UNIVERSIDAD COMPLUTENSE DE MADRID

FACULTAD DE CIENCIAS GEOLÓGICAS

Departamento de Petrología y Geoquímica

TESIS DOCTORAL

The Eclogitic Gneisses of the Cabo Ortegal Complex: provenance and tectonothermal evolution (zircon U-Pb/ Lu-Hf methods)

MEMORIA PARA OPTAR AL GRADO DE DOCTOR

PRESENTADA POR

Richard Albert Roper

Directores

Ricardo Arenas Martín
Sonia Sánchez Martínez
Axel Gerdes

Madrid, 2016

The Eclogitic Gneisses of the Cabo Ortegal Complex:

Provenance and tectonothermal evolution (zircon U-Pb/Lu-Hf methods)

PhD Thesis

Richard Albert Roper

UNIVERSIDAD COMPLUTENSE DE MADRID
FACULTAD DE CIENCIAS GEOLÓGICAS
Departamento de Petrología y Geoquímica

Madrid, 2015

UNIVERSIDAD COMPLUTENSE DE MADRID
FACULTAD DE CIENCIAS GEOLÓGICAS
INSTITUTO DE GEOCIENCIAS
Departamento de Petrología y Geoquímica

PhD Thesis

The Eclogitic Gneisses of the Cabo Ortegal Complex: Provenance and tectonothermal evolution (zircon U-Pb/Lu-Hf methods)

Los Gneises Eclogíticos del Complejo de Cabo Ortegal: Procedencia y evolución tectonotermal (métodos U-Pb/Lu-Hf en circón)

Dissertation submitted for the degree of Doctor of Philosophy in

Geological Sciences

Richard Albert Roper

Supervisors:
Dr. Ricardo Arenas Martín
Dr. Axel Gerdes
Dr. Sonia Sánchez Martínez

Madrid, 2015

UNIVERSIDAD COMPLUTENSE DE MADRID
FACULTAD DE CIENCIAS GEOLÓGICAS
INSTITUTO DE GEOCIENCIAS
Departamento de Petrología y Geoquímica

Tesis Doctoral

The Eclogitic Gneisses of the Cabo Ortegal Complex: Provenance and tectonothermal evolution (zircon U-Pb/Lu-Hf methods)

Los Gneises Eclogíticos del Complejo de Cabo Ortegal: Procedencia y evolución tectonotermal (métodos U-Pb/Lu-Hf en circón)

Disertación presentada para optar al grado de Doctor en

Ciencias Geológicas

Richard Albert Roper

Supervisores:
Dr. Ricardo Arenas Martín
Dr. Axel Gerdes
Dra. Sonia Sánchez Martínez

Madrid, 2015

UNIVERSIDAD COMPLUTENSE DE MADRID
FACULTAD DE CIENCIAS GEOLÓGICAS
INSTITUTO DE GEOCIENCIAS
Departamento de Petrología y Geoquímica

Tesis Doctoral

The Eclogitic Gneisses of the Cabo Ortegal Complex: Provenance and tectonothermal evolution (zircon U-Pb/Lu-Hf methods)

Los Gneises Eclogíticos del Complejo de Cabo Ortegal: Procedencia y evolución tectonotermal (métodos U-Pb/Lu-Hf en circón)

Disertación presentada para optar al grado de Doctor en

Ciencias Geológicas

Richard Albert Roper

Madrid, 2015

Dr. Ricardo Arenas

Dr. Axel Gerdes

Dra. Sonia Sánchez Martínez

To everyone I love

A aquellos que amo

Acknowledgements

La tesis doctoral que aquí presento ha sido fruto de un intenso y largo trabajo, que ha llegado a buen puerto gracias a varias personas que me han apoyado en estos años. En los siguientes párrafos quiero agradecer de manera muy especial a aquéllas personas sin las cuales esta tesis no habría sido la misma, e incluso, no habría sido.

En primer lugar quiero agradecer a mi principal supervisor, Ricardo Arenas. Desde el primer momento apostaste por mí, incluso antes de empezar el máster. No sólo quiero agradecerte que hayas sido un buen director (que no es poco, viendo el panorama), sino que has ido más allá. Además de tomarte muy en serio tu labor de supervisor y de maestro, me has tratado como a un igual, sin palabras fuera de lugar ni de tono, con paciencia, dando ánimos cuando los necesité y abriéndome todas las puertas que pudiste. Mi vida pudo seguir otros muchos derroteros, pero al final estoy escribiendo éstas palabras porque pude seguir el camino que yo quería seguir, el de la ciencia, y te lo agradezco sobre todo a ti Ricardo. Gracias.

I also want to thank another one of my supervisors, Axel Gerdes. From the first moment, you accepted me, you gave me access to the Institut and to the lab and you taught me many things. Thanks to you this PhD is what it is, and has the strength it has. But not only that, you had time for me. And this is not a minor thing, I´m totally aware of it. Thanks for everything you´ve done and thanks for doing more than you "should".

Y además quiero agradecer a mi supervisora Sonia Sánchez Martínez. Gracias por estar siempre disponible para cualquier pregunta que tuviese, por tu disposición a ayudarme y guiarme y por aquellas campañas de campo. Gracias.

Agradezco a todos los miembros del grupo de investigación por el día a día, el trato amigable, y su disposición, al Departamento de Petrología y Geoquímica por acogerme y facilitarme los medios materiales necesarios, con una mención especial a Isabel, Beatriz y Miguel Ángel, a la Facultad de Ciencias Geológicas por formarme (y a Lidia y Wyo por hacer que funcione), y a UCM por concederme la beca predoctoral.

Quiero agradecer al personal del taller de Petrología y Geoquímica, a Marián, Carmen y Pedro, por el excelente trato recibido, por enseñarme todo lo relacionado con la preparación de muestras y de láminas delgadas y por preparar diligentemente aquellas muestras urgentes que en su momento necesité. También agradecer al CAI de Geocronología y Geoquímica Isotópica, a Carmen Galindo, a Chema y a José Antonio. Durante la larga temporada que pasé en el laboratorio aprendí multitud de cosas, preparación de muestras, titraciones, técnicas cromatográficas, análisis con los espectrómetros y un largo etcétera, en el que por supuesto incluyo las técnicas de exhaustiva limpieza. Gracias.

I´m also thankful to all the people I met in Frankfurt, especially to Gerhard Brey for allowing me to work in the Institut, and to Heidi, Wolf and Armin and also to Linda and Zehra for all those very nice moments we spent together. Thanks.

Agradezco a los revisores anónimos de la tesis doctoral y a los revisores internacionales (Gerhard Brey, Ulf Linnemann y Francisco Pereira) por sus excelentes informes. También quiero agradecer a los revisores de los artículos que se presentan en ésta tesis doctoral, que aumentaron considerablemente la calidad de éstos con sus comentarios y apreciaciones.

Agradecer a mi toda mi familia pues sin ellos dudo que hubiese llegado hasta éste punto. Gracias papá, por todo... por contribuir a ser quien soy y sobre todo por aguantar. Thanks mum, you´ve done more than you possibly could, I can´t find the right words to say how much I love you. And to you Tom Tom the drum, where ever you are, we still got a guinness pending... A mis hermanos, Jordan y

Bárbara, por estar siempre al pie del cañón, a Moisés, a Marta, a mis tíos y primos... y por supuesto a mi tío-abuelo Luis. Sin tu ayuda y apoyo incondicionales tanto a mí como a mi familia esta tesis habría sido un sueño inalcanzable.

A mi entorno social, a los Colegas, sobre todo a los geomongers, los miners, al Garrote, y a los geolokos. Y por supuesto a vosotras dos, por vuestra gran amistad, por todo lo vivido y por vivir, por quien sois... y a ti gruñón... ;)

Y por último a ti Sandra. Por corresponderme, por entretejer tu vida con la mía durante este tiempo, por aguantar al grunchón que se mostró al final de la tesis, por ser quien eres... gracias apa... muak!

Index

Abstract

The Variscan belt was formed when several continents interacted to finally form the supercontinent of Pangea. In this general context of continent interaction and orogen development this PhD was projected and is presented in this document. The main objective of this thesis is to explore the origin, the sources and the development of a high-grade metamorphic terrane involved in this orogenesis. This PhD focuses on the Eclogitic Gneisses (Banded Gneisses), which are included in the high-pressure and high-temperature (HP–HT) member of the Upper Allochthon of the Cabo Ortegal Complex (NW Iberia), and also deals with the Eclogite band and the Cariño Gneisses, so that the general tectonothermal evolution is better accounted for.

To address the objectives of this thesis, several methods have been applied. The first group of methods had the aim of recognising and describing the subject of study, from a macroscopic point of view (cartography and detailed representation of geological sections) to a microscopic level (thin section observation and description). When this recognition was carried out and the scientific literature was handled, detailed isotopic experiments were performed. U–Pb, Lu–Hf and Sm–Nd radiogenic methods were applied to make provenance approaches of the detrital materials, to constrain the age of rock formation, the primary sources of magmatic generation and the age and features of the high-grade metamorphic development of the igneous rocks of the studied units.

This PhD document has been organised in an article format, where the majority of the results are presented as articles, from which the PhD candidate is the corresponding author or co-author. This thesis starts with a general introduction and with an exposure of the main objectives posed and methods applied. Afterwards, a general review of the origin and evolution of the NW Iberian terranes, and a detailed study from a macroscopic to a microscopic point of view of the main formation studied, together with a discussion of its tectonothermal evolution and an exhumation modelling is presented. Then, a provenance approach together with a paleogeographic reconstruction proposal, studying the detrital materials of the intermediate-pressure top member of the Upper Allochthon is shown. These provenance studies were also applied to the HP–HT Banded Gneiss formation, mainly to find out which continental fragment subducted in the Devonian. After this work, isotope geochemistry techniques were applied to several igneous rocks that registered the evolution of a long-lived magmatic arc and the deformations attained by the HP–HT subduction-related metamorphic event. Afterwards, a discussion integrating this subduction event in the general framework of the assembly of Pangea is presented. Finally, this PhD finishes exposing an integrated discussion and the general conclusions achieved.

The main conclusions derived from this PhD thesis are that the Upper Allochthon is a single terrane and not a composite one, from which its metasedimentary rocks are derived from the Gondwana mainland, specifically from the West African Craton (WAC). The detritus that constitute the metasedimentary rocks were deposited in a back-arc type basin between *c.* 521–506 Ma. These sediments register the crustal growth events of the WAC and the formation of a volcanic arc system that is considered to be the Cadomian arc. The initial activity of this arc is constrained between *c.* 780 Ma and *c.* 590 Ma, defining the "proto-arc stage", where mainly crustal recycling of the margin of Gondwana where it was built, took place. The "arc-stage" was developed between *c.* 590 and 490 Ma where broad mixing processes took place between the intruding depleted mantle (DM) derived magmas and the old pre-existing crust. The igneous rocks registered part of the magmatic arc activity (D0 event). The first record of acidic magma intrusion has an age of *c.* 512 Ma and has diverse source signatures. It seems that around *c.* 498 Ma an arc-related high-temperature input gave as a result fractional crystallisation of acidic rocks from DM-derived partial melts. The basic magmas started to intrude at *c.* 505 Ma and had different sources, from magmas almost directly derived from the partial melting of the depleted mantle, to isotopically enriched magmas, which could derive from the partial fusion of an

enriched mantle component (probably the subcontinental mantle of Gondwana) and as an important contamination of DM-derived melts with continental crust material, respectively. The metasedimentary rocks were partially melted at around 485–495 Ma. After the magmatic activity finished, the Upper Allochthon did not drift away opening the Rheic Ocean, as it has been proposed by other authors for the Avalonian terranes, but formed part of the extended passive margin of Gondwana until the Devonian. The high-grade metamorphism attained by the Upper Allochthon was driven by the subduction of the margin of Gondwana under the colliding retro-continent. Taking into account the paleogeographic reconstructions proposed by other authors for the Devonian, this retro-continent should be Laurrusia, but it is likely to be another continental fragment of Gondwana. In the context of this high-grade metamorphic event (D1 event) zircon recrystallised at *c.* 395 Ma in the acidic rocks. The basic rocks were transformed into eclogites, which was recorded by a zircon recrystallisation climax at *c.* 393 Ma, most probably near the metamorphic P–T path temperature peak. The high-grade metamorphic event re-melted the leucosomes at high-T conditions between 379 and 403 Ma, with a climax at *c.* 388 Ma. During this subduction event the Upper Allochthon was exhumed as an ultra-HP buoyant plume (D2 event). The progression of the deformational history of the upper units entails the development of large recumbent folds and an important basal thrust (D3 structures). The mentioned subduction event was the first one attained by the margin of Gondwana in the complex history of the early stages of supercontinent assembly.

Resumen

El cinturón Varisco se formó cuando varios continentes interactuaron para acabar formando el supercontinente de Pangea. La tesis que aquí se presenta se enmarca en este contexto general de interacción continental y desarrollo orogénico. El principal objetivo es explorar la formación, las fuentes y el desarrollo de un terreno metamórfico de alto grado involucrado en la orogénesis Varisca. En esta tesis se hace especial hincapié en los Gneises Eclogíticos (Gneises Bandeados), los cuales están incluidos en el miembro de alta presión y alta temperatura (*HP–HT*) del Alóctono Superior del Complejo de Cabo Ortegal (NO de Iberia). También se aborda el estudio de otros miembros del Alóctono Superior, como la banda principal de eclogitas y los Gneises de Cariño, con el fin de tener más herramientas para abordar la evolución tectonotermal general.

Para cumplir con los objetivos de esta tesis se han aplicado varios métodos. El primer grupo de métodos tenían por objetivo reconocer y describir el objeto de estudio, desde un punto de vista macroscópico (cartografía y representación detallada de secciones geológicas) hasta un punto de vista microscópico (observación y descripción de láminas delgadas). Una vez terminado el reconocimiento de las diferentes litologías y de la revisión bibliográfica pertinente, se llevaron a cabo determinaciones isotópicas detalladas. Se aplicaron métodos isotópicos U–Pb, Lu–Hf y Sm–Nd en las formaciones estudiadas para conocer las áreas fuente de los materiales detríticos, las edades de cristalización, las fuentes ígneas primigenias y la edad y las condiciones del metamorfismo de alto grado desarrollado en las rocas ígneas estudiadas.

Esta tesis doctoral ha sido organizada en formato de artículos, en los cuales se han presentado la mayoría de los resultados obtenidos y en los que el doctorando es autor o coautor. Este documento comienza con una introducción general y con la exposición de los principales objetivos y métodos aplicados. A continuación se presenta una revisión general sobre el origen y evolución de los terrenos del NO de Iberia y un estudio detallado desde un punto de vista macro- y microscópico de los Gneises Eclogíticos, junto con una discusión de su evolución tectonotermal y su mecanismo de exhumación. Después se muestra un estudio de procedencia y una propuesta de reconstrucción paleogeográfica de los materiales detríticos del miembro culminante de presión intermedia (*IP*) del Alóctono Superior. Estos estudios también se han realizado en la formación de los Gneises Eclogíticos, para conocer, principalmente, la identidad del fragmento continental que subdujo en el Devónico. Posteriormente se aplicaron técnicas de geoquímica isotópica en varias rocas ígneas que registraron la evolución de un arco magmático longevo y de las deformaciones inducidas por el evento metamórfico subductivo de *HP–HT*. Seguidamente se expone una discusión que integra este evento subductivo en el contexto general del ensamblaje de Pangea. Finalmente, esta tesis doctoral concluye con una discusión integradora y con una síntesis de las conclusiones generales obtenidas.

Las principales conclusiones derivadas de esta tesis doctoral son que el Alóctono Superior no es un terreno compuesto sino uno simple, cuyas rocas detríticas provienen del continente Gondwana, concretamente del Cratón de África Occidental (*WAC*). Los detritos de las rocas metasedimentarias se depositaron en una cuenca de retro arco en torno a *c.* 521–506 Ma. Estos sedimentos registran los eventos de crecimiento cortical del *WAC*, y la formación de un sistema de arcos volcánicos, el cual se considera ser el arco Cadomiense. La actividad inicial de este arco, llamada "fase de proto-arco", tuvo lugar entre *c.* 780 y *c.* 590 Ma, donde principalmente tuvo lugar un reciclado cortical del margen continental de Gondwana. La "fase de arco" se extendió entre *c.* 590 y *c.* 490 Ma, y en ella se produjeron intensos procesos de mezcla entre magmas derivados del manto empobrecido (*DM*) y la corteza continental antigua. Las rocas ígneas registraron parte de la actividad del arco (evento D0). El primer registro de la intrusión de rocas ácidas, que muestra una diversidad de fuentes, es de *c.* 512 Ma. Los datos apuntan a que en torno a *c.* 498 Ma un alto aporte térmico relacionado con la actividad del arco dio lugar a la cristalización fraccionada de rocas ácidas a partir de fundidos parciales

derivados del manto empobrecido. Los magmas básicos, que empezaron a intruir hacia *c.* 505 Ma, tienen diferentes fuentes, desde magmas derivados principalmente de la fusión parcial del manto empobrecido, hasta magmas isotópicamente enriquecidos, probablemente derivados de la fusión parcial de un componente mantélico enriquecido (seguramente el manto subcontinental de Gondwana) y de la contaminación de fundidos derivados del *DM* con materiales de la corteza continental. Las rocas metasedimentarias fundieron parcialmente en torno a *c.* 485–495 Ma. A diferencia de lo esperado, cuando la actividad magmática del arco cesó, la migración del Alóctono Superior no dejó tras de sí un extenso océano, como parece que sí lo hicieron (según otros autores) los terrenos avalonianos, que en su deriva continental dejaron paso a la apertura del Océano Rhéico. El Alóctono Superior formó parte del margen pasivo y extendido de Gondwana hasta el Devónico. El metamorfismo de alto grado que registra este terreno se produjo por la subducción del margen de Gondwana bajo un retro continente. Teniendo en cuenta las reconstrucciones paleogeográficas de otros autores para el Devónico, este retro continente debió de ser Laurrusia, pero es probable que sea otro fragmento continental de Gondwana. En el contexto de este evento metamórfico de alto grado (evento D1) el circón de las rocas ácidas recristalizó a *c.* 395 Ma. Las rocas básicas fueron transformadas en eclogitas mostrando un clímax de recristalización de circón en torno a *c.* 393 Ma, probablemente cerca del pico térmico de la trayectoria metamórfica P–T. El metamorfismo de alto grado volvió a fundir los leucosomas en condiciones de alta temperatura entre 379 y 403 Ma, con un clímax a *c.* 388 Ma. Durante esta subducción el Alóctono Superior fue exhumado como una pluma de ultra alta presión (evento D2). La progresión de la historia deformativa de las unidades superiores condujo al desarrollo de enormes pliegues recumbentes y de un gran cabalgamiento basal (estructuras D3). Este evento de subducción fue el primero que sufrió el margen de Gondwana en la compleja historia de los estadios iniciales del ensamblado supercontinental.

I

Introduction

1.1. Introduction to the PhD Thesis

This PhD thesis explores the generation, the sources and the development of a high-grade metamorphic terrain involved in the Variscan orogen, the mountain belt formed when the last supercontinent, Pangea, assembled. When continents are pieced together to form supercontinents, the oceanic crusts that separate them are consumed by subduction, a process capable of forming extensive volcanic arc systems. When the continents finally collide, their margins are subducted to great depths and mountain belts are developed, favouring a scenario where extreme deformations and high or even ultra-high grade metamorphism can take place. The studied terrain attained very high deformation when the margins of the continents started to interact at the initial stages of their assembly, as well as during the intense decompression attained when the terrain exhumed after pronounced continental subduction.

High-grade terrains contain very valuable information about the history of the orogen in which they were formed, because they register several processes around the cores of the belt itself. But on the other hand, this information is cryptic and difficult to decipher because each process blurs the information recorded

by the previous one, and the high intensity of deformation tangles up structures, compositions and any other primary features.

The high-grade studied terrain is a member of the Cabo Ortegal Complex, which is one of many complexes scattered along the European continent. These complexes include the remnants of the deepest sectors of the mountain chain that sutured Pangea. They are huge nappe piles formed and stacked during the orogen development, disposed as big synformal structures. They can be followed through the NW and SW Iberian Massif, the Armorican, Central, Vosges and Maures Massifs and Corsica in France, the Bohemian Massif in Germany, Poland, Czech Republic and Austria, and the Alps and Sardinia in Italy.

Many theses and investigations have been performed in the last decades, giving a high degree of knowledge of the different units and members of the Cabo Ortegal Complex. From the basis of all this information, new studies with modern techniques are required to clarify and better understand the ages of protolith rock formation, the igneous sources and the detrital provenance of the different units involved in the complex history of these old Variscan remnants. For these reasons the present PhD was planned.

The Cabo Ortegal Complex is one of the five complexes of NW Iberia. Two high-grade terrains are found in this complex, the Basal allochthonous units and the Upper Allochthon, which are separated by an ophiolite belt. The Upper Allochthon terrane is formed by an intermediate-pressure (IP) top member and a high-pressure and high-temperature (HP–HT) bottom member, some of the formations of which are the ones studied in this PhD. The main formation studied is the Banded Gneisses, which is a highly deformed metasedimentary rock terrain with many lithologies included, and from which no previous theses have been done. To better understand the complex evolution of this formation and to englobe it in its general context, its two outlining formations have also been investigated. They are the Cariño Gneisses to the East and the Eclogite band to the West, and both have been studied in previous PhD theses.

In this thesis, different methods have been applied in order to constrain the origin and evolution of the studied terrains. At first, a review article is presented synthesising the geology of the allochthonous terranes of Galicia (NW Iberia). This work is the first article presented, which has been recently submitted (chapter 3), and represents a good introduction to the framework of the issues addressed in the following chapters. The first methods to be used had the objective of recognising the objects to be studied, using cartographic and petrographic techniques. The results derived from applying these methods are presented mainly in chapter 4. Afterwards, and with the objective of knowing which are the source areas of the detrital components of the IP top member of the Upper Allochthon (represented by the Cariño Gneisses), several U–Pb, Lu–Hf and Sm–Nd isotopic experiments were carried out. The results and interpretations derived from this work are presented in chapter 5. These experiments were also carried out on the HP–HT member of the Upper Allochthon, to decipher which continental margin subducted and therefore to make paleogeographic reconstructions of the initial stages of continent interaction of the Variscan orogenesis. These experiments are described and discussed in chapter 6. After having constrained the detrital nature of these rocks, isotopic experiments were carried out on the igneous rocks within two key formations of the HP–HT Upper Allochthon, the Eclogite Band and Banded Gneiss formations. The igneous rocks studied are; several leucosomes, to study the features concerning partial melting and regional foliation development of the high-grade metasedimentary rocks; eclogites, to study the nature of the mafic magmatic evolution and the eclogite facies metamorphism attained; and orthogneisses, to constrain the felsic activity of an important magmatic arc system developed in the initial stages of the Variscan orogen. All this information is shown in chapter 7. To discuss the complex collision between the two main continents involved in the assembly of Pangea, chapter 8 was drawn up, and an integrated discussion of the PhD thesis is presented in chapter 9.

1.2. Article summary

Articles included in this PhD thesis:

Article 1:

Arenas, R., Sánchez Martínez, S., Díez Fernández, R., Gerdes, A., Abati, J., Fernández-Suárez, J., Andonaegui, P., González Cuadra, P., López Carmona, A., Albert, R., Fuenlabrada, J. M., Rubio Pascual, F. J. (2015). Allochthonous terranes involved in the Variscan suture of Galicia (NW Iberia): A review of their origin and tectonothermal evolution.

Article status: **Submitted.**

This article is presented in chapter 3.

Article 2:

Albert, R., Arenas, R., Sánchez Martínez, S., Gerdes, A. (2012). The eclogite facies gneisses of the Cabo Ortegal Complex (NW Iberian Massif): Tectonothermal evolution and exhumation model. *Journal of Iberian Geology* **38(2)**, 389-406.

Article status: **Published.**

This article is presented in chapter 4.

Article 3:

Albert, R., Arenas, R., Gerdes, A., Sánchez Martínez, S., Fernández-Suárez, J., Fuenlabrada, J. M. (2014). Provenance of the Variscan Upper Allochthon (Cabo Ortegal Complex, NW Iberian Massif). *Gondwana Research* **28(4)**, 1434-1448.

Article status: **Published.**

This article is presented in chapter 5.

Article 4:

Albert, R., Arenas, R., Gerdes, A., Sánchez Martínez, S., Marko, L. (2015). Provenance of the HP–HT subducted margin in the Variscan belt (Cabo Ortegal Complex, NW Iberian Massif). *Journal of Metamorphic Geology* **33(9)**, 959-979.

Article status: **Published.**

This article is presented in chapter 6.

Article 5:

Arenas, R., Díez Fernández, R., Sánchez Martínez, S., Gerdes, A., Fernández-Suárez, J., Albert, R. (2014). Two-stage collision: Exploring the birth of Pangea in the Variscan terranes. *Gondwana Research* **25(2)**, 756-763.

Article status: **Published.**

This article is presented in chapter 8.

II

Objectives and methodology

The first step was to know the characteristics of the subject to be studied. To do so a description of the field aspects of the Banded Gneiss formation was carried out, revising the details of its cartography, the characteristics of the different types of lithologies that form part of it, and its distinctive internal structural features. This preliminary approach to the studied object was also applied to the formations that outline the Banded Gneisses, which are the Eclogite Band formation to the West and the Cariño Gneiss formation to the East. This initial approach is fundamental to deal with further investigations.

The next step was to have a better idea of the studied objects, through the microscopic features of the lithologies involved in the Banded Gneisses (and also the Eclogite Band and the Cariño Gneisses). To do so petrographic features were described studying thin-sections of the selected rock specimens. The first set of thin-sections was prepared by the author to focus on the formative aspect of the thesis. These observations allowed to clarify the different deformative fabrics and the temporal evolution of the mineral assemblages. Some microprobe analyses were performed to accurately identify some elusive-classifying minerals.

The knowledge gathered from these studies led to the preparation and the publication of the second article included in this PhD thesis. This paper had a very important role in allowing the author to achieve the necessary abilities to publish scientific results to the scientific community. These results are presented in chapter 4.

After having a good idea of the subject of study through the above-mentioned techniques, the best samples were taken to perform radiogenic isotope geochronology on zircon crystals. At first, it was necessary to separate the zircon grains with several mineral separation techniques. These separations were run by the PhD candidate with the initial supervision and guidance of his PhD supervisors and laboratory technicians. These separation techniques were applied with great care to minimize possible laboratory contamination. Samples were cleaned and dried before being crushed in a jaw crusher and afterwards in a tungsten disc mill. The light fraction was removed by floatability using a Wilfley table, and a Franz model magnetic separator was used, to remove those minerals susceptible to a magnetic field induced by an electric current up to 1.7 A. Minerals with a density below 3325 $kg \cdot m^{-3}$ were removed using CH_2I_2 (diiodomethane) heavy liquid, using pertinent lab equipment due to the toxicity and the difficulty of working with this liquid. These separations were performed at the Complutense University of Madrid. The following techniques were performed at the J.W. Goethe Universität of Frankfurt am Main. Zircon hand picking of all types of zircons was carried out under a binocular microscope before mounting them, depending on their size, in epoxy resin. These mounts were polished to approximately half of the zircon crystal thicknesses. Then the mounts were introduced into a JSM 6490 scanning electron microscope (SEM) to perform cathodoluminiscence (CL) and back-scattered electron (BSE) images to study the internal zoning of the zircon grains in order to choose the best areas for isotope analysis. Isotopic measurements were taken for U–Pb and Lu–Hf isotopes. Both types of measurements were performed with the laser ablation technique. The laser used in both cases was a RESOlution M–50, with 193 nm wavelength ArF excimer (COMpexPro) laser, which provided a maximum space resolution of 23 μm laser spot diameters. The zircon was ablated within a low volume cell in a He stream, which was mixed directly after the ablation cell with N_2 and Ar, before being introduced into an Ar plasma attached to the mass spectrometers. This plasma device ionized the ablated zircon so that the spectrometers could measure the different masses. In the case of U–Pb isotope measurements the mass spectrometer (MS) used was ThermoFinnigan Element 2 sector field MS and for Lu–Hf isotopes the spectrometer used was a ThermoFinnigan Neptune multicollector MS. During the entire PhD project the total amount of U–Pb analyses was around 2600 and the amount of Lu–Hf analyses was around 1400 (in both cases excluding standard analyses). The analytical sequences where sites of ablation and other variables were defined, were programed and performed by the PhD candidate with the supervisors guidance.

Other isotopic experiments applied to the studied rocks were the Nd whole-rock determinations. Sm–Nd geochemistry allowed a theoretical approach to provenance, model ages and a "track of the juvenility" of the different lithologies investigated at a hand-specimen scale. These determinations were performed at the geochronology laboratory (CAI) of the Complutense University of Madrid, and involved several laboratory skill developments. The technique used required clean lab conditions for sample dissolution with ultra-pure acids and conventional ion-exchange chromatography procedures. Rare earth element concentrates were loaded on rhenium filaments onto the sample load system of the thermal ionization mass spectrometer (TIMS-Phoenix HCT040®). A number of 36 Sm–Nd whole-rock determinations were taken during the PhD thesis.

Data processing of the isotopic determinations constituted an important part of the PhD project and careful attention was taken on the calculations involved, such as data reduction, interference corrections, decay equation application, standard deviation corrections, error determinations and so on.

All this work, involving isotope geochemistry, led to the publication of two articles which are presented in chapters 5 and 6. These chapters deal with the main lithology of the Banded Gneiss

formation, the metasedimentary rocks.

The above-mentioned techniques were also applied to several igneous lithologies which are presented in chapter 7. Several leucosomes, eclogites and orthogneisses were studied, building a solid base to monetarise the igneous activity of a magmatic arc. The intention is, to publish these results after the actual PhD thesis is defended. The author has also collaborated in the preparation of two articles, which are presented in this thesis to show the geological context of the studied units (chapter 3) and the implication of these units in the assembly of Pangea (chapter 8).

Another objective was to learn and to be able to communicate ideas and results to the scientific community. To achieve this objective the author performed several congress communications, with posters, and also with oral communications. Some of the meetings were the DEFMET congress (Interrelationship between deformation and metamorphism, held in Granada in 2011), the GEOPilsen conference (held in the Czech Republic in 2013), Gondwana15 meeting (held in Madrid in 2014), GeoFrackfurt2014 (held in Germany in 2014) and a meeting of the Spanish Geological Society (SGE, held in Morocco in 2015).

III

Allochthonous terranes involved in the Variscan suture of Galicia: A review of their origin and tectonothermal evolution

3.1. Introduction

The article presented in this chapter represents the geological framework in which the rest of the thesis is englobed. It is an up to date review of the already published knowledge about the origin and the evolution of the terranes from the allochthonous complexes of Galicia. One of these terranes is the Upper Allochthon (Upper Units), in which the formations studied in this thesis are included.

3.2. Partial conclusions

As this chapter is a review and intends to be the geological framework for this PhD thesis there are no *s.s.* conclusions to mention. Even so a synthesis of the major aspects of the geology concerning the Upper Units of the Cabo Ortegal Complex is presented here on.

The Upper Units (also called Upper Allochthon) represent the thickest terrane of the allochthonous complexes and they are constituted by a variety of units that can be grouped in two main ensembles according to their tectonothermal evolution: an upper ensemble characterised by intermediate pressure metamorphism (IP Upper Units), and a lower ensemble affected by high pressure and high temperature metamorphism (HP-HT

Upper Units). The Upper Units are considered as a single and coherent terrane because of their systematic position above the Ophiolitic Units. In the first descriptions of the allochthonous complexes these units were assigned to a common tectonic setting and interpreted as sections of a back-arc, a fore-arc, or the magmatic arc itself (Arenas et al., 1986). This interpretation has not changed to this day, as many subsequent works have interpreted the origin of the Upper Units in the context of a peri-Gondwanan magmatic arc. The polymetamorphic nature of this terrane has also been demonstrated, first it was affected by a tectonothermal event related to the activity of the magmatic arc, and then by a collisional tectonothermal event present in the Upper Units, but with different characteristics depending on the intensity of deformation and metamorphism.

Intermediate Pressure Upper Units:

In the Cabo Ortegal Complex, the IP Upper Units are represented by the Cariño Gneiss Unit. It is formed by schists and paragneisses, with compositions ranging from pelitic to greywackic, intruded by small massifs of gabbros and granitoids (Castiñeiras, 2005). The metasedimentary rocks still preserve primary sedimentary features, which indicate deposition in a turbiditic system (Vogel, 1967). A maximum depositional age of c. 510 Ma has been obtained for the Cariño paragneisses using U-Pb dating of detrital zircons, with a clear North African provenance (Albert et al., 2015).

High Pressure and High Temperature Upper Units:

The lower part of the Upper Units consists of a HP-HT metamorphic belt. The protoliths are similar to those described in the IP Upper Units, but the intensity of deformation and metamorphism hinders the preservation of primary sedimentary or igneous features, which in only a few cases can be recognised. The main deformation and metamorphic events are also comparable, regardless of their intensity, as well as the isotopic geochronology obtained for them. The second metamorphic event is the one showing HP-HT characteristics. The tectonic fabrics and mineral assemblages of the first Cambrian, arc-related, metamorphic event were in this case affected by strong reworking, and they have been almost completely obliterated. However, the initial existence of this first event can still be detected, mainly due to the presence of relict monazites in high-grade gneisses whose age has been determined by U-Pb.

Equivalent HP-HT units are known to be present in the Variscan belt outlining the Variscan suture, both in the Armorican Massif, French Massif Central and the Bohemian Massif (Ballèvre et al., 2014). In some sectors the presence of mineral assemblages including coesite suggests that ultra-high-P conditions were reached at least locally (Lardeaux et al., 2001). Peak pressures calculated so far for the NW Iberian Massif are close to ultra-high-P values, although evidence of coesite is still missing.

The diversity and tectonothermal evolution of the HP-HT rocks of the Cabo Ortegal Complex were described in great detail in the pioneering work of Vogel (1967), and later by Engels (1972) and Gil Ibarguchi et al. (1990). In this complex, the HP-HT Upper Units include two main juxtaposed counterparts, the Cedeira and Capelada units. Both units have a similar lithological composition but different record of high-P metamorphism. The Capelada Unit occupies the upper structural level, and developed eclogite facies metamorphism, whereas the Cedeira Unit reached only granulite facies conditions.

The eclogitic gneisses of the Capelada Unit (Banded Gneisses) are mainly derived from semipelitic and greywackic sediments, interspersed with granitic and tonalitic orthogneisses (Albert et al., 2012). These gneisses are usually migmatised and show a mylonitic foliation. Mafic rocks occur as numerous eclogite pods or bands within the gneisses and also form a thick layer of eclogite, separating this ensemble from the mafic and ultramafic rocks underneath. In some sectors of this layer, pre-metamorphic mingling processes are still recognizable, as well as some lenses of *augen*gneiss similar to those observed in the IP Upper Units. The U-Pb dating of detrital zircons from the paragneisses reported similar age populations to those obtained in the Cariño Unit (IP Upper Units). Therefore, it is considered that the source area for this sequence was also located in North Africa (Albert et al., 2015).

Allochthonous terranes involved in the Variscan suture of Galicia (NW Iberia): A review of their origin and tectonothermal evolution

Ricardo Arenas[1], Sonia Sánchez Martínez[1], Rubén Díez Fernández[1], Axel Gerdes[2], Jacobo Abati[1], Javier Fernández-Suárez[1], Pilar Andonaegui[1], Pablo González Cuadra[3], Alicia López Carmona[1], Richard Albert[1], José Manuel Fuenlabrada[4], Francisco J.Rubio Pascual[3]

1-Departamento de Petrología y Geoquímica e Instituto de Geociencias (UCM, CSIC), Universidad Complutense, 28040 Madrid, Spain.
(arenas@geo.ucm.es)
2-Institut für Geowissenschaften, Goethe-University Frankfurt, 60438 Frankfurt am Main, Germany.
3-Instituto Geológico y Minero de España (CSIC), 28760 Madrid, Spain.
4-CAI de Geocronología y Geoquímica Isotópica, Universidad Complutense, 28040 Madrid, Spain.

CONTENT

Extended abstract

NW Iberia includes a rather complete section of a Variscan suture, where different terranes with continental or oceanic affinities appear with clear structural relationships. Three groups of terranes, namely Upper, Ophiolitic and Basal units and a frontal tectonic mélange appear in Galicia, in Cabo Ortegal, Órdenes and Malpica-Tui complexes. They constitute a huge allochthonous pile thrust over the Iberian parautochthonous and autochthonous domains, which represent the section of the Gondwanan margin that escaped continental subduction during the Variscan cycle (Schistose Domain of Galicia-Trás-os-Montes and Central Iberian Zone).

In the Upper Units, *c.* 12000 m of terrigenous sediments (Órdenes Series) intruded by large massifs of Cambrian (*c.* 500 Ma) I-type calc-alkaline granitoids (Corredoiras Orthogneiss) and tholeiitic gabbros (Monte Castelo Gabbro), are considered to represent a section of a magmatic arc built up in the periphery of Gondwana during Neoproterozoic-Cambrian times. Nd model ages from the Cambrian topmost turbiditic series (Ares-Sada greywackes) are relatively young (720-1215 Ma) and suggest proximity to some Avalonian terranes. The uppermost part of this terrane was affected by metamorphism ranging between the greenschist facies and the intermediate pressure granulite facies conditions (IP Upper Units), dated at 496-484 Ma. The IP Upper Units can be considered a relic section preserving the Cambrian tectonothermal activity associated with peri-Gondwanan arc activity. That activity was caused by magmatic underplating and followed by accretion of arc slices, which developed counter-clockwise P-T path evolution. However, the lower part of this terrane shows a completely different tectonothermal record, as it was affected by intense high-P and high-T metamorphism (HP-HT Upper Units; Cedeira and Capelada units in the Cabo Ortegal Complex, Sobrado Unit in the Órdenes Complex). This event developed extensive recrystallization under eclogite and granulite facies conditions, the peak pressures being in the range of ultra-high-P metamorphism (proved minimum pressure at 22 Kb, with some indicators of higher values). The high/ultra-high-P metamorphism (*c.* 400 Ma) was followed by drastic and fast exhumation coeval with partial melting (*c.* 390 Ma). The development of extensional detachments (*c.* 375 Ma), recumbent folds and thrusts drove the exhumation of this high-P complex later on.

True MORB ophiolites derived from typical oceanic lithosphere are unknown in the Variscan suture of Galicia. On the contrary, the mafic-ultramafic sequences preserved in NW Iberia were generated in supra-subduction settings, their mafic rocks showing island-arc tholeiitic composition. There exist two critical oceanic to transitional crust-forming events: a Middle-Late Cambrian phase (*c.* 500 Ma, Lower Ophiolitic Units, Vila de Cruces and Bazar unit), and a Middle Devonian phase (*c.* 395 Ma, Upper Ophiolitic Unit, Careón, Purrido and Moeche units). Both types of mafic units were accreted beneath the Upper Units during Variscan convergence, the Upper Ophiolites first (*c.* 391-377 Ma), and then the Lower Ophiolites (*c.* 367 Ma). Due to their buoyant nature, many Devonian ophiolites escaped from early-Variscan subduction, so they are the most common ophiolites preserved in the Variscan suture across Europe. The mafic-ultramafic sequence of the Bazar Unit has been interpreted as peri-Gondwanan oceanic lithosphere accreted beneath the magmatic arc system at 480 Ma. This unit is the only one in NW Iberia showing low-P granulite facies conditions, which has been linked to mid-ocean ridge subduction under Gondwana and the opening of an asthenospheric window.

The Basal Units consist of a thick sequence of Ediacaran-Early Ordovician terrigenous metasedimentary rocks intruded by Cambrian to Ordovician granitoids (calc-alkaline to peralkaline) and minor mafic igneous rocks. These units are considered to outline the most external part of the Gondwanan paleomargin during the Late Devonian. However, detrital zircon age populations along with (very old) Nd model ages obtained from well-preserved turbiditic series (ranging between 1782 and 2223 Ma) indicate a paleoposition further to the East than the arc-related section preserved in the Upper Units. The Basal Units also represent a continental paleosubduction zone affecting a wide and continuous section of the margin at the onset of the Variscan collision (*c.* 370 Ma). Subduction polarity was to the W (present-day coordinates) and

included right-lateral components. Continental layers were imbricated below previously accreted ophiolites, while a variety of C-type eclogites, blueschists and lawsonite bearing metabasites developed. The Basal Units can be subdivided in two main groups according to their tectonothermal evolution: an upper group with high-P and medium-high-T metamorphism (Agualada and Espasante units); and a lower group with high-P and low-medium-T metamorphism (Ceán, Malpica-Tui, Lamas de Abade, Santiago, Cercio, Lalín and Forcarei units). The upper group is considered the closest section to the overlying mantle wedge during Variscan subduction, whereas the lower group accounts for the cooler sections of the subduction wedge. The arrival of thicker, more buoyant continental crust blocked the subduction, leading to several thrusting events that transported the subduction complex onto the adjacent, inner sections of the margin, represented by the parautochthonous sequences of the Schistose Domain.

The Somozas Mélange is a piece of the Variscan continental subduction channel developed between the section of the Gondwanan margin represented by the Basal Units and their respective overlying mantle wedge. The subducted continental margin was exhumed later on and emplaced over the mélange zone. The mélange appears as a unique element at the easternmost contact between the allochthonous terranes and their relative autochthon. The mélange unit consists of *c.* 500 m of serpentinite showing block-in-matrix texture. The blocks are variable in size and include metasedimentary rocks, volcanics, gabbros, granitoids and high-P rocks. As a major plate boundary, and given the nature and sensitive structural position of this unit, multiple tectonic events have left strong imprint on it.

Continental convergence did not decline after Variscan subduction and early Variscan nappe tectonics. The allochthonous pile and the suture zone were transferred onto the Gondwana mainland, thus triggering the thermal and gravitational collapse of the collisional wedge. The convergence continued during the Pennsylvanian, when the entire allochthonous pile was subjected to heterogeneous reworking in strike-slip systems.

Considering the allochthonous character of the nappe pile and the strong deformation associated to the Variscan collision, there are problems to identify the original tectonic setting of some terranes and thence, it is almost impossible to reconstruct the paleogeographic setting during the Variscan and pre-Variscan times in detail. Key features to perform any evolving model for the Variscan convergence should consider the existence of two different high-P metamorphic events, both of them affecting continental or transitional crustal sections that belonged to the margin of Gondwana. On the other hand, the Ophiolitic Units provide evidence for two stages of generation of oceanic or transitional crust precisely within the paleogeographic domain that separated the two sections recording the high-P events. Previous models developed in NW Iberia suggested that the Upper Units represent a peri-Gondwanan terrane drifted away from the main continent during the opening of the Rheic Ocean. The Lower and Upper Ophiolitic units would be generated respectively during the opening (rifting) and the beginning of the closure (by intraoceanic subduction) of this Paleozoic ocean. In those models, the two high-P metamorphic events would be related first to the accretion of the drifted terrane to the southern margin of Laurussia (Upper Units), and then to the subduction of the thinned Gondwanan margin after complete closure of the Rheic Ocean (Basal Units).

The previous models have important problems to explain the high/ultra-high-P metamorphic event and the exhumation of deeply subducted transitional-type sections. On the other hand, the recently discovered participation of an older continental crust in the generation of some protoliths belonging to both types of ophiolitic units (Purrido, Moeche and Vila de Cruces units), along with their highly depleted Sm-Nd isotopic signature, make difficult their relationship to open wide oceanic domains. A two-stage collisional model affecting a wide Gondwanan platform may explain most of the evidences in NW Iberia. This platform would contain Cambrian back-arc sections with transitional crust (*c.* 500 Ma) filled by siliciclastic material, and also the remnants of a previous Ediacaran-Cambrian magmatic arc. Collision of this platform with the southern margin of Laurussia, in a dextral convergence setting, would have caused imbrication

and subduction of transitional crustal sections to high/ultra-high-P depths (*c.* 400 Ma), followed by exhumation and subsequent generation of ephemeral supra-subduction or pull-apart oceanic basins (*c.* 395 Ma), finally closed during the second event of collision and restarted subduction of the Gondwana margin to the North (*c.* 370 Ma). According to this model the Upper Units of NW Iberia would represent the lower plate to the Rheic Ocean suture.

Introduction

Most of the pre-Alpine basement in central and western Europe is formed by the Variscan Orogen. This belt can be followed from Iberia, across Brittany and the French Massif Central, to the Bohemian Massif, also extending towards the basement of the Alps, Corsica and Sardinia (Fig. 1). The orogen was linear in origin, but it was affected by several late to post-orogenic oroclinal bends that hinder correlations across the belt and the understanding of some critical questions about its origin and evolution through time (Matte, 2001: Martínez Catalán, 2011; Weil *et al.*, 2012). It is flanked by two different low-grade thrust belts, a foreland thrust belt to the South represented by the Cantabrian Zone of the Iberian Massif, and an external thrust belt to the North and West forming the Rhenohercynian and South Portuguese zones (Fig. 1). The external limits of these thrust belts, both to the South and North, define a doubly vergent Variscan orogenic front.

The Variscan Orogen has continuity in eastern North America in the Appalachian-Alleghanian Belt. This long orogen was developed during the main stages of the Pangea assembly which occurred by the collision of two large continents, Gondwana to the South and Laurussia to the North. It is considered that the final assembly of Pangea occurred in Carboniferous and

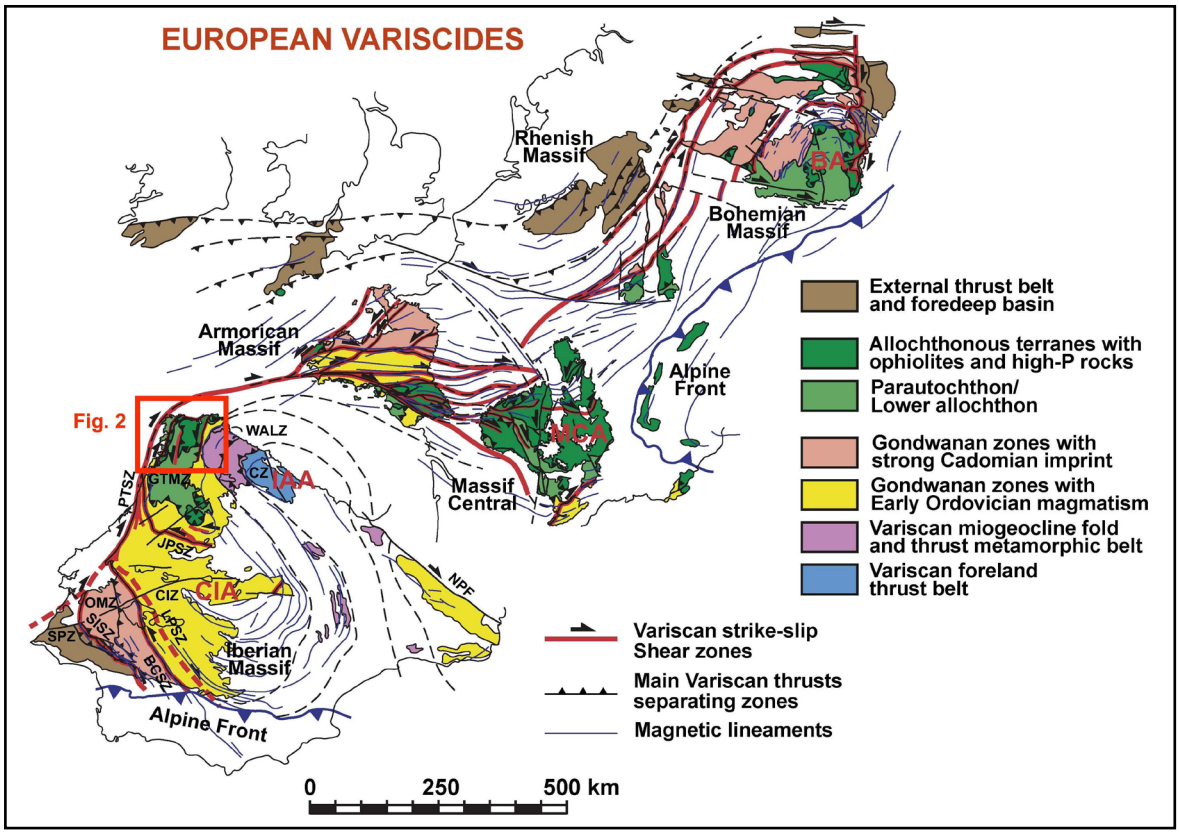

Fig. 1. Terranes and oroclines of the Variscan belt (Martínez Catalán, 2011). Arcs: BA, Bohemian; CIA, Central Iberian; IAA, Ibero-Armorican; MCA, Massif Central. Zones of the Iberian Massif: CIZ, Central Iberian; CZ, Cantabrian; GTMZ, Galicia-Trás-os-Montes; OMZ, Ossa-Morena; SPZ, South Portuguese; WALZ, West Asturian-Leonese. Shear zones and faults: BCSZ, Badajoz-Córdoba; JPSZ, Juzbado-Penalva; LPSZ, Los Pedroches; NPF, North Pyrenean; PTSZ, Porto-Tomar; SISZ, Southern Iberian. Location of the geological map and section presented in Fig. 2 is shown.

Early Permian times, and that the continental collision took place following the closure of the main Paleozoic ocean, the Rheic Ocean. This ocean was generated after Late Cambrian-Early Ordovician times, following the rifting and progressive North drift of Avalonia and other minor peri-Gondwanan terranes (Nance *et al.*, 2010; Stampfli and Borel, 2002; Murphy and Nance, 2008; Murphy *et al.*, 2006).

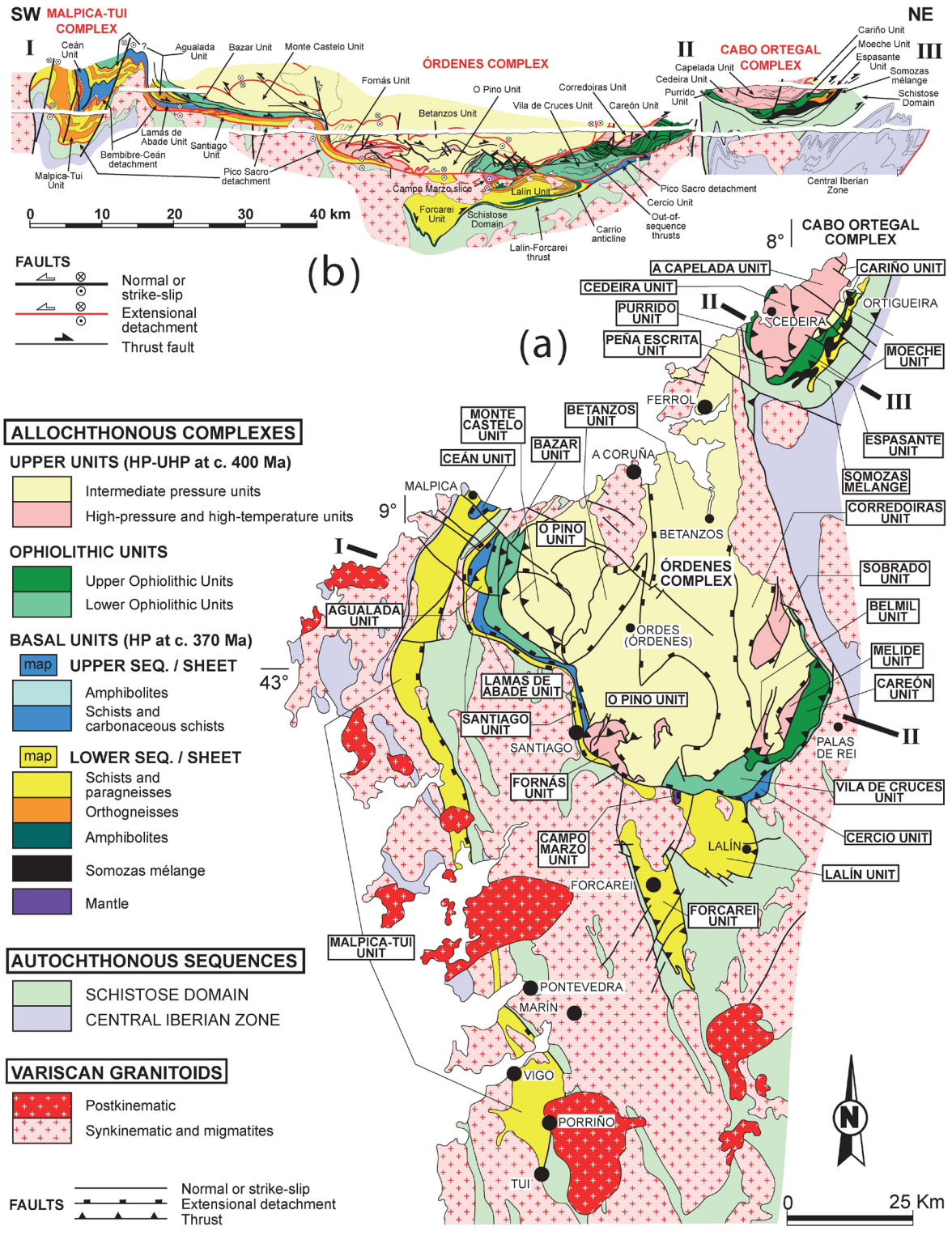

Fig. 2. a Geological map of the allochthonous complexes of the NW Iberian Massif (Galicia region). **b** Composite cross section. The location and name of the most representative units are indicated.

The oldest orogenic events associated with the assembly of Pangea and the distribution of the oceanic domains closed during the collision, can only be deduced from the study of some terranes involved in the Variscan-Appalachian-Alleghanian Orogen. However, the first orogenic stages usually appear strongly overprinted by subsequent events. It is therefore fundamental to identify the terranes and domains where these oldest events can still be recognized. One of the main characteristics of the Variscan Orogen is the presence of a long suture zone outlined by several allochthonous terranes including ophiolites and high-P units (Fig. 1). They preserve the most significant information in relation to the oldest orogenic events and the evolution of the oceanic domains that preceded the collision. Therefore a clear understanding of these terranes is a key issue to increase the knowledge about the characteristics of the initial interaction between Gondwana and Laurussia. On the other hand, the allochthonous terranes also provide information about the Proterozoic and Paleozoic evolution of the continental margins before orogenesis that is valuable for paleogeographic reconstructions.

Different orogenic models have been proposed in the last years for the Variscan Belt, based on the study of the origin and tectonothermal evolution of terranes involved in the orogen (Matte, 1991, 2001; Stampfli *et al.*, 2002; Winchester *et al.*, 2002; Gómez Barreiro *et al.*, 2007; Ballèvre *et al.*, 2009, 2014; Martínez Catalán *et al.*, 2009; Kroner and Romer, 2013; Arenas *et al.*, 2014a). However, an integrated description of the terranes that define the suture zone has not been presented so far. Considering that these terranes are mainly continuous along the whole orogen (Fig. 1), their description for a specific region can be considered as a reference framework that would greatly aid correlations along the Variscan belt. This paper presents an updated and detailed revision of the origin and tectonothermal evolution of the terranes making up the allochthonous complexes of Galicia (NW of the Iberian Massif; Fig. 2). These complexes have been the subject of extensive research in recent decades, with publication of many detailed papers, granting a comprehensive review. The main conclusions reached in this paper can be considered a solid foundation for future progress in the understanding of the Variscan Orogen and, consequently, the assembly of Pangea.

Allochthonous complexes and terranes from Galicia (NW Iberian Massif)

Three allochthonous complexes exist in Galicia in the most internal part of the Variscan Orogen, from East to West the Cabo Ortegal, Órdenes and Malpica-Tui complexes (Fig. 2). These large structures were considered lithological complexes because they contain a stacking of allochthonous units with different origin and contrasted tectonothermal evolution. The Malpica-Tui Complex is included among the allochthonous complexes both for historical reasons, as it was denominated Ancient Complex in the first geological maps of Galicia (Parga Pondal, 1963), and simplicity. However, this complex is different to the others because it is apparently constituted by a single terrane. The three allochthonous complexes show a general synformal structure which has favored their preservation. It is a wide, open, upright synform in the Órdenes Complex, and two narrow upright synforms in the Cabo Ortegal and Malpica-Tui complexes (Fig. 2).

The allochthonous complexes are constituted by a thick stacking of terranes which include ophiolitic units and high-P metamorphic rocks. They are equivalent to other terrane assemblages described in the Variscan Orogen (Fig. 1). These complexes contain the remnants of a Variscan suture, but since this suture is rootless and thrust above an autochthonous-parautochthonous substratum, it is unclear whether it accounts for a primary suture separating large continental landmasses. The complexes were first described as allochthonous structures by Ries and Shackleton (1971), who interpreted them as remnants of a Variscan thrust plate. Some later works proposed an alternative interpretation, according to which the complexes would represent rooted structures related to the activity of a mantle plume developed in an extensional setting (Van Calsteren *et al.*, 1979). However, new research after 1980 has fully confirmed the allochthonous nature of these complexes and their equivalence with residual klippen of a giant nappe pile.

The Parautochthon (also referred to as Schistose Domain) and the allochthonous complexes

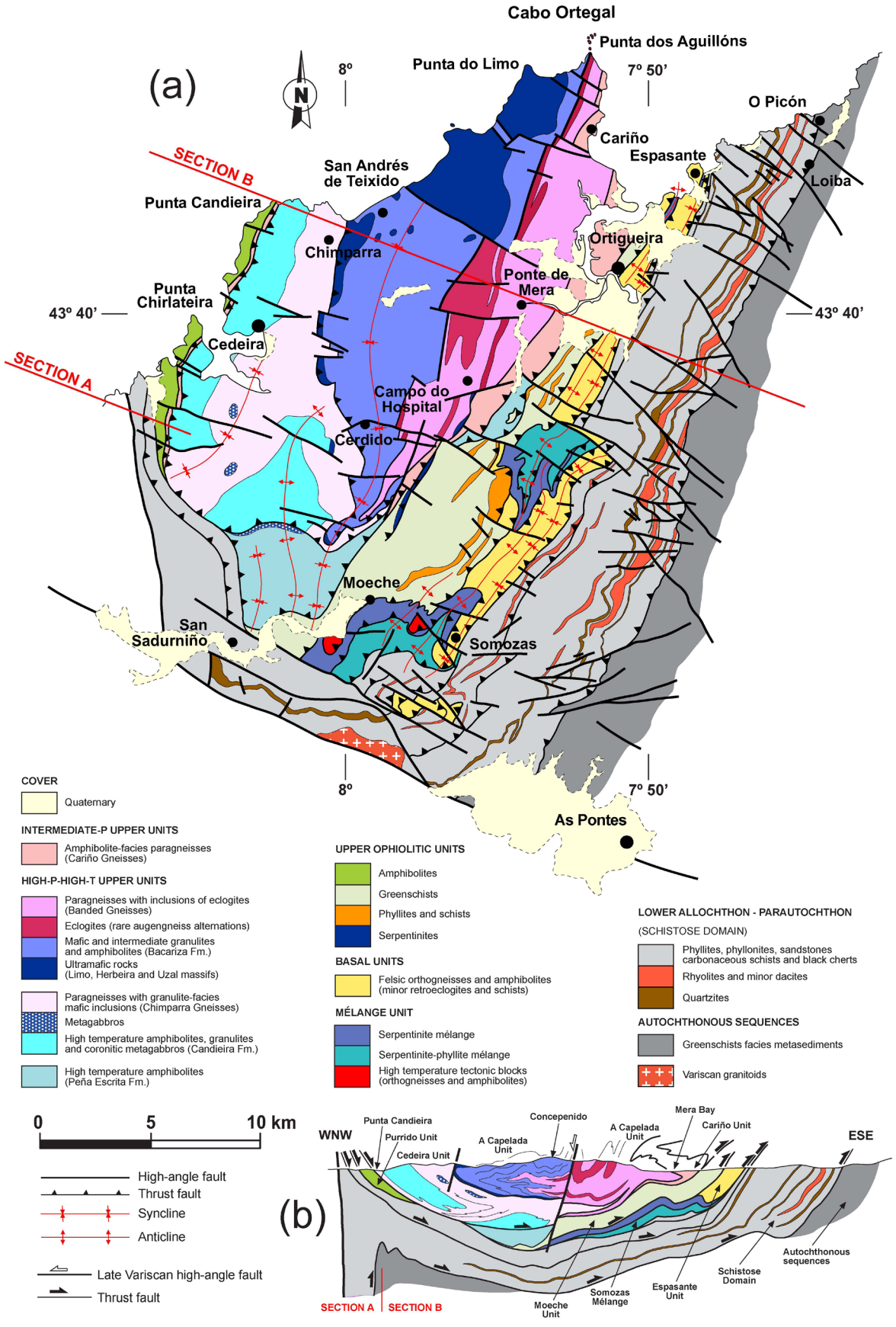

Fig. 3. a Geological map and **b** composite cross section of the Cabo Ortegal Complex. Based in Vogel (1967), Marcos *et al.* (1984), Arenas (1988) and Arenas *et al.* (2014b).

define the Galicia-Trás-os-Montes Zone (Farias *et al.*, 1987), which is emplaced by means of a low-angle thrust over the Central Iberian Zone. This zone and its prolongation towards the foreland across the West Asturian-Leonese Zone and the Cantabrian Zone, represent an autochthonous section of the margin of Gondwana characterized by the presence of thick pre-orogenic sedimentary series ranging in age from the Ediacaran to Devonian, with some magmatic events more abundant around the Cambrian-Ordovician boundary (Pérez–Estaún *et al.*, 1990; Martínez Catalán *et al.*, 1992; Díez Montes, 2007; Rubio Pascual, 2013) (Fig. 1). The Parautochthon consists of pre-orogenic Cambrian to Devonian metasedimentary rock sequences with minor metavolcanic rocks, and younger Late Devonian and Early Carboniferous synorogenic deposits (Farias, 1990; Díez Fernández *et al.*, 2012a and references therein). Stratigraphic, magmatic and faunal similarities between the Parautochthon and the Iberian autochthonous sequences, together with the absence of ophiolites within or at their contact and the lack of evidence for high-P metamorphism, suggest that the two domains were located adjacent to each other, forming part of the same section of the Gondwanan margin. The Iberian autochthonous section and the Parautochthon were variably deformed and metamorphosed during Variscan times, with activity advancing from West to East in present day coordiates. In the Central Iberian Zone, the first deformation and metamorphism was dated at *c.* 359 Ma in the Alcañices Synform using $^{40}Ar/^{39}Ar$ geochronology. Progressively younger ages were obtained in eastern sections of the Central Iberian Zone and in the West Asturian Leonese Zone, with deformation reaching the limit with the Cantabrian Zone at *c.* 321 Ma (Dallmeyer *et al.*, 1997). Both domains were intruded by large massif of synkinematic and postkinematic granitoids.

Terrane typology and correlation

The first studies about the terranes forming part of the allochthonous complexes had a local character, and were focused on the description of the lithological and structural diversity. For a long time the research focused on the description of specific areas of the complexes, without regard to differentiation of the large individual terranes. However, investigating the origin and tectonothermal evolution of the terranes was finally the main objective of later works works. Arenas *et al.* (1986) performed the first correlation and interpretation of the terranes forming part of the allochthonous complexes in Galicia. Such correlation is currently accepted with some simplification and updating, and is based on the distinction of terranes with continental or oceanic nature, the latter represented by several units interpreted as ophiolites. From bottom to top, the terranes included in the Galician allochthonous complexes are named: Basal Units, Ophiolitic Units and Upper Units (Fig. 2). There exists another terrane only present in the leading edge of the large allochthonous pile, and resting below the Basal Units. It is a thick serpentinite mélange, the Somozas Mélange, only described in the eastern part of the Cabo Ortegal Complex (Fig. 2). Both the Basal Units and the Upper Units have a significant proportion of metasedimentary rocks, and they are considered te represent two different terranes with continental affinity. Interpretations regarding the Ophiolitic Units are more complex as recent works have shown they are constituted by oceanic sections with different ages generated in diverse paleogeographic settings.

Further subdivision of the allochthonous terranes is possible considering their age, origin and tectonothermal evolution. The Basal Units include two different lithological successions, a Lower Sequence and an Upper Sequence and two distinct metamorphic groups, a Lower Metamorphic Group (LMG) and an Upper Metamorphic Group (UMG). The Ophiolitic Units are formed by two different groups, the Lower Ophiolitic Units and the Upper Ophiolitic Units. The Upper Units are constituted by a lower set of units affected by high pressure and high temperature metamorphism (HP-HT Upper Units), and an uppermost set characterized by an intermediate pressure tectonothermal evolution (IP Upper Units) (Fig. 2). Moreover, it is also convenient to use the local name of the units in order to perform an accurate description of the terranes. Location of all units described in the allochthonous complexes of Galicia is presented in the synthetic map shown in Fig. 2, and also in the more detailed maps of the Cabo Ortegal (Fig. 3), Órdenes (Fig. 4) and Malpica-Tui (Fig. 5) complexes.

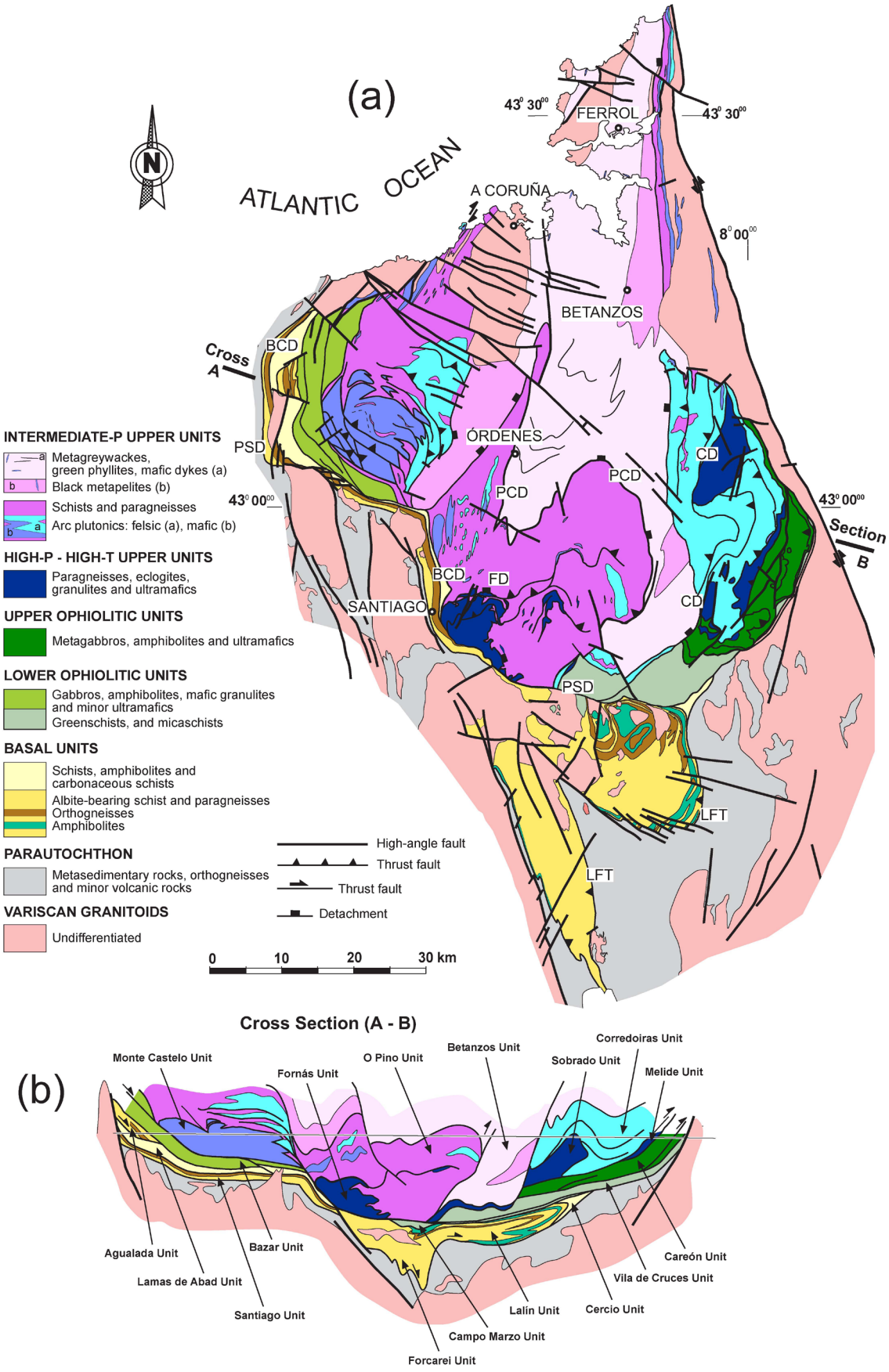

Fig. 4. a Geological map and **b** cross section of the Órdenes Complex. Based on Díaz García (1990), Díaz García *et al.* (2000), Martínez Catalán *et al.* (2002) and Díaz García *et al.* (2010).

The Órdenes Complex

A general map and cross section of the Órdenes Complex, the largest among the allochthonous complexes of the NW Iberian Massif, is shown in Fig. 4. The central part of the complex is occupied by extensive exposures of the Upper Units, which reach a thickness of *c.* 12000 m. The Ponte Carreira Detachment, a shear zone interpreted as an extensional detachment, represents the contact between the Betanzos and O Pino units. The Ponte Carreira Detachment has been dated at *c.* 371 Ma ($^{40}Ar/^{39}Ar$ on muscovite; Gómez Barreiro *et al.*, 2006). Below, the Monte Castelo and Corredoiras units are characterized by higher metamorphic grade. Further down, the HP-HT Upper Units are represented by the Fornás, Belmil, Melide and Sobrado units (Figs. 2 and 4), which are also separated from overlying units by two extensional detachments with intense shearing, the Fornás and Corredoiras detachments (Fig. 4). The Corredoiras Detachment was dated at *c.* 375 Ma ($^{40}Ar/^{39}Ar$ on hornblende; Dallmeyer *et al.*, 1997), while the Fornás Detachment seems older and active until *c.* 382 Ma ($^{40}Ar/^{39}Ar$ on hornblende; Gómez Barreiro *et al.*, 2006).

Under the HP-HT Upper Units, the Upper Ophiolitic Units are represented by the Careón Ophiolite, while the Lower Ophiolitic Units are constituted by the Bazar and Vila de Cruces ophiolites. The relative position of the two groups of ophiolites can be observed SE of the Órdenes Complex, where the Careón and Vila de Cruces ophiolites are in contact. Below the ophiolites, the Basal Units appear as a thick rather continuous set of two juxtaposed sequences with intricate internal structure. They are separated from the rest of the allochthonous units by two extensional detachments, the Bembibre-Ceán and Pico Sacro detachments (Figs. 2 and 4), which probably were active between *c.* 340-317 Ma (Díez Fernández *et al.*, 2012b). The Upper Sequence of the Basal Units is represented by the Lamas de Abade and Cercio units, and the Lower Sequence includes the Santiago, Lalín and Forcarei units (Fig. 4). The Agualada Unit is the structurally counterpart of the Basal Units and is considered part of its Lower Sequence thrust above the Lamas de Abade Unit. The Campo Marzo Unit, formed by *c.* 500 m of ultramafic rocks, is sandwiched between the Basal Units below and the Pico Sacro detachment above (Fig. 4). The lithological constitution and structural position of this unit are key elements for the interpretation of the tectonothermal evolution of the Basal Units, as discussed below.

The contact zone between the Basal Units and the Parautochthon is well exposed at the base of the Lalín and Forcarei units. It is a rather narrow zone characterized by strong ductile shearing interpreted as an important thrust, the Lalín-Forcarei Thrust. This thrust would have transported to the E-SE the thick ensemble formed by the allochthonous complexes over the Parautochthon, and then the whole Galicia-Trás-os-Montes was transferred on top of the Central Iberian Zone following a newly-formed thrust at its base (Martínez Catalán *et al.*, 1996; Dallmeyer *et al.*, 1997). The mylonitic fabric associated to the basal thrust of the Parautocthon has been dated at *c.* 343 Ma ($^{40}Ar/^{39}Ar$; Dallmeyer *et al.*, 1997). The activity of the Lalín-Forcarei thrust has been constrained indirectly by regional data and considered older (*c.* 340 Ma).

The Cabo Ortegal Complex

The Cabo Ortegal Complex is the easternmost among the allochthonous complexes of Galicia and therefore located at the leading edge of such tectonic pile (Figs. 2 and 3). Despite its smaller size, this complex includes a rather complete collection of the allochthonous terranes described in NW Iberia, with excellent outcrops on the Cantabrian coast. The largest exposures are represented by the HP-HT Upper Units, which according to structural and tectonothermal criteria feature two main different units, the Capelada Unit above and the Cedeira Unit in the lower position. It is unclear if a third small unit, the Peña Escrita Unit, located further below, is part of these units or a different one (Figs. 2 and 3). The IP Upper Units are barely represented in this complex, the Cariño Unit being the sole example. The contact between both types of Upper Units is a detachment similar to those described in the Órdenes Complex, but it has not been studied in detail in the Cabo Ortegal Complex.

The ophiolites are only represented by the Upper Ophiolitic Units, which in this case include two units with different lithological composition, the Purrido and Moeche ophiolites. The Basal Units are represented by the Espasante Unit,

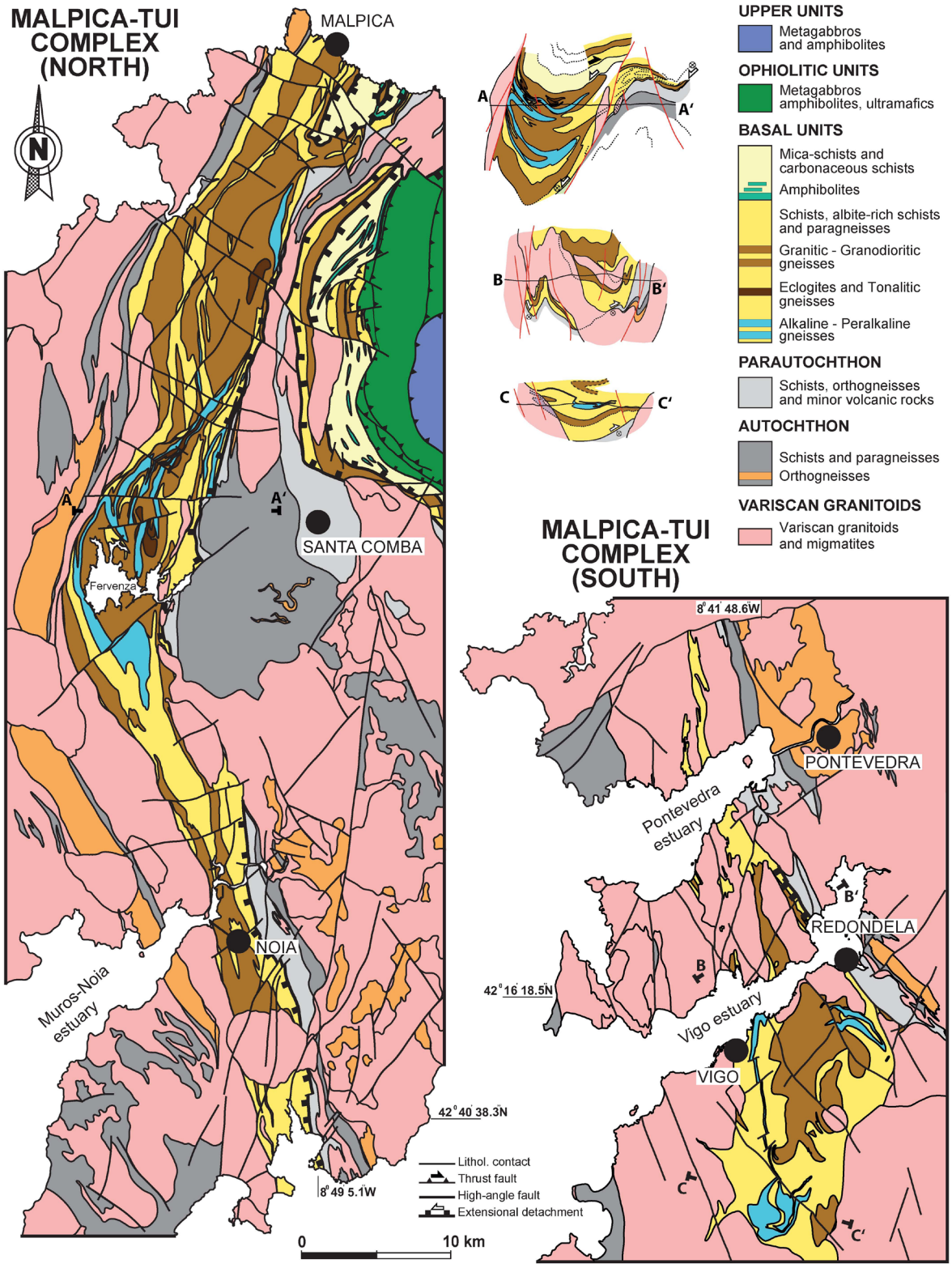

Fig. 5. Geological map and representative cross sections of the Malpica–Tui Complex. Based on Díez Fernández (2011).

which according to its similar lithologies and tectonothermal evolution can be correlated with the Agualada Unit of the Órdenes Complex. The lowest structural level of the Cabo Ortegal Complex is occupied by a thick serpentinite mélange restricted to the advancing front of the allochthonous complexes, the Somozas Mélange. This is an exotic unit for which no equivalent units have

been described so far in the NW Iberian Massif. The contact zone of the Cabo Ortegal Complex with the Parautochthon is broad and shows strong shearing, as evidenced by extensive development of phyllonites in the southern part of the complex. The basal contact of the Parautochthon is strongly deformed too, and well exposed in the coastal section near Loiba village. It is a thrust that emplaced a thick series of metasedimentary and metavolcanic rocks, some of which are Ordovician in age, on top of Silurian fossiliferous ampelites typical of the Central Iberian Zone (Arenas, 1988; Rodríguez *et al.*, 2004; Valverde Vaquero *et al.*, 2005).

The Malpica-Tuy Complex

The Malpica-Tui Complex occupies the core of a narrow synform which extends *c.* 150 km in N-S direction (Figs. 2 and 5). This complex only includes lithologies of the Basal Units, which show here largest variety in terms of composition and tectonic fabrics. The Upper Sequence crops out in the northern sector, in the core of the synform, forming the Ceán Unit (Fig. 2). The rest of the complex is constituted by lithologies of the Lower Sequence, also referred to as the Malpica-Tui Unit (Fig. 2).

The current basal contact of the Malpica-Tui Unit is an extensional fault, the westward continuation of the Pico Sacro Detachment (Fig. 2). This tectonic contact is reworked in strike-slip shear zones that run parallel to the boundaries of the complex and are responsible for its elongated shape. The contact between the Upper and Lower sequences is also an extensional fault that reaches the Órdenes Comples to the East, the Bembibre-Cean Detachment (Fig. 2). The Bembibre-Cean Detachment is cut by the Pico Sacro Detachment (Gómez Barreiro *et al.*, 2010a), and has been dated at *c.* 337 Ma ($^{40}Ar/^{39}Ar$ on muscovite; López Carmona *et al.*, 2014).

Basal Units

They represent a coherent continental terrane that extends from the Malpica-Tui Complex to the eastern part of the Órdenes Complex. It can be also followed discontinuously up to the eastern sector of the Cabo Ortegal Complex (Fig. 2).

Lithologies and chemical composition

The Basal Units are constituted by metasedimentary rocks, orthogneisses and less abundant mafic rocks, all of them grouped in two juxtaposed lithological sequences, a Lower Sequence and an Upper Sequence. The largest lithological variety is found in the Malpica-Tui Complex, where in addition deformation is heterogeneous, thus enabling observation of primary protolith features and reconstruction of the original lithostratigraphy (Díez Fernández *et al.*, 2010; Fig. 6).

In the Malpica-Tui Complex, the Lower Sequence was originally formed by geywackes arranged as siliciclastic turbiditic series together with ampelitic shales, semipelites, and scarcer limestones and cherts. Variscan deformation and metamorphism transformed this rock ensemble to a sequence of albite-bearing schists and paragneisses, graphitic schists, calc-silicate rocks and metacherts. The metasedimentary rocks are intruded by a large variety of granitoids, later transformed into orthogneisses, with compositions ranging between granites, high-K granites, quartz-syenites, granodiorites and tonalites. The sequence also contains less abundant mafic rocks, which now occur as amphibolites, blueschists and variably retrogressed eclogites (Fig. 6a). The granitic rocks define two compositional suites (Floor, 1966; Rodríguez Aller, 2005; Montero *et al.*, 2009), a dominant suite with calc-alkaline composition and intruded by the mafic rocks (*c.* 493 Ma; Abati *et al.*, 2010), and another younger suite with alkaline-peralkaline affinity (*c.* 475-470 Ma; Díez Fernández *et al.*, 2012c). The alkaline-peralkaline granitoids are not intruded by the mafic rocks, which thence can be interpreted as a dyke swarm emplaced in between the two granitic series.

The Lower Sequence described in the Malpica-Tui Complex can be followed in the Santiago and Lalín units of the Órdenes Complex (Arenas *et al.*, 1995). Both units are located in the normal limb of a large recumbent anticlinorium, the Carrio Anticline (Fig. 2). This sequence continues into the Forcarei Unit to depict the reverse limb of that fold (Martínez Catalán *et al.*, 1996). Minor differences between these three units exist, for instance the mafic rocks are more abundant in the Lalín Unit and the alkaline-peralkaline orthogneisses are very rare or absent in the

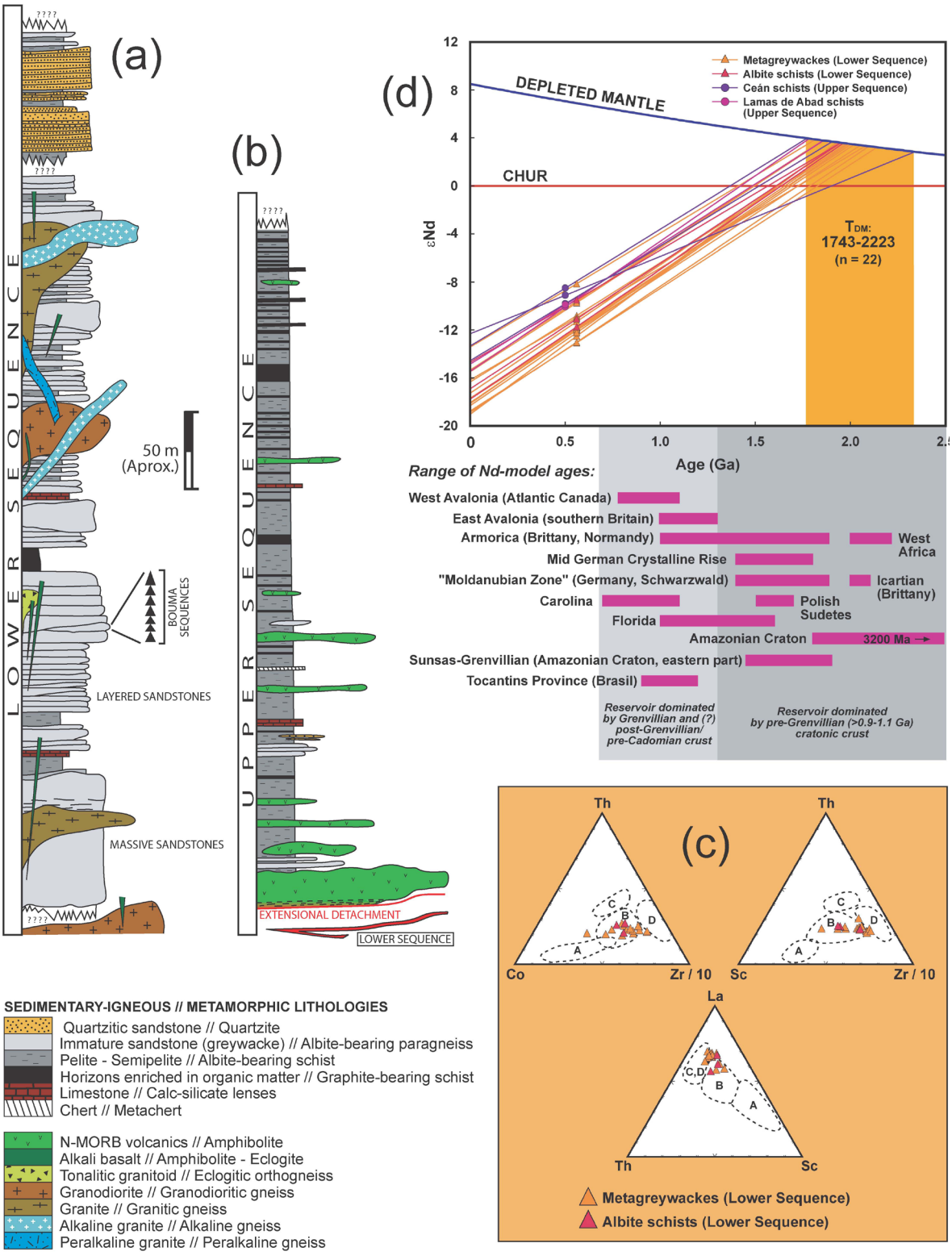

Fig. 6. Idealized stratigraphic columns summarizing the main sedimentological features observed in the **(a)** Lower and **(b)** Upper sequences of the Malpica-Tui Complex. **(c)** Trace element tectonic setting diagrams (Bathia and Crook, 1986) for the metagreywackes and albite-bearing schists and paragneisses from the Lower Sequence of the Malpica-Tui Unit (Fuenlabrada et al., 2012). Tectonic settings: A) oceanic island arcs, B) continental island arcs, C) active continental margins, D) passive margins. **(d)** TDM model ages (DePaolo, 1981) of the metasedimentary rocks of the Basal Units (Fuenlabrada *et al.*, 2012). Triangles and circles show εNd values at 560 and 500 Ma, which are the reference ages for the deposition of the Lower and Upper sequences, respectively. Data for comparative model ages from different regions taken from Linnemann and Romer (2002).

three of them, while in the Forcarei Unit some metaquartzites appear, orthogneisses are very scarce, and the metabasites are restricted to a thin level at the base of the unit (Figs. 2 and 4). The metamorphic evolution is complex and will be described below. Retrogressed eclogites exist in the Santiago Units, but they are completely absent in Lalín and Forcarei units (Rubio Pascual *et al.*, 2002).

In the Ceán Unit, the Upper Sequence is constituted by albite-bearing schists, alternating with graphite-bearing schists and minor metagreywackes, metaquartzites, calc-silicate rocks and metacherts. Alternations of mafic rocks transformed into amphibolites and variably retrogressed blueschists are abundant, notably a thick mafic layer located at the base of the sequence, the Cambre Amphibolites (Fig. 6b). The Upper Sequence is best exposed in the Lamas de Abade and Cercio units (Fig. 2). In the Lamas de Abade Unit lithologies are very similar to those described in the Ceán Unit, but the deformation has a mylonitic character (Gómez Barreiro *et al.*, 2010a). The Cercio Unit contains a fragment of the Upper Sequence similar to the middle and upper part of this sequence as described in the Malpica-Tui Complex, but in this case it is affected by lower metamorphic grade (Díez Fernández *et al.*, 2013).

In the uppermost part of the Basal Units, the Agualada and Espasante units are constituted by variably retrogressed calc-alkaline orthogneisses, schists and paragneisses, amphibolites and eclogites (Martínez Catalán *et al.*, 1996; Arenas *et al.*, 1997). Thin layers of ultramafic rocks occur along lithological contacts limiting the unit.

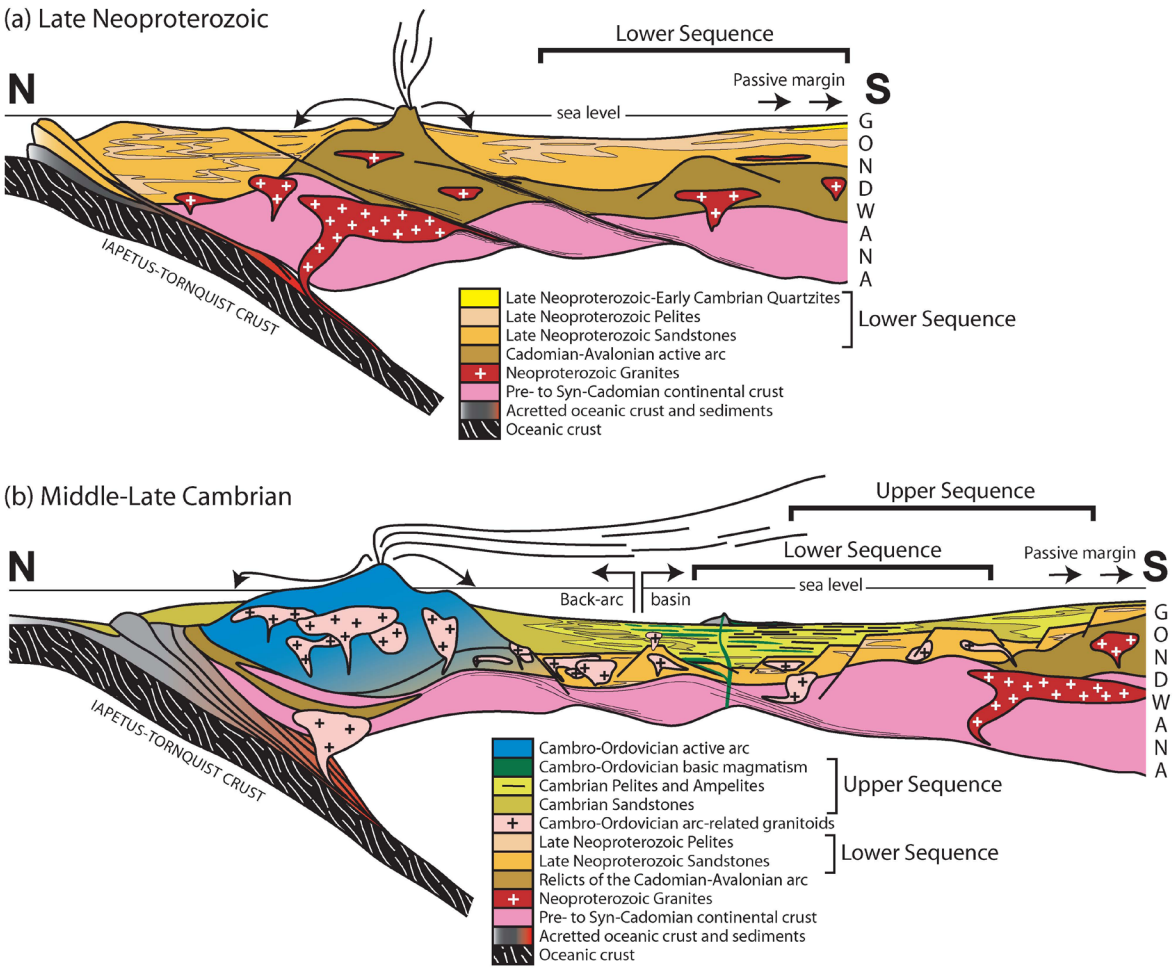

Fig. 7. Cartoon showing the tectonic setting for the **(a)** Lower (Late Neoproterozoic) and **(b)** Upper (Middle-Late Cambrian) sequences of the Basal Units of the allochthonous complexes.

Altogether, the lithologies observed in these two units seem to match those of the Lower Sequence. These units reached the higher metamorphic conditions in the Basal Units. They are currently interpreted as a part of the Lower Sequence subducted to the greatest depths and subsequently thrusted on top of this terrane.

The precise age of the sedimentary protoliths involved in the two lithological sequences is unknown, even though in the Malpica-Tui Complex they still preserve some palinological record (Fombella Blanco, 1984). Using U-Pb geochronology of detrital zircons, maximum depositional ages of Late Neoproterozoic (*c.* 560 Ma) and Late Cambrian to Ordovician (*c.* 500-480 Ma) were obtained for the Lower and Upper sequences respectively (Díez Fernández *et al.*, 2010, 2013). Given that it is intruded by Cambrian granitoids (*c.* 493 Ma), the depositional age of the Lower Sequence can be further constrained to 493-560 Ma.

According to geochemical discriminant diagrams for tectonic setting (Bathia and Crook, 1986), using immobile trace elements (Th-Co-Zr-Sc-La), the metagreywackes of the Lower Sequence have chemical compositions which indicate deposition in an active magmatic arc (Fig. 6c). This arc was formed in the periphery of a continent, probably above thinned continental crust. The calc-alkaline magmatism recorded in the Basal Units would be also connected to the activity of this arc system. However, the compositions of the younger pelitic-semipelitic schists of the Upper Sequence are more typical of sedimentary rocks deposited in a passive margin setting. In relation to PAAS (post-Archean Australian Shale), the metasedimentary rocks of the Basal Units show *c.* 1 values in some significant LILE elements (Rb, Th, Ce, K_2O) and negative anomalies in U, Sr, Hf and TiO_2 (Fuenlabrada *et al.*, 2012). On the other hand, Nd model ages of the metasedimentary rocks in both sequences are very old in the context of the Iberian Massif, as they range between 1743 and 2223 Ma (Fig. 6d). These ages suggest that the original sedimentary basin was located near a cratonic area with dominant Paleoproterozoic and Archean isotopic sources. Considering the age populations obtained in detrital zircons from these metasedimentary rocks (Díez Fernández *et al.*, 2010), the whole dataset is compatible with a paleolocation in the periphery of the West African Craton.

An idealized scheme for the Late Neoproterozoic-Middle-Late Cambrian evolution of the peri-Gondwanan magmatic arcs, including the most probable location of the sedimentary series of the Basal Units, is shown in Fig. 7. Cessation of activity in this arc system occurred in a context of extension affecting the margin of Gondwana, coevally with the rifting and drifting of Avalonia and possibly other smaller terranes of the Variscan Belt. The intrusion of dyke swarms represented by the mafic rocks of the Basal Units, as well as the later intrusion of alkaline to peralkaline granitoids, would be probably related to this event.

High pressure metamorphism

The Basal Units represent a long high-P belt involved in the Variscan Orogen, in turn a typical collisional belt. Considering the crustal affinity and provenance of this terrane, the most probable setting for the origin of the high-P event entails deep subduction of the Gondwanan margin during the Variscan cycle.

Two different metamorphic groups can be distinguished in the Basal Units according to the characteristics of the high-P metamorphism. A Lower Metamorphic Group (LMG) constituted by the Malpica-Tui, Santiago, Lalín, Forcarei, Ceán, Lamas de Abade and Cercio units shows hig-P and low to intermediate-T metamorphism with variable intensity. However, an Upper Metamorphic Group (UMG) formed by the Agualada and Espasante units was affected by high-P and intermediate to high-T metamorphism (Martínez Catalán *et al.*, 1996). The LMG contains abundant high-P metapelites (garnet-phengite-chlorite-chloritoid-quartz-albite-clinozoisite-rutile±glaucophane), blueschists, lawsonite-bearing blueschists, common eclogites, eclogites with phengite and glaucophane and jadeite-bearing orthogneisses (Van der Wegen, 1978; Gil Ibarguchi y Ortega Gironés, 1985; Arenas *et al.*, 1995; Gil Ibarguchi, 1995, Rubio Pascual *et al.*, 2002; Rodríguez Aller, 2005; López Carmona *et al.*, 2010, 2013, 2014) (Fig. 8). The UMG features a variety of eclogites, including types with well developed honeycomb pattern textures (Fig. 8), along with high-P orthogneisses and paragneisses, frequent-

ly migmatitic (Arenas, 1988; Arenas *et al.*, 1997). Some $^{40}Ar/^{39}Ar$ ages obtained in the high-P assemblages have provided minimum age estimations for the high-P metamorphism (*c.* 370-365 Ma; Rodríguez *et al.*, 2003; López Carmona *et al.*, 2014). However, U-Pb data obtained from metamorphic zircon rims from orthogneisses of the Agualada Unit pointed to an age of *c.* 372 Ma, which is somewhat older but probably closer to the real age of the high-P metamorphic event (Abati *et al.*, 2010). In the same unit, the migmatization following the high-P event has been dated at *c.* 351-346 Ma using monazites extracted from paragneisses (Abati and Dunning, 2002).

The thermal structure of the Basal Units seems to reflect the original layout of a continental subduction zone. In the LMG, peak pressures reached during the high-P event increase to the West, from the less pressurized Forcarei Unit to the relatively deeper Lalín and Santiago units up to the deepest Malpica-Tui Unit. Such layout suggests westward subduction polarity (present coordinates; Martínez Catalán *et al.*, 1996). The Malpica-Tui and Santiago units reached eclogite facies conditions, while the Lalín and Forcarei units did not exceed the blueschist metamorphic facies. Blueschist facies conditions were also reached in the Ceán and Lamas de Abade units, located upwards in the original stacking, but the metamorphic conditions recorded in the Cercio Unit during the high-P event are still not clear. According to the higher metamorphic conditions reached by the UMG, these units are interpreted as a piece of the Lower Sequence subducted to greater depths and subsequently thrust onto the Upper Sequence, most probably during still active continental subduction (Arenas *et al.*, 1997).

The original subduction zone has been calculated to dip *c.* 18° using thermal modeling (Alcock *et al.*, 2005). The continental subduction complex was later affected by thermal inversion, which caused extensive migmatization in the Lalín, Agualada and Espasante units. Such inversion was fuelled by conductive heat transfer from the overlying mantle wedge, in part during exhumation of the subduction complex. Remnants of this mantle wedge are still preserved in the ultramafic section preserved in the Campo Marzo Unit (Fig. 2). The reaction history deduced for the high-P pelitic schist from the Ceán Unit, according to thermal modeling in the MnNCKFMASHTO system, is shown in Fig. 9 (López Carmona *et al.*, 2013). Pressure peak conditions in these schists are calculated in *c.* 22 Kbar, but higher pressure values were attained in sectors of the Malpica-Tui (Rodríguez *et al.*, 2003), and probably in the Agualada and Espasante units. The schists of the Ceán Unit also show the regional thermal inversion characteristic of the Basal Units, as can be observed in Figs. 9a, 9b and 9c.

Structural evolution

The regional structure of the Basal Units was first described in the Órdenes Complex (Martínez Catalán *et al.*, 1996). More recent works have expanded the study to the Malpica-Tui Complex (Díez Fernández, 2011; Díez Fernández *et al.*, 2011, 2012d, 2012e) or have provided detailed microstructural descriptions (Llana-Fúnez, 2002; Gómez Barreiro *et al.*, 2010a).

The record of the first deformation that affected the Basal Units (D_1) appears strongly overprinted by subsequent events and with relict character. Remnants in the metasedimentary rocks occur as an internal schistosity within albite porphyroblasts (S_i) grown during decompression. S_i consists of an aligned mineral assemblage of garnet-phengite-chlorite-rutile-clinozoisite (S_1). This high-P foliation and its associated stretching lineation have been also preserved as variably sized resisters in the Malpica-Tui Unit, such as eclogite boudins and pods of eclogitic gneisses. The stretching lineation associated to S_1 trends NE-SW, whereas shear sense indicators suggest a consistent top-to-the-NE kinematics in present coordinates. Such kinematics were developed during westward subduction of the Gondwanan margin, thus supporting that the continental convergence had a dextral component at this stage (Díez Fernández *et al.*, 2012d, 2012e).

In advanced stages of D_1, sections of the continental margin located inboard reached the subduction zone. Progressive accretion of thicker and more buoyant sections of the margin locked the subduction complex. Thrusting of the UMG (Agualada and Espasante units) above the LMG probably occurred during this stage (Martínez Catalán *et al.*, 1996). P-T-t paths obtained in the Agualada, Santiago and Lamas de Abade units

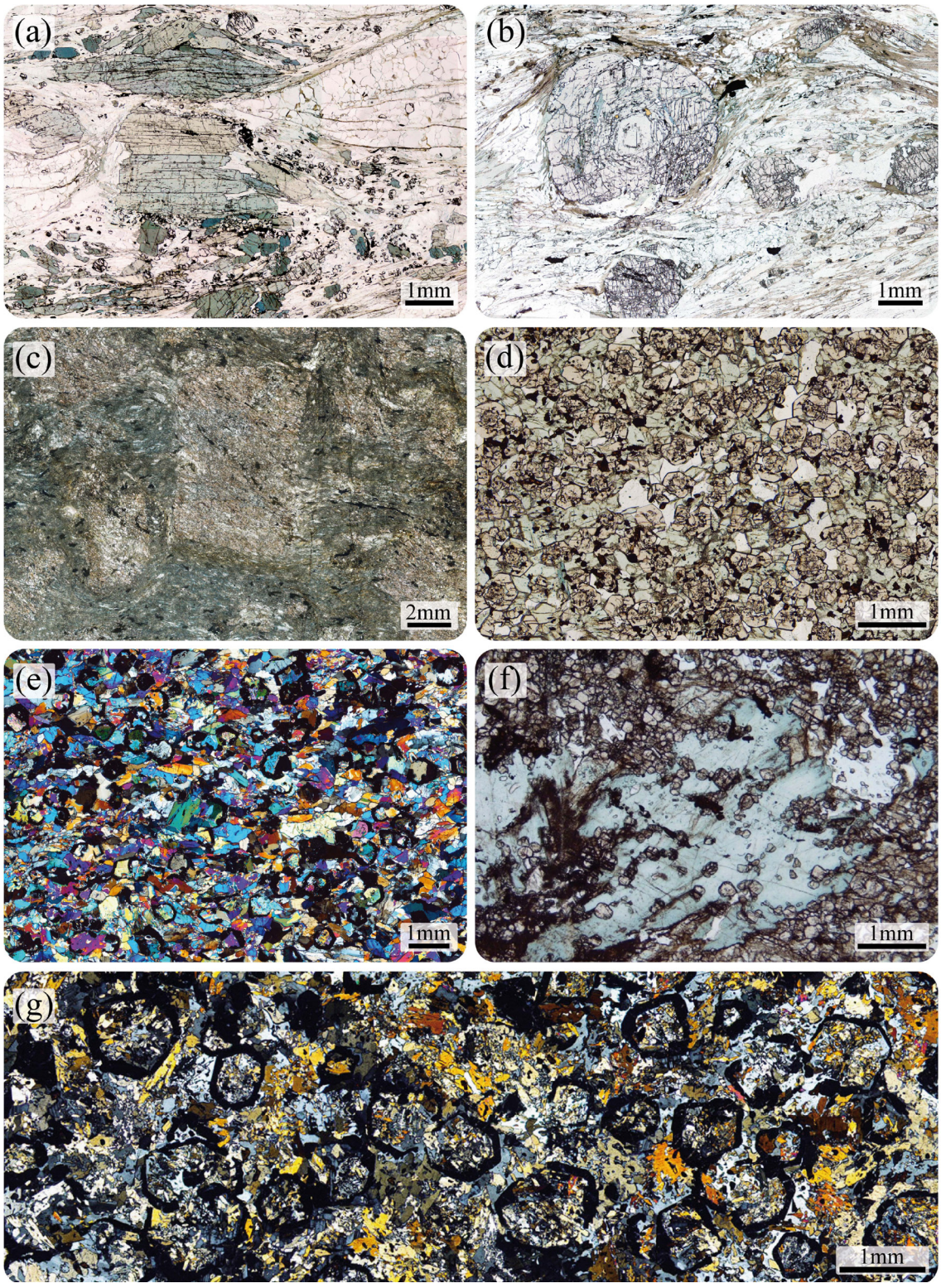

Fig. 8. Thin-section images of the high-pressure lithologies from (**a-f**) the Malpica-Tui and (**g**) Órdenes complexes. Blueschist-facies rocks from the Ceán Unit: (**a**) low-Ca metapelite from the upper structural levels displaying highly pleochroic chloritoid porphyroblasts; (**b**) Glaucophane-chloritoid-bearing garnet micaschist interbedded with the metabasic rocks; (**c**) Retrogressed blueschist with pseudomorphs after lawsonite located at the base of the unit. Eclogites from the Malpica-Tui Unit: (**d-e**) Honeycomb textures in eclogites including garnet, omphacite, rutile, clinozoisite, and white mica; (**f**) A later generation of poikiloblastic glaucophane is occasionally observed. Eclogites from the Agualada Unit: (**g**) retrogressed eclogite displaying primary honeycomb texture formed by omphacite (later transformed to a symplectitic aggregate) surrounding garnet. The eclogitic assemblage is formed by garnet, omphacite, rutile, and quartz. Post-eclogitic parageneses in the amphibolite-facies conditions include hornblende, plagioclase and epidote.

seem to confirm this interpretation (Arenas *et al.*, 1995, 1997). The P-T-t path calculated for the eclogites of the Agualada Unit is compatible with underthrusting of a cooler slice, which in this case would be represented by the Lamas de Abade Unit and correlatives (Fig. 2).

The second deformation phase (D_2) is related to the initial exhumation of the subduction complex. The current regional schistosity observed throughout the Basal Units formed at this stage (S_2). S_2 is generally axial planar to large recumbent folds vergent to the East, which represent the most prominent macroestructures in this terrane (Fig. 10; Díez Fernández *et al.*, 2011). Fig. 10a includes a map and cross section of the northern part of the Malpica-Tui Complex, showing the extensive development of the D_2 folds. The largest recumbent fold is the Carrio Anticline, in the Órdenes Complex, which is located above the Lalín-Forcarei Thrust (Fig. 10b). This thrust is responsible for the emplacement of the Basal Units onto their relative autochthon and some of its associated tectonic fabrics transect the large recumbent folds transported at its hanging wall (Martínez Catalán *et al.*, 1996).

The stretching lineation associated to S_2 shows W-E to NW-SE trending, and consistent top-to-the-E or -SE kinematics in present coordinates (Gómez Barreiro *et al.*, 2010a; Díez Fernández, 2011). During D_2 the thermal inversion detected in the Basal Units took place, both in the Órdenes and the Malpica-Tui complexes. Heat transfer from the overlying mantle wedge preserved in the Campo Marzo Unit occurred during exhumation and thinning of the subduction complex (Fig. 2).

Exhumation of the Basal Units progressed via the development of large extensional detachments (D_3). The Bembibre-Ceán Detachment was active first, and then extension continued in the Pico Sacro Detachment (Gómez Barreiro *et al.*, 2010a; Díez Fernández *et al.*, 2012b) (Figs. 2 and 4). These detachments have associated ductile-fragile fabrics and they can generate local foliation (S_3), even with mylonitic character. Later tectonic activity in the Basal Units consisted in the development of upright folds (D_4). The regional synforms that characterize the cartographic expression of the allochthonous complexes were formed at this stage, in close relation to large strike-slip shear zones that produced intense local overprinting and reworking of previous low-angle faults and, ultimately, cut across the upright structures. The Palas de Rei Shear Zone, in between the Órdenes and Cabo Ortegal complexes, and the Malpica-Lamego Shear Zone, which forms the western limit of the Malpica-Tui Complex (Llana-Fúnez and Marcos, 2001), were generated during this phase of deformation (Fig. 2).

Ophiolitic Units

A classical Wilson Cycle considers that collisional orogens typically contain a single ophiolitic belt, the only remnants of a sutured oceanic domain. However, preservation of old N-MORB oceanic lithosphere is problematic, as its thermal structure favors its total consumption by subduction. Conversely, most of the ophiolites obducted in orogenic belts were generated in supra-subduction settings, either at the last stages during the closure of large oceanic domains or in relation to the opening of ephemeral basins (Leitch, 1984; Pearce *et al.*, 1984). Ophiolitic belts related to the opening of ephemeral pull-apart basins have been specifically referred for the case of the Rheic Ocean (Murphy *et al.*, 2011). Such oceanic lithospheres is buoyant and tends to escape from subduction, and can be easily obducted on continental margins. Since the nature of oceanic tracts may vary along continental margins, oblique continental convergence and collision may result in the incorporation to the orogen of a collection of oceanic sections with different origin and age. Therefore, real geodynamic contexts lead to situations which tend to increase the variety of ophiolitic belts involved in large orogens, which rarely contain a single ophiolite generated at a particular time. This is also the case in the Variscan suture, where several recent papers described a variety of ophiolitic units with lithological and chronological differences. Such diversity indicates variable settings for the generation of oceanic lithosphere during Paleozoic times, the understanding of which seriously called into question the Variscan and pre-Variscan paleogeographic reconstructions during the last years.

In the NW of the Iberian Massif, a group of

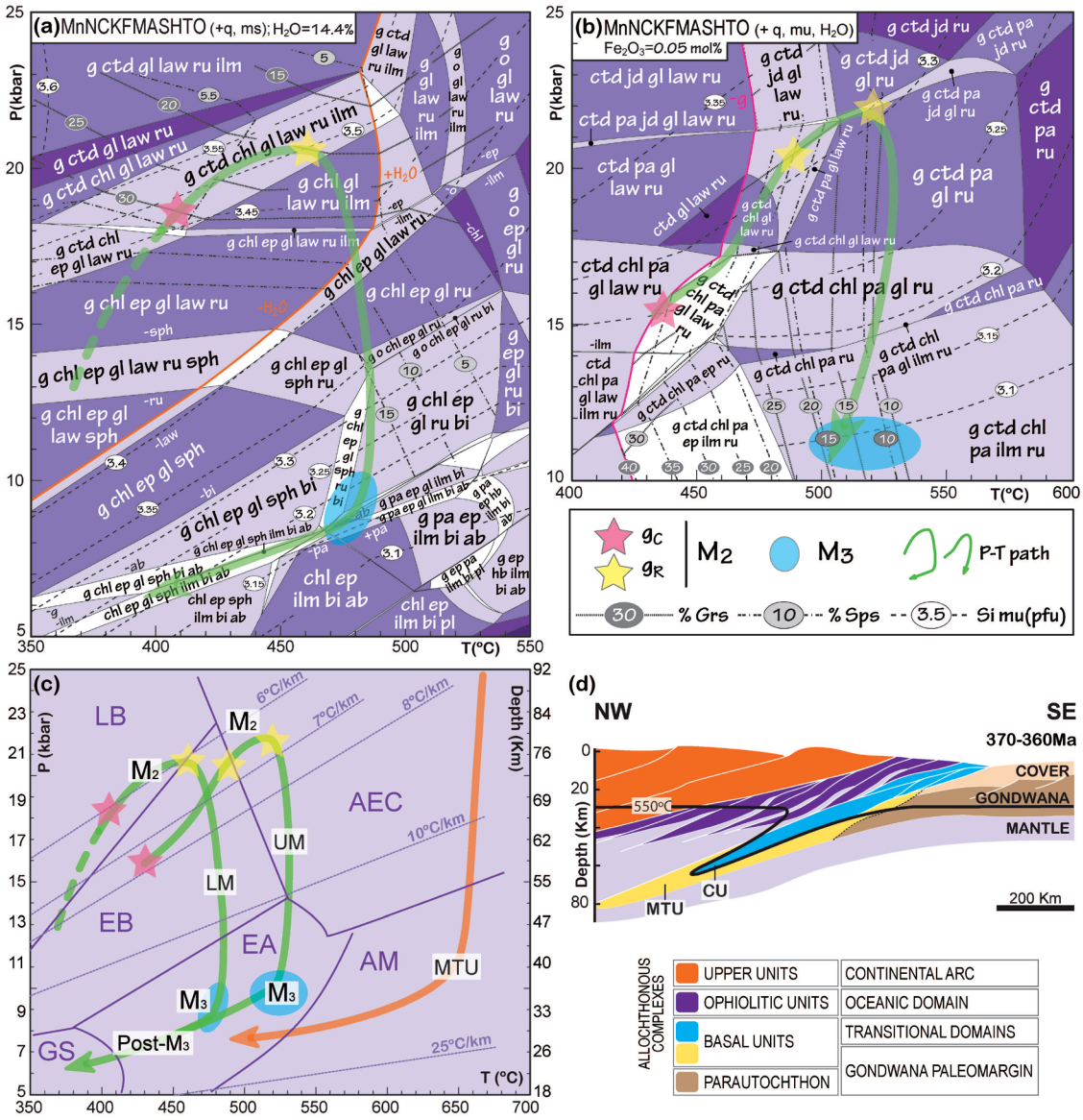

Fig. 9. Metamorphic evolution of the Ceán Unit. (**a**) P-T pseudosection calculated with Thermocalc for the lower metapelites (LM): [SiO_2:57.91; TiO_2:0.76; Al_2O_3:10.11; FeO:6.76; O:0.53; MnO:0.02; MgO:4.38; CaO:2.77; Na_2O:1.23; K_2O:2.95; H_2O:14.40]. (**b**) P-T pseudosection calculated with Thermocalc for the upper metapelites (UM): [SiO_2:69.21; TiO_2:0.67; Al_2O_3:14.82; FeO:7.75; O:0.05; MnO:0.26; MgO:3.08; CaO:0.24; Na_2O:0.99; K_2O:2.93; H_2O in excess]. (**c**) P-T diagram showing the metamorphic paths of the Ceán Unit (LM and UM) and the Malpica-Tui Unit (MTU). Modified from López-Carmona *et al.* (2013). Metamorphic facies field abbreviations: GS, greenschist facies; EA, epidote, amphibolite facies; AM, amphibolite facies; LB, lawsonite blueschist facies; EB, epidote blueschist facies and AEC, amphibole–eclogite facies. After Evans (1990) and Maruyama *et al.* (1996). (**d**) Schematic cross-section of the subduction zone operating in the NW Iberian Massif at *c.* 372 Ma. Modified from Martínez Catalán *et al.* (1996); Arenas *et al.* (1997) and López-Carmona *et al.* (2013).

tectonostratigraphic units constituted by mafic and ultramafic rocks, with little or no presence of metasedimentary rocks, were interpreted as ophiolites in the first descriptions of the terranes included in the allochthonous complexes (Arenas *et al.*, 1986). Two groups of ophiolitic units have been distinguised in Galicia (Arenas *et al.*, 2007a) (Fig. 2), which can be correlated with similar types along the Variscan Orogen. The Upper Ophiolitic Units have Devonian age and represent the most common group along the Variscan Orogen (Murphy *et al.*, 2011). Devonian ophiolites exist in Cornwall (Lizard Ophiolite; Clark *et al.*, 1998; Nutman *et al.*, 2001), Armorican Massif (Drain Ophiolite; Ballèvre *et al.*, 2009, 2014) and Bohemian Massif (Ślęża Ophiolite; Dubińska *et*

al. 2004; Kryza and Pin 2010). These ophiolites have been considered as related to the evolution of the Rheic Ocean, being originated during stages shortly before its closure (Díaz García *et al.*, 1999a; Sánchez Martínez *et al.*, 2007a). The Lower Ophiolitic Units include mafic-ultramafic sequences with Cambrian age and were developed in different geodynamic contexts, either during the opening of the Rheic Ocean (Arenas *et al.*, 2007b), or in previous stages to the opening of this large Paleozoic ocean (Sánchez Martínez *et al.*, 2012). Five ophiolitic units have been described in the NW of the Iberian Massif, Galicia. The Upper Ophiolitic Units are represented by the Careón, Purrido and Moeche ophiolites, while the Lower Ophiolitic Units are formed by the Vila de Cruces and Bazar ophiolites. Other additional ophiolitic units, with similar chronology and meaning, appear in the nearby region of Trás-os-Montes, Portugal (Pin *et al.*, 2006). In the following, the Galician ophiolites will be described separately, as they differ from each other in lithological composition and tectonothermal evolution.

Upper Ophiolitic Units

Careón Ophiolite

This is the ophiolitic unit with the best preserved metaigneous succession in the NW of the Iberian Massif. It is located in the East of the Órdenes Complex (Fig. 4) and is made up of three imbricated slices that repeat an oceanic crust-mantle transition zone, with a total thickness of *c.* 1500 m (Fig. 11). The thicker slice is the Careón Sheet, constituted by *c.* 1000 m of serpentinized ultramafic rocks and isotropic metagabbros, with abundant stocks of pegmatoid gabbros and late pegmatoid gabbros emplaced at all levels of the succession, and scarce wehrlite sills. Diabase and late diabase dykes also appear in all the exposed levels, from the deepest mantle sections to the shallower crustal levels (Fig. 11). The Careón Ophiolite shows a different lithological constitution to the HOT and LOT ophiolitic types described by Nicolas (1989, 1995) (Fig. 11). Therefore, it was interpreted as an ophiolite generated in a supra-subduction zone setting by Díaz García *et al.* (1999a). The intrusion of abundant diabase dykes in all the levels of the Careón Sheet is an additional argument for the generation of this ophiolite in a context of pronounced extension and thinning, above a subduction zone. Using immobile trace element (Hf, Th, Ta) and the diagram of Wood (1980) (Fig. 12a), the gabbros show compositions of typical island-arc tholeiitites, but the younger diabase dykes have transitional compositions to N-MORB. All the studied lithologies show a negative Nb-anomaly in relation to N-MORB, which is consistent with the generation of this ophiolite in an active subduction zone setting (Sánchez Martínez *et al.*, 2007a) (Fig. 12a).

The Careón Ophiolite was the first ophiolite dated in the NW of the Iberian Massif. A protolith age of *c.* 395 Ma was obtained from a sample of pegmatoid gabbro of the Careón Sheet (U-Pb zircon; Díaz García *et al.*, 1999a). The same U-Pb protolith age was reported later for a similar gabbro of the same slice by Pin *et al.* (2002). The three tectonic slices of the Careón Ophiolite show a pervasive foliation, which developed at higher temperature towards the upper part of each slice. In the contact zone with the overlying ultramafic rocks, the gabbros are transformed in garnet-bearing amphibolites. High temperature, corundum-bearing metamorphic soles with a thickness of *c.* 2 m can be locally developed (Fig. 11). P-T conditions reached during imbrication of the ophiolitic slices were estimated at c 11.5 kbar and 650 °C in the garnet amphibolites from the uppermost part of the Careón Sheet (Fig. 11). The stretching lineation of the amphibolites shows a consistent E-W trending, and shear sense indicators in the main fabric point to top-to-the East kinematics in present coordinates (Gómez Barreiro *et al.*, 2010b). The imbrication of the ophiolitic slices occurred at *c.* 377 Ma, according to the $^{40}Ar/^{39}Ar$ dating of hornblende from the amphibolitic foliation (Dallmeyer *et al.*, 1997).

The Careón Ophiolite was originally interpreted as a supra-subduction zone ophiolite generated in an intra-Rheic Ocean subduction zone (Díaz García *et al.*, 1999a; Sánchez Martínez *et al.*, 2007a). (Fig. 13). This subduction zone would have consumed almost all the old and dense lithosphere of the Rheic Ocean, whose common basatic types with N-MORB composition are yet to be found in the Variscan Belt. The youngest oceanic lithosphere generated in this intra-oceanic subduction zone at *c.* 395 Ma was accreted below

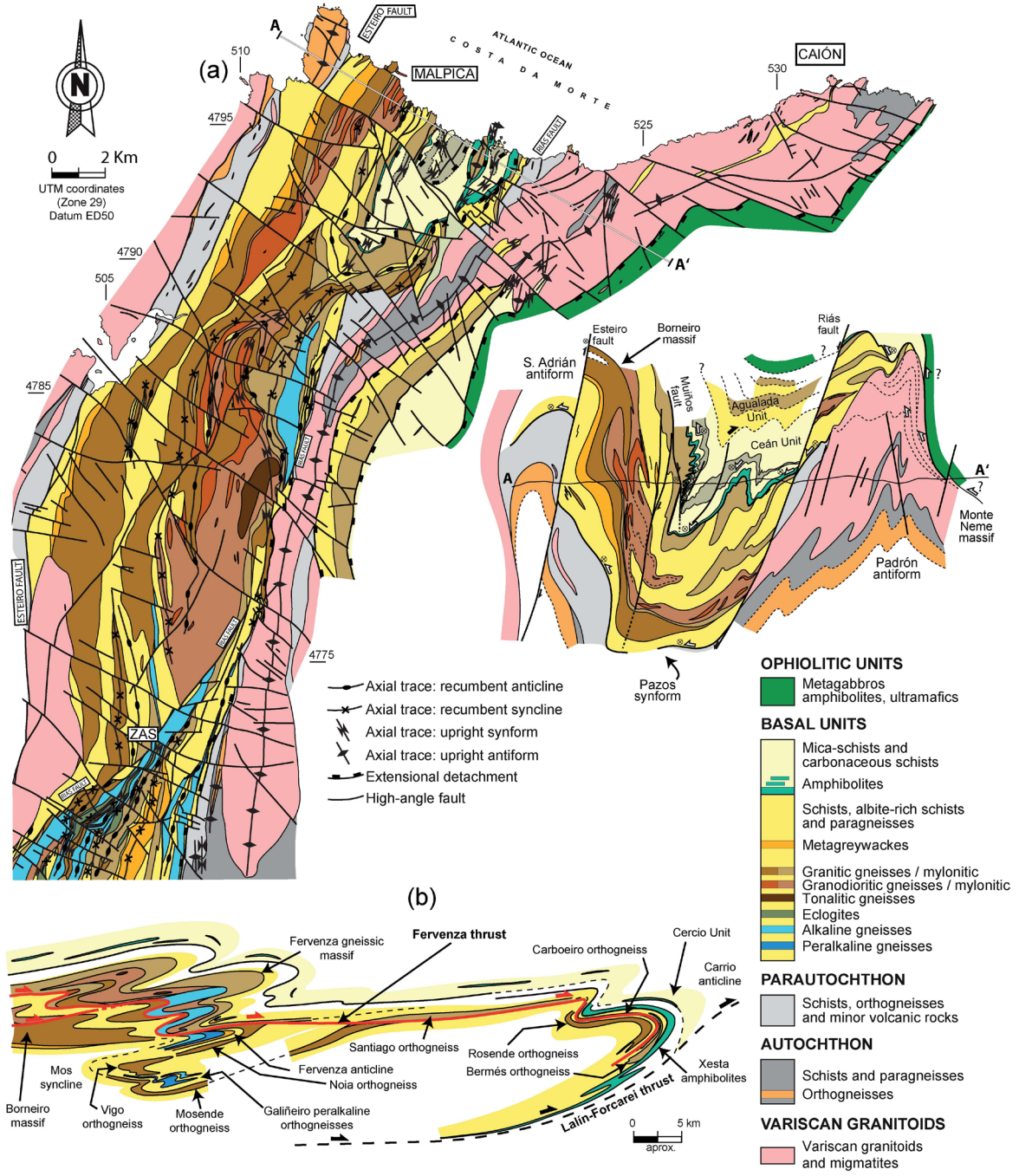

Fig. 10. (**a**) Geological map and cross section of the northern sector of the Malpica–Tui Complex, showing the internal structure of the Basal Units. (**b**) Idealized reconstruction of the internal structure of the Basal Units across the Órdenes and Malpica–Tui complexes during advanced stages of their exhumation (D2). The names of significant structures and gneissic massifs are indicated. Based in Díez Fernández (2011) and Díez Fernández *et al.* (2011).

the margin of Laurussia shortly after its formation, at *c.* 377 Ma. This first interpretation will be discussed in the next chapters in the light to the new data obtained in the other members of the Upper Ophiolitic Units.

Purrido Ophiolite

The Purrido Ophiolite is located in the western part of the Cabo Ortegal Complex (Fig. 3) and consists of *c.* 300 m of monotonous amphibolites and garnet-bearing amphibolites formed after gabbros. Unlike the Careón Ophiolite, well preserved metaigneous types have not been found, but the characteristic amphibolitic types show similar compositions and mineral assemblages in both ophiolites. Therefore, they are considered

as correlatives (Sánchez Martínez *et al.*, 2007b). The mafic rocks have typical compositions of island-arc tholeiites, with slight Nb anomalies (Sánchez Martínez *et al.*, 2007b) (Fig. 12b).

U-Pb zircon dating of a first sample of amphibolites provided a dominant group of zircons with average age of *c.* 1160 Ma, interpreted as the age of the gabbroic protoliths. Minor zircon populations with ages ranging 1.2-1.6 Ga were considered as inherited crystals. Therefore, the Purrido Ophiolite became an enigmatic pre-Rodinian ophiolite preserved in the Variscan suture (Sánchez Martínez *et al.*, 2006). Further research in two amphibolite samples yielded a new, consistent U-Pb zircon age of *c.* 395 Ma, matching the chronology of the Careón Ophiolite (Sánchez Martínez *et al.*, 2011). Moreover, the Lu-Hf zircon data revealed the presence of Paleoproterozoic isotopic sources mixed with juvenile mafic material extracted at *c.* 395 Ma (Fig. 14). The Sm-Nd isotopic geochemistry of these amphibolites also shows an important isotopic heterogeneity for the original mafic material (Sánchez Martínez *et al.*, 2011). On the other hand, the Purrido amphibolites have a well-developed planolinear foliation formed during the accretion of the unit and dated at *c.* 391.3 ± 6.6 Ma ($^{40}Ar/^{39}Ar$ on hornblende Dallmeyer *et al.*, 1997).

The geochemical and geochronological data obtained in the Purrido Ophiolite, can only be interpreted in the context of interaction among Devonian gabbroic magmas and continental crust. Such scenario led to a rethinking of the initial interpretation proposed for the Upper Ophiolitic Units, according to which they would be associated with the activity of an intra-Rheic Ocean subduction zone. Again the new interpretation will be presented and discussed in detail in a later section.

Moeche Ophiolite

The Moeche Ophiolite crops out largely in the eastern part of the Cabo Ortegal Complex (Fig. 3). The structural position relative to the Purrido Ophiolite is not obvious, although they contact in a small coastal section to the West of Cedeira village, where the Moeche Ophiolite occupies a lower structural position (Fig. 3). This ophiolite

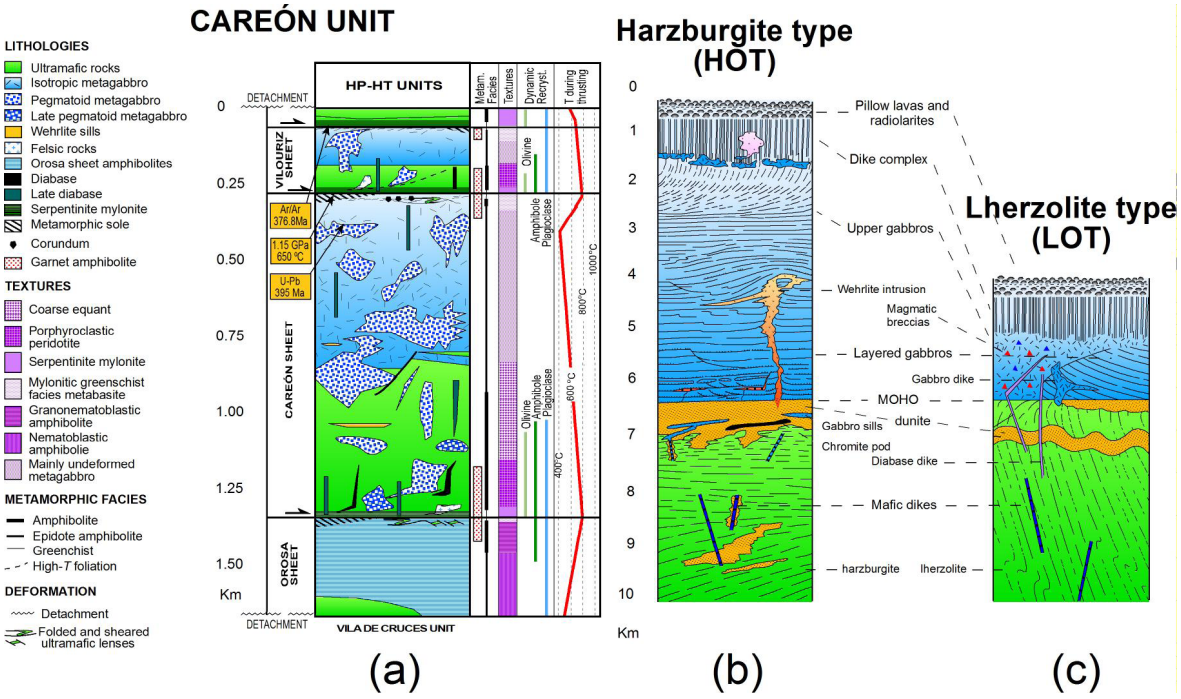

Fig. 11. (**a**) Synthetic column of the Careón Ophiolite showing the main lithologies and imbricates, distribution of metamorphic facies, textures, levels where dynamic recrystallization of main components occurred, and the saw-tooth thermal gradients developed during the earliest stages of thrusting. The U-Pb age of the gabbroic protholiths, $^{40}Ar/^{39}Ar$ age of hornblende in metamorphic soles and the peak P-T conditions reached during the accretion are also shown. Modified from Díaz García *et al.*, (1999a). (**b**) and (**c**) Representative columns for the Harzburgite (HOT) and Lherzolite (LOT) types of ophiolites described by Nicolas (1989, 1995).

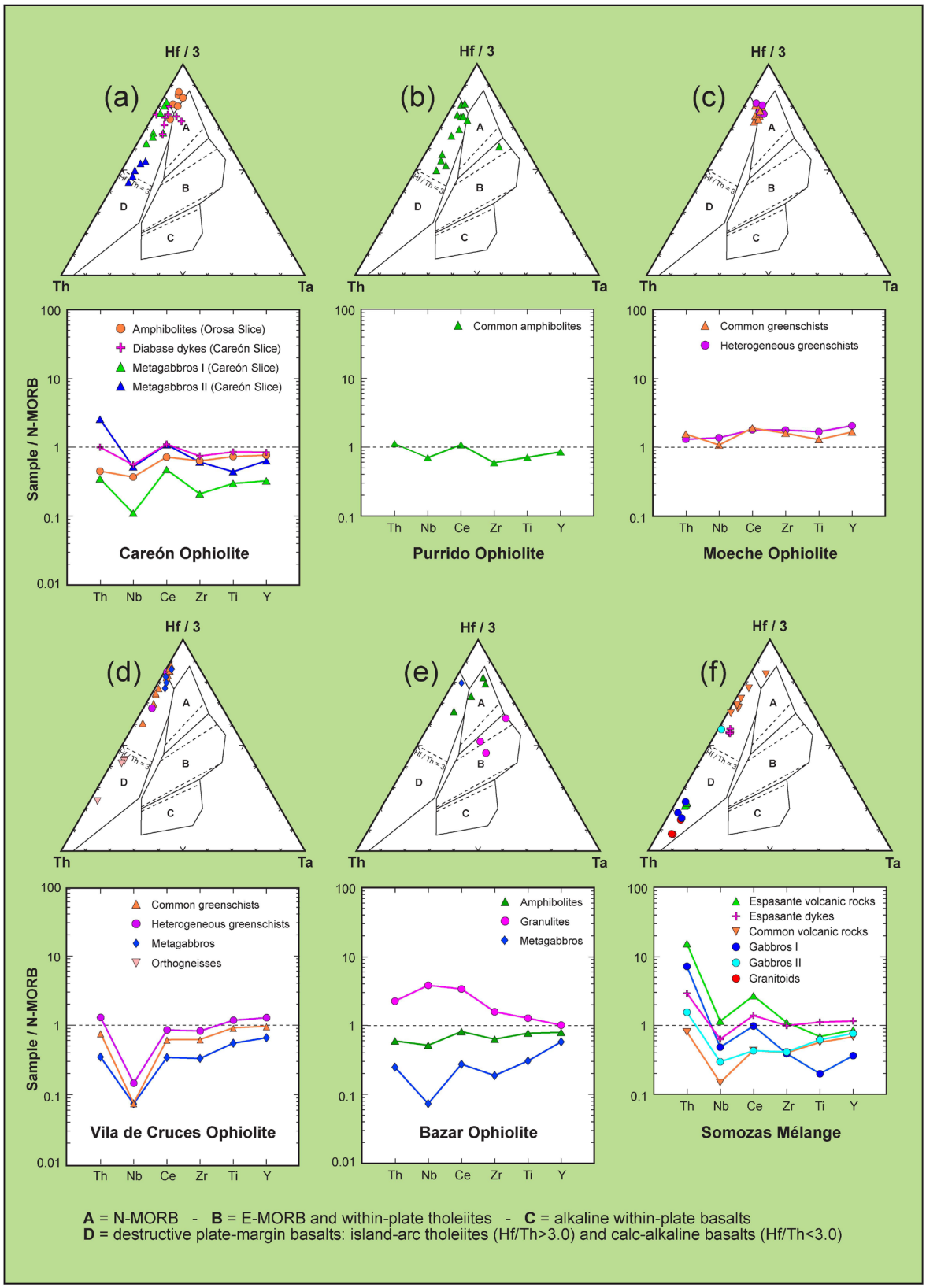

Fig. 12. Hf-Th-Ta diagrams (Wood, 1980) and N-MORB-normalized trace-element patterns (selected elements and normalizing values following Pearce, 1996) for the most representative lithologies of the ophiolites included in the Allochthonous Complexes of Galicia. (**a**) Careón Ophiolite. (**b**) Purrido Ophiolite. (**c**) Moeche Ophiolite. (**d**) Vila de Cruces Ophiolite. (**e**) Bazar Ophiolite. (**f**) Igneous rocks involved in the serpentinitic Somozas Mélange. Modified after Arenas *et al.* (2007b, 2009, 2014b), Sánchez Martínez *et al.* (2007a, 2007b, 2012).

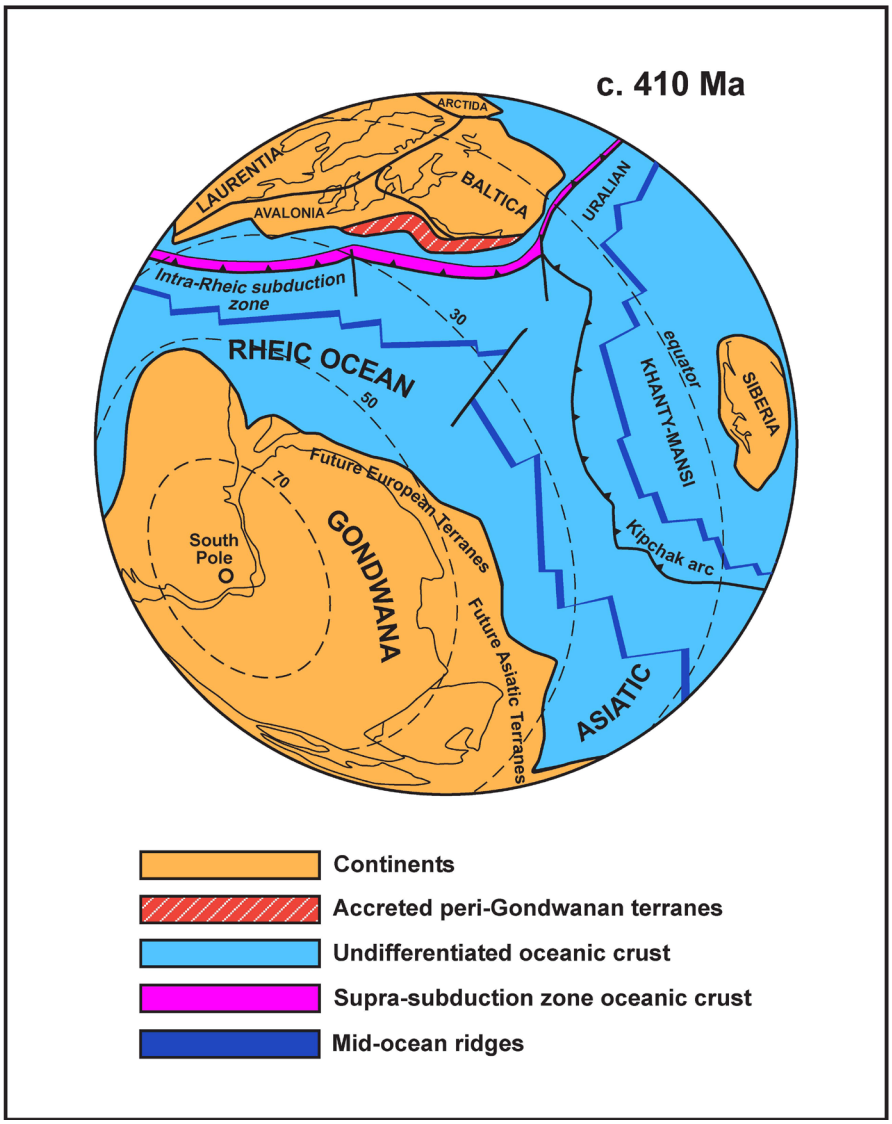

Fig. 13. Paleogeographic reconstruction of the Rheic domain at the Silurian-Devonian transition (modified after Stampfli and Borel, 2002). Note the generation of new oceanic lithosphere associated with intra-oceanic subduction directed to the North (Sánchez Martínez *et al.*, 2007a).

consists of *c.* 500 m of greenschists with some alternations of pelitic phyllites and micaschists and scarce metagabbros and serpentinites. According to the Hf-Th-Ta diagram of Wood (1980), the mafic rocks show transitional compositions between N-MORB and island-arc tholeiites. They also show slight enrichment in trace elements in relation to N-MORB (Sánchez Martínez *et al.*, 2007b) (Fig. 12c).

U-Pb zircon dating of a mylontic greenschist yielded an age of 400 ± 3 Ma (Arenas *et al.*, 2014b), coeval with the protolith ages obtained in the Careón and Purrido ophiolites. Lu–Hf zircon isotope signatures clearly indicate contributions from an old continental source. εHf values are negative (generally below εHf = -5), and thence not compatible with extraction from a juvenile mantle source (Fig. 14). Such Lu-Hf zircon data are similar to those obtained in the Purrido Ophiolite. Also in this case, they are not compatible with the generation of this ophiolite in a setting far from continental domains.

The internal structure of the Moeche Ophiolite is not well known. It shows a mylonitic-ultramylonitic regional schistosity developed in greenschist facies conditions. The presence of this pervasive fabric makes identifying primary igneous features difficult, thus hindering assessments on their basaltic or gabbroic nature. The regional schistosity is axial planar to isoclinal recumbent folds of, at least, decametric size. $^{40}Ar/^{39}Ar$ dating on the mylonitic fabric of the phyllites yielded an age of *c.* 364 Ma (whole rock analysis; Dallmeyer *et al.*, 1997), which is slightly younger than the

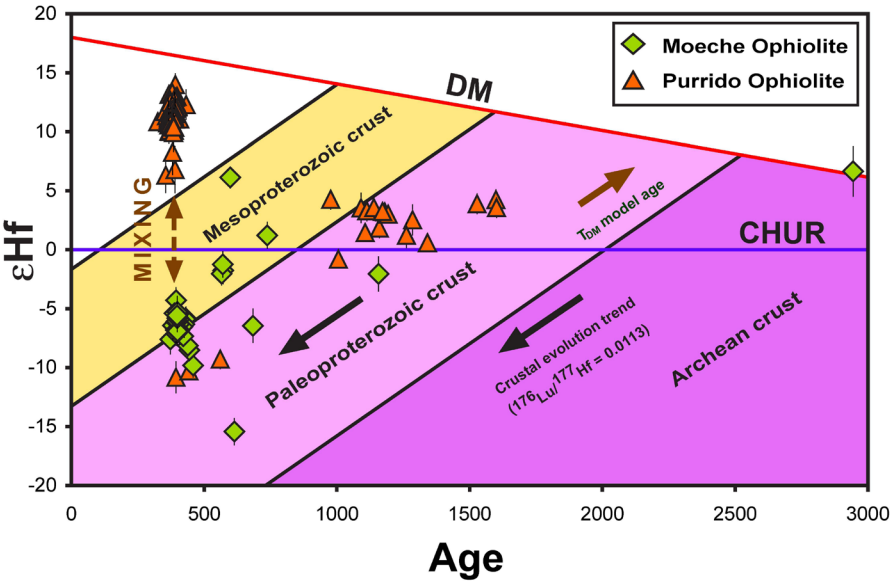

Fig. 14. Initial εHf versus age diagram combining the U-Pb and Lu-Hf isotope data of zircons from the Purrido and Moeche ophiolites. Crustal evolution trends ($^{176}Lu/^{177}Hf$ = 0.0113) for the Archean, Paleoproterozoic and Mesoproterozoic crusts are also shown. Based in Sánchez Martínez *et al.* (2011) and Arenas *et al.* (2014b).

regional fabric of the rest of the Upper Ophiolitic Units.

Lower Ophiolitic Units

Vila de Cruces Ophiolite

Located in the SE of the Órdenes Complex, the Vila de Cruces Ophiolite shows an intricate internal structure formed by two main juxtaposed slices totaling *c.* 4000 m in thickness (Fig. 4). It is mainly composed of greenschist with probable volcanic protoliths, which alternate with phyllites, pelitic micaschists, semipelitic schists with porphyroblasts of albite and garnet and rare metacherts. Other lithologies include some lens-shaped alternations of metagabbro and two layers of tonalitic orthogneiss transitional to gabbro. In the contact zone between the two main slices, some rather thin intercalations of serpentinites occur. Both the mafic and felsic metaigneous rocks have compositions typical of magmas generated in destructive plate margins (Fig. 12d). The greenschists and metagabbros show island-arc tholeiite compositions and a marked negative Nb anomaly in relation to N-MORB (Fig. 12d), supporting a supra-subduction zone setting for this ophiolite (Arenas *et al.*, 2007b).

In the orthogneisses, a first U-Pb zircon study yielded a protolith age of 497 ± 4 Ma (Arenas *et al.*, 2007b). However, based on the discovery of some zircon grains giving inaccurate Mesoproterozoic ages (*c.* 1168-1176 Ma) in two samples of metagabbro, this unit was interpreted as a composite terrane rather than a single ophiolite (Sánchez Martínez, 2009; Sánchez Martínez *et al.*, 2009). Additional U-Pb dating yielded consistent ages of *c.* 500 Ma for one sample of gabbro and three orthogneiss samples (Sánchez Martínez *et al.*, 2013). This age is currently considered as the crystallization age for the igneous protoliths of the Vila de Cruces Ophiolite. In spite of the absence of Lu-Hf zircon data in this unit, the presence of Mesoproterozoic zircons is considered as evidence for interaction of the igneous protoliths with continental crust.

The Vila de Cruces Ophiolite is characterized by a pervasive regional schistosity that transects a previous schistosity. Both planar fabrics are associated with different generations of map-scale recumbent folds and formed under greenschist facies conditions (Arenas *et al.*, 2007b). The P-T values are higher in the upper part of the unit, where they can reach the amphibolite facies or transitional conditions. In these upper levels, the mica-schists contain garnet-chlorite-white mica, but not biotite, which suggest that part of this unit was affected by an initial high-P metamorphic gradient. On the other hand, the regional foliation has been dated at *c.* 363-367 Ma in two phyllite samples ($^{40}Ar/^{39}Ar$ dating on white mica concentrates; Dallmeyer *et al.*, 1997).

The Vila de Cruces Ophiolite is interpreted as a supra-subduction zone ophiolite developed in a Cambrian back-arc opened in the periphery

of Gondwana (Arenas *et al.*, 2007b). Therefore it probably represents a domain of transitional crust, built upon interaction between juvenile mantle magmas and thinned Gondwanan continental crust.

Bazar Ophiolite

The Bazar Ophiolite is located in the western part of the Órdenes Complex (Fig. 4). It consists of a *c.* 5000 m thick imbricate of tectonic slices mainly constituted by mafic rocks and some ultramafic rocks at the base (Díaz García, 1990). The main tectonic slice (Carballo-Bazar; Sánchez Martínez *et al.*, 2009, 2012) is *c.* 4000 m thick and includes metagabbros and amphibolites with high-T foliation. Scarce metric-sized boudins of mafic granoblastic granulites are preserved within the mafic rocks, indicating the existence of a previous granulite-facies metamorphic event. These boudins are wrapped by the high-T foliation and show a mineral assemblage transitional between low and intermediate-P conditions (plagioclase-clinopyroxene-orthopyroxene-hornblende-ilmenite±garnet±olivine). The lower part of the main slice consists of relatively well-preserved gabbros and ultramafic rocks, with minor leucogabbros and rare tonalites. The geochemical features of the most representative lithologies of the Bazar Ophiolite are quite complex. Regarding the most abundant amphibolites and metagabbros, they show compositions equivalent to island-arc tholeiites and N-MORB (Fig. 12e). However, the mafic granulites seem to be transitional between MOR (mid-ocean ridge) and WP (within-plate) basalts, with normalized trace element similar to those of T-MORB generated in plume-ridge interactions (Pearce, 1996) (Fig. 12e).

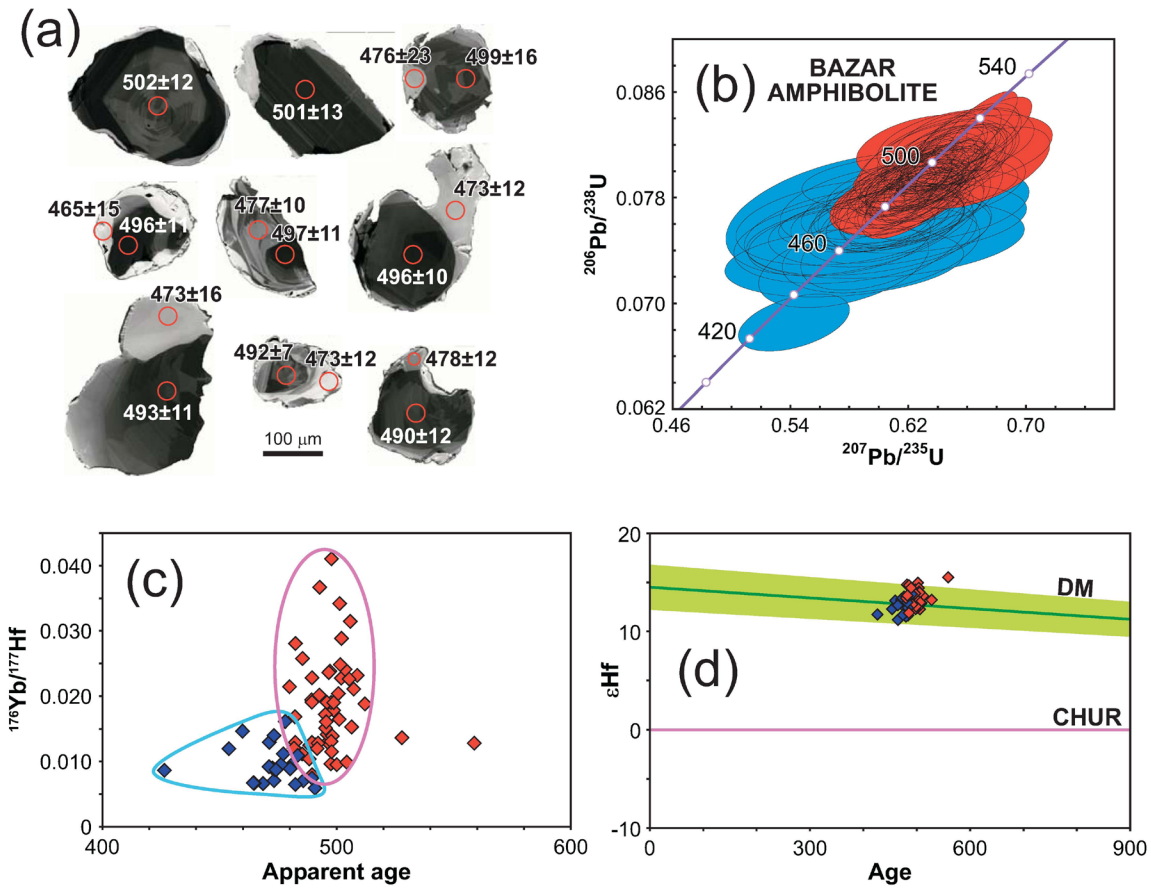

Fig. 15. U-Pb zircon dating and Yb-Lu-Hf isotope data of a metagabbroic amphibolite sample from the Bazar Ophiolite. (**a**) Cathodo-luminiscence images of selected zircons, circles representing the spot size of U-Th-Pb analyses. (**b**) Concordia diagram showing the results of the U-Pb analyses, with two statistically coherent groups of data. (**c**) $^{176}Yb/^{177}Hf$ versus apparent age diagram, the different trends of each group of analyses are encircled. (**d**) εHf versus apparent age plot; the depleted mantle array (DM) is extrapolated from average modern-day values of MORB (Chauvel and Blichert-Toft, 2001), assuming a linear behaviour from εHf = +2 at 4000 Ma (Vervoort and Blichert-Toft, 1999). Red symbols = zircon cores, blue symbols = zircon overgrowths-recrystallized domains. After Sánchez Martínez *et al.* (2012).

Zircon crystals extracted from an amphibolite sample show large cores surrounded by new recrystallized rims with irregular morphology (Fig. 15a). They yielded two groups of concordant U-Pb ages (Fig. 15b), which were treated separately according to their different $^{176}Yb/^{177}Hf$ ratios (Fig. 15c). The first group has an average age of 495 ± 2 Ma, interpreted as the age of the gabbroic protoliths. The second group shows an average age of 475 ± 2, thought to account for the high-T metamorphism (Sánchez Martínez *et al.*, 2012). At variance with the rest of the ophiolites, the Hf isotopic signature of zircons plus the absence of inherited grains point to a juvenile nature of the mafic protoliths of the Bazar Ophiolite as well as an apparent lack of interaction with continental crust (Fig. 15d). These data and the trace element composition suggest that the protoliths of the mafic rocks were generated in an oceanic context.

Taking into account the age, composition and tectonothermal evolution of the Bazar Ophiolite, it seems likely that this unit represents a lithospheric section of a peri-Gondwanan Cambrian ocean. Although its tectonic setting is yet uncertain, the N-MORB compositions shown by the gabbros indicates participation of a mid-ocean-ridge. The development of low to intermediate-P granulitic metamorphism can be explained by overheating related to the accretion of this units to the base of a magmatic arc. Based on the small gap (*c.* 20 Ma) between the formation of mafic protoliths and the high-T metamorphism, it can be suggested that the oceanic lithosphere preserved in the Bazar Ophiolite was remarkably buoyant and prone to escape from accretion. Alternatively, such high-T event could also result from an ephemeral opening of an asthenospheric window after subduction of a mid-ocean-ridge (Fig. 16).

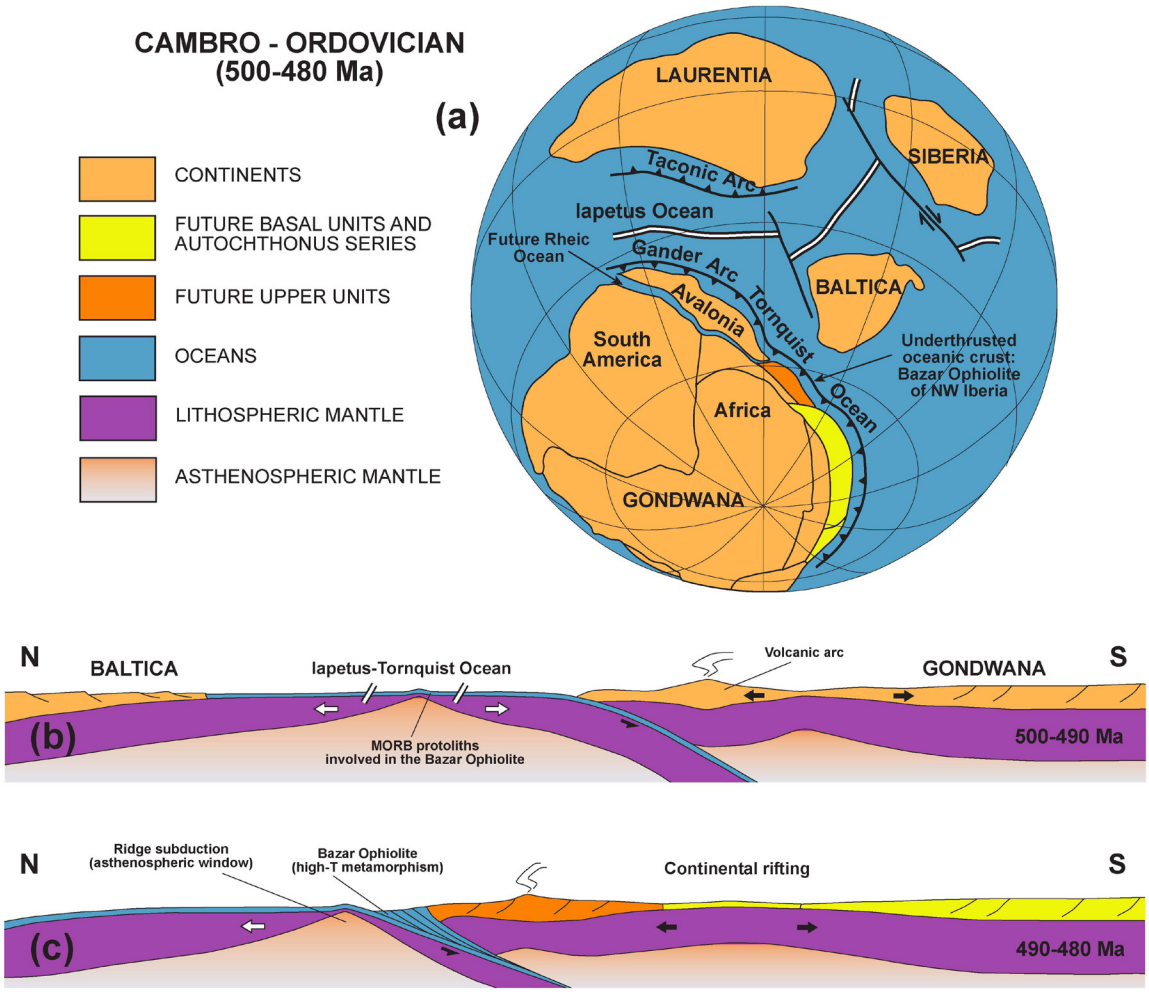

Fig. 16. (**a**) Paleogeographical reconstruction and (**b, c**) two plate sections for the Cambrian-Ordovician boundary. Based on Winchester *et al.* (2002), Arenas *et al.* (2007b), Gómez Barreiro *et al.* (2007) and Sánchez Martínez *et al.*, (2013).

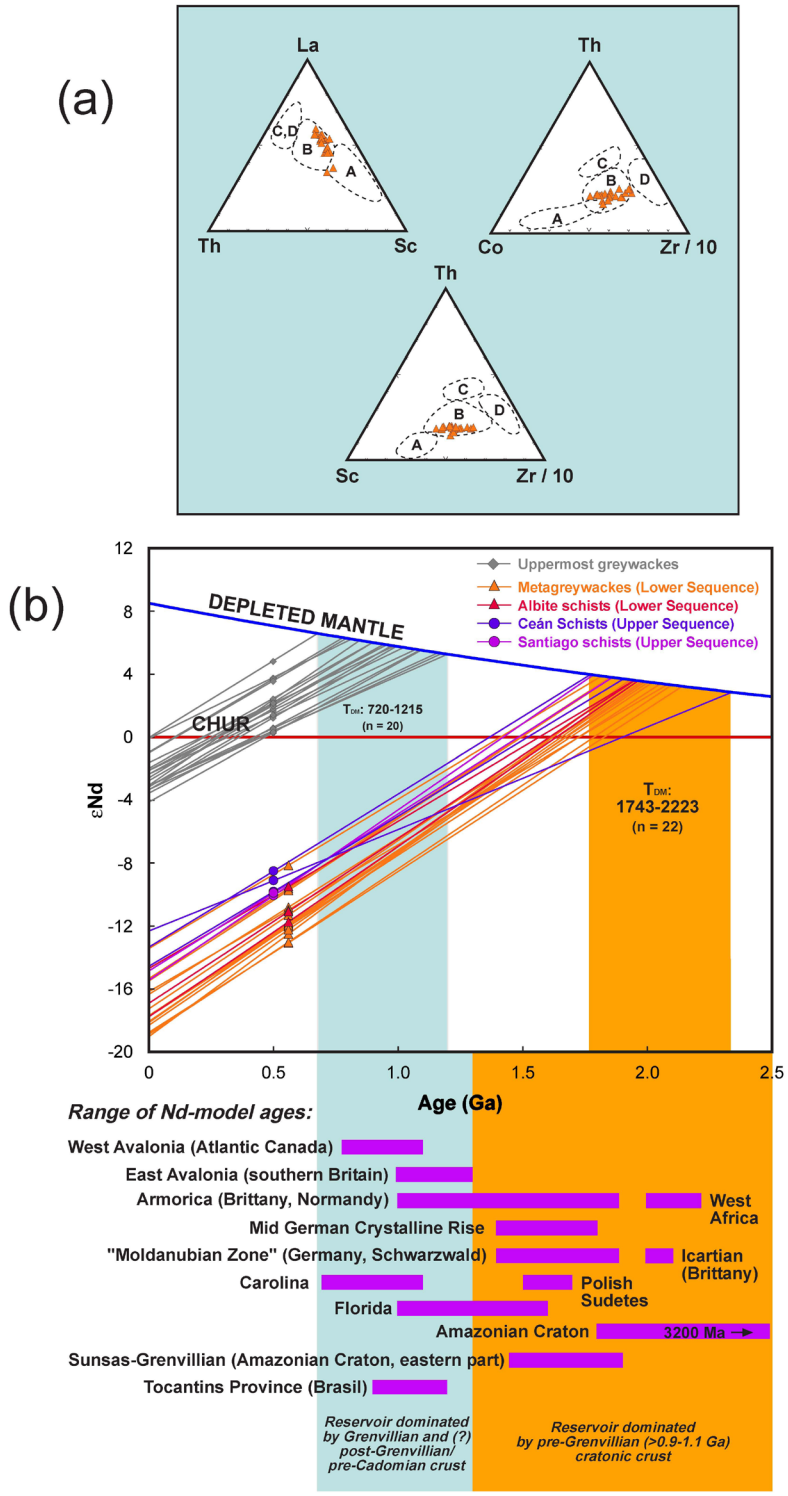

Fig. 17. Geochemical data for the uppermost metagreywackes of the Intermediate-P Upper Units (Betanzos Unit). (**a**) Trace element tectonic setting diagrams (Bathia and Crook, 1986). Tectonic settings: A) oceanic island arcs, B) continental island arcs, C) active continental margins, D) passive margins. (**b**) TDM model ages (DePaolo, 1981) calculated with εNd values at 500 Ma, reference age for the deposition of the metagreywackes. TDM model ages of the metasedimentary rocks of the Basal Units are included for comparison. Data source for comparative model ages from different regions taken from Linnemann and Romer (2002). Modified after Fuenlabrada *et al.* (2010, 2012).

Upper Units

The Upper Units represent the thickest terrane of the allochthonous complexes and also that with the largest exposure. They are constituted by a variety of units that can be grouped in two main ensembles according to their tectonothermal evolution: an upper ensemble characterized by intermediate pressure metamorphism (IP Upper Units), and a lower ensemble affected by high pressure and high temperature metamorphism (HP-HT Upper Units). The Upper Units are considered as a single and coherent terrane because of their systematic position above the Ophiolitic Units. In the first descriptions of the allochthonous complexes these units were assigned to a common tectonic setting and interpreted as sec-

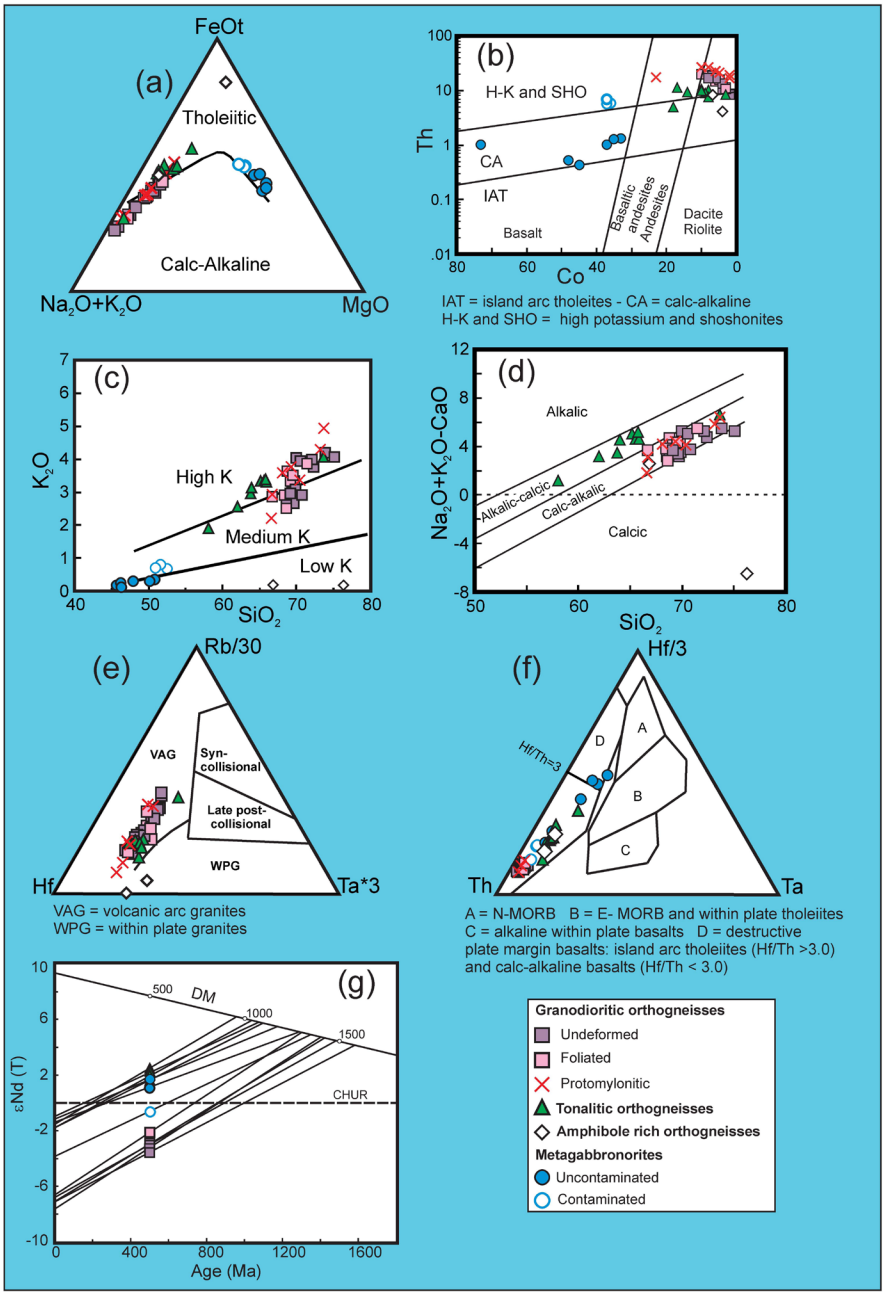

Fig. 18. Geochemical data of metaigneous rocks from the Corredoiras massif (IP Upper Units). (**a**) AFM diagram showing the tholeiitic and calc-alkaline fields after Irvine and Baragar (1971). (**b**) Th-Co discrimination diagram (Hastie *et al.*, 2007). (**c**) SiO_2-K_2O diagram (Peccerillo and Taylor, 1976). (**d**) Na_2O+K_2O-CaO *v.* SiO2 plot (Frost *et al.*, 2001) showing the fields for the alkalic, alkalic-calcic, calc-alkalic and calcic rock series. (**e**) Rb-Hf-Ta diagram (Harris et al., 1986). (**f**) Hf-Th-Ta diagram (Wood, 1980). (**g**) TDM model ages (DePaolo, 1981) calculated with εNd values at 492 Ma. After Andonaegui *et al.* (2012).

tions of a back-arc, a fore-arc, or the magmatic arc itself (Arenas *et al.*, 1986). This interpretation has not changed to this day, as many subsequent works have interpreted the origin of the Upper Units in the context of a peri-Gondwanan magmatic arc. The polymetamorphic nature of this terrane has also been demonstrated, first it was affected by a tectonothermal event related to the activity of the magmatic arc, and then by a collisional tectonothermal event present in any member of the Upper Units, but with different characteristics depending on the intensity of deformation and metamorphism.

Intermediate Pressure Upper Units

Lithologies and chemical composition

In the Órdenes Complex, the Betanzos Unit is constituted by a siliciclastic turbiditic series of greywackes with thin alternations of conglomerates, green phyllites and calc-silicate layers, which in the lower part of the unit ranges to a series of black metapelites and quartzites (Díaz García, 1990; Fuenlabrada *et al.*, 2010). This succession is intruded by abundant diabase dykes of metric size. The maximum depositional age of the greywackes has been calculated at *c.* 530-550 Ma (Middle Cambrian) using U-Pb dating of de-

trital zircons, with source areas located in North Africa (Fernández-Suárez *et al.*, 2003; Fuenlabrada *et al.*, 2010). On the other hand, one of the diabase dykes intruding the greywackes has been dated at *c.* 510 Ma (U-Pb in zircon; Díaz García *et al.*, 2010). The tectonic setting of the greywackic series was studied by means of immobile trace elements (La-Th-Sc; Bathia and Crook, 1986). The greywackes were deposited in a basin fed with material coming from an active continental margin (Fig. 17a). The greywackes have Nd model ages in the range T_{DM} = 720-1215 Ma (Fig. 17b), which are significantly younger than those of the Basal Units (Fig. 17b) and suggest participation of younger source areas or incorporation to the basin of juvenile Nd isotopic sources probably derived from igneous rocks of the magmatic arc.

The O Pino Unit rests below the Betanzos Unit, and is made of pelitic-semipelitic schists and paragneisses intruded by variably sized massifs of granitoids and gabbros, ranging from

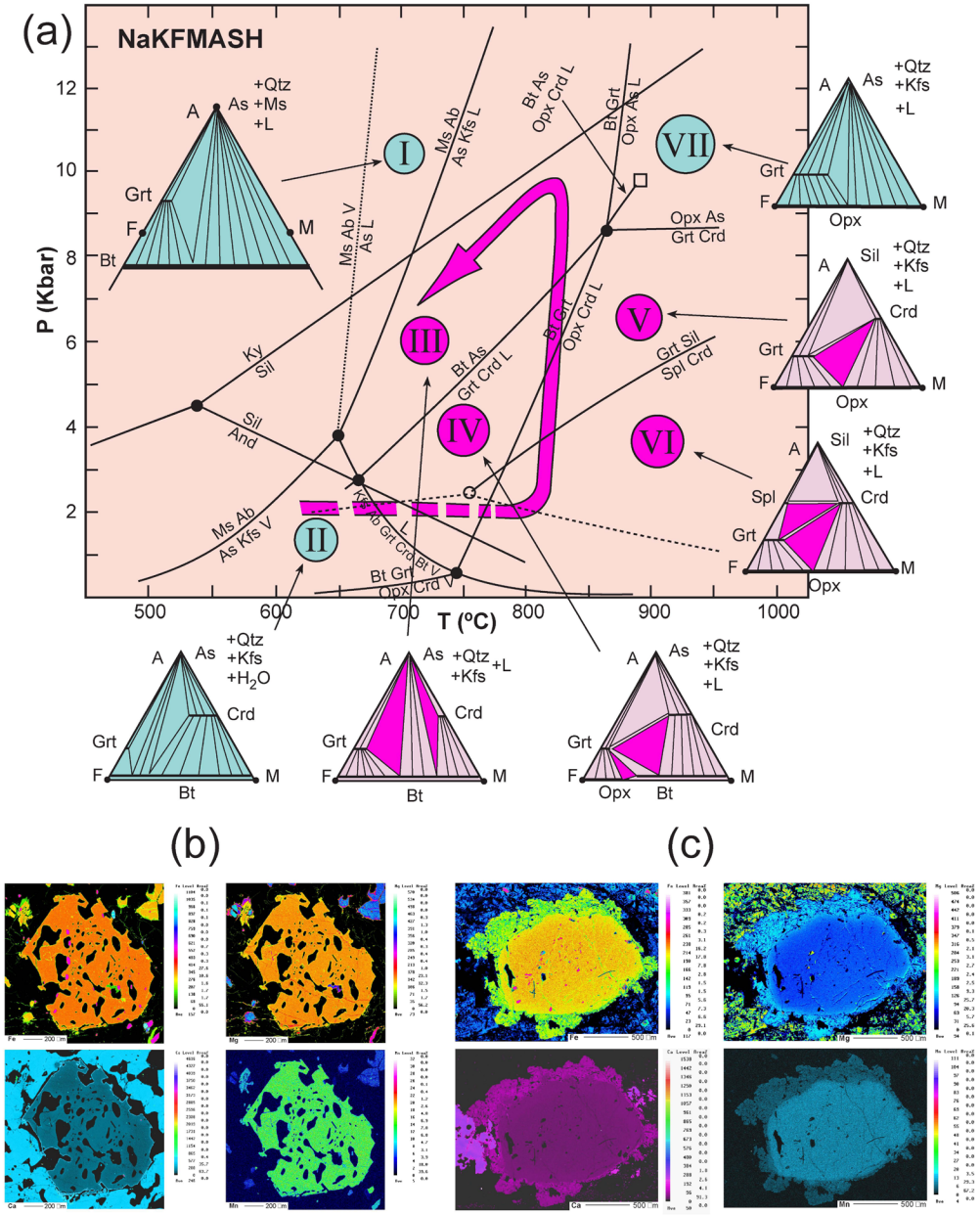

Fig. 19. (**a**) Counter clockwise P-T path calculated for the metapelitic granulites included in the Monte Castelo Gabbro Massif (IP Upper Units). Petrogenetic grid after Spear *et al.* (1999). (**b**) X-ray maps of a granulitic garnet representative of the low-P field VI. It is chemically homogeneous except for a relatively Ca-rich thin rim with growth zoning. (**c**) X-ray maps of a granulitic garnet representative of the baric peak. Note the xenomorphic overgrowth surrounding an unzoned lower pressure core. Modified after Abati *et al.* (2003).

dykes and stocks to large intrusive bodies (Díaz García, 1990; Abati, 2002; Castiñeiras, 2005). The larger igneous massif corresponds to the A Silva granodiorite, located NW of the Órdenes village (Fig. 4), and dated at *c.* 510 Ma (U-Pb in zircon; Castiñeiras *et al.*, 2010). In the Cabo Ortegal Complex, the IP Upper Units are represented by the Cariño Unit, whose lithological constitution is similar to that of the O Pino Unit (Fig. 3). It is formed by a series of schists and paragneiss-

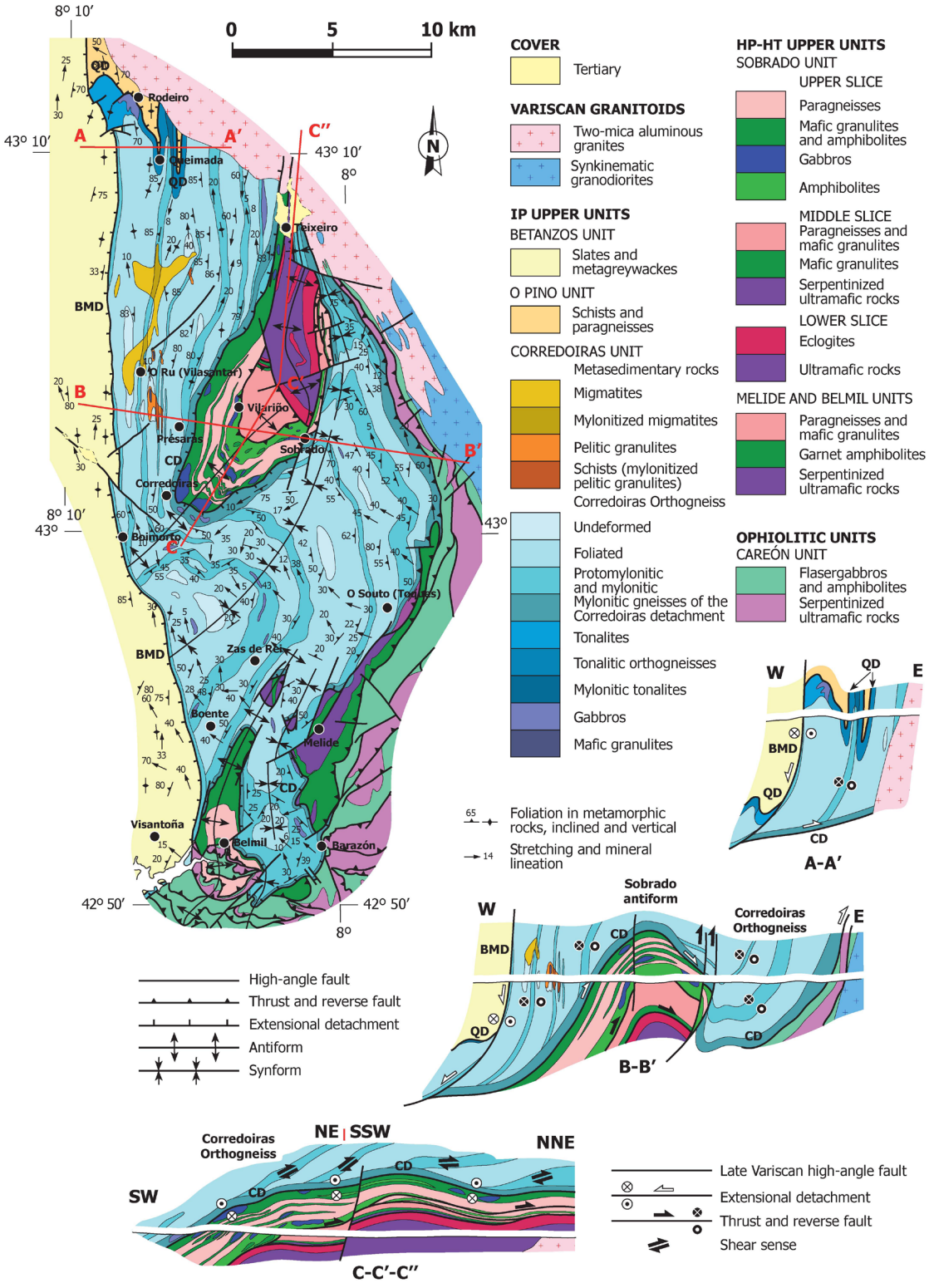

Fig. 20. Geological map and cross sections of the eastern part of the Órdenes Complex. After Díaz García (1999b), Arenas and Martínez Catalán (2002), González Cuadra (2007).

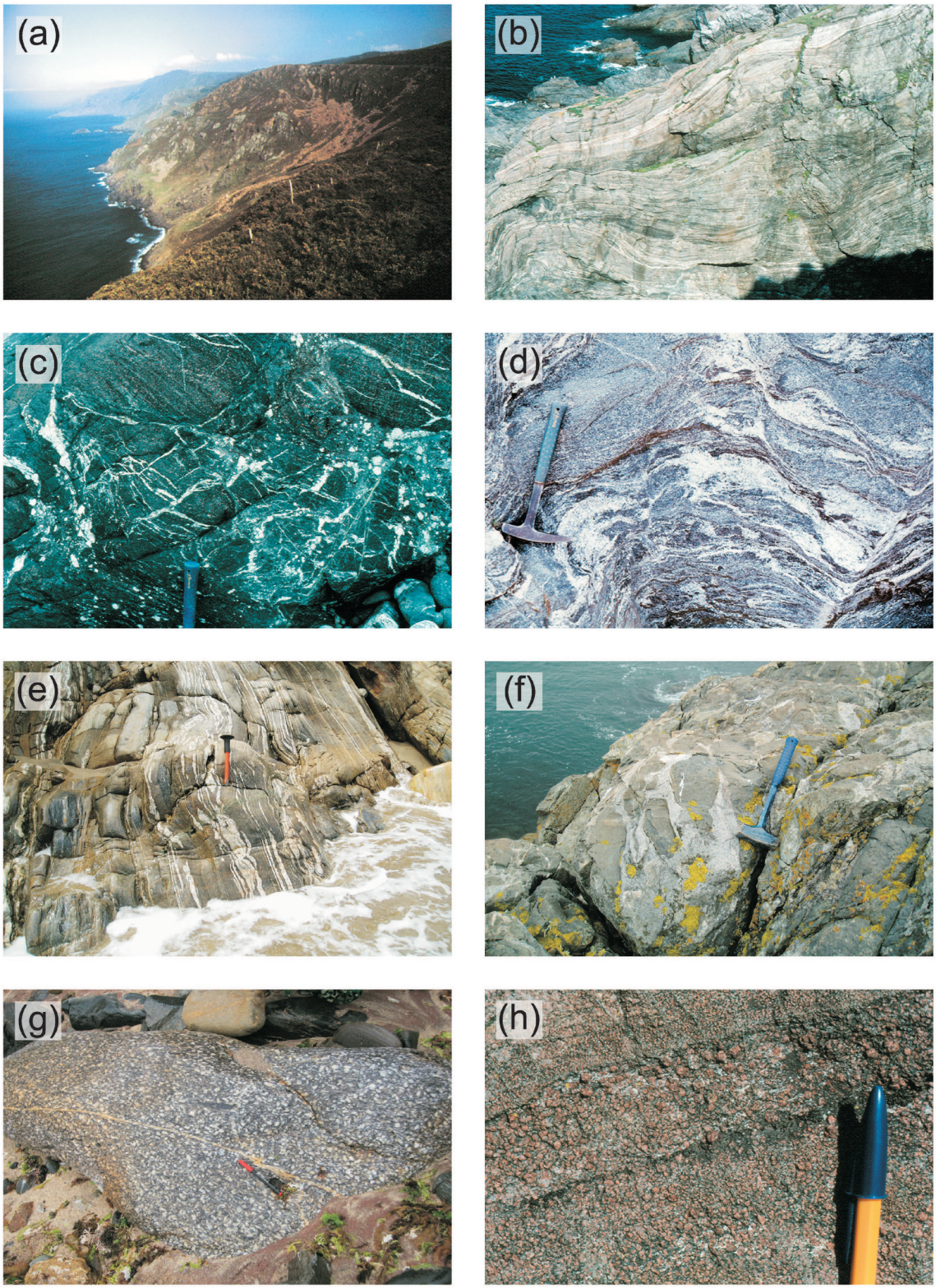

Fig. 21. Some aspects of the HP-HT Upper Units. (**a**) Hinge zone of the large recumbent synform of the Capelada Unit exposed in the coastal section of the Cabo Ortegal Complex. (**b**) Regional mylonitic foliation in the Bacariza Granulites (Capelada Unit). (**c-d**) Decompressive partial melting affecting the granulites of the Bacariza Formation; (**c**) the primary granulitic foliation is well preserved in sectors with limited partial melting, however (**d**) it may be strongly blurred in those subjected to intense partial melting. (**e**) Banded Gneisses in the Masanteo peninsula (Capelada Unit). (**f**) Mingling features exposed in a large metaigneous body preserved in the Banded Gneisses Formation; the HP-HT metamorphism transformed the mafic parts in eclogites. (**g**) Augen gneiss body included in the eclogite layer of the Capelada Unit exposed in the Masanteo peninsula. (**h**) Cpx–Grt rock from the Sobrado Unit, Órdenes Complex.

es, with compositions ranging from pelitic to greywackic, intruded by small massifs of gabbros and granitoids (Castiñeiras, 2005). The metasedimentary rocks still preserve primary sedimentary features, which indicate deposition in a turbiditic system. A maximum depositional age of *c.* 510 Ma has been obtained for the Cariño paragneisses using U-Pb dating of detrital zircons, with clear North African provenance (Albert *et al.*, 2015). Both the turbiditic nature and the maximum depositional age suggest equivalence to the greywackic series of the Betanzos Unit. However, Nd model ages are much older in the Cariño Unit, with an average of *c.* 1730 Ma, which indicates limited contribution of juvenile sources and also a heterogeneous isotopic character of the IP Upper Units (Albert *et al.*, 2015).

The lower sectors of the IP Upper Units are represented by two units with very different constitution, the Monte Castelo and Corredoiras units (Fig. 4). The Monte Castelo Unit includes a large massif of metagabbros with scarce lens-shaped inclusions of migmatitic paragneisses (Díaz García, 1990). The Monte Castelo Gabbro Massif (*c.* 150 km^2) is constituted by fine to medium grained metagabbronorites including types with olivine, amphibole or biotite, with variable textures from granular to intergranular and ophitic. Most of the gabbro massif is not deformed and shows a relatively homogeneous chemical composition characteristic of island-arc tholeiites (Andonaegui *et al.*, 2002). The Monte Castelo Gabbro has been dated at 499 ± 2 Ma (U-Pb in zircon; Abati *et al.*, 1999). The Corredoiras Unit is formed by a large massif of granitic orthogneisses that includes two stocks of gabbro and some large inclusions of migmatitic paragneisses (González Cuadra, 2007). The orthogneiss massif is mainly composed of granodioritic orthogneisses, with small bodies of tonalitic orthogneisses, scarce amphibole-rich orthogneisses and metagabbronorites. The granodioritic and tonalitic orthogneisses have compositions characteristic of I-type granitoids. In some cases, the metagabbronorites show chemical contamination by interaction with felsic magma. All the igneous lithologies included in the Corredoiras Massif have chemical compositions typical of magmas generated in magmatic arcs (Andonaegui *et al.*, 2012) (Fig. 18a-f). On the other hand, Nd model ages (T_{DM} = 949-1578 Ma) fall within the range defined by the Betanzos and Cariño units (Fig. 18g). The granodioritic orthogneisses of the Corredoiras Massif were dated at 492 ± 3 Ma (U-Pb in zircon; Andonaegui *et al.*, 2012).

Tectonothermal evolution: Arc–related event and collisional reworking

The highest levels of the IP Upper Units, represented by the turbiditic series of the Betanzos Unit, are affected by chlorite-zone low-grade metamorphism. They contain a single foliation (S_1), axial planar to West vergent D_1 folds with reverse limbs less than 2 km in wavelength (Matte and Capdevila, 1978; Díaz García *et al.*, 2010). This regional foliation is intersected at high angle by diabase dykes, one of which was dated at *c.* 510 Ma (Díaz García *et al.*, 2010). Therefore, both D_1 and the greenschist facies metamorphism seem to predate the Middle Cambrian. They are probably related to the dynamics of a peri-Gondwanan magmatic arc, also the setting for the protoliths of the Upper Units (Díaz García *et al.*, 2010; Fuenlabrada *et al.*, 2010).

A second regional foliation (S_2) exists from the base of the Betanzos Unit down, formed during a second syn-metamorphic deformation phase (D_2). This schistosity is axial planar to minor folds and contains a stretching lineation trending N-S, and shear sense indicators pointing top-to-the-North. S_2 increases down structure becoming the dominant tectonic fabric until the bottom of the IP Upper Units, with accompanying progressive increase of P-T conditions. In the O Pino Unit, metamorphism reached the amphibolite facies, with regional development of Ky-Sill-bearing mineral assemblages and widespread migmatization over the lowest structural levels. The schists and paragneisses SE of Santiago city contain large idiomorphic crystals of andalusite, also abundant within quartz veins, which appear invariably pseudomorphosed by light blue kyanite, grown in a prograde counter-clockwise P-T path (Castiñeiras, 2005). S_2 has been dated at *c.* 493-496 Ma, in migmatites from the base of the O Pino Unit (U-Pb in monazites; Abati *et al.*, 1999; Abati, 2002).

The Monte Castelo Gabbro Massif contains hectometric metapelitic xenoliths affected by high-T recrystallization during their incorporation to the gabbro body at *c.* 500-505 Ma (U-Pb

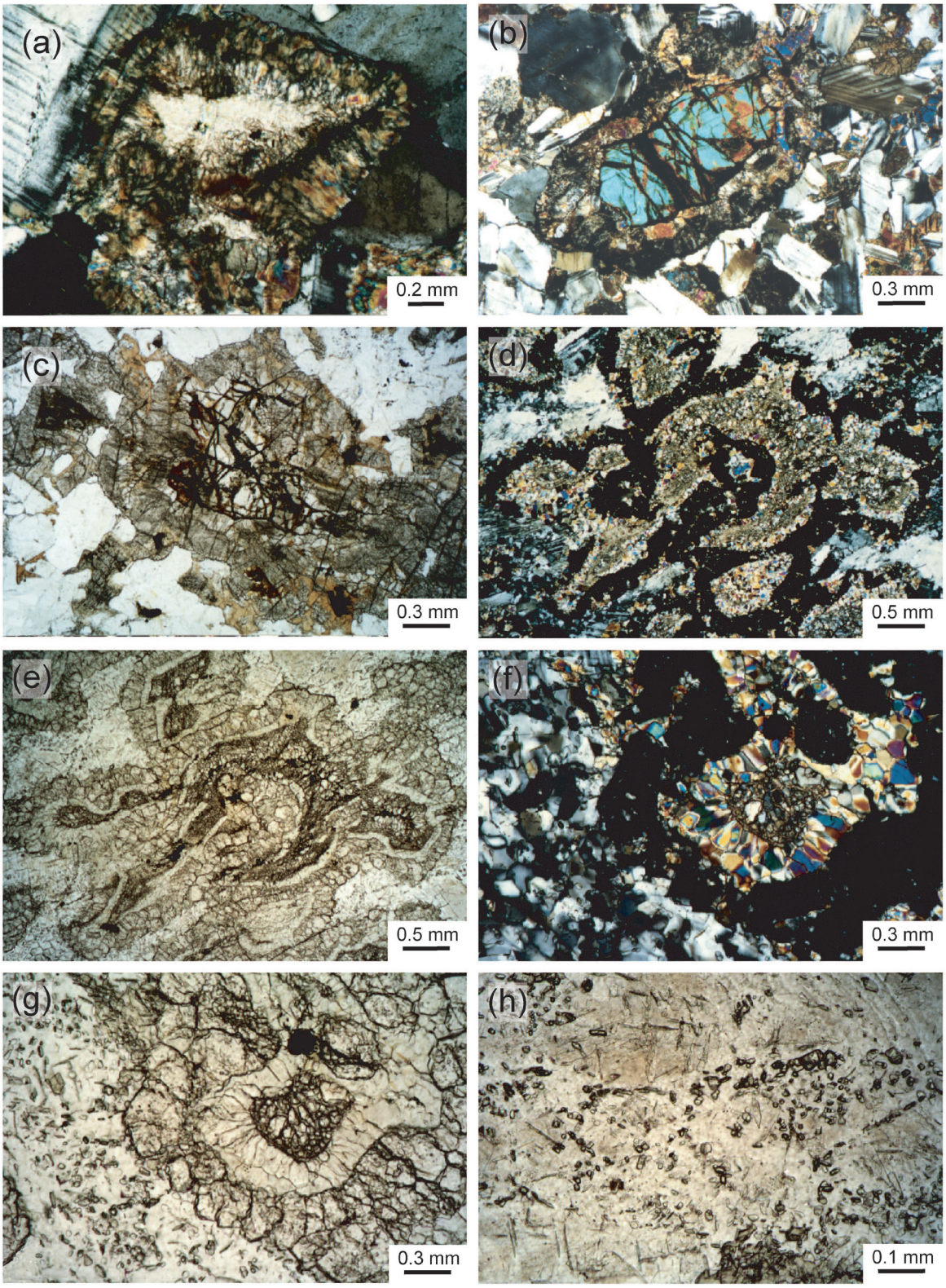

Fig. 22. Textural characteristics of the coronitic metagabbros from the Sobrado Unit, Órdenes Complex. (**a**) Olivine pseudomorph with core region replaced by anthophyllite-tremolite aggregate, and external corona of orthopyroxene-pargasite. (**b-c**) Orthopyroxene-clinopyroxene-garnet-pargasite corona between olivine and plagioclase. (**d-g**) Orthopyroxene aggregates after olivine separated from plagioclase by clinopyroxene (inner) and garnet (outer) coronas. (**h**) Recrystallized plagioclase with abundant inclusions of kyanite and corundum, also visible in (**f**) and (**g**). The development of these coronas is associated to a prograde path with drastic pressure increase (Arenas and Martínez Catalán, 2002).

in zircon; Abati *et al.*, 1999, 2007). These xenoliths were transformed in intermediate-P granulites (*c.* 800 °C and 9.5 kbar) during susequent prograde metamorphism at *c.* 498 Ma (U-Pb in monazite; Abati *et al.*, 1999). The mineral assemblage is formed by spinel-garnet-orthopyroxene-cordierite-sillimanite-biotite, being developed during a counter-clockwise metamorphic path (Abati *et al.*, 2003) (Fig. 19a). The garnet crystals exhibit thick overgrowth rims surrounding previous core domains developed at high-T and low-P conditions (Figs. 19b,c). Counter-clockwise P-T paths are generally associated with magmatic arcs where intense underplating generates strong heating at low pressure. Subsequent subduction of sections of the magmatic arc itself explains the drastic pressure increase, which occurred shortly after the gabbro intrusion. Still during the high-T evolution, the Monte Castelo massif was affected by a new intermediate-P shearing dated at *c.* 482 Ma (Abati *et al.*, 2007). A similar evolution can be recognized in the Corredoiras Unit. The large Corredoiras Orthogneiss Massif recrystallized under intermediate-P granulite facies and includes large xenoliths of pelitic granulites, strongly migmatised, from which identical counter-clockwise P-T paths have been inferred (González Cuadra, 2007). U-Pb dating in monazite obtained from these migmatitic xenoliths yielded an age of 484-493 Ma (Abati *et al.*, 1999), a similar range to that obtained in the Monte Castelo Unit.

Following the two first deformation phases, the tectonothermal evolution of the IP Upper Units is characterized by a new prograde tectonic event with collisional nature (D_3), which seems to be separated in time from the previous arc-related event. Therefore, the IP Upper Units are equivalent to an old basement deformed first during D_1 and D_2 and affected long afterwards by reworking associated to a new thickening event D_3. This evolution has been better identified in the SE part of the Órdenes Complex, in the Corredoiras Unit. There, the orthogneiss massif characteristic of this unit and its large xenoliths of migmatised pelitic granulites appear deformed by a generation of prograde shear zones (Fig. 20). These shear zones are up to 1 km thick and their associated foliation (S_3) exhibits N-S trending stretching lineation and consistent top-to-the-N kinematic indicators. When D_3 affects the metapelitic rocks, S_3 may have mylonitic character and is defined by a prograde mineral assemblage with garnet-staurolite-biotite, preferentially for the case of pelitic granulites formed during the previous cycle (González Cuadra, 2007) (Fig. 20). These shear zones have been interpreted as D_3 thrusts repeating slices of granulitic basement deformed and metamorphosed in Cambrian times (González Cuadra, 2007). There are not isotopic geochronological data in the Corredoiras Unit to constrain the age of the D_3 event in the IP Upper Unit. However, D_3 shear zones are clearly intersected at high angle by the Corredoiras Detachment (Fig. 20), which separate the IP Upper Units from the HP-HT Upper Units in the SE of the Órdenes Complex (Díaz García *et al.*, 1999b; González Cuadra *et al.*, 2007) (Fig. 20). An $^{40}Ar/^{39}Ar$ age of *c.* 375 Ma dating the activity in the Corredoiras Detachment (Dallmeyer *et al.*, 1997), can be taken as a minimum age for D_3.

Equivalent shear zones to those described in the Corredoiras Unit have been described in the O Pino Unit. Thrusting in this case is associated with recumbent folds vergent to the E-NE and accompanied by metamorphism under garnet-bearing amphibolite facies conditions (Gómez Barreiro *et al.*, 2006; Gómez Barreiro, 2007). S_3 in this particular case was dated at *c.* 397 Ma ($^{40}Ar/^{39}Ar$ dating on hornblende; Gómez Barreiro *et al.*, 2006). This is a reference chronology for D_3, which is thought to represent reworking of an old metamorphic basement in a much younger collisional setting. The Ponte Carreira and Corredoiras extensional detachments cut D_3 structures and consequently have been integrated in the gravitational collapse that followed D_3 crustal thickening.

High Pressure and High Temperature Upper Units

The lower part of the Upper Units consists of a HP-HT metamorphic belt. The protoliths are similar to those described in the IP Upper Units, but the intensity of deformation and metamorphism hinders the preservation of primary sedimentary or igneous features, that only in few cases can be recognized. The succession of the main deformation and metamorphic events are also comparable, regardless of their intensity, as well

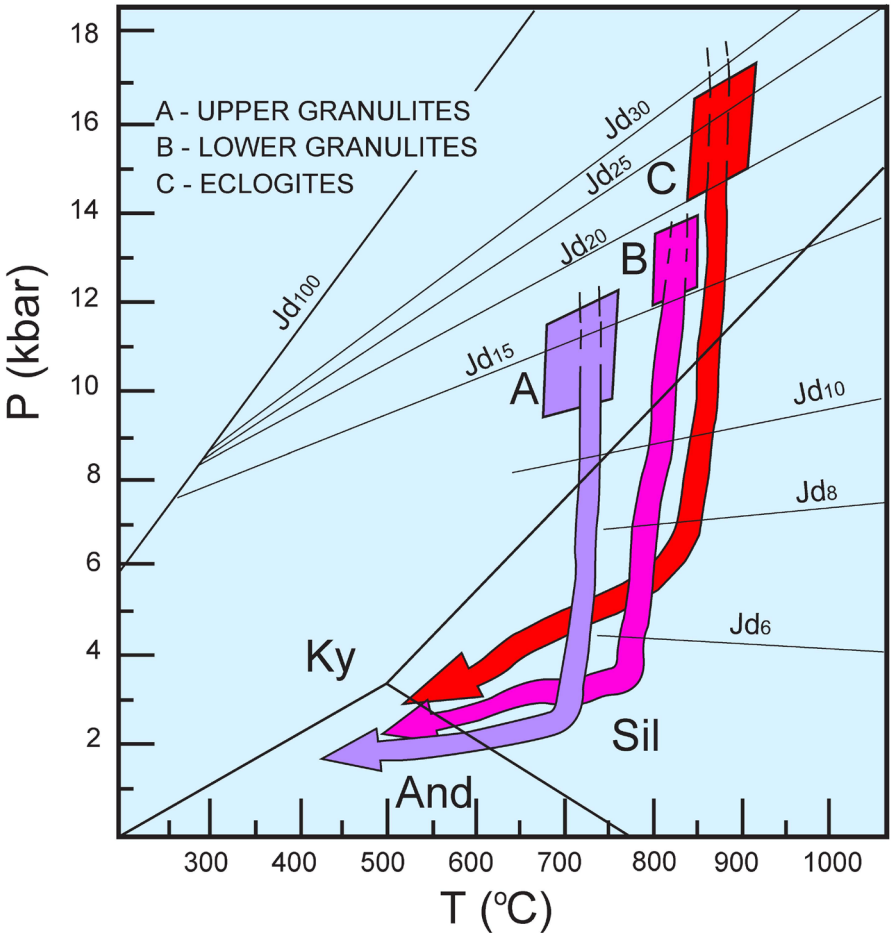

Fig. 23. P-T paths indicating the metamorphic evolution followed by some characteristic HP-HT lithologies from the Sobrado Unit (Órdenes Complex). Boxes in the diagram are indicative of peak conditions. Isopleths of jadeite content in clinopyroxenes coexisting with albite (Xalb=1) and quartz, and stability curves of the Al_2SiO_5 polymorphs are also shown. The P-T paths were calculated using Cpx-Grt thermobarometry (Díaz García *et al.*, 1999b).

as the isotopic geochronology obtained for them. The second metamorphic event is the one showing HP-HT characteristics. The tectonic fabrics and mineral assemblages of the first Cambrian, arc-related, metamorphic event were in this case affected by strong reworking, and they have been almost completely obliterated. However, the initial existence of this first event still can be detected, mainly due to the presence of relict monazites in high grade gneisses whose age has been determined by U-Pb.

Equivalent HP-HT units are known in the Variscan Belt outlining the Variscan suture, both in the Armorican Massif, French Massif Central and the Bohemian Massif (Ballèvre *et al.*, 2014). In some sectors the presence of mineral assemblages including coesite suggests that ultra-high-P conditions were reached at least locally (Lardeaux *et al.*, 2001). Peak pressures calculated so far for the NW Iberian Massif are close to ultra-high-P values, although evidence of coesite is still missing.

Lithologies and tectonothermal evolution

In the western sector of the Órdenes Complex, the Fornás Unit (Figs. 2 and 4) is mainly constituted by migmatitic garnet amphibolites with few mineral relicts of previous high-P granulites (Cpx-Grt-Pl) and coronitic metagabbros. Two kilometric inclusions of metaperidotites and garnet-bearing pyroxenites, and dispersed layers of paragneiss (Grt + Ky + Bt + Pl + Qtz + Kfs + Rt) can also be found in this unit (Gómez Barreiro, 2007).

In the eastern part of the Órdenes Complex, the HP-HT Upper Units are represented by the Sobrado, Melide and Belmil units, formed by similar lithological ensembles but variable thickness and structural complexity (Figs. 2, 4 and 20). The Sobrado Unit shows the most complete, though much thinned, HP-HT succession. It includes three tectonic slices, the intensity of HP metamorphism of which increases from top to bottom (Arenas and Martínez Catalán, 2002). The lower slice is formed by serpentinized ultramafic rocks, eclogites and Cpx-Grt rocks without

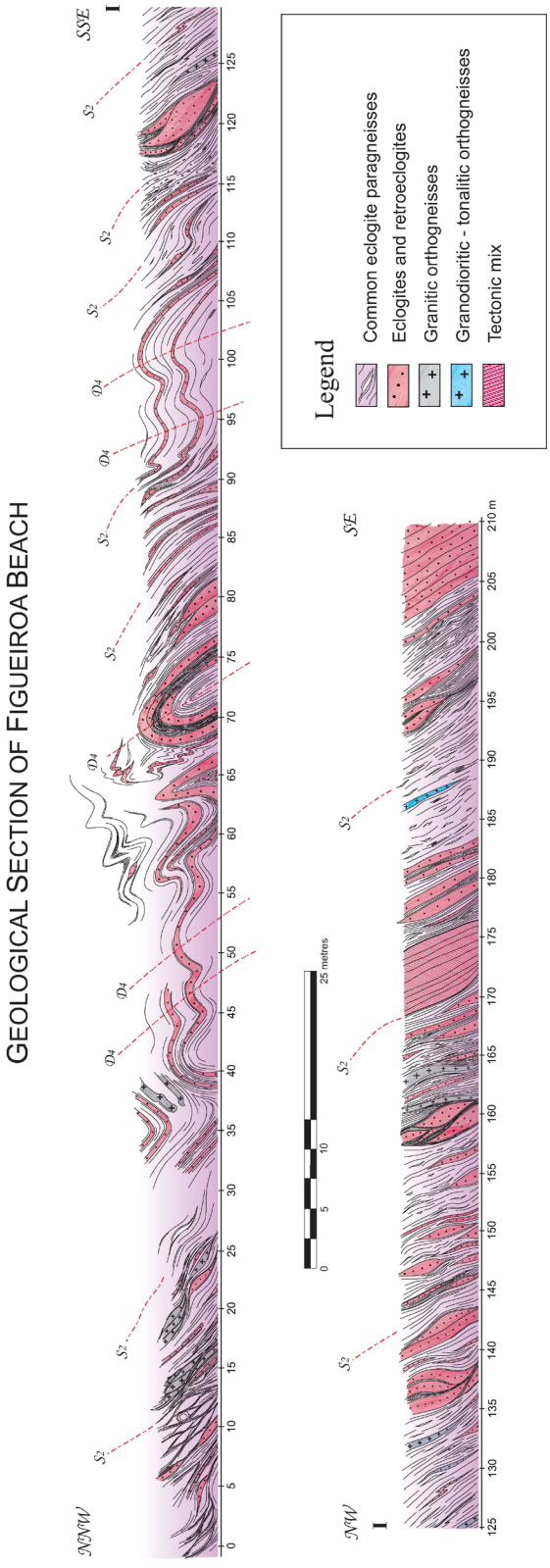

Fig. 24. Detailed section of the Banded Gneisses Formation (Capelada Unit) in the Figueiroa Beach, South of the Masanteo Peninsula (Cabo Ortegal Complex). The regional decompressive mylonitic foliation (S2) is affected by large recumbent folds (not visible in this section) and by upright folds (D4). The HP-HT fabric (S1) is completely overprinted by S2 and can be only observed in few eclogite pods.

omphacite or plagioclase (Fig. 21h). The intermediate slice mainly contains high-P granulites and variably migmatised paragneisses, while the upper slice consists of high-P granulites and paragneisses as well as retrogressive garnet-bearing amphibolites. The mafic layers defined by the granulites and amphibolites preserve lens-shaped inclusions of gabbros up to 2 km long (Fig. 20), and dated at *c.* 515 Ma (U-Pb in zircon; Fernández-Suárez *et al.*, 2007).

The gabbroic rocks of the Sobrado Unit show a rather complete textural evolution, from undeformed types with intact igneous texture and mineralogy (Cpx+Opx+Pl±Ol), through coronitic gabbros and recrystallized coronitic gabbros, to high-P granulites with grano-nematoblastic textures and without any relict of the previous stages. Such variability can be observed both at map scale, where large, intact, lens-shaped gabbro bodies exhibit long tails of high-P granulites, and at outcrop-scale where the whole transition can be observed at metric scale. Transformation from gabbro to coronitic metagabbro of the highest grade (Grt+Opx+Cpx+Prg+Pl+Ky+Crn), entails a sequenze of complex coronitic types, described by Arenas and Martínez Catalán (2002) (Fig. 22). Altogether, they define a prograde P-T path associated to subduction, with a peak pressure calculated at 16 Kbar in this unit (Arenas and Martínez Catalán, 2002). P-T conditions reached during the high-P event have been calculated using Cpx-Grt thermobarometry for each tectonic slice of the Sobrado Unit (Fig. 23). Pressure conditions obtained this way provide only minimum values, but temperature calculations are significant and close to real values or slightly overestimated (Fe^{2+} = Total Fe). These temperatures range between 725 °C in the upper slice, and 850 °C in the intermediate one, to 875 °C in the lower slice. Such range fits well with the strong migmatization experienced during the exhumation and progressive hydration of these units.

The diversity and tectonothermal evolution of the HP-HT rocks of the Cabo Ortegal Complex were described in great detail in the pioneering work of Vogel (1967), and later by Engels (1972) and Gil Ibarguchi *et al.* (1990). In this complex, the HP-HT Upper Units include two main juxtaposed counterparts, the Cedeira and Capelada units (Fig. 3). Both units have a similar litholog-

ical composition but different record of high-P metamorphism. The Capelada Unit occupies the upper structural level, and developed eclogite facies metamorphism, whereas the Cedeira Unit reached only granulite facies conditions. Another possible third HP-HT unit has been also described in the Cabo Ortegal Complex, the Peña Escrita Unit (Fig. 3). This is a small lens-shaped unit which crops-out at the South of the complex, constituted by mafic rocks whose structure and tectonothermal evolution are poorly constrained. Consequently, it is not clear yet whether this is a different unit or a section of either of the two large HP-HT Capelada and Cedeira units.

The Capelada Unit is *c.* 2000 m thick and, from bottom to top contains ultramafic rocks, high-P mafic granulites and eclogitic gneisses and eclogites (Fig. 3). Its lithological constitution and structure resembles that of an attenuated mantle-crust transition. Taking into account the age range of its protoliths (see below), this unit may represent a section of a Cambrian back-arc basin infilled with large amounts of terrigenous sediments, now exposed in the upper structural levels.

The eclogitic gneisses of the Capelada Unit (Banded Gneisses, Figs. 3 and 24) are mainly derived from semipelitic and greywackic sediments, and are intercalated with granitic and tonalitic orthogneisses (Albert *et al.*, 2012). These gneisses are usuallly migmatised and show mylonitic foliation (Figs, 21e and 24). Mafic rocks occur as numerous eclogite pods or bands within the gneisses and also forming a thick layer of eclogite separating this ensemble from the mafic and ultramafic rocks underneath (Figs. 3 and 24). In some sectors of that layer, pre-metamorphic mingling processes are still recognizable (Fig. 21f), as well as some lenses of augengneiss similar to those observed in the IP Upper Units. Mendia (1996) described three main eclogitic types: common eclogites, Fe-Ti eclogites after Fe-Ti gabbros, and Al-Mg eclogites derived from troctolitic gabbros. The high-P mineral assemblage in the later (Grt+Cr-Omp+Qtz+Ky+Zo+White mica+Rt) formed at *c.* 23 kbar (Mendia, 1996). The gabbroic protoliths of these eclogites were dated at *c.* 491-495 Ma (U-Pb in zircon; Ordoñez Casado *et al.*, 2001; Albert *et al.*, 2013), while the granitic protoliths of the orthogneisses yielded ages of *c.* 484-506 Ma (U-Pb in zircon; Albert *et al.*, 2013). On the other hand, U-Pb dating of detrital zircons from the paragneisses reported similar age populations to those obtained in the Cariño Unit (IP Upper Units). Therefore, it is considered that the source area for this sequence was also located in North Africa (Albert *et al.*, submitted).

The high-P granulites of the Capelada Unit are referred as the Bacariza Formation (Fig. 3) The dominant mafic members contain Grt+Cpx-+Pl+Qtz+Zo-Czo+Hbl+Rt±Ky (Fig. 21c), although other associated types with intermediate composition may be found (Puelles, 2004; Puelles *et al.*, 2005). Extensive partial melting and retrogression along with strong shearing experienced during exhumation conferred a heterogeneous character to this formation (Figs. 21c and 21d). The most common lithologies are a variety of amphibolic gneisses, which preserve the HP-HT mineral assemblage in less retrogressed mafic lenses surrounded by a intense mylonitic regional foliation (Fig. 21b). Given the absence of metasedimentary rocks and the presence of metaigneous types, probably derived both from mafic and scarcer granitic protoliths, the most probable precursor for the granulite formation was a plutonic complex associated with a magmatic arc, which is in agreement with the back-arc setting proposed for the whole Capelada Unit. U-Pb zircon dating of a non-retrogressed mafic granulite yielded an age of *c.* 520 Ma, interpreted as the chronology of the gabbroic protoliths (Fernández-Suárez *et al.*, 2007).

The ultramafic rocks of the Capelada Unit occur in three massifs, from North to South the Limo, Herbeira and Uzal massifs (Figs. 3 and 21a). These are structurally connected and altogether represent the largest ultramafic unit identified in the Variscan Belt. The thicker ultramafic succession appears in the Herbeira Massif, being constituted by *c.* 600 m of harzburgites and dunites with many alternations of pyroxenites. It has been interpreted as a section of a mantle wedge above a subduction zone and it is considered as one of the world-class examples of a heterogeneous upper mantle (Girardeau *et al.*, 1989; Girardeau and Gil Ibarguchi, 1991). Some ultramafic layers contain chromitites enrich in Pt-Pd (Moreno *et al.*, 2001). A Sm-Nd isochrone

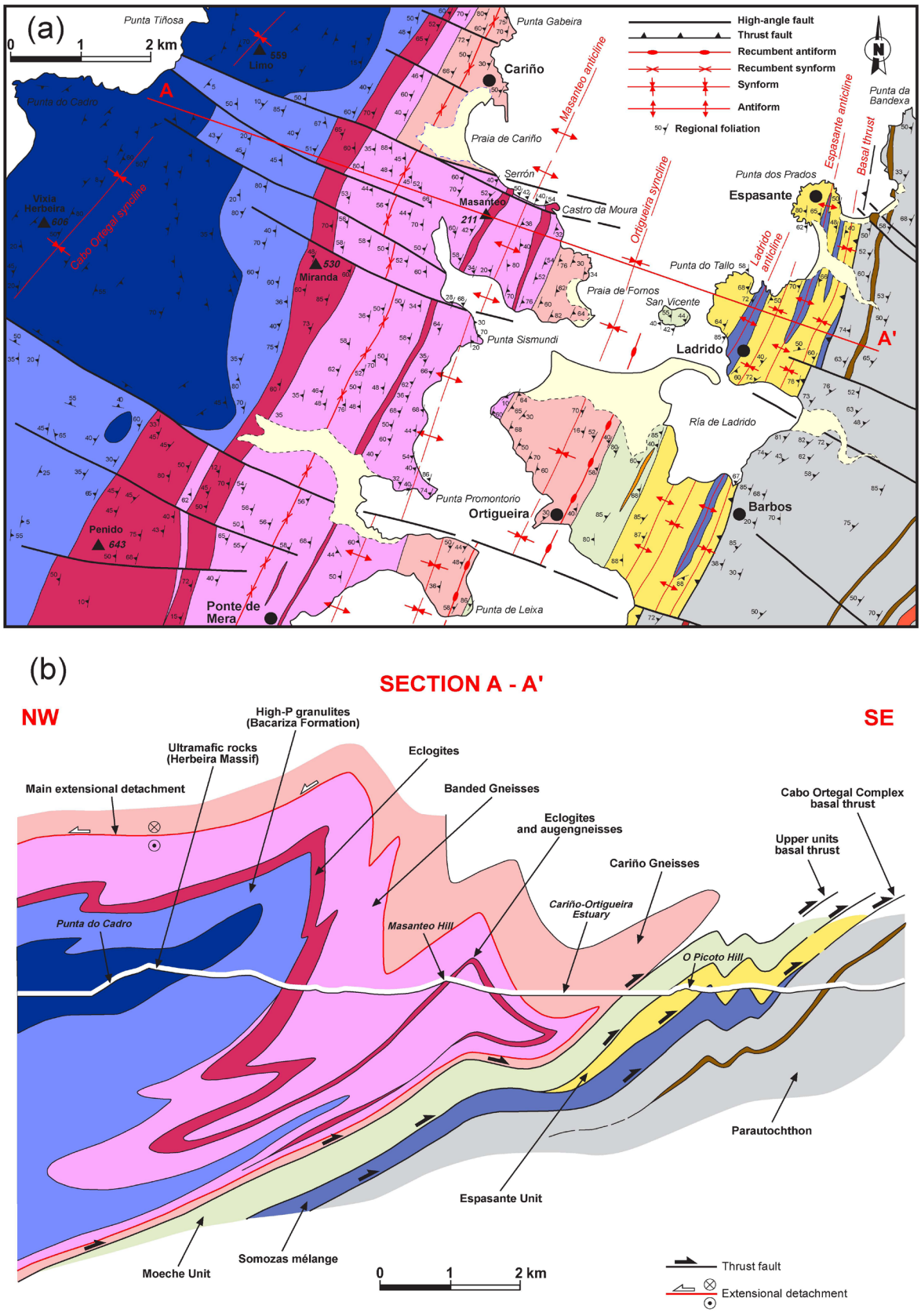

Fig. 25. (**a**) Geological map and (**b**) cross section of the northern part of the Cabo Ortegal Complex.

in the pyroxenite rocks yielded an age of *c.* 500 Ma, interpreted as the chronology of the protoliths (Santos *et al.*, 2002). These data confirm the similar age of this ultramafic section relative to the rest of the formations included in the Capelada Unit.

The Cedeira Unit has a similar thickness to the Capelada Unit and it is constituted by migmatitic gneisses (Chimparra Gneisses) and metabasic rocks, which include high-P granulites, high-T amphibolites and coronitic metagabbros (Candieira Formation) (Fig. 3). The gneissic rocks have comparable composition to the upper gneisses of the Capelada Unit, but very scarce mafic inclusions exist that in this case have mineral assemblages typical of high-P granulites (Vogel, 1967). Coronitic gabbros similar to those of the Sobrado Unit of the Órdenes Complex are locally abundant. The basal part of this unit is a complex tectonic boundary, locally known as the Carreiro Shear Zone, which separates the HP-HT Upper Units from the Purrido Ophiolite (Vogel, 1967) (Fig. 3). This shear zone consists of an imbrication of paragneisses and ultramafic rocks (Azcárraga, 2000). The latter are mylonitic garnet-bearing harzburgites and Ti-clinohumite-bearing orthopyroxenites, with mineral assemblages equilibrated at high to ultra-high-P (Gil Ibarguchi *et al.*, 1999).

The most relevant structural feature in the HP-HT Upper Units is the presence of a widespread mylonitic foliation (Figs. 21b and 24) (Marcos *et al.*, 1984). This mylonitic foliation S_2 reworks and usually obliterates previous tectonic fabrics and mineral assemblages generated during the high-P event (D_1). Any previous tectonothermal record associated with the Cambrian history of these units has been almost entirely overprinted. During the development of S_2, the Bacariza Formation and its equivalents in the Sobrado Unit, as well as all the high-P gneisses, were affected by intense hydration and migmatization. P-T paths contemporary to S_2 depict a drastic isothermal exhumation. D_1 mineral assemblages with Grt+Cpx+Zo+Rt were replaced by more hydrated phases, such as Grt+Hbl+Czo+Spn (Vogel, 1967; Gil Ibarguchi *et al.*, 1990; Arenas, 1991; Mendia, 1996). The stretching lineation associated with S_2 trends NNE-SSW and D_2 kinematic indicators consistently indicate top-to-the-North sense of shearing (Ábalos *et al.*, 1994, 1996). Yet, S_1 prevails in some eclogites and granulites of the Cabo Ortegal Complex and presents, relative to S_2, similar kinematics and stretching lineation trend (Ábalos, 1997; Ábalos *et al.*, 2003). In the same complex, S_2 is affected by a train of large recumbent folds vergent to the East (Fig. 25). The largest of these folds is the recumbent synform of the Capelada Unit, first described by Marcos *et al.* (1984) (Fig. 3). There are other similar folds related to the same generation, as the large recumbent antiform which inverted the position of the Cariño gneisses below the Capelada Unit (Fig. 25). These large folds do not show in general penetrative axial planar foliation, which suggests limited contribution of compressional forces during its nucleation and amplification. An exception exists in the surrounding areas of the hinge zone of the large recumbent synform of the Capelada Unit, where the development of a slightly pervasive axial planar S_2 can be observed in the gneisses of the Cariño Unit. This train of recumbent folds developed during the exhumation of a high-ultra-high-P continental subduction complex, most probably as a result of thrusting over the underlying units (Albert *et al.*, 2012) (Fig. 25).

Chronology of the metamorphic events

The gneissic rocks of the HP-HT Upper Units contain monazite dated at *c.* 500-480 Ma, both in the Cabo Ortegal Complex (Chimparra Gneisses) and the Órdenes Complex (Belmil and Sobrado gneisses) (Fernández-Suárez *et al.*, 2002). No other evidence for such Cambrian tectonothermal activity has been found so far, as the HP-HT event seems to have reworked any previous tectonic fabrics and mineral assemblages. The age of this event coincides with the first tectonothermal event described for the IP Upper Units, so they both can be integrated in the dynamics of a peri-Gondwanan magmatic arc during the Cambrian.

The second HP-HT event has been dated in a variety of rocks. A first age of *c.* 390 Ma obtained in the large eclogite layer of the Cabo Ortegal Complex was interpreted as dating the high-P metamorphism (SHRIMP, U-Pb in zircon; Ordóñez Casado *et al.*, 2001). The same methodology was used later to constrain the age of the high-P event in a mafic granulite of the Sobrado

Unit (*c.* 410-385 Ma), in a similar mafic granulite of the Bacariza Formation (*c.* 410-385 Ma) and in a leucosome related to the post high-P partial melting affecting the same formation (*c.* 397-391 Ma) (Fernández-Suárez *et al.*, 2007). An additional U-Pb zircon age of *c.* 391 Ma has been obtained in a non-retrogressed eclogite body included in the Banded Gneisses Formation (LA-ICP-MS; Albert *et al.*, 2013). Therefore, the real age of the subduction must be contemporary or somewhat younger than the oldest metamorphic ages obtained for rocks recording this event (*c.* 410-400 Ma). The age of exhumation of the subduction complex was bracketed by means of $^{40}Ar/^{39}Ar$ dating of retrogressive hornblende amphiboles associated to S_2 to the range 389-381 Ma (Peucat *et al.*, 1990).

The reported ages indicate that the HP-HT event and subsequent exhumation, are coeval to the collisional event described for the overlying IP Upper Units. It can be concluded that the whole Early to Middle Devonian tectonometamorphic record of the Upper Units accounts for a single collisional event, previous to Variscan deformation *sensu lato*. Taking into account the provenance deduced for the Upper Units, the margin of Gondwana was one of the continents involved in that eo-Variscan collision.

Somozas Mélange

The lowest part of the Cabo Ortegal Complex is formed by a thick mélange unit, only represented in this position within the realm of the allochthonous complexes of NW Iberia. The Somozas Mélange crops out in the eastern sector of the Cabo Ortegal Complex (Fig. 3) and was first described by Arenas *et al.* (1986), and then

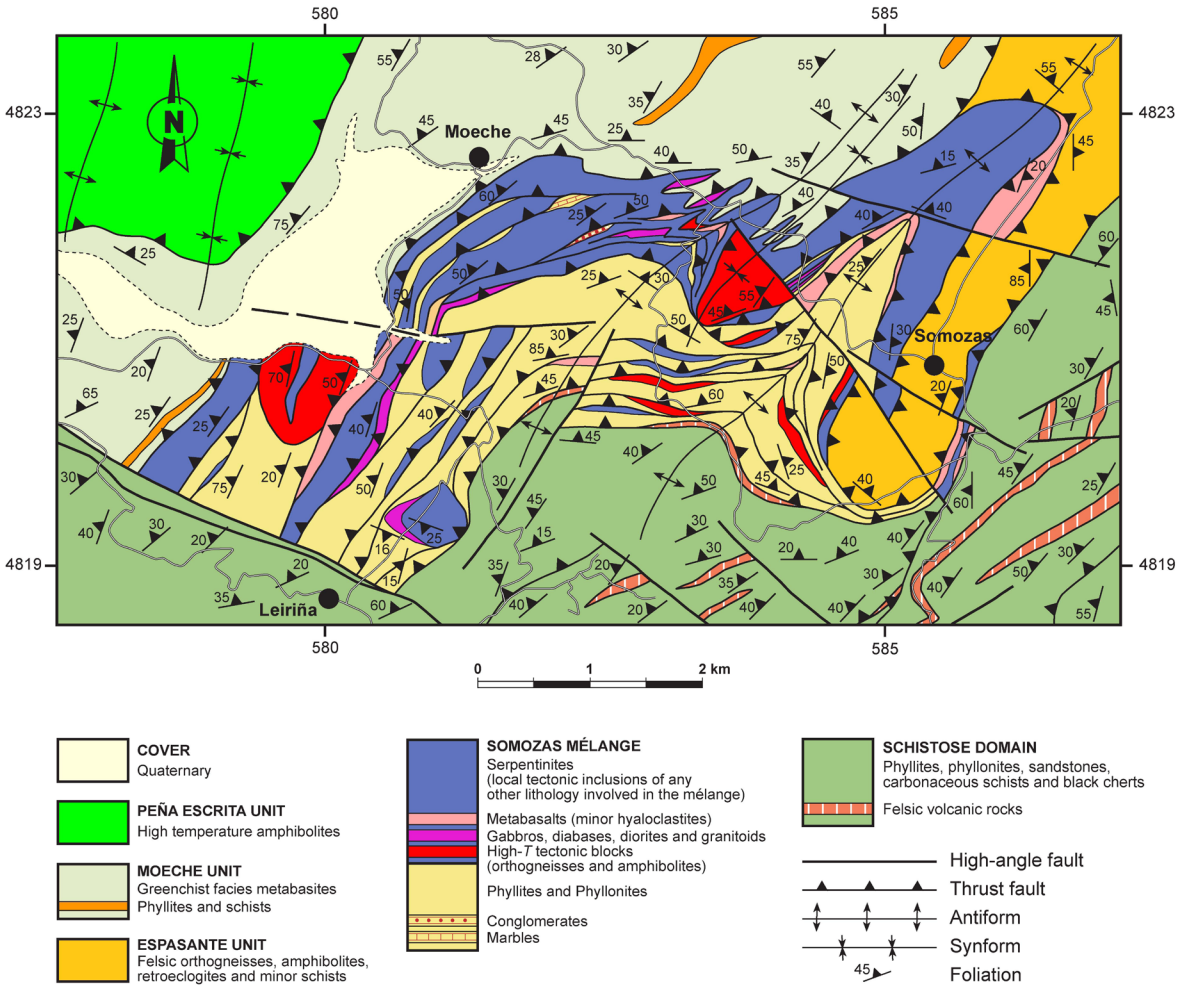

Fig. 26. Detailed geological map of the southern part of the Somozas Mélange (Cabo Ortegal Complex), between the Somozas and Moeche villages.

by Arenas (1988) and Marcos *et al.* (2002). The mélange was revisited by Arenas *et al.* (2009), who provided a detailed mapping, compositional data of igneous rocks and some U-Pb ages. This unit, however, shows unique features at the scale of the allochthonous complexes, the interpretation of its origin and meaning being a real challenge.

The Somozas Mélange is *c.* 1800 m thick, dips gently to the West and intersects the contact between the Basal and Ophiolitic units (Espasante and Moeche units, respectively; Figs. 25 and 26). The upper contact of the mélange is therefore an out-of-sequence thrust that cuts part of the allochthonous pile located above. The mélange unit has two members with different lithologies and meaning (Fig. 26). The upper member is a *c.* 800 m thick serpentinite mélange, consisting of a highly sheared serpentinite matrix that wraps around tectonic blocks with variable thickness, from metric to kilometric (Fig. 26). These blocks are made up of gabbros, diabases, granitoids, metabasalts, andesitic basalts, pillow breccias, pillow lavas, hyaloclastites, marbles, phyllites, sandstones and conglomerates, plus other high-T metamorphic blocks of orthogneisses and amphibolites, some of which contain zoisite and rutile. Many of these tectonic blocks are exotic, as they are unknown in the rest of the allochthonous complexes and Parautochthon. The lower member is a *c.* 1000 m thick mélange with a matrix formed by ocher-colored phyllites or blue phyllonites, and tectonic blocks of the lithologies involved in the upper serpentinite mélange (Fig. 26). No evident high-P rocks have been described so far in the Somozas Mélange, though some of the high-T tectonic blocks reached at least the higher pressure part of the amphibolite facies (Arenas, 1988).

U-Pb zircon dating was performed in a tonalitic orthogneiss from a large high-T tectonic block and two slightly deformed granitoids affected by low grade recrystallization (Arenas *et al.*, 2009). The high-T tonalitic orthogneiss has an age of *c.* 485 Ma (U-Pb in zircon, SHRIMP), while the two granitoids yielded ages of *c.* 499 Ma (U-Pb in zircon, SHRIMP) and *c.* 527 Ma (U-Pb in zircon, LA-ICP-MS). The composition of the igneous rocks involved in the mélange, either volcanic, plutonic or dykes, shows clear affinity with a volcanic arc, a setting also supported by an ubiquitous negative Nb-anomaly (Fig. 12) (Arenas *et al.*, 2009). On the other hand, U-Pb ages of detrital zircons extracted from a tectonic block of conglomerate indicate an Early-Middle Ordovician maximum deposition age and derivation from the West African Craton (Arenas *et al.*, 2009).

The U-Pb ages along with the whole rock geochemical data set favors the hypothesis that the Somozas Mélange contains material derived from a peri-Gondwanan magmatic arc. Although the age of the mélange is unknown, the structural position of this unit suggests a relationship with the subduction and accretionary processes that affected the Basal Units. The development of a serpentinite mélange such as the upper member of this unit implies the existence of a long-lasting subduction process, capable of generating a low-viscosity channel in the overlying mantle wedge (Gerya *et al.*, 2002; Hebert *et al.*, 2009). The lower member was developed later, probably during the imbrication of the upper member with the upper part of the Parautochthon (Fig. 26). Therefore, the age of the mélange should be bracketed between the age of the subduction of the Basal Units (*c.* 370 Ma; Abati *et al.*, 2010) and the age of its basal imbrication. The age of the latter is unknown, but it should be similar or slighty younger than the age of the basal thrust that moved the Parautochthon and the rest of the allochthonous complexes eastwards (*c.* 343 Ma; Dallmeyer *et al.*, 1997).

Provenance of the continental terranes

The provenance of the continental terranes included in the allochthonous complexes has been somewhat enigmatic until recent times. The Variscan Belt was formed by the collision of two large continental masses, Gondwana and Laurussia, and this scenario leads to two different possibilities for the provenance of the terranes located in the most internal part of the belt. Moreover, it is also believed that other suspect terranes located in an intermediate paleogeographic position (*e.g.* microcontinents or volcanic arcs) could have been involved in the orogen too, thus introducing further elements to be taken into account when considering the origin of the allochthonous

terranes.

The provenance of the Upper Units was initially ascribed to a section of the Gondwanan margin surrounding the West Africa Craton (WAC), based on U-Pb data of detrital zircons from the uppermost greywackic series of the Betanzos Unit, in the Órdenes Complex (Fernández-Suárez *et al.*, 2003). Additional U-Pb and Hf isotopes in zircon from the metagreywackes of the Cariño Unit (Cabo Ortegal Complex) have provided firmer grounds to this interpretation. They contain zircon populations with Archean, Eburnean and Cadomian ages, as well as scarce and scattered Mesoproterozoic grains unlikely to represent a major crust generation pulse in the source area of the siliciclastic unit (Albert *et al.*, 2015). Moreover, considering the Sm-Nd isotopic signature and abundant input of juvenile material (Fuenlabrada *et al.*, 2010), it can be concluded that the source area for the Upper Units was also located in the proximity of a volcanic arc (Fig. 27).

In the Basal Units, the U-Pb data of detrital zircons from the metagreywackes are also consistent with source areas in the periphery of the WAC. However, their higher content in Stenian-Tonian zircons was considered indicative of a more easterly provenance, *i.e.* closer to the Sahara Craton (Díez Fernández *et al.*, 2010). On the other hand, Nd model ages obtained in the greywackes of the Basal Units fall in the range 1743-2223 Ma (Fuenlabrada *et al.*, 2012), suggesting dominant WAC isotopic sources, but located far away from any source of juvenile material such as peri-Gondwanan arc system (Fig. 27).

The source area for the Parautochthon and autochthonous domains of the Iberian Massif was probably located further to the East, as they are characterized by higher Stenian-Tonian zircon populations (Fig. 27) (Díez Fernández *et al.*, 2012a; Fernández-Suárez *et al.*, 2014; Shaw *et al.*, 2014).

Paleogeography and Variscan evolution

Previous models dealing with the evolution of the Upper Units considered them as a section of a peri-Gondwanan volcanic arc rifted from the continental margin in Cambrian–Early Ordovician times, and then drifted northward, open-

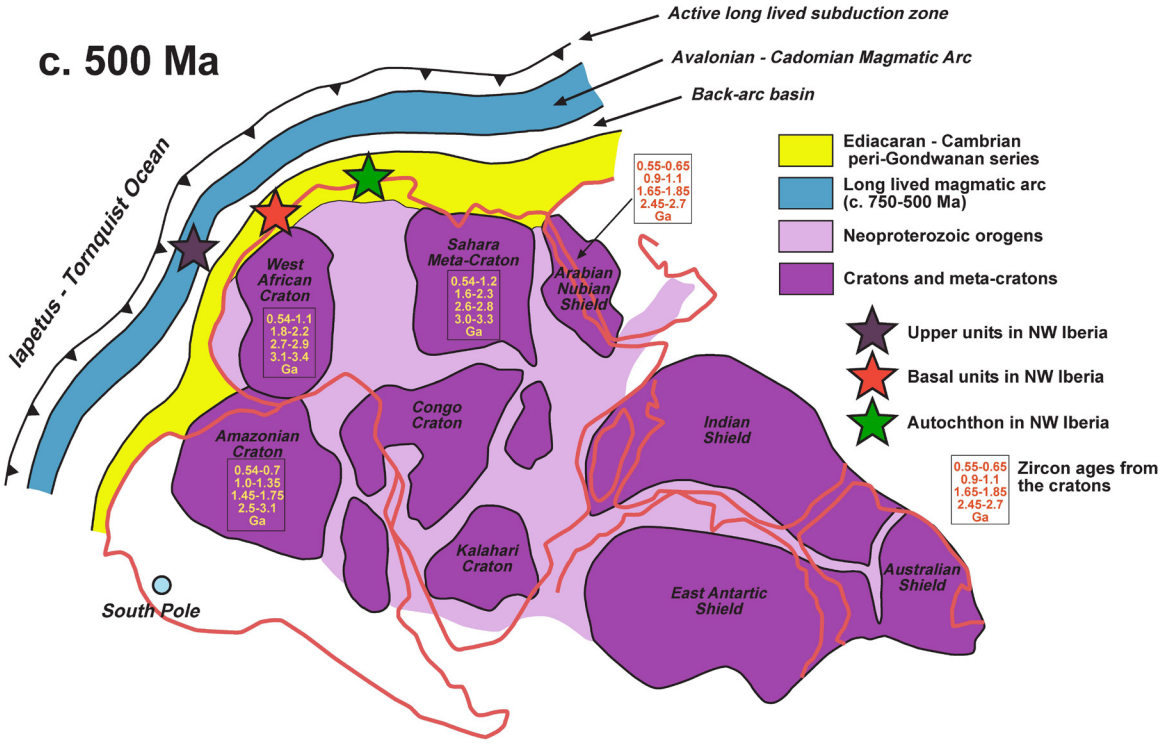

Fig. 27. Cartoon showing the paleoposition of the continental terranes exposed in the NW of the Iberian Massif.

ing the Rheic Ocean in its wake. These events would have coincided with the rift and drift of the Avalonian microcontinent (Fig. 28). The Upper Units, however, would have had a different identity and provenance since they were located further to the East along the paleo-margin of Gondwana (Abati *et al.*, 2007; Gómez Barreiro *et al.*, 2007; Díez Fernández *et al.*, 2010). The high- to ultrahigh-pressure (HP-UHP) metamorphic event that affected the lower section of the Upper Units at *c.* 410-390 Ma would have been generated during the subduction of this terrane under the southern margin of Laurussia, this process indicating the switch from a divergent to a convergent setting in the evolution of the Rheic Ocean (Fig. 28). This geodynamic evolution would imply that the Variscan ophiolitic units of NW Iberia were developed in the realm of the Rheic Ocean. The Cambrian ophiolites – with the exception of the Bazar Ophiolite– would be related to early stages in the opening of this ocean, while the Devonian ophiolites would have been formed during the final stages of its closure (Arenas *et al.*, 2007a). For this reason, it had been proposed that the Devonian ophiolites were formed in a northward dipping intra-Rheic Ocean supra-subduction zone located close to the southern margin of Laurussia (Díaz García *et al.*, 1999a; Sánchez Martínez *et al.*, 2007a). Such intraoceanic subduction zone would have generated buoyant oceanic lithosphere that would have been readily accreted beneath Laurussia and eventually obducted over the external margin of Gondwana (Basal Units) at the beginning of the Variscan cycle (*c.* 370 Ma). Furthermore, the activity of this intraoceanic subduction zone would have consumed a significant tract of the Rheic Ocean, thus explaining the general absence of typical N-MORB lithosphere in the Variscan sutures.

However, the previous models that linked the generation of the Devonian ophiolites to an open-ocean setting were challenged by new isotopic data that revealed interaction of the Devonian gabbroic protoliths with old continental crust (see above). Many of the zircons analyzed in mafic rocks from the Purrido and Moeche ophiolites show Lu-Hf isotopic compositions only compatible with a continental origin. These zircons can be only interpreted as inherited crystals incorporated into the mafic magmas (Sánchez Martínez *et al.*, 2011; Arenas *et al.*, 2014b). Consequently, there is no conclusive evidence to link the generation of the Devonian ophiolites either to the evolution of the Rheic Ocean or to an intraoceanic subduction zone active in a mature ocean basin. If the connection between the Variscan suture of NW Iberia and the evolution of the Rheic Ocean is called into question, so must be the interpretation of the Upper Units as a peri-Gondwanan terrane that drifted away during the opening of this Paleozoic ocean. Moreover, problems also exist in attributing the development of HP–UHP metamorphism in the trailing edge of a rather small terrane to its collision with Laurussia. In this regard, deep seating of continental crust is usually associated with subduction of the thinned margin of a large continent prior to its collision with another large continent (Warren *et al.*, 2008; Beaumont *et al.*, 2009).

The age of the HP-UHP metamorphic event in the Upper Units (no younger than 400-390 Ma) is close to that of the mafic rocks of the Upper Ophiolitic Units (*c.* 400-395 Ma). Yet, the U-Pb geochronology provides the age of the HT zircon growth, which probably occurred sometime after the continental margin sank into the mantle. Accordingly, the peak pressure of the HP event must have been reached prior to 400-390 Ma since this age likely marks a point along the exhumation/decompression path after subduction (Fernández-Suárez *et al.*, 2007). Consequently, this continental subduction predates the generation of the Devonian mafic rocks (Sánchez Martínez *et al.*, 2007a; Martínez Catalán *et al.*, 2009). Considering the new Lu-Hf isotope geochemistry of the Devonian ophiolites (400-395 Ma) and the detailed U-Pb geochronology of the two HP metamorphic events (>400 Ma and ~370 Ma), Arenas *et al.* (2014a) conceived a model of two successive collision events between Gondwana and Laurussia, each of them taking place in a context of oblique convergence and separated by the opening of a rather wide oceanic basin, probably of pull-apart type (Fig. 29).

According to the latter model, the Upper Units became the most external part of the Gondwanan margin, a rather wide continental shelf containing thick turbiditic series intruded by large massifs of gabbros and granitoids. That lithological ensemble resulted from volcanic arc activity in

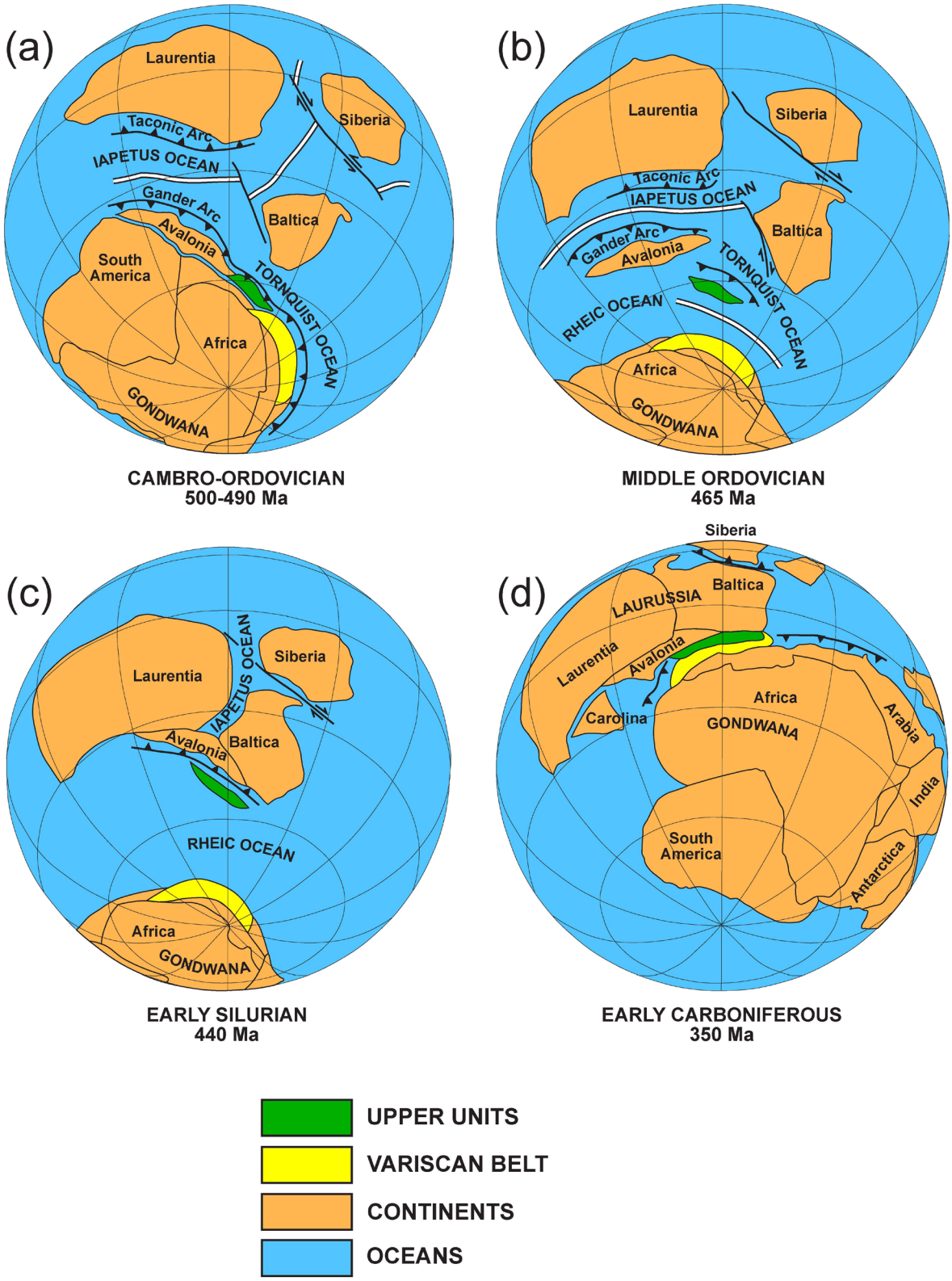

Fig. 28. Paleozoic paleogeography showing the distribution of terranes in the peri-Gondwanan realm and the main stages of the assembly of Pangea. This model interpreted the Upper Units as a far-traveled terrane drifted from Gondwana and finally accreted to the Southern margin of Laurussia. The Rheic Ocean opened in Late Cambrian-Early Ordovician times and widened during drifting to the North of Avalonia and the Upper Units of NW Iberia. (Gómez Barreiro *et al.*, 2007)

Cambrian times, which was followed by significant extension and rift-related magmatism in the back-arc region. This shelf did not witness significant new igneous activity or deformation until the onset of the HP–UHP metamorphic event, and hence it shows the characteristics of a typical passive margin for most of the Ordovician and Silurian. In the geological record covering this time interval there is no evidence suggesting any significant separation of this continental shelf from the Gondwanan mainland. Siluro-Devonian convergence between Gondwana and Laurussia led to a first continental collision before 400-390 Ma, including the dextral, oblique subduction to the North (Ábalos *et al.*, 2003) of the most external and thinned part of the Gondwanan margin accompanied by the first HP–UHP metamorphism (Albert *et al.*, submitted). The collision probably affected the eastern part of Avalonia and the Baltic margin (Fig. 29).

Further lateral motion between Gondwana and Laurussia favored the rapid generation of a rather wide pull-apart basin in Early Devonian times, which we interpret as the tectonic setting for the generation of the *c.* 395 Ma mafic rocks forming the most typical ophiolites found in the Variscan Belt (Fig. 29). The pull-apart basin currently being generated between the North American Plate and the Caribbean Plate can be considered a modern analogue for this setting, although in this case the lateral component is sinistral. The Gonâve microplate occupies the pull-apart basin and comprises oceanic lithosphere with a rather thin or completely absent sedimentary cover (Brink *et al.*, 2002). This oceanic lithosphere is being generated by the activity of the Mid-Cayman Spreading Centre. In this modern analogue, as was probably the case at the beginning of Pangea assembly, the pull-apart basin followed a period of continental convergence responsible for the high-P belts in northern Cuba and Hispaniola (García Casco *et al.*, 2008; Sommer *et al.*, 2011).

Subsequent convergence eventually closed the pull-apart basin and forced the accretion of buoyant oceanic lithosphere beneath the northern continent starting at *c.* 380 Ma (Careón and Purrido ophiolites; Dallmeyer *et al.*, 1997). The accreted oceanic lithosphere is mostly metamorphosed to the amphibolite facies, but the occasional presence of corundum-bearing metamorphic soles indicates the presence of local higher thermal gradients (Díaz García *et al.*, 1999a). Later accretion of more Devonian mafic slices took place under greenschist facies conditions (Moeche Ophiolite), and was followed by the accretion of mafic complexes rimming the continental margin that were formed within the Cambrian peri-Gondwanan volcanic arc (Vila de Cruces Ophiolite). The final outcome was the generation of a complex suture zone that records protracted convergence and is characterized by the presence of a double ophiolitic belt made of lithological sequences with contrasting origin and age: the Upper Ophiolitic Units of Devonian age and the Lower Ophiolitic Units of Cambrian age. The occurrence of a thick serpentinite mélange at the base of the allochthonous pile was interpreted in the context of dextral convergence (Somozas Mélange; Arenas *et al.*, 2009).

Further dextral convergence caused north-directed subduction of the Gondwana margin under Laurussia and the rest of the accreted sections of Cambrian and Devonian ophiolitic ensembles at *c.* 370 Ma (Díez Fernández *et al.*, 2012d, 2012e). This subduction affected a piece of the Gondwanan margin with a more easterly provenance (in Gondwanan margin coordinates; Basal Units; Díez Fernández *et al.*, 2010; Fuenlabrada *et al.*, 2012). This is the suggested setting for the development of the second HP metamorphic event, formed under LIT conditions and generating C-type eclogites, blueschists and HP metapelites (Fig. 29). Continental subduction evolved to a collisional scenario as more internal sections of Gondwana were underthrust. Convergence continued for about 70 m.y. (Dallmeyer *et al.*, 1997) as intracontinental deformation progressed southward, reaching inner sections of Gondwana while building a foreland fold and thrust belt in the external parts of the orogen (Peréz-Estaún *et al.*, 1991).

Conclusions

NW Iberia includes a rather complete section of the Variscan suture, where different terranes with continental or oceanic affinities appear with clear structural relationships between them. Three groups of terranes, namely Upper,

Ophiolitic and Basal units and a frontal tectonic mélange occur in Galicia, in the Cabo Ortegal, Órdenes and Malpica-Tui complexes. They constitute a huge allochthonous pile thrust over the Iberian parautochthonous and autochthonous domains, which represent a section of the Gondwanan margin that escaped continental subduction during the Variscan cycle (Schistose Domain of Galicia-Trás-os-Montes and Central Iberian Zone).

Previous ideas about the final assembly of Pangea call upon a single-stage collision between Gondwana and Laurussia in Carboniferous times. However, the new data regarding the origin and tectonothermal evolution of the allochthonous terranes involved in the Variscan suture of NW Iberia suggest a more complex and longer history for the early stages of supercontinent assembly. According to them, the interaction between the colliding margins started earlier and lasted longer than previously considered. These data are consistent with two successive collisional events separated by the generation of a relatively ephemeral oceanic basin. The first collision occurred in Early Devonian times (before *c.* 400-390 Ma) and caused deep subduction of a section of the margin of Gondwana and the generation of a HP–UHP metamorphic belt (Upper Units of the Variscan suture). Lateral motion between Gondwana and Laurussia favored the opening of a relatively wide pull-apart basin at *c.* 400-395 Ma. The rapid closure of this basin started at *c.* 380 Ma and caused the accretion of buoyant oceanic lithosphere of Devonian age below the northern continent. This oceanic lithosphere is represented by the most common ophiolites found in the Variscan Belt (Upper Ophiolitic Units). Mafic slices with a similar age and showing greenschist facies recrystallization were accreted later, followed by mafic complexes with Cambrian age generated by the activity of peri-Gondwanan volcanic arcs

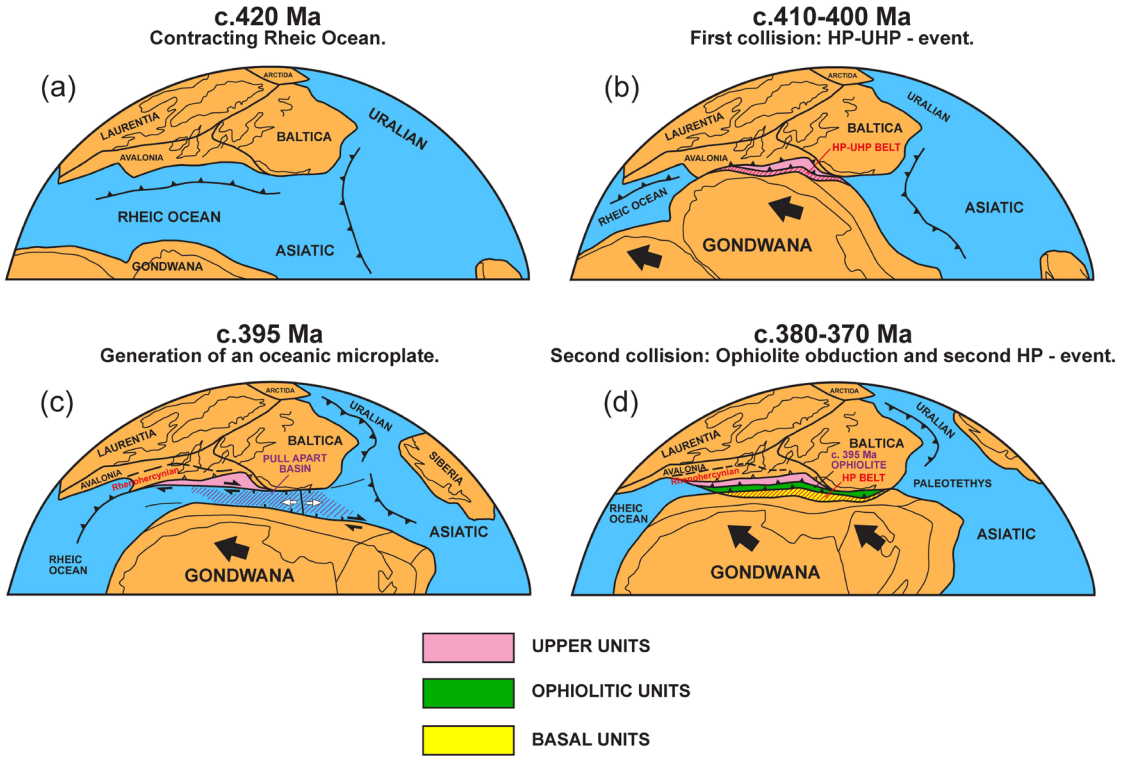

Fig. 29. (**a**) Reconstruction of the Rheic Ocean realm at the Silurian-Devonian boundary, and (**b**) the initial collision between Gondwana and Laurussia at *c.* 410-400 Ma following the complete closure of the Rheic Ocean. This collision caused subduction of a section of the margin of Gondwana and generated the HP-UHP metamorphic belt preserved in the allochthonous Upper Units exposed in the Variscan suture. The true Rheic Ocean suture is not represented in NW Iberia. (**c**) Dextral motion between Gondwana and Laurussia favored the opening of a rather ephemeral pull-apart basin at *c.* 395 Ma, accompanied by generation of new oceanic lithosphere. (**d**) The second and final collision at *c.* 380-370 Ma caused the accretion of buoyant oceanic lithosphere followed by new contnental subduction affecting the margin of Gondwana, thereby developing a second HP-LIT metamorphic belt. The two different HP belts and the ophiolitic units dated at *c.* 395 Ma can be identified in the allochthonous terranes that outline the Variscan Belt from Iberia to the Bohemian Massif.

that progressively reached the collision zone as the basin shrank (Lower Ophiolitic Units). Finally, further convergence led to a new collision with another section of the Gondwanan margin, with generation of a second HP-LIT belt at *c.* 370 Ma (Basal Units). Convergence continued during the Carboniferous and produced the complex intracontinental deformation that characterizes the Variscan Belt. According to structural data and paleogeographic reconstructions for the allochthonous pile of NW Iberia, the Devonian and Carboniferous convergence was accompanied by a dextral lateral component for most of the time. Based on modern analogues of continental interaction, the development of complex collisions, as here suggested for Gondwana and Laurussia during the assembly of Pangea, could have been the rule rather than the exception throughout Earth history.

Acknowledgements

Financial support has been provided by the Spanish project CGL2012-34618 (Ministerio de Economía y Competitividad).

Many of the ideas developed in this work emerged during years of stimulating and friendly discussions with our colleague Florentino Díaz García, who sadly passed away. This paper is a tribute to his memory.

References

Ábalos, B. 1997. Omphacite fabric variation in the Cabo Ortegal eclogite (NW Spain): relationships with strain symmetry during high-pressure deformation. Journal of Structural Geology, 19, 621-637.

Ábalos, B., Mendia, M., Gil Ibarguchi, J.I. 1994. Structure of the Cabo Ortegal eclogite-facies zone (NW Iberia). Comptes Rendus de l'Académie des sciences de Paris, 319, 1231-1238.

Ábalos, B., Azcárraga, J., Gil Ibarguchi, J.I., Mendia, M., Santos Zalduegui, J.F. 1996. Flow stress, strain rate and effective viscosity evaluation in a high-pressure nappe (Cabo Ortegal, Spain). Journal of Metamorphic Geology, 14, 227-248.

Ábalos, B., Puelles, P., Gil Ibarguchi, J.I. 2003. Structural assemblage of high-pressure mantle and crustal rocks in a subduction channel (Cabo Ortegal, NW Spain). Tectonics, 22, 1006, TC001405.

Abati, J. 2002. Petrología Metamórfica y Geocronología de la unidad culminante del Complejo de Órdenes en la región de Carballo (Galicia, NW del Macizo Ibérico). Nova Terra, 20, 269 p.

Abati, J., Dunning, G.R., Arenas, R., Díaz García, F., González Cuadra, P., Martínez Catalán, J.R., Andonaegui, P. 1999. Early Ordovician orogenic event in Galicia (NW Spain): evidence from U-Pb ages in the uppermost unit of the Ordenes Complex. Earth and Planetary Science Letters, 165, 213-228.

Abati, J., Dunning, G.R. 2002. Edad U-Pb en monacitas y rutilos de los paragneises de la Unidad de Agualada (Complejo de Órdenes, NW del Macizo Ibérico). Geogaceta, 32, 95-98.

Abati, J., Arenas, R., Martínez Catalán, J.R., Díaz García, F. 2003. Anticlockwise *P-T* path of granulites from the Monte Castelo Gabbro (Órdenes Complex, NW Spain). Journal of Petrology, 44, 305-327.

Abati, J., Castiñeiras, P., Arenas, R., Fernández-Suárez, J., Gómez-Barreiro, J., Wooden, J. 2007. Using SHRIMP zircon dating to unravel tectonothermal events in arc environments. The early Palaeozoic arc of NW Iberia revisited. Terra Nova, 19, 432-439.

Abati, J., Gerdes, A., Fernández-Suárez, J., Arenas, R., Whitehouse, M.J., Díez Fernández, R. 2010. Magmatism and early-Variscan continental subduction in the northern Gondwana margin recorded in zircons from the basal units of Galicia, NW Spain. Geological Society of America Bulletin, 122, 219-235.

Albert, R., Arenas, R., Sánchez Martínez, S., Gerdes, A. 2012. The eclogite facies gneisses of the Cabo Ortegal Complex (NW Iberian Massif): Tectonothermal evolution and exhumation model. Journal of Iberian Geology, 38, 389-406.

Albert, R., Arenas, R., Gerdes, A., Sánchez Martínez, S. 2013. Refined ages of magmatism and high-P metamorphism in the eclogite facies gneissic formation of the Cabo Ortegal Complex. Proceedings of the Joint Conference of the Czech and German geological societies: Crustal evolution and geodynamic processes in Central Europe. Pilsen, Czech Republic. p. 93.

Albert, R., Arenas, R., Gerdes, A., Sánchez Martínez, S., Fernández-Suárez, J., Fuenlabrada, J.M. 2015. Provenance of the Variscan Upper Allochthon (Cabo Ortegal Complex, NW Iberian Massif). Gondwana Research. (In press). dx.doi.org/10.1016/j.gr.2014.10.016.

Albert, R., Arenas, R. Gerdes, A., Sánchez Martínez, S. Submitted. Provenance of the high-P and high-T unit of the Cabo Ortegal Complex (NW Iberian Massif). Submitted.

Alcock, J., Arenas, R., Martínez Catalán, J.R. 2005. Shear stress in subducting continental margin from high-pressure, moderate-temperature metamorphism in the

Órdenes Complex, Galicia, NW Spain. Tectonophysics, 397, 181-194.

Andonaegui, P., González del Tánago, J., Arenas, R., Abati, J., Martínez Catalán, J.R., Peinado, M., Díaz García, F. 2002. Tectonic setting of the Monte Castelo gabbro (Órdenes Complex, northwestern Iberian Massif): Evidence for an arc-related terrane in the hanging wall to the Variscan suture. In: Martínez Catalán, J.R., Hatcher, R.D. Jr., Arenas, R. and Díaz García, F. (Eds.), Variscan-Appalachian Dynamics: the building of the Late Paleozoic Basement. Geological Society of America Special Paper, 364, 37-56.

Andonaegui, P., Castiñeiras, P., González Cuadra, P., Arenas, R., Sánchez Martínez, S., Abati, J., Díaz García, F., Martínez Catalán, J.R. 2012. The Corredoiras orthogneiss (NW Iberian Massif): Geochemistry and geochronology of the Paleozoic magmatic suite developed in a peri-Gondwanan arc. Lithos, 128-131, 84-99.

Arenas, R. 1988. Evolución petrológica y geoquímica de la unidad alóctona inferior del Complejo Metamórfico Básico – Ultrabásico de Cabo Ortegal (Unidad de Moeche) y del Silúrico Parautóctono (NW de España). Corpus Geologicum Gallaeciae, 4, 543 p.

Arenas, R. 1991. Opposite P,T,t paths of Hercynian metamophism between the upper units of the Cabo Ortegal Complex and their substratum (northwest of the Iberian Massif). Tectonophysics, 191, 347-364.

Arenas, R., Gil Ibarguchi, J.I., González Lodeiro, F., Klein, E., Martínez Catalán, J.R., Ortega Gironés, E., Pablo Maciá, J.G. de, Peinado, M. 1986. Tectonostratigraphic units in the complexes with mafic and related rocks of the NW of the Iberian Massif. Hercynica, 2, 87-110.

Arenas, R., Rubio Pascual, F.J., Díaz García, F., Martínez Catalán, J.R. 1995. High-pressure microinclusions and development of an inverted metamorphic gradient in the Santiago Schists (Órdenes Complex, NW Iberian Massif, Spain): evidence of subduction and syn-collisional decompression. Journal of Metamorphic Geology, 13, 141-164.

Arenas, R., Abati, J., Martínez Catalán, J.R., Díaz García, F., Rubio Pascual, F.J. 1997. P-T evolution of eclogites from the Agualada Unit (Órdenes Complex, NW Iberian Massif, Spain): Implications for crustal subduction. Lithos, 40, 221-242.

Arenas, R., Martínez Catalán, J.R. 2002. Prograde development of corona textures in metagabbros of the Sobrado unit (Órdenes Complex, northwestern Iberian Massif). In: Martínez Catalán, J.R., Hatcher, R.D., Jr, Arenas, R. and Díaz García, F. (Eds.), Variscan-Appalachian Dynamics: the building of the Late Paleozoic Basement. Geological Society of America Special Paper, 364, 73-88.

Arenas, R., Martínez Catalán, J.R., Sánchez Martínez, S., Díaz García, F., Abati, J., Fernández-Suárez, J., Andonaegui, P., Gómez-Barreiro, J. 2007a. Paleozoic ophiolites in the Variscan suture of Galicia (northwest Spain): distribution, characteristics and meaning. In: Hatcher, R.D. Jr., Carlson, M.P., McBride, J.H. and Martínez Catalán, J.R. (Eds.), 4-D Framework of Continental Crust. Geological Society of America Memoir, 200, 425-444.

Arenas, R., Martínez Catalán, J.R., Sánchez Martínez, S., Fernández-Suárez, J., Andonaegui, P., Pearce, J.A., Corfu, F. 2007b. The Vila de Cruces Ophiolite: A remnant of the early Rheic Ocean in the Variscan suture of Galicia (NW Iberian Massif). Journal of Geology, 115, 129-148.

Arenas, R., Sánchez Martínez, S., Castiñeiras, P., Jeffries, T.E., Díez Fernández, R., Andonaegui, P. 2009. The basal tectonic mélange of the Cabo Ortegal Complex (NW Iberian Massif): a key unit in the suture of Pangea. Journal of Iberian Geology, 35, 85-125.

Arenas, R., Díez Fernández, R., Sánchez Martínez, S., Gerdes, A., Fernández-Suárez, J., Albert, R. 2014a. Two-stage collision: Exploring the birth of Pangea in the Variscan terranes. Gondwana Research, 25, 756-763.

Arenas, R., Sánchez Martínez, S., Gerdes, A., Albert, R., Díez Fernández, R., Andonaegui, P. 2014b. Re-interpreting the Devonian ophiolites involved in the Variscan suture: U-Pb and Lu-Hf zircon data of the Moeche Ophiolite (Cabo Ortegal Complex, NW Iberia). International Journal of Earth Sciences. doi: 10.1007/s00531-013-0880-x.

Azcárraga, J. 2000. Evolución tectónica y metamórfica de los mantos inferiores de grado alto y alta presión del complejo de Cabo Ortegal. Nova Terra, 17, 346 p.

Ballèvre, M., Bosse, V., Ducassou, C., Pitra, P. 2009. Palaeozoic history of the Armorican Massif: Models for the tectonic evolution of the suture zones. Comptes Rendus Geoscience, 341, 174-201.

Ballèvre, M., Martínez Catalán, J.R., López Carmona, A., Abati, J., Díez Fernández, R., Ducassou, C., Pitra, P., Arenas, R., Bosse, V., Castiñeiras, P., Fernández-Suárez, P., Gómez Barreiro, J., Paquette, J.L., Peucat, J.J., Poujol, M., Ruffet, G., Sánchez Martínez, S. 2014. Correlation of the nappe stack in the Ibero-Armorican arc across the Bay of Biscay: a joint French-Spanish project. Geological Society of London, Special Publication, 405, 77-113.

Bathia, M.R., Crook, K.A.W. 1986. Trace elements characteristics of greywackes and tectonic setting discrimination of sedimentary basins. Contributions to Mineralogy and Petrology, 92, 181-193.

Beaumont, C., Jamieson, R.A., Butler, J.P. Warren, C.J. 2009. Crustal structure: A key constraint on the mechanism of ultra-high-pressure rock exhumation. Earth and Planetary Science Letters, 287, 116-129.

Brink, U.S. ten, Coleman, D.F., Dillon, W.P. 2002. The nature of the crust under Cayman Trough from gravity. Marine and Petroleum Geology, 19, 971-987.

Castiñeiras, P. 2005. Origen y evolución tectonotermal de las unidades de O Pino y Cariño (Complejos Alóctonos de Galicia). Nova Terra, 28, 279 p.

Castiñeiras, P., Díaz García, F., Gómez Barreiro, J. 2010. REE-assisted U-Pb zircon age (SHRIMP) of an anatetic granodiorite: Constraints on the evolution of the A Silva granodiorite, Iberian allochthonous complexes. Lithos, 116, 153-166.

Clark, A.H., Scott, D.J., Sandeman, H.A., Bromley, A.V., Farrar, E. 1998. Siegenian generation of the Lizard ophiolite: U-Pb zircon age data for plagiogranite, Porthkerries, Cornwall. Journal of de Geological Society, London, 155, 595-598.

Chauvel, C., Blichert-Toft, J. 2001. A hafnium isotope and trace element perspective on melting of the depleted mantle. Earth and Planetary Science Letters, 190, 137-151.

Dallmeyer, R.D., Martínez Catalán, J.R., Arenas, R., Gil Ibarguchi, J.I., Gutiérrez Alonso, G., Farias, P., Aller, J., Bastida, F. 1997. Diachronous Variscan tectonothermal activity in the NW Iberian Massif: evidence from $^{40}Ar/^{39}Ar$ dating of regional fabrics. Tectonophysics, 277, 307-337.

DePaolo, D.J. 1981. Neodymium isotopes in the Colorado Front Range and crust-mantle evolution in the Proterozoic. Nature, 291, 193-196.

Díaz García, F. 1990. La geología del sector occidental del Complejo de Órdenes (Cordillera Hercínica, NW de España). Nova Terra, 3, 230 p.

Díaz García, F., Arenas, R., Martínez Catalán, J.R., González del Tánago, J., Dunning, G.R. 1999a. Tectonic evolution of the Careón Ophiolite (northwest Spain): a remnant of oceanic lithosphere in the Variscan Belt. Journal of Geology, 107, 587-605.

Díaz García, F., Martínez Catalán, J.R., Arenas, R., González Cuadra, P. 1999b. Structural and kinematic analysis of the Corredoiras Detachment: Evidence for early Variscan synconvergent extension in the Órdenes Complex, NW Spain. International Journal of Earth Sciences, 88, 337-351.

Díaz García, F., Martínez Catalán, J.R., Arenas, R., Abati, J., González Cuadra, P. 2000. Geological Map of the Órdenes Complex. In: Arenas, R., Díaz García, F., Martínez Catalán, J.R., Abati, J., González Cuadra, P., Andonaegui, P., González del Tánago, J., Rubio Pascual, F.J., Castiñeiras, P., Gómez Barreiro, J. Structure and evolution of the Órdenes Complex. Basement Tectonics 15, Pre – Conference Field Trip Guide, A Coruña, Spain.

Díaz García, F., Sánchez Martínez, S., Castiñeiras, P., Fuenlabrada, J.M., Arenas, R. 2010. A peri-Gondwanan arc in NW Iberia. II: Assessment of the intra-arc tectonothermal evolution through U-Pb SHRIMP dating of mafic dykes. Gondwana Research, 17, 352-362.

Díez Fernández, R. 2011. Evolución estructural y cinemática de una corteza continental subducida: La Unidad de Malpica – Tui (NO del Macizo Ibérico). Nova Terra, 40, 228 p.

Díez Fernández, R., Martínez Catalán, J.R., Gerdes, A., Abati, J., Arenas, R., Fernández-Suárez, J. 2010. U-Pb ages of detrital zircons from the basal allochthonous units of NW Iberia: Provenance and paleoposition on the northern margin of Gondwana during the Neoproterozoic and Paleozoic. Gondwana Research, 18, 385-399.

Díez Fernández, R., Martínez Catalán, J.R., Arenas, R., Abati, J. 2011. Tectonic evolution of a continental subduction-exhumatio channel: Variscan structure of the basal allochthonous units in NW Spain. Tectonics, 30, TC3009, 3001-3022.

Díez Fernández, R., Martínez Catalán, J.R., Arenas, R., Abati, J., Gerdes, A., Fernández-Suárez, J. 2012a. U-Pb detrital zircon analysis of the lower allochthon of NW Iberia: age constraints, provenance and links with the Variscan mobile belt and Gondwana cratons. Journal of the Geological Society, London, 169, 655-665.

Díez Fernández, R., Martínez Catalán, J.R., Gómez Barreiro, J., Arenas, R. 2012b. Extensional flow during gravitational collapse: A tool for setting plate convergence (Padrón Migmatitic Dome, Variscan Belt, NW Iberia). The Journal of Geology, 120, 83-103.

Díez Fernández, R., Castiñeiras, P., Gómez Barreiro, J. 2012c. Age constraints on Lower Paleozoic convection system: magmatic events in the NW Iberian Gondwana margin. Gondwana Research, 21, 1066-1079.

Díez Fernández, R., Martínez Catalán, J.R., Arenas, R., Abati, J. 2012d. The onset of the assembly of Pangaea in NW Iberia: Constraints on the kinematics of continental subduction. Gondwana Research, 22, 20-25.

Díez Fernández, R. and Martínez Catalán, J.R. 2012e. Stretching lineations in high-pressure belts: the fingerprint of subduction and subsequent events (Malpica–Tui complex, NW Iberia). Journal of the Geological Society, 169, 531-543.

Díez Fernández, R., Foster, D.A., Gómez Barreiro, J., Alonso-García, M. 2013. Rheological control on the tectonic evolution of a continental suture zone: the Variscan example from NW Iberia (Spain). International Journal of Earth Sciences, 102, 1305-1319.

Díez Montes, a. 2007. La geología del Dominio Ollo de Sapo en las comarcas de Sanabria y Terra do Bolo. Nova Terra, 34, 494 p.

Dubińska, E., Bylina, P., Kozlowski, A., Dörr, W., Nejbert, K. 2004. U-Pb dating of serpentinization: Hydrothermal zircon from a metasomatic rodingite shell (Sudetic ophiolite, SW Poland). Chemical Geology, 203, 183-203.

Engels, J.P. 1972. The catazonal polymetamorphic rocks of

Cabo Ortegal (N.W. Spain): A structural and petrofabric study. Leidse Geologische Mededelingen, 48, 83-133.

Evans, B.W. 1990. Phase relations of epidote – blueschists. Lithos, 25, 3-23.

Farias, P. 1990. La geología de la región del Sinforme de Verín (Cordillera Herciniana, NW de España). Nova Terra, 2, 201 p.

Farias, P., Gallastegui, G., gonzález – Lodeiro, F., Marquínez, J., Martín Parra, L.M., Martínez Catalán, J.R., Pablo Maciá, J.G. de, Rodríguez Fernández, L.R. 1987. Aportaciones al conocimiento de la litoestratigrafía y estructura de Galicia Central. Memórias da Facultade de Ciências, Universidade do Porto, 1, 411-431.

Fernández-Suárez, J., Corfu, F., Arenas, R., Marcos, A., Martínez Catalán, J.R., Díaz García, F., Abati, J., Fernández, F.J. 2002. U-Pb evidence for a polyorogenic evolution of the HP-HT units of the NW Iberian Massif. Contributions to Mineralogy and Petrology, 143, 236-253.

Fernández-Suárez, J., Díaz García, F., Jeffries, T.E., Arenas, R., Abati, J. 2003. Constraints on the provenance of the uppermost allochthonous terrane of the NW Iberian Massif: Inferences from detrital zircon U-Pb ages. Terra Nova, 15,138-144.

Fernández-Suárez, J., Arenas, R., Abati, J., Martínez Catalán, J.R., Whitehouse, M.J., Jeffries, T.E. 2007. U-Pb chronometry of polymetamorphic high-pressure granulites: An example from the allochthonous terranes of the NW Iberian Variscan belt. In: Hatcher, R.D. Jr., Carlson, M.P., McBride, J.H. and Martínez Catalán, J.R. (Eds.), 4-D Framework of Continental Crust. Geological Society of America Memoir, 200, 469-488.

Fernández-Suárez, J., Gutiérrez-Alonso, G., Pastor-Galán, D., Hofmann, J.B., Linnemann, U. 2014. The Ediacaran-Early Cambrian detrital zircon record of NW Iberia: possible sources and paleogeographic constraints. International Journal of Earth Sciences, 103, 1335-1357.

Floor, P. 1966. Petrology of an aegirine-riebeckite gneiss-bearing part of the Hesperian Massif: the Galiñeiro and sourrounding areas, Vigo, Spain. Leidse Geologische Mededelingen, 36, 203 p.

Fombella Blanco, M. 1984. Age palynologique du Blastomilonitic Graben, Zone Occidentale de la Galice. Revue de Micropaléontologie, 27, 113-117.

Frost, B.R., Barnes, C.G., Collins, W.J., Arculus, R.J., Ellis, D.J., Frost, C.D. 2001. A geochemical classification for granitic rocks. Journal of Petrology, 42, 2033-2048.

Fuenlabrada, J.M., Arenas, R., Sánchez Martínez, S., Díaz García, F., Castiñeiras, P. 2010. A peri-Gondwana arc in NW Iberia. I: Isotopic and geochemical constraints on the origin of the arc - A sedimentary approach. Gondwana Research, 17, 338-351.

Fuenlabrada, J.M., Arenas, R., Díez Fernández, R., Sánchez Martínez, S., Abati, J., López Carmona, A. 2012. Sm-Nd isotope geochemistry and tectonic setting of the metasedimentary rocks from the basal allochthonous units of NW Iberia (Variscan suture, Galicia). Lithos, 148, 196-208.

García-Casco, A., Iturralde-Vinent, M.A., Pindell, J. 2008. Latest Cretaceous collision/accretion between the Caribbean plate and Caribeana: Origin of metamorphic terranes in the Greater Antilles. International Geology Review, 50, 781-809.

Gerya, T.V., Stöckhert, B., Perchuk, A.L. 2002. Exhumation of high-pressure metamorphic rocks in a subduction channel: A numerical simulation. Tectonics, 21, 6-1-19.

Gil Ibarguchi, J.I. 1995. Petrology of jadeite-metagranite and associated orthogneiss from the Malpica-Tuy allochthon (Nortwest Spain). European Journal of Mineralogy, 7, 403-415.

Gil Ibarguchi, J.I , Ortega Gironés, E. 1985. Petrology, structure and geotectonic implications of glaucophane-bearing eclogites and related rocks from the Malpica-Tuy (MT) unit, Galicia, Nortwest Spain. Chemical Geology, 50, 145-162.

Gil Ibarguchi, J.I., Mendia, M., Girardeau, J., Peucat, J.J. 1990. Petrology of eclogites and clynopiroxene-garnet metabasites from the Cabo Ortegal Complex (northwestern Spain). Lithos, 25, 133-162.

Gil Ibarguchi, J.I., Ábalos, B., Azcárraga, J., Puelles, P. 1999. Deformation, high-pressure metamorphism and exhumation of ultramafic rocks in a deep subduction/collision setting (Cabo Ortegal, NW Spain). Journal of Metamorphic Geology, 17, 747-764.

Girardeau, J., Gil Ibarguchi, J.I., Ben Jamaa, N. 1989. Evidence for a heterogeneous upper mantle in the Cabo Ortegal Complex, Spain. Science, 245, 1231-1233.

Girardeau, J., Gil Ibarguchi, J.I. 1991. Pyroxenite-rich peridotites of the Cabo Ortegal Complex (Nothwest Spain): Evidence for a large-scale upper-mantle heterogeneity. Journal of Petrology, 32, 135-154.

Gómez Barreiro, J. 2007. La Unidad de Fornás: Evolución tectonometamórfica del SO del Complejo de Órdenes. Nova Terra, 32, 291 p.

Gómez-Barreiro, J., Wijbrans, J.R., Castiñeiras, P., Martínez Catalán, J.R., Arenas, R., Díaz García, F., Abati, J. 2006. $^{40}Ar/^{39}Ar$ laserprobe dating of mylonitic fabrics in a polyorogenic terane of NW Iberia. Journal of the Geological Society, London, 163, 61-73.

Gómez-Barreiro, J., Martínez Catalán, J.R., Arenas, R., Castiñeiras, P., Abati, J., Díaz García, F., Wijbrans, J.R. 2007. Tectonic evolution of the upper allochthon of the Órdenes complex (northwestern Iberian Massif): Structural constraints to a polyorogenic peri-Gondwanan terrane. In: Linneman, U., Nance, R.D., Kraft, P. and Zulauf,

G. (Eds.), The evolution of the Rheic Ocean: From Avalonian-Cadomian active margin to Alleghenian-Variscan collision. Geological Society of America Special Paper 423, 315-332.

Gómez Barreiro, J., Martínez Catalán, J.R., Díez Fernández, R., Arenas, R., Díaz García, F. 2010a. Upper crust reworking during gravitational collapse: the Bembibre – Pico Sacro detachment system (NW Iberia). Journal of the Geological Society, London, 167, 769-784.

Gómez Barreiro, J., Martínez Catalán, J.R., Prior, D., Wenk, H.-R., Vogel, S., Díaz García, F., Arenas, R., Sánchez Martínez, S., Lonardelli, I. 2010b. Fabric development in a Middle Devonian intra-oceanic subduction regime: the Careón ophiolite (NW Spain). Journal of Geology, 118,163-186.

González Cuadra, P. 2007. La Unidad de Corredoiras (Complejo de Órdenes, Galicia): Evolución estructural y metamórfica. Nova Terra, 33, 254 p.

Harris, N.B.W., Pearce, J.A., Tindle, A.G. 1986. Geochemical characteristics of collision zone magmatism. In: Coward, M.P. and Reis, A.C. (Eds.), Collision tectonics. Geological Society of London, Special Publication, 19, 67-81.

Hastie, A.R., Kerr, A.C., Pearce, J.A., Mitchell, S.F. 2007. Classification of altered volcanic island arc rocks using immobile trace elements: development of the Th-Co discrimination diagram. Journal of Petrology, 48, 2341-2357.

Hebert, L.B., Antoshechkina, P., Asimow, P, Gurnis, M. 2009. Emergence of a low-viscosity channel in subduction zones through the coupling of mantle flow and thermodynamics. Earth and Planetary Science Letters, 278, 243-256.

Irvine, T.N., Baragar, W.R.A. 1971. A guide to the chemical classification of the common volcanic rocks. Canadian Journal of Earth Sciences, 8, 523-548.

Kroner, U., Romer, R.L. 2013. Two plates – Many subduction zones: The Variscan orogeny reconsidered. Gondwana Research, 24, 298-329.

Kryza, R., Pin, C. 2010. The Central-Sudetic ophiolites (SW Poland): Petrogenetic issues, geochronology and palaeotectonic implications. Gondwana Research, 17, 292-305.

Lardeaux, J.M., Ledru, P., Daniel, I., Duchene, S. 2001. The Variscan French Massif Central-a new addition to the ultra-high pressure metamorphic 'club': exhumation processes and geodynamic consequences. Tectonophysics, 332, 143-167.

Leitch, E.C. 1984. Island arc elements and arc-related ophiolites. Tectonophysics, 106, 177-203.

Linnemann, U., Romer, R.L. 2002. The Cadomian Orogeny in Saxo-Thuringia, Germany: geochemical and Nd-Sr-Pb isotopic characterization of marginal basins with constraints to geotectonic setting and provenance. Tectonophysics, 352, 33-64.

Llana-Fúnez, S. 2002. Quartz c-axis texture mapping of a Variscan regional foliation (Malpica-Tui Unit, NW Spain). Journal of Structural Geology, 24, 1299–1312.

Llana-Fúnez, S., Marcos, A. 2001. The Malpica–Lamego Line: a major crustal-scale shear zone in the Variscan belt of Iberia. Journal of Structural Geology, 23, 1015-1030.

López-Carmona A, Abati J, Reche J. 2010. Petrologic modeling of chloritoid-glaucophane schists from the NW Iberian Massif. Gondwana Research, 17, 377-391.

López Carmona, A., Pitra, P., Abati, J. 2013. Blueschist-facies metapelites from the Malpica-Tui Unit (NW Iberian Massif): phase equilibria modelling and H_2O and Fe_2O_3 influence in high-pressure assemblages. Journal of Metamorphic Geology, 31, 263-280.

López Carmona, A., Abati, J., Pitra, P., Lee, J.K.W. 2014. Retrogressed lawsonite blueschists from the NW Iberian Massif: P-T constraints from numerical modelling and $^{40}Ar/^{39}Ar$ geochronology. Contributions to Mineralogy and Petrology, 167, 987: 1-20.

Llana-Fúnez, S., Marcos, A. 2001. The Malpica – Lamego Line: a major crustal-scale shear zone in the Variscan belt of Iberia. Journal of Structural Geology, 23, 1015-1030.

Marcos, A., Marquínez, J., Pérez-Estaún, A., Pulgar, J.A., Bastida, F. 1984. Nuevas aportaciones al conocimiento de la evolución tectonometamórfica del Complejo de Cabo Ortegal (NW de España). Cuadernos do Laboratorio Xeolóxico de Laxe, 7, 125-137.

Marcos, A., Farias, P., Galán, G., Fernández, F.J., Llana-Fúnez, S. 2002. Tectonic framework of the Cabo Ortegal Complex: A slab of lower crust exhumed in the Variscan orogen (northwestern Iberian Peninsula). In: Martínez Catalán, J.R., Hatcher, R.D. Jr., Arenas, R. and Díaz García, F. (Eds.), Variscan-Appalachian dynamics: the building of the Late Paleozoic basement. Geological Society of America Special Paper, 364, 143-162.

Martínez Catalán, J.R. 2011. Are the oroclines of the Variscan belt related to late Variscan strike-slip tectonics? Terra Nova, 23, 241-247.

Martínez Catalán, J.R., Hacar Rodríguez, M.P., Villar Alonso, P., Pérez – Estaún, A. and gonzález lodeiro, F. 1992. Lower Paleozoic extensional tectonics in the limit between the West Asturian – Leonese and Central Iberian Zones of the Variscan Fold – Belt in NW Spain. Geologische Rundschau, 81, 545-560.

Martínez Catalán J.R., Arenas, R., Díaz García, F., Rubio Pascual, F.J., Abati, J., Marquínez, J. 1996. Variscan exhumation of a subducted Paleozoic continental margin: The basal units of the Órdenes Complex, Galicia, NW Spain. Tectonics, 15, 106-121.

Martínez Catalán, J.R., Díaz García, F., Arenas, R., Abati, J.,

Castiñeiras, P., González Cuadra, P., Gómez Barreiro, J., Rubio Pascual, F. 2002. Thrust and detachment systems in the Ordenes Complex (northwestern Spain): Implications for the Variscan-Appalachian geodynamics. In: Martínez Catalán, J.R., Hatcher, R.D. Jr., Arenas, R. and Díaz García, F. (Eds.), Variscan-Appalachian dynamics: the building of the Late Paleozoic basement. Geological Society of America Special Paper, 364, 163-182.

Martínez Catalán, J.R., Arenas, R., Abati, J., Sánchez Martínez, S., Díaz García, F., Fernández-Suárez, J., González Cuadra, P., Castiñeiras, P., Gómez Barreiro, J., Díez Montes, A., González Clavijo, E., Rubio Pascual, F.J., Andonaegui, P., Jeffries, T.E., Alcock, J.E., Díez Fernández, R., López Carmona, A. 2009. A rootless suture and the loss of the roots of a mountain chain: The Variscan belt of NW Iberia. Comptes Rendus Geoscience, 341, 114-126.

Martínez Catalán, J.R. 2011. Are the oroclines of the Variscan belt related to late Variscan strike-slip tectonics? Terra Nova, 23, 241-247.

Maruyama, S., Liou, J., Terabayashi, M. 1996. Blueschists and eclogites of the world and their exhumation. International Geology Review, 38, 485-594.

Matte Ph. 1991. Accretionary history and crustal evolution of the Variscan belt in Western Europe. Tectonophysics, 196, 309-337.

Matte, Ph. 2001. The Variscan collage and orogeny (480-290 Ma) and the tectonic definition of the Armorica microplate: a review. Terra Nova, 13, 122-128.

Matte, Ph., Capdevila, R. 1978. Tectonique en grands plis couchés et plissements superposés d´âge hercynien dans la série de Ordenes-Betanzos (Galice Occidentale). Cuadernos del Seminario de Estudios Cerámicos de Sargadelos, 27, 193-201.

Mendia, M. 2000. Petrología de la Unidad Eclogítica del Complejo de Cabo Ortegal (NW de España). Nova Terra, 16, 424 p.

Montero, P., Bea, F. Corretgé, L.G., Floor, P., Whitehouse, M.J. 2009. U-Pb ion microprobe dating and Sr and Nd isotope geology of the Galiñeiro Igneous Comlex: A model for the peraluminous/peralkaline duality of the Cambro-Ordovician magmatism of Iberia. Lithos, 107, 227-238.

Moreno, T., Gibbons, W., Prichard, H.M., Lunar, R. 2001. Platiniferous chromitites and the tectonic setting of ultramafic rocks in Cabo Ortegal (North West Spain). Journal of the Geological Society, London, 158, 601-614.

Murphy, J.B., Nance, R.D. 2008. The Pangea conundrum. Geology, 36, 703-706.

Murphy, J.B., Gutiérrez-Alonso, G., Nance, R.D., Fernández-Suárez, J., Keppie, J.D., Quesada, C., Strachan, R.A., Dostal, J. 2006. Origin of the Rheic Ocean: Rifting along a Neoproterozoic suture? Geology, 34, 325-328.

Murphy, J.B., Cousens, B.L., Braid, J.A., Strachan, R.A., Dostal, J., Keppie, J.D., Nance, R.D. 2011. Highly depleted oceanic lithosphere in the Rheic Ocean: Implications for Paleozoic plate reconstructions. Lithos, 123,165-175.

Nance, R.D., Gutiérrez-Alonso, G., Keppi, J.D., Linnemann, U., Murphy, J.B., Quesada, C., Strachan, R.A., Woodcock, N.H. 2010. Evolution of the Rheic Ocean. Gondwana Research, 17,194-222.

Nicolas, A. 1989. Structures of ophiolites and dynamics of oceanic lithosphere. Kluwer Academic Publishers, 367 p.

Nicolas, A, 1995. The mid-oceanic ridges. Mountains below sea level. Springer-Verlag. 200 p.

Nutman, A.P., Green, D.H., Cook, C.A., Styles, M.T., Holdsworth, R.E. 2001. SHRIMP U-Pb zircon dating of the exhumation of the Lizard Peridotite and its emplacement over crustal rocks: Constraints for tectonic models. Journal of the Geological Society, London, 158, 809-820.

Ordóñez Casado, B., Gebauer, D., Schäfer, H.J., Gil Ibarguchi, J.I., Peucat, J.J. 2001. A single Devonian subduction event for the HP/HT metamorphism of the Cabo Ortegal complex within the Iberian Massif. Tectonophysics 332, 359-385.

Pearce, J.A. 1996. A users guide to basalt discrimination diagrams. In: Wyman, D.A. (Ed.), Trace Element Geochemistry of Volcanic Rocks: Application for Massive Sulphide Exploration. Short Course Notes, Geological Association of Canada, 12, 79-113.

Pearce, J.A., Lippard, S.J., Roberts, S. 1984. Characteristics and tectonic significance of supra-subduction zone ophiolites . In: Kokelaar, B.P. and Howells, M.F. (Eds.), Marginal Basin Geology. Geological Society, London, Special Publications, 16, 77-94.

Peccerillo, R., Taylor, S.R. 1976. Geochemistry of Eocene calc-alkaline volcanic rocks from the Kastamonu area, northern Turkey. Contributions to Mineralogy and Petrology, 58, 63-81.

Pérez-Estaún, A., Martinez-Catalán, J.R., Bastida, F. 1991. Crustal thickening and deformation sequence in the footwall to the suture of the Variscan belt of northwest Spain. Tectonophysics, 191, 243–253.

Pin, C., Paquette, J.L., Santos Zalduegui, J.F., Gil Ibarguchi, J.I. 2002. Early Devonian supra-subduction zone ophiolite related to incipient collisional processes in the Western Variscan Belt: The Sierra de Careón unit, Órdenes Complex, Galicia. In: Martínez Catalán, J.R., Hatcher, R.D. Jr., Arenas, R. and Díaz García, F. (Eds.), Variscan-Appalachian dynamics: the building of the Late Paleozoic basement. Geological Society of America Special Paper, 364, 57-71.

Pin, C., Paquette, J.L., Ábalos, B., Santos, J.F., Gil Ibarguchi, J.I. 2006. Composite origin of an early Variscan transported suture: Ophiolitic units of the Morais Nappe

Complex (north Portugal). Tectonics, 25, 1-19.

Parga Pondal, I. 1963. Mapa geológico de Galicia a escala 1/2.000.000. Laboratorio Geológico de Lage.

Pérez – Estaún, A., Bastida, F., Martínez Catalán, J.R., Gutiérrez Marco, J.C., Marcos, A., Pulgar, J.A., 1990. West Asturian – Leonese Zone. Stratigraphy. In: R.D. Dallmeyer and Martínez García, E. (Eds.), Pre – Mesozoic Geology of Iberia. Springer – Verlag. Berlin, 92-102.

Peucat, J.J., Bernard-Griffiths, J., Gil Ibarguchi, J.I., Dallmeyer, R.D., Menot, R.P., Cornichet, J., Iglesias Ponce de León, M. 1990. Geochemical and geochronological cross section of the deep Variscan crust: The Cabo Ortegal high-pressure nappe (northwestern Spain). Tectonophysics, 177, 263-292.

Pin, C., Paquette, J.L., Santos Zalduegui, J.F., Gil Ibarguchi, J.I., 2002. Early Devonian supra-subduction zone ophiolite related to incipient collisional processes in the Western Variscan Belt: The Sierra de Careón unit, Órdenes Complex, Galicia. In: Martínez Catalán, J.R., Hatcher, R.D. Jr., Arenas, R. and Díaz García, F. (Eds), Variscan-Appalachian Dynamics: the building of the Late Paleozoic Basement. Geological Society of America Special Paper 364, 57-71.

Puelles, P. 2004. Deformación, metamorfismo y exhumación de las granulitas de alta presión de la Bacariza (Complejo de Cabo Ortegal, NO de España). Nova terra, 23, 411 p.

Puelles, P., Ábalos, B., Gil Ibarguchi, J.I. 2005. Metamorphic evolution and thermobaric structure of the subduction-related Bacariza high-pressure granulite formation (Cabo Ortagal Complex, NW Spain). Lithos, 84, 125-149.

Ries, A.C., Shackleton, R.M. 1971. Catazonal complexes of north-west Spain and north Portugal, remnants of a Hercynian thrust plate. Nature Physical Sciences, 234, 65-68.

Rodríguez, J., Cosca, M.A., Gil Ibarguchi, J.I., Dallmeyer, R.D. 2003. Strain partitioning and preservation of $^{40}Ar/^{39}Ar$ ages during Variscan exhumation of a subducted crust (Malpica-Tui complex, NW Spain). Lithos, 70, 111-139.

Rodríguez, R., Marcos, A., Farias, P. 2004. Palinological data on the age of the metasediments of the Parautochthonous Thrust Sheet in the Cabo Ortegal area (Galicia, NW Spain). Neues Jarbuch für Geologie und Paläontologie, 10, 437-447.

Rodríguez Aller, J. 2005. Recristalización y deformación de litologías supracorticales sometidas a metamorfismo de alta presión (Complejo de Malpica – Tuy, NO del Macizo Ibérico). Nova Terra, 29, 572 p.

Rubio Pascual, F.J. 2013. Evolución tectonotermal varisca del Sistema Central en Somosierra – Honrubia. Nova Terra, 44, 364 p.

Rubio Pascual, F.J., Arenas, R., Díaz García, F., Martínez Catalán, J.R., Abati, J. 2002. Eclogites and eclogite – amphibolites from the Santiago Unit (Órdenes Complex, NW Iberian Massif, Spain): a case study of contrasting high-pressure metabasites in a context of crustal subduction. In: Martínez Catalán, J.R., Hatcher, R.D. Jr., Arenas, R. and Díaz García, F. (Eds.), Variscan-Appalachian dynamics: the building of the Late Paleozoic basement. Geological Society of America Special Paper, 364, 105-124.

Sánchez Martínez, S. 2009. Geoquímica y geocronología de las ofiolitas de Galicia. Nova Terra, 37, 351 p.

Sánchez Martínez, S., Jeffries, T., Arenas, R., Fernández-Suárez, J., García-Sánchez, R. 2006. A pre-Rodinian ophiolite involved in the Variscan suture of Galicia (Cabo Ortegal Complex, NW Spain). Journal of the Geological Society, London, 163, 737-740.

Sánchez Martínez, S., Arenas, R., Díaz García, F., Martínez Catalán, J.R., Gómez Barreiro, J., Pearce, J. 2007a. The Careón Ophiolite, NW Spain: supra-subduction zone setting for the youngest Rheic Ocean floor. Geology, 35, 53-56.

Sánchez Martínez, S., Arenas, R., Andonaegui, P., Martínez Catalán, J.R., Pearce, J.A. 2007b. Geochemistry of two associated ophiolites from the Cabo Ortegal Complex (Variscan belt of northwest Spain). In: Hatcher, R.D. Jr., Carlson, M.P., McBride, J.H. and Martínez Catalán, J.R. (Eds.), 4-D Framework of Continental Crust. Geological Society of America Memoir, 200, 445-467.

Sánchez Martínez, S., Arenas, R., Fernández-Suárez, J., Jeffries, T.E. 2009. From Rodinia to Pangaea: ophiolites from NW Iberia as witness for a long-lived continental margin. In: Murphy, J.B., Keppie, J.D. and Hynes, A.J. (Eds.), Ancient Orogens and Modern Analogues. Geological Society, London, Special Publications, 327, 317-341.

Sánchez Martínez, S., Arenas, R., Gerdes, A., Castiñeiras, P., Potrel, A., Fernández-Suárez, J. 2011. Isotope geochemistry and revised geochronology of the Purrido Ophiolite (Cabo Ortegal Complex, NW Iberian Massif): Devonian magmatism with mixed sources and involved Mesoproterozoic basement. Journal of the Geological Society, London, 168, 733-750.

Sánchez Martínez. S., Gerdes, A., Arenas, R., Abati, J. 2012. The Bazar Ophiolite of NW Iberia: a relict of the Iapetus-Tornquist Ocean in the Variscan suture. Terra Nova, 24, 283-294.

Sánchez Martínez, S., Arenas, R., Albert, R., Gerdes, A., Potrel, A. 2013. Detailed re-dating of the Vila de Cruces Ophiolite (allochthonous complexes of NW Iberia): The opening of a back-arc basin in the Gondwana shelf. In: Žák, J., Zulauf, G. and Röhling, H.-G. (Eds.), Crustal evolution and geodynamic processes in Central Europe. Proceedings of the Joint conference of the Czech and

German geological societies, Pilsen, Czech Republic, 95.

Santos, J.F., Schärer, U., Gil Ibarguchi, J.I., Girardeau, J. 2002. Genesis of pyroxenite-rich peridotite at Cabo Ortegal (NW Spain): geochemical and Pb-Sr-Nd isotope data. Journal of Petrology, 43, 17-43.

Shaw, J., Gutiérrez-Alonso, G., Johnston, S.T., Pastor Galán, D. 2014. Provenance variability along the Early Ordovician north Gondwana margin; Paleogeographic and tectonic implications of U-Pb detrital zircon ages from the Armorican Quartzite of the Iberian Variscan belt. Geological Society of America Bulletin, 126, 702-719.

Sommer, M., Hüneke, H., Meschede, M., Cobiella-Reguera, J. 2011. Geodynamic model of the northwestern Caribbean: scaled reconstruction of Late Cretaceous to Late Eocene plate boundary relocation in Cuba. Neues Jahrbuch für Geologie und Paläontologie, Monatschefte, 259, 299-312.

Spear, F.S., Kohn, M.J., Cheney, J.T. 1999. P-T paths from anatectic pelites. Contribution to Mineralogy and Petrology, 134, 17-32.

Stampfli, G.M., Von Raumer, J., Borel, G.D. 2002. Paleozoic evolution of pre-Variscan terranes: From Gondwana to the Variscan collision. In: Martínez Catalán, J.R., Hatcher, R.D. Jr., Arenas, R. and Díaz García, F. (Eds.), Variscan-Appalachian dynamics: the building of the Late Paleozoic basement. Geological Society of America Special Paper, 364, 263-280.

Stampfli, G.M., Borel, G.D. 2002. A plate tectonic model for the Paleozoic and Mesozoic constrained by dynamic plate boundaries and restored synthetic oceanic isochrons. Earth and Planetary Science Letters, 196,17-33.

Valverde-Vaquero, P., Marcos, A., Farias, P., Gallastegui, G. 2005. U-Pb dating of Ordovician felsic volcanism in the Schistose Domain of the Galicia – Trás – os – Montes Zone near Cabo Ortegal (NW Spain). Geológica Acta, 3, 27-37.

Van Calsteren, P.W.C., Boelrijk, N.A.I.M., Hebeda, E.H., Priem, H.N.A., Tex, E. Den, Verdurmen, E.A.T.H., Verschure, R.H. 1979. Isotopic dating of older elements (including the Cabo Ortegal mafic – ultramafic complex) in the Hercynian Orogen of NW Spain: manifestations of a presumed Early Paleozoic Mantle plume. Chemical Geology, 24, 35-56.

Van der Wegen, G. 1978. Garnet-bearing metabasites from the Blastomylonitic Graben, Western Galicia, Spain. Scripta Geologica, 45, 1-95.

Vervoort, J.D., Blichert-Toft, J. 1999. Evolution of the depleted mantle: Hf isotope evidence from juvenile rocks through time. Geochimica et Cosmochimica Acta, 63, 533-556.

Vogel, D.E. 1967. Petrology of an eclogite- and pyrigarnite-bearing polymetamorphic rock complex at Cabo Ortegal, NW Spain. Leidse Geologische Mededelingen, 40, 121-213.

Warren, C.J., Beaumont, C., Jamieson, R.A. 2008. Modelling tectonic styles and ultra-high pressure (UHP) rock exhumation during the transition from oceanic subduction to continental collision. Earth and Planetary Science Letters, 267, 129-145.

Weil, A.B., Gutiérrez-Alonso, G., Johnston, S.T., Pastor-Galán, D. 2012. Kinematic constraints on buckling a lithospheric-scale orocline along the northern margin of Gondwana: A geologic synthesis. Tectonophysics, 582, 25-49.

Winchester, J.A., Pharaoh, T.C., Verniers, J. 2002. Palaeozoic amalgamation of Central Europe: an introduction and synthesis of new results from recent geological and geophysical investigations. In: Winchester, J.A., Pharaoh, T.C. and Verniers, J. (Eds.), Palaeozoic Amalgamation of Central Europe. Geological Society, London, Special Publications, 201, 1-18.

Wood, D.A. 1980. The application of a Th-Hf-Ta diagram to problems of tectomagmatic classification and to establishing the nature of crustal contamination of basaltic lavas of the British Tertiary Volcanic Province. Earth and Planetary Science Letters, 50,11-30.

IV

The eclogite facies gneisses of the Cabo Ortegal Complex

4.1. Introduction

This article deals with the tectonothermal evolution of the eclogite facies gneisses (Banded Gneisses) of the Cabo Ortegal Complex. It shows a detailed description of the macroscopic and microscopic features of these gneisses, and two detailed cross-sections performed in excellent exposures on the Cantabrian coast allowing a clear understanding of the lithological constitution and deformations affecting the unit. This work represents the starting point for the following chapters, as it shows the constitution of the main formation studied and a discussion of its tectonothermal evolution, from the knowledge extracted from previous works and from the structural features described. It is also argued and proposed a model for the exhumation of the terrane in which the formation is included.

4.2. Partial conclusions

The high-P conditions that affected parts of Upper Allochthon terrane indicate that they once constituted a subduction complex, developed on a continental or a transitional thinned continental margin containing thick sedimentary series. The deep subduction (D1 event) that this margin underwent necessarily implies the existence of a colliding retro-continent. The

subducted complex experienced a drastic and fast exhumation (D2 event) during the generation of the decompressive mylonitic foliation (S2). This constitutes the most prominent structural feature in the HP–HT units. This pronounced exhumation (calculated in at least *c*. 10 kbar) very likely occurred during continuous subduction of continental or transitional slices, *i.e.* new layers of the same terrane that in a prograde accretionary sequence should be presently located below the HP–HT units. These units are not preserved, at least in NW Iberia, because the HP–HT units rest above ophiolitic units, avoiding the identification of the colliding margins. The progression of exhumation favours the generation of an important extensional detachment, which is represented by the contact between the Cariño Gneisses, in the amphibolite facies and located in the hanging wall, and the eclogite facies gneisses. A sketch is presented showing a model for the exhumation of the eclogite facies gneisses and in general for the HP–HT units of the Cabo Ortegal Complex. The tectonothermal and exhumation history of the HP–HT units fits quite well into the mathematical modelling (other authors) of the exhumation of ultra-high-pressure complexes. The progression of the deformational history of the upper units entails the development of large recumbent folds and a basal thrust (D3 structures). The geometry of both structures seems to indicate that their development could be related to each other and that they represent the final structures developed in the exhumation of the subducted complex. The structures predicted in numerical models have been compared to those explained in this article, where the large regional structures (D3 recumbent folds and basal thrust) and an ultra-HP buoyant plume (HP–HT units), are represented. The progression of the exhumation entails an important change in the nature of the colliding plates, because during this evolution the prograde continental margin was replaced by the under-thrusting of ophiolites. The tectonothermal evolution of the eclogite facies gneisses of the Cabo Ortegal Complex represents an illustrative example of the complex history of these deeply subducted complexes, which are relatively frequent in the suture zone of the Variscan belt. The structural, metamorphic and geochronological patterns in the evolution of this gneissic unit follow almost perfectly the predictions based in numerical experiments about the exhumation of ultra-HP complexes, and consequently, they represent a direct confirmation of the reality of these models.

ISSN (print): 1698-6180. ISSN (online): 1886-7995
www.ucm.es/info/estratig/journal.htm

Journal of Iberian Geology 38 (2) 2012: 389-406
http://dx.doi.org/10.5209/rev_JIGE.2012.v38.n2.40463

The eclogite facies gneisses of the Cabo Ortegal Complex (NW Iberian Massif): Tectonothermal evolution and exhumation model

Los gneises eclogíticos del Complejo de Cabo Ortegal (NW del Macizo Ibérico): Evolución tectonotermal y modelo de exhumación

R. Albert[1], R. Arenas[1], S. Sánchez-Martínez[1], A. Gerdes[2,3]

[1]Departamento de Petrología y Geoquímica and Instituto de Geociencias (UCM, CSIC), Universidad Complutense de Madrid, 28040 Madrid, Spain
[2]Institut für Geowissenschaften, Mineralogie, J.W. Goethe Universität, Frankfurt am Main, Germany.
[3]Department of Earth Sciences, Stellenbosch University, Private Bag X1,Matieland 7602, South Africa.

**corresponding author: r.albert@geo.ucm.es*

Received: 09/09/2012 / Accepted: 18/10/2012

Abstract

The tectonothermal evolution of the eclogite facies gneisses of the Cabo Ortegal Complex has been investigated using new field and petrologic studies. This gneissic unit is included in the high-pressure and high-temperature (HP-HT) upper units of the allochthonous complexes of NW Iberia, a Cambrian arc-derived peri-Gondwanan terrane emplaced above ophiolitic units considered to represent the Rheic Ocean suture. Two detailed cross-sections performed in excellent exposures on the Cantabrian coast allows a clear understanding of the lithological constitution and deformations affecting the unit. The eclogitic gneiss unit is constituted by metasedimentary gneisses with abundant mafic inclusions, felsic rocks and rare ultramafic inclusions. The felsic rocks range from centimetric leucosomes to metric bodies and most of them were generated during extensive partial melting affecting the unit. The first tectonic fabric detected in the unit is a rarely preserved S1 foliation developed during subduction (ca. 400-390 Ma; 22 kbar). A drastic and fast exhumation (ca. 390 Ma; 12-10 kbar) generated a regional mylonitic foliation which represents the most prominent structural feature in the HP-HT upper units. The consecutive generation of extensional detachments, recumbent folds and a basal thrust occurred during the change from continental-type subduction to the underthrusting of ophiolitic units. These consecutive structures are probably related and the consequence of a long and pronounced exhumation of the subducted complex. The tectonothermal evolution of the eclogite facies gneisses of the Cabo Ortegal Complex represents an illustrative example of the intricate history of these deeply subducted units, which are relatively frequent in the suture zone of the Variscan Belt. It is important to remark that the structural, metamorphic and geochronological patterns in the evolution of this gneissic unit follows almost perfectly the

predictions based in numerical experiments about the exhumation of ultra-high-P complexes. Consequently it represents a direct confirmation of these models.

Keywords: Eclogite facies gneisses, tectonothermal evolution, exhumation model, Variscan Belt, Cabo Ortegal Complex

Resumen

La evolución tectonotermal de los gneises eclogíticos del Complejo de Cabo Ortegal ha sido investigada con nuevos estudios de campo y petrológicos. Los gneises están incluidos en las unidades superiores de alta presión y alta temperatura (HP-HT) de los complejos alóctonos del NW de Iberia, consideradas parte de un terreno peri-Gondwánico de edad Cámbrica originado en un contexto de arco magmático. Este terreno se encuentra emplazado sobre diferentes unidades ofiolíticas que representan la sutura del Océano Rheico. Se han realizado dos secciones geológicas detalladas de afloramientos costeros que muestran las litologías constituyentes y las deformaciones que afectan a la formación gnéisica, que aparece constituida por paragneises con abundantes inclusiones máficas, rocas félsicas y escasas inclusiones de rocas ultramáficas. Las rocas félsicas varían desde leucosomas centimétricos hasta cuerpos métricos y la mayoría de ellas fueron generadas durante un proceso de fusión parcial generalizada. La primera fábrica tectónica detectada es una foliación relicta S1, muy raramente preservada, que se considera desarrollada durante un proceso de subducción (ca. 400-390 Ma; 22 kbar). La foliación regional milonítica, la estructura principal en las unidades de HP-HT, fue generada durante una drástica y rápida exhumación (ca. 390 Ma; 12-10 kbar). La generación consecutiva de despegues extensionales, pliegues recumbentes y de un gran cabalgamiento basal, tuvo lugar durante la transición desde la subducción de un margen continental hasta la imbricación de las unidades ofiolíticas. Estas estructuras sucesivas están probablemente relacionadas y son consecuencia de la pronunciada exhumación del complejo subducido. La evolución tectonotermal de los gneises en facies de las eclogitas del Complejo de Cabo Ortegal representa un ejemplo ilustrativo de la intrincada historia de estas unidades subducidas a gran profundidad, relativamente frecuentes en la zona de sutura de la Cadena Varisca. Es importante resaltar que las pautas estructurales, petrológicas y geocronológicas de la evolución de esta unidad gnéisica se ajustan con detalle a los modelos establecidos mediante experimentos numéricos para la exhumación de complejos de ultra-HP. Consecuentemente, la evolución descrita puede considerarse una confirmación directa de la verosimilitud de estos modelos.

Palabras clave: Gneises eclogíticos, evolución tectonotermal, modelo de exhumación, Cadena Varisca, Complejo de Cabo Ortegal

1. Introduction

The presence of terranes affected by high/ultra-high-P metamorphism has been described in different collisional belts, where they represent the orogenic sections subducted to the highest depths and those affected by the oldest deformative and metamorphic events. Formation and exhumation of UHP rocks may occur during oceanic or thinned continental margin subduction either via continuous circulation in lithospheric scale wedges (Platt, 1986, 1993; Allemand and Lardeaux, 1997) or via return flow in low-viscosity overpressured subduction channels (Gerya *et al*., 2002; Gerya and Stöckhert, 2006; Yamato *et al*, 2008). However, some recent papers have stated that the development of ultra-high-P complexes is almost exclusively related to the subduction of thinned continental margins during early stages of continental collision, which necessarily implies the existence of a prograde continental margin facing a retro-continent (Chopin, 2003; Warren *et al*., 2008; Beaumont *et al*., 2009). Numerical modelling of exhumation of UHP units at the transition from oceanic subduction to continental collision indicates that the first order structural style of the orogenic domain is controlled by the penetration of an UHP buoyant plume (slice of subducting pro-continental margin) in the overlying lower pressure nappe pile. Therefore, to unravel the tectonothermal evolution of high/ultra-high-P complexes, an important tool is to investigate the tectonic and metamorphic processes generated during the first stages of the collision, those associated to deep subduction of crustal layers and the generation of thick orogenic wedges that frequently involve sections of lithospheric mantle.

Some high pressure and high temperature gneissic units including mafic rocks, with local ultra-high-pressure mineral assemblages, appear through the Variscan Belt outlining the main suture zone (Fig. 1; Gil Ibarguchi *et al*., 1990; Obrien and Vrana, 1995; Lardeaux *et al*., 2001; Massone, 2001; Arenas and Martínez Catalán, 2002). This type of units contains important information about the tectonothermal evolution of the Variscan or eo-Variscan accretionary complex, mainly because of the extreme metamorphic conditions attained and the superposition of deformational events that they register. The P-T evolution of these gneissic complexes is well described in some cases, but a detailed description of their internal structure and petrological constitution is generally lacking. Considering this and with the aim of a better understanding of the structure and evolution of the Variscan suture, we present a case study of a very good exposure of one of these units, the eclogite facies gneisses of the Cabo Ortegal Complex (Figs. 1 and 2), also previously

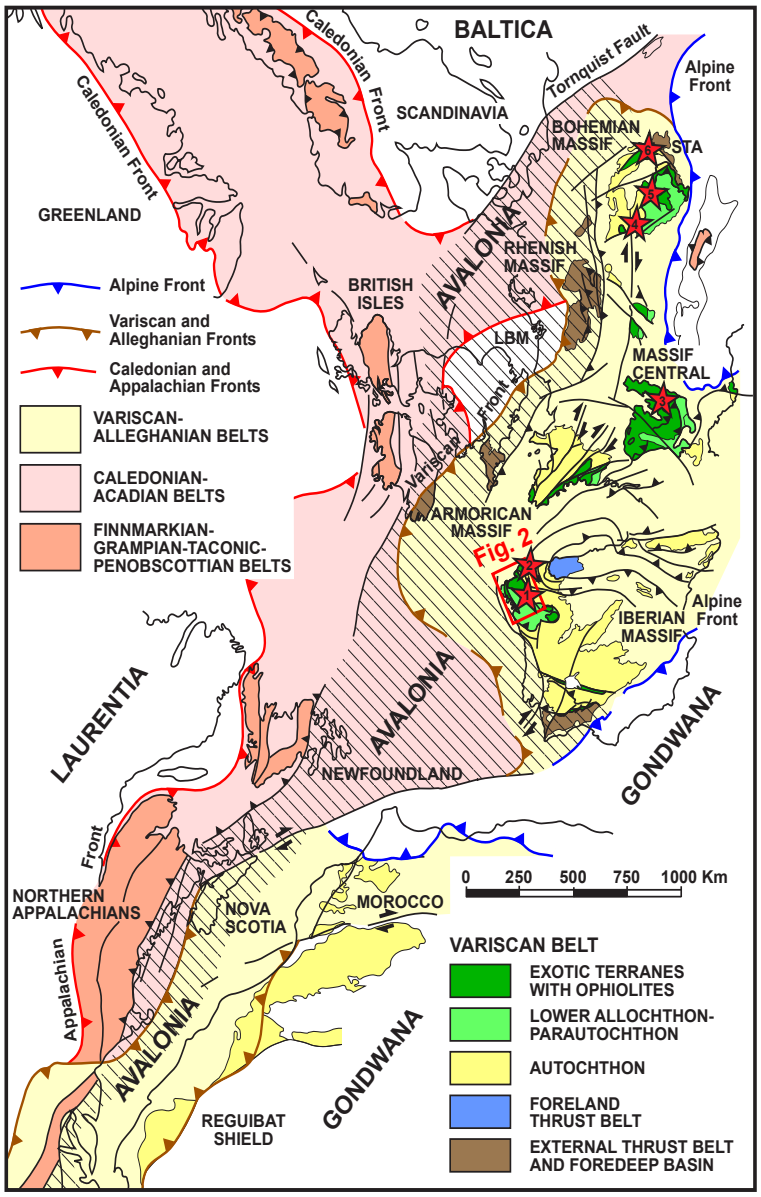

Fig. 1.- Sketch showing the distribution of the Paleozoic orogens in a reconstruction of the Baltica-Laurentia-Gondwana junction developed during the assembly of Pangaea. The distribution of the most important domains described in the Variscan Belt is also shown, together with the inferred position of the microcontinent Avalonia and the studied region in NW Iberia. Modified from Martínez Catalán *et al*. (2002). LBM: London-Brabant Massif. STA: Silesian Terrane Assemblage. High-P and ultra-high-P units involved in the Variscan suture (red stars): 1) High-P and high-T unit of the Sobrado Antiform, Órdenes Complex (Arenas and Martínez Catalán, 2002); 2) Eclogite facies gneisses and related high-P and high-T rocks of the Cabo Ortegal Complex; 3) Coesite-bearing eclogite in the Monts du Lyonnais Unit, French Massif Central (Lardeaux *et al*., 2001); 4) High-P and high-T rocks in the Mariánské Lázně Complex, Bohemian Massif (Timmermann *et al*., 2004); 5) Eclogite facies gneisses bearing Cs + Dia in the Gneiss-Eclogite Unit, Saxonian Erzgebirge, Bohemian Massif (Massone, 2001; Massone, 2003; Massone *et al*., 2007); 6) High-P and high-T rocks in the Gory Sowie Block, Central Sudetes, Bohemian Massif (Kryza and Pin, 2002).

Fig. 1.- Esquema de la distribución de los orógenos Paleozoicos en una reconstrucción de la unión entre Baltica-Laurentia-Gondwana desarrollada durante el ensamblado de Pangea. También se muestra la distribución de los dominios más importantes descritos en la Cadena Varisca, junto con la posición inferida para el microcontinente Avalonia y la región estudiada en el NW de Iberia. Modificado de Martínez Catalán *et al*. (2002). LBM: Macizo de Londres-Brabant. STA: Asociación de terrenos de Silesia. Unidades de alta y ultra-alta-P involucradas en la sutura Varisca (estrellas rojas): 1) Unidad de alta-P y alta-T del Antiforme de Sobrado, Complejo de Órdenes (Arenas y Martínez Catalán, 2002); 2) Gneises en facies de eclogitas y rocas relacionadas de alta-P y alta-T del Complejo de Cabo Ortegal; 3) Eclogita con coesita de la Unidad Monts du Lyonnais, Macizo Central Francés (Lardeaux *et al*., 2001); 4) Rocas de alta-P y alta-T del Complejo de Mariánské Lázně, Macizo de Bohemia (Timmermann *et al*., 2004); 5) Gneises en facies de eclogitas con Cs + Dia de Erzgebirge, Sajonia, Macizo de Bohemia (Massone, 2001; Massone, 2003; Massone *et al*., 2007); 6) Rocas de alta-P y alta-T del Gory Sowie, Sudetes Centrales, Macizo de Bohemia (Kryza and Pin, 2002).

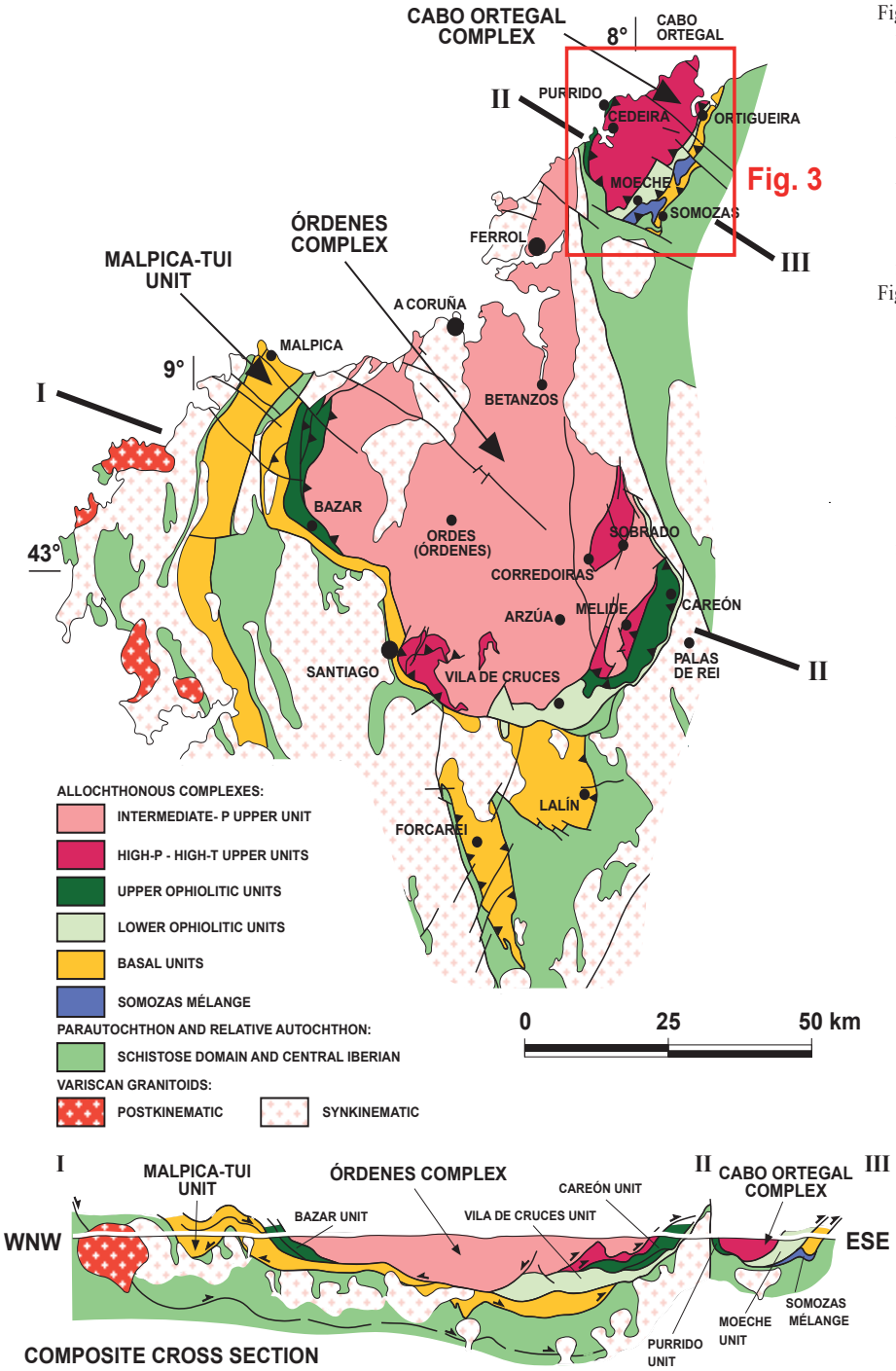

Fig. 2.- Terrane distribution in the allochthonous complexes of NW Iberia (Galicia) and a WNW-ESE oriented general cross-section. The map shows the synformal structure of the complexes where a rootless branch of the Variscan suture is exposed. The location of the geological map presented in figure 3 is also shown.

Fig. 2.- Distribución de terrenos en los complejos alóctonos del NW de Iberia (Galicia) y sección geológica general con orientación WNW-ESE. El mapa muestra la estructura sinformal de los complejos donde aflora una rama desenraizada de la Sutura Varisca. También se indica la localización del mapa geológico de la figura 3.

described as the Banded Gneiss Formation (Vogel, 1967). This gneissic formation appears as a highly sheared complex ensemble of metasedimentary rocks, eclogites and felsic rocks, together with their retrogressed products and abundant melts. The field relations of all of these rocks will be described using two detailed sections obtained in exceptionally good exposures on the Cantabrian coastal section of NW Spain. This information will be discussed and used to present a comprehensive model for the development of mineral assemblages and tectonic fabrics, in relation to the subduction - exhumation of the eclogitic gneisses.

2. Geological context

Five allochthonous complexes preserved at the NW of the Iberian Massif containing ophiolites and high pressure terranes are considered to be remnants of the Variscan suture (Figs. 1 and 2). This suture is rootless and problems exist for a clear correlation with the other suture zones described in the belt, although it is generally accepted that all of them correspond to a unique, more or less complex, oceanic domain, the Rheic Ocean (Simancas *et al*., 2005; Martínez Catalán *et al*., 2009). The allochthonous complexes show a late Variscan synformal structure and they are considered to be large klippens composed of several terranes, stacked in a huge and structurally intricated nappe pile (Fig. 2). These terranes recorded distinctive tectonothermal evolutions and are interpreted as dismembered fragments of a polycyclic Variscan and eo-Variscan accretionary complex. Each of the allochthonous terranes are subdivided in units which receive local names, but they can be correlated along the NW Iberian complexes (Cabo Ortegal, Órdenes, Bragança and Morais complexes, and the Malpica-Tui Unit), following similar basis to those used by Arenas *et al*. (1986). In a downwards structural order these terranes are constituted by: upper units, ophiolitic units and basal units, with a frontal serpentinitic mélange located at the base of the pile, the Somozas Mélange (Arenas *et al*., 2009). Below the allochthonous complexes, the Schistose Domain of Galicia-Trás-os-Montes (or Parautochthon) shows a similar lithological constitution and tectonothermal evolution to those characteristic of the Iberian Autochthon (Central Iberian Zone of the Iberian Massif).

The upper units of the Cabo Ortegal Complex are subdivided in an uppermost member with intermediate pressure metamorphism (IP upper units) and a lower member affected by high pressure and high temperature metamorphism (HP-HT upper units). This terrane is considered a remnant of a Cambrian peri-Gondwanan magmatic arc (Fuenlabrada *et al*., 2010), rifted from the main continent (Gómez Barreiro *et al*., 2007) and affected by a polymetamorphic evolution developed during the magmatic arc stage and later during eo-Variscan times (Abati *et al*., 1999; Fernández Suárez *et al*., 2002). The ophiolitic units are generally subdivided in lower ophiolites and upper ophiolites, with Cambrian (ca. 500 Ma) and Devonian (ca. 395 Ma) ages respectively, and they are considered to represent the opening and closure of the Rheic Ocean (Díaz García *et al*., 1999; Arenas *et al*., 2007; Sánchez Martínez *et al*., 2007, 2011). The basal units represent a section of the most external Gondwanan margin, subducted at ca. 370 Ma during a collisional event considered the first true Variscan deformation recorded in the belt (Arenas *et al*., 1995; Martínez Catalán *et al*., 1996; Abati *et al*., 2010; Díez Fernández *et al*., 2011).

The HP-HT units are constituted by paragneisses, mafic and ultramafic rocks, with some minor felsic bodies (Vogel, 1967; Girardeau *et al*., 1989; Gil Ibarguchi *et al*., 1990). The mafic rocks appear as different types of eclogites and Cpx-Grt granulites (pyrigarnites) and as their retrogressive products which include migmatitic amphibolitic gneisses, amphibolites and scarce greenschists. Gabbros occur in several stages of transformation, from rocks without any evidences of metamorphism to coronitic metagabbros, high-P granulites and amphibolites (Arenas and Martínez Catalán, 2002). In the upper units of the Cabo Ortegal Complex, both IP upper units and HP-HT units are represented. The IP upper units are only represented by amphibolite facies gneisses, the Cariño Gneisses. The HP-HT units include granulite facies gneisses (Chimparra Gneisses) and the deepest eclogite facies gneisses described in this paper (Banded Gneisses, Fig. 3). U-Pb zircon dating of the well preserved gabbros, eclogites and Cpx-Grt granulites indicates an age for the mafic protoliths in the range of 520-490 Ma, with a HP-HT metamorphic event ranging between 400-390 Ma (Santos Zalduegui *et al*., 1996; Ordóñez Casado *et al*., 2001; Fernández Suárez *et al*., 2007). The subsequent decompression of the HP-HT units was very fast, according to other U-Pb ages obtained in leucosomes developed during migmatization of the mafic granulites which are almost indistinguishable from the high-P event and range between 397-390 Ma (Fernández Suárez *et al*., 2007). During their exhumation, the HP-HT units were affected by intense shearing that generated a pervasive mylonitic fabric with regional distribution, followed by the development of large recumbent folds and thrusts (Marcos *et al*., 1984; Ábalos *et al*., 2003, 2011; Puelles *et al*., 2009).

P-T conditions of the eclogite facies metamorphism developed in the HP-HT units were estimated at 780-800 °C and 22 kbar, using classical thermobarometric techniques on the mineral assemblages from the main layer of eclogites (Fig. 3) in the Cabo Ortegal Complex (Mendia, 2000). This is a ca. 300 m thick band of massive eclogites located at the base of the eclogitic gneisses and it shows similar characteristics to other minor eclogites included in the eclogitic gneisses. The Cariño Gneisses, above the eclogitic gneisses, show metamorphic peak conditions calculated at 700 ± 50 °C and 12 ± 1,5 kbar (Castiñeiras, 2005). Consequently it is clear that the Cariño Gneisses were not involved in the HP-HT event and that the contact with the eclogitic gneisses is an important extensional detachment. The metamorphic jump between both

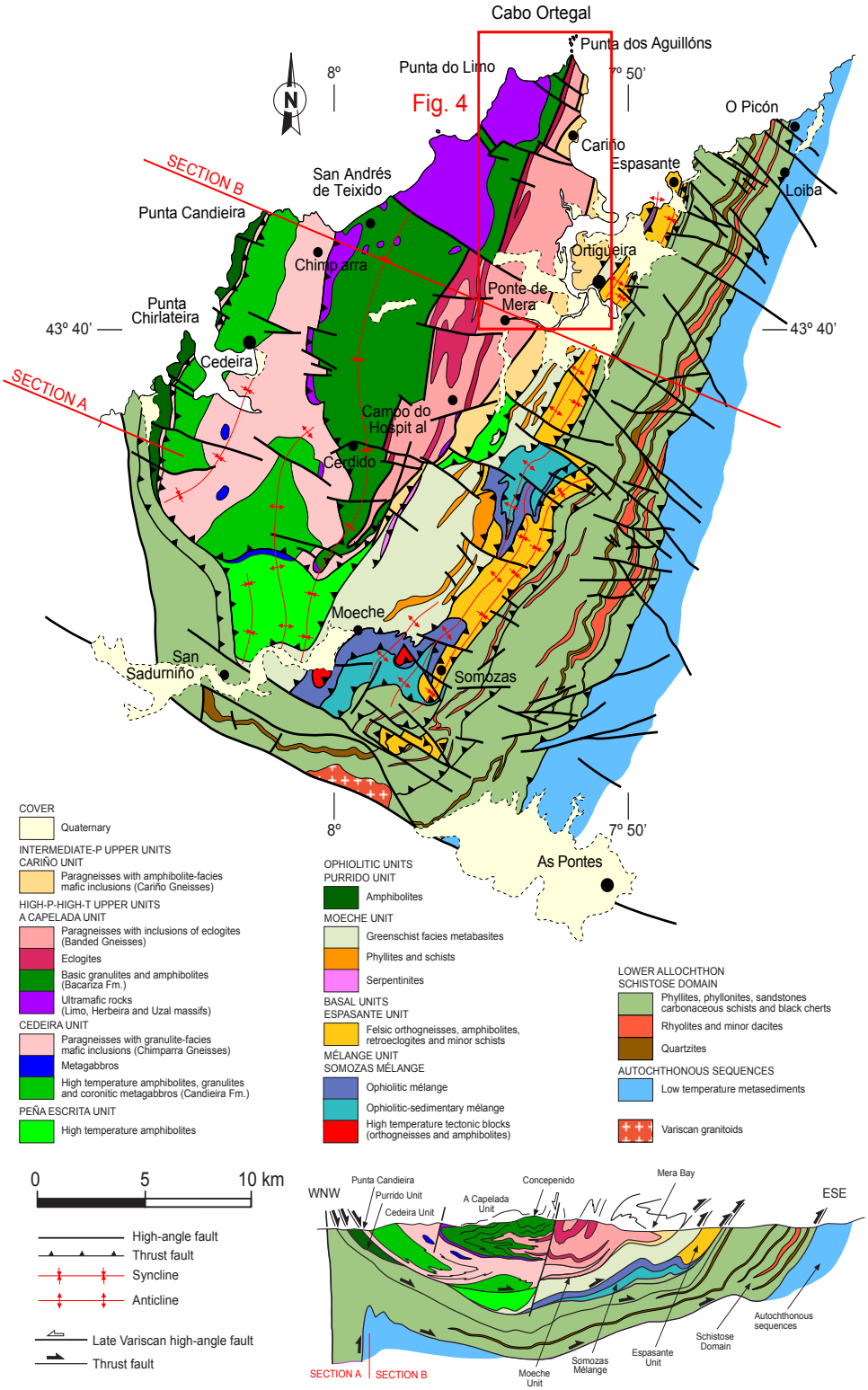

Fig. 3.- Geological map and cross-section of the Cabo Ortegal Complex. The location of the geological map presented in figure 4 is also shown. Modified from Vogel (1967), Marcos *et al*. (1984), Arenas *et al*. (1986, 2009).

Fig. 3.- Mapa geológico y sección transversal del Complejo de Cabo Ortegal. También se indica la localización del mapa geológico de la figura 4. Modificado de Vogel (1967), Marcos *et al*. (1984), Arenas *et al*. (1986, 2009).

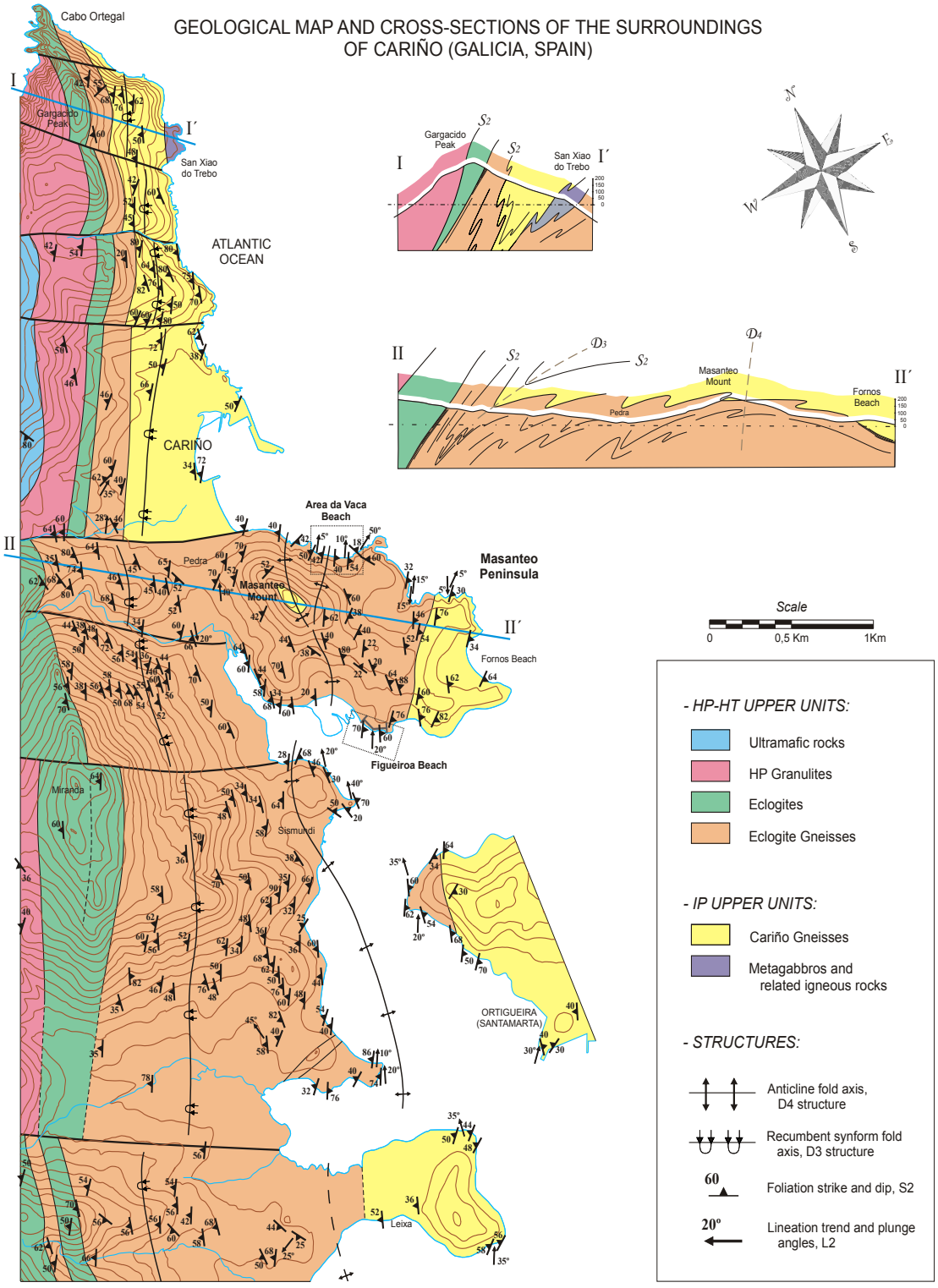

Fig. 4.- Geological map and cross-sections of the northern part of the eclogite facies gneisses. The location of Figueiroa and Area da Vaca sections are also shown.

Fig. 4.- Mapa geológico y secciones transversales de la parte septentrional de los gneises eclogíticos. También se indica la localización de las secciones geológicas de Figueiroa y Area da Vaca.

gneiss formations can thence be calculated in the range of 10 kbar.

3. The eclogite facies gneisses

The eclogite gneisses is a ca. 20 km long and 500-700 m thick unit (Figs. 3 and 4) mainly composed of metasedimentary rocks, eclogites, felsic rocks, abundant melts and their retrogressed products (Fig. 5). Some scarce inclusions of ultramafic rocks also appear in a unique locality. According to the coexistence of Omp + Grt (abbreviations after Kretz, 1983) in the mafic inclusions, this gneiss formation is the only one in the upper units of the Cabo Ortegal Complex that reached eclogite facies conditions. As the mafic inclusions are eclogites and retroeclogites we assume that the metasedimentary rocks were also eclogized, but they do not show any clear petrological evidence of an eclogite facies metamorphism as their mineral assemblages are not diagnostic from a petrographic point of view. This is probably due to the retrogradation processes that took place or because the mineral assemblage is only susceptible to reveal the HP conditions by thermodynamic modeling, which has not been performed. The metasedimentary rocks can be divided into metapelitic and metagreywackic types, and they always appear intensively migmatized and sheared displaying abundant quartzo-feldspathic leucosomes. The original sedimentary sequence was intruded by two main types of magmatic rocks. The first type, much more abundant than the second, was formed by diabasic dikes and gabbros now displayed as eclogites, retrogressed eclogites and rare coronitic metagabbros, while the second type is represented by thin inclusions of orthogneisses probably derived from granitic to tonalitic protoliths.

A unique exposure located in the Masanteo peninsula (Fig. 4) shows a thick mafic body of eclogites scarcely affected by post-peak shearing. The eclogites are intruded by abundant mesocratic melts with tonalitic compositions (Fig. 6f), showing outstanding features similar to those seen in a mingling of basic and felsic rocks. The mafic body does not show in its internal zone the common tight foliation that is generally observed along the formation. Instead this sector exhibits brecciated forms and rounded shapes in contact with the melt. Its mafic parts are well preserved eclogites, but the metamorphic conditions of the melts are not so clear because no distinctive mineral assemblages have been identified yet. However, we believe that the felsic rocks were probably derived from extensive partial melting affecting the metasedimentary gneisses during the first stages of decompression. These melts intruded and brecciated parts of the formation increasing heterogeneity, but their real participation in the gneiss formation can only be appreciated in the rare domains with moderate shearing. According to this data and interpretations, the participation in this formation of felsic material generated by decompressive partial melting can be very important, making difficult the distinction of the pre-metamorphic lithologies and compositions.

3.1. Lithologies and mineral assemblages

The most representative lithology in this formation is a gneiss bearing Qtz+Grt+Pl+Bt+Ky as primary minerals, which is considered a metasedimentary rock (Fig. 5b). According to their different compositions two distinctive gneissic types can be distinguished: one has relatively high alumina content and it is considered metapelitic; the other lacks Ky and the other alumina-rich minerals are scarce and therefore it is thought to be metagreywackic. In the field these gneisses define a banded formation variably migmatized but generally rich in centimetre to decimetre thick leucosomes which always appear sheared by the regional pervasive foliation. Within these gneisses there are two types of basic rocks: variably retrogressed eclogites with Grt+Cpx+Hbl+Pl+Czo+Rt+Ilm+Spn (Fig. 5f and 5g); and what it is thought to be a prograde pre-eclogitic type, coronitic metagabbros composed of Ol+Grt+Pl+Czo+Rt+Ilm+Spn (Fig. 5h and 5i). The eclogitic inclusions are common in most sections of the gneiss formation, but the coronitic metagabbros are very rare. The eclogites and retrogressed eclogites are displayed as variably sized boudins, from decametres to centimetres, and in the case of the thicker inclusions they can contain an internal foliation different to the regional foliation that surrounds the boudins. In the best preserved eclogites it is possible to observe that this internal foliation was developed in eclogite facies conditions, because it is defined by the dimensional orientation of omphacite. Two types of orthogneisses can be distinguished, a granitic one with Qtz+Grt+Pl+Mc+Bt (Fig. 5d) and a tonalitic one with Qtz+Grt+Pl+Hbl+Czo (Fig. 5c). These orthogneisses do not define lenticular boudins as in the case of the mafic inclusions, by the contrary they appear as centimetre to metre thick leucocratic bands within the metasedimentary rocks, intensively sheared by the regional foliation.

3.2. General structure

Detailed geological cross sections

Five consecutive events were developed during the tectonothermal evolution of the eclogite facies gneisses. All of them generated representative structures that can be discussed using the good exposures of the coastal section.

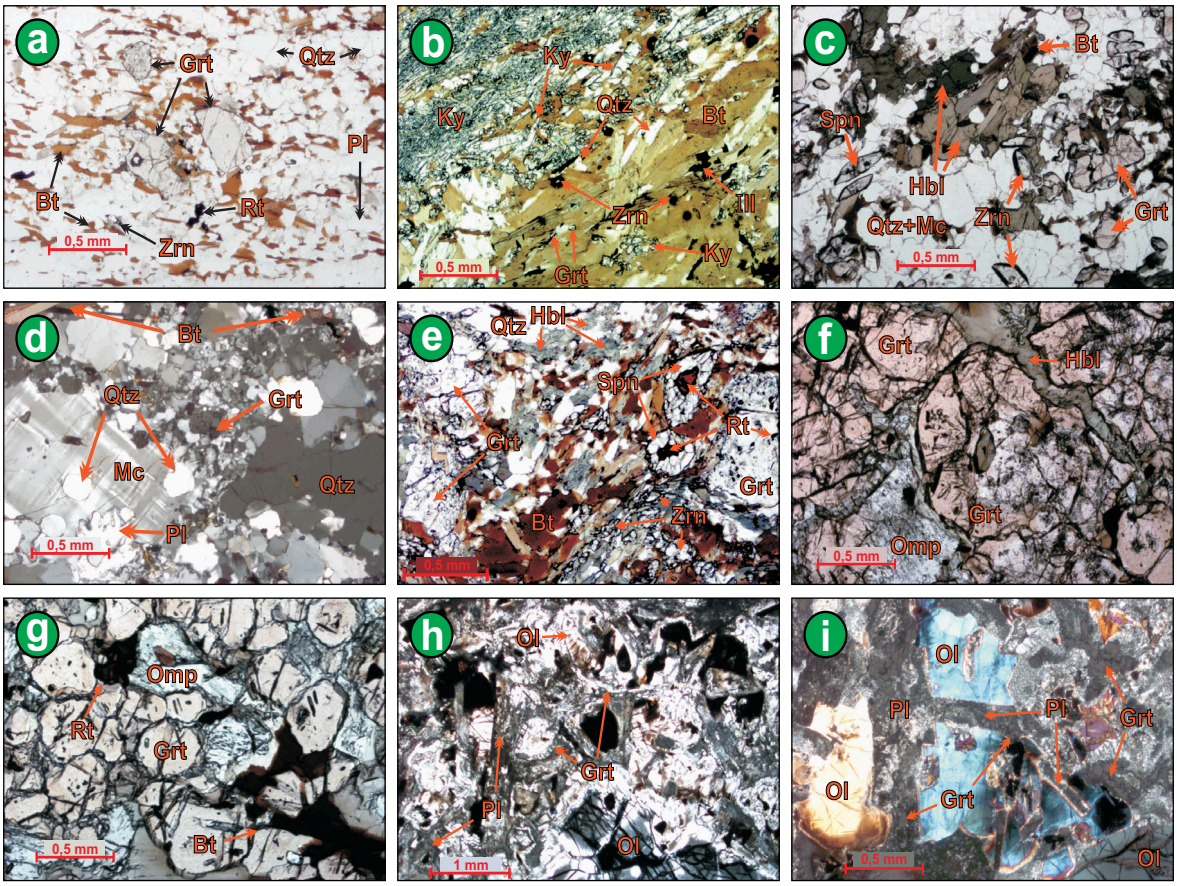

Fig. 5.- Photomicrographs of representative samples. a) Granolepidoblastic paragneiss (Qtz+Grt+Bt+Pl+Rt+Ilm+Spn); this sample lacks quartzo-feldespathic leucosomes and was little affected by D_2 retrogression, it corresponds to the paragneisses within the boudins shown in figures 6c and 6d. b) Banded paragneiss with abundant quartzo-feldespathic leucosomes and biotite rich domains (Qtz+Grt+Ky+Bt+Ms+Pl+Or+Ilm). c) Tonalitic melt intruding eclogites in the North coast of the Masanteo Peninsula (Qtz+Grt+Bt+Ms+Pl+Hbl+Czo+Rt+Ilm+Spn); it corresponds to the felsic rocks in figure 6f. d) Granitic orthogneiss (Qtz+Grt+Bt+Ms+Pl+Kfs+Ilm). e) Amphibole bearing gneiss (Qtz+Grt+Bt+Pl+Kfs+Hbl+Czo+Ilm+Spn). f) Eclogite with Omp, Grt and secondary Hbl; inclusions in Grt are mainly Rt. g) Low retrogressed eclogite (Qtz+Grt+Omp+Hbl+Bt+Rt). h) Coronitic metagabbro with preserved ophitic texture; garnet coronas developed by reaction between Ol (preserved in the section) and Pl (replaced by Ab and Ep). i) A detail in the previous coronitic metagabbro showing the garnet coronas between olivine and plagioclase.

Fig. 5.- Microfotografías de muestras representativas. a) Paragneis granolepidoblástico (Qtz+Grt+Bt+Pl+Rt+Ilm+Spn); esta muestra carece de leucosomas cuarzofeldespáticos y fue poco retrogradada durante D_2, corresponde a los paragneises del interior de los boudins mostrados en las figuras 6c y 6d. b) Paragneis bandeado con abundantes leucosomas cuarzofeldespáticos y dominios ricos en biotita (Qtz+Grt+Ky+Bt+Ms+Pl+Or+Ilm). c) Fundidos tonalíticos intrusivos en eclogitas en la costa Norte de la Península de Masanteo (Qtz+Grt+Bt+Ms+Pl+Hbl+Czo+Rt+Ilm+Spn); corresponden a las rocas félsicas de la figura 6f. d) Ortogneises graníticos (Qtz+Grt+Bt+Ms+Pl+Kfs+Ilm). e) Gneis anfibólico (Qtz+Grt+Bt +Pl+Kfs+Hbl+Czo+Ilm+Spn). f) Eclogita con Omp, Grt y Hbl secundaria; las inclusiones en Grt son mayoritariamente Rt. g) Eclogita poco retrogradada (Qtz+Grt+Omp+Hbl+Bt+Rt). h) Metagabro coronítico con textura ofítica preservada; las coronas de granate se desarrollaron por reacción entre Ol (preservado) y Pl (reemplazada por Ab y Ep). i) Detalle del metagabro coronítico de la figura 6h mostrando las coronas de granate entre el olivino y la plagioclasa.

Two of these exposures have been studied in detail and two geological cross sections have been performed. The geological section of Figueiroa beach (Fig. 7) is located in the South coast of the Masanteo Peninsula (Fig. 4). It is a 210 metre long outcrop representation, which is very close to the eastern boundary of the eclogitic gneisses. This section shows a quasi-homoclinal sequence that dips to the East with an average angle of 50 to 80º trending N to N20ºE. It includes almost all types of lithologies, where orthogneisses are scarce and eclogites are abundant. The most obvious structural feature is a generalized S_2 mylonitic foliation developed during a D_2 deformative event with regional distribution. This S_2 foliation surrounds the larger mafic boudins and appears folded by

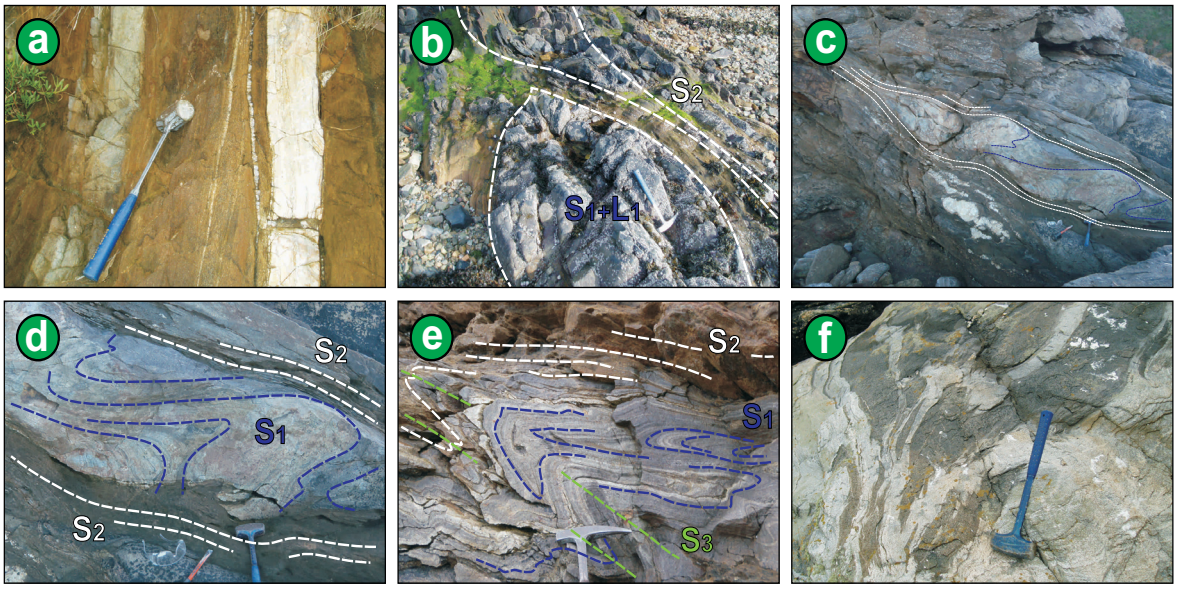

Fig. 6.- Photographs of some representative outcrops of the eclogite facies gneisses in the Masanteo Peninsula (Fig. 4). a) Eclogite (mafic left layer) and orthogneiss (felsic right layer) within paragneisses. b) Eclogite boudin with preserved internal fabric surrounded by the metasedimentary gneisses. c) Slightly sheared gneissic boudin surrounded by the regional S_2 foliation; the boudin preserves an internal fabric interpreted as the relict S_1 foliation, and lacks quartzo-feldespathic leucosomes. d) Enlarged aspect of the previous low deformed gneissic lens; it is surrounded by other highly sheared migmatitic gneisses, the common gneiss type in the eclogite facies gneisses. e) Slightly sheared gneissic lens showing a relict S_1 foliation tightly folded during the regional D_2 event, which produces the S_2 foliation outlining the outcrop; recumbent D_3 folds, without associated axial planar foliation, developed later. f) Large eclogitic outcrop intruded by tonalitic melts and later affected by tight recumbent folds.

Fig. 6.- Fotografías de algunos afloramientos representativos de los gneises eclogíticos en la Península de Masanteo (Fig. 4). a) Eclogita (capa máfica de la izquierda) y ortogneis (capa félsica) entre paragneises. b) Boudin de eclogita con fábrica interna preservada envuelto por los gneises metasedimentarios. c) Boudin gnéisico poco cizallado envuelto por la foliación regional S_2; el boudin preserva una fábrica interna interpretada como la foliación S_1 relicta, y carece de leucosomas cuarzofeldespáticos. d) Aspecto ampliado del boudin gnéisico anterior con escasa deformación; está envuelto por otros gneises migmatíticos intensamente cizallados, que representan el tipo de gneises más común. e) Boudin gnéisico poco cizallado que contiene una foliación relicta S_1 fuertemente plegada durante el evento regional D_2, al que también se asocia la foliación regional S_2 que envuelve al afloramiento; los pliegues recumbentes D_3, sin desarrollo de foliación de plano axial, se generaron posteriormente. f) Gran afloramiento de eclogitas intruidas por líquidos de composición tonalítica y con desarrollo posterior de pliegues recumbentes apretados.

upright folds developed during a D_4 deformation (previous large D_3 recumbent folds are not obvious in these sections. They can be observed in a larger scale in figures 3 and 4). The geological section of Area da Vaca beach is 490 metres long (Fig. 8) and it is situated at the north coast of the Masanteo Peninsula (Fig. 4). In this section the eclogites are not abundant whereas the orthogneisses are very numerous, especially in the central part where the eclogites are missing. At the beginning and at the end of this section two large bodies of eclogites appear. The original contacts with the gneisses were important shear zones, but now they appear overprinted by brittle faults. The whole section defines a wide and open D_4 major antiform, and also shows a folded S_2 foliation that actually surrounds the large mafic bodies. Some of the felsic rocks show syntectonic relations with S_2 suggesting that they were generated during partial melting coeval with this deformative event. Some of the felsic rocks in this section also define D_2 folds, and in few cases an S_2 axial plane foliation can be observed. Other observations supporting this syn-tectonic D_2 nature of some felsic rocks are there post-eclogitic and intrusive nature (Fig. 6f) observed in few outcrops at the north coast of the Masanteo Peninsula (Fig. 4) and that it seems that there development took place synchronously with S_2 due to the observation of elongated mineral aggregates with a highly ductile aspect, which is compatible with a syn-kinematic crystallization of a melt. In the Area da Vaca section and in few cases in the Figueiroa section, the larger eclogitic boudins include an internal foliation previous to the regional one. Considering that in the best preserved boudins this foliation is defined by the minerals forming the eclogitic mineral assemblage, this foliation is considered an S_1 fabric developed during the eclogitic subductive event (D_1).

Structure of the eclogite facies gneisses

Taking into account the lithological and structural data obtained in these two sections, and also the additional in-

formation about the largest structures in the region that can be deduced from the geological maps and the general cross sections (Figs. 3 and 4), the deformative events affecting the eclogitic gneisses can be summarized as follows.

Evidence for an eclogite facies metamorphism and associated fabric ($D_1 – S_1$) can be obtained from some mafic inclusions but only in few cases in the metasedimentary gneisses. During the eclogitic metamorphism a foliation (S_1) and a lineation (L_1) that show a top-to-north sense of movement (Ábalos *et al*., 2003, 2011) were developed in the mafic rocks, being generally difficult to observe. The observation of D_1 features is even more elusive in the metasedimentary rocks, because the next deformational event (D_2) almost totally erased the previous structures and mineral assemblages by intense shearing and retrogradation processes. Only in few outcrops of gneisses in the Masanteo Peninsula, some metric boudins of metasedimentary rocks surrounded by the S_2 foliation but showing little shearing associated to D_2 and preserving D_1 features have been observed (Fig 6d and 6e). In this case the distance between S_1 foliation planes is wider (1-2 cm) than S_2 planes (0.1-1 cm), and the quartzo-feldespathic domains are less differentiated (i.e. quartzo-feldespathic domains due to metamorphic differentiation are less felsic than those from metasedimentary rocks were only D_2 is recognised). It is not possible to observe any mineralogical differences between these gneisses and the same gneisses affected by D_2 shearing, but microscopic textural differences do exist. In the gneisses preserving D_1 features there is no secondary mineral growth, no migmatization is found (i.e. leucosomes due to anatexis are not found), and the lepidoblastic minerals such as Bt are not highly concentrated in the foliation planes. The existence of previous Cambrian deformations in the upper units has been demonstrated by different authors using U-Pb geochronological data (Fernández Suárez *et al*., 2002; Abati *et al*., 2007; Díaz García *et al*., 2010). These deformations were developed during the generation of the protoliths in a Cambrian peri-Gondwanan magmatic arc. However, there is no evidence of any pre-D_1 (D_0) fabric or mineral assemblage in the gneiss formation, in accordance with the extreme metamorphic conditions developed during the eclogite facies metamorphism, except of some igneous minerals preserved in scarce coronitic metagabbros (Fig. 5h and 5i).

The characteristic banding in this formation is a result of the extreme deformation developed during D_2 event. All along this stage the formation experienced mylonitic decompressive shearing and migmatization, developing an S_2 foliation that presently shows a regional distribution. S_2 has an approximately N20ºE strike, and dips to the West or to the East (Fig. 4). Associated to S_2 foliation there is an L_2 lineation with top-to-north sense of movement. This lineation trends N10ºE - N30ºE and has a plunge ranging 5º - 30º, generally due NE. S_2 is a pervasive mylonitic fabric that wraps around the larger eclogite bodies and also generates zones of tectonic mix by extreme shearing and mixing of retrograded mafic rocks, gneisses and melts (m.175, Fig 7). Other than small tight folding, almost isoclinal, there is local formation of sheath folds, both most probably formed by D_2. The generalized migmatization concentrates the quartzo-feldespathic aggregates in large lenses (various centimetres) and in very small pods (up to 1-2 cm), which gives an augen aspect to some parts of these gneisses.

The regional distribution of the gneiss formation is controlled by large recumbent folds with an East vergence (D_3), always folding S_2. The largest of these folds is a kilometric scale recumbent synform which is the most prominent feature in the general structure of the upper units in the Cabo Ortegal Complex (Fig. 3 and sections I-I´ and II-II´ of Fig. 4). This synform was early mapped by Vogel (1967), but its real significance and detailed geometry was presented by Marcos *et al*. (1984). Its axial plane is sub-horizontal and strikes in a N-S direction at regional scale (Fig. 3), although in the eastern part of the complex it dips to the West (Fig. 4). This large recumbent fold rarely developed an axial planar foliation (S_3) that has been observed close to the hinge zone only in the Cariño Gneisses. Another related recumbent fold can be observed in the eastern limit of the upper units, where the Cariño Gneisses appear below the eclogitic gneisses dipping to the West and directly in contact with the Moeche Ophiolite (Fig. 3). These relations necessarily imply that a tight recumbent antiform exists under the large synform. Many evidences of recumbent folding can be seen in the hinge zone of this antiform, near the contact with the Moeche Ophiolite, especially in the Leixa area (Fig. 4). The age of the recumbent folds is not accurately known, but it is certainly younger than the emplacement of the IP upper units over the HP-HT units, because the limit between them is also folded by the large synform (Figs. 3 and 4).

The upper units of the Cabo Ortegal Complex are thrust over the ophiolites represented by the Purrido and Moeche units (Fig. 3). The recumbent antiform of the eastern limit rests directly over the thrust. Evidence of important shearing can be seen in the contact zone. The deformation occurred in greenschist facies conditions and a new mylonitic fabric appears in the Cariño Gneisses and especially in the greenschists of the Moeche Ophiolite. The geometry of the recumbent folds and the thrust seem to indicate that the generation of both types of structures

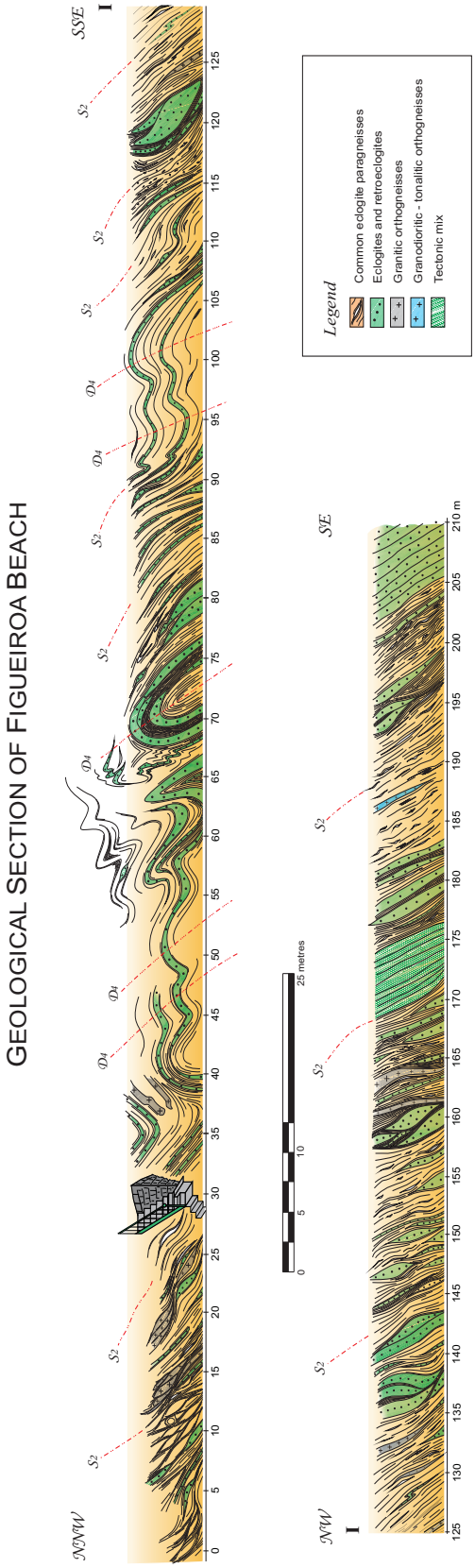

Fig. 7.- Geological section of Figueiroa beach (see location in Fig. 4).
Fig. 7.- Sección geológica de la playa de Figueiroa (véase localización en Fig. 4).

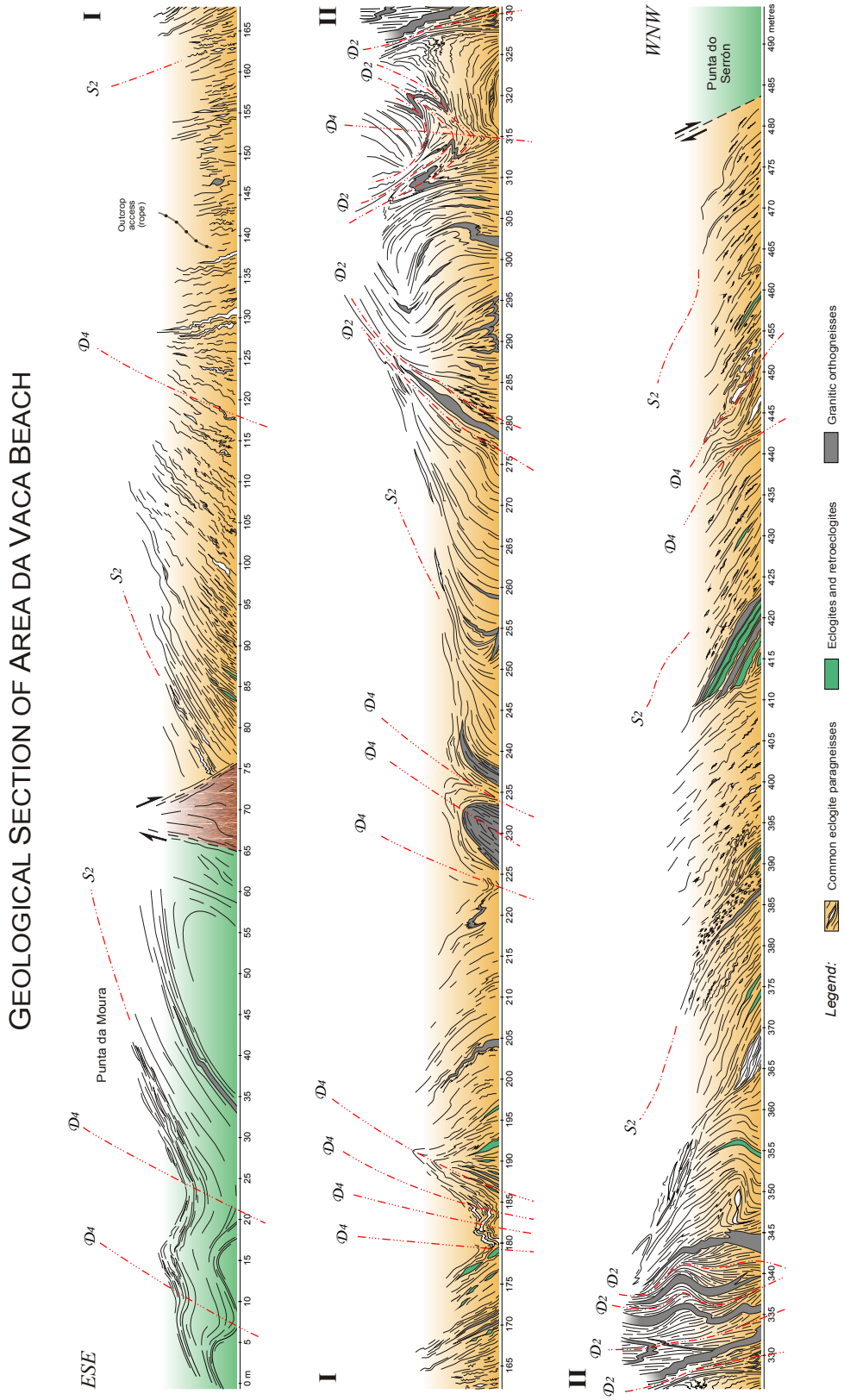

Fig. 8.- Geological section of Area da Vaca beach (see location in Fig. 4).
Fig. 8.- Sección geológica de la playa de Area da Vaca (véase localización en Fig. 4).

could be related, at least in the eastern part of the Cabo Ortegal Complex, the area that represents the front of the allochthonous complexes, the leading edge of the huge allochthonous pile moving to the East from the more internal zones of the orogen. The age of the thrust and the recumbent folds is not completely clear. The recumbent folds are younger than 390 Ma, which is a reference age for the migmatization and the development of the S_2 foliation in the Cabo Ortegal Complex (Peucat *et al*., 1990; Fernández Suárez *et al*., 2007). On the other hand, these folds are also younger than the extensional contact between the Cariño Gneisses and the eclogitic gneisses, as this contact is folded by the large recumbent synform (Figs. 3 and 4). An extensional contact similar to this one and also affecting similar units in the Órdenes Complex was dated at 375 Ma (Corredoiras detachments; Dallmeyer *et al*., 1997). The basal thrust of the upper units cuts the amphibolite facies foliation of the Purrido Unit (upper ophiolites), dated in the range of 391-377 Ma (Peucat *et al*., 1990; Dallmeyer *et al*., 1997). Moreover, the greenschist facies foliation of the Moeche Unit was dated at 364 Ma (Dallmeyer *et al*., 1997). Therefore, the thrust and the associated recumbent folds are probably younger than 375 Ma, but older than 364 Ma.

The S_2 mylonitic foliation, the D_3 recumbent folds and the basal thrust are additionally affected by upright folds (D_4), the largest of which is the huge open synform (klippen) of the Cabo Ortegal Complex (Fig. 3). Another important D_4 fold is the smooth antiform centred in the Masanteo Peninsula (Fig. 4). Minor D_4 folds are also abundant across the two sections represented in figures 7 and 8. There is no axial planar foliation associated to D_4 folds.

4. Discussion: the exhumation of the HP-HT units

The eclogite facies gneisses of the Cabo Ortegal Complex were subducted at a great depth. This is a gneiss formation similar to others described in the Variscan suture zone affected by ultra-high-P metamorphism. The P-T conditions obtained so far in this formation are less extreme than those considered characteristic for the UHP metamorphism, but relatively close (ca. 780-800 °C and 22 kbar). The eclogitic gneiss unit belongs to the upper units of the allochthonous complexes, a large crustal ensemble interpreted as a Cambrian peri-Gondwanan terrane with magmatic arc affinities. The high-P conditions that affected parts of this terrane indicate that they once constituted a subduction complex, developed on a continental or a transitional thinned continental margin containing thick sedimentary series. The deep subduction (D_1 event, see section 3.2) of this margin necessarily implies the existence of a prograde continent colliding with a retro-continent. Taking into account that the NW Iberian Variscan suture is rootless, which is also the situation of similar allochthonous terranes along the Variscan Belt (Fig. 1), and also considering that the upper allochthonous units are presently emplaced above ophiolites, it is not possible to obtain direct evidence about the identity of the involved continents. However, in the context of the gneissic unit and in present coordinates, subduction occurred with 10-30° N direction and top-to-the-North kinematics (Ábalos *et al*., 2011).

The subducted complex experienced a drastic and fast exhumation (D_2 event, see section 3.2) during generation of the decompressive mylonitic foliation (S_2) that constitutes the most prominent structural feature in the HP-HT units. The magnitude of the exhumation registered during D_2 can be calculated in ca. 10 kbar and it was developed in ca. 10 Ma (subduction at ca. 400-390 Ma vs. exhumation at ca. 390 Ma). Such a pronounced exhumation very likely occurred during continuous subduction of continental or transitional slices, i.e. new layers of the same terrane represented by the upper units that in a prograde accretionary sequence should be presently located below the HP-HT units (Platt, 1986). These units are not preserved, at least in NW Iberia, because the HP-HT units rest above ophiolitic units, which avoid direct interpretation of the colliding margins. The progression of exhumation favors the generation of an important extensional detachment, which is represented by the contact between the Cariño Gneisses, in the amphibolite facies and located in the hanging wall, and the eclogite facies gneisses. Similar detachments have been also described in the Órdenes Complex, both inside the intermediate pressure units and also in the contact with the HP-HT units (Martínez Catalán *et al*., 2002). In that contact, the Corredoiras detachment shows almost identical characteristics to the detachment described above of the Banded Gneisses, with an age calculated at ca. 375 Ma ($^{40}Ar/^{39}Ar$ geochronology; Dallmeyer *et al*., 1997). The sketch shown in figure 9 presents a model for the exhumation of the eclogite facies gneisses and in general for the HP-HT units of the Cabo Ortegal Complex (paleogeographic reconstructions at these times have been published in many works, i.e. Gómez Barreiro *et al.*, 2007).

The tectonothermal and exhumation history of the HP-HT units, illustrated by the eclogite facies gneisses, fits quite well to the conclusions obtained by Beaumont *et al*. (2009) in relation to the exhumation of ultra-high-P complexes. Specifically the exhumation rates and the time range obtained for this process in the basis of ge-

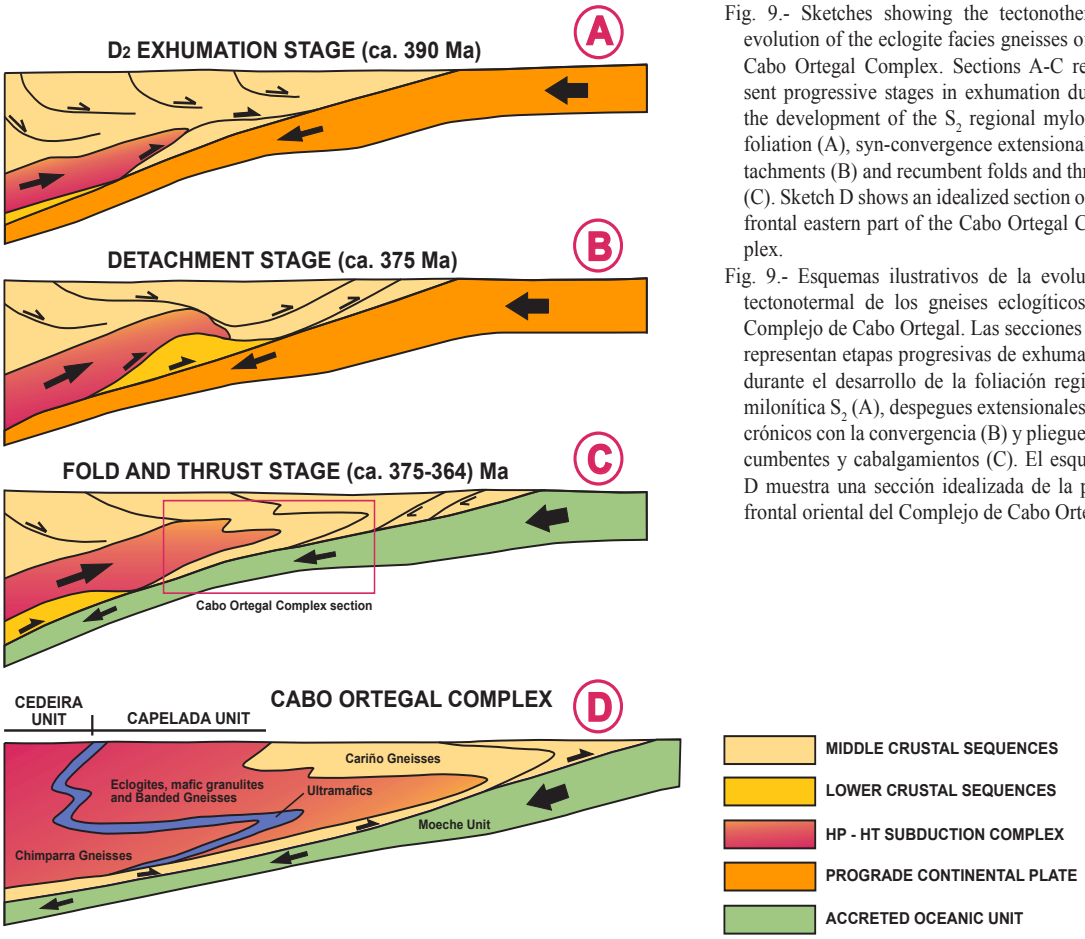

Fig. 9.- Sketches showing the tectonothermal evolution of the eclogite facies gneisses of the Cabo Ortegal Complex. Sections A-C represent progressive stages in exhumation during the development of the S_2 regional mylonitic foliation (A), syn-convergence extensional detachments (B) and recumbent folds and thrusts (C). Sketch D shows an idealized section of the frontal eastern part of the Cabo Ortegal Complex.

Fig. 9.- Esquemas ilustrativos de la evolución tectonotermal de los gneises eclogíticos del Complejo de Cabo Ortegal. Las secciones A-C representan etapas progresivas de exhumación durante el desarrollo de la foliación regional milonítica S_2 (A), despegues extensionales sincrónicos con la convergencia (B) y pliegues recumbentes y cabalgamientos (C). El esquema D muestra una sección idealizada de la parte frontal oriental del Complejo de Cabo Ortegal.

ochronological isotopic data, follows with significant detail the predictions based on numerical experiments. Moreover, as it has been discussed in previous sections, the progression of the deformational history in the upper units entails the development of large recumbent folds and a basal thrust (D_3 structures, see section 3.2 and figures 3 and 4). The geometry of both structures seems to indicate that their development could be related and that they represent the final events in the exhumation of the subducted complex. This is also in good agreement with the structural pattern predicted by the theoretical models (Warren *et al*., 2008; Beaumont *et al*., 2009), but in this case the time range, although uncertain, seems to be larger. Comparison of the structures predicted in these models and those explained in this paper are represented in figure 9, such as a UHP buoyant plume (HP-HT units) or large regional structures (D_3 recumbent folds and basal thrust). The progression of the exhumation entails an important change in the nature of the colliding plates, because during this evolution the prograde continental margin was replaced by the underthrusting of ophiolites (Fig. 9). These ophiolitic slices were initially accreted in amphibolite facies conditions (Purrido Unit), but they were finally replaced, after additional exhumation of the orogenic wedge, by the underthrusting of greenschist facies ophiolites (Moeche Unit). The paleogeographic meaning for this change in the type of subduction, from a continental subduction to the accretion of ophiolitic units, is presently uncertain, although it has been traditionally related to the closure of the Rheic Ocean (Gómez Barreiro *et al*., 2007; Sánchez Martínez *et al*., 2007).

The tectonothermal evolution of the eclogite facies gneisses of the Cabo Ortegal Complex represents an illustrative example of the complex history of these deeply subducted complexes, which are relatively frequent in the suture zone of the Variscan Belt. It is important to remark that the structural, metamorphic and geochronological patterns in the evolution of this gneissic unit follows almost perfectly the predictions based in numerical experiments about the exhumation of ultra-high-P complexes. Consequently, it represents a direct confirmation of the reality of these models.

Acknowledgements

Financial support for this research has been provided by the Spanish project CGL2007-65338-CO2-01/BTE (Ministerio de Economía y Competitividad). Insightful review of the manuscript performed by Jean-Marc Lardeaux and Francisco Martínez are gratefully acknowledged, as well as the editorial work and suggestions of Cesar Casquet. Richard Albert thanks to the Universidad Complutense de Madrid which provided him with a four-year pre-doctoral grant. This study is also a contribution to the IGCP 597 project, Amalgamation and breakup of Pangaea: the type example of the supercontinent cycle.

References

Ábalos, B., Puelles, P., Gil Ibarguchi, J.I. (2003): Structural assemblages of high-pressure mantle and crustal rocks in a subduction channel (Cabo Ortegal, NW Spain). *Tectonics* 22, 1-21. doi: 10.1029/2002tc001405.

Ábalos, B., Fountain, D.M., Gil Ibarguchi, J.I., Puelles, P. (2011): Eclogite as a seismic marker in subduction channels: Seismic velocities, anisotropy, and petrofabric of Cabo Ortegal eclogite tectonites (Spain). *Geological Society of America Bulletin* 123, 439-456. doi: 10.1130/b30226.1.

Abati, J., Dunning, G.R., Arenas, R., Díaz García, F., González Cuadra, P., Martínez Catalán, J.R., Andonaegui, P. (1999): Early Ordovician orogenic event in Galicia (NW Spain): evidence from U-Pb ages in the uppermost unit of the Ordenes Complex. *Earth and Planetary Science Letters* 165, 213-228. doi: 10.1016/s0012-821x(98)00268-4.

Abati, J., Castiñeiras, P., Arenas, R., Fernández-Suárez, J., Gómez Barreiro, J., Wooden, J. (2007): Using SHRIMP-RG U-Pb zircon dating to unravel tectonomagmatic events in arc environments. The early Paleozoic arc of NW Iberia revisited. *Terra Nova* 19, 432-439. doi: 10.1111/j.1365-3121.2007.00768.x.

Abati, J., Gerdes, A., Fernández-Suárez, J., Arenas, R., Whitehouse, M.J., Díez Fernández, R. (2010): Magmatism and early-Variscan continental subduction in the northern Gondwana margin recorded in zircons from the basal units of Galicia, NW Spain. *Geological Society of America Bulletin* 122, 219-235. doi: 10.1130/b26572.1.

Allemand, P., Lardeaux, J.M. (1997): Strain partitioning and metamorphism in a deformable orogenic wedge: Application to the Alpine belt. *Tectonophysics* 280, 157-169. doi: 10.1016/S0040-1951(97)00136-4.

Arenas, R., Gil Ibarguchi, J.I., González Lodeiro, F., Klein, E., Martínez Catalán, J.R., Ortega Gironés, E., Pablo Maciá, J.G. de, Peinado, M. (1986): Tectonostratigraphic units in the complexes with mafic and related rocks of the NW of the Iberian Massif. *Hercynica* II, 87-110.

Arenas, R., Rubio Pascual, F.J., Díaz García, F., Martínez Catalán, J.R. (1995): High-pressure micro-inclusions and development of an inverted metamorphic gradient in the Santiago Schists (Ordenes Complex, NW Iberian Massif, Spain): evidence of subduction and syn-collisional decompression. *Journal of Metamorphic Geology* 13, 141-164. doi: 10.1111/j.1525-1314.1995.tb00211.x.

Arenas, R., Martínez Catalán, J.R. (2002): Prograde development of corona textures in metagabbros of the Sobrado unit (Órdenes Complex, northwestern Iberian Massif). In: Martínez Catalán, J.R., Hatcher, R.D., Jr, Arenas, R. and Díaz García, F. (eds.), *Variscan-Appalachian dynamics: The building of the late Paleozoic basement.* Geological Society of America, Special Paper 364: 73-88. doi:10.1130/0-8137-2364-7.73.

Arenas, R., Martínez Catalán, J.R., Sánchez Martínez, S., Fernández-Suárez, J., Andonaegui, P., Pearce, J.A., Corfu, F. (2007): The Vila de Cruces Ophiolite: A remnant of the early Rheic Ocean in the Variscan suture of Galicia (NW Iberian Massif). *Journal of Geology* 115, 129-148. doi: 10.1086/510645.

Arenas, R., Sánchez Martínez, S., Castiñeiras, P., Jeffries, T.E., Díez Fernández, R., Andonaegui, P. (2009): The basal tectonic mélange of the Cabo Ortegal Complex (NW Iberian Massif): a key unit in the suture of Pangea. *Journal of Iberian Geology* 35, 85-125.

Beaumont, C., Jamieson, R.A., Butler, J.P., Warren, C.J. (2009): Crustal structure: A key constraint on the mechanism of ultra-high-pressure rock exhumation. *Earth and Planetary Science Letters* 287, 116-129. doi: 10.1016/j.epsl.2009.08.001.

Castiñeiras, P. (2005): Origen y evolución tectonotermal de las unidades de O Pino y Cariño (Complejos Alóctonos de Galicia). *Nova Terra* 28: 279 p.

Chopin, C. (2003): Ultrahigh-pressure metamorphism; tracing continental crust into the mantle. *Earth and Planetary Science Letters* 212, 1-14. doi: 10.1016/s0012-821x(03)00261-9.

Dallmeyer, R.D., Martínez Catalán, J.R., Arenas, R., Gil Ibarguchi, J.I., Guiérrez Alonso, G., Farias, P., Bastida, F., Aller, J. (1997): Diachronous Variscan tectonothermal activity in the NW Iberian Massif: Evidence from $^{40}Ar/^{39}Ar$ dating of regional fabrics. *Tectonophysics* 277, 307-337. doi: 10.1016/s0040-1951(97)00035-8.

Díaz García, F., Arenas, R., Martínez Catalán, J.R., González del Tánago, J., Dunning, G. (1999): Tectonic evolution of the Careón ophiolite (Northwest Spain): a remnant of oceanic lithosphere in the Variscan belt. *Journal of Geology* 107, 587-605.

Díaz García, F., Sánchez Martínez, S., Castiñeiras, P., Fuenlabrada, J.M., Arenas, R. (2010): A peri-Gondwanan arc in NW Iberia. II: Assessment of the intra-arc tectonothermal evolution through U-Pb SHRIMP dating of mafic dykes. *Gondwana Research* 17, 352-362. doi: 10.1016/j.gr.2009.09.010.

Díez Fernández, R., Martínez Catalán, J.R., Arenas, R., Abati, J. (2011): Tectonic evolution of a continental subduction-exhumation channel: Variscan structure of the basal allochthonous units in NW Spain. *Tectonics* 30. doi: 10.1029/2010TC002850.

Fernández Suárez, J., Corfu, F., Arenas, R., Marcos, A., Martínez Catalán, J.R., Díaz García, F., Abati, J., Fernández, F.J. (2002): U-Pb evidence for a polyorogenic evolution of the HP-HT units of the NW Iberian Massif. *Contributions to Mineralogy and Petrology* 143, 236-253. doi: 10.1007/s00410-001-0337-2.

Fernández-Suárez, J., Arenas, R., Abati, J., Martínez Catalán, J.R., Whitehouse, M.J., Jeffries, T.E. (2007): U-Pb chronometry of polymetamorphic high-pressure granulites: An example from the allochthonous terranes of the NW Iberian Variscan belt. In: Hatcher, R.D., Jr., Carlson, M.P., McBride, J.H. and Martínez Catalán, J.R. (eds.), *4–D framework of continental crust.* Geological Society of America, Memoir 200: 469-488. doi: 10.1130/2007.1200(24).

Fuenlabrada, J.M., Arenas, R., Sánchez Martínez, S., Díaz García, F., Castiñeiras, P. (2010): A peri-Gondwanan arc in NW Iberia. I: Isotopic and geochemical constraints on the origin of the arc - A sedimentary approach. *Gondwana Research* 17, 338-351. doi: 10.1016/j.gr.2009.09.007.

Gerya, T.V., Stöckhert, B., Perchuk, A.L. (2002): Exhumation of high-pressure metamorphic rocks in a subduction channel: A numerical

simulation. *Tectonics* 21, 6-1-19. doi: 10.1029/2002tc001406.

Gerya, T., Stöckhert, B. (2006): Two-dimensional numerical modeling of tectonic and metamorphic histories at active continental margins. *International Journal of Earth Sciences* 95, 250-274. doi: 10.1007/s00531-005-0035-9.

Gil Ibarguchi, J.I., Mendia, M., Girardeau, J., Peucat, J.J. (1990): Petrology of eclogites and clynopiroxene-garnet metabasites from the Cabo Ortegal Complex (northwestern Spain). *Lithos* 25, 133-162. doi: 10.1016/0024-4937(90)90011-O.

Girardeau, J., Gil Ibarguchi, J.I., Ben Jamaa, N. (1989): Evidence for heterogeneous upper mantle in the Cabo Ortegal Complex, Spain. *Science* 245, 1231-1233. doi: 10.1126/science.245.4923.1231.

Gómez Barreiro, J., Martínez Catalán, J.R., Arenas, R., Castiñeiras, P., Abati, J., Díaz García, F., Wijbrans, J.R. (2007): Tectonic evolution of the upper allochthon of the Órdenes complex (northwestern Iberian Massif): Structural constraints to a polyorogenic peri-Gondwanan terrane, in: Linneman, U., Nance, R.D., Kraft, P. and Zulauf, G. (eds.), *The evolution of the Rheic Ocean: From Avalonian-Cadomian active margin to Alleghenian-Variscan collision*. Geological Society of America, Special Paper 423: 315-332. doi: 10.1130/2007.2423(15).

Kretz, R. (1983): Symbols for rock-forming minerals. *American Mineralogist* 68, 277-279.

Kryza, R., Pin, C. (2002): Mafic rocks in a deep-crustal segment of the Variscides (the Góry Sowie, SW Poland): evidence for crustal contamination in an extensional setting. *International Journal of Earth Science* 91, 1017-1029. doi: 10.1007/s00531-002-0294-7.

Lardeaux, J.M., Ledru, P., Daniel, I., Duchene, S. (2001): The Variscan French Massif Central-a new addition to the ultra-high pressure metamorphic 'club': exhumation processes and geodynamic consequences. *Tectonophysics* 332, 143-167. doi: 10.1016/s0040-1951(00)00253-5.

Marcos, A., Marquínez, J., Pérez-Estaún, A., Pulgar, J.A., Bastida, F. (1984): Nuevas aportaciones al conocimiento de la evolución tectonometamórfica del Complejo de Cabo Ortegal (NW de España). *Cuadernos do Laboratorio Xeolóxico de Laxe* 7, 125-137.

Martínez Catalán, J.R., Arenas, R., Díaz García, F., Rubio Pascual, F.J., Abati, J., Marquínez, J. (1996): Variscan exhumation of a subducted Paleozoic continental margin: The basal units of the Ordenes Complex, Galicia, NW Spain. *Tectonics* 15, 106-121. doi: 10.1029/95tc02617.

Martínez Catalán, J.R., Díaz García, F., Arenas, R., Abati, J., Castiñeiras, P., González Cuadra, P., Gómez Barreiro, J., Rubio Pascual, F. (2002): Thrust and detachment systems in the Ordenes Complex (northwestern Spain): Implications for the Variscan-Appalachian geodynamics, in: Martínez Catalán, J.R., Hatcher, R.D., Jr, Arenas, R. and Díaz García, F. (Eds.), *Variscan-Appalachian dynamics: The building of the late Paleozoic basement.* Geological Society of America, Special Paper 364: 163-182. doi:10.1130/0-8137-2364-7.163.

Martínez Catalán, J.R., Arenas, R., Abati, J., Sánchez Martínez, S., Díaz García, F., Fernández Suárez, J., González Cuadra, P., Castiñeiras, P., Gómez Barreiro, J., Díez Montes, A., González Clavijo, E., Rubio Pascual, F.J., Andonaegui, P., Jeffries, T.E., Alcock, J.E., Díez Fernández, R., López Carmona, A. (2009): A rootless suture and the loss of the roots of a mountain chain: The Variscan belt of NW Iberia. *Comptes Rendus Geoscience* 341, 114-126. doi: 10.1016/j.crte.2008.11.004.Massonne, H.-J. (2001): First find of coesite in the ultrahigh-pressure metamorphic area of the central Erzgebirge, Germany. *European Journal of Mineralogy* 13, 565-570. doi: 10.1127/0935-1221/2001/0013-0565.

Massone, H.-J. (2003): A comparison of the evolution of diamondiferous quartz-rich rocks from the Saxonian Erzgebirge and the Kokchetav Massif: Are so-called diamondiferous gneisses magmatic rocks? *Earth and Planetary Science Letters* 216, 347-364. doi: 10.1016/s0012-821x(03)00512-0.

Massone, H.-J., Kennedy, A., Nasdala, L., Theye, T. (2007): Dating of zircon and monazite from diamondiferous quartzofeldspathic rocks of the Saxonian Erzgebirge - hints at burial and exhumation velocities. *Mineralogical Magazine* 71, 407-425. doi: 10.1180/minmag.2007.071.4.407.

Mendia, M.S. (2000): Petrología de la Unidad Eclogítica del Complejo de Cabo Ortegal (NW de España). *Nova Terra* 16: 424 p.

Obrien, P.J., Vrana, S. (1995): Eclogites with a short-lived granulite facies overprint in the Moldanubian Zone, Czech Republic: petrology, geochemistry and diffusion modelling of garnet zoning. *Geologische Rundschau* 84, 473-488. doi: 10.1007/s005310050019.

Ordóñez Casado, B., Gebauer, D., Schäfer, H.J., Gil Ibarguchi, J.I., Peucat, J.J. (2001): A single Devonian subduction event for the HP/HT metamorphism of the Cabo Ortegal complex within the Iberian Massif. *Tectonophysics* 332, 359-385. doi: 10.1016/S0040-1951(00)00210-9.

Peucat, J.J., Bernard-Griffiths, J., Gil Ibarguchi, J.I., Dallmeyer, R.D., Menot, R.P., Cornichet, J., Iglesias Ponce de León, M., (1990): Geochemical and geochronological cross section of the deep Variscan crust: The Cabo Ortegal high-pressure nappe (northwestern Spain). *Tectonophysics* 177, 263-292. doi: 10.1016/0040-1951(90)90285-g.

Platt, J.P. (1986): Dynamics of orogenic wedges and the uplift of high-pressure metamorphic rocks. *Geological Society of America Bulletin* 97, 1037-1053. doi: 10.1130/0016-7606(1986)97<1037:DOOWAT>2.0.CO;2.

Platt, J.P. (1993): Exhumation of high pressure rocks: a review of concepts and processes. *Terra Nova* 5, 119-133. doi: 10.1111/j.1365-3121.1993.tb00237.x.

Puelles, P., Ábalos, B., Gil Ibarguchi, J.I. (2009): Transposed high-pressure granulite fabrics (Cabo Ortegal, NW Spain): implications on the scales of deformation localization. *Journal of Structural Geology* 31, 776-790. doi: 10.1016/j.jsg.2009.05.001.

Sánchez Martínez, S., Arenas, R., Díaz García, F., Martínez Catalán, J.R., Gómez-Barreiro, J., Pearce, J.A. (2007): Careón Ophiolite, NW Spain: Supra-subduction zone setting for the youngest Rheic ocean floor. *Geology* 35, 53-56. doi: 10.1130/g23024a.1.

Sánchez Martínez, S., Arenas, R., Gerdes, A., Castiñeiras, P., Potrel, A., Fernández-Suárez, J. (2011): Isotope geochemistry and revised geochronology of the Purrido Ophiolite (Cabo Ortegal Complex, NW Iberian Massif): Devonian magmatism with mixed sources and involved Mesoproterozoic basement. *Journal of the Geological Society*, London 168, 733-750. doi: 10.1144/0016-76492010-065.

Santos Zalduegui, J.F., Schärer, U., Gil Ibarguchi, J.I., Girardeau, J. (1996): Origin and evolution of the Paleozoic Cabo Ortegal ultramafic-mafic complex (NW Spain): U-Pb, Rb-Sr and Pb-Pb isotope data. *Chemical Geology* 129, 281-304. doi: 10.1016/0009-2541(95)00144-1.

Simancas, J.F., Tahiri, A., Azor, A., González Lodeiro, F., Martínez Poyatos, D.J., El Hadi, H. (2005): The tectonic frame of the Variscan-Alleghanian orogen in Southern Europe and Northern Africa. *Tectonophysics* 398, 181-198. doi: 10.1016/j.tecto.2005.02.006.

Timmermann, H., Štědrá, V., Gerdes, A., Noble, S.R., Parrish, R.R., Dörr, W. (2004): The problem of dating high-pressure metamorphism: a U-Pb isotope and geochemical study on eclogites and related rocks of the Mariánské Lázně Complex, Czech Republic. *Journal of Petrology* 45, 1311-1338. doi: 10.1093/petrology/egh020.

Vogel, D.E. (1967): Petrology of an eclogite- and pyrigarnite-bearing polymetamorphic rock complex at Cabo Ortegal, NW Spain. *Leidse Geologische Mededelingen* 40, 121-213.

Warren, C.J., Beaumont, C., Jamieson, R.A. (2008): Modelling tectonic styles and ultra-high pressure (UHP) rock exhumation during the transition from oceanic subduction to continental collision. *Earth and Planetary Science Letters* 267, 129-145. doi: 10.1016/j.epsl.2007.11.025.

Yamato, P., Burov, E., Agard, P., Le Pourhiet, L., Jolivet, L. (2008): HP-UHP exhumation during slow continental subduction: Self-consistent thermodynamically and thermomechanically coupled model with application to the Western Alps. *Earth and Planetary Science Letters* 271, 63-74. doi:10.1016/j.epsl.2008.03.049.

V

Provenance of the Variscan Upper Allochthon

5.1. Introduction

This chapter presents an article dealing with provenance studies of the Cariño Gneiss formation. These gneisses represent the intermediate-pressure (IP) Upper Allochthon in the Cabo Ortegal Complex. The main objective of this article is to find out from which continents or cratons the detrital materials of the upper units derive. Back in 2003, an article was published dealing with these issues, studying the upper units from the Órdenes Complex (Fernández-Suárez *et al.*, 2003). This work already concluded that these units are derived from Gondwana but even so this article was planned with the aim of knowing if the Upper Allochthon is in fact a continuous terrane present in the rest of the complexes. It was also required to refine the conclusions proposed increasing the statistical adequacy of the data by analysing more zircon grains with the U–Pb LA-ICP-MS zircon method and to complement the study with Lu–Hf zircon and Sm–Nd whole-rock analyses. With these additional techniques many conclusions have arisen about crustal growth events in the detrital source areas and about the geological environment of the depositional basin.

5.2. Partial conclusions

The protoliths of the metasedimentary rocks of the Cariño Gneiss formation are formed by siliciclastic series that represent the deposition of greywackes by turbidity currents at *c.* 510 Ma. The siliciclastic series were deposited in a peripheral back-arc basin, somewhere between an active volcanic arc and the Northern margin of the West Africa Craton (WAC). In this tectonic setting, detritus arrived from the active part of the volcanic arc and from the mainland. These metasedimentary rocks record Archean, Eburnean, and late or post-Cadomian crust formation events, with a 3.6% Mesoproterozoic zircon input. In the source region of the gneiss formation, the Archean crust formation event is roughly dated at *c.* 3.3–2.9 Ga, which is represented by zircons with *c.* 3.0–2.2 Ga crystallization ages. These Archean materials suffered important crustal reworking processes, supporting an intracratonic or an active margin setting. The recorded Eburnean events represent the intrusion of juvenile Eburnean depleted-mantle derived magmas into an Archean basement, most probably the Archean basement represented by the Cariño Gneiss Archean zircon population. The most probable geodynamic setting is a volcanic arc at the margin of a pre-existing Archean craton. Archean and Paleoproterozoic (Eburnean) zircon populations are most probably derived from the WAC. The Cambrian events recorded in the Cariño Gneisses represent a magmatic arc at the periphery of the North Gondwana margin, specifically the North WAC. This arc records the intrusion of *c.* 525 Ma juvenile DM-derived magmas into the Eburnean and Archean basement of Gondwana. The first stages of the arc were probably linked to the Cadomian arc system, defined in other parts of Europe as to have an activity bracketed between 750 Ma and 540 Ma, and so it could represent a long lasting volcanic-magmatic arc system. Taking into account the Nd model ages published from other metagreywacke series included in the NW Iberian Upper Allochthon, it can be concluded that this terrane contains heterogeneous isotopic sources. These varied sources indicate that different parts of the peri-Gondwanan arc system may be preserved in the Upper Allochthon.

Gondwana Research 28 (2015) 1434–1448

Contents lists available at ScienceDirect

Gondwana Research

journal homepage: www.elsevier.com/locate/gr

Provenance of the Variscan Upper Allochthon (Cabo Ortegal Complex, NW Iberian Massif)

R. Albert [a,*], R. Arenas [a], A. Gerdes [b,c], S. Sánchez Martínez [a], J. Fernández-Suárez [a], J.M. Fuenlabrada [d]

[a] Departamento de Petrología y Geoquímica and Instituto de Geociencias (UCM-CSIC), Universidad Complutense de Madrid, Spain
[b] Institut für Geowissenschaften, Petrologie und Geochemie, J.W. Goethe Universität, Frankfurt am Main, Germany
[c] Department of Earth Sciences, Stellenbosch University, Private Bag X1, Matieland, South Africa
[d] CAI de Geocronología y Geoquímica Isotópica, Universidad Complutense de Madrid, Spain

ARTICLE INFO

Article history:
Received 28 May 2014
Received in revised form 17 October 2014
Accepted 20 October 2014
Available online 15 November 2014

Handling Editor: I. Safonova

Keywords:
Detrital zircons
Provenance
Isotope geochemistry
Variscan Upper Allochthon
Cabo Ortegal Complex

ABSTRACT

This study focuses on the provenance of the uppermost unit of the Upper Allochthon of the Variscan belt with combined U–Pb and Lu–Hf zircon (LA-ICPMS) and Sm–Nd whole-rock analyses. This unit is represented in the Cabo Ortegal Complex (NW Iberia) by the metasiliciclastic Cariño Gneisses which overlap ophiolitic units that represent perigondwanan oceanic domains. The data set indicates a maximum depositional age of c. 510 Ma and a c. 1.73 Ga Sm–Nd model age, typifying a late or post Pan-African (or Cadomian) and Eburnean events, which entailed abundant input of juvenile material involving broad mixing with older crustal sources. The Mesoproterozoic activity is scarce and scattered and therefore unlikely to represent a major crust generation pulse in the source area of the siliciclastic unit. The data set also records an Archean orogenic pulse in its source area followed by a long lasting crust reworking process, where the Eburnean juvenile materials intruded. These data are interpreted as indicative of a West Africa Craton provenance, where the siliciclastic series from which the Cariño Gneisses are derived were probably deposited in a back-arc type basin where detritus was mostly sourced by the continent rather than the magmatic arc.

1. Introduction

The Variscan–Appalachian–Alleghenian orogeny was formed when the Pangea supercontinent assembled during Carboniferous and Early Permian. Part of the European branch of this orogen, the Variscan belt, is well preserved in the Iberian Massif. This Massif exhibits an almost complete section of the southern part (present day coordinates) of the orogen from the most external zones (Autochthon) to the internal sections which are represented by the Parautochthon and the allochthonous complexes.

Our understanding of the sources and provenance of the rock series involved in the Variscan Orogeny has significantly increased in the last few years mostly driven by U–Pb and Lu–Hf zircon (LA-ICPMS) and Sm–Nd whole rock studies. In the NW Iberian Massif most of the provenance studies have been focussed on sedimentary series located below the ophiolitic units, either in the autochthonous domain (Cantabrian zone, CZ, West-Asturian–Leonese zone, WALZ, and Central Iberian zone, CIZ, Fig. 1a, Fernández-Suárez et al., 1999; Gutiérrez-Alonso et al., 2003; Martínez Catalán et al., 2004; Fernández-Suárez et al., 2013; Shaw et al., 2014), the Parautochthon (Díez Fernández et al., 2012b) or the basal units (Díez Fernández et al., 2010). These studies suggest as a main conclusion that the rock series were formed at the periphery of the Gondwanan margin, between the Nubian platform and the periphery of West African Craton (WAC), although their exact location is still a matter of debate. The key for paleogeographic reconstructions is usually focussed on the presence or absence of a Stenian–Tonian zircon population in Ediacaran and post-Ediacaran rock series. Rocks containing this population are usually placed in front of the Sahara Craton or the Nubian Shield (Díez Fernández et al., 2010; Fernández-Suárez et al., 2013; Shaw et al., 2014), whereas those lacking or having an extremely low quantity of it are considered to have a proximal WAC provenance (Abati et al., 2010a, 2012). Nevertheless, the real importance of the isotopic sources has not been completely evaluated in NW Iberia as there are almost no previous studies integrating U–Pb/Lu–Hf (zircon) and Sm–Nd (whole rock) data systematics. This kind of studies is absent in metasedimentary rock series and only very few works have presented some of these combined results for metaigneous rocks (i.e. Sánchez Martínez et al., 2011).

The Upper Allochthon or upper units is located above the ophiolitic units, which are considered to represent the Variscan suture in the NW Iberian Massif. This issue poses first order questions, not only about tectonic settings but also about provenance and sources of the involved rock series. In the Upper Allochthon, two works were carried out separately publishing U–Pb detrital zircon and Sm–Nd whole rock data on metagreywackes (Fernández-Suárez et al., 2003; Fuenlabrada et al.,

* Corresponding author.
E-mail address: r.albert@geo.ucm.es (R. Albert).

http://dx.doi.org/10.1016/j.gr.2014.10.016
1342-937X/

2010). Both studies focussed on the siliciclastic series located at the uppermost structural position of the Órdenes Complex which is situated to the West of the Cabo Ortegal Complex (Fig. 1b–c), where the mentioned series are not represented. According to the data in the works mentioned above, this terrane has been considered as WAC derived, but the young Nd model ages obtained from the metagreywackes (c. 1 Ga) are inconsistent with the old isotopic sources expected from the WAC. This observation requires additional explanations. Also, new and integrated U–Pb/Lu–Hf (zircon) and Sm–Nd (whole rock) data are needed to present a complete picture for the provenance of the upper units, as the previously studied greywacke series are only representative for the uppermost stratigraphic levels of this thick terrane (c. 10,000–12,000 m).

This contribution presents a provenance study of the upper units combining U–Pb and Lu–Hf in zircon (LA-SF-ICPMS) and Sm–Nd whole rock analyses. The rocks studied belong to the Cariño Gneiss formation, which is the top member of the Upper Allochthon of the Cabo Ortegal Complex, different to and occupying a lower position than the metagreywackes previously studied in the Órdenes Complex. This will allow a straightforward comparison and a better understanding of the origin of this terrane.

2. Geological framework of the Upper Allochthon in NW Iberia

The NW sector of the Iberian Massif includes an autochthonous domain, represented by the Cantabrian (CZ), West-Asturian-Leonese (WALZ) and Central Iberian (CIZ, Fig. 1a) zones. This domain is overlain by an allochthonous domain which is represented by the Galicia-Trás-os-Montes Zone (GTOMZ). In the GTOMZ a lower assemblage is considered as the Lower Allochthon or Parautochthon. Above it, a group of five allochthonous complexes include the remnants of the Variscan suture which can be followed throughout Europe, from the Iberian to the Bohemian Massif (Fig. 1a; Martínez Catalán et al., 2009). These allochthonous complexes have an intricate internal structure, but they appear clearly constituted by three terranes with contrasting origin, structure and tectonothermal evolution. The complexes are nappe piles structured as late Variscan synforms, and they are divided upwards as basal, ophiolitic and upper units.

The basal units represent a crustal terrane formed by the subduction of the Gondwanan continental margin below Laurrusia at c. 370 Ma (Gil Ibarguchi and Ortega Gironés, 1985; Arenas et al., 1995; Rodríguez et al., 2003; Abati et al., 2010b; Díez Fernández et al., 2011; López-Carmona et al., 2014). This terrane contains metasedimentary rock series with Ediacaran to Early Ordovician maximum depositional ages (Díez Fernández et al., 2010; 2012b), intruded by abundant calc-alkaline (c. 493 Ma; Abati et al., 2010b) to alkaline–peralkaline (c. 475–470 Ma; Díez Fernández et al., 2012a) granitic bodies.

The ophiolitic units are formed by mafic–ultramafic rock series that have been the object of recent works. They represent a varied assemblage with units formed in different stages in the evolution of the Paleozoic oceans. Part of these ophiolites have been interpreted as Cambrian remnants of the peri-Gondwanan oceans, including sequences accreted at the base of a fore-arc (Sánchez Martínez et al., 2012) and back-arc sequences (Arenas et al., 2007). However the most extended ophiolitic units in NW Iberia, and also along the Variscan suture in the rest of Europe, are c. 395 Ma mafic–ultramafic rock series. The interpretation of these units has changed over time. They were first considered supra-subduction zone ophiolites formed during the last stages of the closure of the Rheic Ocean (Díaz García et al., 1999; Sánchez Martínez et al., 2007). However these ophiolites, according to new U–Pb/Lu–Hf zircon data, have been recently considered to be related to the opening of a long pull-apart basin, which show an interaction of the mafic rocks with an old continental basement (Sánchez Martínez et al., 2011; Arenas et al., 2013, 2014).

The upper units or Upper Allochthon constitutes a terrane with continental-crust affinity which can be divided into high pressure–high temperature (HP–HT) units below and intermediate pressure (IP) units above. The HP–HT base of this terrane is mainly composed of ultramafic rocks, basic, intermediate and acid granulites, eclogites, orthogneisses and paragneisses (Vogel, 1967; Gil Ibarguchi et al., 1990; Peucat et al., 1990; Ábalos et al., 2003). The protolith ages for the igneous rocks are clustered around c. 490 Ma and the age of the HP–HT metamorphism is c. 400–390 Ma (Ordóñez Casado et al., 2001; Fernández-Suárez et al., 2007). The uppermost section of the Upper Allochthon, the IP upper units, is composed of a thick siliciclastic series with greywacke and pelitic members and minor conglomerates (Díaz García, 1990; Díaz García et al., 2010). In the Órdenes Complex the greywackes have chemical compositions characteristic of volcanic-arc settings (Fuenlabrada et al., 2010) and maximum depositional ages in the range of 530–500 Ma (Fernández-Suárez et al., 2003; Fuenlabrada et al., 2010). This series is intruded by large massifs of gabbros with tholeitic arc affinity (Andonaegui et al., 2002) and granitoids with calc-alkaline compositions (Andonaegui et al., 2012). U–Pb dating of these mafic and felsic metaigneous rocks yielded protolith ages at c. 500 Ma (Abati et al., 1999; Andonaegui et al., 2012). A doleritic dyke swarm dated at c. 510 Ma also intrudes into the top greywacke series (Díaz García et al., 2010). The IP upper units metamorphic grade decreases upwards from granulite to greenschist facies, with characteristic counter-clockwise P–T paths interpreted as associated to magmatic underplating in a volcanic arc setting (Abati et al., 2003). This arc-related metamorphic event is dated at c. 496–482 Ma (Abati et al., 1999, 2007). Therefore multiple evidence support the original volcanic-arc setting for the upper units of the allochthonous complexes. This volcanic arc was part of the Early Paleozoic peri-Gondwanan arc system. The uppermost part of the preserved section of this arc seems to be only slightly affected by the Variscan and eo-Variscan activity, whereas the lower part was strongly reworked during the Variscan collision developing a high-P and high-T recrystallization in the Devonian.

Most of the terranes and minor members described in the allochthonous complexes of NW Iberia are present in the Cabo Ortegal Complex, a small but well exposed complex on the Northern Galician coast (Fig. 1a). The upper units are mostly represented by the HP–HT units (Fig. 1b and c). The IP upper units are only represented by the Cariño Gneiss formation, which is the uppermost structural unit of the Cabo Ortegal Complex. It is formed by metasedimentary rocks in amphibolite facies with peak metamorphic conditions at 700 °C and 12 kbar (Castiñeiras, 2005). It is a homogeneous metaturbiditic sequence of centimetre-scale alternations of fine-grained pelitic bands with lepidoblastic texture and medium-grained psamitic bands with granoblastic texture, where the amount of medium-grained bands seems to decrease upwards (Castiñeiras, 2005). On the base of their mineralogical composition the psamitic types are described as quartz- and normal greywackes and the pelitic bands as normal and quartz-poor greywackes (Vogel, 1967). This compositional banding is an inherited sedimentary feature representing the deposition of greywackes by turbidity currents. The limits between sedimentary bands also coincide with the foliation, which is defined by preferential orientation of the rock forming minerals. This foliation strikes N-S to c. N45° and dips up to 75° westwards at the western part of the formation and eastwards at the eastern part defining a wide and open antiform (Fig. 2). The dominant regional lineation plunges c. 5° to 30° with a N20°–N55° trend. The formation is folded in a large recumbent synform with subordinated folds with an East vergence. Its axial plane strikes c. N-S and dips to the West in the western part of the formation. Associated with this synform an axial plane foliation developed locally in the fine-grained bands. This large synform does not only affect the Cariño Gneiss formation but also all of the upper units of the Cabo Ortegal Complex. The synform was earlier mapped by Vogel (1967) and Marcos et al. (1984), and a recent interpretative section has been presented by Arenas et al. (2013).

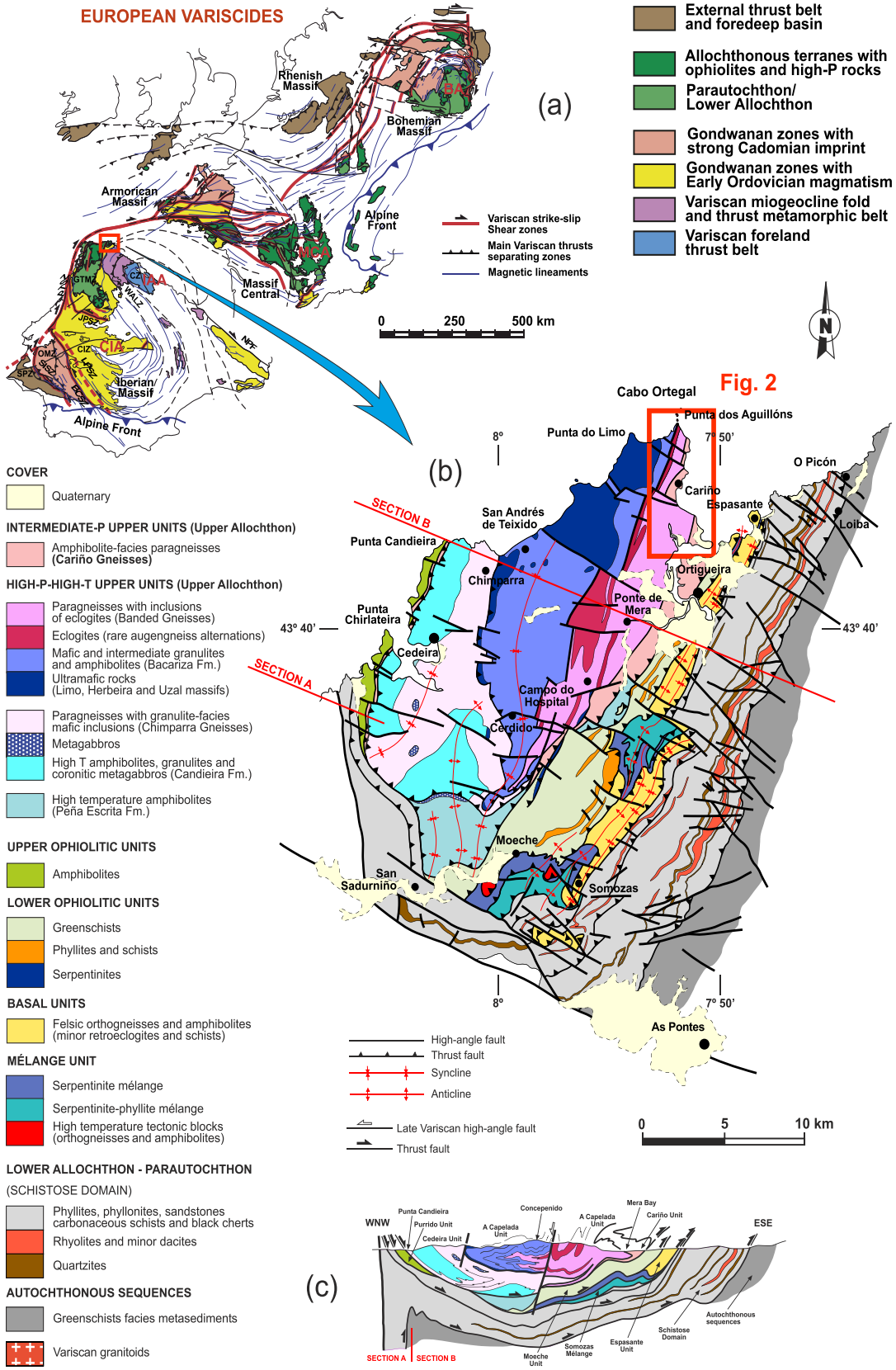
EUROPEAN VARISCIDES
(a)
Rhenish Massif
Bohemian Massif
Armorican Massif
Alpine Front
Massif Central
Iberian Massif
Alpine Front
Variscan strike-slip Shear zones
Main Variscan thrusts separating zones
Magnetic lineaments
0 250 500 km
External thrust belt and foredeep basin
Allochthonous terranes with ophiolites and high-P rocks
Parautochthon/ Lower Allochthon
Gondwanan zones with strong Cadomian imprint
Gondwanan zones with Early Ordovician magmatism
Variscan miogeocline fold and thrust metamorphic belt
Variscan foreland thrust belt
N
Fig. 2
(b)
Cabo Ortegal
Punta dos Aguillóns
Punta do Limo
8°
7° 50'
O Picón
Cariño
Espasante
Loiba
SECTION B
San Andrés de Teixido
Punta Candieira
Chimparra
Ortigueira
Ponte de Mera
Punta Chirlateira
43° 40'
Cedeira
SECTION A
Campo do Hospital
Cerdido
Moeche
San Sadurniño
Somozas
As Pontes
High-angle fault
Thrust fault
Syncline
Anticline
Late Variscan high-angle fault
Thrust fault
0 5 10 km
COVER
Quaternary
INTERMEDIATE-P UPPER UNITS (Upper Allochthon)
Amphibolite-facies paragneisses (Cariño Gneisses)
HIGH-P-HIGH-T UPPER UNITS (Upper Allochthon)
Paragneisses with inclusions of eclogites (Banded Gneisses)
Eclogites (rare augengneiss alternations)
Mafic and intermediate granulites and amphibolites (Bacariza Fm.)
Ultramafic rocks (Limo, Herbeira and Uzal massifs)
Paragneisses with granulite-facies mafic inclusions (Chimparra Gneisses)
Metagabbros
High T amphibolites, granulites and coronitic metagabbros (Candieira Fm.)
High temperature amphibolites (Peña Escrita Fm.)
UPPER OPHIOLITIC UNITS
Amphibolites
LOWER OPHIOLITIC UNITS
Greenschists
Phyllites and schists
Serpentinites
BASAL UNITS
Felsic orthogneisses and amphibolites (minor retroeclogites and schists)
MÉLANGE UNIT
Serpentinite mélange
Serpentinite-phyllite mélange
High temperature tectonic blocks (orthogneisses and amphibolites)
LOWER ALLOCHTHON - PARAUTOCHTHON
(SCHISTOSE DOMAIN)
Phyllites, phyllonites, sandstones carbonaceous schists and black cherts
Rhyolites and minor dacites
Quartzites
AUTOCHTHONOUS SEQUENCES
Greenschists facies metasediments
Variscan granitoids
(c)
WNW
ESE
Punta Candieira
Purrido Unit
Cedeira Unit
A Capelada Unit
Concepenido
A Capelada Unit
Mera Bay
Cariño Unit
Autochthonous sequences
Schistose Domain
Espasante Unit
Somozas Mélange
Moeche Unit
SECTION A
SECTION B

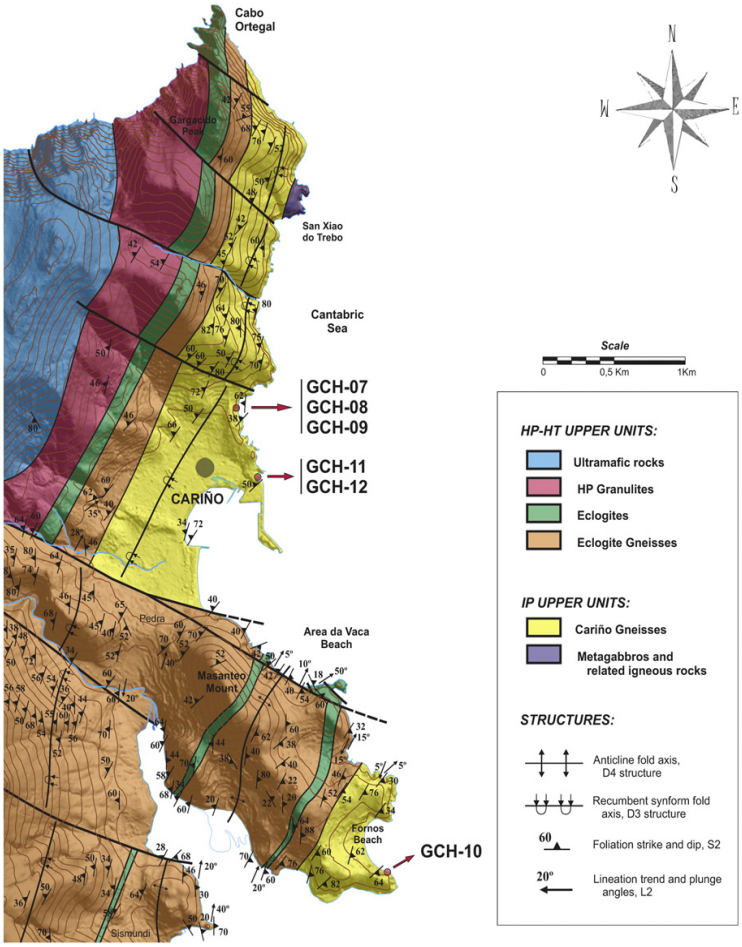

Fig. 2. Geological map of the Northern part of the Cariño Gneiss formation, with the location of the studied samples.

3. Sample description

Six samples were chosen from the Cariño Gneiss formation. The location of these samples is shown in Fig. 2. Samples GCH-07, 08 and 09 were collected at Peiral beach (N43° 44′ 40″, W7° 52′ 2″), samples GCH-11 and 12 from the old shellfish breeding centre (N43° 44′ 23″, W7° 51′ 53″) and sample GCH-10 from Fornos beach (N43° 42′ 41″, W7° 51′ 5″; Simple Cylindrical projection, WGS84 datum). All samples are texturally and compositionally very similar, and were selected from the medium-grained psamitic bands instead of the fine-grained pelitic bands. Microscopically the samples are inequigranular and medium to fine-grained, and show a granoblastic–lepidoblastic texture. Qtz and Pl are the major components. Qtz is slightly undulose and Pl is usually altered. Micas are smaller than Qtz and Pl, Bt is usually retrogressed to Chl, and the preferred orientation that both Bt and Ms define is poorly developed. Grt are strongly corroded and have a dusty appearance due to high abundance of inclusions. Ky and St are very rare in the selected samples but are more abundant in the pelitic bands of these rocks. Other constituents are Spn, Rt, Ilm, Ap, Zrn and opaque matter (mineral abbreviations after Kretz (1983)).

4. Sample preparation and analytical procedures

4.1. Zircon sample preparation

Zircon crystals were separated from bulk samples using conventional mineral separation techniques at the Facultad de Ciencias Geológicas, Universidad Complutense de Madrid (UCM). Samples were cleaned and dried before crushing them in a jaw crusher and in a tungsten disc mill. The light fraction was removed by floatability using a Wilfley table. The magnetic fraction was separated with a hand magnet for the most magnetic minerals and with a Franz model magnetic separator to remove those minerals susceptible to a magnetic field induced by an electric current up to 1.7 A. Minerals with a density below 3325 $kg \cdot m^{-3}$ were removed using CH_2I_2 (diiodomethane) heavy liquid. Zircon hand picking, mounting, imaging and analysis were performed at the J. W. Goethe Universität of Frankfurt am Main (GUF). Hand-picked zircons of all sizes and morphologies were mounted in epoxy filled mounts depending on their size and polished to approximately 50% of their thickness. All

Fig. 1. Geological map of the European Variscides (a) based on Martínez Catalán (2011). Geological map (b) and cross-section (c) of the NW Iberian Cabo Ortegal Complex. The location of Fig. 2 geological map is also shown. Based on Vogel (1967); Marcos et al. (1984); Arenas (1988); Arenas et al. (2013). The Upper Allochthon is formed by the intermediate – P upper units and the high-p – high-T upper units.

zircons studied were documented by back-scattered electron (BSE) and cathodoluminiscence (CL) images using a JSM 6490 scanning electron microscope to study their internal structure in order to choose the best areas for laser ablation.

4.2. U–Pb zircon analyses

Zircons were analysed for U, Th and Pb isotopes at the GUF using a ThermoScientific Element 2 sector field ICP-MS coupled to a Resolution M-50 (Resonetics) 193 nm ArF excimer laser (CompexPro 102, Coherent) system using a slightly modified method as described in Gerdes and Zeh (2006, 2009); Zeh and Gerdes (2012). Laser spot-size was 23 to 33 μm for unknowns, 15 μm for Plešovice, 33 μm for GJ1 and 91500, and 50 μm for Felix standard zircons. Sample surface was cleaned directly before each analysis by four pre-ablation pulses. Ablation was performed in a 0.6 $L \cdot min^{-1}$ He stream, which was mixed directly after the ablation cell with 0.07 $L \cdot min^{-1}$ N_2 and 0.68 $L \cdot min^{-1}$ Ar prior introduction into the Ar plasma of the SF-ICP-MS. The sensitivity achieved was in the range of 8000–12,000 $cps/\mu g \cdot g^{-1}$ for ^{238}U with a 23 μm spot size, at 5.5 Hz and 4–5 $J \cdot cm^{-2}$ using GJ1 zircon. The two-volume ablation cell (Laurin Technic, Australia) of the M50 laser enables detection and sequential sampling of heterogeneous grains (e.g., growth zones) during time resolved data acquisition, due to its quick response time of <1 s (time until maximum signal strength was achieved) and wash-out (<99% of previous signal) time of <3 s. All analyses were common-Pb corrected following the method described in Millonig et al. (2012). ^{204}Hg during the analytical session was about 200 cps. For the analysed sample the common ^{204}Pb contents were mostly near or below the detection limit, and thus a ^{208}Pb-based common Pb correction has been usually applied. The analytical results are presented as supplementary electronic material (Suppl. Electr. Mat., Tables 1 to 6). The accuracy of the method was verified by repeated analyses of reference zircon 91500 (Wiedenbeck et al., 1995), Plešovice (Slama et al., 2008) and in-house standard Felix (Millonig et al., 2012). Data were plotted using Isoplot 3.75 software (Ludwig, 2012).

From the six samples studied a total of 889 zircon cores were dated (Suppl. Electr. Mat., Tables 1 to 6), from which 839 are considered valid analysis (5.6% rejected) in terms of concordance (up to 10% discordance accepted). Following recommendations made by Vermeesch (2004) more than 117 zircons were analysed in each sample to achieve statistical adequacy. Data have been represented for visualization in complete and partial conventional concordia diagrams (from 450 Ma to 750 Ma) for each sample (Fig. 3). Data have also been plotted as adaptive Kernel Density Estimates (KDEs) and Probability Density Plots (PDPs) in Fig. 4, using DesityPlotter5.0 software (Vermeesch, 2012). KDEs were built with bandwidth = 15 Ma and histograms with binwith = 25 Ma. The age assigned to each zircon core was chosen depending on $^{207}Pb/^{206}Pb$ age. If $^{207}Pb/^{206}Pb$ age <1 Ga, $^{206}Pb/^{238}U$ age was chosen, if not $^{207}Pb/^{206}Pb$ age was preferred.

Maximum depositional ages (MDAs) for each sample were calculated following the most conservative method (YC2σ(3+)) reported by Dickinson and Gehrels (2009) with some modifications. MDAs were calculated as the weighted mean of the youngest cluster of zircon ages that can be used to calculate a concordia age with Isoplots normal "ConcAge" tool (i.e. probability of data-point equivalence higher than 0.001), choosing the first (younger) zircon age of the cluster as to have less than 1% age difference with the next zircon age.

No major differences have been found between the studied samples. As all six samples were collected from the same formation it is assumed that the original detritus was derived from the same source area. To support this assumption a comparison between distributions of detrital zircon ages has been performed using a Kolmogorov–Smirnov nonparametric test (Fig. 5a), in a similar way as had been used previously to establish common provenance (Fernández-Suárez et al., 2013 and references therein), and a Cumulative Distribution Plot (CDP) with errors has also been reported (Fig. 5b). This test and plot were performed with a MS Excel© spreadsheet downloaded from the Arizona Laserchron Center webpage (https://sites.google.com/a/laserchron.org/laserchron/).

4.3. Lu–Hf zircon analyses

Hafnium isotope measurements (Suppl. Electr. Mat., Tables 7 to 11) were performed with a Thermo-Finnigan Neptune multicollector ICP-MS at GUF coupled to the same laser as described in the U–Pb method. Laser spots with diameter mostly of 40 μm were drilled with a repetition rate of 5.5 Hz and an energy density of 6 J/cm^2 during 55 s of data acquisition. All data were adjusted relative to the JMC475 of $^{176}Hf/^{177}Hf$ ratio = 0.282160 and quoted uncertainties are quadratic additions of the within run precision of each analysis and the reproducibility of the JMC475 (2 SD = 0.0033%, n = 16). Accuracy and external reproducibility of the method were verified by repeated analysis of reference zircon GJ-1 and Plešovice, (see Suppl. Electr. Mat., Table 12) which are well within the range of solution mode data (Woodhead and Hergt, 2005; Gerdes and Zeh, 2006).

For calculation of epsilon Hf (εHf_t) chosen values for chondritic uniform reservoir (CHUR) are $^{176}Lu/^{177}Hf = 0.0336$ and $^{176}Hf/^{177}Hf = 0.282785$ (Bouvier et al., 2008), and a ^{176}Lu decay constant of 1.867×10^{-11} a^{-1} (average of Scherer et al. (2001) and Soderlund et al. (2004) calculated from terrestrial mineral isochrones). Initial $^{176}Hf/^{177}Hf_t$ and εHf_t for all analysed zircon domains were calculated using the preferred U–Pb ages.

Depleted mantle hafnium model ages (TDM) were calculated using present day $^{176}Hf/^{177}Hf = 0.283164$ value for average MORB (Chauvel et al., 2008) which is assumed to be present day depleted mantle composition. This value corresponds to an initial $\varepsilon Hf_{(t\ =\ 0Ga)} = 13.4$. DM evolution trend was propagated to $\varepsilon Hf_{(t\ =\ 4Ga)} = 0$, because the existence of a voluminous depleted mantle reservoir during Hadean–Early Archean is highly speculative (see Hawkesworth et al. (2010); Kemp et al. (2010) and discussions of Zeh et al. (2011)). TDM values for all data were calculated using a mean $^{176}Lu/^{177}Hf$ of 0.0113 (average continental crust; Rudnick and Gao, 2003) for the zircon crystallization age.

MORB $^{176}Hf/^{177}Hf$ intervals were taken from the Atlantic, Pacific and Indian MORB values (excepting three unusual low values from the Indian Ocean) reported by Chauvel and Blichert-Toft (2001) considering a minimum $^{176}Hf/^{177}Hf = 0.28302$ ($\varepsilon Hf_{(t\ =\ 0Ma)} = 8.3$) and a maximum $^{176}Hf/^{177}Hf = 0.28337$ ($\varepsilon Hf_{(t\ =\ 0Ma)} = 20.7$). These values are propagated to $\varepsilon Hf_{(t\ =\ 4Ga)} = 0$ defining a field (blue discontinuous lines) around the DM-evolution trend where the real DM composition should lie (i.e. error field for DM-evolution line).

4.4. Sm–Nd whole rock analyses

Sample preparation and analyses were performed at the laboratory of Geocronología y Geoquímica Isotópica at the Universidad Complutense de Madrid.

Whole rock samples were dissolved by oven digestion in ultra-pure HF and HNO_3 acids together with the $^{149}Sm/^{150}Nd$ spike in sealed teflon microreactors. Once the samples were dissolved and dried HNO_3 was added to eliminate silica fluorides and after that HCl was added to form chlorine molecules. Then the sample was subjected to a centrifugal process and to a two stage conventional ion-exchange chromatography to concentrate and separate REEs with DOVEX AG-50x12 (200–400 mesh) resin, and to separate Sm from Nd with HEDHP resin. The fractions where Sm and Nd are present in high concentrations are dried and loaded with H_3PO_4 on rhenium filaments in triple disposition, and analysed in a thermal ionization mass spectrometer TIMS-Phoenix HCT040® following a dynamic multicollector method. The measured $^{143}Nd/^{144}Nd$ isotopic ratios were corrected for possible isobaric interferences from ^{142}Ce and ^{144}Sm (only for samples with $^{147}Sm/^{144}Sm$ <0.0001) and normalized to $^{146}Nd/^{144}Nd = 0.7219$

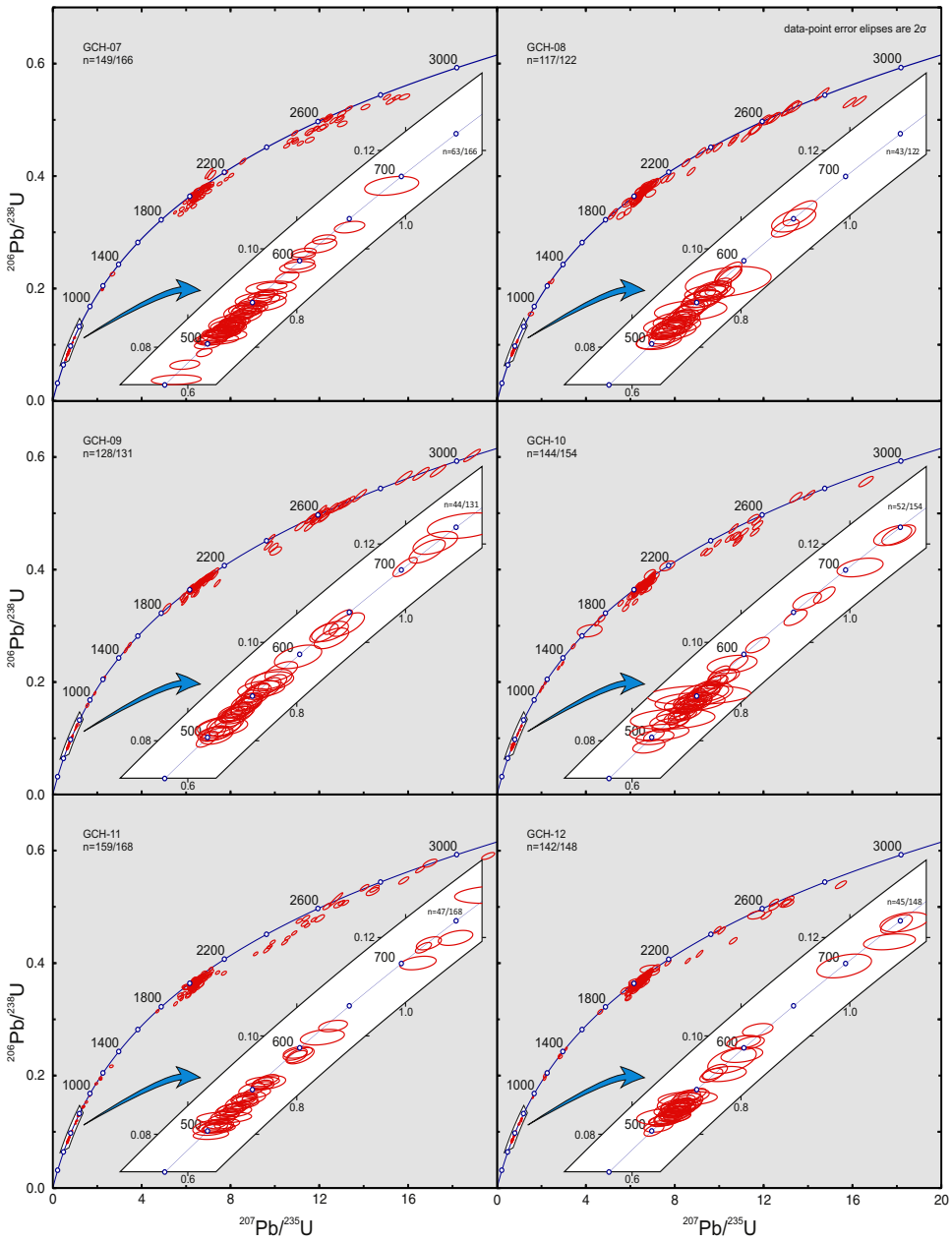

Fig. 3. U–Pb conventional concordia diagrams for samples GCH- 07, 08, 09, 10, 11, and 12. Ellipses represent combined 2σ uncertainties of $^{206}Pb/^{238}U$ and $^{207}Pb/^{235}U$ ratios.

(O'Nions et al., 1977) to correct for mass fractionation. The LaJolla Nd international isotopic standard was analysed during sample measurement, and gave an average value of $^{143}Nd/^{144}Nd = 0.511850$ for 7 replicas, with an internal precision of ±0.00001 (2σ). These values were used to correct the measured ratios for possible sample drift following reference values from Lugmair et al. (1983). The analytic errors for $^{147}Sm/^{144}Nd$ ratio is 0.1 % and for $^{143}Nd/^{144}Nd = 0.006\%$.

Chondritic uniform reservoir (CHUR) present day values considered for this study are $^{147}Sm/^{144}Nd = 0.1967$ (Jacobsen and Wasserburg, 1980) and $^{143}Nd/^{144}Nd = 0.512638$ (Hamilton et al., 1983). The DM evolution trend and DM model ages (TDMs) have been calculated as described by DePaolo (1981) using $^{147}Sm/^{144}Nd$ ratios and MDAs for each sample. A ^{147}Sm decay constant of 6.539×10^{-11} a^{-1} has been used, calculated from ^{147}Sm half-life reported by Lugmair and Marti (1978) and Begemann et al. (2001). MORB epsilon values of +7 to +12 used are those reported by DePaolo and Wasserburg (1976).

5. Results

5.1. U–Pb results

The results of U–Pb dating are given as supplementary electronic material (Suppl. Electr. Mat., Tables 1 to 6) and represented in Fig. 3. In order to allow forward comparisons, the age spectrum has been

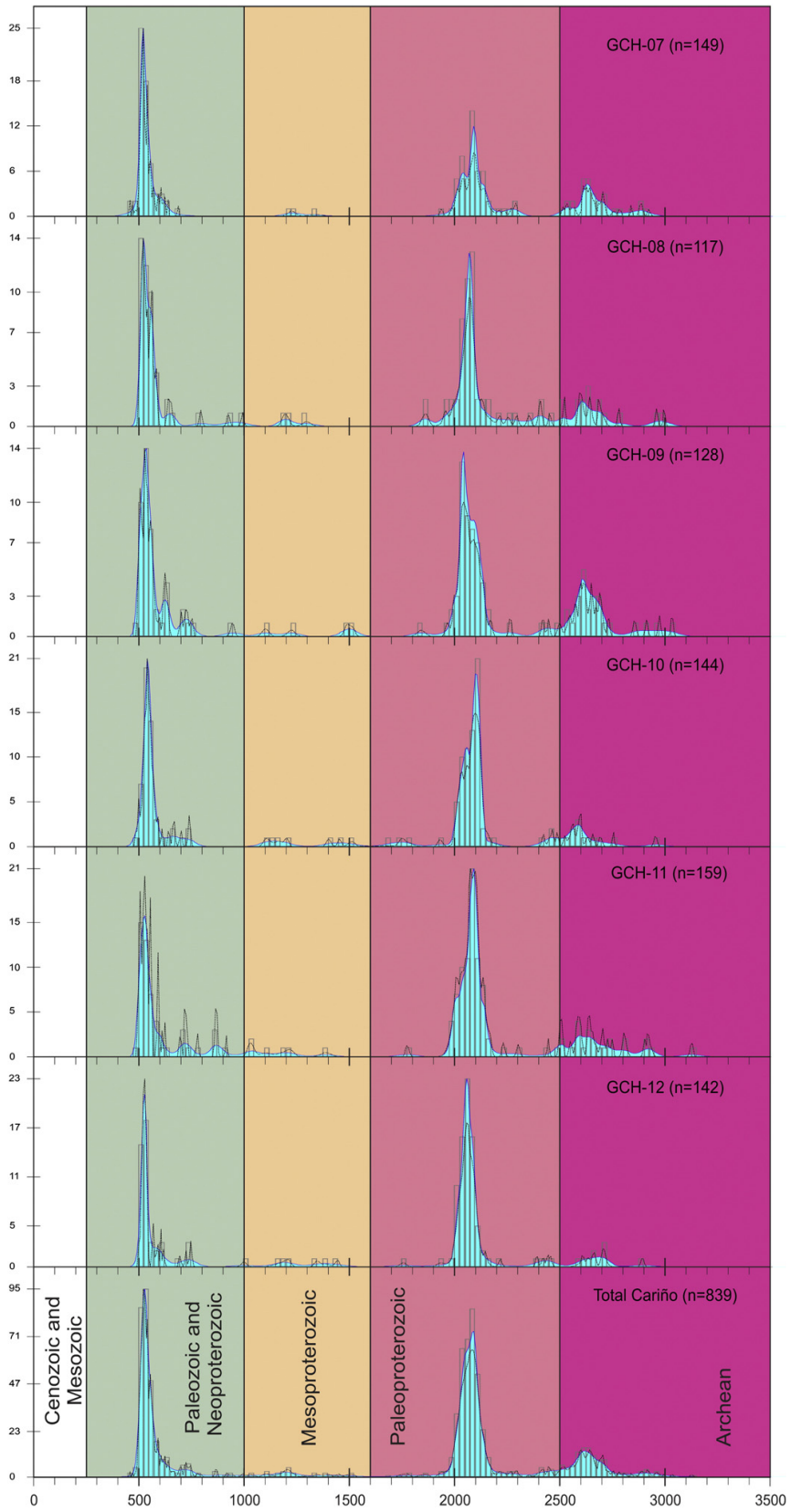
GCH-07 (n=149)
GCH-08 (n=117)
GCH-09 (n=128)
GCH-10 (n=144)
GCH-11 (n=159)
GCH-12 (n=142)
Total Cariño (n=839)
Cenozoic and Mesozoic
Paleozoic and Neoproterozoic
Mesoproterozoic
Paleoproterozoic
Archean
0
500
1000
1500
2000
2500
3000
3500

a)

	GCH-07	GCH-08	GCH-09	GCH-10	GCH-11	GCH-12
GCH-07		0.679	0.257	0.110	0.045	0.053
GCH-08	0.679		0.791	0.902	0.467	0.496
GCH-09	0.257	0.791		0.189	0.422	0.029
GCH-10	0.110	0.902	0.189		0.773	0.202
GCH-11	0.045	0.467	0.422	0.773		0.709
GCH-12	0.053	0.496	0.029	0.202	0.709	

b)

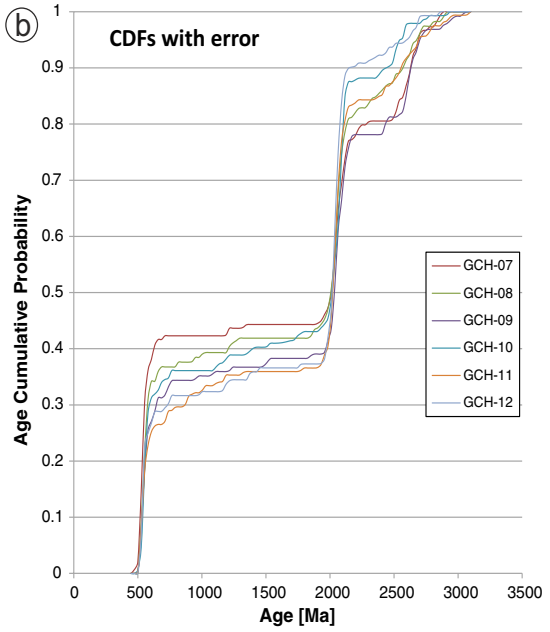

Fig. 5. (a) Results of the Kolmogorov–Smirnoff (K–S) test. This K–S test compares the distribution of detrital zircon ages from detrital samples, and tests the null hypothesis that the distributions are the same. When P < 0.05 it is likely with a 95% confidence level that the samples derive from different populations. (b) Cumulative distribution function (CDF) plot, incorporating measurement uncertainty, showing the probability that a zircon will be younger than a certain age and the similarity between samples.

divided in four major groups: Paleozoic–Neoproterozoic (<1 Ga), Mesoproterozoic (1–1.6 Ga), Paleoproterozoic (1.6–2.5 Ga) and Archean (>2.5 Ga; see Fig. 6). Descriptions of U–Pb results of each sample are as follows.

From sample GCH-07, 166 analyses were performed of which 149 were concordant (<10% discordance, d = 10.2%, d: percentage of discordant analyses). 63 of them are Paleozoic–Neoproterozoic (42.3%), 3 are Mesoproterozoic (2%), 54 are Paleoproterozoic (36.2%) and 29 are Archean (19.5%). MDA_{07} (GCH-07 maximum depositional age) calculated for this sample (see above) is 510.4 ± 2.4 Ma, using 12 ages.

From sample GCH-08, 122 analyses were performed of which 117 were concordant (d = 4.1%). 46 of them are Paleozoic–Neoproterozoic (39.3%), 3 are Mesoproterozoic (2.6%), 53 are Paleoproterozoic (45.3%) and 15 are Archean (12.8%), with a MDA_{08} of 515.6 ± 3.8 Ma, using 15 ages.

From sample GCH-09, 131 analyses were performed of which 128 were concordant (d = 2.3%). 45 of them are Paleozoic–Neoproterozoic (35.2%), 4 are Mesoproterozoic (3.1%), 54 are Paleoproterozoic (42.2%) and 25 are Archean (19.5%), with a MDA_{09} of 507.1 ± 4.2 Ma, using 10 ages.

From sample GCH-10, 154 analyses were performed of which 144 were concordant (d = 6.5%). 52 of them are Paleozoic–Neoproterozoic (36.1%), 7 are Mesoproterozoic (4.9%), 72 are Paleoproterozoic (50%) and 13 are Archean (9%), with a MDA_{10} of 506 ± 10 Ma, using 4 ages.

From sample GCH-11, 168 analyses were performed of which 159 were concordant (d = 5.4%). 51 of them are Paleozoic–Neoproterozoic (32.1%), 6 are Mesoproterozoic (3.8%), 79 are Paleoproterozoic (49.7%) and 23 are Archean (14.5%), with a MDA_{11} of 506.3 ± 2.8 Ma, using 9 ages.

From sample GCH-12, 148 analyses were performed of which 142 were concordant (d = 4.1%). 45 of them are Paleozoic–Neoproterozoic (31.7%), 7 are Mesoproterozoic (4.9%), 81 are Paleoproterozoic (57%) and 9 are Archean (6.3%), with a MDA_{12} of 509.4 ± 7.1 Ma, using 5 ages.

To merge all samples and treat them as a single sample a Kolmogorov–Smirnov test has been performed. Fig. 5a shows its P-values and Fig. 5b the cumulative density function plot (CDF) which includes age errors. P-values indicate that all six samples pass the test with the exception of GCH-07 with GCH-11 (P = 0.044) and GCH-07 with GCH-12 (P = 0.027) comparison. Both P-values are near to 0.05 (value required to pass the test) and taking into account that the other 13 comparisons are satisfactory and the similarity between age distributions observed on KDE, PDP (Fig. 4) and CDF plots (Fig. 5b), it is concluded that all samples are shed from the same source area and that the differences between zircon age populations are explained by sampling bias or/and because each sample is a small fraction of the same thick pile of sediments (i.e. the same formation) located in different parts of the stratigraphic column, and so in different positions in relation to the source area.

Analyses from all samples are summarized in Fig. 6 and add a total of 889 age determinations, from which 839 have less than 10% discordance (d = 5.6%). 36% of the analyses (n = 302) have a Paleozoic–Neoproterozoic age with peaks at 505, 525, 540, 557, 590, maximum abundance at 525 Ma, and a tail with minor peaks between 600 and 800. Mesoproterozoic ages are scattered in the interval age of c. 1.0 to 1.5 Ga and do not define any maxima, comprising 3.6% (n = 30) of the total ages. The main age group is Paleoproterozoic (46.8%, n = 393) and it is constrained between c. 1.98 and 2.17 Ga with a well-defined maximum at 2.09 Ga. The Archean population represents 13.6% (n = 114) of the analyses with maxima at c. 2.6, 2.64 and 2.7 Ga. MDAs calculated for each sample vary from 506 to 516 Ma, with an average of 509.5 ± 3.6 Ma (Fig. 7; calculated as weighted average of all six MDAs with Isoplot software). The conservative way in which these MDAs have been calculated guarantees with a high level of confidence that the age of deposition is c. 510 Ma or younger.

5.2. Lu–Hf results

From the 839 concordant zircon cores analysed with U–Pb method 420 were analysed for Lu–Hf isotopes (Suppl. Electr. Mat., Tables 7 to 11). Around 58% of all analyses have positive εHf (Fig. 8a). When these superchondritic zircon data plot near the DM evolution trend it can be surmised that they were crystallized from magmas more or less directly derived from a depleted mantle source.

Paleozoic–Neoproterozoic zircons (in particular Cambrian–Ediacaran) are arranged in the Hf–U–Pb age diagram in two ways (Fig. 8a and b). First as positive εHf zircons (form 0 to +10 epsilon units) with TDMs from c. 0.65 to 1.2 Ga (average at 0.9 Ga), pointing to a high production of juvenile (depleted mantle derived) magmas between c. 500 and 560 Ma, most of them crystallizing at c. 525 Ma. This observation is consistent with a developed magmatic arc setting. The second way in which these zircons are arranged is with a wide range in their εHf units, from 0 to −16. There is also a small cluster of 7 zircons with εHf of −23 to −26, and a single analyses with εHf = −49. There are

Fig. 4. Kernel density estimation plots (continuous line enclosing the blue area) and probability density plots (dashed line) for all samples and for the combination of all Cariño Gneiss zircons studied.

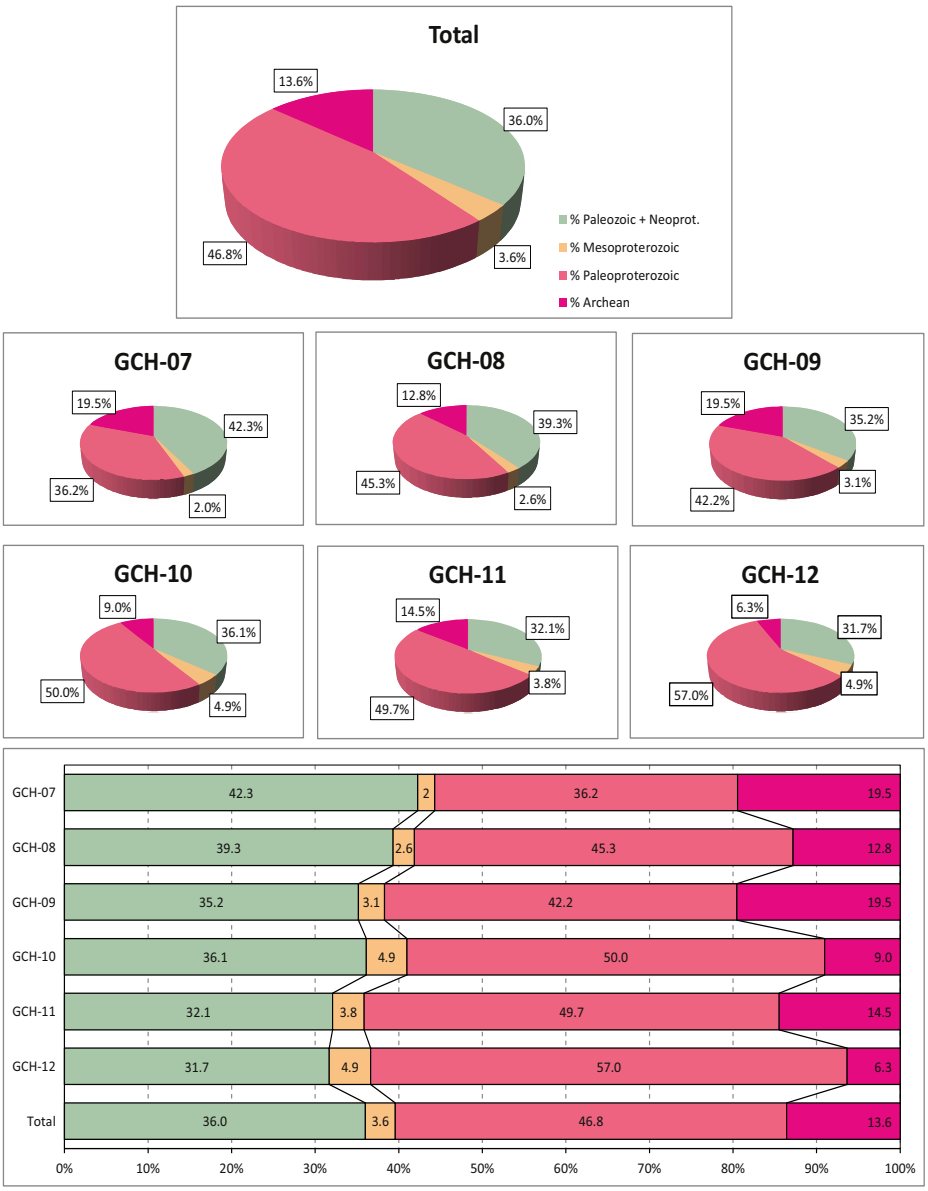

Fig. 6. Percentage of zircon populations represented as bar diagrams and circular plots.

two explanations for the generation of these negative εHf zircons: i) by a mixing process between juvenile magmas and materials with strong negative εHf values and ii) by an intense c. 500 to 560 Ma crustal reworking process of c. 0.8–2.1 Ga DM derived materials. This second explanation is not favoured owing to the very low proportion of Mesoproterozoic zircons in the samples. The first explanation requires the juvenile magmas to mix with a source with an $\varepsilon Hf_{(c.\ 525Ma)} < -16$ to give this wide negative range of εHf to the zircons. If we follow the evolutionary field array in Fig. 8a, this source is represented by the c. 2.09 Ga zircons that lie on the Eburnean crust evolution trend. The other 8 Paleozoic–Neoproterozoic zircons with εHf values below −23 lie on the Archean crust evolution field and therefore were probably formed by recycling Archean crust. Zircons with ages between c. 560–750 Ma plot around or slightly above the CHUR evolution trend, which is in line with an early magmatic arc setting. All these observations are in agreement with the development of a c. 500–750 Ma magmatic arc setting.

Paleoproterozoic 1.9–2.2 Ga zircons are arranged in a similar way as the Paleozoic–Neoproterozoic zircons. Superchondritic clustered zircon data have TDM values from c. 2.0 to 2.6 Ga (average at 2.3 Ga) and resemble a crust formation event where DM derived magma intrusion started at c. 2.17 Ga, with crystallization ages concentrated at 2.09 Ga and finished around 1.98 Ga. This timing falls within the timespan considered for the Eburnean Orogeny (c. 1.8–2.2 Ma; Ennih and Liégeois, 2008). Subchondritic zircon data have εHf values from 0 to −15, and point to a mixing process between the DM derived magmas and older rocks, probably the Archean crust.

Paleoproterozoic and Archean zircon ages range between c. 2.24 and 3.03 Ga and have slightly positive εHf up to +4 and negative εHf down to −15, with TDMs from c. 2.8 to 3.6 Ga (maximum at 3.1 Ga). These

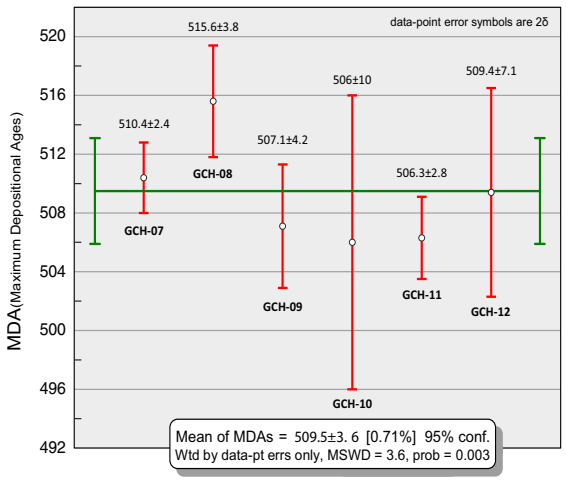

Fig. 7. Maximum depositional ages for each Cariño Gneiss sample (see Sections 4.2 and 5.1) and the weighted average of all samples, which gives a c. 510 Ma MDA for the Cariño Gneiss formation.

analyses are not clustered but they are arranged in a linear trend, which is slightly lower than the average continental crustal evolution trend of $^{176}Lu/^{177}Hf = 0.0113$ used to calculate TDMs in this study. These linearly arranged analyses (vs. cluster superchondritic arrange) point to an Archean crust formation event at c. 3.1 Ga, where its materials underwent subsequent crustal reworking during the Late Archean.

5.3. Sm–Nd results

In crustal evolution models based on Nd isotopic compositions, the main fractionation event during the formation and evolution of continental crust takes place during partial melting of lithospheric mantle to generate the source of crustal rocks (McLennan and Hemming, 1992). The εNd model age of a sedimentary rock represents the average age of the extraction of its components from the mantle. In the case of detrital rocks, model ages usually reflect complex mixtures based on the different age and provenance of their components. The combined interpretation of Nd model ages and detrital zircon ages has proven to be a powerful tool for investigating the evolution of continental crust, especially in orogenic belts (e.g., Linnemann et al., 2004).

Whole rock Sm–Nd analyses were performed on 10 Cariño Gneiss samples. Results (Table 1) have been plotted in Fig. 9. Present day Nd epsilon values ($\varepsilon Nd_{t\ =\ 0Ma}$) vary from −16.0 to −11.4 and εNd for the time of sedimentation ($\varepsilon Nd_{t\ =\ 510Ma}$) varies from −10.2 to −6.3. Depleted mantle model ages (TDM) range between 1.82 and 1.58 Ga, with an average of 1.73 Ga.

Results were plotted together with Sm–Nd data for the uppermost siliciclastic series of the Upper Allochthon of the Órdenes Complex (Fuenlabrada et al., 2010) to establish similarities between detrital units belonging to this terrane (Fig. 9). These low-grade metagreywackes have a Nd TDM average of c. 1 Ga (n = 20) and the Cariño Gneisses an older mean of c. 1.73 Ga (n = 10). This isotopic difference between sedimentary rock series included in the Upper Allochthon and with similar maximum depositional ages is interpreted to reflect changes in the setting of individual series in relation to the peri-Gondwanan arc system. The Cariño Gneisses have a higher input of detritus with older isotopic signatures and therefore it is assumed that this series was deposited closer to the mainland than the top greywacke series of the Órdenes Complex. This last series would have been deposited closer to the most active part of the magmatic arc that shed juvenile detritus into the basin.

6. Provenance of the Upper Allochthon involved in the Variscan suture

According to the data presented in this contribution the maximum depositional age is c. 510 Ma, so its protolith was a Middle Cambrian or younger sedimentary series. Concordia (Fig. 3) and PDP-KDE (Fig. 4) plots reveal two main age populations, with pronounced age peaks at c. 525 Ma (Paleozoic–Neoproterozoic population: 36%) and c. 2.09 Ga (Paleoproterozoic population: 46.8%; Fig. 6). Archean populations compromise around 13.6% of the total Cariño Gneiss zircons and Mesoproterozoic zircons are scarce with only a 3.6%.

The main Archean U–Pb zircon population in the Cariño Gneisses is bracketed at 2.7–2.5 Ga (Fig. 4). The εHf vs. age pattern for these zircons (Fig. 8a) is a linear trend that points to a long lasting continental crust reworking process of juvenile rocks formed at c. 3.3–2.9 Ga (maximum at 3.1 Ga), with limited mixing processes, supporting an intracratonic or an active margin setting. In the Northern WAC, Archean igneous rocks have mainly been reported in the Western Reguibat Shield. Potrel et al. (1998) published ages of around 3 Ga for juvenile magmatic rocks and Schofield et al. (2012) reported main intrusion events at c. 2.9, 2.7 and 2.5 Ga in this area. Based on the above studies, the Western part of the Reguibat Shield is a viable candidate for the provenance of the Cariño Gneiss Archean zircons.

The Cariño Gneiss Paleoproterozoic fraction makes up 46.8% of the total population (Fig. 6). Maximum abundance clusters at c. 2.17–1.98 Ga with a maximum peak at 2.09 Ga (Fig. 4). This Paleoproterozoic population falls within the time span of the Eburnean orogeny (2.2–2.0 Ga according to Egal et al. (2002), or 1.8–2.2 according to Ennih and Liégeois (2008)). This orogenic cycle was defined at the Southern WAC and has been extended to all rocks of the WAC affected by c. 2.0 Ga geological events, so the Paleoproterozoic materials of the Cariño Gneisses are possibly derived from rocks generated or reworked during the Eburnean orogeny. Close similarities are observed when comparisons are made with WAC Eburnean rocks. Eburnean ages between c. 2.1 and 2.04 Ga in igneous and sedimentary rocks have been reported in the Eastern Reguibat Shield (Peucat et al., 2005) and in the Anti-Atlas belt (Thomas et al., 2002; Abati et al., 2012; Avigad et al., 2012), supporting a WAC provenance for the Paleoproterozoic zircons in the Cariño Gneisses. The Cariño Gneiss Lu–Hf data (Fig. 8a) for zircons of Eburnean age (c. 2.13–1.97 Ga) are arranged as a cluster with positive εHf values representing juvenile rocks and few values with negative εHf units suggesting a mixing process of juvenile and reworked rocks, i.e. Eburnean DM derived magmas intruded in an older basement triggering mixing processes. As the most negative εHf value for Eburnean zircons is −15 and the Archean linear arrangement intersects at c. 2 Ga at c. εHf = −15, this old basement could well be represented by the Cariño Gneiss Archean zircons. All these observations are in agreement with the geodynamic setting proposed by Egal et al. (2002), where the Eburnean is an active margin orogen formed by oceanic subduction along the edge of the pre-existing Archean craton. The input of this population in the Cariño Gneisses is much higher than in the other samples (i.e. Abati et al., 2012; Avigad et al., 2012). This is probably due to the deposition of the Cariño Gneisses closer to the Paleoproterozoic source area, i.e. the Northern WAC.

In the Mesoproterozoic Era the WAC became a stable craton (Ennih and Liégeois, 2008) which gave as a result a characteristic c. 1.7–1.0 Ga "magmatic gap" (Linnemann et al., 2008 and references therein). Nevertheless, in some peripheral WAC derived samples, Mesoproterozoic zircons are relatively common in Ediacaran–Ordovician and younger siliciclastic samples. This is the case in NW Iberia, where the provenance of these series is frequently assigned to a provenance from the Saharan metacraton (i.e. Díez Fernández et al., 2010). However, recently a Middle Cambrian sandstone from the Anti-Atlas belt has been reported to contain zircons with Stenian Mesoproterozoic ages from c. 1.1 to 1 Ga (Avigad et al., 2012). Therefore siliciclastic series formed in the Cambrian close to the WAC can also contain this zircon population. In the

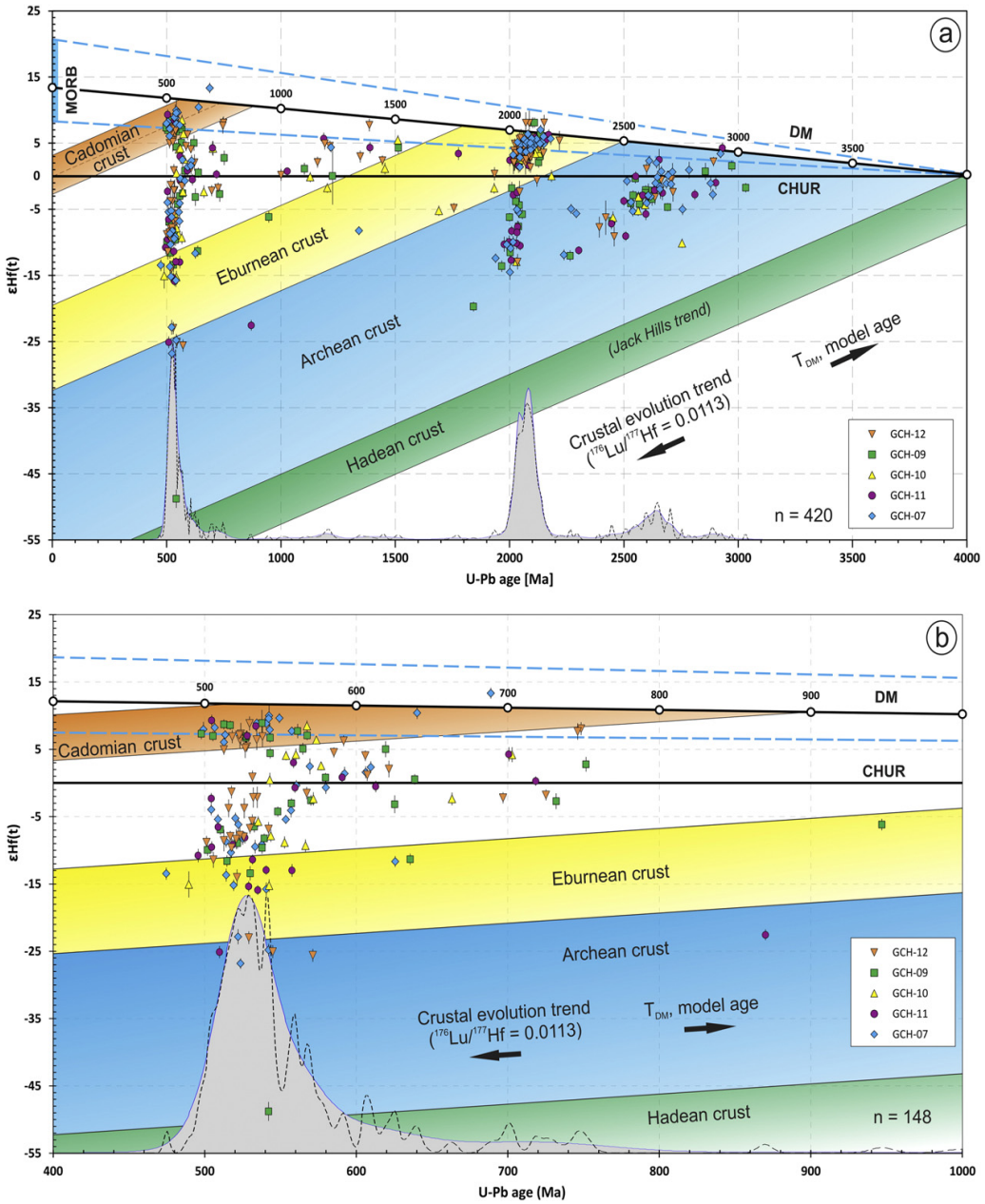

Fig. 8. (a) Hf isotope evolution diagram showing Cariño Gneiss zircon data. Kernel Density Estimation of analysed zircons with Lu–Hf systematics is represented in grey. See text for discussion (Section 5.2) and for constants and parameters used (Section 4.3). CHUR — chondritic uniform reservoir; DM — depleted mantle; MORB — mid-ocean ridge basalt. (b) Hf isotope evolution diagram of analysed zircon grains in the age range of 400–1000 Ma. See text for discussion, and for constants and parameters used.

Cariño Gneisses, the Mesoproterozoic zircons are scarce and scattered, constituting 3.6% of the total population and not defining a clear maximum (Fig. 4). This population is also present in the Parautochthon (Díez Fernández et al., 2012b) and in the Basal Allochthon (basal units) of NW Iberia (Díez Fernández et al., 2010). These populations could derive from cratons adjacent to the WAC, i.e. Amazonian, Saharan or the Arabian–Nubian cratons (Fig. 10), transported by rivers, wind or by a tectonic along-strike transport of terranes during Cadomian orogenic processes (Fernández-Suárez et al., 2002; Gutiérrez-Alonso et al., 2003), or even from unknown Mesoproterozoic igneous rocks in the WAC. In any case the Mesoproterozoic population is still enigmatic but it is present in the siliciclastic derived formations of the allochthonous complexes of NW Iberia, albeit in much lower proportions than in putative coeval rocks of the Autochthon (Fernández-Suárez et al., 2013 and references therein) and it could be a distinctive feature for these rocks.

The Paleozoic–Neoproterozoic fraction constitutes 36% of the Cariño Gneiss zircons, most of them with ages of c. 750–490 Ma and with a

Table 1
Whole rock Nd isotope data of the Cariño Gneiss samples.

Sample	Sm	Nd	$^{147}Sm/^{144}Nd$	$^{143}Nd/^{144}Nd_{(o)}$	2SE(abs)*10^{-6}	$\varepsilon Nd_{(t=0)}$	$\varepsilon Nd_{(t=510)}$	T_{DM}
GCH-07	2.99	16.27	0.1111	0.511841	3	-15.5	-10.0	1783
GCH-08	3.44	18.51	0.1124	0.511879	3	-14.8	-9.3	1751
GCH-09	3.24	17.40	0.1126	0.511876	3	-14.9	-9.4	1758
GCH-10	2.50	13.09	0.1155	0.511869	2	-15.0	-9.7	1821
GCH-11	3.26	18.57	0.1063	0.511856	3	-15.3	-9.4	1683
GCH-12	4.68	24.78	0.1142	0.511968	2	-13.1	-7.7	1645
GCH-27	7.20	36.68	0.1187	0.512054	2	-11.4	-6.3	1584
GCH-28	2.23	11.96	0.1126	0.511834	3	-15.7	-10.2	1821
GCH-29	5.48	27.90	0.1186	0.511962	3	-13.2	-8.1	1731
GCH-30	2.96	16.65	0.1073	0.511815	2	-16.0	-10.2	1757
Average								1733

maximum abundance at c. 525 Ma. These ages coincide with the reported ages for the Cadomian and Pan-African orogenies (c. 750–540 Ma; e.g. Ennih and Liégeois, 2008; Linnemann et al., 2014) but the c. 525 Ma Cariño Gneiss maximum is younger, suggesting a different metacratonic WAC activity or a late development of the Cadomian–Pan-African orogenies. Paleozoic–Neoproterozoic populations in the WAC are very common. For example, merged samples published by Abati et al. (2012) from the Sirwa Window (Anti-Atlas belt) have an age range of c. 540–770 Ma with peaks at c. 560 and 610 Ma. Thomas et al. (2002) reported igneous rock zircon U–Pb ages from the same area with ages of c. 560–580, 610 and 740 Ma, and from the NE flank of the Zenaga inlier (Anti-Atlas belt) two groups of detrital U–Pb ages where published by Avigad et al. (2012). Ages in these samples were c. 532–668 Ma with a peak at 570 Ma and c. 545–750 Ma with a peak at 655 Ma (in addition to Cryogenian and Tonian peaks). Cariño Gneiss zircons with ages between c. 760 and 560 Ma are not abundant and plot in the Lu–Hf diagram (Fig. 8a and b) around the CHUR evolution trend, pointing to a crustal recycling of early Cadomian–Pan-African material. C. 560–500 Ma Cariño Gneiss zircons are very abundant with a maximum peak at c. 525 Ma. The Lu–Hf isotopic pattern (Fig. 8a and b) shows that these Cariño Gneiss zircons are arranged as a cluster with positive εHf values plotting near the DM evolution trend and as a variably negative εHf arrangement. These patterns can be explained by the intrusion of juvenile magmas that triggered mixing process with an Eburnean and Archean crust and with a small proportion of reworked early Cadomian–Pan-African crustal material, consistent with a peripheral arc activity at the Northern WAC.

As discussed by Cawood et al. (2012) convergent margin basins have a high proportion of detrital zircons with ages close to the age of the sediment, where back arc basins have an increasing input of older detritus from the adjoining mainland. The Cariño Gneiss U–Pb age distribution pattern is a strongly bimodal one where the majority of the Paleozoic–Neoproterozoic fraction is concentrated near its MDA, as appreciated by the steep slope of the CDF diagram (Fig. 5b), or the narrow bell shaped curve of the KDE plot (Fig. 4). These observations suggest that the Cariño Gneisses turbiditic greywacke sediments were deposited in a relatively narrow back-arc type basin, where the late/post Cadomian–Pan-African volcanic arc system was very active, shedding its juvenile materials into the basin at the same time as the adjacent WAC furnished the Eburnean and Archean detritus.

Comparison with the Órdenes Complex uppermost unit reveals that the IP Upper Allochthon is heterogeneous. This unit, which was thought to correlate with the Cariño Gneiss unit, has yielded a MDA of 510–530 Ma and was intruded by a swarm of dykes with protolith ages of

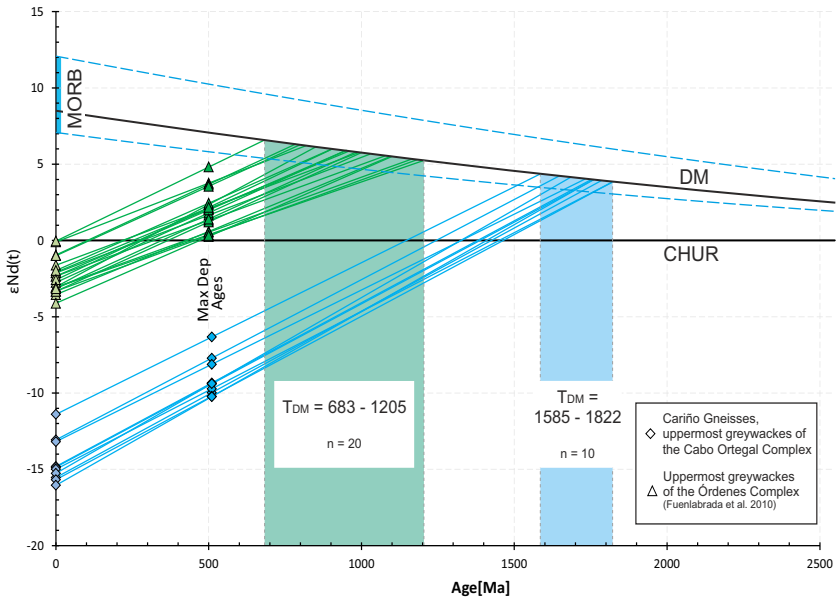

Fig. 9. Sm–Nd isotope evolution diagram showing whole-rock data of 10 metasedimentary rock samples from the Cariño Gneiss formation (Cabo Ortegal Complex, NW Iberian Massif). Whole-rock Sm–Nd data (n = 20) of the uppermost greywackes of the Órdenes Complex (upper units; Fuenlabrada et al., 2010) are included for comparison. Rhombus and triangles show εNd values at present day and at maximum depositional ages. See text for discussion (Section 5.3) and for constants and parameters used (Section 4.4). CHUR — chondritic uniform reservoir; DM — depleted mantle; MORB — mid-ocean ridge basalt.

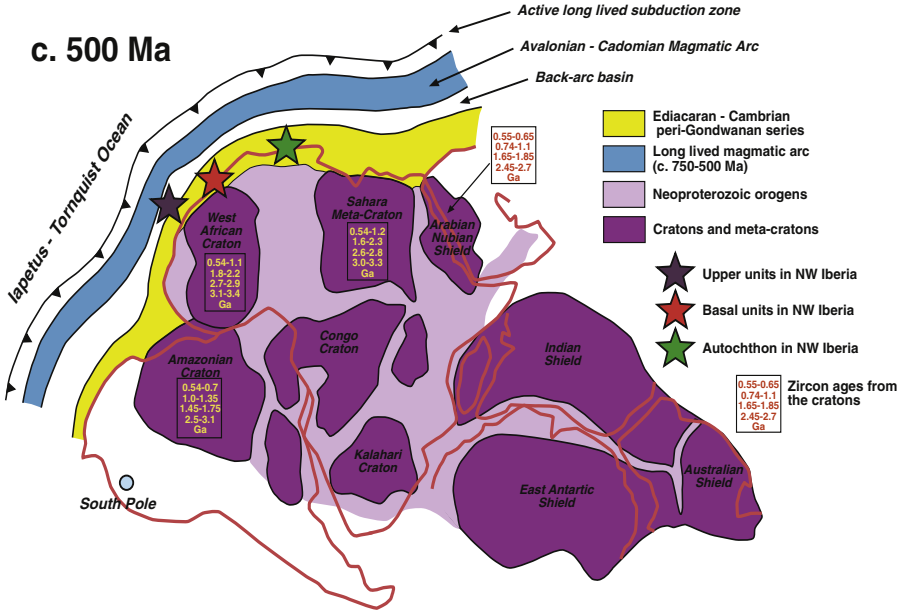

Fig. 10. Sketch showing the proposed paleogeographic position of the upper units and other terranes from the NW Iberian Massif. Paleogeographical context based on Fernández-Suárez et al. (2013). Numbers in squares are zircon ages in Ga from the cratons, from Linnemann et al. (2014) and references therein. New zircon ages have been added to the West African Craton (Avigad et al., 2012) and to the Arabian Nubian Shield (Morag et al., 2012).

c. 510 Ma (Fernández-Suárez et al., 2003; Díaz García et al., 2010; Fuenlabrada et al., 2010). Its zircon population (n = 85) has 81% of Paleozoic–Neoproterozoic zircons, 0% are Mesoproterozoic, 19% are Paleoproterozoic and 0% are Archean ones. This unit has a higher Paleozoic–Neoproterozoic zircon input and younger Nd DM model ages (TDM_{mean} = 1 Ga) than the Cariño Gneisses (TDM_{mean} = 1.73 Ga, Fig. 9). Therefore the IP Upper Allochthon of the NW Iberian complexes is interpreted to represent different stages and positions within the peri-Gondwanan back-arc basin, where the Cariño Gneisses were deposited closer to the stable metacraton (WAC) and the Órdenes Complex Upper Allochthon unit was deposited closer to the arc.

A paleogeographical sketch map of the peri-Gondwanan region at c. 500 Ma is presented in Fig. 10. The sedimentary series included in the upper units were deposited close to a long lived volcanic arc. The Cariño Gneiss protoliths were probably formed in a back-arc basin, in a sedimentary basin with abundant detritus coming from the most active part of the arc and from the mainland. Other siliciclastic series from the Upper Allochthon, such as the Órdenes Complex top metagreywackes, were deposited closer to the active part of the arc, in a domain of the sedimentary basin where the arc was the main sediment supplier. The basal units of the allochthonous complexes contain siliciclastic metagreywacke series with MDA in the range of c. 560–517 Ma and detrital zircon maximum abundance age of c. 650 Ma (Díez Fernández et al., 2010). These siliciclastic series are characterized by Nd TDM model ages in the range of 1.74–2.22 Ga (Fuenlabrada et al., 2012), the oldest model ages reported so far in the NW Iberian terranes, including both the autochthonous and allochthonous domains. These relatively old isotopic sources strongly suggest deposition in a tectonic setting where detritus were sourced dominantly from the Gondwana mainland (Fig. 10). The most frequent siliciclastic series included in the basal units (Díez Fernández et al., 2010) seems to be older that those forming part of the Upper Allochthon. They were deposited closer to the mainland and they do not reflect the most recent activity of the arc during the Middle Cambrian. Finally, according to available zircon data and the dynamic evolution of the Variscan belt, the original setting of the Iberian Autochthon was probably located further to the East, in any transitional region between the West African Craton and the Sahara Craton (Fig. 10; Gómez Barreiro et al., 2007; Díez Fernández et al., 2010; Shaw et al., 2014), or even further East, in the vicinity of the present day Jordan–Israel region (Fernández-Suárez et al., 2013).

7. Conclusions

The protoliths of the Cariño Gneiss formation, the intermediate pressure Upper Allochthon included in the Cabo Ortegal Complex, are formed by siliciclastic series that represent the deposition of greywackes by turbidity currents at c. 510 Ma (maximum depositional age from detrital zircons). Considering the high proportion of Eburnean zircon input and its relatively old whole rock Nd TDM values, the siliciclastic series were deposited in a peripheral back-arc basin somewhere between an active volcanic arc and the Northern margin of the West Africa Craton (WAC). In this tectonic setting, detritus arrived both from the active part of the volcanic arc and from the mainland. These metasedimentary rocks record Archean, Eburnean, and late or post-Cadomian–Pan-African crust formation events, with a 3.6% Mesoproterozoic zircon input.

In the source region of the gneiss formation, the Archean crust formation event is roughly dated at c. 3.3–2.9 Ga, which is represented by zircons with c. 3.0–2.2 Ga crystallization ages. These Archean materials suffered important crustal reworking processes supporting an intracratonic or an active margin setting.

The recorded Eburnean events represent the intrusion of Eburnean juvenile magmas into an Archean basement, most probably the Archean basement represented by the Cariño Gneiss Archean zircons. The most probable geodynamic setting is a volcanic arc at the margin of a pre-existing Archean craton.

Archean and Paleoproterozoic (Eburnean) zircon populations seem to be derived from the WAC. The Cambrian events recorded in the Cariño Gneisses represent a magmatic arc at the periphery of the North Gondwana margin, specifically the North WAC. This arc records the intrusion of c. 525 Ma juvenile magmas into the Eburnean and Archean basement of Gondwana. The first stages of the arc were probably linked to the Cadomian arc system, defined in other parts of Europe

as to have an activity bracketed between 750 Ma and 540 Ma, and so it could represent a long lasting volcanic–magmatic arc system.

Taking into account the Nd TDM model ages published from other metagreywacke series included in the NW Iberian Upper Allochthon, it can be concluded that this terrane contains heterogeneous isotopic sources. These varied sources indicate that different parts of the peri-Gondwanan arc system may be preserved in the Upper Allochthon.

Acknowledgements

Financial support for this research has been provided by the Spanish project CGL2012-34618 (Ministerio de Economía y Competitividad). The authors are grateful to Wilfried Winkler and David Orejana who performed insightful reviews of the manuscript and to Inna Safonova for the excellent editing work. R. Albert is thankful to the Universidad Complutense de Madrid which provided him with a pre-doctoral grant. The authors are also thankful for the technical and laboratory support provided by Linda Marko (GUF) and José Antonio Hernández Jiménez (UCM).

Appendix A. Supplementary data

Supplementary data to this article can be found online at http://dx.doi.org/10.1016/j.gr.2014.10.016.

References

Ábalos, B., Puelles, P., Gil Ibarguchi, J.I., 2003. Structural assemblage of high-pressure mantle and crustal rocks in a subduction channel (Cabo Ortegal, NW Spain). Tectonics 22.

Abati, J., Dunning, G.R., Arenas, R., Díaz García, F., González Cuadra, P., Martínez Catalán, J.R., Andonaegui, P., 1999. Early Ordovician orogenic event in Galicia (NW Spain): evidence from U–Pb ages in the uppermost unit of the Ordenes Complex. Earth and Planetary Science Letters 165, 213–228.

Abati, J., Arenas, R., Martínez Catalán, J.R., Díaz Garca, F., 2003. Anticlockwise P–T path of granulites from the Monte Castelo Gabbro (Ordenes Complex, NW Spain). Journal of Petrology 44, 305–327.

Abati, J., Castiñeiras, P., Arenas, R., Fernández-Suárez, J., Gómez Barreiro, J., Wooden, J.L., 2007. Using SHRIMP zircon dating to unravel tectonothermal events in arc environments. The early Palaeozoic arc of NW Iberia revisited. Terra Nova 19, 432–439.

Abati, J., Aghzer, A.M., Gerdes, A., Ennih, N., 2010a. Detrital zircon ages of Neoproterozoic sequences of the Moroccan Anti-Atlas belt. Precambrian Research 181, 115–128.

Abati, J., Gerdes, A., Fernández-Suárez, J., Arenas, R., Whitehouse, M.J., Díez Fernández, R., 2010b. Magmatism and early-Variscan continental subduction in the northern Gondwana margin recorded in zircons from the basal units of Galicia, NW Spain. Geological Society of America Bulletin 122, 219–235.

Abati, J., Aghzer, A.M., Gerdes, A., Ennih, N., 2012. Insights on the crustal evolution of the West African Craton from Hf isotopes in detrital zircons from the Anti-Atlas belt. Precambrian Research 212, 263–274.

Andonaegui, P., del Tánago, J.G., Arenas, R., Abati, J., Martínez Catalán, J.R., Peinado, M., Díaz García, F., 2002. Tectonic setting of the Monte Castelo gabbro (Ordenes Complex, northwestern Iberian Massif): evidence for an arc-related terrane in the hanging wall to the Variscan suture. In: Martínez Catalán, J.R., Hatcher, R.D., Arenas, R., Díaz García, F. (Eds.), Variscan–Appalachian dynamics: the building of the Late Paleozoic basement: Boulder, Colorado. Geological Society of America Special Paper 364, pp. 37–56.

Andonaegui, P., Castiñeiras, P., González Cuadra, P., Arenas, R., Sánchez Martínez, S., Abati, J., Díaz García, F., Martínez Catalán, J.R., 2012. The Corredoiras orthogneiss (NW Iberian Massif): geochemistry and geochronology of the Paleozoic magmatic suite developed in a peri-Gondwanan arc. Lithos 128–131, 84–99.

Arenas, R., 1988. Evolución petrológica y geoquímica de la unidad alóctona inferior del complejo metamórfico básico–ultrabásico de Cabo Ortegal (Unidad de Moeche) y del Silúrico paraautóctono, Cadena Hercínica Ibérica (NW de España). Corpus Geologicum Gallaeciae 4. Laboratorio Xeolóxico de Laxe, p. 543, (Phd thesis).

Arenas, R., Rubio Pascual, F.J., Díaz García, F., Martínez Catalán, J.R., 1995. High-pressure micro-inclusions and development of an inverted metamorphic gradient in the Santiago Schists (Ordenes Complex, NW Iberian Massif, Spain): evidence of subduction and syncollisional decompression. Journal of Metamorphic Geology 13, 141–164.

Arenas, R., Martínez Catalán, J.R., Sánchez Martínez, S., Fernández-Suárez, J., Andonaegui, P., Pearce, J.A., Corfu, F., 2007. The Vila de Cruces ophiolite: a remnant of the early Rheic Ocean in the Variscan suture of Galicia (northwest Iberian Massif). Journal of Geology 115, 129–148.

Arenas, R., Sánchez Martínez, S., Gerdes, A., Albert, R., Díez Fernández, R., Andonaegui, P., 2013. Re-interpreting the Devonian ophiolites involved in the Variscan suture: U–Pb and Lu–Hf zircon data of the Moeche Ophiolite (Cabo Ortegal Complex, NW Iberia). International Journal of Earth Sciences 103, 1385–1402.

Arenas, R., Díez Fernández, R., Sánchez Martínez, S., Gerdes, A., Fernández-Suárez, J., Albert, R., 2014. Two-stage collision: exploring the birth of Pangea in the Variscan terranes. Gondwana Research 25, 756–763.

Avigad, D., Gerdes, A., Morag, N., Bechstädt, T., 2012. Coupled U–Pb–Hf of detrital zircons of Cambrian sandstones from Morocco and Sardinia: implications for provenance and Precambrian crustal evolution of North Africa. Gondwana Research 21, 690–703.

Begemann, F., Ludwig, K.R., Lugmair, G.W., Min, K., Nyquist, L.E., Patchett, P.J., Renne, P.R., Shih, C.Y., Villa, I.M., Walker, R.J., 2001. Call for an improved set of decay constants for geochronological use. Geochimica et Cosmochimica Acta 65, 111–121.

Bouvier, A., Vervoort, J.D., Patchett, P.J., 2008. The Lu–Hf and Sm–Nd isotopic composition of CHUR: constraints from unequilibrated chondrites and implications for the bulk composition of terrestrial planets. Earth and Planetary Science Letters 273, 48–57.

Castiñeiras, P., 2005. Origen y evolución tectonotermal de las unidades de O Pino y Cariño (Complejos Alóctonos de Galicia). Nova Terra 28. Laboratorio Xeolóxico de Laxe, p. 279, (Phd thesis).

Cawood, P.A., Hawkesworth, C.J., Dhuime, B., 2012. Detrital zircon record and tectonic setting. Geology 40, 875–878.

Chauvel, C., Blichert-Toft, J., 2001. A hafnium isotope and trace element perspective on melting of the depleted mantle. Earth and Planetary Science Letters 190, 137–151.

Chauvel, C., Lewin, E., Carpentier, M., Arndt, N.T., Marini, J.C., 2008. Role of recycled oceanic basalt and sediment in generating the Hf–Nd mantle array. Nature Geoscience 1, 64–67.

DePaolo, D.J., 1981. A neodymium and strontium isotopic study of the mesozoic calc-alkaline granitic batholiths of the Sierra-Nevada and Peninsular ranges, California. Journal of Geophysical Research 86, 470–488.

DePaolo, D.J., Wasserburg, G.J., 1976. Inferences about magma sources and mantle structure from variations of $^{143}Nd/^{144}Nd$. Geophysical Research Letters 3, 743–746.

Díaz García, F., 1990. La geología del sector occidental del Complejo de Órdenes, (Cordillera Hercínica, Noroeste de España). Nova Terra 3. Laboratorio Xeolóxico de Laxe, p. 290, (Phd thesis).

Díaz García, F., Arenas, R., Martínez Catalán, J.R., González del Tánago, J., Dunning, G.R., 1999. Tectonic evolution of the Careon ophiolite (northwest Spain). A remnant of oceanic lithosphere in the Variscan belt. Journal of Geology 107, 587–605.

Díaz García, F., Sánchez Martínez, S., Castiñeiras, P., Fuenlabrada, J.M., Arenas, R., 2010. A peri-Gondwanan arc in NW Iberia. II: assessment of the intra-arc tectonothermal evolution through U–Pb SHRIMP dating of mafic dykes. Gondwana Research 17, 352–362.

Dickinson, W.R., Gehrels, G.E., 2009. Use of U–Pb ages of detrital zircons to infer maximum depositional ages of strata: a test against a Colorado Plateau Mesozoic database. Earth and Planetary Science Letters 288, 115–125.

Díez Fernández, R., Martínez Catalán, J.R., Gerdes, A., Abati, J., Arenas, R., Fernández-Suárez, J., 2010. U–Pb ages of detrital zircons from the Basal allochthonous units of NW Iberia: provenance and paleoposition on the northern margin of Gondwana during the Neoproterozoic and Paleozoic. Gondwana Research 18, 385–399.

Díez Fernández, R., Martínez Catalán, J.R., Arenas, R., Abati, J., 2011. Tectonic evolution of a continental subduction–exhumation channel: Variscan structure of the basal allochthonous units in NW Spain. Tectonics 30, 1–22.

Díez Fernández, R., Castiñeiras, P., Gómez Barreiro, J., 2012a. Age constraints on Lower Paleozoic convection system: magmatic events in the NW Iberian Gondwana margin. Gondwana Research 21, 1066–1079.

Díez Fernández, R., Martínez Catalán, J.R., Arenas, R., Abati, J., Gerdes, A., Fernández-Suárez, J., 2012b. U–Pb detrital zircon analysis of the lower allochthon of NW Iberia: age constraints, provenance and links with the Variscan mobile belt and Gondwanan cratons. Journal of the Geological Society 169, 655–665.

Egal, E., Thieblemont, D., Lahondere, D., Guerrot, C., Costea, C.A., Iliescu, D., Delor, C., Goujou, J.C., Lafon, J.M., Tegyey, M., Diaby, S., Kolie, P., 2002. Late Eburnean granitization and tectonics along the western and northwestern margin of the Archean Kenema-Man domain (Guinea, West African Craton). Precambrian Research 117, 57–84.

Ennih, N., Liégeois, J.-P., 2008. The boundaries of the West African craton, with special reference to the basement of the Moroccan metacratonic Anti-Atlas belt. Geological Society, London, Special Publications 297, 1–17.

Fernández-Suárez, J., Gutiérrez-Alonso, G., Jenner, G.A., Tubrett, M.N., 1999. Crustal sources in Lower Palaeozoic rocks from NW Iberia: insights from laser ablation U–Pb ages of detrital zircons. Journal of the Geological Society 156, 1065–1068.

Fernández-Suárez, J., Gutiérrez Alonso, G., Jeffries, T.E., 2002. The importance of along-margin terrane transport in northern Gondwana: insights from detrital zircon parentage in Neoproterozoic rocks from Iberia and Brittany. Earth and Planetary Science Letters 204, 75–88.

Fernández-Suárez, J., Díaz García, F., Jeffries, T.E., Arenas, R., Abati, J., 2003. Constraints on the provenance of the uppermost allochthonous terrane of the NW Iberian Massif: inferences from detrital zircon U–Pb ages. Terra Nova 15, 138–144.

Fernández-Suárez, J., Arenas, R., Abati, J., Martínez Catalán, J.R., Whitehouse, M.J., Jeffries, T.E., 2007. U–Pb chronometry of polymetamorphic high-pressure granulites: an example from the allochthonous terranes of the NW Iberian Variscan belt. In: Hatcher Jr., R.D., Carlson, M.P., McBride, J.H., Martínez Catalán, J.R. (Eds.), 4-D framework of continental crust. Geological Society of America Memoir 200, pp. 469–488.

Fernández-Suárez, J., Gutiérrez-Alonso, G., Pastor-Galán, D., Hofmann, M., Murphy, J., Linnemann, U., 2013. The Ediacaran–Early Cambrian detrital zircon record of NW Iberia: possible sources and paleogeographic constraints. International Journal of Earth Sciences 103, 1335–1357.

Fuenlabrada, J.M., Arenas, R., Sánchez Martínez, S., Díaz García, F., Castiñeiras, P., 2010. A peri-Gondwanan arc in NW Iberia I: isotopic and geochemical constraints on the origin of the arc-A sedimentary approach. Gondwana Research 17, 338–351.

Fuenlabrada, J.M., Arenas, R., Díez Fernández, R., Sánchez Martínez, S., Abati, J., López Carmona, A., 2012. Sm–Nd isotope geochemistry and tectonic setting of the metasedimentary rocks from the basal allochthonous units of NW Iberia (Variscan suture, Galicia). Lithos 148, 196–208.

Gerdes, A., Zeh, A., 2006. Combined U–Pb and Hf isotope LA-(MC-)ICP-MS analyses of detrital zircons: comparison with SHRIMP and new constraints for the provenance and

age of an Armorican metasediment in Central Germany. Earth and Planetary Science Letters 249, 47–61.
Gerdes, A., Zeh, A., 2009. Zircon formation versus zircon alteration — New insights from combined U–Pb and Lu–Hf in-situ LA-ICP-MS analyses, and consequences for the interpretation of Archean zircon from the Central Zone of the Limpopo Belt. Chemical Geology 261, 230–243.
Gil Ibarguchi, J.I., Ortega Gironés, E., 1985. Petrology, structure and geotectonic implications of glaucophane-bearing eclogites and related rocks from the Malpica—Tuy (MT) Unit, Galicia, northwest Spain. Chemical Geology 50, 145–162.
Gil Ibarguchi, J.I., Mendia, M., Girardeau, J., Peucat, J.J., 1990. Petrology of eclogites and clinopyroxene-garnet metabasites from the Cabo Ortegal Complex (northwestern Spain). Lithos 25, 133–162.
Gómez Barreiro, J., Martínez Catalán, J.R., Arenas, R., Castiñeiras, P., Abati, J., Díaz García, F., Wijbrans, J.R., 2007. Tectonic evolution of the upper allochthon of the Órdenes complex (northwestern Iberian Massif): structural constraints to a polyorogenic peri-Gondwanan terrane. In: Linnemann, U., Nance, R.D., Kraft, P., Zulauf, G. (Eds.), The evolution of the Rheic Ocean: from Avalonian–Cadomian active margin to Alleghenian–Variscan collision. Geological Society of America Special Paper 423, pp. 315–332.
Gutiérrez-Alonso, G., Fernández-Suárez, J., Jeffries, T.E., Jenner, G.A., Tubrett, M.N., Cox, R., Jackson, S.E., 2003. Terrane accretion and dispersal in the northern Gondwana margin. An Early Paleozoic analogue of a long-lived active margin. Tectonophysics 365, 221–232.
Hamilton, P.J., O'Nions, R.K., Bridgwater, D., Nutman, A., 1983. Sm–Nd studies of Archaean metasediments and metavolcanics from West Greenland and their implications for the Earth's early history. Earth and Planetary Science Letters 62, 263–272.
Hawkesworth, C.J., Dhuime, B., Pietranik, A.B., Cawood, P.A., Kemp, A.I.S., Storey, C.D., 2010. The generation and evolution of the continental crust. Journal of the Geological Society 167, 229–248.
Jacobsen, S.B., Wasserburg, G.J., 1980. Sm–Nd isotopic evolution of chondrites. Earth and Planetary Science Letters 50, 139–155.
Kemp, A.I.S., Wilde, S.A., Hawkesworth, C.J., Coath, C.D., Nemchin, A., Pidgeon, R.T., Vervoort, J.D., DuFrane, S.A., 2010. Hadean crustal evolution revisited: new constraints from Pb–Hf isotope systematics of the Jack Hills zircons. Earth and Planetary Science Letters 296, 45–56.
Kretz, R., 1983. Symbols for rock-forming minerals. American Mineralogist 68, 277–279.
Linnemann, U., McNaughton, N.J., Romer, R.L., Gehmlich, M., Drost, K., Tonk, C., 2004. West African provenance for Saxo-Thuringia (Bohemian Massif): did Armorica ever leave pre-Pangean Gondwana? U/Pb-SHRIMP zircon evidence and the Nd-isotopic record. International Journal of Earth Sciences 93, 683–705.
Linnemann, U., Pereira, F., Jeffries, T.E., Drost, K., Gerdes, A., 2008. The Cadomian Orogeny and the opening of the Rheic Ocean: the diacrony of geotectonic processes constrained by LA-ICP-MS U–Pb zircon dating (Ossa-Morena and Saxo-Thuringian Zones, Iberian and Bohemian Massifs). Tectonophysics 461, 21–43.
Linnemann, U., Gerdes, A., Hofmann, M., Marko, L., 2014. The Cadomian Orogen: Neoproterozoic to Early Cambrian crustal growth and orogenic zoning along the periphery of the West African Craton—Constraints from U–Pb zircon ages and Hf isotopes (Schwarzburg Antiform, Germany). Precambrian Research 244, 236–278.
López-Carmona, A., Abati, J., Pitra, P., Lee, J.K.W., 2014. Retrogressed lawsonite blueschists from the NW Iberian Massif: P–T-t constraints from thermodynamic modelling and Ar-40/Ar-39 geochronology. Contributions to Mineralogy and Petrology 167.
Ludwig, K.R., 2012. User's Manual for Isoplot 3.75. A Geochonological Toolkit for Microsoft ExcelBerkeley Geochronology Center Special, Publication No. 5, p. 75.
Lugmair, G.W., Marti, K., 1978. Lunar initial $^{143}Nd/^{144}Nd$: differential evolution of the lunar crust and mantle. Earth and Planetary Science Letters 39, 349–357.
Lugmair, G.W., Shimamura, T., Lewis, R.S., Anders, E., 1983. Sm-146 in the early solar-system — Evidence from neodymium in the Allende meteorite. Science 222, 1015–1018.
Marcos, A., Marquínez, J., Pérez-Estaún, A., Pulgar, J.A., Bastida, F., 1984. Nuevas aportaciones al conocimiento de la evolución tectonometamórfica del Complejo de Cabo Ortegal (NW de España). Cadernos Laboratorio Xeolóxico de Laxe 7, 125–137.
Martínez Catalán, J.R., 2011. Are the oroclines of the Variscan belt related to late Variscan strike-slip tectonics? Terra Nova 23, 241–247.
Martínez Catalán, J.R., Fernández-Suárez, J., Jenner, G.A., Belousova, E., Díez Montes, A., 2004. Provenance constraints from detrital zircon U–Pb ages in the NW Iberian Massif: implications for Palaeozoic plate configuration and Variscan evolution. Journal of the Geological Society 161, 463–476.
Martínez Catalán, J.R., Arenas, R., Abati, J., Sánchez Martínez, S., Díaz García, F., Fernández-Suárez, J., González Cuadra, P., Castiñeiras, P., Gómez Barreiro, J., Díez Montes, A., González Clavijo, E., Rubio Pascual, F.J., Andonaegui, P., Jeffries, T.E., Alcock, J.E., Díez Fernández, R., López Carmona, A., 2009. A rootless suture and the loss of the roots of a mountain chain: the Variscan belt of NW Iberia. Comptes Rendus Geoscience 341, 114–126.
McLennan, S.M., Hemming, S., 1992. Samarium/neodymium elemental and isotopic systematics in sedimentary rocks. Geochimica et Cosmochimica Acta 56, 887–898.
Millonig, L.J., Gerdes, A., Groat, L.A., 2012. U–Th–Pb geochronology of meta-carbonatites and meta-alkaline rocks in the southern Canadian Cordillera: a geodynamic perspective. Lithos 152, 202–217.
Morag, N., Avigad, D., Gerdes, A., Harlavan, Y., 2012. 1000–580 Ma crustal evolution in the northern Arabian–Nubian Shield revealed by U–Pb–Hf of detrital zircons from late Neoproterozoic sediments (Elat area, Israel). Precambrian Research 208–211, 197–212.
O'Nions, R.K., Hamilton, P.J., Evensen, N.M., 1977. Variations in $^{143}Nd/^{144}Nd$ and $^{87}Sr/^{86}Sr$ in oceanic basalts. Earth and Planetary Science Letters 34, 13–22.
Ordóñez Casado, B., Gebauer, D., Schafer, H.J., Gil Ibarguchi, J.I., Peucat, J.J., 2001. A single Devonian subduction event for the HP/HT metamorphism of the Cabo Ortegal complex within the Iberian Massif. Tectonophysics 332, 359–385.
Peucat, J.J., Bernard-Griffiths, J., Gil Ibarguchi, J.I., Dallmeyer, R.D., Menot, R.P., Cornichet, J., Ponce De León, M.I., 1990. Geochemical and geochronological cross section of the deep Variscan crust: the Cabo Ortegal high-pressure nappe (northwestern Spain). Tectonophysics 177, 263–292.
Peucat, J.J., Capdevila, R., Drareni, A., Mahdjoub, Y., Kahoui, M., 2005. The Eglab massif in the West African Craton (Algeria), an original segment of the Eburnean orogenic belt: petrology, geochemistry and geochronology. Precambrian Research 136, 309–352.
Potrel, A., Peucat, J.J., Fanning, C.M., 1998. Archean crustal evolution of the West African Craton: example of the Amsaga Area (Reguibat Rise). U–Pb and Sm–Nd evidence for crustal growth and recycling. Precambrian Research 90, 107–117.
Rodríguez, J., Cosca, M.A., Gil Ibarguchi, J.I., Dallmeyer, R.D., 2003. Strain partitioning and preservation of $^{40}Ar/^{39}Ar$ ages during Variscan exhumation of a subducted crust (Malpica-Tui complex, NW Spain). Lithos 70, 111–139.
Rudnick, R.L., Gao, S., 2003. 3.01 — Composition of the continental crust. In: Holland, H.D., Turekian, K.K. (Eds.), Treatise on Geochemistry. Pergamon, Oxford, pp. 1–64.
Sánchez Martínez, S., Arenas, R., Díaz García, F., Martínez Catalán, J.R., Gómez-Barreiro, J., Pearce, J.A., 2007. Careón ophiolite, NW Spain: suprasubduction zone setting for the youngest Rheic Ocean floor. Geology 35, 53–56.
Sánchez Martínez, S., Arenas, R., Gerdes, A., Castiñeiras, P., Potrel, A., Fernández-Suárez, J., 2011. Isotope geochemistry and revised geochronology of the Purrido Ophiolite (Cabo Ortegal Complex, NW Iberian Massif): Devonian magmatism with mixed sources and involved Mesoproterozoic basement. Journal of the Geological Society 168, 733–750.
Sánchez Martínez, S., Gerdes, A., Arenas, R., Abati, J., 2012. The Bazar Ophiolite of NW Iberia: a relic of the Iapetus–Tornquist Ocean in the Variscan suture. Terra Nova 24, 283–294.
Scherer, E., Munker, C., Mezger, K., 2001. Calibration of the lutetium–hafnium clock. Science 293, 683–687.
Schofield, D.I., Horstwood, M.S.A., Pitfield, P.E.J., Gillespie, M., Darbyshire, F., O'Connor, E.A., Abdouloye, T.B., 2012. U–Pb dating and Sm–Nd isotopic analysis of granitic rocks from the Tiris Complex: new constraints on key events in the evolution of the Reguibat Shield, Mauritania. Precambrian Research 204–205, 1–11.
Shaw, J., Gutiérrez-Alonso, G., Johnston, S.T., Pastor Galán, D., 2014. Provenance variability along the Early Ordovician north Gondwana margin: Paleogeographic and tectonic implications of U–Pb detrital zircon ages from the Armorican Quartzite of the Iberian Variscan belt. Geological Society of America Bulletin 126, 702–719.
Slama, J., Kosler, J., Condon, D.J., Crowley, J.L., Gerdes, A., Hanchar, J.M., Horstwood, M.S.A., Morris, G.A., Nasdala, L., Norberg, N., Schaltegger, U., Schoene, B., Tubrett, M.N., Whitehouse, M.J., 2008. Plešovice zircon — A new natural reference material for U–Pb and Hf isotopic microanalysis. Chemical Geology 249, 1–35.
Soderlund, U., Patchett, J.P., Vervoort, J.D., Isachsen, C.E., 2004. The Lu-176 decay constant determined by Lu–Hf and U–Pb isotope systematics of Precambrian mafic intrusions. Earth and Planetary Science Letters 219, 311–324.
Thomas, R.J., Chevallier, L.P., Gresse, P.G., Harmer, R.E., Eglington, B.M., Armstrong, R.A., de Beer, C.H., Martini, J.E.J., de Kock, G.S., Macey, P.H., Ingram, B.A., 2002. Precambrian evolution of the Sirwa Window, Anti-Atlas Orogen, Morocco. Precambrian Research 118, 1–57.
Vermeesch, P., 2004. How many grains are needed for a provenance study? Earth and Planetary Science Letters 224, 441–451.
Vermeesch, P., 2012. On the visualisation of detrital age distributions. Chemical Geology 312, 190–194.
Vogel, D.E., 1967. Petrology of an eclogite- and pyrigarnite-bearing polymetamorphic rock complex at Cabo Ortegal, NW Spain. Leidse Geol Mededelingen, pp. 121–213, (Phd thesis).
Wiedenbeck, M., Alle, P., Corfu, F., Griffin, W.L., Meier, M., Oberli, F., Vonquadt, A., Roddick, J.C., Speigel, W., 1995. 3 natural zircon standards for U–Th–Pb, Lu–Hf, trace-element and REE analyses. Geostandards Newsletter 19, 1–23.
Woodhead, J.D., Hergt, J.M., 2005. A preliminary appraisal of seven natural zircon reference materials for in situ Hf isotope determination. Geostandards and Geoanalytical Research 29, 183–195.
Zeh, A., Gerdes, A., 2012. U–Pb and Hf isotope record of detrital zircons from gold-bearing sediments of the Pietersburg Greenstone Belt (South Africa)—Is there a common provenance with the Witwatersrand Basin? Precambrian Research 204, 46–56.
Zeh, A., Gerdes, A., Millonig, L., 2011. Hafnium isotope record of the Ancient Gneiss Complex, Swaziland, southern Africa: evidence for Archaean crust–mantle formation and crust reworking between 3.66 and 2.73 Ga. Journal of the Geological Society 168, 953–963.

VI

Provenance of the HP-HT subducted margin in the Variscan belt

6.1. Introduction

The article presented in this chapter deals with provenance investigations on the metasedimentary rocks of the Banded Gneiss formation. This terrain formed part of a passive continental (or transitional) margin between its genesis to the development of the Devonian HP–HT metamorphic recrystallizations. As this metamorphic event was driven by a subduction process the aim of these investigations is to identify the continent that subducted.

6.2. Partial conclusions

Data representative of the West Africa Craton (WAC) shows similar and compatible patterns to those shown by the HP–HT Upper Allochthon presented herein. A similar thorough comparison as the previous chapter has been made between the Banded Gneisses and the WAC detrital and igneous U–Pb zircon data, which allows to confirm once again the WAC provenance for the Upper Allochthon. This comparison has been made for each of the zircon populations, but the comparison of the Mesoproterozoic populations deserves a special mention.

In the Mesoproterozoic Era, the WAC became a stable craton which resulted in a characteristic

c. 1.7–1.0 Ga 'magmatic gap', and therefore Mesoproterozoic zircons are not expected to be present in a WAC derived formation. In the Banded Gneisses the Mesoproterozoic zircon is scarce and scattered, constituting 2.8% of the total population and not defining a clear maximum. Taking into account that this population is isotopically depleted, it could have been derived from the Amazonia craton or from Mesoproterozoic dykes intruding the WAC. Terranes that clearly derive from the Amazonian craton and have similar Neoproterozoic–Cambrian arc developments as the Upper Allochthon (Avalonia and Ganderia), contain isotopically depleted Mesoproterozoic zircon, but not as depleted as the zircon from this study. Dolerite dykes have been recently discovered in the Anti-Atlas belt (WAC) with emplacement ages of *c.* 1.65 Ga and *c.* 1.4 Ga. The $^{176}Hf/^{177}Hf$ *v.* age plot shows that the Banded Gneisses Mesoproterozoic population has an isotopically depleted source that undertook a similar Lu–Hf isotopic evolution as the CHUR and the DM. These observations seem to favour a WAC juvenile DM-derived dyke provenance, rather than an Amazonian or even a Laurentian one. Therefore, the provenance of the Mesoproterozoic population remains enigmatic (because the observations aforementioned are not conclusive), but it does not seem necessary to assign far exotic provenance sources to explain the presence of this small population in the Upper Allochthon (as it has been assigned in previous works).

The zircon detrital signature of the Banded Gneisses has not only been compared with the WAC, but also with cratons and terranes that could potentially be the source areas for its metasedimentary rocks. The high number of zircon grains with mixing patterns at *c.* 1.5 and 1.0 Ga in the Avalonian terranes (Ganderia and Avalonia) and the Laurentian craton are not present in the HP–HT Upper Allochthon spectrum. Therefore, the Upper Allochthon detrital series are not derived from the mentioned source areas.

The Paleozoic–Neoproterozoic zircon population of the Banded Gneisses (with most of its ages of *c.* 780–490 Ma and with a maximum abundance at *c.* 522–512 Ma) coincides with the reported ages for the Cadomian orogeny (*c.* 750–540 Ma), but the *c.* 522–512 Ma Banded Gneisses maximum is younger. Banded Gneisses zircon crystals with ages between *c.* 780 and 590 Ma are not abundant and are interpreted as to be formed by crustal recycling due to the initial development of the Cadomian arc system ('proto–arc' stage). The *c.* 590–490 Ma Banded Gneisses zircon is very abundant ('arc' stage) and their Lu–Hf isotopic patterns are explained by the intrusion of DM-derived magmas that triggered mixing processes with an Eburnean and Archean crust (and with a small proportion of reworked early Cadomian crustal material), consistent with a peripheral arc activity at the Northern WAC. If the magmatic arc is the Cadomian arc, the magmatic activity inferred by the Banded Gneisses lasted at least until *c.* 510 Ma in the NW Iberian section of the Gondwana margin, instead of *c.* 540 Ma (as described in the Bohemian Massif). This could imply a diachronous scissor-like continental arc generation, due to oblique vector of subduction, that propagated westwards (possibility already proposed in the literature), but more likely, it could imply that the *c.* 540–510 Ma arc activity was not registered in the Bohemian Massif sector of the margin of Gondwana, because magmatic activity can strongly vary between segments of the same arc system.

When comparisons are made with the unit overlapping the HP–HT Banded Gneisses (the IP Cariño Gneisses, studied in the previous chapter) big similarities are observed. Their maximum depositional ages (MDAs) are very similar (Cariño Gneisses MDA = 510 Ma, Banded Gneisses MDA = 521 Ma) and as no big differences in their youngest U–Pb ages are appreciated, it seems reasonable to conclude that both units are temporally related. Sm–Nd isotopic experiments also reveal the similarity between the gneissic units as the $\varepsilon Nd_{(t)}$ values for the Banded Gneisses are in the range of those for the Cariño Gneisses. The main difference between their U–Pb age density distributions is that the Banded Gneiss formation has an abundant *c.* 590–540 Ma Ediacaran population and the Cariño Gneiss formation has not. Both formations represent the same section of the Gondwanan margin. Their bimodal detrital populations suggest that both formations had the same geological setting, *i.e.* sedimentation in a back-arc type basin. Banded Gneiss formation was profusely intruded by

acidic and basic magmas (protolith ages of *c.* 506–484 Ma) and Cariño Gneisses were not. All these observations lead one to suppose that they were probably deposited in the same back-arc basin at *c.* 521–506 Ma. The first sediments deposited were those of the Banded Gneiss formation, formed by the mixture of the old components from the WAC and abundant arc related *c.* 590–520 Ma sediments. The Cariño Gneisses protoliths deposited afterwards, filling the same basin with WAC sediments and *c.* 560–510 Ma arc-derived sediments.

Between the time of deposition (*c.* 512–506 Ma) and high-grade metamorphism (*c.* 400–390 Ma), both formations constituted a part of the margin of Gondwana, that changed from a volcanic arc to a passive margin setting at around the Cambrian–Ordovician boundary. The different metamorphic conditions reached by both units indicate that the HP–HT member of the Upper Allochthon was affected by a deep subduction at *c.* 400–390 Ma. Different structures and metamorphic recrystallizations related to this collision have also been described in the IP upper units. In this case, the intensity of deformation was much lower and only limited shear zones and amphibolite facies Barrovian metamorphism were generated. The differentiated tectonothermal evolution recorded in the Cariño and Banded gneiss formations, could have been favoured by the previous structure of the Gondwana margin, achieved during the Cambrian–Ordovician extension. It has been published by other authors that in the Cambrian–Ordovician transition, lithospheric extension induced crustal necking and stretching, compartmenting the Gondwana lithosphere into several continental micro-blocks. During the Devonian collision the thicker sections of the margin were affected by limited accretion and thickening, developing Barrovian metamorphism. The adjacent thinned sections experienced profound subduction directed to the North, favoured by zones of inherited crustal weakness, developing the HP–HT subduction-related metamorphic conditions of the Banded Gneiss formation and its HP–HT equivalents along the Variscan belt. The new provenance data presented in this PhD is conclusive on the origin of the Banded Gneiss formation, whose eclogite facies evolution can only be explained as generated during subduction of the Gondwana margin directed to the North.

Journal of
METAMORPHIC GEOLOGY

J. metamorphic Geol., 2015, **33,** 959–979 doi:10.1111/jmg.12155

Provenance of the HP–HT subducted margin in the Variscan belt (Cabo Ortegal Complex, NW Iberian Massif)

R. ALBERT,[1] R. ARENAS,[1] A. GERDES,[2,3] S. SÁNCHEZ MARTÍNEZ[1] AND L. MARKO[2]
[1]*Departamento de Petrología y Geoquímica & Instituto de Geociencias (UCM, CSIC), Universidad Complutense, 28040, Madrid, Spain (r.albert@geo.ucm.es)*
[2]*Institut für Geowissenschaften, Goethe–University Frankfurt, 60438, Frankfurt, Germany*
[3]*Department of Earth Sciences, Stellenbosch University, Private Bag X1, Matieland, South Africa*

ABSTRACT The Variscan Upper Allochthon is a continental-affinity terrane that recorded a Cambrian–Ediacaran magmatic arc generation, a subsequent transition to a passive margin, and a collision-related high-*P* metamorphism during the Devonian–Carboniferous amalgamation of Pangea. The objective of this article is to decipher which continental margin subducted in the Devonian high-*P*–high-*T* (HP–HT) event. To do so, a provenance study is presented using combined U–Pb ($n = 613$) and Lu–Hf ($n = 463$) isotopic LA–ICP–MS zircon analyses and Sm–Nd whole–rock ($n = 5$) determinations. These analyses have been performed on five samples of the Banded Gneisses (Cabo Ortegal Complex, NW Iberia), which forms a part of the HP–HT bottom member of the Upper Allochthon. Palaeozoic–Neoproterozoic zircon ages (34.7%) have a maximum abundance at 522–512 Ma, peaks at 575, 561, 545 Ma and minor abundance peaks between 780 and 590 Ma, and show from their Lu–Hf compositions a volcanic arc mixing pattern. This arc was probably related to the Cadomian arc system. The Mesoproterozoic population is scarce and scattered (2.8%), and due to its Lu–Hf pattern, it is proposed that this population is also West Africa Craton derived. The Paleoproterozoic population (39.6%) is concentrated at 2.07 Ga and it is linked to the Eburnean Orogeny, where depleted mantle derived magmas intruded an Archean craton margin. This craton is represented by the Archean population (22.8%), which is grouped at 3.0, 2.68-2.61 and 2.52-2.48 Ga, and shows long-term reworking processes and at least two juvenile magma intrusions. These data show that the Variscan Upper Allochthon has a West African provenance and therefore, it strongly suggests that the NW Iberian allochthonous complexes and their correlative European terranes are also West Africa derived. These results allow us to finally clarify that the first high-*P* event, recorded during the eo-Variscan amalgamation of Pangea, was attained by the subduction of the margin of Gondwana under Laurussia.

Key words: Cabo Ortegal; LAICPMS; Lu–Hf; U–Pb; Variscan Allochthon.

INTRODUCTION

The Variscan belt is a long orogen developed during the main stages of the Pangea assembly as a result of the collision of two large continents, Gondwana to the South and Laurussia to the North (Matte, 1991, 2001; Winchester *et al.*, 2002; Martínez Catalán *et al.*, 2009; Arenas *et al.*, 2014a). It is considered that the final assemblage of Pangea took place between Devonian and Early Permian, and that the continental collision followed the closure of the main Palaeozoic ocean, the Rheic Ocean. This ocean was generated after the Late Cambrian–Early Ordovician, after rifting and progressive north drift of Avalonia and other peri-Gondwanan terranes (Stampfli & Borel, 2002; Murphy *et al.*, 2006; Arenas *et al.*, 2007; Murphy & Nance, 2008; Nance *et al.*, 2010). The Variscan belt can be followed from Iberia, across Brittany and the French Massif Central, to the Bohemian Massif, extending towards the basement of the Alps, Corsica and Sardinia (Fig. 1a). The orogen was linear in origin, but it was affected by several late- to post-orogenic oroclinal bends that hinder correlations across the belt (Matte, 2001; Martínez Catalán, 2011; Weil *et al.*, 2013). The Variscan orogen has continuity in eastern North America in the Appalachian–Alleghanian Belt.

The Variscan orogen contains a long suture zone outlined by several allochthonous terranes with ophiolites and high-*P* units (Fig. 1a). They preserve the most significant information in relation to the oldest orogenic events and the evolution of the oceanic domains that preceded the collision. Therefore, a clear understanding of the origin and tectonothermal evolution of these terranes is a key issue to improve the knowledge about the initial interaction between Gondwana and Laurussia. The orogen is characterized by the development of two high-*P* events with

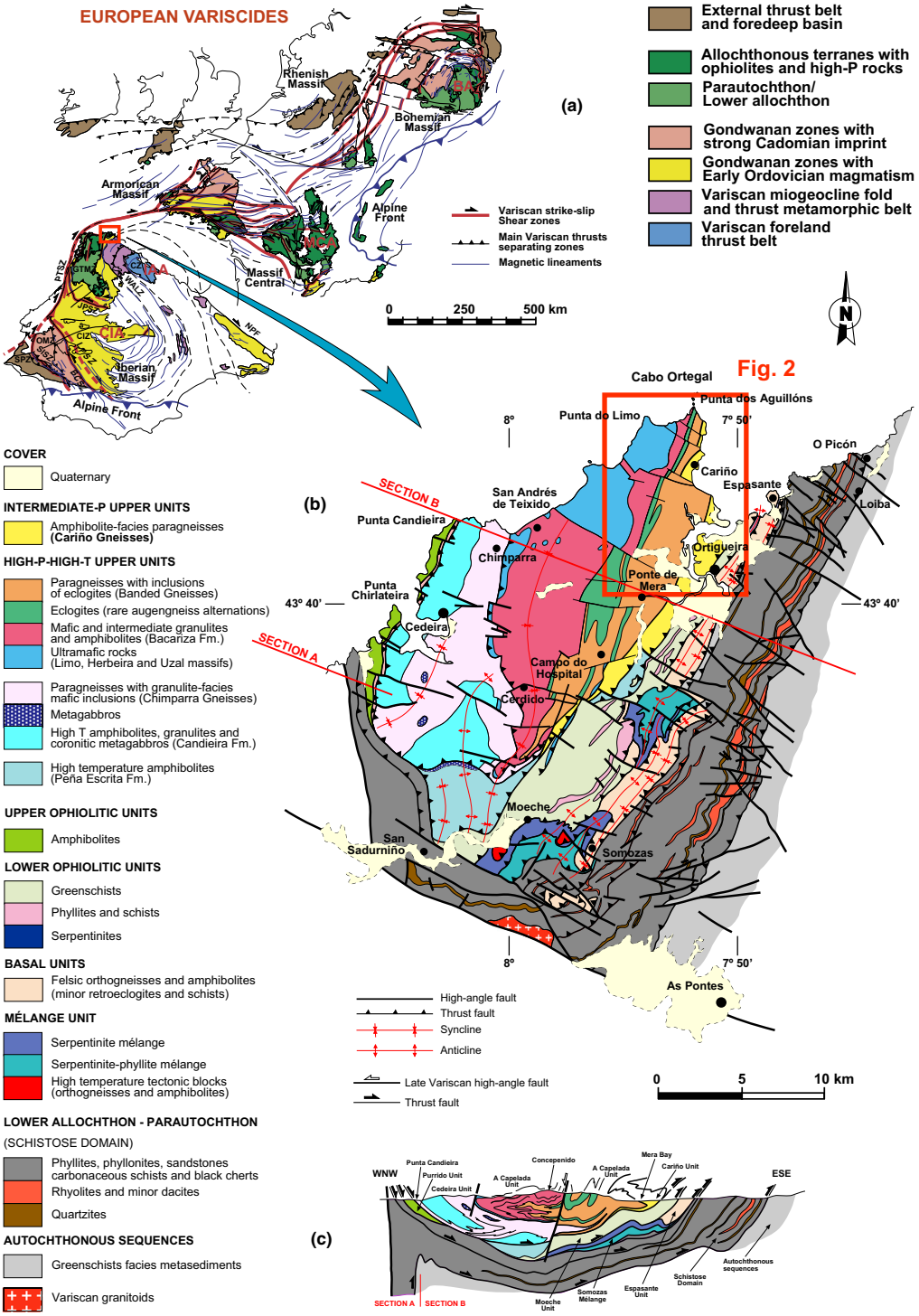

Fig. 1. Geological map of the European Variscides (a) based on Martínez Catalán (2011). Geological map (b) and cross-section (c) of the NW Iberian Cabo Ortegal Complex. The location of Fig. 2 geological map is also shown. Based on Vogel (1967), Marcos *et al.* (1984), Arenas (1988), Arenas *et al.* (2014b). The Upper Allochthon is formed by the intermediate-pressure upper units and the high-*P*–high-*T* upper units.

different ages, preserved in two distinct terranes with continental or transitional characteristics. These high-*P* events were probably generated during two stages of collision between Gondwana and Laurussia, separated in time by the opening of a long, but ephemeral, pull-apart basin at *c*. 395 Ma, with generation of oceanic crust that presently represents the most common ophiolites in the Variscan belt (Sánchez Martínez *et al*., 2011; Arenas *et al*., 2014a,b).

The younger high-*P* event is characteristic of an allochthonous terrane located below the ophiolites, currently described in NW Iberia as the basal units. Dated at *c*. 370 Ma (Rodríguez *et al*., 2003; Abati *et al*., 2010), this high-*P* event generated low to intermediate-*T* mineral assemblages, with extensive development of C-type eclogites, blueschists, high-*P* metapelites and orthogneisses (Gil Ibarguchi & Ortega Gironés, 1985; Arenas *et al*., 1995, 1997; Gil Ibarguchi, 1995; López-Carmona *et al*., 2013, 2014). According to their structural position below the ophiolites, the basal units were interpreted early on as a section of the Gondwanan margin affected by subduction (Arenas *et al*., 1986). This subduction was directed to the North and it can be considered as the first s.s. Variscan event that affected the margin of Gondwana (Martínez Catalán *et al*., 1996; Díez Fernández *et al*., 2011, 2012b).

The interpretation of the older high-*P* event is more problematic. It is a high-*P* and high-*T* (HP–HT) event that appears in the bottom member of a thick allochthonous terrane, which is located above the ophiolites and is described as the Upper Allochthon (or upper units) in the NW Iberian Massif. This high-*P* event has been repeatedly dated at *c*. 400–390 Ma (Ordóñez Casado *et al*., 2001; Fernández-Suárez *et al*., 2007) and generated B-type eclogites, high-*P* granulites, high-*P* gneisses and related high-*P* mineral assemblages in gabbros and ultramafic rocks. The top member of the Upper Allochthon has continental crust-active margin equivalence, but does not show high-*P* assemblages. Instead, it is only affected by intermediate-pressure (IP) metamorphism. The upper units have been traditionally interpreted as a single terrane, because they appear above the ophiolites (Arenas *et al*., in press). However, considering the tectonothermal differences between the top and bottom members of the Upper Allochthon and the frequent cryptic character of many sutures, doubts arise in relation to the single or composite character of this terrane. Preliminary data in the IP upper units indicated a Gondwanan provenance for this terrane (Fernández-Suárez *et al*., 2003). However, no information existed dealing with the provenance of the HP–HT upper units, and so it was not possible to know if this continental–transitional subducted margin represents a section of the Gondwanan margin or a part of the northern colliding continent, Laurussia. Answering this question will ensure a better understanding of the Variscan belt and consequently of the characteristics of the Pangea assembly. It is also important to consider the original linear trend of the belt, and that the allochthonous terranes are rather continuous between Iberia and the Bohemian Massif, with systematic presence of the two high-*P* events described in NW Iberia (Ballèvre *et al*., 2014).

To improve knowledge about the origin and provenance of the HP–HT upper units, a two-step experiment was carried out based on the study of geochronology and isotopic geochemistry of detrital zircon (U–Pb, Lu–Hf) and whole-rock samples (Sm–Nd). The first step consisted of the investigation of the provenance characteristics of the siliciclastic series of the IP upper units, using very well-preserved and representative samples of the Cabo Ortegal Complex, in the NW Iberian Massif (Fig. 1b,c). This study, recently published (Albert *et al*., 2015), confirmed the Gondwanan provenance of the IP upper units providing solid basis for comparison. The investigation of the provenance of the HP–HT upper units of the same complex is the objective of this article. Data derived from this type of investigation should definitively enable one to know if the upper units are in fact a single or a composite terrane, and consequently clarify the Gondwanan or Laurussian provenance of the subducted margin represented by the HP–HT upper units.

GEOLOGICAL FRAMEWORK

The Iberian Massif has been divided into several zones according to stratigraphic, structural, metamorphic and magmatic characteristics (Lotze, 1945, 1950; Julivert *et al*., 1972; Farias *et al*., 1987). The Cantabrian (CZ), West Asturian–Leonese (WALZ) and Central Iberian (CIZ) zones define an autochthonous domain representing a large section of the Gondwanan margin involved in the Variscan deformation (Fig. 1a). They are overlain by an allochthonous thick pile which is represented by the Galicia–Trás–os–Montes Zone (GTOMZ). A similar zone distribution can be followed along the Variscan belt (Martínez Catalán, 2011; Fig. 1a). The lowest unit in the GTOMZ is considered the Lower Allochthon or Parautochthon. Above it, five allochthonous complexes, structured as late Variscan synforms, are observed. In Galicia, they are the Cabo Ortegal, Órdenes and Malpica–Tui complexes (outcropping in an East–West direction), together with the Bragança and Morais complexes in the Trás–os–Montes region of Portugal. They are nappe piles constituted of three main groups of terranes, from bottom to top: basal, ophiolitic and upper units (Martínez Catalán *et al*., 2009; Arenas *et al*., in press). It is assumed that all these zones have been condensed and piled up, thrust from more external positions in relation to the Gondwanan mainland to form what today is known as the Iberian Massif.

The basal units of the allochthonous complexes are formed by metasedimentary rock series with Ediacaran to Early Ordovician maximum depositional ages (MDAs; Díez Fernández *et al.*, 2010), intruded by abundant calcalkaline (*c.* 493 Ma) to alkaline–peralkaline (*c.* 475–470 Ma) granitic bodies (Abati *et al.*, 2010; Díez Fernández *et al.*, 2012a). They represent a continental terrane with Gondwanan provenance, affected by high-*P* and low- to intermediate-*T* metamorphism during north directed Variscan subduction at *c.* 370 Ma (Gil Ibarguchi & Ortega Gironés, 1985; Arenas *et al.*, 1995; Rodríguez *et al.*, 2003; Abati *et al.*, 2010; Díez Fernández *et al.*, 2011; López-Carmona *et al.*, 2014). This subduction took place below ophiolites and other terranes previously docked to the southern margin of Laurussia (Arenas *et al.*, 2014a).

The ophiolitic units are formed by mafic–ultramafic rock series representing a varied ensemble of units formed in different stages of the evolution of the Palaeozoic oceans. Part of these ophiolites have been interpreted as Cambrian remnants of the peri-Gondwanan oceans, including sequences stacked at the base of a fore-arc (Sánchez Martínez *et al.*, 2012) and back-arc sequences (Arenas *et al.*, 2007). However, the most extended ophiolitic units in NW Iberia, and also along the Variscan suture in the rest of Europe, are *c.* 395 Ma mafic–ultramafic rock series. The interpretation of these units has changed over time. They were first considered as supra-subduction zone ophiolites formed during the last stages of the closure of the Rheic Ocean (Díaz García *et al.*, 1999; Sánchez Martínez *et al.*, 2007). However, according to new U–Pb/Lu–Hf zircon data, they have been recently considered as related to the opening of a long pull-apart basin, showing an interaction of the mafic rocks with an old continental basement (Sánchez Martínez *et al.*, 2011; Arenas *et al.*, 2014a,b).

The Upper Allochthon (upper units) is located above the ophiolitic units, and has been traditionally interpreted as a unique terrane with continental crust affinity. According to its tectonothermal evolution, it is divided into HP–HT upper units (bottom member) and IP upper units (top member). However, the traditional interpretation of the upper units as a single terrane can only be considered as preliminary, as the final subdivision of the Upper Allochthon depends on the provenance compatibility for both metamorphic groups, which will be examined according to the new data presented in this article.

The IP upper units, are composed of a thick siliciclastic series with greywacke and pelitic members and minor conglomerates (Díaz García, 1990; Castiñeiras, 2005; Díaz García *et al.*, 2010; Fuenlabrada *et al.*, 2010), intruded by large massifs of arc-derived gabbros and granitoids (Andonaegui *et al.*, 2002, 2012). Their metamorphic grade varies from greenschist facies to granulite facies conditions, with development of extensive migmatization at the lowest levels (Abati *et al.*, 1999, 2003). The IP upper units' tectonothermal evolution has a polymetamorphic nature (Fernández-Suárez *et al.*, 2002), with a first Cambrian event connected with the evolution of a peri-Gondwanan volcanic arc system (Abati *et al.*, 1999, 2007), and a second event related to a collisional eo-Variscan activity (Gómez Barreiro *et al.*, 2006; González Cuadra, 2007; Arenas *et al.*, in press). The IP upper units in the Cabo Ortegal Complex are only represented by the meta-siliciclastic Cariño Gneisses (Vogel, 1967; Castiñeiras, 2005), which have been recently studied in terms of provenance (Albert *et al.*, 2015). The main conclusion is that the sedimentary protoliths are clearly Gondwana derived, with source areas located in the domain of the West African Craton.

The HP–HT upper units are the bottom member of the Upper Allochthon (located above the ophiolites) and they are mainly composed of ultramafic rocks, mafic–intermediate high-*P* granulites, eclogites, HT amphibolites, metagabbros, orthogneisses, abundant migmatitic paragneisses and their retrogressive products (Vogel, 1967; Gil Ibarguchi *et al.*, 1990; Peucat *et al.*, 1990; Ábalos *et al.*, 2003). The protolith ages for the meta-igneous rocks forming part of these units range between 520 and 490 Ma, and the age of the HP–HT metamorphism has been dated to *c.* 400–390 Ma (Ordóñez Casado *et al.*, 2001; Fernández-Suárez *et al.*, 2007; Albert *et al.*, 2013). This HP–HT Middle Devonian tectonothermal event was attained by a subduction process (Gil Ibarguchi *et al.*, 1999), which affected a continental or transitional crust of unknown provenance.

In the Cabo Ortegal Complex, the metasedimentary rocks of the HP–HT upper units are represented by an eclogite facies gneissic formation described as the Banded Gneiss formation (Fig. 1b). They outcrop in the eastern sector of the Cabo Ortegal Complex, with a ~N20° trend and with thicknesses varying between 175 m (North of Cariño) and 1300 m (Masanteo peninsula; Fig. 2). They are formed by intensively deformed migmatitic psammitic–pelitic gneisses with abundant lens-shaped and variably retrogressed eclogite inclusions, with highly sheared alternations of felsic igneous rocks (granitic–tonalitic compositions), and rare inclusions of ultramafic rocks and marbles. The mineral assemblages of these lithologies were described by Vogel (1967). REE patterns of the eclogitic lenses are similar to those of N- and T-type MORBs (Peucat *et al.*, 1990). Pressure conditions for the eclogites of this formation were calculated at ~23 kbar (Mendia *et al.*, 2001), with no clear evidence for development of UHP metamorphism. However, UHP metamorphism has been described in a similar unit in the French Massif Central (Lardeaux *et al.*, 2001). The objective of this article was the study of the provenance of the para-derived eclogitic gneisses of this formation. Comparison of the source areas of these

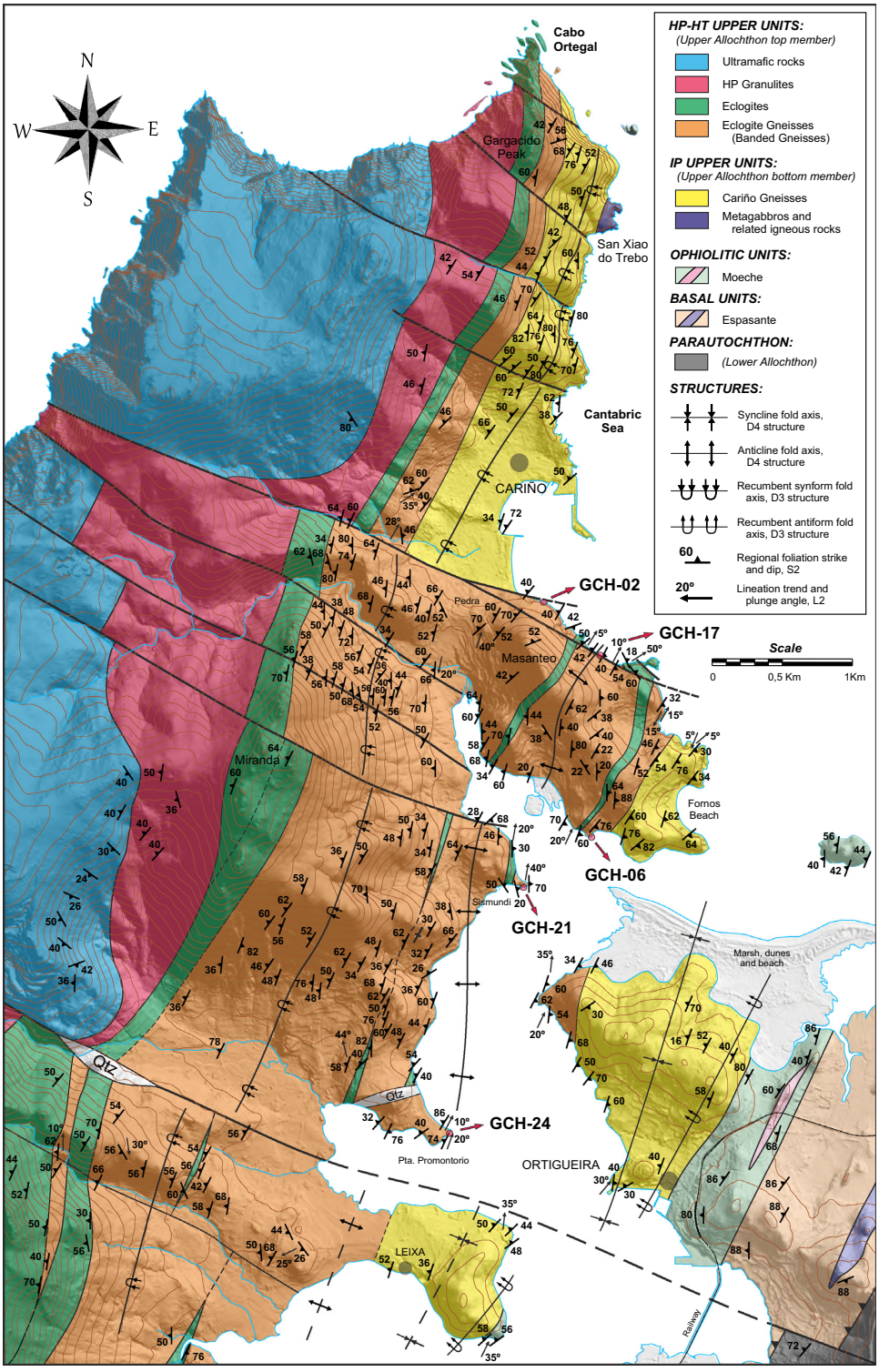

Fig. 2. Geological map of the northern part of the Banded Gneiss formation, with the location of the studied samples.

rocks with those previously obtained for the metasedimentary rock series of the IP upper units is the best method known to find out if the upper units are a single or a composite terrane. Additionally, this comparison should also provide clear information about the Gondwanan or Laurussian provenance of the HP–HT upper units.

SAMPLE DESCRIPTIONS

Five metasedimentary rock samples were chosen from the Banded Gneiss formation, whose location is shown in Fig. 2. Sample GCH–02 (ref. 112974) is from an outcrop south of Cariño beach (43°43′46.1″ N, 7°52′08.5″W). Sample GCH–06 (ref. 112978) is from Figueiroa beach (43°42′39.6″N, 7°51′48.6″W), 10 m east of the Figueiroa beach geological section presented by Albert *et al.* (2012). GCH–17 (ref. 112989) is from the Area da Vaca beach (43°43′31.2″ N, 7°51′44.6″W), at the 270 m point of the Area da Vaca geological section presented by Albert *et al.* (2012). Sample GCH–21 (ref. 113164) is from Sismundi (43°42′25.0″N, 7°52′10.4″W) and sample GCH–24 (ref. 113170) is from Punta Promontorio (43°41′16.3″N, 7°52′39.7″W; in all cases using Simple Cylindrical projection, WGS84 datum; ref: rock collection reference, UCM).

All samples are variably fresh (not altered) fine-grained migmatitic para-gneisses with grano-lepidoblastic texture. To avoid possible problems derived from leucosome generation and the presence of new metamorphic zircon, only the most massive layers, with no evident generation of leucosomatic bands along the foliation, were sampled. They contain a main mineral assemblage formed at the metamorphic peak *P–T* conditions or in the first stages of retrogression, constituted by Qz + Grt + Bt + Pl + Rt ± Ky ± Afs, with Ap + Zrn + Ilm + Py + Gr as accessory phases and Chl + Ms as common retrogressive minerals (mineral abbreviations after Whitney & Evans, 2010).

SAMPLE PREPARATION AND ANALYTICAL PROCEDURES

Zircon sample preparation

Zircon crystals were separated from bulk samples using conventional mineral separation techniques at the Facultad de Ciencias Geológicas, Universidad Complutense de Madrid (UCM). Samples were cleaned and crushed in a jaw crusher and in a tungsten disc mill. The light fraction was removed using a Wilfley table. The magnetic fraction was separated with a hand magnet and with a Franz model magnetic separator to remove those minerals susceptible to a magnetic field induced by an electric current up to 1.7 A. Minerals with a density below 3325 kg m^{-3} were removed using CH_2I_2 (diiodomethane). Zircon hand picking, mounting, imaging and analysis were performed at the Goethe University of Frankfurt am Main (GUF). Hand-picked zircon grains of all sizes and morphologies were mounted in epoxy filled mounts depending on their size and polished to ~50% of their thickness. All grains were documented by back-scattered electron and cathodoluminiscence images using a JSM 6490 scanning electron microscope to study their internal structure to choose the best areas for laser ablation.

U–Pb zircon analyses

Zircon was analysed for U, Th and Pb isotopes at the GUF with a ThermoScientific Element 2 sector field ICP–MS coupled with a RESOlution M–50 (ASI) 193 nm ArF excimer laser system (CompexPro 102, Coherent), using a slightly modified method as described in Gerdes & Zeh (2006, 2009) and Zeh & Gerdes (2012). Laser spot-size was 23–33 μm for unknowns, 15 μm for Plešovice, 33 μm for GJ1 and 91500, and 50 μm for Felix standard zircon. Sample surface was cleaned by four pre-ablation laser pulses. Ablation was performed in a 0.6 l min^{-1} He stream, mixed directly after the ablation cell with 0.07 l min^{-1} N_2 and 0.68 l min^{-1} Ar, prior introduction into the Ar plasma torch. The sensitivity achieved was in the range of 8000–12,000 cps $\mu g\ g^{-1}$ for ^{238}U with a 23 μm spot size, at 5.5 Hz and 4–5 J cm^{-2} using GJ1 zircon. All analyses were common-Pb corrected following the method described in Millonig *et al.* (2012). The ^{204}Hg during the analytical session was ~200 cps. For the analysed sample, the common ^{204}Pb contents were mostly near or below the detection limit, and thus a ^{208}Pb-based common Pb correction has usually been applied. The results are presented in Tables S1–S5. The accuracy of the method was verified by repeated analyses of reference zircon 91500 (Wiedenbeck *et al.*, 1995), Plešovice (Sláma *et al.*, 2008) and in-house standard Felix (Millonig *et al.*, 2012). Data were plotted using Isoplot 3.75 software (Ludwig, 2012).

From the five samples, a total of 729 zircon cores were dated (Tables S1–S5), from which 613 are considered valid analysis (15.9% rejected) in terms of concordance (up to 10% discordance accepted). More than 117 zircon grains were analysed in each sample to achieve statistical adequacy (Vermeesch, 2004). Data have been represented for visualization as Wetherill concordia diagrams for each sample (Fig. 3). Data have also been plotted as adaptive Kernel Density Estimates (aKDEs) and probability density plots (PDPs) in Fig. 4, using DensityPlotter 5.0 software (Vermeesch, 2012). The age assigned to each zircon core was chosen depending on $^{207}Pb/^{206}Pb$ age. If the $^{207}Pb/^{206}Pb$ age was <1 Ga, the $^{206}Pb/^{238}U$ age was chosen, if not $^{207}Pb/^{206}Pb$ age was used. Bar diagrams, are presented in Fig. 5

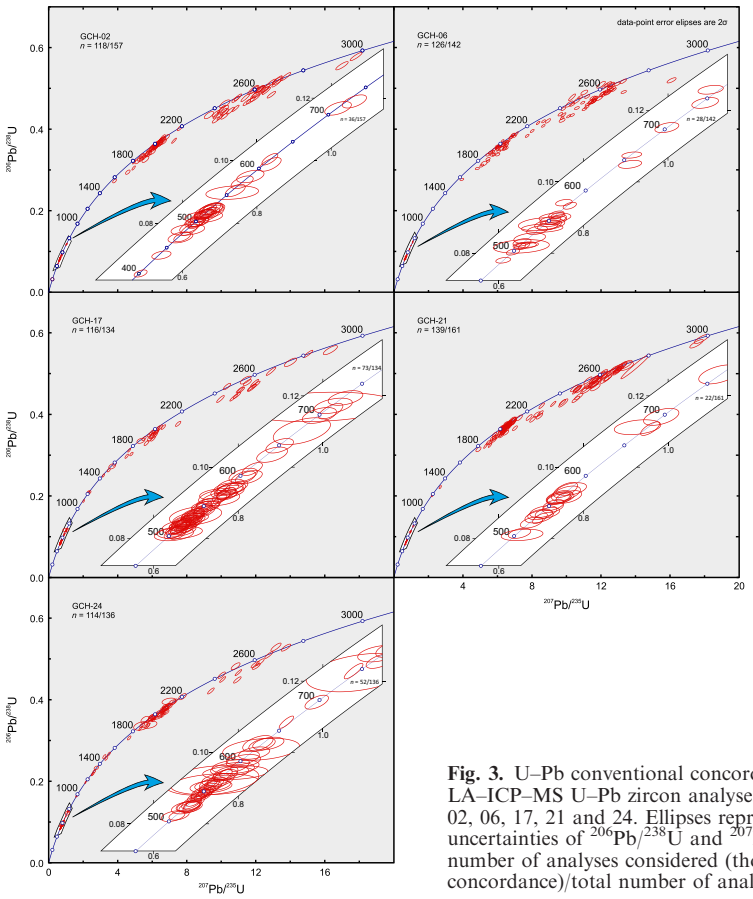

Fig. 3. U–Pb conventional concordia diagrams showing LA–ICP–MS U–Pb zircon analyses from samples GCH–02, 06, 17, 21 and 24. Ellipses represent combined 2σ uncertainties of $^{206}Pb/^{238}U$ and $^{207}Pb/^{235}U$ ratios. *n*, number of analyses considered (those with 90–110% concordance)/total number of analyses.

showing the relative proportions of age populations in each sample and in the combination of all samples. A cumulative density plot is presented in Fig. 6 to represent the relative proportions of zircon populations of each sample of the HP–HT upper allochthon and of the IP Upper Allochthon.

Maximum depositional ages for each sample were calculated following the most conservative method (YC2σ(3 +)) reported by Dickinson & Gehrels (2009), with some modifications. MDAs were calculated as the weighted mean of the youngest group of zircon ages that can be used to calculate a concordia age with Isoplots normal 'ConcAge' tool (i.e. probability of data-point equivalence higher than 0.001). The first (younger) zircon age chosen for the group was the one that had less than 1% age difference with the age of the following zircon. One exception has been made to this rule. In sample GCH-02, one very young age (*c.* 470 Ma) has been ignored (because MDA for this sample was extremely low compared with the rest of the samples), so its MDA changes from 479 ± 11 to 497.4 ± 5.8 Ma.

Lu–Hf zircon analyses

Hafnium isotope measurements (Tables S6–S10) were performed with a ThermoFinnigan. Neptune multi-collector ICP–MS at GUF coupled to the same laser as described in the U–Pb method. Laser spots with diameters mostly of 40 μm were drilled with a repetition rate of 5.5 Hz and an energy density of 6 J cm^{-2} during 55 s of data acquisition. All data were adjusted relative to the JMC475 ratio of $^{176}Hf/^{177}Hf = 0.282160$ and quoted uncertainties are quadratic additions of the within run precision of each analysis and the reproducibility of the JMC475 (2 SD = 0.0033%, $n = 16$). Accuracy and external reproducibility of the method was verified by repeated analysis of reference zircon GJ-1 and Plešovice (Table S11) which are well within the range of solution mode data (Woodhead & Hergt, 2005; Gerdes & Zeh, 2006).

From the zircon cores dated with the U–Pb method, a total of 463 were analysed for Lu–Hf isotopes (Tables S6–S10). Data have been plotted as aKDEs and PDPs in Fig. 7a,b, using Densi-

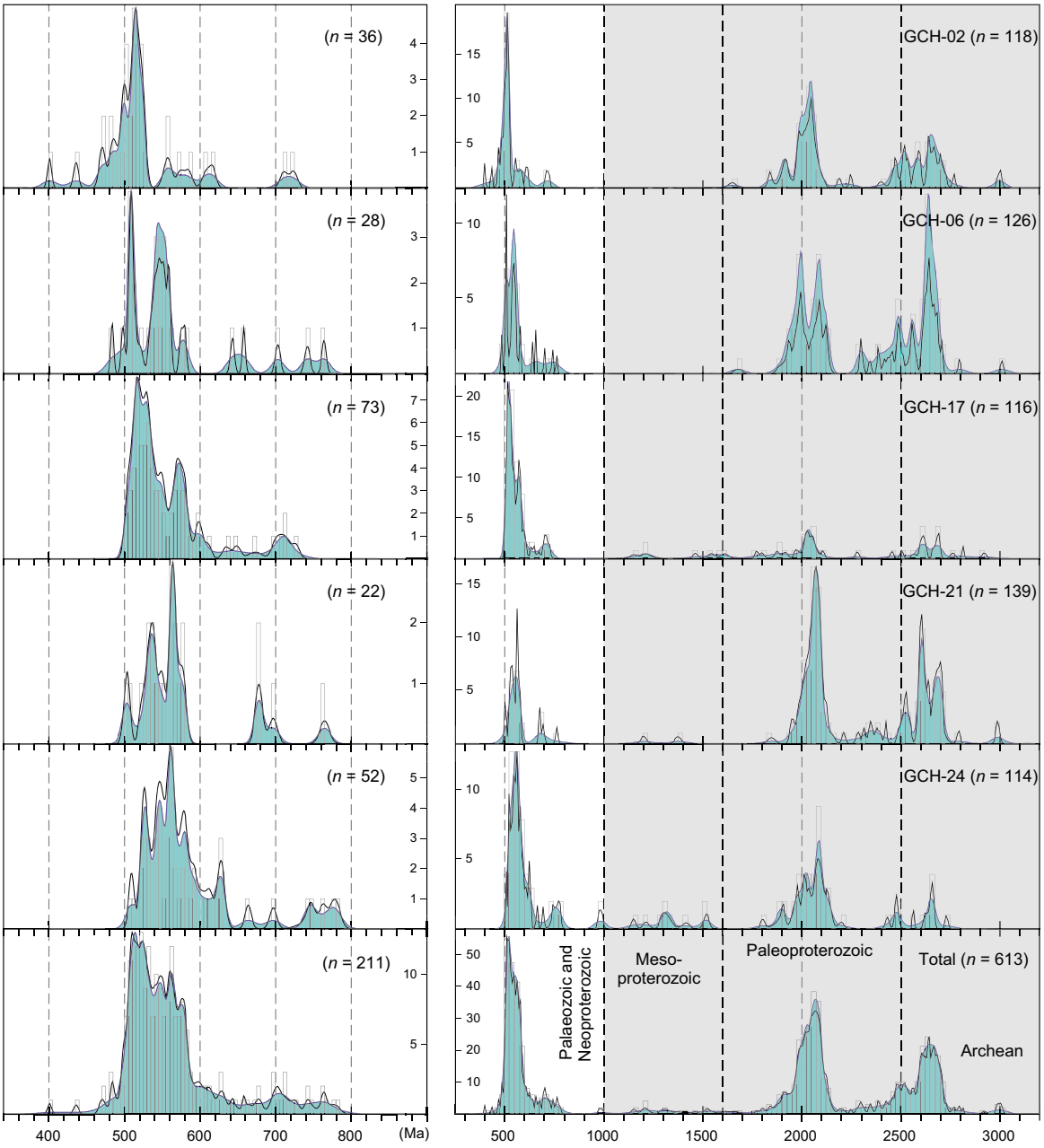

Fig. 4. Adaptive Kernel Density Estimation plots (aKDEs, continuous line enclosing the blue area) and probability density plots (PDPs, dashed line) for all samples and for the combination of all Banded Gneisses zircon studied for U–Pb isotopes. Complete aKDEs (right) were built with bandwidth = 15 Ma and histograms with binwidth = 25 Ma, and partial aKDEs (left, representing a 360–900 Ma time range) with bandwidth = 5 Ma and histograms with binwidth = 5 Ma (DensityPlotter5.0 software; Vermeesch, 2012). Numbers in the vertical axis represent histogram frequency, *n*, number of analyses.

tyPlotter5.0 software (Vermeesch, 2012). To calculate Hf epsilon units (εHf_t), the values chosen for chondritic uniform reservoir (CHUR) are $^{176}Lu/^{177}Hf = 0.0336$ and $^{176}Hf/^{177}Hf = 0.282785$ (Bouvier *et al.*, 2008), and a ^{176}Lu decay constant of 1.867×10^{-11} a^{-1} (average of Scherer *et al.*, 2001 and Söderlund *et al.*, 2004). Initial $^{176}Hf/^{177}Hf_{(t)}$ and $\varepsilon Hf_{(t)}$ for all analysed zircon domains were calculated using the preferred U–Pb ages (Figs 7a,b & 8).

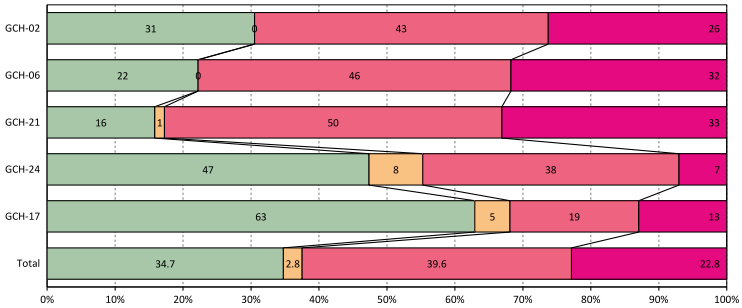

Fig. 5. Relative abundance of Banded Gneisses U–Pb zircon ages for each significant age population represented as bar diagrams, for each sample and for the total U–Pb zircon analyses. Green: Palaeozoic and Neoproterozoic; yellow: Mesoproterozoic; pale pink: Paleoproterozoic; dark pink: Archean population.

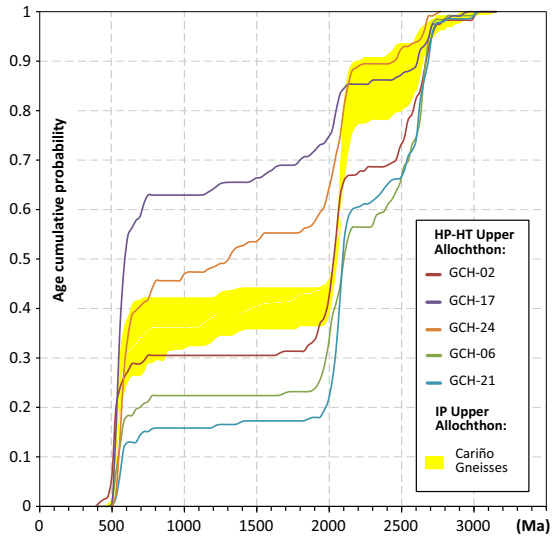

Fig. 6. Cumulative density plots for each of the HP–HT Upper Allochthon samples, and for the IP Upper Allochthon.

Two-stage depleted mantle model ages (T_{DM}) were calculated using present day $^{176}Hf/^{177}Hf = 0.283164$ value for average MORB (Chauvel *et al.*, 2008) which is assumed to be present-day depleted mantle composition. This value corresponds to an initial $\varepsilon Hf_{(t\ =\ 0\ Ga)} = 13.4$. DM evolution trend was propagated to $\varepsilon Hf_{(t\ =\ 4\ Ga)} = 0$, because the existence of a voluminous-depleted mantle reservoir during Hadean is highly speculative (see discussions in Hawkesworth *et al.*, 2010; Kemp *et al.*, 2010 and Zeh *et al.*, 2011). T_{DM} values for all data were calculated using a mean $^{176}Lu/^{177}Hf$ of 0.0113 (average continental crust; Rudnick & Gao, 2003).

MORB $^{176}Hf/^{177}Hf$ interval was taken from the Atlantic, Pacific and Indian MORB values (excepting three unusual low values from the Indian Ocean) reported by Chauvel & Blichert-Toft (2001) considering a minimum $^{176}Hf/^{177}Hf = 0.28302$ ($\varepsilon Hf_{(t\ =\ 0\ Ma)} = 8.3$) and a maximum $^{176}Hf/^{177}Hf = 0.28337$ ($\varepsilon Hf_{(t\ =\ 0\ Ma)} = 20.7$). These values are propagated to $\varepsilon Hf_{(t\ =\ 4\ Ga)} = 0$, defining a field (blue discontinuous lines) around the DM-evolution trend, to provide an indication of the likely range of DM compositions through time.

Sm–Nd whole-rock analyses

Sample preparation and analyses were performed at the laboratory of Geocronología y Geoquímica Isotópica at the UCM. Whole-rock samples were dissolved by oven digestion in ultra-pure HF and HNO_3 acids together with the $^{149}Sm/^{150}Nd$ spike in sealed teflon microreactors. Once the samples were dissolved and dried, HNO_3 was added to eliminate silica fluorides and then HCl was added to form chlorine molecules. The sample was then subjected to a two-stage conventional ion-exchange chromatography. The fractions where Sm and Nd were present in high concentrations were dried and loaded with H_3PO_4 on rhenium filaments in triple disposition, and analysed in a thermal ionization mass spectrometer TIMS-Phoenix HCT040® following a dynamic multicollector method. The measured $^{143}Nd/^{144}Nd$ isotopic ratios were corrected for possible isobaric interferences from ^{142}Ce and ^{144}Sm (only for samples with $^{147}Sm/^{144}Sm$ <0.0001) and normalized to $^{146}Nd/^{144}Nd = 0.7219$ (O'Nions *et al.*, 1977) to correct for mass fractionation. The LaJolla Nd international isotopic standard was analysed during sample measurement, and gave an average value of $^{143}Nd/^{144}Nd = 0.511847$ for nine replicates, with an internal precision of ± 0.000008 (2σ). These values were used to correct the measured ratios for possible instrumental bias following reference values from Lugmair *et al.* (1983). The analytic errors for $^{147}Sm/^{144}Nd$ ratio is 0.1% and for $^{143}Nd/^{144}Nd$ is 0.006%. CHUR present-day values considered for this study are $^{147}Sm/^{144}Nd = 0.1967$ (Jacobsen & Wasserburg, 1980) and $^{143}Nd/^{144}Nd = 0.512638$ (Hamilton *et al.*, 1983). The DM evolution trend and DM model ages (T_{DM}) have been calculated as described by DePaolo (1981) using $^{147}Sm/^{144}Nd$ ratios and MDAs for each sample (Fig. 9). A ^{147}Sm decay constant of 6.539×10^{-11} a^{-1} has been used, calculated from ^{147}Sm half-life reported by Lugmair & Marti (1978) and Begemann *et al.* (2001). MORB epsilon values of +7 to +12 used are those reported by DePaolo & Wasserburg (1976).

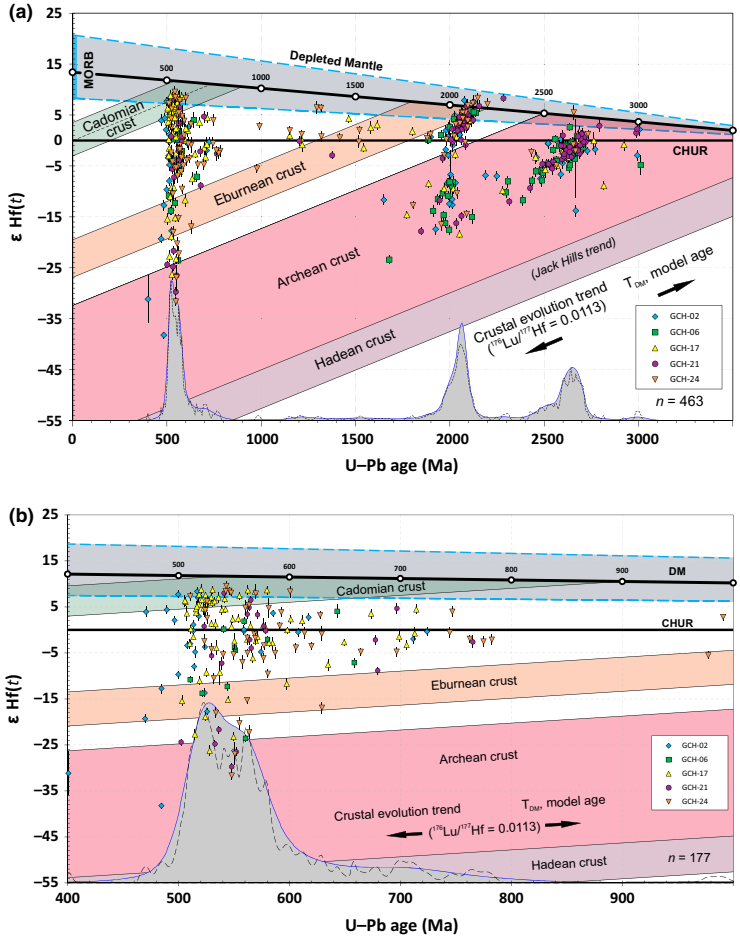

Fig. 7. Hf isotope evolution diagram showing Banded Gneisses combined U–Pb and Lu–Hf zircon data. Error bars are 2σ. Oblique coloured bands represent crustal evolution trends for Hadean, Archean, Eburnean and Cadomian DM derived rocks. Adaptive Kernel Density Estimation of analysed zircon with Lu–Hf systematics is represented in grey (a) Hf isotope evolution diagram of all analysed zircon grains (complete aKDEs were built with bandwidth = 15 Ma and histograms with binwidth = 25 Ma). (b) Hf isotope evolution diagram of analysed zircon grains in the age range of 1000–400 Ma (partial aKDEs were built with bandwidth = 15 Ma and histograms with binwidth = 5 Ma; DensityPlotter5.0 software; Vermeesch, 2012). See text for discussion and for constants and parameters used. CHUR, chondritic uniform reservoir; DM, depleted mantle; MORB, mid ocean ridge basalt.

RESULTS

U–Pb results

U–Pb dating results are given in Tables S1–S5 and represented in Fig. 3. To allow forward comparisons, the age spectrum has been divided into four major groups: Palaeozoic–Neoproterozoic (<1 Ga), Mesoproterozoic (1.6–1 Ga), Paleoproterozoic (2.5–1.6 Ga) and Archean (>2.5 Ga). Descriptions of U–Pb results of each sample are as follows.

From sample GCH–02, 156 analyses were performed, of which 118 were concordant (<10% discordance, d = 24.4%, d: percentage of discordant analyses). Of these, 36 are Palaeozoic–Neoproterozoic (30.5%), 0 are Mesoproterozoic, 51 are Paleoproterozoic (43.2%) and 31 are Archean (26.3%). MDA_{02} (GCH–02 MDA) calculated for this sample, using 11 ages (see above), is 498.4 ± 5.8 Ma.

From sample GCH–06, 142 analyses were performed of which 126 were concordant (<10% discordance, d = 11.3%). Of these, 28 are Palaeozoic–Neoproterozoic (22.2%), 0 are Mesoproterozoic, 58 are Paleoproterozoic (46%) and 40 are Archean (31.7%). MDA_{06} calculated for this sample, using seven ages (see above), is 510.4 ± 3.5 Ma.

From sample GCH–17, 134 analyses were performed, of which 116 were concordant (<10% discordance, d = 13.4%). Of these, 73 are Palaeozoic–Neoproterozoic (62.9%), 6 are Mesoproterozoic (5.2%), 22 are Paleoproterozoic (19%) and 15 are Archean (12.9%). MDA_{17} calculated for this sample, using 24 ages (see above), is 515.4 ± 2.8 Ma.

From sample GCH–21, 161 analyses were performed of which 139 were concordant (<10% discordance, d = 13.7%). Of these, 22 are Palaeozoic–Neoproterozoic (15.8%), 2 are Mesoproterozoic (1.4%), 69 are Paleoproterozoic (49.6%) and 46 are Archean (33.1%). MDA_{21} calculated for this sample, using three ages (see above), is 510 ± 28 Ma.

From sample GCH-24, 136 analyses were performed, of which 114 were concordant (<10% discordance, d = 16.2%). Of these, 54 are Palaeozoic–Neoproterozoic (47.4%), 9 are Mesoproterozoic

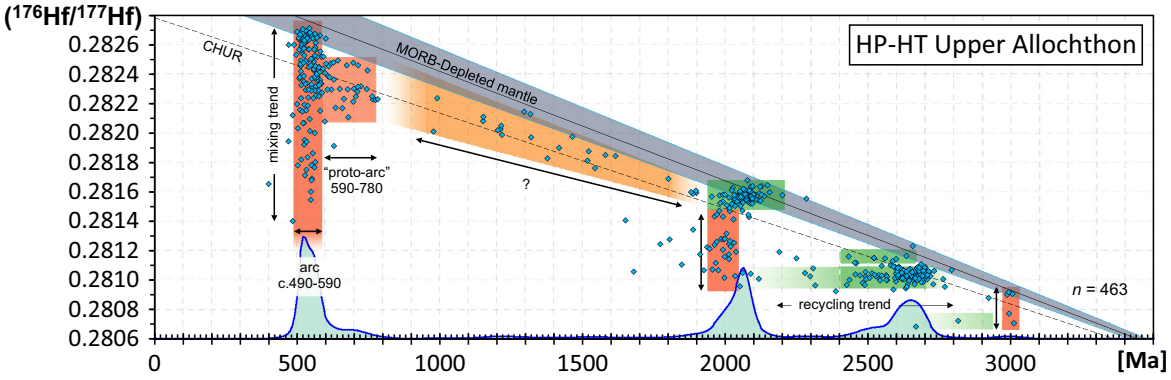

Fig. 8. $^{176}Hf/^{177}Hf$ *v.* age plot for detrital zircon data. Horizontal green shaded areas represent recycling trends with $^{176}Lu/^{177}Hf = 0$. Vertical red shaded areas represent mixing between juvenile and recycled crustal material formed in magmatic arcs. The orange shaded area represents a source that developed through time with a similar $^{176}Lu/^{177}Hf$ ratio as the CHUR and depleted mantle, from which the Mesoproterozoic zircon crystallized.

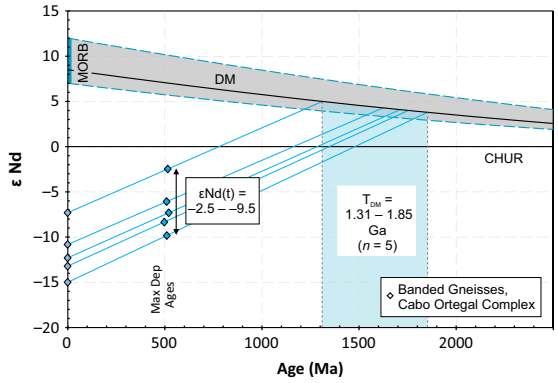

Fig. 9. Sm–Nd isotope evolution diagram showing Banded Gneisses Sm–Nd whole–rock data. Rhombus show εNd values at present day and at maximum depositional ages. See text for discussion and for constants and parameters used. CHUR, chondritic uniform reservoir; DM, depleted mantle; MORB, mid ocean ridge basalt.

(7.9%), 43 are Paleoproterozoic (37.7%) and 8 are Archean (7%). MDA_{24} calculated for this sample, using eight ages (see above), is 520.9 ± 6.7 Ma.

Analyses from all samples are summarized in Figs 5 and 6, and add a total of 729 age determinations, of which 613 were concordant (<10% discordance, d = 15.9%). Of the analyses, 34.7% (n = 213) have a Palaeozoic–Neoproterozoic age with peaks at *c.* 512, 522, 545, 561, 575, maximum abundance at 522–512 Ma, and a tail with minor peaks between 780 and 590 Ma. Mesoproterozoic ages are scattered in the interval age of *c.* 1.6–1.1 Ga and do not define any maximum, comprising 2.8% (n = 17) of the total ages. The main age group is Paleoproterozoic (39.6%, n = 243) and the majority of the ages are constrained between *c.* 21.4 and 1.88 Ga with a well-defined maximum at 2.07 Ga. The Archean population represents 22.8% (n = 140) of the analyses and shows two main groups, one with ages concentrated at 2.52–2.48 Ga (maximum at *c.* 2.51 Ga), and a second group ranging 2.68–2.61 Ga (maximum at 2.64 Ga).

Maximum depositional ages calculated for each of the five samples vary from 521 to 497 Ma. This MDA age spread is relatively high and considering the high deformation attained by these gneisses, an MDA average does not seem to be reliable (MSWD of the average is too high = 8.6). Therefore, the older MDA was chosen (*c.* 521 Ma) to establish the MDA for this formation.

Lu–Hf results

From the 613 concordant zircon cores analysed with the U–Pb method, 463 were analysed for Lu–Hf isotopes (Tables S6–S10). Around 46% of all analyses have positive $\varepsilon Hf_{(t)}$ (Fig. 7a). As these superchondritic zircon data fall in the MORB-depleted mantle field (Fig. 7a), it can be surmised that the zircon crystallized from magmas that were almost directly derived from a depleted mantle source.

Palaeozoic–Neoproterozoic zircon is arranged in the Hf–U–Pb age diagram in two ways (Figs 7a,b & 8). First, as a vertical array of zircon with crystallization ages between *c.* 590 and 490 Ma, with $\varepsilon Hf_{(t)}$ values from +9.5 to −38, and second, with ages of *c.* 780–590 Ma and $\varepsilon Hf_{(t)}$ values from +4 to −10.

A group of zircon values (n = 19), which are mainly Mesoproterozoic (1615–978 Ma), plot around the CHUR evolution trend with $\varepsilon Hf_{(t)}$ from +6.5 to −5.5 (average: +1.2).

Table 1. Whole-rock Sm-Nd isotope data of the Banded Gneiss samples.

Sample	Sm	Nd	$^{147}Sm/^{144}Nd$	$^{143}Nd/^{144}Nd_{(t\ =\ 0)}$	2SE(abs) × 10^{-6}	$\varepsilon Nd_{(t\ =\ 0)}$	$\varepsilon Nd_{(t\ =\ MDA)}$	T_{DM}
GCH-02	4.105	20.736	0.1197	0.511960	2	−13.2	−8.3	1754
GCH-06	4.371	21.356	0.1237	0.512083	2	−10.8	−6.1	1624
GCH-17	4.162	20.429	0.1232	0.512263	2	−7.3	−2.5	1313
GCH-21	3.484	17.993	0.1170	0.511869	1	−15.0	−9.8	1852
GCH-24	1.157	5.756	0.1215	0.512007	2	−12.3	−7.3	1711
Average								1651

Paleoproterozoic 2.14–1.88 Ga zircon population is arranged in two ways. First, as a group with $\varepsilon Hf_{(t)}$ from ~ +8.3 to −3.5 (average: +3.1), composed by 78% (n = 104) of this Paleoproterozoic zircon, and with T_{DM} values, from *c.* 2.56 to 2.02 Ga (average: 2.26 Ga). The older zircon in this group (*c.* 2.1 Ga) has higher $\varepsilon Hf_{(t)}$ values than the younger ones (*c.* 1.9 Ga), showing a steep decrease in their $\varepsilon Hf_{(t)}$ values as the age of the zircon decreases. The other way in which zircon with the same time span (n = 29, 22%) are arranged is with $\varepsilon Hf_{(t)}$ values from −6.7 to −18.4 (average: −12.1), and T_{DM} from 3.44 to 2.76 Ga (average: 3.05 Ga). This group seems to be arranged vertically in the Hf–U–Pb age diagram (Figs 7a & 8).

Paleoproterozoic and Archean zircon (n = 128) has crystallization ages between *c.* 3.01 and 2.19 Ga. Values range from slightly positive $\varepsilon Hf_{(t)}$ up to +5.5 to negative $\varepsilon Hf_{(t)}$ down to −13.8, and have T_{DM} from *c.* 3.69 to 2.62 Ga (average: 3.04 Ga, Fig. 7a). These zircon values are not clustered but arranged in a linear trend, which is lower than the average continental crustal evolution trend of $^{176}Lu/^{177}Hf$ = 0.0113 used to calculate T_{DM} in this study. In fact, this trend corresponds to a $^{176}Lu/^{177}Hf$ = 0, as revealed by the horizontal distribution of this population in the $^{176}Hf/^{177}Hf$ *v.* age plot (Fig. 8). This population can be subdivided – a first group formed by the main Archean U–Pb population (*c.* 2.68–2.61 Ga) with $\varepsilon Hf_{(t)}$ between ~ +5 and −5 and the data following the mentioned linear trend, with decreasing age and $\varepsilon Hf_{(t)}$ values, and a second group formed by zircon with crystallization ages of *c.* 3.0 Ga ($\varepsilon Hf_{(t)}$ from *c.* +2.2 to −4.8) and zircon with T_{DM} of *c.* 3.5 Ga.

Sm–Nd results

Whole-rock Sm–Nd analyses were performed on five Banded Gneisses samples, with results (Table 1) plotted in Fig. 9. Present-day Nd epsilon values ($\varepsilon Nd_{t\ =\ 0\ Ma}$) for four of the samples (not considering GCH-17) vary from −15.0 to −10.8 and εNd for their maximum sedimentation age ($\varepsilon Nd_{t\ =\ MDA}$) varies from −9.8 to −6.1. Their depleted mantle model ages (Nd_{TDM}) range between 1.85 and 1.62 Ga (average of 1.74 Ga). These results are in agreement with previous published data (Nd_{TDM} = 1.70 Ga, Peucat *et al.*, 1990). Sample GCH–17 results are $\varepsilon Nd_{(t\ =\ 0\ Ma)}$ = −7.3, $\varepsilon Nd_{(t\ =\ MDA)}$ = −2.5 and Nd_{TDM} = 1.31 Ga.

DISCUSSION

Provenance of the HP–HT Upper Allochthon

Concordia (Fig. 3) and density plots (PDP–aKDE; Fig. 4) reveal two main age populations, with pronounced age peaks at *c.* 522–512 Ma (Palaeozoic–Neoproterozoic population: 34.7%) and *c.* 2.07 Ga (Paleoproterozoic population: 39.6%; Fig. 5). Archean populations comprise ~22.8% of the total Banded Gneisses zircon, and the Mesoproterozoic population, at only 2.8%, is scarce.

The HP–HT Upper Allochthon zircon detrital signature has been compared in Fig. 10 to cratons and terranes that could potentially be the source areas for the studied meta-sedimentary rocks. Data representative of the Avalonian terranes are those proposed for Ganderia and Avalonia by Willner *et al.* (2013, 2014), and data from the Laurentian craton are from Willner *et al.* (2014). It is noteworthy to highlight the high number of zircon grains with mixing patterns at *c.* 1.5 and 1.0 Ga in these data sets, because they are not present in the HP–HT Upper Allochthon spectrum. Data representative for the West Africa craton are from Abati *et al.* (2012), and show compatible and similar patterns to those shown by the HP–HT Upper Allochthon. Data from a high grade Armorican metasedimentary rock, with a probable WAC provenance (Gerdes & Zeh, 2006), are also plotted for comparison.

The distal (>1 Ga) detrital zircon spectrum

The main Archean U–Pb zircon population (34.7%) in the Banded Gneisses is bracketed at 2.75–2.50 Ga (Fig. 4). The $\varepsilon Hf_{(t)}$ *v.* age pattern for this zircon population (Fig. 7a) is a linear trend that points to an intrusion at *c.* 2.70 Ga ($\varepsilon Hf_{(t)}$ from *c.* +5 to −5) of juvenile magmas (data with T_{DM} of *c.* 3.2–2.8 Ga, maximum at 3.0 Ga) into an older crust triggering limited mixing processes. Its linear evolution from intrusion at *c.* 2.70 to 2.40 Ga could represent a long-lasting continental crust reworking process (and probably other intrusion events at ~2.51 Ga), or Pb-loss processes triggered by high

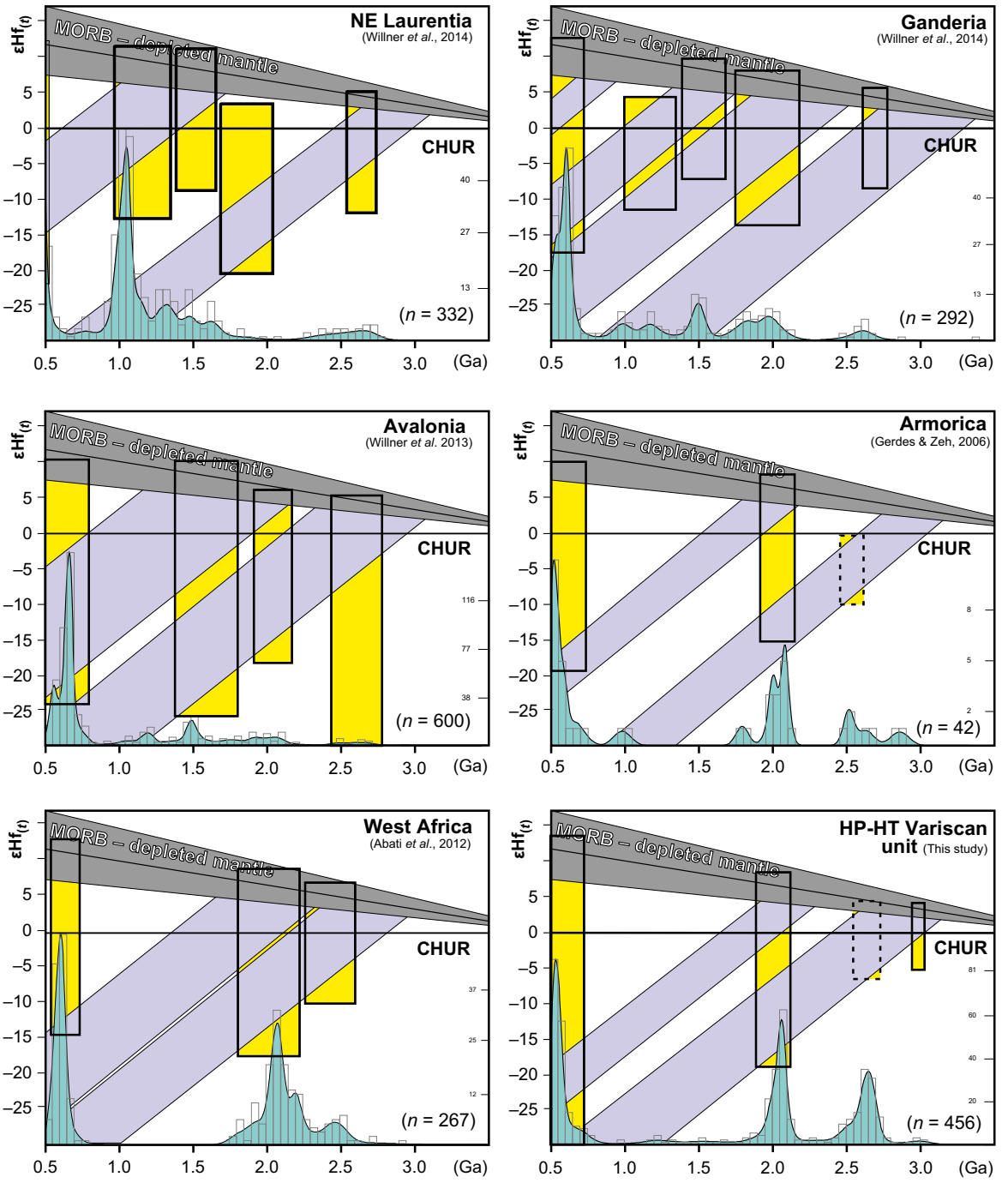

Fig. 10. Schematic $\varepsilon Hf_{(t)}$ *v.* age for detrital zircon from data presented herein and from Gerdes & Zeh (2006), Abati *et al.* (2012) and Willner *et al.* (2013, 2014). Light purple shaded areas represent crustal evolution trends of zircon that might have originated from common crustal domains. Vertical yellow shaded areas represent mixing between juvenile and recycled crustal material, most likely formed in magmatic arcs. Light blue shaded areas at the base of each plot are density distributions of the considered zircon (aKDE, DensityPlotter5.0 software, Vermeesch, 2012). Figure modified from Willner *et al.* (2014).

grade metamorphic events (see the horizontal trend of this population in Fig. 8). There is also a small data set with crystallization ages of *c.* 3.0 Ga ($\varepsilon Hf_{(t)}$ from *c.* +2.2 to −4.8) pointing to a similar geological framework, an intrusion at *c.* 3.0 Ga and a reworking process (data with average T_{DM} of 3.5 Ga). In the Northern WAC, Archean igneous rocks have mainly been reported in the Western Reguibat Rise. The different terranes in this rise contain zircon crystallization ages of *c.* 3.50–3.45, 3.04–2.92, 2.75–2.70 and 2.50–2.46 Ga (Potrel *et al.*, 1996, 1998; Key *et al.*, 2008; Schofield *et al.*, 2012; Bea *et al.*, 2013; Montero *et al.*, 2014). These studies suggest that the Western part of the Reguibat Rise is a viable candidate for the provenance of the Banded Gneisses Archean zircon (despite the *c.* 3.5 Ga population, which is only found in the Banded Gneisses as T_{DM} in some zircon).

The Banded Gneisses Paleoproterozoic fraction makes up 39.6% of the total population (Fig. 5). Maximum abundance clusters at *c.* 2.14–1.88 Ga with a maximum peak at 2.07 Ga (Fig. 4). This Paleoproterozoic population falls within the time span of the Eburnean orogeny (2.2–2.0 Ga according to Egal *et al.*, 2002; or 2.2–1.8 Ga according to Ennih & Liégeois, 2008), so the Paleoproterozoic materials of the Banded Gneisses are possibly derived from rocks generated or reworked during the Eburnean orogeny. Eburnean ages between *c.* 2.1 and 2.04 Ga in igneous and sedimentary rocks have been reported in the Eastern Reguibat Rise (Peucat *et al.*, 2005; Schofield *et al.*, 2006) and in the Anti-Atlas belt (Thomas *et al.*, 2002; Abati *et al.*, 2012; Avigad *et al.*, 2012), supporting a WAC provenance for the Banded Gneisses Paleoproterozoic zircon. The Banded Gneisses Lu–Hf data (Fig. 7a) for zircon of Eburnean age (*c.* 2.20–1.88 Ga, $n = 135$) are arranged as a cluster with positive $\varepsilon Hf_{(t)}$ values ($n = 96/135$) representing juvenile rocks (average T_{DM} of *c.* 2.2 Ga) and few negative $\varepsilon Hf_{(t)}$ values ($n = 39/135$), suggesting a mixing process, i.e. Eburnean DM derived magmas intruding an older crust triggering mixing processes (Fig. 8). As the most negative $\varepsilon Hf_{(t)}$ value for Eburnean zircon is −18, and the Archean linear arrangement intersects at *c.* 2 Ga at $\sim\varepsilon Hf_{(t)} = -17$, this old crust could well be the one represented by the Banded Gneisses Archean zircon. All these observations are in agreement with the geodynamic setting proposed by Egal *et al.* (2002), where the Eburnean is an active margin orogen formed by oceanic subduction along the edge of the pre-existing Archean craton.

In the Mesoproterozoic Era, the WAC became a stable craton (Ennih & Liégeois, 2008) which resulted in a characteristic *c.* 1.7–1.0 Ga 'magmatic gap' (Linnemann *et al.*, 2008 and references therein). Nevertheless, in some peripheral WAC derived samples, Mesoproterozoic zircon is relatively common in Ediacaran–Ordovician (and younger) siliciclastic samples (Anti-Atlas, Avigad *et al.*, 2012; Autochthon, Fernández-Suárez *et al.*, 2013; Parautochthon, Díez Fernández *et al.*, 2012c; Basal allochthonous units, Díez Fernández *et al.*, 2010). In the Banded Gneisses the Mesoproterozoic zircon is scarce and scattered, constituting 2.8% of the total population and not defining a clear maximum (Fig. 4). Taking into account its juvenile character ($\varepsilon Hf_{(t)}$ from +6.5 to −5.5), this population could have been derived from the Amazonia craton or from Mesoproterozoic dykes intruding the WAC. Terranes that clearly derive from the Amazonian craton and have similar Neoproterozoic–Cambrian arc developments as the Upper Allochthon (Avalonia and Ganderia), contain juvenile Mesoproterozoic zircon (Willner *et al.*, 2013, 2014; Fig. 10), but not as juvenile as zircon from this study (Figs 7a & 10). Dolerite dykes have been recently discovered in the Anti-Atlas belt with emplacement ages of *c.* 1.65 Ga (Kouyaté *et al.*, 2013) and *c.* 1.4 Ga (El Bahat *et al.*, 2013; Michard & Gasquet, 2013; Söderlund *et al.*, 2013). The $^{176}Hf/^{177}Hf$ *v.* age plot (Fig. 8) shows that the HP–HT Upper Allochthon Mesoproterozoic population seems to have a source that undertook a similar Lu/Hf isotopic evolution as the CHUR-depleted mantle (with a similar $^{176}Lu/^{177}Hf$ ratio of ~0.033–0.038). These observations seem to favour a WAC juvenile dyke provenance rather than an Amazonian or even a Laurentian source. Therefore, the provenance of the Mesoproterozoic population remains enigmatic (because the observations aforementioned are not conclusive), but it does not seem necessary to assign far exotic provenance sources to explain the presence of this small population in the Upper Allochthon.

The proximal (<1 Ga) detrital zircon spectrum

The Palaeozoic–Neoproterozoic fraction constitutes 34.7% of the Banded Gneisses zircon, most with ages of *c.* 780–490 Ma and with a maximum abundance at *c.* 522–512 Ma. These ages coincide with the reported ages for the Cadomian orogeny (*c.* 750–540 Ma; Linnemann *et al.*, 2014), but the *c.* 522–512 Ma Banded Gneisses maximum is younger, suggesting a different metacratonic WAC activity or, more likely, a late development of the Cadomian orogeny. Palaeozoic–Neoproterozoic populations in the WAC are very common, and range from *c.* 770 to 530 Ma (Anti-Atlas belt, Thomas *et al.*, 2002; Abati *et al.*, 2012; Avigad *et al.*, 2012). The Ganderia and Avalonia terranes are characterized by a *c.* 700–500 Ma development of magmatic arcs that were built on the Amazonian craton sector of the Gondwanan margin (Willner *et al.*, 2013, 2014; Fig. 10). Banded Gneisses zircon with ages between *c.* 780 and 590 Ma are not abundant and fall in the Lu–Hf diagram (Fig. 7a,b) around the CHUR evolution trend ($\varepsilon Hf_{(t)}$ from +4 to

−10), pointing to a crustal recycling due to the initial development of the Cadomian arc system ('proto–arc' stage; Fig. 8). The *c*. 590–490 Ma Banded Gneisses zircon is very abundant and shows a maximum peak at *c*. 522–512 Ma, and other abundant peaks at *c*. 575, 560 and 545 Ma (Fig. 4). The Lu–Hf isotopic pattern (Fig. 7a,b) shows that this Banded Gneisses zircon is arranged vertically, with $\varepsilon Hf_{(t)}$ values up to +9.5 (zircon almost directly derived from a DM source), and $\varepsilon Hf_{(t)}$ values down to −38. These patterns can be explained by the intrusion of juvenile magmas that triggered mixing processes with an Eburnean and Archean crust (and with a small proportion of reworked early Cadomian crustal material), consistent with a peripheral arc activity at the Northern WAC.

According to the data presented here, the MDA for the siliciclastic series of the HP–HT upper units is *c*. 521 Ma. Taking into account crystallization ages of intrusive igneous rocks in this formation (*c*. 506–484 Ma, Albert *et al*., 2013), the protolith of the eclogite facies paragneisses of the Cabo Ortegal Complex was a Middle Cambrian siliciclastic sedimentary series.

As discussed by Cawood *et al*. (2012), convergent margin basins have a high proportion of detrital zircon with ages close to the age of the sediment, where back-arc basins have an increasing input of older detritus from the adjoining mainland. The Banded Gneisses U–Pb age distribution pattern is a strongly bimodal one, where the majority of the Palaeozoic–Neoproterozoic fraction is concentrated near the age of sedimentation (Fig. 4). These observations suggest that the protoliths of the sedimentary rocks involved in the Banded Gneiss formation may have been deposited in a back-arc type basin, where the volcanic arc system was very active, shedding its juvenile materials into the basin at the same time as the adjacent WAC supplied the Eburnean and Archean detritus.

Comparison between the provenance of the IP and the HP–HT upper units of the Cabo Ortegal Complex

When comparisons are made with the unit overlapping the HP–HT Banded Gneisses (the IP Cariño Gneisses, Albert *et al*., 2015) big similarities are observed. Their MDAs are very similar (Cariño Gneisses MDA = 510 Ma, Banded Gneisses MDA = 521 Ma). As no big differences in their youngest U–Pb ages are apparent, it seems reasonable to conclude that both units are temporally related.

Sm–Nd isotopic experiments also reveal the similarity between the gneissic units. The $\varepsilon Nd_{(t)}$ values for the Banded Gneisses (from −6.1 to −9.8, Fig. 9) are in the range of those for the Cariño Gneisses (−7.7 to −10.2, Albert *et al*., 2015), except for sample GCH-17 ($\varepsilon Nd_{(t)} = -2.5$, this study). This higher $\varepsilon Nd_{(t)}$ value is possibly due to the high Palaeozoic–Neoproterozoic juvenile input in the sample. Of the zircon cores analysed with Lu/Hf in this sample, 64% are Palaeozoic–Neoproterozoic ($n = 65/101$) of which 62% are juvenile ($n = 40/65$, $\varepsilon Hf_{(t)} > 0$).

A Kolmogorov–Smirnoff test to evaluate the statistical similarities between age distributions of the samples of the unit studied in the present contribution failed. This does not necessarily imply that the samples do not come from the same detrital sources, but seem to resemble the heterogeneity of the Banded Gneisses in contrast to the homogeneity exhibited by the Cariño Gneisses (see Fig. 6).

The main difference between their U–Pb age density distributions is that the Banded Gneiss formation has an abundant *c*. 590–540 Ma Ediacaran population (Fig. 4) and the Cariño Gneiss formation has not. The Cariño Gneisses were tentatively related to the late or post-activity of the Cadomian Orogen (and in a broader sense to the activity of a Pan-African orogen). The abundance of this Ediacaran population in the Banded Gneisses favours this interpretation. If the magmatic arc, revealed by the isotopic information of the Upper Allochthon detrital units, is the Cadomian magmatic arc (as described by Linnemann *et al*., 2014) the magmatic activity inferred by the Banded Gneisses lasted at least until *c*. 510 Ma in the NW Iberian section of the Gondwana margin, instead of *c*. 540 Ma (as described in the Bohemian Massif, Linnemann *et al*., 2014). This could imply a diachronous scissor-like continental arc generation, due to oblique vector of subduction, that propagated westwards (cf. Linnemann *et al*., 2008). But more likely, it could imply that the *c*. 540–510 Ma arc activity was not registered in the Bohemian Massif sector of the Gondwana margin, because magmatic activity can strongly vary between segments of the same arc system.

Cariño Gneiss and Banded Gneiss formations represent the same section of the Gondwanan margin. Both have the same detrital sources (despite the relative higher abundance of the Banded Gneisses Ediacaran population, see discussion above). Their bimodal detrital populations suggest that both formations had the same geological setting, i.e. sedimentation in a back-arc type basin. Their MDAs and $\varepsilon Nd_{(t)}$ values are very similar (Fig. 9). Banded Gneiss formation was profusely intruded by acid and basic magmas (protolith ages of *c*. 506–484 Ma, see geological context) and Cariño Gneisses were not. All these observations lead one to suppose that they were probably deposited in the same back-arc basin at *c*. 521–506 Ma. The first sediments deposited were those of the Banded Gneiss formation (due to its higher isotopic heterogeneity and higher presence of intruded igneous rocks), formed by the mixture of the old components from the WAC (Eburnean and Archean detritus) and abundant arc related *c*. 590–520 Ma sediments. The Cariño Gneiss protoliths deposited afterwards, filling the same basin with

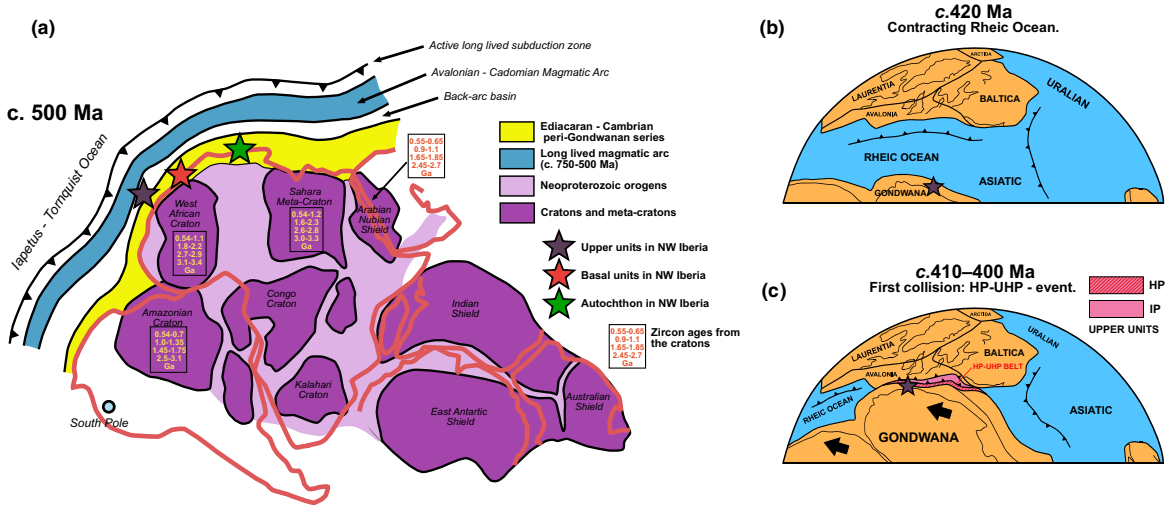

Fig. 11. (a) Sketch showing the proposed paleogeographic position of the upper units (Upper Allochthon) and other terranes from the NW Iberian Massif at *c.* 500 Ma. Simplified paleogeography of Gondwana based on Fernández-Suárez *et al.* (2013). Numbers in squares are zircon ages in Ga from the cratons, from Linnemann *et al.* (2014) and references therein. New zircon ages have been added to the West African Craton (Avigad *et al.*, 2012) and to the Arabian Nubian Shield (Morag *et al.*, 2012). (b & c) Sketch showing the proposed paleogeographic position of the upper units (Upper Allochthon) during the Devonian collision (based on Arenas *et al.*, 2014a).

WAC sediments and *c.* 560–510 Ma arc-derived sediments.

Implications for the Devonian subduction recorded in the Upper Allochthon

The metasedimentary sequences that constitute the gneissic units of the Upper Allochthon, both in the IP upper units (Cariño Gneisses) and in the HP–HT upper units (Banded Gneisses) have the same detrital sources and they seem to have been deposited in a same back-arc basin. Therefore, these units were probably the members of the same sedimentary succession. Between the time of deposition (*c.* 512–506 Ma) and high-grade metamorphism (*c.* 400–390 Ma), both formations constituted a part of the margin of Gondwana. According to the sedimentary and igneous processes recorded in this margin, it changed from a volcanic arc to a passive margin setting at around the Cambrian–Ordovician boundary, after a short event of extension marked by the intrusion of alkaline–peralkaline igneous rocks (Rodríguez Aller, 2005; Abati *et al.*, 2010; Díez Fernández *et al.*, 2012a).

The different metamorphic conditions reached by both units indicate that the HP–HT member of the Upper Allochthon was affected by subduction at *c.* 400–390 Ma. This deep subduction affecting the margin of Gondwana is considered a clear evidence for a first collision between this continent and the southern margin of Laurussia (Arenas *et al.*, 2014a). Different structures and metamorphic recrystallizations related to this collision have also been described in the IP upper units. In this case, the intensity of deformation was much lower and only limited shear zones and amphibolite facies Barrovian metamorphism were generated (Gómez Barreiro *et al.*, 2006; Arenas *et al.*, in press). The differentiated tectonothermal evolution recorded in the Cariño and Banded gneiss formations, could have been favoured by the previous structure of the Gondwana margin, achieved during the Cambrian–Ordovician extension. It has been published (Díez Fernández *et al.*, 2014), that in the Cambrian–Ordovician transition, lithospheric extension induced crustal necking and stretching, compartmenting the Gondwana lithosphere into several continental microblocks. During the Devonian collision the thicker sections of the margin were affected by limited accretion and thickening, developing Barrovian metamorphism. The adjacent thinned sections experienced profound subduction directed to the North, favoured by zones of inherited crustal weakness, developing the HP–HT subduction-related metamorphic conditions of the Banded Gneiss formation and its HP–HT equivalents along the Variscan belt (Fig. 11b,c).

According to previously published structural data of the Banded Gneiss formation, subduction affecting the entire lower section of the Upper Allochthon was probably oblique with a top-to-the-NNE sense of shearing (present day coordinates; Ábalos *et al.*, 2003, 2011). At first, this sense of movement is not

conclusive about the origin of the subducted continental margin, as subduction of either the Gondwanan margin to the North or the Laurussian margin to the South could explain this tectonic evolution. However, the new provenance data presented in this paper is conclusive on the origin of the Banded Gneiss formation, whose eclogite facies evolution can only be explained as generated during subduction of the Gondwana margin directed to the North.

CONCLUSIONS

The sedimentary protoliths of the eclogitic gneisses of the Cabo Ortegal Complex (Banded Gneisses) has a Gondwanan provenance. They were deposited in a sedimentary basin located in the periphery of West Africa. This implies that the margin of Gondwana, which developed a Cambrian–Ediacaran continental–magmatic arc and a subsequent transition to a passive margin, subducted during the Devonian below another continent located to the North, most probably Laurussia. This tectonothermal event represents a first collision related to the final assembly of Pangea, as has been recently proposed (Arenas *et al*., 2014a).

Due to the strong bimodal character of the U–Pb detrital populations and the high amount of ages near to the sedimentation age (Max. Dep. Age = *c*. 521 Ma, Min. Dep. Age = *c*. 506 Ma) the basin where these sediments deposited was probably a back-arc type basin. The Lu–Hf data shows that at this time the Cambrian–Ediacaran population was formed in a continental–magmatic arc and strongly suggests, due to timing and due to its WAC provenance, that the arc system was the Cadomian arc. The igneous activity of the arc lasted at least until Middle Cambrian in the Iberian sector of the Gondwanan margin. Comparing this study with a previous one on the Iberian IP Upper Allochthon (Albert *et al*., 2015), it seems reasonable to propose that the siliciclastic series involved in the HP–HT Upper Allochthon deposited first (due to its isotopic heterogeneity between samples and high amount of basic and acid intrusions). The sedimentary protoliths of the IP Upper Allochthon deposited shortly after than the HP–HT Upper Allochthon (due to its homogeneity and scarce igneous intrusions) in the same basin. The NW Iberian IP Upper Allochthon scarcely registers Ediacaran arc igneous activity, probably because when erosion and sedimentation of the detrital series took place the topographic relief of the Ediacaran part of the arc was dismantled.

Considering the original linear character of the Variscan belt and the presence of a rather continuous equivalent HP–HT unit from the Iberian Massif to the Bohemian Massif, we suggest that the conclusions presented in this article can be extrapolated to the entire Variscan realm.

ACKNOWLEDGMENTS

This work was supported by the Ministerio de Economía y Competividad (Spanish project CGL2012–34618). R. Albert is thankful to the Universidad Complutense de Madrid which provided him with a pre-doctoral grant. The authors are grateful to A.P. Willner and J. Payne who performed insightful reviews of the manuscript and to M. Brown for excellent editing work. The authors are also thankful for the technical and laboratory support provided by J.M. Fuenlabrada and J.A. Hernández Jimenez (TIMS Laboratory, UCM).

REFERENCES

Ábalos, B., Puelles, P. & Gil Ibarguchi, J.I., 2003. Structural assemblage of high-pressure mantle and crustal rocks in a subduction channel (Cabo Ortegal, NW Spain). *Tectonics*, **22,** 21.

Ábalos, B., Fountain, D.M., Gil Ibarguchi, J.I. & Puelles, P., 2011. Eclogite as a seismic marker in subduction channels: seismic velocities, anisotropy, and petrofabric of Cabo Ortegal eclogite tectonites (Spain). *Geological Society of America Bulletin*, **123,** 439–477.

Abati, J., Dunning, G.R., Arenas, R. *et al*., 1999. Early Ordovician orogenic event in Galicia (NW Spain): evidence from U-Pb ages in the uppermost unit of the Ordenes Complex. *Earth and Planetary Science Letters*, **165,** 213–228.

Abati, J., Arenas, R., Martínez Catalán, J.R. & Díaz García, F., 2003. Anticlockwise P-T path of granulites from the Monte Castelo Gabbro (Ordenes Complex, NW Spain). *Journal of Petrology*, **44,** 305–327.

Abati, J., Castiñeiras, P., Arenas, R. *et al*., 2007. Using SHRIMP zircon dating to unravel tectonothermal events in arc environments. The early Palaeozoic arc of NW Iberia revisited. *Terra Nova*, **19,** 432–439.

Abati, J., Gerdes, A., Fernández-Suárez, J. *et al*., 2010. Magmatism and early-Variscan continental subduction in the northern Gondwana margin recorded in zircons from the basal units of Galicia, NW Spain. *Geological Society of America Bulletin*, **122,** 219–235.

Abati, J., Aghzer, A.M., Gerdes, A. & Ennih, N., 2012. Insights on the crustal evolution of the West African Craton from Hf isotopes in detrital zircons from the Anti-Atlas belt. *Precambrian Research*, **212,** 263–274.

Albert, R., Arenas, R., Sánchez Martínez, S. & Gerdes, A., 2012. The eclogite facies gneisses of the Cabo Ortegal Complex (NW Iberian Massif): tectonothermal evolution and exhumation model. *Journal of Iberian Geology*, **38,** 389–406.

Albert, R., Arenas, R., Gerdes, A. & Sánchez Martínez, S., 2013. Refined ages of magmatism and high-P metamorphism in the Eclogite Facies Gneissic Formation of the Cabo Ortegal Complex. Crustal evolution and geodynamic processes in Central Europe. Proceedings of the Joint Conference of the Czech and German geological societies held in Plzen (Pilsen), **82,** 93.

Albert, R., Arenas, R., Gerdes, A. *et al*., 2015 (in press). Provenance of the Variscan Upper Allochthon (Cabo Ortegal Complex, NW Iberian Massif). *Gondwana Research*, doi:10.1016/j.gr.2014.10.016.

Andonaegui, P., del Tánago, J.G., Arenas, R. *et al*., 2002. Tectonic setting of the Monte Castelo gabbro (Ordenes Complex, northwestern Iberian Massif): evidence for an arc-related terrane in the hanging wall to the Variscan suture. In: *Variscan–Appalachian Dynamics: The Building of the Late Paleozoic Basement* (eds Martínez Catalán, J.R., Hatcher,

R.D., Arenas, R. & Díaz García, F.), *Geological Society of America Special Paper*, **364,** 37–56.
Andonaegui, P., Castiñeiras, P., González Cuadra, P. *et al*., 2012. The Corredoiras orthogneiss (NW Iberian Massif): geochemistry and geochronology of the Paleozoic magmatic suite developed in a peri-Gondwanan arc. *Lithos*, **128–131,** 84–99.
Arenas, R., 1988. Evolución petrológica y geoquímica de la unidad alóctona inferior del complejo metamórfico básico–ultrabásico de Cabo Ortegal (Unidad de Moeche) y del Silúrico paraautóctono, Cadena Hercínica Ibérica (NW de España). *Corpus Geologicum Gallaeciae*, **4,** 543.
Arenas, R., Gil Ibarguchi, J.I., González Lodeiro, F. *et al*., 1986. Tectonostratigraphic units in the complexes with mafic and related rocks of the NW of the Iberian Massif. *Hercynica*, **2,** 787–110.
Arenas, R., Rubio Pascual, F.J., Díaz García, F. & Martínez Catalán, J.R., 1995. High-pressure micro-inclusions and development of an inverted metamorphic gradient in the Santiago Schists (Ordenes Complex, NW Iberian Massif, Spain): evidence of subduction and syncollisional decompression. *Journal of Metamorphic Geology*, **13,** 141–164.
Arenas, R., Abati, J., Martínez Catalán, J.R. *et al*., 1997. P-T evolution of eclogites from the Agualada Unit (Ordenes Complex, northwest Iberian Massif, Spain): implications for crustal subduction. *Lithos*, **40,** 221–242.
Arenas, R., Martínez Catalán, J. R., Sánchez Martínez, S. *et al*., 2007. Paleozoic ophiolites in the Variscan suture of Galicia (northwest Spain): distribution, characteristics, and meaning. *4–D Framework of Continental Crust*, **200,** 425–444.
Arenas, R., Díez Fernández, R., Sánchez Martínez, S. *et al*., 2014a. Two-stage collision: exploring the birth of Pangea in the Variscan terranes. *Gondwana Research*, **25,** 756–763.
Arenas, R., Sánchez Martínez, S., Gerdes, A. *et al*., 2014b. Re-interpreting the Devonian ophiolites involved in the Variscan suture: U-Pb and Lu–Hf zircon data of the Moeche Ophiolite (Cabo Ortegal Complex, NW Iberia). *International Journal of Earth Sciences*, **103,** 1385–1402.
Avigad, D., Gerdes, A., Morag, N. & Bechstädt, T., 2012. Coupled U-Pb–Hf of detrital zircons of Cambrian sandstones from Morocco and Sardinia: implications for provenance and Precambrian crustal evolution of North Africa. *Gondwana Research*, **21,** 690–703.
Ballèvre, M., Martínez Catalán, J. R., López-Carmona, A. *et al*., 2014. Correlation of the nappe stack in the Ibero-Armorican arc across the Bay of Biscay: a joint French–Spanish project. *Geological Society (London) Special Publications*, **405,** 77–113.
Bea, F., Montero, P., Haissen, F. & El Archi, A., 2013. 2.46 Ga kalsilite and nepheline syenites from the Awsard pluton, Reguibat rise of the West African Craton, Morocco. Generation of extremely K-rich magmas at the Archean-Proterozoic transition. *Precambrian Research*, **224,** 242–254.
Begemann, F., Ludwig, K.R., Lugmair, G.W. *et al*., 2001. Call for an improved set of decay constants for geochronological use. *Geochimica Et Cosmochimica Acta*, **65,** 111–121.
Bouvier, A., Vervoort, J.D. & Patchett, P.J., 2008. The Lu–Hf and Sm–Nd isotopic composition of CHUR: constraints from unequilibrated chondrites and implications for the bulk composition of terrestrial planets. *Earth and Planetary Science Letters*, **273,** 48–57.
Castiñeiras, P., 2005. Origen y evolución tectonotermal de las unidades de O Pino y Cariño (Complejos Alóctonos de Galicia). *Nova Terra*, **28,** 279.
Cawood, P.A., Hawkesworth, C.J. & Dhuime, B., 2012. Detrital zircon record and tectonic setting. *Geology*, **40,** 875–878.
Chauvel, C. & Blichert-Toft, J., 2001. A hafnium isotope and trace element perspective on melting of the depleted mantle. *Earth and Planetary Science Letters*, **190,** 137–151.
Chauvel, C., Lewin, E., Carpentier, M. *et al*., 2008. Role of recycled oceanic basalt and sediment in generating the Hf–Nd mantle array. *Nature Geoscience*, **1,** 64–67.
DePaolo, D.J., 1981. A neodymium and strontium isotopic study of the mesozoic calc-alkaline granitic batholiths of the Sierra-Nevada and Peninsular ranges, California. *Journal of Geophysical Research*, **86,** 470–488.
DePaolo, D.J. & Wasserburg, G.J., 1976. Inferences about magma sources and mantle structure from variations of $^{143}Nd/^{144}Nd$. *Geophysical Research Letters*, **3,** 743–746.
Díaz García, F., 1990. La geología del sector occidental del Complejo de Órdenes, (Cordillera Hercínica, Noroeste de España). *Nova Terra*, **3,** 290.
Díaz García, F., Arenas, R., Martínez Catalán, J.R. *et al*., 1999. Tectonic evolution of the Careon ophiolite (northwest Spain). A remnant of oceanic lithosphere in the Variscan belt. *Journal of Geology*, **107,** 587–605.
Díaz García, F., Sánchez Martínez, S., Castiñeiras, P. *et al*., 2010. A peri-Gondwanan arc in NW Iberia. II: assessment of the intra-arc tectonothermal evolution through U-Pb SHRIMP dating of mafic dykes. *Gondwana Research*, **17,** 352–362.
Dickinson, W.R. & Gehrels, G.E., 2009. Use of U-Pb ages of detrital zircons to infer maximum depositional ages of strata: a test against a Colorado Plateau Mesozoic database. *Earth and Planetary Science Letters*, **288,** 115–125.
Díez Fernández, R., Martínez Catalán, J.R., Gerdes, A. *et al*., 2010. U-Pb ages of detrital zircons from the Basal allochthonous units of NW Iberia: provenance and paleoposition on the northern margin of Gondwana during the Neoproterozoic and Paleozoic. *Gondwana Research*, **18,** 385–399.
Díez Fernández, R., Martínez Catalán, J.R., Arenas, R. & Abati, J., 2011. Tectonic evolution of a continental subduction–exhumation channel: Variscan structure of the basal allochthonous units in NW Spain. *Tectonics*, **30,** 1–22.
Díez Fernández, R., Castiñeiras, P. & Gómez Barreiro, J., 2012a. Age constraints on Lower Paleozoic convection system: magmatic events in the NW Iberian Gondwana margin. *Gondwana Research*, **21,** 1066–1079.
Díez Fernández, R., Martínez Catalán, J.R., Arenas, R. & Abati, J., 2012b. The onset of the assembly of Pangaea in NW Iberia: constraints on the kinematics of continental subduction. *Gondwana Research*, **22,** 20–25.
Díez Fernández, R., Martínez Catalán, J.R., Arenas, R. *et al*., 2012c. U-Pb detrital zircon analysis of the lower allochthon of NW Iberia: age constraints, provenance and links with the Variscan mobile belt and Gondwanan cratons. *Journal of the Geological Society*, **169,** 655–665.
Díez Fernández, R., Pereira, M.F. & Foster, D.A., 2014. Peralkaline and alkaline magmatism of the Ossa-Morena zone (SW Iberia): age, source, and implications for the Paleozoic evolution of Gondwanan lithosphere. *Lithosphere*, **7,** 73–90.
Egal, E., Thiéblemont, D., Lahondère, D. *et al*., 2002. Late Eburnean granitization and tectonics along the western and northwestern margin of the Archean Kenema-Man domain (Guinea, West African Craton). *Precambrian Research*, **117,** 57–84.
El Bahat, A., Ikenne, M., Söderlund, U. *et al*., 2013. U-Pb baddeleyite ages and geochemistry of dolerite dykes in the Bas Drâa Inlier of the Anti-Atlas of Morocco: newly identified 1380 Ma event in the West African Craton. *Lithos*, **174,** 85–98.
Ennih, N. & Liégeois, J.-P., 2008. The boundaries of the West African craton, with special reference to the basement of the Moroccan metacratonic Anti-Atlas belt. *Geological Society, London, Special Publications*, **297,** 1–17.
Farias, P., Gallastegui, G., González-Lodeiro, F. *et al*., 1987. Aportaciones al conocimiento de la litoestratigrafía y estructura de Galicia Central. *Memórias da Faculdade de Ciências, Universidade do Porto*, **1,** 411–431.
Fernández-Suárez, J., Corfu, F., Arenas, R. *et al*., 2002. U-Pb evidence for a polyorogenic evolution of the HP–HT units

of the NW Iberian Massif. *Contributions to Mineralogy and Petrology*, **143,** 236–253.
Fernández-Suárez, J., Díaz García, F., Jeffries, T.E. *et al*., 2003. Constraints on the provenance of the uppermost allochthonous terrane of the NW Iberian Massif: inferences from detrital zircon U-Pb ages. *Terra Nova*, **15,** 138–144.
Fernández-Suárez, J., Arenas, R., Abati, J. *et al*., 2007. U–Pb chronometry of polymetamorphic high-pressure granulites: an example from the allochthonous terranes of the NW Iberian Variscan belt. In: *4–D Framework of Continental Crust* (eds Hatcher, R.D., Carlson, M.P., McBride, J.H. & Martínez Catalán, J.R.), *Geological Society of America Memoir*, **200,** 469–488.
Fernández-Suárez, J., Gutiérrez-Alonso, G., Pastor-Galán, D. *et al*., 2013. The Ediacaran-Early Cambrian detrital zircon record of NW Iberia: possible sources and paleogeographic constraints. *International Journal of Earth Sciences*, **103,** 1335–1357.
Fuenlabrada, J.M., Arenas, R., Sánchez Martínez, S. *et al*., 2010. A peri-Gondwanan arc in NW Iberia I: isotopic and geochemical constraints on the origin of the arc – a sedimentary approach. *Gondwana Research*, **17,** 338–351.
Gerdes, A. & Zeh, A., 2006. Combined U-Pb and Hf isotope LA–(MC–)ICP–MS analyses of detrital zircons: comparison with SHRIMP and new constraints for the provenance and age of an Annorican metasediment in Central Germany. *Earth and Planetary Science Letters*, **249,** 47–61.
Gerdes, A. & Zeh, A., 2009. Zircon formation versus zircon alteration – new insights from combined U-Pb and Lu–Hf in-situ LA–ICP–MS analyses, and consequences for the interpretation of Archean zircon from the Central Zone of the Limpopo Belt. *Chemical Geology*, **261,** 230–243.
Gil Ibarguchi, J.I., 1995. Petrology of jadeite metagranite and associated orthogneiss from the Malpica–Tuy allochthon (Northwest Spain). *European Journal of Mineralogy*, **7,** 403–416.
Gil Ibarguchi, J.I. & Ortega Gironés, E., 1985. Petrology, structure and geotectonic implications of glaucophane-bearing eclogites and related rocks from the Malpica-Tuy (MT) Unit, Galicia, northwest Spain. *Chemical Geology*, **50,** 145–162.
Gil Ibarguchi, J.I., Mendia, M., Girardeau, J. & Peucat, J.J., 1990. Petrology of eclogites and clinopyroxene–garnet metabasites from the Cabo Ortegal Complex (northwestern Spain). *Lithos*, **25,** 133–162.
Gil Ibarguchi, J.I., Ábalos, B., Azcarraga, J. & Puelles, P., 1999. Deformation, high-pressure metamorphism and exhumation of ultramafic rocks in a deep subduction/collision setting (Cabo Ortegal, NW Spain). *Journal of Metamorphic Geology*, **17,** 747–764.
Gómez Barreiro, J., Wijbrans, J.R., Castiñeiras, P. *et al*., 2006. Ar-40/Ar-39 laserprobe dating of mylonitic fabrics in a polyorogenic terrane of NW Iberia. *Journal of the Geological Society*, **163,** 61–73.
González Cuadra, P., 2007. La Unidad de Corredoiras (Complejo de Órdenes, Galicia): evolución estructural y metamórfica. *Nova Terra*, **33,** 254.
Hamilton, P.J., O'Nions, R.K., Bridgwater, D. & Nutman, A., 1983. Sm–Nd studies of Archaean metasediments and metavolcanics from West Greenland and their implications for the Earth's early history. *Earth and Planetary Science Letters*, **62,** 263–272.
Hawkesworth, C.J., Dhuime, B., Pietranik, A.B. *et al*., 2010. The generation and evolution of the continental crust. *Journal of the Geological Society*, **167,** 229–248.
Jacobsen, S.B. & Wasserburg, G.J., 1980. Sm–Nd isotopic evolution of chondrites. *Earth and Planetary Science Letters*, **50,** 139–155.
Julivert, M., Fontboté, J.M., Ribeiro, A. & Conde, L., 1972. Mapa Tectónico de la Península Ibérica y Baleares E. 1: 1 000 000. Instituto Geológico y Minero de España.
Kemp, A.I.S., Wilde, S.A., Hawkesworth, C.J. *et al*., 2010. Hadean crustal evolution revisited: new constraints from Pb–Hf isotope systematics of the Jack Hills zircons. *Earth and Planetary Science Letters*, **296,** 45–56.
Key, R.M., Loughlin, S.C., Gillespie, M. *et al*., 2008. Two Mesoarchaean terranes in the Reguibat shield of NW Mauritania. *Geological Society, London, Special Publications*, **297,** 33–52.
Kouyaté, D., Söderlund, U., Youbi, N. *et al*., 2013. U-Pb baddeleyite and zircon ages of 2040 Ma, 1650 Ma and 885 Ma on dolerites in the West African Craton (Anti-Atlas inliers): possible links to break-up of Precambrian supercontinents. *Lithos*, **174,** 71–84.
Lardeaux, J.M., Ledru, P., Daniel, I. & Duchene, S., 2001. The Variscan French Massif Central-a new addition to the ultra-high pressure metamorphic 'club': exhumation processes and geodynamic consequences. *Tectonophysics*, **332,** 143–167.
Linnemann, U., Pereira, F., Jeffries, T.E. *et al*., 2008. The Cadomian Orogeny and the opening of the Rheic Ocean: the diacrony of geotectonic processes constrained by LA–ICP–MS U-Pb zircon dating (Ossa–Morena and Saxo-Thuringian Zones, Iberian and Bohemian Massifs). *Tectonophysics*, **461,** 21–43.
Linnemann, U., Gerdes, A., Hofmann, M. & Marko, L., 2014. The Cadomian Orogen: Neoproterozoic to Early Cambrian crustal growth and orogenic zoning along the periphery of the West African Craton—Constraints from U-Pb zircon ages and Hf isotopes (Schwarzburg Antiform, Germany). *Precambrian Research*, **244,** 236–278.
López-Carmona, A., Pitra, P. & Abati, J., 2013. Blueschist–facies metapelites from the MalpicaTui Unit (NW Iberian Massif): phase equilibria modelling and H_2O and Fe_2O_3 influence in high-pressure assemblages. *Journal of Metamorphic Geology*, **31,** 263–280.
López-Carmona, A., Abati, J., Pitra, P. & Lee, J.K.W., 2014. Retrogressed lawsonite blueschists from the NW Iberian Massif: P–T–t constraints from thermodynamic modelling and Ar-40/Ar-39 geochronology. *Contributions to Mineralogy and Petrology*, **167,** 1–20.
Lotze, F., 1945. Zur Gliederung der Varisziden der Iberischen Meseta. *Geotektonische Forschungen*, **6,** 78–92.
Lotze, F., 1950. Observaciones Respecto a la División de los Varíscides de la Meseta Ibérica. (Spanish translation by Ríos. J.M.). *Publicaciones Extranjeras Sobre Geología de España*, **5,** 149–166.
Ludwig, K.R., 2012. User's Manual for Isoplot 3.75. A Geochonological Toolkit for Microsoft Excel. *Berkeley Geochronology Center, Special Publication*, **5,** 75.
Lugmair, G.W. & Marti, K., 1978. Lunar initial $^{143}Nd/^{144}Nd$: differential evolution of the lunar crust and mantle. *Earth and Planetary Science Letters*, **39,** 349–357.
Lugmair, G.W., Shimamura, T., Lewis, R.S. & Anders, E., 1983. Sm–146 in the early solar-system – evidence from neodymium in the Allende meteorite. *Science*, **222,** 1015–1018.
Marcos, A., Marquínez, J., Pérez-Estaún, A. *et al*., 1984. Nuevas aportaciones al conocimiento de la evolución tectonometamórfica del Complejo de Cabo Ortegal (NW de España). *Cadernos Laboratorio Xeolóxico de Laxe*, **7,** 125–137.
Martínez Catalán, J.R., 2011. Are the oroclines of the Variscan belt related to late Variscan strike-slip tectonics? *Terra Nova*, **23,** 241–247.
Martínez Catalán, J.R., Arenas, R., Díaz García, F. *et al*., 1996. Variscan exhumation of a subducted paleozoic continental margin: the basal units of the Ordenes Complex, Galicia, NW Spain. *Tectonics*, **15,** 106–121.
Martínez Catalán, J.R., Arenas, R., Abati, J. *et al*., 2009. A rootless suture and the loss of the roots of a mountain chain: the Variscan belt of NW Iberia. *Comptes Rendus Geoscience*, **341,** 114–126.

Matte, P., 1991. Accretionary history and crustal evolution of the Variscan belt in Western Europe. *Tectonophysics*, **196,** 309–337.

Matte, P., 2001. The Variscan collage and orogeny (480–290 Ma) and the tectonic definition of the Armorica microplate: a review. *Terra Nova*, **13,** 122–128.

Mendia, M., Gil Ibarguchi, J.I. & Ábalos, B., 2001. Metamorfic evolution P–T–d–t and geodynamic meaning of the eclogitic unit of the Cabo Ortegal complex (NW of Spain). *Cadernos Laboratorio Xeolóxico de Laxe*, **26,** 155–178.

Michard, A. & Gasquet, D., 2013. Comment on "U–Pb baddeleyite ages and geochemistry of dolerite dykes in the Bas Drâa Inlier of the Anti-Atlas of Morocco: newly identified 1380 Ma event in the West African Craton" by El Bahat *et al. Lithos*, **174,** 99–100.

Millonig, L.J., Gerdes, A. & Groat, L.A., 2012. U-Th–Pb geochronology of meta-carbonatites and meta-alkaline rocks in the southern Canadian Cordillera: a geodynamic perspective. *Lithos*, **152,** 202–217.

Montero, P., Haissen, F., El Archi, A. *et al*., 2014. Timing of Archean crust formation and cratonization in the Awsard-Tichla zone of the NW Reguibat Rise, West African Craton: a SHRIMP, Nd–Sr isotopes, and geochemical reconnaissance study. *Precambrian Research*, **242,** 112–137.

Morag, N., Avigad, D., Gerdes, A. & Harlavan, Y., 2012. 1000–580 Ma crustal evolution in the northern Arabian-Nubian Shield revealed by U-Pb–Hf of detrital zircons from late Neoproterozoic sediments (Elat area, Israel). *Precambrian Research*, **208–211,** 197–212.

Murphy, J.B. & Nance, R.D., 2008. The Pangea conundrum. *Geology*, **36,** 703–706.

Murphy, J.B., Gutiérrez-Alonso, G., Nance, R.D. *et al*., 2006. Origin of the Rheic Ocean: rifting along a Neoproterozoic suture? *Geology*, **34,** 325–328.

Nance, R.D., Gutiérrez-Alonso, G., Keppie, J.D. *et al*., 2010. Evolution of the Rheic Ocean. *Gondwana Research*, **17,** 194–222.

O'Nions, R.K., Hamilton, P.J. & Evensen, N.M., 1977. Variations in $^{143}Nd/^{144}Nd$ and $^{87}Sr/^{86}Sr$ in oceanic basalts. *Earth and Planetary Science Letters*, **34,** 13–22.

Ordóñez Casado, B., Gebauer, D., Schäfer, H.J. *et al*., 2001. A single Devonian subduction event for the HP/HT metamorphism of the Cabo Ortegal complex within the Iberian Massif. *Tectonophysics*, **332,** 359–385.

Peucat, J.J., Bernard-Griffiths, J., Gil Ibarguchi, J.I. *et al*., 1990. Geochemical and geochronological cross section of the deep Variscan crust: the Cabo Ortegal high-pressure nappe (northwestern Spain). *Tectonophysics*, **177,** 263–292.

Peucat, J.J., Capdevila, R., Drareni, A. *et al*., 2005. The Eglab massif in the West African Craton (Algeria), an original segment of the Eburnean orogenic belt: petrology, geochemistry and geochronology. *Precambrian Research*, **136,** 309–352.

Potrel, A., Peucat, J.J., Fanning, C.M. *et al*., 1996. 3.5 Ga old terranes in the West African Craton, Mauritania. *Journal of the Geological Society*, **153,** 507–510.

Potrel, A., Peucat, J.J. & Fanning, C.M., 1998. Archean crustal evolution of the West African Craton: example of the Amsaga Area (Reguibat Rise). U-Pb and Sm–Nd evidence for crustal growth and recycling. *Precambrian Research*, **90,** 107–117.

Rodríguez Aller, J., 2005. Recristalización y deformación de litologías supracorticales sometidas a metamorfismo de alta presión (Complejo de Malpica – Tuy, NO del Macizo Ibérico). *Nova Terra*, **29,** 572.

Rodríguez, J., Cosca, M.A., Gil Ibarguchi, J.I. & Dallmeyer, R.D., 2003. Strain partitioning and preservation of $^{40}Ar/^{39}Ar$ ages during Variscan exhumation of a subducted crust (Malpica–Tui complex, NW Spain). *Lithos*, **70,** 111–139.

Rudnick, R.L. & Gao, S., 2003. Chapter 3.01 – composition of the continental crust. In: *Treatise on Geochemistry* (eds Holland, H.D. & Turekian, K.K.), pp. 1–64. Pergamon, Oxford.

Sánchez Martínez, S., Arenas, R., Díaz García, F. *et al*., 2007. Careon ophiolite, NW Spain: suprasubduction zone setting for the youngest Rheic Ocean floor. *Geology*, **35,** 53–56.

Sánchez Martínez, S., Arenas, R., Gerdes, A. *et al*., 2011. Isotope geochemistry and revised geochronology of the Purrido Ophiolite (Cabo Ortegal Complex, NW Iberian Massif): Devonian magmatism with mixed sources and involved Mesoproterozoic basement. *Journal of the Geological Society*, **168,** 733–750.

Sánchez Martínez, S., Gerdes, A., Arenas, R. & Abati, J., 2012. The Bazar Ophiolite of NW Iberia: a relic of the Iapetus-Tornquist Ocean in the Variscan suture. *Terra Nova*, **24,** 283–294.

Scherer, E., Münker, C. & Mezger, K., 2001. Calibration of the lutetium–hafnium clock. *Science*, **293,** 683–687.

Schofield, D.I., Horstwood, M.S.A., Pitfield, P.E.J. *et al*., 2006. Timing and kinematics of Eburnean tectonics in the central Reguibat Shield, Mauritania. *Journal of the Geological Society*, **163,** 549–560.

Schofield, D.I., Horstwood, M.S.A., Pitfield, P.E.J. *et al*., 2012. U-Pb dating and Sm–Nd isotopic analysis of granitic rocks from the Tiris Complex: new constraints on key events in the evolution of the Reguibat Shield, Mauritania. *Precambrian Research*, **204–205,** 1–11.

Sláma, J., Košler, J., Condon, D.J. *et al*., 2008. Plešovice zircon – a new natural reference material for U-Pb and Hf isotopic microanalysis. *Chemical Geology*, **249,** 1–35.

Söderlund, U., Patchett, J.P., Vervoort, J.D. *et al*., 2004. The Lu–176 decay constant determined by Lu–Hf and U-Pb isotope systematics of Precambrian mafic intrusions. *Earth and Planetary Science Letters*, **219,** 311–324.

Söderlund, U., Ibanez-Mejia, M., El Bahat, A. *et al*., 2013. Reply to Comment on "U–Pb baddeleyite ages and geochemistry of dolerite dykes in the Bas-Drâa inlier of the Anti-Atlas of Morocco: newly identified 1380 Ma event in the West African Craton" by André Michard and Dominique Gasquet. *Lithos*, **174,** 101–108.

Stampfli, G.M. & Borel, G.D., 2002. A plate tectonic model for the Paleozoic and Mesozoic constrained by dynamic plate boundaries and restored synthetic oceanic isochrons. *Earth and Planetary Science Letters*, **196,** 17–33.

Thomas, R.J., Chevallier, L.P., Gresse, P.G. *et al*., 2002. Precambrian evolution of the Sirwa Window, Anti-Atlas Orogen, Morocco. *Precambrian Research*, **118,** 1–57.

Vermeesch, P., 2004. How many grains are needed for a provenance study? *Earth and Planetary Science Letters*, **224,** 441–451.

Vermeesch, P., 2012. On the visualisation of detrital age distributions. *Chemical Geology*, **312,** 190–194.

Vogel, D.E., 1967. Petrology of an eclogite- and pyrigarnite-bearing polymetamorphic rock complex at Cabo Ortegal, NW Spain. *Leidse Geologische Mededelingen*, **40,** 121–213.

Weil, A.B., Gutiérrez-Alonso, G., Johnston, S.T. & Pastor-Galán, D., 2013. Kinematic constraints on buckling a lithospheric-scale orocline along the northern margin of Gondwana: a geologic synthesis. *Tectonophysics*, **582,** 25–49.

Whitney, D.L. & Evans, B.W., 2010. Abbreviations for names of rock-forming minerals. *American Mineralogist*, **95,** 185–187.

Wiedenbeck, M., Allé, P., Corfu, F. *et al*., 1995. 3 natural zircon standards for U-Th–Pb, Lu–Hf, trace-element and REE analyses. *Geostandards Newsletter*, **19,** 1–23.

Willner, A.P., Barr, S.M., Gerdes, A. *et al*., 2013. Origin and evolution of Avalonia: evidence from U-Pb and Lu–Hf isotopes in zircon from the Mira terrane, Canada, and the Stavelot-Venn Massif, Belgium. *Journal of the Geological Society*, **170,** 769–784.

Willner, A.P., Gerdes, A., Massonne, H.J. *et al*., 2014. Crustal evolution of the Northeast Laurentian Margin and the Peri-Gondwanan microcontinent Ganderia prior to and during

closure of the Iapetus Ocean: detrital Zircon U-Pb and Hf isotope evidence from Newfoundland. *Geoscience Canada*, **41,** 345–364.

Winchester, J.A., Pharaoh, T.C. & Verniers, J., 2002. Palaeozoic amalgamation of Central Europe: an introduction and synthesis of new results from recent geological and geophysical investigations. In: *Palaeozoic Amalgamation of Central Europe* (eds Winchester, J.A., Pharaoh, T.C. & Verniers, J.), **201,** 1–18.

Woodhead, J.D. & Hergt, J.M., 2005. A preliminary appraisal of seven natural zircon reference materials for in situ Hf isotope determination. *Geostandards and Geoanalytical Research*, **29,** 183–195.

Zeh, A. & Gerdes, A., 2012. U-Pb and Hf isotope record of detrital zircons from gold-bearing sediments of the Pietersburg Greenstone Belt (South Africa) – is there a common provenance with the Witwatersrand Basin? *Precambrian Research*, **204,** 46–56.

Zeh, A., Gerdes, A. & Millonig, L., 2011. Hafnium isotope record of the Ancient Gneiss Complex, Swaziland, southern Africa: evidence for Archaean crust–mantle formation and crust reworking between 3.66 and 2.73 Ga. *Journal of the Geological Society*, **168,** 953–963.

SUPPORTING INFORMATION

Additional Supporting Information may be found in the online version of this article at the publisher's web site:

Tables S1–S5. U, Th and Pb LA–ICP–MS data of zircon cores.

Tables S6–S10. Lu, Yb and Hf LA–ICP–MS data of zircon cores.

Table S11. Lu, Yb and Hf LA–ICP–MS data of standards.

Received 5 May 2015; revision accepted 11 August 2015.

VII

Migmatization, eclogitization and magmatism

7.1. Introduction

This chapter deals with the rocks with igneous protoliths from the Banded Gneiss and the Eclogite Band formations (HP–HT Upper Allochthon) of the Cabo Ortegal Complex (NW Iberia). These results will be published in several articles after defending the present PhD thesis.

When the provenance of the Upper Allochthon was investigated through the analysis of detrital zircon from the metasedimentary rocks of the Banded Gneiss (HP–HT; chapter 6) and Cariño Gneiss (IP; chapter 5) formations, it was made evident that a magmatic arc was active at the margin of the Gondwana supercontinent in the Neoproterozoic–Cambrian, from at least *c.* 780 to *c.* 490 Ma. Furthermore, as the HP–HT metasedimentary rocks (Banded Gneisses) have a Gondwanan provenance, it was concluded that the metamorphic event that gave the HP–HT characteristics to the bottom member of the Upper Allochthon was driven by a subduction event, where the margin of Gondwana subducted under the northern continent, most probably Laurrusia.

This chapter aims to assess the conditions of the magmatic arc´s igneous activity, the HP–HT metamorphic event and the generalised

partial melting undergone by the HP–HT Upper Allochthon. To do so an investigation was carried out studying zircon from several orthogneisses, eclogites and leucosomes from the Eclogite Band and Banded Gneiss formations from the HP–HT Upper Allochthon of the Cabo Ortegal Complex (NW Iberia).

7.2. Leucosomes

Concerning the Upper Allochthon HP–HT metamorphic event, the initial hypothesis is that this event took place at *c.* 400–390 Ma. But from the five meta-sedimentary rocks analysed (chapter 6) no Devonian zircon recrystallisation or new zircon formation was found (with the exception of sample GCH-02 where one analysis gave a Devonian age). Taking into account that the meta-sedimentary rock zircon grains have very small rims (making them very difficult to analyse with the LA–ICP–MS actual spatial resolution) and that only the zircon cores were analysed (because those experiments aimed for provenance information) the HP–HT Devonian event cannot be discarded. To advance in what we know about this eclogitic event, or about the expected post-eclogitic migmatization event, and also about the age of the regional foliation development, three leucosomes were analysed from the Banded Gneisses meta-sedimentary rocks, the eclogitic metasedimentary unit of the Cabo Ortegal Upper Allochthon.

There are no previous studies concerning the Banded Gneisses leucosomes, but a Ms concentrate from the metasedimentary rocks was analysed with the $^{40}Ar/^{39}Ar$ method. This experiment, published by Peucat *et al.* (1990) gave an age of 375.9 ± 1.4 Ma, and most probably dates the last stages of regional foliation development of the Banded Gneiss formation.

The abundance of leucosomes in the Banded Gneisses metasedimentary rocks shows that this formation underwent abundant partial anatexis. This abundant leucosomatic production could be a response to temperature input due to the igneous activity of the Neoproterozoic–Cambrian magmatic arc system, or to the temperature input during the HP–HT Devonian metamorphic event, or to a post-eclogitic isothermal decompression during the exhumation of the Banded Gneisses (and most probably of the entire HP–HT Upper Allochthon). These leucosomes are displayed as small pods within the gneisses, called "*augen*" gneisses by Vogel (1967), or as thin more or less continuous veins within the gneisses, giving its planar or plano-linear character. The abundance of leucosomes is a characteristic feature of these gneisses and is the reason why this formation is called the Banded Gneisses.

7.2.1. Sample GCH-25
(Sismundi leucosome)

This sample was collected from *Sismundi* (43°42'25.52"N, 7°52'14.66"W; Simple Cylindrical projection, WGS84 datum; Appx. 1).

This sample is interpreted from field observations as a leucosome, formed by partial melting of the metasedimentary rocks (Fig. 1). This lithology is displayed as centimetre sized leucocratic bands, folded and coherent with the metasedimentary rocks regional foliation (Ref: 114088; Ref: rock collection reference, UCM).

From microscopic observations this sample has Qz and Afs as major constituents (Fig. 2). Both minerals are poikilitic and feldspar is usually altered and shows pertitic exsolutions. Qz contains minor inclusions of Bt, Ap, Zrn and Spn, and Afs contains Grt, Qz, Bt, Ap and Zrn. Minor constituents are Grt, Ap, Bt, Chl, Amp (scarce), Spn and Zrn. Grt is small, idioblastic, has a small amount of inclusions (probably Rt, Ap and Zrn) and it is not surrounded by Bt or other minerals (except feldspar). These observations clearly suggest that Grt grew in this leucosome instead of being a relict mineral mechanically extracted from the metasedimentary rock (mineral abbreviations after Whitney & Evans, 2010).

7.2.1.1. Results

From sample GCH-25, 54 U–Pb analyses were performed of which 35 were concordant (d = 35.2%; d, percentage of discordant analyses; Figs. 3 & 4a,b). Domain II is defined by 26 Devonian analyses constrained between 377 and 403 Ma, and show a well-defined maximum abundance at 387 Ma (all zircon analyses from this population are concordant). Domain I is defined by 7 Cambrian analyses, that show badly defined relative abundance peaks at 496, 490 and 480 Ma (only 7 out of 21 zircon grains from this population were concordant). One analysis is Paleoproterozoic and one is Archean (considered inheritances; only two out of seven zircon grains from this inherited population were concordant; Fig. 4b).

Most of the domain I zircon (Cambrian) show more or less well defined oscillatory zonings. They are normally surrounded by lobulated sinuous rims, which are dark in CL images and bright in BSE images. Domain II (Devonian) zircon is displayed as rims surrounding domain I zircon. They show well defined combined oscillatory and multi-faceted ("soccerball") textures. These rims are the outer features observed and define the crystals exterior habit, which shows well defined crystal faces and the long crystal axis to be between two and five times longer than the

Fig. 1. Field photograph of the studied sample. The hammer is 33 cm long.

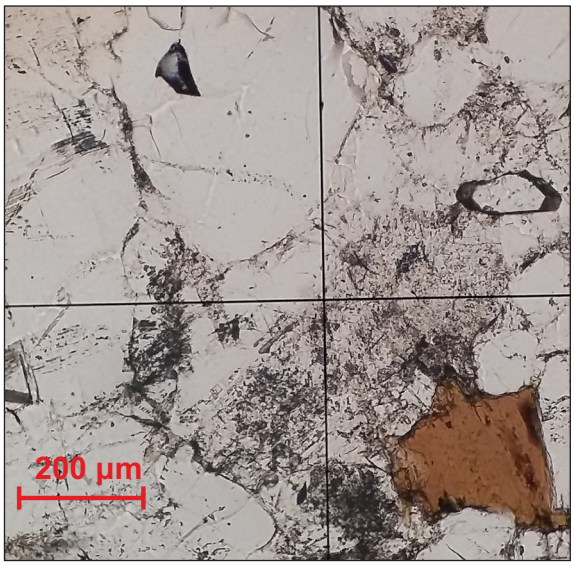

Fig. 2. Photomicrograph of the studied sample.

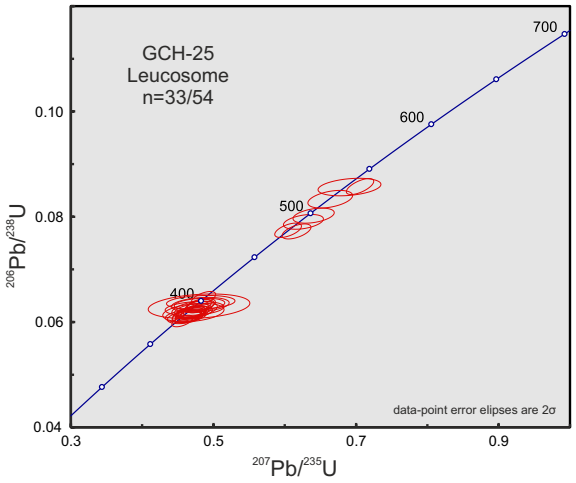

Fig. 3. U-Pb conventional concordia diagram showing U-Pb zircon analyses of the studied sample. Ellipses represent combined 2σ uncertainties of $^{206}Pb/^{238}U$ and $^{207}Pb/^{235}U$ ratios. *n*, number of analyses considered (those with 90–110% concordance)/total number of U–Pb analyses.

short axis (Fig. 5).

Domain II $\varepsilon Hf_{(t)}$ values are high, with values between *c.* +1.9 and +5.6 (average: +3.5; Fig. 6a). Domain I $\varepsilon Hf_{(t)}$ values are lower than those of domain II, with values from -4.4 to +0.6 (average: -1.8; Fig. 6a). $^{176}Hf/^{177}Hf_{(t)}$ ratios for domain II zircon plot around 0.282639 ± 0.000048 (±2 SD; Fig. 6b), and $^{176}Hf/^{177}Hf_{(t)}$ ratios for domain I zircon are lower than those of domain II and plot at 0.282414 ± 0.000088 (±2 SD; Fig. 6b).

U content of domain II analysed zircon is very low, in the range of 15–515 ppm (average: 133 ppm). U content of domain I analysed zircon is also low, in the range of 112–421 ppm (average: 229 ppm; Appx. 4).Domain II Th/U ratios are always below 0.2, and vary from *c.* 0.002 to *c.* 0.065 (average: 0.008); and domain I Th/U ratios are higher and more variable, and vary from *c.* 0.09 to *c.* 0.96 (average: 0.56; Fig. 7a).

$^{176}Lu/^{177}Hf$ ratios of domain II zircon are extremely low and vary from *c.* 0.00003 to *c.* 0.00041 (average: 0.00008; Fig. 7b). $^{176}Lu/^{177}Hf$ ratios of domain I zircon are higher than those of domain II and vary from *c.* 0.00134 to *c.* 0.00185 (average: 0.00158; Fig. 7b). $^{176}Yb/^{177}Hf$ ratios of domain II zircon are extremely low and vary from *c.* 0.0009 to *c.* 0.0126 (average: 0.0025; Appx. 4). $^{176}Yb/^{177}Hf$ ratios of domain I zircon are higher than those of domain II and vary from *c.* 0.0401 to *c.* 0.0557 (average: 0.0474; Appx. 4).

Nd whole-rock model-age is 1.24 Ga and $\varepsilon Nd_{(t)}$ values are: $\varepsilon Nd_{(t=0)}$ = -1.3; $\varepsilon Nd_{(t=387)}$ = +0.7.

7.2.1.2. Discussion

U–Pb ages can be sub-divided into three groups, the old inheritances, the Cambrian domain I zircon and the Devonian domain II zircon. The younger population in this sample, domain II, has the highest $^{176}Hf/^{177}Hf_{(t)}$ ratios, clearly higher than domain I zircon (Fig. 6b). This necessarily implies that domain II zircon are overgrowths,

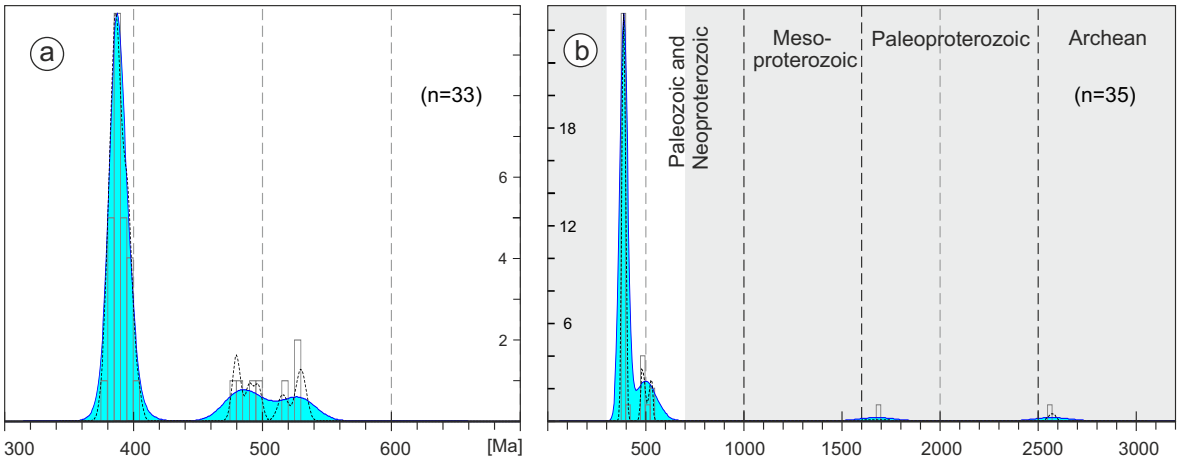

Fig. 4. Adaptative Kernel Density Estimation (aKDE, continuous line enclosing the blue area), Probability Density (PDP, black dashed line) and histogram diagrams of the U–Pb analyses (calculated with DensityPlotter5.0, Vermeesch 2012). Numbers in the vertical axis represent histogram frequency; *n*, number of analyses. **a** Partial plot representing data within a 300–700 Ma time range (bandwidth = 5 Ma, binwidth = 5 Ma). **b** Complete plot (bandwidth = 15 Ma, binwidth = 25 Ma).

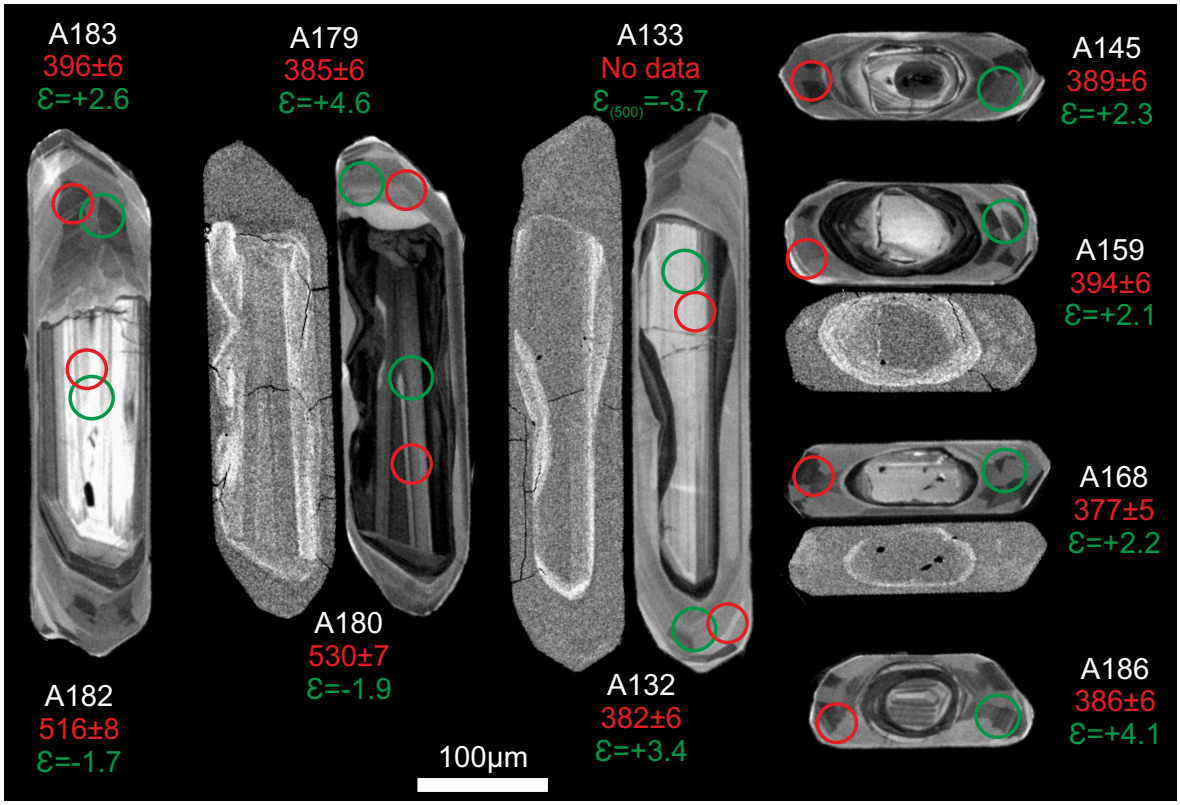

Fig. 5. BSE and CL images of representative zircons from the studied sample. Images without circles are BSE (back-scattered electrons) images, and those with circles are CL (cathodoluminescence) images. Laser ablation pits for U–Pb analyses (red line circles) have 30 μm diameters. Laser ablation pits for Lu–Hf analyses (green line circles) have 33 μm diameters. White numbers are the reference number of the analysis, red numbers are the U–Pb age and its 2σ error (Ma) and the green numbers are the εHf values for the U–Pb age. U–Pb analysis of A133 gave a discordant age, and εHf value was calculated for an assumed 500 Ma age.

from a fluid phase with higher $^{176}Hf/^{177}Hf_{(t)}$ ratios than the fluid from which the cores crystallised, and that they are not a consequence of solid-state recrystallisation of domain I zircon. This is because Hf^{4+} substitutes the cationic position of Zr^{4+} in the Zrn structure and because Hf has almost identical chemical properties, including atomic radii, than Zr. Therefore Hf will almost never be purged from the Zrn crystalline structure during a solid-state recrystallisation process (Hoskin & Schaltegger, 2003; Gerdes & Zeh, 2009). So a solid-state recrystallisation of domain I to form domain II zircon is discarded. Furthermore, the higher $^{176}Hf/^{177}Hf_{(t)}$ ratios of domain II overgrowths imply that the fluid phase from which this zircon grew from was enriched in radiogenic ^{176}Hf. This ^{176}Hf comes from ^{176}Lu decay. As the amount of ^{176}Lu in zircon is very low and the ^{176}Lu decay is very slow (^{176}Lu half-life: *c.* 37.8 Ga), it is very unlikely that the higher amounts of radiogenic domain II ^{176}Hf come from the decay of zircon ^{176}Lu. So, the higher domain II $^{176}Hf/^{177}Hf_{(t)}$ ratios must be a result of incorporating radiogenic ^{176}Hf into the partial melt. This ^{176}Hf should come from the decay of ^{176}Lu liberated from the melted minerals that formed the leucosome. This process is capable of liberating sufficient radiogenic ^{176}Hf to explain domain II $^{176}Hf/^{177}Hf_{(t)}$ ratios (*cf.* with Gerdes & Zeh, 2009; Zeh *et al.*, 2010 and references therein). Domain II has a combined well-defined oscillatory and multi-faceted ("soccerball") textures as shown from the CL images (Fig. 5). These textures favour the interpretation of overgrowth development of domain II zircon. Moreover, the multi-faceted textures point to a high-T overgrowth environment for these rims, as these textures have been related to high-T terrains (Harley *et al.*, 2007). From field and petrographic observations this rock has been interpreted as a leucosome formed by partial melting of the Banded Gneisses metasedimentary

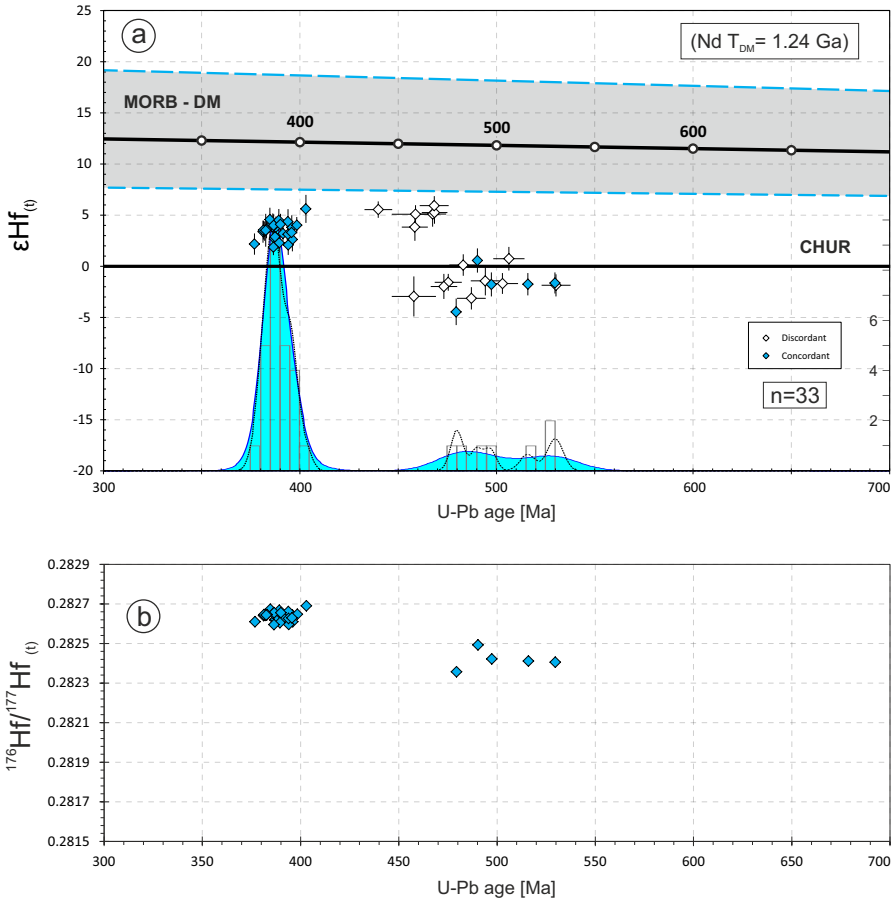

Fig. 6. a εHf *v.* age diagram. Error bars are +2σ and -2σ uncertainties. *n*, number of concordant zircon grains analysed for Lu–Hf isotopes. Numbers in the right vertical axis represent histogram frequency. Top-right rectangle shows Nd whole-rock model-age for the studied sample. MORB εHf interval was taken from Chauvel & Blichert-Toft (2001) considering a minimum $\varepsilon Hf_{(t=0Ma)}$ = +8.3 and a maximum $\varepsilon Hf_{(t=0Ma)}$ = +20.7. These values are propagated to $\varepsilon Hf_{(t=4Ga)}$ = 0 defining a grey field (enclosed by the blue discontinuous lines) around the DM-evolution trend, to provide an indication of the likely range of DM compositions through time. MORB: mid-ocean ridge basalts; DM: depleted mantle; CHUR: chondritic uniform reservoir. **b** $^{176}Hf/^{177}Hf_{(t)}$ *v.* age diagram.

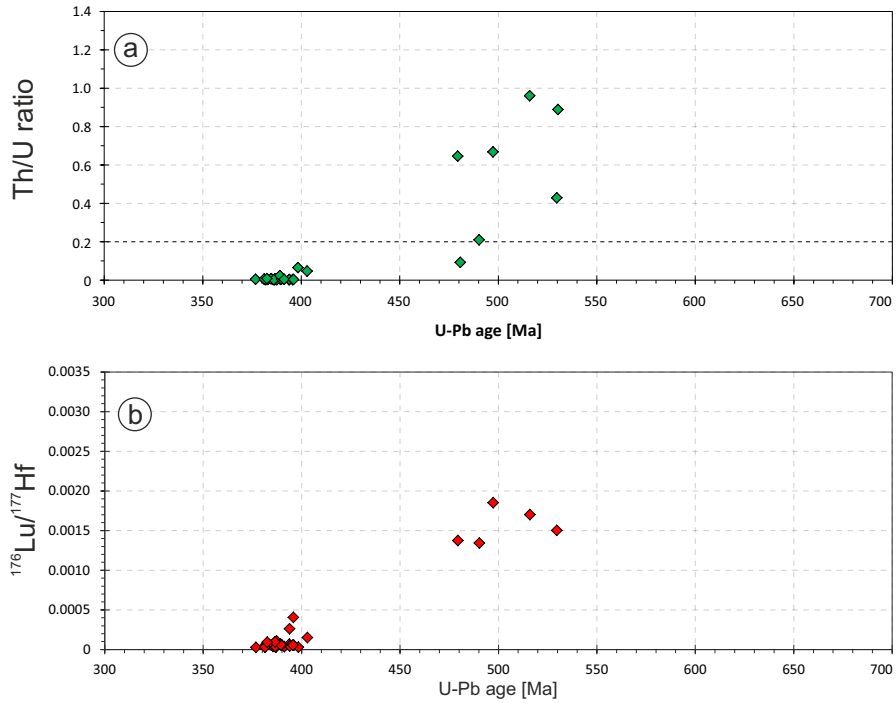

Fig. 7. a Th/U ratios *v.* age diagram (yellow rhombus represent Zrn analysed for U–Th–Pb isotopes and green rhombus represent those analysed for U–Th–Pb and Lu–Hf isotopes). **b** $^{176}Lu/^{177}Hf_{(t)}$ *v.* age diagram.

rocks. The presence of newly formed Grt (Fig. 2) leads one to suppose that the silicate fluid from which this leucosome crystallised had sufficient temperature to contain Grt forming cations. Therefore this partial melting is considered as to have occurred at high-T conditions. The very low Th/U, $^{176}Lu/^{177}Hf$ and $^{176}Yb/^{177}Hf$ ratios of domain II zircon (with respect to domain I cores) implies that domain II zircon is highly depleted in Th and HREE. Therefore these Devonian overgrowths most probably grew coherent or shortly after a rare element partitioning mineral, probably Grt.

Despite having discarded a solid-state recrystallisation process to explain the formation of domain II rims, domain I cores are normally surrounded by lobulated sinuous rims, which are dark in CL images and bright in BSE images (Fig. 5). As atoms with higher atomic number (Z) produce stronger scattering, these rims are brighter in BSE images probably because their heavy atom contents are considerably higher than the rest of the zircon. These rims are interpreted as alteration fronts, formed by the rare element purge triggered by a solid-state recrystallisation (these fronts are not always visible in BSE images). These observations lead one to conclude that the Banded Gneiss metasedimentary rocks underwent partial melting at high-T conditions, triggering solid-state recrystallisation processes in the sedimentary inherited zircon (domain I Cambrian and older zircon) and when the partial melt cooled sufficiently domain II overgrowths formed between 377 and 403 Ma, with a crystallisation climax at *c.* 387 Ma.

7.2.2. Sample GCH-26
(*Figueiroa leucosome)*

This sample was collected from *Figueiroa* beach (43°42'40.50"N, 7°51'48.51"W), at the 185–190 m point of the *Figueiroa* beach geological section (chapter 4).

This sample is interpreted from field observations as a leucosome, formed by partial melting of the Banded Gneisses metasedimentary rocks (Fig. 8). This lithology is displayed as centimetre sized pods ("*augens*"), folded and coherent with the metasedimentary rocks regional foliation (Ref: 114089).

From microscopic observations this sample has a granoblastic texture and has Qz, Afs and Pl as major constituents (Fig. 9). These minerals are poikilitic and feldspar is usually altered and shows pertitic exsolutions. Qz contains minor inclusions of Ap and feldspar contains inclusions of Qz, Bt, Ap and Zrn. Minor constituents are Ap, Bt, white mica, Amp, Rt, and Zrn.

7.2.2.1. Results

From sample GCH-26, 50 U–Pb analyses were performed of which 32 were concordant (*d* = 36%; Figs. 10 & 11a,b). Domain II is defined by 16 Devonian analyses constrained between 379 and 403 Ma, and show a well-defined maximum abundance at 389 Ma. Domain I is defined by 12 Cambrian–Ordovician analyses that show a well-defined maximum abundance at 508 Ma, and a relative abundance peak at 477 Ma. Three analyses are Neoproterozoic, which are considered inheritances (Fig. 11b).

Most of the domain I zircon (Cambrian–Ordovician) show more or less well defined oscillatory zonings, others show patchy-chaotic textures. They are normally surrounded by lobulated sinuous rims, which are dark and also bright in CL images and bright in BSE images. Domain II (Devonian) zircon is displayed as rims surrounding domain I zircon. Their show well defined combined oscillatory and multi-faceted ("soccerball") textures. In some zircon grains these textures are badly defined and even structure-less. These rims are the outer features observed and define the crystals external habit, which normally shows well defined crystal faces and the long crystal axis to be between two and four times longer than the short axis (Fig. 12).

Domain II $\varepsilon Hf_{(t)}$ values are high, with values between *c.* +3.7 and +6.3 (average: +4.9; Fig. 13a). Domain I $\varepsilon Hf_{(t)}$ values are variable, with values of -6.2 to +7.5 (average: +5.0; Fig. 13a). If the two lower values are not considered, domain I values are in the range of +5.1 to +7.5 (average: +6.4; Fig. 13a). $^{176}Hf/^{177}Hf_{(t)}$ ratios for domain II

Fig. 8. Field photograph of the studied sample. The hammer is 13.6 cm long (not considering the blue handle).

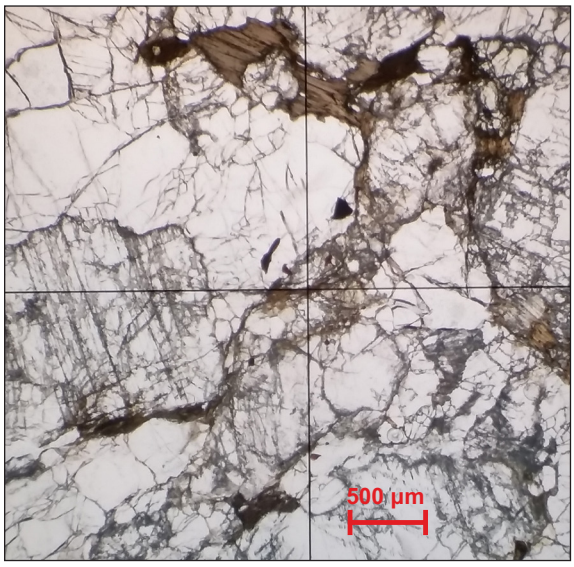

Fig. 9. Photomicrograph of the studied sample.

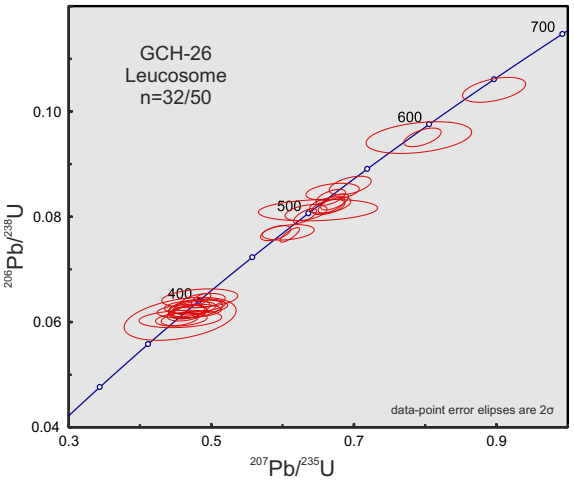

Fig. 10. U-Pb conventional concordia diagram showing U-Pb zircon analyses of the studied sample. Ellipses represent combined 2σ uncertainties of $^{206}Pb/^{238}U$ and $^{207}Pb/^{235}U$ ratios. *n*, number of analyses considered (those with 90–110% concordance)/total number of U–Pb analyses.

zircon plot around 0.282679 ± 0.000037 (±2 SD; Fig. 13b), and $^{176}Hf/^{177}Hf_{(t)}$ ratios for domain I zircon plot at 0.282609 ± 0.000214 (±2 SD; Fig. 13b). If the two lower ratios are not considered, domain I ratios are in the range of 0.282650 ± 0.000036 (±2 SD; Fig. 13b).

Domain II Th/U ratios are always below 0.2, and vary from *c.* 0.004 to *c.* 0.033 (average: 0.011); and domain I Th/U ratios are higher (higher than 0.2) and more variable, from *c.* 0.40 to *c.* 0.92 (average: 0.58; Fig. 14a). U content of domain II analysed zircon is highly variable, in the range of 20–2074 ppm (average: 223 ppm). U content of domain I analysed zircon is variable, but not as much as domain II, in the range of 76–885 ppm (average: 403 ppm; Appx. 4).

$^{176}Lu/^{177}Hf$ ratios of domain II zircon are low and vary from *c.* 0.00013 to *c.* 0.00066 (average: 0.00035; Fig. 14b). $^{176}Lu/^{177}Hf$ ratios of domain I zircon are higher than those of domain II and vary from *c.* 0.00080 to *c.* 0.00230 (average: 0.00154; Fig. 14b). $^{176}Yb/^{177}Hf$ ratios of domain II zircon are low and vary from *c.* 0.0028 to *c.* 0.0206 (average: 0.0098; Appx. 4). $^{176}Yb/^{177}Hf$ ratios of domain I zircon are higher than those of domain II and vary from *c.* 0.0217 to *c.* 0.0657 (average: 0.0447; Appx. 4).

Nd whole-rock model-age is 0.92 Ga and $\varepsilon Nd_{(t)}$ values are: $\varepsilon Nd_{(t=0)} = -1.6$; $\varepsilon Nd_{(t=389)} = +1.6$.

7.2.2.2. Discussion

U–Pb ages can be sub-divided into three groups, the old inheritances, Cambrian–Ordovician domain I zircon and Devonian domain II zircon. The younger population in this sample, domain II, has similar $^{176}Hf/^{177}Hf_{(t)}$ ratios within error than domain I zircon (Fig. 13b). These observations suggest that domain II zircon is a consequence of solid-state recrystallisation of domain I zircon. As explained in the previous sample (leucosome GCH-25), zircon domains altered by pseudomorphic recrystallisation

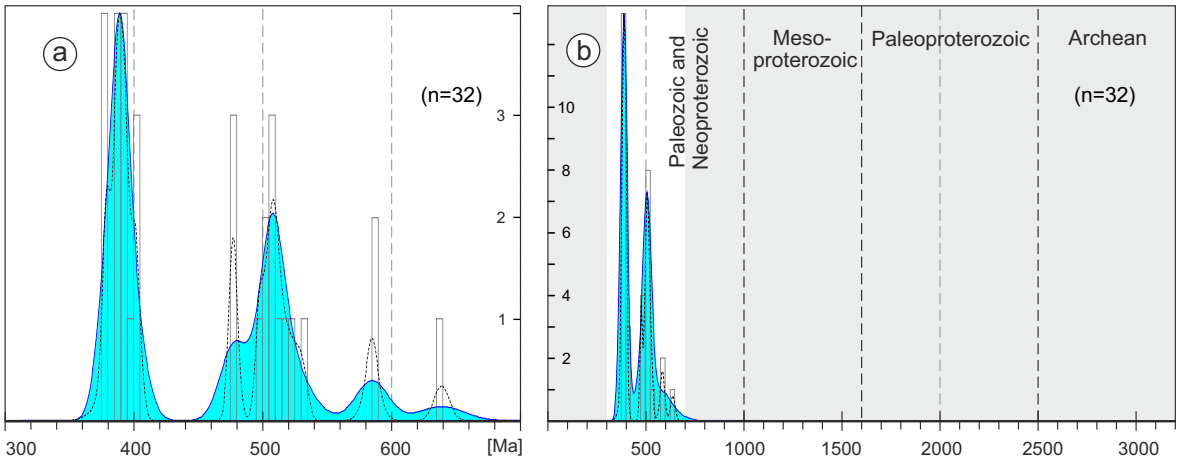

Fig. 11. Adaptative Kernel Density Estimation (aKDE, continuous line enclosing the blue area), Probability Density (PDP, black dashed line) and histogram diagrams of the U–Pb analyses (calculated with DensityPlotter5.0, Vermeesch 2012). Numbers in the vertical axis represent histogram frequency; *n*, number of analyses. **a** Partial plot representing data within a 300–700 Ma time range (bandwidth = 5 Ma, binwidth = 5 Ma). **b** Complete plot (bandwidth = 15 Ma, binwidth = 25 Ma).

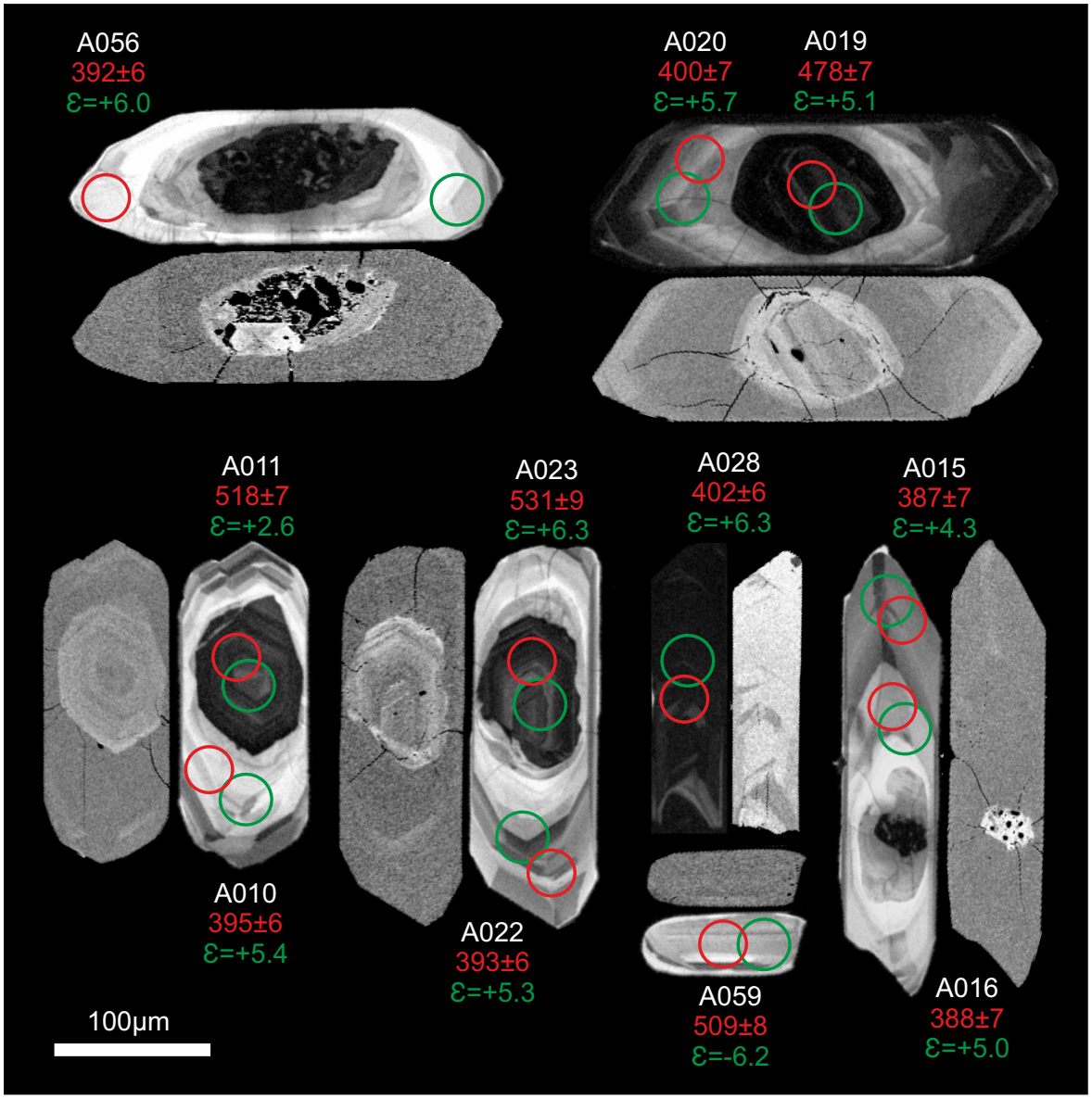

Fig. 12. BSE and CL images of representative zircons from the studied sample. Images without circles are BSE (back-scattered electrons) images, and those with circles are CL (cathodoluminescence) images. Laser ablation pits for U–Pb analyses (red line circles) have 30 μm diameters. Laser ablation pits for Lu–Hf analyses (green line circles) have 33 μm diameters. White numbers are the reference number of the analysis, red numbers are the U–Pb age and its 2σ error (Ma) and the green numbers are the εHf values for the U–Pb age.

conserve their original $^{176}Hf/^{177}Hf_{(t)}$ ratios. Some of the zircon textures favour this interpretation for domain II zircon from this sample. Some of the domain II zircon rims show badly defined oscillatory textures (*e.g.* A056; Fig. 12) and domain I zircon cores are surrounded by alteration fronts (Fig. 12). In some cases domain I cores show patchy chaotic textures, which are interpreted as an extreme development of the alteration fronts (*e.g.* A056, A020, A015; Fig. 12). The process responsible for the development of these textures is the exsolution of enriched REE zircon into depleted REE zircon and xenotime (with the addition of U–Th-silicates as a product, Tomaschek *et al.*, 2003), following the reaction $(Zr,Hf,Y,REE)(Si,P)O_4 \rightarrow (Zr,Hf)SiO_4 + (Y,REE)PO_4$ (Pan, 1997). This process is a consequence of REE purge from the zircon structure triggered by solid-state recrystallisation. Moreover, the chaotic patchy cores are normally surrounded by cracks (BSE images; Fig. 12) that could well be the result of volume change in these cores

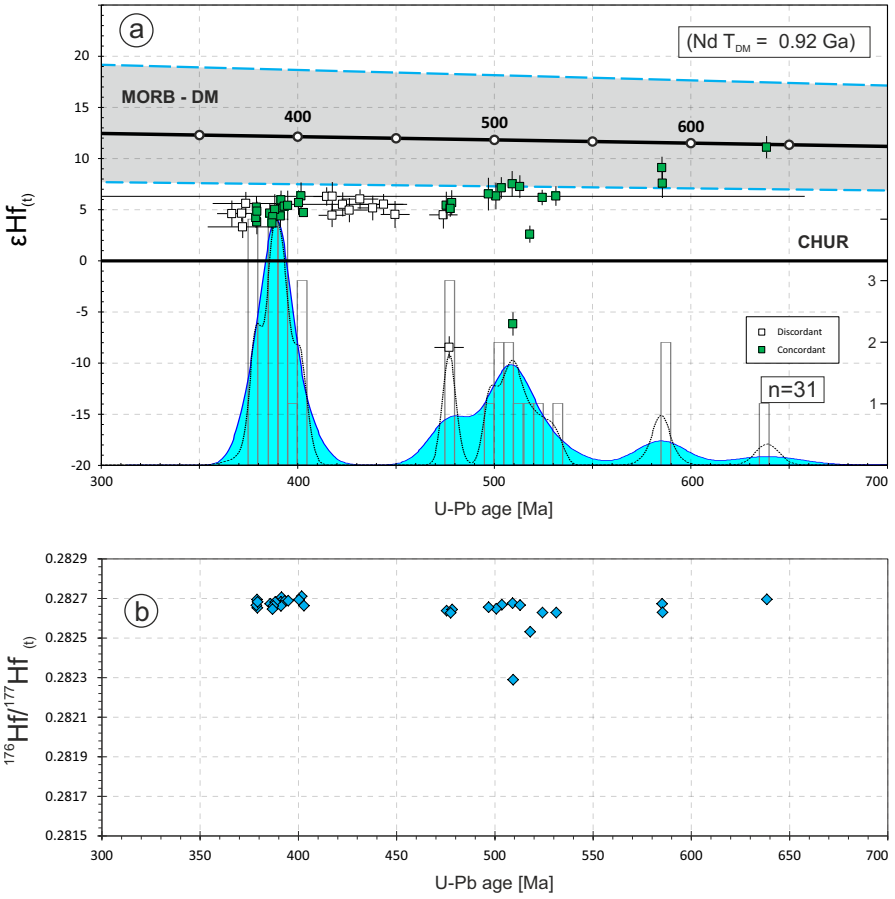

Fig. 13. a εHf *v.* age diagram. Error bars are +2σ and -2σ uncertainties. *n*, number of concordant zircon grains analysed for Lu–Hf isotopes. Numbers in the right vertical axis represent histogram frequency. Top-right rectangle shows Nd whole-rock model-age for the studied sample. MORB εHf interval was taken from Chauvel & Blichert-Toft (2001) considering a minimum $\varepsilon Hf_{(t=0Ma)}$ = +8.3 and a maximum $\varepsilon Hf_{(t=0Ma)}$ = +20.7. These values are propagated to $\varepsilon Hf_{(t=4Ga)}$ = 0 defining a grey field (enclosed by the blue discontinuous lines) around the DM-evolution trend, to provide an indication of the likely range of DM compositions through time. MORB: mid-ocean ridge basalts; DM: depleted mantle; CHUR: chondritic uniform reservoir. **b** $^{176}Hf/^{177}Hf_{(t)}$ *v.* age diagram.

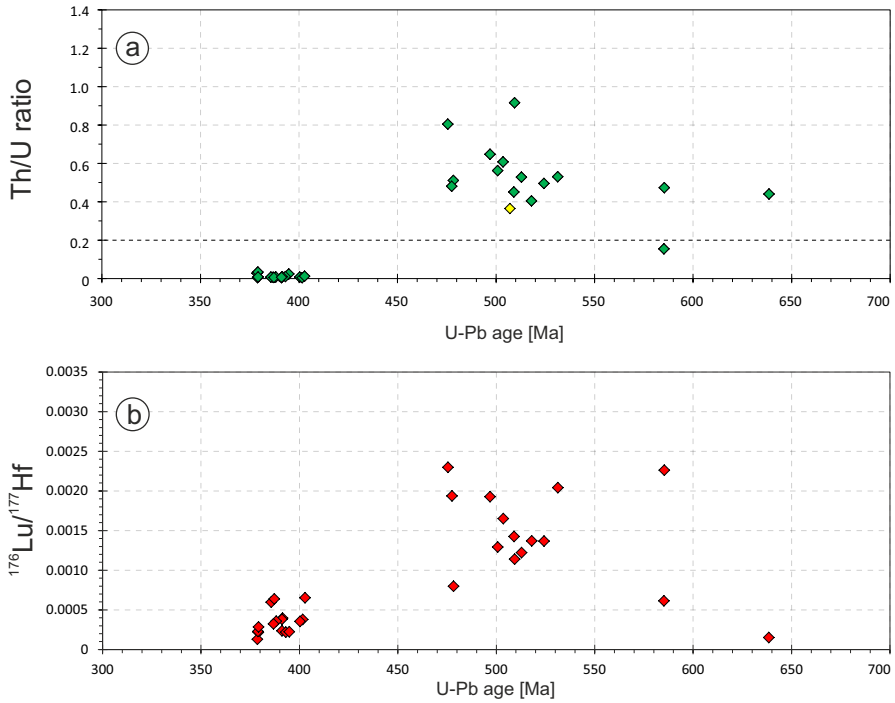

Fig. 14. a Th/U ratios *v.* age diagram (yellow rhombus represent Zrn analysed for U–Th–Pb isotopes and green rhombus represent those analysed for U–Th–Pb and Lu–Hf isotopes). **b** $^{176}Lu/^{177}Hf_{(t)}$ *v.* age diagram.

in response of the zircon exsolution process. From the above-mentioned observations a solid-sate recrystallisation process for the genesis of domain II rims seems proved, but a genesis of these rims by overgrowth cannot be ruled out for the following reasons: (i) domain II rims also show well defined combined oscillatory and sector ("soccerball") textures; (ii) this sample is a leucosome formed by partial melting (and therefore it crystallised from a fluid phase); (iii) $^{176}Hf/^{177}Hf_{(t)}$ ratios in this sample and in the previous sample (GCH-25) of the same zircon domains have the same values within error, and domain II rims from the previous sample were interpreted as overgrowths (both samples are leucosomes formed by the same partial melting event from metasedimentary rocks from the same formation). Furthermore, if a comparison of $^{176}Hf/^{177}Hf_{(t)}$ ratios of cores and rims from the same crystals is made, both processes are evident. Analyses A011 (core) and A010 (rim; Fig. 12) have clearly different $^{176}Hf/^{177}Hf_{(t)}$ ratios (0.282532 and 0.282690 respectively) pointing to a overgrowth genesis of the rim. Analyses A019 (core) and A020 (rim; Fig. 12) have very similar $^{176}Hf/^{177}Hf_{(t)}$ ratios (0.282629, 0.282694) pointing to a very probable solid-state recrystallisation genesis of the rim. From these observations it seems reasonable to propose that both processes were involved in the generation of domain II Devonian rims. In the previous sample (leucosome GCH-25) it was proposed that overgrowth followed solid-state recrystallisation, but from this sample this sequence of events does not seem to have occurred in this order. Zircon dissolution and re-precipitation can occur at the prograde or the retrograde metamorphic path and solid-state recrystallisation usually occurs somewhere near the temperature peak (Harley, 2007). As the cracks observed in BSE images seem to crosscut the entire rims (they have been interpreted as a consequence of solid state recrystallisation) it seems logical to propose that overgrowths crystallised from the partial melt in the prograde metamorphic path and that solid-state recrystallisation occurred afterwards when the system reached the temperature peak.

7.2.3. Sample GCH-32
(Area da Vaca leucosome, 205 m)

This sample was collected from the *Area da Vaca* beach (43°43'29.34"N, 7°51'38.25"W), at the 205 m point of the *Area da Vaca* geological section (chapter 4).

This sample is interpreted from field observations as a leucosome, formed by partial melting of the metasedimentary rocks (Fig. 15). This lithology is displayed as centimetre sized leucocratic bands, folded and coherent with the metasedimentary rocks regional foliation (Ref: 114095).

From microscopic observations this sample has a porphyro-grano-lepidoblastic texture and has Qz and Afs as major constituents (Fig. 16). Qz is displayed as big poikilitic crystals and as small crystals. These two ways in which Qz is present in this sample could be due to a re-partial melting of the leucosome or that the small crystals are inherited from the metasedimentary rock from which this leucosome partially melted from. Poikilitic Qz contains inclusions of Qz, Pl, Grt, Bt and Ap. Afs is poikilitic and contains inclusions of Qz, Bt, Ap and Zrn. It is usually altered and shows pertitic type exsolutions. Minor constituents are Grt, Bt, Ap, Zo, white mica, Chl and Zrn. Grt is displayed in two ways, as relatively big crystals with a high presence of inclusions (Qz and Ap), highly fractured and corroded and rimed with Bt, Qz and white mica; and as relatively small crystals, with almost no inclusions (or very small to be appreciated), which are predominantly present in the Qz-Afs regions.

7.2.3.1. Results

From sample GCH-32, 61 U–Pb analyses were performed of which 30 were concordant (d = 51%; Figs. 17 & 18a,b). Domain II is defined by 14 Devonian analyses constrained between 358 and 408 Ma, and with a well-defined maximum abundance at 394 Ma. Domain I is defined by 13 Cambrian–Ordovician analyses that show a well-defined maximum abundance at 490 Ma, and relative abundance peaks at 486, 496 and 521 Ma. One analysis is Ediacaran and two analyses are Paleoproterozoic (Fig. 18b).

Most of the domain I zircon (Cambrian–Ordovician) shows more or less well defined oscillatory zonings. It is normally surrounded by lobulated sinuous rims, which are dark in CL images and bright in BSE images. Domain II (Devonian) zircon is displayed as rims surrounding domain I zircon and as newly formed dark zircon. It shows well defined combined oscillatory and multi-faceted ("soccerball") textures. In some zircon rims these textures are

Fig. 15. Field photograph of the studied sample. The hammer is 33 cm long.

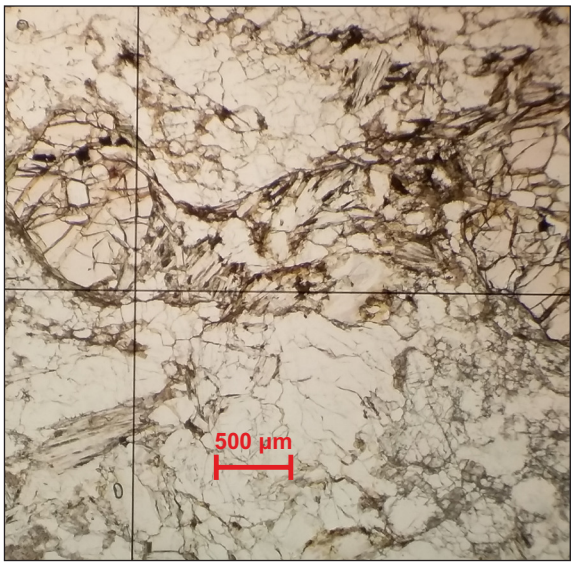

Fig. 16. Photomicrograph of the studied sample.

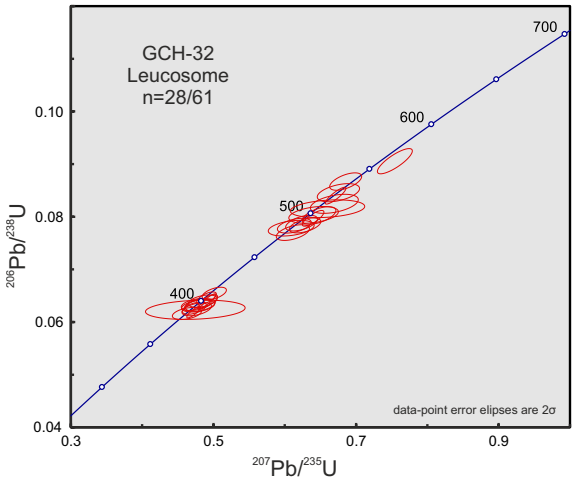

Fig. 17. U-Pb conventional concordia diagram showing U-Pb zircon analyses of the studied sample. Ellipses represent combined 2σ uncertainties of $^{206}Pb/^{238}U$ and $^{207}Pb/^{235}U$ ratios. *n*, number of analyses considered (those with 90–110% concordance)/total number of U–Pb analyses.

badly defined or even structure-less. The domain II rims are the outer features observed and define the crystals outer habit, which normally show well defined crystal faces and the long crystal axis to be between two and four times longer than the short axis (Fig. 19).

Domain II $\varepsilon Hf_{(t)}$ values are between *c.* -3.5 and +3.1 (average: +0.8; Fig. 20a). Domain I $\varepsilon Hf_{(t)}$ values are between *c.* -8.8 and +3.9 (average: 0.0; Fig. 20a). $^{176}Hf/^{177}Hf_{(t)}$ ratios for domain II zircon plot around 0.282559 ± 0.000098 (±2 SD; Fig. 20b), and $^{176}Hf/^{177}Hf_{(t)}$ ratios for domain I zircon plot at 0.282473 ± 0.000233 (±2 SD; Fig. 20b).

U content of domain II analysed zircon is highly variable, in the range of 98–2783 ppm (average: 585 ppm). U content of domain I analysed zircon is also highly variable, in the range of 45–1770 ppm (average: 397 ppm; Appx. 4). Domain II Th/U ratios are always below 0.2, and vary from 0.002 to *c.* 0.034 (average: 0.011), and domain I Th/U ratios are higher and more variable, from *c.* 0.01 to *c.* 1.09 (average: 0.42; Fig. 21a).

$^{176}Lu/^{177}Hf$ ratios of domain II zircon are low and vary from *c.* 0.00002 to 0.00035 (average: 0.00007; Fig. 21b). $^{176}Lu/^{177}Hf$ ratios of domain I zircon are higher than those of domain II, and vary from *c.* 0.00057 to 0.00193 (average: 0.00118; Fig. 21b). $^{176}Yb/^{177}Hf$ ratios of domain II zircon are low and vary from *c.* 0.0006 to 0.0139 (average: 0.0024; Appx. 4). $^{176}Yb/^{177}Hf$ ratios of domain I zircon are higher than those of domain II, and vary from *c.* 0.0162 to 0.0551 (average: 0.0349; Appx. 4).

Nd whole-rock model-age is 1.52 Ga and $\varepsilon Nd_{(t)}$ values are: $\varepsilon Nd_{(t=0)} = -2.9$; $\varepsilon Nd_{(t=394)} = -1.0$.

7.2.3.2. Discussion

U–Pb ages can be sub-divided into three groups, the old inheritances, Cambrian–Ordovician domain I zircon and Devonian domain II zircon. The younger population in this

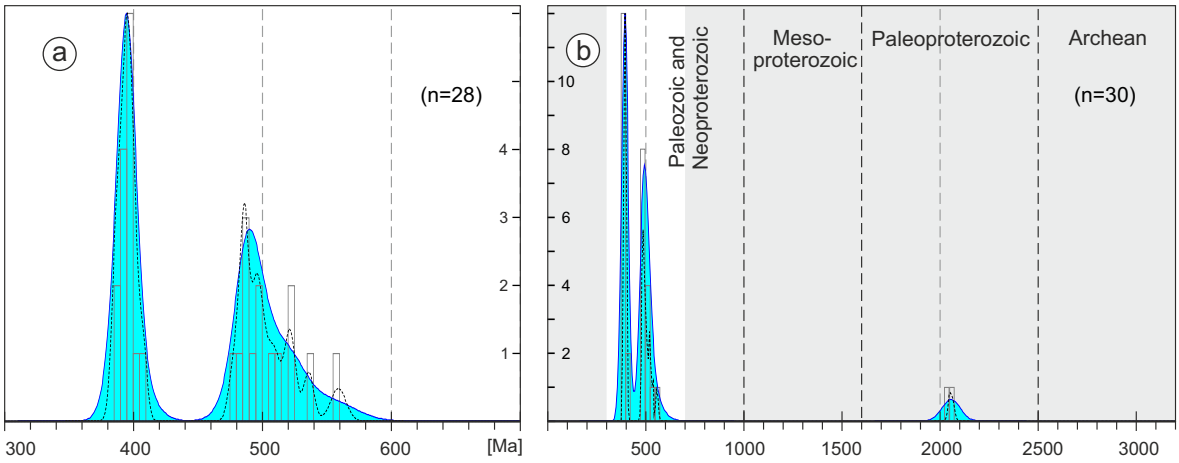

Fig. 18. Adaptative Kernel Density Estimation (aKDE, continuous line enclosing the blue area), Probability Density (PDP, black dashed line) and histogram diagrams of the U–Pb analyses (calculated with DensityPlotter5.0, Vermeesch 2012). Numbers in the vertical axis represent histogram frequency; *n*, number of analyses. **a** Partial plot representing data within a 300–700 Ma time range (bandwidth = 5 Ma, binwidth = 5 Ma). **b** Complete plot (bandwidth = 15 Ma, binwidth = 25 Ma).

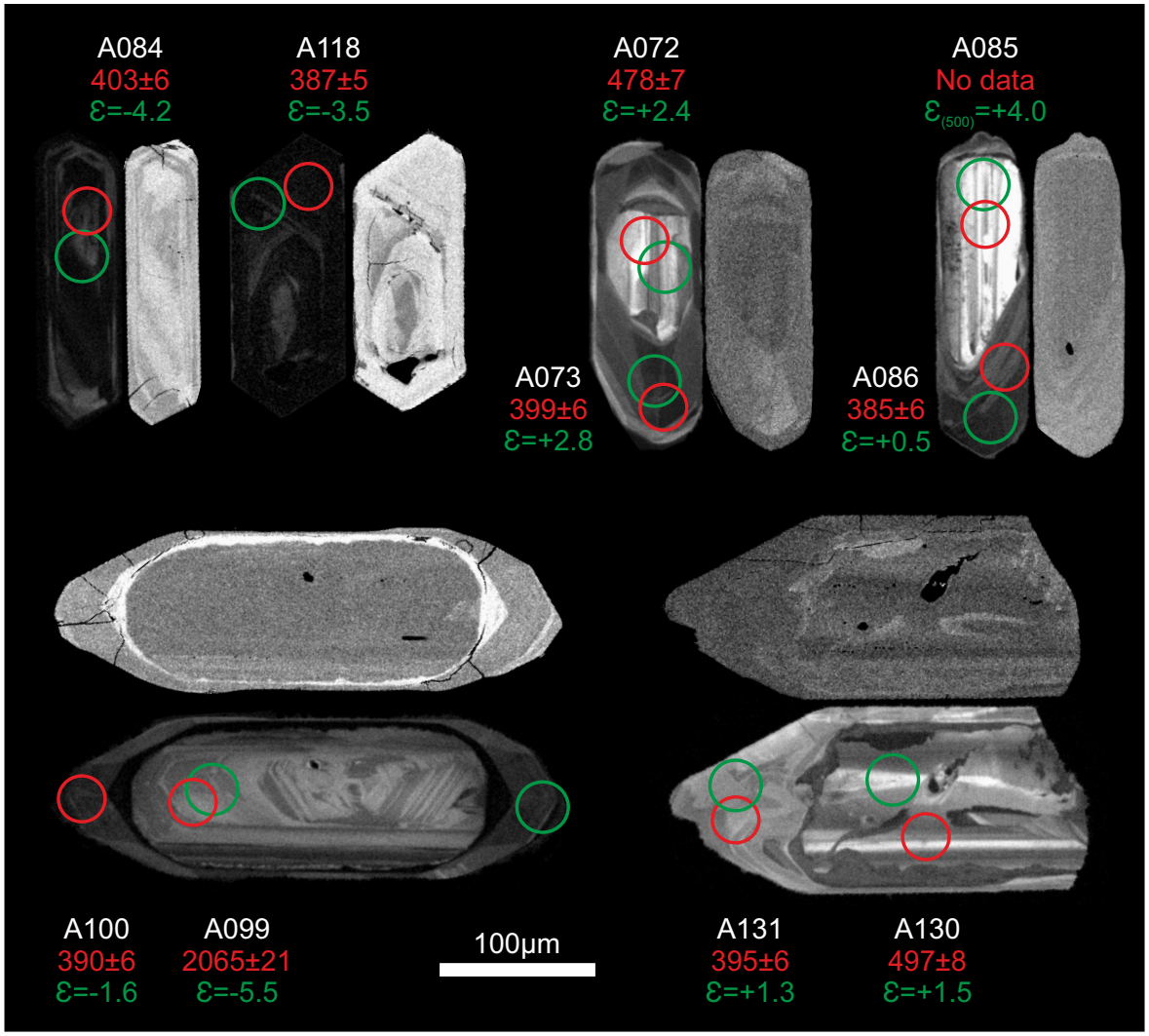

Fig. 19. BSE and CL images of representative zircons from the studied sample. Images without circles are BSE (back-scattered electrons) images, and those with circles are CL (cathodoluminescence) images. Laser ablation pits for U–Pb analyses (red line circles) have 30 μm diameters. Laser ablation pits for Lu–Hf analyses (green line circles) have 33 μm diameters. White numbers are the reference number of the analysis, red numbers are the U–Pb age and its 2σ error (Ma) and the green numbers are the εHf values for the U–Pb age. U–Pb analysis of A085 gave a discordant age, and εHf value was calculated for an assumed 500 Ma age.

sample, domain II, has similar $^{176}Hf/^{177}Hf_{(t)}$ ratios within error than domain I zircon (Fig. 20b), but their $^{176}Hf/^{177}Hf_{(t)}$ ratio variations are very high. This high variation points to solid-state recrystallisation for the generation of domain II zircon, because if this zircon grew from a fluid phase they would have the same $^{176}Hf/^{177}Hf_{(t)}$ ratios, heritage of the assumed chemically-homogenised fluid phase. As this sample is a leucosome and a fluid phase is intrinsically present at its formation, a close look into the zircon of this sample becomes necessary. For example, zircon A099 and its rim A100 (Fig. 19) is a clear case of rim overgrowth, as their $^{176}Hf/^{177}Hf_{(t)}$ ratios are clearly different (0.281308 and 0.282493 respectively). On the other hand, zircon A130 and its rim A131 (0.282515, 0.282574) and zircon A085 and its rim A086 (0.282584, 0.282558; Fig. 19) show almost identical $^{176}Hf/^{177}Hf_{(t)}$ ratios and therefore a solid-state recrystallisation is the most probable process for the formation of the rims. The three zircon grains with lower $^{176}Hf/^{177}Hf_{(t)}$ ratios and $\varepsilon Hf_{(t)}$ values (Fig. 20a,b) with Devonian ages (domain II) are A084, A107 and A118 (Fig. 19). These three zircon grains have the higher U contents (428, 2376 and 2783 ppm

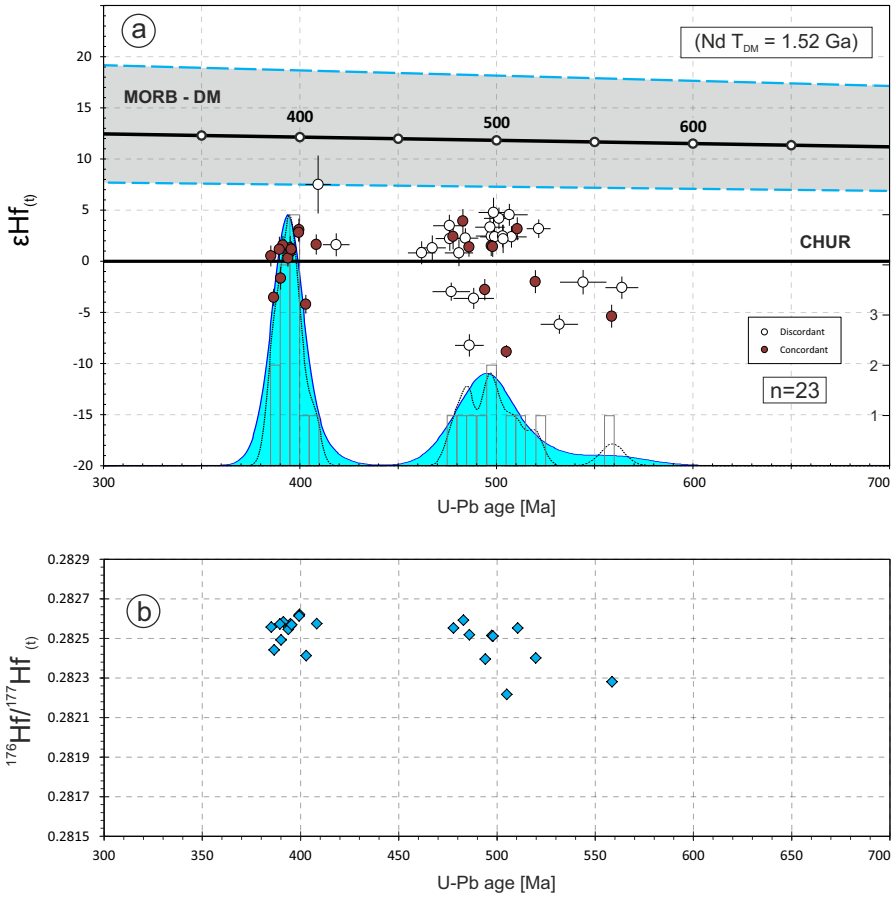

Fig. 20. a εHf *v.* age diagram. Error bars are +2σ and -2σ uncertainties. *n*, number of concordant zircon grains analysed for Lu–Hf isotopes. Numbers in the right vertical axis represent histogram frequency. Top-right rectangle shows Nd whole-rock model-age for the studied sample. MORB εHf interval was taken from Chauvel & Blichert-Toft (2001) considering a minimum $\varepsilon Hf_{(t=0Ma)}$ = +8.3 and a maximum $\varepsilon Hf_{(t=0Ma)}$ = +20.7. These values are propagated to $\varepsilon Hf_{(t=4Ga)}$ = 0 defining a grey field (enclosed by the blue discontinuous lines) around the DM-evolution trend, to provide an indication of the likely range of DM compositions through time. MORB: mid-ocean ridge basalts; DM: depleted mantle; CHUR: chondritic uniform reservoir. **b** $^{176}Hf/^{177}Hf_{(t)}$ *v.* age diagram.

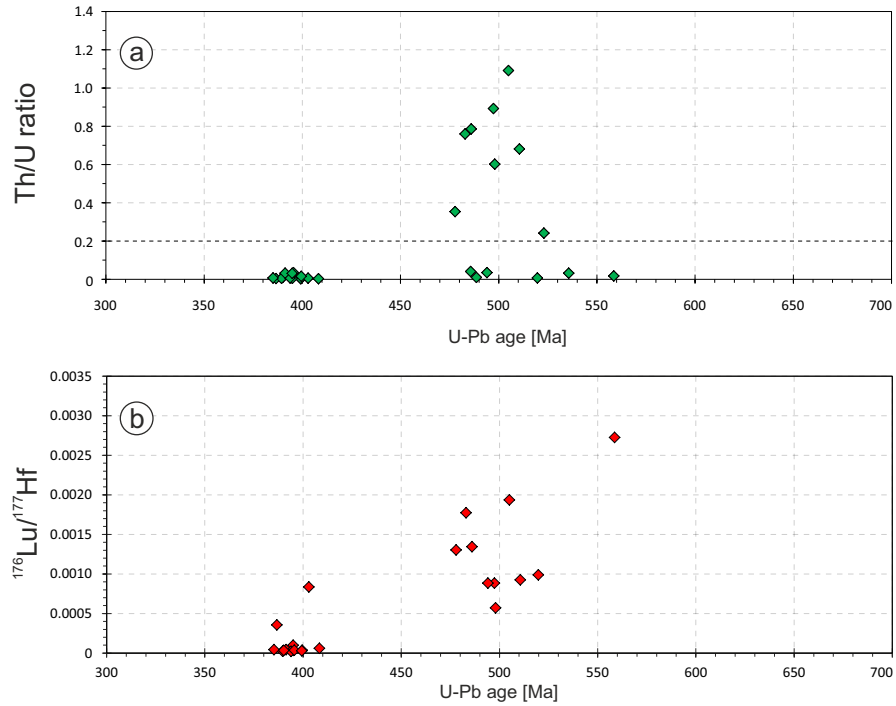

Fig. 21. a Th/U ratios *v.* age diagram (yellow rhombus represent Zrn analysed for U–Th–Pb isotopes and green rhombus represent those analysed for U–Th–Pb and Lu–Hf isotopes). **b** $^{176}Lu/^{177}Hf_{(t)}$ *v.* age diagram.

respectively) and the higher $^{176}Lu/^{177}Hf$ ratios (0.00083, 0.00090, 0.00035) of domain II zircon population. Their textures are clearly different from the rest of domain II rims. They are very dark in the CL images (much darker than the rest of domain II zircon) and their oscillatory growth patterns are faded and blurred. As their chemical contents are different from the rest of the Devonian population, and as other zircon grains with Ordovician–Cambrian ages show the same textural patterns, it is concluded that this zircon was altered by solid-state recrystallisation. Therefore both processes (recrystallisation and overgrowth) are present within zircon with the same ages (Devonian) and from the same sample. As not all the analysed domain II rims have their corresponding domain I core analysed, it is not possible to assess the $^{176}Hf/^{177}Hf_{(t)}$ ratio of the fluid phase from which the overgrowths grew.

7.3. Eclogites

Four eclogites have been studied, two from the Eclogite Band formation and the other two from the Banded Gneiss formation (Cabo Ortegal Complex, NW Iberian Massif; Appx. 1).

The intention of studying these rocks is to better constrain what we know about the age of crystallisation, the nature of the sources and the development of the mafic igneous activity of the magmatic arc that was built at the margin of Gondwana in the Neoproterozoic–Cambrian. Studying these rocks will also give important information about the age and conditions of the metamorphic event that transformed the protoliths of these rocks into eclogites.

In the Eclogite Band formation three types of eclogites have been described (Mendía, 2000): (i) the common MORB-type eclogites (which constitute a *c.* 70% of the formation outcrops and is represented in this PhD by sample GCH-19, section 7.3.1), (ii) the Ky-rich eclogites (which constitute a *c.* 25% of the outcrops and is represented by sample GCH-22, section 7.3.3) and (iii) the Fe–Ti rich eclogites (which constitute a *c.* 5% of the outcrops and have not been studied in this work).

The eclogites from the Banded Gneiss formation (also called eclogite facies gneisses, see chapter 4) are found as variably sized boudins within the meta-sedimentary rocks of this formation. They are generally retrograded and they are represented by the sample GCH-20 (section 7.3.2). There is also an eclogite the outcrop of which is intimately related to an igneous felsic rock by a mingling process (see chapter 4) and is represented by sample GCH-23 (section 7.3.4; the felsic rock is represented by sample GCH-14, described in section 7.4.4).

Previous studies (Bernard-Griffiths *et al.*, 1985; Peucat *et al.*, 1990; Gil Ibarguchi *et al.*, 1990) have shown that the common eclogites from the Eclogite Band formation (represented by sample GCH-19, section 7.3.1) have N-MORB type compositions, unfractionated HREE an LREE depleted patterns, $\varepsilon Nd_{(t=480)}$ values of +10 and $^{87}Sr/^{86}Sr$ ratios of 0.7032–0.7052; and that their protoliths were gabbros or basalts (Mendía, 2000). Ordoñez Casado *et al.* (2001) discussed that as basalts may only contain inherited but not co-magmatic zircon, the protolith must have been gabbroic rocks. Peucat *et al.* (1990) gave a $^{207}Pb/^{206}Pb$ age of 480 ± 5 Ma for these rocks (TIMS technique) and interpreted this age as the age of HP–HT metamorphism. Ordoñez Casado *et al.* (2001) dated the magmatic domains of zircon from this formation at 495 ± 11 Ma (average of eight analyses on five crystals) and the metamorphic domains (rims) at 386 ± 41 Ma (average of four analyses on three crystals; SHRIMP technique).

The Ky-rich eclogites from the Eclogite Band formation (represented by sample GCH-22, section 7.3.3) are richer in Mg and Al and have lower REE and trace element contents than the common N-MORB type eclogites (Gil Ibarguchi *et al.*, 1990). Presumably, they originated from plagioclase-rich cumulates of troctolitic composition with spinel-bearing protoliths (Gil Ibarguchi *et al.*, 1990). Mendía (2000) stated that, from a geochemistry point of view, the eclogites from the Eclogite Band formation are co-genetic, where the Ky-rich eclogites would represent cumulates from the tholeitic series, rich in plagioclase contents and with Sr and Eu positive anomalies. Whole-rock Nd experiments show $\varepsilon Nd_{(t=480)}$ values of *c.* +1 for this lithology (Bernard-Griffiths *et al.*, 1985; Peucat *et al.*, 1990). The eclogitic metamorphism was interpreted to be Early Ordovician, as this type of eclogites was dated at 480 Ma by the TIMS U–Pb zircon aggregate method (Bernard-Griffiths *et al.,* 1985; Peucat *et al.,* 1990). Retrogression under amphibolite-facies conditions has been dated between 410 and 430 Ma by Van Calsteren *et al.* (1979; K–Ar on amphibole concentrates). Ordoñez Casado *et al.* (2001) analysed five magmatic domains on five zircon grains which yielded a mean age of 469 ± 9 Ma, and four spots from high luminescent rim domains of three zircon grains yielded an average age of 380 ± 14 Ma (SHRIMP technique). Whole-rock Nd experiments show values of $\varepsilon Nd_{(t=o)}$ = -0.5 and $\varepsilon Nd_{(t=472)}$ = -1.04 (Ordoñez Casado *et al.,* 2001).

7.3.1. Sample GCH-19
(Ortegal lighthouse eclogite)

This eclogite forms part of the Eclogite Band formation of the HP–HT Upper Allochthon of the Cabo Ortegal Complex, and is representative of the common MORB-type eclogites. This sample is located in the northern part of the Cabo Ortegal Eclogite Band formation (Appx. 1; 43°46'06"N, 7°52'05"W).

This sample is a fine to medium grained rock with oriented porphyro-grano-nematoblastic texture (Ref: 113162). Its major constituents are Grt, Cpx and Zo and its minor constituents are Qz, Amp, Pl, Rt, Ilm, Spn, Czo, Ap and Zrn (Figs. 22 & 23). Grt is idioblastic, colourless to light pink and poikilitic, with many inclusions (mainly Qz, Rt, Zo, Amp and Cpx). It shows de-compressive related coronas with micro- to crypto-crystalline minerals where Amp and Qz have been identified. Cpx is colourless and forms elongated crystals defining the foliation trend. Its borders are rimed by symplectites, which are probably Pl and Amp or Pl and secondary Cpx. These symplectites are a retrograde texture and therefore this Cpx is most probably the primary eclogitic Cpx, *i.e.* Omp. Amp, which is most probably Hbl, is light to dark green and also pale brown. It is slightly pleochroic and it is poikilitic, with inclusions of at least Cpx, Rt, Zo and Ap minerals. Zo is in net contact with Cpx, forms elongated tabular crystals coherent with the foliation trend and it is sometimes partially replaced by Czo. Zo is most probably a primary eclogitic-stable mineral. Rt is relatively abundant, has dark opaque rims, which are most probably Ilm, and very rarely both, Rt and Ilm, are surrounded by Spn. Qz shows undulose extinction, and forms polycrystalline aggregates with lobulated crystal boundaries.

7.3.1.1. Results

From this sample 112 U–Pb analyses were performed of which 59 were concordant (*d* = 47.3%; Figs. 24 & 25a,b). The U–Pb ages are scattered between *c.* 520 to 380 Ma with relative abundances at 505–485, 443–424 and 402–387 Ma (Fig. 25).

Most of the zircon grains in this sample conserve their primary oscillatory igneous zoning but this texture is generally blurred and fainted. Other zircon grains are structure-less. Rims are also found and show fainted oscillatory and structure-less zonings. Alteration fronts are not evident (Fig. 26). No internal features are observed in BSE images.

Epsilon Hf values are high and plot around the MORB-DM evolution trend with values between *c.* +6 and +14 (Fig. 27a). $^{176}Hf/^{177}Hf_{(t)}$ ratios plot

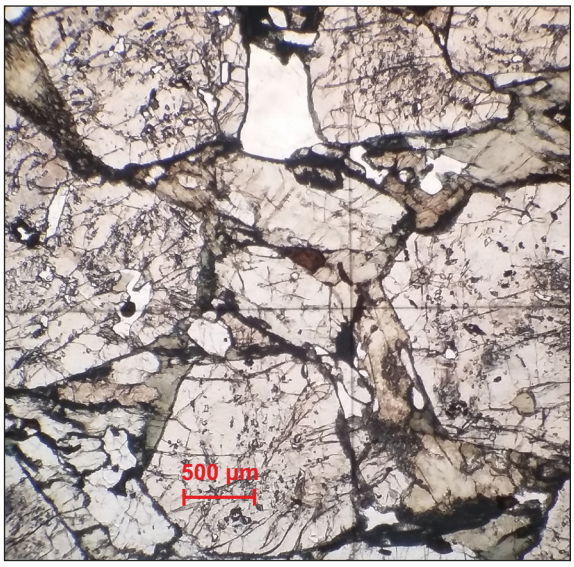

Fig. 22. Photomicrograph of the studied sample.

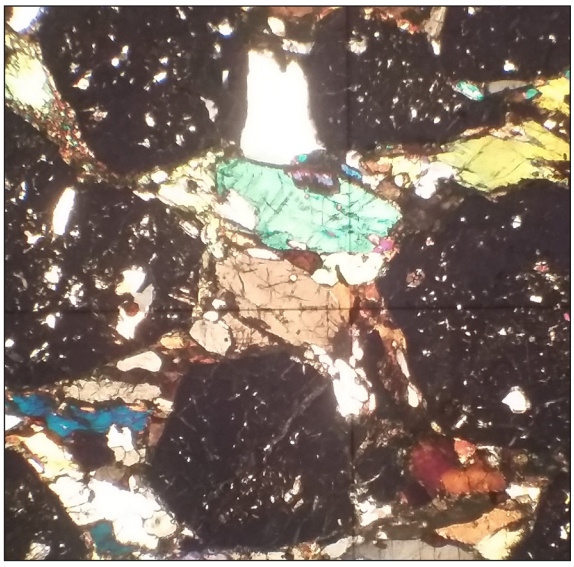

Fig. 23. Cross-polirazed light photomicrograph of the studied sample.

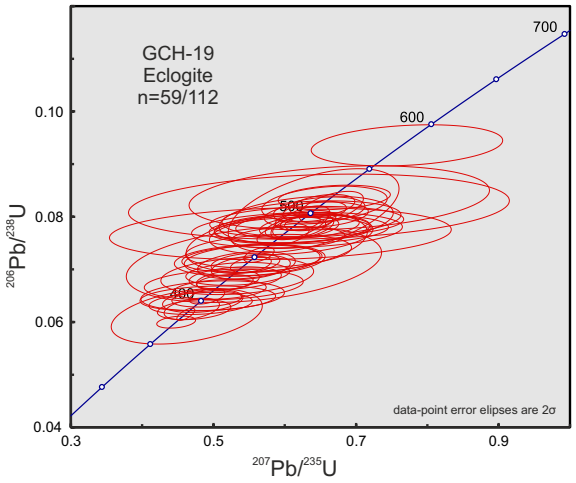

Fig. 24. U-Pb conventional concordia diagram showing U-Pb zircon analyses of the studied sample. Ellipses represent combined 2σ uncertainties of $^{206}Pb/^{238}U$ and $^{207}Pb/^{235}U$ ratios. *n*, number of analyses considered (those with 90–110% concordance)/total number of U–Pb analyses.

around 0.282812 ± 0.000110 (±2 SD) and no variation is observed between zircon grains of different ages (Fig. 27b).

U content of the analysed zircon grains is very low, in the range of 2–390 ppm (average: 32 ppm; Appx. 4). Th/U ratios vary from *c.* 0.002 to 0.7 and no variation is observed between zircon grains of different ages (Fig. 28a).

$^{176}Lu/^{177}Hf$ ratios vary from *c.* 0.0002 to 0.0013 and no variation is observed between zircon grains of different ages (Fig. 28b).

Nd whole-rock experiments failed to calculate a model-age, because the $^{147}Sm/^{144}Nd$ ratio calculated for this sample has a negative slope in the $\varepsilon Nd_{(t)}$ *v.* age plot (higher value than CHURs $^{147}Sm/^{144}Nd$ value of 0.1967; Jacobsen & Wasserburg, 1980). Epsilon value for present day is: $\varepsilon Nd_{(t=0)} = +11.9$.

7.3.1.2. Discussion

U–Pb analyses are scattered but seem to be grouped in at least three sub-subdivisions with relative abundances at 505–485, 443–424 and 402–387 Ma (Figs. 24 & 25a,b). The older ages (*i.e.* 505–485 Ma) are assumed to date the protolith magmatic crystallisation. Zircon with these ages always shows a more or less well-defined oscillatory igneous zoning, but this texture is also displayed by zircon grains with younger ages. The sub-division of zircon with ages of *c.* 443–424 Ma show well defined but also blurred oscillatory zonings, and also structure-less zonings. In some cases the structure-less zonings show diffusion patterns which are probably due to Pb-loss processes. The younger sub-division (*c.* 402–387) also show both type of zonings (oscillatory and structure-less) but in most of the cases they are structure-less or highly blurred oscillatory zonings. Rims are also found and show fainted oscillatory and structure-less zonings, but no alteration fronts are evident between the rims and the cores. Form petrological observations (absence of alteration fronts) and geochemical

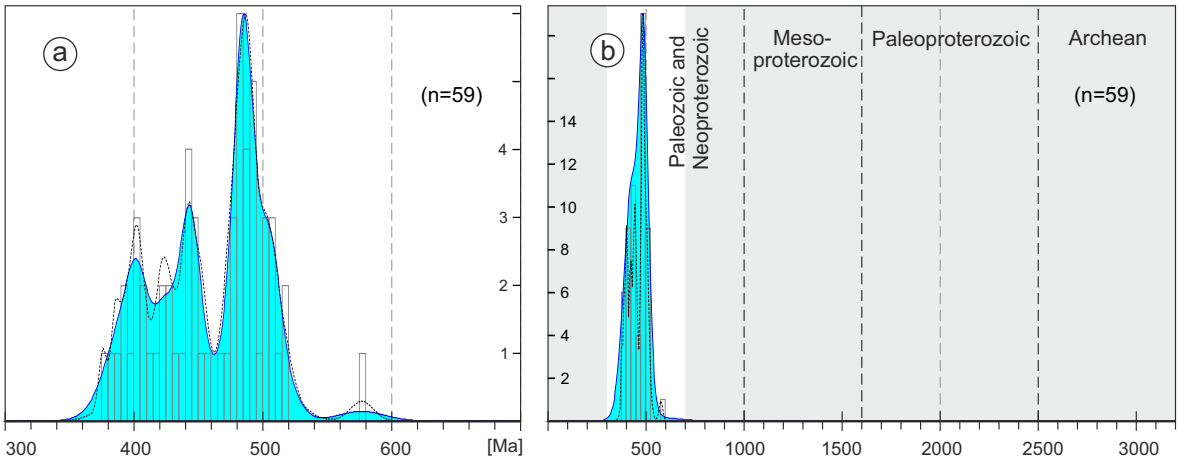

Fig. 25. Adaptative Kernel Density Estimation (aKDE, continuous line enclosing the blue area), Probability Density (PDP, black dashed line) and histogram diagrams of the U–Pb analyses (calculated with DensityPlotter5.0, Vermeesch 2012). Numbers in the vertical axis represent histogram frequency; *n*, number of analyses. **a** Partial plot representing data within a 300–700 Ma time range (bandwidth = 5 Ma, binwidth = 5 Ma). **b** Complete plot (bandwidth = 15 Ma, binwidth = 25 Ma).

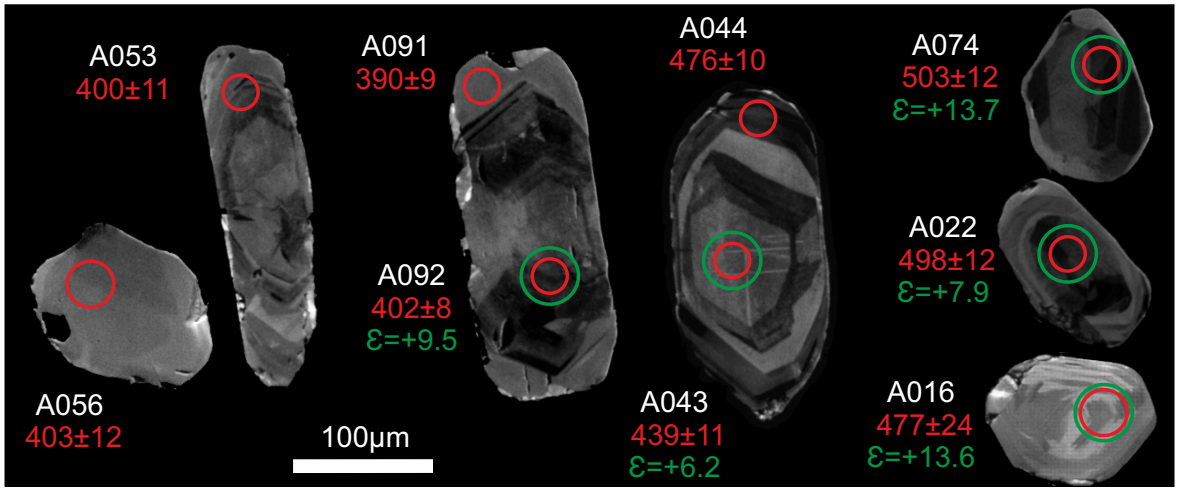

Fig. 26. CL (cathodoluminescence) images of representative zircons from the studied sample. Laser ablation pits for U–Pb analyses (red line circles) have 30 μm diameters. Laser ablation pits for Lu–Hf analyses (green line circles) have 33 μm diameters. White numbers are the reference number of the analysis, red numbers are the U–Pb age and its 2σ error (Ma) and the green numbers are the εHf values for the U–Pb age.

data (no variation of Th/U, $^{176}Lu/^{177}Hf$, $^{176}Yb/^{177}Hf$ and $^{176}Hf/^{177}Hf_{(t)}$ ratios relative to U–Pb ages), these rims were not likely formed by a dissolution-reprecipitation process (*i.e.* they are not *s.s.* overgrowths). Furthermore, this lack of isotopic ratio variations is shown by the whole sample zircon population (Figs. 27 & 28). These observations strongly suggest that a *c.* 387 Ma high-grade metamorphic event induced solid-state zircon pseudomorphic recrystallisation, triggering U–Pb age rejuvenation via Pb-loss processes of the zircon that crystallised in the gabbroic or basaltic protolith at *c.* 485 Ma. Lu–Hf analyses of all 15 concordant zircon domains yielded similar $^{176}Hf/^{177}Hf_{(t)}$ values within error of 0.282812 ± 0.000110 (±2 SD; Fig. 27b). This error is relatively high due to two analyses with slightly lower values (Fig. 27b). This data indicates that all zircon domains were formed from an isotopically almost-homogeneous source. Furthermore, Fig. 27a shows that the protolithic gabbroic-basaltic rock crystallised shortly after it was extracted from a DM source, confirming its MORB affinity (Bernard-Griffiths *et al.*, 1985; Peucat *et al.*, 1990; Gil Ibarguchi *et al.*, 1990; Mendía, 2000).

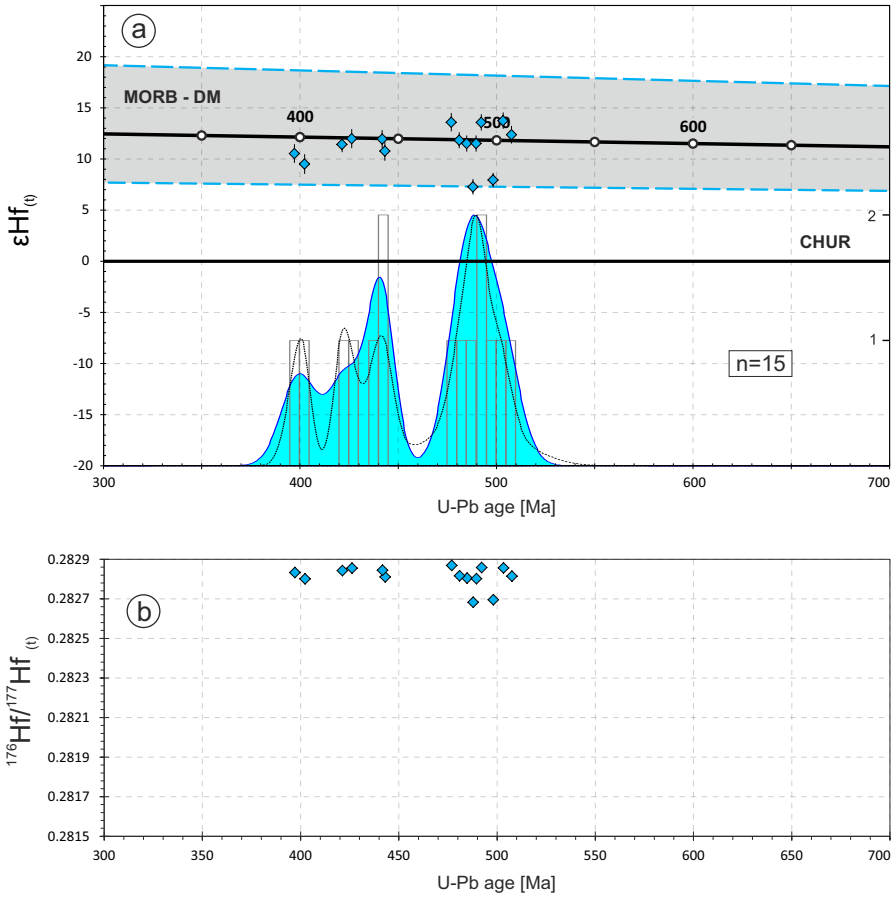

Fig. 27. a εHf *v.* age diagram. Error bars are +2σ and -2σ uncertainties. *n*, number of concordant zircon grains analysed for Lu–Hf isotopes. Numbers in the right vertical axis represent histogram frequency. Top-right rectangle shows Nd whole-rock model-age for the studied sample. MORB εHf interval was taken from Chauvel & Blichert-Toft (2001) considering a minimum $\varepsilon Hf_{(t=0Ma)}$ = +8.3 and a maximum $\varepsilon Hf_{(t=0Ma)}$ = +20.7. These values are propagated to $\varepsilon Hf_{(t=4Ga)}$ = 0 defining a grey field (enclosed by the blue discontinuous lines) around the DM-evolution trend, to provide an indication of the likely range of DM compositions through time. MORB: mid-ocean ridge basalts; DM: depleted mantle; CHUR: chondritic uniform reservoir. **b** $^{176}Hf/^{177}Hf_{(t)}$ *v.* age diagram.

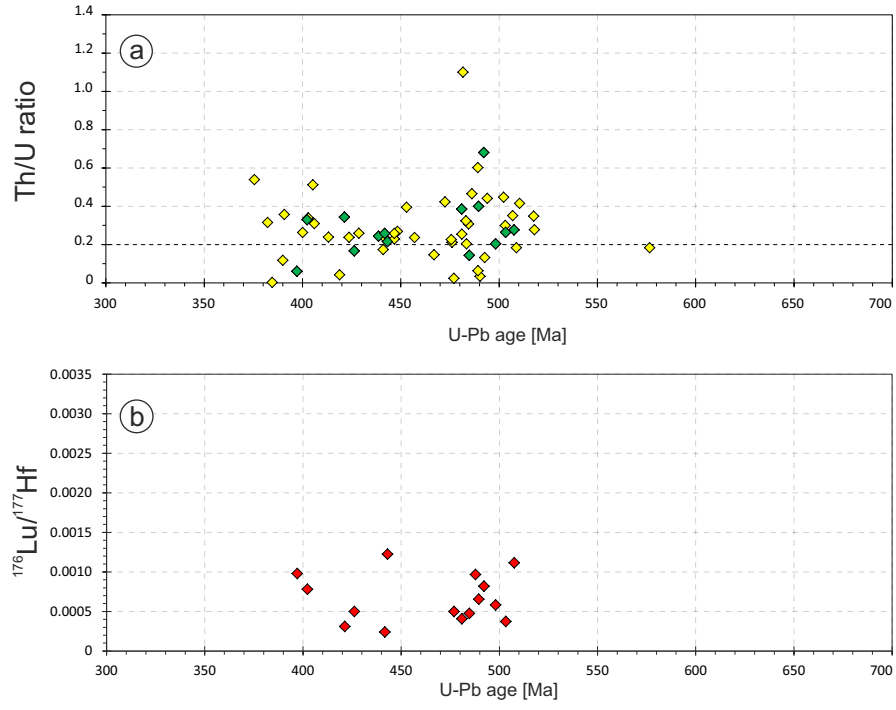

Fig. 28. a Th/U ratios *v.* age diagram (yellow rhombus represent Zrn analysed for U–Th–Pb isotopes and green rhombus represent those analysed for U–Th–Pb and Lu–Hf isotopes). **b** $^{176}Lu/^{177}Hf_{(t)}$ *v.* age diagram.

7.3.2. Sample GCH-20
(Cariño´s beach ultramafic zone eclogite)

This sample is a centimetre size eclogite boudin that outcrops within the Banded Gneiss meta-sedimentary rocks (HP–HT Upper Allochthon, Cabo Ortegal Complex). It is located in the northern part of the *Masanteo* peninsula (Appx. 1; 43°43'46.6"N, 7°52'09.3"W).

The locality or area where this sample outcrops contains the less retrograded eclogites found in the Banded Gneiss formation. The less retrograded sample collected in this area (Fig. 29; Ref: 112682) has a porphyro-nematoblastic texture and has abundant poikilitic Grt, which have colourless "dusty" cores with abundant inclusions (mainly Ap and Rt) and pink rims with less inclusions. This eclogite conserves its primary eclogitic Cpx that show exsolution lamellas and replacement of their crystal borders to weak pleochroic green Amp, with almost no development of symplectites. From a SEM study it can be approached that these Cpx are calcic, with a low Na content and that the exsolution lamellas are also Px, but with less Ca, same Na, and more Mg, Al, Fe and SiO_2 contents. Other minerals identified are Qz, Zo, Rt, Ilm, Spn, Ap, Zrn and relatively big patches of poikilitic non-oriented brown mica.

The sample gathered for isotopic experiments out of which results are presented in this section, is a retrograded eclogite compared with the above-mentioned specimen. It is a fine to medium grained rock with oriented porphyro-grano-nematoblastic texture (Ref: 113163). Its major constituents are Grt and Amp (most probably Hbl) and its minor constituents are Qz, Ap, Rt, Spn, Ilm, brown mica (very scarce) and Zrn (Fig. 30). Grt are subidioblastic to xenoblastic due to corrosion and mineral replacements. They are light pink and poikilitic, with many inclusions (mainly Qz, Rt, and Amp). Amp has a light beige-greenish colour, it is non-pleochroic (or very weakly pleochroic) and shows a moderate to a very high birefringence. They are displayed as small crystals within the matrix together with Qz, Ap, Rt, Ilm, Spn (and probably Pl), and as coarse, poikilitic xenoblastic crystals. These bigger Amp crystals are zoned, with darker borders than their cores and have inclusions of almost all types of minerals within this rock (Qz, Grt, Rt, Spn, Ap and Zrn). They also show exsolution lamellas which are too small to be identified, and show a "dirty" aspect which is more prominent in the centre of the crystals. Qz is relatively abundant and shows weak undulose extinction. It coexists with small Amp crystals, forming the matrix, defining a granoblastic amoeboid texture. Spn, Rt and Ilm are relatively abundant.

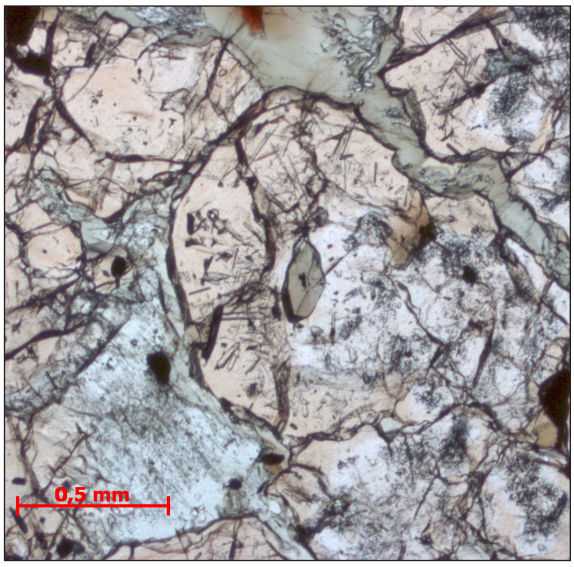

Fig. 29. Photomicrograph of the less retrograded sample.

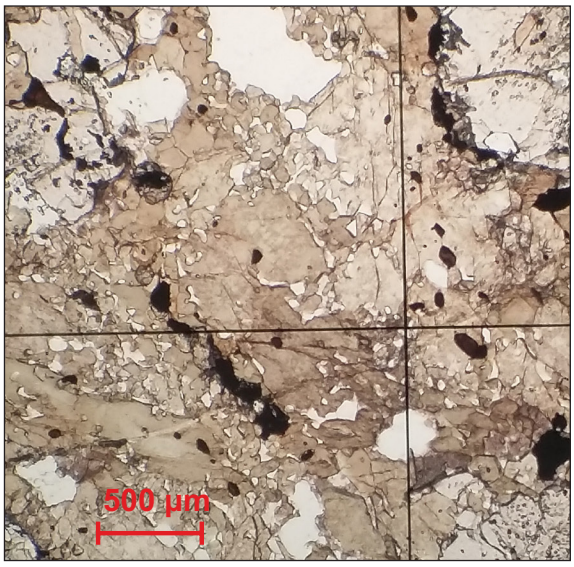

Fig. 30. Photomicrograph of the studied sample.

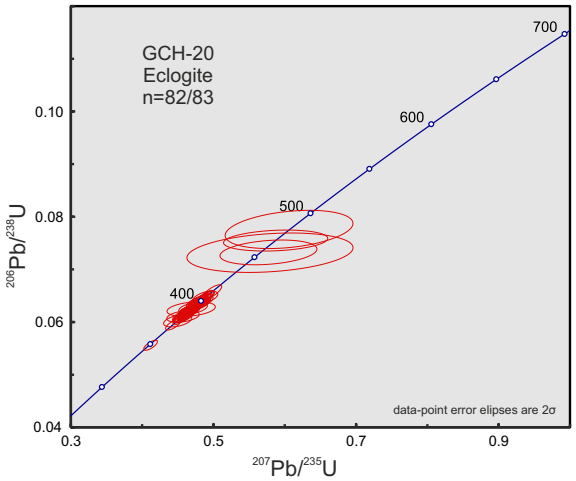

Fig. 31. U-Pb conventional concordia diagram showing U-Pb zircon analyses of the studied sample. Ellipses represent combined 2σ uncertainties of $^{206}Pb/^{238}U$ and $^{207}Pb/^{235}U$ ratios. *n*, number of analyses considered (those with 90–110% concordance)/total number of U–Pb analyses.

7.3.2.1. Results

From this sample (GCH-20), 83 U–Pb analyses were performed of which 82 were concordant (*d* = 1.2%; Figs. 31 & 32). The majority of the U–Pb ages are grouped between 372 and 410 Ma, with a maximum abundance at 390 Ma (domain II; Fig. 32a), and only three zircon grains (domain I) are older than 420 Ma.

Zircon in this sample show highly blurred and fainted dark oscillatory zonings. Most of the textures are so blurred that they can be considered structure-less. Some of the domain II (390 Ma) zircon show overgrowths, that are brighter in the CL images than their cores (they were not analysed because they are too small, *c.* 1 µm; see Fig. 33). Other zircon grains from this same group show structure-less inherited cores (Fig. 33). When zircon of this sample was hand-picked many apatites were selected. The CL images of these apatites show that their REE contents are extremely high, even higher than zircon (their images are darker than the zircon images). No internal features are observed in BSE images.

Domain II $\varepsilon Hf_{(t)}$ values are high and plot around the MORB-DM evolution trend with values between *c.* +7.7 and +12.1 (average: +10.1; Fig. 34a). Domain I $\varepsilon Hf_{(t)}$ values are also high with values of +13.0, +13.1 and +14.2 (average: +13.4; Fig. 34a). $^{176}Hf/^{177}Hf_{(t)}$ ratios for domain II zircon plot around 0.282821 ± 0.000061 (±2 SD; Fig. 34b), and $^{176}Hf/^{177}Hf_{(t)}$ ratios for domain I zircon plot at 0.282859 ± 0.000016 (±2 SD; Fig. 34b).

U content of domain II analysed zircon is very low, 111–655 ppm (average: 409 ppm). U content of domain I analysed zircon is lower than domain II zircon, 6–27 ppm (average: 16 ppm). Domain II Th/U ratios vary from *c.* 0.0002 to 0.01. Domain I Th/U ratios are higher, from *c.* 0.1 to *c.* 0.8 (average: 0.25; Fig. 35a).

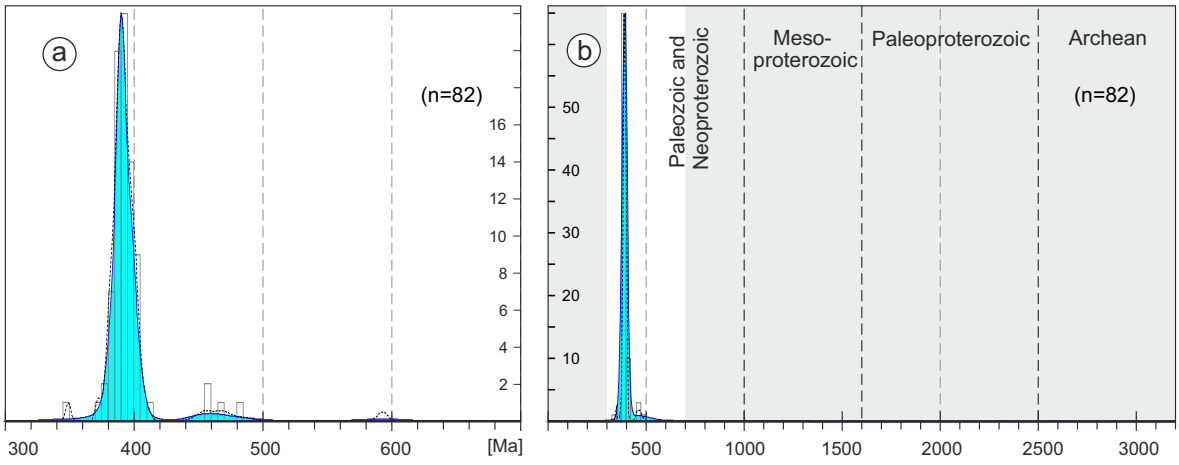

Fig. 32. Adaptative Kernel Density Estimation (aKDE, continuous line enclosing the blue area), Probability Density (PDP, black dashed line) and histogram diagrams of the U–Pb analyses (calculated with DensityPlotter5.0, Vermeesch 2012). Numbers in the vertical axis represent histogram frequency; *n*, number of analyses. **a** Partial plot representing data within a 300–700 Ma time range (bandwidth = 5 Ma, binwidth = 5 Ma). **b** Complete plot (bandwidth = 15 Ma, binwidth = 25 Ma).

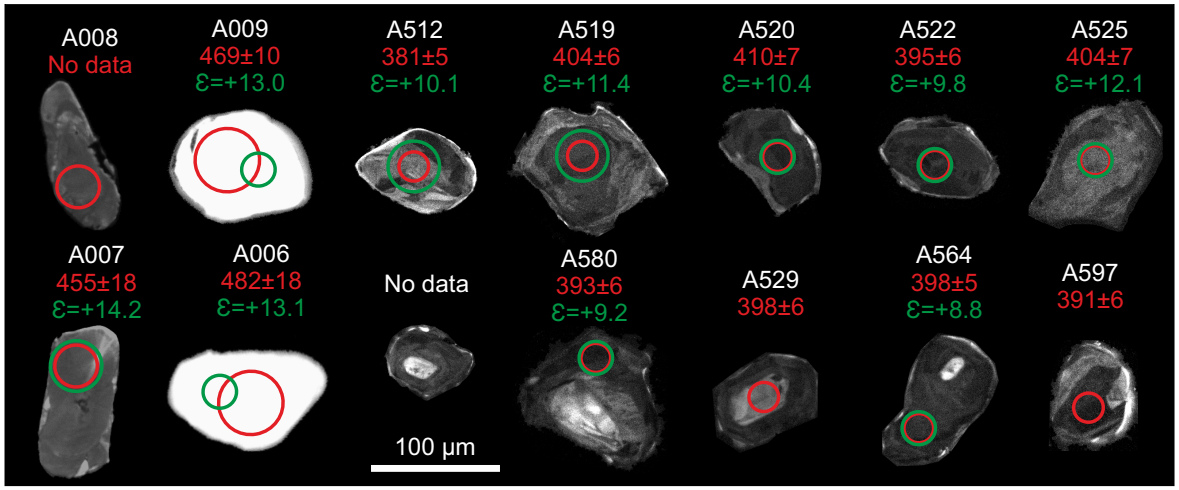

Fig. 33. CL (cathodoluminescence) images of representative zircons from the studied sample. Laser ablation pits for U–Pb analyses (red line circles) have 23, 33 and 50 μm diameters. Laser ablation pits for Lu–Hf analyses (green line circles) have 26 and 33 μm diameters. White numbers are the reference number of the analysis, red numbers are the U–Pb age and its 2σ error (Ma) and the green numbers are the εHf values for the U–Pb age. CL images of A007 and A008 were taken with different SEM parameters than the rest of the Zrn of this sample. Textures of A007 and A008 are the same than A006 and A009.

$^{176}Lu/^{177}Hf$ ratios of domain II zircon are extremely low and vary from *c.* 0.00001 to 0.00005 (Fig. 35b). $^{176}Lu/^{177}Hf$ ratios of domain I zircon are low and vary from *c.* 0.00025 to 0.00037 (Fig. 35b).

Nd whole-rock experiments failed to calculate a model-age, because the $^{147}Sm/^{144}Nd$ ratio calculated for this sample has a negative slope in the $\varepsilon Nd_{(t)}$ *v.* age plot (higher value than CHURs $^{147}Sm/^{144}Nd$ value of 0.1967; Jacobsen & Wasserburg, 1980). Epsilon value for present day is: $\varepsilon Nd_{(t=0)} = +9.4$.

7.3.2.2. Discussion

The majority of the U–Pb ages from this sample are grouped at 390 Ma (domain II; Fig. 32a), and only three zircon grains (domain I) show ages older than 420 Ma.

Domain I zircon is very scarce ($n = 3/19$; zircon analysed with U–Pb and Lu–Hf systematics) and seem to be the remnants of the magmatic protolithic zircon. This assumption is favoured by the fact that they are the older zircon grains in the sample and that they have higher Th/U ratios (from *c.* 0.1 to 0.8) than the younger domain II zircon (Fig. 35a). Their ages are 455, 469 and 482 Ma. Due to their very low U content these analysis are very poor quality and show very high errors. This is most probably due to an intense solid-state Pb-loss process triggered by the HP post-protolith metamorphism. Therefore their ages are not considered to establish a protolith age.

Domain II (*c.* 390 Ma) zircon have low U content (but higher than domain I zircon) and very low Th/U ratios (< 0.01; Fig. 35a). They have lower $^{176}Lu/^{177}Hf$ ratios (*c.* 0.00001; Fig. 35b) and also lower $^{176}Yb/^{177}Hf$ ratios (average: *c.* 0.0015; Appx. 4) than domain I zircon. $^{176}Hf/^{177}Hf_{(t)}$ ratios for all analysed zircon grains plot within error at 0.282821 ± 0.000061 (domain II) and 0.282859 ± 0.000016 (domain I; ±2 SD; Fig. 34b). These very similar $^{176}Hf/^{177}Hf_{(t)}$ ratios between domain I magmatic zircon and domain II metamorphic zircon seem to clearly indicate that domain II zircon was formed by a solid-state recrystallisation process of domain I zircon. This is due to the high immobility of Hf in Zrn, basically because Hf has the same ionic radius than Zr (155 *p*m; Hoskin & Schaltegger, 2003). The lower amount of Lu and Yb with respect to Hf and also of Th with respect of U of domain II zircon in relation to domain I zircon are explained as a consequence of the intense and extreme solid-state recrystallisation process. This process purged from the crystal structure the cations with ionic radii and chemical properties (such as oxidation state) significantly different

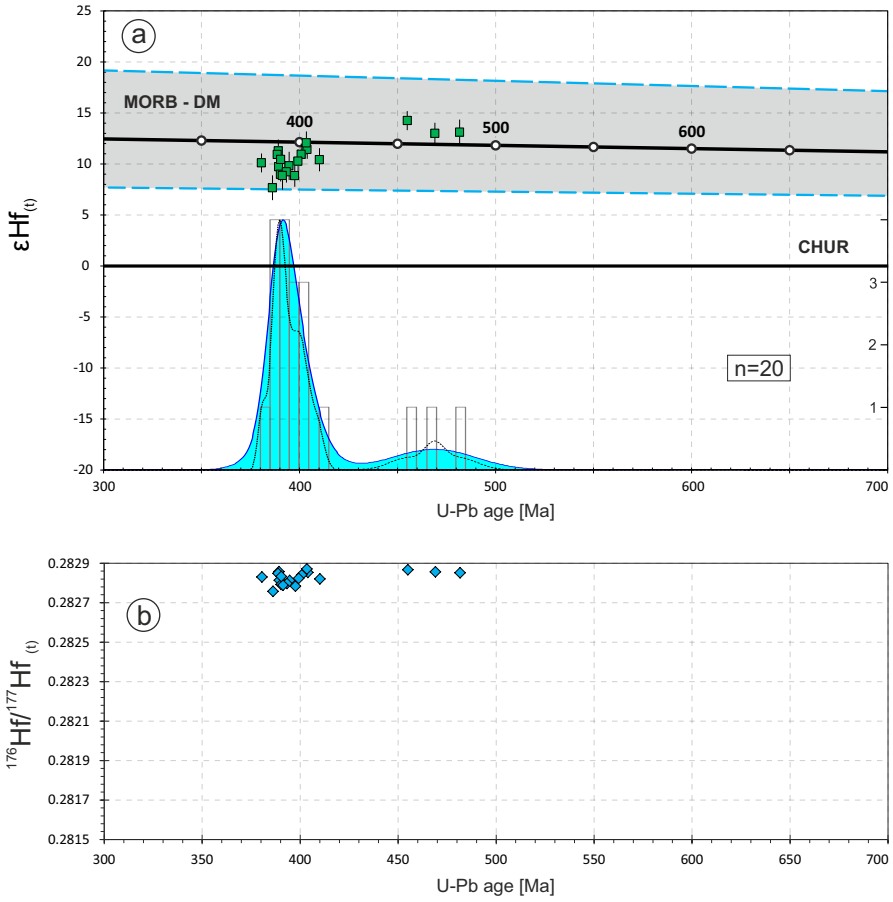

Fig. 34. a εHf *v.* age diagram. Error bars are +2σ and -2σ uncertainties. *n*, number of concordant zircon grains analysed for Lu–Hf isotopes. Numbers in the right vertical axis represent histogram frequency. Top-right rectangle shows Nd whole-rock model-age for the studied sample. MORB εHf interval was taken from Chauvel & Blichert-Toft (2001) considering a minimum $\varepsilon Hf_{(t=0Ma)}$ = +8.3 and a maximum $\varepsilon Hf_{(t=0Ma)}$ = +20.7. These values are propagated to $\varepsilon Hf_{(t=4Ga)}$ = 0 defining a grey field (enclosed by the blue discontinuous lines) around the DM-evolution trend, to provide an indication of the likely range of DM compositions through time. MORB: mid-ocean ridge basalts; DM: depleted mantle; CHUR: chondritic uniform reservoir. **b** $^{176}Hf/^{177}Hf_{(t)}$ *v.* age diagram.

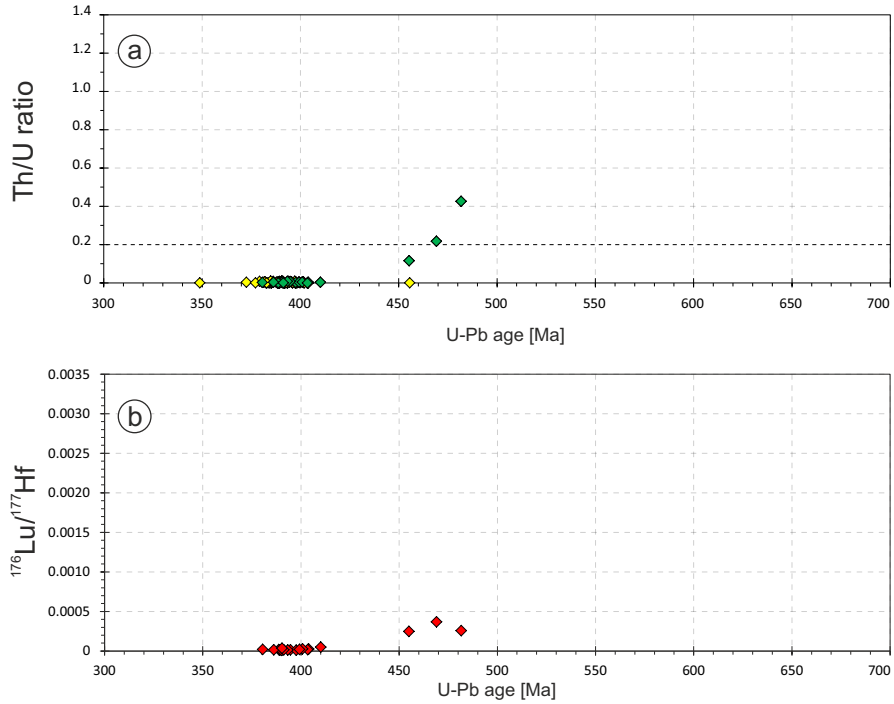

Fig. 35. a Th/U ratios *v.* age diagram (yellow rhombus represent Zrn analysed for U–Th–Pb isotopes and green rhombus represent those analysed for U–Th–Pb and Lu–Hf isotopes). **b** $^{176}Lu/^{177}Hf_{(t)}$ *v.* age diagram.

from those of Zr and Hf (Hoskin & Schaltegger, 2003).

$\varepsilon Hf_{(t)}$ values of all analysed zircon fall into the MORB-depleted mantle field. This observation strongly suggests that the protolith mafic rock was crystallised almost directly from a DM source.

The low amount of zircon grains with a protolith origin (domain I, n = 4/82; zircon only analysed with U–Pb systematics) in contrast to the high amount of zircon formed during the HP metamorphic event (domain II, n = 78/82), suggests that the HP metamorphic event induced an extreme solid-state recrystallisation of the protolith zircon in this sample. Some of the domain II metamorphic zircon conserve xenocrystic cores, which are most probably remains of the magmatic domain II zircon (see Fig. 33).

As stated in the results section when zircon from this sample was hand-picked many Ap crystals were picked by mistake. This error resembles the high amount of Ap in the sample, which from their low luminescence, appreciated from CL images, their REE contents are thought to be very high. The presence of REE enriched Ap in the sample can be explained by the Zrn REE purge triggered by solid-state recrystallisation. Phosphorus and REE are relatively abundant and they are common impurities in zircon, and when these elements were purged from the zircon structure they formed abundant Ap.

7.3.3. Sample GCH-22
(Concepenido eclogite)

This eclogite forms part of the Eclogite Band formation of the HP–HT Upper Allochthon of the Cabo Ortegal Complex, and is commonly named in the literature as the *Concepenido* eclogite, the Ky rich eclogite or the Al–Mg rich eclogite (Mendía, 2000). This sample is located in the southern part of the Cabo Ortegal Eclogite Band formation (Appx. 1; 43°40'41"N, 7°55'57"W).

This type of eclogite outcrops structurally banded. The sample studied is a *c.* 3.5 *c*m band with *c.* 0.5–1.0 *c*m sized garnets (Fig. 36). The 2 *c*m inner band has a foliated green-bluish colour matrix with Px and Ky, and the outer parts have a brownish matrix, which is probably very altered due to deformation. Both parts show idioblastic 0.5–1.0 *c*m sized garnets. These outer parts were removed before geochronology experiments (Ref: 113165).

This sample is a medium to coarse grained rock with oriented porphyro-grano-nematoblastic texture. Its major constituents are Grt, Cpx, Ky and Amp (most probably Hbl) and its minor constituents are Qz, Rt, Ap, Zo, white mica and Zrn (Fig. 37). Grt is abundant, idioblastic to subidioblastic, generally colourless to light pink, and of millimetre or even centimetre-size. It is poikilitic with Qz, Zo and Amp rich cores (other inclusions are Cpx, Ky, Rt, Ap and Opq). It has been described that needle-shaped inclusions of Rt in Grt could outline previous igneous Ti–Aug or Spn (Gil Ibarguchi *et al.*, 1990). Cpx is relatively abundant and forms elongated crystals and ribbons. It is also present as poikilitic crystals with Ky, Qz or Zo inclusions. Other than a small and non-important presence of symplectites at the rims of Cpx, no other textures formed by retrogression were found, and so this Cpx is most probably Omp. Ky is abundant, present as small sub-rounded to elongated crystals generally coherent with the foliation trend. Amp is sub-idiomorphic and is in net contact with the rest of the matrix forming minerals. White mica is poikilitic and also shows net contacts with matrix forming minerals.

7.3.3.1. Results

From this sample (GCH-22), 82 U–Pb analyses were performed of which 76 were concordant (*d* = 7.3%; Figs. 38 & 39). The U–Pb ages show a maximum abundance at 473 (domain I) and relative abundances at 482, 444 (domain I) and 395 Ma (domain II; Fig. 39a).

Most of the zircon grains in this sample conserve a sector zoning (domain I), which is interpreted as a primary igneous texture. These

Fig. 36. Hand specimen photograph of the studied sample. The specimen is *c.* 3.5 cm wide.

Fig. 37. Cross-polarized light photomicrograph of the studied sample.

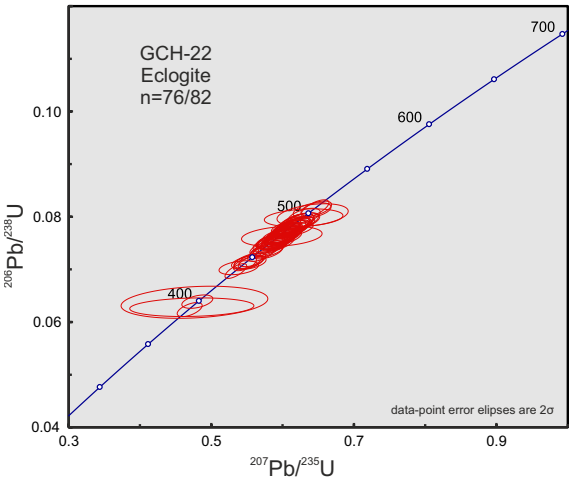

Fig. 38. U-Pb conventional concordia diagram showing U-Pb zircon analyses of the studied sample. Ellipses represent combined 2σ uncertainties of $^{206}Pb/^{238}U$ and $^{207}Pb/^{235}U$ ratios. *n*, number of analyses considered (those with 90–110% concordance)/total number of U–Pb analyses.

zircon domains have white (low U) overgrowths, texturally identical to a second type of zircon which shows an oscillatory blurred and fainted zoning (Fig. 40). These whitish zircon grains and overgrowths are considered as a second zircon type (domain II). No internal features are observed in BSE images.

Epsilon Hf values are *c.* -2 for domain I and *c.* +3 for domain II (Fig. 41a). $^{176}Hf/^{177}Hf_{(t)}$ ratios for domain I plot around 0.282461 ± 0.000019 (±2 SD) and for domain II at 0.282618 ± 0.000001 (±2 SD; Fig. 41b).

Domain I is characterised as showing a sector dark zoning, and having *c.* 450 ppm of U, *c.* 35 ppm of Pb and *c.* 0.2 Th/U ratio. Domain II has an oscillatory blurred zoning, low U (*c.* 30 ppm), low Pb (*c.* 3 ppm) and low Th/U ratios (*c.* 0.01; Fig. 42a & Appx. 4). Th/U ratios are in the range of *c.* 0.2 for domain I and *c.* 0.01 for domain II (Fig. 42a).

$^{176}Lu/^{177}Hf$ ratios are around *c.* 0.00045 for domain I and *c.* 0.00001 for domain II (Fig. 42b). $^{176}Yb/^{177}Hf$ ratios are around *c.* 0.0130 for domain I and *c.* 0.0003 for domain II (Appx. 4).

Nd whole-rock model-age is 1.10 Ga and $\varepsilon Nd_{(t)}$ values are: $\varepsilon Nd_{(t=0)} = -8.0$; $\varepsilon Nd_{(t=473)} = -2.2$.

7.3.3.2. Discussion

U–Pb analyses can be sub-divided into three groups with relative abundances at 482–473, 444 and 395 Ma. The oldest ages (*i.e.* 482–473 Ma) are assumed to be the age of protolith magmatic crystallisation. It can be argued that these zircon grains are metamorphic instead of magmatic (as already stated by Bernard-Griffiths *et al.*, 1985 and Peucat *et al.*, 1990; TIMS, U–Pb discordia line upper intercept). This is possible but highly unlikely, because their textures suggest an igneous origin and no older cores are found, and this would imply that *c.* 480 Ma zircon grains were all formed by metamorphism, which is

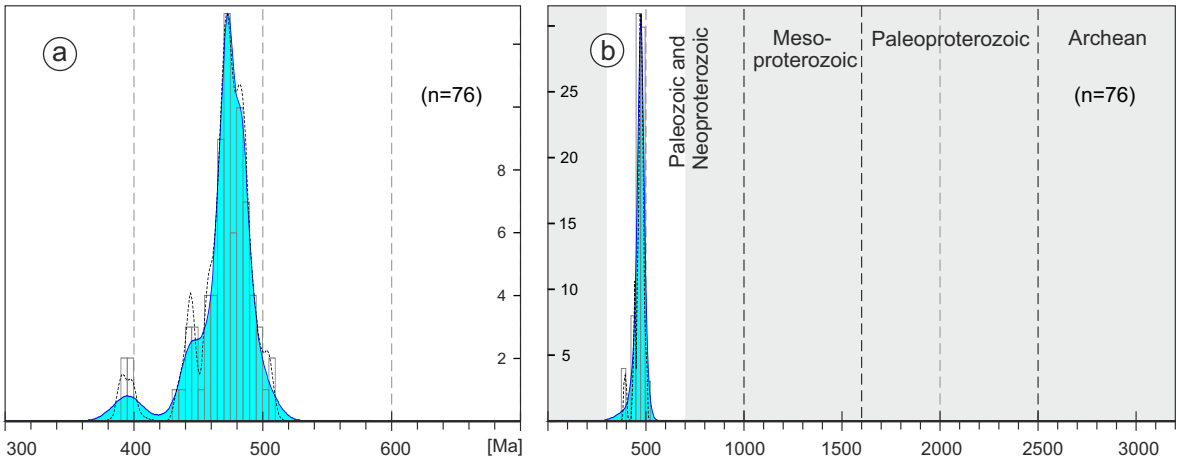

Fig. 39. Adaptative Kernel Density Estimation (aKDE, continuous line enclosing the blue area), Probability Density (PDP, black dashed line) and histogram diagrams of the U–Pb analyses (calculated with DensityPlotter5.0, Vermeesch 2012). Numbers in the vertical axis represent histogram frequency; *n*, number of analyses. **a** Partial plot representing data within a 300–700 Ma time range (bandwidth = 5 Ma, binwidth = 5 Ma). **b** Complete plot (bandwidth = 15 Ma, binwidth = 25 Ma).

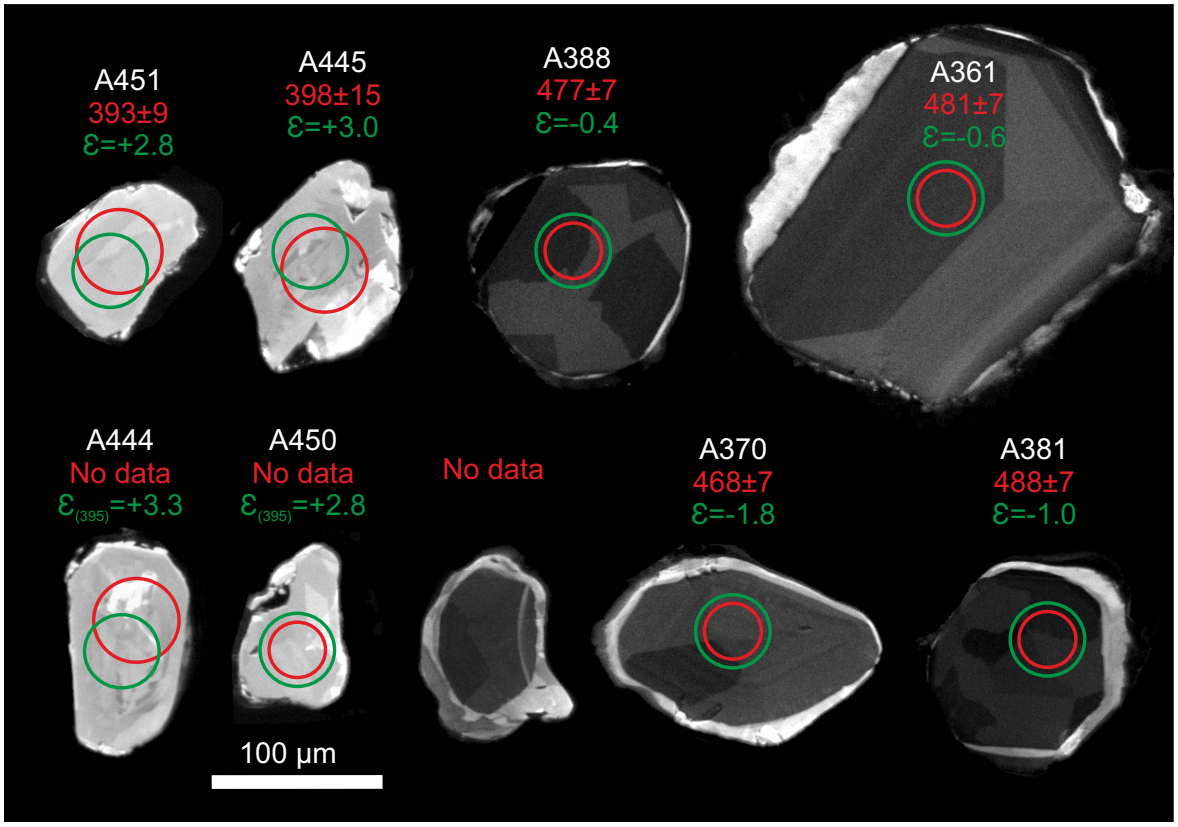

Fig. 40. CL (cathodoluminescence) images of representative zircons from the studied sample. Laser ablation pits for U–Pb analyses (red line circles) have 33 and 50 μm diameters. Laser ablation pits for Lu–Hf analyses (green line circles) have 40 μm diameters. White numbers are the reference number of the analysis, red numbers are the U–Pb age and its 2σ error (Ma) and the green numbers are the εHf values for the U–Pb age. U–Pb analysis of A444 and A450 gave a discordant ages, and εHf value was calculated for an assumed 395 Ma age.

highly improbable.

Zircon with igneous protolith ages (*i.e.* 482–473 Ma) and the zircon group with ages around 444 Ma, correspond to domain I. Lu–Hf analyses of zircon corresponding to this domain (19 concordant analyses) yielded identical $^{176}Hf/^{177}Hf_{(t)}$ within error of 0.282461 ± 0.000019 (±2 SD; Fig. 41b), indicating that these zircon grains were formed from a isotopically homogeneous source. This suggests that domain I zircon in this eclogite crystallised during a single magmatic event at *c.* 482–473 Ma. It also seems to suggest that the magmatic event lasted until *c.* 444 Ma, but this would imply a *c.* 40 Ma duration, and a timespan this long for an igneous crystallisation event is not plausible. A possible explanation (which cannot be supported with the presented data) is that a metamorphic event perhaps took place at around 444 Ma or at 395 Ma, triggering a pseudomorphic zircon alteration process without a fluid phase.

Lu–Hf analyses of zircon corresponding to domain II (4 concordant analyses out of which 2 were analysed for Lu–Hf isotopes) yielded identical $^{176}Hf/^{177}Hf_{(t)}$ within error of 0.282618 ± 0.000001 (±2 SD; Fig. 41b), showing significantly higher $^{176}Hf/^{177}Hf_{(t)}$ ratios than domain I zircon. This implies that the Lu–Hf isotopic system was disturbed during the *c.* 395 Ma zircon crystallisation event. If the rock system did not remain closed this disruption could be due to mixing with external sources with a different Lu–Hf composition. Taking into account that no veins or leucosomes are found in this eclogite it is assumed that the rock system remained closed. If this is true, the higher $^{176}Hf/^{177}Hf_{(t)}$ requires that domain II incorporated additional radiogenic hafnium (^{176}Hf) at its formation. This ^{176}Hf comes from ^{176}Lu decay. Much of the ^{176}Lu remained in the matrix when the protolith

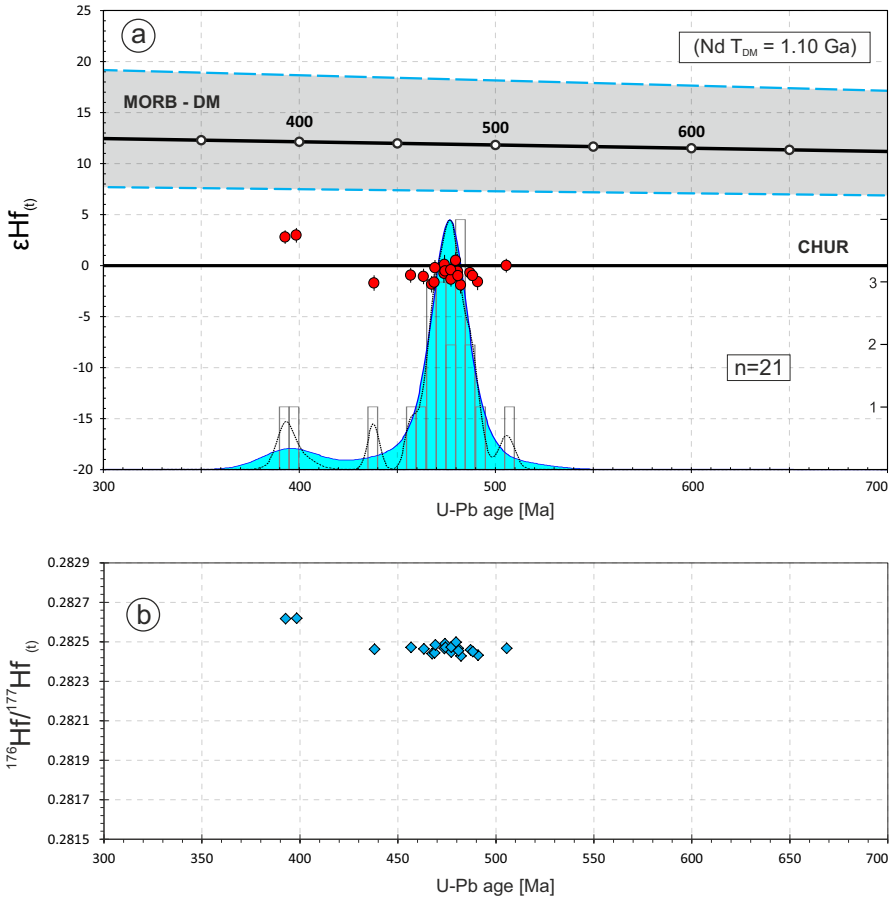

Fig. 41. a εHf *v.* age diagram. Error bars are +2σ and -2σ uncertainties. *n*, number of concordant zircon grains analysed for Lu–Hf isotopes. Numbers in the right vertical axis represent histogram frequency. Top-right rectangle shows Nd whole-rock model-age for the studied sample. MORB εHf interval was taken from Chauvel & Blichert-Toft (2001) considering a minimum $\varepsilon Hf_{(t=0Ma)}$ = +8.3 and a maximum $\varepsilon Hf_{(t=0Ma)}$ = +20.7. These values are propagated to $\varepsilon Hf_{(t=4Ga)}$ = 0 defining a grey field (enclosed by the blue discontinuous lines) around the DM-evolution trend, to provide an indication of the likely range of DM compositions through time. MORB: mid-ocean ridge basalts; DM: depleted mantle; CHUR: chondritic uniform reservoir. **b** $^{176}Hf/^{177}Hf_{(t)}$ *v.* age diagram.

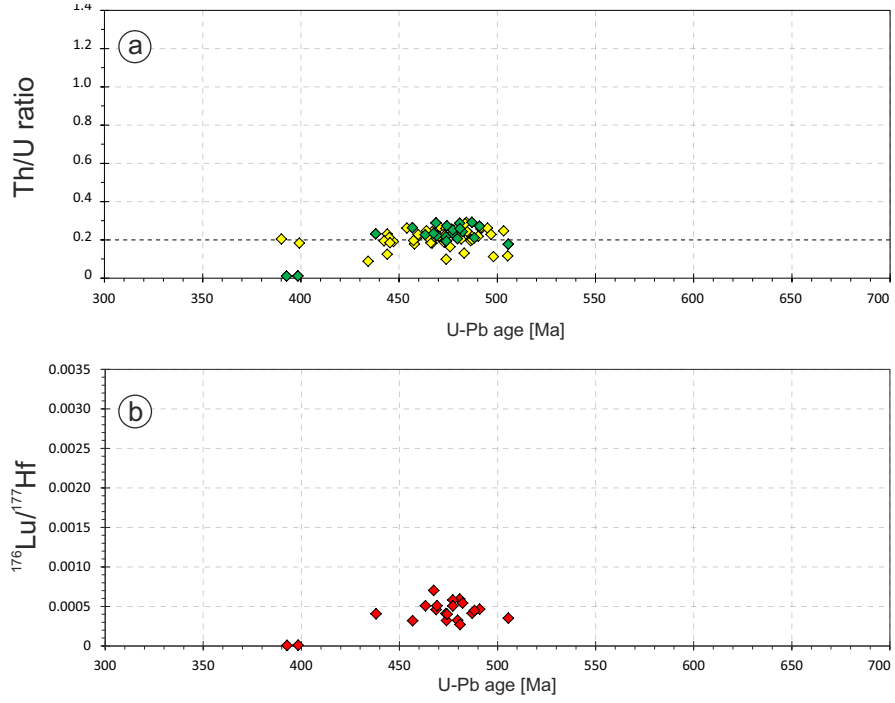

Fig. 42. a Th/U ratios *v.* age diagram (yellow rhombus represent Zrn analysed for U–Th–Pb isotopes and green rhombus represent those analysed for U–Th–Pb and Lu–Hf isotopes). **b** $^{176}Lu/^{177}Hf_{(t)}$ *v.* age diagram.

of this rock crystallised (the majority of the available Hf in a melt is incorporated into zircon, and Lu into other minerals, *i.e.* the matrix). So, the only way in which these domain II zircon achieved its higher $^{176}Hf/^{177}Hf_{(t)}$ is growing in equilibrium with the matrix at *c.* 395 Ma, assisted by a melt phase (another way is a solid state Hf isotope exchange between matrix and domain II, a very unlikely possibility owing the grate and proofed immobility of Hf in zircon, Hoskin & Schaltegger, 2003; Gerdes & Zeh, 2009 and that no inter-element isotopic fractionation is expected). The geological event in which this could happen is most probably the high-grade metamorphism that transformed the basic rock into an eclogite. This interpretation is favoured by the low $^{176}Lu/^{177}Hf$, $^{176}Yb/^{177}Hf$ and Th/U ratios of the *c.* 395 Ma (domain II) zircon (Fig. 42a,b & Appx. 4). These low ratios require that domain II zircon grew together with, or subsequent to, a HREE and Th fractionating phase, most probably metamorphic garnet (Zeh *et al.* 2010). These low ratios can also be achieved by over-growing domain II Zrn from a depleted Th and HREE fluid phase. This scenario is not expected because the first fluids to form should be enriched in these incompatible elements.

As commented in section 7.3, the protolith of this rock was a cumulate of troctolite composition. This composition, very differentiated from a normal gabbroic composition, explains why the magmatic crystallisation age is younger (*c.* 482–473 Ma) than of those co-genetic eclogites with gabbroic protoliths (eclogite GCH-19; *c.* 505–485 Ma).

7.3.4. Sample GCH-23
(Da Moura eclogite)

This sample is located in the northern part of the *Masanteo* peninsula, at *Punta da Moura* (Appx. 1; 43°43'28.7"N, 7°51'20.0"W).

This eclogite forms part of the Banded Gneiss formation mafic rocks. Together with the orthogneiss sample GCH-14 (section 7.4.5) this eclogite constitutes the *Punta da Moura* mingling suite. Field observations suggest that this eclogite was intruded by the orthogneiss (Fig. 43).

This sample is a fine to medium grained rock with oriented porphyro-grano-nematoblastic texture (Ref: 113166). Its major constituents are Grt and Amp (most probably Hbl) and its minor constituents are Qz, Rt, Spn, Ilm, Ap, Pl, Bt or Phl (very scarce) and Zrn (Fig. 44). Grt is xenoblastic due to corrosion and mineral replacements. It is light pink and poikilitic, with many inclusions (mainly Qz and Rt). Amp is beige-brown to green, pleochroic and shows a "dirty" aspect. It is zoned, with darker brown coloured rims, and it is poikilitic, with inclusions of almost all types of minerals within this rock (Qz, Grt, Bt, Spn, Rt, and Zrn). These observations are explained as to be probably due to replacement of the primary eclogitic Cpx to Amp. Amp is also non-poikilitic, displayed as small crystals defining the matrix together with Qz (and probably feldspar). Qz is relatively abundant and has weak undulose extinction. It coexists with small Amp crystals, forming the matrix, defining a granoblastic amoeboid texture. It is also displayed as tabular aggregates coherent with the foliation trend. Spn, Rt and Ilm are relatively abundant.

7.3.4.1. Results

From this sample (GCH-23), 47 U–Pb analyses were performed of which 40 were concordant (*d* = 14.9%; Figs. 45 & 46). The U–Pb ages show two maximum abundance peaks at 508 and 489 Ma and relative abundances at 526 and 469 Ma (Fig. 46).

Most of the zircon in this sample shows convoluted zonings and only in few crystals an oscillatory zoning can be observed, which is always fainted and not well defined (Fig. 47). No internal features are observed in BSE images, other than a relatively high amount of inclusions in the zircon grains.

Epsilon Hf values vary from -5.3 to +7.4, and the majority of them are around +4.8 ± 3.0 (±2 SD; Fig. 48a & Appx. 4). $^{176}Hf/^{177}Hf_{(t)}$ ratios plot around 0.282581 ± 0.000200 (±2 SD) and the majority of them plot around 0.282613 ± 0.000074 (±2 SD; Fig. 48b).

Fig. 43. Field photograph of the studied sample. The hammer is 40.6 cm long.

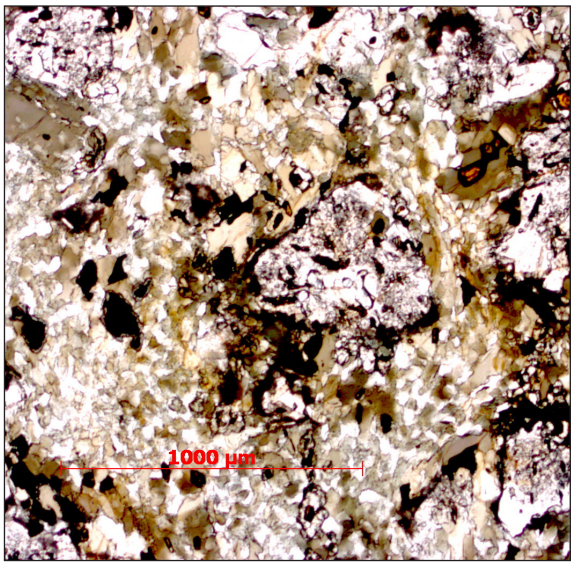

Fig. 44. Photomicrograph of the studied sample.

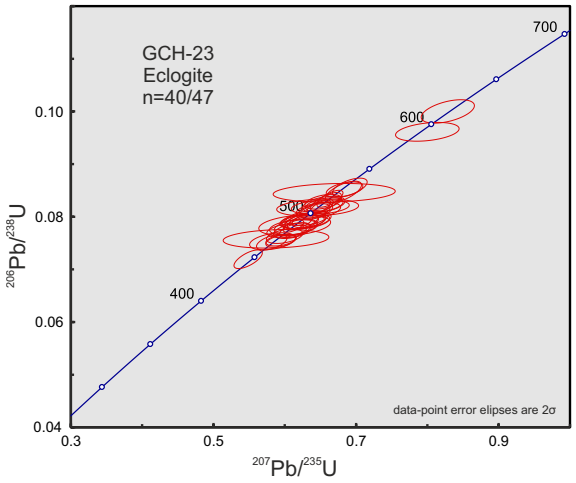

Fig. 45. U-Pb conventional concordia diagram showing U-Pb zircon analyses of the studied sample. Ellipses represent combined 2σ uncertainties of $^{206}Pb/^{238}U$ and $^{207}Pb/^{235}U$ ratios. *n*, number of analyses considered (those with 90–110% concordance)/total number of U–Pb analyses.

Zircon in this sample have around 309 ppm of U (minimum: 23, maximum: 1347), and around 32 ppm of Pb (minimum: 3, maximum: 156; Appx. 4). Th/U ratios are always higher than 0.2 and vary from 0.28 to 9.17 (average: 1.22; Fig. 49a).

$^{176}Lu/^{177}Hf$ ratios vary from 0.00028 to 0.00161 (average: 0.00080; Fig. 49b). $^{176}Yb/^{177}Hf$ ratios vary from 0.0071 to 0.0529 (average: 0.0239; Appx. 4).

Nd whole-rock model-age is 0.78 Ga and $\varepsilon Nd_{(t)}$ values are: $\varepsilon Nd_{(t=0)} = +2.1$; $\varepsilon Nd_{(t=508)} = +4.8$.

7.3.4.2. Discussion

U–Pb analyses can be sub-divided into two major groups with abundance peaks at *c.* 508 and *c.* 489 Ma. Another two minor subdivisions can be observed with peaks at *c.* 526 and *c.* 469 Ma. Fig. 47 shows the textures of 20 crystals, from where it is observed a generalised development of convoluted bright zonings and diffuse and blurred oscillatory dark zonings. The processes that developed these two types of textures could not be dated because U–Pb ages from the analyses taken from each of the texture types could not distinguish two discrete ages. Nevertheless one crystal gave an age of 507 ± 6 Ma on its dark and fainted oscillatory side and an age of 486 ± 9 Ma on its light convoluted side (A141 and A140 respectively; Fig. 47). Taking into account that this mafic rock outcrops together with a *c.* 500 Ma orthogneiss (GCH-14, section 7.4.5) and that both lithologies outcrop together with field relationships interpreted as a mingling process between them, the dark fainted oscillatory zonings seem to be related to the protolith magmatic formation of this mafic rock at *c.* 508 Ma, and the light convoluted textures seem to be related to a high temperature input alteration, triggered by the *c.* 500 Ma felsic intrusion into the mafic rock that ultimately formed the mingling related structures. This temperature input seems to be responsible for the formation of the light

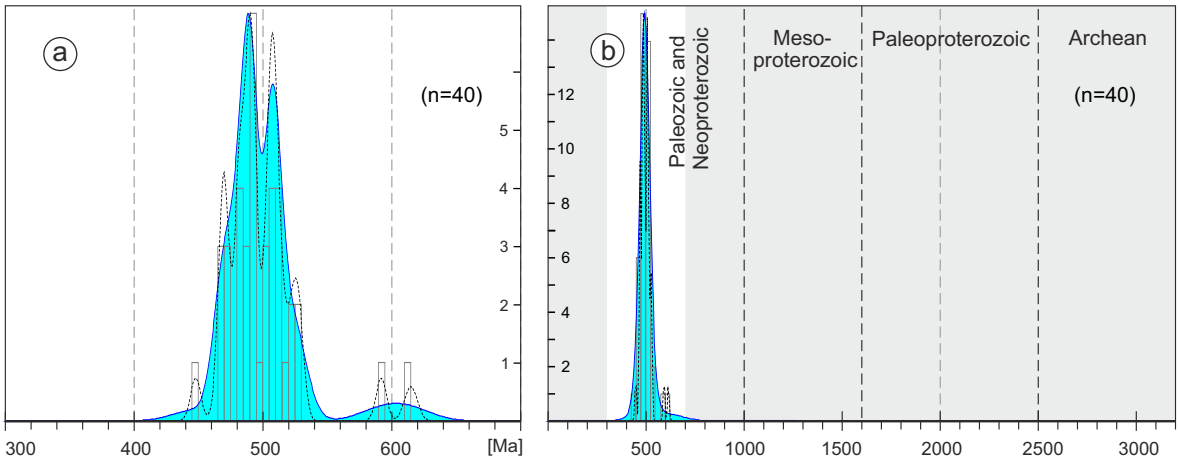

Fig. 46. Adaptative Kernel Density Estimation (aKDE, continuous line enclosing the blue area), Probability Density (PDP, black dashed line) and histogram diagrams of the U–Pb analyses (calculated with DensityPlotter5.0, Vermeesch 2012). Numbers in the vertical axis represent histogram frequency; *n*, number of analyses. **a** Partial plot representing data within a 300–700 Ma time range (bandwidth = 5 Ma, binwidth = 5 Ma). **b** Complete plot (bandwidth = 15 Ma, binwidth = 25 Ma).

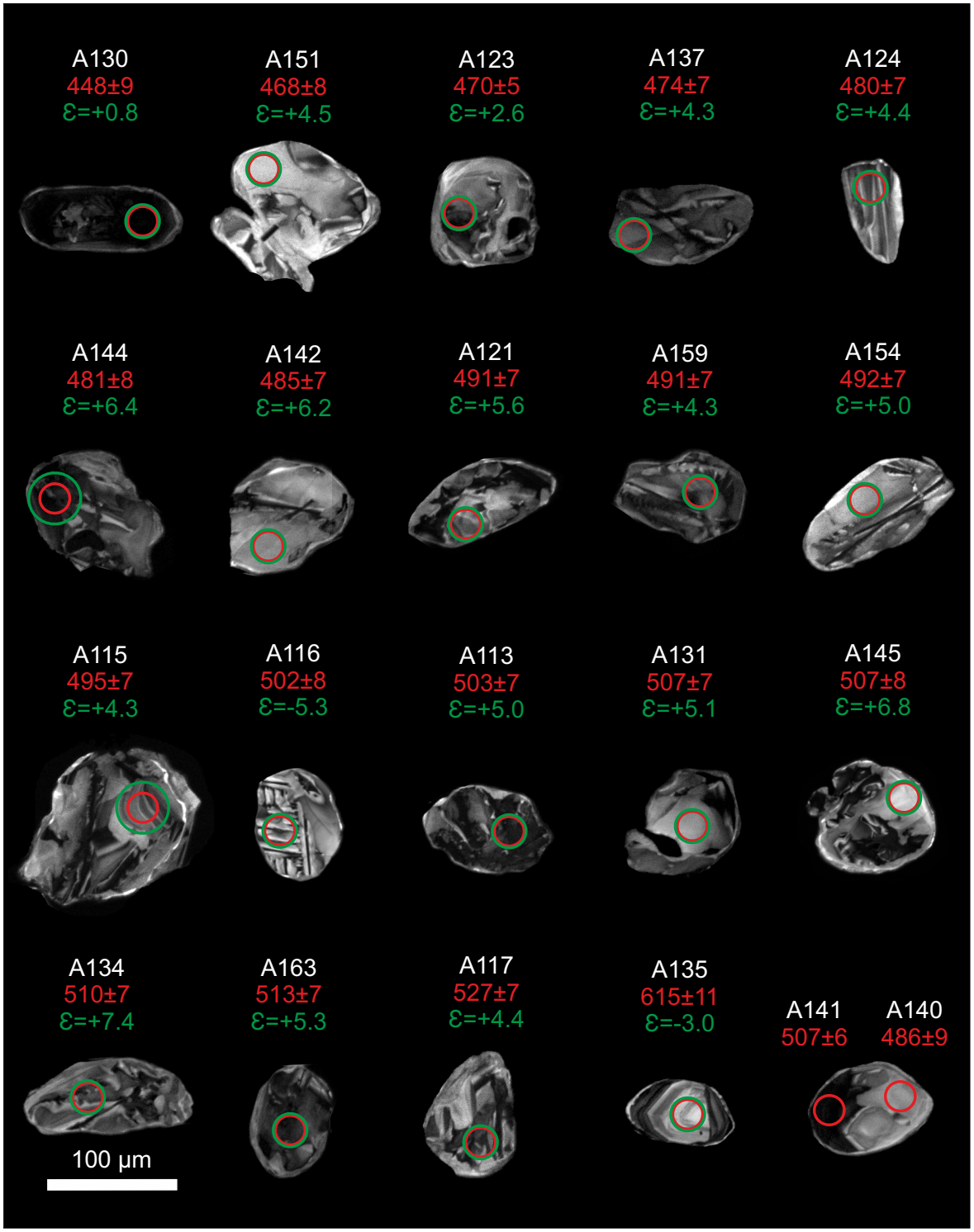

Fig. 47. CL (cathodoluminescence) images of representative zircons from the studied sample. Laser ablation pits for U–Pb analyses (red line circles) have 23 μm diameters. Laser ablation pits for Lu–Hf analyses (green line circles) have 26 and 40 μm diameters. White numbers are the reference number of the analysis, red numbers are the U–Pb age and its 2σ error (Ma) and the green numbers are the εHf values for the U–Pb age.

convoluted zonings at *c.* 489 Ma.

$^{176}Lu/^{177}Hf$, $^{176}Yb/^{177}Hf$, $^{176}Hf/^{177}Hf_{(t)}$ and Th/U ratios do not show any variation related with U–Pb age variations (Figs. 48b, 49a,b & Appx. 4).

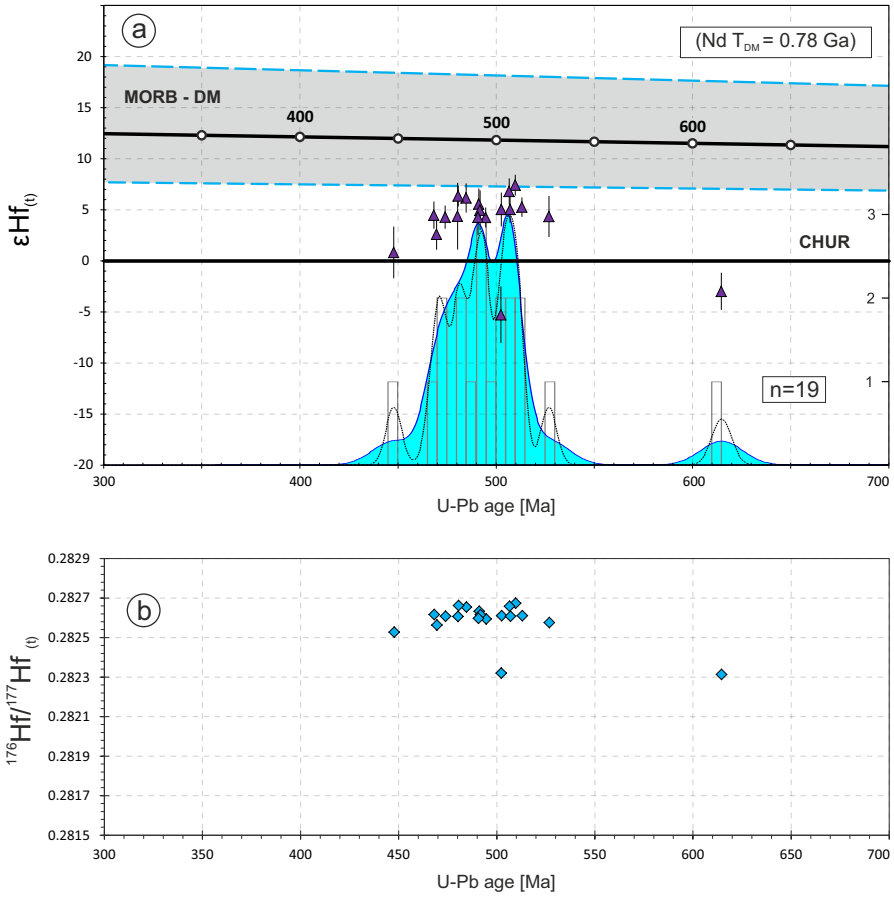

Fig. 48. a εHf *v.* age diagram. Error bars are +2σ and -2σ uncertainties. *n*, number of concordant zircon grains analysed for Lu–Hf isotopes. Numbers in the right vertical axis represent histogram frequency. Top-right rectangle shows Nd whole-rock model-age for the studied sample. MORB εHf interval was taken from Chauvel & Blichert-Toft (2001) considering a minimum $\varepsilon Hf_{(t=0Ma)}$ = +8.3 and a maximum $\varepsilon Hf_{(t=0Ma)}$ = +20.7. These values are propagated to $\varepsilon Hf_{(t=4Ga)}$ = 0 defining a grey field (enclosed by the blue discontinuous lines) around the DM-evolution trend, to provide an indication of the likely range of DM compositions through time. MORB: mid-ocean ridge basalts; DM: depleted mantle; CHUR: chondritic uniform reservoir. **b** $^{176}Hf/^{177}Hf_{(t)}$ *v.* age diagram.

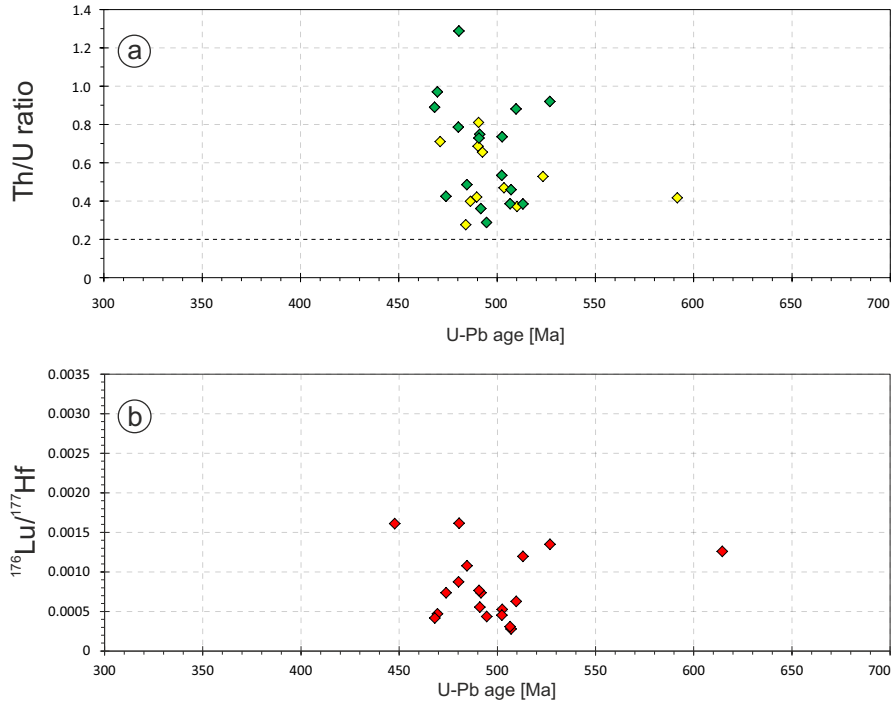

Fig. 49. a Th/U ratios *v.* age diagram (yellow rhombus represent Zrn analysed for U–Th–Pb isotopes and green rhombus represent those analysed for U–Th–Pb and Lu–Hf isotopes). **b** $^{176}Lu/^{177}Hf_{(t)}$ *v.* age diagram.

These observations lead one to conclude that the convoluted light zonings were not formed by a dissolution-recrystallisation process but by a pseudomorphic alteration and most likely with no presence of fluid phases.

7.4. Orthogneisses

In order to investigate the felsic magmatic activity of the Neoproterozoic–Cambrian magmatic arc system, six orthogneisses from the Banded Gneiss formation were studied. Five orthogneisses outcrop at the northern coast of the *Masanteo* peninsula and one from the southern coast (see locations for each sample; Appx. 1).

The nature of these orthogneisses, on the basis of field observations, is thought to be intrusive instead of being the result of a huge leucosomatic production. Studying these rocks will provide important information about the age of crystallisation, the nature of the sources and the development of the felsic igneous activity of the magmatic arc that was built at the margin of Gondwana in the Neoproterozoic–Cambrian.

7.4.1. Sample GCH-01
(Cariño´s beach ultramafic zone orthogneiss)

This sample was collected from the northern coast of the *Masanteo* peninsula (Appx. 1; 43°43'46.6"N, 7°52'07.5"W).

This orthogneiss outcrops as a *c.* 30 centimetre-thick leucocratic felsic rock within the metasedimentary rocks. It is displayed as a boudin wrapped by the metasedimentary rocks with strong regional foliation development (Fig. 50). It shows a different and younger foliation than the regional one. It outcrops at the northern coast of the *Masanteo* peninsula, in the same outcrop as eclogite GCH-20 (section 7.3.2) and the metasedimentary rock GCH-02 (chapter 6).

From microscopic observations this sample has a porphyro-granoblastic texture (Fig. 51; Ref: 112973). Grt porphyroblasts are colourless, subidioblastic and poikilitic, with a high amount of inclusions within their cores (Qz, Chl and Ap). The matrix is formed by Qz, Afs, Pl and small Grt. The grain sizes are varied. Qz, Afs and Pl are displayed as small crystals with straight grain boundaries and triple junctions (granoblastic polygonal texture) but also as bigger crystals with irregular grain boundaries. Other constituents are Zrn, Ap, Chl, Rt and Ilm.

7.4.1.1. Results

From this sample (GCH-01), 165 U–Pb analyses were performed of which 140 were concordant (*d* = 12.1%; Figs. 52 & 53). The U–Pb ages show two maximum abundance peaks at 496 (domain I, zircon age range between 518 and 466 Ma) and 402 Ma (domain II, zircon age range between 410 and 381 Ma; Fig. 53). 16 analyses gave ages between *c.* 700 and *c.* 540 Ma; and three analyses gave Paleoproterozoic ages.

Domain I zircon (*c.* 500 Ma) shows oscillatory and multi-faceted ("soccerball") habits (Fig. 54). These zircon grains are normally surrounded by very bright rims (interpreted as alteration fronts), which have not been analysed due to spatial resolution issues, and another rim, which is darker from CL images than the previous bright rim and domain I zircon. This darker rim is associated with domain II zircon (*c.* 400 Ma). Domain II shows badly defined faded oscillatory zonings. Some zircon grains have dark cores with patchy or chaotic textures, which in BSE images show a high amount of inclusions (Fig. 54).

With the exception of one domain II analysis (A456; 401 Ma; $\varepsilon Hf_{(t)}$ = -7.5) and analyses from zircon with older ages than 540 Ma (which are considered inheritances), all zircon have positive $\varepsilon Hf_{(t)}$ values(Fig. 55a). All domain I zircon plot

Fig. 50. Field photograph of the studied sample. The hammer is 40.6 cm long.

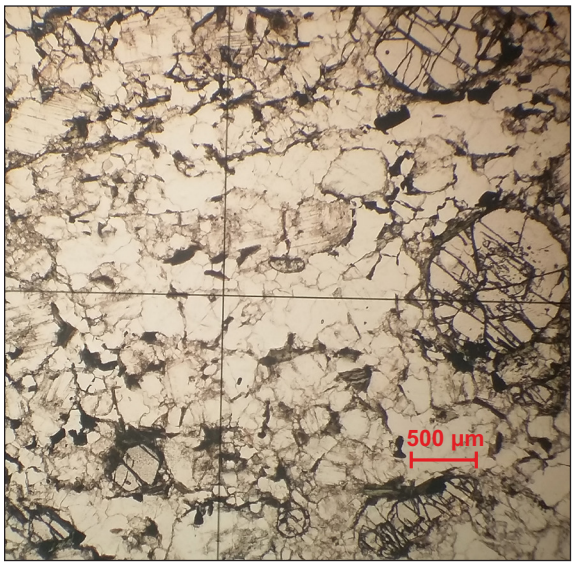

Fig. 51. Phtomicrograph of the studied sample.

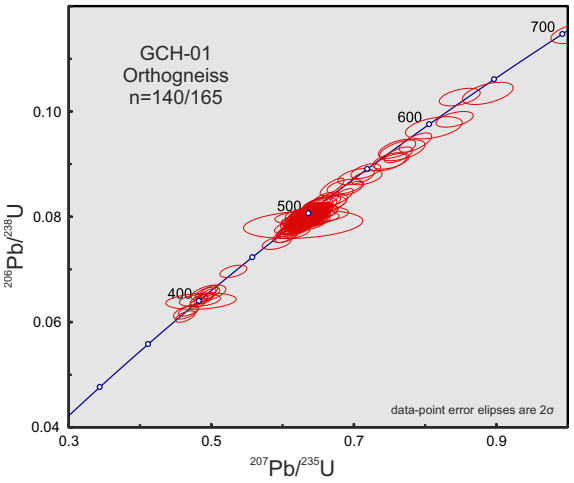

Fig. 52. U-Pb conventional concordia diagram showing U-Pb zircon analyses of the studied sample. Ellipses represent combined 2σ uncertainties of $^{206}Pb/^{238}U$ and $^{207}Pb/^{235}U$ ratios. *n*, number of analyses considered (those with 90–110% concordance)/total number of U–Pb analyses.

within the MORB-depleted mantle field, with $\varepsilon Hf_{(t)}$ values between +7.9 and +11.6. Domain II $\varepsilon Hf_{(t)}$ values are slightly lower than domain I $\varepsilon Hf_{(t)}$ values, with values between +6.8 and +8.3 (Fig. 55a & Appx. 4). $^{176}Hf/^{177}Hf_{(t)}$ ratios for all zircon grains (without considering the above-mentioned exceptions) plot around 0.282745 ± 0.000052 (±2 SD; Fig. 55b).

Domain I zircon has around 255 ppm of U (minimum: 95, maximum: 683) and around 21 ppm of Pb (minimum: 8, maximum: 58). Domain II zircon has higher values, with around 834 ppm of U (minimum: 139, maximum: 1897; and one zircon grain with 42 ppm) and around 51 ppm of Pb (minimum: 11, maximum: 128; and one Zrn with 3 ppm; Appx. 4). All domain I analyses have Th/U ratios higher than 0.2, and vary from 0.23 to 1.00 (average: 0.42; Fig. 56a). The majority of domain II analyses have Th/U ratios lower than 0.2, and vary from 0.003 to 0.62 (average: 0.08; Fig. 56a).

$^{176}Lu/^{177}Hf$ ratios for domain I zircon are higher than 0.00100 and $^{176}Lu/^{177}Hf$ ratios for domain II zircon are lower (with some exceptions) than 0.00013 (Fig. 56b). $^{176}Yb/^{177}Hf$ ratios for domain I zircon plot around *c.* 0.0529, and those for domain II are much lower and plot around *c.* 0.0048 (Appx. 4).

Nd whole-rock model-age is 0.76 Ga and $\varepsilon Nd_{(t)}$ values are: $\varepsilon Nd_{(t=0)} = +4.3$; $\varepsilon Nd_{(t=496)} = +5.7$.

7.4.1.2. Discussion

U–Pb analyses can be sub-divided into two groups, domain I with a maximum abundance age peak at 496 Ma and domain II with a maximum abundance age peak at 402 Ma. Other older analyses (16 between *c.* 700 and 540 Ma and other three Paleoproterozoic) are considered inheritances. Zircon corresponding to domain I show combined oscillatory and multi-faceted or sector ("soccerball") textures (Fig. 54). Bright lobulated sinuous small rims

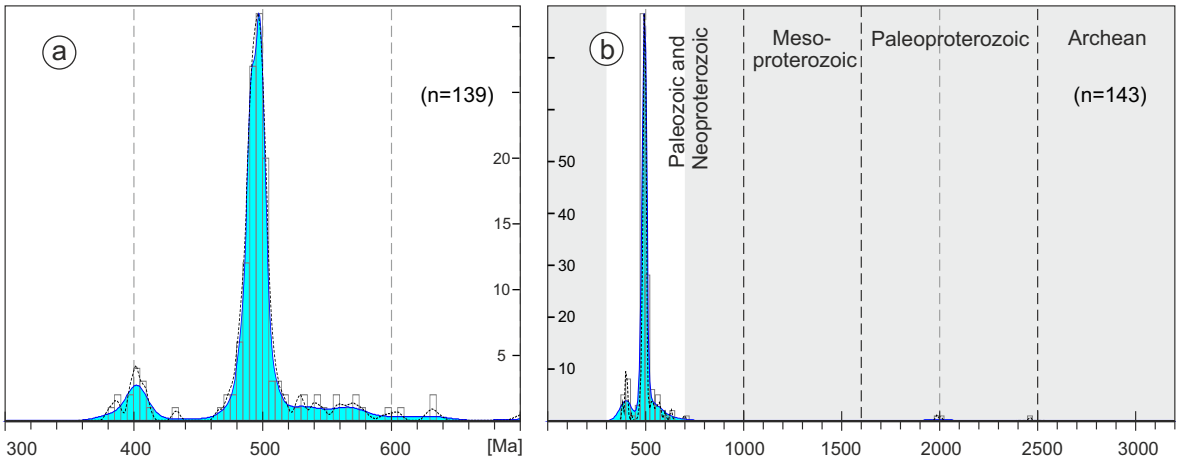

Fig. 53. Adaptative Kernel Density Estimation (aKDE, continuous line enclosing the blue area), Probability Density (PDP, black dashed line) and histogram diagrams of the U–Pb analyses (calculated with DensityPlotter5.0, Vermeesch 2012). Numbers in the vertical axis represent histogram frequency; *n*, number of analyses. **a** Partial plot representing data within a 300–700 Ma time range (bandwidth = 5 Ma, binwidth = 5 Ma). **b** Complete plot (bandwidth = 15 Ma, binwidth = 25 Ma).

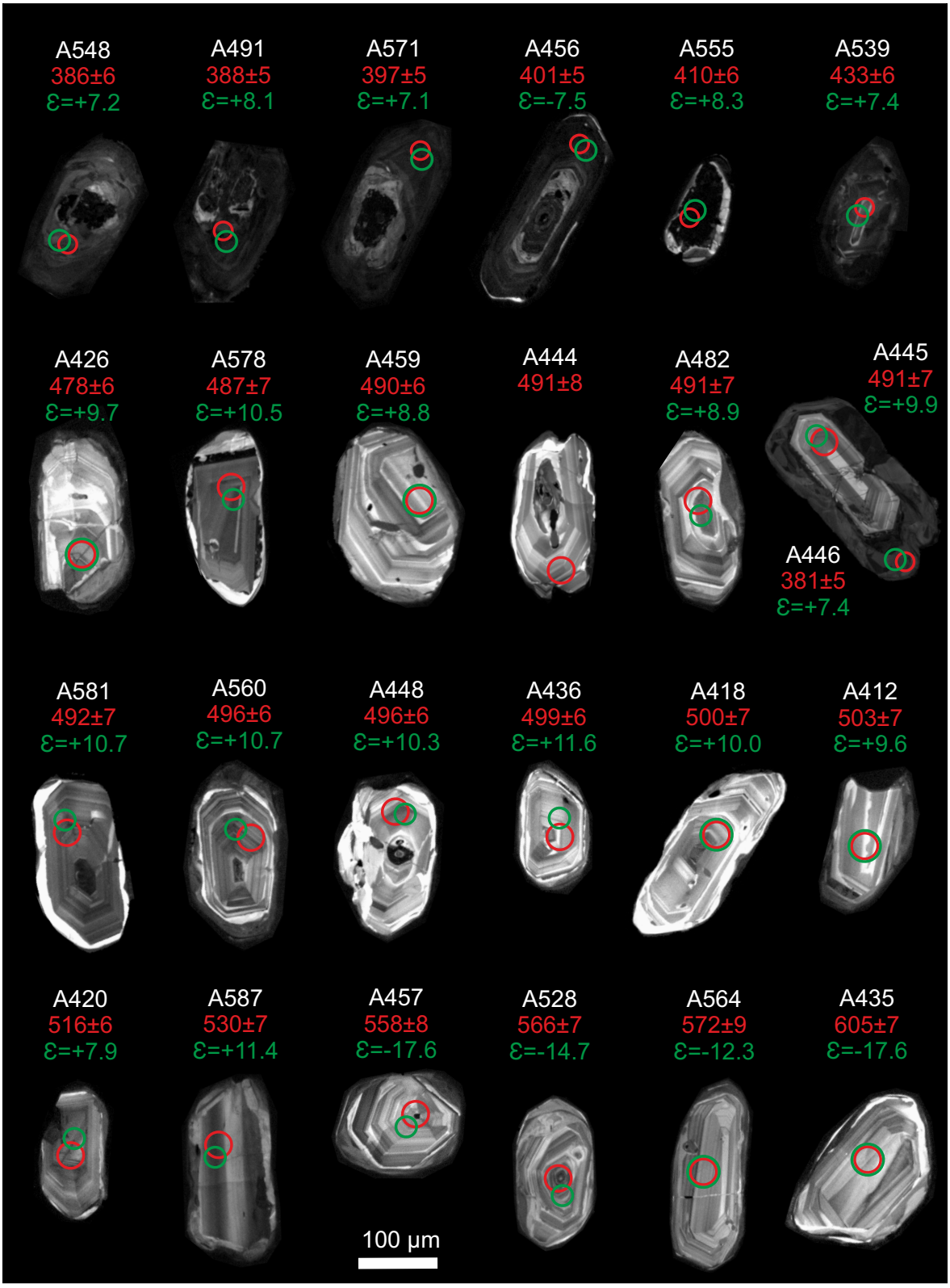

Fig. 54. CL images (cathodoluminescence) of representative zircons from the studied sample. Laser ablation pits for U–Pb analyses (red line circles) have 23 and 33 μm diameters. Laser ablation pits for Lu–Hf analyses (green line circles) have 26 and 40 μm diameters. White numbers are the reference number of the analysis, red numbers are the U–Pb age and its 2σ error (Ma) and the green numbers are the εHf values for the U–Pb age.

are generally observed around domain I zircon textures. Around these bright rims, darker rims are observed, which correspond to domain II and show darker (due to higher U content) faded oscillatory textures.

Domain I zircon is interpreted to represent magmatic protolith zircon. Their textures have been considered to have grown during high-T anatexis (Vavra *et al.*, 1996), to high-T subsolidus growth (Schaltegger *et al.*, 1999) and more recently to have grown from partial melts in ultrahigh-T terrains (*e.g.* Kelly & Harley, 2005). Nevertheless this protolithic zircon is related to the crystallisation of the orthogneiss in an arc development environment at *c.* 496 Ma (the entire Banded Gneiss formation is arc-related). Domain II textures have the same $^{176}Hf/^{177}Hf_{(t)}$ ratios than domain I textures. This implies that these textures are not overgrowths, but instead they are a consequence of a *c.* 402 Ma solid-state recrystallisation (*e.g.* Zeh *et al.*, 2010). This is due to the high immobility of Hf in Zrn, basically because Hf has the same ionic radius than Zr (155 *p*m). The quantities of Lu and Yb HREE with respect to Hf (lower $^{176}Lu/^{177}Hf$ and $^{176}Yb/^{177}Hf$ ratios) and Th with respect of U (lower Th/U ratios) of domain II with respect of domain I are lower. This is explained by the recrystallising event that purged from the crystal structure the cations with ionic radii significantly different from those of Zr and Hf (Hoskin & Schaltegger, 2003).

Other observations that favour this interpretation are the small bright rims that are normally observed between both domains. These rims are interpreted as alteration fronts, where trace elements are enriched in detriment to depletion of domain II darker rims. This trace element partitioning is an effect of the solid-state recrystallisation, where purging of non-essential structural cations takes place (Hoskin & Schaltegger, 2003). Another observation is the textures of the cores of many of the domain II zircon grains. These cores (top row images; Fig. 54) have chaotic patchy dark textures, they are surrounded by bright alteration fronts, and have a high amount of inclusions. These cores are only present in zircon grains where domain II textures are well developed and seem to be the result of extreme cation purge from the protolithic domain I zircon. The inclusions that these cores present are probably exsolutions of rare mineral phases (apatite, xenotime, U–Th-silicates...) from the Zrn structure.

Solid-state recrystallisation can take place at any stage during metamorphism, but it usually dominates the near-peak T region of the metamorphic P–T path (Harley *et al.*, 2007).

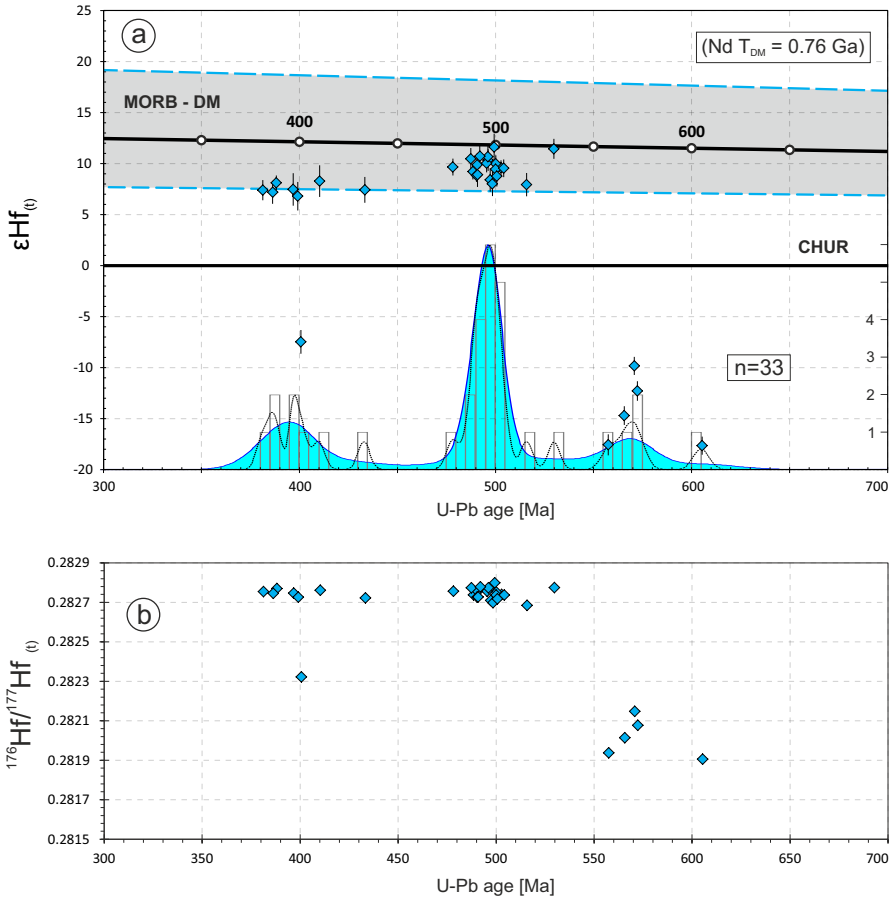

Fig. 55. a εHf *v.* age diagram. Error bars are +2σ and -2σ uncertainties. *n*, number of concordant zircon grains analysed for Lu–Hf isotopes. Numbers in the right vertical axis represent histogram frequency. Top-right rectangle shows Nd whole-rock model-age for the studied sample. MORB εHf interval was taken from Chauvel & Blichert-Toft (2001) considering a minimum $\varepsilon Hf_{(t=0Ma)}$ = +8.3 and a maximum $\varepsilon Hf_{(t=0Ma)}$ = +20.7. These values are propagated to $\varepsilon Hf_{(t=4Ga)}$ = 0 defining a grey field (enclosed by the blue discontinuous lines) around the DM-evolution trend, to provide an indication of the likely range of DM compositions through time. MORB: mid-ocean ridge basalts; DM: depleted mantle; CHUR: chondritic uniform reservoir. **b** $^{176}Hf/^{177}Hf_{(t)}$ *v.* age diagram.

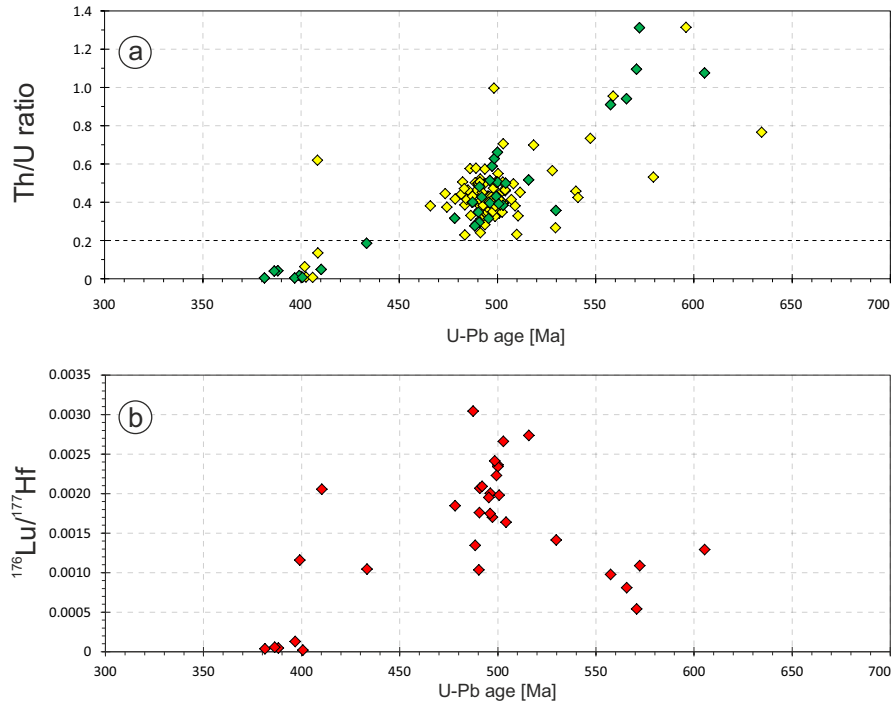

Fig. 56. a Th/U ratios *v.* age diagram (yellow rhombus represent Zrn analysed for U–Th–Pb isotopes and green rhombus represent those analysed for U–Th–Pb and Lu–Hf isotopes). **b** $^{176}Lu/^{177}Hf_{(t)}$ *v.* age diagram.

7.4.2. Sample GCH-03
(Area da Vaca orthogneiss, 100 m)

This sample was collected from the *Area da Vaca* beach (43°43'27.8"N, 7°51'35.1"W), at the 100 m point of the *Area da Vaca* geological section (Appx. 1).

This orthogneiss outcrops as a *c.* 50 centimetre thick melanocratic felsic rock within the metasedimentary rocks. It is displayed as a boudin wrapped by the metasedimentary rocks regional foliation (Fig. 57). It outcrops at the 100 m point of the *Area da Vaca* geological section; chapter 4).

From microscopic observations this sample has a porphyro-grano-lepidoblastic texture (Fig. 58; Ref: 112975). Grt porphyroblasts are xenoblastic and poikilitic, with an extreme amount of inclusions (mainly Qz). The lepidoblastic texture is defined by a great amount of Chl, which is displayed together with Spn and Ap. Qz and Afs are displayed with a granoblastic interlobate texture where Qz is also displayed as elongated poly-crystals. Other constituents are Zrn and small quantities of Rt and Ilm.

7.4.2.1. Results

From this sample (GCH-03), 122 U–Pb analyses were performed of which 119 were concordant (d = 2.5%; Figs. 59 & 60). The U–Pb ages are spread between *c.* 510 and 450 Ma, with a maximum abundance peak at 485 Ma, and with no inherited zircon (Fig. 60a).

The zircon grains from this sample present a wide variety of textures. They show well defined to faded multi-faceted habits ("soccerball habit"). Other zircon grains show badly defined oscillatory zonings and others show transgressive recrystallisation areas that are internally featureless and have sinuous and lobulated edges (A075 and A164; Fig. 61). All zircon grains show bright rims in the CL images and some zircon grains are fragments (A074 and A093; Fig. 61). No internal features are observed in BSE images.

$\varepsilon Hf_{(t)}$ values of all analysed zircon grains are positive with an average value of +4.5 (minimum: +1.3, maximum: +9.2; Fig. 62a). $^{176}Hf/^{177}Hf_{(t)}$ ratios plot around 0.282645 ± 0.000115 (±2 SD; Fig. 62b).

All zircon grains have an average content of U of 538 ppm (minimum: 28, maximum: 2298) and an average of 48 ppm of Pb (minimum: 2.6, maximum: 256; Appx. 4). The majority of the zircon grains have Th/U ratios higher than 0.2, with an average value of 0.52 (minimum: 0.24, maximum: 1.26). Only three analyses have lower Th/U values lower than 0.2 (Fig. 63a).

Fig. 57. Field photograph of the studied sample. The hammer is 40.6 cm long.

Fig. 58. Photomicrograph of the studied sample.

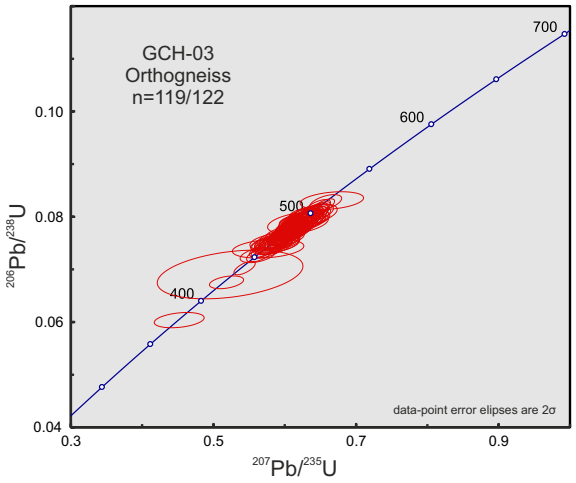

Fig. 59. U-Pb conventional concordia diagram showing U-Pb zircon analyses of the studied sample. Ellipses represent combined 2σ uncertainties of $^{206}Pb/^{238}U$ and $^{207}Pb/^{235}U$ ratios. *n*, number of analyses considered (those with 90–110% concordance)/total number of U–Pb analyses.

$^{176}Lu/^{177}Hf$ ratios plot around 0.00144 ± 0.00134 (±2 SD; Fig. 63b). $^{176}Yb/^{177}Hf$ ratios plot around 0.0456 ± 0.0450 (±2 SD; Appx. 4).

Nd whole-rock model-age is 0.75 Ga and $\varepsilon Nd_{(t)}$ values are: $\varepsilon Nd_{(t=0)} = +2.5$; $\varepsilon Nd_{(t=485)} = +5.0$.

7.4.2.2. Discussion

The U–Pb ages are spread between *c.* 510 and 450 Ma, with a maximum abundance peak at 485 Ma (Fig. 60). The textures shown by the zircon grains in this sample vary from "soccerball", to oscillatory, to transgressive recrystallisation areas. These types of textures could not be linked to specific age ranges or to any chemical variation ratios. The only exception is the transgressive recrystallisation areas, where two U–Pb analyses were performed, with ages of 378 ± 7 and 430 ± 23 Ma (Fig. 61). These areas are interpreted as to be the result of a solid-state recrystallisation event dated in other samples at *c.* 390 Ma. The rest of the ages in this sample, that vary between *c.* 510 and 450 Ma, show a wide spread in their U, Pb, Lu and Yb contents. Their higher $\varepsilon Hf_{(t)}$ values plot in the MORB-depleted mantle field (higher value: +9.2) and their lower values plot very near the CHUR trend (lower value: +1.3; Fig. 62a). Their $^{176}Hf/^{177}Hf_{(t)}$ values also present a high variation and no tendency in their values was found in relation to their U–Pb ages. This wide range in their U–Pb ages and the wide range in their chemical compositions can be explained by a rejuvenation process via Pb-loss triggered by the *c.* 390 Ma recrystallisation event. This explanation does not seem satisfactory due to the very low proportion of discordant analyses (2.5%) and to the high concordance achieved by the U–Pb zircon ages (69 out of 122 analyses are 98–102% concordant). Another explanation could be that the protolith magmatic material started to crystallise zircon with high-T related "soccerball" textures (*e.g.* A046 and A059; Fig. 61) and that before the magmas completely crystallised they were mixed with other magmas with different

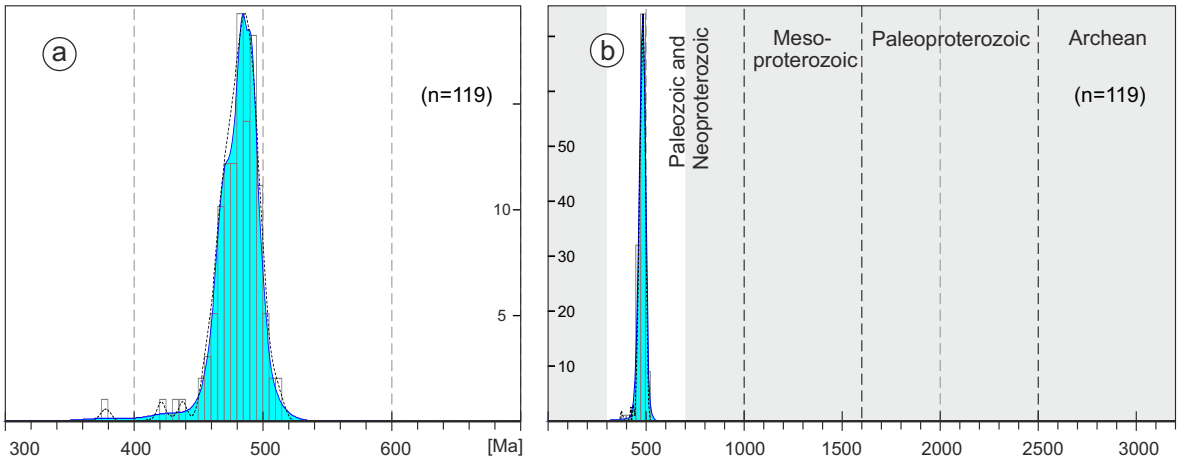

Fig. 60. Adaptative Kernel Density Estimation (aKDE, continuous line enclosing the blue area), Probability Density (PDP, black dashed line) and histogram diagrams of the U–Pb analyses (calculated with DensityPlotter5.0, Vermeesch 2012). Numbers in the vertical axis represent histogram frequency; *n*, number of analyses. **a** Partial plot representing data within a 300–700 Ma time range (bandwidth = 5 Ma, binwidth = 5 Ma). **b** Complete plot (bandwidth = 15 Ma, binwidth = 25 Ma).

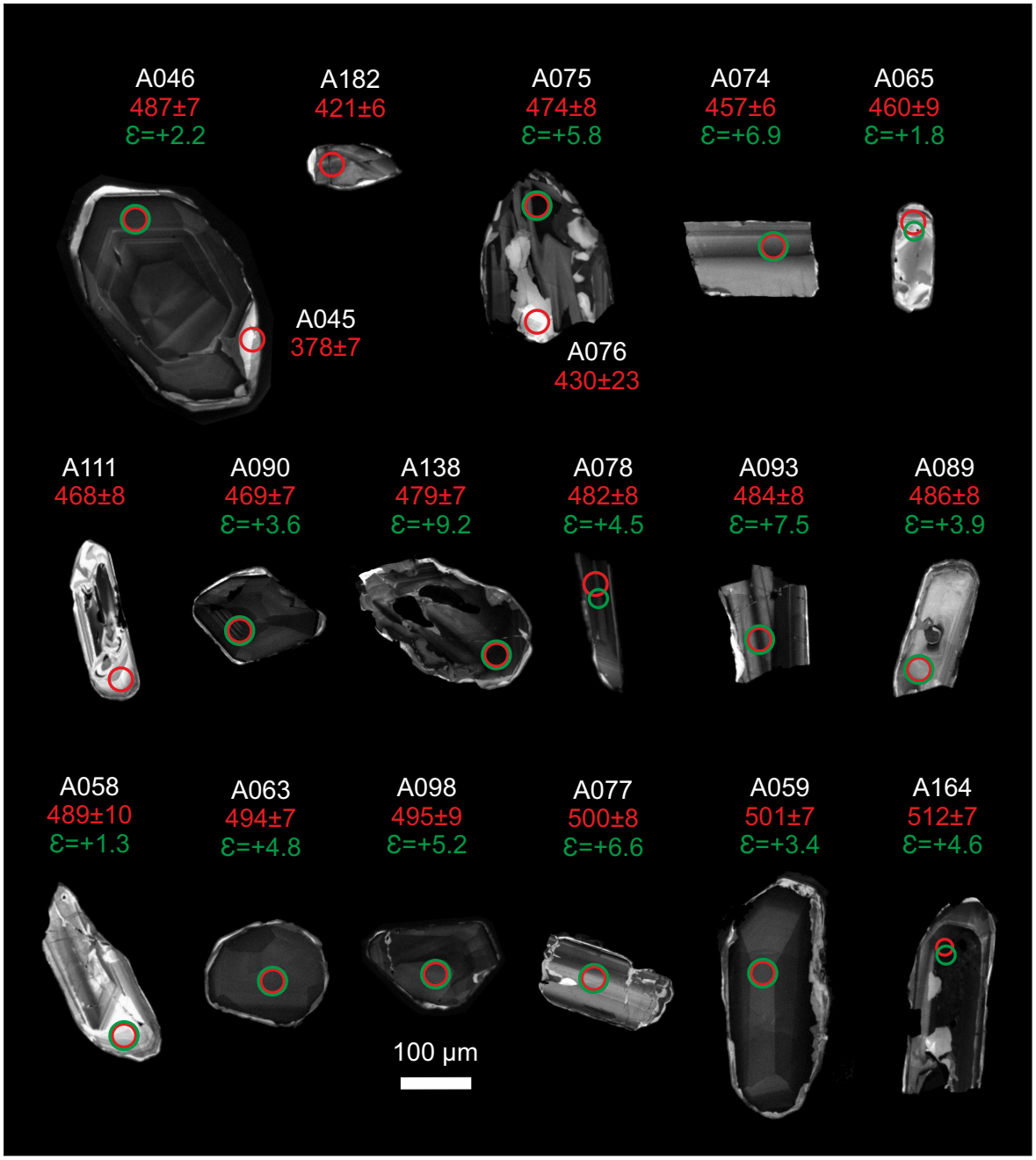

Fig. 61. CL (cathodoluminescence) images of representative zircons from the studied sample. Laser ablation pits for U–Pb analyses (red line circles) have 23 and 33 μm diameters. Laser ablation pits for Lu–Hf analyses (green line circles) have 26 and 40 μm diameters. White numbers are the reference number of the analysis, red numbers are the U–Pb age and its 2σ error (Ma) and the green numbers are the εHf values for the U–Pb age.

compositions, and zircon continued crystallising with oscillatory textures (*e.g.* A111 and A065; Fig. 61). The system cooled very slowly due to a long term high-T input associated with the mixing and the arc environment in which this orthogneiss crystallised and developed. This interpretation seems possible but is not fully supported by the data presented in this work. The only certain conclusions from this sample is that the orthogneiss protolithic material crystallised sometime around *c.* 485 Ma and that a posterior recrystallisation event altered the zircon textures without triggering any rare element purge driven by solid-state recrystallisation processes from the zircon structure.

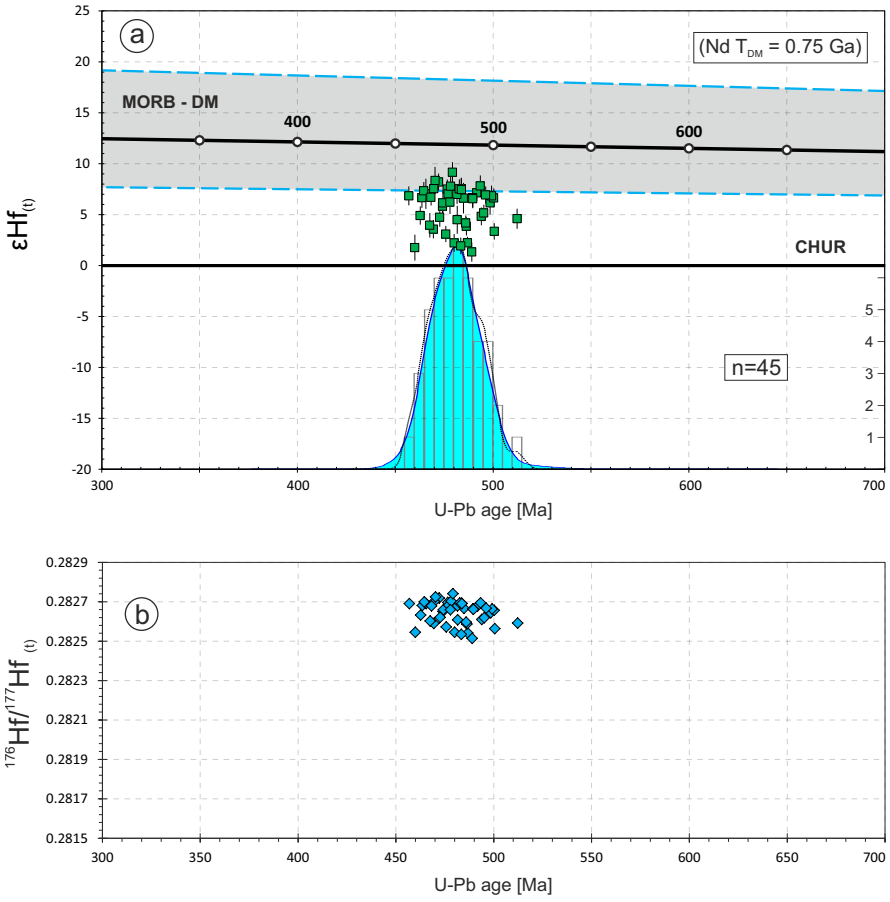

Fig. 62. a εHf *v.* age diagram. Error bars are +2σ and -2σ uncertainties. *n*, number of concordant zircon grains analysed for Lu–Hf isotopes. Numbers in the right vertical axis represent histogram frequency. Top-right rectangle shows Nd whole-rock model-age for the studied sample. MORB εHf interval was taken from Chauvel & Blichert-Toft (2001) considering a minimum $\varepsilon Hf_{(t=0Ma)}$ = +8.3 and a maximum $\varepsilon Hf_{(t=0Ma)}$ = +20.7. These values are propagated to $\varepsilon Hf_{(t=4Ga)}$ = 0 defining a grey field (enclosed by the blue discontinuous lines) around the DM-evolution trend, to provide an indication of the likely range of DM compositions through time. MORB: mid-ocean ridge basalts; DM: depleted mantle; CHUR: chondritic uniform reservoir. **b** $^{176}Hf/^{177}Hf_{(t)}$ *v.* age diagram.

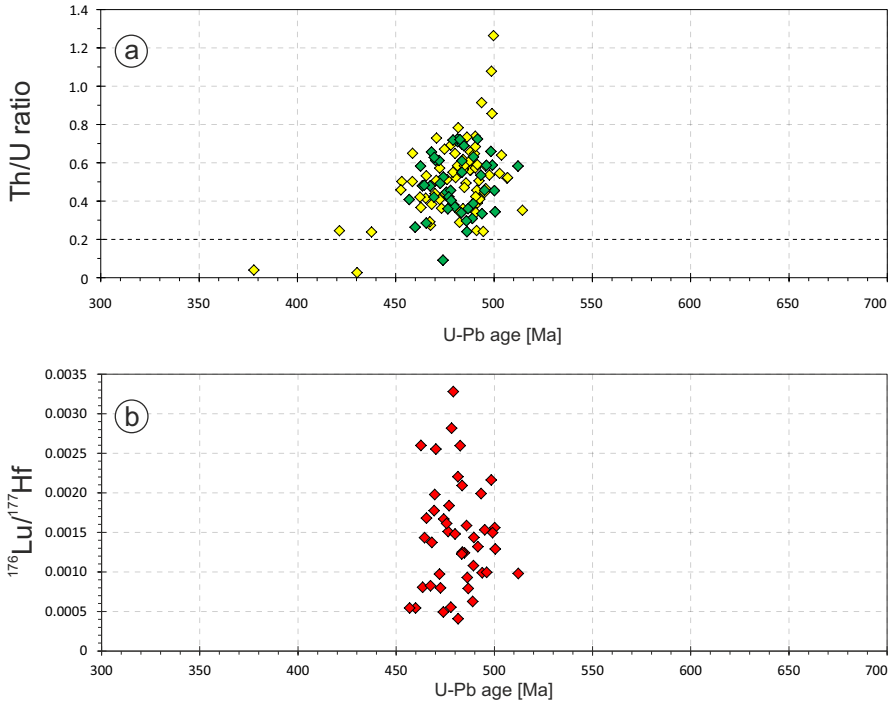

Fig. 63. a Th/U ratios *v.* age diagram (yellow rhombus represent Zrn analysed for U–Th–Pb isotopes and green rhombus represent those analysed for U–Th–Pb and Lu–Hf isotopes). **b** $^{176}Lu/^{177}Hf_{(t)}$ *v.* age diagram.

Another explanation for the chemical variation shown by this sample could be that the protolith of this rock was not really an igneous rock but a sedimentary one. In fact, this sample was collected assuming it was a non-altered metasedimentary rock instead of an orthogneiss (see field photograph, Fig. 57). This confusion may look like a novels geologist mistake but the truth is that the rocks outcropping in this high-grade terrain are frequently cryptic in terms of rock classification. This rock has been classified as an orthogneiss because it has no inherited zircon, but doubts arise, since in arc environments, a sedimentary rock can contain a single zircon population from a unique source area and an igneous rock can have a huge number of inhered zircon grains due to a complex igneous development.

7.4.3. Sample GCH-13
(Figueiroa orthogneiss)

This sample was collected from *Figueiroa* beach (43°42'41.1"N, 7°51'50.3"W), at the 160 m point of the *Figueiroa* beach geological section (chapter 4).

This orthogneiss outcrops as a *c.* 20–30 centimetre thick leucocratic felsic rock intruding the metasedimentary rocks (Fig. 64). It outcrops at the 160 m point of the *Figueiroa* geological section (chapter 4).

From microscopic observations this sample has a grano-lepidoblastic texture (Ref: 112985). Qz and Afs are the major constituents (Fig. 65). The matrix is formed mainly by small crystals of altered Afs and Qz, and altered white mica (most probably Ms). Qz is displayed as tabular elongated amoeboid poly-crystals. Other constituents are Grt and Zrn. Small subidioblastic corroded and altered crystals of Grt were found in small quantities.

7.4.3.1. Results

From this sample (GCH-13), 92 U–Pb analyses were performed of which 87 were concordant (*d* = 5.4%; Figs. 66 & 67). The U–Pb ages are spread between *c.* 530 and 460 Ma, with a maximum abundance peak at 504 Ma and with relative abundances at 536, 486 and 473 Ma (Fig. 67). There are seven analyses with ages older than 600 Ma, which are considered inheritances.

The zircon grains from this sample show a wide variety of textures. Some of the zircon grains show more or less well defined oscillatory growth patterns (*e.g.* A012; Fig. 68), others show sinuous oscillatory patterns (*e.g.* A095; Fig. 68) and others faded oscillatory or even structure-less textures (*e.g.* A047; Fig. 68). The great majority of these zircon grains are fragments (Fig. 68). There is also another type of zircon, which is smaller than the previously described. It is much darker (CL images) and shows a higher number of inclusions (BSE images). Its textures are defined by oscillatory growth patterns which are faded and in some cases sinuous (*e.g.* A019; Fig. 68). No internal features are observed in BSE images, with the exception of the inclusions above-mentioned.

$\varepsilon Hf_{(t)}$ values for all zircon grains plot with an average value of +0.3 (minimum: -12.4, maximum: +8.0; Fig. 69a). $^{176}Hf/^{177}Hf_{(t)}$ ratios plot around 0.282305 ± 0.000883 (±2 SD; Fig. 69b).

All zircon grains have an average content of U of 552 ppm (minimum: 45, maximum: 3570) and an average of 53 ppm of Pb (minimum: 7,

Fig. 64. Field photograph of the studied sample. The hammer is 40.6 cm long.

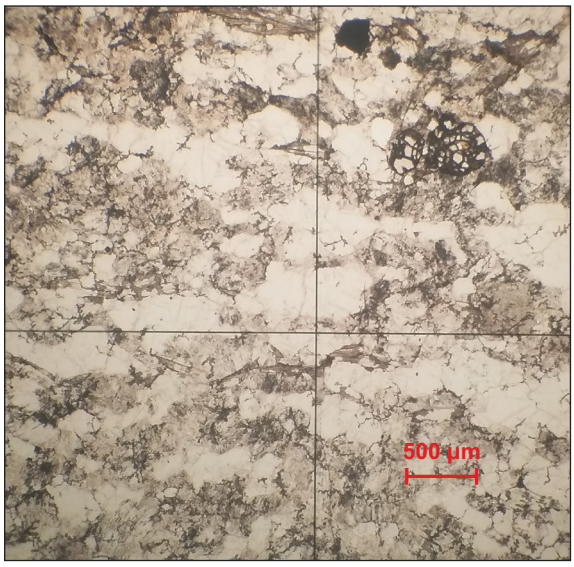

Fig. 65. Phtomicrograph of the studied sample.

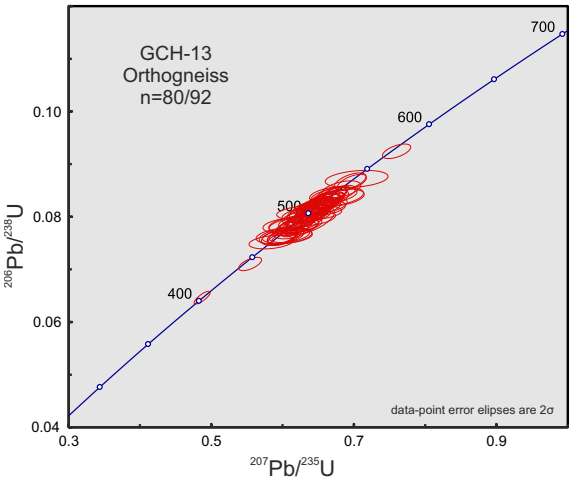

Fig. 66. U-Pb conventional concordia diagram showing U-Pb zircon analyses of the studied sample. Ellipses represent combined 2σ uncertainties of $^{206}Pb/^{238}U$ and $^{207}Pb/^{235}U$ ratios. *n*, number of analyses considered (those with 90–110% concordance)/total number of U–Pb analyses.

maximum: 337; Appx. 4). The majority of the zircon grains have Th/U ratios higher than 0.2, with an average value of 0.82 (minimum: 0.18, maximum: 1.51). Only one analysis has lower Th/U values lower than 0.2 (Fig. 70a).

$^{176}Lu/^{177}Hf$ ratios plot around 0.00122 ± 0.00126 (±2 SD; Fig. 70b). $^{176}Yb/^{177}Hf$ ratios plot around 0.0389 ± 0.0409 (±2 SD; Appx. 4).

Nd whole-rock experiments failed to calculate a model-age, because the $^{147}Sm/^{144}Nd$ ratio calculated for this sample has a negative slope in the $\varepsilon Nd_{(t)}$ *v.* age plot (higher value than CHURs $^{147}Sm/^{144}Nd$ value of 0.1967; Jacobsen & Wasserburg, 1980). Epsilon value for present day is: $\varepsilon Nd_{(t=0)} = -0.6$.

7.4.3.2. Discussion

Zircon from this sample shows a high variety of textures and chemical ratios and values. It has not been possible to relate these observations with certain age ranges. The maximum abundance peak of 504 Ma (Fig. 67) is interpreted as the age of igneous crystallisation of the protolithic felsic magmas. The variety of textures displayed (Fig. 68) points to a complex evolution after crystallisation, and possibly to complex crystallisation processes where a high number of inherited zircon grains may have played an important role. The high variability in their $\varepsilon Hf_{(t)}$ values is not compatible with a direct crystallisation of the whole population of zircon from an homogeneous fluid phase (Fig. 69a). The high and varied Th/U, $^{176}Lu/^{177}Hf$ and $^{176}Yb/^{177}Hf$ ratios constitute evidence that zircon was not subjected to a rare element purge due to solid-state recrystallisation processes (Fig. 70 & Appx. 4). But a pseudomorphic recrystallisation process seems probable and expected from textural observations, as the oscillatory patterns are normally blurred and faded (Fig. 68). Other textural observations such as the alotriomorphic character of zircon habits, point to a fragmentation of the zircon grains due to

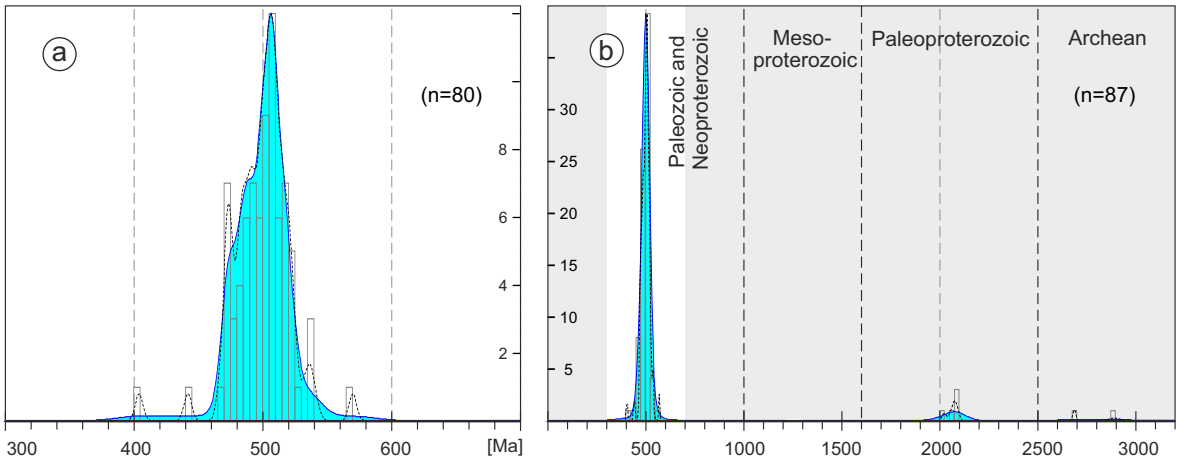

Fig. 67. Adaptative Kernel Density Estimation (aKDE, continuous line enclosing the blue area), Probability Density (PDP, black dashed line) and histogram diagrams of the U–Pb analyses (calculated with DensityPlotter5.0, Vermeesch 2012). Numbers in the vertical axis represent histogram frequency; *n*, number of analyses. **a** Partial plot representing data within a 300–700 Ma time range (bandwidth = 5 Ma, binwidth = 5 Ma). **b** Complete plot (bandwidth = 15 Ma, binwidth = 25 Ma).

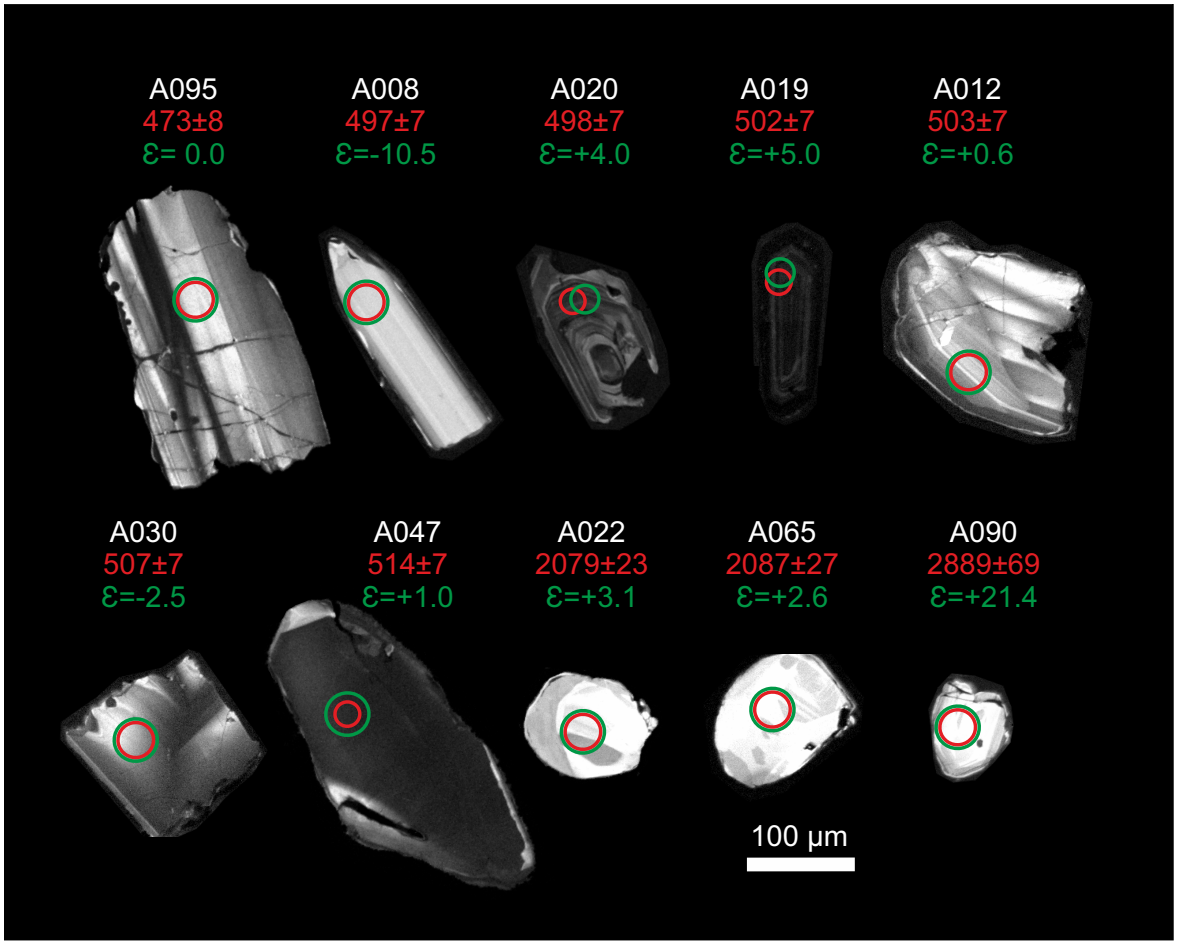

Fig. 68. CL images (cathodoluminescence) of representative zircons from the studied sample. Laser ablation pits for U–Pb analyses (red line circles) have 23 and 33 μm diameters. Laser ablation pits for Lu–Hf analyses (green line circles) have 26 and 40 μm diameters. White numbers are the reference number of the analysis, red numbers are the U–Pb age and its 2σ error (Ma) and the green numbers are the εHf values for the U–Pb age.

fragile deformation, or to an interstitial growth or to a different geological environment for this sample. An immature sedimentary origin could explain the fragmentation of the zircon grains, but this possibility is highly unlikely due to field and microscopic observations that classify this rock as having an igneous origin (see Figs. 64 & 65). The high number of inclusions viewed in BSE images is likely due to have been captured during zircon growth rather than to be a result of zircon impurity exsolution due to solid-state recrystallisation.

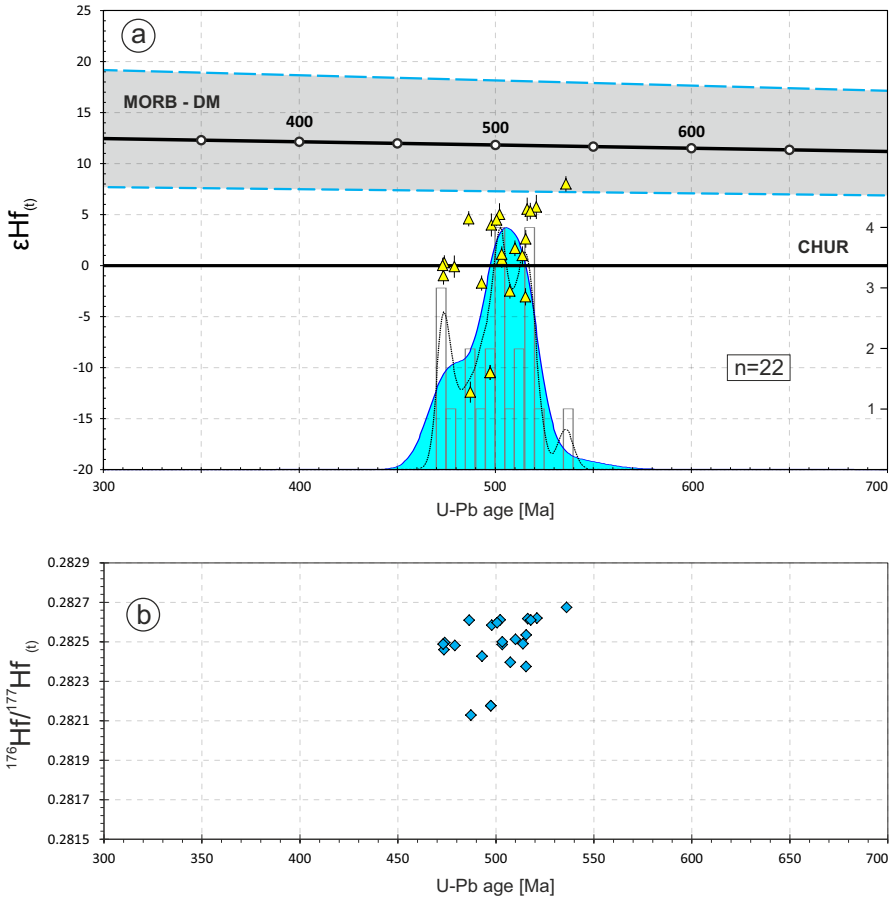

Fig. 69. a εHf *v.* age diagram. Error bars are +2σ and -2σ uncertainties. *n*, number of concordant zircon grains analysed for Lu–Hf isotopes. Numbers in the right vertical axis represent histogram frequency. Top-right rectangle shows Nd whole-rock model-age for the studied sample. MORB εHf interval was taken from Chauvel & Blichert-Toft (2001) considering a minimum $\varepsilon Hf_{(t=0Ma)}$ = +8.3 and a maximum $\varepsilon Hf_{(t=0Ma)}$ = +20.7. These values are propagated to $\varepsilon Hf_{(t=4Ga)}$ = 0 defining a grey field (enclosed by the blue discontinuous lines) around the DM-evolution trend, to provide an indication of the likely range of DM compositions through time. MORB: mid-ocean ridge basalts; DM: depleted mantle; CHUR: chondritic uniform reservoir. **b** $^{176}Hf/^{177}Hf_{(t)}$ *v.* age diagram.

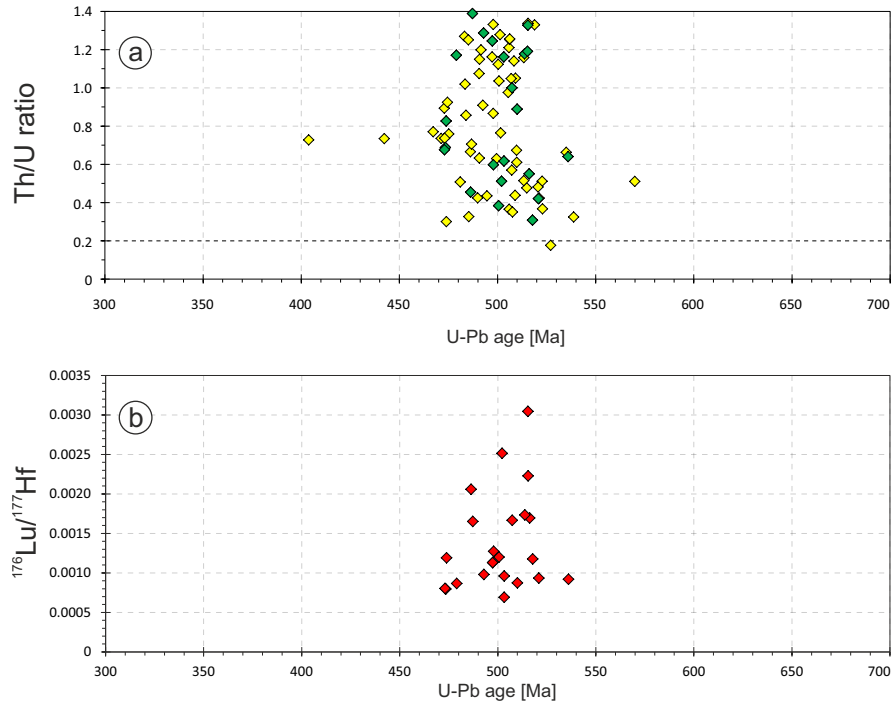

Fig. 70. a Th/U ratios *v.* age diagram (yellow rhombus represent Zrn analysed for U–Th–Pb isotopes and green rhombus represent those analysed for U–Th–Pb and Lu–Hf isotopes). **b** $^{176}Lu/^{177}Hf_{(t)}$ *v.* age diagram.

7.4.4. Sample GCH-14
(Da Moura orthogneiss)

This orthogneiss forms part, together with the eclogite sample GCH-23 (section 7.3.4), of the *Punta da Moura* mingling suite. This sample is located in the northern part of the *Masanteo* peninsula, at *Punta da Moura* (Appx. 1; 43°43'28.6"N, 7°51'20.3"W).

This orthogneiss forms part of the *Punta Da Moura* mingling suite (Fig. 71), and from field observations it seems that this orthogneiss intruded the mafic rock (eclogite GCH-23, section 7.3.4).

This sample is a fine to medium grained rock with porphyro-grano-lepidoblastic texture (Ref: 112986). Its major constituents are Grt and Qz and its minor constituents are Bt, Amp, Zo, Czo, Afs, Pl, white mica, Ap, Rt, Spn and Opq (Fig. 72). Grt is strongly xenoblastic due to corrosion and mineral replacements. It is light pink, poikilitic, with some inclusions of Qz, Spn and Bt, and sometimes shows an atoll texture. Qz is displayed as non-poikilitic aggregates defining a granoblastic interlobate to amoeboid texture. Bt is not oriented and Zo is mainly replaced to Czo. Czo is relatively big (up to 0.5 *c*m) and always shows rims of cryptocrystalline matter. Amp, Rt, Spn and white mica are very small and scarce.

7.4.4.1. Results

From this sample (GCH-14), 108 U–Pb analyses were performed of which 104 were concordant (*d* = 3.7%; Figs. 73 & 74). The U–Pb ages show a maximum abundance peak at 500 Ma and a relative abundance peak at 470 Ma (Fig. 74). One analysis gave an age of 353 Ma and 4 analyses gave ages between 380 and 410 Ma.

Zircon from this sample shows a wide variety of textures. Some of the zircon grains show more or less well defined oscillatory growth patterns (*e.g.* A180; Fig. 75), others show sinuous oscillatory patterns (*e.g.* A199; Fig. 75) and others faded oscillatory or even structure-less textures (*e.g.* A201, A206, A214; Fig. 75). Almost all zircon grains show structure-less bright rims which in some cases are sinuous and transgressive (*e.g.* A185; Fig. 75). No internal features are observed in BSE images, with the exception of a low number of inclusions.

$\varepsilon Hf_{(t)}$ values for all zircon grains are positive with an average value of +0.1 (minimum: -4.7, maximum: +6.9; Fig. 76a). $^{176}Hf/^{177}Hf_{(t)}$ ratios plot around 0.282362 ± 0.000610 (±2 SD; Fig. 76b).

All zircon grains have an average content of U of 223 ppm (minimum: 27, maximum: 915)

Fig. 71. Field photograph of the studied sample. The hammer is 33 cm long.

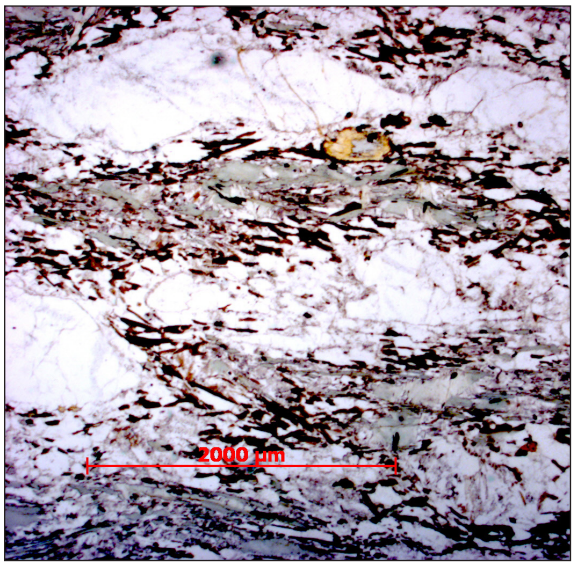

Fig. 72. Phtomicrograph of the studied sample.

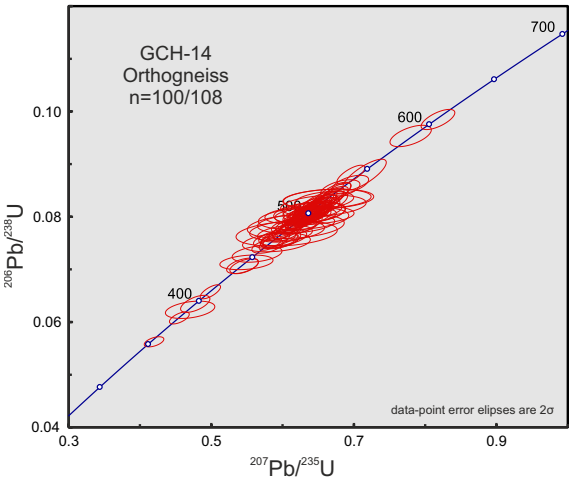

Fig. 73. U-Pb conventional concordia diagram showing U-Pb zircon analyses of the studied sample. Ellipses represent combined 2σ uncertainties of $^{206}Pb/^{238}U$ and $^{207}Pb/^{235}U$ ratios. *n*, number of analyses considered (those with 90–110% concordance)/total number of U–Pb analyses.

and an average of 21 ppm of Pb (minimum: 2, maximum: 103; Appx. 4). Th/U ratios have average values of 0.34 (minimum: 0.001, maximum: 0.94; Fig. 77a).

$^{176}Lu/^{177}Hf$ ratios plot around 0.00141 ± 0.00128 (±2 SD; Fig. 77b). $^{176}Yb/^{177}Hf$ ratios plot around 0.0446 ± 0.0420 (±2 SD; Appx. 4).

Nd whole-rock model-age is 1.08 Ga and $\varepsilon Nd_{(t)}$ values are: $\varepsilon Nd_{(t=0)} = -3.6$; $\varepsilon Nd_{(t=500)} = +0.6$.

7.4.4.2. Discussion

Zircon from this sample shows a high variety of textures and chemical ratios and values. It has not been possible to relate these observations with certain age ranges. The maximum abundance peak of 500 Ma is interpreted as the age of igneous crystallisation of the protolithic felsic magmas. The relative abundance peak of 470 Ma zircon is interpreted as a Pb-loss process triggered by the *c.* 390 Ma HP–HT metamorphic event or by a *c.* 470 Ma metamorphic event that altered the previous protolithic *c.* 500 Ma zircon. This possible *c.* 470 Ma event could be a temperature input related to the arc development in which this sample is related to. Almost all zircon grains show structure-less bright rims which in some cases are sinuous and transgressive. One analysis on a bright rim gave an age of 390 ± 8 Ma (A236; Fig. 75). This age is repeatedly present in many samples and it is interpreted as the age of HP–HT Devonian metamorphism and could explain, by Pb-loss process, the relative abundance of 470 Ma zircon in this sample. This felsic rock outcrops together with a *c.* 507 Ma mafic rock (GCH-23, section 7.3.4) and both lithologies outcrop together with field relationships interpreted as a mingling process between them. It is interpreted that this felsic rock intruded at *c.* 500 Ma the *c.* 507 Ma mafic rock and triggered a high temperature input. Sample GCH-23 also shows a relative abundance of ages at *c.* 470 Ma

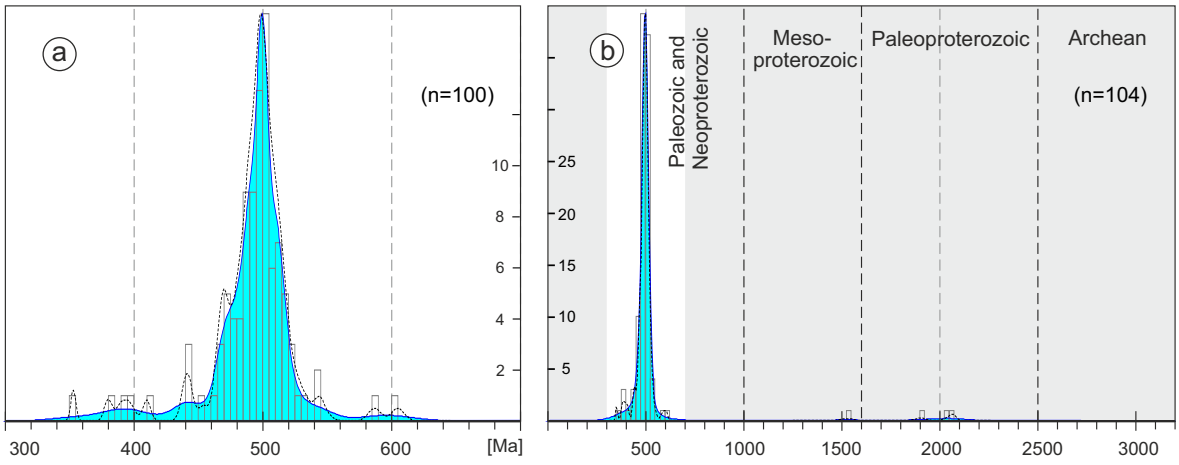

Fig. 74. Adaptative Kernel Density Estimation (aKDE, continuous line enclosing the blue area), Probability Density (PDP, black dashed line) and histogram diagrams of the U–Pb analyses (calculated with DensityPlotter5.0, Vermeesch 2012). Numbers in the vertical axis represent histogram frequency; *n*, number of analyses. **a** Partial plot representing data within a 300–700 Ma time range (bandwidth = 5 Ma, binwidth = 5 Ma). **b** Complete plot (bandwidth = 15 Ma, binwidth = 25 Ma).

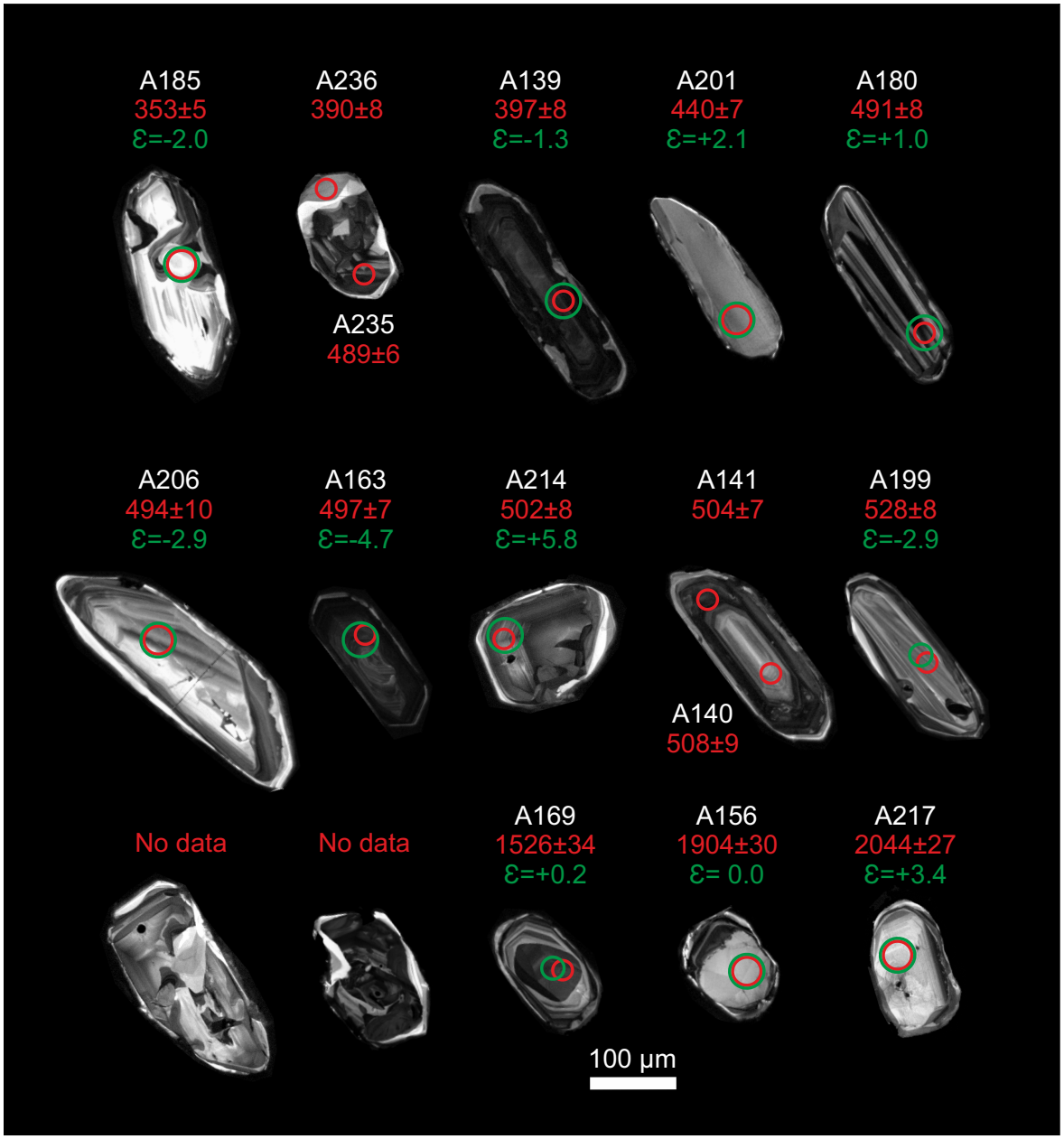

Fig. 75. CL images (cathodoluminescence) of representative zircons from the studied sample. Laser ablation pits for U–Pb analyses (red line circles) have 23 and 33 μm diameters. Laser ablation pits for Lu–Hf analyses (green line circles) have 26 and 40 μm diameters. White numbers are the reference number of the analysis, red numbers are the U–Pb age and its 2σ error (Ma) and the green numbers are the εHf values for the U–Pb age.

which can be related to the mingling process. $^{176}Lu/^{177}Hf$, $^{176}Yb/^{177}Hf$, $^{176}Hf/^{177}Hf_{(t)}$ and Th/U ratios do not show any variation related with U–Pb age variations. These observations leads one to conclude that the convoluted light zonings were not formed by a dissolution-recrystallisation process but by a pseudomorphic alteration and most likely with no presence of fluid phases.

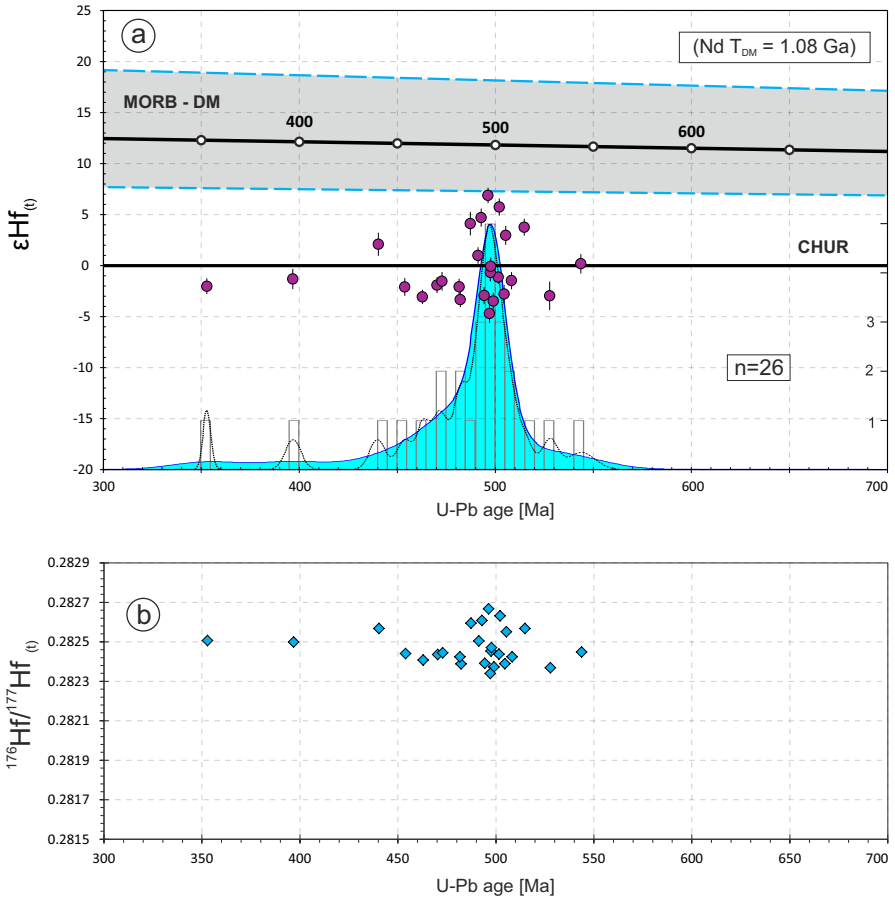

Fig. 76. a εHf *v.* age diagram. Error bars are +2σ and -2σ uncertainties. *n*, number of concordant zircon grains analysed for Lu–Hf isotopes. Numbers in the right vertical axis represent histogram frequency. Top-right rectangle shows Nd whole-rock model-age for the studied sample. MORB εHf interval was taken from Chauvel & Blichert-Toft (2001) considering a minimum $\varepsilon Hf_{(t=0Ma)}$ = +8.3 and a maximum $\varepsilon Hf_{(t=0Ma)}$ = +20.7. These values are propagated to $\varepsilon Hf_{(t=4Ga)}$ = 0 defining a grey field (enclosed by the blue discontinuous lines) around the DM-evolution trend, to provide an indication of the likely range of DM compositions through time. MORB: mid-ocean ridge basalts; DM: depleted mantle; CHUR: chondritic uniform reservoir. **b** $^{176}Hf/^{177}Hf_{(t)}$ *v.* age diagram.

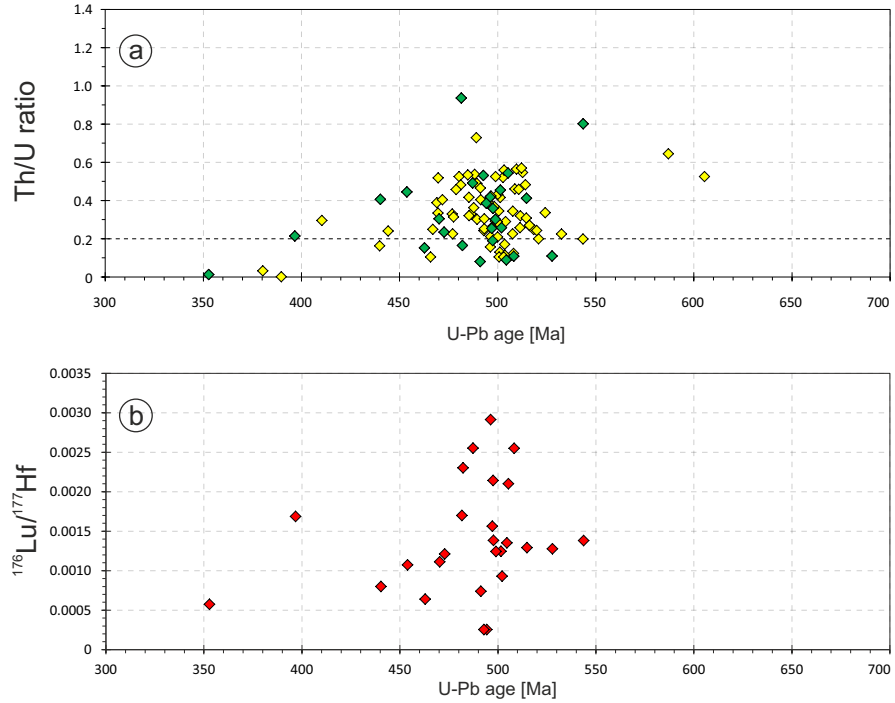

Fig. 77. a Th/U ratios *v.* age diagram (yellow rhombus represent Zrn analysed for U–Th–Pb isotopes and green rhombus represent those analysed for U–Th–Pb and Lu–Hf isotopes). **b** $^{176}Lu/^{177}Hf_{(t)}$ *v.* age diagram.

7.4.5. Sample GCH-18
(Area da Vaca orthogneiss, 275 m)

This sample was collected from the *Area da Vaca* beach (43°43'30.1"N, 7°51'42.4"W), at the 275 m point of the *Area da Vaca* geological section (Appx. 1).

This orthogneiss outcrops as a leucocratic felsic rock intruding the metasedimentary rocks (Fig. 78). It outcrops at the 255 and 275 m points of the *Area da Vaca* geological section; chapter 4).

From microscopic observations this sample has a granoblastic texture (Ref: 112990). Qz and Afs are the major constituents (Fig. 79). The matrix is formed mainly by small crystals of altered Afs and white mica (most probably Ms). Qz is displayed as tabular elongated poly-crystals defining the foliation. Other constituents are Ap and Zrn. Very small transparent tabular crystals with low interference colours were found, and they are thought to be an Als, probably Ky. Very small idioblastic crystals of Grt were found in very small quantities.

7.4.5.1. Results

From this sample (GCH-18), 62 U–Pb analyses were performed of which 60 were concordant (d = 3.2%; Figs. 80 & 81). The U–Pb ages are scattered in the range of 492–524 Ma, with a maximum abundance peak at 506 Ma (Fig. 81), and there are also two inheritances out of which one is concordant with an age of 1152 Ma.

All zircon grains from this sample are idiomorphic and show combined sector and oscillatory growth patterns (except the old inheritances; Fig. 82). Some of the zircon grains show bright borders in BSE images which are probably features from the last stages of the magmatic crystallisation (*e.g.* A478 and A469; Fig. 82). Some zircon grains are slightly corroded (*e.g.* A479; Fig. 82) and show very small and thin bright rims (see details of A478; Fig. 82).

$\varepsilon Hf_{(t)}$ values for all Cambrian zircon grains analysed are negative with an average value of -5.3 (minimum: -6.9, maximum: -2.4; Fig. 83a). $^{176}Hf/^{177}Hf_{(t)}$ ratios for all Cambrian zircon grains plot around 0.282312 ± 0.000042 (±2 SD; Fig. 83b).

All analysed zircon grains have an average content of U of 3171 ppm (minimum: 880, maximum: 6124) and an average value of 238 ppm of Pb (minimum: 66, maximum: 465; Appx. 4). Th/U ratios are lower than 0.2 and have average values of 0.005 (minimum: 0.004, maximum: 0.006; Fig. 84a).

Fig. 78. Field photograph of the studied sample. The boot is *c.* 30 cm long.

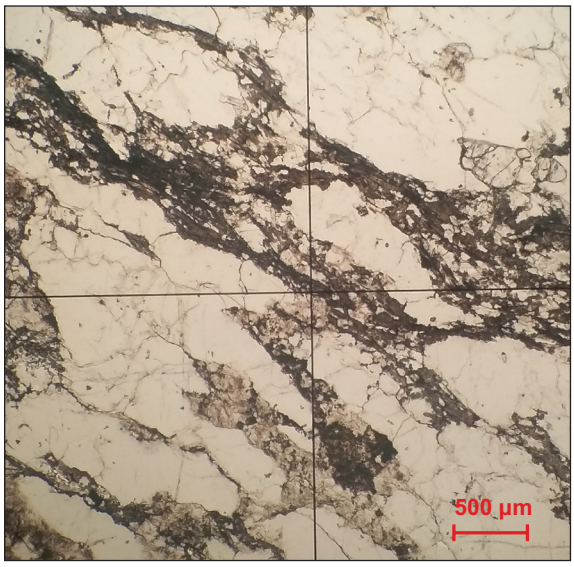

Fig. 79. Photomicrograph of the studied sample.

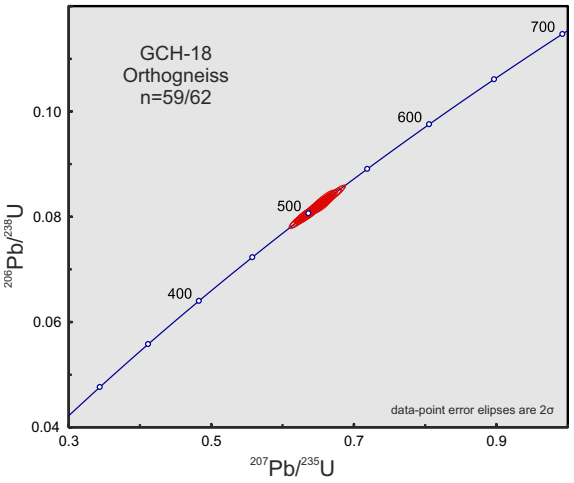

Fig. 80. U-Pb conventional concordia diagram showing U-Pb zircon analyses of the studied sample. Ellipses represent combined 2σ uncertainties of $^{206}Pb/^{238}U$ and $^{207}Pb/^{235}U$ ratios. *n*, number of analyses considered (those with 90–110% concordance)/total number of U–Pb analyses.

$^{176}Lu/^{177}Hf$ ratios for all Cambrian analysed zircon grains plot around 0.00138 ± 0.00062 (±2 SD; Fig. 84b). $^{176}Yb/^{177}Hf$ ratios for all Cambrian zircon grains analysed plot around 0.0433 ± 0.0190 (±2 SD; Appx. 4).

Nd whole-rock model-age is 2.32 Ga and $\varepsilon Nd_{(t)}$ values are: $\varepsilon Nd_{(t=0)}$ = -6.4; $\varepsilon Nd_{(t=506)}$ = -4.4.

7.4.5.2. Discussion

Beside the inheritances this sample has one zircon population with ages between 492 and 524 Ma and with a maximum abundance peak at 506 Ma. The textures that these zircon grains display are sector ("soccerball") growth patterns in the inner parts of the crystals that progressively changes to oscillatory zoning at their external parts (Fig. 82). These growth patterns are perfectly congruent with the geological setting of the formation of this sample, which is a felsic igneous rock whose magmatic protolith intruded the Banded Gneiss metasedimentary rocks. The $^{176}Hf/^{177}Hf_{(t)}$ ratios for this Cambrian population are very similar (0.282312 ± 0.000042; ±2 SD; Fig. 83b), and strongly suggests that all this zircon grew from the same homogeneous fluid phase. All analysed Cambrian zircon grains in this sample are concordant, within a 98–103% degree of concordance, resembling the very good quality of the analyses. Taking into account this high degree of concordance and the zircon textures, there is no evidence of Pb-loss processes. Therefore, the 32 Ma time period between the youngest and oldest zircon grains probably represents the cooling time range of the igneous protolith. This timespan seems to be too long, but the arc environment in which this sample is included could explain this long cooling interval, as the arc system could provide long-lived temperature input. The very low Th/U ratios (average: 0.005) can be interpreted as an evidence of metamorphic growth of the zircon, but the lack of signs of overgrowth or solid-state recrystallisation (no recrystallisation zones or alteration fronts were found) in the zircon

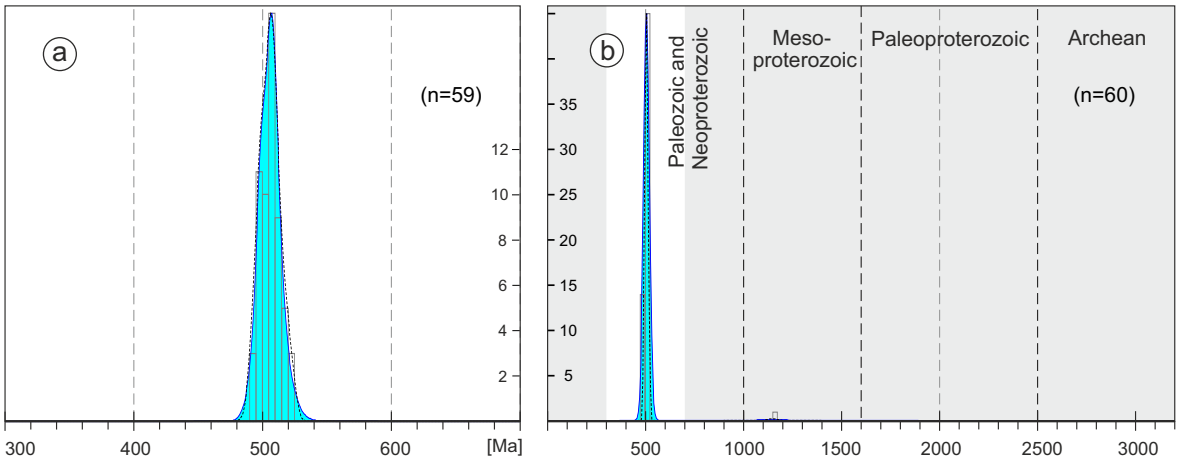

Fig. 81. Adaptative Kernel Density Estimation (aKDE, continuous line enclosing the blue area), Probability Density (PDP, black dashed line) and histogram diagrams of the U–Pb analyses (calculated with DensityPlotter5.0, Vermeesch 2012). Numbers in the vertical axis represent histogram frequency; *n*, number of analyses. **a** Partial plot representing data within a 300–700 Ma time range (bandwidth = 5 Ma, binwidth = 5 Ma). **b** Complete plot (bandwidth = 15 Ma, binwidth = 25 Ma).

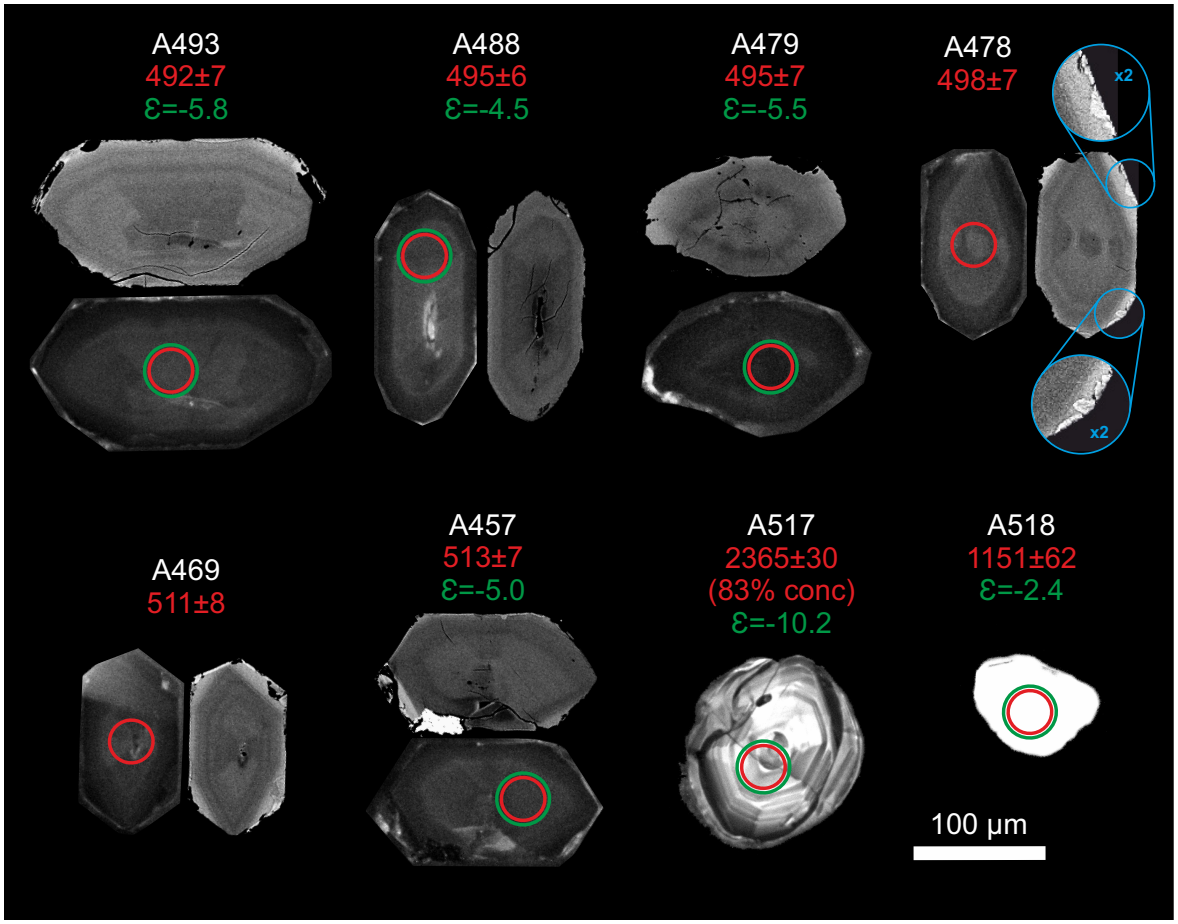

Fig. 82. BSE and CL images of representative zircons from the studied sample. Images without circles are BSE (back-scattered electrons) images, and those with circles are CL (cathodoluminescence) images. Laser ablation pits for U–Pb analyses (red line circles) have 33 μm diameters. Laser ablation pits for Lu–Hf analyses (green line circles) have 40 μm diameters. Blue circles are zoomed areas. White numbers are the reference number of the analysis, red numbers are the U–Pb age and its 2σ error (Ma) and the green numbers are the εHf values for the U–Pb age.

textures or in the chemical data, strongly discards a metamorphic origin or posterior metamorphic alteration of the zircon. The low Th/U ratios are explained by the very high contents of U (average: 3171 ppm). Therefore the zircon from this sample constitutes a clear example of the exception of typical metamorphic Th/U ratios (< 0.02) in magmatic zircon. Even though a metamorphic generation or overprint has been discarded, a post-protolith event must have taken place, because some of the zircon grains show corroded edges (*e.g.* A493; Fig. 82) and very thin rims (see blue zoomed areas in zircon grain A478; Fig. 82). No analytical information could be gathered from these rims. They could represent the only signs of over-imprint effects of zircon from the Devonian metamorphic event that the Upper Allochthon underwent. The low $\varepsilon Hf_{(t)}$ values calculated (average value of -5.3; Fig. 83a) indicates that the protolith material was not juvenile. It could be the result of partial melting of a *c.* 1.46 Ga old juvenile rock (average Hf zircon model-age is 1.46 Ga) or the result of mixing of a juvenile magma and the magma resulting from partial melting of a rock older than 1.46 Ga. It could also be the result of partial melting of sedimentary rocks. If this was the case it would be expected that Nd whole-rock model-age of this sample (Nd_{TDM} = 2.32 Ga) fell in the range of those of the Banded Gneiss metasedimentary rocks (from 1.31 to 1.85 Ga; see chapter 6), and they do not. Therefore it is not possible to give a reason of why the source signal of this rock is not juvenile, but is most probably linked to the complex magmatic development of the magmatic arc in which this orthogneiss was formed.

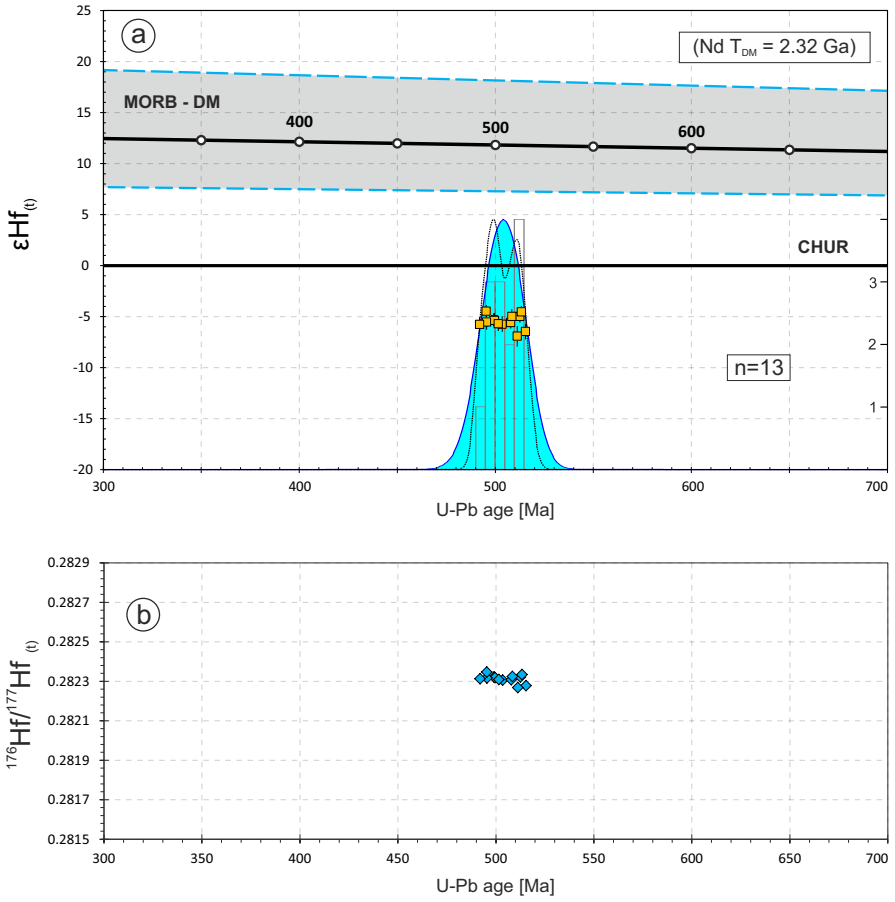

Fig. 83. a εHf *v.* age diagram. Error bars are +2σ and -2σ uncertainties. *n*, number of concordant zircon grains analysed for Lu–Hf isotopes. Numbers in the right vertical axis represent histogram frequency. Top-right rectangle shows Nd whole-rock model-age for the studied sample. MORB εHf interval was taken from Chauvel & Blichert-Toft (2001) considering a minimum $\varepsilon Hf_{(t=0Ma)}$ = +8.3 and a maximum $\varepsilon Hf_{(t=0Ma)}$ = +20.7. These values are propagated to $\varepsilon Hf_{(t=4Ga)}$ = 0 defining a grey field (enclosed by the blue discontinuous lines) around the DM-evolution trend, to provide an indication of the likely range of DM compositions through time. MORB: mid-ocean ridge basalts; DM: depleted mantle; CHUR: chondritic uniform reservoir. **b** $^{176}Hf/^{177}Hf_{(t)}$ *v.* age diagram.

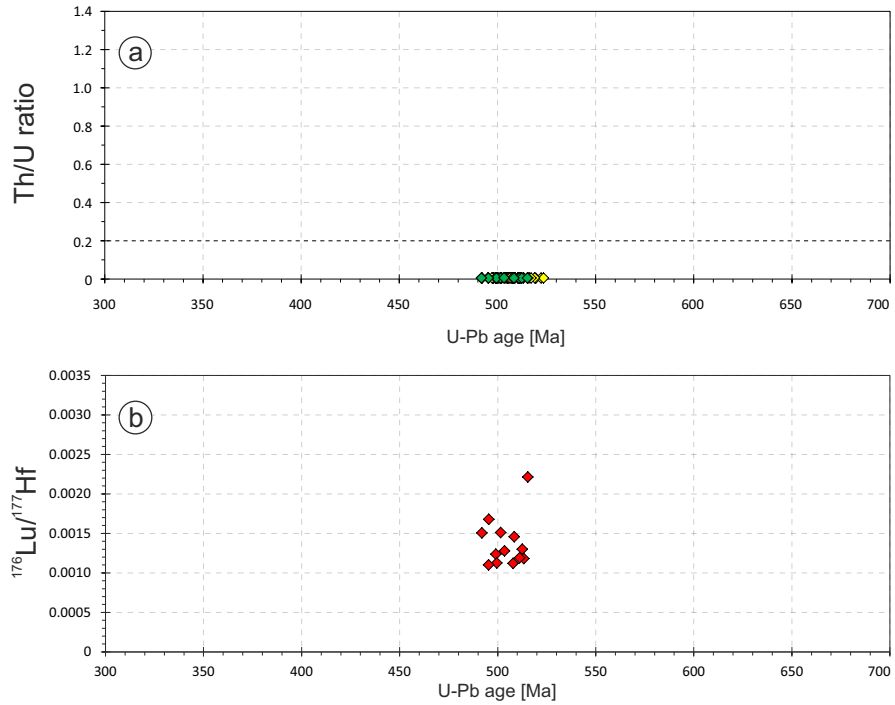

Fig. 84. a Th/U ratios *v.* age diagram (yellow rhombus represent Zrn analysed for U–Th–Pb isotopes and green rhombus represent those analysed for U–Th–Pb and Lu–Hf isotopes). **b** $^{176}Lu/^{177}Hf_{(t)}$ *v.* age diagram.

7.4.6. Sample GCH-31
(Serrón orthogneiss)

This sample was collected from *Punta do Serrón*, *Area da Vaca* beach (43°43'35.8"N, 7°51'49.5"W), at the 490 m point of the *Area da Vaca* geological section (chapter 4).

This orthogneiss outcrops as a porphyritic felsic rock with reddish feldspar centimetre porphyroblasts within a melanocratic matrix. It outcrops in contact with a mafic rock (*Punta do Serrón* mafic rock, meter point 460, *Area da Vaca* geological section; chapter 4). From field observations this mafic rock seems to intrude this orthogneiss (Fig. 85).

From microscopic observations this sample has a porphyro-grano-lepidoblastic texture (Ref: 114094). Qz, Grt and Afs are the major constituents (Fig. 86). Qz is displayed as small matrix-forming crystals in a granoblastic polygonal texture and they are mainly disposed in the porphyroblasts pressure shadows together with Bt, Ap and Grt. Qz is also displayed as tabular elongated poly-crystals coherent with the foliation. Grt and Afs are displayed as porphyroblasts and as small crystals within the matrix. Afs porphyroblasts normally show microcline twinning and they are normally poikilitic, containing mainly Qz and Afs crystals. In other cases this poikilitic texture seems to be a porphyroclastic texture, where the porphyroblasts are crushed or fragmented. The microcline twinning of these porphyroblasts seems to be an over-imposed feature, because it is not evident in all the crystals and in some cases it seems more evident at their outer parts. Other constituents are Bt, white mica, Ap and Zrn. Bt together with Qz tabular poly-crystals define the foliation.

7.4.6.1. Results

From this sample (GCH-31), 64 U–Pb analyses were performed of which 47 were concordant (d = 26.5%; Figs. 87 & 88). The U–Pb ages are scattered in the range of *c.* 470 to 520 Ma, with a maximum abundance peak at 483 Ma (Fig. 88) and two relative abundance peaks at 498 and 512. There are also two concordant zircon inheritances with ages of 635 and 2140 Ma.

Zircon is usually idiomorphic and shows a generally well-defined oscillatory growth pattern. In some cases this texture is blurred and faded. The majority of the zircon grains show rims which are darker than their cores in CL images. The contacts between cores and rims are usually sinuous and transgressive (Fig. 89).

$\varepsilon Hf_{(t)}$ values for all Cambrian zircon grains analysed are negative with an average value of -4.1 (minimum: -28.4, maximum: -0.1; Fig. 90a).

Fig. 85. Field photograph of the studied sample.

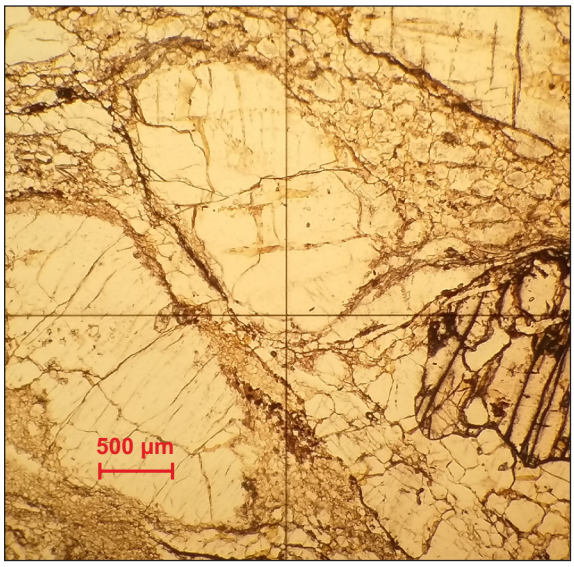

Fig. 86. Phtomicrograph of the studied sample.

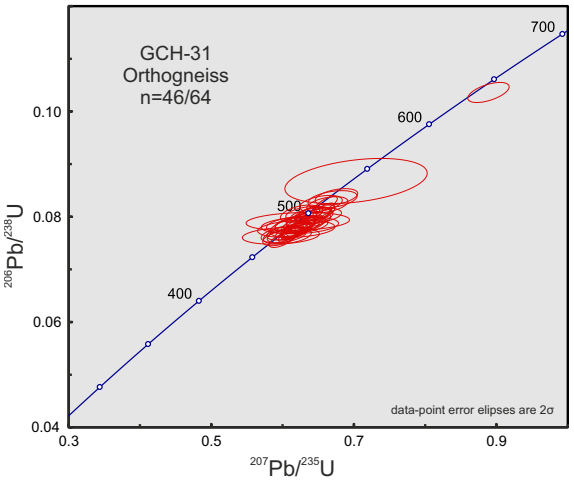

Fig. 87. U-Pb conventional concordia diagram showing U-Pb zircon analyses of the studied sample. Ellipses represent combined 2σ uncertainties of $^{206}Pb/^{238}U$ and $^{207}Pb/^{235}U$ ratios. *n*, number of analyses considered (those with 90–110% concordance)/total number of U–Pb analyses.

If the most negative value is excluded the average value is -2.5 (minimum: -4.7, maximum: -0.1; Fig. 90a). $^{176}Hf/^{177}Hf_{(t)}$ ratios for all Cambrian zircon grains analysed plot around 0.282357 ± 0.000371 (±2 SD; Fig. 90b). If the lowest value is excluded the average value is 0.282403 ± 0.000076 (±2 SD; Fig. 90b).

All analysed Cambrian zircon grains have an average content of U of 262 ppm (minimum: 54, maximum: 1011) and an average value of 21 ppm of Pb (minimum: 5, maximum: 74; Appx. 4). Th/U ratios for all Cambrian zircon grains analysed have average values of 0.45 (minimum: 0.14, maximum: 0.93; Fig. 91a).

$^{176}Lu/^{177}Hf$ ratios for all Cambrian zircon grains analysed plot around 0.00165 ± 0.00117 (±2 SD; Fig. 91b). $^{176}Yb/^{177}Hf$ ratios for all Cambrian zircon grains analysed plot around 0.0486 ± 0.0356 (±2 SD; Appx. 4).

Nd whole-rock model-age is 1.36 Ga and $\varepsilon Nd_{(t)}$ values are: $\varepsilon Nd_{(t=0)}$ = -6.0; $\varepsilon Nd_{(t=483)}$ = -2.1.

7.4.6.2. Discussion

Beside the inheritances, this sample has one zircon population with ages between *c.* 470 and 520 Ma, with a maximum abundance peak at 483 Ma and with two relative abundance peaks at 498 and 512 Ma. The zircon textures (Fig. 89) show that zircon grains from this sample have cores and rim domains, but no age constraints could be established for each domain. The reason for this is that cores and rims show variable ages. For example core A198 has an age of 500 ± 8 Ma and core A219 has an age of 480 ± 7 Ma (Fig. 89). Rims also show this wide time span. Rim A205 has an age of 510 ± 7 Ma and rim A230 has an age of 476 ± 8 Ma (Fig. 89). A similar situation happens when a close look on $^{176}Hf/^{177}Hf_{(t)}$ ratios or $\varepsilon Hf_{(t)}$ values is taken for each of these two domains. In some cases $^{176}Hf/^{177}Hf_{(t)}$ ratios of a rim and a core of the same zircon crystal are very similar, suggesting that rims were formed

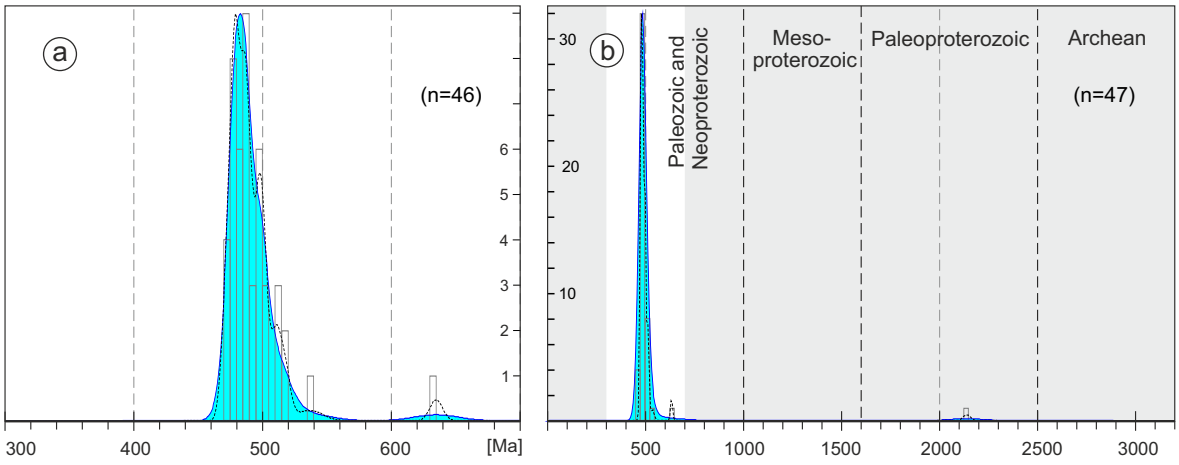

Fig. 88. Adaptative Kernel Density Estimation (aKDE, continuous line enclosing the blue area), Probability Density (PDP, black dashed line) and histogram diagrams of the U–Pb analyses (calculated with DensityPlotter5.0, Vermeesch 2012). Numbers in the vertical axis represent histogram frequency; *n*, number of analyses. **a** Partial plot representing data within a 300–700 Ma time range (bandwidth = 5 Ma, binwidth = 5 Ma). **b** Complete plot (bandwidth = 15 Ma, binwidth = 25 Ma).

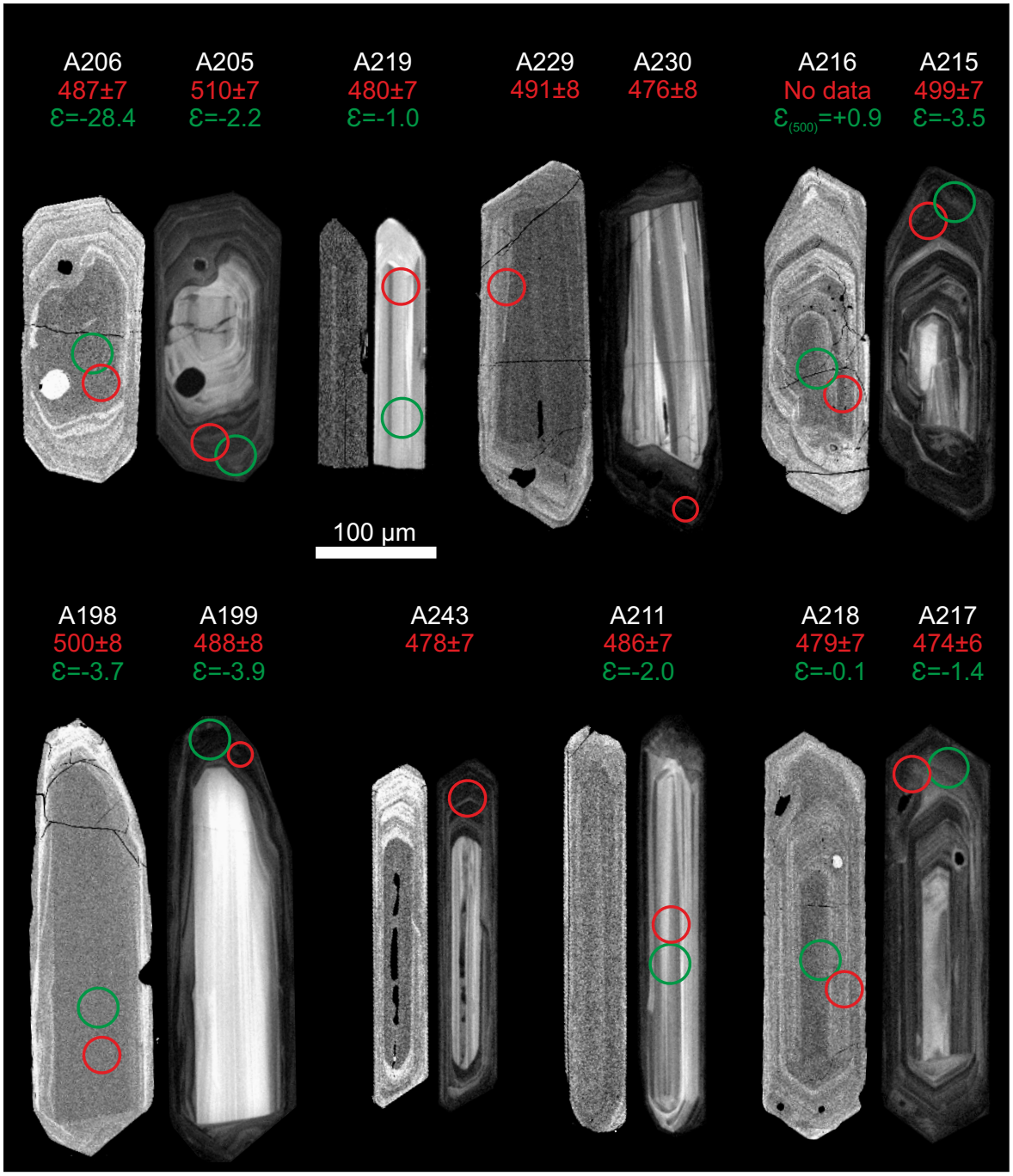

Fig. 89. BSE and CL images of representative zircons from the studied sample. Left images circles are BSE (back-scattered electrons) images, and right imeges are CL (cathodoluminescence) images. Laser ablation pits for U–Pb analyses (red line circles) have 20 and 30 μm diameters. Laser ablation pits for Lu–Hf analyses (green line circles) have 23 and 33 μm diameters. White numbers are the reference number of the analysis, red numbers are the U–Pb age and its 2σ error (Ma) and the green numbers are the εHf values for the U–Pb age. U–Pb analysis of A216 gave a discordant age, and εHf value was calculated for an assumed 500 Ma age.

by a solid-sate recrystallisation process of their corresponding cores. This is the case of core A218 (0.282480) and rim A217 (0.282446; Fig. 89 and Appx. 4). In other cases $^{176}Hf/^{177}Hf_{(t)}$ ratios of cores and rims are totally different (rim A205 and core A206 have $^{176}Hf/^{177}Hf_{(t)}$ ratios of 0.282400 and 0.281676 respectively) implying that the rim is an overgrowth grown from a different liquid phase with a different $^{176}Hf/^{177}Hf_{(t)}$ ratio than its core. Also, Th/U and $^{176}Lu/^{177}Hf$ ratios do not show any correlation with their U–Pb ages (Fig. 91). The only data that

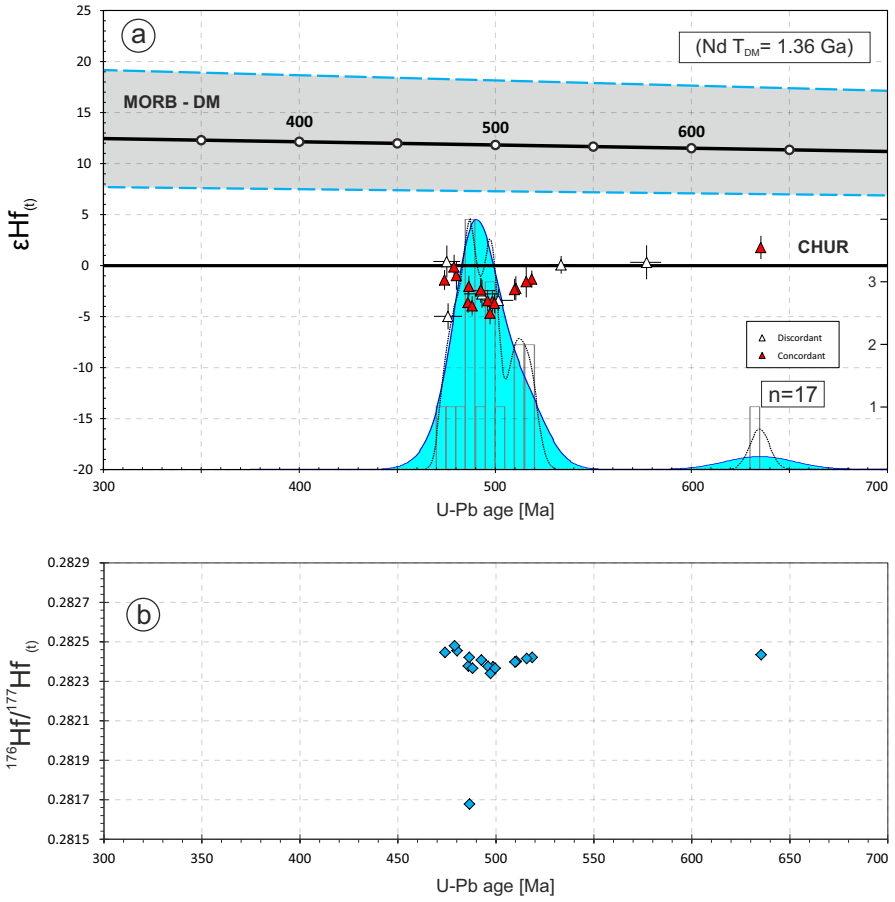

Fig. 90. a εHf *v.* age diagram. Error bars are +2σ and -2σ uncertainties. *n*, number of concordant zircon grains analysed for Lu–Hf isotopes. Numbers in the right vertical axis represent histogram frequency. Top-right rectangle shows Nd whole-rock model-age for the studied sample. MORB εHf interval was taken from Chauvel & Blichert-Toft (2001) considering a minimum $\varepsilon Hf_{(t=0Ma)}$ = +8.3 and a maximum $\varepsilon Hf_{(t=0Ma)}$ = +20.7. These values are propagated to $\varepsilon Hf_{(t=4Ga)}$ = 0 defining a grey field (enclosed by the blue discontinuous lines) around the DM-evolution trend, to provide an indication of the likely range of DM compositions through time. MORB: mid-ocean ridge basalts; DM: depleted mantle; CHUR: chondritic uniform reservoir. **b** $^{176}Hf/^{177}Hf_{(t)}$ *v.* age diagram.

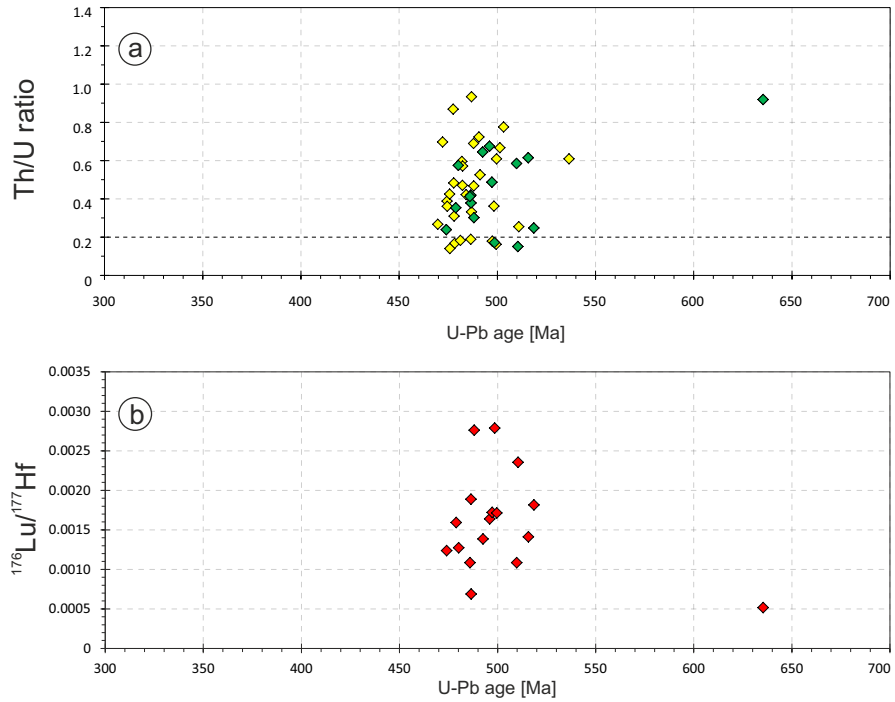

Fig. 91. a Th/U ratios *v.* age diagram (yellow rhombus represent Zrn analysed for U–Th–Pb isotopes and green rhombus represent those analysed for U–Th–Pb and Lu–Hf isotopes). **b** $^{176}Lu/^{177}Hf_{(t)}$ *v.* age diagram.

show a correlation when plotted against U–Pb ages are the $\varepsilon Hf_{(t)}$ values and $^{176}Hf/^{177}Hf_{(t)}$ ratios (Fig. 90). Between *c.* 520 and 500 Ma these ratios decrease when U–Pb ages decrease, and between *c.* 500 and 470 Ma the ratios increase when U–Pb ages decrease. The $^{176}Hf/^{177}Hf_{(t)}$ ratio decrease between *c.* 520 and 500 Ma looks like it can only be explained by continuous zircon crystallisation in a liquid phase that was progressively depleted in its radiogenic ^{176}Hf content. This progressive depletion can be explained or by a *c.* 20 Ma progressive mixing between this liquid phase and another one with lower $^{176}Hf/^{177}Hf_{(t)}$ ratios, or by a continuous contamination of the liquid during *c.* 20 Ma probably due to continuous assimilation of the host-rock. The $^{176}Hf/^{177}Hf_{(t)}$ ratio increase between *c.* 500 and 470 Ma can be explained as, once the rock system crystallised at *c.* 500 Ma it started a *c.* 30 Ma long partial melting process that progressively enriched the partial melt with radiogenic ^{176}Hf, that came from the ^{176}Lu decay from the minerals that were melting to form the partial melt. It is noteworthy to mention that from field observations this orthogneiss was intruded by the *Punta do Serrón* mafic rock (Fig. 85). This outcrop is cartographically related with the *Punta da Moura* mingling suite and the Eclogite Band formation (Appx. 1). This mingling complex is formed by a *c.* 508 Ma mafic rock (sample GCH-23; Zrn crystallisation from *c.* 515 Ma; section 7.3.4) that underwent a *c.* 489 Ma solid state recrystallisation process (that lasted from *c.* 490 to 470 Ma), triggered by the temperature input related with the intrusion of a *c.* 500 Ma felsic rock (sample GCH-14; section 7.4.4). From these observations and interpretations it is proposed that this orthogneiss (GCH-31) was intruded by the mafic protolith magmas that constitute the common eclogites of the Eclogite Band formation (represented by sample GCH-19; section 7.3.1; abundance Zrn peak at 485 Ma, Zrn crystallisation between *c.* 520 and 470 Ma), the *Punta do Serrón* mafic rock (not studied in this work) and the *Punta da Moura* mafic rock (represented by sample GCH-23; section 7.3.4; Zrn crystallisation peak at 508 Ma). When these magmas were cooling and crystallising, felsic magma (sample GCH-14; section 7.4.4) intruded into the mafic rocks in the *Punta da Moura* area at *c.* 500 Ma to form the *Punta da Moura* mingling suite.

7.5. Discussion

7.5.1. Leucosomes

From the first sample studied (GCH-25, section 7.2.1) it was concluded that the metasedimentary rocks (in which the leucosomes are included) underwent partial melting at high-T conditions, triggering solid-state recrystallisation process of the inherited zircon (Cambrian and older zircon). When the partial melt cooled sufficiently, overgrowths formed between 377 and 403 Ma, with a crystallisation climax at *c.* 387 Ma.

From the second sample studied (GCH-26, section 7.2.2) it was concluded that the overgrowths crystallised from the partial melt in the prograde metamorphic path and that solid-state recrystallisation occurred afterwards when the system reached the temperature peak. The overall age for these processes is from 379 to 403 Ma with a crystallisation climax at *c.* 389 Ma.

From the third sample studied (GCH-32, section 7.2.3) it was concluded that both processes (recrystallisation and overgrowth) are present within zircon crystals of the same age (Devonian), and that the overall age for these processes is from 358 to 408 Ma with a crystallisation climax at *c.* 394 Ma.

As all three leucosomes are formed in the same formation, Fig. 92 is presented, which combines the $\varepsilon Hf_{(t)}$ data of the three samples and the U–Pb combined density diagram of these three and of the detrital zircon of the metasedimentary rocks. The youngest zircon population is Devonian and it is constrained between 377 and 408 Ma, with zircon crystallisation climax at *c.* 388 Ma (if the youngest and oldest ages are not considered the time range is 379 to 403 Ma). These ages are interpreted as to be the ages of the migmatization event that the metasedimentary rocks underwent. Taking into account the conclusions for each sample, together with their U–Pb ages it is proposed that this event triggered

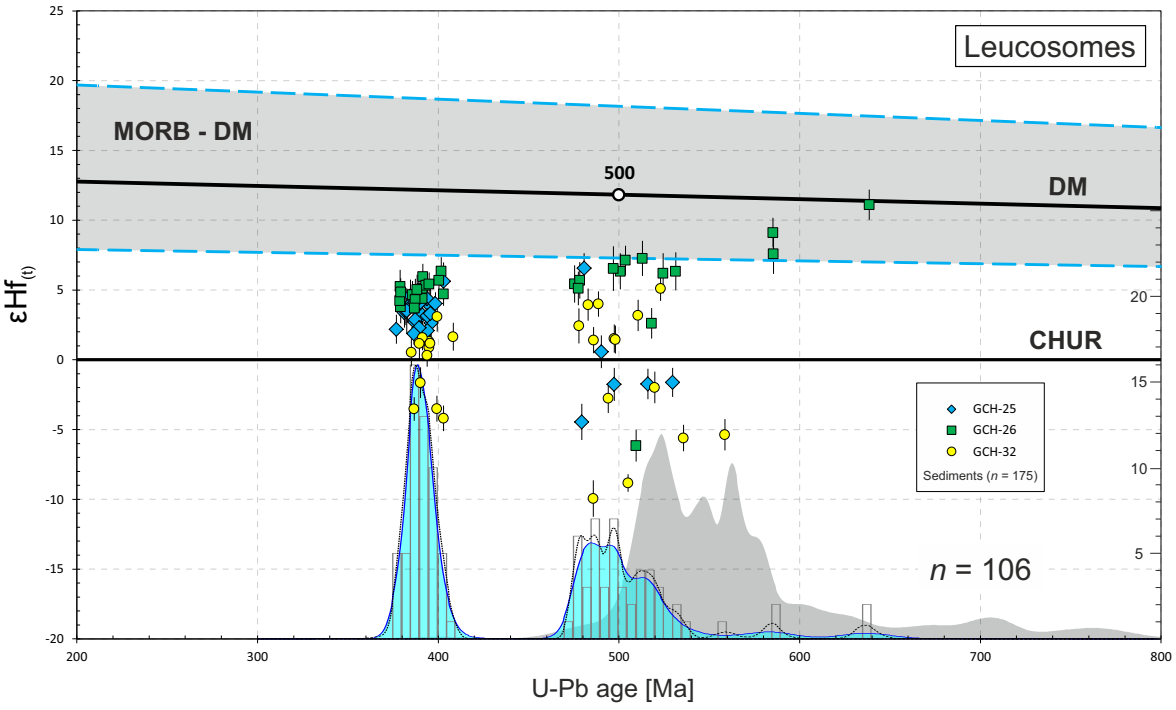

Fig. 92. εHf *v.* age diagram for the three leucosomes studied. Adaptative Kernel Density Estimation (aKDE, continuous line enclosing the blue area, and grey area), Probability Density (PDP, black dashed line) and histogram diagrams of the U–Pb analyses (calculated with DensityPlotter5.0, Vermeesch 2012; bandwidth = 5 Ma, binwidth = 5 Ma). Numbers in the right vertical axis represent histogram frequency; *n*, number of analyses. The grey shaded area is the aKDE for the Eclogite Gneisses detrital zircon. The histogram for the Eclogite Gneisses detrital zircon (not represented) has been normalized to the same hight as the leucosome zircon histogram. Error bars are +2σ and -2σ uncertainties. MORB: mid-ocean ridge basalts; DM: depleted mantle; CHUR: chondritic uniform reservoir.

pseudomorphic recrystallisation of the previous zircon grains, as the metasedimentary rocks were heated at high temperature conditions and partially melted. Afterwards these zircon crystals overgrew when the system cooled sufficiently.

During the study of these leucosomes, the older zircon population (Cambrian–Ordovician) has been assumed to be inherited from the metasedimentary rocks. The wide range of $\varepsilon Hf_{(t)}$ values of this leucosomes zircon population (Fig. 92) seems to favour this interpretation, because the detrital zircon also shows a wide $\varepsilon Hf_{(t)}$ value range. However, the U–Pb density distribution of the leucosomes is not included within the density distribution of the metasedimentary rocks (Fig. 92). If the leucosome zircon population was inherited from the metasedimentary rocks, their U–Pb density distributions should overlap. Moreover, the U–Pb maximum abundance peaks of the leucosome zircon population are *c.* 485 and *c.* 495 Ma, and these ages in the metasedimentary rocks are scarce and almost negligible. It would appear that these observations can only be explained by assuming that the leucosomes were generated at around 485–495 Ma and that they were re-melted at *c.* 388 Ma. Petrographic observations favour this interpretation as the quartz-feldspathic matrix is displayed as big poikilitic crystals and as small crystals defining a granoblastic texture. This interpretation is taken with great care until it can be corroborated with further studies, but it seems clear that some sort of process must have occurred in the Cambrian–Ordovician boundary in the light of the above-mentioned observations.

7.5.2. Eclogites

From the first sample studied (GCH-19, section 7.3.1) it was concluded that a *c.* 387 Ma high-grade metamorphic event induced solid-state zircon pseudomorphic recrystallisations, triggering U–Pb age rejuvenation via Pb-loss processes of the zircons that crystallised in the

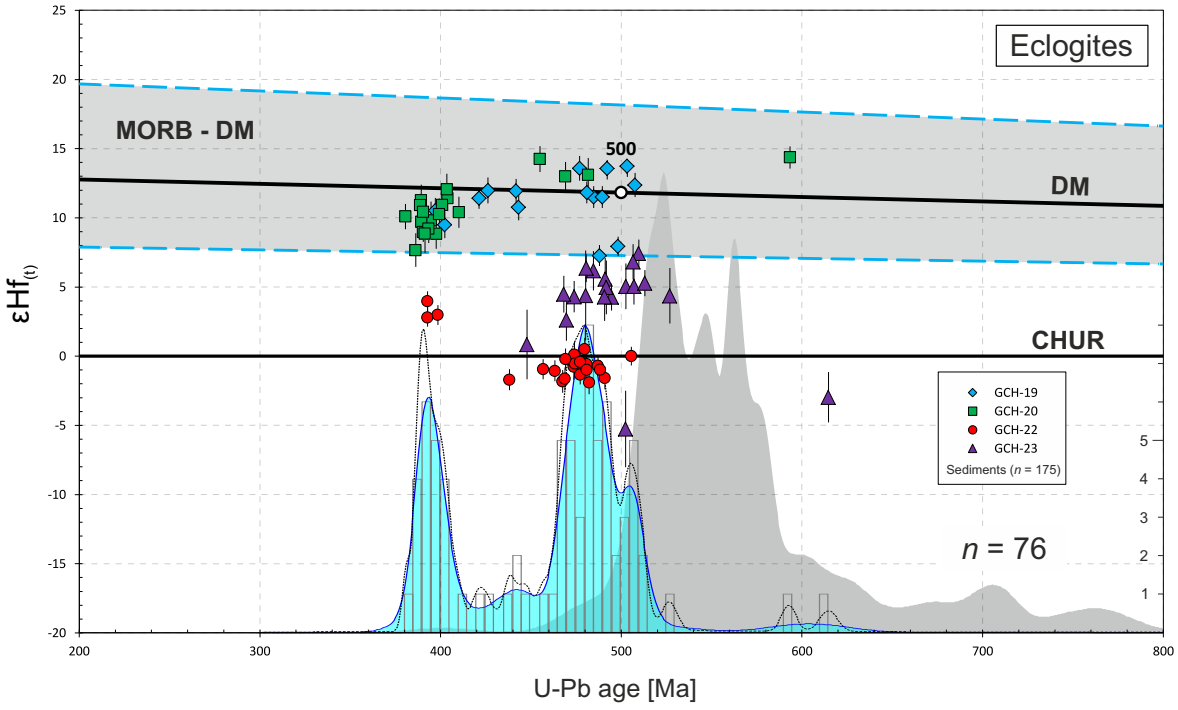

Fig. 93. εHf *v.* age diagram for the four eclogites studied. Adaptative Kernel Density Estimation (aKDE, continuous line enclosing the blue area, and grey area), Probability Density (PDP, black dashed line) and histogram diagrams of the U–Pb analyses (calculated with DensityPlotter5.0, Vermeesch 2012; bandwidth = 5 Ma, binwidth = 5 Ma). Numbers in the right vertical axis represent histogram frequency; *n*, number of analyses. The grey shaded area is the aKDE for the Eclogite Gneisses detrital zircon. The histogram for the Eclogite Gneisses detrital zircon (not represented) has been normalized to the same hight as the eclogite zircon histogram. Error bars are +2σ and -2σ uncertainties. MORB: mid-ocean ridge basalts; DM: depleted mantle; CHUR: chondritic uniform reservoir.

gabbroic or basaltic protolith from 505 to 485 Ma (zircon crystallisation climax at *c*. 485 Ma).

From the second sample studied (GCH-20, section 7.3.2) it was concluded that the protolith mafic rock was crystallised almost directly from a DM source, and that a HP–HT metamorphic event induced extreme zircon solid-state recrystallisation of the protolith zircon between 372 and 410 Ma, with a zircon crystallisation climax at 390 Ma.

From the third sample studied (GCH-22, section 7.3.3) it was concluded that the age of crystallisation of the protolith material is constrained between 482 and 473 Ma, with a zircon crystallisation climax at 473 Ma. This protolithic zircon overgrew at high-T conditions at *c*. 395 Ma together with, or subsequent to, metamorphic Grt.

From the fourth sample studied (GCH-23, section 7.3.4) it was concluded that the protolithic zircon crystallised at around *c*. 508 Ma. This mafic rock was intruded by a felsic rock (GCH-14, section 7.4.4) at *c*. 500 Ma, inducing a high-T input in the mafic rock, which triggered zircon pseudomorphic alteration at *c*. 489 Ma, with no presence of a fluid phase.

The four eclogites have been represented together in Fig. 93, which combines the $\varepsilon Hf_{(t)}$ data of the four samples and the U–Pb combined density diagram of these four and of the detrital zircon of the HP–HT metasedimentary rocks (Banded Gneisses). This combined figure shows a zircon crystallisation climax for the Cambrian–Ordovician eclogite population at *c*. 480 Ma and a relative abundance peak at *c*. 505 Ma. Both ages are interpreted as the ages of the protolith mafic generation, but the possibility of a generation at *c*. 505 Ma and a metamorphic event at *c*. 480 Ma cannot be discarded or proved. The sources of the mafic protolith rocks are varied. Two samples (GCH-19 and GCH-20) show that their protoliths are almost directly derived from a depleted mantle source, most probably by direct partial fusion of it. The geological environment in which these primitive and juvenile protolithic rocks are enclosed is a back-arc type basin where the oceanic crust is generated as the basin widens and evolves. This environment fits perfectly with a juvenile source protolith origin for these eclogites. The other two samples (GCH-22 and GCH-23) have $\varepsilon Hf_{(t)}$ and $\varepsilon Nd_{(t)}$ values not compatible with a juvenile source derivation for the genesis of their protoliths. It seems that the only possible ways to explain a non-juvenile derivation of a basic rock are: (i) as a partial fusion of an enriched mantle component, or (ii) as an important contamination of a depleted mantle partial melt with continental crust material. Both explanations are probable, since in a magmatic arc system, contamination is very possible due to the intrusion of juvenile materials into continental crust ones, the same way as an enriched mantle component is also very probably present in this geological context. This enriched component could be, for example, the subcontinental mantle of Gondwana, which evolved separately from the depleted mantle since the Mesoproterozoic (Nd model ages and the average of Hf zircon model ages fall in the Mesoproterozoic Era).

The zircon crystallisation climax is *c*. 393 Ma for the Devonian eclogite population. This age is interpreted to be the age of maximum zircon crystallisation due to a HP–HT metamorphic event. This metamorphism triggered solid-state recrystallisation of inherited zircon and also zircon overgrowths at high temperature conditions, most probably near the metamorphic path temperature peak.

7.5.3. Orthogneisses

From the first sample studied (GCH-01, section 7.4.1) it was concluded that the magmatic protolith zircon crystallised between 518 and 466 Ma with a crystallisation climax at *c*. 496 Ma. A solid-state recrystallisation of the protolithic zircon triggered by a high-grade metamorphic event took place between 410 and 381 Ma, with a crystallisation climax at *c*. 402 Ma.

From the second sample studied (GCH-03, section 7.4.2) it was concluded that the protolithic zircon crystallised between 510 and 450 Ma, with a crystallisation climax at *c*. 485 Ma, and that a posterior recrystallisation event altered the zircon textures without triggering any rare element purge from the zircon structures.

From the third sample studied (GCH-13, section 7.4.3) it was concluded that the protolithic zircon crystallised between 530 and 460 Ma, with a crystallisation climax at *c.* 504 Ma.

From the fourth sample studied (GCH-14, section 7.4.4) it was concluded that the protolithic zircon crystallised at around *c.* 500 Ma. This orthogneiss forms part of the *Punta da Moura* mingling suite and shows a zircon relative abundance at *c.* 470 Ma. This age could be related to a temperature input associated to the mingling process, to a different *c.* 470 Ma metamorphic event, or to a Pb-loss process triggered by the Devonian HP–HT metamorphic event, which has been dated in this sample with one zircon-rim analysis at *c.* 390 Ma.

From the fifth sample studied (GCH-18, section 7.4.5) it was concluded that the protolith zircon crystallised between 524 and 492 Ma, with a crystallisation climax at *c.* 506 Ma. Due to the high quality of the analysis this time range is considered as a *c.* 32 Ma cooling time of the protolith magmas.

From the sixth sample studied (GCH-31, section 7.4.6) it was concluded that the protolithic zircon cores and rims were crystallised between 520 and 470 Ma, through solid-state recrystallisation and overgrowth processes. From 520 to 500 Ma (with a crystallisation climax at 512 Ma) the cores and rims grew from a magma that was progressively mixed with another less-juvenile liquid or from a magma that was progressively contaminated, probably by a continuous assimilation of the host rock. At *c.* 500 Ma the magmatic system crystallised and from 500 to 470 Ma cores and rims were formed by a *c.* 30 Ma long partial melting process, with a crystallisation climax at 483 Ma. This partial melting process was probably due to the long lasting temperature input related to the magmatic arc system. There is the possibility that this process could be driven by a metamorphic event

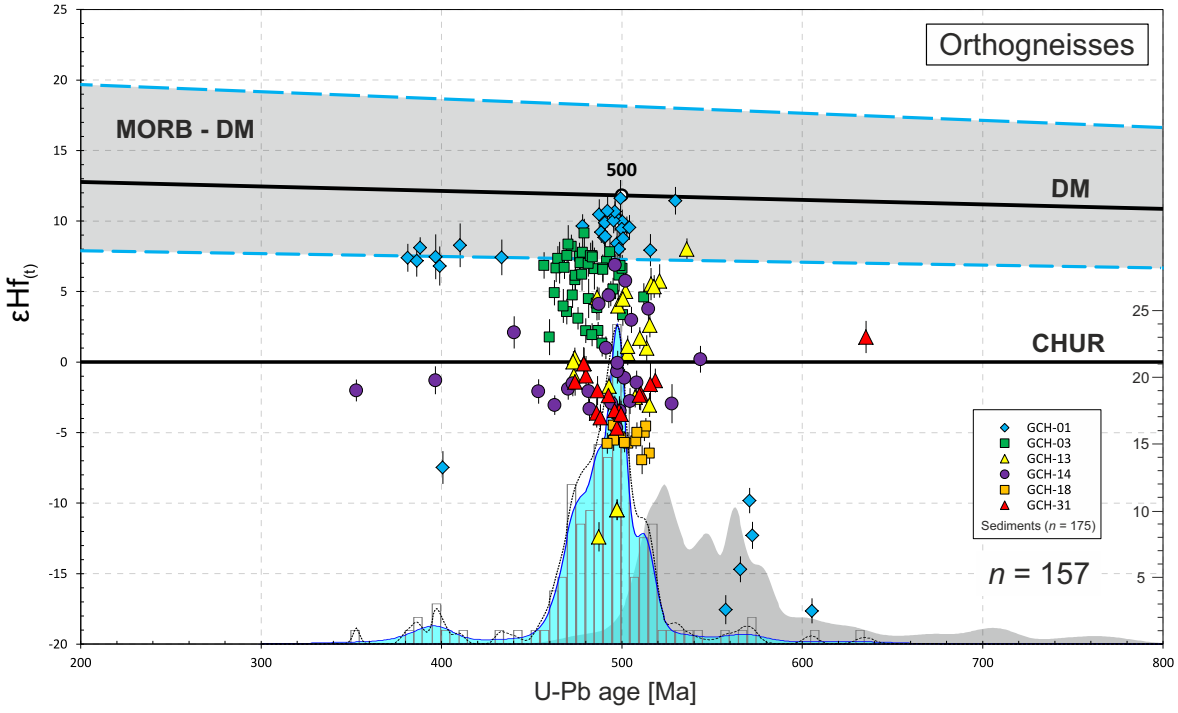

Fig. 94. εHf *v.* age diagram for the six orthogneisses studied. Adaptative Kernel Density Estimation (aKDE, continuous line enclosing the blue area, and grey area), Probability Density (PDP, black dashed line) and histogram diagrams of the U–Pb analyses (calculated with DensityPlotter5.0, Vermeesch 2012; bandwidth = 5 Ma, binwidth = 5 Ma). Numbers in the right vertical axis represent histogram frequency; *n*, number of analyses. The grey shaded area is the aKDE for the Eclogite Gneisses detrital zircon. The histogram for the Eclogite Gneisses detrital zircon (not represented) has been normalized to the same hight as the orthogneiss zircon histogram. Error bars are +2σ and -2σ uncertainties. MORB: mid-ocean ridge basalts; DM: depleted mantle; CHUR: chondritic uniform reservoir.

related to the oceanic crust subduction directed to Gondwana, responsible for the formation of the Cambrian–Ordovician magmatic arc system.

The six orthogneisses have been represented together in Fig. 94, which combines the $\varepsilon Hf_{(t)}$ data of the six samples and the U–Pb combined density diagram of all six and of the detrital zircon of the HP–HT metasedimentary rocks (Banded Gneisses). This combined figure shows a zircon crystallisation climax for the Cambrian–Ordovician orthogneiss population at 498 Ma with a long tail of ages down to *c*. 460–470 Ma and a relative abundance peak at *c*. 512 Ma. These ages are interpreted as the ages of the protolith felsic generation, but the possibility of a generation at *c*. 512 Ma and a later metamorphic event cannot be discarded or proved, but from the above-mentioned discussions it seems probable. If this event took place it was most probably a high-T metamorphic event related to the activity of the magmatic arc system. The sources of the felsic protolith rocks are varied. At around *c*. 512 Ma the sources (as viewed in Fig. 94) are diverse, as would be expected from a felsic arc-related magmatism. At around c. 498 Ma (the zircon crystallisation climax) the sources are also varied, but some of the orthogneiss zircon analyses plot on the MORB-DM evolution array (such as GCH-01 and GCH-03). This implies that the rocks, from which the mentioned juvenile zircon analyses belong to, were almost directly derived from a depleted mantle source. As a felsic rock cannot be a direct product of the partial fusion of the mantle, they must be the result of fractional crystallisation of a basic magma, or more likely the result of the partial fusion of a DM derived mafic rock.The magmatic arc geological environment in which these rocks are related, could explain the high temperature conditions necessary for partially melting mafic rocks. For these reasons it is concluded that from the acidic igneous rocks studied, the magmatic activity of the arc system started at around 512 Ma and finished around 470–460 Ma, and that this activity induced high–T related metamorphism that partially melted previously generated igneous rocks within the same magmatic arc.

The zircon crystallisation climax is *c*. 395 Ma for the Devonian orthogneiss population. This age is interpreted to be the age of maximum zircon crystallisation due to a HP–HT metamorphic event. This metamorphism triggered solid-state recrystallisation of inherited zircon at high temperature conditions, most probably near the metamorphic path temperature peak. It is noteworthy to mention that the orthogneisses are the igneous lithologies that were less affected by this HP–HT metamorphic event.

7.6. General discussion

From the leucosome samples studied, it is interpreted that a first migmatization of the metasedimentary rocks took place at around 485–495 Ma. This process was probably triggered by a temperature input related to the magmatic arc system activity. These leucosomes were re-melted at high-T conditions between 379 and 403 Ma, with a zircon crystallisation climax at *c.* 388 Ma. This second event was most probably related to the HP–HT Devonian metamorphic event.

From the eclogite samples studied, it is interpreted that the Devonian zircon crystallisation climax was triggered by the HP–HT metamorphic event at *c*. 393 Ma, most probably near the metamorphic path temperature peak. The Cambrian–Ordovician eclogite population shows a zircon crystallisation climax at *c*. 480 Ma and a relative abundance peak at *c*. 505 Ma. Both ages are interpreted as the ages of the protolith mafic generation, but the possibility of a generation at *c*. 505 Ma and a metamorphic event at *c*. 480 Ma cannot be discarded or proved. The sources of the mafic protolith rocks are varied. The protoliths are juvenile, with an almost direct derivation from a depleted mantle source, and they are also isotopically enriched. These isotopically enriched sources are interpreted as a partial fusion of an enriched mantle component (probably the subcontinental mantle of Gondwana), or as an important contamination of a depleted mantle partial melt with continental crust material.

From the orthogneiss samples studied, it is interpreted that the Devonian zircon crystallisation climax was triggered by the HP–HT metamorphic event at *c*. 395 Ma. The orthogneisses are the igneous lithologies that were less affected by this HP–HT metamorphic event. The Cambrian–Ordovician orthogneiss population shows a zircon crystallisation climax at 498 Ma with a long tail of ages down to *c*. 460–470 Ma and a relative abundance peak at *c*. 512 Ma. These ages are conservatively interpreted as the ages of protolithic formation, but a more complex evolution is also proposed. The magmatic activity of the arc system started at around 512 Ma and finished around 470–460 Ma, and this activity induced high–T related metamorphism at around 498 Ma that partially melted previously generated igneous rocks within the same magmatic arc up to *c*. 460–470 Ma.

7.7. References

Bernard-Griffiths, J., Peucat, J.J., Cornichet, J., Ponce de Léon, M. I. & Gil Ibarguchi, J. I. (1985). U–Pb, Nd Isotope and REE geochemistry in eclogites from the Cabo Ortegal Complex, Galicia, Spain: An example of REE immobility conserving MORB-like patterns during high-grade metamorphism. *Chemical Geology: Isotope Geoscience section* **52**, 217-225.

Gerdes, A. & Zeh, A. (2009). Zircon formation versus zircon alteration - New insights from combined U–Pb and Lu–Hf in-situ LA–ICP–MS analyses, and consequences for the interpretation of Archean zircon from the Central Zone of the Limpopo Belt. *Chemical Geology* **261**, 230-243.

Gil Ibarguchi, J. I., Mendía, M., Girardeau, J. & Peucat, J. J. (1990). Petrology of eclogites and clinopyroxene-garnet metabasites from the Cabo Ortegal Complex (northwestern Spain). *Lithos* **25**, 133-162.

Harley, S. L., Kelly, N. M. & Möller, A. (2007). Zircon Behaviour and the Thermal Histories of Mountain Chains. *Elements* **3**, 25-30.

Hoskin, P. W. O. & Schaltegger, U. (2003). The Composition of Zircon and Igneous and Metamorphic Petrogenesis. *Reviews in Mineralogy and Geochemistry* **53**, 27-62.

Jacobsen, S. B. & Wasserburg, G. J. (1980). Sm–Nd isotopic evolution of chondrites. *Earth and Planetary Science Letters* **50**, 139-155.

Kelly, N. & Harley, S. (2005). An integrated microtextural and chemical approach to zircon geochronology: refining the Archaean history of the Napier Complex, east Antarctica. *Contributions to Mineralogy and Petrology* **149**, 57-84.

Mendía, M. (2000). Petrología de la Unidad Eclogítica del Complejo de Cabo Ortegal, (NW de España). *Nova Terra* **16**, 424.

Ordóñez Casado, B., Gebauer, D., Schäfer, H. J., Gil Ibarguchi, J. I. & Peucat, J. J. (2001). A single Devonian subduction event for the HP/HT metamorphism of the Cabo Ortegal complex within the Iberian Massif. *Tectonophysics* **332**, 359-385.

Pan, Y. (1997). Zircon- and monazite-forming metamorphic reactions at Manitouwadge, Ontario. *The Canadian Mineralogist* **35**, 105-118.

Peucat, J. J., Bernard-Griffiths, J., Gil Ibarguchi, J. I., Dallmeyer, R. D., Menot, R. P., Cornichet, J. & Ponce De León, M. I. (1990). Geochemical and geochronological cross section of the deep Variscan crust: The Cabo Ortegal high-pressure nappe (northwestern Spain). *Tectonophysics* **177**, 263-292.

Schaltegger, U., Fanning, C. M., Günther, D., Maurin, J. C., Schulmann, K. & Gebauer, D. (1999). Growth, annealing and recrystallisation of zircon and preservation of monazite in high-grade metamorphism: conventional and in-situ U–Pb isotope, cathodoluminescence and microchemical evidence. *Contributions to Mineralogy and Petrology* **134**, 186-201.

Tomaschek, F., Kennedy, A. K., Villa, I. M., Lagos, M. & Ballhaus, C. (2003). Zircons from Syros, Cyclades, Greece - Recrystallisation and Mobilization of Zircon During High-Pressure Metamorphism. *Journal of Petrology* **44**, 1977-2002.

Van Calsteren, P. W. C., Boelrijk, N. A. I. M., Hebeda, E. H., Priem, H. N. A., Den Tex, E., Verdurmen, E. A. T. & Verschure, R. H. (1979). Isotopic dating of older elements (including the Cabo Ortegal mafic-ultramafic complex) in the Hercynian orogen of NW Spain: Manifestations of a presumed Early Paleozoic mantle-plume. *Chemical Geology* **24**, 35-56.

Vavra, G., Gebauer, D., Schmid, R. & Compston, W. (1996). Multiple zircon growth and recrystallisation during polyphase Late Carboniferous to Triassic metamorphism in granulites of the Ivrea Zone (Southern Alps): an ion microprobe (SHRIMP) study. *Contributions to Mineralogy and Petrology* **122**, 337-358.

Vogel, D. E. (1967). Petrology of an eclogite- and pyrigarnite-bearing polymetamorphic rock complex at Cabo Ortegal, NW Spain. *Leidse Geologische Mededelingen* **40**, 121-213.

Whitney, D. L. & Evans, B. W. (2010). Abbreviations for names of rock-forming minerals. *American Mineralogist* **95**, 185-187.

Zeh, A., Gerdes, A., Barton Jr, J. & Klemd, R. (2010). U–Th–Pb and Lu–Hf systematics of zircon from TTG's, leucosomes, meta-anorthosites and quartzites of the Limpopo Belt (South Africa): Constraints for the formation, recycling and metamorphism of Palaeoarchaean crust. *Precambrian Research* **179**, 50-68.

VIII

Two-stage collision: Exploring the birth of Pangea in the Variscan terranes

8.1. Introduction

This article is presented to englobe the Upper Allochthon in the general context of continental interaction in the process of Pangea´s amalgamation. In the Allochthonous Complexes there are two high grade terranes with continental affinity that underwent subduction, the Upper Allochthon (upper units) and the Basal Allochthon (basal units). A modern analogue is shown to address the conditions of the initial stages of the continental assembly.

8.2. Partial conclusions

The subduction event that both terranes underwent is not one, but two events with different ages and P–T conditions. The subduction of the Upper Allochthon terrane reached HP–HT or even ultra-HP–HT conditions and it is *c*. 30 Ma older than the subduction of the Basal Allochthon, which registered HP and low-to-intermediate-T (HP–LIT). In this article it is proposed that the volcanic arc system that in a broad sense the Upper Allochthon represents did not drift away from Gondwana to form the Rheic Ocean in its wake, but instead a relatively small basin was formed, now represented by the Lower Ophiolitic Units. Between the formation of the magmatic arc and the Devonian subduction the

margin of Gondwana was a passive and extended one. The first collision occurred in the Early Devonian (before *c.* 400–390 Ma) and caused deep subduction of a section of the margin of Gondwana and the generation of a HP–UHP metamorphic belt (Upper Allochthon of the Variscan suture). Lateral motion between Gondwana and Laurussia favoured the opening of a relatively wide pull-apart basin at *c.* 400–395 Ma. The rapid closure of this basin started at *c.* 380 Ma and caused the accretion of buoyant oceanic lithosphere of Devonian age below the northern continent. This oceanic lithosphere is represented by the most common ophiolites found in the Variscan Belt (Upper Ophiolitic Units). Mafic slices with a similar age and showing greenschist facies recrystallization were accreted later, followed by mafic complexes with Cambrian age generated by the activity of peri-Gondwanan volcanic arcs that progressively reached the collision zone as the basin shrank (Lower Ophiolitic Units). Finally, further convergence led to a new collision with another section of the Gondwanan margin, with generation of a second HP–LIT belt at *c.* 370 Ma (Basal Units). Convergence continued during the Carboniferous and produced the complex intracontinental deformation that characterizes the Variscan belt. According to structural data and paleogeographic reconstructions for the allochthonous pile of NW Iberia, the Devonian and Carboniferous convergence was accompanied by a dextral lateral component for most of the time.

Gondwana Research 25 (2014) 756–763

Contents lists available at ScienceDirect

Gondwana Research

journal homepage: www.elsevier.com/locate/gr

GR Letter

Two-stage collision: Exploring the birth of Pangea in the Variscan terranes

Ricardo Arenas [a,*], Rubén Díez Fernández [a,b], Sonia Sánchez Martínez [a], Axel Gerdes [c,d], Javier Fernández-Suárez [a], Richard Albert [a]

[a] Departamento de Petrología y Geoquímica and Instituto de Geociencias (UCM, CSIC), Universidad Complutense de Madrid, 28040 Madrid, Spain
[b] IDL, Departamento de Geociências, ECT, Universidade de Évora, Apartado 94, 7001-554 Évora, Portugal
[c] Institut für Geowissenschaften, Mineralogie, J.W. Goethe Universität, Frankfurt am Main, Germany
[d] Department of Earth Sciences, Stellenbosch University, Private Bag X1,Matieland 7602, South Africa

ARTICLE INFO

Article history:
Received 24 June 2013
Received in revised form 1 August 2013
Accepted 4 August 2013
Available online 31 August 2013

Handling Editor: R.D. Nance

Keywords:
Assembly of Pangea
Allochthonous Variscan terranes
NW Iberian Massif

ABSTRACT

The Variscan suture exposed in NW Iberia contains a stack of terranes including two allochthonous units with continental affinity and Gondwanan provenance (Upper and Basal Units), separated by an ophiolite belt where the most common units show protolith ages at c. 395 Ma. Recent Lu–Hf zircon data obtained from these ophiolites indicate interaction between the gabbroic magmas and old continental crust. Hence, the ophiolites could not have originated in a deep ocean basin associated with a mature mid-ocean-ridge or intraoceanic subduction. The tectonothermal evolution of the continental terranes bounding the suture zone records two consecutive events of deep subduction. The Upper Units record an initial high-P/ultra-high-P metamorphic event that occurred before 400–390 Ma, while the Basal Units were affected by a second high-P/low-to-intermediate-T metamorphic event dated at c. 370 Ma. Continental subduction affected the most external margin of Gondwana and developed in a setting of dextral convergence with Laurussia. Development of the two high-P events alternated with the opening of an ephemeral oceanic basin, probably of pull-apart type, in Early Devonian times. This ephemeral oceanic domain is suggested as the setting for the protoliths of the most common ophiolites involved in the Variscan suture. Current ideas for the assembly of Pangea advocate a single collisional event between Gondwana and Laurussia in the Carboniferous. However, the new evidence from the allochthonous terranes of the Variscan belt suggests a more complex scenario for the assembly of the supercontinent, with an interaction between the colliding continental margins that started earlier and lasted longer than previously considered. Based on modern analogs of continental interaction, the development of complex collisions, as here suggested for Gondwana and Laurussia during the assembly of Pangea, could have been the norm rather than the exception throughout Earth history.

1. Introduction

It is broadly accepted that the assembly of Pangea occurred in Carboniferous and Early Permian times, after a long stage of continental convergence that ended with the closure of the Rheic Ocean (e.g. Nance et al., 2010 and references therein) and the collision of Gondwana and Laurussia (Stampfli and Borel, 2002; Murphy and Nance, 2008). This collision resulted in the formation of the Variscan–Appalachian–Alleghanian orogen, which extends from Europe to eastern North America and contains key information for reconstructing the amalgamation history of the supercontinent. In the Variscan belt, the oldest tectonothermal events are preserved in a complex suture zone that can be traced from the Iberian Peninsula to the Bohemian Massif (Fig. 1). This belt is affected by several oroclinal folds, but the original geometry was broadly linear (Matte, 2001; Martínez Catalán, 2011; Weil et al., 2012). The suture zone is made up of a stack of allochthonous terranes with ophiolites and high-P (HP) and ultra-high-P (UHP) metamorphic rocks. One of the most distinctive features of the Variscan belt is the presence of two different events of HP metamorphism that appear to have occurred relatively close in time, but were separated by the development of oceanic basins. This evolution is unusual in large collisional belts, whose tectonothermal evolution is commonly interpreted as reflecting a single HP or UHP metamorphic event associated with subduction of one of the colliding continental margins (Platt, 1986; Beaumont et al., 2009). In the Variscan belt, both HP events and the development of some of the oceanic domains occurred after the earliest Devonian and are thus broadly coeval with the initial stages of the assembly of Pangea.

This paper presents a short summary of the origin and tectonothermal evolution of the allochthonous terranes involved in the Variscan suture, and proposes a conceptual model to integrate part of this history in the context of Pangea formation. The geological section exposed in the NW Iberian Massif is taken as an example and described in some detail, but

* Corresponding author. Tel.: +34 639601919, +34 915442535.
E-mail addresses: arenas@geo.ucm.es (R. Arenas), georuben@usal.es (R. Díez Fernández), s.sanchez@geo.ucm.es (S. Sánchez Martínez), gerdes@em.uni-frankfurt.de (A. Gerdes), jfsuarez@geo.ucm.es (J. Fernández-Suárez), r.albert@geo.ucm.es (R. Albert).

1342-937X/$ – see front matter © 2013 International Association for Gondwana Research. Published by Elsevier B.V. All rights reserved.
http://dx.doi.org/10.1016/j.gr.2013.08.009

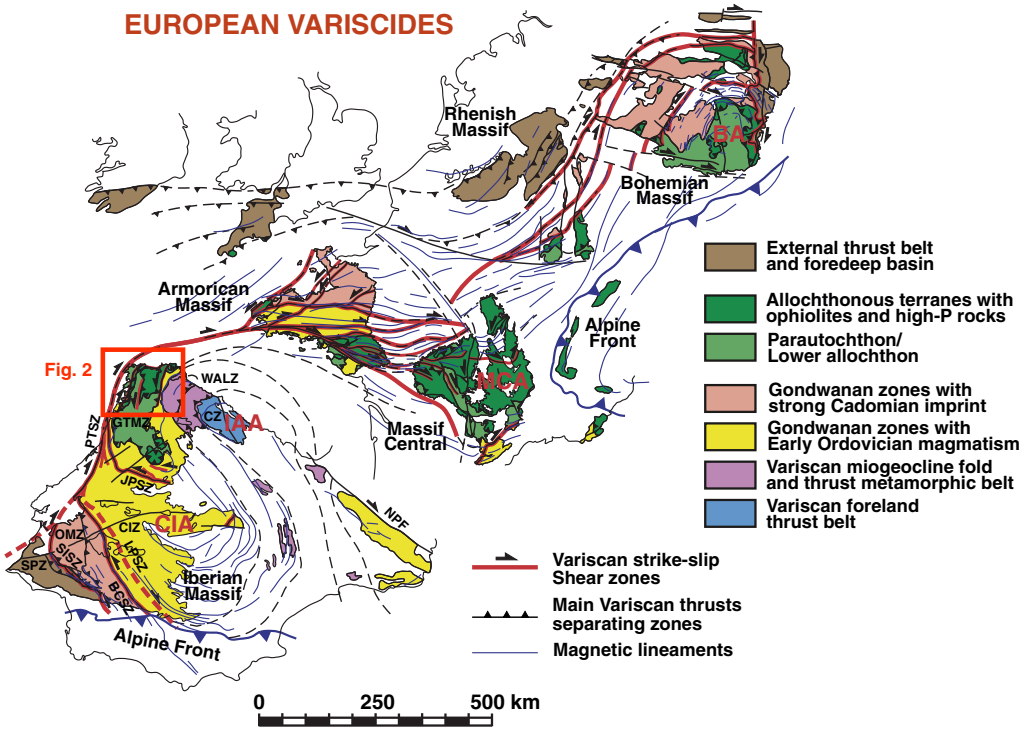

Fig. 1. Terranes and oroclines of the Variscan belt (Martínez Catalán, 2011). Arcs: BA, Bohemian; CIA, Central Iberian; IAA, Ibero-Armorican; MCA, Massif Central. Zones of the Iberian Massif: CIZ, Central Iberian; CZ, Cantabrian; GTMZ, Galicia-Trás-os-Montes; OMZ, Ossa-Morena; SPZ, South Portuguese; WALZ, West Asturian-Leonese. Shear zones and faults: BCSZ, Badajoz-Cordoba; JPSZ, Juzbado-Penalva; LPSZ, Los Pedroches; NPF, North Pyrenean; PTSZ, Porto–Tomar; SISZ, Southern Iberian. Location of the geological map and section presented in Fig. 2 are also shown.

allochthonous terranes are fairly continuous along the suture and largely comparable throughout the European Variscan belt (Faryad and Kachlík, 2013; Kroner and Romer, 2013). Recent isotopic and geochronologic data on the origin of the Ophiolitic Units and U–Pb geochronological constraints on the HP events provide new insights into the early events involved in the formation of Pangea. The history of convergence and collision is probably longer and more complex than previously described.

2. Terranes involved in the Variscan suture

The NW Iberian section of the Variscan belt contains different terranes with contrasting origins and tectonothermal evolution (Arenas et al., 1986; Martínez Catalán et al., 2009). The Central Iberian Zone represents the lowest sequence and together with a parautochthonous domain (or Schistose Domain) defines the main section of the Gondwanan margin involved in the Variscan orogen (Martínez Catalán et al., 2009) (Figs. 1 and 2). On top, a set of allochthonous terranes of alleged exotic nature forms a nappe stack representative of the suture zone (Figs. 1 and 2). Three main groups of terranes have been identified, two of which show continental crustal affinities (Basal and Upper Units). These are separated by ophiolites representing the suture itself (Ophiolitic Units, Fig. 2).

Located immediately below the suture, the Basal Units contain metasedimentary rocks (comprising a thick pile of metagreywackes with minor metapelites, graphitic schist, calc-silicate lenses, metacherts and quartzites), calc-alkaline to alkaline–peralkaline metagranitoids, and some mafic rocks. Maximum depositional ages for the metasedimentary series range between Ediacaran and Early Ordovician (Díez Fernández et al., 2010, 2013), with Nd model ages between 1.78 and 2.22 Ga (Fuenlabrada et al., 2012). Major and trace element geochemistry of the metagreywackes suggest deposition in association with a peri-Gondwanan arc system built upon a thinned continental margin. The calc-alkaline (c. 493 Ma; Abati et al., 2010) and alkaline–peralkaline (c. 475–470 Ma; Díez Fernández et al., 2012a) granitoids were generated within this arc, suggesting an evolution from convergence to continental rifting. The Basal Units are considered to represent a section of the most external margin of Gondwana located somewhere between the West African and Saharan cratons (Díez Fernández et al., 2010). The first tectonothermal event recorded in these units is a HP and low- to intermediate-T (LIT) event dated at c. 370 Ma (Rodríguez et al., 2003; Abati et al., 2010). A variety of HP mica schists and orthogneisses, C-type eclogites and some blueschists were formed at this time (Arenas et al., 1995, 1997; Rodríguez et al., 2003; López Carmona et al., 2013).

Resting on top of the suture zone, the Upper Units consist of a pile, 10–12 km thick, of metasedimentary rocks (mainly metagreywackes), large massifs of calc-alkaline orthogneisses, and gabbros with compositions of island-arc tholeiites, together with medium to high grade mafic rocks, including B-type eclogites (Coleman et al., 1965) and HP granulites, and some ultramafic massifs. The low grade metagreywackes located in the uppermost position have a Middle Cambrian maximum depositional age (Fernández-Suárez et al., 2003), with Nd model ages ranging between 0.72 and 1.22 Ga, and major and trace element compositions typical of active margin settings (Fuenlabrada et al., 2010). Protolith ages for gabbros and granitoids range between 490 and 520 Ma (Fernández-Suárez et al., 2007; Andonaegui et al., 2012). These units were part of a Cambrian peri-Gondwanan magmatic arc, and were located west of the external margin section represented by

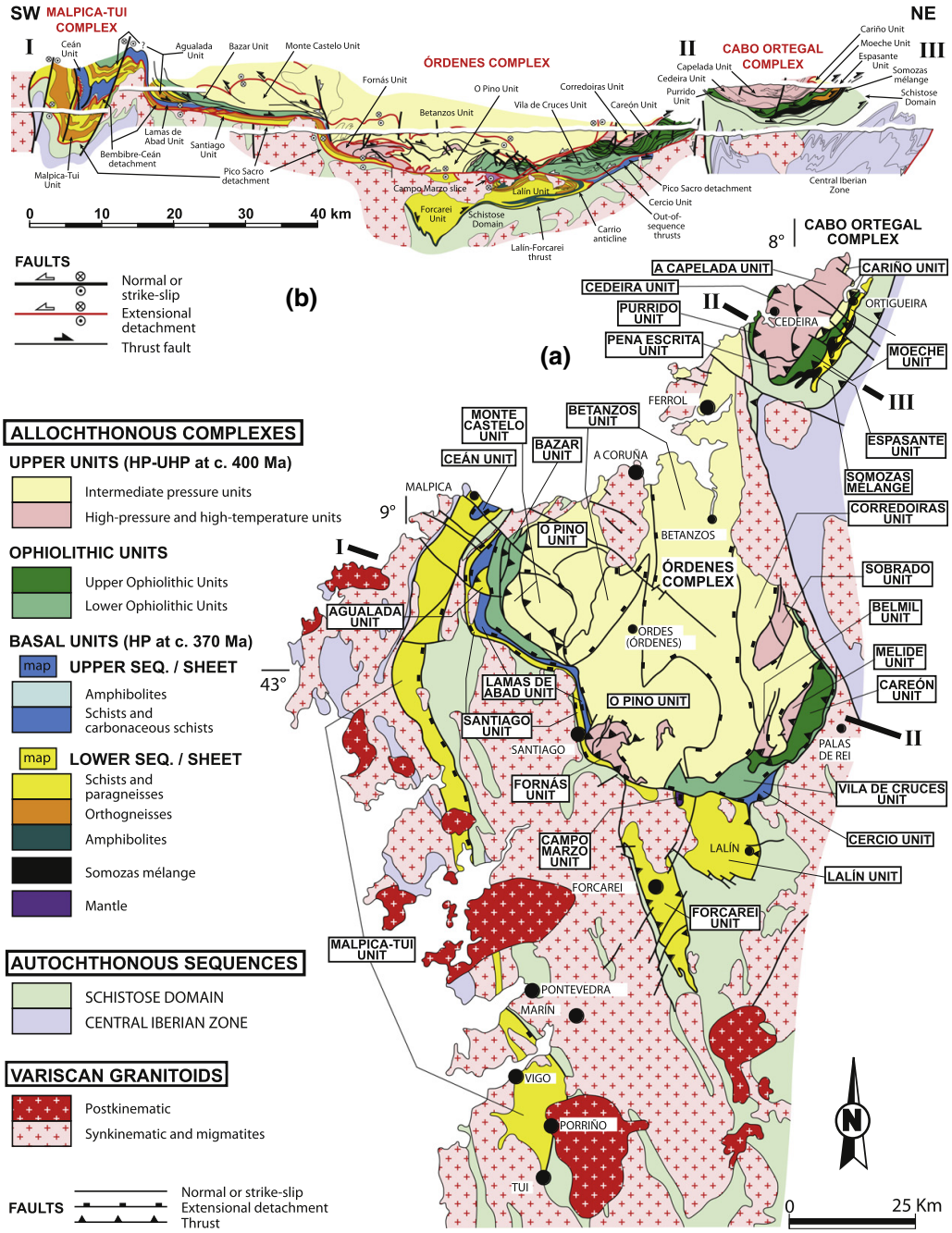

Fig. 2. (a) Geological map of the allochthonous complexes of the NW Iberian Massif (Galicia region), and (b) composite cross section, showing the distribution and general structure of the terranes involved in the Variscan suture. The location and name of the most representative units are indicated.

the Basal Units (Díez Fernández et al., 2010; Fuenlabrada et al., 2010). The Upper Units may be divided into two groups according to metamorphic criteria: an uppermost section with intermediate-P metamorphism ranging from the chlorite zone to the granulite facies, and a lower section showing HP and high-T (HT) metamorphism dated at c. 400–390 Ma (Ordóñez Casado et al., 2001; Fernández-Suárez et al., 2007). The latter metamorphic event reached UHP conditions in other domains of the Variscan belt (Lardeaux et al., 2001). The main tectonothermal events recorded in the uppermost section are Cambrian in age and were probably developed in response to the accretionary dynamics of the peri-Gondwanan arc system (Abati et al., 1999, 2007; Díaz García et al., 2010).

The ophiolites of NW Iberia have received considerable attention in the past few years with papers describing in detail their lithologies, chemical compositions and isotopic geochronology. It is now well-established that their igneous protoliths range quite widely in age, thereby precluding their generation within a single oceanic domain. Two groups of Ophiolitic Units have been distinguished (Fig. 2): an older group (Lower Ophiolitic Units) containing metaigneous rocks of Late Cambrian age (c. 497–495 Ma), and a younger group (Upper Ophiolitic Units) including gabbroic rocks of Devonian age (Emsian–Eifelian; c. 395 Ma).

The Cambrian ophiolites comprise either thick sequences of greenschists (with island-arc tholeiite compositions), with some alternations of phyllites and rare tonalitic orthogneisses (Vila de Cruces Ophiolite; Arenas et al., 2007a; Fig. 2), or c. 4000 m of HT metagabbroic amphibolites with N-MORB affinities and minor ultramafic rocks (Bazar Ophiolite; Sánchez Martínez et al., 2012; Fig. 2). The protoliths of the Vila de Cruces Ophiolite were formed during the opening of a back-arc basin at the periphery of Gondwana. In contrast, based on its chemical composition and structural position, the Bazar Ophiolite probably represents a relic of the Cambrian peri-Gondwanan Iapetus-Tornquist Ocean, accreted below a system of peri-Gondwanan volcanic arcs. This accretion is dated at c. 475 Ma based on U–Pb zircon geochronology for the timing of the HT metamorphism affecting the mafic protoliths. The Lower Ophiolitic Units are interpreted to represent a series of mafic complexes linked to the dynamics affecting the most external margin of Gondwana in Cambrian–Early Ordovician times.

The Middle Devonian ophiolites are the most abundant group found in the Variscan suture (Murphy et al., 2011). In addition to NW Iberia, they occur in the Lizard Complex (Lizard Ophiolite; Clark et al., 1998; Nutman et al., 2001), in the Armorican Massif (Drain Ophiolite; Ballèvre et al., 2009, 2012), and in the Bohemian Massif (Ślęża Ophiolite; Dubińska et al., 2004; Kryza and Pin, 2010). In Galicia (NW Spain), the Careón Ophiolite (395 ± 2 Ma, U–Pb zircon in metagabbro; Díaz García et al., 1999; Pin et al., 2002; Fig. 2) has received special attention and can be considered the type example of the group. It is made up of three imbricate slices, the thickest (c. 1000 m) of which contains a sequence of peridotites overlain by 500 m of isotropic gabbros. Both the peridotites and the gabbros are intruded by stocks of pegmatitic gabbros and numerous doleritic dykes. The ophiolite contains no sheeted dyke complex and no volcanic or sedimentary rocks, at variance with common N-MORB oceanic lithosphere generated at a mid-ocean ridge. The mafic rocks have compositions typical of island-arc tholeiites (Sánchez Martínez et al., 2007). The U–Pb zircon age obtained for this ophiolite is relatively close to the time calculated for its accretion (c. 377 Ma, $^{40}Ar/^{39}Ar$ on hornblende concentrate; Dallmeyer et al., 1997), therefore the unit represents a section of buoyant oceanic lithosphere that escaped subduction beneath Laurussia. New U–Pb zircon data obtained from other upper ophiolites in NW Iberia yielded similar crystallization ages for the mafic protoliths (395 ± 3 Ma for the Purrido Unit: Sánchez Martínez et al., 2011; 400 ± 3 Ma for the Moeche Unit: Arenas et al., in press; Fig. 2). Moreover, a combined isotopic (Lu–Hf in zircon and Sm–Nd in whole rock) study of these ophiolites shows that a suite of Devonian gabbros with juvenile isotopic compositions and mantle provenance (the mafic protoliths of the ophiolites) interacted with old continental crust and were affected by limited mixing (Sánchez Martínez et al., 2011; Arenas et al., in press). The involvement of a continental component is revealed by Paleoproterozoic Hf model ages in some of the zircons, which is inconsistent with the generation of the igneous protoliths in an intra-oceanic setting far removed from continents.

3. A two-stage collision model for the early history of Pangea

The Upper Units have been previously interpreted as a section of a peri-Gondwanan volcanic arc that rifted off the continental margin in Cambrian–Early Ordovician times and drifted northward, opening the Rheic Ocean in its wake. This rifting would have coincided with the rift and drift of the Avalonian microcontinent. The Upper Units, however, would have had a different identity and provenance since they were located further to the east along the paleo-margin of Gondwana (Abati et al., 2007; Gómez Barreiro et al., 2007; Díez Fernández et al., 2010). The HP or UHP metamorphic event that affected the lower section of the Upper Units at c. 400–390 Ma would have been generated during the accretion of this terrane to the southern margin of Laurussia, this process highlighting the switch from a divergent to a convergent setting in the evolution of the Rheic Ocean. The geodynamic evolution hitherto suggested for the Upper Units implies that the ophiolites involved in the Variscan suture were developed in the realm of the Rheic Ocean. The Cambrian ophiolites – with the exception of the Bazar Ophiolite – would be related to early stages in the opening of this ocean, while the Devonian ophiolites would have been formed during the final stages of its closure (Arenas et al., 2007b). For this reason, it has been proposed that the Devonian ophiolites were formed in a northward dipping intra-Rheic Ocean supra-subduction zone located close to the southern margin of Laurussia (Díaz García et al., 1999; Sánchez Martínez et al., 2007). Such intraoceanic subduction zone would have generated buoyant oceanic lithosphere that would have readily accreted beneath Laurussia and eventually been obducted over the external margin of Gondwana (Basal Units) at the beginning of the Variscan deformation (c. 370 Ma). Furthermore, the activity of this intraoceanic subduction zone would have consumed a significant tract of the Rheic Ocean, thus explaining the general absence of typical N-MORB lithosphere in the Variscan suture.

However, the aforementioned models that link the generation of the Devonian ophiolites to an open-ocean setting are inconsistent with the new isotopic data that clearly show the interaction of the gabbroic protoliths with old continental crust. Many of the zircons analyzed in mafic rocks from the Purrido and Moeche ophiolites show Lu–Hf isotopic compositions only compatible with a continental origin. These zircons can be only interpreted as inherited crystals incorporated into the mafic magmas (Sánchez Martínez et al., 2011; Arenas et al., in press). Consequently, there is no conclusive evidence to link the generation of the Devonian ophiolites either to the evolution of the Rheic Ocean or to an intraoceanic subduction zone active in a mature ocean basin. If the connection between the Variscan suture of NW Iberia and the evolution of the Rheic Ocean is called into question, so must the interpretation of the Upper Units as a peri-Gondwanan terrane that drifted away during the opening of this Paleozoic ocean. Moreover, problems also exist in attributing the development of HP–UHP metamorphism in the trailing edge of a rather small terrane to its collision with Laurussia. The tectonothermal evolution expected for the accretion of a small, ribbon terrane to a large continent would be one more compatible with soft collision, without generation of important subduction and, hence, lacking HP–UHP metamorphism. In contrast, the latter is usually associated with deep subduction of the thinned margin of a large continent during its collision with another large continent (Warren et al., 2008; Beaumont et al., 2009).

It is also noteworthy that the age of the HP–UHP metamorphic event in the Upper Units, which is constrained to be no younger than 400–390 Ma (U–Pb zircon; Ordóñez Casado et al., 2001; Fernández-Suárez et al., 2007), is similar to that of the mafic rocks of the Upper Ophiolitic Units, repeatedly dated at c. 400–395 Ma (U–Pb zircon; Díaz García et al., 1999; Pin et al., 2002, 2006; Sánchez Martínez et al., 2011; Arenas et al., in press). In the case of the HP metamorphic event, the U–Pb geochronology provides the age of the HT zircon growth, which occurred sometime after the continental margin became involved in the subduction system. Accordingly, the peak pressure of the HP event must have been reached prior to 400–390 Ma since this age likely marks a point along the exhumation/decompression path (Fernández-Suárez et al., 2007). This subduction must also predate the generation of the Devonian mafic rocks, as expressed in recent papers focused on the origin of the allochthonous terranes of NW Iberia (Sánchez Martínez et al., 2007; Martínez Catalán et al., 2009).

Hence, the new data from the allochthonous terranes of NW Iberia, in particular Lu–Hf isotope geochemistry of the Devonian ophiolites and detailed U–Pb geochronology of the two HP metamorphic events, seem to be more consistent with the development of two successive collision events between Gondwana and Laurussia, each taking place in a context of oblique convergence and separated in time by the opening of a rather wide oceanic basin, probably of pull-apart type.

The allochthonous Upper Units are herein interpreted as the most external part of the Gondwanan margin, a rather wide continental shelf containing thick turbidite series intruded by large massifs of gabbros and granitoids. This lithological succession was formed during the activity of a volcanic arc in Cambrian times, having developed after an important episode of crustal extension and thinning. This continental shelf did not witness significant new igneous activity or deformation until the onset of the HP–UHP metamorphic event, and hence shows the characteristics of a typical passive margin for most of the Ordovician and Silurian. In the geological record covering this time interval there is no evidence suggesting any significant separation of this continental shelf from the Gondwanan mainland. Convergence between Gondwana and Laurussia led to a first continental collision before 400–390 Ma, including the dextral subduction (Ábalos et al., 2003) of the most external and thinned part of the Gondwanan margin to the north accompanied by the first HP–UHP metamorphism. The southern margin of Laurussia acted as the upper plate in the subduction complex and the most important collision probably affected the eastern part of Avalonia and the Baltic margin (Fig. 3).

Renewed dextral motion between Gondwana and Laurussia favored the rapid generation of a rather wide pull-apart basin in Early Devonian times, which we interpret as the tectonic setting for the generation of the c. 395 Ma mafic rocks forming the most typical ophiolites involved in the Variscan suture (Fig. 4). The pull-apart basin currently being generated between the North American Plate and the Caribbean Plate can be considered a modern analog for the suggested tectonic setting, although in this case the lateral component is sinistral. The Gonâve microplate occupies the pull-apart basin and comprises oceanic lithosphere with a rather thin or completely absent sedimentary cover (ten Brink et al., 2002). This oceanic lithosphere is being generated by the activity of the Mid-Cayman Spreading Centre (Fig. 5). In this modern analog, as was probably the case at the beginning of Pangea assembly, the pull-apart basin was generated following an initial collision that produced the high-P belts in northern Cuba and Hispaniola (Fig. 5) (García-Casco et al., 2008; Sommer et al., 2011).

Continued dextral convergence finally caused the closure of the pull-apart basin and the accretion of buoyant oceanic lithosphere beneath the northern continent starting at c. 380 Ma (Careón and Purrido ophiolites; Dallmeyer et al., 1997). The accreted oceanic lithosphere is mostly metamorphosed to the amphibolite facies, but the occasional presence of corundum-bearing metamorphic soles indicates the localized presence of high thermal gradients (Díaz García et al., 1999). Later accretion of new Devonian mafic slices took place under greenschist facies conditions (Moeche Ophiolite), and was followed by the accretion of mafic complexes rimming the continental margin that formed within the Cambrian peri-Gondwanan volcanic arc (Vila de Cruces Ophiolite). The final outcome was the generation of a complex suture zone that records protracted dextral convergence and is characterized by the presence of a double ophiolitic belt of contrasting origin

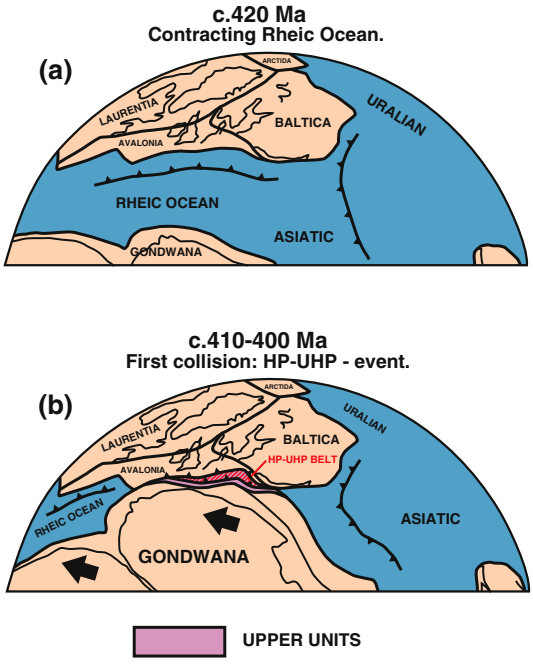

Fig. 3. Reconstructions of (a) the Rheic Ocean realm at the Silurian — Devonian boundary, and (b) the initial collision between Gondwana and Laurussia at c. 410–400 Ma, following the complete closure of the Rheic Ocean. This collision caused subduction of the most external margin of Gondwana and generated the HP–UHP metamorphic belt preserved in the allochthonous Upper Units exposed in the Variscan suture. The true Rheic Ocean suture is not represented in the mapped area of NW Iberia.

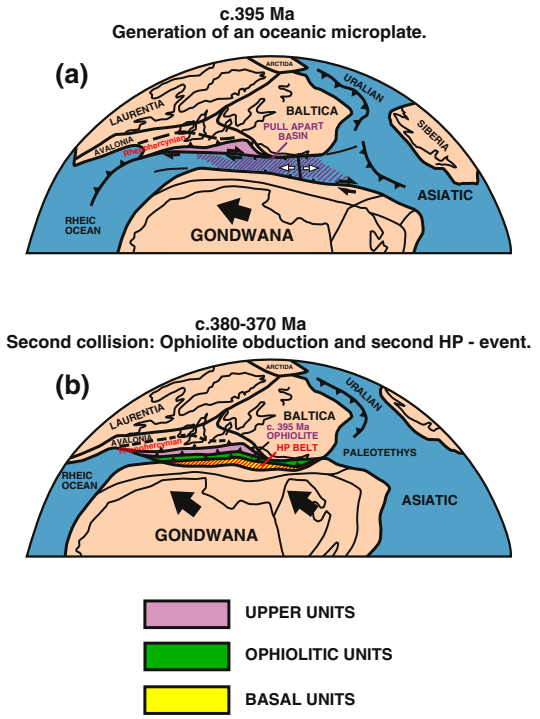

Fig. 4. Reconstructions showing (a) dextral motion between Gondwana and Laurussia, which favored the opening of a rather ephemeral pull-apart basin at c. 395 Ma with generation of new oceanic lithosphere, and (b) the second and final collision at c. 380–370 Ma, which caused the accretion of buoyant oceanic lithosphere followed by new subduction affecting the margin of Gondwana, thereby developing a second HP–LIT metamorphic belt. The two different HP belts and the ophiolitic units dated at c. 395 Ma can be identified in the allochthonous terranes that outline the Variscan suture from Iberia to the Bohemian Massif.

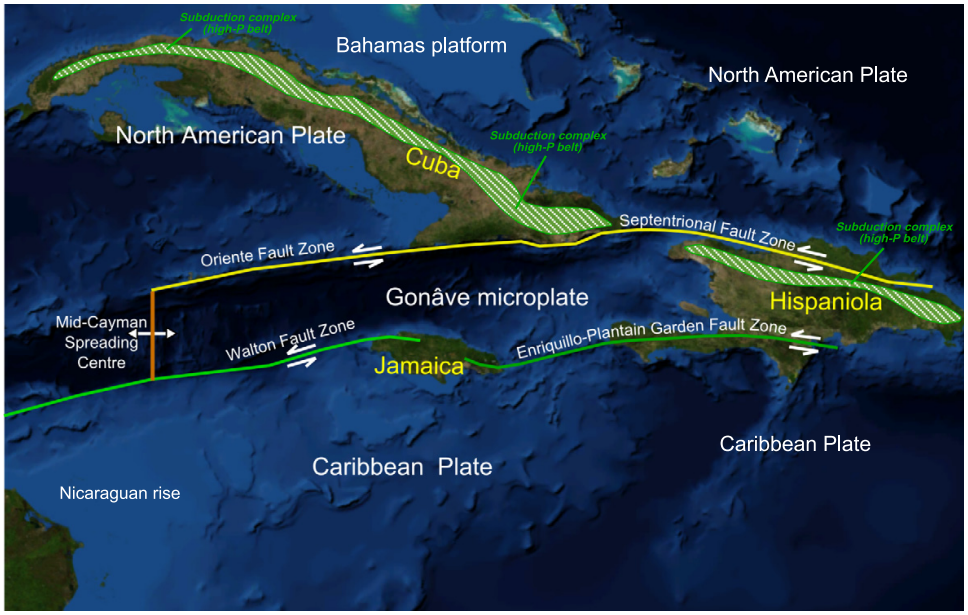

Fig. 5. Sketch showing the present plate distribution in the North Caribbean region. Initial interaction between the North American and Caribbean plates generated the HP terranes and ophiolites located in northern Cuba and Hispaniola. The opening of a long pull-apart basin, which can be followed for more than 2500 km from east to west, transected the HP belts and generated new oceanic lithosphere in the Gonâve microplate. (Modified after an original NASA image with additional information from Wikimedia Commons; see also García-Casco et al. (2008) and references therein for additional information about the geology of the Caribbean region).

and ages: the Upper Ophiolitic Units of Devonian age and the Lower Ophiolitic Units of Cambrian age. The occurrence of a thick serpentinite mélange at the base of the allochthonous pile was interpreted in the context of dextral convergence (Somozas mélange, Fig. 2; Arenas et al., 2009).

The final collision between Gondwana and Laurussia started at c. 370 Ma as a consequence of continued oblique dextral convergence (Díez Fernández et al., 2012b). It caused renewed north-directed subduction affecting a new section of the external Gondwanan margin with a more easterly provenance (in Gondwanan margin coordinates; Basal Units; Díez Fernández et al., 2010; Fuenlabrada et al., 2012). This is the suggested setting for the development of the second HP metamorphic event, formed under LIT conditions and generating C-type eclogites (Coleman et al., 1965), blueschists and HP metapelites (Fig. 4). Convergence continued for about 70 m.y. (Dallmeyer et al., 1997) as intracontinental deformation progressed southward, reaching inner sections of Gondwana while building a foreland fold and thrust belt in the external parts of the orogen.

4. Conclusions

Previous interpretations for the final assembly of Pangea call upon a single-stage collision between Gondwana and Laurussia in Carboniferous times. However, recent data regarding the origin and tectonothermal evolution of the allochthonous terranes involved in the Variscan suture suggest a more complex and longer history for the early stages in the assembly of the supercontinent. These data are consistent with two successive collisional events separated by the generation of a relatively ephemeral oceanic basin. The first collision occurred in Early Devonian times (before c. 400–390 Ma) and caused deep subduction of the most external margin of Gondwana and the generation of a HP–UHP metamorphic belt (Upper Units of the Variscan suture). Continued dextral motion between Gondwana and Laurussia favored the opening of a relatively large pull-apart basin at c. 400–395 Ma. The rapid closure of this basin started at c. 380 Ma and caused the accretion of buoyant oceanic lithosphere of Devonian age below the northern continent. This oceanic lithosphere is represented by the most common ophiolites found in the European Variscan suture (Upper Ophiolitic Units). Mafic slices with a similar age and showing greenschist facies recrystallization were accreted later, followed by mafic complexes with Cambrian age generated by the activity of peri-Gondwanan volcanic arcs that progressively reached the collision zone as the basin shrank (Lower Ophiolitic Units). Finally, renewed dextral convergence led to a new collision with another section of the Gondwanan margin at c. 370 Ma and the generation of a second HP–LIT belt (Basal Units). Convergence continued during the Carboniferous producing the complex intracontinental deformation that characterizes the Variscan belt.

Acknowledgments

Financial support for this research has been provided by the Spanish project CGL2012-34618 (Ministerio de Economía y Competitividad). Insightful reviews of the manuscript performed by Rob Strachan and an anonymous reviewer are gratefully acknowledged, as well as the excellent editing work of R. Damian Nance that significantly improved the final version of the manuscript. This paper is a contribution to Project 597 of the International Geological Correlation Programme: "Amalgamation and Breakup of Pangaea: the type example of the supercontinent".

References

Ábalos, B., Puelles, P., Gil Ibarguchi, J.I., 2003. Structural assemblage of high-pressure mantle and crustal rocks in a subduction channel (Cabo Ortegal, NW Spain). Tectonics 22, 1006. http://dx.doi.org/10.1029/2002tc001405.

Abati, J., Dunning, G.R., Arenas, R., Díaz García, F., González Cuadra, P., Martínez Catalán, J.R., Andonaegui, P., 1999. Early Ordovician orogenic event in Galicia (NW Spain): evidence from U–Pb ages in the uppermost unit of the Ordenes Complex. Earth and Planetary Science Letters 165, 213–228.

Abati, J., Castiñeiras, P., Arenas, R., Fernández-Suárez, J., Gómez Barreiro, J., Wooden, J., 2007. Using SHRIMP-RG U–Pb zircon dating to unravel tectonomagmatic events in

arc environments. The early Paleozoic arc of NW Iberia revisited. Terra Nova 19, 432–439.
Abati, J., Gerdes, A., Fernández-Suárez, J., Arenas, R., Whitehouse, M.J., Díez Fernández, R., 2010. Magmatism and early-Variscan continental subduction in the northern Gondwana margin recorded in zircons from the basal units of Galicia, NW Spain. Geological Society of America Bulletin 122, 219–235.
Andonaegui, P., Castiñeiras, P., González Cuadra, P., Arenas, R., Sánchez Martínez, S., Abati, J., Díaz García, F., Martínez Catalán, J.R., 2012. The Corredoiras orthogneiss (NW Iberian Massif): geochemistry and geochronology of the Paleozoic magmatic suite developed in a peri-Gondwanan arc. Lithos 128–131, 84–99.
Arenas, R., Gil Ibarguchi, J.I., González Lodeiro, F., Klein, E., Martínez Catalán, J.R., Ortega Gironés, E., de Pablo Maciá, J.G., Peinado, M., 1986. Tectonostratigraphic units in the complexes with mafic and related rocks of the NW of the Iberian Massif. Hercynica 2, 87–110.
Arenas, R., Rubio Pascual, F.J., Díaz García, F., Martínez Catalán, J.R., 1995. High-pressure microinclusions and development of an inverted metamorphic gradient in the Santiago Schists (Órdenes Complex, NW Iberian Massif, Spain): evidence of subduction and syn-collisional decompression. Journal of Metamorphic Geology 13, 141–164.
Arenas, R., Abati, J., Martínez Catalán, J.R., Díaz García, F., Rubio Pascual, F.J., 1997. P-T evolution of eclogites from the Agualada Unit (Órdenes Complex, NW Iberian Massif, Spain): implications for crustal subduction. Lithos 40, 221–242.
Arenas, R., Martínez Catalán, J.R., Sánchez Martínez, S., Fernández-Suárez, J., Andonaegui, P., Pearce, J.A., Corfu, F., 2007a. The Vila de Cruces Ophiolite: a remnant of the early Rheic Ocean in the Variscan suture of Galicia (NW Iberian Massif). Journal of Geology 115, 129–148.
Arenas, R., Martínez Catalán, J.R., Sánchez Martínez, S., Díaz García, F., Abati, J., Fernández-Suárez, J., Andonaegui, P., Gómez-Barreiro, J., 2007b. Paleozoic ophiolites in the Variscan suture of Galicia (northwest Spain): distribution, characteristics and meaning. In: Hatcher Jr., R.D., Carlson, M.P., McBride, J.H., Martínez Catalán, J.R. (Eds.), 4-D Framework of Continental Crust. Geological Society of America Memoir, 200, pp. 425–444.
Arenas, R., Sánchez Martínez, S., Castiñeiras, P., Jeffries, T.E., Díez Fernández, R., Andonaegui, P., 2009. The basal tectonic mélange of the Cabo Ortegal Complex (NW Iberian Massif): a key unit in the suture of Pangea. Journal of Iberian Geology 35, 85–125.
Arenas, R., Sánchez Martínez, S., Gerdes, A., Albert, R., Díez Fernández, R., Andonaegui, P., 2013. Re-interpreting the Devonian ophiolites involved in the Variscan suture: U–Pb and Lu–Hf zircon data of the Moeche Ophiolite (Cabo Ortegal Complex, NW Iberia). International Journal of Earth Sciences. http://dx.doi.org/10.1007/s00531-013-0880-x (in press).
Ballèvre, M., Bosse, V., Ducassou, C., Pitra, P., 2009. Palaeozoic history of the Armorican Massif: models for the tectonic evolution of the suture zones. Comptes Rendus Geoscience 341, 174–201.
Ballèvre, M., Bosse, V., Ducassou, C., Paquette, J.L., Peucat, J.J., Pitra, P., Poujol, M., Ruffet, G., 2012. Geometry and correlation of the nappe stack in the Ibero-Armorican arc across the Bay of Biscay: a joint French–Spanish project. Part 1: the data. Géologie de la France 1, 60–61.
Beaumont, C., Jamieson, R.A., Butler, J.P., Warren, C.J., 2009. Crustal structure: a key constraint on the mechanism of ultra-high-pressure rock exhumation. Earth and Planetary Science Letters 287, 116–129.
Clark, A.H., Scott, D.J., Sandeman, H.A., Bromley, A.V., Farrar, E., 1998. Siegenian generation of the Lizard ophiolite: U–Pb zircon age data for plagiogranite, Porthkerries, Cornwall. Journal of the Geological Society of London 155, 595–598.
Coleman, R.G., Lee, D.E., Beatty, L.B., Brannock, W.W., 1965. Eclogites and eclogites — their differences and similarities. Geological Society of America Bulletin 76, 483–508.
Dallmeyer, R.D., Martínez Catalán, J.R., Arenas, R., Gil Ibarguchi, J.I., Gutiérrez Alonso, G., Farias, P., Aller, J., Bastida, F., 1997. Diachronous Variscan tectonothermal activity in the NW Iberian Massif: evidence from $^{40}Ar/^{39}Ar$ dating of regional fabrics. Tectonophysics 277, 307–337.
Díaz García, F., Arenas, R., Martínez Catalán, J.R., González del Tánago, J., Dunning, G.R., 1999. Tectonic evolution of the Careón Ophiolite (northwest Spain): a remnant of oceanic lithosphere in the Variscan Belt. Journal of Geology 107, 587–605.
Díaz García, F., Sánchez Martínez, S., Castiñeiras, P., Fuenlabrada, J.M., Arenas, R., 2010. A peri-Gondwanan arc in NW Iberia. II: assessment of the intra-arc tectonothermal evolution through U–Pb SHRIMP dating of mafic dykes. Gondwana Research 17, 352–362.
Díez Fernández, R., Martínez Catalán, J.R., Gerdes, A., Abati, J., Arenas, R., Fernández-Suárez, J., 2010. U–Pb ages of detrital zircons from the basal allochthonous units of NW Iberia: provenance and paleoposition on the northern margin of Gondwana during the Neoproterozoic and Paleozoic. Gondwana Research 18, 385–399.
Díez Fernández, R., Castiñeiras, P., Gómez Barreiro, J., 2012a. Age constraints on Lower Paleozoic convection system: magmatic events in the NW Iberian Gondwana margin. Gondwana Research 21, 1066–1079.
Díez Fernández, R., Martínez Catalán, J.R., Arenas, R., Abati, J., 2012b. The onset of the assembly of Pangaea in NW Iberia: constraints on the kinematics of continental subduction. Gondwana Research 22, 20–25.
Díez Fernández, R., Foster, D.A., Gómez Barreiro, J., Alonso-García, M., 2013. Rheological control on the tectonic evolution of a continental suture zone: the Variscan example from NW Iberia (Spain). International Journal of Earth Sciences. http://dx.doi.org/10.1007/s00531-013-0885-5.
Dubińska, E., Bylina, P., Kozlowski, A., Dörr, W., Nejbert, K., 2004. U–Pb dating of serpentinization: hydrothermal zircon from a metasomatic rodingite shell (Sudetic ophiolite, SW Poland). Chemical Geology 203, 183–203.
Faryad, S.W., Kachlík, V., 2013. New evidence of blueschist facies rocks and their geoectonic implication for Variscan suture (s) in the Bohemian Massif. Journal of Metamorphic Geology 31, 63–82.
Fernández-Suárez, J., Díaz García, F., Jeffries, T.E., Arenas, R., Abati, J., 2003. Constraints on the provenance of the uppermost allochthonous terrane of the NW Iberian Massif: inferences from detrital zircon U–Pb ages. Terra Nova 15, 138–144.
Fernández-Suárez, J., Arenas, R., Abati, J., Martínez Catalán, J.R., Whitehouse, M.J., Jeffries, T.E., 2007. U–Pb chronometry of polymetamorphic high-pressure granulites: an example from the allochthonous terranes of the NW Iberian Variscan belt. In: Hatcher Jr., R.D., Carlson, M.P., McBride, J.H., Martínez Catalán, J.R. (Eds.), 4–D Framework of Continental Crust. Geological Society of America Memoir, 200, pp. 469–488.
Fuenlabrada, J.M., Arenas, R., Sánchez Martínez, S., Díaz García, F., Castiñeiras, P., 2010. A peri-Gondwana arc in NW Iberia. I: isotopic and geochemical constraints on the origin of the arc — a sedimentary approach. Gondwana Research 17, 338–351.
Fuenlabrada, J.M., Arenas, R., Díez Fernández, R., Sánchez Martínez, S., Abati, J., López Carmona, A., 2012. Sm–Nd isotope geochemistry and tectonic setting of the metasedimentary rocks from the basal allochthonous units of NW Iberia (Variscan suture, Galicia). Lithos 148, 196–208.
García-Casco, A., Iturralde-Vinent, M.A., Pindell, J., 2008. Latest Cretaceous collision/accretion between the Caribbean plate and Caribeana: origin of metamorphic terranes in the Greater Antilles. International Geology Review 50, 781–809.
Gómez Barreiro, J., Martínez Catalán, J.R., Arenas, R., Castiñeiras, P., Abati, J., Díaz García, F., Wijbrans, J.R., 2007. Tectonic evolution of the upper allochthon of the Órdenes complex (northwestern Iberian Massif): Structural constraints to a polyorogenic peri-Gondwanan terrane. In: Linneman, U., Nance, R.D., Kraft, P., Zulauf, G. (Eds.), The Evolution of the Rheic Ocean: From Avalonian-Cadomian Active Margin to Alleghenian-Variscan Collision. Geological Society of America Special Paper, 423, pp. 315–332.
Kroner, U., Romer, R.L., 2013. Two plates — many subduction zones: the Variscan orogeny reconsidered. Gondwana Research 24, 298–329.
Kryza, R., Pin, C., 2010. The Central-Sudetic ophiolites (SW Poland): petrogenetic issues, geochronology and palaeotectonic implications. Gondwana Research 17, 292–305.
Lardeaux, J.M., Ledru, P., Daniel, I., Duchene, S., 2001. The Variscan French Massif Central — a new addition to the ultra-high pressure metamorphic 'club': exhumation processes and geodynamic consequences. Tectonophysics 332, 143–167.
López Carmona, A., Pitra, P., Abati, J., 2013. Blueschist-facies metapelites from the Malpica-Tui Unit (NW Iberian Massif): phase equilibria modelling and H_2O and Fe_2O_3 influence in high-pressure assemblages. Journal of Metamorphic Geology 31, 263–280.
Martínez Catalán, J.R., 2011. Are the oroclines of the Variscan belt related to late Variscan strike-slip tectonics? Terra Nova 23, 241–247.
Martínez Catalán, J.R., Arenas, R., Abati, J., Sánchez Martínez, S., Díaz García, F., Fernández-Suárez, J., González Cuadra, P., Castiñeiras, P., Gómez Barreiro, J., Díez Montes, A., González Clavijo, E., Rubio Pascual, F.J., Andonaegui, P., Jeffries, T.E., Alcock, J.E., Díez Fernández, R., López Carmona, A., 2009. A rootless suture and the loss of the roots of a mountain chain: the Variscan belt of NW Iberia. Comptes Rendus Geoscience 341, 114–126.
Matte, P., 2001. The Variscan collage and orogeny (480–290 Ma) and the tectonic definition of the Armorica microplate: a review. Terra Nova 13, 122–128.
Murphy, J.B., Nance, R.D., 2008. The Pangea conundrum. Geology 36, 703–706.
Murphy, J.B., Cousens, B.L., Braid, J.A., Strachan, R.A., Dostal, J., Keppie, J.D., Nance, R.D., 2011. Highly depleted oceanic lithosphere in the Rheic Ocean: implications for Paleozoic plate reconstructions. Lithos 123, 165–175.
Nance, R.D., Gutiérrez-Alonso, G., Keppi, J.D., Linnemann, U., Murphy, J.B., Quesada, C., Strachan, R.A., Woodcock, N.H., 2010. Evolution of the Rheic Ocean. Gondwana Research 17, 194–222.
Nutman, A.P., Green, D.H., Cook, C.A., Styles, M.T., Holdsworth, R.E., 2001. SHRIMP U–Pb zircon dating of the exhumation of the Lizard Peridotite and its emplacement over crustal rocks: constraints for tectonic models. Journal of the Geological Society of London 158, 809–820.
Ordóñez Casado, B., Gebauer, D., Schäfer, H.J., Gil Ibarguchi, J.I., Peucat, J.J., 2001. A single Devonian subduction event for the HP/HT metamorphism of the Cabo Ortegal complex within the Iberian Massif. Tectonophysics 332, 359–385.
Pin, C., Paquette, J.L., Santos Zalduegui, J.F., Gil Ibarguchi, J.I., 2002. Early Devonian supra-subduction zone ophiolite related to incipient collisional processes in the Western Variscan Belt: the Sierra de Careón unit, Órdenes Complex, Galicia. In: Martínez Catalán, J.R., Hatcher Jr., R.D., Arenas, R., Díaz García, F. (Eds.), Variscan-Appalachian Dynamics: The Building of the Late Paleozoic Basement. Geological Society of America Special Paper, 364, pp. 57–71.
Pin, C., Paquette, J.L., Ábalos, B., Santos, J.F., Gil Ibarguchi, J.I., 2006. Composite origin of an early Variscan transported suture: Ophiolitic units of the Morais Nappe Complex (north Portugal). Tectonics 25, 1–19.
Platt, J.P., 1986. Dynamic of orogenic wedges and the uplift of high-pressure metamorphic rocks. Geological Society of America Bulletin 97, 1037–1053.
Rodríguez, J., Cosca, M.A., Gil Ibarguchi, J.I., Dallmeyer, R.D., 2003. Strain partitioning and preservation of $^{40}Ar/^{39}Ar$ ages during Variscan exhumation of a subducted crust (Malpica-Tui Complex, NW Spain). Lithos 70, 111–139.
Sánchez Martínez, S., Arenas, R., Díaz García, F., Martínez Catalán, J.R., Gómez Barreiro, J., Pearce, J., 2007. The Careón Ophiolite, NW Spain: supra-subduction zone setting for the youngest Rheic Ocean floor. Geology 35, 53–56.
Sánchez Martínez, S., Arenas, R., Gerdes, A., Castiñeiras, P., Potrel, A., Fernández-Suárez, J., 2011. Isotope geochemistry and revised geochronology of the Purrido Ophiolite (Cabo Ortegal Complex, NW Iberian Massif): Devonian magmatism with mixed sources and involved Mesoproterozoic basement. Journal of the Geological Society of London 168, 733–750.

Sánchez Martínez, S., Gerdes, A., Arenas, R., Abati, J., 2012. The Bazar Ophiolite of NW Iberia: a relict of the Iapetus-Tornquist Ocean in the Variscan suture. Terra Nova 24, 283–294.
Sommer, M., Hüneke, H., Meschede, M., Cobiella-Reguera, J., 2011. Geodynamic model of the northwestern Caribbean: scaled reconstruction of Late Cretaceous to Late Eocene plate boundary relocation in Cuba. Neues Jahrbuch für Geologie und Paläontologie, Monatschefte 259, 299–312.
Stampfli, G.M., Borel, G.D., 2002. A plate tectonic model for the Paleozoic and Mesozoic constrained by dynamic plate boundaries and restored synthetic oceanic isochrons. Earth and Planetary Science Letters 196, 17–33.
ten Brink, U.S., Coleman, D.F., Dillon, W.P., 2002. The nature of the crust under Cayman Trough from gravity. Marine and Petroleum Geology 19, 971–987.
Warren, C.J., Beaumont, C., Jamieson, R.A., 2008. Modelling tectonic styles and ultra-high pressure (UHP) rock exhumation during the transition from oceanic subduction to continental collision. Earth and Planetary Science Letters 267, 129–145.
Weil, A.B., Gutiérrez-Alonso, G., Johnston, S.T., Pastor-Galán, D., 2012. Kinematic constraints on buckling a lithospheric-scale orocline along the northern margin of Gondwana: a geologic synthesis. Tectonophysics 582, 25–49.

IX

Final discussion and conclusions

This PhD mainly deals with the study of the HP–HT Banded Gneiss formation of the Upper Allochthon of the Cabo Ortegal Complex. When the metasedimentary rocks from this formation were investigated, the overlapping IP Cariño Gneisses were also taken into account and when the Banded Gneiss igneous rocks were studied the underlying Eclogite Band formation was also investigated. The general discussion and conclusions of all this work are summarised as follows.

The Banded Gneiss and Cariño Gneiss formations have a very similar old detrital spectrum (> 1 Ga) and therefore their detrital provenance will be discussed together. The main Archean population is interpreted as a *c.* 2.70 Ga intrusion of juvenile magmas into an older crust triggering limited mixing processes (Fig. 1). From intrusion at *c.* 2.70 Ga to *c.* 2.40 Ga it seems that this population registers a long lasting crust reworking process and probably other intrusion events at around 2.51 Ga, or Pb-loss processes triggered by high-grade metamorphic events. This Archean population also shows an intrusion at *c.* 3.0 Ga and a reworking process. The provenance of this population has been assigned to the Western Reguibat Rise, in the West Africa

Craton (WAC). The Paleoproterozoic population has been linked to the Eburnean Orogeny and its provenance has been assigned as to be from the Eastern Reguibat Rise (also in the WAC). This population shows that the Eburnean depleted mantle derived magmas intruded at around *c.* 2.07 Ga in the Archean crust, represented by the above-mentioned Archean population, triggering mixing processes (Fig. 1). The Mesoproterozoic population of these metasedimentary rocks is scarce and scattered so problems arise when assigning its provenance, because the WAC has no igneous activity reported at this time, due to becoming a stable craton. Nevertheless, from the isotopic information and from the information of recently discovered dykes it has been proposed that this population is also WAC derived.

The young detrital spectrum (< 1 Ga) from the studied formations is proved to have been derived from the erosion of a magmatic arc. The initial development of this arc has been constrained between *c.* 780 and 590 Ma, defined as the "proto-arc stage", where mainly crustal recycling took place (Fig. 1). Between 590 and 490 Ma, the "arc-stage", intrusion of juvenile magmas took place triggering intense mixing processes with an Eburnean and Archean crust (and with a small proportion of reworked early arc crustal material). This arc is interpreted as having been built in the margin of Gondwana, specifically at the WAC, where a long lived subduction of oceanic crust directed to Gondwana should necessarily have occurred. This arc is proposed to be the Cadomian arc and probably represents a late development of its orogeny compared to where it has been defined (see chapters 5 & 6 for details).

The maximum depositional age for the siliciclastic series of the HP–HT Banded Gneisses is *c.* 521 Ma, and of the IP Cariño Gneisses is *c.* 510 Ma. Taking into account crystallisation ages of intrusive igneous rocks of the Banded Gneisses, the protolith of was a Middle Cambrian siliciclastic sedimentary series.

From the U–Pb age distribution patterns it is proposed that the protoliths of the sedimentary rocks involved in both formations may have been deposited in a back-arc type basin, where the volcanic arc system was very active, shedding its juvenile materials into the basin at the same time as the adjacent WAC supplied the Eburnean and Archean detritus.

The main difference between the U–Pb age distributions of both formations is that the Banded Gneisses has an abundant *c.* 590–540 Ma Ediacaran population and the Cariño Gneiss

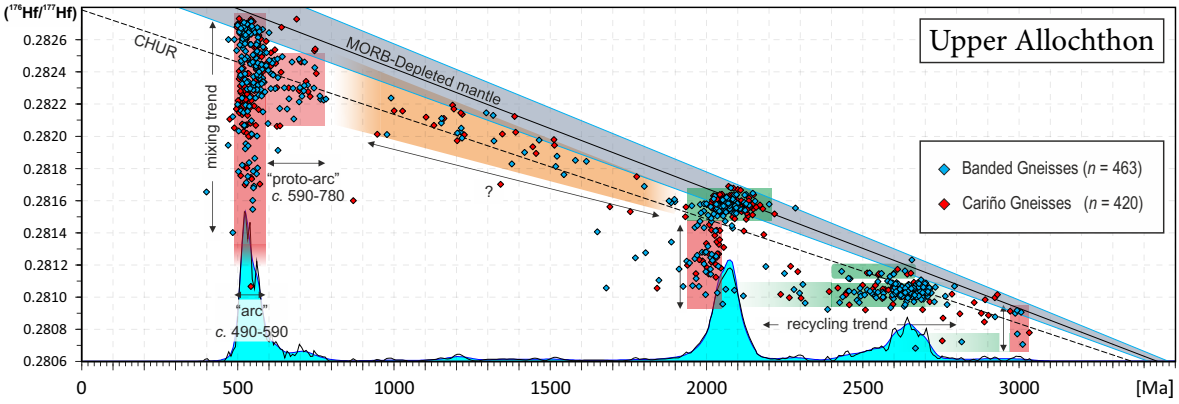

Fig. 1. $^{176}Hf/^{177}Hf$ *v.* age plot for detrital zircon data of the Upper Allochthon. Horizontal green shaded areas represent crustal recycling trends with $^{176}Lu/^{177}Hf = 0$. Vertical red shaded areas represent mixing between juvenile and recycled crustal material formed in magmatic arcs. The orange shaded area represents a source that developed through time with a similar $^{176}Lu/^{177}Hf$ ratio as the CHUR and the DM, from which the Mesoproterozoic zircon crystallized. MORB $^{176}Hf/^{177}Hf$ interval was taken from the Atlantic, Pacific and Indian MORB values (excepting three unusual low values from the Indian Ocean) reported by Chauvel & Blichert-Toft (2001) considering a minimum $^{176}Hf/^{177}Hf = 0.28302$ ($\varepsilon Hf_{(t=0Ma)} = +8.3$) and a maximum $^{176}Hf/^{177}Hf = 0.28337$ ($\varepsilon Hf_{(t=0Ma)} = +20.7$). These values are propagated to $\varepsilon Hf_{(t=4Ga)} = 0$ defining a grey field (enclosed by the blue discontinuous lines) around the DM-evolution trend, to provide an indication of the likely range of DM compositions through time. *n*, number of concordant zircon analyses (90–100% conc.), analysed for Lu–Hf isotopes. MORB: mid-ocean ridge basalts; DM: depleted mantle; CHUR: chondritic uniform reservoir.

formation has not. Both formations were probably deposited in the same back-arc basin at *c.* 521–506 Ma. The first sediments deposited were those of the Banded Gneiss formation (due to its higher isotopic heterogeneity and higher presence of intruded igneous rocks), formed by the mixture of the old components from the WAC (Eburnean and Archean detritus) and abundant arc-related *c.* 590–520 Ma sediments. The Cariño Gneisses protoliths deposited afterwards, filling the same basin with WAC sediments and abundant *c.* 560–510 Ma arc-derived sediments.

When the sediments of these formations were deposited, igneous rocks intruded in the Banded Gneiss formation. The first igneous materials to intrude were the acid magmas, the protoliths of the orthogneisses, at *c.* 512 Ma, and afterwards the basic magmas at *c.* 505 Ma (Fig. 2). Some of the basic magmas are clearly juvenile additions to the crust derived by partial melting of a depleted mantle source. Others, however, have more enriched isotope signatures, which are interpreted as a partial fusion of an enriched mantle component (probably the subcontinental mantle of Gondwana), or as an important contamination of a DM-derived partial melt with continental crust material. The sources of the acid magmas probably divers from depleted to isotopically enriched sources. The intrusive processes continued in the magmatic arc, and at *c.* 498 Ma the orthogneisses show their zircon crystallisation climax. At this time the arc activity induced high-T related metamorphism that partially melted previously generated igneous rocks (generating acid rocks by partially melting basic rocks) until *c.* 460–470 Ma. Due to this high temperature input the sediments partially melted, migmatising at *c.* 495–485 Ma (Fig. 2). The basic rock´s zircon crystallisation climax occurred at

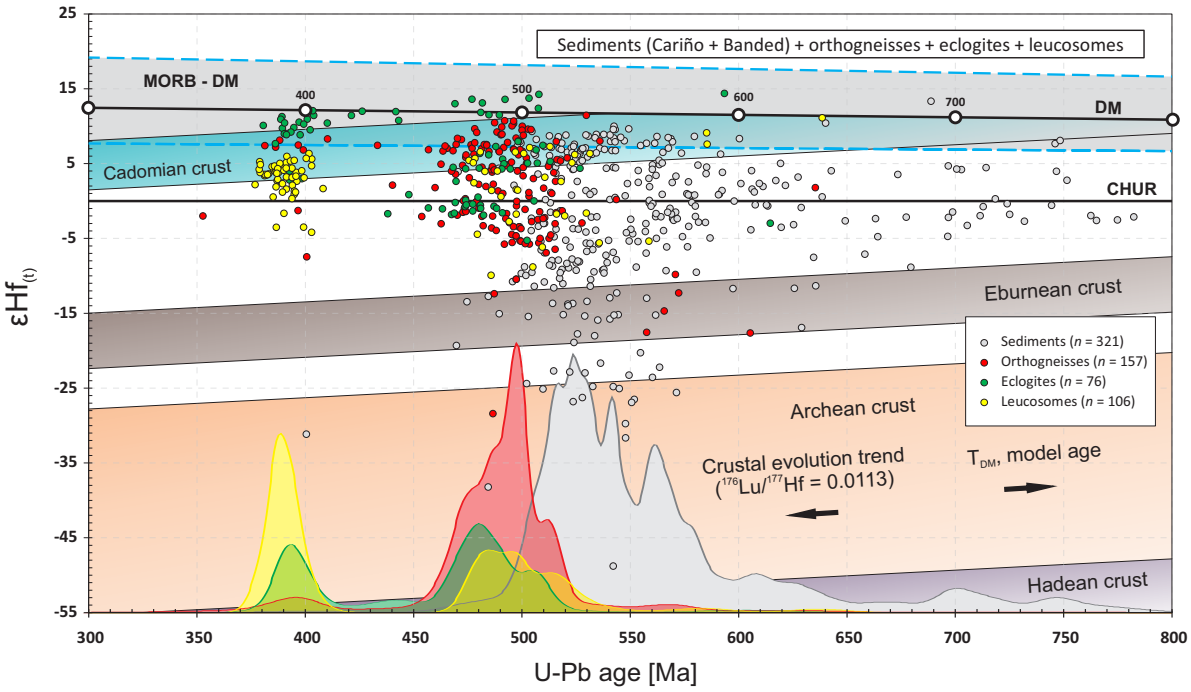

Fig. 2. εHf *v.* age diagram for all the lithologies studied. Density plots at the base of the figure are adaptative Kernel Density Estimations (aKDEs) for each of the lithologies studied (grey: sediments; red: orthogneisses; green: eclogites; yellow: leucosomes). The four aKDEs have been normalized to the same histogram bin heights (histogram diagrams of the U–Pb analyses that have their corresponding Lu–Hf analysis represented in this figure. Histogram diagrams are not represented, and have been calculated with DensityPlotter5.0, Vermeesch 2012; bandwidth = 5 Ma, binwidth = 5 Ma). Coloured inclined shaded areas represent crustal evolution trends for Hadean, Archean, Eburnean and Cadomian DM derived rocks. MORB εHf interval was taken from the Atlantic, Pacific and Indian MORB values (excepting three unusual low values from the Indian Ocean) reported by Chauvel & Blichert-Toft (2001) considering a minimum $\varepsilon Hf_{(t=0Ma)}$ = +8.3 ($^{176}Hf/^{177}Hf$ = 0.28302) and a maximum $\varepsilon Hf_{(t=0Ma)}$ = +20.7 ($^{176}Hf/^{177}Hf$ = 0.28337). These values are propagated to $\varepsilon Hf_{(t=4Ga)}$ = 0 defining a grey field (enclosed by the blue discontinuous lines) around the DM-evolution trend, to provide an indication of the likely range of DM compositions through time. *n*, number of concordant zircon analyses (90–100% conc.), analysed for Lu–Hf isotopes. MORB: mid-ocean ridge basalts; DM: depleted mantle; CHUR: chondritic uniform reservoir.

c. 480 Ma, and it is interpreted as the climax of igneous intrusion, but an effect of the high-T arc-related input cannot be discarded.

From the above-mentioned Cambrian–Ordovician processes to the Devonian no activity is registered. At this time interval the margin of Gondwana was a passive one (already stated in scientific literature) where the Gondwana-directed subduction that formed the Cadomian magmatic arc ended. At the Devonian, part of this arc (which is now the bottom member of the Upper Allochthon) underwent a HP–HT metamorphic event. This event was induced by the subduction of the margin of Gondwana under another continental fragment. The first zircon crystallisation climax due to this metamorphism is shown by the orthogneisses at *c.* 395 Ma, which were very slightly affected, probably because of their low competence. The zircon crystallisation climax of the eclogites has an age of *c.* 393 Ma and most probably took place near the metamorphic path temperature peak. This lithology was severely disturbed by the metamorphic event. The sediments do not show any important zircon recrystallisation at this time, but the leucosomes that they contain were intensively re-melted (and probably new leucosomatic production took place) at high-T conditions. This second migmatisation was the most important one and took place between 403 and 379 Ma, with a zircon crystallisation climax at *c.* 388 Ma (Fig. 2). It is noteworthy to mention that this intense metamorphism induced zircon recrystallisation in the different lithologies heterogeneously. The sediments were almost unaffected and only the leucosomes produced, registered the effects of this metamorphism. The orthogneisses were slightly affected and the eclogites were the ones that best registered the effects of this HP–HT metamorphic event. It looks like this heterogeneity is related to the competence of the lithologies, where a higher competence allows a more effective isotropic compression, and therefore a higher degree of zircon recrystallisation.

The subducted ensemble experienced a drastic and fast exhumation, from which its progression probably favoured the development of the important extensional detachment which constitutes the actual contact between the Banded and the Cariño Gneiss formations. The HP–HT Upper Allochthon was most probably exhumed as an ultra-high-P buoyant plume, returning immediately over the Gondwana subducting plate.

X

Supporting Information

Appx. 1: Map with sample locations
Appx.2. Data Tables for chapter 5 (Tables 1—12)
(only digital version)
Appx.3. Data Tables for chapter 6 (Tables S1—S12)
(only digital version)
Appx.4. Data Tables for chapter 7 (Tables Ig1-U—Ig13-U & Tables Ig1-Hf—Ig13-Hf)
(only digital version)

Appx.1
Map with sample locations

N
W
E
S

Cabo Ortegal
GCH-19
Gargacido Peak
San Xiao do Trebo
Cantabric Sea
GCH-07
GCH-08
GCH-09
GCH-11
GCH-12
CARIÑO
GCH-01
GCH-02
GCH-20
GCH-31
GCH-18
Pedra
GCH-03, GCH-17, GCH-32
GCH-14, GCH-23
Masanteo
Miranda
Scale
0 0,5 Km 1Km
Fornos Beach
GCH-10
GCH-03, GCH-06, GCH-26
Sismundi
GCH-21
GCH-25
Marsh, dunes and beach
Qtz
Qtz
GCH-24
Pta. Promontorio
ORTIGUEIRA
LEIXA
Railway
GCH-22

HP-HT UPPER UNITS:
(Upper Allochthon top member)
- Ultramafic rocks
- HP Granulites
- Eclogites
- Eclogite Gneisses (Banded Gneisses)

IP UPPER UNITS:
(Upper Allochthon bottom member)
- Cariño Gneisses
- Metagabbros and related igneous rocks

OPHIOLITIC UNITS:
- Moeche

BASAL UNITS:
- Espasante

PARAUTOCHTHON:
- *(Lower Allochthon)*

STRUCTURES:
- Syncline fold axis, D4 structure
- Anticline fold axis, D4 structure
- Recumbent synform fold axis, D3 structure
- Recumbent antiform fold axis, D3 structure
- 60 — Regional foliation strike and dip, S2
- 20º — Lineation trend and plunge angle, L2

Appx.2
Data tables for chapter 5
Tables 1-12

Table 1
U, Th and Pb LA-ICP-MS data of zircon cores from sample GCH-07

Grain	^{207}Pb[a] (cps)	U[b] (ppm)	Pb[b] (ppm)	Th[b]/U	^{206}Pbc[c] (%)	$^{207}Pb/^{235}U$[d]	±2s (%)	$^{206}Pb/^{238}U$[d]	±2s (%)	ρ[e] (rho)	$^{207}Pb/^{206}Pb$[d]	±2s (%)	$^{206}Pb/^{238}U$[f]	±2s (Ma)	$^{207}Pb/^{235}U$[f]	±2s (Ma)	$^{207}Pb/^{206}Pb$[f]	±2s (Ma)	Conc.[g] (%)
A368	1661	41	3	0.73	3.3	0.5788	6.5	0.07335	1.1	0.17	0.05724	6.4	456	5	464	24	501	140	91
A188	1518	95	8	0.82	0.1	0.5944	3.8	0.07641	1.0	0.27	0.05642	3.6	475	5	474	14	469	80	101
A295	14192	351	31	0.76	0.2	0.6301	1.9	0.07888	0.9	0.46	0.05794	1.7	489	4	496	7	528	36	93
A288	4157	222	19	0.51	1.2	0.6357	3.0	0.08051	0.9	0.30	0.05727	2.9	499	4	500	12	502	64	99
A280	1888	116	10	0.54	b.d.	0.6441	3.5	0.08138	1.0	0.29	0.05740	3.4	504	5	505	14	507	74	99
A263	1134	66	6	0.73	b.d.	0.6525	5.1	0.08157	1.0	0.21	0.05802	5.0	506	5	510	21	530	109	95
A234	4457	271	22	0.34	b.d.	0.6545	2.4	0.08176	0.9	0.37	0.05806	2.2	507	4	511	10	532	49	95
A313	2625	76	7	0.94	0.1	0.6471	3.1	0.08205	1.2	0.38	0.05720	2.8	508	6	507	12	499	63	102
A204	1422	42	4	0.95	0.0	0.6485	3.8	0.08212	1.4	0.37	0.05727	3.5	509	7	508	15	502	77	101
A317	1121	29	3	1.18	b.d.	0.6673	5.0	0.08232	1.2	0.23	0.05879	4.9	510	6	519	21	559	106	91
A347	2133	65	5	0.38	b.d.	0.6634	3.1	0.08279	0.8	0.25	0.05812	3.0	513	4	517	13	534	67	96
A250	2547	78	7	0.69	b.d.	0.6602	3.2	0.08292	1.2	0.38	0.05774	2.9	514	6	515	13	520	65	99
A306	911	57	5	1.02	b.d.	0.6621	4.4	0.08297	1.0	0.23	0.05788	4.2	514	5	516	18	525	93	98
A321	1172	72	7	1.39	0.0	0.6586	3.4	0.08299	0.9	0.27	0.05755	3.3	514	5	514	14	513	72	100
A316	1455	44	4	0.67	b.d.	0.6655	3.9	0.08302	1.1	0.29	0.05813	3.7	514	6	518	16	535	82	96
A216	884	12	1	0.68	0.0	0.6699	3.1	0.08303	1.5	0.50	0.05851	2.7	514	8	521	13	549	58	94
A281	8959	258	22	0.43	0.0	0.6692	1.7	0.08356	0.8	0.48	0.05808	1.5	517	4	520	7	533	33	97
A343	2464	74	6	0.51	b.d.	0.6681	2.8	0.08368	0.9	0.33	0.05790	2.6	518	5	520	11	526	57	99
A339	1505	91	9	0.93	b.d.	0.6771	3.7	0.08384	1.2	0.32	0.05857	3.5	519	6	525	15	551	76	94
A225	1038	30	3	1.16	b.d.	0.6741	3.7	0.08386	1.5	0.42	0.05830	3.4	519	8	523	15	541	74	96
A364	1901	51	5	0.76	0.5	0.6793	3.0	0.08395	1.1	0.36	0.05869	2.8	520	6	526	13	556	62	94
A304	10248	292	25	0.48	b.d.	0.6795	1.7	0.08395	1.0	0.57	0.05870	1.4	520	5	526	7	556	31	93
A233	2539	152	14	0.85	b.d.	0.6816	2.5	0.08405	0.8	0.34	0.05882	2.4	520	4	528	10	560	51	93
A342	2336	141	12	0.25	b.d.	0.6777	2.9	0.08411	1.0	0.35	0.05843	2.7	521	5	525	12	546	60	95
A312	2722	83	8	0.96	0.0	0.6728	2.3	0.08435	1.0	0.42	0.05785	2.1	522	5	522	10	524	46	100
A299	1527	92	8	0.61	b.d.	0.6737	3.9	0.08438	1.1	0.28	0.05790	3.7	522	5	523	16	526	82	99
A292	11297	646	57	0.57	0.1	0.6763	1.6	0.08462	0.9	0.58	0.05797	1.3	524	5	525	7	528	29	99
A360	2353	56	6	1.19	1.0	0.6822	3.0	0.08482	0.9	0.32	0.05834	2.8	525	5	528	12	542	62	97
A333	5100	147	14	0.89	0.1	0.6799	2.4	0.08482	1.1	0.43	0.05814	2.2	525	5	527	10	535	48	98
A189	855	25	2	0.55	0.1	0.6751	4.5	0.08486	1.6	0.35	0.05770	4.2	525	8	524	18	518	92	101
A260	4441	250	22	0.50	0.3	0.6796	2.5	0.08501	1.0	0.40	0.05798	2.3	526	5	527	10	529	51	99
A366	3202	83	8	0.76	0.6	0.6866	3.4	0.08509	0.9	0.26	0.05853	3.3	526	4	531	14	550	72	96
A352	5199	143	12	0.44	b.d.	0.6861	2.0	0.08521	1.0	0.48	0.05840	1.8	527	5	530	8	545	39	97
A355	2038	59	5	0.38	0.2	0.6823	2.8	0.08522	1.0	0.35	0.05807	2.7	527	5	528	12	532	58	99
A252	2228	63	6	1.09	b.d.	0.6943	3.1	0.08624	0.8	0.25	0.05839	3.0	533	4	535	13	545	65	98
A291	3221	90	8	0.76	b.d.	0.6981	2.4	0.08643	0.9	0.39	0.05858	2.2	534	5	538	10	551	48	97
A262	1505	90	8	0.63	b.d.	0.7059	3.5	0.08644	1.4	0.41	0.05922	3.2	534	7	542	15	575	69	93
A212	2061	25	3	1.00	b.d.	0.7078	2.9	0.08701	0.9	0.31	0.05900	2.7	538	5	543	12	567	60	95
A303	897	25	2	0.82	0.0	0.7012	4.1	0.08733	1.6	0.39	0.05823	3.8	540	8	540	17	539	82	100
A202	2808	78	8	0.87	b.d.	0.7033	2.7	0.08748	1.0	0.38	0.05831	2.5	541	5	541	12	541	55	100
A231	2647	76	7	0.66	b.d.	0.7214	2.3	0.08749	0.9	0.38	0.05981	2.2	541	5	552	10	597	47	91
A227	2256	66	7	1.06	b.d.	0.7081	3.0	0.08774	1.0	0.33	0.05854	2.8	542	5	544	13	550	61	99
A337	12540	330	30	0.44	0.0	0.7074	1.5	0.08775	0.8	0.53	0.05847	1.3	542	4	543	6	547	28	99
A249	33093	656	61	0.41	2.1	0.7022	3.2	0.08779	1.1	0.35	0.05801	3.0	542	6	540	13	530	65	102
A244	1932	52	5	0.78	b.d.	0.7233	2.7	0.08787	0.9	0.35	0.05970	2.5	543	5	553	11	593	54	92
A307	2122	59	6	1.15	b.d.	0.7161	3.3	0.08851	0.9	0.28	0.05868	3.1	547	5	548	14	555	68	98
A296	701	16	2	0.54	0.8	0.7363	4.9	0.08895	1.5	0.31	0.06003	4.7	549	8	560	21	605	101	91
A279	5574	315	40	2.35	0.1	0.7345	2.2	0.08949	0.9	0.40	0.05953	2.1	552	5	559	10	587	45	94
A230	788	21	2	0.90	b.d.	0.7280	4.6	0.08967	1.3	0.29	0.05888	4.4	554	7	555	20	563	96	98
A298	1199	29	3	1.17	0.3	0.7460	3.9	0.09025	1.1	0.27	0.05996	3.8	557	6	566	17	602	82	93
A325	3361	90	9	1.15	b.d.	0.7405	2.2	0.09033	1.0	0.44	0.05945	2.0	557	5	563	10	584	43	95
A187	3121	170	19	1.30	b.d.	0.7437	2.3	0.09083	0.8	0.36	0.05938	2.2	560	5	565	10	581	47	96
A271	949	51	5	0.84	b.d.	0.7528	5.0	0.09205	1.2	0.24	0.05931	4.9	568	7	570	22	579	106	98
A297	2074	57	6	0.96	b.d.	0.7545	3.0	0.09234	0.8	0.25	0.05926	2.9	569	4	571	13	577	63	99
A243	3413	175	20	1.29	b.d.	0.7824	2.3	0.09414	1.1	0.48	0.06027	2.0	580	6	587	10	613	43	95
A179	2113	51	5	0.82	0.2	0.8016	3.4	0.09624	1.0	0.29	0.06041	3.2	592	6	598	15	618	69	96
A357	4025	99	11	1.20	b.d.	0.8052	2.8	0.09689	0.9	0.33	0.06027	2.6	596	5	600	13	613	57	97
A344	5159	127	13	0.63	b.d.	0.8123	2.2	0.09861	0.7	0.33	0.05975	2.1	606	4	604	10	594	45	102
A190	4255	102	12	1.07	0.1	0.8129	2.3	0.09918	0.8	0.33	0.05945	2.2	610	4	604	11	584	47	104
A363	2365	54	7	1.28	0.4	0.8441	2.9	0.1006	1.2	0.40	0.06088	2.6	618	7	621	13	635	57	97
A277	5847	276	32	1.05	0.0	0.8503	2.0	0.1019	0.7	0.36	0.06049	1.9	626	4	625	10	621	41	101

Grain	^{207}Pb[a] (cps)	U[b] (ppm)	Pb[b] (ppm)	Th[b] U	^{206}Pbc[c] (%)	^{207}Pb[d] ^{235}U	±2s (%)	^{206}Pb[d] ^{238}U	±2s (%)	ρ[e] (rho)	^{207}Pb[d] ^{206}Pb	±2s (%)	^{206}Pb[f] ^{238}U	±2s (Ma)	^{207}Pb[f] ^{235}U	±2s (Ma)	^{207}Pb[f] ^{206}Pb	±2s (Ma)	Conc.[g] (%)
A340	3115	148	17	0.80	b.d.	0.8972	2.6	0.1044	0.9	0.36	0.06233	2.4	640	6	650	12	685	51	93
A199	867	37	4	0.74	0.4	0.9746	4.2	0.1128	1.4	0.33	0.06268	3.9	689	9	691	21	697	84	99
A257	7255	64	13	0.42	0.0	2.230	1.9	0.1999	0.9	0.49	0.08090	1.6	1175	10	1190	13	1219	32	96
A361	11592	100	21	0.49	0.0	2.232	1.9	0.1984	0.8	0.45	0.08161	1.7	1167	9	1191	13	1236	33	94
A318	2487	19	6	1.95	b.d.	2.684	3.2	0.2260	1.2	0.38	0.08613	3.0	1314	15	1324	24	1341	58	98
A248	52371	194	66	0.26	b.d.	5.502	1.0	0.3357	0.7	0.65	0.1189	0.8	1866	11	1901	9	1939	14	96
A235	15770	93	36	0.91	0.1	5.756	1.8	0.3328	0.9	0.54	0.1254	1.5	1852	15	1940	15	2035	26	91
A256	9797	63	26	1.24	b.d.	5.804	1.5	0.3416	0.9	0.59	0.1232	1.3	1894	15	1947	13	2004	22	95
A220	22523	75	36	1.87	0.0	5.951	1.3	0.3534	0.7	0.56	0.1221	1.0	1951	12	1969	11	1988	18	98
A246	26810	186	72	0.81	b.d.	6.012	1.1	0.3403	0.7	0.67	0.1281	0.8	1888	12	1978	9	2072	14	91
A311	12040	38	15	0.78	0.0	6.141	1.7	0.3477	1.1	0.66	0.1281	1.3	1924	18	1996	15	2072	22	93
A228	19634	131	56	1.09	b.d.	6.152	1.3	0.3536	0.8	0.59	0.1262	1.1	1952	13	1998	11	2045	19	95
A221	72693	222	88	0.61	0.0	6.177	1.1	0.3611	0.8	0.76	0.1241	0.7	1987	14	2001	10	2016	13	99
A266	76715	486	199	0.76	0.0	6.211	1.1	0.3635	0.9	0.79	0.1239	0.7	1999	15	2006	10	2013	12	99
A268	11744	37	16	1.08	0.1	6.253	1.6	0.3509	0.8	0.50	0.1292	1.4	1939	13	2012	14	2088	24	93
A322	7410	48	22	1.36	0.1	6.256	2.0	0.3654	0.9	0.46	0.1242	1.8	2008	16	2012	18	2017	31	100
A245	10090	32	13	0.71	0.1	6.261	1.7	0.3599	1.0	0.56	0.1262	1.4	1982	17	2013	15	2045	25	97
A207	9760	31	13	1.15	b.d.	6.302	1.7	0.3683	0.8	0.46	0.1241	1.5	2022	14	2019	15	2016	27	100
A267	18776	121	56	1.49	0.1	6.322	1.3	0.3582	0.7	0.55	0.1280	1.1	1974	12	2022	12	2071	20	95
A349	34883	107	56	2.31	0.1	6.334	1.3	0.3667	0.8	0.63	0.1253	1.0	2014	15	2023	12	2033	18	99
A253	10180	32	12	0.47	0.0	6.338	1.7	0.3571	1.0	0.57	0.1287	1.4	1969	17	2024	15	2080	25	95
A270	19367	117	46	0.82	b.d.	6.349	1.6	0.3470	1.0	0.64	0.1327	1.2	1920	16	2025	14	2134	21	90
A367	17336	52	22	0.85	1.7	6.359	2.0	0.3564	0.8	0.41	0.1294	1.9	1965	14	2027	18	2090	33	94
A351	11254	34	14	0.87	0.0	6.386	1.8	0.3577	0.9	0.48	0.1295	1.6	1971	15	2030	16	2091	28	94
A232	10354	68	30	1.11	b.d.	6.411	1.4	0.3673	0.7	0.51	0.1266	1.2	2017	12	2034	12	2051	21	98
A224	18004	24	10	0.85	b.d.	6.412	1.2	0.3571	0.7	0.55	0.1302	1.0	1969	11	2034	11	2101	18	94
A302	33401	105	44	0.77	0.0	6.417	1.2	0.3709	0.9	0.70	0.1255	0.9	2034	15	2035	11	2036	16	100
A215	10102	67	27	0.74	b.d.	6.424	1.6	0.3594	0.9	0.55	0.1296	1.4	1980	16	2036	15	2093	24	95
A326	11364	70	31	1.14	b.d.	6.442	1.6	0.3637	0.9	0.57	0.1285	1.3	2000	16	2038	14	2077	24	96
A210	10553	33	16	1.58	0.0	6.499	1.8	0.3696	1.0	0.52	0.1275	1.6	2027	17	2046	16	2064	28	98
A237	7738	50	23	1.20	0.0	6.502	2.0	0.3736	1.0	0.51	0.1262	1.7	2046	18	2046	17	2046	30	100
A334	21884	142	64	1.37	b.d.	6.506	1.3	0.3641	0.7	0.59	0.1296	1.0	2002	13	2047	11	2093	18	96
A229	4547	14	6	0.97	0.0	6.516	2.3	0.3738	1.3	0.54	0.1264	2.0	2047	22	2048	21	2049	35	100
A301	9831	28	12	0.99	b.d.	6.518	1.5	0.3595	0.8	0.53	0.1315	1.3	1980	14	2048	14	2118	23	93
A310	9337	28	14	1.68	b.d.	6.575	1.6	0.3670	1.0	0.62	0.1299	1.3	2015	17	2056	14	2097	22	96
A222	7915	25	10	0.89	0.0	6.578	1.8	0.3672	1.0	0.58	0.1299	1.4	2016	18	2056	16	2097	25	96
A209	5198	16	7	1.43	0.0	6.609	1.8	0.3684	0.9	0.48	0.1301	1.6	2022	15	2061	16	2100	28	96
A181	14032	43	18	0.92	b.d.	6.648	1.4	0.3706	0.9	0.68	0.1301	1.0	2032	16	2066	12	2100	18	97
A261	10788	31	14	1.16	b.d.	6.672	1.7	0.3629	0.9	0.52	0.1334	1.5	1996	15	2069	15	2143	25	93
A208	6958	42	19	1.03	0.0	6.674	1.9	0.3715	1.0	0.55	0.1303	1.6	2037	18	2069	17	2102	28	97
A274	8869	55	25	1.31	b.d.	6.754	1.4	0.3660	0.8	0.58	0.1338	1.1	2011	14	2080	12	2149	20	94
A305	7400	22	10	1.02	b.d.	6.774	2.0	0.3795	0.7	0.34	0.1294	1.9	2074	12	2082	18	2090	33	99
A255	9722	60	29	1.30	0.0	6.804	1.7	0.3817	0.7	0.43	0.1293	1.5	2084	13	2086	15	2088	27	100
A192	3470	22	10	0.91	0.0	6.811	2.1	0.3776	1.2	0.57	0.1308	1.8	2065	22	2087	19	2109	31	98
A308	8913	26	12	1.07	0.1	6.862	1.7	0.3820	1.0	0.60	0.1303	1.3	2086	18	2094	15	2102	24	99
A247	5344	15	6	0.68	b.d.	6.900	2.0	0.3769	0.8	0.39	0.1328	1.9	2062	14	2099	18	2135	33	97
A323	11010	33	14	0.77	b.d.	6.913	1.5	0.3774	0.9	0.62	0.1328	1.2	2064	16	2100	13	2136	20	97
A193	9523	57	27	1.22	b.d.	6.949	1.8	0.3836	1.0	0.58	0.1314	1.4	2093	19	2105	16	2117	25	99
A345	9110	26	12	1.33	0.0	6.990	1.6	0.3822	0.6	0.39	0.1326	1.5	2087	11	2110	15	2133	26	98
A294	12057	33	14	0.72	0.1	7.011	1.6	0.3732	0.9	0.55	0.1362	1.3	2044	15	2113	14	2180	23	94
A259	51983	348	170	1.28	0.1	7.022	2.0	0.4050	1.9	0.92	0.1257	0.8	2192	35	2114	18	2039	14	107
A362	17740	50	22	0.71	0.0	7.110	1.5	0.3829	0.7	0.43	0.1347	1.4	2090	12	2125	14	2160	24	97
A236	10768	62	26	0.61	b.d.	7.121	1.5	0.3856	0.9	0.58	0.1339	1.2	2102	16	2127	13	2150	21	98
A348	19560	126	54	0.50	0.3	7.153	2.1	0.4021	1.6	0.78	0.1290	1.3	2179	30	2131	19	2085	24	104
A191	32382	86	43	1.51	0.0	7.509	1.2	0.3866	0.8	0.61	0.1409	1.0	2107	14	2174	11	2238	17	94
A314	20371	52	25	0.97	0.2	7.770	1.2	0.4065	0.7	0.62	0.1386	0.9	2199	14	2205	11	2210	16	99
A206	57681	138	57	0.30	0.1	7.808	1.0	0.3948	0.7	0.67	0.1434	0.7	2145	12	2209	9	2269	13	95
A324	22474	57	25	0.46	b.d.	8.031	1.1	0.4016	0.7	0.65	0.1450	0.9	2176	14	2235	10	2288	15	95
A213	71345	159	73	0.37	0.1	8.551	1.3	0.4266	1.0	0.79	0.1454	0.8	2290	20	2291	12	2292	14	100
A185	62563	117	62	0.80	0.0	10.53	1.1	0.4541	0.7	0.66	0.1681	0.8	2414	14	2482	10	2539	14	95
A182	47475	174	90	0.49	0.0	10.69	1.1	0.4633	0.8	0.68	0.1674	0.8	2454	15	2497	10	2531	14	97
A200	114268	412	216	0.43	0.0	10.89	1.0	0.4767	0.8	0.78	0.1656	0.6	2513	17	2514	10	2514	11	100
A273	53807	204	102	0.34	b.d.	10.89	1.1	0.4646	0.8	0.71	0.1700	0.8	2460	16	2514	10	2557	13	96
A309	64673	238	122	0.46	0.1	10.92	1.1	0.4618	0.8	0.70	0.1714	0.8	2448	15	2516	10	2571	13	95

Grain	^{207}Pb[a] (cps)	U[b] (ppm)	Pb[b] (ppm)	Th[b] / U	^{206}Pbc[c] (%)	^{207}Pb[d] / ^{235}U	±2s (%)	^{206}Pb[d] / ^{238}U	±2s (%)	ρ[e] (rho)	^{207}Pb[d] / ^{206}Pb	±2s (%)	^{206}Pb[f] / ^{238}U	±2s (Ma)	^{207}Pb[f] / ^{235}U	±2s (Ma)	^{207}Pb[f] / ^{206}Pb	±2s (Ma)	Conc.[g] (%)
A211	79151	137	76	0.91	b.d.	11.14	1.0	0.4585	0.7	0.71	0.1762	0.7	2433	15	2535	10	2618	12	93
A354	157284	260	142	0.64	b.d.	11.55	0.9	0.4766	0.7	0.78	0.1758	0.6	2513	15	2569	9	2614	10	96
A258	20215	35	21	1.35	b.d.	11.56	1.4	0.4646	0.9	0.61	0.1805	1.1	2460	18	2570	14	2657	19	93
A319	24669	45	26	0.89	0.1	11.56	1.5	0.4791	1.1	0.71	0.1751	1.0	2523	22	2570	14	2607	17	97
A341	124207	428	223	0.26	0.2	11.84	0.9	0.4855	0.6	0.71	0.1769	0.6	2551	14	2592	9	2624	11	97
A356	204509	332	205	1.27	b.d.	11.85	0.9	0.4847	0.7	0.77	0.1773	0.6	2548	15	2593	9	2628	10	97
A327	21627	68	43	1.38	0.2	12.09	1.4	0.4857	0.9	0.66	0.1805	1.0	2552	19	2611	13	2657	17	96
A219	86675	143	85	0.88	b.d.	12.09	1.0	0.4995	0.7	0.70	0.1755	0.7	2612	14	2611	9	2611	11	100
A336	19282	30	20	1.73	0.0	12.20	1.3	0.4883	0.8	0.63	0.1812	1.0	2563	17	2620	12	2664	17	96
A335	34114	108	68	1.22	b.d.	12.36	1.1	0.5022	0.8	0.69	0.1785	0.8	2623	17	2632	11	2639	14	99
A217	238893	384	200	0.06	0.1	12.38	1.1	0.5020	0.9	0.86	0.1789	0.6	2622	20	2634	10	2642	9	99
A269	148016	243	145	0.83	0.1	12.41	0.9	0.5062	0.7	0.75	0.1777	0.6	2640	15	2636	9	2632	10	100
A223	47848	150	113	2.31	b.d.	12.46	0.9	0.5041	0.7	0.74	0.1793	0.6	2631	15	2640	9	2646	10	99
A183	215331	343	193	0.52	b.d.	12.63	1.1	0.4991	0.9	0.85	0.1836	0.6	2610	20	2653	10	2685	9	97
A275	69929	230	132	0.59	0.0	12.91	1.3	0.5016	1.0	0.75	0.1866	0.9	2621	21	2673	12	2713	14	97
A290	73196	111	67	0.87	b.d.	12.93	1.0	0.5044	0.7	0.77	0.1859	0.6	2633	16	2675	9	2707	10	97
A289	31517	48	28	0.67	0.1	13.01	1.2	0.5113	0.9	0.72	0.1845	0.8	2662	19	2680	11	2694	14	99
A186	35846	56	37	1.60	b.d.	13.03	1.4	0.4932	0.8	0.61	0.1917	1.1	2584	18	2682	13	2757	18	94
A254	82453	251	150	0.63	0.0	13.32	1.0	0.5203	0.7	0.76	0.1857	0.6	2700	17	2703	9	2704	11	100
A264	27444	39	26	1.26	b.d.	14.07	1.2	0.5231	0.8	0.65	0.1951	0.9	2712	17	2754	11	2785	15	97
A272	141799	187	139	1.70	0.1	15.04	0.9	0.5409	0.7	0.81	0.2017	0.5	2787	17	2818	9	2840	9	98
A338	53075	69	41	0.42	0.0	15.21	1.1	0.5338	0.9	0.80	0.2067	0.7	2758	20	2829	11	2880	11	96
A251	163799	221	146	0.99	0.0	15.48	0.9	0.5400	0.7	0.74	0.2079	0.6	2783	15	2845	9	2889	10	96
A282	35574	44	31	1.21	0.0	15.83	1.2	0.5412	0.8	0.64	0.2122	0.9	2788	18	2867	12	2923	15	95
A214	*-70*	*3*		*117*	*b.d.*														
A358	*17*	*1*		*0.13*	*b.d.*														
A350	*28018*	*355*	*4*	*0.07*	*0.0*	*0.1108*	*24.6*	*0.00830*	*24*	*0.98*	*0.09676*	*5.5*	*53*	*13*	*107*	*25*	*1563*	*102*	*3*
A201	*2646*	*65*	*6*	*1.00*	*1.6*	*0.6687*	*4.7*	*0.08000*	*1.5*	*0.33*	*0.06062*	*4.4*	*496*	*7*	*520*	*19*	*626*	*95*	*79*
A218	*524*	*19*	*2*	*0.72*	*0.0*	*0.6229*	*4.6*	*0.08137*	*1.7*	*0.36*	*0.05552*	*4.2*	*504*	*8*	*492*	*18*	*433*	*95*	*116*
A293	*1213*	*35*	*3*	*0.99*	*b.d.*	*0.7074*	*3.9*	*0.08401*	*1.0*	*0.26*	*0.06107*	*3.8*	*520*	*5*	*543*	*17*	*642*	*81*	*81*
A203	*1423*	*40*	*4*	*0.74*	*b.d.*	*0.7451*	*3.5*	*0.08747*	*1.2*	*0.35*	*0.06178*	*3.3*	*541*	*6*	*565*	*15*	*667*	*71*	*81*
A353	*1086*	*63*	*6*	*0.63*	*b.d.*	*0.7594*	*3.2*	*0.08750*	*0.9*	*0.29*	*0.06295*	*3.1*	*541*	*5*	*574*	*14*	*706*	*66*	*77*
A226	*3132*	*27*	*3*	*0.62*	*12.4*	*1.2030*	*10.7*	*0.08831*	*3.2*	*0.30*	*0.09878*	*10.3*	*546*	*17*	*802*	*61*	*1601*	*191*	*34*
A205	*24078*	*510*	*43*	*0.14*	*b.d.*	*0.9268*	*1.4*	*0.08864*	*0.8*	*0.61*	*0.07583*	*1.1*	*548*	*4*	*666*	*7*	*1090*	*22*	*50*
A359	*395*	*9*	*1*	*1.40*	*0.0*	*0.8150*	*5.4*	*0.09093*	*2.0*	*0.38*	*0.06501*	*5.0*	*561*	*11*	*605*	*25*	*775*	*106*	*72*
A180	*347*	*19*	*2*	*0.38*	*1.3*	*0.6381*	*10.3*	*0.09874*	*2.4*	*0.24*	*0.04687*	*10.0*	*607*	*14*	*501*	*41*	*43*	*239*	*1424*
A365	*82690*	*226*	*54*	*0.28*	*1.3*	*4.467*	*2.2*	*0.2082*	*1.6*	*0.73*	*0.1556*	*1.5*	*1219*	*18*	*1725*	*19*	*2408*	*26*	*51*
A346	*1340*	*5*	*1*	*0.21*	*b.d.*	*5.059*	*15.5*	*0.1350*	*13*	*0.84*	*0.2718*	*8.4*	*816*	*101*	*1829*	*141*	*3317*	*132*	*25*
A320	*11800*	*89*	*32*	*0.98*	*b.d.*	*5.248*	*1.5*	*0.3015*	*1.0*	*0.66*	*0.1262*	*1.1*	*1699*	*14*	*1860*	*13*	*2046*	*19*	*83*
A315	*51914*	*106*	*54*	*1.10*	*1.0*	*9.676*	*2.0*	*0.4099*	*1.2*	*0.62*	*0.1712*	*1.5*	*2215*	*23*	*2404*	*18*	*2569*	*26*	*86*
A278	*63567*	*251*	*114*	*0.46*	*0.1*	*9.917*	*1.1*	*0.4051*	*0.8*	*0.77*	*0.1776*	*0.7*	*2192*	*15*	*2427*	*10*	*2630*	*11*	*83*
91500[h]	9384	69	13	0.46	0.5	1.838	3.0	0.1786	1.7	0.38	0.07465	2.4	1059	17	1059	20	1059	48	100
Felix[h]	4694	227	26	1.76	0.4	0.6335	4.6	0.08112	3.5	0.34	0.05664	2.3	503	17	498	18	477	51	106
Plesovice[h]	1723	581	30	0.12	0.2	0.3999	2.6	0.05415	2.5	0.37	0.05356	0.9	340	8	342	8	353	20	96

$^{206}Pb/^{238}U$ error is the quadratic additions of the within run precision (2 SE) and the external reproducibility (2 SD) of the reference zircon. $^{207}Pb/^{206}Pb$ error propagation (^{207}Pb signal dependent) following Gerdes & Zeh (2009). $^{207}Pb/^{235}U$ error is the quadratic addition of the $^{207}Pb/^{206}Pb$ and $^{206}Pb/^{238}U$ uncertainty.

[a] Within run background-corrected mean ^{207}Pb signal in cps (counts per second).

[b] U and Pb content and Th/U ratio were calculated relative to GJ-1 reference zircon.

[c] Percentage of the common Pb on the ^{206}Pb. b.d. = below detection limit.

[d] Pb/U and Pb/Pb ratios. Corrected for background, within-run Pb/U fractionation (in case of $^{206}Pb/^{238}U$) and common Pb using Stacy and Kramers (1975) model Pb composition and subsequently normalised to GJ-1 (ID-TIMS value/measured value); $^{207}Pb/^{235}U$ calculated using (($^{207}Pb/^{206}Pb$)*($^{238}U/^{206}Pb$)*137.88).

[e] Rho (ρ) is the ($^{206}Pb/^{238}U$)/($^{207}Pb/^{235}U$) error correlation coefficient.

[f] Pb/U and Pb/Pb ages.

[g] Degree of concordance = (($^{206}Pb/^{238}U$ age)/($^{207}Pb/^{206}Pb$ age)) x 100.

[h] Mean of 13 (91500), 13 (Felix), 13 (Plesovice), and 26 (GJ-1) analyses, respectively.

Table 2
U, Th and Pb LA-ICP-MS data of zircon cores from sample GCH-08

Grain	^{207}Pb[a] (cps)	U[b] (ppm)	Pb[b] (ppm)	$\frac{Th}{U}$[b]	^{206}Pbc[c] (%)	$\frac{^{207}Pb}{^{235}U}$[d]	±2s (%)	$\frac{^{206}Pb}{^{238}U}$[d]	±2s (%)	ρ[e] (rho)	$\frac{^{207}Pb}{^{206}Pb}$[d]	±2s (%)	$\frac{^{206}Pb}{^{238}U}$[f]	±2s (Ma)	$\frac{^{207}Pb}{^{235}U}$[f]	±2s (Ma)	$\frac{^{207}Pb}{^{206}Pb}$[f]	±2s (Ma)	Conc.[g] (%)
A247	1088	35	3	0.44	0.3	0.6492	5.3	0.08128	1.8	0.34	0.05792	4.9	504	9	508	21	527	108	96
A355	1393	47	4	0.56	0.4	0.6436	4.5	0.08132	1.7	0.37	0.05740	4.2	504	8	505	18	507	91	99
A259	1797	59	6	0.68	0.1	0.6546	3.0	0.08175	1.6	0.53	0.05807	2.6	507	8	511	12	532	56	95
A301	1400	48	4	0.55	0.2	0.6653	4.2	0.08245	1.8	0.42	0.05852	3.8	511	9	518	17	549	84	93
A269	2240	70	6	0.35	0.3	0.6597	3.0	0.08304	1.5	0.49	0.05762	2.6	514	7	514	12	515	58	100
A294	2266	67	7	0.61	1.5	0.6778	4.8	0.08330	1.7	0.35	0.05901	4.5	516	8	525	20	567	98	91
A290	4021	115	12	0.65	1.3	0.6624	4.3	0.08337	1.7	0.39	0.05762	4.0	516	8	516	18	515	87	100
A340	1452	46	4	0.52	0.3	0.6660	3.6	0.08352	1.9	0.53	0.05784	3.1	517	9	518	15	524	67	99
A366	1639	52	5	0.61	0.3	0.6750	3.9	0.08364	1.8	0.46	0.05853	3.4	518	9	524	16	550	75	94
A278	2291	68	6	0.28	1.1	0.6674	4.0	0.08388	1.9	0.47	0.05770	3.5	519	9	519	16	519	77	100
A317	5072	316	37	1.13	0.8	0.6732	2.9	0.08403	1.4	0.49	0.05811	2.6	520	7	523	12	534	56	97
A358	795	27	2	0.38	0.1	0.6721	4.3	0.08408	1.9	0.45	0.05797	3.8	520	10	522	18	529	84	98
A313	1551	47	4	0.39	0.3	0.6748	4.5	0.08409	1.7	0.39	0.05821	4.1	520	9	524	18	538	90	97
A250	6587	110	11	0.34	6.7	0.6737	6.4	0.08441	1.8	0.28	0.05789	6.1	522	9	523	26	526	134	99
A261	2013	142	14	0.74	0.0	0.6894	3.2	0.08517	1.6	0.49	0.05871	2.8	527	8	532	13	556	61	95
A309	2157	71	7	0.71	0.1	0.6806	3.0	0.08525	1.9	0.61	0.05790	2.4	527	9	527	13	526	53	100
A321	1223	40	4	0.56	0.3	0.6816	5.1	0.08542	1.7	0.33	0.05787	4.9	528	9	528	21	525	106	101
A258	2574	174	19	0.93	0.1	0.6937	3.5	0.08576	1.8	0.51	0.05867	3.0	530	9	535	15	555	65	96
A337	2073	130	12	0.41	0.3	0.6865	3.7	0.08581	1.6	0.44	0.05802	3.3	531	8	531	15	531	73	100
A293	3868	116	11	0.58	0.3	0.6882	2.7	0.08599	1.8	0.65	0.05804	2.0	532	9	532	11	531	44	100
A312	2155	63	6	0.62	0.6	0.6999	3.6	0.08699	1.6	0.45	0.05836	3.2	538	8	539	15	543	71	99
A343	3082	96	9	0.45	0.8	0.7046	3.3	0.08730	1.6	0.47	0.05853	3.0	540	8	542	14	550	65	98
A307	10107	117	13	0.35	10.5	0.7076	7.7	0.08747	1.9	0.25	0.05867	7.4	541	10	543	33	555	162	97
A372	3188	105	9	0.31	b.d.	0.7068	3.1	0.08764	1.5	0.48	0.05849	2.8	542	8	543	13	548	60	99
A318	2238	144	16	0.88	0.4	0.7101	3.4	0.08792	1.5	0.46	0.05858	3.0	543	8	545	14	551	66	99
A256	1890	63	6	0.23	0.0	0.7149	3.5	0.08825	1.8	0.52	0.05876	3.0	545	9	548	15	558	65	98
A373	1070	31	3	0.62	0.6	0.7268	4.2	0.08952	1.9	0.46	0.05889	3.7	553	10	555	18	563	80	98
A314	1184	36	4	0.57	0.3	0.7298	4.0	0.08981	1.5	0.38	0.05893	3.7	554	8	556	17	565	81	98
A305	19822	827	95	0.69	3.0	0.7281	4.0	0.08987	1.7	0.42	0.05876	3.6	555	9	555	17	558	79	99
A253	7511	446	42	0.32	0.3	0.7339	2.2	0.09050	1.4	0.65	0.05881	1.7	558	8	559	10	560	37	100
A308	1258	37	4	0.44	0.3	0.7444	3.3	0.09091	1.4	0.42	0.05938	3.0	561	8	565	15	581	66	97
A335	10647	423	51	0.82	4.0	0.7423	5.0	0.09107	1.5	0.29	0.05911	4.8	562	8	564	22	571	105	98
A267	7190	228	21	0.25	1.5	0.7433	3.1	0.09139	1.5	0.48	0.05899	2.7	564	8	564	14	567	59	99
A265	1835	112	13	0.81	b.d.	0.7477	3.7	0.09157	1.7	0.46	0.05922	3.3	565	9	567	16	575	72	98
A349	2623	179	19	0.77	b.d.	0.7507	2.9	0.09169	1.5	0.53	0.05938	2.4	566	8	569	13	581	52	97
A266	3569	113	11	0.39	b.d.	0.7584	2.6	0.09227	1.6	0.60	0.05961	2.1	569	9	573	11	590	45	96
A365	15438	76	14	0.68	21.1	0.7767	8.3	0.09331	2.7	0.33	0.06037	7.8	575	15	584	37	617	169	93
A360	4750	140	13	0.17	0.2	0.7783	2.4	0.09447	1.7	0.70	0.05975	1.7	582	9	585	11	595	36	98
A377	2752	88	10	0.74	0.2	0.7771	2.6	0.09454	1.6	0.63	0.05962	2.0	582	9	584	12	590	44	99
A319	2466	77	8	0.41	b.d.	0.7767	2.6	0.09506	1.9	0.73	0.05926	1.8	585	11	584	12	577	39	101
A288	10598	561	66	0.50	0.4	0.8815	2.4	0.1042	1.4	0.60	0.06133	1.9	639	9	642	11	651	40	98
A344	1983	105	13	0.62	b.d.	0.8970	3.7	0.1058	1.8	0.50	0.06147	3.2	648	11	650	18	656	69	99
A292	7826	196	24	0.61	0.2	0.9084	2.8	0.1072	1.9	0.69	0.06147	2.0	656	12	656	14	656	43	100
A311	3905	74	12	0.90	0.1	1.203	2.6	0.1314	1.6	0.60	0.06638	2.1	796	12	802	15	818	44	97
A249	27718	191	37	0.28	9.3	1.514	6.5	0.1546	1.8	0.28	0.07106	6.3	926	15	936	41	959	128	97
A254	10422	283	49	0.26	0.1	1.662	2.2	0.1667	1.4	0.65	0.07232	1.7	994	13	994	14	995	34	100
A257	13488	262	56	0.28	0.1	2.278	2.1	0.2056	1.5	0.71	0.08036	1.5	1206	17	1206	15	1206	30	100
A342	11288	111	24	0.27	0.1	2.284	2.2	0.2077	1.8	0.84	0.07977	1.2	1216	20	1207	16	1191	24	102
A322	12461	163	35	0.15	2.1	2.469	2.6	0.2126	1.6	0.62	0.08426	2.0	1242	18	1263	19	1298	40	96
A376	24370	110	46	0.86	1.0	5.161	2.4	0.3297	1.7	0.69	0.1135	1.7	1837	27	1846	21	1856	31	99
A368	8477	36	15	0.93	0.0	5.281	2.1	0.3355	1.5	0.74	0.1142	1.4	1865	25	1866	18	1867	25	100
A324	4689	19	8	1.05	b.d.	5.567	2.7	0.3293	1.6	0.58	0.1226	2.2	1835	25	1911	24	1995	39	92
A357	28361	102	47	0.82	2.8	5.853	3.2	0.3526	1.8	0.55	0.1204	2.7	1947	30	1954	28	1962	48	99
A252	33494	261	132	1.35	0.4	5.867	1.8	0.3545	1.4	0.82	0.1200	1.0	1956	24	1956	15	1957	18	100
A273	12146	89	38	0.80	0.6	5.871	2.3	0.3367	1.6	0.68	0.1264	1.7	1871	25	1957	20	2049	30	91
A255	20900	76	30	0.30	0.1	6.100	1.9	0.3613	1.6	0.84	0.1225	1.0	1988	27	1990	17	1993	18	100
A362	9315	34	15	0.61	0.1	6.147	2.2	0.3554	1.5	0.70	0.1254	1.6	1960	26	1997	19	2035	28	96
A353	28803	106	42	0.45	0.3	6.155	1.8	0.3505	1.3	0.75	0.1274	1.2	1937	22	1998	16	2062	21	94
A275	6876	49	20	0.41	0.9	6.187	3.3	0.3577	1.6	0.49	0.1254	2.9	1971	27	2003	29	2035	50	97
A260	12434	101	39	0.24	0.2	6.216	1.9	0.3637	1.5	0.77	0.1240	1.2	1999	26	2007	17	2014	22	99
A300	9631	35	15	0.63	0.2	6.221	2.2	0.3516	1.6	0.72	0.1283	1.5	1942	27	2007	20	2075	27	94

Grain	^{207}Pb[a] (cps)	U[b] (ppm)	Pb[b] (ppm)	$\frac{Th}{U}$[b]	^{206}Pbc[c] (%)	$\frac{^{207}Pb}{^{235}U}$[d]	±2s (%)	$\frac{^{206}Pb}{^{238}U}$[d]	±2s (%)	ρ[e] (rho)	$\frac{^{207}Pb}{^{206}Pb}$[d]	±2s (%)	$\frac{^{206}Pb}{^{238}U}$[f]	±2s (Ma)	$\frac{^{207}Pb}{^{235}U}$[f]	±2s (Ma)	$\frac{^{207}Pb}{^{206}Pb}$[f]	±2s (Ma)	Conc.[g] (%)
A346	10498	38	16	0.43	0.2	6.251	2.0	0.3651	1.6	0.79	0.1242	1.2	2006	27	2012	17	2017	22	99
A325	3522	25	11	0.59	0.0	6.270	3.4	0.3567	1.9	0.56	0.1275	2.8	1966	32	2014	30	2064	49	95
A338	29913	220	92	0.55	0.1	6.287	1.9	0.3562	1.5	0.77	0.1280	1.2	1964	25	2017	17	2071	21	95
A264	13458	101	45	0.75	0.1	6.376	2.1	0.3640	1.6	0.74	0.1270	1.4	2001	27	2029	19	2057	25	97
A263	11316	40	17	0.48	0.0	6.402	1.9	0.3680	1.4	0.73	0.1262	1.3	2020	24	2033	17	2045	23	99
A323	16758	125	56	0.71	0.1	6.438	1.9	0.3637	1.5	0.81	0.1284	1.1	2000	26	2037	17	2076	19	96
A367	28700	102	45	0.68	0.0	6.440	1.6	0.3595	1.4	0.86	0.1299	0.8	1980	24	2038	15	2097	15	94
A302	7793	59	26	0.68	0.2	6.460	2.5	0.3684	1.6	0.66	0.1272	1.9	2022	29	2040	22	2059	33	98
A333	11617	37	19	1.06	1.3	6.461	3.1	0.3729	1.5	0.49	0.1257	2.7	2043	27	2041	28	2038	48	100
A347	12024	43	17	0.35	0.1	6.473	2.0	0.3655	1.5	0.77	0.1284	1.2	2008	26	2042	17	2077	22	97
A280	17595	129	58	0.74	0.1	6.480	1.9	0.3643	1.5	0.79	0.1290	1.2	2002	26	2043	17	2085	21	96
A296	13611	101	47	0.85	0.1	6.484	2.1	0.3667	1.5	0.71	0.1282	1.5	2014	26	2044	18	2074	26	97
A262	12358	43	20	0.81	0.3	6.491	2.1	0.3696	1.5	0.74	0.1274	1.4	2028	27	2045	18	2062	24	98
A274	13170	71	33	0.49	4.9	6.502	3.7	0.3737	1.7	0.46	0.1262	3.3	2047	30	2046	33	2046	58	100
A352	12114	43	18	0.50	0.2	6.504	2.2	0.3731	1.8	0.80	0.1264	1.4	2044	31	2046	20	2049	24	100
A271	48648	355	160	0.64	0.1	6.512	2.2	0.3765	2.0	0.91	0.1255	0.9	2060	36	2048	20	2035	17	101
A351	6267	22	10	0.75	0.2	6.525	2.6	0.3708	1.5	0.59	0.1276	2.1	2033	26	2049	23	2066	36	98
A295	17517	125	57	0.65	0.2	6.548	2.2	0.3748	1.7	0.79	0.1267	1.4	2052	31	2052	20	2053	24	100
A345	7500	28	12	0.64	0.1	6.586	2.4	0.3717	1.7	0.69	0.1285	1.7	2037	29	2057	21	2078	31	98
A298	15445	49	23	0.63	1.7	6.587	2.5	0.3739	1.5	0.61	0.1278	2.0	2048	27	2058	22	2068	35	99
A326	6139	44	19	0.52	0.2	6.615	2.6	0.3708	1.9	0.73	0.1294	1.7	2033	33	2061	23	2090	31	97
A306	18424	63	27	0.47	0.5	6.637	2.1	0.3773	1.5	0.69	0.1276	1.6	2064	26	2064	19	2065	27	100
A279	42902	132	58	0.51	0.9	6.694	1.8	0.3767	1.6	0.85	0.1289	1.0	2061	28	2072	16	2083	17	99
A375	15959	59	27	0.72	0.3	6.700	2.1	0.3769	1.6	0.78	0.1289	1.3	2062	29	2073	19	2084	23	99
A350	17067	59	25	0.40	0.1	6.749	1.9	0.3808	1.5	0.80	0.1285	1.1	2080	27	2079	17	2078	19	100
A276	21969	125	57	0.35	4.9	6.752	3.8	0.3786	2.0	0.53	0.1293	3.2	2070	36	2079	34	2089	57	99
A299	12610	43	19	0.50	0.0	6.797	2.1	0.3773	1.6	0.74	0.1306	1.4	2064	28	2085	19	2107	25	98
A297	10229	25	12	0.50	6.1	6.799	3.9	0.3825	1.6	0.42	0.1289	3.5	2088	29	2086	35	2083	61	100
A272	8931	64	29	0.56	0.0	6.866	2.0	0.3835	1.5	0.77	0.1299	1.3	2092	27	2094	18	2096	22	100
A316	78583	338	127	0.08	4.2	6.908	2.7	0.3691	1.5	0.55	0.1357	2.3	2025	26	2100	25	2174	40	93
A320	6865	23	10	0.58	0.2	6.912	2.9	0.3846	2.0	0.68	0.1303	2.1	2098	36	2100	26	2103	37	100
A277	22467	157	71	0.58	0.2	7.038	1.7	0.3855	1.5	0.84	0.1324	1.0	2102	26	2116	16	2130	17	99
A361	10307	33	15	0.45	0.1	7.058	2.4	0.3867	1.9	0.79	0.1324	1.5	2108	34	2119	22	2130	26	99
A303	9220	29	13	0.52	0.1	7.162	2.4	0.3878	1.6	0.68	0.1340	1.7	2112	29	2132	21	2150	30	98
A327	16878	55	23	0.27	b.d.	7.549	1.8	0.3939	1.4	0.77	0.1390	1.1	2141	25	2179	16	2215	19	97
A354	10324	29	13	0.34	0.2	7.796	2.0	0.3975	1.6	0.81	0.1422	1.2	2158	30	2208	18	2255	20	96
A304	33205	93	46	0.55	0.0	8.506	1.7	0.4236	1.3	0.80	0.1456	1.0	2277	26	2287	15	2295	18	99
A369	62862	163	68	0.05	0.1	8.737	1.7	0.4080	1.5	0.86	0.1553	0.9	2206	27	2311	16	2405	15	92
A378	50397	132	62	0.18	0.2	9.169	1.9	0.4414	1.7	0.86	0.1507	1.0	2357	33	2355	18	2354	17	100
A251	31802	77	39	0.38	0.1	9.610	1.6	0.4478	1.4	0.88	0.1557	0.8	2385	28	2398	15	2409	13	99
A315	33567	80	39	0.24	0.0	9.935	1.7	0.4511	1.4	0.84	0.1597	0.9	2400	28	2429	16	2453	15	98
A371	55935	118	62	0.38	b.d.	10.60	1.5	0.4613	1.4	0.90	0.1667	0.7	2445	28	2489	14	2525	11	97
A379	77304	173	89	0.26	0.0	10.68	1.5	0.4663	1.4	0.90	0.1661	0.7	2467	28	2496	14	2519	11	98
A334	147965	285	175	0.82	0.1	11.21	1.6	0.4690	1.5	0.92	0.1733	0.6	2479	30	2541	15	2590	10	96
A348	23118	46	26	0.52	0.2	11.57	1.9	0.4820	1.5	0.81	0.1741	1.1	2536	32	2570	18	2597	18	98
A356	25715	51	31	0.75	0.1	11.65	1.9	0.4830	1.6	0.83	0.1749	1.0	2540	33	2576	18	2605	17	98
A363	61168	116	65	0.28	0.1	12.04	1.8	0.4993	1.5	0.84	0.1749	1.0	2611	33	2607	17	2605	16	100
A248	67423	112	81	1.15	2.1	12.21	1.9	0.4995	1.4	0.72	0.1773	1.3	2612	30	2621	18	2628	22	99
A289	59136	109	62	0.32	0.1	12.38	1.8	0.5022	1.7	0.93	0.1789	0.6	2623	36	2634	17	2642	11	99
A268	31168	116	74	0.69	0.1	12.47	1.9	0.5034	1.6	0.84	0.1796	1.0	2628	34	2640	18	2649	17	99
A291	154530	270	182	0.79	0.3	13.05	1.6	0.5157	1.5	0.92	0.1835	0.6	2681	32	2683	15	2685	10	100
A339	34402	58	34	0.24	0.8	13.23	2.3	0.5208	2.1	0.89	0.1842	1.0	2702	46	2696	22	2691	17	100
A341	51694	81	49	0.32	2.3	13.38	2.0	0.5222	1.5	0.76	0.1859	1.3	2708	34	2707	19	2706	22	100
A310	90273	145	90	0.33	0.1	14.63	1.8	0.5455	1.7	0.94	0.1945	0.6	2806	39	2792	17	2781	10	101
A336	93204	261	163	0.32	0.1	15.88	1.5	0.5304	1.4	0.90	0.2171	0.7	2743	31	2869	15	2959	11	93
A364	211000	262	163	0.26	0.1	16.32	1.6	0.5329	1.4	0.90	0.2221	0.7	2754	32	2896	15	2996	11	92
A282	8707	111	4	0.19	3.5	0.1417	7.7	0.02074	6.8	0.88	0.04955	3.6	132	9	135	10	174	85	76
A281	3311	117	8	0.16	b.d.	0.5729	4.8	0.07170	2.1	0.43	0.05795	4.3	446	9	460	18	528	95	85
A374	329	7	4	10.97	b.d.	1.524	19.6	0.09434	6.8	0.34	0.1172	18.4	581	38	940	128	1914	330	30
A270	44404	566	140	0.12	0.0	3.909	2.5	0.2458	2.3	0.89	0.1153	1.2	1417	29	1616	21	1885	21	75
A370	53552	221	66	0.26	0.0	5.809	3.1	0.2729	3.0	0.96	0.1544	0.8	1556	42	1948	27	2395	14	65
91500[h]	8378	74	13	0.29	0.5	1.850	1.8	0.1795	1.4	0.54	0.07477	0.9	1064	14	1063	12	1062	18	100

Grain	^{207}Pb[a] (cps)	U[b] (ppm)	Pb[b] (ppm)	Th[b] U	^{206}Pbc[c] (%)	^{207}Pb[d] / ^{235}U	±2s (%)	^{206}Pb[d] / ^{238}U	±2s (%)	ρ[e] (rho)	^{207}Pb[d] / ^{206}Pb	±2s (%)	^{206}Pb[f] / ^{238}U	±2s (Ma)	^{207}Pb[f] / ^{235}U	±2s (Ma)	^{207}Pb[f] / ^{206}Pb	±2s (Ma)	Conc.[g] (%)
Felix[h]	12482	435	68	2.47	0.2	0.6484	3.0	0.08211	3.0	0.43	0.05728	3.0	509	15	507	12	502	65	102
Plesovice[h]	2852	651	34	0.09	1.3	0.3989	4.1	0.05419	2.2	0.48	0.05339	2.9	340	7	341	12	345	64	99

$^{206}Pb/^{238}U$ error is the quadratic additions of the within run precision (2 SE) and the external reproducibility (2 SD) of the reference zircon. $^{207}Pb/^{206}Pb$ error propagation (^{207}Pb signal dependent) following Gerdes & Zeh (2009). $^{207}Pb/^{235}U$ error is the quadratic addition of the $^{207}Pb/^{206}Pb$ and $^{206}Pb/^{238}U$ uncertainty.

[a] Within run background-corrected mean ^{207}Pb signal in cps (counts per second).

[b] U and Pb content and Th/U ratio were calculated relative to GJ-1 reference zircon.

[c] Percentage of the common Pb on the ^{206}Pb. b.d. = below detection limit.

[d] Pb/U and Pb/Pb ratios. Corrected for background, within-run Pb/U fractionation (in case of $^{206}Pb/^{238}U$) and common Pb using Stacy and Kramers (1975) model Pb composition and subsequently normalised to GJ-1 (ID-TIMS value/measured value); $^{207}Pb/^{235}U$ calculated using (($^{207}Pb/^{206}Pb$)*($^{238}U/^{206}Pb$)*137.88).

[e] Rho (ρ) is the ($^{206}Pb/^{238}U$)/($^{207}Pb/^{235}U$) error correlation coefficient.

[f] Pb/U and Pb/Pb ages.

[g] Degree of concordance = (($^{206}Pb/^{238}U$ age)/($^{207}Pb/^{206}Pb$ age)) x 100.

[h] Mean of 13 (91500), 13 (Felix), 13 (Plesovice), and 23 (GJ-1) analyses, respectively.

Table 3
U, Th and Pb LA-ICP-MS data of zircon cores from sample GCH-09

Grain	^{207}Pb[a] (cps)	U[b] (ppm)	Pb[b] (ppm)	Th/U[b]	$^{206}Pb_c$[c] (%)	$^{207}Pb/^{235}U$[d]	±2s (%)	$^{206}Pb/^{238}U$[d]	±2s (%)	ρ[e] (rho)	$^{207}Pb/^{206}Pb$[d]	±2s (%)	$^{206}Pb/^{238}U$[f]	±2s (Ma)	$^{207}Pb/^{235}U$[f]	±2s (Ma)	$^{207}Pb/^{206}Pb$[f]	±2s (Ma)	Conc.[g] (%)
A389	3067	108	9	0.38	0.2	0.6351	2.5	0.08028	1.6	0.64	0.05738	2.0	498	8	499	10	506	43	98
A023	1218	137	13	0.62	0.0	0.6528	3.8	0.08095	1.7	0.45	0.05848	3.4	502	8	510	15	548	73	92
A408	8094	239	20	0.25	2.3	0.6478	3.8	0.08138	1.5	0.39	0.05773	3.5	504	7	507	15	520	76	97
A464	1790	56	5	0.50	0.9	0.6471	2.8	0.08143	1.6	0.56	0.05764	2.3	505	8	507	11	516	51	98
A012	2382	263	21	0.20	0.1	0.6531	3.8	0.08156	1.4	0.39	0.05807	3.5	505	7	510	15	533	76	95
A467	7484	252	21	0.29	0.1	0.6553	1.9	0.08238	1.4	0.75	0.05769	1.3	510	7	512	8	518	28	98
A380	1746	39	4	0.30	3.8	0.6553	5.3	0.08268	2.1	0.40	0.05749	4.8	512	10	512	21	510	106	100
A011	1316	139	12	0.40	0.6	0.6637	5.7	0.08278	1.8	0.32	0.05815	5.4	513	9	517	23	536	118	96
A043	1250	124	11	0.41	0.5	0.6700	4.0	0.08312	2.2	0.55	0.05846	3.3	515	11	521	16	547	73	94
A435	1562	55	5	0.50	0.1	0.6654	3.7	0.08348	1.8	0.49	0.05781	3.3	517	9	518	15	523	72	99
A030	1548	168	15	0.42	b.d.	0.6782	3.4	0.08427	1.6	0.46	0.05837	3.0	522	8	526	14	544	66	96
A432	1299	42	4	0.80	0.2	0.6884	3.6	0.08521	1.7	0.48	0.05859	3.2	527	9	532	15	552	69	95
A478	6221	204	20	0.59	0.0	0.6818	2.2	0.08527	1.4	0.61	0.05799	1.8	527	7	528	9	530	39	100
A470	1781	55	5	0.65	0.3	0.6810	3.0	0.08528	1.4	0.47	0.05792	2.7	528	7	527	13	527	59	100
A416	2284	71	7	0.40	1.3	0.6891	3.9	0.08569	1.6	0.42	0.05832	3.6	530	8	532	16	542	78	98
A403	4481	140	13	0.38	0.2	0.6884	3.2	0.08570	1.9	0.60	0.05826	2.6	530	10	532	13	540	56	98
A430	2772	93	9	0.47	b.d.	0.6935	3.2	0.08594	1.8	0.56	0.05853	2.6	531	9	535	13	550	58	97
A431	2502	76	8	0.65	0.4	0.6895	2.4	0.08614	1.5	0.60	0.05805	1.9	533	8	533	10	532	43	100
A040	1685	176	16	0.32	0.0	0.7065	3.2	0.08700	2.0	0.64	0.05890	2.5	538	10	543	13	563	53	95
A025	1397	71	7	0.43	b.d.	0.7039	3.1	0.08701	1.6	0.53	0.05867	2.6	538	8	541	13	555	57	97
A032	2054	221	22	0.64	b.d.	0.7078	3.3	0.08726	1.7	0.52	0.05883	2.8	539	9	543	14	561	61	96
A009	5046	523	44	0.12	0.1	0.7150	2.6	0.08774	1.6	0.62	0.05911	2.0	542	8	548	11	571	45	95
A017	5330	526	50	0.40	0.7	0.7093	2.6	0.08791	1.6	0.60	0.05852	2.1	543	8	544	11	549	46	99
A490	2042	66	7	0.62	b.d.	0.7085	3.3	0.08792	1.7	0.51	0.05845	2.8	543	9	544	14	547	62	99
A472	1224	40	4	0.76	0.1	0.7184	3.4	0.08876	1.7	0.49	0.05870	3.0	548	9	550	15	556	65	99
A463	3185	108	11	0.66	b.d.	0.7253	3.1	0.08958	1.8	0.56	0.05872	2.6	553	9	554	13	557	56	99
A422	2134	66	6	0.41	0.1	0.7257	2.6	0.08977	1.8	0.68	0.05863	1.9	554	10	554	11	553	42	100
A459	1720	51	5	0.56	0.2	0.7366	3.5	0.09028	1.7	0.49	0.05918	3.1	557	9	560	15	574	67	97
A458	3308	78	7	0.13	3.4	0.7349	4.8	0.09050	1.5	0.31	0.05890	4.6	558	8	559	21	563	100	99
A451	2407	76	7	0.29	b.d.	0.7457	2.8	0.09097	1.6	0.58	0.05945	2.3	561	9	566	12	583	49	96
A027	3720	180	18	0.51	0.1	0.7552	2.9	0.09156	1.7	0.57	0.05982	2.4	565	9	571	13	597	51	95
A018	1545	152	17	0.75	0.6	0.7500	4.8	0.09205	1.7	0.36	0.05909	4.5	568	9	568	21	571	98	99
A486	1461	43	5	0.86	b.d.	0.7539	4.1	0.09246	1.8	0.44	0.05914	3.7	570	10	570	18	572	80	100
A394	2910	83	9	0.54	0.1	0.7716	3.2	0.09410	1.7	0.54	0.05947	2.7	580	9	581	14	584	58	99
A421	2754	57	6	0.44	2.5	0.8026	4.4	0.09704	2.0	0.45	0.05999	3.9	597	11	598	20	603	85	99
A021	2672	235	27	0.58	0.2	0.8640	3.0	0.1008	1.7	0.57	0.06214	2.5	619	10	632	14	679	53	91
A457	5336	157	17	0.39	0.5	0.8502	2.5	0.1019	1.5	0.61	0.06053	2.0	625	9	625	12	622	43	100
A419	3031	82	11	1.09	b.d.	0.8613	3.2	0.1022	1.6	0.51	0.06111	2.8	627	10	631	15	643	59	98
A013	2295	191	21	0.38	0.1	0.8923	3.0	0.1036	1.9	0.63	0.06245	2.3	636	11	648	14	690	49	92
A031	10810	952	111	0.63	0.3	0.8760	2.5	0.1041	2.0	0.79	0.06101	1.5	639	12	639	12	640	33	100
A400	12212	292	32	0.12	b.d.	0.9994	1.8	0.1153	1.4	0.76	0.06285	1.2	704	9	704	9	703	25	100
A452	4164	88	12	0.57	0.2	1.040	2.6	0.1185	1.7	0.63	0.06368	2.0	722	11	724	14	731	43	99
A493	1800	39	6	0.67	0.1	1.055	3.2	0.1202	1.6	0.50	0.06367	2.8	732	11	732	17	731	58	100
A041	6269	132	19	0.39	4.3	1.109	5.1	0.1237	1.7	0.34	0.06506	4.8	752	12	758	27	776	100	97
A462	982	15	3	0.79	b.d.	1.552	3.6	0.1582	1.9	0.53	0.07113	3.1	947	17	951	22	961	62	99
A022	8791	369	67	0.20	0.0	1.891	2.1	0.1798	1.5	0.69	0.07630	1.5	1066	14	1078	14	1103	30	97
A019	7137	235	51	0.33	0.0	2.311	2.4	0.2065	1.6	0.67	0.08116	1.8	1210	18	1216	17	1225	35	99
A398	8395	57	15	0.25	0.1	3.294	2.0	0.2568	1.6	0.82	0.09305	1.1	1473	21	1480	16	1489	21	99
A492	14543	97	28	0.36	0.1	3.452	1.9	0.2656	1.4	0.73	0.09426	1.3	1519	19	1516	15	1513	25	100
A436	25701	108	42	0.52	1.8	5.127	3.1	0.3302	2.3	0.75	0.1126	2.0	1839	37	1841	26	1842	37	100
A410	22459	84	33	0.37	0.1	5.853	1.7	0.3519	1.4	0.83	0.1206	1.0	1944	24	1954	15	1966	17	99
A415	78573	288	130	1.09	0.0	5.934	1.8	0.3435	1.7	0.91	0.1253	0.8	1903	28	1966	16	2033	14	94
A461	15886	56	24	0.68	0.0	5.971	1.6	0.3469	1.3	0.84	0.1249	0.8	1920	22	1972	14	2027	15	95
A474	33067	127	56	0.85	0.5	6.067	3.9	0.3580	3.7	0.96	0.1229	1.1	1973	63	1986	34	1999	20	99
A010	40153	494	237	0.99	0.2	6.170	1.7	0.3634	1.4	0.79	0.1232	1.1	1998	24	2000	15	2002	19	100
A485	8132	29	13	0.69	0.2	6.192	2.1	0.3652	1.7	0.78	0.1230	1.3	2007	29	2003	19	2000	24	100
A479	17794	65	31	0.90	0.7	6.235	1.9	0.3657	1.4	0.76	0.1236	1.2	2009	25	2009	17	2009	22	100
A407	47358	175	75	0.58	b.d.	6.240	1.5	0.3632	1.3	0.86	0.1246	0.8	1997	22	2010	13	2023	14	99
A381	10947	41	17	0.43	0.2	6.281	2.1	0.3631	1.6	0.74	0.1255	1.4	1997	27	2016	19	2035	25	98
A388	17069	63	29	0.84	0.2	6.290	2.0	0.3632	1.6	0.81	0.1256	1.2	1997	28	2017	18	2037	21	98
A434	8638	32	14	0.66	b.d.	6.314	2.0	0.3651	1.5	0.74	0.1254	1.3	2007	25	2020	18	2035	24	99

Grain	^{207}Pb[a] (cps)	U[b] (ppm)	Pb[b] (ppm)	Th[b] U	^{206}Pbc[c] (%)	^{207}Pb[d] ^{235}U	±2s (%)	^{206}Pb[d] ^{238}U	±2s (%)	ρ[e] (rho)	^{207}Pb[d] ^{206}Pb	±2s (%)	^{206}Pb[f] ^{238}U	±2s (Ma)	^{207}Pb[f] ^{235}U	±2s (Ma)	^{207}Pb[f] ^{206}Pb	±2s (Ma)	Conc.[g] (%)
A405	10562	38	19	1.12	0.2	6.350	2.1	0.3666	1.6	0.73	0.1256	1.4	2013	27	2025	19	2038	25	99
A404	13963	49	22	0.71	0.4	6.367	2.0	0.3667	1.6	0.82	0.1259	1.1	2014	28	2028	18	2042	20	99
A406	8895	33	14	0.54	0.1	6.370	2.3	0.3666	1.6	0.67	0.1260	1.7	2014	27	2028	21	2043	31	99
A007	12483	153	67	0.62	0.0	6.371	2.1	0.3669	1.7	0.81	0.1259	1.2	2015	29	2028	18	2042	22	99
A395	14745	51	19	0.24	0.0	6.376	1.8	0.3573	1.5	0.82	0.1294	1.0	1969	25	2029	16	2090	18	94
A008	20499	245	99	0.35	0.1	6.411	1.9	0.3699	1.6	0.82	0.1257	1.1	2029	28	2034	17	2039	20	100
A491	16908	54	26	0.88	0.3	6.419	2.2	0.3703	1.7	0.76	0.1257	1.4	2031	30	2035	20	2039	25	100
A396	26079	92	39	0.63	0.0	6.458	1.5	0.3570	1.3	0.85	0.1312	0.8	1968	22	2040	13	2114	14	93
A393	25307	91	37	0.37	0.0	6.471	1.8	0.3692	1.5	0.86	0.1271	0.9	2026	27	2042	16	2059	16	98
A444	26292	92	38	0.37	0.2	6.474	2.0	0.3728	1.7	0.85	0.1260	1.0	2042	29	2042	17	2042	18	100
A382	14396	50	22	0.59	0.3	6.499	2.1	0.3659	1.5	0.74	0.1288	1.4	2010	27	2046	18	2082	24	97
A473	33607	127	55	0.67	0.0	6.505	1.7	0.3711	1.4	0.80	0.1271	1.0	2035	24	2047	15	2059	18	99
A426	20632	78	34	0.60	0.1	6.505	1.8	0.3697	1.6	0.86	0.1276	0.9	2028	28	2047	16	2065	16	98
A476	24653	86	37	0.53	0.3	6.517	1.7	0.3737	1.5	0.86	0.1265	0.9	2047	26	2048	15	2050	16	100
A391	18481	69	30	0.59	0.0	6.519	1.9	0.3732	1.5	0.81	0.1267	1.1	2044	27	2049	17	2053	20	100
A487	16390	58	25	0.44	0.1	6.528	1.7	0.3714	1.4	0.79	0.1275	1.1	2036	24	2050	15	2063	19	99
A417	17168	58	25	0.53	0.3	6.539	1.9	0.3698	1.5	0.79	0.1282	1.2	2028	26	2051	17	2074	21	98
A469	14468	51	21	0.29	0.7	6.564	2.3	0.3752	1.8	0.81	0.1269	1.3	2054	32	2055	20	2055	23	100
A397	14251	50	24	0.83	0.3	6.616	2.1	0.3765	1.7	0.78	0.1275	1.3	2060	30	2062	19	2063	24	100
A427	20560	72	32	0.60	0.0	6.639	1.8	0.3762	1.4	0.81	0.1280	1.0	2058	25	2065	16	2071	18	99
A418	10607	39	18	0.69	0.1	6.698	2.0	0.3781	1.5	0.75	0.1285	1.3	2067	26	2072	18	2078	23	100
A044	18832	243	100	0.32	b.d.	6.724	2.1	0.3796	1.7	0.81	0.1285	1.2	2074	30	2076	19	2077	22	100
A428	30304	102	51	0.90	0.1	6.782	1.7	0.3792	1.4	0.82	0.1297	1.0	2072	25	2083	15	2094	17	99
A414	39372	105	57	1.21	0.5	6.784	2.1	0.3811	1.9	0.89	0.1291	1.0	2082	33	2084	19	2086	17	100
A028	16718	90	38	0.45	0.1	6.792	1.9	0.3784	1.5	0.80	0.1302	1.1	2069	27	2085	17	2100	20	98
A392	17363	59	27	0.61	0.4	6.806	1.9	0.3814	1.5	0.77	0.1294	1.2	2083	26	2086	17	2090	21	100
A024	9116	47	22	0.64	0.3	6.859	2.1	0.3828	1.6	0.75	0.1299	1.4	2089	29	2093	19	2097	25	100
A029	49537	262	114	0.52	0.0	6.895	1.6	0.3771	1.4	0.89	0.1326	0.8	2063	26	2098	15	2133	13	97
A016	17011	202	86	0.40	0.1	6.897	1.9	0.3830	1.6	0.85	0.1306	1.0	2090	29	2098	17	2106	17	99
A465	7737	27	12	0.62	0.1	6.917	2.2	0.3848	1.7	0.75	0.1304	1.5	2099	30	2101	20	2103	26	100
A455	15096	50	21	0.24	0.1	6.952	1.9	0.3854	1.4	0.75	0.1308	1.3	2102	26	2105	17	2109	22	100
A460	23695	79	39	0.85	0.2	6.997	1.9	0.3871	1.6	0.85	0.1311	1.0	2109	28	2111	17	2113	17	100
A433	11418	38	19	0.82	0.2	7.030	2.4	0.3862	1.7	0.72	0.1320	1.6	2105	31	2115	21	2125	29	99
A026	16129	85	38	0.51	0.1	7.060	2.1	0.3875	1.6	0.76	0.1322	1.4	2111	28	2119	19	2127	24	99
A020	7502	83	39	0.69	0.0	7.075	2.3	0.3865	1.6	0.72	0.1328	1.6	2106	29	2121	20	2135	28	99
A466	18052	64	27	0.28	0.0	7.161	1.8	0.3919	1.4	0.77	0.1325	1.2	2132	26	2132	16	2132	20	100
A413	100441	347	145	0.26	0.2	7.287	1.8	0.3895	1.6	0.89	0.1357	0.8	2120	28	2147	16	2173	14	98
A456	26277	73	33	0.40	0.0	7.312	1.7	0.3960	1.4	0.82	0.1339	1.0	2151	26	2150	16	2150	17	100
A468	73651	222	88	0.19	0.0	7.407	1.6	0.3755	1.4	0.91	0.1431	0.7	2055	25	2162	14	2265	11	91
A039	80658	621	303	0.30	0.0	9.710	1.6	0.4423	1.4	0.89	0.1592	0.7	2361	28	2408	15	2447	12	96
A475	60444	151	80	0.48	0.1	9.811	1.6	0.4542	1.4	0.90	0.1567	0.7	2414	29	2417	15	2420	12	100
A437	47701	110	55	0.32	0.4	9.936	1.8	0.4390	1.5	0.82	0.1642	1.0	2346	29	2429	17	2499	17	94
A447	136745	277	133	0.09	2.9	10.04	2.1	0.4329	1.4	0.65	0.1682	1.6	2319	27	2439	20	2540	27	91
A006	42543	283	151	0.32	0.3	11.13	1.7	0.4770	1.4	0.83	0.1692	0.9	2514	29	2534	16	2550	16	99
A390	90554	183	98	0.32	0.3	11.56	1.6	0.4765	1.5	0.89	0.1759	0.7	2512	30	2569	15	2615	12	96
A480	39771	81	43	0.25	0.1	11.58	1.6	0.4898	1.4	0.90	0.1714	0.7	2570	31	2571	15	2571	12	100
A424	201358	403	220	0.29	0.1	11.64	1.5	0.4907	1.3	0.90	0.1720	0.7	2574	28	2576	14	2577	11	100
A484	62623	117	65	0.34	0.1	11.84	1.8	0.4906	1.6	0.92	0.1751	0.7	2573	34	2592	17	2607	12	99
A489	72148	137	82	0.55	0.4	11.87	1.7	0.4955	1.6	0.90	0.1737	0.8	2594	34	2594	17	2594	13	100
A454	67973	130	71	0.24	0.0	11.90	1.6	0.4945	1.3	0.84	0.1746	0.9	2590	28	2597	15	2602	14	100
A471	35742	65	41	0.77	0.4	11.90	1.8	0.4883	1.5	0.85	0.1768	0.9	2563	32	2597	17	2623	15	98
A488	183181	355	209	0.46	0.2	12.07	1.8	0.5036	1.7	0.95	0.1739	0.6	2629	36	2610	17	2595	10	101
A450	69448	141	80	0.33	0.0	12.18	1.6	0.5008	1.4	0.90	0.1763	0.7	2617	31	2618	15	2619	11	100
A420	37417	71	39	0.27	0.1	12.19	1.7	0.4923	1.4	0.84	0.1796	0.9	2580	30	2619	16	2649	15	97
A477	21229	41	26	0.73	b.d.	12.24	1.7	0.4994	1.4	0.82	0.1778	1.0	2611	31	2623	16	2633	16	99
A015	43610	255	162	0.74	0.0	12.25	1.5	0.4944	1.4	0.87	0.1797	0.7	2589	29	2624	15	2650	12	98
A399	75462	140	82	0.37	0.1	12.58	1.8	0.5077	1.6	0.92	0.1798	0.7	2647	36	2649	17	2651	12	100
A446	36573	67	47	0.99	0.1	12.78	1.7	0.5104	1.5	0.91	0.1817	0.7	2658	33	2664	16	2668	11	100
A449	53532	98	65	0.79	0.1	12.92	1.7	0.5131	1.5	0.88	0.1827	0.8	2670	32	2674	16	2677	13	100
A423	90102	168	101	0.38	0.1	13.14	1.5	0.5173	1.4	0.90	0.1842	0.7	2688	30	2690	15	2691	11	100
A481	66964	118	69	0.32	0.1	13.14	1.7	0.5167	1.5	0.90	0.1844	0.7	2685	33	2690	16	2693	12	100
A038	59232	334	200	0.38	0.0	13.32	1.7	0.5204	1.5	0.88	0.1856	0.8	2701	33	2702	16	2704	13	100
A411	57565	96	63	0.60	0.1	13.82	1.8	0.5312	1.7	0.93	0.1886	0.7	2746	38	2737	17	2730	11	101
A412	29238	46	30	0.42	0.0	15.81	2.0	0.5628	1.8	0.90	0.2037	0.9	2878	41	2865	19	2856	14	101

Grain	^{207}Pb[a] (cps)	U[b] (ppm)	Pb[b] (ppm)	Th[b] U	^{206}Pbc[c] (%)	^{207}Pb[d] ^{235}U	±2s (%)	^{206}Pb[d] ^{238}U	±2s (%)	ρ[e] (rho)	^{207}Pb[d] ^{206}Pb	±2s (%)	^{206}Pb[f] ^{238}U	±2s (Ma)	^{207}Pb[f] ^{235}U	±2s (Ma)	^{207}Pb[f] ^{206}Pb	±2s (Ma)	Conc.[g] (%)
A409	85501	123	88	0.65	0.1	16.58	1.8	0.5700	1.6	0.90	0.2109	0.8	2908	38	2911	17	2912	13	100
A014	40795	183	136	0.72	0.1	17.35	1.7	0.5752	1.5	0.91	0.2188	0.7	2929	36	2955	16	2972	11	99
A429	51779	64	47	0.43	0.2	18.88	1.6	0.6026	1.5	0.92	0.2273	0.6	3040	37	3036	16	3033	10	100
A402	*120*	*3*	*0*	*0.53*	*0.2*	*0.9426*	*16.8*	*0.08735*	*5.2*	*0.31*	*0.07826*	*15.9*	*540*	*27*	*674*	*86*	*1154*	*316*	*47*
A438	*22949*	*92*	*29*	*0.17*	*0.3*	*5.076*	*1.8*	*0.3057*	*1.4*	*0.78*	*0.1204*	*1.1*	*1719*	*21*	*1832*	*15*	*1963*	*20*	*88*
A042	*110366*	*1215*	*374*	*0*	*0.2*	*5.348*	*1.7*	*0.3134*	*1.5*	*0.9*	*0.1237*	*0.7*	*1758*	*24*	*1877*	*14*	*2011*	*12*	*87*
91500[h]	8378	74	13	0.29	0.5	1.850	1.8	0.1795	1.4	0.54	0.07477	0.9	1064	14	1063	12	1062	18	100
Felix[h]	12482	435	68	2.47	0.2	0.6484	3.0	0.08211	3.0	0.43	0.05728	3.0	509	15	507	12	502	65	102
Plesovice[h]	2852	651	34	0.09	1.3	0.3989	4.1	0.05419	2.2	0.48	0.05339	2.9	340	7	341	12	345	64	99

$^{206}Pb/^{238}U$ error is the quadratic additions of the within run precision (2 SE) and the external reproducibility (2 SD) of the reference zircon. $^{207}Pb/^{206}Pb$ error propagation (^{207}Pb signal dependent) following Gerdes & Zeh (2009). $^{207}Pb/^{235}U$ error is the quadratic addition of the $^{207}Pb/^{206}Pb$ and $^{206}Pb/^{238}U$ uncertainty.

[a] Within run background-corrected mean ^{207}Pb signal in cps (counts per second).

[b] U and Pb content and Th/U ratio were calculated relative to GJ-1 reference zircon.

[c] Percentage of the common Pb on the ^{206}Pb. b.d. = below detection limit.

[d] Pb/U and Pb/Pb ratios. Corrected for background, within-run Pb/U fractionation (in case of $^{206}Pb/^{238}U$) and common Pb using Stacy and Kramers (1975) model Pb composition and subsequently normalised to GJ-1 (ID-TIMS value/measured value); $^{207}Pb/^{235}U$ calculated using (($^{207}Pb/^{206}Pb$)*($^{238}U/^{206}Pb$)*137.88).

[e] Rho (ρ) is the ($^{206}Pb/^{238}U$)/($^{207}Pb/^{235}U$) error correlation coefficient.

[f] Pb/U and Pb/Pb ages.

[g] Degree of concordance = (($^{206}Pb/^{238}U$ age)/($^{207}Pb/^{206}Pb$ age)) x 100.

Table 4
U, Th and Pb LA-ICP-MS data of zircon cores from sample GCH-10

Grain	^{207}Pb[a] (cps)	U[b] (ppm)	Pb[b] (ppm)	Th[b]/U	^{206}Pb[c] (%)	$^{207}Pb/^{235}U$[d]	±2s (%)	$^{206}Pb/^{238}U$[d]	±2s (%)	ρ[e] (rho)	$^{207}Pb/^{206}Pb$[d]	±2s (%)	$^{206}Pb/^{238}U$[f]	±2s (Ma)	$^{207}Pb/^{235}U$[f]	±2s (Ma)	$^{207}Pb/^{206}Pb$[f]	±2s (Ma)	Conc.[g] (%)
A253	1521	75	7	0.96	b.d.	0.6307	3.8	0.07889	1.4	0.38	0.05798	3.5	490	7	497	15	529	78	93
A302	21871	1714	146	0.45	2.4	0.6419	4.5	0.08068	1.5	0.33	0.05770	4.2	500	7	503	18	518	92	97
A268	3448	177	16	0.88	0.0	0.6401	2.4	0.08106	1.2	0.50	0.05727	2.1	502	6	502	10	502	46	100
A345	2465	223	20	0.69	0.4	0.6500	6.8	0.08170	1.6	0.24	0.05770	6.6	506	8	509	28	518	146	98
A306	2046	96	9	1.05	0.0	0.6604	2.9	0.08314	1.3	0.46	0.05761	2.6	515	7	515	12	515	57	100
A252	1742	83	8	1.37	2.1	0.6681	4.3	0.08400	1.5	0.35	0.05769	4.1	520	8	520	18	518	89	100
A334	3631	337	33	1.09	0.0	0.6874	2.3	0.08403	1.4	0.60	0.05933	1.8	520	7	531	10	579	40	90
A299	4940	159	16	0.92	2.8	0.6745	9.4	0.08443	2.0	0.21	0.05794	9.2	523	10	523	39	527	202	99
A261	5245	233	23	1.13	0.0	0.6838	2.2	0.08485	1.6	0.73	0.05845	1.5	525	8	529	9	547	33	96
A325	4284	420	40	0.92	0.0	0.6812	2.7	0.08486	1.4	0.51	0.05822	2.4	525	7	527	11	538	52	98
A217	6283	601	54	0.57	0.7	0.6816	4.4	0.08525	1.4	0.32	0.05798	4.2	527	7	528	18	529	92	100
A271	5880	289	27	0.89	0.0	0.6866	2.4	0.08532	1.2	0.49	0.05836	2.1	528	6	531	10	543	46	97
A321	6405	294	26	0.53	0.4	0.7032	1.9	0.08574	1.3	0.67	0.05949	1.4	530	6	541	8	585	30	91
A254	4044	199	19	0.78	0.0	0.7027	3.0	0.08579	1.4	0.48	0.05940	2.6	531	7	540	13	582	57	91
A170	6945	357	33	0.69	0.0	0.6921	2.7	0.08658	1.6	0.60	0.05797	2.2	535	8	534	11	529	47	101
A200	3132	153	14	0	b.d.	0.7073	2.8	0.08690	1.4	0.5	0.05904	2.4	537	7	543	12	568	52	95
A311	9759	452	46	1.19	0.0	0.7069	2.0	0.08691	1.2	0.60	0.05899	1.6	537	6	543	9	567	35	95
A304	7795	369	34	0.71	0.0	0.7070	2.1	0.08695	1.3	0.61	0.05897	1.7	537	7	543	9	566	37	95
A303	4098	361	35	0.90	0.2	0.7068	2.9	0.08718	1.3	0.44	0.05881	2.6	539	7	543	12	560	58	96
A266	1314	125	13	1.26	b.d.	0.6980	4.5	0.08732	1.5	0.33	0.05798	4.3	540	8	538	19	529	94	102
A173	1250	63	6	1.15	b.d.	0.7119	4.0	0.08765	1.6	0.41	0.05891	3.6	542	8	546	17	564	79	96
A309	2711	267	27	1.11	b.d.	0.7065	3.1	0.08780	1.3	0.42	0.05836	2.9	542	7	543	13	543	62	100
A315	429	21	2	1.32	0.0	0.7064	7.4	0.08788	1.8	0.24	0.05830	7.2	543	9	543	32	541	158	100
A295	2792	269	25	0.66	b.d.	0.7139	2.8	0.08798	1.3	0.46	0.05885	2.5	544	7	547	12	561	54	97
A337	10318	871	78	0.40	1.1	0.7115	4.1	0.08803	1.6	0.39	0.05862	3.8	544	8	546	17	553	82	98
A202	16001	785	77	0.93	0.0	0.7118	1.9	0.08833	1.3	0.66	0.05844	1.5	546	7	546	8	546	32	100
A203	1214	61	6	1.02	0.0	0.7152	3.6	0.08847	1.4	0.40	0.05863	3.3	546	8	548	15	553	71	99
A278	3359	335	32	0.73	0.0	0.7170	2.6	0.08881	1.3	0.52	0.05856	2.2	548	7	549	11	551	48	100
A344	23309	1826	170	0.63	0.0	0.7173	1.8	0.08908	1.4	0.78	0.05840	1.1	550	7	549	8	545	24	101
A313	6517	212	22	0.74	8.4	0.7231	10.8	0.08928	1.8	0.16	0.05874	10.6	551	9	552	47	557	231	99
A179	576	59	6	0.85	0.0	0.7350	5.6	0.08953	2.2	0.39	0.05954	5.1	553	11	559	24	587	111	94
A307	2853	135	13	0.66	0.4	0.7316	3.3	0.08965	1.6	0.47	0.05919	2.9	553	8	557	14	574	64	96
A190	1306	64	7	1.20	b.d.	0.7415	4.0	0.08969	1.6	0.40	0.05997	3.6	554	8	563	17	602	79	92
A212	3565	182	18	0.75	b.d.	0.7364	2.8	0.08999	1.4	0.50	0.05935	2.4	556	7	560	12	580	53	96
A244	7346	687	62	0.39	b.d.	0.7377	2.4	0.09040	1.4	0.57	0.05918	2.0	558	7	561	10	574	43	97
A230	4074	82	8	0.95	0.0	0.7426	2.5	0.09052	1.2	0.48	0.05950	2.2	559	7	564	11	586	48	95
A251	4106	191	20	1.10	0.0	0.7369	2.7	0.09079	1.3	0.48	0.05887	2.4	560	7	561	12	562	52	100
A301	11254	490	46	0.45	0.0	0.7448	2.0	0.09153	1.5	0.74	0.05902	1.4	565	8	565	9	568	30	99
A204	5909	263	28	1.09	0.0	0.7547	2.3	0.09186	1.3	0.54	0.05959	2.0	567	7	571	10	589	42	96
A310	7103	324	30	0.43	0.0	0.7551	2.1	0.09202	1.2	0.57	0.05951	1.7	567	6	571	9	586	37	97
A249	4287	186	18	0.60	b.d.	0.7662	2.7	0.09274	1.5	0.54	0.05993	2.3	572	8	578	12	601	50	95
A178	3592	164	16	0.64	b.d.	0.7683	3.1	0.09307	1.3	0.44	0.05987	2.8	574	7	579	14	599	60	96
A234	8827	399	42	0.98	0.0	0.7600	2.1	0.09361	1.4	0.67	0.05888	1.5	577	8	574	9	563	33	102
A312	20387	1131	128	0.93	3.6	0.7839	4.8	0.09552	1.6	0.33	0.05952	4.5	588	9	588	22	586	98	100
A267	14400	572	64	1.18	0.0	0.7957	1.8	0.09574	1.2	0.70	0.06027	1.3	589	7	594	8	613	27	96
A314	7464	289	32	1.00	0.0	0.8304	2.1	0.09944	1.3	0.60	0.06057	1.7	611	8	614	10	624	37	98
A290	11604	430	67	2.66	0.0	0.9004	1.9	0.1050	1.2	0.64	0.06217	1.5	644	8	652	9	680	32	95
A318	4868	170	22	1.27	0.0	0.9217	2.3	0.1084	1.3	0.56	0.06169	1.9	663	8	663	11	663	41	100
A227	13847	243	30	0.94	0.0	0.9534	1.7	0.1096	1.2	0.73	0.06312	1.2	670	8	680	8	712	25	94
A327	1750	59	9	1.95	0.0	1.019	3.4	0.1152	1.3	0.40	0.06414	3.1	703	9	713	18	746	66	94
A199	4852	319	52	1.92	0.0	1.079	2.6	0.1217	1.4	0.52	0.06428	2.3	740	10	743	14	751	48	99
A276	6480	438	55	0.50	0.3	1.090	2.3	0.1218	1.4	0.59	0.06490	1.9	741	10	749	12	771	39	96
A211	22935	176	34	0.49	0.3	1.941	1.8	0.1844	1.3	0.73	0.07637	1.2	1091	13	1095	12	1105	25	99
A235	6794	110	23	0.70	b.d.	2.028	2.4	0.1904	1.3	0.54	0.07727	2.0	1123	13	1125	16	1128	39	100
A270	8217	262	54	0.51	b.d.	2.162	2.0	0.1987	1.3	0.63	0.07891	1.6	1168	14	1169	14	1170	31	100
A260	38343	563	115	0.32	0.0	2.260	1.6	0.2044	1.2	0.78	0.08023	1.0	1199	13	1200	11	1203	19	100
A243	17808	446	107	0.52	0.0	2.763	1.7	0.2252	1.3	0.77	0.08897	1.1	1309	15	1346	12	1403	20	93
A339	23819	259	68	0.86	0.1	2.936	1.6	0.2330	1.3	0.81	0.09139	1.0	1350	16	1391	12	1455	18	93
A288	6844	143	41	0.66	0.0	3.424	2.2	0.2636	1.4	0.63	0.09419	1.7	1508	18	1510	17	1512	32	100
A296	5062	16	7	0.79	13.8	4.163	11.0	0.2913	3.0	0.28	0.1037	10.6	1648	44	1667	94	1691	195	97
A323	14298	222	76	0.86	0.0	4.491	1.8	0.3044	1.2	0.68	0.1070	1.3	1713	19	1729	15	1749	24	98

Grain	^{207}Pb[a] (cps)	U[b] (ppm)	Pb[b] (ppm)	Th[b] U	^{206}Pbc[c] (%)	^{207}Pb[d] ^{235}U	±2s (%)	^{206}Pb[d] ^{238}U	±2s (%)	ρ[e] (rho)	^{207}Pb[d] ^{206}Pb	±2s (%)	^{206}Pb[f] ^{238}U	±2s (Ma)	^{207}Pb[f] ^{235}U	±2s (Ma)	^{207}Pb[f] ^{206}Pb	±2s (Ma)	Conc.[g] (%)
A224	4477	33	13	1.47	0.0	4.689	2.8	0.3130	1.6	0.56	0.1087	2.3	1755	24	1765	24	1777	42	99
A291	16811	215	80	0.65	0.0	5.558	1.8	0.3403	1.3	0.71	0.1184	1.2	1888	21	1910	15	1933	22	98
A297	19398	105	42	1.15	0.2	5.779	2.0	0.3318	1.5	0.72	0.1263	1.4	1847	24	1943	18	2047	25	90
A167	54040	316	122	0.72	0.0	5.894	1.6	0.3417	1.3	0.84	0.1251	0.8	1895	22	1960	14	2030	15	93
A189	6520	30	14	1.50	b.d.	6.038	2.5	0.3540	1.8	0.71	0.1237	1.8	1954	30	1981	22	2010	31	97
A247	22662	243	97	0.67	0.6	6.134	2.7	0.3540	1.5	0.57	0.1257	2.2	1954	26	1995	23	2038	38	96
A255	58333	330	117	0.15	b.d.	6.156	1.5	0.3562	1.2	0.84	0.1253	0.8	1964	21	1998	13	2034	14	97
A322	21012	110	46	0.99	0.0	6.167	1.6	0.3601	1.3	0.79	0.1242	1.0	1983	22	2000	14	2018	18	98
A265	24111	251	107	1.20	0.0	6.212	1.6	0.3426	1.3	0.79	0.1315	1.0	1899	21	2006	14	2118	17	90
A187	51009	597	232	0.52	0.0	6.216	1.4	0.3594	1.2	0.82	0.1254	0.8	1980	20	2007	13	2035	14	97
A256	9838	52	23	1.18	1.5	6.226	2.5	0.3624	1.4	0.54	0.1246	2.1	1994	23	2008	22	2023	38	99
A166	9073	50	20	0.78	b.d.	6.232	2.1	0.3570	1.4	0.64	0.1266	1.6	1968	23	2009	19	2051	29	96
A191	32824	386	165	1.01	0.0	6.244	1.7	0.3624	1.3	0.77	0.1250	1.1	1994	23	2011	15	2028	19	98
A174	25690	146	69	1.66	0.0	6.251	1.7	0.3573	1.3	0.79	0.1269	1.0	1970	22	2012	15	2055	18	96
A246	46443	515	234	1.43	0.0	6.277	1.5	0.3670	1.2	0.80	0.1240	0.9	2015	21	2015	14	2015	17	100
A169	43086	239	90	0.21	b.d.	6.297	2.0	0.3695	1.7	0.87	0.1236	1.0	2027	30	2018	17	2009	17	101
A317	35705	165	76	1.68	0.4	6.313	1.9	0.3669	1.6	0.85	0.1248	1.0	2015	27	2020	16	2026	17	99
A231	10479	122	57	1.47	0.0	6.382	1.9	0.3670	1.3	0.65	0.1261	1.5	2015	22	2030	17	2045	26	99
A207	27852	310	128	0.83	0.3	6.390	1.7	0.3635	1.4	0.80	0.1275	1.0	1999	24	2031	15	2064	18	97
A316	6651	36	16	1.27	0.0	6.426	2.3	0.3674	1.3	0.57	0.1269	1.9	2017	22	2036	20	2055	33	98
A281	24456	253	107	0.86	0.3	6.428	1.7	0.3688	1.2	0.71	0.1264	1.2	2024	21	2036	15	2049	21	99
A205	24020	134	56	0.84	0.0	6.463	1.8	0.3676	1.3	0.71	0.1275	1.2	2018	22	2041	16	2064	22	98
A326	9966	52	25	1.68	0.4	6.511	2.5	0.3733	1.3	0.51	0.1265	2.2	2045	23	2047	23	2050	39	100
A168	8186	44	19	1.04	b.d.	6.517	2.3	0.3691	1.3	0.56	0.1281	1.9	2025	23	2048	20	2072	33	98
A282	15710	165	72	0.88	0.0	6.556	1.8	0.3740	1.3	0.74	0.1271	1.2	2048	23	2053	16	2059	21	99
A209	30385	168	69	0.76	0.0	6.558	1.6	0.3606	1.2	0.77	0.1319	1.0	1985	20	2054	14	2123	18	93
A192	7435	82	37	1.32	0.0	6.588	2.2	0.3654	1.5	0.68	0.1308	1.6	2008	26	2058	20	2109	29	95
A182	6713	38	16	0.91	0.0	6.599	2.2	0.3722	1.4	0.65	0.1286	1.7	2040	25	2059	19	2079	29	98
A275	14429	75	34	1.21	0.0	6.611	2.1	0.3647	1.2	0.57	0.1315	1.7	2004	21	2061	19	2118	30	95
A335	7684	81	35	0.92	0.0	6.613	2.1	0.3766	1.7	0.81	0.1273	1.2	2061	30	2061	18	2062	21	100
A245	9736	100	45	1.10	0.0	6.617	2.2	0.3702	1.5	0.69	0.1296	1.6	2030	27	2062	20	2093	29	97
A341	8955	45	19	0.78	0.0	6.620	1.9	0.3696	1.3	0.68	0.1299	1.4	2027	22	2062	17	2097	24	97
A208	8955	48	19	0.57	b.d.	6.639	2.4	0.3699	1.3	0.55	0.1302	2.0	2029	23	2065	21	2100	35	97
A223	2761	15	6	0.92	0.0	6.642	3.8	0.3658	1.6	0.42	0.1317	3.4	2010	27	2065	34	2121	60	95
A289	4023	21	9	0.92	0.0	6.647	2.7	0.3765	1.6	0.59	0.1281	2.2	2060	28	2066	24	2071	38	99
A273	9825	105	50	1.52	0.0	6.661	1.9	0.3778	1.4	0.73	0.1279	1.3	2066	25	2067	17	2069	24	100
A186	9981	109	50	1.18	0.0	6.679	2.1	0.3747	1.5	0.75	0.1293	1.4	2051	27	2070	18	2088	24	98
A262	32363	350	179	2.02	0.0	6.683	1.7	0.3716	1.3	0.75	0.1304	1.1	2037	22	2070	15	2104	19	97
A342	28468	281	133	1.42	0.0	6.688	1.5	0.3755	1.2	0.79	0.1292	0.9	2055	21	2071	13	2087	16	98
A229	22815	114	50	1.03	0.0	6.693	1.7	0.3722	1.4	0.79	0.1304	1.0	2040	24	2072	15	2103	18	97
A219	13619	33	14	0.99	b.d.	6.709	2.0	0.3730	1.3	0.68	0.1305	1.5	2043	24	2074	18	2104	26	97
A338	20982	205	86	0.73	0.3	6.709	1.6	0.3736	1.3	0.81	0.1302	0.9	2046	23	2074	14	2101	17	97
A343	105551	1062	415	0.31	0.1	6.714	1.5	0.3783	1.3	0.87	0.1287	0.7	2068	23	2074	13	2081	13	99
A250	34790	342	153	1.03	0.2	6.729	1.8	0.3776	1.3	0.71	0.1293	1.3	2065	23	2077	16	2088	22	99
A220	18386	97	46	1.36	0.0	6.740	1.5	0.3786	1.3	0.84	0.1291	0.8	2070	23	2078	14	2086	15	99
A333	43948	226	101	1.07	0.0	6.769	1.8	0.3809	1.6	0.88	0.1289	0.9	2081	28	2082	16	2083	15	100
A206	17710	91	40	0.94	0.0	6.844	2.0	0.3801	1.5	0.73	0.1306	1.4	2077	26	2091	18	2106	24	99
A171	10015	53	24	1.02	0.0	6.853	2.2	0.3756	1.5	0.67	0.1323	1.6	2056	26	2093	20	2129	29	97
A183	4908	26	11	0.88	0.0	6.854	2.2	0.3821	1.4	0.64	0.1301	1.7	2086	25	2093	19	2099	29	99
A300	15449	79	35	0.97	0.0	6.860	1.7	0.3832	1.2	0.73	0.1298	1.1	2091	22	2093	15	2096	20	100
A277	23561	220	105	1.36	0.0	6.870	1.7	0.3802	1.3	0.81	0.1310	1.0	2077	24	2095	15	2112	17	98
A185	2947	15	7	0.65	b.d.	6.875	3.0	0.3917	1.7	0.57	0.1273	2.5	2131	31	2095	27	2061	43	103
A263	10664	105	45	0.77	b.d.	6.887	2.0	0.3786	1.3	0.68	0.1319	1.4	2070	24	2097	18	2124	25	97
A259	14485	145	61	0.65	0.0	6.889	2.1	0.3839	1.5	0.71	0.1302	1.5	2094	26	2097	19	2100	26	100
A210	10469	52	23	0.82	0.0	6.893	1.9	0.3789	1.3	0.67	0.1319	1.4	2071	23	2098	17	2124	25	98
A177	11994	128	56	0.96	0.0	6.895	2.0	0.3779	1.4	0.67	0.1323	1.5	2067	24	2098	18	2129	26	97
A176	5254	28	13	1.07	0.0	6.897	2.0	0.3816	1.4	0.70	0.1311	1.4	2084	25	2098	18	2112	25	99
A257	7279	77	35	1.04	0.0	6.905	2.1	0.3858	1.4	0.68	0.1298	1.5	2104	25	2099	18	2095	27	100
A226	6431	66	31	1.13	b.d.	6.911	2.1	0.3847	1.3	0.62	0.1303	1.6	2098	23	2100	19	2102	28	100
A248	14330	71	34	1.33	0.0	6.948	1.9	0.3844	1.2	0.62	0.1311	1.5	2097	21	2105	17	2113	26	99
A233	55041	268	114	0.53	0.0	6.963	1.7	0.3899	1.5	0.87	0.1295	0.8	2122	27	2107	15	2091	15	101
A298	15444	75	36	1.31	0.0	6.975	1.6	0.3859	1.2	0.76	0.1311	1.0	2104	22	2108	14	2112	18	100
A319	45770	218	99	1.00	0.0	7.000	1.4	0.3855	1.2	0.87	0.1317	0.7	2102	22	2111	13	2121	12	99
A320	31393	142	61	0.69	0.0	7.042	1.6	0.3797	1.2	0.76	0.1345	1.0	2075	22	2117	14	2158	18	96

Grain	^{207}Pb[a] (cps)	U[b] (ppm)	Pb[b] (ppm)	Th[b] U	^{206}Pbc[c] (%)	^{207}Pb[d] / ^{235}U	±2s (%)	^{206}Pb[d] / ^{238}U	±2s (%)	ρ[e] (rho)	^{207}Pb[d] / ^{206}Pb	±2s (%)	^{206}Pb[f] / ^{238}U	±2s (Ma)	^{207}Pb[f] / ^{235}U	±2s (Ma)	^{207}Pb[f] / ^{206}Pb	±2s (Ma)	Conc.[g] (%)
A236	3214	34	17	1.33	0.0	7.042	2.9	0.3880	1.6	0.54	0.1316	2.4	2114	28	2117	26	2120	43	100
A193	1897	19	9	0.90	0.0	7.655	3.6	0.4067	1.8	0.49	0.1365	3.1	2200	33	2191	33	2183	55	101
A292	105175	366	168	0.34	0.0	9.325	1.4	0.4313	1.2	0.87	0.1568	0.7	2312	24	2370	13	2421	12	95
A228	55937	197	96	0.64	0.0	9.500	1.6	0.4314	1.2	0.76	0.1597	1.1	2312	24	2388	15	2453	18	94
A279	251212	1666	810	0.42	0.1	9.928	1.3	0.4470	1.2	0.88	0.1611	0.6	2382	23	2428	12	2467	10	97
A264	111713	377	187	0.42	0.0	10.46	1.5	0.4556	1.2	0.81	0.1666	0.9	2420	25	2477	14	2523	15	96
A165	205875	697	355	0.36	0.0	10.64	1.6	0.4731	1.5	0.92	0.1631	0.6	2497	30	2492	15	2488	11	100
A225	25038	83	49	1.38	0.0	10.72	1.8	0.4597	1.3	0.71	0.1691	1.3	2438	26	2499	17	2548	22	96
A308	66606	204	104	0.47	0.1	10.80	1.4	0.4596	1.2	0.87	0.1705	0.7	2438	24	2506	13	2562	11	95
A237	153709	961	463	0.25	0.0	10.82	1.6	0.4496	1.4	0.90	0.1745	0.7	2394	28	2507	15	2601	11	92
A305	71392	211	109	0.60	0.1	10.88	1.4	0.4545	1.2	0.86	0.1736	0.7	2415	25	2513	13	2593	12	93
A340	94306	277	158	1.09	b.d.	11.11	1.5	0.4665	1.3	0.85	0.1728	0.8	2468	27	2533	14	2585	13	95
A201	82807	267	136	0.15	b.d.	11.53	1.8	0.4903	1.3	0.73	0.1706	1.2	2572	28	2567	17	2564	20	100
A258	62218	377	200	0.60	0.0	11.60	1.4	0.4665	1.2	0.85	0.1804	0.7	2468	25	2573	13	2656	12	93
A222	88144	263	144	0.59	0.0	11.68	1.5	0.4863	1.2	0.83	0.1743	0.8	2555	26	2579	14	2599	14	98
A181	48186	298	160	0.49	0.0	11.73	1.6	0.4789	1.3	0.83	0.1777	0.9	2522	28	2583	15	2631	15	96
A184	30719	84	60	1.79	0.0	13.45	1.7	0.5284	1.4	0.83	0.1846	0.9	2735	31	2712	16	2694	15	102
A280	76591	366	248	1.27	b.d.	14.05	1.5	0.5326	1.3	0.90	0.1914	0.6	2753	29	2753	14	2754	11	100
A213	65275	145	95	0.69	0.0	16.61	1.6	0.5566	1.3	0.84	0.2165	0.9	2852	31	2913	16	2955	14	97
A274	*1451*	*140*	*13*	*0.58*	*b.d.*	*0.7658*	*3.1*	*0.08760*	*1.4*	*0.46*	*0.06340*	*2.8*	*541*	*8*	*577*	*14*	*722*	*59*	*75*
A293	*1208*	*49*	*8*	*3.50*	*0.0*	*0.8266*	*4.7*	*0.09498*	*1.5*	*0.32*	*0.06312*	*4.5*	*585*	*8*	*612*	*22*	*712*	*95*	*82*
A269	*51083*	*252*	*86*	*0.70*	*31.4*	*0.9346*	*8.3*	*0.1052*	*3.5*	*0.43*	*0.06445*	*7.5*	*645*	*22*	*670*	*42*	*756*	*159*	*85*
A294	*257*	*6*	*1*	*0.18*	*3.1*	*0.7704*	*16.4*	*0.1642*	*3.0*	*0.18*	*0.03403*	*16.1*	*980*	*27*	*580*	*75*	*-788*	*457*	*-124*
A175	*60325*	*523*	*150*	*0.88*	*b.d.*	*4.050*	*1.9*	*0.2550*	*1.5*	*0.83*	*0.1152*	*1.0*	*1464*	*20*	*1644*	*15*	*1883*	*19*	*78*
A272	*24707*	*162*	*54*	*0.65*	*0.0*	*5.133*	*1.7*	*0.2982*	*1.3*	*0.77*	*0.1248*	*1.1*	*1683*	*19*	*1842*	*15*	*2026*	*19*	*83*
A180	*30835*	*353*	*241*	*1.43*	*1.0*	*5.150*	*5.8*	*0.7185*	*4.2*	*0.72*	*0.0520*	*4.0*	*3490*	*113*	*1844*	*50*	*285*	*91*	*1226*
A324	*64275*	*624*	*222*	*0.73*	*0.2*	*6.482*	*1.8*	*0.3011*	*1.3*	*0.73*	*0.1561*	*1.2*	*1697*	*19*	*2043*	*16*	*2414*	*21*	*70*
A188	*152087*	*505*	*242*	*0.94*	*0.4*	*9.748*	*1.9*	*0.3994*	*1.7*	*0.92*	*0.1770*	*0.8*	*2166*	*32*	*2411*	*18*	*2625*	*13*	*83*
A221	*37253*	*119*	*56*	*0.58*	*0.0*	*9.865*	*1.6*	*0.4045*	*1.4*	*0.85*	*0.1769*	*0.9*	*2190*	*26*	*2422*	*15*	*2624*	*15*	*83*
91500[h]	8532	69	13	0.45	0.3	1.853	3.8	0.1791	2.4	0.61	0.07503	3.1	1062	23	1064	25	1069	63	99
Felix[h]	4019	203	23	1.93	0.4	0.6208	6.4	0.08063	3.9	0.48	0.05583	3.4	500	19	490	25	445	75	113
Plesovice[h]	2881	1038	54	0.16	0.2	0.4045	3.8	0.05489	3.8	0.53	0.05345	1.6	344	13	345	11	348	35	99

$^{206}Pb/^{238}U$ error is the quadratic additions of the within run precision (2 SE) and the external reproducibility (2 SD) of the reference zircon. $^{207}Pb/^{206}Pb$ error propagation (^{207}Pb signal dependent) following Gerdes & Zeh (2009). $^{207}Pb/^{235}U$ error is the quadratic addition of the $^{207}Pb/^{206}Pb$ and $^{206}Pb/^{238}U$ uncertainty.

[a] Within run background-corrected mean ^{207}Pb signal in cps (counts per second).

[b] U and Pb content and Th/U ratio were calculated relative to GJ-1 reference zircon.

[c] Percentage of the common Pb on the ^{206}Pb. b.d. = below detection limit.

[d] Pb/U and Pb/Pb ratios. Corrected for background, within-run Pb/U fractionation (in case of $^{206}Pb/^{238}U$) and common Pb using Stacy and Kramers (1975) model Pb composition and subsequently normalised to GJ-1 (ID-TIMS value/measured value); $^{207}Pb/^{235}U$ calculated using (($^{207}Pb/^{206}Pb$)*($^{238}U/^{206}Pb$)*137.88).

[e] Rho (ρ) is the ($^{206}Pb/^{238}U$)/($^{207}Pb/^{235}U$) error correlation coefficient.

[f] Pb/U and Pb/Pb ages.

[g] Degree of concordance = (($^{206}Pb/^{238}U$ age)/($^{207}Pb/^{206}Pb$ age)) x 100.

[h] Mean of 13 (91500), 13 (Felix), 9 (Plesovice), and 23 (GJ-1) analyses, respectively.

Table 5
U, Th and Pb LA-ICP-MS data of zircon cores from sample GCH-11

Grain	^{207}Pb[a] (cps)	U[b] (ppm)	Pb[b] (ppm)	Th/U[b]	$^{206}Pb_c$[c] (%)	$^{207}Pb/^{235}U$[d]	±2s (%)	$^{206}Pb/^{238}U$[d]	±2s (%)	ρ[e] (rho)	$^{207}Pb/^{206}Pb$[d]	±2s (%)	$^{206}Pb/^{238}U$[f]	±2s (Ma)	$^{207}Pb/^{235}U$[f]	±2s (Ma)	$^{207}Pb/^{206}Pb$[f]	±2s (Ma)	Conc.[g] (%)
A415	1260	52	5	1.24	0.0	0.6423	4.1	0.07993	1.0	0.24	0.05828	4.0	496	5	504	17	540	88	92
A526	3895	187	17	0.92	0.0	0.6426	2.2	0.08114	0.9	0.39	0.05744	2.1	503	4	504	9	508	45	99
A503	2266	45	4	1.07	0.0	0.6570	3.7	0.08127	1.0	0.25	0.05863	3.6	504	5	513	15	553	79	91
A369	1427	67	6	0.88	0.1	0.6496	4.1	0.08138	0.9	0.22	0.05790	4.0	504	4	508	17	526	89	96
A397	2807	134	11	0.59	b.d.	0.6510	2.7	0.08142	1.0	0.38	0.05799	2.5	505	5	509	11	529	56	95
A374	666	31	3	0.92	0.2	0.6465	4.7	0.08142	1.6	0.34	0.05759	4.4	505	8	506	19	514	98	98
A499	1534	72	7	1.04	b.d.	0.6502	3.8	0.08155	1.3	0.35	0.05783	3.5	505	6	509	15	523	78	97
A416	1554	32	3	1.33	b.d.	0.6635	3.9	0.08214	1.0	0.26	0.05858	3.8	509	5	517	16	552	82	92
A419	8168	377	32	0.55	0.0	0.6618	1.6	0.08228	1.0	0.61	0.05833	1.3	510	5	516	6	542	27	94
A515	3307	143	12	0.56	0.6	0.6617	3.1	0.08297	1.0	0.33	0.05785	2.9	514	5	516	12	524	63	98
A508	5063	158	15	0.80	4.7	0.6668	6.2	0.08343	1.1	0.18	0.05796	6.1	517	6	519	25	528	133	98
A394	1506	68	6	0.92	b.d.	0.6681	3.2	0.08375	1.1	0.35	0.05785	3.0	518	6	520	13	524	65	99
A450	3982	161	15	0.86	0.2	0.6763	2.1	0.08377	0.7	0.36	0.05855	2.0	519	4	525	9	550	43	94
A525	2395	106	9	0.44	0.2	0.6708	2.5	0.08424	0.9	0.36	0.05775	2.4	521	5	521	10	520	52	100
A513	3080	122	12	0.86	0.7	0.6881	3.5	0.08467	1.1	0.31	0.05894	3.3	524	5	532	14	565	71	93
A523	10864	468	44	0.84	0.2	0.6853	1.9	0.08479	0.9	0.49	0.05862	1.7	525	5	530	8	553	36	95
A517	2605	118	11	0.89	0.2	0.6785	3.3	0.08493	1.2	0.37	0.05794	3.1	525	6	526	14	528	67	100
A396	1258	59	5	0.54	0.0	0.6805	3.1	0.08511	1.1	0.36	0.05799	2.9	527	6	527	13	529	64	100
A413	6862	310	26	0.30	0.0	0.6836	2.2	0.08537	0.9	0.42	0.05808	2.0	528	5	529	9	533	44	99
A372	4178	187	18	0.94	0.1	0.6908	2.6	0.08552	0.8	0.33	0.05859	2.4	529	4	533	11	552	53	96
A391	4766	218	19	0.52	b.d.	0.6981	2.0	0.08595	0.7	0.36	0.05891	1.9	532	4	538	9	564	41	94
A392	3043	142	13	0.75	b.d.	0.7105	2.3	0.08632	0.8	0.37	0.05970	2.1	534	4	545	10	593	46	90
A382	1105	51	5	0.90	b.d.	0.6987	3.4	0.08654	1.4	0.41	0.05856	3.1	535	7	538	14	551	69	97
A490	2350	101	10	0.72	0.1	0.7021	2.5	0.08688	0.8	0.32	0.05861	2.3	537	4	540	10	553	51	97
A493	1499	70	8	1.44	b.d.	0.7109	3.7	0.08733	1.3	0.35	0.05904	3.4	540	7	545	16	569	75	95
A535	5563	240	22	0.59	0.1	0.7063	2.0	0.08737	0.8	0.41	0.05863	1.8	540	4	543	8	553	39	98
A432	3224	137	13	0.75	0.0	0.7044	2.8	0.08747	0.9	0.34	0.05841	2.6	541	5	541	12	545	57	99
A480	19257	824	68	0.08	0.3	0.7130	1.5	0.08750	0.7	0.45	0.05910	1.3	541	3	547	6	571	29	95
A559	4399	182	18	0.78	0.1	0.7273	2.8	0.08845	1.0	0.34	0.05963	2.6	546	5	555	12	590	56	93
A519	2155	89	10	1.33	0.1	0.7173	2.7	0.08916	1.2	0.45	0.05835	2.4	551	6	549	12	543	53	101
A505	3460	143	16	1.32	0.5	0.7376	2.3	0.08983	0.8	0.34	0.05955	2.2	555	4	561	10	587	47	94
A542	4631	410	41	0.84	0.4	0.7367	2.0	0.09007	0.8	0.42	0.05932	1.8	556	4	560	9	579	40	96
A412	6617	282	32	1.48	0.0	0.7369	2.2	0.09034	1.1	0.48	0.05916	1.9	558	6	561	10	573	42	97
A483	1210	49	6	1.97	b.d.	0.7488	3.4	0.09052	1.2	0.37	0.06000	3.1	559	7	568	15	603	68	93
A404	1594	71	7	1	b.d.	0.7375	3.4	0.09069	0.9	0.3	0.05898	3.3	560	5	561	15	566	72	99
A488	6103	238	25	0.91	0.4	0.7483	2.0	0.09116	0.9	0.43	0.05954	1.8	562	5	567	9	587	40	96
A510	7535	280	30	0.81	0.0	0.8004	1.9	0.09578	1.1	0.56	0.06061	1.6	590	6	597	9	625	34	94
A393	1316	54	6	0.74	b.d.	0.8061	2.6	0.09597	1.4	0.53	0.06092	2.2	591	8	600	12	637	48	93
A520	4584	175	20	1.15	b.d.	0.7972	2.3	0.09626	1.0	0.45	0.06006	2.0	592	6	595	10	606	44	98
A492	2651	99	12	1.33	0.4	0.8022	2.7	0.09665	1.0	0.37	0.06020	2.5	595	6	598	12	611	55	97
A421	2209	82	9	0.88	b.d.	0.8472	3.9	0.09973	1.3	0.33	0.06161	3.7	613	8	623	18	661	79	93
A457	3942	147	17	0.89	b.d.	0.8668	2.5	0.1020	0.9	0.37	0.06162	2.3	626	6	634	12	661	50	95
A461	3893	110	14	0.68	0.1	1.023	2.7	0.1148	1.0	0.37	0.06463	2.5	701	7	716	14	762	52	92
A504	19485	571	73	0.76	0.0	1.033	1.2	0.1179	0.7	0.63	0.06353	0.9	718	5	720	6	726	19	99
A533	7361	224	32	1.20	0.0	1.043	1.8	0.1188	0.9	0.51	0.06366	1.6	724	6	726	9	730	33	99
A471	3800	108	14	0.66	b.d.	1.092	2.4	0.1199	1.0	0.44	0.06607	2.1	730	7	750	13	809	45	90
A445	4171	75	11	0.41	3.6	1.157	4.7	0.1287	1.1	0.24	0.06519	4.6	781	8	781	26	781	96	100
A449	4060	91	20	2.82	0.1	1.366	1.8	0.1436	0.9	0.48	0.06900	1.6	865	7	874	11	899	32	96
A448	2289	53	12	2.71	0.0	1.362	3.5	0.1445	1.3	0.37	0.06836	3.2	870	10	873	21	880	67	99
A475	9060	193	29	0.51	0.1	1.408	1.9	0.1449	0.8	0.44	0.07050	1.7	872	7	892	11	943	34	92
A509	3002	24	4	0.69	0.6	1.508	3.2	0.1528	1.1	0.33	0.07157	3.1	917	9	934	20	974	62	94
A438	12969	242	41	0.47	b.d.	1.662	1.4	0.1641	0.8	0.56	0.07349	1.1	979	7	994	9	1027	23	95
A500	17540	322	58	0.70	0.0	1.714	1.7	0.1681	0.9	0.54	0.07396	1.4	1002	8	1014	11	1040	28	96
A469	4751	68	14	0.60	1.4	1.956	2.7	0.1856	0.9	0.34	0.07643	2.6	1098	9	1100	19	1106	51	99
A474	3979	58	13	1.21	b.d.	2.146	2.6	0.1955	1.0	0.39	0.07961	2.4	1151	11	1164	18	1187	48	97
A529	6455	87	18	0.56	0.1	2.163	1.9	0.1935	0.7	0.38	0.08107	1.8	1140	8	1169	14	1223	35	93
A468	4691	53	12	0.64	0.2	2.636	2.6	0.2165	0.9	0.34	0.08832	2.4	1263	10	1311	19	1389	47	91
A377	25632	170	66	1.37	b.d.	4.709	1.2	0.3145	0.8	0.61	0.1086	1.0	1763	12	1769	10	1776	18	99
A527	49317	261	104	1.13	0.1	5.526	1.3	0.3276	0.9	0.71	0.1223	0.9	1827	15	1905	11	1991	16	92
A429	9895	53	22	1.11	0.1	5.745	1.8	0.3433	0.9	0.48	0.1214	1.6	1903	14	1938	16	1976	28	96
A561	8648	45	21	1.82	0.0	5.757	1.8	0.3391	0.9	0.49	0.1231	1.5	1883	14	1940	15	2002	27	94

Grain	^{207}Pb[a] (cps)	U[b] (ppm)	Pb[b] (ppm)	Th[b] U	^{206}Pbc[c] (%)	^{207}Pb[d] ^{235}U	±2s (%)	^{206}Pb[d] ^{238}U	±2s (%)	ρ[e] (rho)	^{207}Pb[d] ^{206}Pb	±2s (%)	^{206}Pb[f] ^{238}U	±2s (Ma)	^{207}Pb[f] ^{235}U	±2s (Ma)	^{207}Pb[f] ^{206}Pb	±2s (Ma)	Conc.[g] (%)
A456	49847	267	104	0.92	0.0	5.797	1.1	0.3362	0.8	0.74	0.1251	0.7	1868	13	1946	10	2030	13	92
A537	11375	57	24	1.04	0.0	5.906	1.5	0.3458	0.7	0.49	0.1239	1.3	1914	12	1962	13	2013	23	95
A541	15947	76	31	0.89	0.7	6.022	2.0	0.3559	0.9	0.42	0.1227	1.9	1963	14	1979	18	1996	33	98
A481	5905	28	12	1.12	0.7	6.058	3.3	0.3583	1.0	0.31	0.1226	3.1	1974	18	1984	29	1995	56	99
A423	14591	60	25	0.48	3.9	6.059	3.0	0.3571	1.0	0.32	0.1231	2.8	1968	16	1984	26	2001	50	98
A401	10229	22	9	0.85	b.d.	6.091	1.7	0.3419	1.0	0.60	0.1292	1.4	1896	17	1989	15	2087	24	91
A428	23145	114	56	2.07	0.0	6.110	1.4	0.3436	0.9	0.65	0.1290	1.1	1904	15	1992	13	2084	19	91
A437	18057	100	43	1.15	0.0	6.155	1.2	0.3597	0.8	0.62	0.1241	1.0	1981	13	1998	11	2016	17	98
A465	13581	72	29	0.81	b.d.	6.165	1.3	0.3569	0.7	0.56	0.1253	1.1	1968	12	2000	11	2033	19	97
A536	6838	14	5	0.57	0.1	6.167	1.6	0.3483	0.9	0.54	0.1284	1.4	1927	15	2000	14	2076	24	93
A403	47995	236	87	0.30	0.1	6.180	1.0	0.3540	0.7	0.70	0.1266	0.7	1954	12	2002	9	2051	12	95
A444	25503	132	51	0.50	b.d.	6.188	1.3	0.3578	0.8	0.64	0.1254	1.0	1972	14	2003	11	2035	17	97
A512	10375	51	21	0.98	0.1	6.228	1.7	0.3544	0.9	0.50	0.1274	1.5	1956	15	2008	15	2063	26	95
A521	50338	243	88	0.26	0.0	6.233	1.1	0.3525	0.8	0.66	0.1283	0.8	1946	13	2009	10	2074	15	94
A487	14762	75	26	0.00	0.1	6.235	1.5	0.3556	0.8	0.54	0.1271	1.2	1962	14	2009	13	2059	22	95
A395	25194	131	52	0.60	0.0	6.236	1.2	0.3663	0.7	0.59	0.1235	1.0	2012	12	2009	11	2007	17	100
A376	32580	160	61	0.50	b.d.	6.248	1.0	0.3530	0.8	0.76	0.1284	0.7	1949	13	2011	9	2076	11	94
A418	78362	786	332	0.88	0.0	6.255	0.9	0.3670	0.7	0.75	0.1236	0.6	2015	12	2012	8	2009	11	100
A516	10882	52	24	1.37	0.1	6.256	1.8	0.3602	0.9	0.51	0.1260	1.5	1983	16	2012	16	2042	27	97
A414	10356	22	9	0.73	b.d.	6.287	1.5	0.3530	0.8	0.50	0.1292	1.3	1949	13	2017	14	2087	23	93
A433	12852	65	25	0.32	0.8	6.293	2.2	0.3629	1.1	0.47	0.1258	2.0	1996	18	2017	20	2040	35	98
A462	10466	22	9	0.64	0.0	6.325	1.6	0.3501	0.9	0.53	0.1310	1.4	1935	14	2022	14	2112	24	92
A555	47639	470	207	1.02	0.2	6.336	1.3	0.3706	1.0	0.74	0.1240	0.9	2032	17	2023	12	2015	16	101
A560	15419	32	13	0.73	0.1	6.352	1.3	0.3519	0.8	0.62	0.1309	1.0	1944	13	2026	11	2110	17	92
A380	9557	21	13	3.74	0.4	6.367	1.7	0.3658	0.9	0.52	0.1262	1.5	2010	16	2028	15	2046	26	98
A531	12326	24	10	0.99	b.d.	6.381	1.5	0.3550	0.7	0.50	0.1304	1.3	1958	12	2030	13	2103	22	93
A476	9788	20	8	0.73	b.d.	6.388	1.7	0.3593	0.9	0.54	0.1290	1.5	1979	16	2031	15	2084	26	95
A379	7736	39	18	1.60	0.1	6.398	2.1	0.3675	1.3	0.61	0.1263	1.6	2018	22	2032	18	2047	29	99
A378	11308	54	25	1.63	0.0	6.399	1.6	0.3615	1.1	0.67	0.1284	1.2	1989	18	2032	14	2076	21	96
A407	4863	23	9	0.85	0.2	6.401	2.3	0.3587	0.9	0.39	0.1294	2.1	1976	15	2032	21	2090	38	95
A548	5694	26	11	1.02	b.d.	6.405	2.3	0.3574	1.2	0.54	0.1300	1.9	1970	21	2033	20	2098	34	94
A478	15297	54	26	0.97	5.5	6.406	3.5	0.3646	1.0	0.29	0.1274	3.3	2004	17	2033	31	2063	58	97
A486	10566	54	25	1.49	0.0	6.410	2.0	0.3709	0.8	0.40	0.1253	1.8	2034	14	2034	17	2033	32	100
A502	17072	35	15	1.05	b.d.	6.411	1.4	0.3641	0.8	0.55	0.1277	1.2	2002	13	2034	12	2066	20	97
A373	7688	38	16	0.85	0.0	6.418	2.0	0.3644	1.0	0.48	0.1277	1.7	2003	17	2035	18	2067	31	97
A522	17047	77	35	1.24	0.5	6.441	1.9	0.3665	0.9	0.48	0.1275	1.7	2013	16	2038	17	2064	30	98
A557	5284	10	4	0.80	0.8	6.446	2.2	0.3704	0.9	0.39	0.1262	2.1	2031	15	2039	20	2046	37	99
A558	12587	61	24	0.69	0.1	6.453	1.5	0.3607	0.8	0.55	0.1298	1.3	1985	15	2040	14	2095	23	95
A489	18782	86	38	1.04	0.5	6.470	1.4	0.3721	0.7	0.52	0.1261	1.2	2039	13	2042	13	2044	21	100
A511	25918	112	48	0.95	0.3	6.475	1.5	0.3589	0.8	0.57	0.1308	1.2	1977	14	2042	13	2109	21	94
A482	15100	31	13	0.70	0.0	6.500	1.2	0.3687	0.8	0.65	0.1279	0.9	2023	13	2046	10	2069	16	98
A427	10475	21	9	0.84	0.0	6.520	1.7	0.3671	0.7	0.41	0.1288	1.6	2016	12	2049	15	2082	28	97
A459	12520	60	28	1.40	0.1	6.525	1.6	0.3672	0.9	0.58	0.1289	1.3	2016	16	2049	14	2082	22	97
A546	17319	79	36	1.38	0.0	6.561	1.3	0.3667	0.6	0.46	0.1297	1.2	2014	11	2054	12	2094	21	96
A370	14465	29	12	0.80	0.1	6.561	1.6	0.3658	0.7	0.44	0.1301	1.4	2010	12	2054	14	2099	25	96
A460	9709	48	21	1.03	0.0	6.575	1.9	0.3682	1.0	0.55	0.1295	1.6	2021	18	2056	17	2091	27	97
A371	24855	115	47	0.71	0.0	6.582	1.3	0.3646	0.8	0.57	0.1309	1.1	2004	13	2057	12	2110	19	95
A424	16788	79	34	0.96	b.d.	6.588	1.5	0.3647	1.0	0.64	0.1310	1.2	2004	17	2058	14	2111	21	95
A446	11592	56	27	1.73	0.0	6.588	1.6	0.3711	1.0	0.61	0.1288	1.3	2035	17	2058	14	2081	22	98
A410	8262	39	17	1.13	b.d.	6.597	1.8	0.3690	0.7	0.40	0.1297	1.6	2025	12	2059	16	2093	28	97
A464	18713	86	38	1.05	b.d.	6.598	1.1	0.3733	0.7	0.62	0.1282	0.9	2045	12	2059	10	2073	15	99
A434	14128	71	35	1.70	0.0	6.621	1.5	0.3755	1.0	0.65	0.1279	1.2	2055	17	2062	13	2069	20	99
A491	22709	105	48	1.21	0.1	6.621	1.3	0.3683	0.9	0.68	0.1304	0.9	2021	15	2062	11	2103	17	96
A543	7501	35	15	0.94	b.d.	6.625	1.8	0.3671	0.8	0.46	0.1309	1.6	2016	14	2063	16	2110	27	96
A381	13483	64	28	0.91	0.2	6.625	1.5	0.3704	0.8	0.53	0.1297	1.3	2031	14	2063	14	2094	23	97
A451	21371	123	48	0.53	0.3	6.636	2.6	0.3619	2.2	0.84	0.1330	1.4	1991	38	2064	23	2138	25	93
A539	9170	42	20	1.51	0.4	6.644	2.0	0.3614	1.1	0.55	0.1333	1.6	1989	19	2065	17	2142	28	93
A470	17287	35	15	0.94	0.1	6.734	1.5	0.3760	0.7	0.46	0.1299	1.3	2058	12	2077	13	2096	23	98
A452	13482	28	12	0.78	b.d.	6.752	1.4	0.3733	0.8	0.54	0.1312	1.2	2045	13	2079	13	2114	21	97
A477	55304	269	110	0.57	0.0	6.757	1.1	0.3752	0.7	0.68	0.1306	0.8	2054	13	2080	9	2106	14	98
A532	51719	239	102	0.75	0.1	6.758	1.2	0.3775	0.8	0.64	0.1298	0.9	2065	14	2080	11	2096	16	99
A398	5142	24	10	0.74	0.0	6.781	2.2	0.3713	0.9	0.40	0.1324	2.0	2036	15	2083	20	2131	35	96
A467	14712	70	31	1.01	b.d.	6.807	1.4	0.3825	0.7	0.51	0.1291	1.2	2088	13	2087	12	2086	21	100
A501	15492	30	12	0.65	b.d.	6.824	1.3	0.3801	0.7	0.59	0.1302	1.0	2077	13	2089	11	2101	18	99

Grain	^{207}Pb[a] (cps)	U[b] (ppm)	Pb[b] (ppm)	Th[b] U	^{206}Pbc[c] (%)	^{207}Pb[d] ^{235}U	±2s (%)	^{206}Pb[d] ^{238}U	±2s (%)	ρ[e] (rho)	^{207}Pb[d] ^{206}Pb	±2s (%)	^{206}Pb[f] ^{238}U	±2s (Ma)	^{207}Pb[f] ^{235}U	±2s (Ma)	^{207}Pb[f] ^{206}Pb	±2s (Ma)	Conc.[g] (%)
A524	70097	308	125	0.50	b.d.	6.866	0.9	0.3752	0.7	0.76	0.1327	0.6	2054	12	2094	8	2134	10	96
A540	18073	82	35	0.85	b.d.	6.899	1.3	0.3747	0.8	0.63	0.1335	1.0	2052	15	2099	12	2145	18	96
A422	27455	125	57	1.06	b.d.	6.970	1.2	0.3798	0.8	0.70	0.1331	0.9	2075	15	2108	11	2139	15	97
A514	10154	43	20	1.10	0.0	7.017	1.7	0.3809	0.9	0.50	0.1336	1.5	2080	15	2114	16	2146	26	97
A389	23829	104	44	0.66	b.d.	7.060	1.2	0.3778	0.9	0.73	0.1355	0.8	2066	15	2119	11	2171	14	95
A406	11541	50	23	0.95	b.d.	7.114	1.5	0.3834	1.0	0.70	0.1346	1.1	2092	19	2126	13	2159	18	97
A506	41866	185	85	0.96	0.0	7.115	1.1	0.3897	0.7	0.61	0.1324	0.9	2122	12	2126	10	2130	15	100
A530	45531	376	165	0.78	0.0	7.419	1.1	0.3831	0.7	0.62	0.1404	0.8	2091	12	2163	10	2233	14	94
A409	38772	223	95	0.58	0.1	7.705	1.2	0.3820	0.7	0.62	0.1463	0.9	2086	13	2197	11	2303	16	91
A447	100655	337	161	0.74	0.0	9.131	0.9	0.4164	0.7	0.72	0.1591	0.6	2244	12	2351	8	2446	11	92
A425	53950	168	79	0.44	0.0	9.653	1.4	0.4242	1.2	0.84	0.1651	0.8	2279	23	2402	13	2508	13	91
A538	79480	229	118	0.96	0.0	9.760	1.0	0.4291	0.7	0.66	0.1650	0.7	2302	13	2412	9	2507	13	92
A405	59245	191	90	0.38	0.0	9.896	1.0	0.4370	0.7	0.72	0.1643	0.7	2337	14	2425	9	2500	11	93
A518	73444	214	103	0.39	0.1	10.44	1.1	0.4368	0.9	0.80	0.1733	0.6	2336	17	2474	10	2590	11	90
A485	72345	211	104	0.45	0.0	10.57	0.9	0.4445	0.7	0.71	0.1725	0.7	2371	13	2486	9	2582	11	92
A426	187309	523	251	0.21	0.0	10.87	0.9	0.4533	0.7	0.78	0.1740	0.6	2410	14	2512	8	2596	9	93
A388	47652	138	72	0.47	0.0	11.09	1.0	0.4746	0.7	0.66	0.1694	0.8	2504	14	2530	10	2552	13	98
A408	33471	94	53	0.95	0.1	11.34	1.1	0.4701	0.8	0.73	0.1750	0.8	2484	17	2552	11	2606	13	95
A466	30310	84	48	0.90	0.0	11.40	1.2	0.4798	0.9	0.72	0.1723	0.8	2527	18	2556	11	2580	14	98
A484	102084	274	157	1.06	0.0	11.45	0.9	0.4668	0.6	0.72	0.1780	0.6	2469	13	2561	8	2634	10	94
A547	127540	334	175	0.40	0.0	11.75	0.9	0.4771	0.7	0.74	0.1786	0.6	2514	14	2585	8	2640	10	95
A458	17213	44	31	2.43	b.d.	12.01	1.5	0.4794	1.1	0.73	0.1817	1.0	2525	23	2605	14	2669	17	95
A417	58647	314	193	1.06	b.d.	12.35	1.3	0.5008	1.0	0.77	0.1788	0.8	2617	21	2631	12	2642	13	99
A463	152796	782	491	1.10	0.0	12.75	2.0	0.5132	1.9	0.96	0.1801	0.6	2670	41	2661	19	2654	10	101
A528	17829	42	26	1.00	0.1	12.87	1.4	0.5040	0.9	0.68	0.1852	1.0	2631	21	2670	13	2700	17	97
A420	74326	176	99	0.45	0.1	13.00	1.0	0.5071	0.7	0.74	0.1859	0.6	2644	15	2679	9	2706	11	98
A472	160878	790	443	0.37	0.0	13.16	1.0	0.5070	0.7	0.73	0.1883	0.7	2644	16	2691	10	2727	11	97
A507	230924	1092	623	0.20	b.d.	14.03	1.1	0.5338	0.9	0.79	0.1906	0.7	2757	20	2752	11	2748	12	100
A375	13180	29	18	0.66	0.0	14.40	1.7	0.5272	1.1	0.67	0.1981	1.2	2729	25	2776	16	2810	20	97
A556	55219	116	79	1.16	0.2	14.48	1.2	0.5321	0.9	0.77	0.1973	0.8	2750	21	2781	12	2804	13	98
A390	115498	230	169	1.53	0.1	15.80	1.2	0.5467	1.0	0.80	0.2095	0.7	2812	22	2865	11	2902	11	97
A454	163722	361	250	1.06	0.0	16.53	1.0	0.5660	0.8	0.81	0.2118	0.6	2891	19	2908	9	2919	9	99
A400	24674	47	35	1.21	0.0	16.98	1.5	0.5775	1.0	0.67	0.2133	1.1	2939	24	2934	15	2930	18	100
A534	51914	35	25	0.68	0.1	19.60	1.2	0.5903	0.9	0.70	0.2408	0.9	2991	20	3072	12	3125	14	96
A453	*1540*	*29*	*3*	*0.74*	*b.d.*	*0.7287*	*3.5*	*0.08386*	*1.3*	*0.36*	*0.06302*	*3.3*	*519*	*6*	*556*	*15*	*709*	*69*	*73*
A399	*1804*	*60*	*6*	*0.61*	*0.1*	*0.9388*	*3.2*	*0.09413*	*1.2*	*0.37*	*0.07233*	*3.0*	*580*	*7*	*672*	*16*	*995*	*61*	*58*
A554	*14030*	*262*	*38*	*0.64*	*0.0*	*1.384*	*2.5*	*0.1328*	*2.3*	*0.90*	*0.07562*	*1.1*	*804*	*17*	*882*	*15*	*1085*	*22*	*74*
A402	*10529*	*99*	*25*	*0.30*	*1.4*	*3.344*	*2.3*	*0.2422*	*0.8*	*0.35*	*0.1001*	*2.2*	*1398*	*10*	*1491*	*18*	*1627*	*40*	*86*
A544	*40564*	*314*	*87*	*1.17*	*0.3*	*3.355*	*2.3*	*0.2131*	*2.1*	*0.90*	*0.1142*	*1.0*	*1246*	*24*	*1494*	*18*	*1867*	*18*	*67*
A455	*79133*	*708*	*142*	*0.15*	*0.3*	*3.669*	*1.1*	*0.1969*	*0.7*	*0.61*	*0.1351*	*0.9*	*1159*	*7*	*1565*	*9*	*2166*	*16*	*54*
A436	*10932*	*49*	*27*	*3.14*	*0.0*	*5.992*	*2.1*	*0.3338*	*1.1*	*0.53*	*0.1302*	*1.7*	*1857*	*18*	*1975*	*18*	*2101*	*31*	*88*
A479	*14651*	*53*	*29*	*2.00*	*0.1*	*8.442*	*1.6*	*0.3801*	*0.9*	*0.61*	*0.1611*	*1.2*	*2077*	*17*	*2280*	*14*	*2467*	*21*	*84*
A431	*25348*	*92*	*39*	*0.61*	*0.7*	*9.382*	*1.6*	*0.3668*	*1.0*	*0.65*	*0.1855*	*1.2*	*2014*	*17*	*2376*	*14*	*2703*	*20*	*75*
91500[h]	9384	69	13	0.46	0.5	1.838	3.0	0.1786	1.7	0.38	0.07465	2.4	1059	17	1059	20	1059	48	100
Felix[h]	4694	227	26	1.76	0.4	0.6335	4.6	0.08112	3.5	0.34	0.05664	2.3	503	17	498	18	477	51	106
Plesovice[h]	1723	581	30	0.12	0.2	0.3999	2.6	0.05415	2.5	0.37	0.05356	0.9	340	8	342	8	353	20	96

$^{206}Pb/^{238}U$ error is the quadratic additions of the within run precision (2 SE) and the external reproducibility (2 SD) of the reference zircon. $^{207}Pb/^{206}Pb$ error propagation (^{207}Pb signal dependent) following Gerdes & Zeh (2009). $^{207}Pb/^{235}U$ error is the quadratic addition of the $^{207}Pb/^{206}Pb$ and $^{206}Pb/^{238}U$ uncertainty.

[a] Within run background-corrected mean ^{207}Pb signal in cps (counts per second).

[b] U and Pb content and Th/U ratio were calculated relative to GJ-1 reference zircon.

[c] Percentage of the common Pb on the ^{206}Pb. b.d. = below detection limit.

[d] Pb/U and Pb/Pb ratios. Corrected for background, within-run Pb/U fractionation (in case of $^{206}Pb/^{238}U$) and common Pb using Stacy and Kramers (1975) model Pb composition and subsequently normalised to GJ-1 (ID-TIMS value/measured value); $^{207}Pb/^{235}U$ calculated using (($^{207}Pb/^{206}Pb$)*($^{238}U/^{206}Pb$)*137.88).

[e] Rho (ρ) is the ($^{206}Pb/^{238}U$)/($^{207}Pb/^{235}U$) error correlation coefficient.

[f] Pb/U and Pb/Pb ages.

[g] Degree of concordance = (($^{206}Pb/^{238}U$ age)/($^{207}Pb/^{206}Pb$ age)) x 100.

Table 6
U, Th and Pb LA-ICP-MS data of zircon cores from sample GCH-12

Grain	^{207}Pb[a] (cps)	U[b] (ppm)	Pb[b] (ppm)	$\frac{Th}{U}$[b]	^{206}Pbc[c] (%)	$\frac{^{207}Pb}{^{235}U}$[d]	±2s (%)	$\frac{^{206}Pb}{^{238}U}$[d]	±2s (%)	ρ[e] (rho)	$\frac{^{207}Pb}{^{206}Pb}$[d]	±2s (%)	$\frac{^{206}Pb}{^{238}U}$[f]	±2s (Ma)	$\frac{^{207}Pb}{^{235}U}$[f]	±2s (Ma)	$\frac{^{207}Pb}{^{206}Pb}$[f]	±2s (Ma)	Conc.[g] (%)
A065	2833	112	10	1.08	0.2	0.6402	2.3	0.08086	1.3	0.54	0.05742	2.0	501	6	502	9	508	43	99
A010b	4732	377	34	0.76	1.1	0.6484	3.3	0.08161	1.2	0.35	0.05763	3.1	506	6	507	13	516	69	98
A026	970	37	3	0.65	0.2	0.6591	3.6	0.08278	1.1	0.30	0.05775	3.4	513	5	514	15	520	75	99
A127	1737	81	7	0.75	b.d.	0.6560	3.1	0.08278	1.2	0.39	0.05748	2.8	513	6	512	12	510	62	101
A017	1112	44	4	0.92	0.0	0.6667	3.2	0.08330	1.5	0.46	0.05805	2.9	516	7	519	13	532	63	97
A116	3224	141	13	0.89	b.d.	0.6648	3.0	0.08348	1.4	0.45	0.05776	2.7	517	7	518	12	521	60	99
A122	994	39	4	1.19	0.6	0.6573	6.1	0.08361	1.6	0.27	0.05702	5.9	518	8	513	25	492	129	105
A165	1952	95	9	0.93	0.1	0.6786	3.5	0.08362	1.1	0.31	0.05886	3.4	518	5	526	15	562	73	92
A107	2142	95	9	0.94	b.d.	0.6655	2.9	0.08370	1.5	0.50	0.05767	2.5	518	7	518	12	517	55	100
A049	1984	74	7	1.08	0.5	0.6802	3.4	0.08413	1.5	0.44	0.05864	3.0	521	7	527	14	554	66	94
A117	2993	133	13	1.00	0.1	0.6820	3.0	0.08423	1.4	0.47	0.05873	2.6	521	7	528	12	557	57	94
A014	2947	108	9	0.40	0.2	0.6754	2.3	0.08448	1.2	0.52	0.05799	1.9	523	6	524	9	529	42	99
A018	4421	154	14	0.69	0.3	0.6787	2.4	0.08453	1.1	0.48	0.05823	2.1	523	6	526	10	538	45	97
A057	2891	112	10	0.86	0.1	0.6825	2.5	0.08454	1.1	0.44	0.05856	2.2	523	5	528	10	551	49	95
A054	780	31	3	1.01	b.d.	0.6780	3.6	0.08466	1.6	0.44	0.05809	3.2	524	8	526	15	533	71	98
A118	1764	75	7	0.88	0.3	0.6784	4.6	0.08499	1.4	0.30	0.05789	4.4	526	7	526	19	526	96	100
A043	5858	224	23	1.35	0.1	0.6794	2.2	0.08502	1.3	0.57	0.05796	1.8	526	6	526	9	528	39	100
A031	1803	67	6	0.75	0.1	0.6803	3.2	0.08514	1.2	0.38	0.05795	3.0	527	6	527	13	528	66	100
A092	1822	143	14	1.14	0.1	0.6888	3.3	0.08533	1.5	0.45	0.05854	3.0	528	8	532	14	550	65	96
A145	7545	330	33	1.15	0.7	0.6873	4.2	0.08555	1.3	0.30	0.05827	4.0	529	7	531	18	540	88	98
A008b	3351	146	13	0.56	0.0	0.6856	2.4	0.08562	1.2	0.49	0.05808	2.1	530	6	530	10	533	45	99
A061	2765	115	11	0.90	0.0	0.6885	2.7	0.08568	1.3	0.49	0.05828	2.4	530	7	532	11	540	52	98
A080	1607	66	6	0.92	0.1	0.6898	4.3	0.08593	1.2	0.28	0.05823	4.1	531	6	533	18	538	91	99
A158	3303	155	14	0.60	b.d.	0.7060	2.5	0.08593	1.2	0.47	0.05959	2.2	531	6	542	11	589	48	90
A006	2354	86	8	0.79	b.d.	0.6901	2.9	0.08604	1.2	0.42	0.05818	2.6	532	6	533	12	536	57	99
A159	4383	210	20	0.96	0.0	0.6927	2.2	0.08635	1.0	0.47	0.05818	1.9	534	5	534	9	537	42	100
A143	3282	299	27	0.62	0.1	0.6925	2.8	0.08642	1.4	0.51	0.05811	2.4	534	7	534	12	534	53	100
A050	768	28	3	1.05	0.6	0.6883	5.0	0.08646	1.9	0.37	0.05774	4.6	535	10	532	21	520	102	103
A019	2810	104	10	0.87	0.2	0.6993	3.3	0.08706	1.3	0.38	0.05825	3.0	538	7	538	14	539	66	100
A013b	6995	137	15	0.68	6.9	0.7021	6.3	0.08726	1.3	0.21	0.05836	6.2	539	7	540	27	543	135	99
A006b	7382	288	28	0.77	0.8	0.7010	2.9	0.08773	1.2	0.42	0.05795	2.6	542	6	539	12	528	57	103
A160	3573	159	17	1.29	0.1	0.7131	3.3	0.08779	1.3	0.39	0.05891	3.0	542	7	547	14	564	66	96
A157	8299	368	33	0.43	0.1	0.7187	2.0	0.08821	1.0	0.52	0.05910	1.7	545	5	550	8	571	37	95
A162	3556	161	17	0.99	b.d.	0.7455	2.3	0.09198	1.2	0.54	0.05878	1.9	567	7	566	10	559	42	101
A135	4243	224	26	1.16	2.8	0.7691	4.3	0.09225	1.4	0.31	0.06047	4.1	569	7	579	19	620	89	92
A015	3352	96	11	1.24	1.3	0.7526	2.5	0.09267	1.3	0.55	0.05890	2.1	571	7	570	11	563	45	101
A125	775	31	4	1.33	0.0	0.7836	4.6	0.09503	2.3	0.49	0.05981	4.0	585	13	588	21	597	88	98
A156	1917	77	8	0.88	0.1	0.8017	3.9	0.09613	1.3	0.33	0.06048	3.7	592	7	598	18	621	80	95
A007b	3221	112	12	0.90	0.1	0.8163	2.7	0.09856	1.1	0.40	0.06006	2.5	606	6	606	12	606	53	100
A123	3729	139	16	1.04	0.2	0.8050	3.1	0.09878	1.1	0.35	0.05911	3.0	607	6	600	14	571	64	106
A155	11389	407	49	1.32	0.7	0.8309	2.8	0.1012	1.1	0.38	0.05953	2.6	622	6	614	13	586	55	106
A113	1808	53	7	1.01	b.d.	0.9898	4.1	0.1142	1.7	0.42	0.06288	3.8	697	11	699	21	704	80	99
A130	5578	286	41	1.27	1.0	1.073	3.6	0.1191	1.1	0.30	0.06537	3.5	725	8	740	19	786	73	92
A022	5299	127	19	1.44	b.d.	1.086	2.2	0.1227	1.3	0.59	0.06421	1.8	746	9	747	12	748	38	100
A161	3603	104	14	0.83	0.2	1.100	3.3	0.1231	1.3	0.40	0.06482	3.0	748	9	753	18	768	63	97
A112	19980	364	58	0.30	0.0	1.613	1.6	0.1613	1.0	0.65	0.07251	1.2	964	9	975	10	1000	25	96
A140	3819	56	11	0.26	b.d.	2.142	2.2	0.1947	1.3	0.60	0.07979	1.8	1147	14	1163	15	1192	35	96
A114	2288	30	6	0.65	0.5	2.165	3.1	0.2000	1.6	0.50	0.07852	2.7	1175	17	1170	22	1160	53	101
A141	17732	484	102	0.42	0.1	2.277	1.7	0.2047	1.1	0.66	0.08069	1.3	1201	12	1205	12	1214	25	99
A078	10692	108	32	1.62	0.0	2.803	1.7	0.2353	1.2	0.69	0.08639	1.2	1362	14	1356	13	1347	24	101
A075	6554	62	15	0.42	0.2	2.839	2.7	0.2335	1.2	0.43	0.08818	2.5	1353	15	1366	21	1386	47	98
A064	13818	125	33	0.54	0.1	3.101	1.5	0.2475	1.0	0.71	0.09088	1.0	1426	13	1433	11	1444	20	99
A124	17538	224	91	1.61	0.2	4.641	2.0	0.3133	1.1	0.57	0.1074	1.6	1757	17	1757	17	1756	30	100
A007	8255	32	13	0.81	1.2	5.732	2.4	0.3507	1.4	0.56	0.1185	2.0	1938	23	1936	21	1934	35	100
A139	41519	447	149	0.04	b.d.	5.893	1.3	0.3382	1.0	0.79	0.1264	0.8	1878	16	1960	11	2048	14	92
A166	14719	80	33	1.18	0.3	5.904	2.0	0.3379	1.2	0.58	0.1267	1.6	1877	19	1962	17	2053	29	91
A152	6711	39	17	1.64	0.0	5.916	2.2	0.3464	1.3	0.58	0.1239	1.8	1917	21	1964	19	2012	32	95
A111	24804	125	44	0.18	0.0	5.941	1.4	0.3466	1.0	0.74	0.1243	0.9	1919	17	1967	12	2019	16	95
A085	4051	20	11	3.23	0.2	5.990	2.8	0.3547	1.1	0.40	0.1225	2.6	1957	19	1974	25	1993	46	98
A076	29761	138	56	0.87	0.1	6.015	1.5	0.3543	1.2	0.75	0.1231	1.0	1955	20	1978	13	2002	18	98
A025	1223	5	2	0.00	1.0	6.036	3.1	0.3519	2.4	0.76	0.1244	2.0	1944	40	1981	27	2020	35	96

Grain	^{207}Pb[a] (cps)	U[b] (ppm)	Pb[b] (ppm)	Th[b]/U	^{206}Pbc[c] (%)	$^{207}Pb/^{235}U$[d]	±2s (%)	$^{206}Pb/^{238}U$[d]	±2s (%)	ρ[e] (rho)	$^{207}Pb/^{206}Pb$[d]	±2s (%)	$^{206}Pb/^{238}U$[f]	±2s (Ma)	$^{207}Pb/^{235}U$[f]	±2s (Ma)	$^{207}Pb/^{206}Pb$[f]	±2s (Ma)	Conc.[g] (%)
A132	14121	74	30	0.79	0.2	6.055	1.8	0.3530	1.1	0.62	0.1244	1.4	1949	19	1984	16	2020	25	96
A024	6360	25	11	1.07	0.2	6.146	2.6	0.3511	1.3	0.5	0.1270	2.2	1940	22	1997	23	2056	39	94
A108	12110	56	23	0.86	0.6	6.159	1.9	0.3587	1.2	0.60	0.1245	1.5	1976	20	1999	17	2022	27	98
A045	4262	17	8	1.17	0.4	6.187	3.0	0.3610	1.7	0.57	0.1243	2.4	1987	29	2003	26	2019	43	98
A062	12132	51	23	1.35	0.5	6.194	1.8	0.3607	1.2	0.64	0.1246	1.4	1985	20	2004	16	2023	25	98
A134	14140	71	31	1.19	0.4	6.198	1.9	0.3545	1.1	0.60	0.1268	1.5	1956	19	2004	17	2054	27	95
A151	70400	362	154	1.10	0.0	6.229	1.4	0.3584	1.1	0.83	0.1260	0.8	1975	19	2009	12	2044	13	97
A041	3959	17	7	0.75	0.7	6.231	4.0	0.3628	1.3	0.33	0.1246	3.7	1995	23	2009	35	2023	66	99
A094	10519	49	21	1.10	0.0	6.235	1.8	0.3552	1.1	0.59	0.1273	1.5	1960	18	2009	16	2061	26	95
A131	46915	227	106	1.71	0.4	6.239	1.3	0.3556	1.0	0.79	0.1272	0.8	1961	17	2010	11	2060	14	95
A053	12809	56	25	1.34	b.d.	6.248	1.9	0.3596	1.4	0.74	0.1260	1.3	1980	24	2011	17	2043	23	97
A095	28093	262	95	0.15	0.2	6.268	1.6	0.3594	1.2	0.72	0.1265	1.1	1979	20	2014	14	2050	20	97
A060	25991	87	46	1.95	6.3	6.271	4.5	0.3664	1.3	0.30	0.1241	4.3	2012	23	2014	40	2017	76	100
A167	16433	77	34	1.10	1.3	6.294	2.2	0.3622	1.2	0.53	0.1260	1.9	1993	20	2018	19	2043	33	98
A101	14914	142	54	0.32	0.1	6.298	1.6	0.3660	1.1	0.69	0.1248	1.1	2011	18	2018	14	2026	20	99
A144	29183	308	119	0.47	0.1	6.304	1.5	0.3603	1.0	0.64	0.1269	1.2	1983	17	2019	13	2056	21	96
A154	10660	55	22	0.74	0.0	6.305	1.6	0.3546	1.1	0.68	0.1290	1.2	1957	19	2019	14	2084	21	94
A023	6829	27	11	0.71	0.5	6.325	3.0	0.3632	1.5	0.48	0.1263	2.7	1997	25	2022	27	2047	47	98
A126	8815	41	19	1.54	0.2	6.343	2.1	0.3599	1.3	0.60	0.1278	1.7	1982	22	2024	19	2068	30	96
A040	48833	209	81	0.40	0.1	6.350	1.3	0.3684	1.1	0.80	0.1250	0.8	2022	18	2025	12	2029	14	100
A129	4840	24	10	0.67	0.0	6.362	2.2	0.3602	1.2	0.55	0.1281	1.8	1983	21	2027	20	2072	32	96
A115	6307	29	12	0.69	0.2	6.363	2.3	0.3682	1.4	0.60	0.1253	1.8	2021	24	2027	20	2034	32	99
A109	31232	143	57	0.58	0.1	6.365	1.3	0.3638	1.0	0.79	0.1269	0.8	2000	18	2027	11	2055	14	97
A133	9776	46	19	0.97	0.3	6.372	2.5	0.3651	1.4	0.57	0.1266	2.1	2006	24	2028	22	2051	36	98
A029	27008	107	45	0.93	0.4	6.372	1.5	0.3624	1.1	0.75	0.1275	1.0	1993	20	2028	13	2064	18	97
A087	15681	67	31	1.43	0.5	6.391	2.3	0.3679	1.3	0.59	0.1260	1.9	2019	23	2031	20	2043	33	99
A046	20708	90	38	0.92	0.1	6.401	2.0	0.3648	1.2	0.62	0.1272	1.5	2005	21	2032	17	2060	27	97
A088	6961	30	13	0.79	0.4	6.402	2.1	0.3674	1.5	0.72	0.1264	1.5	2017	27	2033	19	2049	26	98
A074	9241	38	17	0.95	0.8	6.406	2.2	0.3673	1.5	0.65	0.1265	1.7	2017	25	2033	20	2050	30	98
A072	5133	23	10	0.72	0.0	6.413	2.5	0.3683	1.3	0.49	0.1263	2.2	2022	22	2034	23	2047	39	99
A055	14249	58	25	1.13	0.5	6.422	2.0	0.3608	1.1	0.54	0.1291	1.7	1986	18	2035	17	2086	29	95
A056	17560	73	31	0.94	0.3	6.443	2.0	0.3719	1.4	0.70	0.1257	1.4	2038	24	2038	18	2038	25	100
A097	12351	55	23	0.81	0.3	6.446	2.3	0.3671	1.3	0.58	0.1273	1.9	2016	23	2039	20	2062	33	98
A090	6263	28	12	0.98	0.1	6.448	2.0	0.3677	1.3	0.64	0.1272	1.5	2018	22	2039	17	2059	27	98
A138	6463	29	14	1.69	0.4	6.448	3.4	0.3622	1.6	0.47	0.1291	3.0	1992	28	2039	31	2086	53	96
A047	50745	206	84	0.72	0.0	6.472	1.4	0.3624	1.1	0.82	0.1295	0.8	1994	19	2042	12	2091	14	95
A077	4860	22	10	1.19	b.d.	6.472	2.3	0.3722	1.1	0.48	0.1261	2.0	2040	19	2042	20	2044	35	100
A013	8205	32	14	0.91	0.1	6.483	1.8	0.3689	1.2	0.67	0.1275	1.3	2024	21	2044	16	2063	23	98
A083	25218	108	40	0.26	0.3	6.493	1.7	0.3627	1.1	0.63	0.1298	1.4	1995	19	2045	15	2096	24	95
A052	10709	44	19	1.07	0.1	6.501	1.9	0.3684	1.2	0.66	0.1280	1.4	2022	21	2046	16	2070	25	98
A016	7834	30	13	0.83	0.3	6.503	2.4	0.3739	1.3	0.57	0.1261	1.9	2048	24	2046	21	2045	34	100
A038	6032	23	10	1.09	0.0	6.542	1.9	0.3669	1.2	0.62	0.1293	1.5	2015	21	2052	17	2088	27	96
A012	10037	38	16	0.75	0.2	6.550	1.9	0.3729	1.1	0.57	0.1274	1.6	2043	19	2053	17	2062	28	99
A137	26719	131	53	0.74	0.1	6.567	1.4	0.3656	1.1	0.80	0.1303	0.8	2009	19	2055	12	2102	15	96
A142	9468	45	21	1.23	0.1	6.580	1.8	0.3722	1.1	0.61	0.1282	1.4	2040	19	2057	16	2074	25	98
A128	10814	50	21	0.84	b.d.	6.580	2.0	0.3692	1.2	0.62	0.1293	1.6	2026	22	2057	18	2088	28	97
A153	19747	98	43	1.06	0.0	6.607	1.5	0.3730	1.0	0.70	0.1284	1.0	2044	18	2060	13	2077	18	98
A099	6090	28	12	1.11	b.d.	6.610	2.5	0.3721	1.5	0.59	0.1288	2.0	2039	26	2061	22	2082	36	98
A073	15401	68	29	0.73	0.1	6.617	1.7	0.3742	1.2	0.68	0.1283	1.3	2049	20	2062	15	2074	22	99
A044	34644	296	121	0.54	0.1	6.629	1.5	0.3769	1.2	0.83	0.1276	0.8	2062	21	2063	13	2065	14	100
A119	12658	56	24	0.77	0.1	6.631	1.8	0.3747	1.2	0.70	0.1283	1.3	2052	22	2063	16	2075	22	99
A066	6235	26	11	0.69	0.0	6.644	2.3	0.3774	1.4	0.58	0.1277	1.9	2064	24	2065	21	2066	34	100
A032	10590	42	18	0.77	b.d.	6.688	1.9	0.3755	1.2	0.64	0.1292	1.5	2055	22	2071	17	2087	26	98
A089	23011	108	49	1.10	0.2	6.719	1.8	0.3814	1.3	0.76	0.1278	1.1	2083	24	2075	16	2068	20	101
A096	19731	85	37	1.00	0.1	6.720	1.7	0.3726	1.1	0.68	0.1308	1.2	2042	20	2075	15	2109	22	97
A110	43415	189	80	0.88	b.d.	6.758	1.3	0.3664	1.0	0.81	0.1337	0.8	2013	18	2080	11	2148	13	94
A012b	7536	33	14	1.00	0.0	6.766	2.2	0.3763	1.3	0.62	0.1304	1.7	2059	24	2081	19	2104	30	98
A082	50146	209	89	0.88	0.2	6.779	1.3	0.3798	1.0	0.82	0.1295	0.7	2075	19	2083	11	2091	13	99
A091	33016	278	122	1.00	0.2	6.804	1.6	0.3749	1.2	0.74	0.1316	1.1	2053	21	2086	15	2120	19	97
A014b	13212	57	26	1.05	0.1	6.810	1.9	0.3824	1.2	0.61	0.1292	1.5	2088	21	2087	17	2087	27	100
A011b	11930	49	22	0.87	0.6	6.837	2.0	0.3825	1.1	0.56	0.1296	1.7	2088	20	2091	18	2093	29	100
A079	27017	225	96	0.60	0.1	6.866	1.6	0.3856	1.2	0.75	0.1291	1.0	2102	21	2094	14	2086	18	101
A009b	28453	65	36	0.91	10.1	6.873	5.2	0.3894	1.4	0.28	0.1280	5.0	2120	26	2095	47	2071	88	102
A084	35012	149	66	0.91	0.0	6.879	1.3	0.3817	1.1	0.79	0.1307	0.8	2084	19	2096	12	2107	14	99

Grain	^{207}Pb[a] (cps)	U[b] (ppm)	Pb[b] (ppm)	Th[b] U	^{206}Pbc[c] (%)	^{207}Pb[d] / ^{235}U	±2s (%)	^{206}Pb[d] / ^{238}U	±2s (%)	ρ[e] (rho)	^{207}Pb[d] / ^{206}Pb	±2s (%)	^{206}Pb[f] / ^{238}U	±2s (Ma)	^{207}Pb[f] / ^{235}U	±2s (Ma)	^{207}Pb[f] / ^{206}Pb	±2s (Ma)	Conc.[g] (%)
A009	13008	51	23	1.12	0.3	6.884	1.9	0.3840	1.3	0.68	0.1300	1.4	2095	23	2097	17	2098	25	100
A010	3502	13	6	0.44	b.d.	7.102	2.4	0.3844	1.3	0.52	0.1340	2.0	2097	22	2124	21	2151	35	97
A098	14726	57	25	0.71	0.5	7.138	2.2	0.3911	1.3	0.60	0.1324	1.8	2128	24	2129	20	2130	31	100
A042	22529	78	33	0.42	0.0	7.691	1.5	0.4006	1.1	0.78	0.1392	0.9	2172	21	2196	13	2218	16	98
A039	112544	341	146	0.29	0.1	8.586	1.1	0.4040	1.0	0.85	0.1541	0.6	2187	18	2295	10	2392	10	91
A163	345229	851	376	0.29	0.0	9.116	1.4	0.4165	1.2	0.90	0.1587	0.6	2245	23	2350	13	2442	10	92
A051	107052	594	278	0.08	0.0	9.921	1.3	0.4591	1.1	0.80	0.1567	0.8	2436	21	2427	12	2421	13	101
A030	62001	174	88	0.53	0.1	10.11	1.4	0.4580	1.2	0.86	0.1602	0.7	2431	24	2445	13	2457	12	99
A164	49963	153	91	1.79	0.1	10.63	1.4	0.4396	1.1	0.79	0.1754	0.8	2349	21	2491	13	2610	14	90
A081	82142	144	92	0.66	5.7	11.67	2.7	0.4855	1.2	0.44	0.1743	2.4	2551	25	2578	26	2599	40	98
A086	41287	98	60	1.30	0.0	12.12	1.6	0.4853	1.2	0.78	0.1811	1.0	2550	26	2613	15	2663	16	96
A059	27260	60	36	0.97	0.1	12.46	1.5	0.5000	1.0	0.67	0.1807	1.1	2614	21	2640	14	2660	18	98
A017b	46112	111	68	0.96	0.0	12.46	1.4	0.5073	1.0	0.76	0.1781	0.9	2645	23	2640	13	2636	15	100
A120	55297	127	76	0.82	b.d.	13.02	1.4	0.5074	1.2	0.80	0.1862	0.9	2646	25	2681	14	2709	14	98
A027	16212	31	24	2.39	0.2	13.04	2.0	0.5060	1.1	0.55	0.1869	1.7	2640	24	2682	19	2715	28	97
A093	21917	98	60	0.85	0.1	13.10	1.7	0.5112	1.2	0.73	0.1858	1.1	2662	27	2687	16	2706	19	98
A121	59312	114	77	1.12	0.1	15.48	1.3	0.5393	1.0	0.78	0.2082	0.8	2781	23	2845	13	2892	13	96
A058	*-35*																		
A020	*821*	*27*	*2*	*0.63*	*b.d.*	*0.7978*	*5.0*	*0.08466*	*1.5*	*0.30*	*0.06835*	*4.8*	*524*	*7*	*596*	*23*	*879*	*99*	*60*
A015b	*14759*	*301*	*49*	*5.56*	*2.3*	*0.6748*	*4.6*	*0.08655*	*1.5*	*0.32*	*0.05655*	*4.3*	*535*	*8*	*524*	*19*	*474*	*96*	*113*
A016b	*15858*	*205*	*26*	*1.04*	*15.8*	*0.8276*	*10.3*	*0.08780*	*1.9*	*0.19*	*0.06836*	*10*	*543*	*10*	*612*	*49*	*880*	*210*	*62*
A021	*136*	*5*	*1*	*0.80*	*b.d.*	*0.8860*	*12.7*	*0.09786*	*2.8*	*0.22*	*0.06566*	*12*	*602*	*16*	*644*	*63*	*796*	*260*	*76*
A136	*38867*	*257*	*59*	*0.56*	*1.2*	*3.027*	*2.6*	*0.2043*	*2.0*	*0.79*	*0.1074*	*1.6*	*1199*	*22*	*1414*	*20*	*1756*	*29*	*68*
91500[h]	8681	72	13	0.44	0.4	1.835	3.6	0.1782	2.7	0.67	0.07470	2.0	1057	26	1058	24	1060	40	100
Felix[h]	7868	410	60	3.53	0.2	0.6419	2.8	0.08134	2.6	0.62	0.05724	1.7	504	13	503	11	501	37	101
Plesovice[h]	2176	529	27	0.14	0.4	0.3942	2.3	0.05381	1.9	0.50	0.05313	2.0	338	6	337	7	334	45	102

$^{206}Pb/^{238}U$ error is the quadratic additions of the within run precision (2 SE) and the external reproducibility (2 SD) of the reference zircon. $^{207}Pb/^{206}Pb$ error propagation (^{207}Pb signal dependent) following Gerdes & Zeh (2009). $^{207}Pb/^{235}U$ error is the quadratic addition of the $^{207}Pb/^{206}Pb$ and $^{206}Pb/^{238}U$ uncertainty.

[a] Within run background-corrected mean ^{207}Pb signal in cps (counts per second).

[b] U and Pb content and Th/U ratio were calculated relative to GJ-1 reference zircon.

[c] Percentage of the common Pb on the ^{206}Pb. b.d. = below detection limit.

[d] Pb/U and Pb/Pb ratios. Corrected for background, within-run Pb/U fractionation (in case of $^{206}Pb/^{238}U$) and common Pb using Stacy and Kramers (1975) model Pb composition and subsequently normalised to GJ-1 (ID-TIMS value/measured value); $^{207}Pb/^{235}U$ calculated using (($^{207}Pb/^{206}Pb$)*($^{238}U/^{206}Pb$)*137.88).

[e] Rho (ρ) is the ($^{206}Pb/^{238}U$)/($^{207}Pb/^{235}U$) error correlation coefficient.

[f] Pb/U and Pb/Pb ages.

[g] Degree of concordance = (($^{206}Pb/^{238}U$ age)/($^{207}Pb/^{206}Pb$ age)) x 100.

[h] Mean of 4 (91500), 5 (Felix), 5 (Plesovice), and 10 (GJ-1) analyses, respectively.

Table 7

Lu, Yb and Hf LA-MC-ICPMS data of zircon cores from sample GCH-07

Grain	$^{176}Yb/^{177}Hf$ [a]	±2σ	$^{176}Lu/^{177}Hf$ [a]	±2σ	$^{178}Hf/^{177}Hf$	$^{180}Hf/^{177}Hf$	Sig_{Hf} [b] (V)	$^{176}Hf/^{177}Hf$	±2σ [c]	$^{176}Hf/^{177}Hf_{(t)}$ [d]	$\varepsilon Hf_{(t)}$	±2σ [c] (εHf)	T_{DM} [e] (Ga)	age [f] (Ma)	±2σ (Ma)	U-Pb [g] conc	Lu-Hf [h] seq
A179_seq4_40	0.0296	24	0.00085	5	1.46728	1.88693	9	0.282460	29	0.282451	1.4	1.0	1.16	592	6	96	4
A180_seq4_26	0.0043	4	0.00014	1	1.46721	1.88659	4	0.282506	45	0.282505	3.6	1.6	1.04	607	14	1424	4
A181_seq4_40	0.0133	12	0.00046	3	1.46717	1.88677	12	0.281580	18	0.281561	4.3	0.6	2.23	2100	18	97	4
A182_seq4_40	0.0107	9	0.00035	2	1.46724	1.88698	13	0.281065	27	0.281048	-3.9	0.9	3.04	2531	14	97	4
A183_seq4_40	0.0273	22	0.00103	6	1.46725	1.88681	11	0.281079	22	0.281026	-1.1	0.8	3.01	2685	9	97	4
A184_seq4_40	0.0087	7	0.00032	2	1.46718	1.88664	13	0.281015	23	0.280999	-4.1	0.8	3.10	2600	10	98	4
A185_seq4_40	0.0082	7	0.00024	2	1.46720	1.88688	16	0.281016	22	0.281005	-5.3	0.8	3.12	2539	14	95	4
A186_seq4_40	0.0318	26	0.00100	6	1.46719	1.88678	12	0.280922	25	0.280869	-5.0	0.9	3.28	2757	18	94	4
A187_seq4_40	0.0160	13	0.00056	3	1.46724	1.88673	11	0.282427	23	0.282421	-0.4	0.8	1.23	560	5	96	4
A188_seq4_40	0.0287	27	0.00097	7	1.46723	1.88696	11	0.282114	25	0.282105	-13.5	0.9	1.88	475	5	101	4
A189_seq4_40	0.0114	10	0.00040	3	1.46718	1.88681	11	0.282224	26	0.282220	-8.3	0.9	1.63	525	8	101	4
A190_seq4_40	0.0169	14	0.00051	3	1.46720	1.88686	9	0.282472	25	0.282466	2.3	0.9	1.12	610	4	104	4
A191_seq4_40	0.0074	6	0.00023	1	1.46717	1.88675	12	0.281026	23	0.281017	-11.9	0.8	3.24	2238	17	94	4
A192_seq4_40	0.0138	11	0.00047	3	1.46712	1.88670	12	0.281583	22	0.281564	4.6	0.8	2.23	2109	31	98	4
A193_seq4_40	0.0154	14	0.00049	4	1.46718	1.88677	12	0.281589	22	0.281569	4.9	0.8	2.21	2117	25	99	4
A199_seq4_40	0.0328	29	0.00111	8	1.46720	1.88671	13	0.282741	22	0.282727	13.3	0.8	0.57	689	9	99	4
A200_seq4_40	0.0194	16	0.00057	4	1.46716	1.88675	13	0.281177	20	0.281149	-0.8	0.7	2.85	2514	11	100	4
A201_seq4_40	0.0418	41	0.00149	13	1.46719	1.88667	9	0.282098	30	0.282085	-13.7	1.1	1.91	496	7	79	4
A202_seq4_40	0.0199	18	0.00074	5	1.46721	1.88666	11	0.282006	28	0.281999	-15.8	1.0	2.05	541	5	100	4
A203_seq4_40	0.0133	11	0.00042	3	1.46718	1.88664	12	0.282676	19	0.282672	8.1	0.7	0.75	541	6	81	4
A204_seq4_40	0.0206	16	0.00067	4	1.46720	1.88681	10	0.282318	21	0.282312	-5.4	0.8	1.46	509	7	101	4
A205_seq4_40	0.0278	22	0.00091	5	1.46721	1.88671	15	0.281074	19	0.281055	-36.8	0.7	3.64	1090	22	50	4
A206_seq4_40	0.0083	7	0.00026	2	1.46721	1.88675	16	0.281203	21	0.281192	-5.0	0.8	2.88	2269	13	95	4
A207_seq4_40	0.0074	6	0.00023	1	1.46717	1.88682	16	0.281595	19	0.281586	3.2	0.7	2.22	2016	27	100	4
A208_seq4_40	0.0138	11	0.00046	3	1.46728	1.88676	11	0.281614	27	0.281596	5.5	0.9	2.17	2102	28	97	4
A209_seq4_40	0.0236	19	0.00075	4	1.46718	1.88687	12	0.281614	29	0.281584	5.1	1.0	2.19	2100	28	96	4
A210_seq4_40	0.0401	34	0.00129	9	1.46719	1.88670	11	0.281673	28	0.281622	5.6	1.0	2.13	2064	28	98	4
A211_seq4_40	0.0101	9	0.00027	2	1.46712	1.88671	14	0.281029	24	0.281016	-3.1	0.9	3.06	2618	12	93	4
A212_seq4_40	0.0184	15	0.00057	4	1.46715	1.88672	12	0.282193	20	0.282188	-9.1	0.7	1.69	538	5	95	4
A213_seq4_40	0.0017	1	0.00003	0	1.46719	1.88666	15	0.281158	19	0.281157	-5.7	0.7	2.94	2292	14	100	4
A214_seq4_40	0.1449	116	0.00303	18	1.46719	1.88667	9	0.282499	31	0.282499	-10.1	1.1	1.30	-	-	-	4
A215_seq4_40	0.0057	5	0.00018	1	1.46722	1.88693	12	0.281582	20	0.281575	4.6	0.7	2.21	2093	24	95	4
A216_seq4_40	0.0238	21	0.00081	5	1.46716	1.88675	10	0.282082	27	0.282074	-13.7	1.0	1.92	514	8	94	4
A217_seq4_40	0.0248	20	0.00088	5	1.46720	1.88673	17	0.281186	23	0.281142	2.0	0.8	2.80	2642	9	99	4
A218_seq4_40	0.0091	7	0.00029	2	1.46723	1.88676	11	0.282656	17	0.282653	6.6	0.6	0.80	504	8	116	4
A219_seq4_40	0.0159	13	0.00048	3	1.46720	1.88685	11	0.281195	21	0.281172	2.3	0.8	2.76	2611	11	100	4
A220_seq4_40	0.0089	7	0.00026	2	1.46717	1.88676	12	0.281233	29	0.281224	-10.3	1.0	2.95	1988	18	98	4
A221_seq4_40	0.0146	12	0.00048	3	1.46721	1.88683	16	0.281234	26	0.281216	-10.0	0.9	2.95	2016	13	99	4
A222_seq4_40	0.0205	17	0.00062	4	1.46723	1.88680	12	0.281620	26	0.281595	5.4	0.9	2.17	2097	25	96	4
A223_seq4_40	0.0261	21	0.00079	5	1.46720	1.88689	13	0.281119	25	0.281079	-0.2	0.9	2.92	2646	10	99	4
A224_seq4_40	0.0095	8	0.00031	2	1.46720	1.88677	12	0.281607	21	0.281594	5.5	0.7	2.17	2101	18	94	4
A225_seq4_40	0.0231	19	0.00073	4	1.46717	1.88673	12	0.282036	24	0.282028	-15.2	0.8	2.01	519	8	96	4
A226_seq4_40	0.0108	11	0.00035	3	1.46719	1.88672	10	0.282225	25	0.282214	15.9	0.9	1.18	1601	191	34	4
A227_seq4_40	0.0172	14	0.00057	4	1.46718	1.88687	12	0.281748	26	0.281743	-24.8	0.9	2.54	542	5	99	4
A228_seq4_40	0.0119	10	0.00044	3	1.46722	1.88679	12	0.281533	22	0.281516	1.4	0.8	2.35	2045	19	95	4
A229_seq4_40	0.0176	16	0.00058	4	1.46721	1.88675	11	0.281632	27	0.281609	4.8	0.9	2.16	2049	35	100	4
A230_seq4_40	0.0104	9	0.00037	2	1.46723	1.88658	14	0.282287	18	0.282283	-5.4	0.7	1.50	554	7	98	4
A231_seq4_40	0.0158	13	0.00046	3	1.46718	1.88683	14	0.282698	24	0.282693	8.8	0.8	0.70	541	5	91	4
A232_seq4_40	0.0134	12	0.00043	3	1.46721	1.88677	12	0.281599	23	0.281582	3.8	0.8	2.22	2051	21	98	4
A233_seq4_40	0.0307	25	0.00098	6	1.46722	1.88692	11	0.282318	24	0.282309	-5.2	0.8	1.46	520	4	93	4
A234_seq4_40	0.0120	10	0.00037	2	1.46719	1.88680	14	0.282702	22	0.282698	8.2	0.8	0.71	507	4	95	4
A235_seq4_40	0.0640	63	0.00240	20	1.46719	1.88680	10	0.281721	24	0.281628	5.1	0.9	2.13	2035	26	91	4
A236_seq4_40	0.0318	26	0.00110	7	1.46714	1.88662	13	0.281591	24	0.281546	4.9	0.8	2.24	2150	21	98	4
A237_seq4_40	0.0193	19	0.00063	5	1.46714	1.88668	11	0.281611	24	0.281587	3.9	0.9	2.21	2046	30	100	4
A243_seq4_40	0.0167	13	0.00050	3	1.46721	1.88671	14	0.282405	26	0.282400	-0.7	0.9	1.26	580	6	95	4
A244_seq4_40	0.0190	16	0.00062	4	1.46720	1.88681	14	0.282673	23	0.282666	7.9	0.8	0.76	543	5	92	4
A245_seq4_40	0.0170	14	0.00061	4	1.46719	1.88677	14	0.281580	23	0.281557	2.8	0.8	2.27	2045	25	97	4
A246_seq4_40	0.0403	33	0.00129	8	1.46716	1.88680	11	0.281618	22	0.281567	3.8	0.8	2.24	2072	14	91	4
A247_seq4_40	0.0075	6	0.00027	2	1.46724	1.88689	13	0.281577	27	0.281566	5.2	1.0	2.21	2135	33	97	4
A248_seq4_40	0.0005	0	0.00001	0	1.46717	1.88674	16	0.281197	20	0.281197	-12.4	0.7	3.02	1939	14	96	4
A249_seq4_40	0.2364	197	0.00793	50	1.46723	1.88679	13	0.282806	44	0.282725	10.0	1.6	0.64	542	6	102	4
A250_seq4_40	0.0235	19	0.00070	4	1.46716	1.88667	13	0.282670	20	0.282663	7.1	0.7	0.77	514	6	99	4

Grain	$^{176}Yb/^{177}Hf$ [a]	±2σ	$^{176}Lu/^{177}Hf$ [a]	±2σ	$^{178}Hf/^{177}Hf$	$^{180}Hf/^{177}Hf$	Sig_{Hf} [b] (V)	$^{176}Hf/^{177}Hf$	±2σ [c]	$^{176}Hf/^{177}Hf_{(t)}$ [d]	$\varepsilon Hf_{(t)}$ [d]	±2σ [c] (εHf)	T_{DM} [e] (Ga)	age [f] (Ma)	±2σ (Ma)	U-Pb [g] conc	Lu-Hf [n] seq
A251_seq4_40	0.0199	16	0.00060	4	1.46720	1.88679	12	0.280878	23	0.280845	-2.8	0.8	3.27	2889	10	96	4
A252_seq4_40	0.0434	35	0.00138	8	1.46718	1.88676	11	0.282195	28	0.282182	-9.5	1.0	1.70	533	4	98	4
A253_seq4_40	0.0073	6	0.00028	2	1.46715	1.88672	13	0.281644	20	0.281633	6.4	0.7	2.10	2080	25	95	5
A257_seq4_40	0.0181	14	0.00061	4	1.46718	1.88669	12	0.282148	21	0.282134	4.3	0.7	1.51	1219	32	96	5
A258_seq4_40	0.0106	12	0.00035	3	1.46714	1.88664	11	0.281050	26	0.281033	-1.6	0.9	3.01	2657	19	93	5
A259_seq4_40	0.0190	15	0.00071	4	1.46721	1.88684	10	0.281354	22	0.281327	-5.5	0.8	2.72	2039	14	107	5
A261_seq4_40	0.0132	11	0.00052	3	1.46725	1.88679	10	0.281579	22	0.281558	5.1	0.8	2.22	2143	25	93	5
A264_seq4_40	0.0148	13	0.00053	4	1.46707	1.88630	6	0.281046	35	0.281018	0.9	1.2	2.98	2785	15	97	5
A265_seq4_40	0.0117	10	0.00046	3	1.46714	1.88641	8	0.281213	24	0.281196	-10.9	0.8	2.99	2005	12	100	5
A267_seq4_40	0.0181	16	0.00060	4	1.46717	1.88681	12	0.281621	23	0.281597	4.9	0.8	2.18	2071	20	95	5
A274_seq4_40	0.0180	17	0.00061	5	1.46727	1.88693	11	0.281603	24	0.281578	6.0	0.9	2.18	2149	20	94	5
A275_seq4_26	0.0236	26	0.00078	7	1.46718	1.88628	6	0.281098	38	0.281057	0.6	1.4	2.94	2713	14	97	5
A276_seq4_26	0.0058	5	0.00018	1	1.46718	1.88647	6	0.281104	33	0.281097	-14.5	1.2	3.19	2002	18	100	5
A277_seq4_40	0.0308	34	0.00100	9	1.46719	1.88653	9	0.282072	23	0.282061	-11.7	0.8	1.90	626	4	101	5
A280_seq4_40	0.0117	9	0.00045	3	1.46719	1.88680	11	0.282359	23	0.282355	-4.0	0.8	1.38	504	5	99	5
A281_seq4_40	0.0262	22	0.00087	5	1.46718	1.88666	11	0.282175	25	0.282167	-10.3	0.9	1.74	517	4	97	5
A282_seq4_40	0.0204	17	0.00070	5	1.46717	1.88676	11	0.281035	20	0.280996	3.4	0.7	2.95	2923	15	95	5
A288_seq4_26	0.0116	10	0.00040	3	1.46710	1.88637	6	0.282699	31	0.282695	8.0	1.1	0.72	499	4	99	5
A289_seq4_40	0.0245	27	0.00080	7	1.46720	1.88687	14	0.281096	19	0.281055	0.1	0.7	2.95	2694	14	99	5
A290_seq4_40	0.0199	18	0.00062	4	1.46720	1.88670	13	0.281041	24	0.281010	-1.2	0.9	3.03	2707	10	97	5
A291_seq4_40	0.0323	28	0.00105	7	1.46724	1.88681	12	0.282710	19	0.282699	8.9	0.7	0.69	534	5	97	5
A292_seq4_40	0.0216	19	0.00086	6	1.46721	1.88674	14	0.281706	22	0.281697	-26.8	0.8	2.64	524	5	99	5
A293_seq4_40	0.0237	20	0.00073	5	1.46718	1.88669	11	0.282675	19	0.282668	7.5	0.7	0.76	520	5	81	5
A294_seq4_40	0.0174	14	0.00057	3	1.46719	1.88673	12	0.281572	27	0.281549	5.7	0.9	2.22	2180	23	94	5
A296_seq4_40	0.0108	9	0.00045	3	1.46716	1.88657	10	0.282715	21	0.282711	9.6	0.7	0.66	549	8	91	5
A297_seq4_26	0.0252	20	0.00102	6	1.46713	1.88652	6	0.282507	33	0.282496	2.5	1.2	1.08	569	4	99	5
A298_seq4_26	0.0116	9	0.00042	3	1.46704	1.88623	6	0.282323	29	0.282318	-4.1	1.0	1.43	557	6	93	5
A299_seq4_26	0.0091	8	0.00033	2	1.46720	1.88642	6	0.282284	30	0.282281	-6.2	1.1	1.52	522	5	99	5
A300_seq4_26	0.0129	16	0.00045	5	1.46709	1.88633	7	0.282247	28	0.282242	-6.8	1.0	1.58	556	4	101	5
A301_seq4_26	0.0125	11	0.00041	3	1.46717	1.88678	11	0.281604	30	0.281587	5.6	1.1	2.17	2118	23	93	5
A310_seq4_40	0.0121	10	0.00042	3	1.46719	1.88669	12	0.281621	22	0.281604	5.7	0.8	2.15	2097	22	96	5
A311_seq4_40	0.0114	9	0.00038	2	1.46723	1.88678	12	0.281578	25	0.281563	3.7	0.9	2.25	2072	22	93	5
A312_seq4_26	0.0120	10	0.00046	3	1.46714	1.88649	6	0.281815	32	0.281811	-22.8	1.1	2.42	522	5	100	5
A315_seq4_26	0.0254	145	0.00090	45	1.46710	1.88637	5	0.281037	45	0.280993	-5.0	1.6	3.13	2569	26	86	5
A316_seq4_26	0.0078	7	0.00028	2	1.46706	1.88608	6	0.282218	24	0.282215	-8.7	0.9	1.65	514	6	96	5
A318_seq4_26	0.0084	7	0.00030	2	1.46717	1.88664	13	0.281708	19	0.281700	-8.3	0.7	2.30	1341	58	98	5
A319_seq4_26	0.0154	19	0.00050	5	1.46707	1.88650	6	0.281052	34	0.281027	-2.9	1.2	3.04	2607	17	97	5
A323_seq4_40	0.0081	7	0.00031	2	1.46722	1.88671	11	0.281628	22	0.281615	7.0	0.8	2.11	2136	20	97	5
A325_seq4_40	0.0233	19	0.00076	5	1.46720	1.88663	14	0.282659	18	0.282651	7.7	0.6	0.78	557	5	95	5
A326_seq4_40	0.0271	25	0.00094	7	1.46719	1.88683	11	0.281638	23	0.281601	5.1	0.8	2.17	2077	24	96	5
A327_seq4_40	0.0099	8	0.00033	2	1.46724	1.88671	11	0.281037	27	0.281020	-2.0	0.9	3.03	2657	17	96	5
A334_seq4_40	0.0072	6	0.00027	2	1.46721	1.88694	11	0.281570	26	0.281559	4.0	0.9	2.24	2093	18	96	5
A335_seq4_40	0.0261	22	0.00085	5	1.46718	1.88682	12	0.281101	25	0.281058	-1.1	0.9	2.97	2639	14	99	5
A336_seq4_40	0.0135	11	0.00047	3	1.46724	1.88671	10	0.281115	23	0.281092	0.7	0.8	2.89	2664	17	96	5
A337_seq4_40	0.0287	23	0.00104	6	1.46718	1.88681	14	0.282724	21	0.282713	9.6	0.8	0.66	542	4	99	5
A338_seq4_40	0.0528	70	0.00197	27	1.46715	1.88635	11	0.281007	31	0.280898	-1.1	1.1	3.17	2880	11	96	5
A340_seq4_40	0.0392	31	0.00129	8	1.46721	1.88676	12	0.282691	26	0.282675	10.4	0.9	0.70	640	6	93	5
A344_seq4_40	0.0196	16	0.00062	4	1.46713	1.88674	9	0.282455	25	0.282447	1.6	0.9	1.16	606	4	102	5
A345_seq4_40	0.0101	8	0.00038	3	1.46726	1.88686	13	0.281573	23	0.281558	4.9	0.8	2.23	2133	26	98	5
A347_seq4_40	0.0116	9	0.00039	2	1.46724	1.88680	13	0.282637	24	0.282633	6.1	0.9	0.83	513	4	96	5
A349_seq4_40	0.0290	35	0.00097	10	1.46725	1.88683	11	0.281380	22	0.281343	-5.1	0.8	2.69	2033	18	99	5
A350_seq4_26	0.0271	26	0.00102	9	1.46716	1.88636	7	0.281629	35	0.281598	-6.8	1.2	2.41	1563	102	3	5
A351_seq4_40	0.0139	12	0.00047	3	1.46719	1.88663	11	0.281607	22	0.281588	5.0	0.8	2.19	2091	28	94	5

Grain	$^{176}Yb/^{177}Hf$ [a]	±2σ	$^{176}Lu/^{177}Hf$ [a]	±2σ	$^{178}Hf/^{177}Hf$	$^{180}Hf/^{177}Hf$	Sig_{Hf} [b] (V)	$^{176}Hf/^{177}Hf$	±2σ[c]	$^{176}Hf/^{177}Hf_{(t)}$ [d]	$\varepsilon Hf_{(t)}$ [d]	±2σ [c] (εHf)	T_{DM} [e] (Ga)	age[f] (Ma)	±2σ (Ma)	U-Pb [g] conc	Lu-Hf [h] seq

Quoted uncertainties (absolute) relate to the last quoted figure. The effect of the inter-element fractionation on Lu/Hf was estimated to be about 6 % or less based on analyses of the GJ-1 and Plesoviče zircon. Accuracy and reproducibility was checked by repeated analyses of reference zircon GJ-1 and Plesoviče (data given as mean with 2 standard deviation uncertainties).

[a] $^{176}Yb/^{177}Hf = (^{176}Yb/^{173}Yb)_{true} \times (^{173}Yb/^{177}Hf)_{meas} \times (M_{173(Yb)}/M_{177(Hf)})^{\beta(Hf)}$, $\beta(Hf) = \ln((^{179}Hf/^{177}Hf_{true})/(^{179}Hf/^{177}Hf_{measured})) / \ln(M_{179(Hf)}/M_{177(Hf)})$, M = mass of respective isotopes. The $^{176}Lu/^{177}Hf$ was calculated in a similar way using $^{175}Lu/^{177}Hf$ and β(Yb).

[b] Mean Hf signal in volts.

[c] Uncertainties are quadratic additions of the within-run precision and the daily reproducibility of the 40ppb-JMC475 solution. Uncertainties for the JMC475 quoted at 2SD (2 standard deviation).

[d] Initial $^{176}Hf/^{177}Hf$ and εHf calculated using the apparent U-Pb age determined by LA-ICP-MS dating (see column f), and the CHUR parameters: $^{176}Lu/^{177}Hf = 0.0336$, and $^{176}Hf/^{177}Hf = 0.282785$ (Bouvier et al. 2008).

[e] Two stage model age in Ga using measured $^{176}Lu/^{177}Lu$ of each spot (first stage = age of zircon), a value of 0.0113 for the average continental crust (second stage, values compiled from Rudnick and Gao (2003), and depleted mantle $^{176}Lu/^{177}Lu = 0.0379$, and $^{176}Hf/^{177}Hf = 0.283164$.

[f] Apparent U-Pb age determined by LA-ICP-MS.

[g] U-Pb age concordance (%).

[h] Sequence in which Lu-Hf analyses were performed. Standard analyses for each sequence are showed on Table 12.

Table 8

Lu, Yb and Hf LA-MC-ICPMS data of zircon cores from sample GCH-09

Grain	$^{176}Yb/^{177}Hf$ [a]	±2σ	$^{176}Lu/^{177}Hf$ [a]	±2σ	$^{178}Hf/^{177}Hf$	$^{180}Hf/^{177}Hf$	Sig_{Hf} [b] (V)	$^{176}Hf/^{177}Hf$	±2σ [c]	$^{176}Hf/^{177}Hf_{(t)}$ [d]	$\varepsilon Hf_{(t)}$ [d]	±2σ [c] (εHf)	T_{DM} [e] (Ga)	age [f] (Ma)	±2σ (Ma)	U-Pb [g] conc	Lu-Hf [n] seq
A6_seq2	0.0205	28	0.00064	8	1.46717	1.88678	12	0.281168	21	0.281137	-0.3	0.7	2.86	2550	16	99	1
A7_26_seq2	0.0209	22	0.00069	6	1.46707	1.88619	6	0.281382	25	0.281356	-4.4	0.9	2.67	2042	22	99	1
A8_40_seq2	0.0144	12	0.00047	3	1.46715	1.88682	11	0.281285	23	0.281267	-7.6	0.8	2.84	2039	20	100	1
A9_26_seq2	0.0062	7	0.00020	2	1.46710	1.88652	7	0.281067	40	0.281065	-48.8	1.4	3.82	542	8	95	1
A10_40_seq2	0.0130	11	0.00044	3	1.46718	1.88683	17	0.281197	22	0.281181	-11.5	0.8	3.02	2002	19	100	1
A11_40_seq2	0.0153	13	0.00052	3	1.46718	1.88670	12	0.282713	21	0.282708	8.7	0.7	0.69	513	9	96	1
A12_40_seq2	0.0101	8	0.00035	2	1.46719	1.88662	15	0.282667	21	0.282663	7.0	0.8	0.78	505	7	95	1
A13_40_seq2	0.0134	11	0.00045	3	1.46720	1.88685	11	0.282069	24	0.282064	-11.3	0.8	1.89	636	11	92	1
A14_40_seq2	0.0176	14	0.00059	4	1.46717	1.88689	13	0.280945	23	0.280911	1.6	0.8	3.10	2972	11	99	1
A15_40_seq2	0.0212	17	0.00066	4	1.46723	1.88687	14	0.281070	26	0.281036	-1.6	0.9	3.01	2650	12	98	1
A16_40_seq2	0.0171	14	0.00063	4	1.46717	1.88671	12	0.281594	20	0.281569	4.7	0.7	2.22	2106	17	99	1
A17_40_seq2	0.0405	33	0.00138	8	1.46714	1.88657	15	0.282646	21	0.282632	6.7	0.7	0.82	543	8	99	1
A18_40_seq2	0.0194	16	0.00062	4	1.46718	1.88674	13	0.282633	20	0.282627	7.1	0.7	0.82	568	9	99	1
A19_40_seq2	0.0316	25	0.00105	6	1.46692	1.88678	14	0.282032	122	0.282008	0.0	4.3	1.75	1225	35	99	1
A20_40_seq2	0.0186	16	0.00061	4	1.46715	1.88675	11	0.281621	27	0.281597	6.3	1.0	2.15	2135	28	99	1
A21_40_seq2	0.0109	9	0.00036	2	1.46722	1.88681	8	0.282540	33	0.282536	5.0	1.2	0.98	619	10	91	1
A22_40_seq2	0.0177	14	0.00064	4	1.46719	1.88675	13	0.282131	25	0.282118	1.1	0.9	1.59	1103	30	97	1
A23_40_seq2	0.0114	10	0.00040	3	1.46718	1.88668	11	0.282192	25	0.282188	-9.9	0.9	1.71	502	8	92	1
A24_40_seq2	0.0325	28	0.00119	8	1.46717	1.88662	10	0.281614	29	0.281567	4.4	1.0	2.23	2097	25	100	1
A25_40_seq2	0.0079	6	0.00027	2	1.46720	1.88671	12	0.282177	26	0.282174	-9.6	0.9	1.72	538	8	97	1
A26_40_seq2	0.0142	13	0.00048	4	1.46718	1.88664	12	0.281502	22	0.281483	2.1	0.8	2.38	2127	24	99	1
A27_40_seq2	0.0560	47	0.00204	13	1.46716	1.88655	10	0.282594	25	0.282572	5.1	0.9	0.93	565	9	95	1
A28_40_seq2	0.0362	31	0.00127	8	1.46713	1.88669	10	0.281719	22	0.281669	8.1	0.8	2.02	2100	20	98	1
A29_40_seq2	0.0100	8	0.00034	2	1.46718	1.88676	14	0.281518	22	0.281504	3.0	0.8	2.33	2133	13	97	1
A30_40_seq2	0.0171	14	0.00060	4	1.46712	1.88658	11	0.282210	24	0.282204	-8.9	0.9	1.67	522	8	96	1
A31_40_seq2	0.0189	17	0.00072	5	1.46716	1.88672	12	0.282406	22	0.282397	0.5	0.8	1.24	639	12	100	1
A32_40_seq2	0.0158	13	0.00052	3	1.46719	1.88678	10	0.282218	20	0.282212	-8.2	0.7	1.64	539	9	96	1
A38_40_seq2	0.0441	36	0.00140	9	1.46724	1.88683	12	0.281125	20	0.281052	0.2	0.7	2.95	2704	13	100	1
A39_40_seq2	0.0123	10	0.00041	2	1.46717	1.88675	12	0.281043	24	0.281024	-6.8	0.8	3.13	2447	12	96	1
A40_26_seq2	0.0214	20	0.00081	6	1.46712	1.88647	5	0.282705	56	0.282697	8.9	2.0	0.70	538	10	95	1
A41_40_seq2	0.0189	18	0.00073	6	1.46722	1.88691	13	0.282399	31	0.282388	2.8	1.1	1.21	752	12	97	1
A42_40_seq2	0.0076	11	0.00022	3	1.46715	1.88668	16	0.281580	20	0.281571	2.6	0.7	2.26	2011	12	87	1
A43_40_seq2	0.0137	12	0.00047	3	1.46722	1.88671	11	0.282138	24	0.282133	-11.6	0.9	1.81	515	11	94	1
A44_40_seq2	0.0213	17	0.00084	5	1.46717	1.88644	13	0.281581	24	0.281548	3.3	0.8	2.27	2077	22	100	1
A381_seq1_40	0.0089	7	0.00032	2	1.46717	1.88662	12	0.281548	27	0.281536	1.8	1.0	2.32	2035	25	98	5
A382_seq1_40	0.0109	9	0.00037	2	1.46720	1.88697	12	0.281580	25	0.281566	4.0	0.9	2.23	2082	24	97	5
A389_seq1_40	0.0145	12	0.00047	3	1.46718	1.88674	11	0.282682	23	0.282678	7.3	0.8	0.75	498	8	98	5
A394_seq1_40	0.0230	21	0.00071	5	1.46719	1.88659	10	0.282449	20	0.282442	0.8	0.7	1.18	580	9	99	5
A397_seq1_40	0.0156	15	0.00055	4	1.46723	1.88681	12	0.281627	19	0.281605	5.0	0.7	2.17	2063	24	100	5
A399_seq1_40	0.0137	17	0.00050	5	1.46720	1.88676	13	0.281077	25	0.281052	-1.0	0.9	2.98	2651	12	100	5
A404_seq1_40	0.0120	11	0.00040	3	1.46716	1.88648	12	0.281559	23	0.281544	2.3	0.8	2.30	2042	20	99	5
A406_seq1_40	0.0124	13	0.00044	4	1.46721	1.88682	13	0.281616	22	0.281598	4.3	0.8	2.19	2043	31	99	5
A410_seq1_26	0.0045	4	0.00015	1	1.46712	1.88646	7	0.281151	25	0.281146	-13.6	0.9	3.11	1966	17	99	5
A412_seq1_26	0.0120	13	0.00048	4	1.46712	1.88627	6	0.280991	37	0.280965	0.7	1.3	3.05	2856	14	101	5
A416_seq1_26	0.0147	13	0.00062	4	1.46712	1.88621	6	0.282078	30	0.282072	-13.4	1.1	1.92	530	8	98	5
A417_seq1_40	0.0120	10	0.00046	3	1.46724	1.88665	12	0.281648	22	0.281630	6.1	0.8	2.11	2074	21	98	5
A423_seq1_40	0.0150	12	0.00050	3	1.46717	1.88670	15	0.280948	17	0.280922	-4.7	0.6	3.21	2691	11	100	5
A428_seq1_40	0.0230	31	0.00077	9	1.46719	1.88669	12	0.281596	19	0.281565	4.3	0.7	2.23	2094	17	99	5
A429_seq1_40	0.0162	14	0.00058	4	1.46718	1.88685	14	0.280812	20	0.280779	-1.7	0.7	3.33	3033	10	100	5
A431_seq1_40	0.0257	22	0.00087	6	1.46714	1.88671	11	0.282275	24	0.282266	-6.5	0.9	1.54	533	8	100	5
A432_seq1_40	0.0134	12	0.00044	3	1.46720	1.88679	12	0.282647	25	0.282642	6.7	0.9	0.81	527	9	95	5
A433_seq1_40	0.0176	16	0.00063	5	1.46717	1.88669	11	0.281563	19	0.281538	4.0	0.7	2.27	2125	29	99	5
A434_seq1_40	0.0090	7	0.00031	2	1.46721	1.88671	11	0.281607	20	0.281595	3.9	0.7	2.20	2035	24	99	5
A435_seq1_40	0.0296	24	0.00101	6	1.46719	1.88678	9	0.282711	19	0.282701	8.6	0.7	0.70	517	9	99	5
A436_seq1_40	0.0122	11	0.00042	3	1.46720	1.88652	13	0.281069	21	0.281054	-19.7	0.7	3.34	1842	37	100	5
A447_seq1_40	0.0478	41	0.00160	11	1.46718	1.88671	15	0.281149	21	0.281072	-2.9	0.8	2.99	2540	27	91	5
A448_seq1_40	0.0191	16	0.00068	4	1.46721	1.88685	13	0.281077	23	0.281044	-4.1	0.8	3.05	2530	18	99	5

Grain	$^{176}Yb/^{177}Hf$ [a]	±2σ	$^{176}Lu/^{177}Hf$ [a]	±2σ	$^{178}Hf/^{177}Hf$	$^{180}Hf/^{177}Hf$	Sig_{Hf} [b] (V)	$^{176}Hf/^{177}Hf$	±2σ [c]	$^{176}Hf/^{177}Hf_{(t)}$ [d]	$\varepsilon Hf_{(t)}$ [d]	±2σ [c] (εHf)	T_{DM} [e] (Ga)	age [f] (Ma)	±2σ (Ma)	U-Pb [g] conc	Lu-Hf [h] seq
A451_seq1_40	0.0193	16	0.00065	4	1.46716	1.88654	10	0.282656	30	0.282649	7.7	1.1	0.78	561	9	96	5
A455_seq1_40	0.0348	29	0.00133	9	1.46722	1.88684	12	0.281717	22	0.281663	8.1	0.8	2.03	2109	22	100	5
A457_seq1_40	0.0549	45	0.00176	11	1.46721	1.88705	12	0.282322	37	0.282301	-3.2	1.3	1.44	625	9	100	5
A459_seq1_40	0.0216	18	0.00087	6	1.46714	1.88659	12	0.282357	21	0.282348	-3.0	0.7	1.37	557	9	97	5
A460_seq1_40	0.0181	15	0.00065	4	1.46718	1.88676	13	0.281604	21	0.281578	5.1	0.7	2.20	2113	17	100	5
A461_seq1_40	0.0147	12	0.00051	3	1.46719	1.88666	13	0.281402	21	0.281382	-3.8	0.8	2.62	2027	15	95	5
A462_seq1_40	0.0093	8	0.00029	2	1.46718	1.88662	12	0.282017	24	0.282012	-6.2	0.9	1.86	947	17	99	5
A465_seq1_40	0.0162	17	0.00056	5	1.46720	1.88687	12	0.281597	26	0.281575	4.8	0.9	2.21	2103	26	100	5
A467_seq1_40	0.0206	17	0.00079	5	1.46716	1.88671	13	0.282275	21	0.282268	-6.9	0.8	1.55	510	7	98	5
A468_seq1_40	0.0091	7	0.00027	2	1.46720	1.88658	16	0.281007	23	0.280995	-12.0	0.8	3.27	2265	11	91	5
A469_seq1_40	0.0100	8	0.00033	2	1.46718	1.88654	12	0.281321	21	0.281308	-5.8	0.7	2.75	2055	23	100	5
A470_seq1_40	0.0239	19	0.00081	5	1.46721	1.88674	14	0.282656	25	0.282648	6.9	0.9	0.80	528	7	100	5
A471_seq1_40	0.0108	9	0.00035	2	1.46718	1.88667	13	0.281019	28	0.281001	-3.5	1.0	3.09	2623	15	98	5
A472_seq1_40	0.0560	45	0.00183	11	1.46723	1.88667	10	0.282338	21	0.282319	-4.2	0.8	1.43	548	9	99	5
A476_seq1_40	0.0394	33	0.00145	9	1.46724	1.88678	11	0.281663	26	0.281606	4.7	0.9	2.17	2050	16	100	5
A477_seq1_40	0.0100	8	0.00033	2	1.46723	1.88678	12	0.281047	22	0.281031	-2.2	0.8	3.03	2633	16	99	5
A479_seq1_40	0.0299	28	0.00097	7	1.46718	1.88668	11	0.281487	27	0.281449	-1.8	1.0	2.50	2009	22	100	5
A480_seq1_40	0.0094	8	0.00033	2	1.46719	1.88678	14	0.281062	19	0.281046	-3.1	0.7	3.02	2571	12	100	5
A483_seq1_26	0.0219	19	0.00074	5	1.46714	1.88651	7	0.281052	23	0.281016	-4.2	0.8	3.09	2568	15	99	5
A484_seq1_26	0.0245	26	0.00081	7	1.46711	1.88621	6	0.281089	29	0.281049	-2.2	1.0	3.00	2607	12	99	5
A485_seq1_40	0.0138	11	0.00046	3	1.46723	1.88667	12	0.281349	18	0.281332	-6.2	0.7	2.73	2000	24	100	5
A486_seq1_40	0.0185	16	0.00059	4	1.46716	1.88645	11	0.282359	22	0.282352	-2.6	0.8	1.36	570	10	100	5
A487_seq1_40	0.0154	19	0.00054	6	1.46719	1.88661	11	0.281606	24	0.281585	4.2	0.8	2.21	2063	19	99	5
A488_seq1_40	0.0340	33	0.00111	9	1.46723	1.88695	15	0.281113	20	0.281058	-2.1	0.7	2.99	2595	10	101	5
A489_seq1_40	0.0275	35	0.00084	10	1.46719	1.88675	13	0.281089	25	0.281047	-2.5	0.9	3.01	2594	13	100	5
A490_seq1_40	0.0135	11	0.00043	3	1.46717	1.88661	14	0.282572	22	0.282567	4.4	0.8	0.95	543	9	99	5
A491_seq1_40	0.0344	30	0.00121	8	1.46717	1.88650	12	0.281607	20	0.281560	2.8	0.7	2.27	2039	25	100	5
A492_seq1_40	0.0095	8	0.00029	2	1.46722	1.88677	12	0.281951	26	0.281943	4.3	0.9	1.75	1513	25	100	5
A493_seq1_40	0.0241	22	0.00084	6	1.46713	1.88622	6	0.282258	33	0.282246	-2.7	1.2	1.50	732	11	100	5

Quoted uncertainties (absolute) relate to the last quoted figure. The effect of the inter-element fractionation on Lu/Hf was estimated to be about 6 % or less based on analyses of the GJ-1 and Plesoviče zircon. Accuracy and reproducibility was checked by repeated analyses of reference zircon GJ-1 and Plesoviče (data given as mean with 2 standard deviation uncertainties).

(a) $^{176}Yb/^{177}Hf = (^{176}Yb/^{173}Yb)_{true} \times (^{173}Yb/^{177}Hf)_{meas} \times (M_{173(Yb)}/M_{177(Hf)})^{\beta(Hf)}$, $\beta(Hf) = \ln((^{179}Hf/^{177}Hf_{true})/(^{179}Hf/^{177}Hf_{measured})) / \ln(M_{179(Hf)}/M_{177(Hf)})$, M = mass of respective isotopes. The $^{176}Lu/^{177}Hf$ was calculated in a similar way using $^{175}Lu/^{177}Hf$ and β(Yb).

(b) Mean Hf signal in volts.

(c) Uncertainties are quadratic additions of the within-run precision and the daily reproducibility of the 40ppb-JMC475 solution. Uncertainties for the JMC475 quoted at 2SD (2 standard deviation).

(d) Initial $^{176}Hf/^{177}Hf$ and εHf calculated using the apparent U-Pb age determined by LA-ICP-MS dating (see column f), and the CHUR parameters: $^{176}Lu/^{177}Hf = 0.0336$, and $^{176}Hf/^{177}Hf = 0.282785$ (Bouvier et al. 2008).

(e) Two stage model age in Ga using measured $^{176}Lu/^{177}Lu$ of each spot (first stage = age of zircon), a value of 0.0113 for the average continental crust (second stage, values compiled from Rudnick and Gao (2003), and depleted mantle $^{176}Lu/^{177}Lu = 0.0379$, and $^{176}Hf/^{177}Hf = 0.283164$.

(f) Apparent U-Pb age determined by LA-ICP-MS.

(g) U-Pb age concordance (%).

(h) Sequence in which Lu-Hf analyses were performed. Standard analyses for each sequence are showed on Table 12.

Table 9

Lu, Yb and Hf LA-MC-ICPMS data of zircon cores from sample GCH-10

Grain	$^{176}Yb/^{177}Hf$ [a]	±2σ	$^{176}Lu/^{177}Hf$ [a]	±2σ	$^{178}Hf/^{177}Hf$	$^{180}Hf/^{177}Hf$	Sig_{Hf} [b] (V)	$^{176}Hf/^{177}Hf$	±2σ [c]	$^{176}Hf/^{177}Hf_{(t)}$ [d]	$\varepsilon Hf_{(t)}$ [d]	±2σ [c] (εHf)	T_{DM} [e] (Ga)	age [f] (Ma)	±2σ (Ma)	U-Pb [g] conc	Lu-Hf [n] seq
A166_seq3_40	0.0093	7	0.00034	2	1.46713	1.88662	13	0.281557	29	0.281543	2.5	1.0	2.29	2051	29	96	3
A167_seq3_40	0.0132	11	0.00044	3	1.46711	1.88669	15	0.281140	18	0.281123	-12.9	0.7	3.12	2030	15	93	3
A168_seq3_40	0.0160	13	0.00057	4	1.46721	1.88683	11	0.281615	25	0.281593	4.7	0.9	2.19	2072	33	98	3
A170_seq3_40	0.0336	28	0.00109	7	1.46717	1.88665	11	0.282297	23	0.282286	-5.7	0.8	1.50	535	8	101	3
A176_seq3_40	0.0157	14	0.00053	4	1.46717	1.88665	12	0.281566	21	0.281545	4.0	0.7	2.26	2112	25	99	3
A177_seq3_40	0.0174	14	0.00062	4	1.46714	1.88652	12	0.281546	23	0.281521	3.5	0.8	2.30	2129	26	97	3
A178_seq3_40	0.0269	22	0.00104	6	1.46715	1.88682	19	0.282615	17	0.282604	6.4	0.6	0.86	574	7	96	3
A179_seq3_40	0.0066	6	0.00022	1	1.46714	1.88661	10	0.282189	25	0.282187	-8.8	0.9	1.69	553	11	94	3
A182_seq3_40	0.0143	13	0.00049	4	1.46718	1.88671	11	0.281562	20	0.281543	3.1	0.7	2.28	2079	29	98	3
A188_seq3_40	0.0263	23	0.00091	6	1.46717	1.88653	12	0.281061	25	0.281015	-2.9	0.9	3.06	2625	13	83	3
A190_seq3_40	0.0314	28	0.00105	8	1.46712	1.88661	11	0.282562	20	0.282551	4.1	0.7	0.98	554	8	92	3
A193_seq3_40	0.0102	9	0.00037	2	1.46712	1.88680	8	0.281403	26	0.281388	0.0	0.9	2.54	2183	55	101	3
A201_seq3_40	0.0022	7	0.00006	2	1.46713	1.88673	14	0.281053	24	0.281049	-3.1	0.9	3.02	2564	20	100	3
A204_seq3_40	0.0211	18	0.00078	5	1.46711	1.88678	11	0.282173	26	0.282165	-9.3	0.9	1.72	567	7	96	3
A208_seq3_40	0.0093	8	0.00038	3	1.46716	1.88638	10	0.281591	25	0.281576	4.8	0.9	2.21	2100	35	97	3
A210_seq3_40	0.0106	10	0.00038	3	1.46722	1.88654	12	0.281559	21	0.281543	4.2	0.8	2.26	2124	25	98	3
A214_seq3_40	0.0712	68	0.00225	17	1.46711	1.88661	10	0.282504	22	0.282504	-9.9	0.8	1.29	-	-	-	3
A220_seq3_40	0.0295	27	0.00101	8	1.46711	1.88683	11	0.281642	24	0.281603	5.4	0.9	2.16	2086	15	99	3
A228_seq3_40	0.0089	7	0.00030	2	1.46716	1.88664	10	0.281049	26	0.281035	-6.3	0.9	3.10	2453	18	94	3
A229_seq3_40	0.0433	35	0.00148	9	1.46714	1.88664	10	0.281611	26	0.281552	4.0	0.9	2.25	2103	18	97	3
A234_seq3_40	0.0288	26	0.00114	8	1.46717	1.88663	14	0.282505	19	0.282493	2.5	0.7	1.08	577	8	102	3
A235_seq3_40	0.0283	25	0.00089	6	1.46716	1.88663	12	0.282085	22	0.282066	-0.1	0.8	1.68	1128	39	100	3
A248_seq3_40	0.0191	16	0.00065	4	1.46714	1.88659	13	0.281576	24	0.281550	4.1	0.8	2.25	2113	26	99	3
A249_seq3_40	0.0284	24	0.00112	7	1.46715	1.88672	14	0.282370	28	0.282358	-2.4	1.0	1.35	572	8	95	3
A251_seq3_40	0.0347	40	0.00121	12	1.46716	1.88671	8	0.282564	26	0.282551	4.2	0.9	0.97	560	7	100	3
A253_seq3_40	0.0168	15	0.00059	4	1.46692	1.88567	10	0.282056	54	0.282051	-15.1	1.9	1.97	490	7	93	3
A260_seq3_40	0.0046	4	0.00012	1	1.46715	1.88664	16	0.281974	21	0.281972	-1.8	0.7	1.83	1203	19	100	3
A263_seq3_40	0.0288	24	0.00117	7	1.46708	1.88623	10	0.281618	27	0.281571	5.1	0.9	2.21	2124	25	97	3
A272_seq3_40	0.0248	20	0.00095	6	1.46716	1.88653	13	0.281643	21	0.281606	4.1	0.7	2.18	2026	19	83	3
A280_seq3_40	0.0153	12	0.00048	3	1.46719	1.88670	13	0.280753	20	0.280727	-10.1	0.7	3.56	2754	11	100	3
A281_seq3_40	0.0100	8	0.00040	2	1.46717	1.88674	14	0.281571	25	0.281555	2.8	0.9	2.27	2049	21	99	3
A288_seq3_40	0.0197	16	0.00073	4	1.46718	1.88670	13	0.281998	21	0.281977	5.5	0.7	1.69	1512	32	100	3
A291_seq3_40	0.0140	11	0.00047	3	1.46714	1.88671	12	0.281517	23	0.281499	-1.8	0.8	2.43	1933	22	98	3
A293_seq3_40	0.0358	33	0.00120	9	1.46713	1.88658	12	0.282378	29	0.282365	-1.8	1.0	1.33	585	8	82	3
A294_seq3_40	0.0104	8	0.00035	2	1.46713	1.88658	11	0.281968	29	0.281961	-7.2	1.0	1.95	980	27	-124	3
A295_seq3_40	0.0135	12	0.00052	4	1.46713	1.88643	13	0.282226	26	0.282221	-7.8	0.9	1.62	544	7	97	3
A296_seq3_40	0.0249	28	0.00089	9	1.46712	1.88653	10	0.281589	22	0.281560	-5.2	0.8	2.42	1691	195	97	3
A298_seq3_40	0.0236	20	0.00075	5	1.46716	1.88673	15	0.281560	39	0.281530	3.4	1.4	2.29	2112	18	100	3
A305_seq3_40	0.0111	9	0.00036	2	1.46714	1.88661	12	0.281014	25	0.280997	-4.3	0.9	3.11	2593	12	93	3
A308_seq3_40	0.0097	8	0.00032	2	1.46720	1.88655	13	0.281007	22	0.280992	-5.2	0.8	3.14	2562	11	95	3
A309_seq3_40	0.0252	27	0.00095	8	1.46714	1.88671	9	0.282022	27	0.282012	-15.2	0.9	2.03	542	7	100	3
A310_seq3_40	0.0523	42	0.00163	10	1.46720	1.88672	11	0.282684	23	0.282666	8.5	0.8	0.74	567	6	97	3
A315_seq3_40	0.0176	21	0.00065	7	1.46717	1.88655	8	0.282462	29	0.282456	0.5	1.0	1.17	543	9	100	3
A318_seq3_40	0.0258	21	0.00082	5	1.46710	1.88658	11	0.282310	27	0.282300	-2.4	0.9	1.42	663	8	100	3
A327_seq3_40	0.0316	29	0.00117	9	1.46712	1.88664	8	0.282475	31	0.282460	4.2	1.1	1.09	703	9	94	3
A335_seq3_40	0.0138	11	0.00047	3	1.46716	1.88678	11	0.281617	23	0.281599	4.7	0.8	2.18	2062	21	100	3
A339_seq3_40	0.0208	17	0.00067	4	1.46712	1.88654	14	0.281911	25	0.281892	1.2	0.9	1.88	1455	18	93	3
A343_seq3_40	0.0398	35	0.00152	11	1.46721	1.88683	17	0.281611	26	0.281551	3.5	0.9	2.26	2081	13	99	3

Grain	$\frac{^{176}Yb}{^{177}Hf}$ [a]	±2σ	$\frac{^{176}Lu}{^{177}Hf}$ [a]	±2σ	$\frac{^{178}Hf}{^{177}Hf}$	$\frac{^{180}Hf}{^{177}Hf}$	Sig_{Hf} [b] (V)	$\frac{^{176}Hf}{^{177}Hf}$	±2σ [c]	$\frac{^{176}Hf}{^{177}Hf_{(t)}}$ [d]	$\varepsilon Hf_{(t)}$ [d]	±2σ [c] (εHf)	T_{DM} [e] (Ga)	age [f] (Ma)	±2σ (Ma)	U-Pb [g] conc	Lu-Hf [h] seq

Quoted uncertainties (absolute) relate to the last quoted figure. The effect of the inter-element fractionation on Lu/Hf was estimated to be about 6 % or less based on analyses of the GJ-1 and Plesoviče zircon. Accuracy and reproducibility was checked by repeated analyses of reference zircon GJ-1 and Plesoviče (data given as mean with 2 standard deviation uncertainties).

(a) $^{176}Yb/^{177}Hf = (^{176}Yb/^{173}Yb)_{true} \times (^{173}Yb/^{177}Hf)_{meas} \times (M_{173(Yb)}/M_{177(Hf)})^{\beta(Hf)}$, $\beta(Hf) = \ln((^{179}Hf/^{177}Hf_{true})/(^{179}Hf/^{177}Hf_{measured})) / \ln(M_{179(Hf)}/M_{177(Hf)})$, M = mass of respective isotopes. The $^{176}Lu/^{177}Hf$ was calculated in a similar way using $^{175}Lu/^{177}Hf$ and β(Yb).

(b) Mean Hf signal in volts.

(c) Uncertainties are quadratic additions of the within-run precision and the daily reproducibility of the 40ppb-JMC475 solution. Uncertainties for the JMC475 quoted at 2SD (2 standard deviation).

(d) Initial $^{176}Hf/^{177}Hf$ and εHf calculated using the apparent U-Pb age determined by LA-ICP-MS dating (see column f), and the CHUR parameters: $^{176}Lu/^{177}Hf = 0.0336$, and $^{176}Hf/^{177}Hf = 0.282785$ (Bouvier et al. 2008).

(e) Two stage model age in Ga using measured $^{176}Lu/^{177}Lu$ of each spot (first stage = age of zircon), a value of 0.0113 for the average continental crust (second stage, values compiled from Rudnick and Gao (2003), and depleted mantle $^{176}Lu/^{177}Lu = 0.0379$, and $^{176}Hf/^{177}Hf = 0.283164$.

(f) Apparent U-Pb age determined by LA-ICP-MS.

(g) U-Pb age concordance (%).

(h) Sequence in which Lu-Hf analyses were performed. Standard analyses for each sequence are showed on Table 12.

Table 10

Lu, Yb and Hf LA-MC-ICPMS data of zircon cores from sample GCH-11

Grain	$^{176}Yb/^{177}Hf$ [a]	±2σ	$^{176}Lu/^{177}Hf$ [a]	±2σ	$^{178}Hf/^{177}Hf$	$^{180}Hf/^{177}Hf$	Sig_{Hf} [b] (V)	$^{176}Hf/^{177}Hf$	±2σ [c]	$^{176}Hf/^{177}Hf_{(t)}$ [d]	$\varepsilon Hf_{(t)}$ [d]	±2σ [c] (εHf)	T_{DM} [e] (Ga)	age [f] (Ma)	±2σ (Ma)	U-Pb [g] conc	Lu-Hf [n] seq
A369_seq4_40	0.0176	20	0.00059	5	1.46713	1.88679	12	0.282408	23	0.282402	-2.3	0.8	1.29	504	4	96	4
A370_seq4_40	0.0316	25	0.00112	7	1.46714	1.88689	9	0.281623	23	0.281578	4.8	0.8	2.20	2099	25	96	4
A371_seq4_40	0.0067	6	0.00030	2	1.46726	1.88696	14	0.281586	27	0.281574	4.9	1.0	2.21	2110	19	95	4
A372_seq4_40	0.0164	15	0.00060	4	1.46719	1.88686	14	0.282023	23	0.282017	-15.4	0.8	2.02	529	4	96	4
A373_seq4_40	0.0257	21	0.00095	6	1.46721	1.88672	11	0.281647	26	0.281609	5.2	0.9	2.16	2067	31	97	4
A374_seq4_40	0.0164	13	0.00055	3	1.46717	1.88665	11	0.282203	24	0.282197	-9.5	0.9	1.69	505	8	98	4
A375_seq4_40	0.0050	4	0.00017	1	1.46719	1.88667	13	0.280906	22	0.280896	-2.8	0.8	3.20	2810	20	97	4
A376_seq4_40	0.0089	8	0.00029	2	1.46721	1.88683	15	0.281611	22	0.281600	5.1	0.8	2.17	2076	11	94	4
A377_seq4_40	0.0537	46	0.00173	11	1.46721	1.88689	11	0.281807	27	0.281748	3.4	1.0	2.02	1776	18	99	4
A378_seq4_40	0.0212	20	0.00066	5	1.46720	1.88684	12	0.281609	24	0.281583	4.5	0.8	2.20	2076	21	96	4
A379_seq4_40	0.0088	7	0.00031	2	1.46716	1.88670	13	0.281581	21	0.281569	3.3	0.7	2.24	2047	29	99	4
A380_seq4_40	0.0178	15	0.00055	4	1.46720	1.88703	11	0.281202	20	0.281180	-10.5	0.7	3.00	2046	26	98	4
A381_seq4_40	0.0111	9	0.00038	2	1.46713	1.88661	11	0.281561	26	0.281546	3.6	0.9	2.27	2094	23	97	4
A382_seq4_40	0.0204	21	0.00066	6	1.46710	1.88672	13	0.282005	20	0.281998	-15.9	0.7	2.06	535	7	97	4
A388_seq4_40	0.0101	8	0.00032	2	1.46714	1.88672	13	0.281160	21	0.281144	0.0	0.7	2.84	2552	13	98	4
A389_seq4_40	0.0615	52	0.00231	15	1.46711	1.88669	10	0.281667	23	0.281572	6.3	0.8	2.18	2171	14	95	4
A390_seq4_40	0.0359	30	0.00106	7	1.46717	1.88660	10	0.280946	28	0.280886	-1.0	1.0	3.18	2902	11	97	4
A391_seq4_40	0.0127	10	0.00040	2	1.46719	1.88679	14	0.282132	21	0.282128	-11.4	0.7	1.81	532	4	94	4
A392_seq4_40	0.0161	13	0.00058	3	1.46719	1.88681	13	0.282693	22	0.282687	8.5	0.8	0.72	534	4	90	4
A393_seq4_40	0.0139	11	0.00044	3	1.46716	1.88669	9	0.282441	26	0.282436	0.8	0.9	1.19	591	8	93	4
A394_seq4_40	0.0149	13	0.00046	3	1.46716	1.88670	11	0.282204	24	0.282199	-9.2	0.9	1.68	518	6	99	4
A395_seq4_40	0.0096	8	0.00033	2	1.46716	1.88659	15	0.281157	22	0.281144	-12.7	0.8	3.09	2007	17	100	4
A396_seq4_40	0.0195	16	0.00061	4	1.46715	1.88679	11	0.282230	24	0.282224	-8.1	0.9	1.63	527	6	100	4
A397_seq4_40	0.0221	18	0.00068	4	1.46717	1.88672	12	0.282736	23	0.282730	9.3	0.8	0.65	505	5	95	4
A398_seq4_40	0.0053	4	0.00019	1	1.46720	1.88700	12	0.281570	25	0.281563	5.0	0.9	2.22	2131	35	96	4
A399_seq4_40	0.0210	17	0.00064	4	1.46717	1.88691	11	0.282410	27	0.282403	-0.6	1.0	1.26	580	7	58	4
A400_seq4_40	0.0170	14	0.00055	3	1.46718	1.88690	11	0.281046	23	0.281015	4.3	0.8	2.91	2930	18	100	4
A401_seq4_40	0.0071	7	0.00026	2	1.46726	1.88689	11	0.281590	25	0.281579	4.6	0.9	2.21	2087	24	91	4
A402_seq4_40	0.0070	6	0.00023	1	1.46720	1.88674	14	0.281668	25	0.281661	-3.1	0.9	2.26	1627	40	86	4
A403_seq4_40	0.0281	23	0.00090	5	1.46724	1.88696	18	0.281643	17	0.281608	4.8	0.6	2.17	2051	12	95	4
A404_seq4_40	0.0109	9	0.00034	2	1.46719	1.88673	13	0.282416	21	0.282412	-0.7	0.8	1.25	560	5	99	4
A405_seq4_40	0.0103	8	0.00029	2	1.46711	1.88673	16	0.281088	20	0.281074	-3.8	0.7	3.00	2500	11	93	4
A406_seq4_40	0.0100	9	0.00033	2	1.46714	1.88680	13	0.281570	22	0.281557	5.5	0.8	2.22	2159	18	97	4
A407_seq4_40	0.0098	8	0.00032	2	1.46717	1.88669	15	0.281603	24	0.281591	5.1	0.8	2.18	2090	38	95	4
A408_seq4_40	0.0089	7	0.00027	2	1.46715	1.88653	12	0.281039	19	0.281026	-3.0	0.7	3.05	2606	13	95	4
A409_seq4_40	0.0051	4	0.00014	1	1.46718	1.88680	16	0.280999	18	0.280993	-11.2	0.6	3.25	2303	16	91	4
A410_seq4_40	0.0112	9	0.00038	2	1.46713	1.88669	12	0.281599	22	0.281584	4.9	0.8	2.19	2093	28	97	4
A411_seq4_40	0.0130	11	0.00043	3	1.46712	1.88667	13	0.281562	25	0.281545	4.6	0.9	2.25	2139	15	90	4
A412_seq4_40	0.0516	44	0.00179	12	1.46724	1.88673	10	0.282085	27	0.282066	-13.0	0.9	1.92	558	6	97	4
A413_seq4_40	0.0075	7	0.00030	2	1.46711	1.88672	11	0.282653	21	0.282650	7.0	0.8	0.79	528	5	99	4
A414_seq4_40	0.0080	7	0.00027	2	1.46717	1.88683	13	0.281605	20	0.281595	5.1	0.7	2.18	2087	23	93	4
A415_seq4_40	0.0254	23	0.00082	6	1.46719	1.88667	10	0.282176	28	0.282168	-10.8	1.0	1.75	496	5	92	4
A416_seq4_40	0.0160	19	0.00054	6	1.46724	1.88699	12	0.282284	17	0.282279	-6.5	0.6	1.53	509	5	92	4
A417_seq4_40	0.0190	16	0.00062	4	1.46717	1.88651	14	0.281066	20	0.281034	-1.8	0.7	3.01	2642	13	99	4
A418_seq4_40	0.0234	19	0.00076	5	1.46717	1.88684	16	0.281296	21	0.281267	-8.3	0.8	2.85	2009	11	100	4
A419_seq4_40	0.0088	7	0.00032	2	1.46711	1.88670	14	0.281757	26	0.281754	-25.1	0.9	2.53	510	5	94	4
A420_seq4_40	0.0503	41	0.00156	10	1.46717	1.88688	18	0.281125	21	0.281044	0.0	0.7	2.96	2706	11	98	4
A421_seq4_40	0.0107	9	0.00028	2	1.46722	1.88675	13	0.282387	24	0.282384	-0.5	0.9	1.28	613	8	93	4
A422_seq4_40	0.0200	16	0.00070	4	1.46715	1.88675	15	0.281591	22	0.281562	5.2	0.8	2.21	2139	15	97	4
A423_seq4_40	0.0098	8	0.00033	2	1.46714	1.88661	13	0.281586	25	0.281574	2.4	0.9	2.26	2001	50	98	4
A424_seq4_40	0.0113	9	0.00037	2	1.46716	1.88671	14	0.281603	21	0.281588	5.5	0.8	2.18	2111	21	95	4
A425_seq4_40	0.0018	1	0.00003	0	1.46719	1.88668	15	0.280921	21	0.280920	-9.1	0.7	3.30	2508	13	91	4
A426_seq4_40	0.0023	2	0.00006	0	1.46719	1.88691	16	0.280958	26	0.280955	-5.7	0.9	3.19	2596	9	93	4
A427_seq4_40	0.0190	15	0.00063	4	1.46720	1.88686	12	0.281597	23	0.281572	4.2	0.8	2.22	2082	28	97	4
A428_seq4_40	0.0133	28	0.00048	9	1.46714	1.88653	13	0.281516	24	0.281497	1.6	0.9	2.37	2084	19	91	4
A429_seq4_40	0.0091	7	0.00027	2	1.46715	1.88663	13	0.281242	32	0.281232	-10.3	1.1	2.94	1976	28	96	4
A430_seq4_40	0.0103	8	0.00032	2	1.46718	1.88669	14	0.281240	27	0.281228	-10.0	1.0	2.93	1998	14	98	4

Grain	$^{176}Yb/^{177}Hf$ [a]	±2σ	$^{176}Lu/^{177}Hf$ [a]	±2σ	$^{178}Hf/^{177}Hf$	$^{180}Hf/^{177}Hf$	Sig_{Hf} [b] (V)	$^{176}Hf/^{177}Hf$	±2σ [c]	$^{176}Hf/^{177}Hf_{(t)}$ [d]	$\varepsilon Hf_{(t)}$ [d]	±2σ [c] (εHf)	T_{DM} [e] (Ga)	age [f] (Ma)	±2σ (Ma)	U-Pb [g] conc	Lu-Hf [h] seq
A431_seq4_40	0.0137	16	0.00042	4	1.46727	1.88718	12	0.281001	33	0.280980	-2.4	1.2	3.09	2703	20	75	4
A432_seq4_40	0.0156	13	0.00051	3	1.46718	1.88663	17	0.282084	19	0.282079	-12.9	0.7	1.90	541	5	99	4
A433_seq4_26	0.0056	7	0.00019	2	1.46721	1.88633	8	0.281532	28	0.281524	1.5	1.0	2.34	2040	35	98	4
A434_seq4_40	0.0306	25	0.00101	6	1.46721	1.88684	16	0.281575	21	0.281535	2.6	0.7	2.30	2069	20	99	4
A435_seq4_40	0.0018	2	0.00003	0	1.46718	1.88678	14	0.281157	26	0.281155	-5.3	0.9	2.93	2310	11	90	4
A436_seq4_26	0.0074	6	0.00024	2	1.46709	1.88634	8	0.281372	29	0.281362	-2.8	1.0	2.63	2101	31	88	4
A437_seq4_40	0.0215	18	0.00065	4	1.46721	1.88672	12	0.281441	28	0.281416	-2.8	1.0	2.56	2016	17	98	4
A438_seq4_40	0.0182	15	0.00054	3	1.46720	1.88667	17	0.282165	17	0.282155	0.7	0.6	1.55	1027	23	95	4
A444_seq4_40	0.0225	21	0.00074	6	1.46723	1.88686	10	0.281297	27	0.281268	-7.7	0.9	2.84	2035	17	97	5
A446_seq4_40	0.0164	23	0.00059	7	1.46724	1.88685	12	0.281586	22	0.281562	3.8	0.8	2.24	2081	22	98	5
A447_seq4_40	0.0083	7	0.00029	2	1.46718	1.88679	13	0.281027	24	0.281013	-7.2	0.8	3.15	2446	11	92	5
A448_seq4_40	0.0124	10	0.00042	3	1.46717	1.88674	14	0.281605	23	0.281598	-22.6	0.8	2.69	870	10	99	5
A453_seq4_40	0.0168	13	0.00058	4	1.46717	1.88670	11	0.282380	24	0.282374	-2.9	0.8	1.34	519	6	73	5
A456_seq4_40	0.0142	12	0.00047	3	1.46721	1.88688	14	0.281220	26	0.281202	-10.1	0.9	2.97	2030	13	92	5
A458_seq4_40	0.0336	29	0.00107	7	1.46725	1.88713	14	0.281052	31	0.280997	-2.5	1.1	3.07	2669	17	95	5
A459_seq4_40	0.0234	23	0.00077	6	1.46719	1.88689	12	0.281611	23	0.281581	4.6	0.8	2.20	2082	22	97	5
A460_seq4_40	0.0144	13	0.00051	3	1.46715	1.88678	12	0.281566	20	0.281545	3.5	0.7	2.27	2091	27	97	5
A461_seq4_40	0.0232	29	0.00089	10	1.46720	1.88707	15	0.282475	30	0.282463	4.3	1.1	1.09	701	7	92	5
A462_seq4_40	0.0076	6	0.00029	2	1.46724	1.88661	12	0.281610	21	0.281598	5.8	0.7	2.16	2112	24	92	5
A463_seq4_40	0.0256	31	0.00084	10	1.46725	1.88709	8	0.281191	46	0.281148	2.5	1.6	2.79	2654	10	101	5
A465_seq4_40	0.0092	9	0.00028	2	1.46714	1.88649	15	0.281257	23	0.281246	-8.5	0.8	2.88	2033	19	97	5
A468_seq4_40	0.0278	22	0.00089	5	1.46723	1.88674	10	0.282047	24	0.282024	4.3	0.9	1.65	1389	47	91	5
A474_seq4_40	0.0477	43	0.00155	11	1.46718	1.88669	10	0.282227	25	0.282192	5.7	0.9	1.41	1187	48	97	5
A479_seq4_40	0.0145	16	0.00043	4	1.46717	1.88659	11	0.281082	30	0.281061	-5.0	1.1	3.04	2467	21	84	5
A482_seq4_40	0.0189	15	0.00062	4	1.46717	1.88657	13	0.281600	19	0.281576	4.0	0.7	2.22	2069	16	98	5
A483_seq4_40	0.0139	11	0.00043	3	1.46722	1.88666	11	0.282522	22	0.282518	3.0	0.8	1.04	559	7	93	5
A484_seq4_40	0.0113	9	0.00037	2	1.46717	1.88672	15	0.281050	21	0.281032	-2.1	0.7	3.02	2634	10	94	5
A485_seq4_40	0.0561	46	0.00182	11	1.46721	1.88676	14	0.281134	26	0.281044	-2.9	0.9	3.02	2582	11	92	5
A486_seq4_40	0.0174	14	0.00055	3	1.46718	1.88653	11	0.281436	22	0.281415	-2.5	0.8	2.55	2033	32	100	5
A489_seq4_40	0.0248	21	0.00094	6	1.46721	1.88682	13	0.281617	21	0.281581	3.7	0.7	2.22	2044	21	100	5
A491_seq4_40	0.0205	18	0.00070	5	1.46718	1.88671	12	0.281607	20	0.281579	4.9	0.7	2.20	2103	17	96	5
A502_seq4_40	0.0146	12	0.00050	3	1.46719	1.88675	11	0.281558	26	0.281538	2.7	0.9	2.30	2066	20	97	5
A504_seq4_40	0.0134	15	0.00057	5	1.46717	1.88673	13	0.282347	19	0.282339	0.3	0.7	1.32	718	5	99	5

Quoted uncertainties (absolute) relate to the last quoted figure. The effect of the inter-element fractionation on Lu/Hf was estimated to be about 6 % or less based on analyses of the GJ-1 and Plesoviče zircon. Accuracy and reproducibility was checked by repeated analyses of reference zircon GJ-1 and Plesoviče (data given as mean with 2 standard deviation uncertainties).

(a) $^{176}Yb/^{177}Hf = (^{176}Yb/^{173}Yb)_{true} \times (^{173}Yb/^{177}Hf)_{meas} \times (M_{173(Yb)}/M_{177(Hf)})^{\beta(Hf)}$, $\beta(Hf) = \ln((^{179}Hf/^{177}Hf_{true})/(^{179}Hf/^{177}Hf_{measured})) / \ln(M_{179(Hf)}/M_{177(Hf)})$, M = mass of respective isotopes. The $^{176}Lu/^{177}Hf$ was calculated in a similar way using $^{175}Lu/^{177}Hf$ and β(Yb).

(b) Mean Hf signal in volts.

(c) Uncertainties are quadratic additions of the within-run precision and the daily reproducibility of the 40ppb-JMC475 solution. Uncertainties for the JMC475 quoted at 2SD (2 standard deviation).

(d) Initial $^{176}Hf/^{177}Hf$ and εHf calculated using the apparent U-Pb age determined by LA-ICP-MS dating (see column f), and the CHUR parameters: $^{176}Lu/^{177}Hf = 0.0336$, and $^{176}Hf/^{177}Hf = 0.282785$ (Bouvier et al. 2008).

(e) Two stage model age in Ga using measured $^{176}Lu/^{177}Lu$ of each spot (first stage = age of zircon), a value of 0.0113 for the average continental crust (second stage, values compiled from Rudnick and Gao (2003), and depleted mantle $^{176}Lu/^{177}Lu = 0.0379$, and $^{176}Hf/^{177}Hf = 0.283164$.

(f) Apparent U-Pb age determined by LA-ICP-MS.

(g) U-Pb age concordance (%).

(h) Sequence in which Lu-Hf analyses were performed. Standard analyses for each sequence are showed on Table 12.

Table 11

Lu, Yb and Hf LA-MC-ICPMS data of zircon cores from sample GCH-12

Grain	$^{176}Yb/^{177}Hf$ [a]	±2σ	$^{176}Lu/^{177}Hf$ [a]	±2σ	$^{178}Hf/^{177}Hf$	$^{180}Hf/^{177}Hf$	Sig_{Hf} [b] (V)	$^{176}Hf/^{177}Hf$	±2σ [c]	$^{176}Hf/^{177}Hf_{(t)}$ [d]	$\varepsilon Hf_{(t)}$ [d]	±2σ [c] (εHf)	T_{DM} [e] (Ga)	age [f] (Ma)	±2σ (Ma)	U-Pb [g] conc	Lu-Hf [n] seq
A6_seq5_40	0.0240	20	0.00088	6	1.46716	1.88694	13	0.282258	31	0.282249	-6.9	1.1	1.57	542	6	103	4
A7_seq5_40	0.0440	39	0.00148	10	1.46718	1.88677	12	0.282534	22	0.282517	4.1	0.8	1.02	606	6	100	4
A8_seq5_26	0.0152	13	0.00051	3	1.46712	1.88643	7	0.282706	30	0.282701	8.8	1.1	0.69	530	6	99	4
A9_seq5_26	0.0109	13	0.00041	4	1.46706	1.88637	6	0.281704	45	0.281687	8.1	1.6	2.00	2071	88	102	4
A10_seq5_26	0.0262	21	0.00098	6	1.46714	1.88646	7	0.282153	34	0.282144	-11.4	1.2	1.79	506	6	98	4
A11_seq5_26	0.0197	19	0.00066	5	1.46701	1.88648	6	0.281569	34	0.281543	3.4	1.2	2.27	2093	29	100	4
A12_seq5_40	0.0150	14	0.00050	4	1.46722	1.88685	11	0.281594	22	0.281574	4.8	0.8	2.21	2104	30	98	4
A14_seq5_40	0.0211	19	0.00070	5	1.46718	1.88689	12	0.281566	25	0.281538	3.1	0.9	2.29	2087	27	100	4
A15_seq5_26	0.0144	12	0.00055	4	1.46720	1.88641	6	0.281873	36	0.281867	-20.5	1.3	2.31	535	8	113	4
A17_seq5_40	0.0183	18	0.00056	4	1.46714	1.88679	11	0.281029	32	0.281001	-3.2	1.1	3.08	2636	15	100	4
A006_seq5a_40	0.0163	13	0.00061	4	1.46722	1.88679	6	0.282395	42	0.282388	-2.2	1.5	1.30	532	6	99	5
A007_seq5a_40	0.0094	8	0.00034	2	1.46720	1.88659	9	0.281572	28	0.281559	0.4	1.0	2.32	1934	35	100	5
A008_seq5a_40	0.0171	16	0.00065	5	1.46720	1.88677	8	0.281556	39	0.281531	2.5	1.4	2.31	2072	23	101	5
A009_seq5a_40	0.0205	17	0.00070	5	1.46713	1.88685	8	0.281575	37	0.281547	3.7	1.3	2.26	2098	25	100	5
A010_seq5a_40	0.0226	20	0.00086	6	1.46720	1.88680	7	0.281670	34	0.281635	8.1	1.2	2.06	2151	35	97	5
A011_seq5a_40	0.0171	14	0.00066	4	1.46718	1.88649	7	0.281630	32	0.281604	4.7	1.1	2.17	2055	30	98	5
A012_seq5a_40	0.0150	12	0.00052	3	1.46723	1.88670	7	0.281627	38	0.281607	5.0	1.3	2.16	2062	28	99	5
A013_seq5a_40	0.0132	11	0.00044	3	1.46720	1.88678	9	0.281603	32	0.281585	4.3	1.1	2.20	2063	23	98	5
A014_seq5a_40	0.0207	17	0.00070	4	1.46719	1.88686	9	0.282663	22	0.282656	7.1	0.8	0.78	523	6	99	5
A015_seq5a_40	0.0125	11	0.00041	3	1.46716	1.88642	9	0.281706	27	0.281702	-25.6	0.9	2.61	571	7	101	5
A016_seq5a_40	0.0160	13	0.00053	3	1.46718	1.88651	9	0.281598	31	0.281577	3.5	1.1	2.23	2045	34	100	5
A017_seq5a_40	0.0173	16	0.00055	4	1.46719	1.88660	8	0.282359	38	0.282353	-3.8	1.3	1.38	516	7	97	5
A018_seq5a_40	0.0324	26	0.00103	6	1.46710	1.88649	7	0.282246	38	0.282236	-7.8	1.3	1.60	523	6	97	5
A019_seq5a_40	0.0310	25	0.00099	6	1.46725	1.88680	10	0.282650	43	0.282640	6.9	1.5	0.81	538	7	100	5
A020_seq5a_40	0.0084	8	0.00029	2	1.46718	1.88651	8	0.282234	42	0.282232	-7.9	1.5	1.61	524	7	60	5
A021_seq5a_40	0.0212	20	0.00074	6	1.46717	1.88673	7	0.282224	38	0.282216	-6.7	1.4	1.61	602	16	76	5
A022_seq5a_40	0.0707	63	0.00244	17	1.46715	1.88641	8	0.282564	35	0.282530	7.7	1.2	0.94	746	9	100	5
A023_seq5a_40	0.0078	6	0.00026	2	1.46716	1.88658	7	0.281599	38	0.281588	4.0	1.4	2.21	2047	47	98	5
A024_seq5a_40	0.0359	29	0.00135	8	1.46709	1.88634	6	0.281597	34	0.281544	2.6	1.2	2.29	2056	39	94	5
A025_seq5a_40	0.0015	2	0.00004	1	1.46716	1.88655	14	0.281554	37	0.281552	2.1	1.3	2.29	2020	35	96	5
A026_seq5a_40	0.0127	10	0.00041	3	1.46721	1.88684	8	0.282224	45	0.282220	-8.5	1.6	1.64	513	5	99	5
A027_seq5a_40	0.0205	17	0.00065	4	1.46717	1.88666	7	0.281004	40	0.280971	-2.4	1.4	3.10	2715	28	97	5
A028_seq5a_40	0.0158	13	0.00064	4	1.46724	1.88662	8	0.281144	33	0.281119	-13.0	1.2	3.13	2035	14	97	5
A029_seq5a_40	0.0116	9	0.00040	2	1.46717	1.88677	9	0.281601	31	0.281585	4.3	1.1	2.20	2064	18	97	5
A030_seq5a_40	0.0127	10	0.00038	2	1.46719	1.88667	8	0.280968	42	0.280951	-9.1	1.5	3.26	2457	12	99	5
A031_seq5a_40	0.0177	15	0.00057	3	1.46722	1.88676	7	0.282604	41	0.282599	5.2	1.5	0.89	527	6	100	5
A032_seq5a_40	0.0094	8	0.00031	2	1.46722	1.88659	8	0.281614	44	0.281602	5.4	1.6	2.16	2087	26	98	5
A038_seq5a_40	0.0215	26	0.00069	8	1.46719	1.88687	7	0.281587	49	0.281560	3.9	1.7	2.24	2088	27	96	5
A039_seq5a_40	0.0133	11	0.00039	2	1.46724	1.88654	9	0.281051	45	0.281033	-7.7	1.6	3.13	2392	10	91	5
A040_seq5a_40	0.0366	30	0.00125	8	1.46712	1.88660	8	0.281634	28	0.281585	3.5	1.0	2.22	2029	14	100	5
A041_seq5a_40	0.0142	14	0.00042	3	1.46717	1.88658	7	0.281570	37	0.281554	2.2	1.3	2.29	2023	66	99	5
A042_seq5a_40	0.0223	18	0.00081	5	1.46720	1.88659	7	0.281550	41	0.281516	5.4	1.5	2.27	2218	16	98	5
A043_seq5a_40	0.0549	46	0.00173	11	1.46719	1.88668	7	0.282364	42	0.282347	-3.8	1.5	1.39	526	6	100	5
A044_seq5a_40	0.0348	34	0.00109	9	1.46714	1.88640	7	0.281612	41	0.281569	3.7	1.5	2.24	2065	14	100	5
A045_seq5a_40	0.0140	11	0.00042	3	1.46715	1.88673	7	0.281620	36	0.281604	3.9	1.3	2.19	2019	43	98	5
A046_seq5a_40	0.0261	22	0.00085	6	1.46726	1.88703	7	0.281619	48	0.281586	4.2	1.7	2.21	2060	27	97	5
A047_seq5a_40	0.0379	31	0.00125	8	1.46721	1.88644	7	0.281578	42	0.281528	2.9	1.5	2.30	2091	14	95	5
A048_seq5a_40	0.0316	32	0.00099	9	1.46709	1.88632	7	0.281557	50	0.281518	2.0	1.8	2.33	2069	27	97	5
A049_seq5a_40	0.0185	16	0.00059	4	1.46717	1.88649	6	0.282227	42	0.282221	-8.3	1.5	1.63	521	7	94	5
A050_seq5a_40	0.0109	9	0.00035	2	1.46713	1.88657	7	0.282392	45	0.282388	-2.1	1.6	1.30	535	10	103	5
A051_seq5a_26	0.0323	31	0.00118	9	1.46698	1.88599	4	0.281110	73	0.281055	-6.3	2.6	3.08	2421	13	101	5
A052_seq5a_40	0.0189	18	0.00064	5	1.46726	1.88686	6	0.281649	45	0.281624	5.8	1.6	2.12	2070	25	98	5
A053_seq5a_40	0.0159	13	0.00053	3	1.46728	1.88705	6	0.281433	47	0.281412	-2.4	1.7	2.55	2043	23	97	5
A054_seq5a_40	0.0106	9	0.00035	2	1.46722	1.88656	6	0.282664	46	0.282661	7.3	1.6	0.77	524	8	98	5
A055_seq5a_40	0.0179	19	0.00060	6	1.46718	1.88668	6	0.281701	52	0.281677	8.0	1.9	2.01	2086	29	95	5
A056_seq5a_40	0.0125	11	0.00044	3	1.46715	1.88653	7	0.281594	40	0.281577	3.4	1.4	2.23	2038	25	100	5
A057_seq5a_40	0.0398	32	0.00123	7	1.46723	1.88666	7	0.282649	36	0.282637	6.4	1.3	0.82	523	5	95	5

Grain	$^{176}Yb/^{177}Hf$ [a]	±2σ	$^{176}Lu/^{177}Hf$ [a]	±2σ	$^{178}Hf/^{177}Hf$	$^{180}Hf/^{177}Hf$	Sig_{Hf} [b] (V)	$^{176}Hf/^{177}Hf$	±2σ [c]	$^{176}Hf/^{177}Hf_{(t)}$ [d]	$\varepsilon Hf_{(t)}$ [d]	±2σ [c] (εHf)	T_{DM} [e] (Ga)	age [f] (Ma)	±2σ (Ma)	U-Pb [g] conc	Lu-Hf [n] seq
A058_seq5a_40	0.0339	27	0.00082	5	1.46713	1.88645	5	0.282467	-	-	-	-	-	-	-	-	5
A059_seq5a_40	0.0217	20	0.00064	5	1.46720	1.88663	6	0.281045	34	0.281012	-2.2	1.2	3.05	2660	18	98	5
A060_seq5a_40	0.0400	43	0.00134	12	1.46704	1.88654	6	0.281604	49	0.281553	2.0	1.7	2.29	2017	76	100	5
A061_seq5a_40	0.0131	11	0.00042	3	1.46722	1.88685	13	0.282265	22	0.282261	-6.7	0.8	1.55	530	7	98	5
A062_seq5a_40	0.0245	25	0.00078	7	1.46722	1.88688	11	0.281659	22	0.281629	4.9	0.8	2.14	2023	25	98	5
A064_seq5a_40	0.0280	23	0.00084	5	1.46712	1.88668	13	0.281957	22	0.281934	2.4	0.8	1.80	1444	20	99	5
A065_seq5a_40	0.0252	22	0.00082	5	1.46715	1.88667	12	0.282228	26	0.282221	-8.8	0.9	1.64	501	6	99	5
A066_seq5a_40	0.0142	12	0.00045	3	1.46716	1.88678	13	0.281609	24	0.281591	4.5	0.9	2.19	2066	34	100	5
A073_seq5a_40	0.0125	10	0.00043	3	1.46720	1.88672	15	0.281589	22	0.281571	4.0	0.8	2.23	2074	22	99	5
A074_seq5a_26	0.0391	40	0.00133	12	1.46709	1.88647	5	0.281690	37	0.281638	5.8	1.3	2.11	2050	30	98	5
A075_seq5a_40	0.0290	25	0.00119	8	1.46724	1.88690	11	0.282153	27	0.282122	7.7	1.0	1.46	1386	47	98	5
A077_seq5a_40	0.0140	14	0.00048	4	1.46721	1.88708	11	0.281606	25	0.281588	3.9	0.9	2.21	2044	35	100	5
A078_seq5a_40	0.0159	13	0.00052	3	1.46724	1.88684	11	0.282026	26	0.282013	3.0	0.9	1.69	1347	24	101	5
A079_seq5a_40	0.0460	45	0.00149	11	1.46714	1.88651	11	0.281620	34	0.281561	3.9	1.2	2.24	2086	18	101	5
A080_seq5a_40	0.0128	10	0.00042	3	1.46720	1.88684	12	0.282294	28	0.282290	-5.7	1.0	1.50	531	6	99	5
A081_seq5a_40	0.0094	14	0.00030	4	1.46711	1.88673	11	0.281161	25	0.281146	1.1	0.9	2.82	2599	40	98	5
A082_seq5a_40	0.0246	20	0.00092	6	1.46716	1.88675	13	0.281522	23	0.281486	1.4	0.8	2.39	2091	13	99	5
A084_seq5a_40	0.0286	25	0.00102	7	1.46719	1.88672	13	0.281608	24	0.281567	4.6	0.8	2.22	2107	14	99	5
A086_seq5a_26	0.0272	25	0.00084	6	1.46715	1.88668	6	0.281099	35	0.281056	-0.6	1.3	2.96	2663	16	96	5
A089_seq5a_26	0.0384	32	0.00126	8	1.46706	1.88624	6	0.281622	31	0.281572	3.9	1.1	2.23	2068	20	101	5
A090_seq5a_40	0.0163	14	0.00052	3	1.46717	1.88680	13	0.281590	20	0.281569	3.6	0.7	2.24	2059	27	98	5
A091_seq5a_26	0.0122	11	0.00046	4	1.46711	1.88660	7	0.281428	26	0.281409	-0.7	0.9	2.52	2120	19	97	5
A092_seq5a_40	0.0199	17	0.00071	5	1.46719	1.88671	12	0.282611	21	0.282604	5.4	0.7	0.88	528	8	96	5
A093_seq5a_40	0.0263	28	0.00081	7	1.46719	1.88684	13	0.281074	19	0.281032	-0.4	0.7	2.99	2706	19	98	5
A096_seq5a_40	0.0110	13	0.00039	4	1.46722	1.88710	13	0.281577	25	0.281562	4.5	0.9	2.23	2109	22	97	5
A097_seq5a_40	0.0229	22	0.00086	7	1.46723	1.88692	11	0.281631	22	0.281597	4.6	0.8	2.18	2062	33	98	5
A098_seq5a_40	0.0433	37	0.00147	10	1.46718	1.88681	11	0.281603	21	0.281543	4.3	0.7	2.26	2130	31	100	5
A099_seq5a_40	0.0291	35	0.00095	10	1.46720	1.88694	12	0.281623	23	0.281585	4.7	0.8	2.20	2082	36	98	5
A101_seq5a_40	0.0085	12	0.00026	3	1.46719	1.88692	13	0.281567	20	0.281557	2.4	0.7	2.28	2026	20	99	5
A107_seq5a_40	0.0158	18	0.00050	5	1.46719	1.88682	12	0.282658	27	0.282653	6.9	1.0	0.79	518	7	100	5
A110_seq5a_26	0.0309	29	0.00111	9	1.46718	1.88679	6	0.281555	27	0.281510	3.5	1.0	2.31	2148	13	94	5
A112_seq5a_26	0.0079	7	0.00026	2	1.46713	1.88645	9	0.282162	26	0.282157	0.2	0.9	1.56	1000	25	96	5
A113_seq5a_40	0.0096	8	0.00037	2	1.46718	1.88665	11	0.282288	23	0.282283	-2.2	0.8	1.44	697	11	99	5
A114_seq5a_40	0.0173	14	0.00054	3	1.46716	1.88669	12	0.282121	24	0.282109	2.1	0.8	1.58	1160	53	101	5
A115_seq5a_40	0.0349	31	0.00134	10	1.46715	1.88662	10	0.281659	25	0.281607	4.4	0.9	2.17	2034	32	99	5
A116_seq5a_40	0.0235	21	0.00079	6	1.46716	1.88647	14	0.282244	22	0.282236	-7.9	0.8	1.61	517	7	99	5
A117_seq5a_26	0.0204	19	0.00073	6	1.46719	1.88655	6	0.282068	34	0.282060	-14.0	1.2	1.94	521	7	94	5
A118_seq5a_40	0.0140	20	0.00043	5	1.46722	1.88689	14	0.282231	22	0.282227	-8.0	0.8	1.62	526	7	100	5
A119_seq5a_40	0.0139	12	0.00048	3	1.46717	1.88689	13	0.281568	25	0.281549	3.2	0.9	2.27	2075	22	99	5
A120_seq5a_40	0.0448	38	0.00144	9	1.46725	1.88680	16	0.281103	22	0.281029	-0.5	0.8	2.99	2709	14	98	5
A121_seq5a_40	0.0333	27	0.00105	6	1.46714	1.88655	12	0.281041	20	0.280983	2.2	0.7	2.99	2892	13	96	5
A122_seq5a_40	0.0166	15	0.00052	4	1.46719	1.88679	12	0.282426	27	0.282421	-1.3	1.0	1.25	518	8	105	5
A123_seq5a_40	0.0203	16	0.00059	4	1.46720	1.88671	13	0.282442	26	0.282436	1.2	0.9	1.18	607	6	106	5
A124_seq5a_40	0.0228	19	0.00091	6	1.46719	1.88672	16	0.281560	21	0.281530	-4.8	0.7	2.45	1756	30	100	5
A125_seq5a_40	0.0376	33	0.00122	8	1.46723	1.88687	12	0.282557	22	0.282544	4.5	0.8	0.98	585	13	98	5
A127_seq5a_40	0.0150	12	0.00048	3	1.46721	1.88677	12	0.282607	22	0.282602	5.0	0.8	0.89	513	6	101	5
A128_seq5a_40	0.0261	21	0.00090	6	1.46721	1.88676	12	0.281631	22	0.281595	5.2	0.8	2.17	2088	28	97	5
A130_seq5a_40	0.0283	24	0.00098	7	1.46716	1.88672	14	0.282290	23	0.282277	-1.8	0.8	1.44	725	8	92	5
A133_seq5a_40	0.0105	9	0.00035	2	1.46723	1.88703	14	0.281610	21	0.281596	4.4	0.7	2.19	2051	36	98	5
A140_seq5a_40	0.0105	9	0.00036	2	1.46716	1.88665	11	0.282176	26	0.282168	4.9	0.9	1.45	1192	35	96	5
A141_seq5a_40	0.0339	28	0.00106	7	1.46719	1.88667	17	0.282168	22	0.282144	4.6	0.8	1.49	1214	25	99	5
A142_seq5a_40	0.0268	26	0.00092	7	1.46708	1.88608	10	0.281603	36	0.281567	3.8	1.3	2.24	2074	25	98	5
A143_seq5a_40	0.0319	37	0.00114	11	1.46723	1.88695	7	0.282641	43	0.282630	6.4	1.5	0.83	534	7	100	5
A145_seq5a_40	0.0208	17	0.00082	5	1.46721	1.88690	11	0.281811	26	0.281802	-23.0	0.9	2.43	529	7	98	5
A153_seq5a_40	0.0187	23	0.00076	8	1.46711	1.88647	11	0.281607	27	0.281578	4.3	0.9	2.21	2077	18	98	5
A155_seq5a_26	0.0290	26	0.00104	7	1.46711	1.88649	7	0.282464	35	0.282451	2.1	1.2	1.14	622	6	106	5
A156_seq5a_40	0.0296	26	0.00107	7	1.46714	1.88663	12	0.282600	23	0.282588	6.3	0.8	0.89	592	7	95	5
A157_seq5a_40	0.0216	18	0.00089	6	1.46720	1.88683	13	0.281742	27	0.281733	-25.1	1.0	2.56	545	5	95	5
A158_seq5a_26	0.0171	14	0.00061	4	1.46716	1.88624	6	0.282481	27	0.282475	0.9	1.0	1.14	531	6	90	5
A161_seq5a_40	0.0531	48	0.00197	15	1.46716	1.88651	14	0.282568	27	0.282540	8.1	1.0	0.91	748	9	97	5

Grain	$^{176}Yb/^{177}Hf$ [a]	±2σ	$^{176}Lu/^{177}Hf$ [a]	±2σ	$^{178}Hf/^{177}Hf$	$^{180}Hf/^{177}Hf$	Sig_{Hf} [b] (V)	$^{176}Hf/^{177}Hf$	±2σ [c]	$^{176}Hf/^{177}Hf_{(t)}$ [d]	$\varepsilon Hf_{(t)}$ [d]	±2σ [c] (εHf)	T_{DM} [e] (Ga)	age [f] (Ma)	±2σ (Ma)	U-Pb [g] conc	Lu-Hf [h] seq
A162_seq5a_40	0.0184	16	0.00069	5	1.46716	1.88676	12	0.282392	26	0.282385	-1.5	0.9	1.30	567	7	101	5
A165_seq5a_26	0.0085	8	0.00031	2	1.46715	1.88645	6	0.282191	44	0.282188	-9.6	1.6	1.70	518	5	92	5
A167_seq5a_26	0.0159	21	0.00056	6	1.46716	1.88675	7	0.281658	34	0.281637	5.6	1.2	2.11	2043	33	98	5

Quoted uncertainties (absolute) relate to the last quoted figure. The effect of the inter-element fractionation on Lu/Hf was estimated to be about 6 % or less based on analyses of the GJ-1 and Plesoviče zircon. Accuracy and reproducibility was checked by repeated analyses of reference zircon GJ-1 and Plesoviče (data given as mean with 2 standard deviation uncertainties).

(a) $^{176}Yb/^{177}Hf = (^{176}Yb/^{173}Yb)_{true} \times (^{173}Yb/^{177}Hf)_{meas} \times (M_{173(Yb)}/M_{177(Hf)})^{\beta(Hf)}$, $\beta(Hf) = \ln((^{179}Hf/^{177}Hf_{true})/(^{179}Hf/^{177}Hf_{measured})) / \ln(M_{179(Hf)}/M_{177(Hf)})$, M = mass of respective isotopes. The $^{176}Lu/^{177}Hf$ was calculated in a similar way using $^{175}Lu/^{177}Hf$ and β(Yb).

(b) Mean Hf signal in volts.

(c) Uncertainties are quadratic additions of the within-run precision and the daily reproducibility of the 40ppb-JMC475 solution. Uncertainties for the JMC475 quoted at 2SD (2 standard deviation).

(d) Initial $^{176}Hf/^{177}Hf$ and εHf calculated using the apparent U-Pb age determined by LA-ICP-MS dating (see column f), and the CHUR parameters: $^{176}Lu/^{177}Hf = 0.0336$, and $^{176}Hf/^{177}Hf = 0.282785$ (Bouvier et al. 2008).

(e) Two stage model age in Ga using measured $^{176}Lu/^{177}Lu$ of each spot (first stage = age of zircon), a value of 0.0113 for the average continental crust (second stage, values compiled from Rudnick and Gao (2003), and depleted mantle $^{176}Lu/^{177}Lu = 0.0379$, and $^{176}Hf/^{177}Hf = 0.283164$.

(f) Apparent U-Pb age determined by LA-ICP-MS.

(g) U-Pb age concordance (%).

(h) Sequence in which Lu-Hf analyses were performed. Standard analyses for each sequence are showed on Table 12.

Table 12
Lu, Yb and Hf LA-MC-ICPMS data of standards

Grain	$^{176}Yb/^{177}Hf$ [a]	±2σ	$^{176}Lu/^{177}Hf$ [a]	±2σ	$^{178}Hf/^{177}Hf$	$^{180}Hf/^{177}Hf$	Sig_{Hf} [b] (V)	$^{176}Hf/^{177}Hf$	±2σ [c]	$^{176}Hf/^{177}Hf_{(t)}$ [d]	$\varepsilon Hf_{(t)}$ [d]	±2σ [c] (εHf)	T_{DM} [e] (Ga)	age [f] (Ma)
01-Nov														
GJ1-40-1	0.0072	6	0.00025	1	1.46721	1.88688	10	0.282009	25	0.282006	-14.0	0.9	2.01	606
GJ1-40-2	0.0072	6	0.00025	1	1.46721	1.88693	11	0.282019	25	0.282016	-13.7	0.9	2.00	606
GJ1-40-3	0.0077	6	0.00024	1	1.46716	1.88669	11	0.281993	24	0.281990	-14.6	0.9	2.05	606
GJ1-40-4	0.0082	7	0.00025	1	1.46712	1.88657	12	0.281987	24	0.281984	-14.8	0.9	2.06	606
GJ1-40-5	0.0069	6	0.00023	1	1.46715	1.88661	9	0.282025	21	0.282022	-13.5	0.8	1.98	606
GJ1-40-6	0.0069	6	0.00024	1	1.46717	1.88678	10	0.282027	27	0.282025	-13.4	0.9	1.98	606
GJ1-40-7	0.0072	6	0.00025	1	1.46714	1.88673	8	0.282026	27	0.282024	-13.4	1.0	1.98	606
GJ1-40-8	0.0073	6	0.00025	1	1.46708	1.88645	9	0.282011	31	0.282008	-14.0	1.1	2.01	606
GJ1-40-9	0.0076	6	0.00025	1	1.46719	1.88679	9	0.282016	27	0.282013	-13.8	1.0	2.00	606
GJ1-40-10	0.0078	6	0.00025	1	1.46722	1.88672	9	0.282029	24	0.282026	-13.3	0.9	1.98	606
02-Nov														
GJ1_40_90_1	0.0070	6	0.00024	1	1.46721	1.88677	8	0.281996	24	0.281993	-14.5	0.8	2.04	606
GJ1_40_90_2	0.0075	6	0.00025	2	1.46701	1.88634	5	0.281981	45	0.281978	-15.0	1.6	2.07	606
GJ1_40_90_3	0.0074	6	0.00025	1	1.46707	1.88663	8	0.282015	26	0.282013	-13.8	0.9	2.00	606
GJ1_40_90_4	0.0072	6	0.00025	2	1.46717	1.88679	8	0.282032	29	0.282029	-13.2	1.0	1.97	606
GJ1_40_90_5	0.0078	6	0.00025	1	1.46720	1.88687	9	0.282002	30	0.281999	-14.3	1.1	2.03	606
GJ1_40_90_6	0.0068	5	0.00023	1	1.46709	1.88668	8	0.282026	26	0.282024	-13.4	0.9	1.98	606
GJ1_40_90_7	0.0069	6	0.00023	1	1.46720	1.88676	9	0.282026	24	0.282023	-13.4	0.8	1.98	606
GJ1_40_90_8	0.0076	6	0.00025	1	1.46723	1.88678	9	0.282011	29	0.282008	-14.0	1.0	2.01	606
GJ1_40_90_9	0.0073	6	0.00023	1	1.46716	1.88667	9	0.282022	25	0.282019	-13.6	0.9	1.99	606
GJ1_40_90_10	0.0073	6	0.00024	1	1.46715	1.88667	9	0.282018	26	0.282016	-13.7	0.9	2.00	606
GJ1_40_90_11	0.0071	6	0.00023	1	1.46716	1.88667	9	0.282015	25	0.282012	-13.8	0.9	2.00	606
05-Nov														
GJ1_6_100_100_line	0.0071	6	0.00025	2	1.46722	1.88687	14	0.282013	19	0.282010	-13.9	0.7	2.01	606
GJ1_6_100_100_line_2	0.0074	6	0.00025	1	1.46719	1.88687	16	0.281986	17	0.281983	-14.9	0.6	2.06	606
GJ1_40-5-90_1	0.0076	6	0.00026	2	1.46713	1.88657	10	0.281987	26	0.281984	-14.8	0.9	2.06	606
GJ1_40-5-90_2	0.0074	6	0.00026	2	1.46721	1.88668	10	0.282002	21	0.281999	-14.3	0.8	2.03	606
GJ1_40-5-90_3	0.0073	6	0.00025	2	1.46711	1.88662	7	0.282022	38	0.282020	-13.6	1.4	1.99	606
GJ1_40-5-90_4	0.0072	6	0.00025	2	1.46718	1.88674	8	0.282017	31	0.282014	-13.8	1.1	2.00	606
GJ1_40-5-90_5	0.0078	6	0.00025	2	1.46717	1.88661	10	0.282012	23	0.282009	-13.9	0.8	2.01	606
GJ1_40-5-90_6	0.0075	6	0.00025	2	1.46721	1.88663	9	0.282028	26	0.282025	-13.4	0.9	1.98	606
GJ1_40-5-90_7	0.0079	6	0.00025	2	1.46722	1.88673	10	0.282029	25	0.282026	-13.3	0.9	1.98	606
GJ1_40-5-90_8	0.0079	6	0.00025	1	1.46713	1.88669	10	0.281998	23	0.281995	-14.4	0.8	2.04	606
GJ1_40-5-90_9	0.0074	6	0.00025	2	1.46717	1.88678	8	0.282018	29	0.282016	-13.7	1.0	2.00	606
GJ1_40-5-90_10	0.0079	6	0.00025	1	1.46722	1.88674	9	0.282001	36	0.281998	-14.3	1.3	2.03	606
GJ1_40-5-90_11	0.0078	6	0.00025	1	1.46718	1.88662	9	0.282038	31	0.282035	-13.0	1.1	1.96	606
GJ1_40-5-90_12	0.0080	7	0.00024	1	1.46717	1.88656	11	0.282003	34	0.282001	-14.2	1.2	2.02	606
GJ1_40-5-90_13	0.0079	6	0.00024	1	1.46722	1.88686	10	0.282020	27	0.282017	-13.6	1.0	1.99	606
06-Nov														
GJ1_5_100_100_1	0.0082	7	0.00025	1	1.46715	1.88689	13	0.281995	22	0.281992	-14.6	0.8	2.04	606
GJ1_40-5-90_1	0.0077	6	0.00024	1	1.46715	1.88662	11	0.281997	24	0.281995	-14.4	0.9	2.04	606
GJ1_40-5-90_2	0.0074	6	0.00025	2	1.46722	1.88665	7	0.282028	32	0.282025	-13.4	1.1	1.98	606
GJ1_40-5-90_3	0.0073	6	0.00025	2	1.46724	1.88682	8	0.282012	29	0.282009	-13.9	1.0	2.01	606
GJ1_40-5-90_4	0.0076	6	0.00025	2	1.46717	1.88683	9	0.282019	27	0.282016	-13.7	0.9	2.00	606
GJ1_40-5-90_5	0.0074	6	0.00025	2	1.46719	1.88676	9	0.282028	23	0.282025	-13.4	0.8	1.98	606
GJ1_40-5-90_7	0.0073	6	0.00025	1	1.46720	1.88672	10	0.282021	25	0.282018	-13.6	0.9	1.99	606
GJ1_40-5-90_8	0.0072	6	0.00025	1	1.46718	1.88671	10	0.281988	22	0.281985	-14.8	0.8	2.05	606
GJ1_40-5-90_9	0.0070	6	0.00024	1	1.46716	1.88658	9	0.282009	37	0.282006	-14.0	1.3	2.01	606
GJ1_40-5-90_10	0.0069	6	0.00024	1	1.46717	1.88662	10	0.282016	29	0.282013	-13.8	1.0	2.00	606
GJ1_40-5-90_11	0.0071	6	0.00024	1	1.46720	1.88679	11	0.282026	25	0.282023	-13.4	0.9	1.98	606
GJ1_40-5-90_12	0.0069	6	0.00023	1	1.46721	1.88694	11	0.282034	26	0.282031	-13.1	0.9	1.97	606
GJ1_40-5-90_13	0.0066	5	0.00023	1	1.46721	1.88653	10	0.282028	23	0.282025	-13.4	0.8	1.98	606
GJ1_40-5-90_14	0.0067	5	0.00023	1	1.46715	1.88662	10	0.282024	28	0.282022	-13.5	1.0	1.98	606

Grain	$^{176}Yb/^{177}Hf$ [a]	±2σ	$^{176}Lu/^{177}Hf$ [a]	±2σ	$^{178}Hf/^{177}Hf$	$^{180}Hf/^{177}Hf$	Sig_{Hf} [b] (V)	$^{176}Hf/^{177}Hf$	±2σ [c]	$^{176}Hf/^{177}Hf_{(t)}$ [d]	$\varepsilon Hf_{(t)}$ [d]	±2σ [c] (εHf)	T_{DM} [e] (Ga)	age [f] (Ma)
01-Nov														
GJ1_40-5-90_15	0.0070	6	0.00023	1	1.46712	1.88666	10	0.282014	26	0.282012	-13.8	0.9	2.00	606
GJ1_40-5-90_16	0.0072	6	0.00024	1	1.46724	1.88673	10	0.282028	22	0.282025	-13.4	0.8	1.98	606
GJ1_40-5-90_17	0.0072	6	0.00024	1	1.46713	1.88660	10	0.282011	20	0.282009	-14.0	0.7	2.01	606
GJ1_40-5-90_18	0.0074	6	0.00025	1	1.46722	1.88679	10	0.282035	23	0.282032	-13.1	0.8	1.96	606
GJ1_40-5-90_19	0.0076	6	0.00025	1	1.46721	1.88666	10	0.282020	24	0.282017	-13.7	0.8	1.99	606
GJ1_40-5-90_20	0.0076	6	0.00025	1	1.46715	1.88665	10	0.282030	23	0.282027	-13.3	0.8	1.97	606
GJ1_40-5-90_21	0.0075	6	0.00025	1	1.46720	1.88667	10	0.282025	21	0.282022	-13.5	0.7	1.98	606
GJ1_40-5-90_22	0.0075	6	0.00025	1	1.46718	1.88660	10	0.282010	33	0.282008	-14.0	1.2	2.01	606
GJ1_40-5-90_23	0.0075	6	0.00025	1	1.46718	1.88676	11	0.282000	21	0.281997	-14.4	0.7	2.03	606
07-Nov														
GJ1-100-100-5_1	0.0084	7	0.00026	2	1.46717	1.88687	14	0.282012	23	0.282009	-13.9	0.8	2.01	606
GJ1-100-100-5_2	0.0080	7	0.00026	2	1.46718	1.88658	11	0.281993	19	0.281990	-14.6	0.7	2.05	606
GJ1-100-100-5_3	0.0074	6	0.00023	1	1.46725	1.88637	9	0.282029	24	0.282026	-13.3	0.9	1.98	606
GJ1-100-100-5_4	0.0072	6	0.00026	2	1.46721	1.88655	4	0.282028	55	0.282025	-13.4	1.9	1.98	606
GJ1-100-90-5_10	0.0065	5	0.00023	1	1.46718	1.88650	10	0.282031	24	0.282028	-13.3	0.9	1.97	606
GJ1-100-90-5_11	0.0071	6	0.00024	1	1.46715	1.88673	11	0.282001	21	0.281998	-14.3	0.8	2.03	606
GJ1-100-90-5_12	0.0076	6	0.00025	1	1.46718	1.88676	10	0.282010	20	0.282008	-14.0	0.7	2.01	606
GJ1-100-90-5_13	0.0075	6	0.00025	1	1.46722	1.88665	10	0.282003	22	0.282000	-14.3	0.8	2.03	606
GJ1-100-90-5_14	0.0076	6	0.00025	1	1.46715	1.88665	10	0.282012	27	0.282009	-13.9	1.0	2.01	606
GJ1-100-90-5_15	0.0075	6	0.00025	1	1.46720	1.88661	10	0.282020	25	0.282017	-13.6	0.9	1.99	606
GJ1-100-90-5_16	0.0073	6	0.00025	1	1.46720	1.88677	9	0.282008	25	0.282005	-14.1	0.9	2.02	606
GJ1-100-90-5_17	0.0074	6	0.00025	1	1.46713	1.88660	10	0.282003	26	0.282001	-14.2	0.9	2.02	606
GJ1-100-90-5_18	0.0076	6	0.00025	1	1.46725	1.88679	10	0.282017	21	0.282015	-13.7	0.7	2.00	606
GJ1-100-90-5_19	0.0076	6	0.00025	1	1.46720	1.88680	10	0.282016	23	0.282013	-13.8	0.8	2.00	606
GJ1-100-90-5_20	0.0069	6	0.00025	1	1.46718	1.88655	10	0.282002	22	0.282000	-14.3	0.8	2.03	606
GJ1-100-90-5_21	0.0070	6	0.00025	1	1.46717	1.88648	10	0.282010	23	0.282007	-14.0	0.8	2.01	606
GJ1-100-90-5_22	0.0068	5	0.00025	1	1.46725	1.88674	9	0.282024	22	0.282021	-13.5	0.8	1.99	606
GJ1-100-90-5_23	0.0068	5	0.00024	1	1.46715	1.88669	10	0.282013	24	0.282010	-13.9	0.9	2.01	606
GJ1-100-90-5_24	0.0066	5	0.00024	1	1.46724	1.88660	10	0.282015	29	0.282012	-13.8	1.0	2.00	606
GJ1-100-90-5_25	0.0068	5	0.00024	1	1.46717	1.88655	11	0.281996	19	0.281993	-14.5	0.7	2.04	606
GJ1-100-90-5_26	0.0074	6	0.00025	1	1.46719	1.88650	10	0.282015	23	0.282012	-13.8	0.8	2.00	606
GJ1-100-90-5_5	0.0080	7	0.00025	1	1.46713	1.88661	11	0.282021	23	0.282018	-13.6	0.8	1.99	606
GJ1-100-90-5_6	0.0076	6	0.00025	2	1.46716	1.88663	10	0.282016	27	0.282013	-13.8	1.0	2.00	606
GJ1-100-90-5_7	0.0070	6	0.00025	2	1.46719	1.88652	8	0.281997	23	0.281994	-14.5	0.8	2.04	606
GJ1-100-90-5_8	0.0077	6	0.00025	2	1.46716	1.88656	10	0.282016	21	0.282013	-13.8	0.7	2.00	606
GJ1-100-90-5_9	0.0079	6	0.00025	2	1.46721	1.88651	10	0.282003	23	0.282000	-14.3	0.8	2.03	606
Mean	0.0074	8	0.00025	2	1.46718	1.88668	10	0.282014	26	0.282011	-13.9	0.9	2.00	
85														
01-Nov														
Plesovice 26_2	0.0050	4	0.00012	1	1.46710	1.88640	7	0.282457	24	0.282456	-4.1	0.9	1.25	338
Plesovice 32_1	0.0042	3	0.00010	1	1.46721	1.88669	13	0.282461	23	0.282460	-4.0	0.8	1.24	338
Plesovice 40_6	0.0061	5	0.00014	1	1.46720	1.88676	16	0.282469	26	0.282468	-3.7	0.9	1.23	338
Plesovice 40_7	0.0062	5	0.00014	1	1.46715	1.88667	16	0.282462	18	0.282461	-3.9	0.6	1.24	338
Plesovice 40_8	0.0062	5	0.00013	1	1.46716	1.88672	15	0.282444	20	0.282443	-4.6	0.7	1.28	338
Plesovice 40_9	0.0061	5	0.00013	1	1.46714	1.88675	14	0.282449	23	0.282448	-4.4	0.8	1.27	338
Plesovice 40_10	0.0077	6	0.00017	1	1.46712	1.88652	13	0.282454	22	0.282453	-4.2	0.8	1.26	338
Plesovice 48_4	0.0064	5	0.00015	1	1.46718	1.88682	26	0.282465	15	0.282464	-3.8	0.5	1.24	338
Plesovice 48_5	0.0065	5	0.00015	1	1.46717	1.88682	26	0.282455	17	0.282454	-4.2	0.6	1.26	338
02-Nov														
Plesovice_40_90_1	0.0073	6	0.00017	1	1.46716	1.88668	13	0.282478	20	0.282477	-3.4	0.7	1.21	338
Plesovice_40_90_2	0.0076	6	0.00017	1	1.46720	1.88659	12	0.282456	22	0.282455	-4.2	0.8	1.25	338
Plesovice_40_90_3	0.0035	3	0.00008	0	1.46718	1.88672	12	0.282464	23	0.282463	-3.9	0.8	1.24	338

Grain	$^{176}Yb/^{177}Hf$ [a]	±2σ	$^{176}Lu/^{177}Hf$ [a]	±2σ	$^{178}Hf/^{177}Hf$	$^{180}Hf/^{177}Hf$	Sig_{Hf} [b] (V)	$^{176}Hf/^{177}Hf$	±2σ [c]	$^{176}Hf/^{177}Hf_{(t)}$ [d]	$\varepsilon Hf_{(t)}$ [d]	±2σ [c] (εHf)	T_{DM} [e] (Ga)	age [f] (Ma)
01-Nov														
Plesovice_40_90_4	0.0059	5	0.00014	1	1.46718	1.88675	13	0.282460	17	0.282459	-4.0	0.6	1.25	338
Plesovice_40_90_5	0.0053	4	0.00013	1	1.46721	1.88667	12	0.282450	21	0.282449	-4.4	0.8	1.26	338
05-Nov														
Plesovice_40-5-90_1	0.0037	3	0.00008	1	1.46718	1.88673	15	0.282470	23	0.282469	-3.6	0.8	1.23	338
Plesovice_40-5-90_2	0.0046	4	0.00011	1	1.46717	1.88670	11	0.282452	31	0.282452	-4.3	1.1	1.26	338
Plesovice_40-5-90_3	0.0060	5	0.00015	1	1.46725	1.88682	14	0.282463	28	0.282462	-3.9	1.0	1.24	338
Plesovice_40-5-90_4	0.0035	3	0.00008	0	1.46713	1.88687	14	0.282466	24	0.282465	-3.8	0.9	1.23	338
Plesovice_40-5-90_5	0.0025	2	0.00006	0	1.46723	1.88694	14	0.282480	25	0.282480	-3.3	0.9	1.20	338
Plesovice_40-5-90_6	0.0057	5	0.00013	1	1.46727	1.88698	13	0.282515	29	0.282514	-2.1	1.0	1.14	338
Plesovice_40-5-90_7	0.0038	3	0.00009	1	1.46717	1.88670	13	0.282442	22	0.282441	-4.6	0.8	1.28	338
06-Nov														
Plesovice_40-5-90_1	0.0055	4	0.00012	1	1.46719	1.88672	13	0.282471	23	0.282470	-3.6	0.8	1.22	338
Plesovice_40-5-90_2	0.0035	3	0.00008	0	1.46718	1.88697	11	0.282463	34	0.282462	-3.9	1.2	1.24	338
Plesovice_40-5-90_3	0.0079	6	0.00017	1	1.46718	1.88674	14	0.282446	20	0.282445	-4.5	0.7	1.27	338
Plesovice_40-5-90_4	0.0126	10	0.00029	2	1.46719	1.88684	12	0.282460	27	0.282458	-4.1	0.9	1.25	338
Plesovice_40-5-90_5	0.0056	5	0.00013	1	1.46724	1.88698	13	0.282482	32	0.282481	-3.2	1.1	1.20	338
Plesovice_40-5-90_6	0.0047	4	0.00011	1	1.46721	1.88689	13	0.282477	28	0.282477	-3.4	1.0	1.21	338
Plesovice_40-5-90_7	0.0025	2	0.00006	0	1.46716	1.88683	15	0.282448	46	0.282448	-4.4	1.6	1.27	338
Plesovice_40-5-90_7bis	0.0063	5	0.00014	1	1.46724	1.88692	13	0.282481	23	0.282480	-3.3	0.8	1.20	338
Plesovice_40-5-90_8	0.0052	4	0.00012	1	1.46721	1.88677	13	0.282478	22	0.282478	-3.4	0.8	1.21	338
Plesovice_40-5-90_9	0.0049	4	0.00011	1	1.46721	1.88679	13	0.282490	27	0.282489	-2.9	1.0	1.19	338
Plesovice_40-5-90_10	0.0031	3	0.00007	0	1.46716	1.88673	14	0.282472	24	0.282472	-3.5	0.8	1.22	338
Plesovice_40-5-90_11	0.0079	6	0.00018	1	1.46721	1.88693	13	0.282497	26	0.282496	-2.7	0.9	1.17	338
07-Nov														
Plesovice-100-100-5_1	0.0034	3	0.00008	0	1.46717	1.88671	15	0.282465	22	0.282465	-3.8	0.8	1.23	338
Plesovice-100-90-5_2	0.0049	4	0.00012	1	1.46719	1.88685	14	0.282469	17	0.282468	-3.7	0.6	1.23	338
Plesovice-100-90-5_3	0.0036	3	0.00008	1	1.46716	1.88672	13	0.282468	22	0.282467	-3.7	0.8	1.23	338
Plesovice-100-90-5_4	0.0039	3	0.00009	1	1.46720	1.88670	15	0.282455	20	0.282454	-4.2	0.7	1.25	338
Plesovice-100-90-5_5	0.0051	4	0.00012	1	1.46724	1.88685	13	0.282481	26	0.282480	-3.3	0.9	1.20	338
Plesovice-100-90-5_6	0.0055	4	0.00013	1	1.46717	1.88679	13	0.282459	23	0.282458	-4.0	0.8	1.25	338
Plesovice-100-90-5_7	0.0053	4	0.00013	1	1.46724	1.88680	13	0.282493	20	0.282493	-2.8	0.7	1.18	338
Plesovice-100-90-5_8	0.0059	5	0.00014	1	1.46717	1.88676	14	0.282456	25	0.282455	-4.1	0.9	1.25	338
Mean	0.0054	37	0.00012	8	1.46719	1.88677	14	0.282466	31	0.282466	-3.8	1.1	1.23	
41														

Quoted uncertainties (absolute) relate to the last quoted figure. The effect of the inter-element fractionation on Lu/Hf was estimated to be about 6 % or less based on analyses of the GJ-1 and Plesoviče zircon. Accuracy and reproducibility was checked by repeated analyses of reference zircon GJ-1 and Plesoviče (data given as mean with 2 standard deviation uncertainties).

(a) $^{176}Yb/^{177}Hf = (^{176}Yb/^{173}Yb)_{true} \times (^{173}Yb/^{177}Hf)_{meas} \times (M_{173(Yb)}/M_{177(Hf)})^{\beta(Hf)}$, $\beta(Hf) = \ln((^{179}Hf/^{177}Hf_{true})/(^{179}Hf/^{177}Hf_{measured})) / \ln(M_{179(Hf)}/M_{177(Hf)})$, M = mass of respective isotopes. The $^{176}Lu/^{177}Hf$ was calculated in a similar way using $^{175}Lu/^{177}Hf$ and β(Yb).

(b) Mean Hf signal in volts.

(c) Uncertainties are quadratic additions of the within-run precision and the daily reproducibility of the 40ppb-JMC475 solution. Uncertainties for the JMC475 quoted at 2SD (2 standard deviation).

(d) Initial $^{176}Hf/^{177}Hf$ and εHf calculated using the apparent U-Pb age determined by LA-ICP-MS dating (see column f), and the CHUR parameters: $^{176}Lu/^{177}Hf = 0.0336$, and $^{176}Hf/^{177}Hf = 0.282785$ (Bouvier et al. 2008).

(e) Two stage model age in Ga using measured $^{176}Lu/^{177}Lu$ of each spot (first stage = age of zircon), a value of 0.0113 for the average continental crust (second stage, values compiled from Rudnick and Gao (2003), and depleted mantle $^{176}Lu/^{177}Lu = 0.0379$, and $^{176}Hf/^{177}Hf = 0.283164$.

(f) Apparent U-Pb age determined by LA-ICP-MS.

Appx. 3
Data tables for chapter 6
Tables S1-S12

Table S1

U, Th and Pb LA-ICP-MS data of zircon cores from sample GCH-02

Grain	^{207}Pb[a] (cps)	U[b] (ppm)	Pb[b] (ppm)	Th[b] U	^{206}Pbc[c] (%)	^{207}Pb[d] ^{235}U	±2σ (%)	^{206}Pb[d] ^{238}U	±2σ (%)	ρ[e] (rho)	^{207}Pb[d] ^{206}Pb	±2σ (%)	^{206}Pb[f] ^{238}U	±2σ (Ma)	^{207}Pb[f] ^{235}U	±2σ (Ma)	^{207}Pb[f] ^{206}Pb	±2σ (Ma)	Con (%
A324	3926	578	37	0.23	0.1	0.4871	2.9	0.0641	1.4	0.49	0.0551	2.6	401	6	403	10	417	57	96
A318	5372	461	35	0.25	2.2	0.5431	3.9	0.0699	1.5	0.39	0.0563	3.6	436	6	440	14	465	79	94
A250	722	89	8	0.47	b.d.	0.5942	4.6	0.0756	1.9	0.41	0.0570	4.2	470	9	474	18	492	92	95
A266	3699	481	36	0.22	b.d.	0.5988	3.1	0.0757	1.6	0.54	0.0574	2.6	471	7	476	12	505	57	93
A294	2582	88	7	0.14	3.9	0.6142	6.0	0.0780	1.9	0.31	0.0571	5.7	484	9	486	24	495	126	98
A260	1218	143	13	0.58	0.2	0.6180	3.0	0.0781	1.9	0.64	0.0574	2.3	484	9	489	12	508	50	95
A271	1530	184	17	0.64	0.0	0.6191	3.5	0.0789	1.9	0.53	0.0569	3.0	489	9	489	14	489	66	10
A204	5113	277	25	0.56	0.1	0.6365	2.7	0.0800	1.7	0.62	0.0577	2.1	496	8	500	11	518	46	96
A207	1184	123	11	0.54	0.7	0.6374	4.1	0.0806	1.9	0.46	0.0573	3.6	500	9	501	16	505	79	99
A334	3938	204	16	0.16	0.8	0.6380	3.0	0.0806	1.6	0.53	0.0574	2.6	500	8	501	12	508	56	98
A346	1931	203	20	0.77	0.4	0.6397	4.0	0.0806	1.5	0.39	0.0576	3.7	500	7	502	16	513	80	98
A202	1799	98	9	0.62	0.3	0.6415	2.6	0.0806	1.5	0.58	0.0577	2.2	500	7	503	11	519	47	96
A336	5414	537	48	0.39	1.1	0.6456	3.0	0.0819	1.6	0.53	0.0572	2.6	508	8	506	12	497	57	10
A351	4829	131	12	0.20	6.6	0.6568	6.3	0.0821	1.8	0.29	0.0580	6.1	509	9	513	26	529	133	96
A319	5026	540	51	0.54	0.2	0.6573	3.0	0.0829	1.6	0.51	0.0575	2.6	513	8	513	12	512	57	10
A235	3130	338	30	0.38	0.0	0.6577	2.6	0.0824	1.8	0.70	0.0579	1.9	510	9	513	11	525	41	97
A335	6099	330	35	0.86	0.9	0.6580	3.4	0.0829	1.7	0.49	0.0576	2.9	513	8	513	14	515	64	10
A248	1161	62	6	0.61	0.2	0.6609	3.7	0.0830	1.5	0.40	0.0578	3.4	514	7	515	15	521	75	99
A326	2546	138	11	0.18	0.0	0.6612	2.9	0.0831	1.4	0.50	0.0577	2.5	515	7	515	12	518	54	99
A243	2333	257	23	0.41	b.d.	0.6674	2.6	0.0835	1.5	0.59	0.0580	2.1	517	8	519	11	530	46	97
A211	555	31	3	0.59	0.0	0.6686	3.8	0.0830	2.2	0.57	0.0585	3.1	514	11	520	16	547	69	94
A291	4727	231	22	0.58	0.4	0.6697	2.8	0.0835	1.7	0.60	0.0581	2.2	517	8	521	12	535	49	97
A290	480	47	4	0.42	0.7	0.6720	4.8	0.0837	2.1	0.45	0.0582	4.3	518	11	522	20	538	94	96
A356	7374	794	70	0.34	0.1	0.6758	1.9	0.0843	1.5	0.79	0.0582	1.1	522	7	524	8	535	25	97
A300	1203	125	13	0.68	0.3	0.6773	3.8	0.0846	2.0	0.51	0.0581	3.3	524	10	525	16	532	72	98
A308	2475	267	24	0.39	0.2	0.6790	2.9	0.0850	1.6	0.54	0.0580	2.4	526	8	526	12	528	54	99
A253	1339	75	7	0.65	0.1	0.6792	3.4	0.0846	1.7	0.49	0.0582	3.0	523	8	526	14	538	65	97
A252	1476	165	17	0.73	0.3	0.6794	4.1	0.0846	1.7	0.42	0.0583	3.7	523	9	526	17	539	81	97
A349	5194	191	23	0.51	11.8	0.7334	7.9	0.0899	2.0	0.25	0.0592	7.6	555	10	559	34	574	166	97
A236	4391	426	44	0.54	b.d.	0.7417	3.0	0.0906	1.8	0.59	0.0594	2.4	559	9	563	13	582	52	96
A254	3326	146	17	0.73	0.1	0.7601	3.2	0.0932	1.8	0.56	0.0592	2.7	574	10	574	14	574	58	10
A344	706	32	3	0.68	0.5	0.7822	3.8	0.0950	1.7	0.45	0.0597	3.4	585	10	587	17	594	74	99
A189	10929	482	53	0.46	b.d.	0.8347	2.1	0.1005	1.5	0.71	0.0603	1.5	617	9	616	10	613	32	10
A233	3628	180	20	0.54	b.d.	0.8358	2.9	0.0989	1.8	0.63	0.0613	2.2	608	10	617	13	650	48	93
A355	4604	149	20	0.62	0.3	1.0180	2.9	0.1167	1.5	0.53	0.0633	2.4	711	10	713	15	718	52	99
A313	6364	411	58	0.69	0.3	1.0620	2.5	0.1189	1.4	0.58	0.0648	2.0	724	10	735	13	768	43	94
A209	9512	85	27	0.52	0.4	3.8190	2.4	0.2730	1.4	0.61	0.1014	1.9	1556	20	1597	19	1651	35	94
A309	6755	100	35	0.58	0.8	4.5870	2.4	0.2945	1.5	0.62	0.1130	1.8	1664	22	1747	20	1847	33	90
A314	23982	374	127	0.43	0.4	4.9250	1.7	0.3047	1.4	0.83	0.1172	0.9	1715	21	1807	14	1914	17	90
A353	28906	216	72	0.22	0.1	4.9570	1.6	0.3196	1.3	0.85	0.1125	0.8	1788	21	1812	13	1840	15	97
A203	4334	32	11	0.38	0.6	5.1510	2.5	0.3214	1.7	0.66	0.1162	1.9	1796	26	1844	22	1899	34	95
A210	7180	44	18	0.80	0.9	5.2920	2.5	0.3278	1.5	0.61	0.1171	2.0	1828	24	1868	22	1912	36	96
A350	16283	101	44	1.00	0.3	5.3590	1.9	0.3261	1.4	0.74	0.1192	1.3	1819	23	1878	17	1944	23	94
A220	9166	59	29	1.46	0.8	5.4040	2.2	0.3346	1.5	0.68	0.1171	1.6	1860	24	1885	19	1913	29	97
A214	35617	250	86	0.18	0.1	5.4180	1.7	0.3332	1.5	0.90	0.1180	0.8	1854	25	1888	15	1925	13	96
A201	36812	238	80	0.11	0.2	5.5650	1.6	0.3308	1.5	0.90	0.1220	0.7	1842	23	1911	14	1986	12	93
A205	5500	40	14	0.28	0.3	5.6090	2.9	0.3261	2.0	0.68	0.1248	2.1	1819	31	1918	25	2025	38	90
A264	14874	205	77	0.43	0.1	5.7100	1.8	0.3406	1.5	0.79	0.1216	1.1	1890	24	1933	16	1980	20	95
A289	25770	389	151	0.52	0.3	5.7580	2.3	0.3411	1.9	0.83	0.1224	1.3	1892	32	1940	20	1992	23	95
A223	4898	31	12	0.35	1.0	5.7640	3.0	0.3391	1.8	0.61	0.1233	2.4	1882	30	1941	26	2004	42	94
A227	6476	83	34	0.57	0.3	5.8270	2.2	0.3478	1.6	0.73	0.1215	1.5	1924	26	1950	19	1979	26	97
A193	46520	288	112	0.48	0.0	5.8420	1.7	0.3419	1.4	0.85	0.1239	0.9	1896	24	1953	15	2013	16	94
A320	24886	280	115	0.45	1.2	5.9770	2.1	0.3541	1.5	0.70	0.1224	1.5	1954	25	1972	19	1992	27	98
A297	7948	51	21	0.59	0.3	5.9880	2.3	0.3523	1.6	0.70	0.1233	1.6	1945	27	1974	20	2004	29	97
A333	5670	34	14	0.51	0.5	5.9980	2.6	0.3446	1.6	0.62	0.1262	2.1	1909	27	1976	23	2046	36	93
A277	14122	176	73	0.54	0.0	6.0300	2.0	0.3572	1.5	0.74	0.1224	1.3	1969	25	1980	17	1992	24	99
A325	8992	115	48	0.56	0.1	6.0860	2.2	0.3563	1.5	0.66	0.1239	1.7	1965	25	1988	20	2013	30	98
A258	11567	176	67	0.37	0.2	6.1000	2.3	0.3529	1.7	0.76	0.1253	1.5	1949	29	1990	20	2033	26	96
A272	13991	175	80	0.96	0.1	6.1260	1.8	0.3616	1.3	0.76	0.1229	1.1	1990	23	1994	15	1998	20	10
A301	8684	99	41	0.44	0.4	6.1890	2.2	0.3596	1.6	0.72	0.1248	1.6	1980	28	2003	20	2026	28	98
A269	7855	89	39	0.67	0.3	6.1970	2.2	0.3583	1.6	0.71	0.1254	1.6	1974	27	2004	20	2035	28	97
A317	10589	129	51	0.42	0.1	6.1970	2.2	0.3555	1.6	0.72	0.1264	1.5	1961	26	2004	19	2049	26	96
A261	15568	87	40	0.85	0.1	6.2060	1.8	0.3626	1.5	0.79	0.1241	1.1	1995	25	2005	16	2016	20	99
A293	22370	131	50	0.30	0.2	6.2370	1.8	0.3568	1.5	0.84	0.1268	1.0	1967	26	2010	16	2054	17	96
A274	7694	92	39	0.63	0.2	6.2650	2.1	0.3603	1.5	0.72	0.1261	1.5	1984	26	2014	19	2045	26	97
A267	4871	60	25	0.51	0.0	6.2880	2.3	0.3649	1.6	0.69	0.1250	1.7	2005	27	2017	20	2028	29	99
A281	47445	284	120	0.56	0.1	6.2950	1.7	0.3649	1.4	0.87	0.1251	0.8	2005	25	2018	15	2030	15	99

Grain	^{207}Pb[a] (cps)	U[b] (ppm)	Pb[b] (ppm)	Th[b] U	^{206}Pbc[c] (%)	^{207}Pb[d] ^{235}U	±2σ (%)	^{206}Pb[d] ^{238}U	±2σ (%)	ρ[e] (rho)	^{207}Pb[d] ^{206}Pb	±2σ (%)	^{206}Pb[f] ^{238}U	±2σ (Ma)	^{207}Pb[f] ^{235}U	±2σ (Ma)	^{207}Pb[f] ^{206}Pb	±2σ (Ma)	Con (%
A348	85569	987	399	0.42	0.0	6.3430	1.5	0.3635	1.3	0.91	0.1266	0.6	1999	23	2024	13	2051	11	97
A296	20571	140	64	0.85	b.d.	6.4080	2.2	0.3687	1.9	0.86	0.1261	1.1	2023	33	2033	19	2044	20	99
A217	9473	103	43	0.46	0.1	6.4330	2.0	0.3630	1.4	0.70	0.1285	1.4	1996	24	2037	18	2078	25	96
A206	10654	120	51	0.46	0.2	6.4460	2.0	0.3693	1.5	0.77	0.1266	1.3	2026	27	2039	18	2051	23	99
A247	8111	91	42	0.84	0.2	6.4500	2.4	0.3652	1.5	0.62	0.1281	1.9	2007	25	2039	21	2072	33	97
A338	9803	113	51	0.75	0.2	6.4540	2.1	0.3667	1.5	0.71	0.1276	1.5	2014	26	2040	18	2066	26	97
A188	7752	45	22	0.99	0.0	6.5670	2.4	0.3739	1.8	0.74	0.1274	1.6	2048	31	2055	21	2062	29	99
A237	4947	52	24	0.70	0.3	6.5770	2.8	0.3730	1.7	0.59	0.1279	2.3	2044	29	2056	25	2069	40	99
A268	9167	110	45	0.38	0.2	6.5790	2.2	0.3735	1.6	0.72	0.1278	1.5	2046	27	2057	19	2067	26	99
A259	17825	99	41	0.33	0.0	6.5937	2.1	0.3784	1.7	0.84	0.1264	1.1	2069	31	2059	18	2048	20	10
A185	4599	53	23	0.57	b.d.	6.6040	2.7	0.3691	1.6	0.58	0.1298	2.2	2025	27	2060	24	2095	39	97
A218	10972	118	52	0.58	0.2	6.8240	2.1	0.3800	1.5	0.69	0.1302	1.5	2077	26	2089	19	2101	27	99
A184	99724	519	206	0.25	b.d.	7.2660	1.6	0.3716	1.4	0.90	0.1418	0.7	2037	25	2145	14	2249	12	91
A229	134362	1576	653	0.15	0.0	7.6150	1.7	0.4031	1.4	0.82	0.1370	1.0	2183	26	2187	16	2190	17	10
A230	79074	378	168	0.08	0.0	9.2880	2.4	0.4344	1.7	0.70	0.1551	1.7	2325	33	2367	22	2403	29	97
A347	23079	176	93	0.68	b.d.	9.6900	1.8	0.4224	1.4	0.81	0.1664	1.0	2272	28	2406	16	2521	17	90
A341	30302	119	60	0.50	0.5	9.6920	1.8	0.4376	1.5	0.81	0.1606	1.1	2340	29	2406	17	2462	18	95
A263	72698	609	296	0.36	0.0	9.7000	1.5	0.4331	1.3	0.91	0.1624	0.6	2320	26	2407	13	2481	10	93
A360	46067	354	179	0.51	0.0	9.9370	1.5	0.4289	1.3	0.90	0.1680	0.6	2301	26	2429	14	2538	11	91
A226	141066	1082	495	0.04	0.0	10.0100	1.9	0.4493	1.8	0.94	0.1616	0.6	2392	36	2436	18	2473	11	97
A246	52309	374	191	0.42	0.0	10.1300	1.7	0.4434	1.4	0.87	0.1656	0.8	2366	29	2446	15	2514	14	94
A340	8723	37	18	0.26	0.2	10.1500	2.3	0.4488	1.7	0.77	0.1640	1.5	2390	35	2449	21	2498	24	96
A343	40385	152	74	0.31	0.4	10.1900	1.7	0.4320	1.4	0.84	0.1711	0.9	2315	28	2452	16	2569	16	90
A292	48507	194	94	0.30	0.2	10.2100	1.9	0.4409	1.7	0.89	0.1680	0.8	2355	33	2454	17	2538	14	93
A200	34994	134	63	0.05	0.3	10.2100	2.4	0.4619	1.7	0.73	0.1604	1.6	2448	36	2454	22	2460	28	10
A222	54891	206	104	0.37	0.1	10.5400	1.8	0.4453	1.6	0.87	0.1718	0.9	2374	31	2484	17	2575	15	92
A354	54046	172	88	0.36	0.0	10.8300	1.6	0.4510	1.4	0.90	0.1742	0.7	2400	28	2509	15	2598	12	92
A359	56108	416	206	0.13	0.0	10.8300	1.6	0.4731	1.3	0.82	0.1661	0.9	2497	27	2509	15	2518	15	99
A270	44524	160	86	0.36	0.0	10.9700	1.6	0.4780	1.4	0.88	0.1664	0.8	2519	30	2520	15	2521	13	10
A278	198040	1513	798	0.30	0.0	11.4000	1.9	0.4771	1.7	0.90	0.1732	0.8	2515	35	2556	17	2589	13	97
A304	27100	167	97	0.60	0.4	11.4900	1.6	0.4654	1.4	0.86	0.1791	0.8	2463	28	2564	15	2644	13	93
A262	19389	119	68	0.52	0.1	11.7200	1.8	0.4706	1.5	0.85	0.1807	0.9	2486	32	2582	17	2659	15	93
A191	54417	185	100	0.26	0.0	11.8400	2.1	0.4963	1.9	0.90	0.1730	0.9	2598	40	2592	20	2587	15	10
A288	49959	343	196	0.42	0.3	11.9300	1.8	0.4967	1.6	0.89	0.1742	0.8	2600	34	2599	17	2598	14	10
A282	15820	49	29	0.70	0.1	11.9600	2.0	0.4773	1.6	0.84	0.1817	1.1	2516	34	2601	19	2668	18	94
A315	27596	179	140	1.73	b.d.	11.9800	1.8	0.4841	1.6	0.85	0.1795	0.9	2545	33	2603	17	2648	16	96
A279	24403	150	82	0.29	0.1	12.1800	2.6	0.4898	2.2	0.87	0.1804	1.3	2570	47	2619	24	2656	21	97
A305	36308	208	124	0.45	1.2	12.2200	1.9	0.4977	1.6	0.83	0.1780	1.1	2604	35	2621	18	2635	18	99
A327	314064	846	442	0.09	0.0	12.2500	1.5	0.4975	1.4	0.92	0.1786	0.6	2603	31	2624	15	2640	10	99
A357	42111	247	159	0.82	0.1	12.2600	1.7	0.4980	1.5	0.87	0.1785	0.8	2605	31	2624	16	2639	14	99
A342	87674	255	247	2.59	0.1	12.5400	1.5	0.4965	1.3	0.89	0.1832	0.7	2599	29	2646	14	2682	11	97
A190	25093	71	42	0.49	0.2	12.5600	1.8	0.5005	1.6	0.88	0.1820	0.9	2616	35	2647	17	2671	15	98
A275	155189	890	520	0.47	0.0	12.6200	1.6	0.4936	1.5	0.93	0.1854	0.6	2586	32	2652	15	2702	9	96
A307	39420	243	138	0.25	0.4	12.8700	1.9	0.5123	1.7	0.89	0.1821	0.8	2667	37	2670	18	2672	14	10
A306	73680	453	278	0.73	0.1	12.9100	1.6	0.4844	1.4	0.88	0.1933	0.7	2546	29	2673	15	2770	12	92
A216	89312	245	154	0.59	0.0	13.2000	1.6	0.5124	1.5	0.89	0.1869	0.8	2667	32	2694	16	2715	12	98
A257	76520	452	257	0.20	0.2	13.2500	1.7	0.5209	1.6	0.92	0.1845	0.7	2703	35	2698	16	2694	11	10
A299	15140	85	51	0.41	0.0	13.2700	1.9	0.5186	1.5	0.78	0.1856	1.2	2693	33	2699	18	2704	20	10
A244	72030	405	239	0.26	0.0	13.7400	1.7	0.5288	1.6	0.90	0.1885	0.8	2736	35	2732	16	2729	12	10
A187	40983	177	119	0.46	b.d.	17.0000	1.7	0.5555	1.5	0.86	0.2219	0.9	2848	35	2935	17	2994	14	95
A311	54802	219	148	0.33	0.2	17.8200	1.6	0.5781	1.4	0.90	0.2236	0.7	2941	34	2980	15	3007	11	98
A251	15452	310	5	0.29	0.3	0.0346	137.4	0.0021	137.4	1.00	0.1184	3.9	14	19	35	48	1932	70	1
A280	2057	124	14	0.57	6.1	1.2720	7.0	0.0874	1.8	0.26	0.1055	6.7	540	10	833	41	1723	124	31
A310	26794	295	57	0.17	0.0	3.4650	1.9	0.1837	1.5	0.83	0.1368	1.0	1087	15	1519	15	2187	18	50
A312	44650	608	140	0.11	0.0	3.8650	1.8	0.2237	1.5	0.86	0.1253	0.9	1301	18	1606	14	2034	16	64
A255	15703	294	88	0.52	0.0	4.1900	2.1	0.2517	1.7	0.82	0.1208	1.2	1447	22	1672	17	1967	21	74
A219	11487	193	57	0.53	0.0	4.2860	2.3	0.2498	1.8	0.77	0.1244	1.5	1437	23	1691	19	2021	26	71
A302	35156	251	71	0.48	0.2	4.5660	1.8	0.2417	1.5	0.85	0.1370	0.9	1396	19	1743	15	2190	16	64
A273	26795	427	127	0.22	0.0	4.7490	1.9	0.2830	1.6	0.86	0.1217	1.0	1606	23	1776	16	1982	18	81
A186	*14954*	*182*	*54*	*0.46*	*0.0*	*4.7790*	*2.4*	*0.2445*	*2.1*	*0.87*	*0.1418*	*1.2*	*1410*	*27*	*1781*	*20*	*2249*	*20*	*63*
A339	*54979*	*838*	*266*	*0.36*	*0.2*	*4.9710*	*1.8*	*0.2886*	*1.4*	*0.78*	*0.1249*	*1.1*	*1635*	*21*	*1814*	*16*	*2028*	*20*	*81*
A221	*63836*	*462*	*149*	*0.33*	*0.0*	*5.0890*	*1.6*	*0.2958*	*1.4*	*0.88*	*0.1248*	*0.8*	*1671*	*21*	*1834*	*14*	*2026*	*14*	*82*
A337	*46911*	*745*	*203*	*0.21*	*1.5*	*5.2130*	*2.3*	*0.2448*	*1.6*	*0.71*	*0.1544*	*1.6*	*1412*	*20*	*1855*	*20*	*2396*	*27*	*59*
A352	*13260*	*75*	*27*	*0.30*	*b.d.*	*6.1460*	*2.1*	*0.3307*	*1.5*	*0.70*	*0.1348*	*1.5*	*1842*	*24*	*1997*	*19*	*2161*	*26*	*85*
A358	*38192*	*448*	*146*	*0.07*	*0.0*	*6.3940*	*2.0*	*0.3205*	*1.7*	*0.87*	*0.1447*	*1.0*	*1792*	*27*	*2031*	*18*	*2284*	*17*	*78*
A276	*49212*	*528*	*173*	*0.13*	*0.0*	*6.5660*	*1.8*	*0.3127*	*1.5*	*0.79*	*0.1523*	*1.1*	*1754*	*22*	*2055*	*16*	*2372*	*19*	*74*
A234	*9358*	*96*	*37*	*0.40*	*0.0*	*6.9700*	*2.6*	*0.3323*	*1.9*	*0.74*	*0.1521*	*1.7*	*1850*	*31*	*2108*	*23*	*2370*	*30*	*78*
A212	*18007*	*86*	*33*	*0.31*	*0.6*	*7.2850*	*2.4*	*0.3448*	*1.8*	*0.77*	*0.1532*	*1.5*	*1910*	*30*	*2147*	*22*	*2382*	*26*	*80*

Grain	^{207}Pb[a] (cps)	U[b] (ppm)	Pb[b] (ppm)	Th[b]/U	$^{206}Pb_c$[c] (%)	$^{207}Pb/^{235}U$[d]	±2σ (%)	$^{206}Pb/^{238}U$[d]	±2σ (%)	ρ[e] (rho)	$^{207}Pb/^{206}Pb$[d]	±2σ (%)	$^{206}Pb/^{238}U$[f]	±2σ (Ma)	$^{207}Pb/^{235}U$[f]	±2σ (Ma)	$^{207}Pb/^{206}Pb$[f]	±2σ (Ma)	Con (%
A232	*82683*	*673*	*236*	*0.11*	*0.2*	*7.7530*	*2.8*	*0.3271*	*1.5*	*0.54*	*0.1719*	*2.4*	*1825*	*24*	*2203*	*26*	*2576*	*39*	*7*
A245	*25484*	*247*	*101*	*0.30*	*0.1*	*7.7970*	*1.8*	*0.3683*	*1.4*	*0.78*	*0.1535*	*1.1*	*2021*	*24*	*2208*	*16*	*2386*	*19*	*8*
A224	*22282*	*102*	*42*	*0.40*	*0.6*	*8.1360*	*1.8*	*0.3643*	*1.4*	*0.80*	*0.1620*	*1.1*	*2003*	*25*	*2246*	*16*	*2476*	*18*	*8*
A183	*31622*	*128*	*64*	*0.76*	*0.3*	*8.5660*	*1.9*	*0.3917*	*1.6*	*0.86*	*0.1586*	*0.9*	*2131*	*29*	*2293*	*17*	*2441*	*16*	*8*
A249	*25294*	*206*	*91*	*0.44*	*0.2*	*8.6540*	*1.9*	*0.3789*	*1.6*	*0.85*	*0.1657*	*1.0*	*2071*	*28*	*2302*	*17*	*2514*	*17*	*8*
A322	*20492*	*166*	*82*	*0.77*	*b.d.*	*8.9280*	*2.0*	*0.3817*	*1.7*	*0.85*	*0.1696*	*1.1*	*2084*	*31*	*2331*	*19*	*2554*	*18*	*8*
A225	*32915*	*121*	*51*	*0.26*	*0.2*	*9.0000*	*2.0*	*0.3834*	*1.8*	*0.88*	*0.1702*	*0.9*	*2092*	*32*	*2338*	*18*	*2560*	*16*	*8*
A345	13226	114	51	0.55	0.1	9.0190	2.0	0.3767	1.6	0.80	0.1737	1.2	2061	28	2340	18	2593	19	7
A316	106084	905	435	0.60	0.1	9.0210	2.6	0.3949	2.3	0.90	0.1657	1.1	2146	42	2340	24	2514	19	8
A303	95033	611	256	0.29	0.0	9.4900	2.1	0.3612	1.5	0.72	0.1906	1.5	1988	26	2387	20	2747	24	7
A256	52924	366	172	0.32	0.3	9.6690	2.0	0.4117	1.6	0.81	0.1703	1.2	2223	30	2404	18	2561	19	8
A295	63538	228	111	0.40	0.1	9.7360	1.7	0.4214	1.5	0.85	0.1676	0.9	2267	28	2410	16	2534	15	8
A321	68533	510	228	0.19	0.0	9.8100	1.6	0.4134	1.4	0.89	0.1721	0.7	2230	27	2417	15	2578	12	8
A208	85654	658	298	0.29	0.1	9.8760	1.6	0.4041	1.5	0.92	0.1772	0.6	2188	27	2423	15	2627	11	8
A231	63014	466	220	0.44	0.1	9.8980	1.6	0.4011	1.5	0.92	0.1790	0.7	2174	28	2425	15	2643	11	8
A323	136865	1048	459	0.16	0.0	9.9100	1.7	0.4072	1.5	0.90	0.1765	0.7	2202	29	2426	16	2620	12	8
A228	26232	207	102	0.40	0.2	10.2300	2.2	0.4301	1.9	0.88	0.1724	1.0	2306	38	2455	21	2581	17	8
A265	57376	379	192	0.52	0.3	10.3400	1.7	0.4183	1.4	0.86	0.1794	0.9	2253	27	2466	16	2647	14	8
A213	63200	227	116	0.52	0.1	10.4100	1.7	0.4234	1.6	0.91	0.1782	0.7	2276	30	2472	16	2637	12	8
A199	24080	172	85	0.37	0.0	10.5800	1.8	0.4307	1.5	0.82	0.1782	1.0	2309	29	2487	17	2636	17	8
91500[h]	7017	61	11	0.25	0.4	1.8607	5.0	0.1807	5.7	0.61	0.0747	2.9	1071	56	1067	33	1060	58	10
Felix[h]	6593	361	52	2.09	0.4	0.6274	10.0	0.0808	7.9	0.43	0.0563	5.1	501	38	494	39	464	114	11
Plesovice[h]	2330	904	49	0.09	0.2	0.4243	10.5	0.0572	9.9	0.51	0.0538	1.5	359	35	359	32	362	33	9
GJ-1[h]	6697	306	28	0.03	0.2	0.8144	2.1	0.0983	1.3	0.49	0.0601	2.2	604	7	605	10			

$^{206}Pb/^{238}U$ error is the quadratic additions of the within run precision (2 SE) and the external reproducibility (2 SD) of the reference zircon. $^{207}Pb/^{206}Pb$ error propagation (^{207}Pb signal dependent) following Gerdes & Zeh (2009). $^{207}Pb/^{235}U$ error is the quadratic addition of the $^{207}Pb/^{206}Pb$ and $^{206}Pb/^{238}U$ uncertainty.

[a] Within run background-corrected mean ^{207}Pb signal in cps (counts per second).

[b] U and Pb content and Th/U ratio were calculated relative to GJ-1 reference zircon.

[c] Percentage of the common Pb on the ^{206}Pb. b.d. = below detection limit.

[d] Pb/U and Pb/Pb ratios. Corrected for background, within-run Pb/U fractionation (in case of $^{206}Pb/^{238}U$) and common Pb using Stacy and Kramers (1975) model Pb composition and subsequently normalised to GJ-1 (ID-TIMS value/measured value); $^{207}Pb/^{235}U$ calculated using (($^{207}Pb/^{206}Pb$)*($^{238}U/^{206}Pb$)*137.88).

[e] Rho (ρ) is the ($^{206}Pb/^{238}U$)/($^{207}Pb/^{235}U$) error correlation coefficient.

[f] Pb/U and Pb/Pb ages.

[g] Degree of concordance = (($^{206}Pb/^{238}U$ age)/($^{207}Pb/^{206}Pb$ age)) x 100.

[h] Mean of 13 (91500), 13 (Felix), 13 (Plesovice), and 26 (GJ-1) analyses, respectively.

Table S2

U, Th and Pb LA-ICP-MS data of zircon cores from sample GCH-06

Grain	^{207}Pb[a] (cps)	U[b] (ppm)	Pb[b] (ppm)	Th[b] / U	^{206}Pbc[c] (%)	^{207}Pb[d] / ^{235}U	±2σ (%)	^{206}Pb[d] / ^{238}U	±2σ (%)	ρ[e] (rho)	^{207}Pb[d] / ^{206}Pb	±2σ (%)	^{206}Pb[f] / ^{238}U	±2σ (Ma)	^{207}Pb[f] / ^{235}U	±2σ (Ma)	^{207}Pb[f] / ^{206}Pb	±2σ (Ma)	Conc. (%)
A178	4707	306	28	1.10	0.5	0.6106	2.4	0.0780	0.8	0.35	0.0568	2.2	484	4	484	9	482	49	100
A139	7501	225	25	1.97	0.2	0.6337	2.0	0.0804	0.9	0.43	0.0572	1.8	498	4	498	8	499	40	100
A165	7015	224	21	1.00	0.1	0.6499	1.8	0.0819	0.9	0.51	0.0576	1.5	507	4	508	7	514	33	99
A098	1010	21	3	2.81	1.4	0.6534	8.3	0.0819	1.9	0.23	0.0579	8.0	508	9	511	34	524	177	97
A136	8137	104	11	1.70	0.0	0.6601	1.7	0.0821	1.0	0.61	0.0583	1.3	509	5	515	7	542	29	94
A167	2072	62	6	1.36	0.5	0.6613	3.4	0.0822	0.9	0.25	0.0584	3.3	509	4	515	14	543	72	94
A058	1094	57	5	0.73	0.0	0.6672	3.3	0.0824	0.8	0.23	0.0587	3.2	510	4	519	13	557	69	92
A135	5066	312	30	1.13	0.3	0.6550	2.7	0.0830	1.0	0.39	0.0572	2.5	514	5	512	11	500	54	103
A031	861	42	4	0.78	0.3	0.6731	4.6	0.0842	1.4	0.32	0.0580	4.3	521	7	523	19	529	95	98
A121	2469	72	8	1.58	0.2	0.6905	2.9	0.0864	1.1	0.39	0.0579	2.7	534	6	533	12	527	58	101
A151	13535	505	52	0.79	5.5	0.7028	5.7	0.0870	1.1	0.19	0.0586	5.6	538	6	540	24	551	122	98
A032	4035	184	17	0.51	0.1	0.7148	2.7	0.0875	0.9	0.34	0.0593	2.6	541	5	548	12	577	56	94
A030	2074	96	9	0.83	0.2	0.7165	3.6	0.0880	1.2	0.34	0.0590	3.4	544	6	549	16	569	74	96
A171	929	22	2	1.06	1.5	0.7012	6.4	0.0881	1.7	0.26	0.0577	6.2	544	9	540	27	519	136	105
A142	4516	117	11	0.50	1.0	0.7210	2.7	0.0884	0.8	0.30	0.0592	2.6	546	4	551	11	574	56	95
A044	3463	345	31	0.48	b.d.	0.7286	2.0	0.0891	1.0	0.51	0.0593	1.7	550	5	556	9	578	38	95
A024	1141	51	5	0.99	b.d.	0.7289	3.5	0.0893	1.1	0.31	0.0592	3.4	551	6	556	15	576	73	96
A160	3104	84	9	1.25	b.d.	0.7402	2.2	0.0896	1.1	0.49	0.0599	1.9	553	6	563	9	599	41	92
A048	1162	53	6	1.12	0.1	0.7329	4.2	0.0900	1.2	0.28	0.0591	4.0	556	6	558	18	569	88	98
A014	7102	333	38	1.65	0.0	0.7400	1.8	0.0906	0.7	0.39	0.0593	1.7	559	4	562	8	576	36	97
A050	5796	530	47	0.29	b.d.	0.7360	2.0	0.0908	0.9	0.46	0.0588	1.8	560	5	560	9	559	39	100
A166	10167	271	26	0.42	0.1	0.7679	1.7	0.0933	0.8	0.51	0.0597	1.4	575	5	579	7	592	31	97
A021	3789	357	37	0.81	b.d.	0.7540	2.1	0.0942	0.8	0.37	0.0581	2.0	580	4	571	9	533	43	109
A097	5057	114	15	1.34	0.1	0.9106	2.5	0.1049	0.9	0.36	0.0630	2.3	643	5	657	12	708	49	91
A164	5642	237	27	0.53	0.4	0.9145	2.1	0.1075	0.7	0.31	0.0617	2.0	658	4	659	10	663	43	99
A122	5541	114	17	1.74	0.1	0.9975	2.3	0.1152	1.0	0.43	0.0628	2.1	703	7	703	12	701	45	100
A086	6685	130	19	1.31	0.1	1.0880	2.4	0.1221	1.0	0.43	0.0647	2.1	742	7	748	13	763	45	97
A154	6213	110	16	1.06	0.2	1.1010	2.2	0.1258	0.8	0.36	0.0635	2.1	764	6	754	12	725	44	105
A017	20011	191	57	0.52	2.2	3.9390	2.3	0.2773	0.8	0.33	0.1030	2.2	1578	11	1622	19	1680	41	94
A060	10063	59	22	1.16	1.1	4.8390	2.1	0.3040	0.8	0.38	0.1155	1.9	1711	12	1792	17	1887	34	91
A170	12523	47	16	0.54	1.1	5.0920	1.8	0.3111	1.0	0.55	0.1187	1.5	1746	15	1835	15	1937	27	90
A118	3175	11	4	0.58	1.8	5.2230	2.9	0.3162	1.5	0.51	0.1198	2.5	1771	23	1856	25	1953	44	91
A046	11071	65	29	1.55	0.6	5.4500	1.9	0.3377	0.8	0.41	0.1171	1.7	1875	13	1893	17	1912	31	98
A092	8889	68	24	0.44	0.2	5.4570	1.8	0.3273	0.9	0.50	0.1209	1.6	1825	15	1894	16	1970	28	93
A125	32838	117	46	1.06	0.3	5.4630	1.5	0.3222	0.8	0.53	0.1230	1.2	1800	12	1895	13	2000	22	90
A109	12141	88	36	1.09	0.6	5.6000	1.9	0.3427	0.9	0.49	0.1185	1.7	1900	15	1916	17	1934	30	98
A049	113475	1440	506	0.25	0.0	5.6470	1.2	0.3451	0.9	0.81	0.1187	0.7	1911	15	1923	10	1936	12	99
A131	9654	34	15	1.53	0.0	5.7250	1.7	0.3380	0.9	0.52	0.1229	1.5	1877	15	1935	15	1998	26	94
A029	36426	227	93	1.06	0.1	5.7650	1.0	0.3446	0.7	0.66	0.1213	0.8	1909	11	1941	9	1976	14	97
A108	25518	39	14	0.48	0.2	5.8080	1.5	0.3380	1.0	0.65	0.1246	1.1	1877	16	1948	13	2024	20	93
A155	18273	128	56	1.43	0.1	5.8360	1.4	0.3515	0.8	0.54	0.1204	1.2	1942	13	1952	12	1962	21	99
A042	24824	287	111	0.49	0.2	5.9610	1.4	0.3581	0.8	0.61	0.1207	1.1	1973	14	1970	12	1967	19	100
A113	80566	560	207	0.32	0.0	5.9810	1.1	0.3559	0.8	0.72	0.1219	0.7	1963	13	1973	9	1984	13	99
A043	48273	541	210	0.59	0.0	5.9840	1.3	0.3545	1.0	0.78	0.1224	0.8	1956	17	1973	11	1992	14	98
A062	12209	129	45	0.26	0.2	6.0160	1.7	0.3382	0.9	0.51	0.1290	1.5	1878	14	1978	15	2085	26	90
A007	8505	48	28	3.39	0.1	6.0400	2.0	0.3535	1.1	0.57	0.1239	1.6	1951	19	1982	17	2013	29	97
A080	14770	53	19	0.21	b.d.	6.0540	1.9	0.3576	1.3	0.67	0.1228	1.4	1971	22	1984	17	1997	25	99
A085	20485	70	27	0.57	0.1	6.0750	1.3	0.3593	0.7	0.51	0.1226	1.1	1979	11	1987	11	1995	19	99
A022	13768	75	31	0.93	0.4	6.0820	1.6	0.3466	0.8	0.51	0.1273	1.4	1918	13	1988	14	2061	24	93
A126	48585	162	69	0.99	0.0	6.1350	1.0	0.3626	0.8	0.77	0.1227	0.7	1995	14	1995	9	1996	12	100
A176	14071	47	20	0.97	0.0	6.1600	1.4	0.3579	0.9	0.61	0.1248	1.1	1972	15	1999	12	2026	20	97
A138	18443	60	27	1.20	0.0	6.1900	1.4	0.3616	0.8	0.58	0.1242	1.2	1990	14	2003	12	2017	20	99
A040	8577	44	18	0.84	0.1	6.2150	2.0	0.3527	1.2	0.59	0.1278	1.6	1948	20	2007	18	2068	28	94
A163	126261	423	160	0.24	0.0	6.3000	1.0	0.3717	0.7	0.67	0.1229	0.8	2037	12	2018	9	1999	14	102
A045	6500	32	15	1.23	0.2	6.3240	2.1	0.3626	1.0	0.50	0.1265	1.8	1994	18	2022	18	2050	32	97
A101	14663	43	17	0.52	0.0	6.3270	1.5	0.3608	1.0	0.65	0.1272	1.1	1986	17	2022	13	2059	20	96
A006	9127	46	19	0.94	0.0	6.4000	1.6	0.3524	1.0	0.63	0.1317	1.2	1946	17	2032	14	2121	22	92
A095	31944	100	43	0.88	0.1	6.4130	1.1	0.3683	0.8	0.70	0.1263	0.8	2022	14	2034	10	2047	14	99
A009	37615	200	75	0.23	0.0	6.4280	1.1	0.3644	0.8	0.78	0.1280	0.7	2003	14	2036	10	2070	12	97
A145	19697	60	35	3.05	0.0	6.4490	1.3	0.3557	0.9	0.67	0.1315	1.0	1962	15	2039	12	2118	17	93
A059	5521	27	11	0.92	b.d.	6.4790	1.8	0.3536	1.0	0.53	0.1329	1.5	1952	16	2043	16	2137	27	91
A119	71868	221	80	0.04	0.0	6.5260	1.5	0.3658	1.0	0.65	0.1294	1.2	2010	17	2049	13	2090	20	96
A116	18971	121	57	1.48	0.0	6.5460	1.2	0.3617	0.8	0.67	0.1313	0.9	1990	14	2052	11	2115	15	94
A018	15835	79	32	0.51	0.1	6.5580	1.5	0.3700	0.6	0.43	0.1285	1.4	2029	11	2054	14	2078	24	98
A110	20939	68	29	0.79	b.d.	6.6320	1.2	0.3712	0.6	0.52	0.1296	1.1	2035	11	2064	11	2092	19	97
A016	16017	79	34	0.68	0.0	6.7590	1.2	0.3792	0.8	0.62	0.1293	0.9	2072	13	2080	11	2088	17	99
A120	16721	102	48	1.31	0.1	6.8020	1.5	0.3807	0.9	0.61	0.1296	1.2	2080	17	2086	13	2092	21	99
A156	41230	123	59	1.34	0.2	6.8900	1.4	0.3859	1.0	0.73	0.1295	0.9	2104	18	2097	12	2091	17	101

Grain	^{207}Pb[a] (cps)	U[b] (ppm)	Pb[b] (ppm)	Th[b] / U	^{206}Pbc[c] (%)	^{207}Pb[d] / ^{235}U	±2σ (%)	^{206}Pb[d] / ^{238}U	±2σ (%)	ρ[e] (rho)	^{207}Pb[d] / ^{206}Pb	±2σ (%)	^{206}Pb[f] / ^{238}U	±2σ (Ma)	^{207}Pb[f] / ^{235}U	±2σ (Ma)	^{207}Pb[f] / ^{206}Pb	±2σ (Ma)	Conc. (%)
A096	17830	113	55	1.48	b.d.	6.9020	1.4	0.3857	0.7	0.55	0.1298	1.1	2103	13	2099	12	2095	20	100
A077	14484	43	20	0.99	b.d.	6.9840	1.3	0.3832	0.7	0.54	0.1322	1.1	2091	12	2109	11	2127	19	98
A111	59717	352	182	1.64	b.d.	7.0970	1.3	0.3891	1.0	0.80	0.1323	0.8	2119	18	2124	11	2128	13	100
A011	59006	263	110	0.48	0.1	7.7220	1.2	0.3840	0.8	0.70	0.1458	0.8	2095	15	2199	11	2298	14	91
A162	193691	1041	420	0.13	0.1	8.0140	1.1	0.3960	0.8	0.72	0.1468	0.8	2151	15	2233	10	2308	14	93
A169	141858	352	148	0.11	0.0	8.3560	1.0	0.4155	0.8	0.80	0.1458	0.6	2240	16	2270	9	2298	10	97
A112	126835	622	255	0.02	0.0	8.6550	1.0	0.4084	0.7	0.68	0.1537	0.7	2208	13	2302	9	2388	12	92
A099	82252	387	171	0.28	0.1	8.6710	1.0	0.4196	0.7	0.69	0.1499	0.8	2259	14	2304	10	2345	13	96
A081	88144	198	85	0.11	0.2	8.9230	1.4	0.4205	1.1	0.75	0.1539	0.9	2263	20	2330	13	2390	16	95
A175	72625	145	66	0.15	0.0	9.6430	1.1	0.4369	0.8	0.71	0.1601	0.8	2337	16	2401	11	2457	14	95
A158	113353	236	108	0.29	0.0	9.7430	0.9	0.4273	0.7	0.73	0.1653	0.6	2294	13	2411	9	2511	11	91
A152	72287	136	60	0.14	0.0	9.7430	1.4	0.4217	0.9	0.61	0.1675	1.1	2268	17	2411	13	2533	19	90
A072	87374	183	85	0.12	b.d.	9.8210	1.1	0.4503	0.8	0.71	0.1582	0.8	2397	16	2418	10	2436	13	98
A174	82762	176	92	1.00	0.0	9.8250	1.2	0.4352	1.0	0.85	0.1637	0.6	2329	20	2419	11	2494	10	93
A140	84360	165	78	0.38	0.0	10.1200	1.0	0.4319	0.7	0.77	0.1699	0.6	2314	14	2446	9	2556	10	91
A159	94238	213	100	0.08	b.d.	10.1700	1.8	0.4619	1.3	0.76	0.1597	1.2	2448	27	2450	16	2453	19	100
A177	68721	132	63	0.42	0.1	10.3200	1.1	0.4345	0.7	0.66	0.1722	0.8	2326	14	2464	10	2579	13	90
A114	146130	288	164	0.96	0.4	10.3200	1.6	0.4784	1.4	0.87	0.1565	0.8	2520	29	2464	15	2418	13	104
A133	46703	92	48	0.59	0.0	10.3300	1.2	0.4611	0.8	0.68	0.1624	0.9	2445	17	2465	11	2481	15	99
A055	60869	382	189	0.24	0.0	10.6000	1.5	0.4702	1.2	0.80	0.1635	0.9	2484	25	2489	14	2492	16	100
A078	40643	157	83	0.75	0.1	10.6000	1.1	0.4519	0.7	0.60	0.1702	0.9	2403	13	2489	10	2560	15	94
A168	56783	112	60	0.62	0.0	10.8000	1.1	0.4786	0.6	0.56	0.1637	0.9	2521	13	2506	10	2494	15	101
A010	47138	152	79	0.50	0.0	10.9400	0.9	0.4652	0.6	0.67	0.1706	0.7	2462	12	2518	9	2564	11	96
A028	34393	225	125	0.68	0.0	11.0300	1.5	0.4902	1.0	0.65	0.1631	1.1	2572	21	2525	14	2489	19	103
A094	63572	110	53	0.21	b.d.	11.0400	1.0	0.4495	0.7	0.66	0.1782	0.8	2393	14	2527	10	2636	13	91
A084	62599	111	65	1.24	0.0	11.1700	1.0	0.4549	0.7	0.71	0.1781	0.7	2417	15	2538	10	2636	12	92
A023	39244	115	77	1.84	0.1	11.2000	1.1	0.4802	0.8	0.73	0.1691	0.7	2528	17	2540	10	2549	12	99
A129	59465	224	119	0.70	0.0	11.2200	1.0	0.4607	0.7	0.65	0.1766	0.8	2443	14	2541	10	2621	13	93
A083	203698	336	164	0.12	0.0	11.3900	1.2	0.4668	0.9	0.78	0.1770	0.7	2470	19	2556	11	2625	12	94
A153	117410	436	220	0.33	0.0	11.4500	0.9	0.4652	0.7	0.73	0.1786	0.6	2462	14	2561	8	2640	10	93
A039	27086	80	44	0.70	0.1	11.4700	1.7	0.4680	1.2	0.70	0.1778	1.2	2475	24	2562	16	2633	20	94
A025	63468	184	98	0.51	0.2	11.5200	1.2	0.4767	0.8	0.70	0.1752	0.8	2513	17	2566	11	2608	14	96
A065	70607	215	112	0.48	0.1	11.5500	1.1	0.4676	0.9	0.78	0.1792	0.7	2473	18	2569	10	2645	11	93
A073	77483	277	148	0.57	0.1	11.5900	1.0	0.4685	0.7	0.71	0.1793	0.7	2477	15	2571	10	2647	12	94
A082	109583	174	94	0.64	b.d.	11.6100	1.1	0.4759	0.9	0.79	0.1769	0.7	2509	19	2573	11	2624	12	96
A134	103814	352	185	0.46	0.0	11.6400	1.0	0.4726	0.8	0.75	0.1786	0.7	2495	16	2576	9	2640	11	95
A132	75875	209	113	0.65	0.0	11.6600	1.1	0.4766	0.8	0.68	0.1774	0.8	2512	16	2577	11	2628	14	96
A127	74128	133	73	0.66	0.0	11.9100	1.3	0.4761	1.0	0.79	0.1814	0.8	2510	21	2597	12	2666	13	94
A027	77945	482	261	0.25	0.1	12.0000	1.7	0.5092	1.3	0.80	0.1709	1.0	2653	29	2604	16	2567	17	103
A051	82134	441	248	0.62	0.0	12.0700	1.4	0.4863	1.2	0.88	0.1800	0.7	2555	25	2610	13	2653	11	96
A137	110086	190	100	0.30	0.0	12.0800	1.0	0.4880	0.7	0.76	0.1796	0.6	2562	15	2611	9	2649	10	97
A054	155341	868	468	0.28	0.1	12.1800	1.5	0.5037	1.3	0.91	0.1754	0.6	2629	29	2618	14	2610	10	101
A015	85939	245	132	0.43	0.0	12.1900	1.3	0.4858	1.1	0.88	0.1820	0.6	2552	24	2619	12	2671	10	96
A115	73937	117	66	0.59	0.1	12.3100	1.1	0.4927	0.7	0.62	0.1812	0.9	2582	15	2628	10	2664	14	97
A076	19676	32	19	0.85	b.d.	12.3500	1.4	0.4905	0.9	0.63	0.1826	1.1	2573	19	2631	14	2676	19	96
A008	82055	205	116	0.53	1.1	12.3600	1.2	0.4883	0.8	0.67	0.1835	0.9	2564	17	2632	11	2685	14	95
A057	51762	287	175	0.86	0.0	12.4100	1.3	0.5104	1.0	0.76	0.1764	0.9	2658	22	2636	12	2619	14	101
A088	133707	213	112	0.13	0.0	12.5000	1.0	0.5015	0.6	0.64	0.1808	0.8	2620	14	2643	9	2660	13	99
A066	39755	215	118	0.36	0.0	12.5400	1.1	0.5018	0.8	0.69	0.1812	0.8	2622	17	2646	11	2664	13	98
A038	58946	161	93	0.70	b.d.	12.5400	1.2	0.4959	0.9	0.74	0.1834	0.8	2596	19	2646	11	2684	14	97
A041	70978	390	225	0.54	0.0	12.5700	1.1	0.5080	0.9	0.81	0.1795	0.7	2648	20	2648	11	2648	11	100
A075	32892	111	70	1.13	0.0	12.5800	1.3	0.5099	0.9	0.66	0.1789	1.0	2656	19	2648	13	2643	17	101
A117	93943	288	173	0.91	0.1	12.6400	1.3	0.4997	0.9	0.69	0.1834	0.9	2613	19	2653	12	2684	15	97
A064	126213	340	213	1.19	0.0	12.7300	1.0	0.4968	0.8	0.80	0.1859	0.6	2600	17	2660	9	2706	10	96
A091	70903	109	65	0.65	0.3	12.9400	1.1	0.5112	0.7	0.67	0.1835	0.8	2662	16	2675	10	2685	13	99
A012	60316	152	89	0.50	0.1	13.2800	1.2	0.5175	0.9	0.78	0.1861	0.7	2688	20	2700	11	2708	12	99
A157	66320	97	58	0.89	0.1	13.3100	1.0	0.4913	0.6	0.62	0.1965	0.8	2577	13	2702	9	2797	12	92
A123	101485	131	81	0.65	0.1	16.0800	1.3	0.5199	1.0	0.75	0.2243	0.9	2699	22	2882	13	3012	14	90
A161	*2789*	*84*	*7*	*0.55*	*0.7*	*0.5616*	*4.7*	*0.0761*	*1.0*	*0.22*	*0.0536*	*4.6*	*473*	*5*	*453*	*17*	*352*	*104*	*134*
A079	*13372*	*105*	*36*	*0.81*	*0.8*	*5.0220*	*1.8*	*0.2974*	*0.7*	*0.41*	*0.1225*	*1.6*	*1678*	*11*	*1823*	*15*	*1992*	*29*	*84*
A090	*19901*	*68*	*23*	*0.56*	*b.d.*	*5.4770*	*1.5*	*0.3094*	*0.8*	*0.55*	*0.1284*	*1.3*	*1738*	*13*	*1897*	*13*	*2076*	*23*	*84*
A047	*14757*	*83*	*30*	*0.63*	*0.1*	*5.5900*	*1.6*	*0.3225*	*0.8*	*0.47*	*0.1257*	*1.4*	*1802*	*12*	*1915*	*14*	*2039*	*25*	*88*
A124	*5979*	*23*	*9*	*1.24*	*0.0*	*5.7630*	*2.3*	*0.3107*	*1.1*	*0.47*	*0.1345*	*2.1*	*1744*	*17*	*1941*	*20*	*2158*	*36*	*81*
A144	*6490*	*20*	*8*	*0.91*	*b.d.*	*5.8590*	*1.9*	*0.3259*	*1.0*	*0.54*	*0.1304*	*1.6*	*1818*	*16*	*1955*	*17*	*2103*	*28*	*86*
A130	*53980*	*373*	*137*	*0.59*	*0.1*	*6.8090*	*1.1*	*0.3369*	*0.7*	*0.62*	*0.1466*	*0.9*	*1872*	*11*	*2087*	*10*	*2306*	*15*	*81*
A107	*176243*	*476*	*158*	*0.09*	*0.0*	*6.8570*	*1.2*	*0.3258*	*0.8*	*0.68*	*0.1527*	*0.9*	*1818*	*13*	*2093*	*11*	*2376*	*15*	*77*
A089	*70574*	*155*	*66*	*0.97*	*b.d.*	*7.8820*	*1.2*	*0.3736*	*0.9*	*0.74*	*0.1530*	*0.8*	*2046*	*16*	*2218*	*11*	*2380*	*14*	*86*

Grain	^{207}Pb[a] (cps)	U[b] (ppm)	Pb[b] (ppm)	Th[b] / U	^{206}Pbc[c] (%)	$^{207}Pb/^{235}U$[d]	±2σ (%)	$^{206}Pb/^{238}U$[d]	±2σ (%)	ρ[e] (rho)	$^{207}Pb/^{206}Pb$[d]	±2σ (%)	$^{206}Pb/^{238}U$[f]	±2σ (Ma)	$^{207}Pb/^{235}U$[f]	±2σ (Ma)	$^{207}Pb/^{206}Pb$[f]	±2σ (Ma)	Conc. (%)
A143	*83708*	*190*	*78*	*0.15*	*b.d.*	*8.6590*	*1.1*	*0.3947*	*0.6*	*0.59*	*0.1591*	*0.9*	*2145*	*12*	*2303*	*10*	*2446*	*15*	*88*
A087	*79415*	*347*	*140*	*0.34*	*0.4*	*8.6980*	*2.0*	*0.3636*	*1.1*	*0.57*	*0.1735*	*1.6*	*1999*	*19*	*2307*	*18*	*2592*	*27*	*77*
A141	*12930*	*29*	*15*	*1.57*	*1.1*	*8.7890*	*2.0*	*0.3978*	*1.3*	*0.63*	*0.1602*	*1.5*	*2159*	*23*	*2316*	*18*	*2458*	*26*	*88*
A056	*31360*	*109*	*50*	*0.42*	*0.1*	*9.5390*	*1.0*	*0.4129*	*0.7*	*0.69*	*0.1676*	*0.7*	*2228*	*13*	*2391*	*9*	*2533*	*12*	*88*
A074	*89065*	*178*	*81*	*0.52*	*0.1*	*9.6900*	*1.0*	*0.3978*	*0.6*	*0.61*	*0.1767*	*0.8*	*2159*	*12*	*2406*	*9*	*2622*	*13*	*82*
91500[h]	9367	69	13	0.46	0.6	1.8167	9.0	0.1777	2.9	0.28	0.0741	8.1	1055	28	1051	59	1043	166	102
Felix[h]	4705	227	26	1.76	0.6	0.6073	10.8	0.0813	4.8	0.27	0.0542	8.9	504	23	482	42	376	206	151
Plesovice[h]	1707	575	30	0.12	0.2	0.4114	2.2	0.0555	2.4	0.41	0.0538	0.6	348	8	350	6	361	13	97
GJ-1[h]	7212	286	26	0.02	0.1	0.8151	1.5	0.0984	0.5	0.31	0.0601	1.5	605	3	605	7			

$^{206}Pb/^{238}U$ error is the quadratic additions of the within run precision (2 SE) and the external reproducibility (2 SD) of the reference zircon. $^{207}Pb/^{206}Pb$ error propagation (^{207}Pb signal dependent) following Gerdes & Zeh (2009). $^{207}Pb/^{235}U$ error is the quadratic addition of the $^{207}Pb/^{206}Pb$ and $^{206}Pb/^{238}U$ uncertainty.

[a] Within run background-corrected mean ^{207}Pb signal in cps (counts per second).

[b] U and Pb content and Th/U ratio were calculated relative to GJ-1 reference zircon.

[c] Percentage of the common Pb on the ^{206}Pb. b.d. = below detection limit.

[d] Pb/U and Pb/Pb ratios. Corrected for background, within-run Pb/U fractionation (in case of $^{206}Pb/^{238}U$) and common Pb using Stacy and Kramers (1975) model Pb composition and subsequently normalised to GJ-1 (ID-TIMS value/measured value); $^{207}Pb/^{235}U$ calculated using (($^{207}Pb/^{206}Pb$)*($^{238}U/^{206}Pb$)*137.88).

[e] Rho (ρ) is the ($^{206}Pb/^{238}U$)/($^{207}Pb/^{235}U$) error correlation coefficient.

[f] Pb/U and Pb/Pb ages.

[g] Degree of concordance = (($^{206}Pb/^{238}U$ age)/($^{207}Pb/^{206}Pb$ age)) x 100.

[h] Mean of 12 (91500), 13 (Felix), 13 (Plesovice), and 26 (GJ-1) analyses, respectively.

Table S3

U, Th and Pb LA-ICP-MS data of zircon cores from sample GCH-17

Grain	^{207}Pb[a] (cps)	U[b] (ppm)	Pb[b] (ppm)	Th/U[b]	^{206}Pbc[c] (%)	$^{207}Pb/^{235}U$[d]	±2σ (%)	$^{206}Pb/^{238}U$[d]	±2σ (%)	ρ[e] (rho)	$^{207}Pb/^{206}Pb$[d]	±2σ (%)	$^{206}Pb/^{238}U$[f]	±2σ (Ma)	$^{207}Pb/^{235}U$[f]	±2σ (Ma)	$^{207}Pb/^{206}Pb$[f]	±2σ (Ma)	Conc. (%)
s2A591	6015	314	27	0.42	0.2	0.6575	2.3	0.0811	1.4	0.60	0.0588	1.8	503	7	513	9	559	40	90
s3A350	568	28	3	1.08	0.0	0.6480	5.9	0.0812	1.8	0.32	0.0579	5.6	503	9	507	24	525	122	96
s2A589	2450	137	12	0.46	b.d.	0.6482	2.9	0.0816	1.7	0.57	0.0576	2.4	506	8	507	12	515	53	98
s3A359	768	34	3	0.81	1.1	0.6621	6.6	0.0817	1.8	0.27	0.0588	6.3	506	9	516	27	559	138	91
s2A541	2318	121	10	0.33	0.1	0.6545	3.2	0.0819	1.7	0.53	0.0580	2.7	507	8	511	13	528	59	96
s3A400	1136	53	5	1.15	b.d.	0.6643	4.4	0.0823	1.7	0.37	0.0585	4.1	510	8	517	18	549	90	93
s3A371	1912	93	8	0.50	b.d.	0.6655	3.2	0.0825	1.4	0.44	0.0585	2.8	511	7	518	13	549	62	93
s2A533	6190	311	30	0.67	0.2	0.6586	2.3	0.0829	1.5	0.66	0.0576	1.8	513	8	514	9	516	38	99
s2A583	8503	425	36	0.28	0.2	0.6608	2.2	0.0830	1.5	0.68	0.0577	1.6	514	7	515	9	519	36	99
s2A590	3242	167	15	0.46	0.1	0.6622	3.0	0.0831	1.7	0.55	0.0578	2.5	515	8	516	12	522	55	99
s2A593	6975	350	30	0.24	0.7	0.6743	3.0	0.0831	1.5	0.49	0.0588	2.6	515	7	523	12	561	56	92
s2A546	3205	127	14	0.91	2.2	0.6612	5.1	0.0833	1.8	0.36	0.0576	4.8	516	9	515	21	515	105	100
s3A357	5142	247	23	0.97	0.0	0.6707	2.1	0.0833	1.4	0.67	0.0584	1.6	516	7	521	9	545	34	95
s2A570	13730	571	52	0.44	1.1	0.6621	3.3	0.0834	2.3	0.68	0.0576	2.4	516	11	516	13	514	53	101
s3A398	2195	97	9	0.98	0.0	0.6623	3.1	0.0837	1.3	0.42	0.0574	2.8	518	6	516	13	508	62	102
s2A573	1245	66	6	0.70	0.1	0.6676	3.8	0.0837	1.6	0.41	0.0578	3.5	518	8	519	16	523	76	99
s2A531	11300	579	64	1.02	b.d.	0.6739	2.0	0.0838	1.5	0.75	0.0583	1.3	519	7	523	8	541	28	96
s2A597	1160	64	6	0.42	0.0	0.6754	4.0	0.0841	1.6	0.41	0.0583	3.6	520	8	524	16	540	80	96
s3A393	5052	238	24	1.34	0.0	0.6727	2.8	0.0842	1.4	0.49	0.0580	2.4	521	7	522	11	528	53	99
s3A373	1618	79	7	0.62	b.d.	0.6825	3.8	0.0844	1.5	0.41	0.0587	3.5	522	8	528	16	554	76	94
s3A366	2257	105	11	1.64	0.0	0.6755	3.4	0.0847	1.3	0.39	0.0579	3.2	524	7	524	14	524	70	100
s2A563	1731	88	8	0.45	0.3	0.6755	3.9	0.0847	1.8	0.46	0.0578	3.5	524	9	524	16	523	76	100
s2A581	7606	355	33	0.46	0.7	0.6760	2.3	0.0848	1.5	0.66	0.0578	1.8	525	8	524	10	522	39	100
s2A521	3508	176	17	0.63	0.2	0.6781	2.8	0.0849	1.6	0.58	0.0580	2.3	525	8	526	12	528	50	99
s3A389	2714	123	11	0.74	b.d.	0.6995	2.6	0.0852	1.4	0.54	0.0596	2.2	527	7	538	11	588	47	90
s2A554	3752	174	19	0.83	1.7	0.6805	4.3	0.0853	1.8	0.42	0.0578	3.9	528	9	527	18	523	86	101
s2A559	9485	518	48	0.51	0.1	0.7016	2.1	0.0856	1.4	0.69	0.0595	1.5	529	7	540	9	584	32	91
s2A588	8925	451	46	0.75	0.1	0.6936	2.2	0.0856	1.4	0.62	0.0588	1.7	530	7	535	9	558	38	95
s3A354	1519	71	7	0.99	b.d.	0.6979	3.7	0.0857	1.3	0.34	0.0590	3.5	530	7	538	16	569	77	93
s3A349	6488	315	28	0.56	b.d.	0.6835	2.3	0.0858	1.3	0.56	0.0578	1.9	531	7	529	9	522	42	102
s3A392	4872	227	22	0.96	0.0	0.6954	2.3	0.0861	1.3	0.58	0.0586	1.9	532	7	536	10	552	41	97
s2A526	2533	127	16	1.41	0.2	0.6954	3.0	0.0862	1.6	0.55	0.0585	2.5	533	8	536	13	548	55	97
s3A397	290	13	2	2.28	0.0	0.6992	7.2	0.0864	2.5	0.34	0.0587	6.8	534	13	538	31	557	148	96
s3A381	2264	105	10	0.69	b.d.	0.6926	3.1	0.0865	1.3	0.43	0.0581	2.8	535	7	534	13	534	61	100
s2A575	2354	120	12	0.67	0.3	0.6938	3.3	0.0867	1.6	0.48	0.0580	2.9	536	8	535	14	531	63	101
s2A538	7292	337	29	0.15	0.9	0.6956	2.7	0.0869	1.5	0.54	0.0581	2.3	537	8	536	11	532	50	101
s3A370	3220	147	17	1.75	0.0	0.7043	2.8	0.0872	1.3	0.48	0.0586	2.5	539	7	541	12	552	54	98
s3A408	3009	130	12	0.75	0.0	0.7223	2.6	0.0876	1.5	0.57	0.0598	2.2	542	8	552	11	595	47	91
s2A585	3008	152	15	0.49	0.0	0.7173	2.7	0.0877	1.5	0.57	0.0593	2.2	542	8	549	11	578	48	94
s2A529	5555	276	26	0.46	b.d.	0.7171	2.5	0.0881	1.5	0.62	0.0590	2.0	544	8	549	11	568	43	96
s2A561	4017	188	20	0.74	0.3	0.7142	2.8	0.0887	1.6	0.56	0.0584	2.3	548	8	547	12	546	50	100
s2A542	4332	214	23	0.74	0.0	0.7159	2.3	0.0888	1.5	0.66	0.0584	1.8	549	8	548	10	546	38	100
s3A362	2166	100	11	1.45	0.0	0.7224	3.8	0.0890	1.3	0.36	0.0589	3.5	549	7	552	16	563	77	98
s3A409	4008	177	21	2.03	0.0	0.7339	2.4	0.0891	1.3	0.56	0.0597	2.0	550	7	559	10	594	44	93
s3A364	1554	71	7	1.13	b.d.	0.7307	3.2	0.0897	1.5	0.46	0.0591	2.9	554	8	557	14	570	63	97
s3A346	2407	110	12	1.54	0.0	0.7269	2.9	0.0899	1.3	0.44	0.0587	2.6	555	7	555	13	555	58	100
s3A372	21956	904	89	0.71	0.0	0.7576	1.7	0.0910	1.2	0.72	0.0604	1.2	562	7	573	7	616	25	91
s3A399	982	44	4	0.36	b.d.	0.7596	4.7	0.0912	1.7	0.36	0.0604	4.4	562	9	574	21	619	96	91
s3A394	1344	48	5	0.85	b.d.	0.7431	4.0	0.0916	1.7	0.43	0.0589	3.6	565	9	564	18	562	79	101
s3A360	4739	198	21	1.07	0.0	0.7609	2.4	0.0919	1.5	0.62	0.0600	1.9	567	8	575	10	605	40	94
s3A395	5220	216	23	0.98	0.0	0.7740	2.6	0.0922	1.3	0.50	0.0609	2.2	569	7	582	11	634	48	90
s3A407	1475	62	7	1.12	0.0	0.7533	4.8	0.0924	1.4	0.29	0.0592	4.6	570	8	570	21	572	100	99
s2A545	8269	382	34	0.09	0.2	0.7719	2.4	0.0926	1.4	0.59	0.0605	1.9	571	8	581	11	620	42	92
s2A576	10112	456	49	0.61	0.4	0.7717	2.3	0.0927	1.4	0.59	0.0604	1.9	572	8	581	10	616	41	93
s3A361	2048	85	9	1.24	0.1	0.7747	4.2	0.0931	1.6	0.37	0.0603	3.9	574	9	582	19	616	83	93
s3A390	10090	428	47	1.27	0.0	0.7621	2.0	0.0935	1.3	0.67	0.0591	1.5	576	7	575	9	572	32	101
s3A403	2273	88	10	1.20	0.0	0.7799	3.3	0.0938	1.5	0.45	0.0603	3.0	578	8	585	15	615	64	94
s2A527	2824	121	12	0.37	0.3	0.7845	3.4	0.0940	1.5	0.42	0.0606	3.1	579	8	588	16	623	67	93
s3A380	2837	115	12	0.78	b.d.	0.7718	3.1	0.0941	1.3	0.42	0.0595	2.8	580	7	581	14	586	61	99
s2A523	3793	157	26	2.17	b.d.	0.7961	2.8	0.0944	1.5	0.55	0.0612	2.3	582	8	595	12	645	49	90
s3A363	2307	94	11	1.26	0.0	0.7829	3.3	0.0949	1.5	0.45	0.0598	2.9	585	8	587	15	597	64	98
s2A578	5948	270	24	0.04	0.1	0.8122	2.9	0.0971	1.6	0.54	0.0607	2.4	597	9	604	13	628	53	95
s2A528	3634	150	16	0.49	0.1	0.8253	3.2	0.0972	1.6	0.49	0.0616	2.7	598	9	611	15	660	59	91
s2A564	2494	96	12	1.04	1.1	0.8118	3.4	0.0977	1.7	0.49	0.0603	2.9	601	9	603	15	612	64	98
s2A520	6524	290	34	0.66	0.1	0.8333	2.4	0.0995	1.5	0.63	0.0608	1.8	611	9	615	11	631	40	97
s2A536	2433	94	11	0.53	b.d.	0.8804	3.4	0.1035	1.7	0.50	0.0617	2.9	635	10	641	16	664	63	96
s2A562	3482	131	18	0.92	0.2	0.8982	3.0	0.1060	1.6	0.53	0.0615	2.5	649	10	651	14	656	54	99
s2A572	1061	18	3	0.65	7.1	0.9507	5.8	0.1101	2.8	0.48	0.0626	5.1	673	18	678	29	695	109	97

Grain	$^{207}Pb^{a}$ (cps)	U^{b} (ppm)	Pb^{b} (ppm)	$\frac{Th}{U}^{b}$	$^{206}Pbc^{c}$ (%)	$\frac{^{207}Pb}{^{235}U}^{d}$	±2σ (%)	$\frac{^{206}Pb}{^{238}U}^{d}$	±2σ (%)	ρ^{e} (rho)	$\frac{^{207}Pb}{^{206}Pb}^{d}$	±2σ (%)	$\frac{^{206}Pb}{^{238}U}^{f}$	±2σ (Ma)	$\frac{^{207}Pb}{^{235}U}^{f}$	±2σ (Ma)	$\frac{^{207}Pb}{^{206}Pb}^{f}$	±2σ (Ma)	Conc. (%)
s2A524	6912	283	40	0.97	0.2	0.9921	3.3	0.1145	1.6	0.48	0.0629	2.9	699	10	700	17	703	62	99
s2A560	7038	243	35	0.83	0.1	1.0190	2.3	0.1157	1.5	0.67	0.0639	1.7	706	10	714	12	739	36	95
s2A543	26493	118	29	0.39	19.3	0.9922	15.0	0.1169	2.9	0.19	0.0615	14.7	713	19	700	79	658	315	108
s3A369	2829	93	21	4.82	0.0	1.0250	3.6	0.1172	1.5	0.42	0.0635	3.3	714	10	716	19	723	69	99
s3A404	13057	391	49	0.54	0.7	1.0540	3.2	0.1194	1.4	0.44	0.0640	2.9	727	10	731	17	741	60	98
s2A580	6154	106	20	0.25	0.0	2.0240	2.2	0.1877	1.5	0.66	0.0782	1.7	1109	15	1124	15	1152	34	96
s2A584	29310	471	104	0.35	1.4	2.3100	2.5	0.2077	1.5	0.61	0.0806	2.0	1217	17	1215	18	1213	38	100
s2A571	6701	91	21	0.40	2.8	2.3310	4.1	0.2091	1.6	0.39	0.0809	3.8	1224	18	1222	30	1218	74	100
s2A525	13887	152	43	0.53	0.1	3.1700	1.8	0.2503	1.3	0.74	0.0919	1.2	1440	17	1450	14	1465	23	98
s3A375	9437	85	25	0.85	0.0	3.4750	2.1	0.2631	1.3	0.62	0.0958	1.6	1505	17	1522	17	1544	31	98
s3A402	2824	27	9	1.74	0.1	3.6750	4.4	0.2728	1.9	0.44	0.0977	3.9	1555	27	1566	36	1581	74	98
s3A358	8718	74	23	0.74	b.d.	3.8150	2.2	0.2780	1.5	0.66	0.0995	1.7	1581	20	1596	18	1615	31	98
s2A540	17329	133	54	1.13	0.1	4.5170	1.8	0.2975	1.4	0.78	0.1101	1.2	1679	21	1734	15	1801	21	93
s3A352	45475	315	107	0.66	0.0	4.6650	1.5	0.3122	1.2	0.81	0.1084	0.9	1751	19	1761	13	1772	16	99
s3A376	48438	362	119	0.69	0.0	4.7920	1.7	0.3028	1.2	0.72	0.1148	1.1	1705	18	1784	14	1876	21	91
s3A351	2946	34	12	0.34	1.1	5.3420	3.6	0.3354	1.5	0.43	0.1155	3.2	1864	25	1876	31	1888	58	99
s3A388	15029	87	32	0.61	0.0	5.5220	1.8	0.3407	1.3	0.70	0.1176	1.3	1890	21	1904	16	1919	23	98
s2A532	23672	144	53	0.37	0.0	5.6680	2.1	0.3299	1.6	0.77	0.1246	1.3	1838	26	1927	18	2023	23	91
s3A377	17180	95	42	1.50	0.0	5.8380	1.7	0.3501	1.3	0.76	0.1209	1.1	1935	21	1952	15	1970	19	98
s2A547	8738	52	22	0.80	0.0	5.9470	3.2	0.3448	2.5	0.81	0.1251	1.9	1910	42	1968	28	2030	33	94
s2A558	21563	126	59	1.05	0.1	5.9590	1.9	0.3466	1.5	0.82	0.1247	1.0	1918	25	1970	16	2024	19	95
s3A347	9520	53	22	1.01	0.0	5.9930	2.0	0.3561	1.5	0.74	0.1220	1.4	1964	26	1975	18	1986	25	99
s3A374	21700	115	50	1.36	0.0	6.0410	1.6	0.3525	1.3	0.78	0.1243	1.0	1946	21	1982	14	2019	18	96
s2A574	23702	126	61	1.17	0.4	6.0420	1.9	0.3407	1.5	0.78	0.1286	1.2	1890	25	1982	17	2079	21	91
s2A534	15047	84	33	0.44	0.6	6.0830	2.8	0.3487	1.7	0.60	0.1265	2.2	1928	28	1988	24	2050	39	94
s3A353	31340	196	77	0.76	0.0	6.1930	1.6	0.3547	1.2	0.78	0.1266	1.0	1957	21	2003	14	2052	17	95
s2A598	4080	25	12	0.97	0.0	6.1980	2.6	0.3595	1.5	0.58	0.1250	2.1	1980	26	2004	23	2029	38	98
s3A356	10418	109	44	0.82	b.d.	6.2200	2.0	0.3554	1.5	0.74	0.1270	1.3	1960	25	2007	18	2056	23	95
s2A587	38186	219	88	0.38	0.2	6.3140	1.8	0.3651	1.5	0.85	0.1254	0.9	2006	26	2020	16	2035	17	99
s2A530	29432	173	67	0.25	b.d.	6.4470	1.9	0.3673	1.6	0.88	0.1273	0.9	2017	28	2039	17	2061	16	98
s3A367	36882	181	80	1.13	0.0	6.6470	1.6	0.3689	1.3	0.83	0.1307	0.9	2024	22	2066	14	2107	15	96
s3A348	47582	236	98	0.65	0.2	7.4990	1.7	0.3768	1.4	0.80	0.1443	1.0	2061	24	2173	15	2280	18	90
s2A592	76198	287	144	0.40	0.2	9.9510	1.8	0.4377	1.6	0.88	0.1649	0.9	2340	32	2430	17	2506	14	93
s3A406	55065	183	95	0.57	0.0	10.3300	1.7	0.4684	1.4	0.81	0.1599	1.0	2476	28	2464	16	2455	17	101
s2A537	135736	427	212	0.30	0.0	10.7200	1.7	0.4412	1.6	0.92	0.1762	0.7	2356	31	2499	16	2617	11	90
s2A595	67888	216	114	0.51	0.0	10.9100	1.7	0.4468	1.5	0.90	0.1772	0.7	2381	30	2516	16	2627	12	91
s2A594	67100	221	120	0.53	0.0	11.0700	1.6	0.4600	1.4	0.89	0.1746	0.7	2440	28	2529	15	2602	12	94
s2A596	52324	180	92	0.31	0.0	11.1400	1.6	0.4597	1.3	0.85	0.1758	0.8	2438	27	2535	15	2613	14	93
s2A566	90519	683	359	0.21	b.d.	11.4100	2.2	0.4841	1.6	0.72	0.1710	1.6	2545	34	2557	21	2567	26	99
s3A379	25612	73	49	2.00	0.0	11.5100	1.7	0.4780	1.3	0.76	0.1747	1.1	2518	26	2566	16	2603	18	97
s2A548	68463	195	108	0.47	0.1	11.7500	1.6	0.4662	1.4	0.90	0.1829	0.7	2467	29	2585	15	2679	11	92
s2A577	56368	169	95	0.54	0.1	11.7800	1.8	0.4651	1.6	0.89	0.1837	0.8	2462	33	2587	17	2686	13	92
s2A565	73576	215	146	1.17	0.0	11.9300	1.6	0.4774	1.5	0.93	0.1813	0.6	2516	31	2599	15	2665	10	94
s2A586	67158	196	110	0.49	0.0	12.0100	1.6	0.4729	1.5	0.91	0.1842	0.7	2496	31	2605	15	2691	11	93
s3A396	162686	410	238	0.64	0.2	12.8800	1.8	0.5056	1.6	0.92	0.1847	0.7	2638	35	2671	17	2696	11	98
s2A522	27419	79	48	0.45	0.0	14.0100	2.1	0.5277	1.6	0.77	0.1925	1.3	2732	36	2750	20	2764	22	99
s3A365	180878	388	257	0.92	0.0	15.0300	1.5	0.5483	1.4	0.92	0.1988	0.6	2818	31	2817	14	2817	10	100
s2A568	42017	126	85	0.59	0.1	16.3200	2.1	0.5575	1.6	0.79	0.2123	1.3	2856	38	2896	20	2923	20	98
s2A555	*6967*	*76*	*11*	*0.83*	*20.6*	*0.6318*	*11.9*	*0.0843*	*2.6*	*0.22*	*0.0543*	*11.6*	*522*	*13*	*497*	*48*	*385*	*261*	*136*
s3A368	*892*	*42*	*4*	*0.62*	*b.d.*	*0.7493*	*3.7*	*0.0848*	*1.5*	*0.41*	*0.0641*	*3.3*	*525*	*8*	*568*	*16*	*745*	*70*	*70*
s2A539	*2141*	*94*	*9*	*0.61*	*1.4*	*0.7442*	*5.1*	*0.0850*	*1.9*	*0.37*	*0.0635*	*4.7*	*526*	*9*	*565*	*22*	*725*	*99*	*72*
s3A410	*1103*	*42*	*5*	*1.21*	*b.d.*	*0.8553*	*6.2*	*0.0965*	*1.4*	*0.22*	*0.0643*	*6.0*	*594*	*8*	*628*	*29*	*751*	*127*	*79*
s3A382	*75*	*4*	*0*	*0.80*	*b.d.*	*0.9398*	*24.5*	*0.0986*	*4.2*	*0.17*	*0.0691*	*24.1*	*606*	*24*	*673*	*128*	*902*	*497*	*67*
s3A391	*4053*	*59*	*11*	*0.74*	*5.9*	*1.5090*	*6.1*	*0.1482*	*1.7*	*0.27*	*0.0739*	*5.8*	*891*	*14*	*934*	*38*	*1037*	*118*	*86*
s3A401	*457*	*7*	*1*	*0.90*	*0.0*	*2.0580*	*5.3*	*0.1545*	*1.8*	*0.34*	*0.0966*	*5.0*	*926*	*16*	*1135*	*37*	*1559*	*94*	*59*
s3A378	*47494*	*401*	*102*	*0.55*	*0.0*	*4.2170*	*2.0*	*0.2367*	*1.4*	*0.73*	*0.1292*	*1.4*	*1369*	*18*	*1677*	*16*	*2087*	*24*	*66*
s3A405	*160559*	*847*	*271*	*0.20*	*0.0*	*5.8740*	*1.4*	*0.3123*	*1.2*	*0.85*	*0.1364*	*0.7*	*1752*	*19*	*1957*	*12*	*2182*	*13*	*80*
s2A557	*325163*	*236*	*81*	*0.39*	*0.0*	*6.1360*	*1.8*	*0.3019*	*1.7*	*0.95*	*0.1474*	*0.6*	*1701*	*26*	*1995*	*16*	*2316*	*10*	*73*
s2A569	*48476*	*230*	*89*	*0.30*	*0.0*	*6.9740*	*2.0*	*0.3521*	*1.6*	*0.81*	*0.1437*	*1.2*	*1944*	*27*	*2108*	*18*	*2272*	*20*	*86*
s2A567	*50772*	*220*	*86*	*0.25*	*0.1*	*7.6650*	*2.0*	*0.3565*	*1.7*	*0.86*	*0.1559*	*1.0*	*1966*	*29*	*2193*	*18*	*2412*	*17*	*81*
s2A544	*104874*	*520*	*194*	*0.08*	*0.1*	*7.7510*	*2.3*	*0.3580*	*1.9*	*0.83*	*0.1570*	*1.3*	*1973*	*33*	*2203*	*21*	*2424*	*22*	*81*
s2A556	*42377*	*162*	*71*	*0.47*	*0.1*	*8.3520*	*1.9*	*0.3706*	*1.5*	*0.79*	*0.1635*	*1.2*	*2032*	*26*	*2270*	*17*	*2492*	*20*	*82*
s2A535	*56368*	*202*	*95*	*0.42*	*2.1*	*8.6670*	*2.0*	*0.3920*	*1.5*	*0.74*	*0.1604*	*1.4*	*2132*	*27*	*2304*	*18*	*2460*	*23*	*87*
s2A579	*96410*	*336*	*160*	*0.46*	*0.2*	*9.4330*	*1.6*	*0.3972*	*1.5*	*0.93*	*0.1722*	*0.6*	*2156*	*28*	*2381*	*15*	*2580*	*10*	*84*
s2A582	*91554*	*328*	*146*	*0.33*	*0.0*	*10.170*	*1.9*	*0.3912*	*1.5*	*0.83*	*0.1886*	*1.0*	*2129*	*28*	*2451*	*17*	*2730*	*17*	*78*
s3A411	*108130*	*329*	*172*	*0.46*	*0.0*	*12.670*	*1.7*	*0.4678*	*1.5*	*0.88*	*0.1964*	*0.8*	*2474*	*30*	*2655*	*16*	*2797*	*13*	*88*

Grain	^{207}Pb[a] (cps)	U[b] (ppm)	Pb[b] (ppm)	Th[b]/U	^{206}Pbc[c] (%)	$^{207}Pb/^{235}U$[d]	±2σ (%)	$^{206}Pb/^{238}U$[d]	±2σ (%)	ρ[e] (rho)	$^{207}Pb/^{206}Pb$[d]	±2σ (%)	$^{206}Pb/^{238}U$[f]	±2σ (Ma)	$^{207}Pb/^{235}U$[f]	±2σ (Ma)	$^{207}Pb/^{206}Pb$[f]	±2σ (Ma)	Conc. (%)
s2																			
91500[h]	7017	61	11	0.25	0.4	1.8607	5.0	0.1807	5.7	0.61	0.0747	2.9	1071	56	1067	33	1060	58	101
Felix[h]	6593	361	52	2.09	0.4	0.6274	10.0	0.0808	7.9	0.43	0.0563	5.1	501	38	494	39	464	114	110
Plesovice[h]	2330	904	49	0.09	0.2	0.4243	10.5	0.0572	9.9	0.51	0.0538	1.5	359	35	359	32	362	33	99
GJ-1[h]	6697	306	28	0.03	0.2	0.8144	2.1	0.0983	1.3	0.49	0.0601	2.2	604	7	605	10			
s3																			
91500[h]	8532	69	13	0.45	0.3	1.8103	6.1	0.1784	3.8	0.61	0.0736	4.4	1058	37	1049	40	1030	89	103
Felix[h]	4019	203	23	1.93	0.4	0.6109	10.3	0.0808	4.3	0.35	0.0548	7.7	501	21	484	40	402	176	132
Plesovice[h]	2881	1038	54	0.16	0.2	0.4045	3.8	0.0549	3.8	0.53	0.0535	1.6	344	13	345	11	348	35	99
GJ-1[h]	6932	290	26	0.02	0.1	0.8158	2.0	0.0984	1.1	0.47	0.0601	2.1	605	6	606	9			

$^{206}Pb/^{238}U$ error is the quadratic additions of the within run precision (2 SE) and the external reproducibility (2 SD) of the reference zircon. $^{207}Pb/^{206}Pb$ error propagation (^{207}Pb signal dependent) following Gerdes & Zeh (2009). $^{207}Pb/^{235}U$ error is the quadratic addition of the $^{207}Pb/^{206}Pb$ and $^{206}Pb/^{238}U$ uncertainty.

[a] Within run background-corrected mean ^{207}Pb signal in cps (counts per second).

[b] U and Pb content and Th/U ratio were calculated relative to GJ-1 reference zircon.

[c] Percentage of the common Pb on the ^{206}Pb. b.d. = below detection limit.

[d] Pb/U and Pb/Pb ratios. Corrected for background, within-run Pb/U fractionation (in case of $^{206}Pb/^{238}U$) and common Pb using Stacy and Kramers (1975) model Pb composition and subsequently normalised to GJ-1 (ID-TIMS value/measured value); $^{207}Pb/^{235}U$ calculated using (($^{207}Pb/^{206}Pb$)*($^{238}U/^{206}Pb$)*137.88).

[e] Rho (ρ) is the ($^{206}Pb/^{238}U$)/($^{207}Pb/^{235}U$) error correlation coefficient.

[f] Pb/U and Pb/Pb ages.

[g] Degree of concordance = (($^{206}Pb/^{238}U$ age)/($^{207}Pb/^{206}Pb$ age)) x 100.

[h] Mean for s2 (sequence 2) of 13 (91500), 13 (Felix), 13 (Plesovice), and 26 (GJ-1) analyses, respectively, and mean for s3 (sequence 3) of 11 (91500), 11 (Felix), 9 (Plesovice), and 26 (GJ-1) analyses, respectively.

U, Th and Pb LA-ICP-MS data of zircon cores from sample GCH-21

Grain	^{207}Pb[a] (cps)	U[b] (ppm)	Pb[b] (ppm)	Th[b]/U	^{206}Pbc[c] (%)	^{207}Pb[d]/^{235}U	±2σ (%)	^{206}Pb[d]/^{238}U	±2σ (%)	ρ[e] (rho)	^{207}Pb[d]/^{206}Pb	±2σ (%)	^{206}Pb[f]/^{238}U	±2σ (Ma)	^{207}Pb[f]/^{235}U	±2σ (Ma)	^{207}Pb[f]/^{206}Pb	±2σ (Ma)	Conc.[g] (%)
A108	1249	59	5	1.01	0.1	0.6549	6.2	0.0810	1.6	0.26	0.0586	5.9	502	8	512	25	554	130	91
A171	1259	70	6	0.89	b.d.	0.6488	3.3	0.0815	1.4	0.42	0.0578	3.0	505	7	508	13	521	66	97
A084	1934	86	9	1.40	0.1	0.6770	3.2	0.0845	1.5	0.47	0.0581	2.8	523	8	525	13	534	62	98
A112	8381	743	64	0.39	b.d.	0.6971	2.0	0.0856	1.4	0.67	0.0590	1.5	530	7	537	9	569	33	93
A135	1787	165	17	1.14	0.2	0.6951	4.0	0.0862	1.7	0.43	0.0585	3.6	533	9	536	17	549	78	97
A164	3831	191	19	1.12	0.0	0.6976	3.4	0.0868	1.4	0.40	0.0583	3.2	536	7	537	14	542	69	99
A203	1486	84	8	0.79	b.d.	0.7148	3.3	0.0872	1.4	0.43	0.0595	3.0	539	7	548	14	584	65	92
A086	2839	122	12	0.91	0.1	0.7051	3.7	0.0875	1.5	0.41	0.0584	3.4	541	8	542	16	546	74	99
A079	3527	305	26	0.20	0.0	0.7279	2.8	0.0887	1.3	0.48	0.0595	2.4	548	7	555	12	586	53	93
A081	2117	94	9	0.83	b.d.	0.7291	2.8	0.0894	1.4	0.50	0.0592	2.4	552	7	556	12	573	53	96
A090	3018	131	13	0.97	b.d.	0.7421	3.1	0.0911	1.4	0.43	0.0591	2.8	562	7	564	14	571	62	98
A166	1827	93	10	1.45	b.d.	0.7411	3.1	0.0913	1.6	0.51	0.0589	2.6	563	8	563	13	562	57	100
A185	2081	106	11	0.87	b.d.	0.7454	3.5	0.0915	1.4	0.40	0.0591	3.2	564	8	566	15	571	71	99
A192	974	47	5	0.78	0.4	0.7429	3.4	0.0916	1.6	0.48	0.0588	3.0	565	9	564	15	560	65	101
A018	1615	28	3	1.58	0.0	0.7654	3.2	0.0917	1.6	0.48	0.0606	2.8	565	8	577	14	624	61	91
A051	1279	104	11	0.97	b.d.	0.7585	3.7	0.0926	1.8	0.50	0.0594	3.2	571	10	573	16	581	69	98
A181	1027	84	11	2.08	1.1	0.7576	3.1	0.0936	1.8	0.60	0.0587	2.5	577	10	573	14	556	54	104
A160	1237	58	6	1.22	b.d.	0.7719	3.7	0.0939	1.5	0.41	0.0596	3.4	578	8	581	17	590	74	98
A154	9243	718	89	0.96	0.0	0.9578	1.9	0.1108	1.4	0.73	0.0627	1.3	677	9	682	10	698	28	97
A083	8648	186	22	0.25	3.9	0.9279	4.8	0.1112	1.5	0.32	0.0605	4.6	679	10	667	24	623	99	109
A165	2275	170	24	1.53	b.d.	0.9840	3.5	0.1141	1.7	0.49	0.0625	3.0	697	11	696	18	692	65	101
A199	2234	147	22	1.29	b.d.	1.1210	3.5	0.1260	1.7	0.49	0.0645	3.1	765	12	763	19	758	65	101
A085	6449	89	19	0.52	0.1	2.2260	2.0	0.2012	1.4	0.69	0.0803	1.4	1182	15	1189	14	1203	28	98
A061	10812	118	27	0.50	0.1	2.6800	2.1	0.2216	1.4	0.68	0.0877	1.6	1290	17	1323	16	1377	30	94
A124	5832	38	12	0.17	0.1	4.8950	2.5	0.3143	1.5	0.61	0.1130	2.0	1762	23	1801	21	1848	36	95
A020	94052	990	325	0.24	0.1	5.3220	1.9	0.3235	1.7	0.89	0.1193	0.9	1807	27	1872	17	1946	16	93
A122	15160	85	33	1.02	0.1	5.4730	1.9	0.3309	1.5	0.76	0.1200	1.2	1843	24	1896	17	1956	22	94
A152	112003	1431	459	0.08	0.0	5.5660	1.5	0.3242	1.3	0.86	0.1245	0.8	1810	21	1911	13	2022	14	90
A134	23516	147	53	0.64	0.1	5.6020	1.8	0.3324	1.5	0.83	0.1222	1.0	1850	25	1916	16	1989	18	93
A101	5520	31	12	0.83	0.0	5.7580	2.5	0.3410	1.4	0.58	0.1225	2.0	1891	24	1940	22	1993	36	95
A130	15143	177	68	0.86	b.d.	5.7950	2.0	0.3374	1.5	0.74	0.1246	1.3	1874	24	1946	17	2023	24	93
A188	56623	726	290	0.90	0.2	5.8100	1.5	0.3454	1.3	0.86	0.1220	0.8	1913	22	1948	13	1985	14	96
A161	13204	82	35	1.24	0.1	5.8270	1.7	0.3509	1.3	0.75	0.1204	1.1	1939	21	1950	15	1963	20	99
A049	13652	73	28	0.67	0.1	5.8430	2.0	0.3435	1.3	0.64	0.1234	1.5	1904	21	1953	18	2005	27	95
A180	23029	155	67	1.49	0.1	5.9770	1.8	0.3454	1.4	0.78	0.1255	1.1	1912	23	1973	15	2036	19	94
A184	42957	273	122	1.41	0.0	6.1480	1.5	0.3622	1.3	0.87	0.1231	0.7	1992	22	1997	13	2002	13	100
A175	16419	101	36	0.15	0.0	6.1820	1.7	0.3576	1.3	0.78	0.1254	1.1	1971	23	2002	15	2034	19	97
A204	27136	163	60	0.31	0.0	6.1980	1.6	0.3506	1.3	0.82	0.1282	0.9	1938	22	2004	14	2074	16	93
A055	5391	23	10	1.39	1.0	6.2040	2.9	0.3536	1.6	0.54	0.1273	2.4	1952	26	2005	25	2060	43	95
A063	5739	29	11	0.75	0.2	6.2130	2.0	0.3486	1.4	0.70	0.1293	1.5	1928	24	2006	18	2088	26	92
A065	22798	110	41	0.22	b.d.	6.2420	2.0	0.3653	1.7	0.86	0.1239	1.0	2007	29	2010	17	2013	18	100
A048	21742	102	53	2.34	0.2	6.2440	1.8	0.3650	1.4	0.76	0.1241	1.2	2006	23	2011	16	2015	20	100
A178	11791	66	29	1.21	0.7	6.2670	2.3	0.3673	1.4	0.62	0.1237	1.8	2017	25	2014	20	2011	32	100
A205	9566	60	33	2.54	0.0	6.2820	2.4	0.3661	1.5	0.61	0.1245	1.9	2011	25	2016	21	2021	34	100
A075	15182	79	33	1.00	0.0	6.2970	1.8	0.3557	1.3	0.73	0.1284	1.2	1962	22	2018	16	2076	22	94
A186	8750	54	22	0.79	0.1	6.3040	1.8	0.3569	1.3	0.72	0.1281	1.3	1968	23	2019	16	2072	23	95
A099	11477	57	26	1.42	0.3	6.3060	1.9	0.3602	1.3	0.71	0.1270	1.3	1983	23	2019	17	2057	24	96
A182	28541	159	69	1.06	0.4	6.3090	2.2	0.3612	1.6	0.71	0.1267	1.5	1988	27	2020	19	2052	27	97
A137	12290	29	12	0.99	0.2	6.3770	1.7	0.3632	1.3	0.78	0.1273	1.1	1998	23	2029	15	2061	19	97
A157	12430	61	29	1.75	0.2	6.3790	2.0	0.3573	1.4	0.69	0.1295	1.5	1969	24	2029	18	2091	26	94
A144	32788	177	69	0.47	0.2	6.3950	1.6	0.3616	1.3	0.78	0.1283	1.0	1990	22	2032	14	2075	18	96
A046	6694	32	13	0.82	0.0	6.3950	2.2	0.3673	1.4	0.62	0.1263	1.8	2017	24	2032	20	2047	31	99
A096	18439	93	42	1.32	b.d.	6.3980	1.9	0.3702	1.4	0.74	0.1253	1.3	2030	24	2032	17	2034	22	100
A126	9382	46	21	1.22	0.1	6.4460	2.0	0.3670	1.4	0.70	0.1274	1.4	2015	24	2039	18	2062	25	98
A120	15832	76	32	0.80	0.1	6.4680	1.9	0.3727	1.6	0.83	0.1259	1.1	2042	28	2041	17	2041	19	100
A202	18525	112	51	1.37	0.1	6.4750	2.0	0.3741	1.5	0.76	0.1255	1.3	2049	27	2042	18	2036	23	101
A173	46295	271	106	0.40	0.0	6.4900	1.6	0.3730	1.4	0.85	0.1262	0.9	2043	25	2045	15	2046	15	100
A172	41743	238	96	0.78	0.9	6.4920	2.0	0.3553	1.4	0.72	0.1325	1.4	1960	24	2045	17	2131	24	92
A116	22383	110	48	1.07	0.2	6.5170	1.9	0.3687	1.4	0.73	0.1282	1.3	2023	24	2048	17	2073	23	98
A167	22619	113	54	1.51	1.0	6.5270	2.1	0.3668	1.3	0.65	0.1290	1.6	2014	23	2050	18	2085	28	97
A128	10745	54	25	1.38	b.d.	6.5280	1.9	0.3635	1.4	0.73	0.1302	1.3	1999	24	2050	17	2101	23	95
A123	34303	170	77	1.24	0.2	6.5490	1.9	0.3742	1.3	0.72	0.1269	1.3	2049	23	2053	17	2056	23	100
A042	25506	52	22	0.83	0.2	6.5690	1.7	0.3731	1.3	0.73	0.1277	1.2	2044	22	2055	15	2066	21	99
A113	6038	63	25	0.57	b.d.	6.5700	2.3	0.3723	1.4	0.63	0.1280	1.8	2040	25	2055	20	2071	32	99
A032	18226	87	36	0.65	0.2	6.5870	1.8	0.3751	1.3	0.74	0.1274	1.2	2053	24	2058	16	2062	21	100
A073	14077	66	28	0.81	0.2	6.5920	1.8	0.3758	1.3	0.76	0.1272	1.1	2056	24	2058	16	2060	20	100
A183	28215	263	118	0.82	2.9	6.6210	2.4	0.3707	1.4	0.58	0.1295	1.9	2033	24	2062	21	2092	34	97

Grain	^{207}Pb[a] (cps)	U[b] (ppm)	Pb[b] (ppm)	Th[b]/U	$^{206}Pb_c$[c] (%)	$^{207}Pb/^{235}U$[d]	±2σ (%)	$^{206}Pb/^{238}U$[d]	±2σ (%)	ρ[e] (rho)	$^{207}Pb/^{206}Pb$[d]	±2σ (%)	$^{206}Pb/^{238}U$[f]	±2σ (Ma)	$^{207}Pb/^{235}U$[f]	±2σ (Ma)	$^{207}Pb/^{206}Pb$[f]	±2σ (Ma)	Conc.[g] (%)
A022	20804	93	43	1.19	0.4	6.6230	1.8	0.3771	1.4	0.77	0.1274	1.1	2063	24	2062	16	2062	20	100
A169	5689	27	13	1.38	1.8	6.6240	2.3	0.3713	1.7	0.72	0.1294	1.6	2036	29	2063	21	2090	28	97
A155	11987	65	27	0.69	0.1	6.6270	2.1	0.3748	1.4	0.68	0.1282	1.6	2052	25	2063	19	2074	27	99
A056	10348	47	22	1.22	0.2	6.6390	2.1	0.3734	1.4	0.68	0.1289	1.6	2045	25	2065	19	2084	28	98
A153	28418	152	61	0.54	0.0	6.6410	1.6	0.3725	1.3	0.79	0.1293	1.0	2041	22	2065	14	2088	17	98
A098	11409	56	24	0.86	b.d.	6.6540	1.8	0.3788	1.3	0.74	0.1274	1.2	2071	24	2067	16	2063	22	100
A177	28307	114	53	0.70	6.0	6.6730	3.7	0.3776	1.4	0.39	0.1282	3.4	2065	26	2069	33	2073	60	100
A200	14293	165	76	1.24	0.0	6.6780	1.9	0.3745	1.4	0.76	0.1293	1.2	2050	25	2070	17	2089	21	98
A159	25231	144	68	1.37	b.d.	6.7040	1.7	0.3770	1.4	0.79	0.1290	1.1	2062	24	2073	15	2084	19	99
A021	4543	20	8	0.59	b.d.	6.8290	2.4	0.3823	1.5	0.61	0.1295	1.9	2087	26	2089	22	2092	34	100
A040	5521	24	11	0.92	0.2	6.8650	2.2	0.3867	1.5	0.66	0.1287	1.7	2108	26	2094	20	2081	29	101
A190	17178	93	40	0.61	1.2	6.8810	2.9	0.3829	2.3	0.79	0.1303	1.8	2090	40	2096	26	2102	31	99
A125	8804	44	19	0.75	0.1	6.8950	2.0	0.3844	1.7	0.83	0.1301	1.1	2097	30	2098	18	2099	19	100
A191	46244	255	126	1.65	b.d.	6.9200	1.5	0.3797	1.3	0.87	0.1322	0.7	2075	23	2101	13	2127	13	98
A145	10686	53	23	0.75	0.0	6.9260	1.8	0.3863	1.3	0.70	0.1300	1.3	2106	23	2102	16	2099	23	100
A115	16167	75	32	0.65	0.0	6.9410	1.7	0.3816	1.3	0.78	0.1319	1.1	2084	24	2104	15	2124	19	98
A162	28522	148	63	0.86	0.0	7.0090	1.7	0.3661	1.3	0.78	0.1389	1.0	2011	23	2113	15	2213	18	91
A174	8530	42	20	1.44	b.d.	7.2550	2.1	0.3916	1.5	0.71	0.1344	1.5	2130	27	2143	19	2156	25	99
A092	5529	23	11	1.10	0.0	7.8300	1.8	0.3924	1.5	0.81	0.1447	1.1	2134	27	2212	17	2285	18	93
A121	40361	329	132	0.15	0.1	8.0460	1.9	0.3882	1.6	0.84	0.1503	1.0	2115	28	2236	17	2349	17	90
A138	12294	49	22	0.59	0.1	8.2770	1.8	0.3996	1.4	0.74	0.1502	1.2	2167	25	2262	17	2349	21	92
A054	36795	263	106	0.11	0.0	8.4310	1.8	0.3956	1.5	0.81	0.1546	1.1	2149	27	2279	17	2397	18	90
A088	58872	494	205	0.18	0.0	8.4790	1.6	0.4024	1.4	0.84	0.1528	0.9	2180	25	2284	15	2378	15	92
A062	74976	545	238	0.22	0.0	8.5610	1.6	0.4213	1.4	0.87	0.1474	0.8	2267	26	2292	14	2316	14	98
A028	222483	1512	656	0.08	0.0	9.2280	1.4	0.4257	1.3	0.91	0.1572	0.6	2286	24	2361	13	2426	10	94
A023	53933	165	81	0.71	b.d.	9.7640	1.6	0.4296	1.4	0.87	0.1648	0.8	2304	27	2413	15	2506	13	92
A053	27403	187	90	0.62	0.1	9.8110	2.2	0.4280	1.9	0.87	0.1663	1.1	2297	37	2417	21	2520	19	91
A074	60279	379	211	1.02	0.1	10.4500	1.7	0.4640	1.5	0.86	0.1634	0.9	2457	30	2476	16	2491	15	99
A142	31496	103	51	0.56	0.0	10.5400	1.8	0.4368	1.5	0.85	0.1749	0.9	2336	29	2483	16	2605	16	90
A030	103946	587	280	0.15	0.0	10.5900	1.9	0.4597	1.8	0.94	0.1671	0.7	2438	36	2488	18	2528	11	96
A077	15338	46	22	0.13	b.d.	10.6200	1.8	0.4624	1.4	0.77	0.1665	1.2	2450	28	2490	17	2523	19	97
A060	27281	158	81	0.48	0.1	10.6400	1.8	0.4634	1.5	0.86	0.1666	0.9	2455	32	2493	17	2524	15	97
A118	54993	336	167	0.51	0.0	10.7100	1.9	0.4442	1.5	0.83	0.1749	1.0	2369	31	2499	17	2605	17	91
A052	29790	184	95	0.58	0.1	10.7900	2.1	0.4629	1.8	0.85	0.1691	1.1	2452	37	2505	20	2548	18	96
A189	81741	337	184	0.92	0.0	11.1000	2.1	0.4596	1.5	0.71	0.1752	1.4	2438	30	2532	19	2608	24	93
A025	50455	262	129	0.22	0.1	11.1100	1.7	0.4633	1.5	0.90	0.1740	0.7	2454	31	2533	16	2596	12	95
A094	50737	284	145	0.25	0.0	11.2400	1.7	0.4835	1.4	0.83	0.1685	1.0	2542	30	2543	16	2543	16	100
A076	25894	145	79	0.71	0.0	11.2800	1.7	0.4706	1.3	0.76	0.1738	1.1	2486	27	2546	16	2595	19	96
A109	32539	40	23	1.01	b.d.	11.3900	1.6	0.4706	1.3	0.84	0.1755	0.9	2486	28	2555	15	2611	15	95
A141	12558	40	23	1.12	0.0	11.5500	2.0	0.4745	1.4	0.70	0.1766	1.5	2503	30	2569	19	2621	24	96
A117	80390	583	308	0.51	0.0	11.5900	1.9	0.4852	1.6	0.84	0.1733	1.0	2550	34	2572	18	2590	17	98
A091	30295	80	41	0.27	0.0	11.6000	1.7	0.4814	1.3	0.78	0.1748	1.1	2533	28	2573	16	2605	18	97
A201	32237	205	128	1.47	0.1	11.6100	1.8	0.4722	1.5	0.83	0.1783	1.0	2493	30	2573	17	2637	16	95
A151	8431	25	14	0.98	0.0	11.6700	1.9	0.4662	1.5	0.76	0.1816	1.3	2467	30	2578	18	2667	21	92
A058	58559	145	76	0.33	0.8	11.6800	2.2	0.4772	1.9	0.84	0.1775	1.2	2515	39	2579	21	2630	20	96
A179	25381	161	88	0.63	0.0	11.7000	1.7	0.4862	1.3	0.77	0.1744	1.1	2554	28	2580	16	2601	18	98
A156	47116	269	168	1.34	0.0	11.7700	1.9	0.4898	1.7	0.89	0.1743	0.9	2570	36	2586	18	2599	14	99
A050	25462	62	35	0.75	0.3	11.7700	1.8	0.4843	1.5	0.81	0.1763	1.1	2546	31	2587	17	2619	18	97
A111	43137	125	73	1.06	b.d.	11.8400	1.5	0.4819	1.3	0.86	0.1782	0.8	2535	28	2592	14	2636	13	96
A170	56342	188	113	1.02	b.d.	11.9800	1.5	0.4965	1.3	0.86	0.1750	0.8	2599	28	2603	15	2606	13	100
A059	70515	190	113	0.79	b.d.	12.1100	1.8	0.5010	1.5	0.83	0.1753	1.0	2618	32	2613	17	2609	17	100
A089	25810	68	42	1.27	0.0	12.1100	1.7	0.4980	1.4	0.82	0.1764	0.9	2605	30	2613	16	2619	16	99
A072	57764	151	96	1.41	0.0	12.2000	1.5	0.4940	1.3	0.91	0.1791	0.6	2588	29	2620	14	2644	10	98
A158	69833	205	115	0.69	0.1	12.2100	1.7	0.4843	1.4	0.82	0.1829	1.0	2546	29	2621	16	2679	16	95
A097	82517	416	252	0.98	0.1	12.2800	1.5	0.4975	1.4	0.90	0.1791	0.7	2603	29	2626	14	2644	11	98
A045	98036	234	142	1.13	b.d.	12.3800	1.5	0.4886	1.3	0.88	0.1838	0.7	2565	28	2634	14	2688	12	95
A107	31355	76	44	0.69	0.0	12.4100	1.6	0.4908	1.4	0.83	0.1833	0.9	2574	29	2636	15	2683	15	96
A039	40524	93	60	1.31	0.1	12.5600	1.7	0.5032	1.4	0.81	0.1811	1.0	2627	30	2648	16	2663	16	99
A026	47490	122	73	0.80	0.1	12.7500	1.6	0.5080	1.4	0.88	0.1821	0.8	2648	30	2661	15	2672	13	99
A044	53410	55	33	0.91	0.2	12.7800	1.6	0.5112	1.3	0.79	0.1813	1.0	2662	27	2663	15	2665	16	100
A082	113495	285	163	0.58	b.d.	12.9300	1.4	0.5044	1.3	0.89	0.1859	0.7	2633	28	2674	14	2706	11	97
A133	44088	225	148	1.37	0.2	12.9500	1.5	0.5076	1.4	0.89	0.1851	0.7	2646	30	2676	14	2699	11	98
A163	31503	166	107	1.17	0.0	12.9700	1.8	0.5140	1.5	0.81	0.1830	1.1	2674	32	2677	17	2680	18	100
A139	33022	93	53	0.59	0.0	12.9700	1.6	0.5098	1.4	0.83	0.1846	0.9	2656	30	2678	15	2694	15	99
A136	42620	224	128	0.48	0.0	13.0800	1.5	0.5097	1.4	0.91	0.1862	0.6	2655	30	2686	14	2709	10	98
A038	53374	121	105	3.29	b.d.	13.2100	1.7	0.5165	1.5	0.89	0.1854	0.8	2684	33	2694	16	2702	13	99
A168	39906	109	67	0.86	b.d.	13.2100	1.8	0.5199	1.6	0.85	0.1843	1.0	2699	34	2695	18	2692	16	100
A066	28640	44	32	0.90	5.1	13.3900	3.0	0.5181	1.7	0.58	0.1874	2.4	2691	38	2707	28	2720	40	99
A087	13070	31	21	1.59	0.1	13.4400	2.2	0.5223	1.6	0.74	0.1866	1.5	2709	36	2711	21	2713	24	100
A114	94668	357	220	0.71	0.1	13.9900	4.9	0.5176	4.8	0.98	0.1960	1.0	2689	106	2749	48	2793	17	96

Grain	^{207}Pb[a] (cps)	U[b] (ppm)	Pb[b] (ppm)	Th[b] / U	^{206}Pbc[c] (%)	$^{207}Pb/^{235}U$[d]	±2σ (%)	$^{206}Pb/^{238}U$[d]	±2σ (%)	ρ[e] (rho)	$^{207}Pb/^{206}Pb$[d]	±2σ (%)	$^{206}Pb/^{238}U$[f]	±2σ (Ma)	$^{207}Pb/^{235}U$[f]	±2σ (Ma)	$^{207}Pb/^{206}Pb$[f]	±2σ (Ma)	Conc.[g] (%)
A127	16465	32	21	0.52	0.1	17.5300	1.8	0.5731	1.5	0.81	0.2218	1.1	2921	35	2964	18	2994	17	98
A031	24930	41	27	0.51	0.2	17.8300	2.0	0.5850	1.6	0.81	0.2210	1.2	2969	38	2981	19	2988	19	99
A024	*19833*	*695*	*59*	*0.09*	*0.0*	*0.7636*	*2.6*	*0.0900*	*1.4*	*0.52*	*0.0615*	*2.2*	*555*	*7*	*576*	*12*	*658*	*48*	*84*
A095	*1182*	*40*	*4*	*0.89*	*0.0*	*1.0120*	*5.6*	*0.0982*	*1.6*	*0.28*	*0.0747*	*5.4*	*604*	*9*	*710*	*29*	*1061*	*108*	*57*
A119	*20676*	*160*	*29*	*0.91*	*15.2*	*1.6000*	*11.3*	*0.1238*	*2.1*	*0.18*	*0.0937*	*11.1*	*752*	*15*	*970*	*73*	*1503*	*210*	*50*
A100	*6316*	*138*	*31*	*0.50*	*0.0*	*2.9510*	*2.5*	*0.2095*	*1.7*	*0.66*	*0.1021*	*1.9*	*1226*	*19*	*1395*	*19*	*1663*	*35*	*74*
A064	*4738*	*28*	*7*	*0.50*	*0.2*	*4.0360*	*2.7*	*0.2228*	*1.9*	*0.69*	*0.1314*	*2.0*	*1297*	*22*	*1642*	*22*	*2117*	*34*	*61*
A057	*12017*	*179*	*47*	*0.39*	*b.d.*	*4.2350*	*2.0*	*0.2499*	*1.6*	*0.79*	*0.1229*	*1.2*	*1438*	*21*	*1681*	*17*	*1999*	*22*	*72*
A193	*5783*	*85*	*28*	*0.79*	*b.d.*	*4.9790*	*2.9*	*0.2864*	*2.1*	*0.70*	*0.1261*	*2.1*	*1624*	*30*	*1816*	*25*	*2044*	*37*	*79*
A187	*19247*	*129*	*44*	*0.91*	*0.4*	*5.0280*	*2.4*	*0.2904*	*1.6*	*0.67*	*0.1256*	*1.8*	*1644*	*23*	*1824*	*21*	*2037*	*32*	*81*
A132	*15019*	*87*	*32*	*1.02*	*b.d.*	*5.2350*	*2.1*	*0.3086*	*1.6*	*0.74*	*0.1230*	*1.4*	*1734*	*24*	*1858*	*18*	*2001*	*26*	*87*
A131	*19589*	*237*	*73*	*0.11*	*b.d.*	*5.2510*	*2.0*	*0.3097*	*1.6*	*0.79*	*0.1230*	*1.3*	*1739*	*24*	*1861*	*17*	*2000*	*22*	*87*
A043	*149737*	*1349*	*404*	*0.07*	*0.0*	*6.1250*	*2.0*	*0.2965*	*1.8*	*0.92*	*0.1498*	*0.8*	*1674*	*27*	*1994*	*17*	*2344*	*13*	*71*
A027	*121806*	*917*	*276*	*0.16*	*0.1*	*6.4550*	*2.1*	*0.2879*	*2.0*	*0.94*	*0.1626*	*0.7*	*1631*	*28*	*2040*	*19*	*2483*	*12*	*66*
A176	*81646*	*398*	*131*	*0.17*	*b.d.*	*6.8290*	*3.2*	*0.3165*	*2.6*	*0.80*	*0.1565*	*1.9*	*1773*	*40*	*2090*	*29*	*2418*	*32*	*73*
A140	*80810*	*356*	*114*	*0.13*	*0.1*	*6.9700*	*1.8*	*0.3103*	*1.5*	*0.82*	*0.1629*	*1.1*	*1742*	*23*	*2108*	*17*	*2486*	*18*	*70*
A110	*54764*	*471*	*180*	*0.38*	*b.d.*	*7.1810*	*1.5*	*0.3566*	*1.3*	*0.89*	*0.1461*	*0.7*	*1966*	*22*	*2134*	*13*	*2300*	*12*	*85*
A080	*21664*	*172*	*71*	*0.78*	*0.0*	*7.5800*	*2.0*	*0.3542*	*1.6*	*0.80*	*0.1552*	*1.2*	*1954*	*27*	*2183*	*18*	*2404*	*20*	*81*
A029	*124541*	*892*	*326*	*0.06*	*0.0*	*7.7980*	*1.8*	*0.3605*	*1.7*	*0.91*	*0.1569*	*0.8*	*1984*	*28*	*2208*	*17*	*2422*	*13*	*82*
A041	*58326*	*214*	*86*	*0.29*	*0.0*	*8.0080*	*2.3*	*0.3824*	*2.1*	*0.94*	*0.1519*	*0.8*	*2088*	*38*	*2232*	*21*	*2367*	*14*	*88*
A129	*23482*	*78*	*36*	*0.54*	*b.d.*	*9.7930*	*1.8*	*0.4126*	*1.4*	*0.79*	*0.1721*	*1.1*	*2227*	*27*	*2416*	*17*	*2579*	*19*	*86*
A047	*171938*	*439*	*191*	*0.19*	*0.3*	*10.120*	*1.5*	*0.4081*	*1.4*	*0.90*	*0.1799*	*0.7*	*2206*	*26*	*2446*	*14*	*2652*	*11*	*83*
A019	*25582*	*72*	*35*	*1.24*	*0.1*	*10.140*	*2.4*	*0.3733*	*2.2*	*0.91*	*0.1970*	*1.0*	*2045*	*38*	*2447*	*22*	*2801*	*16*	*73*
A093	*64490*	*401*	*176*	*0.17*	*b.d.*	*10.210*	*1.9*	*0.4173*	*1.5*	*0.80*	*0.1774*	*1.1*	*2248*	*28*	*2454*	*17*	*2629*	*19*	*86*
91500[h]	8676	77	14	0.44	0.3	1.8408	3.8	0.1792	3.3	0.56	0.0745	1.9	1062	32	1060	25	1055	38	101
Felix[h]	8886	509	76	3.98	0.1	0.6348	6.8	0.0807	7.3	0.50	0.0571	1.2	500	35	499	27	494	26	101
Plesovice[h]	2366	866	45	0.15	0.4	0.3935	2.3	0.0539	1.7	0.47	0.0529	2.3	339	6	337	7	326	52	104
GJ-1[h]	7647	340	31	0.02	0.1	0.8142	1.8	0.0984	0.9	0.42	0.0600	1.6	605	5	605	8			

$^{206}Pb/^{238}U$ error is the quadratic additions of the within run precision (2 SE) and the external reproducibility (2 SD) of the reference zircon. $^{207}Pb/^{206}Pb$ error propagation (^{207}Pb signal dependent) following Gerdes & Zeh (2009). $^{207}Pb/^{235}U$ error is the quadratic addition of the $^{207}Pb/^{206}Pb$ and $^{206}Pb/^{238}U$ uncertainty.

[a] Within run background-corrected mean ^{207}Pb signal in cps (counts per second).

[b] U and Pb content and Th/U ratio were calculated relative to GJ-1 reference zircon.

[c] Percentage of the common Pb on the ^{206}Pb. b.d. = below detection limit.

[d] Pb/U and Pb/Pb ratios. Corrected for background, within-run Pb/U fractionation (in case of $^{206}Pb/^{238}U$) and common Pb using Stacy and Kramers (1975) model Pb composition and subsequently normalised to GJ-1 (ID-TIMS value/measured value); $^{207}Pb/^{235}U$ calculated using (($^{207}Pb/^{206}Pb$)*($^{238}U/^{206}Pb$)*137.88).

[e] Rho (ρ) is the ($^{206}Pb/^{238}U$)/($^{207}Pb/^{235}U$) error correlation coefficient.

[f] Pb/U and Pb/Pb ages.

[g] Degree of concordance = (($^{206}Pb/^{238}U$ age)/($^{207}Pb/^{206}Pb$ age)) x 100.

[h] Mean of 9 (91500), 9 (Felix), 9 (Plesovice), and 18 (GJ-1) analyses, respectively.

Table S5

U, Th and Pb LA-ICP-MS data of zircon cores from sample GCH-24

Grain	^{207}Pb[a] (cps)	U[b] (ppm)	Pb[b] (ppm)	Th[b] U	^{206}Pbc[c] (%)	$^{207}Pb/^{235}U$[d]	±2σ (%)	$^{206}Pb/^{238}U$[d]	±2σ (%)	ρ[e] (rho)	$^{207}Pb/^{206}Pb$[d]	±2σ (%)	$^{206}Pb/^{238}U$[f]	±2σ (Ma)	$^{207}Pb/^{235}U$[f]	±2σ (Ma)	$^{207}Pb/^{206}Pb$[f]	±2σ (Ma)	Conc.[g] (%)
A273	3608	217	20	0.89	0.7	0.6460	3.5	0.0822	1.5	0.42	0.0570	3.2	509	7	506	14	493	71	103
A326	6533	416	39	0.95	1.1	0.6602	3.0	0.0824	1.3	0.45	0.0581	2.6	510	7	515	12	534	58	96
A293	1382	96	9	0.82	b.d.	0.6760	4.1	0.0845	1.7	0.41	0.0580	3.7	523	9	524	17	530	82	99
A280	2323	320	28	0.62	b.d.	0.6875	3.3	0.0847	1.4	0.44	0.0589	2.9	524	7	531	14	563	64	93
A249	1695	113	10	0.71	b.d.	0.6837	3.4	0.0849	1.4	0.43	0.0584	3.0	526	7	529	14	544	67	97
A245	6153	296	27	0.58	1.3	0.6808	3.3	0.0849	1.4	0.43	0.0581	3.0	526	7	527	14	535	66	98
A303	4673	322	37	2.01	b.d.	0.6922	2.5	0.0854	1.4	0.55	0.0588	2.1	528	7	534	10	560	45	94
A233	1364	134	17	2.65	0.6	0.6958	3.1	0.0856	2.4	0.77	0.0589	2.0	530	12	536	13	565	43	94
A288	1416	97	11	1.69	0.0	0.6901	2.8	0.0860	1.7	0.61	0.0582	2.2	532	9	533	12	538	49	99
A268	5182	662	69	1.38	b.d.	0.6947	2.1	0.0863	1.3	0.62	0.0584	1.7	534	7	536	9	544	36	98
A346	3664	280	39	3.33	0.0	0.7000	2.4	0.0874	1.3	0.55	0.0581	2.0	540	7	539	10	534	44	101
A340	3632	280	28	1.19	b.d.	0.7077	2.3	0.0878	1.3	0.55	0.0585	1.9	542	7	543	10	547	41	99
A313	5519	407	36	0.39	b.d.	0.7162	2.3	0.0879	1.4	0.58	0.0591	1.9	543	7	548	10	571	41	95
A349	4809	381	37	0.90	b.d.	0.7106	2.5	0.0883	1.4	0.54	0.0584	2.1	546	7	545	11	543	47	100
A221	6458	360	32	0.44	b.d.	0.7206	2.3	0.0886	1.4	0.62	0.0590	1.8	547	8	551	10	567	40	97
A317	2295	166	17	1.02	b.d.	0.7118	2.7	0.0887	1.5	0.56	0.0582	2.2	548	8	546	12	537	49	102
A324	8003	1119	108	0.82	b.d.	0.7302	1.9	0.0890	1.3	0.71	0.0595	1.3	549	7	557	8	586	29	94
A338	7476	575	53	0.62	b.d.	0.7244	2.2	0.0892	1.3	0.61	0.0589	1.7	551	7	553	9	564	37	98
A357	4362	327	30	0.54	0.4	0.7306	2.7	0.0899	1.3	0.50	0.0590	2.3	555	7	557	12	566	51	98
A274	2977	360	45	2.07	0.2	0.7340	2.9	0.0903	1.4	0.47	0.0590	2.6	557	7	559	13	565	56	99
A276	4679	275	33	1.07	5.6	0.7357	5.5	0.0905	1.6	0.29	0.0590	5.3	558	9	560	24	567	115	98
A298	5413	271	27	0.70	3.1	0.7394	4.7	0.0908	1.5	0.31	0.0591	4.4	560	8	562	20	570	96	98
A219	8438	471	43	0.47	b.d.	0.7383	2.0	0.0910	1.4	0.68	0.0588	1.5	562	7	561	9	560	32	100
A248	6176	351	40	1.60	0.0	0.7446	2.3	0.0911	1.4	0.60	0.0593	1.8	562	7	565	10	578	39	97
A267	10044	273	41	1.17	20.2	0.7454	11.5	0.0911	2.7	0.23	0.0593	11.1	562	14	566	51	579	242	97
A281	2189	254	26	0.93	0.1	0.7415	3.6	0.0913	1.6	0.44	0.0589	3.3	563	9	563	16	563	71	100
A294	5532	695	81	1.78	0.0	0.7357	1.9	0.0914	1.4	0.73	0.0584	1.3	564	7	560	8	545	28	103
A354	15794	130	27	1.07	33.5	0.7371	12.4	0.0922	3.7	0.30	0.0580	11.8	568	20	561	55	530	259	107
A247	2373	247	34	2.54	b.d.	0.7588	3.4	0.0923	1.6	0.48	0.0596	3.0	569	9	573	15	590	65	96
A319	1635	112	12	1.12	b.d.	0.7487	3.8	0.0924	1.5	0.39	0.0588	3.5	570	8	567	17	559	75	102
A237	5627	649	64	0.69	0.0	0.7646	2.3	0.0935	1.5	0.66	0.0593	1.7	576	8	577	10	578	37	100
A266	2238	137	15	1.02	b.d.	0.7690	3.1	0.0936	1.4	0.44	0.0596	2.8	577	8	579	14	588	61	98
A257	2524	284	27	0.40	b.d.	0.7706	3.1	0.0942	1.5	0.50	0.0593	2.6	580	9	580	14	579	57	100
A309	1993	126	14	1.09	b.d.	0.7902	3.5	0.0944	1.4	0.40	0.0607	3.2	581	8	591	16	630	70	92
A321	3997	121	16	1.44	7.8	0.7931	7.9	0.0944	1.7	0.21	0.0610	7.7	581	9	593	36	638	167	91
A282	1307	146	18	1.66	0.2	0.7866	5.4	0.0953	1.6	0.29	0.0599	5.2	587	9	589	24	598	112	98
A341	766	114	14	1.60	b.d.	0.7938	5.7	0.0960	1.7	0.29	0.0600	5.5	591	9	593	26	602	118	98
A244	11814	1196	144	1.74	0.7	0.8042	2.3	0.0963	1.3	0.60	0.0606	1.8	593	8	599	10	625	39	95
A315	1372	89	9	0.34	b.d.	0.8124	4.1	0.0976	1.5	0.37	0.0604	3.8	600	9	604	19	617	82	97
A339	1630	99	13	1.93	0.5	0.8114	3.9	0.0985	1.6	0.42	0.0597	3.5	606	9	603	18	594	77	102
A356	3192	210	23	0.76	1.2	0.8379	3.6	0.0998	1.4	0.39	0.0609	3.3	613	8	618	17	634	71	97
A265	7648	87	14	0.95	19.1	0.8543	8.7	0.1009	2.5	0.29	0.0614	8.3	620	15	627	42	653	179	95
A311	4873	581	75	1.73	0.1	0.8564	3.0	0.1022	1.5	0.49	0.0608	2.6	627	9	628	14	631	56	100
A292	2570	142	15	0.60	0.8	0.8714	3.5	0.1025	1.4	0.41	0.0617	3.2	629	9	636	17	663	68	95
A305	1112	50	6	1.16	2.0	0.8466	3.5	0.1025	1.8	0.52	0.0599	3.0	629	11	623	16	600	64	105
A344	28845	3491	374	0.33	0.0	0.9141	1.5	0.1085	1.3	0.84	0.0611	0.8	664	8	659	7	642	18	103
A226	3853	158	20	0.88	0.1	0.9858	2.3	0.1141	1.4	0.61	0.0627	1.8	697	9	697	12	697	39	100
A270	42511	196	58	1.49	32.1	1.0870	9.5	0.1224	3.6	0.38	0.0644	8.8	744	25	747	51	754	185	99
A323	14113	1351	162	0.29	b.d.	1.0730	1.7	0.1228	1.4	0.85	0.0634	0.9	747	10	740	9	722	19	103
A243	4299	331	47	1.01	b.d.	1.1350	2.3	0.1256	1.3	0.57	0.0655	1.9	763	9	770	13	791	40	96
A271	2043	167	24	0.97	b.d.	1.1330	3.6	0.1277	1.5	0.41	0.0643	3.3	775	11	769	20	752	70	103
A296	4749	202	27	0.60	b.d.	1.1640	2.7	0.1290	1.5	0.55	0.0654	2.3	782	11	784	15	788	47	99
A316	6499	239	54	2.68	0.0	1.6010	2.4	0.1638	1.4	0.57	0.0709	2.0	978	12	971	15	954	40	102
A269	6000	167	28	0.48	b.d.	1.6600	2.4	0.1662	1.4	0.58	0.0725	1.9	991	13	993	15	999	40	99
A222	17778	338	70	0.57	b.d.	2.1290	1.7	0.1975	1.3	0.79	0.0782	1.0	1162	14	1158	11	1152	20	101
A318	9879	222	47	0.47	b.d.	2.2770	2.0	0.2045	1.3	0.66	0.0807	1.5	1200	14	1205	14	1215	30	99
A235	10694	362	82	0.53	b.d.	2.5170	1.8	0.2170	1.3	0.72	0.0841	1.3	1266	15	1277	13	1295	24	98
A214	4405	68	21	2.29	0.0	2.5680	2.2	0.2189	1.4	0.67	0.0851	1.6	1276	17	1292	16	1318	31	97
A246	4935	80	21	1.04	b.d.	2.6370	2.6	0.2245	1.3	0.51	0.0852	2.2	1306	15	1311	19	1320	43	99
A306	6032	81	25	1.63	3.1	2.7560	3.9	0.2329	1.6	0.42	0.0859	3.5	1349	20	1344	29	1335	68	101
A333	5662	195	55	0.72	b.d.	3.2210	2.3	0.2606	1.5	0.66	0.0896	1.7	1493	20	1462	18	1418	33	105
A322	9915	296	89	1.13	0.0	3.3370	2.1	0.2562	1.5	0.71	0.0945	1.5	1470	19	1490	16	1518	28	97
A290	12664	350	104	0.84	0.0	3.4850	2.0	0.2670	1.5	0.73	0.0947	1.4	1525	20	1524	16	1522	25	100
A353	15926	185	62	0.60	0.1	4.6600	1.8	0.3064	1.3	0.74	0.1103	1.2	1723	20	1760	15	1805	22	95
A216	62718	919	302	0.15	0.1	5.3170	1.6	0.3301	1.4	0.89	0.1168	0.7	1839	23	1872	14	1908	13	96
A351	97428	270	168	0.94	18.8	5.3780	6.9	0.3359	2.6	0.37	0.1161	6.4	1867	42	1881	61	1897	116	98
A260	14389	211	78	0.67	1.1	5.4190	2.2	0.3378	1.4	0.63	0.1163	1.7	1876	23	1888	19	1901	31	99

Grain	^{207}Pb[a] (cps)	U[b] (ppm)	Pb[b] (ppm)	Th[b] / U	^{206}Pbc[c] (%)	^{207}Pb[d] / ^{235}U	±2σ (%)	^{206}Pb[d] / ^{238}U	±2σ (%)	ρ[e] (rho)	^{207}Pb[d] / ^{206}Pb	±2σ (%)	^{206}Pb[f] / ^{238}U	±2σ (Ma)	^{207}Pb[f] / ^{235}U	±2σ (Ma)	^{207}Pb[f] / ^{206}Pb	±2σ (Ma)	Conc.[g] (%)
A264	3450	49	22	1.64	3.6	5.5720	3.4	0.3514	1.9	0.56	0.1150	2.8	1941	32	1912	30	1880	51	103
A229	164646	2247	748	0.09	0.0	5.6480	1.4	0.3367	1.3	0.91	0.1217	0.6	1871	21	1923	12	1981	10	94
A279	33024	548	181	0.03	b.d.	5.7730	1.5	0.3380	1.3	0.83	0.1239	0.9	1877	21	1942	13	2013	15	93
A263	17585	274	105	0.63	b.d.	5.7730	1.7	0.3490	1.3	0.77	0.1200	1.1	1930	23	1942	15	1956	20	99
A253	49515	171	97	1.87	15.5	5.8360	6.1	0.3389	2.1	0.35	0.1249	5.7	1881	35	1952	54	2027	101	93
A277	9686	151	63	1.05	b.d.	5.8980	2.0	0.3536	1.4	0.73	0.1210	1.3	1952	24	1961	17	1971	24	99
A297	8826	71	30	1.23	b.d.	5.9680	2.3	0.3555	1.5	0.65	0.1218	1.7	1961	25	1971	20	1982	30	99
A259	11540	74	29	0.63	1.5	5.9944	3.2	0.3567	1.8	0.56	0.1219	2.6	1967	30	1975	28	1984	47	99
A212	29669	194	75	0.64	0.3	6.0280	1.5	0.3528	1.3	0.83	0.1239	0.9	1948	21	1980	14	2014	15	97
A308	18205	285	122	1.19	0.0	6.0750	1.7	0.3548	1.4	0.79	0.1242	1.1	1957	23	1987	15	2017	19	97
A230	35749	239	96	0.84	b.d.	6.0940	1.5	0.3515	1.3	0.84	0.1258	0.8	1942	21	1989	13	2040	14	95
A310	5788	44	20	1.53	0.1	6.1080	2.3	0.3604	1.5	0.67	0.1229	1.7	1984	26	1991	20	1999	30	99
A295	20569	155	75	1.85	0.1	6.1830	1.7	0.3568	1.3	0.79	0.1257	1.0	1967	23	2002	15	2038	18	97
A289	35943	159	80	1.10	10.1	6.2000	5.0	0.3592	1.7	0.34	0.1252	4.7	1978	29	2005	44	2032	82	97
A304	10921	85	39	1.49	0.1	6.3050	1.9	0.3670	1.4	0.73	0.1246	1.3	2015	24	2019	17	2023	23	100
A227	8973	60	26	1.19	0.0	6.3710	2.0	0.3644	1.4	0.71	0.1268	1.4	2003	25	2028	18	2054	25	97
A213	19351	52	22	0.89	0.1	6.4550	1.7	0.3645	1.3	0.77	0.1284	1.1	2004	22	2040	15	2077	19	96
A291	10929	80	31	0.40	0.6	6.4630	2.2	0.3632	1.4	0.63	0.1291	1.7	1997	24	2041	20	2085	30	96
A258	24229	179	81	1.31	b.d.	6.6000	1.9	0.3742	1.5	0.79	0.1279	1.2	2049	27	2059	17	2070	21	99
A337	63523	968	440	1.39	0.0	6.6310	1.6	0.3629	1.4	0.87	0.1325	0.8	1996	23	2064	14	2132	13	94
A300	18293	125	57	1.08	1.6	6.6570	2.6	0.3776	1.4	0.56	0.1279	2.1	2065	25	2067	23	2069	37	100
A254	11915	76	33	0.87	0.0	6.6660	1.8	0.3725	1.3	0.74	0.1298	1.2	2041	23	2068	16	2095	21	97
A250	10909	66	34	1.90	1.4	6.7380	2.3	0.3794	1.4	0.61	0.1288	1.8	2074	25	2078	20	2081	32	100
A208	6549	40	15	0.14	b.d.	6.7480	2.7	0.3782	1.5	0.57	0.1294	2.2	2068	27	2079	24	2090	39	99
A223	14882	88	37	0.73	0.1	6.7560	1.8	0.3800	1.4	0.76	0.1289	1.1	2076	24	2080	16	2084	20	100
A301	18986	263	109	0.54	0.9	6.7560	1.9	0.3776	1.4	0.72	0.1298	1.3	2065	24	2080	17	2095	23	99
A262	9535	62	26	0.83	0.0	6.7710	1.9	0.3722	1.4	0.73	0.1319	1.3	2040	24	2082	17	2124	22	96
A251	18230	107	44	0.67	0.4	6.7940	2.1	0.3696	1.3	0.64	0.1333	1.6	2028	23	2085	19	2142	28	95
A325	9703	74	32	0.85	0.6	6.8610	2.3	0.3839	1.5	0.67	0.1296	1.7	2094	27	2094	20	2093	30	100
A299	16346	102	51	1.46	3.2	6.8660	3.4	0.3835	1.5	0.43	0.1298	3.1	2093	26	2094	31	2096	54	100
A307	10313	74	34	1.12	0.0	6.9510	2.0	0.3855	1.4	0.73	0.1308	1.3	2102	26	2105	17	2108	23	100
A327	42501	211	111	0.92	8.6	6.9700	4.8	0.3964	1.6	0.34	0.1275	4.5	2152	29	2108	43	2064	79	104
A218	6554	39	19	1.39	0.0	7.1480	2.4	0.3933	1.4	0.59	0.1318	1.9	2138	26	2130	22	2122	34	101
A275	19940	260	117	0.78	0.1	7.2950	1.8	0.3955	1.4	0.77	0.1338	1.1	2149	25	2148	16	2148	19	100
A347	8652	71	33	0.86	b.d.	7.7490	2.3	0.4077	1.5	0.65	0.1378	1.8	2204	28	2202	21	2200	31	100
A302	61872	642	278	0.11	0.0	9.3970	1.7	0.4217	1.4	0.86	0.1616	0.9	2268	28	2378	16	2473	14	92
A342	21887	252	130	0.61	0.0	10.0200	1.8	0.4603	1.4	0.81	0.1578	1.0	2441	29	2436	16	2433	17	100
A220	75374	295	151	0.71	0.1	10.0800	1.4	0.4498	1.3	0.89	0.1626	0.7	2394	26	2442	13	2483	11	96
A232	14022	54	32	1.24	0.3	10.8300	1.9	0.4823	1.4	0.74	0.1628	1.3	2537	30	2508	18	2485	22	102
A236	75117	539	280	0.73	0.2	10.9300	1.7	0.4487	1.4	0.86	0.1767	0.8	2390	28	2517	15	2622	14	91
A314	67044	309	168	0.84	0.0	10.9900	1.4	0.4666	1.3	0.91	0.1708	0.6	2469	27	2522	13	2565	10	96
A211	64679	214	131	1.31	0.0	11.9600	1.6	0.4862	1.3	0.83	0.1784	0.9	2554	28	2601	15	2638	15	97
A206	31923	103	62	1.19	0.0	12.0300	1.6	0.4820	1.3	0.81	0.1810	0.9	2536	26	2607	15	2662	15	95
A210	53266	170	112	1.75	b.d.	12.2400	1.6	0.4923	1.4	0.85	0.1803	0.9	2580	30	2623	15	2655	14	97
A345	35120	150	92	0.92	0.5	12.7600	1.6	0.5100	1.4	0.90	0.1815	0.7	2656	30	2662	15	2666	11	100
A255	43467	336	197	0.53	0.1	13.1700	1.9	0.5292	1.5	0.83	0.1805	1.0	2738	35	2692	18	2657	17	103
A215	38681	116	70	0.67	0.0	13.7500	1.6	0.5280	1.3	0.81	0.1889	1.0	2733	30	2733	16	2733	16	100
A355	*11361*	*1311*	*105*	*0.52*	*0.4*	*0.7243*	*3.1*	*0.0764*	*1.5*	*0.47*	*0.0688*	*2.7*	*474*	*7*	*553*	*13*	*892*	*56*	*53*
A335	*8407*	*493*	*46*	*0.85*	*3.1*	*0.6901*	*5.1*	*0.0816*	*1.5*	*0.29*	*0.0613*	*4.8*	*506*	*7*	*533*	*21*	*651*	*104*	*78*
A256	*10231*	*776*	*86*	*1.16*	*6.2*	*0.8256*	*6.8*	*0.0929*	*1.7*	*0.25*	*0.0645*	*6.6*	*573*	*9*	*611*	*32*	*756*	*139*	*76*
A225	*194*	*8*	*1*	*0.83*	*b.d.*	*1.6290*	*18.0*	*0.0999*	*4.3*	*0.24*	*0.1183*	*17.5*	*614*	*25*	*982*	*120*	*1930*	*313*	*32*
A348	*747*	*48*	*7*	*2.51*	*0.1*	*0.9685*	*5.7*	*0.1065*	*2.0*	*0.35*	*0.0660*	*5.3*	*652*	*12*	*688*	*29*	*805*	*112*	*81*
A312	*33035*	*386*	*66*	*0.66*	*16.0*	*1.0570*	*6.8*	*0.1115*	*2.6*	*0.39*	*0.0688*	*6.3*	*682*	*17*	*733*	*36*	*891*	*130*	*76*
A224	*12087*	*651*	*89*	*0.42*	*0.0*	*1.5610*	*2.2*	*0.1341*	*1.5*	*0.68*	*0.0844*	*1.6*	*811*	*12*	*955*	*14*	*1303*	*32*	*62*
A272	*12823*	*558*	*82*	*0.37*	*0.4*	*1.5850*	*2.5*	*0.1421*	*1.7*	*0.67*	*0.0809*	*1.9*	*857*	*14*	*964*	*16*	*1219*	*37*	*70*
A352	*21885*	*485*	*73*	*0.43*	*0.2*	*2.1240*	*2.1*	*0.1423*	*1.5*	*0.73*	*0.1083*	*1.4*	*858*	*12*	*1157*	*15*	*1771*	*26*	*48*
A231	*16630*	*271*	*47*	*0.52*	*0.0*	*2.2100*	*2.2*	*0.1584*	*1.8*	*0.82*	*0.1012*	*1.2*	*948*	*16*	*1184*	*15*	*1645*	*23*	*58*
A209	*25942*	*763*	*118*	*0.09*	*0.0*	*2.5600*	*2.5*	*0.1561*	*2.1*	*0.86*	*0.1189*	*1.3*	*935*	*18*	*1289*	*18*	*1940*	*22*	*48*
A261	*23564*	*827*	*151*	*0.37*	*0.2*	*3.0750*	*3.1*	*0.1771*	*1.5*	*0.49*	*0.1259*	*2.7*	*1051*	*15*	*1426*	*24*	*2041*	*48*	*52*
A252	*20501*	*221*	*55*	*0.42*	*0.2*	*3.7000*	*2.2*	*0.2376*	*1.4*	*0.66*	*0.1129*	*1.7*	*1374*	*18*	*1571*	*18*	*1847*	*30*	*74*
A343	*17704*	*386*	*105*	*0.56*	*0.0*	*5.0930*	*1.9*	*0.2465*	*1.4*	*0.76*	*0.1499*	*1.2*	*1420*	*18*	*1835*	*16*	*2344*	*21*	*61*
A217	*21719*	*69*	*36*	*3.66*	*b.d.*	*5.6100*	*3.6*	*0.3009*	*2.4*	*0.66*	*0.1352*	*2.7*	*1696*	*36*	*1918*	*32*	*2167*	*47*	*78*
A350	*162798*	*2207*	*674*	*0.53*	*0.1*	*5.9020*	*2.3*	*0.2749*	*2.1*	*0.93*	*0.1557*	*0.8*	*1565*	*30*	*1962*	*20*	*2410*	*14*	*65*
A334	*134075*	*1714*	*603*	*2.12*	*0.0*	*6.4770*	*2.1*	*0.2822*	*1.9*	*0.92*	*0.1664*	*0.8*	*1603*	*27*	*2043*	*19*	*2522*	*13*	*64*
A336	*179316*	*2154*	*780*	*0.48*	*0.0*	*7.8040*	*1.8*	*0.3311*	*1.6*	*0.90*	*0.1709*	*0.8*	*1844*	*25*	*2209*	*16*	*2567*	*13*	*72*
A234	*29853*	*293*	*105*	*0.55*	*0.0*	*8.1500*	*2.3*	*0.3111*	*1.9*	*0.85*	*0.1900*	*1.2*	*1746*	*29*	*2248*	*21*	*2742*	*20*	*64*
A320	*89037*	*433*	*186*	*0.30*	*0.1*	*9.2390*	*2.2*	*0.3985*	*1.5*	*0.68*	*0.1682*	*1.6*	*2162*	*28*	*2362*	*21*	*2540*	*28*	*85*
A228	*530*	-	-	-	-	-	-	-	-	-	-	-	-	-	-	-	-	-	-

Grain	^{207}Pb[a] (cps)	U[b] (ppm)	Pb[b] (ppm)	Th[b] / U	^{206}Pbc[c] (%)	$^{207}Pb/^{235}U$[d]	±2σ (%)	$^{206}Pb/^{238}U$[d]	±2σ (%)	ρ[e] (rho)	$^{207}Pb/^{206}Pb$[d]	±2σ (%)	$^{206}Pb/^{238}U$[f]	±2σ (Ma)	$^{207}Pb/^{235}U$[f]	±2σ (Ma)	$^{207}Pb/^{206}Pb$[f]	±2σ (Ma)	Conc.[g] (%)
91500[h]	8676	77	14	0.44	0.3	1.8408	3.8	0.1792	3.3	0.56	0.0745	1.9	1062	32	1060	25	1055	38	101
Felix[h]	8886	509	76	3.98	0.1	0.6348	6.8	0.0807	7.3	0.50	0.0571	1.2	500	35	499	27	494	26	101
Plesovice[h]	2366	866	45	0.15	0.4	0.3935	2.3	0.0539	1.7	0.47	0.0529	2.3	339	6	337	7	326	52	104
GJ-1[h]	7647	340	31	0.02	0.1	0.8142	1.8	0.0984	0.9	0.42	0.0600	1.6	605	5	605	8			

$^{206}Pb/^{238}U$ error is the quadratic additions of the within run precision (2 SE) and the external reproducibility (2 SD) of the reference zircon. $^{207}Pb/^{206}Pb$ error propagation (^{207}Pb signal dependent) following Gerdes & Zeh (2009). $^{207}Pb/^{235}U$ error is the quadratic addition of the $^{207}Pb/^{206}Pb$ and $^{206}Pb/^{238}U$ uncertainty.

[a] Within run background-corrected mean ^{207}Pb signal in cps (counts per second).

[b] U and Pb content and Th/U ratio were calculated relative to GJ-1 reference zircon.

[c] Percentage of the common Pb on the ^{206}Pb. b.d. = below detection limit.

[d] Pb/U and Pb/Pb ratios. Corrected for background, within-run Pb/U fractionation (in case of $^{206}Pb/^{238}U$) and common Pb using Stacy and Kramers (1975) model Pb composition and subsequently normalised to GJ-1 (ID-TIMS value/measured value); $^{207}Pb/^{235}U$ calculated using (($^{207}Pb/^{206}Pb$)*($^{238}U/^{206}Pb$)*137.88).

[e] Rho (ρ) is the ($^{206}Pb/^{238}U$)/($^{207}Pb/^{235}U$) error correlation coefficient.

[f] Pb/U and Pb/Pb ages.

[g] Degree of concordance = (($^{206}Pb/^{238}U$ age)/($^{207}Pb/^{206}Pb$ age)) x 100.

[h] Mean of 9 (91500), 9 (Felix), 9 (Plesovice), and 18 (GJ-1) analyses, respectively.

Table S6

Lu, Yb and Hf LA-MC-ICPMS data of zircon cores from sample GCH-02

Grain	$^{176}Yb/^{177}Hf$ [a]	±2σ	$^{176}Lu/^{177}Hf$ [a]	±2σ	$^{178}Hf/^{177}Hf$	$^{180}Hf/^{177}Hf$	Sig_{Hf} [b] (V)	$^{176}Hf/^{177}Hf$	±2σ [c]	$^{176}Hf/^{177}Hf_{(t)}$ [d]	$\varepsilon Hf_{(t)}$ [d]	±2σ [c] (εHf)	T_{DM} [e] (Ga)	age [f] (Ma)	±2σ (Ma)	U-Pb [g] conc	Lu-Hf [n] seq
A183_40_seq2	*0.0350*	*29*	*0.00110*	*7*	*1.46720*	*1.88675*	*8*	*0.281108*	*27*	*0.281056*	*-5.8*	*1.0*	*3.07*	*2441*	*16*	*87*	*2*
A184_40_seq2	0.0063	5	0.00021	1	1.46721	1.88662	11	0.281156	26	0.281147	-7.0	0.9	2.98	2249	12	91	2
A185_40_seq2	0.0103	8	0.00036	2	1.46724	1.88669	11	0.281647	25	0.281632	6.7	0.9	2.10	2095	39	97	2
A187b_40_seq2	0.0159	13	0.00055	3	1.46720	1.88666	10	0.280802	28	0.280770	-2.9	1.0	3.36	2994	14	95	2
A188_40_seq2	0.0107	9	0.00040	3	1.46719	1.88675	13	0.281613	21	0.281598	4.7	0.8	2.18	2062	29	99	2
A189_40_seq2	0.0215	18	0.00069	5	1.46719	1.88690	14	0.282481	22	0.282473	2.7	0.8	1.10	617	9	101	2
A190_40_seq2	0.0135	11	0.00046	3	1.46717	1.88650	10	0.281103	24	0.281080	0.4	0.8	2.91	2671	15	98	2
A191_40_seq2	0.0129	10	0.00043	3	1.46723	1.88673	11	0.281149	32	0.281128	0.2	1.1	2.86	2587	15	100	2
A193_40_seq2	0.0082	7	0.00023	1	1.46717	1.88665	14	0.281151	22	0.281142	-12.7	0.8	3.09	2013	16	94	2
A200_40_seq2	0.0010	2	0.00003	1	1.46723	1.88690	15	0.281115	25	0.281113	-3.3	0.9	2.95	2460	28	100	2
A201_40_seq2	0.0054	4	0.00020	1	1.46717	1.88692	13	0.281286	26	0.281279	-8.4	0.9	2.84	1986	12	93	2
A202_40_seq2	0.0161	14	0.00054	4	1.46725	1.88680	11	0.282202	23	0.282197	-9.7	0.8	1.69	500	7	96	2
A203_40_seq2	0.0215	18	0.00080	5	1.46721	1.88671	10	0.281620	21	0.281591	0.7	0.7	2.27	1899	34	95	2
A204_40_seq2	0.0250	20	0.00081	5	1.46723	1.88667	11	0.282539	25	0.282531	2.1	0.9	1.04	496	8	96	2
A206_40_seq2	0.0123	10	0.00046	3	1.46716	1.88671	11	0.281571	22	0.281553	2.8	0.8	2.27	2051	23	99	2
A209_40_seq2	0.0165	19	0.00054	5	1.46713	1.88655	9	0.281421	30	0.281405	-11.7	1.1	2.74	1651	35	94	2
A214_40_seq2	0.0240	20	0.00083	5	1.46721	1.88666	13	0.281095	30	0.281065	-17.4	1.0	3.28	1925	13	96	2
A216_40_seq2	0.0311	25	0.00101	6	1.46717	1.88658	11	0.281104	23	0.281052	0.5	0.8	2.94	2715	12	98	2
A217_40_seq2	0.0226	18	0.00088	5	1.46724	1.88696	12	0.281712	25	0.281677	7.9	0.9	2.02	2078	25	96	2
A218_40_seq2	0.0126	10	0.00043	3	1.46717	1.88663	11	0.281595	20	0.281578	4.9	0.7	2.20	2101	27	99	2
A226_40_seq2	0.0023	2	0.00007	0	1.46718	1.88653	13	0.281033	22	0.281030	-5.9	0.8	3.10	2473	11	97	2
A227_40_seq2	0.0110	9	0.00036	2	1.46712	1.88631	11	0.281483	19	0.281469	-1.8	0.7	2.47	1979	26	97	2
A229_40_seq2	0.0132	11	0.00038	2	1.46711	1.88650	13	0.281206	26	0.281190	-6.9	0.9	2.92	2190	17	100	2
A233_40_seq2	0.0215	18	0.00091	6	1.46717	1.88669	10	0.282398	25	0.282387	-0.5	0.9	1.27	608	10	93	2
A236_40_seq2	0.0277	24	0.00107	7	1.46718	1.88667	11	0.282436	24	0.282425	-0.3	0.9	1.22	559	9	96	2
A237_40_seq2	0.0165	14	0.00055	4	1.46718	1.88683	11	0.281592	21	0.281570	3.8	0.8	2.23	2069	40	99	2
A234_seq2_40	*0.0029*	*5*	*0.00009*	*2*	*1.46721*	*1.88688*	*13*	*0.281036*	*23*	*0.281032*	*-8.3*	*0.8*	*3.15*	*2370*	*30*	*78*	*2*
A235_seq2_40	0.0326	26	0.00096	6	1.46717	1.88688	11	0.282388	21	0.282379	-3.0	0.7	1.33	510	9	97	2
A236_seq2_26	0.0194	17	0.00078	5	1.46704	1.88609	6	0.282443	30	0.282435	0.1	1.1	1.20	559	9	96	2
A237_seq2_26	0.0207	18	0.00069	5	1.46713	1.88649	6	0.281620	35	0.281593	4.7	1.2	2.19	2069	40	99	2
A243_seq2_40	0.0264	21	0.00082	5	1.46720	1.88678	13	0.282703	22	0.282695	8.4	0.8	0.71	517	8	97	2
A244_seq2_40	0.0207	20	0.00061	5	1.46719	1.88678	21	0.281003	20	0.280971	-2.1	0.7	3.10	2729	12	100	2
A245_seq2_40	*0.0149*	*14*	*0.00048*	*4*	*1.46717*	*1.88685*	*12*	*0.281187*	*28*	*0.281166*	*-3.2*	*1.0*	*2.88*	*2386*	*19*	*85*	*2*
A246_seq2_40	0.0223	18	0.00070	4	1.46712	1.88662	12	0.281079	23	0.281046	-4.4	0.8	3.05	2514	14	94	2
A247_seq2_40	0.0182	15	0.00062	4	1.46721	1.88678	12	0.281568	24	0.281543	3.0	0.9	2.28	2072	33	97	2
A248_seq2_40	0.0223	19	0.00074	5	1.46713	1.88668	11	0.282244	24	0.282236	-8.0	0.8	1.61	514	7	99	2
A249_seq2_26	*0.0076*	*7*	*0.00025*	*2*	*1.46715*	*1.88645*	*6*	*0.281061*	*29*	*0.281049*	*-4.3*	*1.0*	*3.05*	*2514*	*17*	*82*	*2*
A250_seq2_40	0.0123	11	0.00043	3	1.46724	1.88689	14	0.281947	25	0.281943	-19.3	0.9	2.19	470	9	95	2
A251_seq2_26	*0.0372*	*41*	*0.00124*	*12*	*1.46707*	*1.88637*	*7*	*0.281723*	*29*	*0.281678*	*4.5*	*1.0*	*2.08*	*1932*	*70*	*1*	*2*
A252_seq2_40	0.0210	22	0.00077	7	1.46717	1.88665	13	0.282076	25	0.282068	-13.7	0.9	1.93	523	9	97	2
A253_seq2_26	0.0122	13	0.00046	4	1.46710	1.88632	7	0.282579	40	0.282574	4.2	1.4	0.94	523	8	97	2
A254_seq2_26	0.0632	68	0.00201	19	1.46712	1.88643	6	0.282310	32	0.282288	-4.8	1.1	1.48	574	10	100	2
A256_seq2_26	*0.0106*	*9*	*0.00038*	*2*	*1.46706*	*1.88645*	*7*	*0.281050*	*40*	*0.281032*	*-3.8*	*1.4*	*3.06*	*2561*	*19*	*87*	*2*
A257_seq2_26	0.0458	37	0.00148	9	1.46709	1.88635	8	0.281062	21	0.280986	-2.4	0.7	3.08	2694	11	100	2
A258_seq2_26	0.0122	10	0.00044	3	1.46714	1.88656	6	0.281565	30	0.281548	2.2	1.1	2.29	2033	26	96	2
A259_seq2_26	0.0271	31	0.00085	9	1.46704	1.88628	6	0.281573	27	0.281540	2.3	0.9	2.30	2048	20	101	2
A260_seq2_26	0.0173	21	0.00060	6	1.46704	1.88632	6	0.282125	29	0.282120	-12.7	1.0	1.84	484	9	95	2
A261_seq2_26	0.0386	32	0.00123	8	1.46704	1.88636	5	0.281516	33	0.281469	-1.0	1.2	2.46	2016	20	99	2
A262_seq2_26	0.0193	20	0.00064	6	1.46706	1.88644	5	0.281055	33	0.281022	-1.9	1.2	3.03	2659	15	93	2
A263_seq2_26	0.0143	12	0.00047	3	1.46711	1.88666	7	0.281002	26	0.280980	-7.5	0.9	3.20	2481	10	93	2
A264_seq2_26	0.0157	13	0.00064	4	1.46713	1.88646	6	0.281599	30	0.281575	1.9	1.1	2.26	1980	20	95	2
A266_seq2_26	0.0416	36	0.00134	9	1.46711	1.88629	6	0.282611	31	0.282599	3.9	1.1	0.92	471	7	93	2
A267_seq2_40	0.0133	11	0.00047	3	1.46718	1.88673	10	0.281537	22	0.281519	1.1	0.8	2.35	2028	29	99	2
A268_seq2_40	0.0063	5	0.00022	1	1.46717	1.88683	16	0.281590	22	0.281581	4.2	0.8	2.21	2067	26	99	2
A269_seq2_40	0.0233	19	0.00078	5	1.46715	1.88658	12	0.281583	21	0.281553	2.4	0.7	2.28	2035	28	97	2
A270_seq2_40	0.0107	10	0.00036	3	1.46717	1.88673	12	0.281166	27	0.281148	-0.6	0.9	2.85	2521	13	100	2
A271_seq2_40	0.0172	14	0.00061	4	1.46720	1.88681	13	0.282606	25	0.282600	4.4	0.9	0.91	489	9	100	2
A272_seq2_40	0.0107	9	0.00033	2	1.46713	1.88651	14	0.281170	24	0.281157	-12.5	0.9	3.07	1998	20	100	2
A273_seq2_40	*0.0015*	*1*	*0.00004*	*0*	*1.46717*	*1.88674*	*17*	*0.281566*	*22*	*0.281565*	*1.6*	*0.8*	*2.28*	*1982*	*18*	*81*	*2*
A274_seq2_40	0.0122	10	0.00039	3	1.46711	1.88665	12	0.281554	18	0.281538	2.2	0.6	2.31	2045	26	97	2
A275_seq2_26	0.0158	15	0.00055	4	1.46715	1.88647	7	0.281058	22	0.281029	-0.6	0.8	3.00	2702	9	96	2
A277_seq2_40	0.0164	13	0.00053	3	1.46719	1.88662	13	0.281450	18	0.281430	-2.9	0.6	2.54	1992	24	99	2
A278_seq2_26	0.0164	13	0.00052	3	1.46716	1.88637	8	0.280959	26	0.280934	-6.7	0.9	3.24	2589	13	97	2

Grain	$^{176}Yb/^{177}Hf$ [a]	±2σ	$^{176}Lu/^{177}Hf$ [a]	±2σ	$^{178}Hf/^{177}Hf$	$^{180}Hf/^{177}Hf$	Sig_{Hf} [b] (V)	$^{176}Hf/^{177}Hf$	±2σ [c]	$^{176}Hf/^{177}Hf_{(t)}$ [d]	$\varepsilon Hf_{(t)}$ [d]	±2σ [c] (εHf)	T_{DM} [e] (Ga)	age [f] (Ma)	±2σ (Ma)	U-Pb [g] conc	Lu-Hf [h] seq
A279_seq2_26	0.0305	27	0.00101	7	1.46711	1.88642	7	0.281052	28	0.281001	-2.7	1.0	3.07	2656	21	97	2
A280_seq2_26	*0.0251*	*27*	*0.00088*	*8*	*1.46707*	*1.88635*	*5*	*0.282408*	*44*	*0.282379*	*24.6*	*1.6*	*0.79*	*1723*	*124*	*31*	*2*
A281_seq2_40	0.0128	11	0.00042	3	1.46716	1.88658	13	0.281269	20	0.281252	-8.3	0.7	2.87	2030	15	99	2
A282_seq2_26	0.0141	14	0.00045	4	1.46712	1.88637	6	0.280704	32	0.280681	-13.8	1.1	3.69	2668	18	94	2
A288_seq2_26	0.0329	48	0.00102	13	1.46712	1.88636	6	0.281094	33	0.281044	-2.5	1.2	3.02	2598	14	100	2
A289_seq2_26	0.0256	26	0.00092	8	1.46711	1.88662	7	0.281614	32	0.281579	2.4	1.1	2.25	1992	23	95	2
A290_seq2_40	0.0241	20	0.00076	5	1.46714	1.88678	14	0.282550	25	0.282543	3.0	0.9	1.01	518	11	96	2
A291_seq2_26	0.0610	57	0.00200	15	1.46714	1.88649	6	0.282677	33	0.282657	7.0	1.2	0.78	517	8	97	2
A292_seq2_26	0.0264	21	0.00084	5	1.46712	1.88659	8	0.281056	28	0.281015	-5.0	1.0	3.10	2538	14	93	2
A293_seq2_26	0.0097	8	0.00036	2	1.46711	1.88642	7	0.281517	27	0.281503	1.1	0.9	2.37	2054	17	96	2
A294_seq2_26	0.0018	2	0.00007	0	1.46708	1.88636	21	0.281401	17	0.281400	-38.2	0.6	3.21	484	9	98	2
A296_seq2_26	0.0195	33	0.00071	11	1.46719	1.88664	6	0.281596	24	0.281568	3.2	0.8	2.25	2044	20	99	2
A297_seq2_40	0.0110	9	0.00036	2	1.46723	1.88905	12	0.281328	134	0.281314	-6.7	4.8	2.76	2004	29	97	2
A298_seq2_40	*0.0166*	*15*	*0.00054*	*4*	*1.46719*	*1.88676*	*12*	*0.281095*	*28*	*0.281095*	*-59.7*	*1.0*	*3.94*	-	-	-	*2*
A299_seq2_26	0.0256	27	0.00084	8	1.46713	1.88654	6	0.281085	25	0.281042	-0.1	0.9	2.97	2704	20	100	2
A300_seq2_40	0.0155	14	0.00048	4	1.46720	1.88681	13	0.282355	21	0.282350	-3.7	0.7	1.38	524	10	98	2
A301_seq2_40	0.0217	18	0.00080	5	1.46720	1.88676	10	0.281658	25	0.281627	4.9	0.9	2.14	2026	28	98	2
A304_seq2_26	0.0171	14	0.00055	3	1.46709	1.88655	5	0.281038	34	0.281010	-2.6	1.2	3.06	2644	13	93	2
A305_seq2_40	0.0187	15	0.00061	4	1.46716	1.88659	12	0.281084	19	0.281054	-1.3	0.7	2.98	2635	18	99	2
A306_seq2_26	0.0111	10	0.00041	3	1.46714	1.88658	6	0.280975	30	0.280953	-1.7	1.1	3.11	2770	12	92	2
A307_seq2_26	0.0550	45	0.00178	11	1.46713	1.88641	8	0.281090	27	0.280999	-2.4	1.0	3.07	2672	14	100	2
A308_seq2_40	0.0178	15	0.00060	4	1.46721	1.88676	13	0.281958	21	0.281952	-17.8	0.7	2.15	526	8	99	2
A311_seq2_26	0.0300	28	0.00106	8	1.46715	1.88644	7	0.280967	34	0.280906	2.2	1.2	3.09	3007	11	98	2
A313_seq2_26	0.0138	18	0.00052	6	1.46710	1.88662	7	0.282325	26	0.282318	-0.4	0.9	1.36	724	10	94	2
A315_seq2_40	0.0097	8	0.00030	2	1.46717	1.88683	13	0.281023	25	0.281008	-2.6	0.9	3.06	2648	16	96	2
A317_seq2_40	0.0094	8	0.00033	2	1.46718	1.88686	13	0.281576	22	0.281563	3.1	0.8	2.26	2049	26	96	2
A319_seq2_40	0.0346	29	0.00106	7	1.46715	1.88696	12	0.282504	25	0.282493	1.1	0.9	1.11	513	8	100	2
A320_seq2_26	0.0192	17	0.00065	5	1.46715	1.88656	5	0.281558	29	0.281533	0.7	1.0	2.34	1992	27	98	2
A324_seq2_26	0.0074	10	0.00020	3	1.46714	1.88675	6	0.281654	133	0.281652	-31.2	4.7	2.77	401	6	96	2
A325_seq2_26	0.0075	6	0.00023	1	1.46712	1.88656	7	0.281182	37	0.281173	-11.6	1.3	3.03	2013	30	98	2
A326_seq2_26	0.0092	8	0.00035	2	1.46718	1.88671	6	0.282328	36	0.282325	-4.8	1.3	1.43	515	7	99	2
A327_seq2_26	0.0202	19	0.00067	5	1.46715	1.88666	7	0.281006	30	0.280972	-4.1	1.1	3.14	2640	10	99	2
A333_seq2_40	0.0234	26	0.00081	8	1.46720	1.88681	11	0.281610	29	0.281578	3.6	1.0	2.23	2046	36	93	2
A334_seq2_40	0.0349	34	0.00109	9	1.46720	1.88688	12	0.282698	24	0.282688	7.7	0.9	0.73	500	8	98	2
A335_seq2_40	0.0680	57	0.00212	14	1.46716	1.88656	14	0.282475	17	0.282455	-0.2	0.6	1.18	513	8	100	2
A336_seq2_26	0.0319	27	0.00100	7	1.46714	1.88648	8	0.282379	25	0.282370	-3.4	0.9	1.35	508	8	102	2
A338_seq2_40	0.0189	15	0.00066	4	1.46717	1.88686	13	0.281620	24	0.281594	4.6	0.8	2.19	2066	26	97	2
A342_seq2_26	0.0228	25	0.00064	6	1.46719	1.88677	5	0.281084	28	0.281051	-0.3	1.0	2.96	2682	11	97	2
A344_seq2_40	0.0277	23	0.00085	5	1.46716	1.88682	12	0.282528	19	0.282519	3.6	0.7	1.03	585	10	99	2
A345_seq2_40	*0.0070*	*7*	*0.00022*	*2*	*1.46720*	*1.88696*	*12*	*0.281067*	*26*	*0.281056*	*-2.2*	*0.9*	*3.00*	*2593*	*19*	*79*	*2*
A347_seq2_40	0.0223	19	0.00069	5	1.46720	1.88684	11	0.281182	23	0.281149	-0.6	0.8	2.85	2521	17	90	2
A348_seq2_26	0.0372	55	0.00116	16	1.46715	1.88620	6	0.281627	30	0.281581	3.8	1.1	2.22	2051	11	97	2
A354_seq2_26	0.0110	12	0.00036	3	1.46714	1.88644	6	0.281008	31	0.280990	-4.5	1.1	3.12	2598	12	92	2
A355_seq2_26	0.0278	30	0.00100	10	1.46712	1.88652	6	0.282293	29	0.282280	-2.0	1.0	1.44	711	10	99	2
A357_seq2_26	0.0208	24	0.00067	7	1.46705	1.88628	6	0.281040	24	0.281006	-2.9	0.9	3.07	2639	14	99	2
A360_seq2_40	0.0132	11	0.00050	3	1.46719	1.88675	12	0.281057	23	0.281032	-4.3	0.8	3.07	2538	11	91	2

Quoted uncertainties (absolute) relate to the last quoted figure. The effect of the inter-element fractionation on Lu/Hf was estimated to be about 6 % or less based on analyses of the GJ-1 and Plesoviče zircon. Accuracy and reproducibility was checked by repeated analyses of reference zircon GJ-1 and Plesoviče (data given as mean with 2 standard deviation uncertainties).

(a) $^{176}Yb/^{177}Hf = (^{176}Yb/^{173}Yb)_{true} \times (^{173}Yb/^{177}Hf)_{meas} \times (M_{173(Yb)}/M_{177(Hf)})^{\beta(Hf)}$, $\beta(Hf) = \ln((^{179}Hf/^{177}Hf_{true})/(^{179}Hf/^{177}Hf_{measured})) / \ln(M_{179(Hf)}/M_{177(Hf)})$, M = mass of respective isotopes. The $^{176}Lu/^{177}Hf$ was calculated in a similar way using $^{175}Lu/^{177}Hf$ and β(Yb).

(b) Mean Hf signal in volts.

(c) Uncertainties are quadratic additions of the within-run precision and the daily reproducibility of the 40ppb-JMC475 solution. Uncertainties for the JMC475 quoted at 2SD (2 standard deviation).

(d) Initial $^{176}Hf/^{177}Hf$ and εHf calculated using the apparent U-Pb age determined by LA-ICP-MS dating (see column f), and the CHUR parameters: $^{176}Lu/^{177}Hf$ = 0.0336, and $^{176}Hf/^{177}Hf$ = 0.282785 (Bouvier et al. 2008).

(e) Two stage model age in Ga using measured $^{176}Lu/^{177}Lu$ of each spot (first stage = age of zircon), a value of 0.0113 for the average continental crust (second stage, values compiled from Rudnick and Gao (2003), and depleted mantle $^{176}Lu/^{177}Lu$ = 0.0379, and $^{176}Hf/^{177}Hf$ = 0.283164.

(f) Apparent U-Pb age determined by LA-ICP-MS.

(g) U-Pb age concordance (%).

(h) Sequence in which Lu-Hf analyses were performed. Standard analyses for each sequence are showed on Table 12.

Table S7

Lu, Yb and Hf LA-MC-ICPMS data of zircon cores from sample GCH-06

Grain	$^{176}Yb/^{177}Hf$ [a]	±2σ	$^{176}Lu/^{177}Hf$ [a]	±2σ	$^{178}Hf/^{177}Hf$	$^{180}Hf/^{177}Hf$	Sig_{Hf} [b] (V)	$^{176}Hf/^{177}Hf$	±2σ [c]	$^{176}Hf/^{177}Hf_{(t)}$ [d]	$\varepsilon Hf_{(t)}$ [d]	±2σ [c] (εHf)	T_{DM} [e] (Ga)	age [f] (Ma)	±2σ (Ma)	U-Pb [g] conc	Lu-Hf [n] seq
A006_seq4_40	0.0111	9	0.00039	2	1.46716	1.88694	10	0.281603	28	0.281587	5.7	1.0	2.17	2121	22	92	4
A007_seq4_40	0.0083	7	0.00026	2	1.46729	1.88702	12	0.281255	28	0.281245	-9.0	1.0	2.89	2013	29	97	4
A008_seq4_40	0.0351	28	0.00129	8	1.46719	1.88692	11	0.281100	23	0.281034	-0.8	0.8	2.99	2685	14	95	4
A010_seq4_40	0.0079	6	0.00027	2	1.46716	1.88661	13	0.281045	22	0.281032	-3.7	0.8	3.06	2564	11	96	4
A011_seq4_26	0.0235	21	0.00081	6	1.46715	1.88625	7	0.281060	26	0.281025	-10.2	0.9	3.19	2298	14	91	4
A012_seq4_26	0.0380	31	0.00126	8	1.46717	1.88642	6	0.281069	27	0.281003	-1.4	1.0	3.04	2708	12	99	4
A014_seq4_40	0.0524	44	0.00176	11	1.46713	1.88670	11	0.282505	23	0.282486	1.9	0.8	1.10	559	4	97	4
A015_seq4_40	0.0183	15	0.00054	4	1.46718	1.88673	12	0.281052	26	0.281025	-1.5	0.9	3.02	2671	10	96	4
A016_seq4_40	0.0156	12	0.00060	4	1.46714	1.88672	14	0.281593	22	0.281569	4.3	0.8	2.23	2088	17	99	4
A017_seq4_40	0.0338	30	0.00106	8	1.46714	1.88640	12	0.281089	23	0.281056	-23.4	0.8	3.40	1680	41	94	4
A018_seq4_40	0.0050	4	0.00018	1	1.46716	1.88680	12	0.281575	19	0.281567	4.0	0.7	2.23	2078	24	98	4
A019_seq4_40	*0.0139*	*12*	*0.00045*	*3*	*1.46718*	*1.88678*	*15*	*0.281155*	*25*	*0.281134*	*-4.1*	*0.9*	*2.94*	*2393*	*12*	*89*	4
A021_seq4_40	0.0555	45	0.00156	9	1.46720	1.88685	11	0.282378	21	0.282361	-2.1	0.7	1.34	580	4	109	4
A022_seq4_40	0.0251	25	0.00088	7	1.46720	1.88672	12	0.281601	26	0.281567	3.5	0.9	2.24	2061	24	93	4
A023_seq4_40	0.0284	24	0.00092	6	1.46719	1.88686	10	0.281140	22	0.281095	-1.9	0.8	2.94	2549	12	99	4
A024_seq4_40	0.0106	9	0.00035	2	1.46715	1.88653	12	0.282317	19	0.282314	-4.4	0.7	1.44	551	6	96	4
A025_seq4_40	0.0161	13	0.00050	3	1.46720	1.88674	14	0.281113	23	0.281089	-0.7	0.8	2.92	2608	14	96	4
A027_seq4_40	0.0276	25	0.00088	6	1.46706	1.88625	7	0.281065	28	0.281022	-4.0	1.0	3.07	2567	17	103	4
A028_seq4_40	0.0027	3	0.00008	1	1.46715	1.88633	6	0.280969	31	0.280966	-7.9	1.1	3.22	2489	19	103	4
A029_seq4_40	0.0202	18	0.00065	4	1.46718	1.88691	11	0.281089	26	0.281065	-16.2	0.9	3.26	1976	14	97	4
A030_seq4_40	0.0152	15	0.00057	5	1.46719	1.88669	13	0.282101	25	0.282095	-12.3	0.9	1.87	544	6	96	4
A031_seq4_40	0.0150	13	0.00049	3	1.46717	1.88675	12	0.282072	21	0.282067	-13.8	0.8	1.93	521	7	98	4
A032_seq4_40	0.0154	13	0.00069	4	1.46721	1.88679	15	0.282457	22	0.282450	0.2	0.8	1.18	541	5	94	4
A038_seq4_40	0.0147	12	0.00045	3	1.46718	1.88679	13	0.281059	22	0.281036	-0.8	0.8	2.99	2684	14	97	4
A039_seq4_40	0.0265	25	0.00083	7	1.46719	1.88678	12	0.280984	28	0.280942	-5.3	1.0	3.20	2633	20	94	4
A040_seq4_40	0.0163	13	0.00049	3	1.46709	1.88671	14	0.281585	20	0.281566	3.7	0.7	2.24	2068	28	94	4
A041_seq4_40	0.0504	40	0.00163	10	1.46715	1.88667	16	0.281158	24	0.281075	-0.2	0.8	2.93	2648	11	100	4
A042_seq4_40	0.0110	10	0.00034	3	1.46717	1.88669	16	0.281127	24	0.281115	-14.7	0.9	3.17	1967	19	100	4
A043_seq4_40	0.0131	11	0.00039	2	1.46715	1.88661	15	0.281221	23	0.281206	-10.9	0.8	2.98	1992	14	98	4
A044_seq4_26	0.0127	10	0.00045	3	1.46721	1.88624	7	0.282336	24	0.282331	-3.8	0.8	1.41	550	5	95	4
A045_seq4_26	0.0259	21	0.00087	6	1.46715	1.88631	6	0.281600	31	0.281566	3.3	1.1	2.25	2050	32	97	4
A046_seq4_26	0.0221	21	0.00068	5	1.46710	1.88643	6	0.281198	32	0.281173	-13.9	1.1	3.08	1912	31	98	4
A047_seq4_40	*0.0236*	*23*	*0.00071*	*6*	*1.46718*	*1.88659*	*12*	*0.281623*	*18*	*0.281596*	*4.1*	*0.6*	*2.20*	*2039*	*25*	*88*	4
A049_seq4_26	0.0024	2	0.00007	0	1.46708	1.88633	6	0.281225	30	0.281223	-11.6	1.1	2.97	1936	12	99	4
A050_seq4_40	0.0195	18	0.00078	6	1.46719	1.88662	13	0.281774	19	0.281766	-23.6	0.7	2.49	560	5	100	4
A051_seq4_26	0.0415	40	0.00141	12	1.46707	1.88648	8	0.281098	28	0.281026	-1.9	1.0	3.03	2653	11	96	4
A054_seq4_40	0.0244	21	0.00077	6	1.46717	1.88665	17	0.281057	24	0.281019	-3.1	0.8	3.06	2610	10	101	4
A055_seq4_40	0.0366	51	0.00116	15	1.46703	1.88629	7	0.281077	30	0.281022	-5.8	1.1	3.11	2492	16	100	4
A056_seq4_26	*0.0153*	*14*	*0.00046*	*3*	*1.46707*	*1.88627*	*7*	*0.281036*	*34*	*0.281014*	*-5.1*	*1.2*	*3.11*	*2533*	*12*	*88*	4
A057_seq4_40	0.0077	8	0.00021	2	1.46723	1.88684	15	0.281014	20	0.281004	-3.5	0.7	3.09	2619	14	101	4
A058_seq4_40	0.0137	13	0.00053	4	1.46714	1.88650	12	0.282163	19	0.282158	-10.8	0.7	1.76	510	4	92	4
A059_seq4_40	0.0164	13	0.00054	3	1.46714	1.88680	12	0.281592	21	0.281570	5.4	0.8	2.20	2137	27	91	4
A060_seq4_40	0.0164	13	0.00056	3	1.46718	1.88667	12	0.281605	21	0.281585	0.2	0.7	2.29	1887	34	91	4
A062_seq4_26	0.0107	10	0.00040	3	1.46715	1.88646	7	0.281570	35	0.281554	3.6	1.3	2.26	2085	26	90	4
A064_seq4_26	0.0160	16	0.00053	5	1.46714	1.88642	6	0.281083	30	0.281056	0.4	1.1	2.94	2706	10	96	4
A065_seq4_26	0.0159	14	0.00050	3	1.46712	1.88630	7	0.281070	33	0.281044	-1.4	1.2	2.99	2645	11	93	4
A066_seq4_26	0.0088	7	0.00023	1	1.46711	1.88580	8	0.280982	216	0.280970	-3.6	7.7	3.13	2664	13	98	4
A072_seq4_26	0.0167	16	0.00057	4	1.46706	1.88623	7	0.281027	27	0.281000	-7.9	0.9	3.18	2436	13	98	4
A073_seq4_26	0.0377	31	0.00121	8	1.46703	1.88624	7	0.281060	23	0.280998	-3.0	0.8	3.08	2647	12	94	4
A074_seq4_26	*0.0418*	*36*	*0.00135*	*9*	*1.46707*	*1.88645*	*7*	*0.281086*	*25*	*0.281018*	*-2.9*	*0.9*	*3.06*	*2622*	*13*	*82*	4
A075_seq4_40	0.0225	20	0.00066	5	1.46717	1.88676	11	0.281102	28	0.281068	-0.6	1.0	2.95	2643	17	101	4
A076_seq4_40	0.0334	32	0.00099	8	1.46714	1.88679	11	0.281139	27	0.281088	0.9	1.0	2.89	2676	19	96	4
A077_seq4_40	0.0132	13	0.00043	3	1.46724	1.88692	13	0.281597	22	0.281579	5.5	0.8	2.19	2127	19	98	4
A078_seq4_40	0.0167	16	0.00055	4	1.46721	1.88670	13	0.281173	20	0.281146	0.2	0.7	2.83	2560	15	94	4
A079_seq4_40	*0.0213*	*17*	*0.00074*	*4*	*1.46714*	*1.88655*	*12*	*0.281616*	*24*	*0.281588*	*2.7*	*0.9*	*2.23*	*1992*	*29*	*84*	4
A080_seq4_26	0.0027	6	0.00008	2	1.46710	1.88630	7	0.281018	26	0.281015	-17.5	0.9	3.35	1997	25	99	4
A082_seq4_26	0.0278	25	0.00092	6	1.46711	1.88654	8	0.281114	31	0.281068	-1.1	1.1	2.96	2624	12	96	4
A083_seq4_40	0.0766	65	0.00251	16	1.46712	1.88672	18	0.281191	20	0.281065	-1.2	0.7	2.96	2625	12	94	4
A084_seq4_40	0.0213	27	0.00062	7	1.46716	1.88667	12	0.281194	22	0.281163	2.6	0.8	2.76	2636	12	92	4
A085_seq4_40	0.0104	8	0.00034	2	1.46723	1.88674	12	0.281290	24	0.281277	-8.3	0.8	2.84	1995	19	99	4
A094_seq4_26	0.0084	7	0.00029	2	1.46720	1.88635	6	0.280968	30	0.280953	-4.9	1.1	3.18	2636	13	91	4
A097_seq4_26	0.0106	10	0.00039	3	1.46713	1.88671	6	0.282498	43	0.282493	4.0	1.5	1.05	643	5	91	4
A107_seq4_26	*0.0242*	*22*	*0.00083*	*6*	*1.46707*	*1.88638*	*6*	*0.281057*	*29*	*0.281019*	*-8.6*	*1.0*	*3.17*	*2376*	*15*	*77*	4

Grain	$^{176}Yb/^{177}Hf$ [a]	±2σ	$^{176}Lu/^{177}Hf$ [a]	±2σ	$^{178}Hf/^{177}Hf$	$^{180}Hf/^{177}Hf$	Sig_{Hf} [b] (V)	$^{176}Hf/^{177}Hf$	±2σ [c]	$^{176}Hf/^{177}Hf_{(t)}$ [d]	$\varepsilon Hf_{(t)}$ [d]	±2σ [c] (εHf)	T_{DM} [e] (Ga)	age [f] (Ma)	±2σ (Ma)	U-Pb [g] conc	Lu-Hf [h] seq
A108_seq4_26	0.0143	12	0.00060	4	1.46709	1.88633	7	0.281632	33	0.281609	4.2	1.2	2.18	2024	20	93	4
A112_seq4_26	0.0096	26	0.00034	9	1.46713	1.88647	8	0.280938	29	0.280922	-11.8	1.0	3.35	2388	12	92	4
A116_seq4_26	0.0710	118	0.00244	37	1.46716	1.88656	6	0.281643	34	0.281545	4.0	1.2	2.26	2115	15	94	4
A118_seq4_40	0.0299	24	0.00112	7	1.46719	1.88665	9	0.281608	28	0.281567	1.1	1.0	2.29	1953	44	91	4
A123_seq4_40	0.0200	17	0.00066	4	1.46725	1.88658	12	0.280744	53	0.280706	-4.8	1.9	3.48	3012	14	90	4
A125_seq4_40	0.0198	42	0.00058	12	1.46715	1.88663	7	0.281602	41	0.281580	2.6	1.5	2.24	2000	22	90	4
A138_seq4_26	0.0107	9	0.00036	2	1.46707	1.88647	5	0.281279	36	0.281265	-8.2	1.3	2.85	2017	20	99	4
A145_seq4_26	0.0008	1	0.00002	0	1.46722	1.88656	5	0.281008	41	0.281007	-15.0	1.4	3.31	2118	17	93	4
A155_seq4_26	0.0162	20	0.00051	5	1.46719	1.88670	6	0.281257	29	0.281238	-10.4	1.0	2.93	1962	21	99	4
A161_seq4_26	*0.0349*	*83*	*0.00119*	*27*	*1.46711*	*1.88621*	*7*	*0.282213*	*40*	*0.282203*	*-10.1*	*1.4*	*1.69*	*473*	*5*	*134*	4
A162_seq4_26	0.0020	3	0.00005	1	1.46714	1.88625	8	0.281081	31	0.281078	-8.1	1.1	3.08	2308	14	93	4
A163_seq4_26	0.0208	20	0.00072	6	1.46705	1.88635	6	0.281307	35	0.281279	-8.1	1.2	2.83	1999	14	102	4
A164_seq4_26	0.0210	17	0.00076	5	1.46709	1.88639	7	0.282178	30	0.282169	-7.1	1.1	1.68	658	4	99	4
A168_seq4_26	0.0252	21	0.00084	5	1.46713	1.88619	6	0.281044	38	0.281005	-6.4	1.4	3.14	2494	15	101	4
A175_seq4_26	0.0074	6	0.00024	1	1.46710	1.88645	7	0.281048	25	0.281037	-6.1	0.9	3.10	2457	14	95	4
A177_seq4_26	0.0166	13	0.00058	4	1.46719	1.88628	7	0.281127	31	0.281099	-1.0	1.1	2.92	2579	13	90	4

Quoted uncertainties (absolute) relate to the last quoted figure. The effect of the inter-element fractionation on Lu/Hf was estimated to be about 6 % or less based on analyses of the GJ-1 and Plesoviče zircon. Accuracy and reproducibility was checked by repeated analyses of reference zircon GJ-1 and Plesoviče (data given as mean with 2 standard deviation uncertainties).

[a] $^{176}Yb/^{177}Hf = (^{176}Yb/^{173}Yb)_{true} \times (^{173}Yb/^{177}Hf)_{meas} \times (M_{173(Yb)}/M_{177(Hf)})^{\beta(Hf)}$, $\beta(Hf) = \ln((^{179}Hf/^{177}Hf_{true})/(^{179}Hf/^{177}Hf_{measured})) / \ln(M_{179(Hf)}/M_{177(Hf)})$, M = mass of respective isotopes. The $^{176}Lu/^{177}Hf$ was calculated in a similar way using $^{175}Lu/^{177}Hf$ and β(Yb).

[b] Mean Hf signal in volts.

[c] Uncertainties are quadratic additions of the within-run precision and the daily reproducibility of the 40ppb-JMC475 solution. Uncertainties for the JMC475 quoted at 2SD (2 standard deviation).

[d] Initial $^{176}Hf/^{177}Hf$ and εHf calculated using the apparent U-Pb age determined by LA-ICP-MS dating (see column f), and the CHUR parameters: $^{176}Lu/^{177}Hf$ = 0.0336, and $^{176}Hf/^{177}Hf$ = 0.282785 (Bouvier et al. 2008).

[e] Two stage model age in Ga using measured $^{176}Lu/^{177}Lu$ of each spot (first stage = age of zircon), a value of 0.0113 for the average continental crust (second stage, values compiled from Rudnick and Gao (2003), and depleted mantle $^{176}Lu/^{177}Lu$ = 0.0379, and $^{176}Hf/^{177}Hf$ = 0.283164.

[f] Apparent U-Pb age determined by LA-ICP-MS.

[g] U-Pb age concordance (%).

[h] Sequence in which Lu-Hf analyses were performed. Standard analyses for each sequence are showed on Table 12.

Table S8

Lu, Yb and Hf LA-MC-ICPMS data of zircon cores from sample GCH-17

Grain	$^{176}Yb/^{177}Hf$ [a]	±2σ	$^{176}Lu/^{177}Hf$ [a]	±2σ	$^{178}Hf/^{177}Hf$	$^{180}Hf/^{177}Hf$	Sig_{Hf} [b] (V)	$^{176}Hf/^{177}Hf$	±2σ [c]	$^{176}Hf/^{177}Hf_{(t)}$ [d]	$\varepsilon Hf_{(t)}$ [d]	±2σ [c] (εHf)	T_{DM} [e] (Ga)	age [f] (Ma)	±2σ (Ma)	U-Pb [g] conc	Lu-Hf [h] seq
A346_seq3_40	0.0372	31	0.00113	7	1.46718	1.88674	13	0.282656	24	0.282644	7.4	0.8	0.79	555	7	100	3
A348_seq3_40	0.0238	29	0.00071	8	1.46719	1.88674	15	0.281077	25	0.281046	-9.9	0.9	3.16	2280	18	90	3
A349_seq3_40	0.0413	36	0.00140	10	1.46726	1.88697	11	0.282709	24	0.282695	8.7	0.9	0.70	531	7	102	3
A351_seq3_40	0.0075	6	0.00021	1	1.46717	1.88664	13	0.281349	22	0.281341	-8.5	0.8	2.76	1888	58	99	3
A352_seq3_40	0.0184	15	0.00055	3	1.46722	1.88674	17	0.281262	20	0.281243	-14.6	0.7	3.00	1772	16	99	3
A353_seq3_40	0.0061	5	0.00017	1	1.46715	1.88667	14	0.280962	21	0.280956	-18.4	0.7	3.44	2052	17	95	3
A354_seq3_40	0.0185	19	0.00060	5	1.46719	1.88671	15	0.282623	22	0.282617	5.9	0.8	0.86	530	7	93	3
A356_seq3_40	0.0260	25	0.00091	7	1.46718	1.88683	12	0.281584	28	0.281549	2.8	1.0	2.28	2056	23	95	3
A357_seq3_40	0.1435	116	0.00404	24	1.46724	1.88640	8	0.282603	23	0.282564	3.7	0.8	0.97	516	7	95	3
A358_seq3_40	0.0177	15	0.00054	3	1.46720	1.88675	11	0.281859	26	0.281842	3.1	0.9	1.90	1615	31	98	3
A359_seq3_26	0.0072	8	0.00026	2	1.46710	1.88644	7	0.282641	25	0.282639	6.1	0.9	0.82	506	9	91	3
A360_seq3_26	0.0165	13	0.00059	4	1.46715	1.88670	7	0.282260	28	0.282254	-6.1	1.0	1.55	567	8	94	3
A362_seq3_26	0.0198	18	0.00075	6	1.46716	1.88653	7	0.281789	27	0.281781	-23.3	1.0	2.47	549	7	98	3
A363_seq3_26	0.0337	38	0.00109	10	1.46713	1.88671	8	0.282347	37	0.282335	-2.9	1.3	1.39	585	8	98	3
A364_seq3_40	0.0209	17	0.00066	4	1.46719	1.88652	15	0.282513	25	0.282506	2.5	0.9	1.07	554	8	97	3
A365_seq3_40	0.0229	19	0.00065	4	1.46721	1.88675	18	0.280756	24	0.280721	-8.9	0.8	3.54	2817	10	100	3
A366_seq3_40	0.0200	18	0.00063	4	1.46718	1.88661	16	0.281927	25	0.281920	-18.9	0.9	2.21	524	7	100	3
A367_seq3_40	0.0198	17	0.00061	4	1.46720	1.88658	14	0.281573	26	0.281549	4.0	0.9	2.26	2107	15	96	3
A368_seq3_40	*0.0106*	*9*	*0.00034*	*2*	*1.46713*	*1.88649*	*14*	*0.282625*	*24*	*0.282622*	*5.9*	*0.8*	*0.85*	*525*	*8*	*70*	3
A369_seq3_26	0.0304	27	0.00104	7	1.46717	1.88609	5	0.282474	30	0.282460	4.5	1.1	1.09	714	10	99	3
A370_seq3_26	0.0191	17	0.00063	4	1.46714	1.88642	7	0.282575	28	0.282569	4.4	1.0	0.95	539	7	98	3
A371_seq3_40	0.0107	9	0.00035	2	1.46715	1.88659	16	0.282471	26	0.282468	0.2	0.9	1.16	511	7	93	3
A372_seq3_26	0.0234	23	0.00086	6	1.46711	1.88639	7	0.282381	30	0.282372	-2.1	1.0	1.32	562	7	91	3
A373_seq3_26	0.0162	13	0.00051	3	1.46704	1.88589	7	0.282593	39	0.282588	4.7	1.4	0.92	522	8	94	3
A374_seq3_26	0.0117	11	0.00034	3	1.46707	1.88616	8	0.281240	29	0.281227	-9.5	1.0	2.93	2019	18	96	3
A375_seq3_26	0.0159	13	0.00054	3	1.46711	1.88642	7	0.281777	24	0.281761	-1.5	0.9	2.10	1544	31	98	3
A377_seq3_26	0.0126	11	0.00040	3	1.46708	1.88647	7	0.281275	29	0.281260	-9.5	1.0	2.88	1970	19	98	3
A378_seq3_40	*0.0036*	*6*	*0.00009*	*2*	*1.46717*	*1.88663*	*19*	*0.280945*	*22*	*0.280942*	*-18.1*	*0.8*	*3.45*	*2087*	*24*	*66*	3
A379_seq3_40	0.0072	7	0.00020	2	1.46718	1.88674	16	0.281079	30	0.281070	-1.5	1.1	2.96	2603	18	97	3
A380_seq3_40	0.0213	19	0.00066	4	1.46723	1.88685	19	0.282670	26	0.282663	8.6	0.9	0.75	580	7	99	3
A382_seq3_40	*0.0176*	*14*	*0.00058*	*4*	*1.46714*	*1.88661*	*13*	*0.282320*	*22*	*0.282313*	*-3.2*	*0.8*	*1.42*	*606*	*24*	*67*	3
A389_seq3_26	0.0269	22	0.00085	5	1.46709	1.88623	7	0.282641	24	0.282633	6.4	0.8	0.83	527	7	90	3
A390_seq3_26	0.0438	46	0.00170	14	1.46709	1.88642	6	0.282467	40	0.282449	1.0	1.4	1.17	576	7	101	3
A391_seq3_26	*0.0169*	*17*	*0.00049*	*4*	*1.46711*	*1.88614*	*5*	*0.282277*	*30*	*0.282268*	*5.0*	*1.0*	*1.33*	*1037*	*118*	*86*	3
A392_seq3_26	0.0151	13	0.00049	3	1.46707	1.88627	9	0.282631	27	0.282626	6.2	0.9	0.84	532	7	97	3
A393_seq3_26	0.0856	72	0.00286	18	1.46711	1.88650	6	0.282669	27	0.282641	6.5	1.0	0.81	521	7	99	3
A394_seq3_26	0.0142	13	0.00048	3	1.46712	1.88646	7	0.282459	25	0.282454	0.9	0.9	1.16	565	9	101	3
A395_seq3_26	0.0897	83	0.00261	19	1.46716	1.88652	6	0.282689	44	0.282661	8.3	1.5	0.75	569	7	90	3
A397_seq3_26	0.0270	22	0.00090	6	1.46712	1.88619	5	0.282347	43	0.282338	-3.9	1.5	1.40	534	13	96	3
A398_seq3_26	0.0328	31	0.00108	8	1.46711	1.88608	7	0.282626	38	0.282616	5.6	1.3	0.87	518	6	102	3
A399_seq3_26	0.0162	17	0.00051	5	1.46714	1.88640	6	0.282679	28	0.282674	8.6	1.0	0.73	562	9	91	3
A400_seq3_26	0.0157	14	0.00050	4	1.46710	1.88632	7	0.282383	29	0.282379	-3.0	1.0	1.33	510	8	93	3
A401_seq3_26	*0.0101*	*9*	*0.00034*	*2*	*1.46695*	*1.88604*	*5*	*0.281116*	*38*	*0.281106*	*-24.4*	*1.3*	*3.36*	*1559*	*94*	*59*	3
A402_seq3_26	0.0194	18	0.00065	5	1.46709	1.88624	7	0.281869	34	0.281850	2.5	1.2	1.91	1581	74	98	3
A403_seq3_26	0.0184	17	0.00066	5	1.46711	1.88637	8	0.282448	30	0.282441	0.7	1.1	1.18	578	8	94	3
A405_seq3_26	*0.0119*	*10*	*0.00035*	*2*	*1.46713*	*1.88664*	*8*	*0.281127*	*43*	*0.281112*	*-9.8*	*1.5*	*3.08*	*2182*	*13*	*80*	3
A406_seq3_26	0.0149	14	0.00049	4	1.46715	1.88653	6	0.281140	37	0.281117	-3.3	1.3	2.94	2455	17	101	3
A407_seq3_26	0.0140	12	0.00044	3	1.46710	1.88639	13	0.282363	24	0.282359	-2.4	0.8	1.35	570	8	99	3
A408_seq3_26	0.0339	29	0.00122	8	1.46714	1.88638	7	0.282646	25	0.282634	6.7	0.9	0.82	542	8	91	3
A409_seq3_26	0.0790	143	0.00245	42	1.46700	1.88637	6	0.282394	49	0.282369	-2.5	1.7	1.33	550	7	93	3
A410_seq3_26	*0.0224*	*19*	*0.00071*	*5*	*1.46711*	*1.88644*	*7*	*0.282467*	*31*	*0.282459*	*1.7*	*1.1*	*1.14*	*594*	*8*	*79*	3
A520_seq2_26	0.0204	20	0.00076	6	1.46710	1.88645	6	0.282463	31	0.282454	1.9	1.1	1.14	611	9	97	2
A521_seq2_26	0.0219	18	0.00074	5	1.46704	1.88650	6	0.282200	27	0.282193	-9.3	1.0	1.69	525	8	99	2
A522_seq2_26	0.0125	18	0.00048	6	1.46709	1.88611	7	0.281030	45	0.281005	0.0	1.6	3.01	2764	22	99	2
A523_seq2_40	0.0500	42	0.00165	11	1.46711	1.88683	13	0.282356	26	0.282338	-2.8	0.9	1.38	582	8	90	2
A524_seq2_26	0.0201	30	0.00076	10	1.46720	1.88664	6	0.282312	34	0.282302	-1.5	1.2	1.40	699	10	99	2
A525_seq2_40	0.0286	23	0.00092	6	1.46720	1.88680	14	0.282000	20	0.281975	4.3	0.7	1.71	1465	23	98	2
A526_seq2_26	0.0340	31	0.00118	9	1.46711	1.88648	6	0.282496	32	0.282484	1.2	1.1	1.12	533	8	97	2
A528_seq2_40	0.0143	12	0.00047	3	1.46714	1.88680	17	0.282412	21	0.282407	0.0	0.7	1.24	598	9	91	2
A529_seq2_40	0.0185	15	0.00073	4	1.46718	1.88682	13	0.282020	20	0.282012	-15.2	0.7	2.03	544	8	96	2
A530_seq2_26	0.0207	37	0.00069	11	1.46719	1.88668	8	0.281608	35	0.281581	4.1	1.3	2.21	2061	16	98	2
A531_seq2_40	0.0901	74	0.00277	17	1.46719	1.88686	13	0.282173	25	0.282146	-11.0	0.9	1.78	519	7	96	2
A533_seq2_40	0.0135	11	0.00049	3	1.46719	1.88661	16	0.282423	19	0.282419	-1.5	0.7	1.25	513	8	99	2

Grain	$^{176}Yb/^{177}Hf$ [a]	±2σ	$^{176}Lu/^{177}Hf$ [a]	±2σ	$^{178}Hf/^{177}Hf$	$^{180}Hf/^{177}Hf$	Sig_{Hf} [b] (V)	$^{176}Hf/^{177}Hf$	±2σ [c]	$^{176}Hf/^{177}Hf_{(t)}$ [d]	$\varepsilon Hf_{(t)}$ [d]	±2σ [c] (εHf)	T_{DM} [e] (Ga)	age [f] (Ma)	±2σ (Ma)	U-Pb [g] conc	Lu-Hf [h] seq
A534_seq2_26	0.0198	17	0.00068	5	1.46712	1.88634	6	0.281607	35	0.281580	3.8	1.3	2.22	2050	39	94	2
A536_seq2_26	0.0248	22	0.00085	6	1.46707	1.88629	8	0.282182	35	0.282172	-7.5	1.2	1.68	635	10	96	2
A538_seq2_26	0.0301	25	0.00109	7	1.46712	1.88627	7	0.282196	72	0.282185	-9.3	2.5	1.70	537	8	101	2
A540_seq2_40	0.0469	45	0.00158	12	1.46716	1.88672	12	0.281741	22	0.281687	1.8	0.8	2.13	1801	21	93	2
A541_seq2_40	0.0195	23	0.00063	8	1.46712	1.88636	14	0.282573	45	0.282567	3.6	1.6	0.97	507	8	96	2
A542_seq2_40	0.0379	30	0.00122	7	1.46716	1.88675	13	0.282517	22	0.282505	2.3	0.8	1.07	549	8	100	2
A543_seq2_26	0.0483	42	0.00158	11	1.46700	1.88616	9	0.282335	37	0.282314	-0.8	1.3	1.37	713	19	108	2
A545_seq2_26	0.0776	66	0.00260	17	1.46713	1.88653	8	0.282410	32	0.282383	-1.5	1.1	1.30	571	8	92	2
A546_seq2_40	0.0387	39	0.00119	10	1.46717	1.88672	14	0.282599	20	0.282588	4.5	0.7	0.92	516	9	100	2
A547_seq2_40	0.0207	26	0.00072	7	1.46713	1.88670	14	0.281575	22	0.281547	2.1	0.8	2.30	2030	33	94	2
A548_seq2_40	0.0271	29	0.00086	8	1.46716	1.88664	14	0.281105	24	0.281061	0.0	0.8	2.94	2679	11	92	2
A554_seq2_26	0.0293	28	0.00106	8	1.46709	1.88622	8	0.281721	31	0.281710	-26.3	1.1	2.61	528	9	101	2
A555_seq2_26	*0.0256*	*21*	*0.00083*	*5*	*1.46702*	*1.88622*	*7*	*0.282557*	*28*	*0.282549*	*3.3*	*1.0*	*0.99*	*522*	*13*	*136*	2
A559_seq2_26	0.0151	13	0.00057	4	1.46715	1.88668	7	0.282657	27	0.282652	7.1	1.0	0.79	529	7	91	2
A560_seq2_26	0.0302	25	0.00112	7	1.46713	1.88642	7	0.282262	31	0.282247	-3.3	1.1	1.51	706	10	95	2
A561_seq2_40	0.0188	17	0.00066	5	1.46722	1.88681	15	0.282466	25	0.282459	0.7	0.9	1.16	548	8	100	2
A562_seq2_40	0.0243	29	0.00091	9	1.46712	1.88668	14	0.282311	20	0.282300	-2.7	0.7	1.43	649	10	99	2
A563_seq2_40	0.0272	24	0.00087	6	1.46712	1.88653	14	0.282677	21	0.282669	7.6	0.8	0.76	524	9	100	2
A564_seq2_40	0.0440	39	0.00138	10	1.46725	1.88683	11	0.282487	25	0.282472	2.3	0.9	1.11	601	9	98	2
A565_seq2_40	0.0280	22	0.00086	5	1.46722	1.88684	13	0.281092	28	0.281048	-0.8	1.0	2.98	2665	10	94	2
A566_seq2_40	0.0176	20	0.00052	5	1.46718	1.88697	16	0.281023	19	0.280997	-4.9	0.7	3.12	2567	26	99	2
A568_seq2_40	0.0113	18	0.00038	5	1.46717	1.88675	15	0.280898	30	0.280877	-0.8	1.1	3.19	2923	20	98	2
A570_seq2_40	0.0169	14	0.00066	4	1.46715	1.88647	16	0.282610	29	0.282604	5.1	1.0	0.89	516	11	101	2
A571_seq2_26	0.0242	20	0.00079	5	1.46716	1.88649	7	0.282006	37	0.281988	-0.9	1.3	1.80	1218	74	100	2
A572_seq2_40	0.0430	37	0.00138	10	1.46720	1.88692	9	0.282477	30	0.282460	3.5	1.1	1.10	673	18	97	2
A573_seq2_40	0.0165	15	0.00059	4	1.46724	1.88688	14	0.282682	18	0.282677	7.7	0.6	0.75	518	8	99	2
A574_seq2_26	0.0425	95	0.00144	31	1.46706	1.88669	6	0.281589	34	0.281532	2.7	1.2	2.30	2079	21	91	2
A575_seq2_26	0.0179	15	0.00058	4	1.46717	1.88642	8	0.282652	31	0.282646	7.1	1.1	0.80	536	8	101	2
A577_seq2_26	0.0304	24	0.00101	6	1.46717	1.88646	7	0.281159	30	0.281107	1.8	1.1	2.85	2686	13	92	2
A578_seq2_26	0.0074	15	0.00023	5	1.46708	1.88630	10	0.282080	34	0.282078	-11.7	1.2	1.88	597	9	95	2
A580_seq2_40	0.0149	12	0.00046	3	1.46714	1.88671	14	0.282091	21	0.282081	0.9	0.8	1.64	1152	34	96	2
A581_seq2_40	0.0511	43	0.00175	11	1.46716	1.88678	14	0.282631	24	0.282613	5.6	0.9	0.87	525	8	100	2
A584_seq2_40	0.0249	21	0.00070	5	1.46712	1.88634	17	0.282041	46	0.282025	0.3	1.6	1.73	1213	38	100	2
A585_seq2_40	0.0266	30	0.00081	8	1.46716	1.88670	18	0.282578	20	0.282570	4.5	0.7	0.94	542	8	94	2
A586_seq2_26	0.0279	27	0.00088	7	1.46717	1.88663	7	0.281047	25	0.281001	-1.9	0.9	3.06	2691	11	93	2
A587_seq2_26	0.0330	55	0.00116	17	1.46718	1.88669	9	0.281548	50	0.281504	0.7	1.8	2.38	2035	17	99	2
A588_seq2_26	0.0420	36	0.00143	10	1.46717	1.88680	16	0.282505	21	0.282491	1.4	0.7	1.11	530	7	95	2
A589_seq2_26	0.0187	23	0.00059	6	1.46717	1.88670	8	0.282652	35	0.282646	6.4	1.2	0.81	506	8	98	2
A590_seq2_26	0.0144	13	0.00056	4	1.46702	1.88627	6	0.281824	32	0.281819	-22.7	1.1	2.41	515	8	99	2
A591_seq2_26	0.0275	23	0.00098	6	1.46714	1.88612	8	0.282041	33	0.282032	-15.4	1.2	2.01	503	7	90	2
A592_seq2_26	0.0075	30	0.00022	9	1.46713	1.88667	8	0.281024	41	0.281014	-5.7	1.5	3.12	2506	14	93	2
A594_seq2_26	0.0137	16	0.00046	4	1.46720	1.88664	6	0.281081	26	0.281058	-1.9	0.9	2.99	2602	12	94	2
A595_seq2_26	0.0304	26	0.00097	6	1.46709	1.88663	6	0.281052	30	0.281003	-3.3	1.1	3.08	2627	12	91	2
A596_seq2_40	0.0104	18	0.00033	5	1.46727	1.88687	15	0.281098	25	0.281081	-0.8	0.9	2.94	2613	14	93	2
A597_seq2_40	0.0233	23	0.00077	6	1.46724	1.88705	12	0.282713	30	0.282706	8.8	1.1	0.69	520	8	96	2
A598_seq2_40	0.0235	20	0.00074	5	1.46719	1.88673	11	0.281440	24	0.281411	-2.7	0.8	2.56	2029	38	98	2

Quoted uncertainties (absolute) relate to the last quoted figure. The effect of the inter-element fractionation on Lu/Hf was estimated to be about 6 % or less based on analyses of the GJ-1 and Plesoviče zircon. Accuracy and reproducibility was checked by repeated analyses of reference zircon GJ-1 and Plesoviče (data given as mean with 2 standard deviation uncertainties).

(a) $^{176}Yb/^{177}Hf = (^{176}Yb/^{173}Yb)_{true} \times (^{173}Yb/^{177}Hf)_{meas} \times (M_{173(Yb)}/M_{177(Hf)})^{\beta(Hf)}$, $\beta(Hf) = \ln((^{179}Hf/^{177}Hf_{true})/(^{179}Hf/^{177}Hf_{measured})) / \ln(M_{179(Hf)}/M_{177(Hf)})$, M = mass of respective isotopes. The $^{176}Lu/^{177}Hf$ was calculated in a similar way using $^{175}Lu/^{177}Hf$ and β(Yb).

(b) Mean Hf signal in volts.

(c) Uncertainties are quadratic additions of the within-run precision and the daily reproducibility of the 40ppb-JMC475 solution. Uncertainties for the JMC475 quoted at 2SD (2 standard deviation).

(d) Initial $^{176}Hf/^{177}Hf$ and εHf calculated using the apparent U-Pb age determined by LA-ICP-MS dating (see column f), and the CHUR parameters: $^{176}Lu/^{177}Hf$ = 0.0336, and $^{176}Hf/^{177}Hf$ = 0.282785 (Bouvier et al. 2008).

(e) Two stage model age in Ga using measured $^{176}Lu/^{177}Lu$ of each spot (first stage = age of zircon), a value of 0.0113 for the average continental crust (second stage, values compiled from Rudnick and Gao (2003), and depleted mantle $^{176}Lu/^{177}Lu$ = 0.0379, and $^{176}Hf/^{177}Hf$ = 0.283164.

(f) Apparent U-Pb age determined by LA-ICP-MS.

(g) U-Pb age concordance (%).

(h) Sequence in which Lu-Hf analyses were performed. Standard analyses for each sequence are showed on Table 12.

Table S9

Lu, Yb and Hf LA-MC-ICPMS data of zircon cores from sample GCH-21

Grain	$^{176}Yb/^{177}Hf$ [a]	±2σ	$^{176}Lu/^{177}Hf$ [a]	±2σ	$^{178}Hf/^{177}Hf$	$^{180}Hf/^{177}Hf$	Sig_{Hf} [b] (V)	$^{176}Hf/^{177}Hf$	±2σ [c]	$^{176}Hf/^{177}Hf_{(t)}$ [d]	$\varepsilon Hf_{(t)}$ [d]	±2σ [c] (εHf)	T_{DM} [e] (Ga)	age [f] (Ma)	±2σ (Ma)	U-Pb [g] conc	Lu-Hf [n] seq
A18_seq5_40	0.0063	5	0.00021	1	1.46719	1.88689	11	0.282319	26	0.282317	-4.0	0.9	1.43	565	8	91	5
A20_seq5_40	0.0080	7	0.00024	2	1.46715	1.88663	14	0.281219	27	0.281211	-11.8	1.0	2.99	1946	16	93	5
A21_seq5_40	0.0109	9	0.00039	3	1.46717	1.88679	11	0.281544	26	0.281529	2.9	0.9	2.30	2092	34	100	5
A22_seq5_40	0.0262	21	0.00084	5	1.46719	1.88682	11	0.281631	28	0.281598	4.7	1.0	2.18	2062	20	100	5
A25_seq5_40	0.0350	28	0.00106	6	1.46719	1.88671	16	0.281140	22	0.281088	-1.0	0.8	2.93	2596	12	95	5
A26_seq5_40	0.0128	17	0.00038	4	1.46715	1.88669	11	0.281041	24	0.281022	-1.6	0.9	3.03	2672	13	99	5
A28_seq5_40	0.0143	30	0.00045	9	1.46713	1.88643	15	0.280986	26	0.280965	-9.4	0.9	3.25	2426	10	94	5
A30_seq5_40	0.0008	1	0.00002	0	1.46721	1.88674	15	0.281025	24	0.281024	-4.9	0.8	3.09	2528	11	96	5
A31_seq5_40	0.0214	19	0.00072	5	1.46720	1.88662	11	0.280940	30	0.280899	1.5	1.1	3.11	2988	19	99	5
A32_seq5_40	0.0182	15	0.00057	4	1.46720	1.88685	12	0.281071	25	0.281049	-14.8	0.9	3.25	2062	21	100	5
A38_seq5_40	0.0484	53	0.00128	12	1.46722	1.88684	9	0.281151	30	0.281085	1.4	1.1	2.88	2702	13	99	5
A39_seq5_40	0.0157	14	0.00049	3	1.46715	1.88681	11	0.281081	26	0.281056	-0.6	0.9	2.96	2663	16	99	5
A40_seq5_40	0.0171	14	0.00054	3	1.46720	1.88695	11	0.281590	31	0.281568	4.1	1.1	2.23	2081	29	101	5
A42_seq5_40	0.0092	7	0.00031	2	1.46713	1.88658	10	0.281589	30	0.281577	4.0	1.1	2.22	2066	21	99	5
A44_seq5_40	0.0249	21	0.00076	5	1.46713	1.88657	10	0.281055	24	0.281016	-2.0	0.9	3.04	2665	16	100	5
A45_seq5_40	0.0243	20	0.00075	5	1.46716	1.88661	14	0.281023	27	0.280984	-2.6	0.9	3.09	2688	12	95	5
A48_seq5_40	0.0499	49	0.00152	12	1.46722	1.88661	10	0.281547	29	0.281488	-0.3	1.0	2.42	2015	20	100	5
A49_seq5_26	0.0385	34	0.00122	9	1.46708	1.88659	5	0.281555	34	0.281508	0.2	1.2	2.38	2005	27	95	5
A50_seq5_40	0.0143	12	0.00045	3	1.46717	1.88664	10	0.281046	28	0.281024	-2.8	1.0	3.05	2619	18	97	5
A51_seq5_40	0.0104	9	0.00034	2	1.46716	1.88665	11	0.282522	26	0.282518	3.3	0.9	1.03	571	10	98	5
A52_seq5_40	0.0045	4	0.00010	1	1.46718	1.88689	15	0.281035	24	0.281029	-4.2	0.9	3.07	2548	18	96	5
A55_seq5_40	0.0095	8	0.00034	2	1.46718	1.88666	10	0.281484	27	0.281470	0.1	1.0	2.43	2060	43	95	5
A56_seq5_40	0.0280	23	0.00093	6	1.46723	1.88682	11	0.281608	24	0.281571	4.2	0.8	2.22	2084	28	98	5
A59_seq5_40	0.0242	24	0.00073	6	1.46717	1.88664	12	0.281060	24	0.281023	-3.0	0.9	3.05	2609	17	100	5
A60_seq5_40	0.0209	17	0.00065	4	1.46717	1.88664	12	0.281066	25	0.281035	-4.6	0.9	3.07	2524	15	97	5
A61_seq5_40	0.0141	11	0.00045	3	1.46715	1.88650	11	0.281839	21	0.281827	-2.9	0.8	2.04	1377	30	94	5
A62_seq5_40	0.0339	29	0.00102	7	1.46718	1.88664	15	0.281008	22	0.280963	-12.0	0.8	3.31	2316	14	98	5
A63_seq5_40	0.0083	7	0.00025	2	1.46718	1.88686	10	0.281577	29	0.281567	4.2	1.0	2.23	2088	26	92	5
A65_seq5_40	0.0017	1	0.00004	0	1.46723	1.88686	14	0.281562	23	0.281561	2.2	0.8	2.28	2013	18	100	5
A66_seq5_40	0.0221	20	0.00069	5	1.46719	1.88688	10	0.281062	31	0.281026	-0.3	1.1	2.99	2720	40	99	5
A72_seq5_40	0.0242	25	0.00072	6	1.46716	1.88676	10	0.281030	23	0.280994	-3.2	0.8	3.09	2644	10	98	5
A73_seq5_40	0.0098	8	0.00034	2	1.46716	1.88664	11	0.281566	28	0.281553	3.0	1.0	2.27	2060	20	100	5
A74_seq5_40	0.0164	14	0.00053	3	1.46715	1.88660	11	0.281080	25	0.281055	-4.6	0.9	3.05	2491	15	99	5
A75_seq5_40	0.0153	12	0.00050	3	1.46712	1.88651	10	0.281567	26	0.281547	3.2	0.9	2.27	2076	22	94	5
A76_seq5_40	0.0249	22	0.00075	5	1.46715	1.88677	13	0.281050	24	0.281013	-3.7	0.9	3.08	2595	19	96	5
A78_seq5_40	0.0089	7	0.00028	2	1.46718	1.88684	12	0.281054	25	0.281040	-2.2	0.9	3.01	2618	15	100	5
A79_seq5_40	0.0253	21	0.00076	5	1.46720	1.88677	14	0.281607	22	0.281599	-29.7	0.8	2.81	548	7	93	5
A81_seq5_40	0.0100	8	0.00031	2	1.46714	1.88663	12	0.281691	26	0.281688	-26.5	0.9	2.64	552	7	96	5
A82_seq5_40	0.0615	53	0.00193	13	1.46716	1.88658	14	0.281123	22	0.281023	-0.7	0.8	3.01	2706	11	97	5
A83_seq5_40	0.0186	15	0.00064	4	1.46719	1.88663	14	0.282114	21	0.282106	-8.8	0.8	1.79	679	10	109	5
A84_seq5_40	0.0239	25	0.00073	6	1.46717	1.88659	11	0.282485	22	0.282477	0.8	0.8	1.13	523	8	98	5
A85_seq5_40	0.0176	14	0.00053	3	1.46720	1.88673	11	0.282031	26	0.282019	-0.1	0.9	1.74	1203	28	98	5
A86_seq5_40	0.0219	19	0.00076	5	1.46718	1.88669	11	0.282677	28	0.282669	8.0	1.0	0.75	541	8	99	5
A87_seq5_40	0.0218	18	0.00065	4	1.46715	1.88665	11	0.281092	21	0.281058	0.6	0.8	2.93	2713	24	100	5
A89_seq5_40	0.0150	12	0.00046	3	1.46720	1.88663	9	0.281071	27	0.281048	-1.9	1.0	3.00	2619	16	99	5
A90_seq5_40	0.0097	8	0.00033	2	1.46717	1.88670	10	0.282530	28	0.282527	3.4	1.0	1.02	562	7	98	5
A91_seq5_26	0.0083	8	0.00028	2	1.46702	1.88613	7	0.281096	40	0.281082	-1.0	1.4	2.94	2605	18	97	5
A92_seq5_40	0.0084	7	0.00029	2	1.46717	1.88678	14	0.281566	21	0.281553	8.3	0.8	2.16	2285	18	93	5
A94_seq5_40	0.0092	8	0.00031	2	1.46706	1.88655	8	0.281011	33	0.280996	-5.5	1.2	3.14	2543	16	100	5
A96_seq5_40	0.0200	16	0.00066	4	1.46716	1.88678	16	0.281578	17	0.281552	2.4	0.6	2.28	2034	22	100	5
A97_seq5_40	0.0219	21	0.00066	5	1.46720	1.88682	15	0.281069	22	0.281036	-1.7	0.8	3.01	2644	11	98	5
A98_seq5_40	0.0195	17	0.00060	4	1.46713	1.88672	14	0.281551	23	0.281527	2.2	0.8	2.32	2063	22	100	5
A108_seq5_40	0.0129	11	0.00042	3	1.46720	1.88689	12	0.281783	19	0.281779	-24.4	0.7	2.49	502	8	91	5
A111_seq5_40	0.0215	18	0.00064	4	1.46720	1.88691	17	0.281087	20	0.281055	-1.3	0.7	2.98	2636	13	96	5
A112_seq5_40	0.0438	39	0.00162	12	1.46718	1.88673	11	0.282308	25	0.282292	-5.6	0.9	1.49	530	7	93	5
A113_seq5_40	0.0127	10	0.00044	3	1.46718	1.88677	14	0.281570	21	0.281553	3.3	0.8	2.27	2071	32	99	5
A114_seq5_26	0.0318	37	0.00100	10	1.46726	1.88670	6	0.281120	36	0.281067	2.9	1.3	2.88	2793	17	96	5
A115_seq5_40	0.0114	12	0.00041	3	1.46722	1.88691	15	0.281555	20	0.281539	4.0	0.7	2.27	2124	19	98	5
A116_seq5_40	0.0198	22	0.00069	6	1.46716	1.88670	15	0.281571	21	0.281544	3.0	0.7	2.28	2073	23	98	5
A117_seq5_40	0.0135	12	0.00038	3	1.46718	1.88689	15	0.281110	19	0.281092	-1.0	0.7	2.93	2590	17	98	5
A120_seq5_26	0.0239	27	0.00083	8	1.46710	1.88626	7	0.281567	31	0.281534	1.9	1.1	2.32	2041	19	100	5
A123_seq5_40	0.0244	23	0.00078	6	1.46717	1.88665	14	0.281615	22	0.281585	4.1	0.8	2.21	2056	23	100	5

Grain	$^{176}Yb/^{177}Hf$ [a]	±2σ	$^{176}Lu/^{177}Hf$ [a]	±2σ	$^{178}Hf/^{177}Hf$	$^{180}Hf/^{177}Hf$	Sig_{Hf} [b] (V)	$^{176}Hf/^{177}Hf$	±2σ [c]	$^{176}Hf/^{177}Hf_{(t)}$ [d]	$\varepsilon Hf_{(t)}$ [d]	±2σ [c] (εHf)	T_{DM} [e] (Ga)	age [f] (Ma)	±2σ (Ma)	U-Pb [g] conc	Lu-Hf [h] seq
A124_seq5_40	0.0071	6	0.00022	1	1.46711	1.88659	12	0.281111	20	0.281103	-17.8	0.7	3.24	1848	36	95	5
A125_seq5_40	0.0162	15	0.00059	5	1.46719	1.88686	13	0.281583	25	0.281560	4.2	0.9	2.24	2099	19	100	5
A126_seq5_40	0.0161	17	0.00050	4	1.46716	1.88691	12	0.281601	21	0.281582	4.1	0.7	2.21	2062	25	98	5
A127_seq5_40	0.0124	13	0.00043	4	1.46714	1.88667	14	0.280941	22	0.280916	2.2	0.8	3.08	2994	17	98	5
A133_seq5_40	0.0627	52	0.00181	12	1.46715	1.88666	11	0.281177	24	0.281084	1.2	0.9	2.89	2699	11	98	5
A135_seq5_40	0.0151	13	0.00048	3	1.46719	1.88705	14	0.281754	20	0.281749	-24.8	0.7	2.53	533	9	97	5
A136_seq5_40	0.0269	22	0.00087	5	1.46718	1.88669	12	0.281079	20	0.281033	-0.3	0.7	2.98	2709	10	98	5
A137_seq5_40	0.0190	15	0.00058	3	1.46722	1.88685	13	0.281587	19	0.281564	3.5	0.7	2.25	2061	19	97	5
A139_seq5_40	0.0176	15	0.00059	4	1.46723	1.88698	12	0.281092	23	0.281061	0.3	0.8	2.94	2694	15	99	5
A141_seq5_40	0.0038	3	0.00012	1	1.46718	1.88686	14	0.281017	20	0.281011	-3.1	0.7	3.07	2621	24	96	5
A142_seq5_40	0.0039	3	0.00013	1	1.46716	1.88690	15	0.281028	20	0.281021	-3.2	0.7	3.06	2605	16	90	5
A143_seq5_26	0.0084	7	0.00028	2	1.46718	1.88661	8	0.281041	32	0.281027	-2.2	1.1	3.03	2636	12	99	5
A144_seq5_40	0.0078	7	0.00030	2	1.46717	1.88672	19	0.281560	18	0.281548	3.2	0.6	2.27	2075	18	96	5
A145_seq5_40	0.0204	19	0.00066	5	1.46720	1.88672	13	0.281607	24	0.281581	4.9	0.8	2.20	2099	23	100	5
A153_seq5_40	0.0212	17	0.00074	5	1.46713	1.88648	8	0.281548	29	0.281519	2.5	1.0	2.32	2088	17	98	5
A154_seq5_26	0.0345	29	0.00120	8	1.46710	1.88662	7	0.282312	29	0.282296	-2.2	1.0	1.42	677	9	97	5
A155_seq5_26	0.0512	58	0.00183	18	1.46713	1.88652	6	0.281638	33	0.281566	3.8	1.2	2.24	2074	27	99	5
A156_seq5_26	0.0236	27	0.00077	7	1.46713	1.88661	6	0.281180	28	0.281142	1.0	1.0	2.82	2599	14	99	5
A158_seq5_26	0.0197	19	0.00069	5	1.46720	1.88659	6	0.281041	31	0.281006	-2.0	1.1	3.05	2679	16	95	5
A159_seq5_26	0.0086	20	0.00031	6	1.46708	1.88655	7	0.281439	27	0.281427	-0.9	1.0	2.51	2084	19	99	5
A160_seq5_40	0.0240	20	0.00077	5	1.46718	1.88671	12	0.282423	20	0.282414	-0.2	0.7	1.23	578	8	98	5
A161_seq5_40	0.0222	18	0.00069	4	1.46718	1.88685	11	0.281457	25	0.281432	-3.5	0.9	2.55	1963	20	99	5
A163_seq5_26	0.0225	24	0.00071	6	1.46719	1.88652	6	0.281119	32	0.281083	0.8	1.2	2.90	2680	18	100	5
A164_seq5_26	0.0198	20	0.00075	7	1.46709	1.88645	6	0.281842	24	0.281835	-21.7	0.8	2.37	536	7	99	5
A165_seq5_26	0.0240	20	0.00085	6	1.46715	1.88650	5	0.282488	33	0.282477	4.7	1.2	1.06	697	11	101	5
A166_seq5_40	0.0291	29	0.00093	7	1.46716	1.88677	13	0.282577	17	0.282567	4.9	0.6	0.94	563	8	100	5
A168_seq5_26	0.0301	28	0.00096	7	1.46721	1.88675	6	0.281076	36	0.281027	-0.9	1.3	3.01	2692	16	100	5
A169_seq5_26	0.0208	17	0.00071	5	1.46716	1.88651	6	0.281664	34	0.281636	6.7	1.2	2.09	2090	28	97	5
A170_seq5_26	0.0190	18	0.00059	5	1.46716	1.88648	7	0.281064	30	0.281035	-2.7	1.1	3.03	2606	13	100	5
A173_seq5_26	0.0079	15	0.00023	4	1.46713	1.88649	8	0.281573	26	0.281564	3.1	0.9	2.26	2046	15	100	5
A174_seq5_26	0.0192	17	0.00065	4	1.46714	1.88646	6	0.281622	31	0.281595	6.7	1.1	2.14	2156	25	99	5
A175_seq5_26	0.0028	2	0.00011	1	1.46712	1.88621	6	0.281031	29	0.281027	-16.3	1.0	3.31	2034	19	97	5
A177_seq5_26	0.0126	11	0.00043	3	1.46713	1.88664	7	0.281599	35	0.281582	4.4	1.3	2.21	2073	60	100	5
A181_seq5_26	0.0408	38	0.00134	10	1.46714	1.88647	5	0.282459	34	0.282444	0.8	1.2	1.18	577	10	104	5
A182_seq5_26	0.0175	15	0.00063	4	1.46715	1.88642	7	0.281628	27	0.281603	4.6	1.0	2.17	2052	27	97	5
A183_seq5_26	0.0171	19	0.00063	6	1.46709	1.88633	7	0.281592	27	0.281566	4.2	1.0	2.23	2092	34	97	5
A185_seq5_26	0.0182	15	0.00071	4	1.46709	1.88653	6	0.282377	29	0.282369	-2.1	1.0	1.33	564	8	99	5
A191_seq5_26	0.0470	52	0.00158	15	1.46723	1.88660	6	0.281700	39	0.281636	7.5	1.4	2.07	2127	13	98	5
A192_seq5_40	0.0194	19	0.00074	6	1.46720	1.88681	11	0.282620	19	0.282612	6.5	0.7	0.85	565	9	101	5
A199_seq5_26	0.0379	36	0.00129	10	1.46708	1.88642	6	0.282247	40	0.282228	-2.6	1.4	1.52	765	12	101	5
A200_seq5_26	0.0126	14	0.00051	4	1.46707	1.88655	5	0.281622	35	0.281602	5.4	1.3	2.16	2089	21	98	5
A202_seq5_26	0.0275	24	0.00101	7	1.46709	1.88647	5	0.281613	43	0.281574	3.2	1.5	2.24	2036	23	101	5
A203_seq5_26	0.0136	11	0.00056	3	1.46704	1.88630	5	0.282246	38	0.282241	-7.2	1.4	1.59	539	7	92	5

Quoted uncertainties (absolute) relate to the last quoted figure. The effect of the inter-element fractionation on Lu/Hf was estimated to be about 6 % or less based on analyses of the GJ-1 and Plesoviče zircon. Accuracy and reproducibility was checked by repeated analyses of reference zircon GJ-1 and Plesoviče (data given as mean with 2 standard deviation uncertainties).

(a) $^{176}Yb/^{177}Hf = (^{176}Yb/^{173}Yb)_{true} \times (^{173}Yb/^{177}Hf)_{meas} \times (M_{173(Yb)}/M_{177(Hf)})^{\beta(Hf)}$, $\beta(Hf) = \ln((^{179}Hf/^{177}Hf_{true})/(^{179}Hf/^{177}Hf_{measured})) / \ln(M_{179(Hf)}/M_{177(Hf)})$, M = mass of respective isotopes. The $^{176}Lu/^{177}Hf$ was calculated in a similar way using $^{175}Lu/^{177}Hf$ and β(Yb).

(b) Mean Hf signal in volts.

(c) Uncertainties are quadratic additions of the within-run precision and the daily reproducibility of the 40ppb-JMC475 solution. Uncertainties for the JMC475 quoted at 2SD (2 standard deviation).

(d) Initial $^{176}Hf/^{177}Hf$ and εHf calculated using the apparent U-Pb age determined by LA-ICP-MS dating (see column f), and the CHUR parameters: $^{176}Lu/^{177}Hf$ = 0.0336, and $^{176}Hf/^{177}Hf$ = 0.282785 (Bouvier et al. 2008).

(e) Two stage model age in Ga using measured $^{176}Lu/^{177}Lu$ of each spot (first stage = age of zircon), a value of 0.0113 for the average continental crust (second stage, values compiled from Rudnick and Gao (2003), and depleted mantle $^{176}Lu/^{177}Lu$ = 0.0379, and $^{176}Hf/^{177}Hf$ = 0.283164.

(f) Apparent U-Pb age determined by LA-ICP-MS.

(g) U-Pb age concordance (%).

(h) Sequence in which Lu-Hf analyses were performed. Standard analyses for each sequence are showed on Table 12.

Table S10

Lu, Yb and Hf LA-MC-ICPMS data of zircon cores from sample GCH-24

Grain	$^{176}Yb/^{177}Hf$ [a]	±2σ	$^{176}Lu/^{177}Hf$ [a]	±2σ	$^{178}Hf/^{177}Hf$	$^{180}Hf/^{177}Hf$	Sig_{Hf} [b] (V)	$^{176}Hf/^{177}Hf$	±2σ [c]	$^{176}Hf/^{177}Hf_{(t)}$ [d]	$\varepsilon Hf_{(t)}$ [d]	±2σ [c] (εHf)	T_{DM} [e] (Ga)	age [f] (Ma)	±2σ (Ma)	U-Pb [g] conc	Lu-Hf [n] seq
A208bis_seq5_40	0.0003	0	0.00001	0	1.46717	1.88673	14	0.281042	21	0.281041	-14.5	0.7	3.26	2090	39	99	5
A210_seq5_40	0.0099	8	0.00031	2	1.46722	1.88693	15	0.281069	19	0.281053	-0.8	0.7	2.97	2655	14	97	5
A214_seq5_40	0.0109	9	0.00034	2	1.46713	1.88676	13	0.282136	21	0.282128	6.4	0.7	1.48	1318	31	97	5
A215_seq5_40	0.0190	16	0.00059	4	1.46719	1.88690	11	0.281091	23	0.281061	1.2	0.8	2.92	2733	16	100	5
A218_seq5_40	0.0122	15	0.00040	4	1.46717	1.88687	11	0.281650	25	0.281634	7.3	0.9	2.08	2122	34	101	5
A219_seq5_40	0.0036	3	0.00011	1	1.46720	1.88689	17	0.282002	21	0.282000	-15.2	0.7	2.04	562	7	100	5
A221_seq5_40	0.0108	9	0.00037	2	1.46722	1.88694	14	0.282671	22	0.282667	8.1	0.8	0.75	547	8	97	5
A222_seq5_40	0.0163	13	0.00053	3	1.46721	1.88684	15	0.282121	23	0.282109	1.9	0.8	1.59	1152	20	101	5
A223_seq5_40	0.0199	16	0.00074	5	1.46715	1.88671	13	0.281637	21	0.281608	5.5	0.7	2.15	2084	20	100	5
A226_seq5_40	0.0355	64	0.00108	18	1.46720	1.88687	14	0.282226	28	0.282212	-4.7	1.0	1.58	697	9	100	5
A227_seq5_40	0.0201	16	0.00072	4	1.46722	1.88683	11	0.281594	20	0.281566	3.4	0.7	2.25	2054	25	97	5
A233_seq5_26	0.0367	49	0.00136	14	1.46714	1.88669	5	0.282347	35	0.282334	-4.2	1.2	1.41	530	12	94	5
A235_seq5_26	0.0190	16	0.00064	4	1.46717	1.88659	6	0.282160	34	0.282145	6.5	1.2	1.45	1295	24	98	5
A237_seq5_26	0.0177	17	0.00074	6	1.46718	1.88665	6	0.282257	29	0.282249	-6.1	1.0	1.56	576	8	100	5
A243_seq5_26	0.0357	35	0.00123	10	1.46717	1.88638	6	0.282266	24	0.282248	-1.9	0.8	1.48	763	9	96	5
A244_seq5_26	0.0318	42	0.00129	15	1.46717	1.88661	7	0.282534	31	0.282519	3.8	1.1	1.02	593	8	95	5
A245_seq5_26	0.0208	18	0.00072	5	1.46722	1.88658	7	0.282635	37	0.282628	6.2	1.3	0.84	526	7	98	5
A246_seq5_26	0.0179	15	0.00057	3	1.46723	1.88659	6	0.281983	28	0.281969	0.8	1.0	1.79	1320	43	99	5
A247_seq5_26	0.0267	36	0.00090	11	1.46715	1.88644	6	0.282386	30	0.282377	-1.7	1.1	1.31	569	9	96	5
A248_seq5_26	0.0245	29	0.00088	9	1.46716	1.88671	7	0.282392	24	0.282383	-1.7	0.8	1.30	562	7	97	5
A249_seq5_26	0.0103	9	0.00035	3	1.46707	1.88648	5	0.282531	35	0.282527	2.6	1.2	1.04	526	7	97	5
A250_seq5_26	0.0380	56	0.00122	17	1.46716	1.88649	4	0.281492	31	0.281444	-0.3	1.1	2.47	2081	32	100	5
A254_seq5_40	0.0126	10	0.00043	3	1.46717	1.88683	13	0.281571	25	0.281554	3.9	0.9	2.25	2095	21	97	5
A255_seq5_40	0.0184	15	0.00061	4	1.46712	1.88672	13	0.281261	40	0.281230	5.5	1.4	2.62	2657	17	103	5
A257_seq5_40	0.0128	12	0.00042	4	1.46718	1.88674	18	0.282154	26	0.282150	-9.5	0.9	1.75	580	9	100	5
A258_seq5_26	0.0259	28	0.00091	8	1.46709	1.88668	7	0.281619	29	0.281583	4.3	1.0	2.21	2070	21	99	5
A263_seq5_40	0.0241	22	0.00080	6	1.46719	1.88682	15	0.281100	34	0.281070	-16.5	1.2	3.26	1956	20	99	5
A264_seq5_40	0.0231	20	0.00075	5	1.46715	1.88691	11	0.281624	29	0.281597	0.4	1.0	2.27	1880	51	103	5
A265_seq5_40	0.0198	19	0.00066	5	1.46719	1.88693	13	0.282303	23	0.282295	-3.5	0.8	1.45	620	15	95	5
A266_seq5_40	0.0564	53	0.00203	16	1.46717	1.88668	11	0.282347	24	0.282325	-3.4	0.9	1.41	577	8	98	5
A267_seq5_40	0.0175	14	0.00057	3	1.46720	1.88675	15	0.282295	23	0.282289	-5.0	0.8	1.48	562	14	97	5
A268_seq5_40	0.0359	45	0.00125	12	1.46725	1.88692	13	0.281952	34	0.281940	-18.0	1.2	2.17	534	7	98	5
A269_seq5_40	0.0228	18	0.00075	5	1.46719	1.88699	13	0.282250	20	0.282236	2.8	0.7	1.41	991	13	99	5
A270_seq5_26	0.0274	30	0.00095	8	1.46716	1.88676	7	0.282312	32	0.282298	-0.6	1.1	1.39	744	25	99	5
A271_seq5_40	0.0308	25	0.00097	6	1.46725	1.88690	12	0.282238	32	0.282224	-2.5	1.1	1.52	775	11	103	5
A274_seq5_26	0.0313	34	0.00106	11	1.46709	1.88624	6	0.282248	40	0.282237	-7.0	1.4	1.59	557	7	99	5
A275_seq5_26	0.0250	27	0.00098	11	1.46714	1.88636	8	0.281685	29	0.281645	8.3	1.0	2.05	2148	19	100	5
A277_seq5_40	0.0260	21	0.00079	5	1.46719	1.88681	14	0.281475	24	0.281445	-2.9	0.8	2.52	1971	24	99	5
A278_seq5_26	0.0324	28	0.00103	7	1.46714	1.88657	8	0.281121	27	0.281121	-58.8	0.9	3.89	-	-	-	5
A280_seq5_26	0.0231	53	0.00076	16	1.46708	1.88620	9	0.282582	44	0.282575	4.3	1.5	0.94	524	7	93	5
A281_seq5_26	0.0294	25	0.00098	7	1.46720	1.88687	14	0.282594	22	0.282584	5.4	0.8	0.91	563	9	100	5
A282_seq5_26	0.0233	19	0.00075	5	1.46715	1.88651	7	0.282283	35	0.282275	-5.0	1.2	1.50	587	9	98	5
A288_seq5_26	0.0226	23	0.00076	7	1.46709	1.88656	5	0.282161	33	0.282154	-10.5	1.2	1.76	532	9	99	5
A289_seq5_40	0.0175	14	0.00058	4	1.46719	1.88671	14	0.281598	30	0.281576	3.2	1.1	2.24	2032	82	97	5
A290_seq5_40	0.0165	13	0.00061	4	1.46723	1.88712	14	0.281892	21	0.281874	2.0	0.7	1.88	1522	25	100	5
A292_seq5_40	0.0154	12	0.00054	3	1.46720	1.88661	10	0.282370	44	0.282363	-0.9	1.6	1.31	629	9	95	5
A293_seq5_26	0.0286	28	0.00104	8	1.46718	1.88645	5	0.282398	40	0.282387	-2.4	1.4	1.31	523	9	99	5
A294_seq5_26	0.0258	23	0.00096	6	1.46703	1.88644	7	0.281812	42	0.281802	-22.2	1.5	2.42	564	7	103	5
A295_seq5_26	0.0106	13	0.00033	4	1.46714	1.88633	6	0.281203	32	0.281191	-10.3	1.1	2.99	2038	18	97	5
A296_seq5_26	0.0384	48	0.00119	13	1.46719	1.88654	8	0.282248	31	0.282231	-2.1	1.1	1.51	782	11	99	5
A297_seq5_26	0.0196	17	0.00061	4	1.46710	1.88659	7	0.281546	31	0.281523	0.2	1.1	2.36	1982	30	99	5
A298_seq5_26	0.0276	23	0.00093	6	1.46711	1.88653	8	0.282578	45	0.282568	4.8	1.6	0.94	560	8	98	5
A299_seq5_26	0.0205	26	0.00077	9	1.46721	1.88648	5	0.281668	35	0.281637	6.9	1.3	2.09	2096	54	100	5
A300_seq5_40	0.0637	53	0.00196	12	1.46718	1.88689	12	0.281691	26	0.281613	5.4	0.9	2.15	2069	37	100	5
A301_seq5_26	0.0153	12	0.00052	3	1.46717	1.88663	8	0.281540	23	0.281520	2.7	0.8	2.32	2095	23	99	5
A304_seq5_40	0.0447	36	0.00148	9	1.46717	1.88692	11	0.281573	24	0.281516	0.9	0.9	2.36	2023	23	100	5
A305_seq5_40	0.0133	12	0.00045	3	1.46716	1.88658	12	0.281916	36	0.281910	-16.9	1.3	2.19	629	11	105	5
A309_seq5_26	0.0268	23	0.00091	6	1.46717	1.88659	7	0.282563	59	0.282553	4.8	2.1	0.96	581	8	92	5
A311_seq5_40	0.0510	43	0.00177	11	1.46721	1.88695	11	0.282500	23	0.282479	3.2	0.8	1.09	627	9	100	5
A313_seq5_40	0.0411	53	0.00137	16	1.46724	1.88706	15	0.282726	29	0.282712	9.5	1.0	0.66	543	7	95	5
A314_seq5_40	0.0241	21	0.00073	5	1.46717	1.88671	15	0.281035	22	0.280999	-4.9	0.8	3.12	2565	10	96	5
A315_seq5_40	0.0431	35	0.00137	8	1.46720	1.88681	11	0.282657	34	0.282642	8.3	1.2	0.78	600	9	97	5

Grain	$^{176}Yb/^{177}Hf$ [a]	±2σ	$^{176}Lu/^{177}Hf$ [a]	±2σ	$^{178}Hf/^{177}Hf$	$^{180}Hf/^{177}Hf$	Sig_{Hf} [b] (V)	$^{176}Hf/^{177}Hf$	±2σ[c]	$^{176}Hf/^{177}Hf_{(t)}$ [d]	$\varepsilon Hf_{(t)}$ [d]	±2σ [c] (εHf)	T_{DM} [e] (Ga)	age[f] (Ma)	±2σ (Ma)	U-Pb [g] conc	Lu-Hf [h] seq
A316_seq5_40	0.0127	12	0.00040	3	1.46720	1.88686	12	0.282017	24	0.282010	-5.5	0.8	1.86	978	12	102	5
A317_seq5_40	0.0160	13	0.00052	3	1.46719	1.88706	13	0.281551	25	0.281545	-31.7	0.9	2.92	548	8	102	5
A318_seq5_40	0.0140	11	0.00044	3	1.46719	1.88690	14	0.282060	24	0.282050	1.3	0.8	1.68	1215	30	99	5
A319_seq5_40	0.0262	37	0.00084	10	1.46724	1.88698	14	0.282658	24	0.282649	7.9	0.8	0.78	570	8	102	5
A322_seq5_26	0.0374	34	0.00127	9	1.46706	1.88641	7	0.281848	36	0.281811	-0.3	1.3	2.01	1518	28	97	5
A323_seq5_26	0.0638	80	0.00214	22	1.46713	1.88631	6	0.282455	33	0.282425	4.0	1.2	1.14	747	10	103	5
A324_seq5_26	0.0248	20	0.00093	7	1.46707	1.88652	8	0.282297	35	0.282288	-5.3	1.2	1.49	549	7	94	5
A326_seq5_40	0.0282	38	0.00098	12	1.46722	1.88674	13	0.282678	25	0.282669	7.3	0.9	0.76	510	7	96	5
A327_seq5_40	0.0397	33	0.00116	8	1.46715	1.88660	13	0.281664	41	0.281619	5.5	1.5	2.14	2064	79	104	5
A333_seq5_40	0.0195	16	0.00053	3	1.46713	1.88651	13	0.281913	23	0.281899	0.5	0.8	1.88	1418	33	105	5
A338_seq5_26	0.0246	25	0.00092	7	1.46719	1.88625	9	0.281687	70	0.281678	-26.9	2.5	2.66	551	7	98	5
A339_seq5_26	0.0403	36	0.00124	9	1.46713	1.88607	7	0.282308	29	0.282294	-3.8	1.0	1.46	606	9	102	5
A340_seq5_40	0.0254	28	0.00090	9	1.46716	1.88684	10	0.282690	20	0.282681	8.4	0.7	0.73	542	7	99	5
A341_seq5_40	0.0168	16	0.00053	4	1.46715	1.88658	14	0.282444	20	0.282438	0.9	0.7	1.18	591	9	98	5
A342_seq5_40	0.0056	4	0.00016	1	1.46719	1.88672	16	0.281167	23	0.281159	-2.3	0.8	2.87	2433	17	100	5
A344_seq5_40	0.0462	38	0.00142	9	1.46715	1.88660	17	0.282249	23	0.282231	-4.8	0.8	1.56	664	8	103	5
A345_seq5_26	0.0191	17	0.00061	4	1.46712	1.88685	5	0.281043	33	0.281012	-2.1	1.2	3.05	2666	11	100	5
A346_seq5_40	0.0618	57	0.00187	14	1.46724	1.88690	11	0.282315	27	0.282296	-5.3	1.0	1.48	540	7	101	5
A347_seq5_26	0.0246	22	0.00083	6	1.46715	1.88658	6	0.281611	30	0.281576	7.1	1.1	2.16	2200	31	100	5
A349_seq5_40	0.0257	23	0.00082	6	1.46715	1.88653	12	0.282690	25	0.282681	8.5	0.9	0.72	546	7	100	5
A351_seq5_40	0.0546	67	0.00201	21	1.46720	1.88664	10	0.281680	24	0.281607	1.2	0.9	2.24	1897	116	98	5
A353_seq5_40	0.0137	11	0.00043	3	1.46721	1.88674	14	0.281290	21	0.281275	-12.7	0.7	2.93	1805	22	95	5
A354_seq5_40	0.0276	30	0.00102	10	1.46719	1.88678	11	0.282410	21	0.282399	-1.0	0.7	1.27	568	20	107	5
A356_seq5_26	0.0211	19	0.00071	5	1.46718	1.88666	6	0.282387	35	0.282379	-0.7	1.2	1.29	613	8	97	5
A357_seq5_26	0.0095	10	0.00033	3	1.46710	1.88615	8	0.281866	37	0.281863	-20.3	1.3	2.31	555	7	98	5

Quoted uncertainties (absolute) relate to the last quoted figure. The effect of the inter-element fractionation on Lu/Hf was estimated to be about 6 % or less based on analyses of the GJ-1 and Plesoviče zircon. Accuracy and reproducibility was checked by repeated analyses of reference zircon GJ-1 and Plesoviče (data given as mean with 2 standard deviation uncertainties).

[a] $^{176}Yb/^{177}Hf = (^{176}Yb/^{173}Yb)_{true} \times (^{173}Yb/^{177}Hf)_{meas} \times (M_{173(Yb)}/M_{177(Hf)})^{\beta(Hf)}$, $\beta(Hf) = \ln((^{179}Hf/^{177}Hf_{true})/(^{179}Hf/^{177}Hf_{measured})) / \ln(M_{179(Hf)}/M_{177(Hf)})$, M = mass of respective isotopes. The $^{176}Lu/^{177}Hf$ was calculated in a similar way using $^{175}Lu/^{177}Hf$ and β(Yb).

[b] Mean Hf signal in volts.

[c] Uncertainties are quadratic additions of the within-run precision and the daily reproducibility of the 40ppb-JMC475 solution. Uncertainties for the JMC475 quoted at 2SD (2 standard deviation).

[d] Initial $^{176}Hf/^{177}Hf$ and εHf calculated using the apparent U-Pb age determined by LA-ICP-MS dating (see column f), and the CHUR parameters: $^{176}Lu/^{177}Hf$ = 0.0336, and $^{176}Hf/^{177}Hf$ = 0.282785 (Bouvier et al. 2008).

[e] Two stage model age in Ga using measured $^{176}Lu/^{177}Lu$ of each spot (first stage = age of zircon), a value of 0.0113 for the average continental crust (second stage, values compiled from Rudnick and Gao (2003), and depleted mantle $^{176}Lu/^{177}Lu$ = 0.0379, and $^{176}Hf/^{177}Hf$ = 0.283164.

[f] Apparent U-Pb age determined by LA-ICP-MS.

[g] U-Pb age concordance (%).

[h] Sequence in which Lu-Hf analyses were performed. Standard analyses for each sequence are showed on Table 12.

Table S11

Lu, Yb and Hf LA-MC-ICPMS data of standards

Grain	$^{176}Yb/^{177}Hf$ [a]	±2σ	$^{176}Lu/^{177}Hf$ [a]	±2σ	$^{178}Hf/^{177}Hf$	$^{180}Hf/^{177}Hf$	Sig_{Hf} [b] (V)	$^{176}Hf/^{177}Hf$	±2σ [c]	$^{176}Hf/^{177}Hf_{(t)}$ [d]	$\varepsilon Hf_{(t)}$ [d]	±2σ [c] (εHf)	T_{DM} [e] (Ga)	age [f] (Ma)
01-Nov														
GJ1-40-1	0.0072	6	0.00025	1	1.46721	1.88688	10	0.282009	25	0.282006	-14.0	0.9	2.01	606
GJ1-40-2	0.0072	6	0.00025	1	1.46721	1.88693	11	0.282019	25	0.282016	-13.7	0.9	2.00	606
GJ1-40-3	0.0077	6	0.00024	1	1.46716	1.88669	11	0.281993	24	0.281990	-14.6	0.9	2.05	606
GJ1-40-4	0.0082	7	0.00025	1	1.46712	1.88657	12	0.281987	24	0.281984	-14.8	0.9	2.06	606
GJ1-40-5	0.0069	6	0.00023	1	1.46715	1.88661	9	0.282025	21	0.282022	-13.5	0.8	1.98	606
GJ1-40-6	0.0069	6	0.00024	1	1.46717	1.88678	10	0.282027	27	0.282025	-13.4	0.9	1.98	606
GJ1-40-7	0.0072	6	0.00025	1	1.46714	1.88673	8	0.282026	27	0.282024	-13.4	1.0	1.98	606
GJ1-40-8	0.0073	6	0.00025	1	1.46708	1.88645	9	0.282011	31	0.282008	-14.0	1.1	2.01	606
GJ1-40-9	0.0076	6	0.00025	1	1.46719	1.88679	9	0.282016	27	0.282013	-13.8	1.0	2.00	606
GJ1-40-10	0.0078	6	0.00025	1	1.46722	1.88672	9	0.282029	24	0.282026	-13.3	0.9	1.98	606
02-Nov														
GJ1_40_90_1	0.0070	6	0.00024	1	1.46721	1.88677	8	0.281996	24	0.281993	-14.5	0.8	2.04	606
GJ1_40_90_2	0.0075	6	0.00025	2	1.46701	1.88634	5	0.281981	45	0.281978	-15.0	1.6	2.07	606
GJ1_40_90_3	0.0074	6	0.00025	1	1.46707	1.88663	8	0.282015	26	0.282013	-13.8	0.9	2.00	606
GJ1_40_90_4	0.0072	6	0.00025	2	1.46717	1.88679	8	0.282032	29	0.282029	-13.2	1.0	1.97	606
GJ1_40_90_5	0.0078	6	0.00025	1	1.46720	1.88687	9	0.282002	30	0.281999	-14.3	1.1	2.03	606
GJ1_40_90_6	0.0068	5	0.00023	1	1.46709	1.88668	8	0.282026	26	0.282024	-13.4	0.9	1.98	606
GJ1_40_90_7	0.0069	6	0.00023	1	1.46720	1.88676	9	0.282026	24	0.282023	-13.4	0.8	1.98	606
GJ1_40_90_8	0.0076	6	0.00025	1	1.46723	1.88678	9	0.282011	29	0.282008	-14.0	1.0	2.01	606
GJ1_40_90_9	0.0073	6	0.00023	1	1.46716	1.88667	9	0.282022	25	0.282019	-13.6	0.9	1.99	606
GJ1_40_90_10	0.0073	6	0.00024	1	1.46715	1.88667	9	0.282018	26	0.282016	-13.7	0.9	2.00	606
GJ1_40_90_11	0.0071	6	0.00023	1	1.46716	1.88667	9	0.282015	25	0.282012	-13.8	0.9	2.00	606
05-Nov														
GJ1_6_100_100_line	0.0071	6	0.00025	2	1.46722	1.88687	14	0.282013	19	0.282010	-13.9	0.7	2.01	606
GJ1_6_100_100_line_2	0.0074	6	0.00025	1	1.46719	1.88687	16	0.281986	17	0.281983	-14.9	0.6	2.06	606
GJ1_40-5-90_1	0.0076	6	0.00026	2	1.46713	1.88657	10	0.281987	26	0.281984	-14.8	0.9	2.06	606
GJ1_40-5-90_2	0.0074	6	0.00026	2	1.46721	1.88668	10	0.282002	21	0.281999	-14.3	0.8	2.03	606
GJ1_40-5-90_3	0.0073	6	0.00025	2	1.46711	1.88662	7	0.282022	38	0.282020	-13.6	1.4	1.99	606
GJ1_40-5-90_4	0.0072	6	0.00025	2	1.46718	1.88674	8	0.282017	31	0.282014	-13.8	1.1	2.00	606
GJ1_40-5-90_5	0.0078	6	0.00025	2	1.46717	1.88661	10	0.282012	23	0.282009	-13.9	0.8	2.01	606
GJ1_40-5-90_6	0.0075	6	0.00025	2	1.46721	1.88663	9	0.282028	26	0.282025	-13.4	0.9	1.98	606
GJ1_40-5-90_7	0.0079	6	0.00025	2	1.46722	1.88673	10	0.282029	25	0.282026	-13.3	0.9	1.98	606
GJ1_40-5-90_8	0.0079	6	0.00025	1	1.46713	1.88669	10	0.281998	23	0.281995	-14.4	0.8	2.04	606
GJ1_40-5-90_9	0.0074	6	0.00025	2	1.46717	1.88678	8	0.282018	29	0.282016	-13.7	1.0	2.00	606
GJ1_40-5-90_10	0.0079	6	0.00025	1	1.46722	1.88674	9	0.282001	36	0.281998	-14.3	1.3	2.03	606
GJ1_40-5-90_11	0.0078	6	0.00025	1	1.46718	1.88662	9	0.282038	31	0.282035	-13.0	1.1	1.96	606
GJ1_40-5-90_12	0.0080	7	0.00024	1	1.46717	1.88656	11	0.282003	34	0.282001	-14.2	1.2	2.02	606
GJ1_40-5-90_13	0.0079	6	0.00024	1	1.46722	1.88686	10	0.282020	27	0.282017	-13.6	1.0	1.99	606
06-Nov														
GJ1_5_100_100_1	0.0082	7	0.00025	1	1.46715	1.88689	13	0.281995	22	0.281992	-14.6	0.8	2.04	606
GJ1_40-5-90_1	0.0077	6	0.00024	1	1.46715	1.88662	11	0.281997	24	0.281995	-14.4	0.9	2.04	606
GJ1_40-5-90_2	0.0074	6	0.00025	2	1.46722	1.88665	7	0.282028	32	0.282025	-13.4	1.1	1.98	606
GJ1_40-5-90_3	0.0073	6	0.00025	2	1.46724	1.88682	8	0.282012	29	0.282009	-13.9	1.0	2.01	606
GJ1_40-5-90_4	0.0076	6	0.00025	2	1.46717	1.88683	9	0.282019	27	0.282016	-13.7	0.9	2.00	606
GJ1_40-5-90_5	0.0074	6	0.00025	2	1.46719	1.88676	9	0.282028	23	0.282025	-13.4	0.8	1.98	606
GJ1_40-5-90_7	0.0073	6	0.00025	1	1.46720	1.88672	10	0.282021	25	0.282018	-13.6	0.9	1.99	606
GJ1_40-5-90_8	0.0072	6	0.00025	1	1.46718	1.88671	10	0.281988	22	0.281985	-14.8	0.8	2.05	606
GJ1_40-5-90_9	0.0070	6	0.00024	1	1.46716	1.88658	9	0.282009	37	0.282006	-14.0	1.3	2.01	606
GJ1_40-5-90_10	0.0069	6	0.00024	1	1.46717	1.88662	10	0.282016	29	0.282013	-13.8	1.0	2.00	606
GJ1_40-5-90_11	0.0071	6	0.00024	1	1.46720	1.88679	11	0.282026	25	0.282023	-13.4	0.9	1.98	606
GJ1_40-5-90_12	0.0069	6	0.00023	1	1.46721	1.88694	11	0.282034	26	0.282031	-13.1	0.9	1.97	606
GJ1_40-5-90_13	0.0066	5	0.00023	1	1.46721	1.88653	10	0.282028	23	0.282025	-13.4	0.8	1.98	606
GJ1_40-5-90_14	0.0067	5	0.00023	1	1.46715	1.88662	10	0.282024	28	0.282022	-13.5	1.0	1.98	606
GJ1_40-5-90_15	0.0070	6	0.00023	1	1.46712	1.88666	10	0.282014	26	0.282012	-13.8	0.9	2.00	606
GJ1_40-5-90_16	0.0072	6	0.00024	1	1.46724	1.88673	10	0.282028	22	0.282025	-13.4	0.8	1.98	606

Grain	$^{176}Yb/^{177}Hf$ [a]	±2σ	$^{176}Lu/^{177}Hf$ [a]	±2σ	$^{178}Hf/^{177}Hf$	$^{180}Hf/^{177}Hf$	Sig_{Hf} [b] (V)	$^{176}Hf/^{177}Hf$	±2σ [c]	$^{176}Hf/^{177}Hf_{(t)}$ [d]	$\varepsilon Hf_{(t)}$ [d]	±2σ [c] (εHf)	T_{DM} [e] (Ga)	age [f] (Ma)
GJ1_40-5-90_17	0.0072	6	0.00024	1	1.46713	1.88660	10	0.282011	20	0.282009	-14.0	0.7	2.01	606
GJ1_40-5-90_18	0.0074	6	0.00025	1	1.46722	1.88679	10	0.282035	23	0.282032	-13.1	0.8	1.96	606
GJ1_40-5-90_19	0.0076	6	0.00025	1	1.46721	1.88666	10	0.282020	24	0.282017	-13.7	0.8	1.99	606
GJ1_40-5-90_20	0.0076	6	0.00025	1	1.46715	1.88665	10	0.282030	23	0.282027	-13.3	0.8	1.97	606
GJ1_40-5-90_21	0.0075	6	0.00025	1	1.46720	1.88667	10	0.282025	21	0.282022	-13.5	0.7	1.98	606
GJ1_40-5-90_22	0.0075	6	0.00025	1	1.46718	1.88660	10	0.282010	33	0.282008	-14.0	1.2	2.01	606
GJ1_40-5-90_23	0.0075	6	0.00025	1	1.46718	1.88676	11	0.282000	21	0.281997	-14.4	0.7	2.03	606
07-Nov														
GJ1-100-100-5_1	0.0084	7	0.00026	2	1.46717	1.88687	14	0.282012	23	0.282009	-13.9	0.8	2.01	606
GJ1-100-100-5_2	0.0080	7	0.00026	2	1.46718	1.88658	11	0.281993	19	0.281990	-14.6	0.7	2.05	606
GJ1-100-100-5_3	0.0074	6	0.00023	1	1.46725	1.88637	9	0.282029	24	0.282026	-13.3	0.9	1.98	606
GJ1-100-100-5_4	0.0072	6	0.00026	2	1.46721	1.88655	4	0.282028	55	0.282025	-13.4	1.9	1.98	606
GJ1-100-90-5_10	0.0065	5	0.00023	1	1.46718	1.88650	10	0.282031	24	0.282028	-13.3	0.9	1.97	606
GJ1-100-90-5_11	0.0071	6	0.00024	1	1.46715	1.88673	11	0.282001	21	0.281998	-14.3	0.8	2.03	606
GJ1-100-90-5_12	0.0076	6	0.00025	1	1.46718	1.88676	10	0.282010	20	0.282008	-14.0	0.7	2.01	606
GJ1-100-90-5_13	0.0075	6	0.00025	1	1.46722	1.88665	10	0.282003	22	0.282000	-14.3	0.8	2.03	606
GJ1-100-90-5_14	0.0076	6	0.00025	1	1.46715	1.88665	10	0.282012	27	0.282009	-13.9	1.0	2.01	606
GJ1-100-90-5_15	0.0075	6	0.00025	1	1.46720	1.88661	10	0.282020	25	0.282017	-13.6	0.9	1.99	606
GJ1-100-90-5_16	0.0073	6	0.00025	1	1.46720	1.88677	9	0.282008	25	0.282005	-14.1	0.9	2.02	606
GJ1-100-90-5_17	0.0074	6	0.00025	1	1.46713	1.88660	10	0.282003	26	0.282001	-14.2	0.9	2.02	606
GJ1-100-90-5_18	0.0076	6	0.00025	1	1.46725	1.88679	10	0.282017	21	0.282015	-13.7	0.7	2.00	606
GJ1-100-90-5_19	0.0076	6	0.00025	1	1.46720	1.88680	10	0.282016	23	0.282013	-13.8	0.8	2.00	606
GJ1-100-90-5_20	0.0069	6	0.00025	1	1.46718	1.88655	10	0.282002	22	0.282000	-14.3	0.8	2.03	606
GJ1-100-90-5_21	0.0070	6	0.00025	1	1.46717	1.88648	10	0.282010	23	0.282007	-14.0	0.8	2.01	606
GJ1-100-90-5_22	0.0068	5	0.00025	1	1.46725	1.88674	9	0.282024	22	0.282021	-13.5	0.8	1.99	606
GJ1-100-90-5_23	0.0068	5	0.00024	1	1.46715	1.88669	10	0.282013	24	0.282010	-13.9	0.9	2.01	606
GJ1-100-90-5_24	0.0066	5	0.00024	1	1.46724	1.88660	10	0.282015	29	0.282012	-13.8	1.0	2.00	606
GJ1-100-90-5_25	0.0068	5	0.00024	1	1.46717	1.88655	11	0.281996	19	0.281993	-14.5	0.7	2.04	606
GJ1-100-90-5_26	0.0074	6	0.00025	1	1.46719	1.88650	10	0.282015	23	0.282012	-13.8	0.8	2.00	606
GJ1-100-90-5_5	0.0080	7	0.00025	1	1.46713	1.88661	11	0.282021	23	0.282018	-13.6	0.8	1.99	606
GJ1-100-90-5_6	0.0076	6	0.00025	2	1.46716	1.88663	10	0.282016	27	0.282013	-13.8	1.0	2.00	606
GJ1-100-90-5_7	0.0070	6	0.00025	2	1.46719	1.88652	8	0.281997	23	0.281994	-14.5	0.8	2.04	606
GJ1-100-90-5_8	0.0077	6	0.00025	2	1.46716	1.88656	10	0.282016	21	0.282013	-13.8	0.7	2.00	606
GJ1-100-90-5_9	0.0079	6	0.00025	2	1.46721	1.88651	10	0.282003	23	0.282000	-14.3	0.8	2.03	606
Mean	0.0074	8	0.00025	2	1.46718	1.88668	10	0.282014	26	0.282011	-13.9	0.9	2.00	
85														
01-Nov														
Plesovice 26_2	0.0050	4	0.00012	1	1.46710	1.88640	7	0.282457	24	0.282456	-4.1	0.9	1.25	338
Plesovice 32_1	0.0042	3	0.00010	1	1.46721	1.88669	13	0.282461	23	0.282460	-4.0	0.8	1.24	338
Plesovice 40_6	0.0061	5	0.00014	1	1.46720	1.88676	16	0.282469	26	0.282468	-3.7	0.9	1.23	338
Plesovice 40_7	0.0062	5	0.00014	1	1.46715	1.88667	16	0.282462	18	0.282461	-3.9	0.6	1.24	338
Plesovice 40_8	0.0062	5	0.00013	1	1.46716	1.88672	15	0.282444	20	0.282443	-4.6	0.7	1.28	338
Plesovice 40_9	0.0061	5	0.00013	1	1.46714	1.88675	14	0.282449	23	0.282448	-4.4	0.8	1.27	338
Plesovice 40_10	0.0077	6	0.00017	1	1.46712	1.88652	13	0.282454	22	0.282453	-4.2	0.8	1.26	338
Plesovice 48_4	0.0064	5	0.00015	1	1.46718	1.88682	26	0.282465	15	0.282464	-3.8	0.5	1.24	338
Plesovice 48_5	0.0065	5	0.00015	1	1.46717	1.88682	26	0.282455	17	0.282454	-4.2	0.6	1.26	338
02-Nov														
Plesovice_40_90_1	0.0073	6	0.00017	1	1.46716	1.88668	13	0.282478	20	0.282477	-3.4	0.7	1.21	338
Plesovice_40_90_2	0.0076	6	0.00017	1	1.46720	1.88659	12	0.282456	22	0.282455	-4.2	0.8	1.25	338
Plesovice_40_90_3	0.0035	3	0.00008	0	1.46718	1.88672	12	0.282464	23	0.282463	-3.9	0.8	1.24	338
Plesovice_40_90_4	0.0059	5	0.00014	1	1.46718	1.88675	13	0.282460	17	0.282459	-4.0	0.6	1.25	338
Plesovice_40_90_5	0.0053	4	0.00013	1	1.46721	1.88667	12	0.282450	21	0.282449	-4.4	0.8	1.26	338
05-Nov														
Plesovice_40-5-90_1	0.0037	3	0.00008	1	1.46718	1.88673	15	0.282470	23	0.282469	-3.6	0.8	1.23	338
Plesovice_40-5-90_2	0.0046	4	0.00011	1	1.46717	1.88670	11	0.282452	31	0.282452	-4.3	1.1	1.26	338

Grain	$^{176}Yb/^{177}Hf$ [a]	±2σ	$^{176}Lu/^{177}Hf$ [a]	±2σ	$^{178}Hf/^{177}Hf$	$^{180}Hf/^{177}Hf$	Sig_{Hf} [b] (V)	$^{176}Hf/^{177}Hf$	±2σ [c]	$^{176}Hf/^{177}Hf_{(t)}$ [d]	$\varepsilon Hf_{(t)}$	±2σ [c] (εHf)	T_{DM} [e] (Ga)	age [f] (Ma)
Plesovice_40-5-90_3	0.0060	5	0.00015	1	1.46725	1.88682	14	0.282463	28	0.282462	-3.9	1.0	1.24	338
Plesovice_40-5-90_4	0.0035	3	0.00008	0	1.46713	1.88687	14	0.282466	24	0.282465	-3.8	0.9	1.23	338
Plesovice_40-5-90_5	0.0025	2	0.00006	0	1.46723	1.88694	14	0.282480	25	0.282480	-3.3	0.9	1.20	338
Plesovice_40-5-90_6	0.0057	5	0.00013	1	1.46727	1.88698	13	0.282515	29	0.282514	-2.1	1.0	1.14	338
Plesovice_40-5-90_7	0.0038	3	0.00009	1	1.46717	1.88670	13	0.282442	22	0.282441	-4.6	0.8	1.28	338
06-Nov														
Plesovice_40-5-90_1	0.0055	4	0.00012	1	1.46719	1.88672	13	0.282471	23	0.282470	-3.6	0.8	1.22	338
Plesovice_40-5-90_2	0.0035	3	0.00008	0	1.46718	1.88697	11	0.282463	34	0.282462	-3.9	1.2	1.24	338
Plesovice_40-5-90_3	0.0079	6	0.00017	1	1.46718	1.88674	14	0.282446	20	0.282445	-4.5	0.7	1.27	338
Plesovice_40-5-90_4	0.0126	10	0.00029	2	1.46719	1.88684	12	0.282460	27	0.282458	-4.1	0.9	1.25	338
Plesovice_40-5-90_5	0.0056	5	0.00013	1	1.46724	1.88698	13	0.282482	32	0.282481	-3.2	1.1	1.20	338
Plesovice_40-5-90_6	0.0047	4	0.00011	1	1.46721	1.88689	13	0.282477	28	0.282477	-3.4	1.0	1.21	338
Plesovice_40-5-90_7	0.0025	2	0.00006	0	1.46716	1.88683	15	0.282448	46	0.282448	-4.4	1.6	1.27	338
Plesovice_40-5-90_7bis	0.0063	5	0.00014	1	1.46724	1.88692	13	0.282481	23	0.282480	-3.3	0.8	1.20	338
Plesovice_40-5-90_8	0.0052	4	0.00012	1	1.46721	1.88677	13	0.282478	22	0.282478	-3.4	0.8	1.21	338
Plesovice_40-5-90_9	0.0049	4	0.00011	1	1.46721	1.88679	13	0.282490	27	0.282489	-2.9	1.0	1.19	338
Plesovice_40-5-90_10	0.0031	3	0.00007	0	1.46716	1.88673	14	0.282472	24	0.282472	-3.5	0.8	1.22	338
Plesovice_40-5-90_11	0.0079	6	0.00018	1	1.46721	1.88693	13	0.282497	26	0.282496	-2.7	0.9	1.17	338
07-Nov														
Plesovice-100-100-5_1	0.0034	3	0.00008	0	1.46717	1.88671	15	0.282465	22	0.282465	-3.8	0.8	1.23	338
Plesovice-100-90-5_2	0.0049	4	0.00012	1	1.46719	1.88685	14	0.282469	17	0.282468	-3.7	0.6	1.23	338
Plesovice-100-90-5_3	0.0036	3	0.00008	1	1.46716	1.88672	13	0.282468	22	0.282467	-3.7	0.8	1.23	338
Plesovice-100-90-5_4	0.0039	3	0.00009	1	1.46720	1.88670	15	0.282455	20	0.282454	-4.2	0.7	1.25	338
Plesovice-100-90-5_5	0.0051	4	0.00012	1	1.46724	1.88685	13	0.282481	26	0.282480	-3.3	0.9	1.20	338
Plesovice-100-90-5_6	0.0055	4	0.00013	1	1.46717	1.88679	13	0.282459	23	0.282458	-4.0	0.8	1.25	338
Plesovice-100-90-5_7	0.0053	4	0.00013	1	1.46724	1.88680	13	0.282493	20	0.282493	-2.8	0.7	1.18	338
Plesovice-100-90-5_8	0.0059	5	0.00014	1	1.46717	1.88676	14	0.282456	25	0.282455	-4.1	0.9	1.25	338
Mean	0.0054	37	0.00012	8	1.46719	1.88677	14	0.282466	31	0.282466	-3.8	1.1	1.23	
41														

Quoted uncertainties (absolute) relate to the last quoted figure. The effect of the inter-element fractionation on Lu/Hf was estimated to be about 6 % or less based on analyses of the GJ-1 and Plesoviče zircon. Accuracy and reproducibility was checked by repeated analyses of reference zircon GJ-1 and Plesoviče (data given as mean with 2 standard deviation uncertainties).

(a) $^{176}Yb/^{177}Hf = (^{176}Yb/^{173}Yb)_{true} \times (^{173}Yb/^{177}Hf)_{meas} \times (M_{173(Yb)}/M_{177(Hf)})^{\beta(Hf)}$, $\beta(Hf) = \ln((^{179}Hf/^{177}Hf_{true})/(^{179}Hf/^{177}Hf_{measured})) / \ln(M_{179(Hf)}/M_{177(Hf)})$, M = mass of respective isotopes. The $^{176}Lu/^{177}Hf$ was calculated in a similar way using $^{175}Lu/^{177}Hf$ and β(Yb).

(b) Mean Hf signal in volts.

(c) Uncertainties are quadratic additions of the within-run precision and the daily reproducibility of the 40ppb-JMC475 solution. Uncertainties for the JMC475 quoted at 2SD (2 standard deviation).

(d) Initial $^{176}Hf/^{177}Hf$ and εHf calculated using the apparent U-Pb age determined by LA-ICP-MS dating (see column f), and the CHUR parameters: $^{176}Lu/^{177}Hf = 0.0336$, and $^{176}Hf/^{177}Hf = 0.282785$ (Bouvier et al. 2008).

(e) Two stage model age in Ga using measured $^{176}Lu/^{177}Lu$ of each spot (first stage = age of zircon), a value of 0.0113 for the average continental crust (second stage, values compiled from Rudnick and Gao (2003), and depleted mantle $^{176}Lu/^{177}Lu = 0.0379$, and $^{176}Hf/^{177}Hf = 0.283164$.

(f) Apparent U-Pb age determined by LA-ICP-MS.

Appx.4
Data tables for chapter 7
Tables Ig1-U—Ig13-U
Tables Ig1-Hf—Ig13-Hf

Table Ig1-U

U, Th and Pb LA-ICP-MS data of zircon crystals from sample GCH-25

Grain	^{207}Pb[a] (cps)	U[b] (ppm)	Pb[b] (ppm)	Th[b] / U	$^{206}Pb_c$[c] (%)	$^{207}Pb/^{235}U$[d]	±2σ (%)	$^{206}Pb/^{238}U$[d]	±2σ (%)	ρ[e] (rho)	$^{207}Pb/^{206}Pb$[d]	±2σ (%)	$^{206}Pb/^{238}U$[f]	±2σ (Ma)	$^{207}Pb/^{235}U$[f]	±2σ (Ma)	$^{207}Pb/^{206}Pb$[f]	±2σ (Ma)	Conc.[g] (%)
A168	5252	230	13	0.00	0.3	0.4564	2.6	0.0602	1.5	0.56	0.0550	2.2	377	5	382	8	412	49	92
A170	2570	98	6	0.01	1.1	0.4604	4.4	0.0609	1.6	0.37	0.0548	4.1	381	6	385	14	404	92	94
A142	3001	129	7	0.00	0.3	0.4643	3.2	0.0610	1.5	0.46	0.0553	2.8	381	5	387	10	422	62	90
A132	1875	79	4	0.00	0.2	0.4626	3.6	0.0611	1.6	0.43	0.0550	3.3	382	6	386	12	411	74	93
A140	1694	59	3	0.01	1.6	0.4612	5.0	0.0611	1.6	0.31	0.0547	4.8	383	6	385	16	400	108	96
A163	2588	110	6	0.00	0.4	0.4651	4.0	0.0612	1.6	0.41	0.0551	3.6	383	6	388	13	416	81	92
A179	2130	75	4	0.01	1.0	0.4671	3.6	0.0615	1.7	0.46	0.0551	3.2	385	6	389	12	416	71	92
A186	3788	159	9	0.00	0.2	0.4688	2.7	0.0616	1.5	0.54	0.0552	2.3	386	6	390	9	419	51	92
A171	2811	122	7	0.00	0.2	0.4684	3.6	0.0617	1.6	0.46	0.0550	3.2	386	6	390	12	414	71	93
A143	2817	134	8	0.00	0.1	0.4690	3.7	0.0618	1.5	0.41	0.0551	3.4	386	6	391	12	414	75	93
A164	489	15	1	0.01	1.8	0.4719	7.4	0.0618	2.3	0.31	0.0554	7.1	387	9	392	25	427	158	90
A181	2517	104	6	0.00	0.4	0.4724	3.7	0.0619	1.5	0.42	0.0554	3.3	387	6	393	12	427	74	91
A172	3572	152	9	0.00	0.3	0.4733	4.4	0.0619	1.5	0.34	0.0554	4.1	387	6	393	14	430	92	90
A173	3028	140	7	0.00	0.0	0.4729	3.2	0.0620	1.5	0.47	0.0553	2.8	388	6	393	10	426	63	91
A165	2506	93	5	0.02	0.9	0.4715	4.5	0.0622	1.7	0.37	0.0550	4.2	389	6	392	15	410	94	95
A145	3203	134	8	0.00	0.2	0.4756	3.0	0.0623	1.6	0.51	0.0554	2.6	389	6	395	10	428	58	91
A151	2902	116	7	0.00	0.4	0.4735	5.5	0.0624	2.1	0.37	0.0551	5.1	390	8	394	18	415	114	94
A187	2154	92	5	0.00	0.6	0.4735	7.1	0.0626	1.7	0.24	0.0549	6.9	391	7	394	23	407	154	96
A160	17139	143	13	0.00	25.2	0.4798	12.1	0.0630	3.0	0.25	0.0552	11.8	394	12	398	41	422	262	93
A144	3221	132	8	0.00	0.1	0.4806	3.5	0.0630	1.6	0.46	0.0553	3.1	394	6	398	11	425	68	93
A159	2700	117	7	0.00	0.2	0.4793	3.0	0.0630	1.6	0.54	0.0552	2.5	394	6	398	10	418	57	94
A134	3903	96	6	0.00	5.6	0.4817	6.8	0.0633	1.8	0.26	0.0552	6.6	396	7	399	23	420	148	94
A195	3185	137	8	0.00	0.2	0.4828	3.4	0.0633	1.5	0.44	0.0553	3.0	396	6	400	11	424	68	93
A183	3666	153	9	0.00	0.7	0.4805	6.0	0.0634	1.5	0.25	0.0550	5.8	396	6	398	20	412	131	96
A155	3055	109	7	0.06	1.4	0.4822	8.1	0.0638	1.7	0.21	0.0549	8.0	398	6	400	27	407	178	98
A141	12911	515	31	0.05	0.7	0.4860	2.9	0.0645	1.6	0.57	0.0546	2.4	403	6	402	10	398	53	101
A169	3173	112	9	0.65	0.0	0.6165	2.7	0.0772	1.5	0.56	0.0579	2.2	479	7	488	10	527	49	91
A156	8931	302	22	0.09	0.6	0.6047	2.5	0.0774	1.4	0.57	0.0566	2.1	481	7	480	10	478	46	101
A167	14848	421	33	0.21	0.8	0.6262	3.7	0.0790	1.5	0.40	0.0575	3.4	490	7	494	14	510	74	96
A184	6330	214	18	0.67	0.0	0.6405	3.7	0.0802	1.5	0.39	0.0579	3.4	497	7	503	15	527	74	94
A182	5216	155	15	0.96	0.6	0.6638	3.9	0.0833	1.6	0.42	0.0578	3.5	516	8	517	16	521	77	99
A185	6308	185	16	0.43	1.1	0.6908	5.2	0.0856	1.6	0.30	0.0585	5.0	530	8	533	22	548	109	97
A180	6458	211	20	0.89	0.0	0.7056	2.2	0.0857	1.4	0.65	0.0597	1.7	530	7	542	9	592	37	90
A174	101181	68	56	0.01	42.2	4.0180	14.4	0.2832	11.0	0.76	0.1029	9.3	1608	158	1638	124	1677	172	96
A176	48910	100	51	0.76	0.4	10.1800	2.0	0.4309	1.7	0.83	0.1713	1.1	2310	32	2451	19	2571	19	90
A152	*4093*	*87*	*8*	*0.64*	*0.7*	*0.8955*	*6.9*	*0.0699*	*1.7*	*0.25*	*0.0929*	*6.6*	*436*	*7*	*649*	*34*	*1485*	*126*	*29*
A177	*3151*	*126*	*8*	*0.03*	*0.4*	*0.5564*	*4.0*	*0.0706*	*1.6*	*0.41*	*0.0572*	*3.6*	*440*	*7*	*449*	*15*	*497*	*80*	*88*
A133	*21890*	*83*	*15*	*0.42*	*1.8*	*3.6570*	*5.5*	*0.0730*	*3.7*	*0.68*	*0.3635*	*4.0*	*454*	*16*	*1562*	*45*	*3764*	*61*	*12*
A135	*2111*	*35*	*3*	*0.25*	*10.6*	*0.5947*	*12.8*	*0.0736*	*2.5*	*0.20*	*0.0586*	*12.6*	*458*	*11*	*474*	*50*	*551*	*275*	*83*
A136	*1219*	*53*	*4*	*0.00*	*0.2*	*0.5930*	*13.7*	*0.0738*	*2.7*	*0.20*	*0.0583*	*13.5*	*459*	*12*	*473*	*53*	*541*	*294*	*85*
A188	*3618*	*112*	*9*	*0.59*	*0.1*	*0.6852*	*3.6*	*0.0752*	*1.5*	*0.42*	*0.0661*	*3.3*	*468*	*7*	*530*	*15*	*808*	*69*	*58*
A137	*3171*	*98*	*7*	*0.33*	*b.d.*	*0.6475*	*4.0*	*0.0754*	*1.6*	*0.40*	*0.0623*	*3.7*	*468*	*7*	*507*	*16*	*685*	*79*	*68*
A153	*4556*	*163*	*12*	*0.06*	*0.7*	*0.6303*	*3.4*	*0.0754*	*1.4*	*0.43*	*0.0607*	*3.0*	*468*	*7*	*496*	*13*	*627*	*65*	*75*
A139	*7620*	*249*	*19*	*0.31*	*1.6*	*0.6345*	*3.6*	*0.0762*	*1.5*	*0.41*	*0.0604*	*3.3*	*473*	*7*	*499*	*14*	*618*	*71*	*77*
A162	*6771*	*216*	*17*	*0.59*	*0.0*	*0.6499*	*2.5*	*0.0765*	*1.5*	*0.61*	*0.0616*	*2.0*	*475*	*7*	*508*	*10*	*660*	*42*	*72*
A161	*3736*	*112*	*9*	*0.62*	*0.1*	*0.7140*	*3.2*	*0.0778*	*1.5*	*0.47*	*0.0666*	*2.9*	*483*	*7*	*547*	*14*	*824*	*60*	*59*
A157	*3242*	*104*	*9*	*0.51*	*0.1*	*0.6810*	*3.0*	*0.0785*	*1.6*	*0.51*	*0.0629*	*2.6*	*487*	*7*	*527*	*13*	*705*	*56*	*69*
A178	*3316*	*104*	*9*	*0.60*	*b.d.*	*0.6705*	*3.8*	*0.0797*	*1.5*	*0.40*	*0.0610*	*3.5*	*494*	*7*	*521*	*16*	*640*	*76*	*77*
A138	*2612*	*79*	*7*	*0.45*	*b.d.*	*0.6948*	*2.9*	*0.0812*	*1.6*	*0.56*	*0.0621*	*2.4*	*503*	*8*	*536*	*12*	*677*	*51*	*74*
A154	*2739*	*62*	*6*	*0.54*	*0.9*	*0.8165*	*7.0*	*0.0817*	*1.6*	*0.23*	*0.0725*	*6.8*	*506*	*8*	*606*	*32*	*999*	*138*	*51*
A158	*11321*	*44*	*12*	*0.53*	*b.d.*	*4.2470*	*2.7*	*0.2388*	*1.8*	*0.68*	*0.1290*	*2.0*	*1380*	*23*	*1683*	*22*	*2084*	*35*	*66*
A175	*35258*	*66*	*33*	*0.92*	*0.6*	*10.010*	*2.4*	*0.4251*	*1.9*	*0.80*	*0.1707*	*1.5*	*2283*	*37*	*2435*	*23*	*2565*	*24*	*89*
A166	*620657*	*64*	*435*	*0.02*	*89.2*	*266.60*	*13.6*	*2.3090*	*9.3*	*0.68*	*0.8372*	*10.0*	*7714*	*433*	*5675*	*148*	*4986*	*142*	*155*

Grain	^{207}Pb[a] (cps)	U[b] (ppm)	Pb[b] (ppm)	Th[b] U	^{206}Pbc[c] (%)	^{207}Pb[d] / ^{235}U	±2σ (%)	^{206}Pb[d] / ^{238}U	±2σ (%)	ρ[e] (rho)	^{207}Pb[d] / ^{206}Pb	±2σ (%)	^{206}Pb[f] / ^{238}U	±2σ (Ma)	^{207}Pb[f] / ^{235}U	±2σ (Ma)	^{207}Pb[f] / ^{206}Pb	±2σ (Ma)	Conc.[g] (%)
91500[h]	14383	68	13	0.47	0.4	0.1781	3.4	1.8782	14.1	0.08	14.5260	0.6	1057	33	1072	98	1101	325	99
BB-16[h]	11251	302	28	0.40	0.0	0.0912	2.7	0.7668	3.3	0.06	1.5659	0.7	563	14	578	15	638	34	88
Plesovice[h]	17536	3943	198	0.20	3.0	0.0530	7.3	0.2289	70.7	0.03	65.9345	0.2	333	24	207	136			
GJ-1[h]	11801	290	26	0.02	0.4	0.0984	1.3	0.8153	2.3	0.06	1.4809	0.5	605	8	605	11			

$^{206}Pb/^{238}U$ error is the quadratic additions of the within run precision (2 SE) and the external reproducibility (2 SD) of the reference zircon. $^{207}Pb/^{206}Pb$ error propagation (^{207}Pb signal dependent) following Gerdes & Zeh (2009). $^{207}Pb/^{235}U$ error is the quadratic addition of the $^{207}Pb/^{206}Pb$ and $^{206}Pb/^{238}U$ uncertainty.

[a] Within run background-corrected mean ^{207}Pb signal in cps (counts per second).

[b] U and Pb content and Th/U ratio were calculated relative to GJ-1 reference zircon.

[c] Percentage of the common Pb on the ^{206}Pb. b.d. = below detection limit.

[d] Pb/U and Pb/Pb ratios. Corrected for background, within-run Pb/U fractionation (in case of $^{206}Pb/^{238}U$) and common Pb using Stacy and Kramers (1975) model Pb composition and subsequently normalised to GJ-1 (ID-TIMS value/measured value); $^{207}Pb/^{235}U$ calculated using (($^{207}Pb/^{206}Pb$)*($^{238}U/^{206}Pb$)*137.88).

[e] Rho (ρ) is the ($^{206}Pb/^{238}U$)/($^{207}Pb/^{235}U$) error correlation coefficient.

[f] Pb/U and Pb/Pb ages.

[g] Degree of concordance = (($^{206}Pb/^{238}U$ age)/($^{207}Pb/^{206}Pb$ age)) x 100.

[h] Mean of 9 (91500), 9 (BB-16), 9 (Plesovice), and 18 (GJ-1) analyses, respectively.

Table Ig2-U

U, Th and Pb LA-ICP-MS data of zircon crystals from sample GCH-26

Grain	^{207}Pb[a] (cps)	U[b] (ppm)	Pb[b] (ppm)	Th[b]/U	^{206}Pbc[c] (%)	^{207}Pb[d]/^{235}U	±2σ (%)	^{206}Pb[d]/^{238}U	±2σ (%)	ρ[e] (rho)	^{207}Pb[d]/^{206}Pb	±2σ (%)	^{206}Pb[f]/^{238}U	±2σ (Ma)	^{207}Pb[f]/^{235}U	±2σ (Ma)	^{207}Pb[f]/^{206}Pb	±2σ (Ma)	Conc.[g] (%)
A30	3078	96	6	0.03	2.2	0.4581	6.5	0.0605	1.8	0.27	0.0549	6.2	379	6	383	21	408	139	93
A25	5685	482	27	0.00	0.9	0.4560	4.7	0.0606	1.7	0.35	0.0546	4.4	379	6	382	15	397	98	95
A51	1592	70	4	0.03	7.3	0.4568	10.4	0.0606	2.2	0.21	0.0547	10.1	379	8	382	34	399	227	95
A21	439	33	2	0.01	0.8	0.4564	14.1	0.0606	5.5	0.39	0.0546	13.0	379	20	382	46	397	290	96
A57	1238	47	3	0.01	0.9	0.4660	4.9	0.0617	2.0	0.40	0.0548	4.5	386	7	388	16	405	101	95
A07	2756	113	6	0.01	0.5	0.4678	4.0	0.0619	1.7	0.42	0.0549	3.6	387	6	390	13	406	80	95
A15	1727	64	4	0.01	0.8	0.4673	4.5	0.0619	1.7	0.39	0.0547	4.2	387	7	389	15	401	93	97
A16	979	45	3	0.01	0.4	0.4692	7.9	0.0621	1.7	0.22	0.0548	7.7	388	6	391	26	404	172	96
A17	3215	138	8	0.00	1.2	0.4779	6.5	0.0626	2.3	0.35	0.0554	6.1	391	9	397	22	429	137	91
A24	933	40	2	0.01	0.5	0.4696	5.0	0.0626	2.0	0.41	0.0544	4.6	391	8	391	16	389	102	100
A56	1036	40	2	0.01	0.7	0.4763	5.1	0.0626	1.7	0.32	0.0552	4.9	392	6	396	17	419	109	93
A22	3335	123	7	0.01	1.5	0.4787	7.6	0.0629	1.7	0.22	0.0552	7.4	393	6	397	25	421	166	93
A10	997	40	2	0.02	0.7	0.4843	6.0	0.0632	1.6	0.26	0.0556	5.8	395	6	401	20	436	129	91
A20	3701	149	9	0.01	0.8	0.4891	5.1	0.0641	1.7	0.34	0.0554	4.8	400	7	404	17	426	107	94
A28	24426	2074	121	0.00	0.1	0.4857	2.3	0.0643	1.4	0.63	0.0548	1.8	402	6	402	8	404	40	100
A06	1273	20	1	0.01	1.5	0.4840	9.0	0.0645	2.3	0.25	0.0544	8.7	403	9	401	30	389	195	104
A60	24423	330	28	0.80	0.0	0.6102	1.8	0.0766	1.5	0.80	0.0578	1.1	476	7	484	7	522	24	91
A19	24815	717	56	0.48	0.7	0.5904	2.9	0.0769	1.5	0.52	0.0557	2.5	478	7	471	11	440	56	109
A27	9092	604	48	0.51	0.6	0.6079	4.9	0.0770	1.6	0.32	0.0572	4.7	478	7	482	19	501	103	96
A41	28013	361	33	0.65	0.3	0.6316	2.1	0.0801	1.4	0.70	0.0572	1.5	497	7	497	8	498	33	100
A46	17849	205	17	0.56	1.0	0.6330	3.8	0.0808	1.5	0.40	0.0568	3.5	501	7	498	15	485	77	103
A58	28601	284	31	0.61	12.9	0.6498	10.5	0.0813	2.0	0.19	0.0580	10.3	504	10	508	43	530	226	95
A55	8875	276	23	0.36	0.1	0.6640	2.9	0.0818	1.4	0.50	0.0588	2.5	507	7	517	12	561	54	90
A39	11620	371	31	0.45	0.0	0.6688	2.3	0.0822	1.5	0.64	0.0590	1.8	509	7	520	9	568	39	90
A59	2593	76	7	0.92	0.2	0.6669	3.5	0.0822	1.6	0.44	0.0588	3.2	509	8	519	15	560	69	91
A32	7163	230	20	0.53	0.0	0.6731	2.4	0.0828	1.5	0.64	0.0589	1.8	513	7	523	10	565	40	91
A11	13322	885	74	0.40	0.2	0.6676	2.6	0.0837	1.5	0.58	0.0579	2.1	518	7	519	10	525	46	99
A09	14105	156	14	0.50	1.9	0.6703	4.6	0.0847	1.6	0.34	0.0574	4.3	524	8	521	19	506	94	104
A23	9860	613	55	0.53	0.6	0.6950	3.5	0.0859	1.7	0.48	0.0587	3.0	531	9	536	15	555	66	96
A49	2248	94	9	0.15	1.7	0.7913	7.6	0.0950	2.6	0.34	0.0604	7.2	585	14	592	35	618	155	95
A48	5045	148	14	0.47	0.0	0.7964	2.7	0.0951	1.5	0.57	0.0608	2.2	585	9	595	12	631	48	93
A14	2701	27	3	0.44	0.2	0.8968	4.0	0.1041	1.9	0.46	0.0625	3.6	639	11	650	20	690	76	93
A12	*12566*	*491*	*12*	*0.42*	*6.0*	*0.1543*	*12.6*	*0.0204*	*6.5*	*0.51*	*0.0548*	*10.8*	*130*	*8*	*146*	*17*	*405*	*242*	*32*
A26	*678*	*11*	*2*	*0.04*	*14.5*	*0.5500*	*27.6*	*0.0585*	*26.6*	*0.97*	*0.0682*	*7.2*	*366*	*96*	*445*	*105*	*874*	*149*	*42*
A13	*508*	*4*	*0*	*0.05*	*9.7*	*0.0593*	*4.6*	*0.3818*	*17.4*	*0.05*	*16.781*	*0.3*	*371*	*17*	*328*	*50*	*33*	*402*	*1133*
A47	*1283*	*8*	*1*	*0.06*	*11.9*	*0.4691*	*18.4*	*0.0594*	*4.9*	*0.27*	*0.0573*	*17.8*	*372*	*18*	*391*	*62*	*502*	*391*	*74*
A43	*4051*	*130*	*9*	*0.01*	*7.1*	*0.4900*	*9.7*	*0.0597*	*4.6*	*0.48*	*0.0596*	*8.5*	*374*	*17*	*405*	*33*	*588*	*185*	*64*
A50	*4141*	*294*	*19*	*0.12*	*0.1*	*0.5839*	*2.8*	*0.0665*	*1.7*	*0.61*	*0.0637*	*2.2*	*415*	*7*	*467*	*11*	*733*	*47*	*57*
A42	*2117*	*147*	*9*	*0.01*	*0.6*	*0.5200*	*3.8*	*0.0669*	*1.7*	*0.45*	*0.0564*	*3.4*	*417*	*7*	*425*	*13*	*467*	*76*	*89*
A31	*1468*	*30*	*2*	*0.01*	*6.6*	*0.5293*	*12.9*	*0.0669*	*2.3*	*0.18*	*0.0574*	*12.7*	*418*	*9*	*431*	*46*	*506*	*278*	*83*
A40	*383*	*4*	*0*	*0.05*	*2.7*	*0.5645*	*22.8*	*0.0678*	*7.5*	*0.33*	*0.0604*	*21.5*	*423*	*31*	*454*	*87*	*618*	*464*	*68*
A18	*1759*	*52*	*3*	*0.04*	*1.2*	*0.6040*	*15.7*	*0.0684*	*2.9*	*0.18*	*0.0641*	*15.4*	*426*	*12*	*480*	*62*	*745*	*326*	*57*
A45	*18552*	*1243*	*81*	*0.03*	*0.2*	*0.5918*	*3.2*	*0.0693*	*2.3*	*0.71*	*0.0620*	*2.3*	*432*	*9*	*472*	*12*	*673*	*48*	*64*
A54	*9377*	*647*	*45*	*0.46*	*1.0*	*0.6006*	*3.6*	*0.0703*	*1.8*	*0.51*	*0.0619*	*3.1*	*438*	*8*	*478*	*14*	*672*	*65*	*65*
A08	*1446*	*57*	*4*	*0.01*	*0.6*	*0.0713*	*1.7*	*0.5695*	*4.5*	*0.06*	*4.1588*	*0.4*	*444*	*7*	*458*	*17*	*529*	*91*	*84*
A44	*11717*	*758*	*53*	*0.40*	*0.0*	*0.5952*	*2.1*	*0.0722*	*1.7*	*0.81*	*0.0598*	*1.2*	*450*	*7*	*474*	*8*	*595*	*27*	*76*
A52	*15971*	*958*	*79*	*0.57*	*1.2*	*0.6205*	*3.8*	*0.0763*	*1.6*	*0.41*	*0.0590*	*3.5*	*474*	*7*	*490*	*15*	*566*	*76*	*84*
A29	*3223*	*107*	*10*	*1.27*	*0.0*	*0.6574*	*4.0*	*0.0768*	*1.5*	*0.37*	*0.0621*	*3.7*	*477*	*7*	*513*	*16*	*677*	*79*	*70*
A53	*613*	*18*	*2*	*0.06*	*6.7*	*0.8876*	*22.0*	*0.0870*	*13.9*	*0.63*	*0.0740*	*17.0*	*537*	*72*	*645*	*111*	*1042*	*343*	*52*
A38	*190962*	*278*	*150*	*0.38*	*67.9*	*1.5790*	*15.4*	*0.0899*	*7.2*	*0.47*	*0.1274*	*13.6*	*555*	*38*	*962*	*101*	*2062*	*240*	*27*

Grain	$^{207}Pb^{a}$ (cps)	U^{b} (ppm)	Pb^{b} (ppm)	$\frac{Th}{U}^{b}$	$^{206}Pbc^{c}$ (%)	$\frac{^{207}Pb}{^{235}U}^{d}$	±2σ (%)	$\frac{^{206}Pb}{^{238}U}^{d}$	±2σ (%)	ρ[e] (rho)	$\frac{^{207}Pb}{^{206}Pb}^{d}$	±2σ (%)	$\frac{^{206}Pb}{^{238}U}^{f}$	±2σ (Ma)	$\frac{^{207}Pb}{^{235}U}^{f}$	±2σ (Ma)	$\frac{^{207}Pb}{^{206}Pb}^{f}$	±2σ (Ma)	Conc.[g] (%)
91500[h]	14383	68	13	0.47	0.4	0.1781	3.4	1.8782	14.1	0.08	14.5260	0.6	1057	33	1072	98	1101	325	99
BB-16[h]	11251	302	28	0.40	0.0	0.0912	2.7	0.7668	3.3	0.06	1.5659	0.7	563	14	578	15	638	34	88
Plesovice[h]	17536	3943	198	0.20	3.0	0.0530	7.3	0.2289	70.7	0.03	65.9345	0.2	333	24	207	136			
GJ-1[h]	11801	290	26	0.02	0.4	0.0984	1.3	0.8153	2.3	0.06	1.4809	0.5	605	8	605	11			

$^{206}Pb/^{238}U$ error is the quadratic additions of the within run precision (2 SE) and the external reproducibility (2 SD) of the reference zircon. $^{207}Pb/^{206}Pb$ error propagation (^{207}Pb signal dependent) following Gerdes & Zeh (2009). $^{207}Pb/^{235}U$ error is the quadratic addition of the $^{207}Pb/^{206}Pb$ and $^{206}Pb/^{238}U$ uncertainty.

[a] Within run background-corrected mean ^{207}Pb signal in cps (counts per second).

[b] U and Pb content and Th/U ratio were calculated relative to GJ-1 reference zircon.

[c] Percentage of the common Pb on the ^{206}Pb. b.d. = below detection limit.

[d] Pb/U and Pb/Pb ratios. Corrected for background, within-run Pb/U fractionation (in case of $^{206}Pb/^{238}U$) and common Pb using Stacy and Kramers (1975) model Pb composition and subsequently normalised to GJ-1 (ID-TIMS value/measured value); $^{207}Pb/^{235}U$ calculated using $(({}^{207}Pb/{}^{206}Pb)*({}^{238}U/{}^{206}Pb)*137.88)$.

[e] Rho (ρ) is the $({}^{206}Pb/{}^{238}U)/({}^{207}Pb/{}^{235}U)$ error correlation coefficient.

[f] Pb/U and Pb/Pb ages.

[g] Degree of concordance = $(({}^{206}Pb/{}^{238}U \text{ age})/({}^{207}Pb/{}^{206}Pb \text{ age})) \times 100$.

[h] Mean of 9 (91500), 9 (BB-16), 9 (Plesovice), and 18 (GJ-1) analyses, respectively.

Table Ig3-U

U, Th and Pb LA-ICP-MS data of zircon crystals from sample GCH-32

Grain	^{207}Pb[a] (cps)	U[b] (ppm)	Pb[b] (ppm)	Th[b]/U	^{206}Pbc[c] (%)	$^{207}Pb/^{235}U$[d]	±2σ (%)	$^{206}Pb/^{238}U$[d]	±2σ (%)	ρ[e] (rho)	$^{207}Pb/^{206}Pb$[d]	±2σ (%)	$^{206}Pb/^{238}U$[f]	±2σ (Ma)	$^{207}Pb/^{235}U$[f]	±2σ (Ma)	$^{207}Pb/^{206}Pb$[f]	±2σ (Ma)	Conc.[g] (%)
A086	4135	181	10	0.01	0.4	0.4628	3.6	0.0616	1.5	0.42	0.0545	3.3	385	6	386	12	392	74	98
A118	65500	2783	157	0.00	0.0	0.4721	1.7	0.0618	1.4	0.85	0.0554	0.9	387	5	393	5	428	19	90
A116	10008	156	11	0.00	17.5	0.4745	12.0	0.0623	2.4	0.20	0.0553	11.8	390	9	394	40	423	263	92
A100	12530	408	24	0.01	1.9	0.4764	3.5	0.0624	1.6	0.46	0.0554	3.1	390	6	396	12	428	70	91
A127	4308	171	10	0.03	1.0	0.4731	2.9	0.0626	1.5	0.52	0.0548	2.5	391	6	393	10	406	56	96
A110	6275	213	13	0.01	2.2	0.4784	4.0	0.0630	1.5	0.37	0.0551	3.7	394	6	397	13	415	82	95
A129	7048	291	17	0.03	0.6	0.4729	2.4	0.0632	1.4	0.59	0.0543	2.0	395	6	393	8	383	44	103
A131	2211	98	5	0.00	0.0	0.4816	3.6	0.0632	1.6	0.44	0.0553	3.2	395	6	399	12	424	71	93
A075	6524	230	14	0.03	1.0	0.4758	3.6	0.0633	1.5	0.41	0.0545	3.3	396	6	395	12	393	74	101
A107	64525	2376	140	0.00	0.3	0.4912	2.0	0.0639	1.8	0.90	0.0558	0.9	399	7	406	7	443	20	90
A073	8515	372	22	0.00	0.3	0.4920	2.3	0.0639	1.6	0.70	0.0558	1.6	399	6	406	8	446	36	90
A128	4621	183	11	0.01	0.7	0.4848	3.4	0.0639	1.5	0.43	0.0550	3.1	399	6	401	11	412	69	97
A084	10202	428	25	0.00	0.3	0.4902	2.3	0.0645	1.5	0.64	0.0551	1.8	403	6	405	8	417	39	97
A115	7142	293	18	0.00	0.2	0.5011	2.8	0.0654	1.5	0.53	0.0556	2.3	408	6	412	9	436	52	94
A072	3357	107	8	0.35	0.4	0.6113	3.1	0.0770	1.6	0.51	0.0576	2.7	478	7	484	12	515	59	93
A061	2301	82	7	0.76	0.0	0.6090	4.3	0.0778	1.6	0.36	0.0568	4.0	483	7	483	17	483	89	100
A096	5523	187	14	0.04	0.6	0.6133	3.2	0.0783	1.5	0.46	0.0568	2.8	486	7	486	12	485	62	100
A062	4853	163	14	0.79	0.0	0.6284	2.9	0.0783	1.5	0.51	0.0582	2.5	486	7	495	11	537	54	90
A126	3949	146	11	0.01	0.3	0.6235	2.9	0.0788	1.5	0.53	0.0574	2.5	489	7	492	11	508	55	96
A108	39056	1131	83	0.03	0.1	0.6398	1.9	0.0797	1.5	0.79	0.0583	1.2	494	7	502	8	539	26	92
A130	4480	136	12	0.89	0.0	0.6480	3.0	0.0802	1.7	0.57	0.0586	2.5	497	8	507	12	552	54	90
A111	1412	45	4	0.60	0.1	0.6404	4.4	0.0803	1.6	0.37	0.0578	4.1	498	8	503	18	523	91	95
A088	4051	128	12	1.09	0.2	0.6599	6.5	0.0815	1.7	0.26	0.0587	6.2	505	8	515	26	557	136	91
A064	2347	80	7	0.68	0.0	0.6695	4.1	0.0824	1.8	0.44	0.0589	3.7	511	9	520	17	564	80	91
A124	60174	1770	137	0.01	0.3	0.6713	1.8	0.0840	1.6	0.88	0.0580	0.8	520	8	521	7	529	19	98
A065	4617	156	13	0.24	0.1	0.6752	3.6	0.0845	1.7	0.46	0.0579	3.2	523	8	524	15	527	70	99
A123	40634	1028	84	0.03	1.4	0.6854	2.7	0.0867	1.6	0.58	0.0574	2.2	536	8	530	11	506	48	106
A097	39503	982	83	0.02	b.d.	0.7544	2.7	0.0905	2.2	0.82	0.0605	1.5	559	12	571	12	620	33	90
A122	48121	179	67	0.72	0.0	5.8180	1.8	0.3340	1.4	0.80	0.1263	1.1	1858	23	1949	15	2048	19	91
A099	37973	127	52	0.72	0.0	6.4920	1.9	0.3690	1.4	0.78	0.1276	1.2	2025	25	2045	17	2065	21	98
A113	*24517*	*98*	*13*	*0.01*	*40.0*	*0.6362*	*23.1*	*0.0598*	*5.4*	*0.23*	*0.0772*	*22.5*	*374*	*20*	*500*	*96*	*1127*	*447*	*33*
A117	*2411*	*104*	*6*	*0.00*	*0.5*	*0.5121*	*3.7*	*0.0655*	*1.6*	*0.44*	*0.0567*	*3.3*	*409*	*6*	*420*	*13*	*479*	*74*	*86*
A082	*4781*	*83*	*7*	*0.76*	*0.0*	*0.9818*	*10.3*	*0.0658*	*1.7*	*0.17*	*0.1082*	*10.1*	*411*	*7*	*695*	*53*	*1769*	*185*	*23*
A119	*1551*	*168*	*10*	*0.00*	*0.2*	*0.0807*	*183*	*0.0660*	*1.5*	*0.01*	*0.0089*	*183*	*412*	*6*	*79*	*150*	-	-	-
A076	*3095*	*116*	*7*	*0.14*	*1.6*	*0.5615*	*4.3*	*0.0671*	*1.7*	*0.39*	*0.0607*	*4.0*	*418*	*7*	*452*	*16*	*630*	*86*	*66*
A114	*3532*	*105*	*9*	*0.72*	*0.0*	*0.6753*	*3.0*	*0.0743*	*1.6*	*0.53*	*0.0659*	*2.5*	*462*	*7*	*524*	*12*	*804*	*53*	*57*
A087	*4495*	*143*	*12*	*0.95*	*0.0*	*0.6388*	*2.7*	*0.0752*	*1.5*	*0.57*	*0.0616*	*2.2*	*467*	*7*	*502*	*11*	*661*	*47*	*71*
A085	*2306*	*76*	*6*	*0.73*	*0.1*	*0.6627*	*4.4*	*0.0766*	*1.8*	*0.42*	*0.0627*	*4.0*	*476*	*8*	*516*	*18*	*699*	*84*	*68*
A093	*2872*	*96*	*8*	*0.58*	*0.0*	*0.6448*	*3.8*	*0.0767*	*1.6*	*0.40*	*0.0610*	*3.5*	*476*	*7*	*505*	*15*	*639*	*76*	*74*
A091	*43642*	*1303*	*95*	*0.02*	*3.0*	*0.7360*	*6.0*	*0.0768*	*2.1*	*0.35*	*0.0695*	*5.6*	*477*	*10*	*560*	*26*	*914*	*115*	*52*
A080	*4737*	*158*	*14*	*0.84*	*0.0*	*0.6411*	*3.0*	*0.0775*	*1.5*	*0.52*	*0.0600*	*2.5*	*481*	*7*	*503*	*12*	*605*	*55*	*79*
A074	*2254*	*74*	*6*	*0.68*	*0.0*	*0.6446*	*3.3*	*0.0780*	*1.4*	*0.44*	*0.0600*	*2.9*	*484*	*7*	*505*	*13*	*602*	*64*	*80*
A090	*3228*	*102*	*9*	*1.01*	*0.0*	*0.6677*	*3.1*	*0.0783*	*1.6*	*0.50*	*0.0618*	*2.7*	*486*	*7*	*519*	*13*	*668*	*58*	*73*
A094	*2531*	*51*	*5*	*0.73*	*0.0*	*1.0500*	*9.5*	*0.0785*	*1.7*	*0.18*	*0.0970*	*9.4*	*487*	*8*	*729*	*51*	*1567*	*176*	*31*
A121	*34105*	*878*	*64*	*0.04*	*1.1*	*0.5502*	*3.8*	*0.0787*	*2.2*	*0.58*	*0.0507*	*3.1*	*488*	*10*	*445*	*14*	*227*	*71*	*215*
A081	*2541*	*80*	*7*	*0.57*	*b.d.*	*0.6922*	*4.1*	*0.0801*	*1.6*	*0.38*	*0.0627*	*3.8*	*497*	*8*	*534*	*17*	*697*	*81*	*71*
A125	*1694*	*89*	*7*	*0.70*	*0.0*	*0.3919*	*7.7*	*0.0802*	*1.6*	*0.21*	*0.0354*	*7.5*	*497*	*8*	*336*	*22*	*-674*	*208*	*-74*
A079	*4441*	*141*	*12*	*0.49*	*0.0*	*0.6786*	*2.9*	*0.0804*	*1.6*	*0.55*	*0.0612*	*2.4*	*498*	*8*	*526*	*12*	*647*	*52*	*77*
A101	*2977*	*94*	*8*	*0.73*	*0.1*	*0.6991*	*3.6*	*0.0805*	*1.5*	*0.42*	*0.0630*	*3.3*	*499*	*7*	*538*	*15*	*708*	*70*	*70*
A109	*2265*	*72*	*6*	*0.61*	*0.0*	*0.7109*	*3.3*	*0.0809*	*1.6*	*0.48*	*0.0638*	*2.9*	*501*	*8*	*545*	*14*	*734*	*62*	*68*
A098	*2080*	*64*	*6*	*0.68*	*0.0*	*0.7004*	*3.7*	*0.0812*	*1.6*	*0.42*	*0.0626*	*3.4*	*503*	*8*	*539*	*16*	*694*	*71*	*73*
A077	*2601*	*75*	*6*	*0.60*	*0.0*	*0.7374*	*2.8*	*0.0812*	*1.6*	*0.58*	*0.0659*	*2.3*	*503*	*8*	*561*	*12*	*802*	*49*	*63*
A078	*2957*	*87*	*8*	*0.65*	*6.0*	*0.7897*	*9.2*	*0.0817*	*1.9*	*0.21*	*0.0701*	*9.0*	*507*	*9*	*591*	*42*	*930*	*184*	*54*
A112	*2396*	*74*	*6*	*0.59*	*0.1*	*0.7138*	*3.4*	*0.0819*	*1.6*	*0.47*	*0.0632*	*3.0*	*508*	*8*	*547*	*14*	*715*	*63*	*71*
A066	*2118*	*59*	*5*	*0.65*	*1.3*	*0.6523*	*16.9*	*0.0843*	*2.4*	*0.14*	*0.0562*	*16.7*	*521*	*12*	*510*	*70*	*459*	*371*	*114*
A120	*2417*	*56*	*5*	*0.67*	*0.5*	*0.9534*	*4.0*	*0.0848*	*1.6*	*0.42*	*0.0815*	*3.6*	*525*	*8*	*680*	*20*	*1233*	*70*	*43*
A089	*1827*	*50*	*4*	*0.09*	*2.0*	*0.7639*	*6.3*	*0.0860*	*1.9*	*0.30*	*0.0644*	*6.0*	*532*	*10*	*576*	*28*	*755*	*127*	*70*
A095	*934*	*26*	*2*	*0.60*	*b.d.*	*0.8039*	*4.9*	*0.0867*	*2.0*	*0.41*	*0.0673*	*4.4*	*536*	*10*	*599*	*22*	*846*	*93*	*63*
A063	*5977*	*159*	*16*	*0.98*	*0.0*	*0.8014*	*3.7*	*0.0881*	*1.5*	*0.41*	*0.0660*	*3.4*	*544*	*8*	*598*	*17*	*806*	*71*	*67*
A083	*3380*	*64*	*7*	*0.70*	*1.2*	*1.2310*	*6.6*	*0.0900*	*1.9*	*0.29*	*0.0992*	*6.3*	*556*	*10*	*815*	*37*	*1609*	*117*	*35*
A092	*7774*	*200*	*19*	*0.50*	*2.6*	*0.8166*	*4.8*	*0.0914*	*1.5*	*0.32*	*0.0648*	*4.6*	*564*	*8*	*606*	*22*	*768*	*97*	*73*

Grain	^{207}Pb[a] (cps)	U[b] (ppm)	Pb[b] (ppm)	Th[b] U	^{206}Pbc[c] (%)	^{207}Pb[d] / ^{235}U	±2σ (%)	^{206}Pb[d] / ^{238}U	±2σ (%)	ρ[e] (rho)	^{207}Pb[d] / ^{206}Pb	±2σ (%)	^{206}Pb[f] / ^{238}U	±2σ (Ma)	^{207}Pb[f] / ^{235}U	±2σ (Ma)	^{207}Pb[f] / ^{206}Pb	±2σ (Ma)	Conc.[g] (%)
91500[h]	14383	68	13	0.47	0.4	0.1781	3.4	1.8782	14.1	0.08	14.5260	0.6	1057	33	1072	98	1101	325	99
BB-16[h]	11251	302	28	0.40	0.0	0.0912	2.7	0.7668	3.3	0.06	1.5659	0.7	563	14	578	15	638	34	88
Plesovice[h]	17536	3943	198	0.20	3.0	0.0530	7.3	0.2289	70.7	0.03	65.9345	0.2	333	24	207	136			
GJ-1[h]	11801	290	26	0.02	0.4	0.0984	1.3	0.8153	2.3	0.06	1.4809	0.5	605	8	605	11			

$^{206}Pb/^{238}U$ error is the quadratic additions of the within run precision (2 SE) and the external reproducibility (2 SD) of the reference zircon. $^{207}Pb/^{206}Pb$ error propagation (^{207}Pb signal dependent) following Gerdes & Zeh (2009). $^{207}Pb/^{235}U$ error is the quadratic addition of the $^{207}Pb/^{206}Pb$ and $^{206}Pb/^{238}U$ uncertainty.

[a] Within run background-corrected mean ^{207}Pb signal in cps (counts per second).

[b] U and Pb content and Th/U ratio were calculated relative to GJ-1 reference zircon.

[c] Percentage of the common Pb on the ^{206}Pb. b.d. = below detection limit.

[d] Pb/U and Pb/Pb ratios. Corrected for background, within-run Pb/U fractionation (in case of $^{206}Pb/^{238}U$) and common Pb using Stacy and Kramers (1975) model Pb composition and subsequently normalised to GJ-1 (ID-TIMS value/measured value); $^{207}Pb/^{235}U$ calculated using $(^{207}Pb/^{206}Pb)*(^{238}U/^{206}Pb)*137.88$).

[e] Rho (ρ) is the $(^{206}Pb/^{238}U)/(^{207}Pb/^{235}U)$ error correlation coefficient.

[f] Pb/U and Pb/Pb ages.

[g] Degree of concordance = $(^{206}Pb/^{238}U$ age$)/(^{207}Pb/^{206}Pb$ age$)$ x 100.

[h] Mean of 9 (91500), 9 (BB-16), 9 (Plesovice), and 18 (GJ-1) analyses, respectively.

Table Ig4-U

U, Th and Pb LA-ICP-MS data of zircon crystals from sample GCH-19

Grain	^{207}Pb[a] (cps)	U[b] (ppm)	Pb[b] (ppm)	$\frac{Th}{U}$[b]	^{206}Pbc[c] (%)	$\frac{^{207}Pb}{^{235}U}$[d]	±2σ (%)	$\frac{^{206}Pb}{^{238}U}$[d]	±2σ (%)	ρ[e] (rho)	$\frac{^{207}Pb}{^{206}Pb}$[d]	±2σ (%)	$\frac{^{206}Pb}{^{238}U}$[f]	±2σ (Ma)	$\frac{^{207}Pb}{^{235}U}$[f]	±2σ (Ma)	$\frac{^{207}Pb}{^{206}Pb}$[f]	±2σ (Ma)	Conc.[g] (%)
A502	4131	69	5	0.54	2.7	0.4477	5.0	0.0600	1.5	0.31	0.0541	4.7	376	6	376	16	376	106	100
A040	141	3	0	0.32	5.5	0.4626	18.7	0.0611	7.0	0.38	0.0549	17.3	382	26	386	62	409	388	93
A511	7872	390	22	0.00	0.1	0.4613	2.2	0.0615	1.5	0.69	0.0544	1.6	385	6	385	7	389	36	99
A091	420	32	2	0.12	1.3	0.4729	8.9	0.0624	2.5	0.28	0.0550	8.6	390	9	393	29	412	191	95
A051	733	63	4	0.36	0.9	0.4696	6.7	0.0625	2.7	0.40	0.0545	6.2	391	10	391	22	392	139	100
A503	369	4	0	0.06	6.3	0.4820	12.3	0.0635	2.7	0.22	0.0550	12.0	397	10	399	41	413	268	96
A053	664	32	2	0.26	6.7	0.4850	9.5	0.0640	2.8	0.29	0.0549	9.1	400	11	402	32	410	203	98
A092	781	53	4	0.33	3.4	0.4907	8.2	0.0644	1.9	0.24	0.0553	7.9	402	8	405	28	423	177	95
A056	282	6	0	0.34	6.9	0.4921	15.8	0.0645	3.0	0.19	0.0553	15.5	403	12	406	54	426	346	95
A052	1086	96	7	0.51	0.2	0.4909	4.1	0.0649	1.9	0.45	0.0549	3.7	405	7	405	14	407	83	100
A047	1157	4	0	0.31	22.7	0.4989	16.5	0.0650	3.6	0.22	0.0557	16.1	406	14	411	57	439	358	92
A015	397	6	0	0.24	3.2	0.5090	10.4	0.0662	2.3	0.22	0.0558	10.2	413	9	418	36	443	226	93
A020	92	3	0	0.04	1.9	0.5145	17.7	0.0671	3.5	0.20	0.0556	17.4	419	14	421	63	436	386	96
A055	472	34	3	0.34	2.0	0.5162	6.2	0.0675	1.8	0.29	0.0554	6.0	421	7	423	22	429	133	98
A507	738	13	1	0.24	2.1	0.5202	6.9	0.0679	2.3	0.33	0.0555	6.6	424	9	425	24	434	146	98
A032	196	7	0	0.17	1.6	0.5306	10.0	0.0684	2.5	0.25	0.0563	9.6	426	10	432	36	464	213	92
A023	175	3	0	0.26	9.9	0.5334	16.4	0.0688	4.2	0.26	0.0563	15.9	429	17	434	60	463	352	93
A504	470	6	1	1.68	3.0	0.5340	11.1	0.0692	2.6	0.23	0.0560	10.8	431	11	434	40	453	240	95
A043	330	22	2	0.24	1.5	0.5525	8.2	0.0704	2.7	0.33	0.0569	7.7	439	11	447	30	488	170	90
A048	561	5	0	0.17	5.1	0.5463	10.3	0.0708	3.0	0.29	0.0560	9.8	441	13	443	37	451	218	98
A050	1081	83	6	0.24	0.7	0.5525	4.2	0.0709	1.8	0.41	0.0565	3.9	442	7	447	15	472	85	94
A509	635	4	0	0.26	10.1	0.5568	26.3	0.0709	8.3	0.32	0.0569	24.9	442	36	449	100	489	550	90
A024	294	21	2	0.22	1.5	0.5449	7.2	0.0712	2.2	0.31	0.0555	6.9	443	10	442	26	434	153	102
A041	595	3	0	0.26	13.2	0.5509	15.7	0.0718	3.5	0.22	0.0557	15.3	447	15	446	58	440	340	102
A084	436	10	1	0.23	5.9	0.5543	14.0	0.0718	3.4	0.24	0.0560	13.6	447	15	448	52	453	302	98
A013	139	4	0	0.27	2.8	0.5540	14.5	0.0720	2.9	0.20	0.0558	14.2	448	13	448	54	444	316	101
A510	2208	37	3	0.39	0.4	0.5639	3.1	0.0728	1.6	0.52	0.0562	2.6	453	7	454	11	460	58	98
A038	319	6	1	0.24	7.2	0.5773	16.5	0.0735	3.6	0.22	0.0570	16.1	457	16	463	63	491	355	93
A049	151	4	0	0.15	2.3	0.5888	17.6	0.0751	6.2	0.35	0.0569	16.5	467	28	470	69	486	364	96
A054	340	20	2	0.42	2.4	0.6048	10.7	0.0760	2.2	0.21	0.0577	10.5	472	10	480	42	518	231	91
A044	453	35	3	0.23	0.7	0.5977	5.0	0.0766	2.2	0.45	0.0566	4.5	476	10	476	19	476	99	100
A042	294	2	0	0.21	8.9	0.6091	15.4	0.0766	4.1	0.26	0.0576	14.8	476	19	483	61	516	326	92
A016	155	3	0	0.02	6.2	0.5939	33.0	0.0768	5.3	0.16	0.0561	32.6	477	24	473	133	456	722	105
A029	206	11	1	0.38	3.3	0.6111	14.7	0.0775	2.6	0.17	0.0572	14.5	481	12	484	58	500	319	96
A088	268	4	0	0.25	9.0	0.6172	19.6	0.0775	3.5	0.18	0.0578	19.2	481	16	488	79	522	422	92
A079	830	10	1	1.10	10.9	0.6197	16.6	0.0776	2.9	0.17	0.0579	16.3	482	13	490	67	527	358	91
A061	445	4	0	0.32	7.7	0.6107	14.6	0.0778	2.9	0.20	0.0569	14.3	483	14	484	58	488	315	99
A095	810	54	4	0.20	1.0	0.6150	5.6	0.0779	2.1	0.38	0.0573	5.2	483	10	487	22	502	115	96
A046	565	30	3	0.31	3.3	0.6202	7.3	0.0780	2.2	0.30	0.0576	7.0	484	10	490	29	516	153	94
A012	537	41	3	0.14	0.4	0.6259	5.6	0.0781	2.3	0.42	0.0581	5.1	485	11	494	22	535	111	91
A065	357	22	2	0.47	2.3	0.6179	11.4	0.0783	2.6	0.23	0.0572	11.1	486	12	489	45	500	245	97
A075	2316	184	17	0.60	0.3	0.6217	3.7	0.0788	1.5	0.40	0.0572	3.4	489	7	491	15	499	75	98
A077	927	73	5	0.06	0.3	0.6218	5.4	0.0789	3.3	0.62	0.0572	4.3	489	16	491	21	499	94	98
A039	1218	89	8	0.40	0.4	0.6335	4.3	0.0789	1.6	0.37	0.0582	4.0	490	8	498	17	538	88	91
A080	269	5	0	0.03	5.5	0.6308	17.6	0.0790	3.0	0.17	0.0579	17.4	490	14	497	72	526	381	93
A045	1118	81	8	0.68	0.5	0.6291	5.5	0.0793	1.9	0.35	0.0575	5.2	492	9	496	22	511	114	96
A058	267	4	0	0.13	9.2	0.6301	15.8	0.0794	4.6	0.29	0.0575	15.1	493	22	496	64	512	333	96
A089	292	4	0	0.44	8.9	0.6375	16.1	0.0796	3.5	0.22	0.0581	15.7	494	16	501	66	532	344	93
A022	369	20	2	0.20	2.2	0.6442	9.3	0.0804	2.5	0.27	0.0582	8.9	498	12	505	37	535	195	93
A109	690	47	4	0.45	0.8	0.6418	5.7	0.0810	1.9	0.34	0.0575	5.3	502	9	503	23	509	117	99
A506	307	6	1	0.30	8.2	0.6405	15.3	0.0812	8.0	0.52	0.0572	13.0	503	39	503	62	500	287	101
A074	279	17	1	0.26	1.6	0.6482	8.1	0.0812	2.6	0.32	0.0579	7.7	503	12	507	33	526	168	96
A081	285	6	1	0.35	3.4	0.6651	5.6	0.0818	3.0	0.54	0.0590	4.7	507	15	518	23	566	102	90
A508	2818	7	2	0.28	43.4	0.6480	33.7	0.0819	6.2	0.18	0.0574	33.1	508	30	507	144	506	728	100
A096	866	57	5	0.18	0.7	0.6528	5.7	0.0821	2.1	0.37	0.0577	5.3	509	10	510	23	516	116	99
A076	184	11	1	0.42	2.4	0.6557	11.0	0.0824	3.4	0.31	0.0577	10.4	510	17	512	45	519	229	98
A060	446	4	0	0.35	20.4	0.6765	25.4	0.0836	5.9	0.23	0.0587	24.7	518	30	525	110	556	540	93
A027	348	21	2	0.28	1.4	0.6694	9.6	0.0837	2.3	0.24	0.0580	9.3	518	11	520	40	531	204	98
A505	141	3	0	0.18	0.0	0.7714	14.2	0.0936	3.4	0.24	0.0598	13.8	577	19	581	65	596	299	97
A064	*212*	*16*	*1*	*0.23*	*0.1*	*0.6583*	*21.9*	*0.0526*	*11.3*	*0.52*	*0.0908*	*18.8*	*330*	*37*	*514*	*92*	*1443*	*358*	*23*
A083	*187*	*3*	*0*	*0.08*	*15.4*	*0.2472*	*63.2*	*0.0551*	*5.2*	*0.08*	*0.0325*	*62.9*	*346*	*18*	*224*	*136*	*-917*	*###*	*-38*
A501	*14638*	*3*	*3*	*0.21*	*45.6*	*0.3758*	*123*	*0.0555*	*31.1*	*0.25*	*0.0492*	*119*	*348*	*106*	*324*	*414*	*155*	*###*	*224*
A017	*158*	*3*	*0*	*0.46*	*b.d.*	*0.9542*	*16.6*	*0.0601*	*5.4*	*0.33*	*0.1151*	*15.7*	*376*	*20*	*680*	*86*	*1882*	*283*	*20*
A117	*261*	*5*	*0*	*0.19*	*6.1*	*0.9350*	*17.6*	*0.0626*	*4.6*	*0.26*	*0.1084*	*17.0*	*391*	*17*	*670*	*90*	*1772*	*310*	*22*
A110	*190*	*5*	*3*	*0.26*	*13.4*	*92*	*18.5*	*0.0663*	*4.7*	*0.25*	*10*	*17.9*	*414*	*19*	*4601*	*205*	*-*	*-*	*-*
A118	*298*	*12*	*8*	*0.25*	*16.3*	*93*	*18.7*	*0.0670*	*5.5*	*0.29*	*10*	*17.9*	*418*	*22*	*4612*	*207*	*-*	*-*	*-*
A112	*302*	*3*	*0*	*0.05*	*17.1*	*0.7189*	*35.7*	*0.0670*	*12.8*	*0.36*	*0.0778*	*33.4*	*418*	*52*	*550*	*164*	*1141*	*663*	*37*

Grain	^{207}Pb[a] (cps)	U[b] (ppm)	Pb[b] (ppm)	Th[b] / U	^{206}Pbc[c] (%)	^{207}Pb[d] / ^{235}U	±2σ (%)	^{206}Pb[d] / ^{238}U	±2σ (%)	ρ[e] (rho)	^{207}Pb[d] / ^{206}Pb	±2σ (%)	^{206}Pb[f] / ^{238}U	±2σ (Ma)	^{207}Pb[f] / ^{235}U	±2σ (Ma)	^{207}Pb[f] / ^{206}Pb	±2σ (Ma)	Conc.[g] (%)
A062	*225*	*5*	*0*	*0.13*	*4.8*	*0.5320*	*12.8*	*0.0674*	*3.6*	*0.28*	*0.0573*	*12.2*	*420*	*15*	*433*	*46*	*502*	*269*	*84*
A101	*224*	*4*	*3*	*0.16*	*15.4*	*94*	*17.2*	*0.0675*	*3.4*	*0.20*	*10*	*16.9*	*421*	*14*	*4619*	*190*	-	-	-
A124	*850*	*3*	*1*	*0.05*	*48.0*	*0.6857*	*69.6*	*0.0693*	*8.0*	*0.11*	*0.0718*	*69.1*	*432*	*33*	*530*	*338*	*980*	*###*	*44*
A057	*189*	*3*	*0*	*0.32*	*6.0*	*0.5547*	*23.0*	*0.0700*	*5.2*	*0.23*	*0.0575*	*22.4*	*436*	*22*	*448*	*87*	*509*	*492*	*86*
A116	*448*	*6*	*1*	*0.20*	*8.9*	*0.5613*	*15.1*	*0.0710*	*3.6*	*0.24*	*0.0573*	*14.7*	*442*	*15*	*452*	*57*	*505*	*323*	*88*
A085	*351*	*5*	*0*	*0.18*	*8.8*	*0.5884*	*7.4*	*0.0712*	*4.3*	*0.58*	*0.0599*	*6.0*	*444*	*18*	*470*	*28*	*600*	*130*	*74*
A108	*259*	*14*	*1*	*0.58*	*1.9*	*0.6109*	*9.7*	*0.0717*	*3.1*	*0.32*	*0.0618*	*9.2*	*446*	*13*	*484*	*38*	*668*	*197*	*67*
A113	*233*	*4*	*0*	*0.05*	*13.2*	*0.3616*	*60.6*	*0.0728*	*5.4*	*0.09*	*0.0361*	*60.4*	*453*	*23*	*313*	*178*	*-627*	*###*	*-72*
A097	*416*	*12*	*1*	*0.92*	*b.d.*	*0.9751*	*109*	*0.0737*	*20.9*	*0.19*	*0.0959*	*107*	*459*	*93*	*691*	*782*	*1546*	*###*	*30*
A123	*579*	*39*	*3*	*0.20*	*0.8*	*0.6437*	*6.9*	*0.0747*	*2.1*	*0.30*	*0.0625*	*6.6*	*464*	*9*	*505*	*28*	*692*	*140*	*67*
A059	*339*	*4*	*0*	*0.35*	*13.1*	*0.6102*	*22.5*	*0.0757*	*4.3*	*0.19*	*0.0585*	*22.1*	*470*	*19*	*484*	*91*	*548*	*484*	*86*
A098	*150*	*11*	*1*	*0.61*	*b.d.*	*0.8950*	*21.3*	*0.0761*	*4.2*	*0.20*	*0.0853*	*20.9*	*473*	*19*	*649*	*108*	*1322*	*404*	*36*
A107	*207*	*5*	*0*	*0.33*	*b.d.*	*1.0280*	*12.2*	*0.0761*	*3.0*	*0.24*	*0.0980*	*11.8*	*473*	*14*	*718*	*65*	*1585*	*220*	*30*
A115	*300*	*4*	*0*	*0.25*	*18.2*	*0.0041*	*####*	*0.0762*	*5.5*	*0.00*	*0.0004*	*4676*	*473*	*25*	*4*	*216*	-	-	-
A014	*759*	*3*	*0*	*0.29*	*17.3*	*0.7016*	*19.2*	*0.0766*	*3.6*	*0.19*	*0.0664*	*18.8*	*476*	*17*	*540*	*84*	*820*	*393*	*58*
A019	*708*	*3*	*1*	*0.43*	*12.6*	*1.7640*	*22.7*	*0.0769*	*8.1*	*0.35*	*0.1664*	*21.3*	*478*	*37*	*1032*	*159*	*2521*	*357*	*19*
A119	*132*	*8*	*1*	*0.13*	*b.d.*	*0.8716*	*11.8*	*0.0777*	*3.6*	*0.30*	*0.0814*	*11.2*	*482*	*17*	*636*	*57*	*1231*	*220*	*39*
A028	*303*	*20*	*2*	*0.97*	*2.5*	*0.6722*	*8.7*	*0.0780*	*3.1*	*0.36*	*0.0625*	*8.1*	*484*	*14*	*522*	*36*	*693*	*172*	*70*
A122	*1076*	*79*	*7*	*0.37*	*b.d.*	*0.6778*	*4.6*	*0.0781*	*1.7*	*0.37*	*0.0629*	*4.3*	*485*	*8*	*525*	*19*	*706*	*91*	*69*
A073	*136*	*7*	*5*	*0.23*	*12.2*	*109.60*	*18.3*	*0.0791*	*4.4*	*0.24*	*10.050*	*17.7*	*490*	*21*	*4778*	*203*	-	-	-
A090	*253*	*4*	*0*	*0.19*	*12.1*	*0.3589*	*41.0*	*0.0793*	*6.4*	*0.16*	*0.0328*	*40.5*	*492*	*30*	*311*	*116*	*-892*	*###*	*-55*
A111	*242*	*4*	*0*	*0.35*	*7.3*	*0.9854*	*16.9*	*0.0795*	*5.7*	*0.34*	*0.0899*	*15.9*	*493*	*27*	*696*	*89*	*1423*	*303*	*35*
A072	*194*	*3*	*0*	*0.26*	*9.0*	*0.6208*	*30.5*	*0.0808*	*5.1*	*0.17*	*0.0558*	*30.1*	*501*	*25*	*490*	*126*	*442*	*669*	*113*
A086	*295*	*5*	*0*	*0.13*	*5.8*	*0.6732*	*6.2*	*0.0809*	*3.1*	*0.50*	*0.0603*	*5.4*	*502*	*15*	*523*	*26*	*616*	*117*	*81*
A121	*300*	*19*	*2*	*0.36*	*b.d.*	*1.0090*	*9.1*	*0.0819*	*2.2*	*0.25*	*0.0894*	*8.8*	*507*	*11*	*708*	*47*	*1412*	*168*	*36*
A120	*183*	*3*	*0*	*0.05*	*5.2*	*0.9557*	*17.0*	*0.0861*	*3.7*	*0.22*	*0.0805*	*16.6*	*532*	*19*	*681*	*88*	*1210*	*327*	*44*
A114	*260*	*3*	*0*	*0.13*	*1.0*	*1.7780*	*16.4*	*0.0870*	*6.4*	*0.39*	*0.1482*	*15.1*	*538*	*33*	*1037*	*112*	*2325*	*259*	*23*
A010	*672*	*3*	*2*	*0.28*	*45.6*	*123.60*	*16.4*	*0.0892*	*6.8*	*0.42*	*10.050*	*14.9*	*551*	*36*	*4900*	*180*	-	-	-
A078	*339*	*4*	*1*	*0.32*	*9.2*	*0.8091*	*7.4*	*0.0920*	*4.0*	*0.54*	*0.0638*	*6.2*	*567*	*22*	*602*	*34*	*734*	*131*	*77*
A066	*147*	*3*	*0*	*0.18*	*2.5*	*1.3060*	*32.6*	*0.0933*	*25.9*	*0.79*	*0.1015*	*19.8*	*575*	*144*	*849*	*207*	*1652*	*368*	*35*
A087	*2027*	*8*	*2*	*0.32*	*19.9*	*1.9690*	*13.1*	*0.0986*	*3.6*	*0.27*	*0.1449*	*12.6*	*606*	*21*	*1105*	*92*	*2287*	*217*	*26*
A082	*586*	*2*	*1*	*0.09*	*16.0*	*9.9700*	*102*	*0.1300*	*26.7*	*0.26*	*0.5564*	*98.1*	*788*	*201*	*2432*	*###*	*4398*	*###*	*18*
A026	*2604*	*4*	*-*	*0.19*	*92.5*	*-*	*-*	*-*	*-*	*-*	*0.6295*	*94.4*	*-*	*-*	*-*	*-*	*4578*	*###*	*-*
A021	*305*	*-*	*-*	*-*	*-*	*-*	*-*	*-*	*-*	*-*	*-*	*-*	*-*	*-*	*-*	*-*	*-*	*-*	*-*
A030	*148*	*3*	*-*	*0.07*	*b.d.*	*-*	*-*	*-*	*-*	*-*	*0.1932*	*139*	*-*	*-*	*-*	*-*	*2770*	*###*	*-*
A099	*153*	*5*	*-*	*0.53*	*10.1*	*-*	*-*	*-*	*-*	*-*	*0.5727*	*97.8*	*-*	*-*	*-*	*-*	*4440*	*###*	*-*
A500	*603919*	*3*	*34*	*0.19*	*299.3*	*-1387.0*	*55.8*	*-11.40*	*41.6*	*0.75*	*0.8823*	*37.2*	*-*	*-*	*-*	*-*	*5061*	*526*	*-*
A018	*-*	*-*	*-*	*-*	*-*	*-*	*-*	*-*	*-*	*-*	*-*	*-*	*-*	*-*	*-*	*-*	*-*	*-*	*-*
A025	*124*	*-*	*-*	*-*	*-*	*-*	*-*	*-*	*-*	*-*	*-*	*-*	*-*	*-*	*-*	*-*	*-*	*-*	*-*
A031	*609*	*-*	*-*	*-*	*-*	*-*	*-*	*-*	*-*	*-*	*-*	*-*	*-*	*-*	*-*	*-*	*-*	*-*	*-*
A063	*203*	*3*	*-*	*0.39*	*16.1*	*-*	*-*	*-*	*-*	*-*	*10.050*	*16.1*	*-*	*-*	*-*	*-*	*-*	*-*	*-*
A093	*-*	*-*	*-*	*-*	*-*	*-*	*-*	*-*	*-*	*-*	*-*	*-*	*-*	*-*	*-*	*-*	*-*	*-*	*-*
A094	*-*	*-*	*-*	*-*	*-*	*-*	*-*	*-*	*-*	*-*	*-*	*-*	*-*	*-*	*-*	*-*	*-*	*-*	*-*
A100	*120*	*5*	*-*	*0.08*	*62.1*	*-*	*-*	*-*	*-*	*-*	*10.050*	*58.0*	*-*	*-*	*-*	*-*	*-*	*-*	*-*
A499	*20820*	*3*	*-*	*0.25*	*95.6*	*-*	*-*	*-*	*-*	*-*	*10.050*	*15.4*	*-*	*-*	*-*	*-*	*-*	*-*	*-*
91500[h]	8378	74	13	0.29	0.5	0.1795	1.4	1.8499	1.8	0.07	0.9148	0.5	1064	14	1063	12	1062	18	100
Felix[h]	12482	435	68	2.47	0.2	0.0821	3.0	0.6484	3.0	0.06	2.9654	0.4	509	15	507	12	502	65	102
Plesovice[h]	2852	651	34	0.09	1.3	0.0542	2.2	0.3989	4.1	0.05	2.8587	0.5	340	7	341	12	345	64	99
GJ-1[h]	9719	290	27	0.04	0.1	0.0984	1.2	0.8151	2.4	0.06	2.2245	0.5	605	7	605	11			

$^{206}Pb/^{238}U$ error is the quadratic additions of the within run precision (2 SE) and the external reproducibility (2 SD) of the reference zircon. $^{207}Pb/^{206}Pb$ error propagation (^{207}Pb signal dependent) following Gerdes & Zeh (2009). $^{207}Pb/^{235}U$ error is the quadratic addition of the $^{207}Pb/^{206}Pb$ and $^{206}Pb/^{238}U$ uncertainty.

[a] Within run background-corrected mean ^{207}Pb signal in cps (counts per second).

[b] U and Pb content and Th/U ratio were calculated relative to GJ-1 reference zircon.

[c] Percentage of the common Pb on the ^{206}Pb. b.d. = below detection limit.

[d] Pb/U and Pb/Pb ratios. Corrected for background, within-run Pb/U fractionation (in case of $^{206}Pb/^{238}U$) and common Pb using Stacy and Kramers (1975) model Pb composition and subsequently normalised to GJ-1 (ID-TIMS value/measured value); $^{207}Pb/^{235}U$ calculated using (($^{207}Pb/^{206}Pb$)*($^{238}U/^{206}Pb$)*137.88).

[e] Rho (ρ) is the ($^{206}Pb/^{238}U$)/($^{207}Pb/^{235}U$) error correlation coefficient.

[f] Pb/U and Pb/Pb ages.

[g] Degree of concordance = (($^{206}Pb/^{238}U$ age)/($^{207}Pb/^{206}Pb$ age)) x 100.

[h] Mean of 13 (91500), 13 (Felix), 13 (Plesovice), and 26(GJ-1) analyses, respectively.

Table Ig5-U

U, Th and Pb LA-ICP-MS data of zircon crystals from sample GCH-20

Grain	^{207}Pb[a] (cps)	U[b] (ppm)	Pb[b] (ppm)	Th[b]/U	^{206}Pbc[c] (%)	$^{207}Pb/^{235}U$[d]	±2σ (%)	$^{206}Pb/^{238}U$[d]	±2σ (%)	ρ[e] (rho)	$^{207}Pb/^{206}Pb$[d]	±2σ (%)	$^{206}Pb/^{238}U$[f]	±2σ (Ma)	$^{207}Pb/^{235}U$[f]	±2σ (Ma)	$^{207}Pb/^{206}Pb$[f]	±2σ (Ma)	Conc.[g] (%)
A537	9919	508	26	0.00	0.3	0.4119	1.9	0.0556	1.4	0.73	0.0537	1.3	349	5	350	6	360	29	97
A534	7412	383	21	0.00	0.0	0.4434	1.9	0.0595	1.3	0.70	0.0541	1.4	372	5	373	6	374	31	100
A563	10454	395	23	0.00	2.3	0.4499	3.6	0.0602	1.6	0.44	0.0542	3.2	377	6	377	11	378	73	100
A545	8283	403	22	0.01	0.0	0.4538	1.9	0.0606	1.5	0.78	0.0543	1.2	379	5	380	6	385	27	99
A512	6459	318	18	0.00	0.1	0.4556	2.2	0.0608	1.3	0.59	0.0543	1.8	381	5	381	7	385	40	99
A574	5770	275	15	0.00	0.6	0.4554	2.1	0.0609	1.3	0.64	0.0543	1.6	381	5	381	7	381	37	100
A531	6640	333	19	0.01	0.1	0.4567	2.1	0.0610	1.4	0.67	0.0543	1.6	382	5	382	7	382	36	100
A579	9762	408	24	0.00	2.5	0.4573	4.1	0.0611	1.5	0.36	0.0543	3.8	382	5	382	13	384	85	100
A573	12474	553	32	0.00	1.2	0.4578	2.7	0.0612	1.5	0.56	0.0543	2.2	383	6	383	9	383	50	100
A539	9498	462	26	0.00	0.1	0.4576	2.1	0.0612	1.6	0.76	0.0543	1.4	383	6	383	7	381	31	100
A521	9716	492	28	0.00	0.0	0.4601	2.0	0.0613	1.4	0.73	0.0544	1.3	384	5	384	6	389	30	99
A542	7434	364	20	0.00	0.0	0.4616	2.0	0.0615	1.5	0.73	0.0545	1.4	385	5	385	6	390	31	99
A567	9362	460	26	0.01	0.1	0.4610	2.0	0.0615	1.5	0.72	0.0543	1.4	385	6	385	7	385	32	100
A532	7526	370	21	0.00	0.0	0.4626	2.1	0.0616	1.4	0.67	0.0545	1.6	385	5	386	7	391	35	99
A558	10259	511	29	0.00	0.1	0.4624	2.0	0.0617	1.5	0.78	0.0544	1.2	386	6	386	6	387	28	100
A570	12863	653	37	0.00	0.2	0.4626	2.0	0.0617	1.5	0.78	0.0544	1.2	386	6	386	6	385	27	100
A518	6129	291	17	0.01	0.2	0.4632	2.0	0.0617	1.4	0.70	0.0544	1.4	386	5	386	6	388	32	99
A559	6751	328	19	0.00	0.1	0.4628	1.9	0.0618	1.4	0.74	0.0544	1.3	386	5	386	6	386	29	100
A535	10021	491	28	0.00	0.1	0.4655	1.8	0.0620	1.4	0.77	0.0545	1.2	388	5	388	6	390	26	99
A516	11223	521	30	0.00	0.3	0.4661	2.2	0.0620	1.4	0.65	0.0545	1.6	388	5	388	7	392	37	99
A547	8050	334	19	0.00	1.1	0.4655	2.6	0.0621	1.4	0.53	0.0544	2.2	388	5	388	8	387	50	100
A586	10513	439	26	0.00	1.0	0.4660	2.7	0.0621	1.6	0.60	0.0544	2.2	388	6	388	9	389	49	100
A517	10470	516	29	0.00	0.0	0.4664	2.2	0.0621	1.9	0.85	0.0544	1.1	389	7	389	7	389	25	100
A560	9393	454	26	0.00	0.0	0.4668	1.8	0.0621	1.3	0.75	0.0545	1.2	389	5	389	6	391	27	99
A515	9331	444	26	0.01	0.6	0.4666	2.2	0.0621	1.4	0.65	0.0545	1.7	389	5	389	7	390	37	100
A528	4471	214	12	0.00	0.1	0.4666	2.4	0.0622	1.6	0.67	0.0545	1.7	389	6	389	8	390	39	100
A544	6256	311	18	0.01	0.1	0.4667	1.9	0.0622	1.3	0.71	0.0544	1.3	389	5	389	6	389	30	100
A565	3540	167	10	0.00	0.1	0.4667	2.4	0.0622	1.4	0.57	0.0544	2.0	389	5	389	8	388	45	100
A526	10457	502	29	0.00	0.2	0.4675	2.0	0.0622	1.6	0.81	0.0545	1.2	389	6	389	6	391	26	100
A578	7067	341	20	0.01	0.7	0.4671	2.3	0.0623	1.6	0.69	0.0544	1.7	389	6	389	8	388	38	100
A530	6749	321	18	0.00	0.1	0.4676	2.1	0.0623	1.6	0.76	0.0545	1.4	389	6	390	7	390	31	100
A524	7377	367	21	0.01	0.1	0.4681	2.0	0.0623	1.3	0.66	0.0545	1.5	390	5	390	6	391	33	100
A557	6300	318	18	0.01	0.1	0.4684	2.4	0.0623	1.5	0.62	0.0545	1.9	390	6	390	8	392	43	99
A566	9135	450	26	0.00	0.2	0.4692	1.9	0.0624	1.4	0.77	0.0545	1.2	390	5	391	6	393	27	99
A543	7463	380	22	0.00	0.2	0.4693	2.0	0.0624	1.5	0.75	0.0545	1.3	390	6	391	7	393	30	99
A594	6885	313	18	0.01	0.2	0.4694	2.0	0.0624	1.4	0.71	0.0545	1.4	390	5	391	7	393	32	99
A572	14326	347	23	0.01	6.4	0.4688	5.9	0.0625	1.8	0.30	0.0544	5.6	391	7	390	19	389	126	100
A587	10027	483	28	0.00	0.1	0.4695	1.9	0.0625	1.5	0.78	0.0545	1.2	391	6	391	6	391	26	100
A561	7058	361	21	0.01	0.0	0.4699	2.0	0.0625	1.3	0.67	0.0545	1.5	391	5	391	6	393	33	100
A582	10745	538	31	0.01	0.6	0.4701	2.1	0.0625	1.5	0.72	0.0546	1.4	391	6	391	7	394	32	99
A597	4210	196	11	0.00	0.5	0.4699	2.4	0.0625	1.6	0.69	0.0545	1.7	391	6	391	8	392	39	100
A568	9664	476	27	0.01	0.0	0.4697	1.9	0.0625	1.4	0.70	0.0545	1.4	391	5	391	6	391	31	100
A590	9003	439	25	0.00	0.2	0.4702	1.8	0.0626	1.5	0.82	0.0545	1.1	391	6	391	6	391	24	100
A533	9238	457	26	0.00	0.1	0.4713	1.9	0.0626	1.6	0.84	0.0546	1.0	392	6	392	6	395	23	99
A584	14005	480	29	0.00	2.6	0.4715	3.5	0.0627	1.4	0.42	0.0546	3.2	392	6	392	11	395	71	99
A513	10289	509	29	0.00	0.1	0.4718	2.2	0.0627	1.7	0.77	0.0546	1.4	392	6	392	7	396	31	99
A591	11172	563	32	0.00	0.0	0.4718	2.1	0.0627	1.6	0.75	0.0546	1.4	392	6	392	7	394	31	100
A593	7994	418	24	0.00	0.1	0.4728	1.9	0.0629	1.6	0.83	0.0545	1.0	393	6	393	6	392	23	100
A580	10029	515	30	0.01	0.1	0.4732	2.1	0.0629	1.6	0.76	0.0546	1.4	393	6	393	7	394	31	100
A585	11542	594	34	0.00	0.0	0.4734	1.8	0.0629	1.5	0.83	0.0546	1.0	393	6	394	6	394	23	100
A595	9419	476	27	0.01	0.0	0.4734	1.9	0.0630	1.4	0.76	0.0545	1.2	394	5	394	6	393	27	100
A541	7551	332	19	0.01	0.6	0.4744	2.3	0.0630	1.6	0.68	0.0546	1.7	394	6	394	8	396	39	99
A589	5606	263	15	0.00	0.0	0.4741	2.0	0.0631	1.5	0.75	0.0545	1.3	394	6	394	7	392	30	100
A522	9349	447	26	0.01	0.3	0.4753	2.2	0.0632	1.6	0.73	0.0546	1.5	395	6	395	7	395	33	100
A588	8017	375	22	0.01	0.2	0.4758	2.0	0.0633	1.6	0.77	0.0546	1.3	395	6	395	7	394	29	100
A554	7482	363	21	0.00	0.2	0.4768	2.1	0.0633	1.5	0.71	0.0546	1.5	396	6	396	7	398	33	100
A540	14398	562	34	0.00	1.5	0.4774	2.7	0.0634	1.4	0.53	0.0547	2.3	396	6	396	9	398	51	99
A523	7582	361	21	0.00	0.1	0.4772	1.9	0.0634	1.5	0.77	0.0546	1.2	396	6	396	6	397	27	100
A576	12211	591	34	0.00	0.0	0.4786	1.7	0.0635	1.4	0.81	0.0547	1.0	397	5	397	6	398	23	100
A569	10352	513	30	0.01	0.0	0.4788	2.0	0.0635	1.6	0.79	0.0547	1.2	397	6	397	7	398	27	100
A581	10952	429	26	0.00	1.2	0.4789	2.9	0.0636	1.5	0.53	0.0546	2.5	397	6	397	10	396	55	100
A564	9275	458	27	0.00	0.1	0.4800	2.1	0.0636	1.4	0.68	0.0547	1.5	398	5	398	7	401	34	99
A529	4964	248	15	0.01	0.1	0.4799	2.6	0.0636	1.4	0.56	0.0547	2.1	398	6	398	8	400	48	99
A577	4562	214	12	0.00	0.0	0.4806	2.3	0.0637	1.5	0.65	0.0547	1.8	398	6	398	8	400	39	100
A527	13417	655	38	0.01	0.0	0.4813	1.8	0.0639	1.4	0.79	0.0546	1.1	399	5	399	6	398	25	100
A575	2291	111	7	0.00	0.1	0.4822	2.9	0.0639	1.7	0.57	0.0547	2.4	399	7	400	10	401	54	99
A514	6194	303	18	0.00	0.1	0.4819	2.0	0.0639	1.5	0.73	0.0547	1.4	399	6	399	7	399	31	100

Grain	^{207}Pb[a] (cps)	U[b] (ppm)	Pb[b] (ppm)	Th[b] / U	^{206}Pbc[c] (%)	$^{207}Pb/^{235}U$[d]	±2σ (%)	$^{206}Pb/^{238}U$[d]	±2σ (%)	ρ[e] (rho)	$^{207}Pb/^{206}Pb$[d]	±2σ (%)	$^{206}Pb/^{238}U$[f]	±2σ (Ma)	$^{207}Pb/^{235}U$[f]	±2σ (Ma)	$^{207}Pb/^{206}Pb$[f]	±2σ (Ma)	Conc.[g] (%)
A583	6266	315	18	0.00	0.5	0.4827	2.3	0.0640	1.6	0.69	0.0547	1.7	400	6	400	8	401	38	100
A562	6844	322	19	0.01	0.0	0.4841	2.0	0.0642	1.6	0.79	0.0547	1.2	401	6	401	7	401	27	100
A536	10991	532	31	0.00	0.3	0.4840	2.2	0.0642	1.6	0.75	0.0547	1.4	401	6	401	7	399	32	100
A546	6227	295	17	0.01	0.2	0.4855	2.3	0.0643	1.6	0.70	0.0548	1.6	401	6	402	8	404	36	99
A538	11235	541	32	0.00	0.0	0.4857	1.9	0.0643	1.3	0.69	0.0548	1.4	402	5	402	6	402	30	100
A571	7715	383	23	0.00	0.0	0.4879	2.2	0.0646	1.7	0.77	0.0548	1.4	404	7	403	7	403	31	100
A525	8446	398	24	0.00	0.1	0.4876	2.3	0.0646	1.8	0.78	0.0548	1.4	404	7	403	8	402	32	100
A519	12534	634	38	0.00	0.1	0.4886	2.0	0.0647	1.4	0.71	0.0548	1.4	404	6	404	7	404	31	100
A556	7402	334	20	0.00	1.2	0.4884	3.0	0.0647	1.5	0.51	0.0548	2.5	404	6	404	10	403	57	100
A520	9728	452	27	0.00	0.1	0.4981	2.2	0.0657	1.7	0.77	0.0550	1.4	410	7	410	8	412	32	100
A07	206	6	1	0.12	9.1	0.5794	16.4	0.0732	4.2	0.25	0.0574	15.9	455	18	464	63	508	349	90
A555	42836	411	42	0.00	21.3	0.5772	9.6	0.0732	2.6	0.27	0.0572	9.3	456	12	463	36	498	204	92
A09	775	27	2	0.22	6.6	0.5873	10.2	0.0755	2.2	0.21	0.0564	9.9	469	10	469	39	469	220	100
A06	949	14	2	0.43	16.3	0.6061	12.1	0.0776	3.8	0.32	0.0567	11.5	482	18	481	47	478	253	101
A08	*-680*	*5*	*0*	*0.16*	*4.2*	*1.6240*	*-*	*0.0608*	*19.4*	*-*	*0.1936*	*-*	*381*	*72*	*980*	*-*	*2773*	*-*	*14*
91500[h]	8378	74	13	0.29	0.5	0.1795	1.4	1.8499	1.8	0.07	0.9148	0.5	1064	14	1063	12	1062	18	100
Felix[h]	12482	435	68	2.47	0.2	0.0821	3.0	0.6484	3.0	0.06	2.9654	0.4	509	15	507	12	502	65	102
Plesovice[h]	2852	651	34	0.09	1.3	0.0542	2.2	0.3989	4.1	0.05	2.8587	0.5	340	7	341	12	345	64	99
GJ-1[h]	9719	290	27	0.04	0.1	0.0984	1.2	0.8151	2.4	0.06	2.2245	0.5	605	7	605	11			

$^{206}Pb/^{238}U$ error is the quadratic additions of the within run precision (2 SE) and the external reproducibility (2 SD) of the reference zircon. $^{207}Pb/^{206}Pb$ error propagation (^{207}Pb signal dependent) following Gerdes & Zeh (2009). $^{207}Pb/^{235}U$ error is the quadratic addition of the $^{207}Pb/^{206}Pb$ and $^{206}Pb/^{238}U$ uncertainty.

[a] Within run background-corrected mean ^{207}Pb signal in cps (counts per second).

[b] U and Pb content and Th/U ratio were calculated relative to GJ-1 reference zircon.

[c] Percentage of the common Pb on the ^{206}Pb. b.d. = below detection limit.

[d] Pb/U and Pb/Pb ratios. Corrected for background, within-run Pb/U fractionation (in case of $^{206}Pb/^{238}U$) and common Pb using Stacy and Kramers (1975) model Pb composition and subsequently normalised to GJ-1 (ID-TIMS value/measured value); $^{207}Pb/^{235}U$ calculated using (($^{207}Pb/^{206}Pb$)*($^{238}U/^{206}Pb$)*137.88).

[e] Rho (ρ) is the ($^{206}Pb/^{238}U$)/($^{207}Pb/^{235}U$) error correlation coefficient.

[f] Pb/U and Pb/Pb ages.

[g] Degree of concordance = (($^{206}Pb/^{238}U$ age)/($^{207}Pb/^{206}Pb$ age)) x 100.

[h] Mean of 13 (91500), 13 (Felix), 13 (Plesovice), and 26(GJ-1) analyses, respectively.

Table Ig6-U

U, Th and Pb LA-ICP-MS data of zircon crystals from sample GCH-22

Grain	^{207}Pb[a] (cps)	U[b] (ppm)	Pb[b] (ppm)	Th[b] U	^{206}Pbc[c] (%)	^{207}Pb[d] ^{235}U	±2σ (%)	^{206}Pb[d] ^{238}U	±2σ (%)	ρ[e] (rho)	^{207}Pb[d] ^{206}Pb	±2σ (%)	^{206}Pb[f] ^{238}U	±2σ (Ma)	^{207}Pb[f] ^{235}U	±2σ (Ma)	^{207}Pb[f] ^{206}Pb	±2σ (Ma)	Conc.[g] (%)
A428	2432	182	11	0.20	0.2	0.4698	3.0	0.0624	1.7	0.57	0.0546	2.5	390	7	391	10	397	56	98
A451	310	33	2	0.01	3.7	0.4728	15.0	0.0628	2.3	0.15	0.0546	14.9	393	9	393	50	395	333	99
A445	848	35	3	0.01	14.6	0.4765	17.6	0.0638	3.9	0.22	0.0542	17.2	398	15	396	60	380	387	105
A430	2544	355	23	0.18	1.3	0.4805	3.7	0.0639	1.6	0.44	0.0546	3.3	399	6	398	12	394	74	101
A421	13715	1248	84	0.09	0.5	0.5345	2.3	0.0697	1.6	0.71	0.0556	1.6	434	7	435	8	437	36	99
A422	4592	490	36	0.23	2.1	0.5386	4.2	0.0703	1.5	0.37	0.0556	3.9	438	6	438	15	434	87	101
A434	2869	366	26	0.19	0.2	0.5473	2.4	0.0710	1.5	0.60	0.0559	1.9	442	6	443	9	448	43	99
A437	2111	287	20	0.23	0.2	0.5527	3.6	0.0713	1.5	0.41	0.0562	3.3	444	6	447	13	461	72	96
A366	4198	536	37	0.12	0.1	0.5550	2.5	0.0713	1.4	0.56	0.0565	2.1	444	6	448	9	470	46	94
A424	2872	354	25	0.21	0.2	0.5528	3.0	0.0715	1.5	0.48	0.0561	2.7	445	6	447	11	456	59	98
A420	2576	166	12	0.18	0.1	0.5516	2.9	0.0715	1.7	0.56	0.0559	2.4	445	7	446	11	450	54	99
A372	2969	400	28	0.19	0.1	0.5577	2.7	0.0718	1.5	0.53	0.0563	2.3	447	6	450	10	465	51	96
A395	4598	513	39	0.26	0.8	0.5696	2.7	0.0730	1.6	0.59	0.0566	2.2	454	7	458	10	477	48	95
A392	4073	507	38	0.26	0.0	0.5788	3.0	0.0734	1.6	0.52	0.0572	2.6	457	7	464	11	498	57	92
A425	7062	945	69	0.20	0.1	0.5695	2.1	0.0735	1.4	0.66	0.0562	1.6	457	6	458	8	459	36	100
A390	2944	359	26	0.18	0.2	0.5749	2.8	0.0736	1.4	0.52	0.0567	2.3	458	6	461	10	478	52	96
A412	3175	405	30	0.21	0.1	0.5807	3.0	0.0738	1.5	0.51	0.0571	2.6	459	7	465	11	495	57	93
A398	2883	366	27	0.23	0.2	0.5749	2.9	0.0739	1.5	0.51	0.0564	2.5	460	7	461	11	468	56	98
A380	2995	374	28	0.23	b.d.	0.5862	2.8	0.0745	1.5	0.52	0.0571	2.4	463	7	468	11	494	53	94
A402	3729	472	36	0.25	0.0	0.5820	3.3	0.0746	1.4	0.43	0.0566	3.0	464	6	466	12	474	66	98
A393	3116	390	29	0.22	0.0	0.5826	2.9	0.0747	1.8	0.64	0.0566	2.2	464	8	466	11	475	49	98
A365	3114	387	29	0.18	0.1	0.5900	3.0	0.0750	1.6	0.54	0.0571	2.5	466	7	471	11	494	56	94
A403	3774	447	33	0.18	0.1	0.5933	3.2	0.0751	1.6	0.52	0.0573	2.7	467	7	473	12	503	60	93
A382	3124	373	28	0.24	0.0	0.5921	2.6	0.0751	1.5	0.59	0.0572	2.1	467	7	472	10	498	45	94
A370	3127	181	14	0.23	0.3	0.5881	3.2	0.0752	1.5	0.46	0.0567	2.8	468	7	470	12	480	62	97
A414	3228	390	30	0.23	0.2	0.5873	3.4	0.0752	1.6	0.47	0.0566	3.0	468	7	469	13	476	66	98
A371	3219	383	29	0.22	0.3	0.5888	3.4	0.0753	1.7	0.50	0.0567	2.9	468	8	470	13	481	64	97
A401	3288	409	31	0.23	0.1	0.5853	3.1	0.0753	1.6	0.52	0.0564	2.6	468	7	468	12	467	58	100
A378	3737	451	35	0.29	0.2	0.5904	2.7	0.0754	1.5	0.57	0.0568	2.2	469	7	471	10	482	49	97
A389	2975	372	28	0.22	b.d.	0.5951	2.8	0.0755	1.5	0.54	0.0572	2.3	469	7	474	10	498	51	94
A391	2775	331	25	0.22	0.1	0.5933	2.3	0.0757	1.4	0.64	0.0569	1.7	470	7	473	9	486	38	97
A376	3640	212	16	0.27	0.1	0.5988	2.7	0.0758	1.4	0.50	0.0573	2.3	471	6	476	10	504	51	93
A375	3064	372	28	0.21	0.1	0.5974	2.7	0.0759	1.5	0.54	0.0571	2.3	472	7	476	10	494	50	96
A397	3183	382	29	0.19	b.d.	0.5988	2.7	0.0761	1.5	0.56	0.0570	2.2	473	7	476	10	493	49	96
A406	3274	198	15	0.22	0.0	0.5936	2.7	0.0762	1.6	0.58	0.0565	2.2	473	7	473	10	472	49	100
A410	3599	364	28	0.22	1.4	0.5991	3.8	0.0762	1.7	0.44	0.0570	3.4	473	8	477	14	492	75	96
A377	2996	355	27	0.20	0.3	0.5979	3.1	0.0762	1.5	0.48	0.0569	2.7	473	7	476	12	487	59	97
A368	3320	401	33	0.22	0.1	0.5996	2.8	0.0763	1.6	0.58	0.0570	2.3	474	7	477	11	492	50	96
A426	3699	221	17	0.26	0.1	0.6009	2.9	0.0763	1.5	0.50	0.0571	2.5	474	7	478	11	497	55	95
A408	61010	1879	190	0.10	11.7	0.5990	7.7	0.0763	2.1	0.27	0.0570	7.4	474	9	477	30	490	164	97
A363	4182	515	39	0.19	0.1	0.5964	2.4	0.0763	1.5	0.63	0.0567	1.8	474	7	475	9	479	41	99
A369	3886	228	18	0.27	0.2	0.5980	2.8	0.0764	1.5	0.52	0.0568	2.4	474	7	476	11	484	53	98
A405	3468	431	33	0.23	0.0	0.6038	2.7	0.0764	1.7	0.61	0.0574	2.2	474	8	480	11	505	48	94
A433	4055	229	18	0.25	0.2	0.6017	3.4	0.0765	1.6	0.49	0.0570	3.0	475	8	478	13	492	65	97
A417	2946	178	13	0.16	0.1	0.6012	2.7	0.0766	1.6	0.58	0.0569	2.2	476	7	478	11	487	49	98
A411	7231	840	67	0.25	0.1	0.6057	2.9	0.0768	1.7	0.60	0.0572	2.3	477	8	481	11	500	51	95
A388	3349	395	31	0.23	b.d.	0.6075	2.7	0.0769	1.5	0.57	0.0573	2.2	477	7	482	10	504	49	95
A374	3468	428	33	0.25	0.1	0.6012	2.5	0.0769	1.5	0.60	0.0567	2.0	477	7	478	9	481	44	99
A432	3697	439	34	0.26	0.3	0.6010	2.6	0.0771	1.5	0.58	0.0565	2.1	479	7	478	10	473	47	101
A407	3509	424	33	0.21	0.0	0.6070	2.6	0.0773	1.5	0.57	0.0570	2.1	480	7	482	10	491	46	98
A429	3208	181	14	0.22	0.2	0.6049	2.6	0.0774	1.5	0.57	0.0567	2.1	481	7	480	10	479	47	100
A361	4344	516	41	0.29	0.1	0.6066	2.3	0.0774	1.6	0.67	0.0568	1.7	481	7	481	9	484	38	99
A416	3563	442	35	0.26	b.d.	0.6063	2.9	0.0775	1.6	0.55	0.0568	2.4	481	7	481	11	482	53	100
A367	3667	449	35	0.20	0.1	0.6063	2.8	0.0776	1.4	0.48	0.0567	2.5	482	6	481	11	480	54	100
A404	3713	456	36	0.26	0.2	0.6127	2.9	0.0776	1.4	0.49	0.0573	2.5	482	7	485	11	502	55	96
A364	2486	300	24	0.24	b.d.	0.6122	3.1	0.0777	1.7	0.55	0.0572	2.6	482	8	485	12	498	58	97
A394	5165	474	37	0.13	2.5	0.6137	3.9	0.0778	1.5	0.39	0.0572	3.6	483	7	486	15	499	79	97
A409	3876	465	37	0.28	0.2	0.6098	2.2	0.0779	1.5	0.67	0.0568	1.6	484	7	483	8	483	35	100
A427	4466	235	19	0.29	0.6	0.6111	2.9	0.0780	1.4	0.49	0.0568	2.5	484	7	484	11	484	56	100
A413	2913	340	27	0.24	0.1	0.6146	3.2	0.0781	1.5	0.47	0.0571	2.8	485	7	486	12	495	62	98
A400	3198	387	31	0.23	0.0	0.6192	2.8	0.0783	1.6	0.57	0.0574	2.3	486	7	489	11	506	50	96
A418	3274	185	14	0.20	0.2	0.6171	2.7	0.0784	1.5	0.55	0.0571	2.3	486	7	488	11	495	51	98
A396	3461	420	33	0.20	0.1	0.6180	3.0	0.0784	1.5	0.49	0.0572	2.6	486	7	489	12	498	57	98
A362	8447	1016	82	0.29	b.d.	0.6258	2.2	0.0785	1.5	0.68	0.0578	1.7	487	7	493	9	523	36	93
A415	3803	457	36	0.20	0.1	0.6179	2.6	0.0785	1.4	0.56	0.0571	2.1	487	7	489	10	494	47	99
A381	3142	378	30	0.21	0.1	0.6201	3.3	0.0787	1.4	0.43	0.0572	3.0	488	7	490	13	497	66	98
A373	3140	353	28	0.22	0.6	0.6211	3.1	0.0790	1.6	0.52	0.0570	2.6	490	8	491	12	492	58	100

Grain	^{207}Pb[a] (cps)	U[b] (ppm)	Pb[b] (ppm)	Th[b] / U	^{206}Pbc[c] (%)	^{207}Pb[d] / ^{235}U	±2σ (%)	^{206}Pb[d] / ^{238}U	±2σ (%)	ρ[e] (rho)	^{207}Pb[d] / ^{206}Pb	±2σ (%)	^{206}Pb[f] / ^{238}U	±2σ (Ma)	^{207}Pb[f] / ^{235}U	±2σ (Ma)	^{207}Pb[f] / ^{206}Pb	±2σ (Ma)	Conc.[g] (%)
A379	3785	463	37	0.27	b.d.	0.6220	2.9	0.0791	1.5	0.54	0.0570	2.4	491	7	491	11	492	53	100
A399	3730	459	37	0.26	0.0	0.6276	3.2	0.0792	1.6	0.49	0.0574	2.8	492	7	495	13	509	61	97
A436	3186	402	32	0.26	0.0	0.6281	2.9	0.0793	1.5	0.52	0.0575	2.5	492	7	495	11	510	54	96
A423	8523	459	43	0.26	8.4	0.6296	7.2	0.0798	1.7	0.24	0.0572	6.9	495	8	496	28	500	153	99
A435	3382	418	34	0.23	0.2	0.6303	2.9	0.0801	1.5	0.52	0.0571	2.5	497	7	496	12	494	55	101
A447	28836	1078	108	0.11	9.9	0.6422	6.4	0.0803	2.2	0.34	0.0580	6.0	498	10	504	26	529	131	94
A449	3482	371	31	0.25	0.2	0.6415	3.4	0.0812	1.5	0.44	0.0573	3.0	503	7	503	14	503	67	100
A452	6733	762	60	0.12	0.3	0.6473	2.7	0.0815	1.4	0.53	0.0576	2.3	505	7	507	11	514	51	98
A419	6675	386	31	0.18	0.2	0.6457	2.4	0.0816	1.6	0.66	0.0574	1.8	506	8	506	10	507	40	100
A444	*439*	*16*	*1*	*0.02*	*2.6*	*0.6424*	*12.1*	*0.0562*	*4.3*	*0.35*	*0.0829*	*11.3*	*352*	*15*	*504*	*49*	*1267*	*221*	*28*
A431	*69852*	*1309*	*170*	*0.36*	*22.2*	*0.5345*	*14.6*	*0.0681*	*4.7*	*0.32*	*0.0569*	*13.8*	*425*	*19*	*435*	*53*	*489*	*304*	*87*
A438	*1561*	*12*	*10*	*0.01*	*36.8*	*113.40*	*32.9*	*0.0813*	*9.6*	*0.29*	*10.120*	*31.5*	*504*	*47*	*4813*	*401*	-	-	-
A446	*172*	*10*	-	*0.02*	*3957*	-	-	-	-	-	*10.120*	####	-	-	-	-	-	-	-
A448	*89*	-	-	-	-	-	-	-	-	-	-	-	-	-	-	-	-	-	-
A450	-	-	-	-	-	-	-	-	-	-	-	-	-	-	-	-	-	-	-
91500[h]	7004	61	11	0.25	0.4	0.1794	2.1	1.8382	3.2	0.07	1.5934	0.6	1063	20	1059	21	1050	32	101
Felix[h]	6572	361	52	2.08	0.4	0.0810	3.3	0.6372	3.3	0.06	2.2877	0.5	502	16	501	13	492	50	102
Plesovice[h]	2310	955	49	0.08	0.1	0.0542	1.5	0.4000	1.6	0.05	1.3002	0.5	340	5	342	5	351	29	97
GJ-1[h]	6697	306	28	0.03	0.2	0.0983	1.3	0.8144	2.1	0.06	2.1705	0.5	604	7	605	10			

$^{206}Pb/^{238}U$ error is the quadratic additions of the within run precision (2 SE) and the external reproducibility (2 SD) of the reference zircon. $^{207}Pb/^{206}Pb$ error propagation (^{207}Pb signal dependent) following Gerdes & Zeh (2009). $^{207}Pb/^{235}U$ error is the quadratic addition of the $^{207}Pb/^{206}Pb$ and $^{206}Pb/^{238}U$ uncertainty.

[a] Within run background-corrected mean ^{207}Pb signal in cps (counts per second).

[b] U and Pb content and Th/U ratio were calculated relative to GJ-1 reference zircon.

[c] Percentage of the common Pb on the ^{206}Pb. b.d. = below detection limit.

[d] Pb/U and Pb/Pb ratios. Corrected for background, within-run Pb/U fractionation (in case of $^{206}Pb/^{238}U$) and common Pb using Stacy and Kramers (1975) model Pb composition and subsequently normalised to GJ-1 (ID-TIMS value/measured value); $^{207}Pb/^{235}U$ calculated using (($^{207}Pb/^{206}Pb$)*($^{238}U/^{206}Pb$)*137.88).

[e] Rho (ρ) is the ($^{206}Pb/^{238}U$)/($^{207}Pb/^{235}U$) error correlation coefficient.

[f] Pb/U and Pb/Pb ages.

[g] Degree of concordance = (($^{206}Pb/^{238}U$ age)/($^{207}Pb/^{206}Pb$ age)) x 100.

[h] Mean of 13 (91500), 13 (Felix), 13 (Plesovice), and 26(GJ-1) analyses, respectively.

Table Ig7-U

U, Th and Pb LA-ICP-MS data of zircon crystals from sample GCH-23

Grain	$^{207}Pb^{a}$ (cps)	U^{b} (ppm)	Pb^{b} (ppm)	$\underline{Th}^{b}$ U	$^{206}Pbc^{c}$ (%)	$\underline{^{207}Pb}^{d}$ ^{235}U	±2σ (%)	$\underline{^{206}Pb}^{d}$ ^{238}U	±2σ (%)	ρ[e] (rho)	$\underline{^{207}Pb}^{d}$ ^{206}Pb	±2σ (%)	$\underline{^{206}Pb}^{f}$ ^{238}U	±2σ (Ma)	$\underline{^{207}Pb}^{f}$ ^{235}U	±2σ (Ma)	$\underline{^{207}Pb}^{f}$ ^{206}Pb	±2σ (Ma)	Conc.[g] (%)
A130	13733	788	132	9.17	0.2	0.5487	3.0	0.0719	2.0	0.68	0.0553	2.2	448	9	444	11	425	49	105
A152	11880	1347	156	2.79	0.5	0.5818	3.0	0.0752	1.6	0.53	0.0562	2.5	467	7	466	11	458	56	102
A151	1637	93	8	0.89	0.0	0.5829	4.5	0.0753	1.8	0.39	0.0561	4.2	468	8	466	17	457	92	102
A119	3593	440	43	1.56	0.0	0.5943	2.9	0.0754	1.3	0.46	0.0572	2.5	469	6	474	11	498	56	94
A123	3766	473	41	0.97	0.0	0.5950	2.9	0.0756	1.2	0.41	0.0571	2.7	470	5	474	11	496	59	95
A160	2476	112	9	0.71	2.5	0.5878	10.3	0.0758	1.9	0.18	0.0562	10.1	471	9	469	39	462	224	102
A137	2051	126	10	0.42	b.d.	0.5998	3.5	0.0763	1.5	0.42	0.0570	3.2	474	7	477	13	492	70	96
A124	1861	237	20	0.79	b.d.	0.6108	3.5	0.0774	1.6	0.44	0.0573	3.2	480	7	484	14	502	70	96
A144	6999	402	38	1.29	0.3	0.6029	3.8	0.0774	1.4	0.36	0.0565	3.5	481	6	479	15	472	78	102
A122	3832	452	44	1.56	b.d.	0.6144	2.9	0.0775	1.5	0.52	0.0575	2.5	481	7	486	11	512	54	94
A162	972	55	4	0.28	0.2	0.6123	4.5	0.0780	1.5	0.34	0.0569	4.2	484	7	485	17	489	93	99
A142	1061	65	5	0.49	b.d.	0.6154	4.0	0.0781	1.6	0.39	0.0572	3.7	485	7	487	16	498	81	97
A158	8787	612	68	2.20	0.0	0.6122	1.9	0.0782	1.2	0.62	0.0568	1.5	486	6	485	8	482	34	101
A140	811	46	4	0.40	b.d.	0.6140	6.7	0.0784	2.0	0.30	0.0568	6.4	486	9	486	26	485	141	100
A125	3772	452	36	0.42	b.d.	0.6256	2.9	0.0789	1.4	0.50	0.0575	2.5	490	7	493	11	511	54	96
A128	3000	338	29	0.69	b.d.	0.6190	2.7	0.0790	1.6	0.59	0.0568	2.2	490	8	489	11	485	49	101
A120	1593	192	17	0.81	b.d.	0.6243	4.1	0.0791	1.4	0.34	0.0573	3.8	491	6	493	16	502	85	98
A159	2862	160	14	0.73	b.d.	0.6236	3.0	0.0791	1.6	0.51	0.0572	2.6	491	7	492	12	498	57	98
A121	2028	211	19	0.75	0.1	0.6296	4.3	0.0792	1.5	0.35	0.0577	4.1	491	7	496	17	518	89	95
A154	892	111	9	0.36	0.0	0.6261	4.2	0.0793	1.5	0.37	0.0573	3.9	492	7	494	16	503	85	98
A164	2196	130	11	0.65	0.1	0.6377	3.5	0.0794	1.6	0.45	0.0583	3.1	493	7	501	14	539	68	91
A115	1483	181	14	0.29	b.d.	0.6312	3.8	0.0798	1.5	0.38	0.0574	3.5	495	7	497	15	507	78	98
A116	1924	230	19	0.53	0.2	0.6423	3.2	0.0811	1.6	0.51	0.0575	2.7	502	8	504	13	510	60	99
A113	2760	348	31	0.74	0.0	0.6422	2.7	0.0811	1.4	0.51	0.0574	2.3	503	7	504	11	509	52	99
A157	1837	103	9	0.47	b.d.	0.6472	3.9	0.0812	1.5	0.38	0.0578	3.6	504	7	507	16	521	80	97
A145	665	80	7	0.39	b.d.	0.6462	7.3	0.0818	1.6	0.22	0.0573	7.1	507	8	506	29	504	156	100
A131	997	119	10	0.46	b.d.	0.6499	5.1	0.0818	1.4	0.27	0.0576	4.9	507	7	508	21	514	108	99
A141	9223	510	66	3.00	0.0	0.6478	2.1	0.0819	1.3	0.63	0.0574	1.6	507	6	507	8	506	36	100
A127	8744	1027	122	2.51	0.0	0.6522	2.0	0.0819	1.3	0.66	0.0577	1.5	508	6	510	8	520	33	98
A134	2625	300	28	0.88	b.d.	0.6556	3.3	0.0823	1.3	0.41	0.0578	3.0	510	7	512	13	522	66	98
A156	1589	91	7	0.37	b.d.	0.6548	3.7	0.0824	1.5	0.41	0.0577	3.4	510	7	511	15	517	74	99
A143	5431	311	33	1.71	b.d.	0.6576	2.7	0.0827	1.8	0.68	0.0577	2.0	512	9	513	11	517	44	99
A163	3565	410	34	0.38	b.d.	0.6540	3.2	0.0829	1.4	0.43	0.0573	2.9	513	7	511	13	501	64	102
A153	10187	542	65	2.37	0.0	0.6634	2.3	0.0834	1.6	0.70	0.0577	1.6	517	8	517	9	517	35	100
A138	1809	99	9	0.53	0.2	0.6694	10.4	0.0846	1.7	0.16	0.0574	10.3	523	9	520	43	507	227	103
A114	3670	414	44	1.45	0.0	0.6823	3.0	0.0847	1.9	0.64	0.0584	2.3	524	10	528	13	545	51	96
A117	3313	360	34	0.92	b.d.	0.6839	3.1	0.0852	1.4	0.46	0.0582	2.7	527	7	529	13	539	60	98
A155	3617	223	24	1.58	0.0	0.6913	2.9	0.0856	1.7	0.58	0.0586	2.3	529	9	534	12	552	51	96
A118	1485	143	14	0.42	0.8	0.8000	4.6	0.0961	1.5	0.33	0.0604	4.3	592	9	597	21	616	93	96
A135	1180	23	3	1.74	b.d.	0.8287	3.7	0.1000	1.8	0.49	0.0601	3.2	615	11	613	17	606	69	101
A133	*3169*	*412*	*30*	*0.29*	*0.4*	*0.5849*	*2.7*	*0.0735*	*1.3*	*0.48*	*0.0577*	*2.4*	*457*	*6*	*468*	*10*	*519*	*52*	*88*
A139	*630*	*35*	*3*	*0.40*	*b.d.*	*0.6293*	*5.7*	*0.0776*	*1.8*	*0.31*	*0.0588*	*5.4*	*482*	*8*	*496*	*23*	*559*	*118*	*86*
A126	*3537*	*128*	*14*	*0.67*	*13.6*	*0.5837*	*13.3*	*0.0781*	*2.6*	*0.19*	*0.0542*	*13.0*	*484*	*12*	*467*	*51*	*381*	*292*	*127*
A132	*1083*	*67*	*5*	*0.46*	*b.d.*	*0.6541*	*4.2*	*0.0782*	*1.7*	*0.41*	*0.0607*	*3.9*	*485*	*8*	*511*	*17*	*629*	*83*	*77*
A161	*1427*	*108*	*10*	*0.52*	*2.4*	*0.6685*	*5.1*	*0.0801*	*1.7*	*0.35*	*0.0605*	*4.7*	*497*	*8*	*520*	*21*	*622*	*102*	*80*
A136	*637*	*35*	*3*	*0.69*	*0.4*	*0.7794*	*4.8*	*0.0816*	*1.9*	*0.39*	*0.0693*	*4.4*	*505*	*9*	*585*	*22*	*908*	*91*	*56*
A129	*3142*	*61*	*10*	*0.91*	*b.d.*	*1.9110*	*3.6*	*0.1386*	*1.6*	*0.43*	*0.1000*	*3.3*	*837*	*12*	*1085*	*25*	*1624*	*61*	*52*

Grain	^{207}Pb[a] (cps)	U[b] (ppm)	Pb[b] (ppm)	Th[b] / U	^{206}Pbc[c] (%)	$^{207}Pb/^{235}U$[d]	±2σ (%)	$^{206}Pb/^{238}U$[d]	±2σ (%)	ρ[e] (rho)	$^{207}Pb/^{206}Pb$[d]	±2σ (%)	$^{206}Pb/^{238}U$[f]	±2σ (Ma)	$^{207}Pb/^{235}U$[f]	±2σ (Ma)	$^{207}Pb/^{206}Pb$[f]	±2σ (Ma)	Conc.[g] (%)
91500[h]	8532	69	13	0.45	0.3	0.1784	3.8	1.8103	6.1	0.07	4.3867	0.6	1058	37	1049	40	1030	89	103
Felix[h]	4019	203	23	1.93	0.4	0.0808	4.3	0.6109	10.3	0.05	7.7221	0.4	501	21	484	40	402	176	132
Plesovice[h]	2881	1038	54	0.16	0.2	0.0549	3.8	0.4045	3.8	0.05	1.5557	0.5	344	13	345	11	348	35	99
GJ-1[h]	6932	290	26	0.02	0.1	0.0984	1.1	0.8158	2.0	0.06	2.0856	0.5	605	6	606	9			

$^{206}Pb/^{238}U$ error is the quadratic additions of the within run precision (2 SE) and the external reproducibility (2 SD) of the reference zircon. $^{207}Pb/^{206}Pb$ error propagation (^{207}Pb signal dependent) following Gerdes & Zeh (2009). $^{207}Pb/^{235}U$ error is the quadratic addition of the $^{207}Pb/^{206}Pb$ and $^{206}Pb/^{238}U$ uncertainty.

[a] Within run background-corrected mean ^{207}Pb signal in cps (counts per second).

[b] U and Pb content and Th/U ratio were calculated relative to GJ-1 reference zircon.

[c] Percentage of the common Pb on the ^{206}Pb. b.d. = below detection limit.

[d] Pb/U and Pb/Pb ratios. Corrected for background, within-run Pb/U fractionation (in case of $^{206}Pb/^{238}U$) and common Pb using Stacy and Kramers (1975) model Pb composition and subsequently normalised to GJ-1 (ID-TIMS value/measured value); $^{207}Pb/^{235}U$ calculated using (($^{207}Pb/^{206}Pb$)*($^{238}U/^{206}Pb$)*137.88).

[e] Rho (ρ) is the ($^{206}Pb/^{238}U$)/($^{207}Pb/^{235}U$) error correlation coefficient.

[f] Pb/U and Pb/Pb ages.

[g] Degree of concordance = (($^{206}Pb/^{238}U$ age)/($^{207}Pb/^{206}Pb$ age)) x 100.

[h] Mean of 11 (91500), 11 (Felix), 9 (Plesovice), and 26 (GJ-1) analyses, respectively.

Table Ig8-U

U, Th and Pb LA-ICP-MS data of zircon crystals from sample GCH-01

Grain	^{207}Pb[a] (cps)	U[b] (ppm)	Pb[b] (ppm)	Th[b] U	^{206}Pbc[c] (%)	^{207}Pb[d] / ^{235}U	±2σ (%)	^{206}Pb[d] / ^{238}U	±2σ (%)	ρ[e] (rho)	^{207}Pb[d] / ^{206}Pb	±2σ (%)	^{206}Pb[f] / ^{238}U	±2σ (Ma)	^{207}Pb[f] / ^{235}U	±2σ (Ma)	^{207}Pb[f] / ^{206}Pb	±2σ (Ma)	Conc.[g] (%)
A446	4522	558	31	0.00	0.0	0.4637	2.5	0.0609	1.5	0.59	0.0552	2.0	381	5	387	8	420	44	91
A548	3404	400	23	0.04	0.5	0.4649	3.1	0.0618	1.7	0.56	0.0546	2.6	386	6	388	10	396	58	98
A491	5018	613	35	0.04	0.0	0.4684	2.4	0.0621	1.4	0.57	0.0547	2.0	388	5	390	8	401	45	97
A571	6357	781	45	0.00	0.0	0.4815	2.0	0.0635	1.2	0.57	0.0550	1.7	397	5	399	7	413	38	96
A584	6900	139	11	0.02	11.6	0.4859	8.3	0.0639	2.0	0.24	0.0552	8.1	399	8	402	28	419	180	95
A541	9679	741	48	0.01	4.0	0.4844	4.9	0.0640	1.5	0.31	0.0549	4.6	400	6	401	16	407	104	98
A456	9150	1145	67	0.01	b.d.	0.4832	2.1	0.0641	1.3	0.62	0.0547	1.7	401	5	400	7	398	37	101
A554	7789	927	56	0.06	0.1	0.4895	2.2	0.0643	1.3	0.56	0.0552	1.9	402	5	405	8	420	41	96
A449	7144	922	54	0.01	b.d.	0.4919	2.0	0.0644	1.4	0.69	0.0554	1.5	402	5	406	7	428	32	94
A540	7626	901	54	0.01	0.0	0.4939	2.2	0.0650	1.6	0.73	0.0551	1.5	406	6	408	7	417	34	97
A468	17139	1897	128	0.62	0.6	0.4951	2.8	0.0654	1.4	0.51	0.0549	2.5	408	6	408	10	409	55	100
A481	802	42	3	0.13	0.3	0.4965	4.0	0.0654	1.9	0.48	0.0550	3.5	409	8	409	14	414	79	99
A555	10757	1334	81	0.05	0.0	0.4968	2.1	0.0657	1.4	0.66	0.0548	1.6	410	6	410	7	405	35	101
A539	4223	480	32	0.18	b.d.	0.5315	2.9	0.0695	1.4	0.47	0.0554	2.6	433	6	433	10	430	57	101
A545	4334	215	16	0.38	b.d.	0.5923	2.8	0.0749	1.3	0.47	0.0573	2.5	466	6	472	11	504	55	92
A415	4532	228	18	0.44	b.d.	0.6045	2.4	0.0762	1.3	0.52	0.0575	2.0	473	6	480	9	512	45	92
A434	3228	174	13	0.37	0.0	0.6063	2.1	0.0763	1.4	0.68	0.0576	1.5	474	6	481	8	515	34	92
A426	3993	203	15	0.32	b.d.	0.6164	3.0	0.0770	1.3	0.44	0.0581	2.7	478	6	488	12	532	60	90
A567	4053	191	15	0.42	b.d.	0.6097	2.4	0.0771	1.3	0.52	0.0574	2.1	478	6	483	9	507	45	94
A511	4552	213	17	0.44	b.d.	0.6190	2.5	0.0776	1.3	0.50	0.0579	2.2	482	6	489	10	525	48	92
A416	6958	358	28	0.50	0.0	0.6131	2.2	0.0777	1.2	0.55	0.0572	1.9	482	6	486	9	501	41	96
A460	6547	314	25	0.47	0.2	0.6129	2.0	0.0778	1.4	0.70	0.0571	1.4	483	6	485	8	496	31	97
A483	4706	232	18	0.39	b.d.	0.6205	2.7	0.0779	1.4	0.50	0.0578	2.4	483	6	490	11	522	52	93
A532	4726	251	19	0.23	0.1	0.6090	2.7	0.0779	1.3	0.49	0.0567	2.3	483	6	483	10	481	51	101
A575	3970	186	15	0.41	b.d.	0.6219	2.4	0.0780	1.5	0.60	0.0578	1.9	484	7	491	9	522	43	93
A577	6246	290	23	0.46	0.0	0.6212	2.2	0.0781	1.2	0.57	0.0577	1.8	485	6	491	8	517	39	94
A530	4254	193	16	0.57	0.0	0.6293	2.4	0.0783	1.4	0.61	0.0583	1.9	486	7	496	9	540	41	90
A471	2459	122	9	0.33	b.d.	0.6281	2.6	0.0784	1.5	0.59	0.0581	2.1	486	7	495	10	534	46	91
A525	31380	286	37	0.43	23.7	0.6294	10.9	0.0785	2.8	0.26	0.0582	10.5	487	13	496	44	536	230	91
A455	3921	190	15	0.40	b.d.	0.6257	2.9	0.0785	1.4	0.48	0.0578	2.6	487	7	493	11	523	56	93
A453	5554	284	22	0.43	0.0	0.6229	2.1	0.0785	1.3	0.63	0.0575	1.6	487	6	492	8	512	36	95
A578	4362	211	17	0.40	b.d.	0.6222	2.6	0.0785	1.5	0.61	0.0575	2.0	487	7	491	10	509	45	96
A417	2009	101	8	0.28	0.4	0.6298	4.2	0.0787	1.6	0.38	0.0580	3.9	489	7	496	17	531	85	92
A533	6828	322	26	0.50	0.4	0.6294	2.3	0.0788	1.3	0.56	0.0580	2.0	489	6	496	9	529	43	92
A524	7584	361	30	0.58	0.0	0.6256	2.2	0.0788	1.2	0.54	0.0576	1.9	489	6	493	9	513	41	95
A484	4078	203	16	0.29	b.d.	0.6249	2.8	0.0789	1.4	0.51	0.0575	2.4	489	7	493	11	510	52	96
A583	5996	272	22	0.46	0.2	0.6316	2.7	0.0789	1.4	0.51	0.0581	2.3	489	6	497	10	533	50	92
A521	6382	307	25	0.50	0.0	0.6284	2.1	0.0790	1.3	0.60	0.0577	1.7	490	6	495	8	518	37	95
A459	3127	159	12	0.35	b.d.	0.6296	3.1	0.0790	1.3	0.44	0.0578	2.7	490	6	496	12	521	60	94
A515	4073	395	32	0.49	b.d.	0.6248	2.9	0.0791	1.5	0.51	0.0573	2.5	490	7	493	12	504	56	97
A445	3556	171	13	0.29	b.d.	0.6368	3.1	0.0791	1.4	0.47	0.0584	2.7	491	7	500	12	545	60	90
A486	6597	304	24	0.36	0.7	0.6353	2.4	0.0791	1.3	0.54	0.0583	2.1	491	6	499	10	539	45	91
A482	5601	275	22	0.48	b.d.	0.6259	2.6	0.0791	1.4	0.53	0.0574	2.2	491	7	494	10	506	49	97
A447	10593	523	42	0.48	0.0	0.6318	2.2	0.0791	1.5	0.66	0.0579	1.7	491	7	497	9	526	37	93
A556	2533	95	8	0.50	0.1	0.6252	2.8	0.0791	1.7	0.62	0.0573	2.2	491	8	493	11	503	48	98
A473	5784	286	23	0.39	b.d.	0.6348	2.4	0.0792	1.4	0.59	0.0582	1.9	491	7	499	9	536	42	92
A591	3976	191	15	0.38	b.d.	0.6320	3.1	0.0792	1.5	0.47	0.0579	2.8	491	7	497	12	526	60	93
A444	3806	181	14	0.39	b.d.	0.6366	2.9	0.0792	1.6	0.54	0.0583	2.5	491	8	500	12	542	54	91
A546	2857	131	10	0.29	b.d.	0.6295	3.1	0.0792	1.3	0.41	0.0577	2.8	491	6	496	12	517	61	95
A570	5905	257	21	0.52	b.d.	0.6351	2.1	0.0792	1.5	0.70	0.0582	1.5	491	7	499	8	536	33	92
A527	2950	106	9	0.24	2.3	0.6327	4.4	0.0792	1.5	0.33	0.0580	4.2	491	7	498	18	528	92	93
A501	5564	267	21	0.41	b.d.	0.6263	2.3	0.0792	1.3	0.57	0.0574	1.9	491	6	494	9	505	41	97
A504	3478	189	15	0.31	0.2	0.6323	4.2	0.0792	1.4	0.35	0.0579	3.9	492	7	498	17	525	86	94
A522	4798	225	18	0.38	b.d.	0.6391	2.6	0.0793	1.5	0.56	0.0585	2.2	492	7	502	11	548	48	90
A581	5357	252	20	0.43	0.0	0.6263	2.6	0.0793	1.4	0.55	0.0573	2.1	492	7	494	10	502	47	98
A479	5451	265	21	0.45	0.0	0.6342	2.6	0.0794	1.4	0.53	0.0580	2.2	492	7	499	10	528	49	93
A517	4510	213	17	0.40	0.0	0.6341	2.5	0.0794	1.3	0.52	0.0579	2.2	493	6	499	10	527	47	93
A518	4739	223	18	0.38	b.d.	0.6282	2.1	0.0794	1.3	0.63	0.0574	1.7	493	6	495	8	506	37	97
A464	6246	323	26	0.49	0.0	0.6360	2.3	0.0795	1.4	0.60	0.0580	1.8	493	6	500	9	531	40	93
A576	2159	107	8	0.28	b.d.	0.6294	3.2	0.0796	1.3	0.41	0.0574	2.9	494	6	496	13	506	64	98
A428	10527	508	42	0.57	0.0	0.6291	2.2	0.0796	1.4	0.66	0.0573	1.6	494	7	496	8	504	35	98
A542	4393	204	16	0.40	b.d.	0.6341	2.9	0.0796	1.2	0.43	0.0577	2.6	494	6	499	12	520	58	95
A589	8223	407	32	0.34	b.d.	0.6360	2.1	0.0797	1.6	0.74	0.0579	1.4	494	8	500	8	526	31	94
A582	3023	143	11	0.33	b.d.	0.6394	3.0	0.0797	1.3	0.44	0.0582	2.7	494	6	502	12	537	59	92
A561	5752	144	13	0.35	5.1	0.6349	5.8	0.0798	1.4	0.25	0.0577	5.6	495	7	499	23	519	123	95
A526	4279	212	17	0.40	b.d.	0.6337	2.6	0.0798	1.4	0.55	0.0576	2.1	495	7	498	10	514	47	96
A557	5459	244	20	0.43	0.3	0.6442	2.5	0.0799	1.4	0.55	0.0585	2.1	495	7	505	10	549	46	90

Grain	^{207}Pb[a] (cps)	U[b] (ppm)	Pb[b] (ppm)	Th[b] / U	$^{206}Pb_c$[c] (%)	^{207}Pb[d] / ^{235}U	±2σ (%)	^{206}Pb[d] / ^{238}U	±2σ (%)	ρ[e] (rho)	^{207}Pb[d] / ^{206}Pb	±2σ (%)	^{206}Pb[f] / ^{238}U	±2σ (Ma)	^{207}Pb[f] / ^{235}U	±2σ (Ma)	^{207}Pb[f] / ^{206}Pb	±2σ (Ma)	Conc.[g] (%)
A470	3445	176	14	0.31	b.d.	0.6355	3.2	0.0799	1.4	0.42	0.0577	2.9	495	7	499	13	518	64	96
A512	6270	302	24	0.40	0.1	0.6298	2.5	0.0799	1.3	0.50	0.0572	2.2	496	6	496	10	498	48	100
A537	3298	150	12	0.40	b.d.	0.6342	3.0	0.0800	1.4	0.48	0.0575	2.6	496	7	499	12	512	58	97
A451	5723	282	23	0.43	0.0	0.6449	2.6	0.0800	1.4	0.53	0.0585	2.2	496	7	505	10	548	48	91
A438	3866	190	15	0.36	b.d.	0.6363	2.4	0.0800	1.3	0.55	0.0577	2.0	496	6	500	10	519	44	96
A560	8611	400	33	0.51	0.0	0.6434	1.9	0.0800	1.3	0.68	0.0583	1.4	496	6	504	8	542	30	92
A448	3918	189	15	0.39	0.0	0.6436	3.1	0.0800	1.3	0.41	0.0583	2.8	496	6	505	12	543	62	91
A519	3815	179	14	0.35	b.d.	0.6440	2.8	0.0800	1.4	0.49	0.0584	2.5	496	7	505	11	544	54	91
A505	4292	191	16	0.43	b.d.	0.6350	2.5	0.0801	1.4	0.57	0.0575	2.0	497	7	499	10	510	45	97
A475	5191	259	21	0.34	b.d.	0.6458	2.5	0.0802	1.3	0.50	0.0584	2.2	497	6	506	10	545	48	91
A465	5823	534	45	0.59	0.0	0.6466	2.4	0.0802	1.4	0.57	0.0585	2.0	497	7	506	10	548	44	91
A535	4339	206	17	0.41	0.0	0.6334	3.0	0.0802	1.4	0.46	0.0573	2.6	497	7	498	12	502	58	99
A419	6411	326	26	0.41	b.d.	0.6357	2.7	0.0802	1.5	0.54	0.0575	2.2	498	7	500	11	509	49	98
A547	5701	263	22	0.50	b.d.	0.6395	2.9	0.0802	1.3	0.46	0.0578	2.6	498	6	502	12	522	57	95
A502	3766	176	14	0.35	b.d.	0.6359	2.7	0.0803	1.3	0.48	0.0575	2.4	498	6	500	11	510	52	98
A458	3713	178	14	0.39	b.d.	0.6321	3.1	0.0803	1.5	0.48	0.0571	2.8	498	7	497	12	496	61	100
A452	5495	272	22	0.47	0.0	0.6371	2.5	0.0803	1.4	0.57	0.0576	2.1	498	7	501	10	512	46	97
A566	3210	146	12	0.39	b.d.	0.6444	2.1	0.0803	1.4	0.66	0.0582	1.6	498	7	505	9	536	35	93
A488	9483	458	42	1.00	0.0	0.6368	2.1	0.0804	1.3	0.62	0.0575	1.7	498	6	500	8	510	36	98
A534	10870	240	22	0.34	6.3	0.6488	5.6	0.0804	1.5	0.27	0.0586	5.4	498	7	508	23	550	118	91
A514	7382	683	58	0.63	0.0	0.6385	2.5	0.0804	1.4	0.58	0.0576	2.0	498	7	501	10	515	44	97
A538	2974	139	11	0.32	b.d.	0.6385	2.8	0.0805	1.6	0.55	0.0576	2.3	499	7	501	11	513	51	97
A466	5064	253	21	0.41	b.d.	0.6428	2.1	0.0805	1.3	0.61	0.0579	1.7	499	6	504	8	527	37	95
A489	3180	157	13	0.38	b.d.	0.6336	2.9	0.0805	1.5	0.52	0.0571	2.5	499	7	498	11	495	55	101
A463	3460	163	13	0.36	b.d.	0.6430	2.9	0.0805	1.2	0.42	0.0579	2.6	499	6	504	11	527	57	95
A462	13250	667	55	0.51	0.0	0.6344	1.9	0.0805	1.4	0.71	0.0571	1.4	499	7	499	8	497	30	101
A436	4466	215	17	0.43	0.0	0.6436	2.3	0.0805	1.3	0.57	0.0580	1.9	499	6	505	9	528	42	95
A543	5651	279	23	0.42	b.d.	0.6458	2.7	0.0806	1.4	0.52	0.0582	2.3	499	7	506	11	536	50	93
A559	5328	255	21	0.43	0.0	0.6453	2.2	0.0806	1.4	0.61	0.0581	1.8	500	7	506	9	533	39	94
A529	5695	263	22	0.50	b.d.	0.6314	2.4	0.0806	1.3	0.52	0.0568	2.1	500	6	497	10	485	45	103
A424	5460	265	23	0.66	0.0	0.6348	2.1	0.0807	1.3	0.61	0.0571	1.7	500	6	499	9	495	38	101
A418	4379	199	16	0.50	0.1	0.6529	3.2	0.0807	1.5	0.48	0.0587	2.8	500	7	510	13	556	61	90
A580	5596	254	21	0.55	b.d.	0.6475	2.2	0.0807	1.3	0.61	0.0582	1.7	500	6	507	9	537	38	93
A565	3698	181	15	0.39	b.d.	0.6439	3.0	0.0808	1.3	0.43	0.0578	2.7	501	6	505	12	523	59	96
A558	4198	202	16	0.34	1.0	0.6536	3.1	0.0808	1.4	0.46	0.0587	2.7	501	7	511	12	555	59	90
A478	4821	239	19	0.39	b.d.	0.6367	2.5	0.0809	1.2	0.49	0.0571	2.1	501	6	500	10	495	47	101
A503	5846	274	22	0.35	b.d.	0.6447	2.2	0.0809	1.3	0.60	0.0578	1.8	501	6	505	9	522	39	96
A544	5074	254	21	0.41	b.d.	0.6366	2.3	0.0809	1.3	0.57	0.0571	1.9	502	6	500	9	494	42	102
A507	4409	220	18	0.35	b.d.	0.6413	2.8	0.0811	1.6	0.58	0.0574	2.3	502	8	503	11	506	50	99
A432	7627	382	31	0.46	b.d.	0.6512	1.9	0.0811	1.4	0.72	0.0583	1.3	503	7	509	8	540	29	93
A508	6084	287	24	0.50	0.0	0.6548	2.1	0.0811	1.3	0.62	0.0586	1.6	503	6	511	8	550	35	91
A412	3039	149	12	0.38	b.d.	0.6513	2.6	0.0811	1.5	0.56	0.0582	2.2	503	7	509	11	538	47	93
A487	3929	194	16	0.40	b.d.	0.6447	2.7	0.0811	1.3	0.49	0.0576	2.3	503	6	505	11	516	51	97
A563	8265	376	33	0.71	0.0	0.6529	2.3	0.0811	1.4	0.62	0.0584	1.8	503	7	510	9	543	40	93
A509	4894	235	19	0.39	b.d.	0.6491	2.3	0.0812	1.4	0.60	0.0580	1.9	503	7	508	9	530	41	95
A536	4777	230	19	0.46	0.0	0.6402	2.4	0.0813	1.4	0.60	0.0571	1.9	504	7	502	9	496	41	102
A510	5384	253	21	0.46	0.0	0.6459	2.4	0.0813	1.3	0.53	0.0576	2.1	504	6	506	10	515	45	98
A425	6201	314	26	0.50	b.d.	0.6486	2.1	0.0814	1.3	0.62	0.0578	1.7	504	6	508	9	523	37	96
A454	4360	219	18	0.41	b.d.	0.6464	2.4	0.0818	1.3	0.53	0.0573	2.0	507	6	506	10	503	45	101
A437	5724	280	23	0.50	b.d.	0.6499	2.7	0.0820	1.3	0.49	0.0575	2.4	508	7	508	11	510	53	100
A429	3120	158	13	0.38	b.d.	0.6531	3.0	0.0822	1.4	0.47	0.0577	2.6	509	7	510	12	517	58	99
A485	6197	293	24	0.23	0.4	0.6695	2.7	0.0823	1.8	0.67	0.0590	2.0	510	9	520	11	567	44	90
A423	2853	142	12	0.33	b.d.	0.6618	3.5	0.0824	1.4	0.41	0.0582	3.2	510	7	516	14	539	69	95
A469	3383	338	28	0.45	b.d.	0.6593	2.8	0.0826	1.5	0.52	0.0579	2.4	512	7	514	11	526	53	97
A420	8427	410	35	0.52	0.0	0.6615	2.3	0.0833	1.3	0.57	0.0576	1.9	516	6	516	9	514	41	100
A461	8767	403	36	0.70	0.0	0.6831	2.0	0.0837	1.5	0.75	0.0592	1.3	518	7	529	8	573	29	90
A421	8444	408	36	0.56	0.0	0.6966	2.1	0.0854	1.3	0.60	0.0592	1.7	528	6	537	9	574	37	92
A562	22975	1708	142	0.27	0.0	0.6701	2.1	0.0856	1.6	0.77	0.0568	1.3	530	8	521	8	482	29	110
A587	3563	165	14	0.36	b.d.	0.6880	3.0	0.0857	1.3	0.46	0.0583	2.6	530	7	532	12	539	58	98
A573	4124	163	15	0.46	b.d.	0.7187	2.5	0.0874	1.3	0.51	0.0597	2.1	540	7	550	11	591	46	91
A568	3683	332	29	0.42	b.d.	0.7038	3.0	0.0876	1.4	0.49	0.0583	2.6	541	7	541	12	541	57	100
A467	10738	997	95	0.73	0.0	0.7174	2.4	0.0886	1.3	0.55	0.0587	2.0	547	7	549	10	557	43	98
A457	3685	155	16	0.91	0.0	0.7525	2.5	0.0903	1.5	0.59	0.0604	2.0	558	8	570	11	618	43	90
A476	2574	97	10	0.95	b.d.	0.7526	2.8	0.0906	1.4	0.51	0.0603	2.4	559	8	570	12	613	51	91
A528	6455	253	26	0.94	0.0	0.7634	2.1	0.0917	1.3	0.62	0.0604	1.7	566	7	576	9	617	36	92
A574	2275	84	9	1.09	b.d.	0.7688	3.4	0.0926	1.8	0.52	0.0602	2.9	571	10	579	15	611	63	93
A564	4532	178	20	1.31	0.0	0.7614	2.8	0.0929	1.6	0.57	0.0595	2.3	572	9	575	12	585	50	98
A586	6850	560	55	0.53	b.d.	0.7872	2.4	0.0941	1.6	0.67	0.0607	1.8	579	9	590	11	629	38	92
A585	2159	148	18	1.31	b.d.	0.8130	4.0	0.0969	1.8	0.44	0.0609	3.6	596	10	604	18	635	77	94
A435	6190	233	27	1.07	0.0	0.8423	2.5	0.0985	1.2	0.49	0.0620	2.2	605	7	620	12	675	47	90

Grain	^{207}Pb[a] (cps)	U[b] (ppm)	Pb[b] (ppm)	Th[b]/U	^{206}Pbc[c] (%)	$^{207}Pb/^{235}U$[d]	±2σ (%)	$^{206}Pb/^{238}U$[d]	±2σ (%)	ρ[e] (rho)	$^{207}Pb/^{206}Pb$[d]	±2σ (%)	$^{206}Pb/^{238}U$[f]	±2σ (Ma)	$^{207}Pb/^{235}U$[f]	±2σ (Ma)	$^{207}Pb/^{206}Pb$[f]	±2σ (Ma)	Conc.[g] (%)
A569	3614	273	34	1.41	0.0	0.8495	2.8	0.1027	1.3	0.48	0.0600	2.4	630	8	624	13	604	53	104
A590	2641	90	10	0.76	b.d.	0.8889	3.3	0.1034	1.7	0.51	0.0623	2.8	635	10	646	16	685	60	93
A433	3723	116	15	0.81	b.d.	1.0130	2.9	0.1149	1.4	0.50	0.0639	2.5	701	10	710	15	739	52	95
A588	58253	295	99	0.21	0.0	5.5590	1.6	0.3265	1.3	0.82	0.1235	0.9	1821	20	1910	13	2007	16	91
A422	81365	440	158	0.46	0.0	5.7050	1.4	0.3386	1.2	0.86	0.1222	0.7	1880	19	1932	12	1988	13	95
A579	22492	73	37	0.83	0.0	9.5590	1.7	0.4310	1.3	0.77	0.1609	1.1	2310	25	2393	16	2465	18	94
A572	*6729*	*357*	*23*	*0.39*	*0.1*	*0.4962*	*2.6*	*0.0624*	*2.2*	*0.84*	*0.0577*	*1.4*	*390*	*8*	*409*	*9*	*516*	*30*	*76*
A450	*8005*	*391*	*30*	*0.45*	*0.2*	*0.6159*	*2.6*	*0.0750*	*1.3*	*0.49*	*0.0596*	*2.3*	*466*	*6*	*487*	*10*	*588*	*50*	*79*
A520	*6730*	*309*	*24*	*0.43*	*0.4*	*0.6028*	*3.2*	*0.0752*	*1.3*	*0.42*	*0.0582*	*2.9*	*467*	*6*	*479*	*12*	*536*	*63*	*87*
A490	*4023*	*189*	*14*	*0.38*	*0.0*	*0.6311*	*2.0*	*0.0762*	*1.3*	*0.66*	*0.0601*	*1.5*	*474*	*6*	*497*	*8*	*605*	*32*	*78*
A500	*8433*	*372*	*30*	*0.47*	*0.9*	*0.6390*	*3.2*	*0.0765*	*1.3*	*0.42*	*0.0606*	*2.9*	*475*	*6*	*502*	*13*	*626*	*62*	*76*
A472	*16513*	*1718*	*125*	*0.58*	*b.d.*	*0.6186*	*1.9*	*0.0766*	*1.3*	*0.71*	*0.0586*	*1.3*	*476*	*6*	*489*	*7*	*551*	*29*	*86*
A413	*3681*	*158*	*13*	*0.39*	*1.6*	*0.6449*	*3.9*	*0.0776*	*1.4*	*0.35*	*0.0603*	*3.6*	*482*	*6*	*505*	*16*	*615*	*78*	*78*
A516	*16071*	*227*	*24*	*0.34*	*12.8*	*0.6538*	*8.0*	*0.0789*	*1.8*	*0.23*	*0.0601*	*7.8*	*490*	*9*	*511*	*33*	*607*	*168*	*81*
A480	*3142*	*147*	*12*	*0.27*	*0.9*	*0.6593*	*3.4*	*0.0793*	*1.5*	*0.44*	*0.0603*	*3.1*	*492*	*7*	*514*	*14*	*616*	*66*	*80*
A414	*5841*	*162*	*14*	*0.37*	*5.1*	*0.6944*	*5.6*	*0.0796*	*1.5*	*0.27*	*0.0633*	*5.4*	*494*	*7*	*535*	*24*	*717*	*114*	*69*
A427	*5708*	*269*	*22*	*0.38*	*0.3*	*0.6842*	*3.0*	*0.0801*	*1.3*	*0.44*	*0.0620*	*2.7*	*496*	*6*	*529*	*13*	*674*	*58*	*74*
A477	*2983*	*130*	*10*	*0.34*	*0.2*	*0.7096*	*2.4*	*0.0801*	*1.4*	*0.58*	*0.0643*	*2.0*	*497*	*7*	*544*	*10*	*750*	*42*	*66*
A493	*5346*	*232*	*19*	*0.37*	*4.8*	*0.6584*	*7.5*	*0.0809*	*1.6*	*0.21*	*0.0590*	*7.3*	*501*	*8*	*514*	*31*	*568*	*159*	*88*
A430	*4310*	*199*	*17*	*0.38*	*0.5*	*0.7131*	*2.5*	*0.0817*	*1.3*	*0.52*	*0.0633*	*2.1*	*506*	*6*	*547*	*10*	*720*	*45*	*70*
A523	*11260*	*393*	*35*	*0.70*	*1.7*	*0.7626*	*3.1*	*0.0820*	*1.4*	*0.44*	*0.0675*	*2.8*	*508*	*7*	*576*	*14*	*852*	*58*	*60*
A492	*6350*	*277*	*24*	*0.49*	*0.0*	*0.6771*	*2.5*	*0.0824*	*1.3*	*0.53*	*0.0596*	*2.1*	*510*	*6*	*525*	*10*	*589*	*45*	*87*
A431	*5415*	*257*	*22*	*0.42*	*0.0*	*0.7095*	*2.4*	*0.0826*	*1.4*	*0.58*	*0.0623*	*2.0*	*511*	*7*	*544*	*10*	*685*	*42*	*75*
A506	*5424*	*227*	*19*	*0.40*	*0.5*	*0.7558*	*3.1*	*0.0839*	*1.4*	*0.44*	*0.0653*	*2.8*	*520*	*7*	*572*	*14*	*784*	*58*	*66*
A499	*6540*	*191*	*18*	*0.51*	*9.9*	*0.8210*	*13.1*	*0.0892*	*5.2*	*0.39*	*0.0668*	*12.0*	*551*	*27*	*609*	*62*	*830*	*251*	*66*
A474	*3330*	*141*	*15*	*1.09*	*0.0*	*0.7145*	*2.5*	*0.0905*	*1.4*	*0.54*	*0.0572*	*2.1*	*559*	*7*	*547*	*11*	*501*	*47*	*112*
A531	*7122*	*247*	*24*	*0.62*	*b.d.*	*0.7998*	*2.1*	*0.0931*	*1.3*	*0.64*	*0.0623*	*1.6*	*574*	*7*	*597*	*9*	*685*	*34*	*84*
A513	*30789*	*351*	*66*	*0.22*	*4.2*	*1.9970*	*3.9*	*0.1757*	*1.5*	*0.38*	*0.0825*	*3.6*	*1043*	*14*	*1115*	*27*	*1256*	*71*	*83*
91500[h]	8532	69	13	0.45	0.3	0.1784	3.8	1.8103	6.1	0.07	4.3867	0.6	1058	37	1049	40	1030	89	103
Felix[h]	4019	203	23	1.93	0.4	0.0808	4.3	0.6109	10.3	0.05	7.7221	0.4	501	21	484	40	402	176	132
Plesovice[h]	2881	1038	54	0.16	0.2	0.0549	3.8	0.4045	3.8	0.05	1.5557	0.5	344	13	345	11	348	35	99
GJ-1[h]	6932	290	26	0.02	0.1	0.0984	1.1	0.8158	2.0	0.06	2.0856	0.5	605	6	606	9			

$^{206}Pb/^{238}U$ error is the quadratic additions of the within run precision (2 SE) and the external reproducibility (2 SD) of the reference zircon. $^{207}Pb/^{206}Pb$ error propagation (^{207}Pb signal dependent) following Gerdes & Zeh (2009). $^{207}Pb/^{235}U$ error is the quadratic addition of the $^{207}Pb/^{206}Pb$ and $^{206}Pb/^{238}U$ uncertainty.

[a] Within run background-corrected mean ^{207}Pb signal in cps (counts per second).

[b] U and Pb content and Th/U ratio were calculated relative to GJ-1 reference zircon.

[c] Percentage of the common Pb on the ^{206}Pb. b.d. = below detection limit.

[d] Pb/U and Pb/Pb ratios. Corrected for background, within-run Pb/U fractionation (in case of $^{206}Pb/^{238}U$) and common Pb using Stacy and Kramers (1975) model Pb composition and subsequently normalised to GJ-1 (ID-TIMS value/measured value); $^{207}Pb/^{235}U$ calculated using (($^{207}Pb/^{206}Pb$)*($^{238}U/^{206}Pb$)*137.88).

[e] Rho (ρ) is the ($^{206}Pb/^{238}U$)/($^{207}Pb/^{235}U$) error correlation coefficient.

[f] Pb/U and Pb/Pb ages.

[g] Degree of concordance = (($^{206}Pb/^{238}U$ age)/($^{207}Pb/^{206}Pb$ age)) x 100.

[h] Mean of 11 (91500), 11 (Felix), 9 (Plesovice), and 26 (GJ-1) analyses, respectively.

Table Ig9-U

U, Th and Pb LA-ICP-MS data of zircon crystals from sample GCH-03

Grain	^{207}Pb[a] (cps)	U[b] (ppm)	Pb[b] (ppm)	Th[b] / U	^{206}Pbc[c] (%)	$^{207}Pb/^{235}U$[d]	±2σ (%)	$^{206}Pb/^{238}U$[d]	±2σ (%)	ρ[e] (rho)	$^{207}Pb/^{206}Pb$[d]	±2σ (%)	$^{206}Pb/^{238}U$[f]	±2σ (Ma)	$^{207}Pb/^{235}U$[f]	±2σ (Ma)	$^{207}Pb/^{206}Pb$[f]	±2σ (Ma)	Conc.[g] (%)
A045	2184	184	12	0.04	4.4	0.4520	6.3	0.0604	2.0	0.31	0.0543	6.0	378	7	379	20	383	135	99
A182	2830	156	11	0.25	1.9	0.5184	3.8	0.0676	1.5	0.39	0.0557	3.5	421	6	424	13	439	77	96
A076	853	28	3	0.03	7.3	0.5234	15.9	0.0690	5.5	0.34	0.0550	15.0	430	23	427	57	411	335	105
A131	11187	1650	119	0.24	0.1	0.5437	2.2	0.0703	1.5	0.67	0.0561	1.7	438	6	441	8	457	37	96
A126	1410	163	13	0.46	0.2	0.5623	3.6	0.0727	1.6	0.45	0.0561	3.2	453	7	453	13	455	72	99
A116	3590	460	38	0.50	0.5	0.5646	2.6	0.0728	1.6	0.60	0.0562	2.1	453	7	455	10	462	46	98
A074	3137	405	32	0.41	0.0	0.5724	3.1	0.0734	1.4	0.45	0.0565	2.8	457	6	460	12	473	62	97
A066	4322	555	46	0.50	b.d.	0.5712	2.6	0.0737	1.6	0.63	0.0562	2.0	458	7	459	10	460	45	100
A137	5452	329	28	0.65	0.2	0.5730	2.1	0.0737	1.6	0.74	0.0564	1.4	459	7	460	8	467	31	98
A065	1062	93	8	0.26	3.9	0.5767	7.1	0.0740	2.0	0.28	0.0566	6.8	460	9	462	27	474	151	97
A083	5597	575	47	0.42	1.6	0.5798	3.4	0.0744	1.7	0.50	0.0566	3.0	462	8	464	13	474	66	98
A100	6255	676	58	0.58	0.8	0.5836	3.0	0.0744	1.6	0.53	0.0569	2.6	463	7	467	11	487	57	95
A165	1858	216	17	0.37	0.1	0.5862	3.4	0.0744	1.8	0.51	0.0571	2.9	463	8	468	13	496	65	93
A073	2666	348	29	0.48	b.d.	0.5811	3.2	0.0746	1.8	0.57	0.0565	2.7	464	8	465	12	473	59	98
A082	3182	162	14	0.48	1.1	0.5811	4.1	0.0747	1.6	0.38	0.0564	3.8	465	7	465	15	468	83	99
A171	1051	121	10	0.41	0.5	0.5889	4.3	0.0748	1.7	0.39	0.0571	4.0	465	8	470	16	494	88	94
A060	1144	145	11	0.28	0.4	0.5872	4.7	0.0749	1.9	0.41	0.0569	4.3	466	9	469	18	487	94	96
A118	4844	551	47	0.53	0.5	0.5839	2.8	0.0749	1.4	0.49	0.0565	2.4	466	6	467	10	474	53	98
A115	1594	92	7	0.29	1.1	0.5848	3.8	0.0752	1.7	0.44	0.0564	3.4	467	7	468	14	468	75	100
A108	2092	253	21	0.48	0.1	0.5890	3.3	0.0752	1.6	0.48	0.0568	2.9	468	7	470	13	484	64	97
A111	710	82	6	0.27	0.5	0.5864	4.9	0.0753	1.8	0.36	0.0565	4.6	468	8	469	19	473	101	99
A173	5043	313	27	0.66	b.d.	0.5932	2.4	0.0753	1.6	0.67	0.0571	1.8	468	7	473	9	496	39	94
A079	2895	163	13	0.38	0.2	0.5915	3.8	0.0754	1.6	0.42	0.0569	3.5	468	7	472	15	489	77	96
A090	5950	726	59	0.42	0.2	0.5914	2.6	0.0755	1.7	0.63	0.0568	2.0	469	7	472	10	483	45	97
A085	4467	564	50	0.63	b.d.	0.5887	2.7	0.0756	1.7	0.62	0.0565	2.1	470	8	470	10	472	47	99
A172	3535	207	17	0.44	0.1	0.5905	2.6	0.0756	1.8	0.68	0.0566	1.9	470	8	471	10	477	43	99
A113	5620	290	26	0.61	0.7	0.5985	3.1	0.0757	1.6	0.51	0.0574	2.7	470	7	476	12	505	59	93
A134	4340	200	18	0.51	2.0	0.5896	3.9	0.0757	1.8	0.46	0.0565	3.5	471	8	471	15	470	77	100
A162	7601	916	83	0.73	b.d.	0.5982	2.3	0.0758	1.5	0.66	0.0573	1.7	471	7	476	9	502	38	94
A072	6682	846	74	0.61	0.1	0.5955	2.3	0.0760	1.6	0.66	0.0568	1.8	472	7	474	9	485	39	97
A133	8634	1063	87	0.41	0.0	0.5956	2.3	0.0760	1.6	0.71	0.0568	1.6	472	7	474	9	485	36	97
A180	3139	395	34	0.57	0.1	0.6032	3.3	0.0760	1.5	0.45	0.0576	2.9	472	7	479	13	513	64	92
A084	3488	422	36	0.49	0.0	0.5950	2.6	0.0761	1.6	0.63	0.0567	2.0	473	8	474	10	481	45	98
A159	3750	460	37	0.36	0.0	0.6002	2.6	0.0762	1.6	0.61	0.0571	2.1	473	7	477	10	497	45	95
A075	9572	1221	88	0.09	b.d.	0.5983	2.2	0.0763	1.7	0.76	0.0569	1.4	474	8	476	8	486	32	97
A081	2423	313	27	0.53	0.0	0.6009	3.3	0.0763	1.5	0.45	0.0571	2.9	474	7	478	13	495	65	96
A175	13868	1659	151	0.67	0.5	0.5978	2.0	0.0764	1.4	0.69	0.0567	1.5	475	6	476	8	481	33	99
A181	2211	272	22	0.44	0.2	0.5996	3.1	0.0765	1.7	0.55	0.0569	2.6	475	8	477	12	486	58	98
A091	5978	700	60	0.45	0.9	0.6029	2.3	0.0766	1.7	0.71	0.0571	1.6	476	8	479	9	495	36	96
A129	5900	707	61	0.51	0.2	0.6011	2.3	0.0767	1.4	0.60	0.0569	1.8	476	6	478	9	487	40	98
A047	1891	234	19	0.36	b.d.	0.6017	3.9	0.0767	1.6	0.41	0.0569	3.5	477	7	478	15	487	78	98
A140	3569	439	36	0.42	0.0	0.6029	2.8	0.0768	1.4	0.51	0.0570	2.4	477	7	479	11	490	53	97
A087	2872	361	30	0.42	0.0	0.6012	3.0	0.0768	1.6	0.52	0.0568	2.6	477	7	478	12	483	57	99
A178	2915	350	29	0.46	0.2	0.6052	3.3	0.0770	1.6	0.47	0.0570	2.9	478	7	481	13	493	65	97
A170	4903	614	56	0.69	0.2	0.6035	2.5	0.0770	1.6	0.63	0.0569	1.9	478	7	479	9	487	42	98
A094	5761	691	57	0.40	0.2	0.6018	2.6	0.0770	1.5	0.58	0.0567	2.1	478	7	478	10	479	46	100
A138	8071	486	45	0.72	0.1	0.6048	2.3	0.0772	1.5	0.67	0.0569	1.7	479	7	480	9	486	37	99
A127	3434	410	36	0.55	0.3	0.6033	2.9	0.0772	1.7	0.58	0.0567	2.3	479	8	479	11	480	52	100
A119	1427	170	14	0.38	b.d.	0.6096	3.6	0.0772	1.8	0.49	0.0573	3.1	480	8	483	14	501	69	96
A053	4932	568	47	0.37	0.5	0.6079	2.6	0.0773	1.5	0.60	0.0570	2.1	480	7	482	10	493	45	97
A097	9694	1168	106	0.65	b.d.	0.6078	2.0	0.0773	1.5	0.74	0.0570	1.3	480	7	482	8	492	30	98
A122	4925	469	42	0.52	1.8	0.6098	3.5	0.0774	1.7	0.49	0.0572	3.0	480	8	483	13	497	67	97
A109	3780	474	42	0.58	0.1	0.6085	2.5	0.0775	1.5	0.62	0.0569	1.9	481	7	483	10	488	43	99
A096	6577	779	72	0.72	0.1	0.6087	2.5	0.0775	1.5	0.63	0.0569	1.9	481	7	483	10	489	43	98
A078	8467	1024	94	0.71	0.1	0.6092	2.1	0.0776	1.6	0.76	0.0570	1.4	482	8	483	8	490	31	98
A169	9077	1064	101	0.78	0.5	0.6083	2.3	0.0776	1.5	0.67	0.0569	1.7	482	7	483	9	486	37	99
A179	1685	194	16	0.29	0.0	0.6134	3.6	0.0777	1.7	0.48	0.0573	3.1	482	8	486	14	501	69	96
A061	4311	519	42	0.34	b.d.	0.6110	2.7	0.0777	1.6	0.60	0.0570	2.1	483	7	484	10	492	47	98
A099	6997	858	79	0.72	b.d.	0.6102	2.4	0.0777	1.6	0.66	0.0569	1.8	483	7	484	9	489	39	99
A121	1269	32	3	0.34	0.7	0.6128	3.4	0.0779	1.6	0.47	0.0571	3.0	483	8	485	13	494	67	98
A174	9889	1072	100	0.70	1.7	0.6130	3.5	0.0779	1.6	0.46	0.0571	3.1	484	7	485	14	494	68	98
A093	4711	566	52	0.61	b.d.	0.6138	2.6	0.0779	1.7	0.67	0.0571	1.9	484	8	486	10	497	42	97
A112	2877	175	15	0.55	b.d.	0.6120	3.0	0.0779	1.8	0.59	0.0570	2.4	484	8	485	12	490	53	99
A130	3165	391	32	0.36	0.1	0.6157	2.4	0.0780	1.5	0.63	0.0573	1.9	484	7	487	9	501	42	97
A166	4864	572	51	0.62	0.2	0.6139	2.8	0.0780	1.6	0.59	0.0571	2.2	484	8	486	11	494	50	98
A145	2910	307	28	0.56	1.2	0.6151	3.8	0.0780	1.8	0.47	0.0572	3.3	484	8	487	15	498	73	97
A167	8384	497	44	0.57	b.d.	0.6169	2.0	0.0780	1.6	0.81	0.0573	1.2	484	8	488	8	504	26	96

Grain	^{207}Pb[a] (cps)	U[b] (ppm)	Pb[b] (ppm)	Th[b] U	^{206}Pbc[c] (%)	$^{207}Pb/^{235}U$[d]	±2σ (%)	$^{206}Pb/^{238}U$[d]	±2σ (%)	ρ[e] (rho)	$^{207}Pb/^{206}Pb$[d]	±2σ (%)	$^{206}Pb/^{238}U$[f]	±2σ (Ma)	$^{207}Pb/^{235}U$[f]	±2σ (Ma)	$^{207}Pb/^{206}Pb$[f]	±2σ (Ma)	Conc.[g] (%)
A049	5844	672	61	0.69	0.1	0.6136	1.9	0.0781	1.4	0.72	0.0570	1.3	485	6	486	7	491	29	99
A062	6456	804	69	0.47	0.0	0.6127	2.3	0.0781	1.6	0.68	0.0569	1.7	485	7	485	9	487	37	100
A161	2186	230	21	0.58	0.1	0.6140	3.4	0.0781	2.0	0.57	0.0570	2.8	485	9	486	13	491	63	99
A095	8058	992	86	0.49	0.0	0.6154	2.3	0.0783	1.7	0.75	0.0570	1.5	486	8	487	9	493	33	99
A132	6010	774	62	0.30	b.d.	0.6088	2.3	0.0783	1.6	0.72	0.0564	1.6	486	8	483	9	468	35	104
A135	13475	1591	149	0.73	0.1	0.6174	2.0	0.0783	1.6	0.78	0.0572	1.3	486	7	488	8	498	28	98
A089	1144	134	11	0.24	0.1	0.6196	3.5	0.0783	1.7	0.50	0.0574	3.0	486	8	490	14	505	66	96
A046	4203	522	43	0.36	0.2	0.6166	3.0	0.0784	1.5	0.50	0.0570	2.6	487	7	488	12	492	57	99
A101	6032	670	61	0.61	0.3	0.6186	2.4	0.0785	1.6	0.69	0.0571	1.7	487	8	489	9	497	38	98
A154	7897	468	41	0.56	0.1	0.6232	2.1	0.0786	1.4	0.68	0.0575	1.5	488	7	492	8	511	34	96
A080	7250	849	78	0.66	0.0	0.6212	2.1	0.0786	1.7	0.79	0.0573	1.3	488	8	491	8	503	29	97
A151	7187	820	73	0.56	0.4	0.6263	2.4	0.0787	1.6	0.67	0.0577	1.8	488	8	494	10	519	39	94
A058	722	83	7	0.31	0.3	0.6186	5.6	0.0788	2.1	0.38	0.0569	5.2	489	10	489	22	489	115	100
A056	1834	201	17	0.39	0.7	0.6233	3.6	0.0789	1.5	0.42	0.0573	3.3	489	7	492	14	504	72	97
A124	5517	689	62	0.63	0.2	0.6213	2.4	0.0789	1.6	0.65	0.0571	1.9	490	7	491	10	496	41	99
A055	3301	378	35	0.65	0.1	0.6230	3.3	0.0790	1.7	0.51	0.0572	2.8	490	8	492	13	499	62	98
A153	9604	1147	108	0.74	0.1	0.6291	1.9	0.0791	1.4	0.76	0.0577	1.2	490	7	496	7	519	27	94
A057	1886	216	20	0.57	0.2	0.6247	4.3	0.0791	2.0	0.45	0.0573	3.8	491	9	493	17	503	85	97
A107	2750	325	30	0.68	b.d.	0.6218	3.3	0.0791	1.6	0.50	0.0570	2.8	491	8	491	13	493	63	100
A048	3054	329	29	0.42	0.5	0.6202	3.2	0.0791	1.6	0.51	0.0569	2.8	491	8	490	13	486	61	101
A157	1086	137	11	0.34	0.0	0.6231	4.1	0.0791	2.1	0.50	0.0571	3.6	491	10	492	16	497	79	99
A051	2207	113	10	0.41	0.4	0.6245	3.8	0.0791	1.6	0.42	0.0572	3.5	491	8	493	15	500	76	98
A136	1884	89	7	0.25	1.9	0.6290	4.0	0.0792	2.9	0.72	0.0576	2.8	491	14	495	16	515	61	95
A152	3124	392	34	0.46	b.d.	0.6276	2.9	0.0792	1.5	0.53	0.0575	2.4	491	7	495	11	510	54	96
A052	3215	141	12	0.39	2.3	0.6245	4.2	0.0792	1.5	0.37	0.0572	3.9	491	7	493	16	498	86	99
A092	3595	418	38	0.59	b.d.	0.6237	2.7	0.0792	1.6	0.58	0.0571	2.2	492	8	492	11	495	49	99
A050	8416	502	47	0.72	0.5	0.6257	2.5	0.0792	1.6	0.63	0.0573	2.0	492	8	493	10	502	43	98
A168	4907	255	23	0.51	0.5	0.6244	2.6	0.0794	1.5	0.58	0.0571	2.1	492	7	493	10	494	47	100
A155	4947	281	24	0.41	0.4	0.6261	2.3	0.0794	1.6	0.68	0.0572	1.7	493	7	494	9	498	37	99
A086	6675	586	55	0.53	1.7	0.6371	3.4	0.0795	1.6	0.47	0.0581	3.0	493	7	500	13	533	65	92
A142	11942	929	96	0.91	1.9	0.6345	3.6	0.0796	1.7	0.47	0.0578	3.2	494	8	499	14	523	70	94
A063	4880	591	49	0.33	b.d.	0.6240	2.0	0.0796	1.4	0.72	0.0568	1.4	494	7	492	8	485	30	102
A160	10183	1206	98	0.24	0.1	0.6288	2.0	0.0797	1.5	0.78	0.0572	1.2	495	7	495	8	499	28	99
A098	4554	505	44	0.46	0.3	0.6309	2.8	0.0798	1.8	0.66	0.0573	2.1	495	9	497	11	504	46	98
A088	7300	870	75	0.44	0.0	0.6301	2.4	0.0798	1.6	0.65	0.0572	1.8	495	7	496	9	501	40	99
A123	7715	891	78	0.46	0.2	0.6312	2.5	0.0799	1.6	0.66	0.0573	1.9	496	8	497	10	502	41	99
A114	4420	522	47	0.58	0.0	0.6311	2.3	0.0799	1.6	0.70	0.0573	1.7	496	8	497	9	501	36	99
A143	2291	236	22	0.59	0.2	0.6283	3.4	0.0800	1.7	0.49	0.0570	3.0	496	8	495	14	490	66	101
A110	3898	419	38	0.54	1.1	0.6310	3.3	0.0803	1.7	0.51	0.0570	2.8	498	8	497	13	492	62	101
A064	2929	343	32	0.66	b.d.	0.6327	2.6	0.0804	1.8	0.71	0.0571	1.8	498	9	498	10	495	40	101
A120	15355	1745	185	1.08	0.3	0.6326	2.0	0.0804	1.5	0.76	0.0571	1.3	499	7	498	8	493	29	101
A163	7889	710	73	0.86	1.8	0.6414	4.1	0.0805	2.0	0.48	0.0578	3.6	499	9	503	16	522	79	96
A117	4166	486	46	0.59	0.5	0.6351	3.8	0.0805	1.5	0.40	0.0572	3.4	499	7	499	15	500	76	100
A128	18836	2298	255	1.26	0.1	0.6348	1.7	0.0806	1.4	0.86	0.0571	0.9	500	7	499	7	496	19	101
A077	1950	213	19	0.45	0.6	0.6426	3.3	0.0807	1.7	0.52	0.0578	2.8	500	8	504	13	521	61	96
A059	4224	500	42	0.34	b.d.	0.6417	2.6	0.0807	1.5	0.58	0.0576	2.1	501	7	503	11	516	47	97
A139	5869	732	66	0.54	0.0	0.6423	2.3	0.0811	1.5	0.65	0.0574	1.8	503	7	504	9	507	39	99
A176	7832	927	86	0.64	0.1	0.6469	2.1	0.0813	1.6	0.74	0.0577	1.4	504	8	507	9	519	32	97
A141	6216	302	27	0.52	0.1	0.6518	2.3	0.0818	1.6	0.73	0.0578	1.6	507	8	510	9	523	34	97
A054	6523	792	72	0.52	0.0	0.6460	2.3	0.0818	1.5	0.63	0.0573	1.8	507	7	506	9	502	39	101
A164	3540	423	39	0.58	0.0	0.6573	2.8	0.0827	1.5	0.53	0.0576	2.4	512	7	513	11	516	52	99
A156	4876	374	35	0.35	4.2	0.6661	5.5	0.0831	1.7	0.30	0.0582	5.2	514	8	518	22	536	114	96
A177	*392*	*33*	*2*	*0.06*	*7.7*	*0.5273*	*18.6*	*0.0670*	*3.4*	*0.18*	*0.0571*	*18.3*	*418*	*14*	*430*	*67*	*493*	*403*	*85*
A158	*1585*	*193*	*14*	*0.25*	*0.1*	*0.5866*	*4.2*	*0.0732*	*2.1*	*0.50*	*0.0581*	*3.6*	*455*	*9*	*469*	*16*	*535*	*79*	*85*
A144	*16017*	*238*	*40*	*0.43*	*29.9*	*0.8357*	*12.8*	*0.0832*	*3.7*	*0.29*	*0.0728*	*12.3*	*515*	*18*	*617*	*61*	*1009*	*248*	*51*

Grain	^{207}Pb[a] (cps)	U[b] (ppm)	Pb[b] (ppm)	Th[b] U	^{206}Pbc[c] (%)	^{207}Pb[d] / ^{235}U	±2σ (%)	^{206}Pb[d] / ^{238}U	±2σ (%)	ρ[e] (rho)	^{207}Pb[d] / ^{206}Pb	±2σ (%)	^{206}Pb[f] / ^{238}U	±2σ (Ma)	^{207}Pb[f] / ^{235}U	±2σ (Ma)	^{207}Pb[f] / ^{206}Pb	±2σ (Ma)	Conc.[g] (%)
91500[h]	7004	61	11	0.25	0.4	0.1794	2.1	1.8382	3.2	0.07	1.5934	0.6	1063	20	1059	21	1050	32	101
Felix[h]	6572	361	52	2.08	0.4	0.0810	3.3	0.6372	3.3	0.06	2.2877	0.5	502	16	501	13	492	50	102
Plesovice[h]	2310	955	49	0.08	0.1	0.0542	1.5	0.4000	1.6	0.05	1.3002	0.5	340	5	342	5	351	29	97
GJ-1[h]	6697	306	28	0.03	0.2	0.0983	1.3	0.8144	2.1	0.06	2.1705	0.5	604	7	605	10			

$^{206}Pb/^{238}U$ error is the quadratic additions of the within run precision (2 SE) and the external reproducibility (2 SD) of the reference zircon. $^{207}Pb/^{206}Pb$ error propagation (^{207}Pb signal dependent) following Gerdes & Zeh (2009). $^{207}Pb/^{235}U$ error is the quadratic addition of the $^{207}Pb/^{206}Pb$ and $^{206}Pb/^{238}U$ uncertainty.

[a] Within run background-corrected mean ^{207}Pb signal in cps (counts per second).

[b] U and Pb content and Th/U ratio were calculated relative to GJ-1 reference zircon.

[c] Percentage of the common Pb on the ^{206}Pb. b.d. = below detection limit.

[d] Pb/U and Pb/Pb ratios. Corrected for background, within-run Pb/U fractionation (in case of $^{206}Pb/^{238}U$) and common Pb using Stacy and Kramers (1975) model Pb composition and subsequently normalised to GJ-1 (ID-TIMS value/measured value); $^{207}Pb/^{235}U$ calculated using (($^{207}Pb/^{206}Pb$)*($^{238}U/^{206}Pb$)*137.88).

[e] Rho (ρ) is the ($^{206}Pb/^{238}U$)/($^{207}Pb/^{235}U$) error correlation coefficient.

[f] Pb/U and Pb/Pb ages.

[g] Degree of concordance = (($^{206}Pb/^{238}U$ age)/($^{207}Pb/^{206}Pb$ age)) x 100.

[h] Mean of 13 (91500), 13 (Felix), 13 (Plesovice), and 26(GJ-1) analyses, respectively.

Table Ig10-U

U, Th and Pb LA-ICP-MS data of zircon crystals from sample GCH-13

Grain	^{207}Pb[a] (cps)	U[b] (ppm)	Pb[b] (ppm)	Th/U[b]	^{206}Pbc[c] (%)	$^{207}Pb/^{235}U$[d]	±2σ (%)	$^{206}Pb/^{238}U$[d]	±2σ (%)	ρ[e] (rho)	$^{207}Pb/^{206}Pb$[d]	±2σ (%)	$^{206}Pb/^{238}U$[f]	±2σ (Ma)	$^{207}Pb/^{235}U$[f]	±2σ (Ma)	$^{207}Pb/^{206}Pb$[f]	±2σ (Ma)	Conc.[g] (%)
A112	13331	1969	138	0.73	0.0	0.4873	1.9	0.0646	1.5	0.80	0.0547	1.1	404	6	403	6	399	25	101
A096	14103	1608	125	0.73	0.3	0.5546	2.4	0.0710	1.5	0.62	0.0566	1.9	442	6	448	9	477	41	93
A044	13830	1215	105	0.77	2.0	0.5844	4.4	0.0752	1.4	0.32	0.0564	4.2	467	6	467	17	467	92	100
A066	3603	222	18	0.73	0.0	0.5990	2.6	0.0759	1.4	0.52	0.0573	2.2	471	6	477	10	502	49	94
A094	3131	183	16	0.89	0.1	0.6022	2.3	0.0761	1.5	0.63	0.0574	1.8	473	7	479	9	506	40	93
A095	1638	87	7	0.68	0.4	0.5977	3.7	0.0761	1.7	0.46	0.0569	3.3	473	8	476	14	489	73	97
A073	2146	130	11	0.74	b.d.	0.6003	3.0	0.0762	1.4	0.48	0.0572	2.6	473	7	477	11	498	58	95
A072	2848	179	15	0.69	b.d.	0.5998	2.9	0.0762	1.4	0.48	0.0571	2.5	473	6	477	11	495	55	96
A046	2672	118	11	0.83	2.6	0.6068	4.7	0.0763	1.5	0.31	0.0577	4.5	474	7	482	18	518	98	91
A111	10386	1056	83	0.30	2.1	0.5984	4.2	0.0763	1.7	0.40	0.0569	3.9	474	8	476	16	487	86	97
A093	3462	150	14	0.92	3.3	0.6021	5.3	0.0764	1.7	0.32	0.0572	5.0	475	8	479	20	498	111	95
A042	1701	224	19	0.76	b.d.	0.6095	3.8	0.0765	1.5	0.39	0.0578	3.5	475	7	483	15	522	78	91
A023	5615	314	29	1.17	0.7	0.6125	3.3	0.0772	1.4	0.43	0.0576	2.9	479	7	485	13	514	65	93
A051	10866	1166	95	0.51	0.3	0.6148	2.1	0.0775	1.4	0.64	0.0576	1.6	481	6	487	8	513	36	94
A078	6866	418	39	1.27	0.0	0.6173	1.9	0.0778	1.4	0.73	0.0575	1.3	483	6	488	7	512	28	94
A108	1943	253	23	1.02	b.d.	0.6194	3.7	0.0779	1.5	0.40	0.0577	3.4	483	7	489	14	518	74	93
A040	16350	1688	140	0.86	0.9	0.6088	2.7	0.0780	1.7	0.63	0.0566	2.1	484	8	483	10	477	46	101
A074	8101	482	45	1.25	0.0	0.6128	2.0	0.0782	1.3	0.65	0.0569	1.5	485	6	485	8	486	34	100
A062	14324	1530	119	0.33	0.1	0.6278	2.1	0.0782	1.6	0.76	0.0582	1.4	485	7	495	8	538	30	90
A098	18093	1574	131	0.66	2.7	0.6160	4.6	0.0783	1.6	0.35	0.0570	4.3	486	8	487	18	493	95	99
A027	5854	538	45	0.45	2.9	0.6116	5.2	0.0784	1.6	0.30	0.0566	5.0	486	7	485	20	476	110	102
A100	5241	615	52	0.70	0.1	0.6120	2.3	0.0784	1.4	0.60	0.0566	1.8	487	6	485	9	475	40	102
A091	4831	226	22	1.39	1.7	0.6179	4.9	0.0785	1.7	0.35	0.0571	4.6	487	8	489	19	495	102	98
A082	25694	2263	185	0.42	2.2	0.6202	3.4	0.0790	1.4	0.40	0.0570	3.1	490	6	490	13	490	68	100
A076	4232	256	23	1.07	0.0	0.6241	2.3	0.0791	1.5	0.63	0.0572	1.8	491	7	492	9	501	40	98
A077	2336	140	12	0.63	0.3	0.6257	2.7	0.0791	1.4	0.51	0.0574	2.3	491	7	493	11	506	52	97
A016	1444	88	8	1.15	0.1	0.6305	3.3	0.0791	1.8	0.54	0.0578	2.8	491	9	496	13	522	62	94
A015	22326	1391	133	1.20	1.5	0.6391	4.3	0.0793	2.7	0.62	0.0585	3.4	492	13	502	17	548	73	90
A053	2528	161	14	0.91	b.d.	0.6279	2.8	0.0794	1.5	0.53	0.0574	2.4	493	7	495	11	505	52	98
A045	4869	589	57	1.29	0.0	0.6303	2.1	0.0795	1.4	0.66	0.0575	1.6	493	7	496	8	512	35	96
A056	11059	458	40	0.43	3.4	0.6370	4.8	0.0798	1.5	0.32	0.0579	4.5	495	7	500	19	527	99	94
A052	3162	369	35	1.16	b.d.	0.6333	2.6	0.0802	1.4	0.54	0.0573	2.2	497	7	498	10	502	48	99
A008	1616	99	10	1.24	0.0	0.6341	3.6	0.0802	1.5	0.41	0.0573	3.3	497	7	499	14	505	73	99
A058	2192	232	21	0.87	0.2	0.6442	2.1	0.0803	1.5	0.72	0.0582	1.5	498	7	505	9	537	32	93
A039	4311	240	23	1.33	b.d.	0.6360	2.6	0.0803	1.5	0.59	0.0574	2.1	498	7	500	10	509	46	98
A020	7211	602	54	0.60	2.9	0.6332	4.4	0.0803	1.5	0.34	0.0572	4.1	498	7	498	17	499	91	100
A097	31345	3570	307	0.63	0.2	0.6380	1.9	0.0806	1.4	0.77	0.0574	1.2	500	7	501	7	508	26	98
A089	648	79	8	1.12	0.0	0.6369	3.9	0.0807	1.8	0.47	0.0572	3.5	500	9	500	16	500	76	100
A029	3958	428	36	0.38	1.5	0.6375	5.8	0.0808	1.5	0.25	0.0573	5.7	501	7	501	23	502	125	100
A006	4598	282	26	1.03	0.0	0.6453	2.8	0.0808	1.5	0.53	0.0579	2.4	501	7	506	11	527	52	95
A024	5226	316	31	1.28	0.0	0.6389	2.2	0.0809	1.3	0.61	0.0573	1.7	501	7	502	9	503	38	100
A007	5691	626	57	0.76	0.5	0.6384	3.7	0.0809	1.8	0.48	0.0572	3.2	502	9	501	15	500	71	100
A019	11922	1433	120	0.51	0.0	0.6436	2.1	0.0810	1.5	0.69	0.0576	1.5	502	7	505	8	515	34	97
A038	2943	177	17	1.16	0.0	0.6448	3.0	0.0812	1.3	0.42	0.0576	2.7	503	6	505	12	515	60	98
A012	2384	140	12	0.62	0.4	0.6428	3.1	0.0812	1.4	0.45	0.0574	2.7	503	7	504	12	508	60	99
A054	2612	155	14	0.98	b.d.	0.6460	2.6	0.0816	1.4	0.53	0.0574	2.2	506	7	506	10	508	48	99
A110	3841	431	42	1.21	0.0	0.6491	2.6	0.0816	1.3	0.52	0.0577	2.2	506	7	508	10	517	49	98
A032	4262	401	34	0.36	2.3	0.6519	4.6	0.0817	1.5	0.33	0.0579	4.3	506	7	510	19	526	95	96
A107	2804	307	30	1.25	0.2	0.6461	3.4	0.0817	1.6	0.47	0.0574	3.0	506	8	506	14	506	65	100
A109	2973	326	32	1.25	b.d.	0.6450	3.1	0.0817	1.6	0.52	0.0573	2.6	506	8	505	12	502	58	101
A055	2713	163	16	1.05	0.0	0.6528	3.6	0.0818	1.4	0.41	0.0579	3.3	507	7	510	14	525	72	97
A028	3416	419	36	0.57	0.0	0.6507	2.6	0.0819	1.6	0.64	0.0577	2.0	507	8	509	10	516	44	98
A030	3209	194	18	1.00	b.d.	0.6491	2.7	0.0819	1.4	0.50	0.0575	2.3	507	7	508	11	511	51	99
A011	3720	436	36	0.35	0.5	0.6531	2.7	0.0819	1.4	0.53	0.0578	2.3	508	7	510	11	523	50	97
A101	3912	448	43	1.14	0.1	0.6482	2.9	0.0821	1.4	0.48	0.0573	2.6	508	7	507	12	503	57	101
A084	1989	212	18	0.44	b.d.	0.6513	3.5	0.0822	1.6	0.46	0.0575	3.1	509	8	509	14	511	68	100
A031	2498	152	14	1.05	b.d.	0.6626	3.5	0.0822	1.4	0.41	0.0585	3.2	509	7	516	14	547	69	93
A059	11921	1291	114	0.67	b.d.	0.6540	2.2	0.0823	1.6	0.72	0.0576	1.5	510	8	511	9	516	33	99
A088	3209	371	32	0.61	0.4	0.6496	2.8	0.0823	1.5	0.52	0.0573	2.4	510	7	508	11	501	53	102
A049	2650	314	29	0.89	b.d.	0.6528	2.7	0.0823	1.3	0.48	0.0575	2.4	510	6	510	11	511	52	100
A063	1978	232	23	1.16	b.d.	0.6598	2.7	0.0829	1.6	0.59	0.0577	2.2	513	8	514	11	519	48	99
A041	3344	404	35	0.51	b.d.	0.6583	2.8	0.0829	1.3	0.47	0.0576	2.5	513	7	514	11	514	55	100
A047	3805	483	48	1.18	0.0	0.6599	2.4	0.0830	1.5	0.62	0.0577	1.9	514	7	515	10	518	42	99
A087	15478	1738	149	0.48	0.0	0.6709	1.8	0.0832	1.3	0.73	0.0585	1.2	515	7	521	7	549	27	94
A021	3562	422	42	1.19	0.0	0.6622	2.9	0.0832	1.5	0.50	0.0577	2.5	515	7	516	12	519	55	99
A018	3920	475	48	1.33	b.d.	0.6623	3.1	0.0833	1.5	0.50	0.0577	2.6	515	8	516	12	518	58	99
A075	10579	628	63	1.34	b.d.	0.6629	1.9	0.0833	1.2	0.63	0.0577	1.5	516	6	516	8	520	32	99

Grain	^{207}Pb[a] (cps)	U[b] (ppm)	Pb[b] (ppm)	Th[b] U	^{206}Pbc[c] (%)	$^{207}Pb/^{235}U$[d]	±2σ (%)	$^{206}Pb/^{238}U$[d]	±2σ (%)	ρ[e] (rho)	$^{207}Pb/^{206}Pb$[d]	±2σ (%)	$^{206}Pb/^{238}U$[f]	±2σ (Ma)	$^{207}Pb/^{235}U$[f]	±2σ (Ma)	$^{207}Pb/^{206}Pb$[f]	±2σ (Ma)	Conc.[g] (%)
A010	2486	293	25	0.55	b.d.	0.6677	3.1	0.0834	1.7	0.55	0.0581	2.5	516	8	519	12	533	56	97
A043	1391	156	13	0.31	b.d.	0.6808	4.1	0.0836	1.6	0.39	0.0590	3.7	518	8	527	17	568	81	91
A083	1389	156	16	1.33	b.d.	0.6764	4.5	0.0838	1.7	0.38	0.0585	4.1	519	9	525	19	549	90	94
A081	4127	464	40	0.48	b.d.	0.6710	2.4	0.0841	1.4	0.58	0.0579	2.0	521	7	521	10	524	43	99
A009	3909	503	43	0.42	b.d.	0.6712	4.1	0.0842	1.5	0.37	0.0578	3.8	521	8	521	17	524	82	99
A025	4921	562	48	0.42	0.3	0.6682	2.6	0.0842	1.4	0.54	0.0576	2.2	521	7	520	11	513	48	102
A080	3771	459	40	0.51	b.d.	0.6800	2.7	0.0845	1.4	0.54	0.0584	2.3	523	7	527	11	544	49	96
A048	11077	1209	103	0.37	0.3	0.6783	1.7	0.0845	1.3	0.75	0.0582	1.1	523	6	526	7	538	25	97
A064	3032	317	26	0.18	0.4	0.6825	3.3	0.0852	1.5	0.47	0.0581	2.9	527	8	528	14	533	63	99
A079	11838	1323	121	0.66	b.d.	0.6973	2.4	0.0865	1.4	0.60	0.0584	1.9	535	7	537	10	546	42	98
A050	2845	306	28	0.64	b.d.	0.6948	2.6	0.0867	1.5	0.58	0.0581	2.1	536	8	536	11	534	47	100
A060	6171	517	47	0.32	3.3	0.7039	5.1	0.0872	1.5	0.30	0.0586	4.9	539	8	541	22	551	107	98
A057	8213	853	81	0.51	b.d.	0.7600	2.1	0.0924	1.2	0.57	0.0596	1.7	570	7	574	9	590	38	97
A061	21200	125	54	0.84	0.0	6.4660	1.9	0.3764	1.5	0.75	0.1246	1.3	2060	26	2041	17	2023	23	102
A017	12094	70	31	1.01	b.d.	6.6720	2.4	0.3769	1.6	0.67	0.1284	1.8	2062	28	2069	21	2076	31	99
A065	7985	45	19	0.71	b.d.	6.7350	2.1	0.3781	1.4	0.68	0.1292	1.5	2067	25	2077	19	2087	27	99
A022	10591	62	28	1.02	b.d.	6.7660	1.8	0.3815	1.3	0.69	0.1286	1.3	2083	23	2081	16	2079	23	100
A026	8037	97	48	1.51	b.d.	6.7940	2.1	0.3869	1.4	0.65	0.1274	1.6	2109	25	2085	19	2062	28	102
A014	91021	540	337	0.82	b.d.	13.1200	1.9	0.5177	1.8	0.91	0.1838	0.8	2689	39	2688	19	2688	13	100
A090	16235	52	39	0.80	0.0	16.0400	4.6	0.5597	1.8	0.38	0.2078	4.2	2866	41	2879	45	2889	69	99
A013	*8705*	*391*	*32*	*0.52*	*3.0*	*0.6298*	*4.1*	*0.0742*	*1.4*	*0.35*	*0.0616*	*3.8*	*461*	*6*	*496*	*16*	*658*	*82*	*70*
A092	*2930*	*95*	*9*	*1.00*	*6.3*	*0.6346*	*7.3*	*0.0771*	*1.8*	*0.25*	*0.0597*	*7.1*	*479*	*8*	*499*	*29*	*593*	*154*	*81*
A099	*8357*	*217*	*25*	*1.68*	*8.0*	*0.6638*	*8.6*	*0.0809*	*1.6*	*0.19*	*0.0595*	*8.5*	*501*	*8*	*517*	*36*	*587*	*184*	*85*
A085	*3636*	*132*	*13*	*0.92*	*6.3*	*0.7143*	*7.4*	*0.0824*	*1.6*	*0.21*	*0.0629*	*7.2*	*511*	*8*	*547*	*32*	*703*	*154*	*73*
A086	*4765*	*477*	*42*	*0.59*	*7.3*	*0.7070*	*10.7*	*0.0834*	*2.2*	*0.21*	*0.0615*	*10.5*	*516*	*11*	*543*	*46*	*657*	*225*	*79*
91500[h]	8532	69	13	0.45	0.3	0.1784	3.8	1.8103	6.1	0.07	4.3867	0.6	1058	37	1049	40	1030	89	103
Felix[h]	4019	203	23	1.93	0.4	0.0808	4.3	0.6109	10.3	0.05	7.7221	0.4	501	21	484	40	402	176	132
Plesovice[h]	2881	1038	54	0.16	0.2	0.0549	3.8	0.4045	3.8	0.05	1.5557	0.5	344	13	345	11	348	35	99
GJ-1[h]	6932	290	26	0.02	0.1	0.0984	1.1	0.8158	2.0	0.06	2.0856	0.5	605	6	606	9			

$^{206}Pb/^{238}U$ error is the quadratic additions of the within run precision (2 SE) and the external reproducibility (2 SD) of the reference zircon. $^{207}Pb/^{206}Pb$ error propagation (^{207}Pb signal dependent) following Gerdes & Zeh (2009). $^{207}Pb/^{235}U$ error is the quadratic addition of the $^{207}Pb/^{206}Pb$ and $^{206}Pb/^{238}U$ uncertainty.

[a] Within run background-corrected mean ^{207}Pb signal in cps (counts per second).

[b] U and Pb content and Th/U ratio were calculated relative to GJ-1 reference zircon.

[c] Percentage of the common Pb on the ^{206}Pb. b.d. = below detection limit.

[d] Pb/U and Pb/Pb ratios. Corrected for background, within-run Pb/U fractionation (in case of $^{206}Pb/^{238}U$) and common Pb using Stacy and Kramers (1975) model Pb composition and subsequently normalised to GJ-1 (ID-TIMS value/measured value); $^{207}Pb/^{235}U$ calculated using (($^{207}Pb/^{206}Pb$)*($^{238}U/^{206}Pb$)*137.88).

[e] Rho (ρ) is the ($^{206}Pb/^{238}U$)/($^{207}Pb/^{235}U$) error correlation coefficient.

[f] Pb/U and Pb/Pb ages.

[g] Degree of concordance = (($^{206}Pb/^{238}U$ age)/($^{207}Pb/^{206}Pb$ age)) x 100.

[h] Mean of 11 (91500), 11 (Felix), 9 (Plesovice), and 26 (GJ-1) analyses, respectively.

Table Ig11-U

U, Th and Pb LA-ICP-MS data of zircon crystals from sample GCH-14

Grain	^{207}Pb[a] (cps)	U[b] (ppm)	Pb[b] (ppm)	Th[b] U	^{206}Pbc[c] (%)	^{207}Pb[d] ^{235}U	±2σ (%)	^{206}Pb[d] ^{238}U	±2σ (%)	ρ[e] (rho)	^{207}Pb[d] ^{206}Pb	±2σ (%)	^{206}Pb[f] ^{238}U	±2σ (Ma)	^{207}Pb[f] ^{235}U	±2σ (Ma)	^{207}Pb[f] ^{206}Pb	±2σ (Ma)	Conc.[g] (%)
A185	3968	171	9	0.01	0.4	0.4198	2.7	0.0563	1.4	0.52	0.0541	2.3	353	5	356	8	377	51	94
A245	6904	381	22	0.03	0.5	0.4553	2.5	0.0608	1.5	0.61	0.0543	2.0	380	6	381	8	385	44	99
A236	1760	106	7	0.00	4.2	0.4704	6.0	0.0623	2.2	0.36	0.0547	5.6	390	8	391	20	401	126	97
A139	6348	209	14	0.21	1.5	0.4776	3.5	0.0635	2.1	0.59	0.0546	2.8	397	8	396	12	395	64	100
A228	3620	137	10	0.30	0.3	0.4988	2.3	0.0658	1.7	0.71	0.0550	1.7	410	7	411	8	413	37	99
A142	5686	174	12	0.16	1.1	0.5461	3.0	0.0706	1.6	0.55	0.0561	2.5	440	7	442	11	456	55	96
A201	3639	113	9	0.41	0.4	0.5439	3.3	0.0707	1.7	0.51	0.0558	2.9	440	7	441	12	445	64	99
A220	10165	304	23	0.24	3.9	0.5494	5.5	0.0713	1.6	0.29	0.0559	5.3	444	7	445	20	447	118	99
A129	2018	65	5	0.45	2.3	0.5643	5.1	0.0729	1.8	0.35	0.0561	4.7	454	8	454	19	457	105	99
A227	4498	156	12	0.15	0.9	0.5788	3.1	0.0744	1.5	0.48	0.0564	2.7	463	7	464	12	468	60	99
A175	8237	324	23	0.10	0.1	0.5830	2.2	0.0749	1.4	0.64	0.0564	1.7	466	6	466	8	469	38	99
A143	3692	124	10	0.25	1.6	0.5915	6.6	0.0751	1.9	0.30	0.0571	6.3	467	9	472	25	495	138	94
A159	1319	49	4	0.39	0.4	0.5959	3.7	0.0755	1.5	0.41	0.0573	3.4	469	7	475	14	502	75	93
A231	1608	101	8	0.33	1.6	0.5901	4.3	0.0756	1.7	0.40	0.0566	3.9	470	8	471	16	477	86	98
A136	5708	484	41	0.52	b.d.	0.5913	2.6	0.0756	1.5	0.60	0.0567	2.1	470	7	472	10	481	45	98
A131	2028	141	11	0.30	0.7	0.5973	3.9	0.0757	1.9	0.49	0.0573	3.4	470	9	476	15	501	74	94
A166	2362	82	7	0.40	0.9	0.5944	3.3	0.0760	1.6	0.47	0.0568	2.9	472	7	474	13	482	65	98
A221	8775	419	35	0.23	3.2	0.6003	4.6	0.0761	1.7	0.37	0.0572	4.2	473	8	477	18	500	93	95
A154	2865	146	13	0.33	3.8	0.6034	5.2	0.0768	1.7	0.33	0.0570	4.9	477	8	479	20	491	109	97
A234	29331	458	55	0.23	20.8	0.6058	9.6	0.0768	2.5	0.27	0.0572	9.2	477	12	481	37	499	203	96
A167	4163	149	12	0.31	0.5	0.6031	3.1	0.0769	1.7	0.54	0.0569	2.6	478	8	479	12	487	57	98
A200	7239	267	22	0.46	0.0	0.6029	2.1	0.0771	1.5	0.71	0.0567	1.5	479	7	479	8	480	33	100
A170	10002	167	17	0.53	8.1	0.6064	7.1	0.0774	2.0	0.29	0.0568	6.8	480	9	481	27	485	150	99
A230	4482	331	28	0.48	0.3	0.6068	2.8	0.0775	1.8	0.62	0.0568	2.2	481	8	482	11	483	49	100
A233	13043	915	90	0.94	0.3	0.6072	2.4	0.0776	2.0	0.80	0.0568	1.5	482	9	482	9	483	32	100
A183	4403	150	11	0.16	0.2	0.6074	2.1	0.0777	1.5	0.69	0.0567	1.5	482	7	482	8	481	34	100
A232	7508	443	40	0.53	0.6	0.6125	2.3	0.0781	1.4	0.61	0.0569	1.8	485	7	485	9	487	40	100
A226	13306	221	27	0.42	18.1	0.6186	9.0	0.0782	2.4	0.27	0.0574	8.6	485	11	489	35	506	190	96
A189	2479	71	6	0.32	1.7	0.6159	4.2	0.0782	1.6	0.38	0.0571	3.9	486	7	487	16	496	85	98
A173	1614	59	5	0.33	0.2	0.6208	4.0	0.0784	1.8	0.44	0.0574	3.6	487	8	490	16	508	79	96
A243	4533	155	14	0.49	0.6	0.6167	2.6	0.0785	1.7	0.65	0.0570	2.0	487	8	488	10	490	44	99
A210	3189	110	9	0.36	0.0	0.6189	2.6	0.0786	1.6	0.61	0.0571	2.1	488	8	489	10	495	46	99
A244	9992	292	31	0.54	9.3	0.6190	7.2	0.0787	1.9	0.26	0.0571	6.9	488	9	489	28	494	152	99
A235	9165	673	63	0.73	0.2	0.6194	2.0	0.0788	1.3	0.67	0.0570	1.5	489	6	489	8	491	33	100
A219	8400	308	27	0.49	0.0	0.6215	1.8	0.0789	1.4	0.77	0.0572	1.2	489	7	491	7	497	26	98
A223	9746	275	23	0.30	1.8	0.6317	3.1	0.0789	1.5	0.49	0.0581	2.7	490	7	497	12	532	59	92
A180	7097	274	21	0.08	0.3	0.6218	2.3	0.0792	1.6	0.70	0.0570	1.7	491	8	491	9	490	37	100
A133	3624	257	22	0.46	0.0	0.6238	2.7	0.0792	1.5	0.56	0.0571	2.3	491	7	492	11	497	50	99
A176	2658	98	8	0.40	0.0	0.6243	2.7	0.0792	1.6	0.59	0.0572	2.2	491	7	493	10	498	47	99
A212	6027	206	18	0.53	0.3	0.6260	2.3	0.0794	1.4	0.59	0.0572	1.9	493	7	494	9	498	42	99
A213	2572	83	7	0.24	0.1	0.6260	2.5	0.0795	1.8	0.72	0.0571	1.7	493	8	494	10	496	38	99
A237	10656	317	27	0.30	0.7	0.6341	2.4	0.0795	1.5	0.65	0.0578	1.8	493	7	499	9	524	39	94
A207	4795	347	28	0.25	1.5	0.6254	3.3	0.0795	1.7	0.51	0.0570	2.9	493	8	493	13	493	63	100
A206	5306	74	8	0.39	10.0	0.6295	8.2	0.0797	2.2	0.26	0.0573	7.9	494	10	496	33	503	175	98
A186	3337	236	21	0.42	0.2	0.6347	2.7	0.0800	1.5	0.58	0.0575	2.2	496	7	499	11	512	48	97
A205	5888	216	17	0.16	0.0	0.6317	2.1	0.0800	1.4	0.65	0.0572	1.6	496	7	497	8	501	36	99
A127	2944	90	7	0.21	0.3	0.6413	3.4	0.0801	1.7	0.50	0.0581	2.9	496	8	503	14	534	64	93
A222	6925	96	8	0.38	0.7	0.6321	2.7	0.0801	1.7	0.64	0.0573	2.0	497	8	497	11	502	45	99
A202	2966	95	8	0.42	1.1	0.6302	3.8	0.0801	1.5	0.40	0.0571	3.5	497	7	496	15	495	77	100
A163	6222	444	36	0.25	0.4	0.6315	2.5	0.0802	1.5	0.61	0.0571	2.0	497	7	497	10	497	43	100
A143	4319	137	11	0.19	0.7	0.6337	3.4	0.0802	1.4	0.42	0.0573	3.1	497	7	498	13	503	67	99
A144	3910	96	9	0.36	4.3	0.6323	5.6	0.0803	1.5	0.27	0.0572	5.4	498	7	498	22	497	118	100
A137	5304	36	3	0.27	8.2	0.6378	8.0	0.0803	1.8	0.23	0.0576	7.8	498	9	501	32	516	171	97
A225	6636	222	19	0.37	0.4	0.6339	2.7	0.0804	1.5	0.53	0.0572	2.3	498	7	499	11	500	51	100
A162	5972	219	18	0.29	0.0	0.6360	2.2	0.0805	1.4	0.65	0.0573	1.7	499	7	500	9	504	37	99
A153	2980	108	9	0.30	0.3	0.6360	3.3	0.0805	1.5	0.46	0.0573	2.9	499	7	500	13	504	65	99
A224	1581	51	5	0.53	0.9	0.6362	3.7	0.0805	1.6	0.44	0.0573	3.3	499	8	500	15	505	73	99
A229	4382	151	13	0.29	0.3	0.6367	2.2	0.0806	1.5	0.69	0.0573	1.6	500	7	500	9	502	35	100
A188	2478	83	7	0.21	0.2	0.6367	3.1	0.0806	1.9	0.62	0.0573	2.5	500	9	500	12	501	54	100
A165	2119	76	7	0.43	0.2	0.6371	3.6	0.0807	1.6	0.45	0.0573	3.3	500	8	501	15	503	72	99
A246	15849	518	44	0.35	0.3	0.6386	2.3	0.0808	2.0	0.84	0.0574	1.3	501	9	501	9	505	28	99
A211	2379	27	2	0.10	3.5	0.6376	6.4	0.0808	2.1	0.32	0.0573	6.1	501	10	501	26	501	134	100
A177	4936	339	27	0.13	0.1	0.6391	2.6	0.0808	1.9	0.73	0.0573	1.8	501	9	502	10	505	39	99
A187	2882	209	18	0.42	0.5	0.6399	3.1	0.0809	1.5	0.49	0.0574	2.7	501	7	502	13	506	60	99
A126	1067	35	3	0.45	2.0	0.6445	5.6	0.0809	1.9	0.35	0.0578	5.2	501	9	505	22	522	115	96
A214	2114	152	13	0.26	0.4	0.6403	3.0	0.0810	1.7	0.55	0.0573	2.5	502	8	502	12	505	56	100
A160	2514	86	8	0.52	0.1	0.6439	2.9	0.0811	1.7	0.61	0.0576	2.3	503	8	505	11	514	50	98

Grain	^{207}Pb[a] (cps)	U[b] (ppm)	Pb[b] (ppm)	Th[b]/U	^{206}Pbc[c] (%)	$^{207}Pb/^{235}U$[d]	±2σ (%)	$^{206}Pb/^{238}U$[d]	±2σ (%)	ρ[e] (rho)	$^{207}Pb/^{206}Pb$[d]	±2σ (%)	$^{206}Pb/^{238}U$[f]	±2σ (Ma)	$^{207}Pb/^{235}U$[f]	±2σ (Ma)	$^{207}Pb/^{206}Pb$[f]	±2σ (Ma)	Conc.[g] (%)
A178	10300	355	28	0.10	0.2	0.6407	1.9	0.0812	1.5	0.78	0.0573	1.2	503	7	503	7	501	26	100
A209	5287	171	16	0.56	0.5	0.6436	3.2	0.0812	1.7	0.52	0.0575	2.8	503	8	505	13	510	61	99
A155	5409	160	13	0.17	3.7	0.6419	5.2	0.0813	1.6	0.31	0.0573	5.0	504	8	503	21	503	110	100
A141	11705	421	33	0.11	0.5	0.6424	2.4	0.0813	1.5	0.62	0.0573	1.8	504	7	504	9	504	40	100
A216	11514	345	29	0.29	0.5	0.6454	1.9	0.0813	1.5	0.81	0.0576	1.1	504	7	506	8	513	25	98
A191	2821	211	16	0.09	0.1	0.6435	2.9	0.0814	1.9	0.67	0.0573	2.1	504	9	504	12	504	47	100
A125	4538	168	15	0.54	0.1	0.6459	2.9	0.0815	1.6	0.55	0.0575	2.5	505	8	506	12	509	54	99
A132	4089	146	12	0.23	0.1	0.6485	2.3	0.0819	1.6	0.68	0.0574	1.7	508	8	508	9	507	37	100
A140	1387	50	4	0.34	0.3	0.6495	3.9	0.0819	1.8	0.46	0.0575	3.5	508	9	508	16	510	76	100
A130	5100	363	29	0.12	0.1	0.6493	2.5	0.0820	1.6	0.65	0.0574	1.9	508	8	508	10	508	42	100
A151	11425	406	32	0.11	0.0	0.6503	2.2	0.0820	1.7	0.75	0.0575	1.5	508	8	509	9	511	32	99
A182	9855	136	15	0.46	9.9	0.6573	7.5	0.0821	2.0	0.27	0.0581	7.2	509	10	513	30	532	157	96
A157	4139	153	14	0.56	0.0	0.6519	2.6	0.0823	1.5	0.56	0.0575	2.1	510	7	510	10	510	47	100
A192	6802	453	41	0.46	0.1	0.6525	2.4	0.0825	2.0	0.83	0.0574	1.4	511	10	510	10	507	30	101
A164	5055	168	14	0.26	0.6	0.6541	3.1	0.0826	1.6	0.51	0.0575	2.7	511	8	511	13	509	59	101
A135	10465	745	64	0.32	0.1	0.6600	2.0	0.0826	1.5	0.77	0.0579	1.3	512	8	515	8	528	28	97
A128	6891	224	21	0.57	0.2	0.6554	2.5	0.0827	1.5	0.62	0.0575	1.9	512	8	512	10	510	43	100
A172	5053	151	14	0.55	1.8	0.6599	3.9	0.0828	2.1	0.54	0.0578	3.3	513	10	515	16	522	71	98
A208	9842	355	32	0.48	0.0	0.6599	2.1	0.0830	1.7	0.83	0.0576	1.2	514	8	515	8	516	25	100
A190	5007	170	15	0.31	0.1	0.6642	2.7	0.0831	1.8	0.68	0.0580	1.9	515	9	517	11	528	43	97
A179	6148	296	28	0.41	3.4	0.6585	5.1	0.0831	1.6	0.32	0.0575	4.9	515	8	514	21	509	107	101
A215	8237	110	11	0.27	9.6	0.6623	7.6	0.0834	1.8	0.24	0.0576	7.4	516	9	516	31	515	163	100
A215	8231	48	5	0.27	9.9	0.6646	7.8	0.0834	1.8	0.23	0.0578	7.6	516	9	517	32	523	166	99
A171	4660	156	13	0.25	0.0	0.6678	2.3	0.0837	1.7	0.74	0.0578	1.5	518	8	519	9	523	33	99
A134	4057	165	14	0.24	0.1	0.6684	3.3	0.0840	2.5	0.75	0.0577	2.2	520	12	520	14	519	48	100
A181	8975	577	49	0.20	0.8	0.6721	2.4	0.0842	1.6	0.64	0.0579	1.9	521	8	522	10	527	41	99
A193	8025	586	52	0.34	0.0	0.6766	2.4	0.0847	1.6	0.69	0.0579	1.7	524	8	525	10	527	37	100
A199	3015	239	20	0.11	0.2	0.6810	3.3	0.0853	1.6	0.50	0.0579	2.9	528	8	527	14	526	63	100
A158	2554	83	7	0.23	0.3	0.6949	3.0	0.0861	1.6	0.54	0.0585	2.6	533	8	536	13	549	56	97
A152	8740	640	56	0.20	0.1	0.6959	2.3	0.0880	1.7	0.73	0.0574	1.6	544	9	536	10	506	34	107
A184	5356	146	15	0.80	0.1	0.7151	3.5	0.0880	2.7	0.79	0.0589	2.1	544	14	548	15	565	46	96
A161	2466	153	17	0.64	0.0	0.7797	3.0	0.0953	1.7	0.57	0.0593	2.5	587	10	585	14	579	54	101
A203	3666	96	11	0.52	0.1	0.8180	2.4	0.0985	1.6	0.67	0.0603	1.7	605	9	607	11	612	38	99
A169	19873	105	30	0.37	1.5	3.2950	2.4	0.2518	1.6	0.67	0.0949	1.8	1448	21	1480	19	1526	34	95
A156	14935	63	25	0.58	0.3	5.4960	2.3	0.3420	1.6	0.69	0.1165	1.7	1896	26	1900	20	1904	30	100
A217	9148	37	14	0.52	b.d.	5.7170	2.2	0.3288	1.6	0.71	0.1261	1.6	1833	25	1934	19	2044	27	90
A145	33818	261	103	0.31	0.1	6.4150	1.7	0.3639	1.4	0.84	0.1278	0.9	2001	24	2034	15	2068	16	97
A138	*9928*	*292*	*20*	*0.29*	*5.4*	*0.3795*	*9.3*	*0.0591*	*6.3*	*0.68*	*0.0466*	*6.8*	*370*	*23*	*327*	*26*	*27*	*163*	*1390*
A174	*4614*	*147*	*11*	*0.25*	*2.7*	*0.5551*	*5.0*	*0.0702*	*1.7*	*0.34*	*0.0574*	*4.7*	*437*	*7*	*448*	*18*	*506*	*103*	*86*
A143	*4397*	*139*	*11*	*0.17*	*0.3*	*0.6436*	*4.2*	*0.0791*	*1.6*	*0.37*	*0.0590*	*4.0*	*491*	*7*	*505*	*17*	*568*	*86*	*86*
A152	*8740*	*640*	*56*	*0.20*	*0.1*	*0.6959*	*2.3*	*0.0880*	*1.7*	*0.73*	*0.0574*	*1.6*	*544*	*9*	*536*	*10*	*506*	*34*	*107*
A218	*24715*	*155*	*24*	*0.26*	*30.5*	*0.1474*	*312*	*0.1096*	*4.5*	*0.01*	*0.0097*	*312*	*671*	*29*	*140*	*520*	-	-	-
A168	*15455*	*112*	*24*	*0.42*	*0.3*	*2.4470*	*5.2*	*0.1823*	*4.7*	*0.91*	*0.0974*	*2.1*	*1079*	*47*	*1257*	*38*	*1574*	*40*	*69*
A204	*3046*	*3*	-	*0.00*	*78.8*	-	-	-	-	-	*0.4476*	*119*	-	-	-	-	*4077*	*###*	-
91500[h]	8378	74	13	0.29	0.5	0.1795	1.4	1.8499	1.8	0.07	0.9148	0.5	1064	14	1063	12	1062	18	100
Felix[h]	12482	435	68	2.47	0.2	0.0821	3.0	0.6484	3.0	0.06	2.9654	0.4	509	15	507	12	502	65	102
Plesovice[h]	2852	651	34	0.09	1.3	0.0542	2.2	0.3989	4.1	0.05	2.8587	0.5	340	7	341	12	345	64	99
GJ-1[h]	9719	290	27	0.04	0.1	0.0984	1.2	0.8151	2.4	0.06	2.2245	0.5	605	7	605	11			

$^{206}Pb/^{238}U$ error is the quadratic additions of the within run precision (2 SE) and the external reproducibility (2 SD) of the reference zircon. $^{207}Pb/^{206}Pb$ error propagation (^{207}Pb signal dependent) following Gerdes & Zeh (2009). $^{207}Pb/^{235}U$ error is the quadratic addition of the $^{207}Pb/^{206}Pb$ and $^{206}Pb/^{238}U$ uncertainty.

[a] Within run background-corrected mean ^{207}Pb signal in cps (counts per second).

[b] U and Pb content and Th/U ratio were calculated relative to GJ-1 reference zircon.

[c] Percentage of the common Pb on the ^{206}Pb. b.d. = below detection limit.

[d] Pb/U and Pb/Pb ratios. Corrected for background, within-run Pb/U fractionation (in case of $^{206}Pb/^{238}U$) and common Pb using Stacy and Kramers (1975) model Pb composition and subsequently normalised to GJ-1 (ID-TIMS value/measured value); $^{207}Pb/^{235}U$ calculated using (($^{207}Pb/^{206}Pb$)*($^{238}U/^{206}Pb$)*137.88).

[e] Rho (ρ) is the ($^{206}Pb/^{238}U$)/($^{207}Pb/^{235}U$) error correlation coefficient.

[f] Pb/U and Pb/Pb ages.

[g] Degree of concordance = (($^{206}Pb/^{238}U$ age)/($^{207}Pb/^{206}Pb$ age)) x 100.

[h] Mean of 13 (91500), 13 (Felix), 13 (Plesovice), and 26(GJ-1) analyses, respectively.

Table Ig12-U

U, Th and Pb LA-ICP-MS data of zircon crystals from sample GCH-18

Grain	^{207}Pb[a] (cps)	U[b] (ppm)	Pb[b] (ppm)	Th[b] U	$^{206}Pb_c$[c] (%)	^{207}Pb[d] ^{235}U	±2σ (%)	^{206}Pb[d] ^{238}U	±2σ (%)	ρ[e] (rho)	^{207}Pb[d] ^{206}Pb	±2σ (%)	^{206}Pb[f] ^{238}U	±2σ (Ma)	^{207}Pb[f] ^{235}U	±2σ (Ma)	^{207}Pb[f] ^{206}Pb	±2σ (Ma)	Conc.[g] (%)
A493	28759	1603	117	0.00	0.0	0.6232	1.7	0.0793	1.5	0.85	0.0570	0.9	492	7	492	7	492	20	100
A508	48987	2679	195	0.00	0.3	0.6233	1.8	0.0793	1.6	0.88	0.0570	0.9	492	8	492	7	491	19	100
A505	38442	2179	158	0.00	0.0	0.6227	1.7	0.0794	1.5	0.87	0.0569	0.9	492	7	492	7	488	19	101
A488	34791	3891	285	0.01	0.0	0.6312	1.6	0.0799	1.3	0.86	0.0573	0.8	495	6	497	6	504	18	98
A479	47041	5376	395	0.01	0.1	0.6295	1.7	0.0799	1.5	0.88	0.0572	0.8	495	7	496	7	497	18	100
A501	30791	1820	134	0.01	0.0	0.6296	1.7	0.0802	1.5	0.87	0.0569	0.9	497	7	496	7	489	19	102
A502	42521	2454	181	0.00	0.0	0.6348	1.7	0.0803	1.5	0.86	0.0574	0.9	498	7	499	7	505	19	98
A499	32321	1881	138	0.01	0.0	0.6305	1.8	0.0803	1.5	0.85	0.0570	0.9	498	7	496	7	490	20	102
A478	45511	5167	380	0.01	b.d.	0.6325	1.7	0.0803	1.5	0.92	0.0571	0.7	498	7	498	7	497	15	100
A485	25080	3023	223	0.00	0.0	0.6313	1.7	0.0803	1.5	0.86	0.0570	0.9	498	7	497	7	492	20	101
A507	29413	1639	121	0.01	0.0	0.6308	1.7	0.0803	1.5	0.89	0.0570	0.8	498	7	497	7	490	17	102
A473	29549	3412	252	0.01	0.0	0.6360	1.7	0.0805	1.4	0.81	0.0573	1.0	499	7	500	7	504	22	99
A454	34190	4039	299	0.01	0.1	0.6369	1.7	0.0805	1.4	0.84	0.0574	0.9	499	7	500	7	506	20	99
A506	39111	2237	165	0.01	0.0	0.6365	1.8	0.0805	1.6	0.89	0.0574	0.8	499	8	500	7	505	18	99
A465	25989	2800	209	0.01	0.4	0.6368	1.8	0.0806	1.4	0.78	0.0573	1.1	500	7	500	7	504	25	99
A483	33894	3880	287	0.00	0.0	0.6352	1.7	0.0806	1.5	0.88	0.0572	0.8	500	7	499	7	498	18	100
A504	37380	2099	155	0.01	b.d.	0.6357	1.7	0.0807	1.5	0.84	0.0572	0.9	500	7	500	7	498	21	100
A472	45390	5205	386	0.00	0.0	0.6392	1.7	0.0808	1.5	0.90	0.0574	0.7	501	7	502	7	507	16	99
A471	37247	4191	311	0.00	0.0	0.6402	1.9	0.0809	1.6	0.85	0.0574	1.0	501	8	502	8	507	22	99
A462	39218	4505	335	0.01	b.d.	0.6377	1.7	0.0810	1.5	0.90	0.0571	0.7	502	7	501	7	495	16	101
A477	33773	1899	141	0.01	0.0	0.6386	1.7	0.0810	1.6	0.90	0.0572	0.7	502	8	501	7	498	16	101
A461	35478	1995	149	0.01	b.d.	0.6405	1.8	0.0812	1.5	0.85	0.0572	0.9	503	7	503	7	499	21	101
A510	44537	2451	183	0.01	b.d.	0.6416	1.8	0.0813	1.5	0.88	0.0572	0.8	504	7	503	7	501	19	101
A484	43736	5096	380	0.01	0.0	0.6421	1.6	0.0813	1.4	0.88	0.0573	0.8	504	7	504	6	502	17	100
A486	37044	880	66	0.01	0.1	0.6457	1.7	0.0814	1.4	0.84	0.0575	0.9	505	7	506	7	512	20	99
A466	40323	4422	332	0.00	0.0	0.6463	1.7	0.0815	1.5	0.87	0.0575	0.8	505	7	506	7	512	19	99
A481	40795	4540	339	0.01	0.1	0.6461	1.9	0.0815	1.6	0.85	0.0575	1.0	505	8	506	7	510	22	99
A476	31440	1725	129	0.01	0.0	0.6465	1.6	0.0816	1.4	0.89	0.0575	0.7	506	7	506	6	509	16	99
A482	37859	4509	338	0.01	0.0	0.6443	1.9	0.0816	1.6	0.86	0.0573	0.9	506	8	505	7	501	21	101
A455	39695	4665	350	0.01	0.0	0.6488	1.6	0.0817	1.4	0.86	0.0576	0.8	506	7	508	7	514	18	99
A487	32688	3731	280	0.01	0.0	0.6447	1.7	0.0818	1.5	0.86	0.0572	0.9	507	7	505	7	499	19	102
A491	32647	3800	286	0.01	b.d.	0.6510	1.7	0.0819	1.5	0.86	0.0577	0.9	507	7	509	7	517	20	98
A459	39586	2095	158	0.01	0.2	0.6500	1.6	0.0819	1.4	0.85	0.0576	0.9	507	7	508	7	513	19	99
A490	30001	3391	255	0.01	0.0	0.6495	1.7	0.0819	1.4	0.83	0.0575	0.9	507	7	508	7	511	21	99
A456	35242	3925	295	0.00	b.d.	0.6467	1.7	0.0819	1.5	0.89	0.0573	0.8	508	7	506	7	502	17	101
A516	42336	2350	177	0.00	0.0	0.6473	1.9	0.0819	1.7	0.90	0.0573	0.8	508	8	507	8	503	18	101
A467	31300	3607	271	0.01	0.0	0.6524	1.8	0.0820	1.5	0.80	0.0577	1.1	508	7	510	7	520	25	98
A474	34609	3914	295	0.01	b.d.	0.6534	1.6	0.0820	1.3	0.86	0.0578	0.8	508	7	511	6	521	18	98
A489	37148	900	68	0.01	0.0	0.6481	1.7	0.0821	1.5	0.88	0.0573	0.8	508	7	507	7	503	18	101
A509	38970	2160	163	0.01	b.d.	0.6515	1.6	0.0821	1.5	0.89	0.0576	0.8	509	7	509	7	513	17	99
A458	30963	1756	132	0.01	0.0	0.6471	1.8	0.0821	1.6	0.88	0.0572	0.9	509	8	507	7	498	19	102
A453	38693	4386	332	0.01	0.2	0.6490	1.6	0.0822	1.4	0.88	0.0573	0.8	509	7	508	7	502	17	101
A492	36855	2029	153	0.01	b.d.	0.6564	1.6	0.0824	1.4	0.86	0.0578	0.8	510	7	512	6	521	18	98
A469	38650	2133	161	0.01	0.0	0.6528	1.8	0.0824	1.6	0.88	0.0575	0.9	511	8	510	7	509	19	100
A515	47271	2575	195	0.01	0.0	0.6527	1.6	0.0825	1.4	0.89	0.0574	0.7	511	7	510	7	506	16	101
A512	40020	2292	173	0.00	0.0	0.6572	1.7	0.0825	1.5	0.87	0.0578	0.8	511	7	513	7	521	19	98
A513	46167	2550	193	0.00	0.0	0.6527	1.7	0.0826	1.6	0.89	0.0573	0.8	512	8	510	7	504	17	101
A511	31776	1795	136	0.00	b.d.	0.6570	1.7	0.0826	1.5	0.86	0.0577	0.9	512	7	513	7	518	19	99
A500	29613	1644	125	0.01	b.d.	0.6528	1.7	0.0827	1.4	0.84	0.0573	0.9	512	7	510	7	502	21	102
A457	53027	6124	465	0.00	b.d.	0.6562	1.6	0.0828	1.5	0.90	0.0575	0.7	513	7	512	7	511	16	100
A468	32939	3695	281	0.01	0.0	0.6602	1.7	0.0829	1.4	0.82	0.0578	1.0	513	7	515	7	521	22	98
A503	46136	2497	191	0.00	0.0	0.6605	1.6	0.0832	1.4	0.89	0.0576	0.7	515	7	515	6	513	16	100
A514	26217	1492	114	0.01	0.0	0.6568	1.9	0.0833	1.7	0.90	0.0572	0.8	516	9	513	8	499	18	103
A464	38717	4495	344	0.01	0.0	0.6630	1.7	0.0834	1.5	0.86	0.0577	0.9	516	7	516	7	517	20	100
A460	51005	2733	209	0.00	0.0	0.6624	1.7	0.0835	1.5	0.86	0.0575	0.9	517	7	516	7	511	19	101
A475	36685	4102	317	0.01	0.3	0.6671	1.8	0.0838	1.5	0.82	0.0577	1.0	519	7	519	7	519	23	100
A463	44070	4977	383	0.00	b.d.	0.6699	1.6	0.0839	1.4	0.88	0.0579	0.8	520	7	521	6	525	16	99
A480	47025	5371	416	0.00	b.d.	0.6738	1.6	0.0844	1.4	0.88	0.0579	0.8	522	7	523	7	526	17	99
A470	39664	4317	335	0.00	0.0	0.6754	1.6	0.0846	1.4	0.88	0.0579	0.8	524	7	524	6	526	17	99
A518	2094	35	8	0.45	0.0	2.1190	3.6	0.1966	1.7	0.48	0.0782	3.1	1157	18	1155	25	1151	62	101
A519	*5150*	*165*	*17*	*0.44*	*3.8*	*0.7494*	*5.3*	*0.0889*	*1.7*	*0.33*	*0.0611*	*5.0*	*549*	*9*	*568*	*23*	*644*	*108*	*85*
A517	*46509*	*193*	*85*	*0.51*	*2.9*	*7.4940*	*2.3*	*0.3583*	*1.5*	*0.66*	*0.1517*	*1.8*	*1974*	*26*	*2172*	*21*	*2365*	*30*	*83*

Grain	^{207}Pb[a] (cps)	U[b] (ppm)	Pb[b] (ppm)	Th[b] U	^{206}Pbc[c] (%)	$^{207}Pb/^{235}U$[d]	±2σ (%)	$^{206}Pb/^{238}U$[d]	±2σ (%)	ρ[e] (rho)	$^{207}Pb/^{206}Pb$[d]	±2σ (%)	$^{206}Pb/^{238}U$[f]	±2σ (Ma)	$^{207}Pb/^{235}U$[f]	±2σ (Ma)	$^{207}Pb/^{206}Pb$[f]	±2σ (Ma)	Conc.[g] (%)
91500[h]	7004	61	11	0.25	0.4	0.1794	2.1	1.8382	3.2	0.07	1.5934	0.6	1063	20	1059	21	1050	32	101
Felix[h]	6572	361	52	2.08	0.4	0.0810	3.3	0.6372	3.3	0.06	2.2877	0.5	502	16	501	13	492	50	102
Plesovice[h]	2310	955	49	0.08	0.1	0.0542	1.5	0.4000	1.6	0.05	1.3002	0.5	340	5	342	5	351	29	97
GJ-1[h]	6697	306	28	0.03	0.2	0.0983	1.3	0.8144	2.1	0.06	2.1705	0.5	604	7	605	10			

$^{206}Pb/^{238}U$ error is the quadratic additions of the within run precision (2 SE) and the external reproducibility (2 SD) of the reference zircon. $^{207}Pb/^{206}Pb$ error propagation (^{207}Pb signal dependent) following Gerdes & Zeh (2009). $^{207}Pb/^{235}U$ error is the quadratic addition of the $^{207}Pb/^{206}Pb$ and $^{206}Pb/^{238}U$ uncertainty.

[a] Within run background-corrected mean ^{207}Pb signal in cps (counts per second).

[b] U and Pb content and Th/U ratio were calculated relative to GJ-1 reference zircon.

[c] Percentage of the common Pb on the ^{206}Pb. b.d. = below detection limit.

[d] Pb/U and Pb/Pb ratios. Corrected for background, within-run Pb/U fractionation (in case of $^{206}Pb/^{238}U$) and common Pb using Stacy and Kramers (1975) model Pb composition and subsequently normalised to GJ-1 (ID-TIMS value/measured value); $^{207}Pb/^{235}U$ calculated using (($^{207}Pb/^{206}Pb$)*($^{238}U/^{206}Pb$)*137.88).

[e] Rho (ρ) is the ($^{206}Pb/^{238}U$)/($^{207}Pb/^{235}U$) error correlation coefficient.

[f] Pb/U and Pb/Pb ages.

[g] Degree of concordance = (($^{206}Pb/^{238}U$ age)/($^{207}Pb/^{206}Pb$ age)) x 100.

[h] Mean of 13 (91500), 13 (Felix), 13 (Plesovice), and 26(GJ-1) analyses, respectively.

Table Ig13-U

U, Th and Pb LA-ICP-MS data of zircon crystals from sample GCH-31

Grain	^{207}Pb[a] (cps)	U[b] (ppm)	Pb[b] (ppm)	$\frac{Th}{U}$[b]	^{206}Pbc[c] (%)	$\frac{^{207}Pb}{^{235}U}$[d]	±2σ (%)	$\frac{^{206}Pb}{^{238}U}$[d]	±2σ (%)	ρ[e] (rho)	$\frac{^{207}Pb}{^{206}Pb}$[d]	±2σ (%)	$\frac{^{206}Pb}{^{238}U}$[f]	±2σ (Ma)	$\frac{^{207}Pb}{^{235}U}$[f]	±2σ (Ma)	$\frac{^{207}Pb}{^{206}Pb}$[f]	±2σ (Ma)	Conc.[g] (%)
A258	8632	300	22	0.27	0.1	0.5990	2.4	0.0756	1.5	0.63	0.0575	1.9	470	7	477	9	510	42	92
A249	3499	121	10	0.70	0.1	0.5964	3.3	0.0760	1.6	0.49	0.0569	2.9	472	7	475	13	488	64	97
A217	13160	455	34	0.24	0.4	0.5956	3.1	0.0763	1.4	0.45	0.0566	2.8	474	6	474	12	476	62	100
A228	9010	284	22	0.39	0.4	0.6095	4.2	0.0764	1.6	0.38	0.0579	3.8	474	7	483	16	525	84	90
A260	5268	155	12	0.36	1.0	0.5977	7.4	0.0764	1.7	0.23	0.0568	7.2	475	8	476	28	482	159	99
A257	11541	375	29	0.43	0.0	0.6113	2.3	0.0766	1.6	0.69	0.0579	1.7	476	7	484	9	526	36	91
A230	8730	293	21	0.14	0.3	0.6019	4.3	0.0766	1.6	0.38	0.0570	4.0	476	8	478	17	491	88	97
A232	8842	298	26	0.87	0.0	0.6143	2.1	0.0769	1.4	0.69	0.0579	1.5	478	7	486	8	527	33	91
A248	6174	234	18	0.48	0.0	0.6082	2.5	0.0769	1.5	0.59	0.0573	2.0	478	7	482	10	504	45	95
A247	15568	513	39	0.31	0.6	0.6018	3.2	0.0770	1.5	0.46	0.0567	2.9	478	7	478	12	480	63	100
A243	29735	1011	74	0.17	0.1	0.6154	1.9	0.0770	1.5	0.77	0.0579	1.2	478	7	487	7	528	26	91
A218	7388	249	19	0.35	0.0	0.6170	2.4	0.0771	1.5	0.62	0.0580	1.9	479	7	488	9	531	41	90
A219	1878	72	6	0.58	0.0	0.6181	2.8	0.0773	1.5	0.54	0.0580	2.4	480	7	489	11	529	52	91
A223	25001	806	60	0.18	0.3	0.6182	2.6	0.0775	1.5	0.57	0.0578	2.1	481	7	489	10	524	46	92
A221	3431	121	10	0.60	b.d.	0.6203	2.9	0.0776	1.5	0.52	0.0580	2.5	482	7	490	11	528	54	91
A251	7414	272	22	0.47	0.0	0.6236	2.4	0.0777	1.5	0.62	0.0582	1.9	482	7	492	9	538	41	90
A225	12397	255	22	0.57	3.7	0.6192	7.2	0.0777	1.7	0.24	0.0578	6.9	482	8	489	28	522	152	92
A237	11768	283	22	0.42	0.6	0.6134	4.1	0.0780	1.9	0.46	0.0570	3.7	484	9	486	16	493	81	98
A212	4120	130	10	0.41	0.0	0.6254	3.5	0.0783	1.6	0.45	0.0579	3.1	486	7	493	14	527	68	92
A227	7033	207	16	0.19	1.0	0.6244	7.1	0.0784	1.7	0.24	0.0578	6.9	486	8	493	28	521	151	93
A211	6269	198	16	0.42	b.d.	0.6275	2.3	0.0784	1.5	0.67	0.0581	1.7	486	7	495	9	532	37	91
A206	7715	260	20	0.38	0.0	0.6295	2.2	0.0784	1.5	0.67	0.0582	1.6	487	7	496	9	539	35	90
A256	6723	193	17	0.93	0.8	0.6206	5.7	0.0785	1.7	0.30	0.0574	5.4	487	8	490	22	506	119	96
A263	13296	445	35	0.33	0.6	0.6135	3.2	0.0785	1.5	0.45	0.0567	2.9	487	7	486	13	480	64	101
A233	2163	73	6	0.69	0.0	0.6329	3.5	0.0786	1.7	0.48	0.0584	3.0	488	8	498	14	544	66	90
A246	10987	353	29	0.47	b.d.	0.6332	2.0	0.0786	1.5	0.75	0.0584	1.3	488	7	498	8	545	29	90
A199	3237	101	8	0.30	0.6	0.6233	4.4	0.0787	1.6	0.36	0.0575	4.1	488	8	492	17	510	90	96
A229	3785	122	10	0.72	0.6	0.6214	9.5	0.0791	1.8	0.19	0.0570	9.4	491	8	491	38	491	207	100
A226	3549	123	10	0.53	b.d.	0.6304	3.2	0.0792	1.5	0.48	0.0577	2.8	491	7	496	13	520	62	94
A220	2223	80	7	0.65	0.0	0.6364	4.0	0.0794	1.5	0.38	0.0581	3.7	493	7	500	16	534	81	92
A208	4047	132	11	0.68	0.0	0.6448	3.3	0.0800	1.5	0.46	0.0585	2.9	496	7	505	13	547	64	91
A204	3291	109	9	0.49	0.0	0.6476	2.7	0.0802	1.5	0.58	0.0586	2.2	497	7	507	11	551	48	90
A245	7493	237	18	0.18	0.1	0.6469	4.5	0.0802	1.5	0.34	0.0585	4.3	497	7	507	18	548	93	91
A253	5782	138	11	0.36	0.6	0.6418	3.2	0.0804	1.6	0.48	0.0579	2.8	498	7	503	13	527	62	95
A215	16355	544	42	0.17	0.2	0.6373	2.4	0.0804	1.5	0.59	0.0575	2.0	499	7	501	10	510	43	98
A231	9365	289	22	0.16	0.4	0.6357	4.0	0.0806	1.4	0.36	0.0572	3.7	499	7	500	16	500	82	100
91500 198	1473	54	5	0.61	b.d.	0.6245	3.6	0.0806	1.7	0.46	0.0562	3.2	500	8	493	14	461	71	108
A255	3680	125	11	0.67	0.0	0.6490	3.1	0.0809	1.5	0.49	0.0582	2.7	501	7	508	12	537	59	93
A261	11608	358	31	0.78	0.0	0.6575	1.9	0.0812	1.4	0.75	0.0587	1.2	503	7	513	8	557	27	90
BB-16 197	2806	98	8	0.59	0.0	0.6628	3.6	0.0823	1.5	0.42	0.0584	3.2	510	7	516	15	545	70	93
A205	14190	452	35	0.15	0.1	0.6606	2.0	0.0824	1.4	0.71	0.0581	1.4	510	7	515	8	535	31	95
A264	10416	300	24	0.26	0.5	0.6539	3.7	0.0825	1.5	0.41	0.0575	3.4	511	8	511	15	511	75	100
lesovice 19	2433	81	7	0.62	b.d.	0.6702	4.2	0.0833	1.6	0.39	0.0584	3.9	516	8	521	17	543	85	95
A201	10884	337	27	0.25	0.2	0.6756	3.6	0.0838	1.5	0.42	0.0585	3.3	519	8	524	15	548	71	95
A235	9873	162	16	0.61	7.3	0.7031	11.6	0.0868	4.0	0.35	0.0588	10.9	537	21	541	50	558	237	96
A209	7366	180	21	0.92	0.0	0.8888	2.7	0.1036	1.5	0.56	0.0622	2.2	635	9	646	13	682	47	93
A200	6630	24	9	0.79	0.1	6.4360	2.6	0.3506	1.6	0.59	0.1331	2.1	1938	26	2037	23	2140	37	91
A259	*24981*	*747*	*50*	*0.12*	*0.1*	*0.5641*	*2.1*	*0.0703*	*1.8*	*0.87*	*0.0582*	*1.0*	*438*	*8*	*454*	*8*	*538*	*23*	*81*
A250	*3461*	*47*	*4*	*0.63*	*0.0*	*1.3800*	*7.6*	*0.0711*	*1.8*	*0.23*	*0.1409*	*7.4*	*443*	*8*	*881*	*46*	*2238*	*128*	*20*
A244	*2940*	*91*	*7*	*0.91*	*0.0*	*0.6713*	*3.5*	*0.0714*	*1.6*	*0.46*	*0.0682*	*3.1*	*445*	*7*	*522*	*14*	*874*	*64*	*51*
A234	*6461*	*225*	*17*	*0.62*	*0.1*	*0.5924*	*2.7*	*0.0718*	*1.4*	*0.53*	*0.0599*	*2.3*	*447*	*6*	*472*	*10*	*598*	*50*	*75*
A224	*12054*	*346*	*25*	*0.18*	*0.7*	*0.5686*	*3.9*	*0.0752*	*1.5*	*0.39*	*0.0548*	*3.6*	*467*	*7*	*457*	*15*	*405*	*81*	*115*
A236	*38485*	*492*	*45*	*0.31*	*9.5*	*0.6025*	*9.6*	*0.0753*	*1.9*	*0.20*	*0.0580*	*9.4*	*468*	*9*	*479*	*37*	*531*	*206*	*88*
A216	*5811*	*179*	*14*	*0.52*	*b.d.*	*0.6514*	*2.9*	*0.0765*	*1.5*	*0.51*	*0.0618*	*2.5*	*475*	*7*	*509*	*12*	*666*	*53*	*71*
A213	*3848*	*120*	*10*	*0.76*	*0.0*	*0.6309*	*3.2*	*0.0766*	*1.6*	*0.48*	*0.0597*	*2.8*	*476*	*7*	*497*	*13*	*594*	*61*	*80*
A252	*2232*	*63*	*5*	*0.65*	*b.d.*	*0.6980*	*4.1*	*0.0776*	*1.7*	*0.41*	*0.0652*	*3.7*	*482*	*8*	*538*	*17*	*782*	*79*	*62*
A202	*3313*	*112*	*9*	*0.67*	*0.0*	*0.6470*	*3.1*	*0.0794*	*1.5*	*0.50*	*0.0591*	*2.7*	*492*	*7*	*507*	*12*	*571*	*58*	*86*
A203	*9402*	*279*	*21*	*0.19*	*0.8*	*0.6640*	*3.5*	*0.0795*	*1.9*	*0.55*	*0.0606*	*3.0*	*493*	*9*	*517*	*14*	*624*	*64*	*79*
A222	*12584*	*435*	*34*	*0.28*	*2.3*	*0.6054*	*4.5*	*0.0799*	*1.5*	*0.32*	*0.0549*	*4.2*	*496*	*7*	*481*	*17*	*410*	*95*	*121*
A214	*4149*	*113*	*9*	*0.20*	*2.5*	*0.7143*	*4.6*	*0.0809*	*1.6*	*0.34*	*0.0640*	*4.3*	*502*	*8*	*547*	*20*	*743*	*92*	*68*
A254	*5736*	*169*	*14*	*0.25*	*4.3*	*0.6904*	*7.2*	*0.0825*	*1.6*	*0.22*	*0.0607*	*7.0*	*511*	*8*	*533*	*30*	*630*	*151*	*81*
A207	*5350*	*155*	*13*	*0.18*	*1.7*	*0.7261*	*3.7*	*0.0863*	*1.5*	*0.40*	*0.0610*	*3.4*	*534*	*8*	*554*	*16*	*641*	*73*	*83*
A210	*7375*	*174*	*18*	*0.80*	*0.0*	*0.8002*	*2.4*	*0.0937*	*1.5*	*0.63*	*0.0620*	*1.9*	*577*	*8*	*597*	*11*	*673*	*40*	*86*
A262	*46795*	*133*	*50*	*0.74*	*0.0*	*7.0020*	*1.8*	*0.3276*	*1.5*	*0.84*	*0.1550*	*1.0*	*1827*	*24*	*2112*	*16*	*2402*	*17*	*76*

Grain	^{207}Pb[a] (cps)	U[b] (ppm)	Pb[b] (ppm)	Th[b] / U	^{206}Pbc[c] (%)	$^{207}Pb/^{235}U$[d]	±2σ (%)	$^{206}Pb/^{238}U$[d]	±2σ (%)	ρ[e] (rho)	$^{207}Pb/^{206}Pb$[d]	±2σ (%)	$^{206}Pb/^{238}U$[f]	±2σ (Ma)	$^{207}Pb/^{235}U$[f]	±2σ (Ma)	$^{207}Pb/^{206}Pb$[f]	±2σ (Ma)	Conc.[g] (%)
91500[h]	14383	68	13	0.47	0.4	0.1781	3.4	1.8782	14.1	0.08	14.5260	0.6	1057	33	1072	98	1101	325	99
BB-16[h]	11251	302	28	0.40	0.0	0.0912	2.7	0.7668	3.3	0.06	1.5659	0.7	563	14	578	15	638	34	88
Plesovice[h]	17536	3943	198	0.20	3.0	0.0530	7.3	0.2289	70.7	0.03	65.9345	0.2	333	24	207	136			
GJ-1[h]	11801	290	26	0.02	0.4	0.0984	1.3	0.8153	2.3	0.06	1.4809	0.5	605	8	605	11			

$^{206}Pb/^{238}U$ error is the quadratic additions of the within run precision (2 SE) and the external reproducibility (2 SD) of the reference zircon. $^{207}Pb/^{206}Pb$ error propagation (^{207}Pb signal dependent) following Gerdes & Zeh (2009). $^{207}Pb/^{235}U$ error is the quadratic addition of the $^{207}Pb/^{206}Pb$ and $^{206}Pb/^{238}U$ uncertainty.

[a] Within run background-corrected mean ^{207}Pb signal in cps (counts per second).

[b] U and Pb content and Th/U ratio were calculated relative to GJ-1 reference zircon.

[c] Percentage of the common Pb on the ^{206}Pb. b.d. = below detection limit.

[d] Pb/U and Pb/Pb ratios. Corrected for background, within-run Pb/U fractionation (in case of $^{206}Pb/^{238}U$) and common Pb using Stacy and Kramers (1975) model Pb composition and subsequently normalised to GJ-1 (ID-TIMS value/measured value); $^{207}Pb/^{235}U$ calculated using (($^{207}Pb/^{206}Pb$)*($^{238}U/^{206}Pb$)*137.88).

[e] Rho (ρ) is the ($^{206}Pb/^{238}U$)/($^{207}Pb/^{235}U$) error correlation coefficient.

[f] Pb/U and Pb/Pb ages.

[g] Degree of concordance = (($^{206}Pb/^{238}U$ age)/($^{207}Pb/^{206}Pb$ age)) x 100.

[h] Mean of 9 (91500), 9 (BB-16), 9 (Plesovice), and 18 (GJ-1) analyses, respectively.

Table lg1-Hf

Lu, Yb and Hf LA-MC-ICPMS data of zircon crystals from sample GCH-25

Grain	$^{176}Yb/^{177}Hf$ [a]	±2σ	$^{176}Lu/^{177}Hf$ [a]	±2σ	$^{178}Hf/^{177}Hf$	$^{180}Hf/^{177}Hf$	Sig_{Hf} [b] (V)	$^{176}Hf/^{177}Hf$	±2σ [c]	$^{176}Hf/^{177}Hf_{(t)}$ [d]	$\varepsilon Hf_{(t)}$ [d]	±2σ [c] (εHf)	T_{DM} [e] (Ga)	age [f] (Ma)	±2σ (Ma)	U-Pb [g] conc	Lu-Hf [h] seq
GCH-25_195	0.0126	16	0.00041	5	1.46709	1.88655	6	0.282647	33	0.282644	3.8	1.2	0.86	396	6	93	6
GCH-25_194	0.0851	77	0.00267	20	1.46708	1.88651	5	0.282628	38	0.282605	3.8	1.3	0.91	458	7	46	6
GCH-25_188	0.0192	17	0.00067	5	1.46714	1.88667	5	0.282641	35	0.282635	5.1	1.2	0.85	468	7	58	6
GCH-25_187	0.0011	1	0.00004	0	1.46709	1.88651	7	0.282630	20	0.282629	3.2	0.7	0.89	391	7	96	6
GCH-25_186	0.0015	1	0.00004	0	1.46714	1.88663	7	0.282659	22	0.282658	4.1	0.8	0.84	386	6	92	6
GCH-25_185	0.0443	54	0.00150	16	1.46720	1.88654	6	0.282420	29	0.282405	-1.6	1.0	1.27	530	8	97	6
GCH-25_184	0.0557	53	0.00185	14	1.46706	1.88662	5	0.282439	33	0.282422	-1.8	1.2	1.25	497	7	94	6
GCH-25_183	0.0017	1	0.00005	0	1.46717	1.88674	7	0.282610	33	0.282610	2.6	1.2	0.93	396	6	96	6
GCH-25_182	0.0509	80	0.00170	24	1.46711	1.88653	5	0.282427	31	0.282411	-1.7	1.1	1.27	516	8	99	6
GCH-25_181	0.0010	1	0.00003	0	1.46715	1.88670	7	0.282618	26	0.282618	2.7	0.9	0.91	387	6	91	6
GCH-25_180	0.0531	45	0.00174	11	1.46703	1.88651	5	0.282416	31	0.282398	-1.9	1.1	1.29	530	7	90	6
GCH-25_179	0.0018	2	0.00006	0	1.46712	1.88667	7	0.282673	33	0.282672	4.6	1.2	0.81	385	6	92	6
GCH-25_178	0.0360	53	0.00122	17	1.46706	1.88667	6	0.282445	40	0.282433	-1.4	1.4	1.23	494	7	77	6
GCH-25_177	0.0019	2	0.00006	1	1.46712	1.88641	7	0.282665	23	0.282665	5.6	0.8	0.80	440	7	88	6
GCH-25_176	0.0104	8	0.00036	2	1.46717	1.88683	6	0.281036	32	0.281018	-4.1	1.1	3.08	2571	19	90	6
GCH-25_175	0.0245	20	0.00084	5	1.46711	1.88653	8	0.281115	28	0.281074	-2.2	1.0	2.97	2565	24	89	6
GCH-25_174	0.0022	2	0.00007	0	1.46699	1.88654	7	0.282600	33	0.282598	31.3	1.2	0.37	1677	172	96	6
GCH-25_173	0.0018	2	0.00006	0	1.46712	1.88658	7	0.282649	30	0.282649	3.8	1.1	0.85	388	6	91	6
GCH-25_172	0.0033	4	0.00011	1	1.46708	1.88641	7	0.282623	31	0.282623	2.9	1.1	0.91	387	6	90	6
GCH-25_171	0.0022	2	0.00008	1	1.46691	1.88639	6	0.282652	37	0.282651	3.9	1.3	0.85	386	6	93	6
GCH-25_170	0.0014	1	0.00005	0	1.46716	1.88657	7	0.282641	31	0.282641	3.4	1.1	0.87	381	6	94	6
GCH-25_169	0.0402	36	0.00137	10	1.46709	1.88654	6	0.282370	37	0.282357	-4.4	1.3	1.39	479	7	91	6
GCH-25_168	0.0009	1	0.00003	0	1.46705	1.88672	6	0.282610	29	0.282610	2.2	1.0	0.94	377	5	92	6
GCH-25_167	0.0401	61	0.00134	18	1.46704	1.88638	5	0.282505	33	0.282492	0.6	1.2	1.12	490	7	96	6
GCH-25_166	0.0026	3	0.00009	1	1.46710	1.88645	7	0.282656	27	0.282646	112.3	0.9	-1.81	4986	142	155	6
GCH-25_165	0.0021	3	0.00007	1	1.46710	1.88644	7	0.282668	31	0.282667	4.5	1.1	0.82	389	6	95	6
GCH-25_164	*0.0012*	*1*	*0.00004*	*0*	*1.46709*	*1.88661*	*6*	*0.282655*	*31*	*0.282655*	*4.0*	*1.1*	*0.84*	*387*	*9*	*90*	6
GCH-25_163	0.0022	2	0.00007	1	1.46705	1.88659	7	0.282646	24	0.282646	3.6	0.9	0.86	383	6	92	6
GCH-25_162	0.0391	33	0.00131	8	1.46706	1.88652	6	0.282453	23	0.282441	-1.6	0.8	1.22	475	7	72	6
GCH-25_161	0.0442	42	0.00148	12	1.46717	1.88676	5	0.282498	30	0.282484	0.1	1.0	1.14	483	7	59	6
GCH-25_160	0.0023	3	0.00007	1	1.46692	1.88645	6	0.282661	34	0.282661	4.4	1.2	0.83	394	12	93	6
GCH-25_159	0.0014	2	0.00004	0	1.46709	1.88664	6	0.282597	27	0.282596	2.1	1.0	0.95	394	6	94	6
GCH-25_158	*0.0215*	*21*	*0.00076*	*6*	*1.46709*	*1.88659*	*6*	*0.281981*	*31*	*0.281950*	*17.7*	*1.1*	*1.47*	*2084*	*35*	*66*	6
GCH-25_157	0.0317	27	0.00108	7	1.46715	1.88673	5	0.282400	31	0.282390	-3.1	1.1	1.32	487	7	69	6
GCH-25_156	0.0012	1	0.00004	0	1.46715	1.88655	7	0.282668	30	0.282668	6.6	1.1	0.78	481	7	101	6
GCH-25_155	0.0010	1	0.00003	0	1.46708	1.88653	7	0.282648	23	0.282648	4.0	0.8	0.85	398	6	98	6
GCH-25_154	*0.0373*	*43*	*0.00127*	*13*	*1.46713*	*1.88662*	*5*	*0.282499*	*33*	*0.282487*	*0.8*	*1.2*	*1.12*	*506*	*8*	*51*	6
GCH-25_153	0.0013	1	0.00004	0	1.46711	1.88663	7	0.282639	31	0.282638	5.3	1.1	0.84	468	7	75	6
GCH-25_152	*0.0515*	*43*	*0.00173*	*11*	*1.46716*	*1.88675*	*6*	*0.282420*	*30*	*0.282371*	*18.8*	*1.1*	*0.92*	*1485*	*126*	*29*	6
GCH-25_151	0.0016	1	0.00006	0	1.46706	1.88667	7	0.282656	29	0.282656	4.1	1.0	0.84	390	8	94	6
GCH-25_145	0.0017	2	0.00006	1	1.46714	1.88671	7	0.282605	27	0.282605	2.3	0.9	0.94	389	6	91	6
GCH-25_144	0.0071	15	0.00026	5	1.46722	1.88668	7	0.282628	34	0.282626	3.1	1.2	0.90	394	6	93	6
GCH-25_143	*0.0027*	*5*	*0.00010*	*2*	*1.46711*	*1.88673*	*7*	*0.282596*	*22*	*0.282595*	*1.9*	*0.8*	*0.96*	*386*	*6*	*93*	6
GCH-25_142	0.0009	1	0.00003	0	1.46713	1.88659	7	0.282645	26	0.282645	3.5	0.9	0.86	381	5	90	6
GCH-25_141	0.0048	8	0.00015	3	1.46693	1.88634	7	0.282691	39	0.282690	5.6	1.4	0.77	403	6	101	6
GCH-25_140	0.0030	3	0.00009	1	1.46688	1.88609	8	0.282644	45	0.282644	3.5	1.6	0.87	383	6	96	6
GCH-25_139	0.0300	30	0.00101	8	1.46708	1.88651	7	0.282440	35	0.282431	-2.0	1.2	1.24	473	7	77	6
GCH-25_138	0.0558	45	0.00187	12	1.46708	1.88666	5	0.282438	29	0.282421	-1.7	1.0	1.25	503	8	74	6
GCH-25_137	0.0012	1	0.00004	0	1.46706	1.88650	7	0.282658	26	0.282658	5.9	0.9	0.80	468	7	68	6
GCH-25_136	0.0024	8	0.00008	3	1.46706	1.88654	7	0.282641	25	0.282640	5.1	0.9	0.84	459	12	85	6
GCH-25_135	0.0510	78	0.00173	24	1.46714	1.88630	7	0.282428	55	0.282414	-2.9	2.0	1.28	458	11	83	6
GCH-25_134	0.0016	2	0.00006	1	1.46707	1.88647	6	0.282630	28	0.282630	3.3	1.0	0.89	396	7	94	6
GCH-25_133	0.0387	32	0.00132	8	1.46716	1.88676	5	0.282379	35	0.282283	69.4	1.2	-0.16	3764	61	12	6
GCH-25_132	0.0014	1	0.00005	0	1.46714	1.88667	7	0.282642	27	0.282642	3.4	1.0	0.87	382	6	93	6

Grain	$^{176}Yb/^{177}Hf$ [a]	±2σ	$^{176}Lu/^{177}Hf$ [a]	±2σ	$^{178}Hf/^{177}Hf$	$^{180}Hf/^{177}Hf$	Sig_{Hf} [b] (V)	$^{176}Hf/^{177}Hf$	±2σ [c]	$^{176}Hf/^{177}Hf_{(t)}$ [d]	$\varepsilon Hf_{(t)}$ [d]	±2σ [c] (εHf)	T_{DM} [e] (Ga)	age [f] (Ma)	±2σ (Ma)	U-Pb [g] conc	Lu-Hf [h] seq

Quoted uncertainties (absolute) relate to the last quoted figure. The effect of the inter-element fractionation on Lu/Hf was estimated to be about 6 % or less based on analyses of the GJ-1 and Plesoviče zircon. Accuracy and reproducibility was checked by repeated analyses of reference zircon GJ-1 and Plesoviče (data given as mean with 2 standard deviation uncertainties).

(a) $^{176}Yb/^{177}Hf = (^{176}Yb/^{173}Yb)_{true} \times (^{173}Yb/^{177}Hf)_{meas} \times (M_{173(Yb)}/M_{177(Hf)})^{\beta(Hf)}$, $\beta(Hf) = \ln((^{179}Hf/^{177}Hf_{true})/(^{179}Hf/^{177}Hf_{measured})) / \ln(M_{179(Hf)}/M_{177(Hf)})$, M = mass of respective isotopes. The $^{176}Lu/^{177}Hf$ was calculated in a similar way using $^{175}Lu/^{177}Hf$ and β(Yb).

(b) Mean Hf signal in volts.

(c) Uncertainties are quadratic additions of the within-run precision and the daily reproducibility of the 40ppb-JMC475 solution. Uncertainties for the JMC475 quoted at 2SD (2 standard deviation).

(d) Initial $^{176}Hf/^{177}Hf$ and εHf calculated using the apparent U-Pb age determined by LA-ICP-MS dating (see column f), and the CHUR parameters: $^{176}Lu/^{177}Hf$ = 0.0336, and $^{176}Hf/^{177}Hf$ = 0.282785 (Bouvier et al. 2008).

(e) Two stage model age in Ga using measured $^{176}Lu/^{177}Lu$ of each spot (first stage = age of zircon), a value of 0.0113 for the average continental crust (second stage, values compiled from Rudnick and Gao (2003), and depleted mantle $^{176}Lu/^{177}Lu$ = 0.0379, and $^{176}Hf/^{177}Hf$ = 0.283164.

(f) Apparent U-Pb age determined by LA-ICP-MS.

(g) U-Pb age concordance (%).

(h) Sequence in which Lu-Hf analyses were performed. Standard analyses for each sequence are showed on Table 12.

Table Ig2-Hf

Lu, Yb and Hf LA-MC-ICPMS data of zircon crystals from sample GCH-26

Grain	$^{176}Yb/^{177}Hf$ [a]	±2σ	$^{176}Lu/^{177}Hf$ [a]	±2σ	$^{178}Hf/^{177}Hf$	$^{180}Hf/^{177}Hf$	Sig_{Hf} [b] (V)	$^{176}Hf/^{177}Hf$	±2σ [c]	$^{176}Hf/^{177}Hf_{(t)}$ [d]	$\varepsilon Hf_{(t)}$ [d]	±2σ [c] (εHf)	T_{DM} [e] (Ga)	age [f] (Ma)	±2σ (Ma)	U-Pb [g] conc	Lu-Hf [h] seq
GCH-26_60	0.0657	57	0.00230	15	1.46706	1.88660	6	0.282659	38	0.282639	5.4	1.3	0.84	476	7	91	6
GCH-26_59	0.0324	35	0.00114	10	1.46711	1.88663	6	0.282301	32	0.282290	-6.2	1.1	1.50	509	8	91	6
GCH-26_58	0.0481	42	0.00165	11	1.46711	1.88659	5	0.282685	30	0.282669	7.1	1.1	0.77	504	10	95	6
GCH-26_57	0.0149	13	0.00060	4	1.46710	1.88652	8	0.282678	28	0.282674	4.7	1.0	0.81	386	7	95	6
GCH-26_56	0.0099	9	0.00040	3	1.46707	1.88659	8	0.282710	26	0.282707	6.0	0.9	0.74	392	6	93	6
GCH-26_54	0.0036	3	0.00015	1	1.46698	1.88641	7	0.282656	34	0.282655	5.2	1.2	0.82	438	8	65	6
GCH-26_53	0.0108	10	0.00056	4	1.46702	1.88634	5	0.282695	38	0.282684	19.8	1.3	0.50	1042	343	52	6
GCH-26_52	0.0622	55	0.00213	15	1.46704	1.88645	4	0.282633	38	0.282614	4.5	1.3	0.89	474	7	84	6
GCH-26_51	0.0057	6	0.00022	2	1.46712	1.88667	6	0.282655	34	0.282654	3.8	1.2	0.85	379	8	95	6
GCH-26_50	0.0114	10	0.00038	3	1.46714	1.88672	6	0.282705	25	0.282702	6.3	0.9	0.74	415	7	57	6
GCH-26_49	0.0162	28	0.00062	10	1.46704	1.88660	6	0.282680	30	0.282673	9.1	1.1	0.72	585	14	95	6
GCH-26_48	*0.0669*	*60*	*0.00226*	*16*	*1.46692*	*1.88610*	*3*	*0.282655*	*41*	*0.282630*	*7.6*	*1.4*	*0.81*	*585*	*9*	*93*	6
GCH-26_47	0.0055	6	0.00027	3	1.46713	1.88684	6	0.282647	31	0.282645	3.3	1.1	0.87	372	18	74	6
GCH-26_46	0.0357	30	0.00129	8	1.46715	1.88666	4	0.282661	37	0.282648	6.3	1.3	0.81	501	7	103	6
GCH-26_45	0.0093	9	0.00033	3	1.46708	1.88659	6	0.282687	27	0.282684	6.0	0.9	0.77	432	9	64	6
GCH-26_44	0.0494	42	0.00171	11	1.46715	1.88656	5	0.282645	37	0.282630	4.5	1.3	0.87	450	7	76	6
GCH-26_43	0.0070	6	0.00026	2	1.46706	1.88656	7	0.282710	32	0.282708	5.6	1.1	0.74	374	17	64	6
GCH-26_42	0.0218	20	0.00125	9	1.46722	1.88669	6	0.282658	33	0.282648	4.5	1.2	0.84	417	7	89	6
GCH-26_41	0.0550	101	0.00193	33	1.46718	1.88661	4	0.282674	45	0.282656	6.5	1.6	0.79	497	7	100	6
GCH-26_40	0.0121	11	0.00067	5	1.46699	1.88652	6	0.282680	33	0.282675	5.5	1.2	0.79	423	31	68	6
GCH-26_39	0.0403	33	0.00143	9	1.46708	1.88634	4	0.282690	41	0.282677	7.5	1.4	0.75	509	7	90	6
GCH-26_38	0.0250	21	0.00098	6	1.46703	1.88649	4	0.282569	39	0.282530	37.8	1.4	0.31	2062	240	27	6
GCH-26_32	0.0356	56	0.00122	18	1.46719	1.88666	4	0.282679	35	0.282667	7.3	1.3	0.77	513	7	91	6
GCH-26_31	0.0130	15	0.00059	6	1.46708	1.88673	6	0.282705	31	0.282700	6.3	1.1	0.74	418	9	83	6
GCH-26_30	0.0028	3	0.00013	1	1.46710	1.88680	6	0.282667	31	0.282666	4.2	1.1	0.82	379	6	93	6
GCH-26_29	0.0409	46	0.00143	14	1.46701	1.88673	4	0.282259	36	0.282246	-8.4	1.3	1.60	477	7	70	6
GCH-26_28	0.0137	11	0.00038	2	1.46704	1.88647	7	0.282714	29	0.282711	6.3	1.0	0.73	402	6	100	6
GCH-26_27	0.0217	22	0.00080	7	1.46710	1.88670	4	0.282651	37	0.282644	5.7	1.3	0.83	478	7	96	6
GCH-26_26	0.0064	7	0.00026	2	1.46698	1.88644	5	0.282687	33	0.282685	4.6	1.2	0.79	366	96	42	6
GCH-26_25	0.0056	6	0.00023	2	1.46706	1.88670	6	0.282696	34	0.282695	5.2	1.2	0.77	379	6	95	6
GCH-26_24	0.0058	5	0.00024	1	1.46703	1.88650	7	0.282685	31	0.282683	5.1	1.1	0.79	391	8	100	6
GCH-26_23	0.0596	48	0.00204	13	1.46697	1.88625	4	0.282649	38	0.282629	6.3	1.4	0.83	531	9	96	6
GCH-26_22	*0.0065*	*6*	*0.00022*	*2*	*1.46708*	*1.88665*	*6*	*0.282690*	*27*	*0.282688*	*5.3*	*1.0*	*0.77*	*393*	*6*	*93*	6
GCH-26_21	0.0074	7	0.00029	2	1.46713	1.88658	7	0.282685	28	0.282683	4.9	1.0	0.79	379	20	96	6
GCH-26_20	0.0112	10	0.00036	3	1.46707	1.88658	7	0.282696	26	0.282694	5.7	0.9	0.76	400	7	94	6
GCH-26_19	0.0630	78	0.00194	19	1.46697	1.88634	5	0.282646	34	0.282629	5.1	1.2	0.86	478	7	109	6
GCH-26_18	0.0108	9	0.00039	2	1.46705	1.88671	7	0.282660	23	0.282657	5.0	0.8	0.82	426	12	57	6
GCH-26_17	0.0102	10	0.00038	3	1.46707	1.88669	6	0.282665	22	0.282663	4.4	0.8	0.83	391	9	91	6
GCH-26_16	*0.0099*	*9*	*0.00036*	*3*	*1.46699*	*1.88643*	*6*	*0.282685*	*30*	*0.282683*	*5.0*	*1.1*	*0.79*	*388*	*6*	*96*	6
GCH-26_15	0.0169	15	0.00064	5	1.46699	1.88632	6	0.282668	42	0.282663	4.3	1.5	0.83	387	7	97	6
GCH-26_14	0.0034	3	0.00015	1	1.46711	1.88660	7	0.282698	31	0.282696	11.1	1.1	0.66	639	11	93	6
GCH-26_13	0.0052	5	0.00025	2	1.46697	1.88628	6	0.282684	47	0.282683	4.6	1.7	0.80	371	17	1133	6
GCH-26_12	0.0080	8	0.00030	2	1.46711	1.88650	8	0.282685	28	0.282685	-0.7	1.0	0.89	130	8	32	6
GCH-26_11	0.0372	34	0.00137	10	1.46704	1.88644	5	0.282546	31	0.282532	2.6	1.1	1.03	518	7	99	6
GCH-26_10	0.0060	5	0.00023	2	1.46707	1.88660	8	0.282691	24	0.282690	5.4	0.8	0.77	395	6	91	6
GCH-26_9	0.0421	37	0.00137	9	1.46704	1.88651	4	0.282643	41	0.282629	6.2	1.4	0.84	524	8	104	6
GCH-26_8	0.0012	1	0.00004	0	1.46707	1.88652	6	0.282662	26	0.282662	5.5	0.9	0.81	444	7	84	6
GCH-26_7	0.0090	8	0.00032	3	1.46711	1.88668	8	0.282649	21	0.282646	3.7	0.8	0.86	387	6	95	6
GCH-26_6	0.0206	38	0.00066	10	1.46718	1.88664	8	0.282669	24	0.282664	4.7	0.9	0.82	403	9	104	6

Quoted uncertainties (absolute) relate to the last quoted figure. The effect of the inter-element fractionation on Lu/Hf was estimated to be about 6 % or less based on analyses of the GJ-1 and Plesoviče zircon. Accuracy and reproducibility was checked by repeated analyses of reference zircon GJ-1 and Plesoviče (data given as mean with 2 standard deviation uncertainties).

(a) $^{176}Yb/^{177}Hf = (^{176}Yb/^{173}Yb)_{true} \times (^{173}Yb/^{177}Hf)_{meas} \times (M_{173(Yb)}/M_{177(Hf)})^{\beta(Hf)}$, $\beta(Hf) = \ln((^{179}Hf/^{177}Hf_{true})/(^{179}Hf/^{177}Hf_{measured})) / \ln(M_{179(Hf)}/M_{177(Hf)})$, M = mass of respective isotopes. The $^{176}Lu/^{177}Hf$ was calculated in a similar way using $^{175}Lu/^{177}Hf$ and β(Yb).

(b) Mean Hf signal in volts.

(c) Uncertainties are quadratic additions of the within-run precision and the daily reproducibility of the 40ppb-JMC475 solution. Uncertainties for the JMC475 quoted at 2SD (2 standard deviation).

(d) Initial $^{176}Hf/^{177}Hf$ and εHf calculated using the apparent U-Pb age determined by LA-ICP-MS dating (see column f), and the CHUR parameters: $^{176}Lu/^{177}Hf$ = 0.0336, and $^{176}Hf/^{177}Hf$ = 0.282785 (Bouvier et al. 2008).

(e) Two stage model age in Ga using measured $^{176}Lu/^{177}Lu$ of each spot (first stage = age of zircon), a value of 0.0113 for the average continental crust (second stage, values compiled from Rudnick and Gao (2003), and depleted mantle $^{176}Lu/^{177}Lu$ = 0.0379, and $^{176}Hf/^{177}Hf$ = 0.283164.

(f) Apparent U-Pb age determined by LA-ICP-MS.

(g) U-Pb age concordance (%).

(h) Sequence in which Lu-Hf analyses were performed. Standard analyses for each sequence are showed on Table 12.

Table Ig3-Hf

Lu, Yb and Hf LA-MC-ICPMS data of zircon crystals from sample GCH-32

Grain	$^{176}Yb/^{177}Hf$ [a]	±2σ	$^{176}Lu/^{177}Hf$ [a]	±2σ	$^{178}Hf/^{177}Hf$	$^{180}Hf/^{177}Hf$	Sig_{Hf} [b] (V)	$^{176}Hf/^{177}Hf$	±2σ [c]	$^{176}Hf/^{177}Hf_{(t)}$ [d]	$\varepsilon Hf_{(t)}$ [d]	±2σ [c] (εHf)	T_{DM} [e] (Ga)	age [f] (Ma)	±2σ (Ma)	U-Pb [g] conc	Lu-Hf [h] seq
GCH-32_131	0.0010	1	0.00003	0	1.46701	1.88668	6	0.282574	33	0.282574	1.3	1.2	1.00	395	6	93	6
GCH-32_130	0.0269	66	0.00088	21	1.46714	1.88675	6	0.282523	29	0.282515	1.5	1.0	1.07	497	8	90	6
GCH-32_129	0.0032	4	0.00010	1	1.46709	1.88642	9	0.282562	27	0.282561	0.9	1.0	1.02	395	6	103	6
GCH-32_128	0.0013	2	0.00003	0	1.46691	1.88617	7	0.282621	31	0.282621	3.1	1.1	0.90	399	6	97	6
GCH-32_127	0.0016	1	0.00004	0	1.46709	1.88656	7	0.282584	26	0.282584	1.6	0.9	0.98	391	6	96	6
GCH-32_126	0.0014	1	0.00003	0	1.46699	1.88635	7	0.282590	26	0.282590	4.0	0.9	0.93	489	7	96	6
GCH-32_125	0.0377	56	0.00124	17	1.46715	1.88674	5	0.282553	30	0.282542	2.5	1.1	1.02	497	8	-74	6
GCH-32_124	0.0292	28	0.00099	9	1.46704	1.88647	9	0.282411	32	0.282401	-2.0	1.1	1.28	520	8	98	6
GCH-32_123	0.0657	63	0.00207	15	1.46713	1.88661	8	0.282310	27	0.282289	-5.6	0.9	1.50	536	8	106	6
GCH-32_122	0.0198	17	0.00063	4	1.46711	1.88671	5	0.281281	34	0.281256	-7.8	1.2	2.86	2048	19	91	6
GCH-32_121	0.0528	43	0.00160	10	1.46714	1.88643	7	0.282390	29	0.282375	-3.6	1.0	1.35	488	10	215	6
GCH-32_120	0.0382	35	0.00127	9	1.46709	1.88639	6	0.282568	39	0.282538	19.0	1.4	0.70	1233	70	43	6
GCH-32_119	0.0033	3	0.00007	0	1.46710	1.88681	5	0.282569	-	-	-	-	-	-	-	-	6
GCH-32_118	0.0139	15	0.00035	3	1.46710	1.88664	11	0.282445	24	0.282442	-3.5	0.8	1.26	387	5	90	6
GCH-32_117	0.0016	2	0.00006	1	1.46692	1.88600	3	0.282740	80	0.282740	7.5	2.8	0.67	409	6	86	6
GCH-32_116	0.0007	1	0.00002	0	1.46711	1.88653	7	0.282573	35	0.282573	1.2	1.2	1.00	390	9	92	6
GCH-32_115	0.0019	2	0.00006	0	1.46713	1.88659	7	0.282575	28	0.282575	1.7	1.0	0.99	408	6	94	6
GCH-32_114	0.0223	18	0.00075	5	1.46714	1.88662	6	0.282524	32	0.282518	0.8	1.1	1.08	462	7	57	6
GCH-32_113	0.0059	9	0.00011	1	1.46666	1.88559	4	0.282693	75	0.282690	22.0	2.6	0.45	1127	447	33	6
GCH-32_112	0.0286	23	0.00096	6	1.46724	1.88660	5	0.282542	30	0.282533	2.4	1.0	1.03	508	8	71	6
GCH-32_111	0.0162	13	0.00057	3	1.46704	1.88651	5	0.282517	28	0.282512	1.5	1.0	1.08	498	8	95	6
GCH-32_110	0.0006	1	0.00002	0	1.46710	1.88667	8	0.282546	23	0.282546	0.3	0.8	1.05	394	6	95	6
GCH-32_109	0.0231	23	0.00076	6	1.46710	1.88651	5	0.282595	30	0.282588	4.2	1.0	0.93	501	8	68	6
GCH-32_108	0.0278	52	0.00088	16	1.46709	1.88647	10	0.282404	30	0.282396	-2.8	1.0	1.31	494	7	92	6
GCH-32_107	0.0308	32	0.00090	8	1.46711	1.88658	7	0.282441	26	0.282435	-3.5	0.9	1.27	399	7	90	6
GCH-32_101	0.0405	41	0.00135	11	1.46702	1.88637	5	0.282551	27	0.282538	2.4	1.0	1.02	499	7	70	6
GCH-32_100	0.0011	1	0.00003	0	1.46710	1.88652	7	0.282493	31	0.282493	-1.6	1.1	1.16	390	6	91	6
GCH-32_99	0.0098	8	0.00033	2	1.46717	1.88676	5	0.281321	31	0.281308	-5.5	1.1	2.75	2065	21	98	6
GCH-32_98	0.0335	33	0.00110	9	1.46712	1.88664	5	0.282548	31	0.282538	2.5	1.1	1.02	503	8	73	6
GCH-32_97	0.0841	200	0.00272	66	1.46712	1.88667	10	0.282310	32	0.282281	-5.4	1.1	1.50	559	12	90	6
GCH-32_96	0.0084	15	0.00033	6	1.46710	1.88672	8	0.282201	37	0.282198	-9.9	1.3	1.69	486	7	100	6
GCH-32_95	0.0155	13	0.00059	4	1.46707	1.88632	5	0.281822	41	0.281816	-22.3	1.4	2.41	536	10	63	6
GCH-32_94	0.0288	26	0.00092	7	1.46713	1.88654	6	0.282573	33	0.282545	26.9	1.2	0.53	1567	176	31	6
GCH-32_93	0.0440	53	0.00140	15	1.46715	1.88658	6	0.282560	34	0.282548	2.2	1.2	1.02	476	7	74	6
GCH-32_92	0.0355	30	0.00116	8	1.46711	1.88667	6	0.282369	31	0.282357	-2.6	1.1	1.35	564	8	73	6
GCH-32_91	0.0531	45	0.00191	13	1.46711	1.88659	9	0.282418	25	0.282401	-3.0	0.9	1.30	477	10	52	6
GCH-32_90	0.0301	38	0.00107	12	1.46709	1.88660	6	0.282257	31	0.282247	-8.2	1.1	1.60	486	7	73	6
GCH-32_89	0.0436	62	0.00158	21	1.46703	1.88642	6	0.282292	26	0.282276	-6.2	0.9	1.52	532	10	70	6
GCH-32_88	0.0551	53	0.00193	16	1.46716	1.88673	11	0.282236	18	0.282217	-8.8	0.6	1.65	505	8	91	6
GCH-32_87	0.0366	37	0.00121	10	1.46713	1.88669	6	0.282539	34	0.282528	1.3	1.2	1.06	467	7	71	6
GCH-32_86	0.0015	1	0.00004	0	1.46709	1.88666	7	0.282558	29	0.282558	0.5	1.0	1.03	385	6	98	6
GCH-32_85	0.0175	29	0.00060	9	1.46713	1.88666	6	0.282589	30	0.282584	3.5	1.1	0.95	476	8	68	6
GCH-32_84	0.0222	22	0.00083	7	1.46708	1.88654	8	0.282419	26	0.282413	-4.2	0.9	1.31	403	6	97	6
GCH-32_83	0.0407	38	0.00137	10	1.46705	1.88646	5	0.282595	30	0.282553	28.1	1.0	0.49	1609	117	35	6
GCH-32_82	0.0309	32	0.00104	9	1.46705	1.88659	5	0.282542	26	0.282507	30.2	0.9	0.51	1769	185	23	6
GCH-32_81	0.0736	79	0.00242	22	1.46703	1.88651	5	0.282589	33	0.282566	3.3	1.2	0.97	497	8	71	6
GCH-32_80	0.0218	30	0.00075	9	1.46712	1.88660	6	0.282512	37	0.282505	0.8	1.3	1.10	481	7	79	6
GCH-32_79	0.0224	18	0.00077	5	1.46696	1.88634	6	0.282613	41	0.282606	4.8	1.4	0.89	498	8	77	6
GCH-32_78	0.0277	26	0.00093	7	1.46712	1.88637	5	0.282603	30	0.282595	4.6	1.1	0.91	507	9	54	6
GCH-32_77	0.0290	24	0.00098	6	1.46698	1.88647	5	0.282539	39	0.282530	2.2	1.4	1.04	503	8	63	6
GCH-32_76	0.0014	1	0.00004	0	1.46710	1.88655	7	0.282568	32	0.282567	1.6	1.1	1.00	418	7	66	6
GCH-32_75	0.0012	2	0.00003	0	1.46705	1.88646	7	0.282569	22	0.282569	1.2	0.8	1.01	396	6	101	6
GCH-32_74	0.0180	35	0.00060	11	1.46715	1.88679	6	0.282550	27	0.282544	2.3	1.0	1.02	484	7	80	6
GCH-32_73	0.0011	1	0.00003	0	1.46709	1.88672	8	0.282614	25	0.282613	2.8	0.9	0.92	399	6	90	6
GCH-32_72	0.0388	34	0.00130	9	1.46714	1.88669	5	0.282564	35	0.282553	2.4	1.3	1.01	478	7	93	6
GCH-32_66	0.0339	32	0.00114	9	1.46710	1.88670	5	0.282558	34	0.282547	3.2	1.2	1.00	521	12	114	6
GCH-32_65	0.0036	3	0.00012	1	1.46714	1.88668	8	0.282601	25	0.282599	5.1	0.9	0.89	523	8	99	6
GCH-32_64	0.0273	26	0.00092	7	1.46710	1.88662	5	0.282562	32	0.282553	3.2	1.1	0.99	511	9	91	6
GCH-32_63	0.0260	24	0.00100	8	1.46699	1.88665	5	0.282395	27	0.282384	-2.0	1.0	1.31	544	8	67	6
GCH-32_62	0.0401	33	0.00134	8	1.46707	1.88658	5	0.282531	27	0.282519	1.4	0.9	1.07	486	7	90	6
GCH-32_61	0.0529	43	0.00177	11	1.46711	1.88639	5	0.282608	33	0.282592	3.9	1.2	0.93	483	7	100	6

Grain	$\frac{^{176}Yb}{^{177}Hf}$ [a]	±2σ	$\frac{^{176}Lu}{^{177}Hf}$ [a]	±2σ	$\frac{^{178}Hf}{^{177}Hf}$	$\frac{^{180}Hf}{^{177}Hf}$	Sig_{Hf} [b] (V)	$\frac{^{176}Hf}{^{177}Hf}$	±2σ [c]	$\frac{^{176}Hf}{^{177}Hf_{(t)}}$ [d]	$\varepsilon Hf_{(t)}$ [d]	±2σ [c] (εHf)	T_{DM} [e] (Ga)	age [f] (Ma)	±2σ (Ma)	U-Pb [g] conc	Lu-Hf [h] seq

Quoted uncertainties (absolute) relate to the last quoted figure. The effect of the inter-element fractionation on Lu/Hf was estimated to be about 6 % or less based on analyses of the GJ-1 and Plesoviče zircon. Accuracy and reproducibility was checked by repeated analyses of reference zircon GJ-1 and Plesoviče (data given as mean with 2 standard deviation uncertainties).

(a) $^{176}Yb/^{177}Hf = (^{176}Yb/^{173}Yb)_{true} \times (^{173}Yb/^{177}Hf)_{meas} \times (M_{173(Yb)}/M_{177(Hf)})^{\beta(Hf)}$, $\beta(Hf) = \ln((^{179}Hf/^{177}Hf_{true})/(^{179}Hf/^{177}Hf_{measured})) / \ln(M_{179(Hf)}/M_{177(Hf)})$, M = mass of respective isotopes. The $^{176}Lu/^{177}Hf$ was calculated in a similar way using $^{175}Lu/^{177}Hf$ and β(Yb).

(b) Mean Hf signal in volts.

(c) Uncertainties are quadratic additions of the within-run precision and the daily reproducibility of the 40ppb-JMC475 solution. Uncertainties for the JMC475 quoted at 2SD (2 standard deviation).

(d) Initial $^{176}Hf/^{177}Hf$ and εHf calculated using the apparent U-Pb age determined by LA-ICP-MS dating (see column f), and the CHUR parameters: $^{176}Lu/^{177}Hf$ = 0.0336, and $^{176}Hf/^{177}Hf$ = 0.282785 (Bouvier et al. 2008).

(e) Two stage model age in Ga using measured $^{176}Lu/^{177}Lu$ of each spot (first stage = age of zircon), a value of 0.0113 for the average continental crust (second stage, values compiled from Rudnick and Gao (2003), and depleted mantle $^{176}Lu/^{177}Lu$ = 0.0379, and $^{176}Hf/^{177}Hf$ = 0.283164.

(f) Apparent U-Pb age determined by LA-ICP-MS.

(g) U-Pb age concordance (%).

(h) Sequence in which Lu-Hf analyses were performed. Standard analyses for each sequence are showed on Table 12.

Table Ig4-Hf

Lu, Yb and Hf LA-MC-ICPMS data of zircon crystals from sample GCH-19

Grain	$^{176}Yb/^{177}Hf$ [a]	±2σ	$^{176}Lu/^{177}Hf$ [a]	±2σ	$^{178}Hf/^{177}Hf$	$^{180}Hf/^{177}Hf$	Sig_{Hf} [b] (V)	$^{176}Hf/^{177}Hf$	±2σ [c]	$^{176}Hf/^{177}Hf_{(t)}$ [d]	$\varepsilon Hf_{(t)}$ [d]	±2σ [c] (εHf)	T_{DM} [e] (Ga)	age [f] (Ma)	±2σ (Ma)	U-Pb [g] conc	Lu-Hf [h] seq
A10_40_seq1	0.0051	4	0.00023	1	1.46722	1.88681	10	0.282856	30	0.282856	2.5	1.1	0.61	0	0	0	1
A11_40_seq1	0.0072	8	0.00036	3	1.46719	1.88666	11	0.282881	24	0.282881	3.4	0.9	0.56	0	0	No data	1
A12_40_seq1	0.0092	7	0.00047	3	1.46717	1.88675	14	0.282809	22	0.282805	11.5	0.8	0.51	485	11	91	1
A14_40_seq1	0.0071	6	0.00032	2	1.46721	1.88685	10	0.282865	25	0.282860	21.0	0.9	0.25	820	393	58	1
A16_40_seq1	0.0100	9	0.00050	4	1.46714	1.88678	11	0.282873	25	0.282868	13.6	0.9	0.38	477	24	105	1
A21_40_seq1	0.0041	3	0.00020	1	1.46717	1.88673	10	0.282842	20	0.282842	2.0	0.7	0.63	0	0	0	1
A22_40_seq1	0.0129	10	0.00058	4	1.46719	1.88659	13	0.282701	20	0.282695	7.9	0.7	0.72	498	12	93	1
A24_40_seq1	0.0246	26	0.00122	11	1.46716	1.88672	11	0.282820	26	0.282810	10.8	0.9	0.51	443	10	102	1
A26_40_seq1	0.0074	7	0.00038	3	1.46714	1.88667	11	0.282862	25	0.282862	2.7	0.9	0.60	0	0	0	1
A29_40_seq1	0.0088	7	0.00041	2	1.46709	1.88649	11	0.282820	22	0.282816	11.8	0.8	0.49	481	12	96	1
A32_40_seq1	0.0096	8	0.00050	3	1.46718	1.88670	10	0.282859	26	0.282855	12.0	0.9	0.43	426	10	92	1
A39_40_seq1	0.0124	17	0.00065	7	1.46719	1.88688	11	0.282808	22	0.282802	11.5	0.8	0.51	490	8	91	1
A43_40_seq1	0.0240	21	0.00097	7	1.46714	1.88658	11	0.282692	21	0.282683	6.2	0.8	0.75	439	11	90	1
A45_40_seq1	0.0161	13	0.00082	5	1.46713	1.88681	16	0.282866	23	0.282858	13.6	0.8	0.40	492	9	96	1
A55_40_seq1	0.0060	6	0.00031	3	1.46717	1.88674	12	0.282845	22	0.282842	11.4	0.8	0.46	421	7	98	1
A74_40_seq1	0.0078	8	0.00037	3	1.46713	1.88684	12	0.282859	22	0.282856	13.7	0.8	0.40	503	12	96	1
A92_40_seq1	0.0156	13	0.00078	5	1.46716	1.88672	10	0.282806	27	0.282800	9.5	1.0	0.55	402	8	95	1
A97_40_seq1	0.0064	5	0.00032	2	1.46717	1.88665	10	0.282840	24	0.282830	36.5	0.8	-0.04	1546	###	30	1
A503_40_seq1	0.0183	15	0.00098	6	1.46721	1.88696	10	0.282840	26	0.282832	10.5	0.9	0.49	397	10	96	1
A508_40_seq1	0.0211	18	0.00112	7	1.46721	1.88675	11	0.282825	25	0.282814	12.4	0.9	0.48	508	30	100	1
A509_40_seq1	0.0054	5	0.00024	2	1.46718	1.88664	11	0.282846	25	0.282844	11.9	0.9	0.45	442	36	90	1

Quoted uncertainties (absolute) relate to the last quoted figure. The effect of the inter-element fractionation on Lu/Hf was estimated to be about 6 % or less based on analyses of the GJ-1 and Plesoviče zircon. Accuracy and reproducibility was checked by repeated analyses of reference zircon GJ-1 and Plesoviče (data given as mean with 2 standard deviation uncertainties).

(a) $^{176}Yb/^{177}Hf = (^{176}Yb/^{173}Yb)_{true} \times (^{173}Yb/^{177}Hf)_{meas} \times (M_{173(Yb)}/M_{177(Hf)})^{\beta(Hf)}$, $\beta(Hf) = \ln((^{179}Hf/^{177}Hf_{true})/(^{179}Hf/^{177}Hf_{measured})) / \ln(M_{179(Hf)}/M_{177(Hf)})$, M = mass of respective isotopes. The $^{176}Lu/^{177}Hf$ was calculated in a similar way using $^{175}Lu/^{177}Hf$ and β(Yb).

(b) Mean Hf signal in volts.

(c) Uncertainties are quadratic additions of the within-run precision and the daily reproducibility of the 40ppb-JMC475 solution. Uncertainties for the JMC475 quoted at 2SD (2 standard deviation).

(d) Initial $^{176}Hf/^{177}Hf$ and εHf calculated using the apparent U-Pb age determined by LA-ICP-MS dating (see column f), and the CHUR parameters: $^{176}Lu/^{177}Hf$ = 0.0336, and $^{176}Hf/^{177}Hf$ = 0.282785 (Bouvier et al. 2008).

(e) Two stage model age in Ga using measured $^{176}Lu/^{177}Lu$ of each spot (first stage = age of zircon), a value of 0.0113 for the average continental crust (second stage, values compiled from Rudnick and Gao (2003), and depleted mantle $^{176}Lu/^{177}Lu$ = 0.0379, and $^{176}Hf/^{177}Hf$ = 0.283164.

(f) Apparent U-Pb age determined by LA-ICP-MS.

(g) U-Pb age concordance (%).

(h) Sequence in which Lu-Hf analyses were performed. Standard analyses for each sequence are showed on Table 12.

Table Ig5-Hf

Lu, Yb and Hf LA-MC-ICPMS data of zircon crystals from sample GCH-20

Grain	$^{176}Yb/^{177}Hf$ [a]	±2σ	$^{176}Lu/^{177}Hf$ [a]	±2σ	$^{178}Hf/^{177}Hf$	$^{180}Hf/^{177}Hf$	Sig_{Hf} [b] (V)	$^{176}Hf/^{177}Hf$	±2σ[c]	$^{176}Hf/^{177}Hf_{(t)}$ [d]	$\varepsilon Hf_{(t)}$ [d]	±2σ [c] (εHf)	T_{DM} [e] (Ga)	age[f] (Ma)	±2σ (Ma)	U-Pb [g] conc	Lu-Hf [h] seq
A6_26_seq1	0.0054	4	0.00026	2	1.46704	1.88653	5	0.282854	35	0.282852	13.1	1.2	0.42	482	18	101	1
A7_40_seq1	0.0053	5	0.00025	2	1.46713	1.88685	11	0.282870	26	0.282867	14.2	0.9	0.37	455	18	90	1
A8_26_seq1	0.0275	47	0.00097	14	1.46700	1.88612	6	0.282858	31	0.282840	23.9	1.1	0.22	980	-	14	1
A9_26_seq1	0.0080	7	0.00037	3	1.46716	1.88627	5	0.282860	30	0.282856	13.0	1.1	0.41	469	10	100	1
A512_40_seq1	0.0007	1	0.00002	0	1.46716	1.88659	13	0.282831	26	0.282831	10.1	0.9	0.50	381	5	99	1
A519_40_seq1	0.0009	1	0.00003	0	1.46718	1.88674	12	0.282854	26	0.282853	11.4	0.9	0.45	404	6	100	1
A520_26_seq1	0.0016	2	0.00005	0	1.46706	1.88611	7	0.282821	32	0.282821	10.4	1.1	0.51	410	7	100	1
A522_26_seq1	0.0005	0	0.00001	0	1.46713	1.88650	7	0.282814	39	0.282813	9.8	1.4	0.53	395	6	100	1
A525_26_seq1	0.0006	1	0.00002	0	1.46708	1.88637	6	0.282872	32	0.282872	12.1	1.1	0.41	404	7	100	1
A526_26_seq1	0.0004	0	0.00001	0	1.46705	1.88649	6	0.282858	32	0.282858	11.3	1.1	0.44	389	6	100	1
A528_40_seq1	0.0006	1	0.00002	0	1.46713	1.88659	12	0.282849	23	0.282849	10.9	0.8	0.46	389	6	100	1
A530_40_seq1	0.0005	0	0.00001	0	1.46712	1.88644	13	0.282815	24	0.282815	9.7	0.9	0.53	389	6	100	1
A543_40_seq1	0.0003	0	0.00001	0	1.46722	1.88680	15	0.282793	20	0.282793	9.0	0.7	0.57	390	6	99	1
A548_40_seq1	0.0007	1	0.00002	0	1.46716	1.88677	13	0.282817	23	0.282816	14.4	0.8	0.44	593	8	99	1
A559_40_seq1	0.0005	1	0.00002	0	1.46709	1.88640	12	0.282758	34	0.282758	7.7	1.2	0.64	386	5	100	1
A562_26_seq1	0.0010	1	0.00003	0	1.46714	1.88659	6	0.282842	30	0.282842	10.9	1.1	0.47	401	6	100	1
A564_26_seq1	0.0003	0	0.00001	0	1.46711	1.88650	6	0.282785	31	0.282785	8.8	1.1	0.58	398	5	99	1
A575_26_seq1	0.0006	1	0.00002	0	1.46703	1.88626	6	0.282824	32	0.282824	10.3	1.1	0.51	399	7	99	1
A580_26_seq1	0.0004	0	0.00001	0	1.46707	1.88646	7	0.282798	30	0.282798	9.2	1.0	0.56	393	6	100	1
A590_26_seq1	0.0005	0	0.00001	0	1.46706	1.88614	6	0.282789	39	0.282789	8.9	1.4	0.58	391	6	100	1
A594_26_seq1	0.0010	2	0.00003	1	1.46714	1.88622	6	0.282834	29	0.282834	10.4	1.0	0.49	390	5	99	1

Quoted uncertainties (absolute) relate to the last quoted figure. The effect of the inter-element fractionation on Lu/Hf was estimated to be about 6 % or less based on analyses of the GJ-1 and Plesoviče zircon. Accuracy and reproducibility was checked by repeated analyses of reference zircon GJ-1 and Plesoviče (data given as mean with 2 standard deviation uncertainties).

(a) $^{176}Yb/^{177}Hf = (^{176}Yb/^{173}Yb)_{true} \times (^{173}Yb/^{177}Hf)_{meas} \times (M_{173(Yb)}/M_{177(Hf)})^{\beta(Hf)}$, $\beta(Hf) = \ln((^{179}Hf/^{177}Hf_{true})/(^{179}Hf/^{177}Hf_{measured})) / \ln(M_{179(Hf)}/M_{177(Hf)})$, M = mass of respective isotopes. The $^{176}Lu/^{177}Hf$ was calculated in a similar way using $^{175}Lu/^{177}Hf$ and β(Yb).

(b) Mean Hf signal in volts.

(c) Uncertainties are quadratic additions of the within-run precision and the daily reproducibility of the 40ppb-JMC475 solution. Uncertainties for the JMC475 quoted at 2SD (2 standard deviation).

(d) Initial $^{176}Hf/^{177}Hf$ and εHf calculated using the apparent U-Pb age determined by LA-ICP-MS dating (see column f), and the CHUR parameters: $^{176}Lu/^{177}Hf$ = 0.0336, and $^{176}Hf/^{177}Hf$ = 0.282785 (Bouvier et al. 2008).

(e) Two stage model age in Ga using measured $^{176}Lu/^{177}Lu$ of each spot (first stage = age of zircon), a value of 0.0113 for the average continental crust (second stage, values compiled from Rudnick and Gao (2003), and depleted mantle $^{176}Lu/^{177}Lu$ = 0.0379, and $^{176}Hf/^{177}Hf$ = 0.283164.

(f) Apparent U-Pb age determined by LA-ICP-MS.

(g) U-Pb age concordance (%).

(h) Sequence in which Lu-Hf analyses were performed. Standard analyses for each sequence are showed on Table 12.

Table Ig6-Hf

Lu, Yb and Hf LA-MC-ICPMS data of zircon crystals from sample GCH-22

Grain	$^{176}Yb/^{177}Hf$ [a]	±2σ	$^{176}Lu/^{177}Hf$ [a]	±2σ	$^{178}Hf/^{177}Hf$	$^{180}Hf/^{177}Hf$	Sig_{Hf} [b] (V)	$^{176}Hf/^{177}Hf$	±2σ [c]	$^{176}Hf/^{177}Hf_{(t)}$ [d]	$\varepsilon Hf_{(t)}$ [d]	±2σ [c] (εHf)	T_{DM} [e] (Ga)	age [f] (Ma)	±2σ (Ma)	U-Pb [g] conc	Lu-Hf [h] seq
A361_40_seq2	0.0175	14	0.00059	4	1.46718	1.88687	12	0.282471	21	0.282466	-0.6	0.8	1.17	481	7	99	2
A362_40_seq2	0.0110	9	0.00041	3	1.46720	1.88676	13	0.282462	21	0.282458	-0.7	0.7	1.19	487	7	93	2
A363_40_seq2	0.0083	7	0.00032	2	1.46724	1.88667	12	0.282492	27	0.282489	0.1	0.9	1.13	474	7	99	2
A364_40_seq2	0.0165	14	0.00054	3	1.46716	1.88657	11	0.282433	24	0.282428	-1.9	0.8	1.25	482	8	97	2
A368_40_seq2	0.0117	9	0.00041	2	1.46719	1.88685	12	0.282469	26	0.282465	-0.8	0.9	1.18	474	7	96	2
A369_40_seq2	0.0117	10	0.00040	3	1.46717	1.88673	12	0.282475	22	0.282471	-0.5	0.8	1.17	474	7	98	2
A370_40_seq2	0.0214	17	0.00070	4	1.46718	1.88666	13	0.282445	23	0.282439	-1.8	0.8	1.23	468	7	97	2
A374_40_seq2	0.0174	14	0.00058	3	1.46719	1.88678	13	0.282452	20	0.282447	-1.3	0.7	1.21	477	7	99	2
A378_40_seq2	0.0135	11	0.00046	3	1.46717	1.88676	13	0.282448	23	0.282444	-1.6	0.8	1.22	469	7	97	2
A379_40_seq2	0.0133	11	0.00046	3	1.46713	1.88670	12	0.282435	23	0.282431	-1.6	0.8	1.24	491	7	100	2
A380_40_seq2	0.0151	12	0.00051	3	1.46718	1.88670	13	0.282468	22	0.282463	-1.1	0.8	1.19	463	7	94	2
A381_40_seq2	0.0131	10	0.00045	3	1.46719	1.88681	12	0.282454	19	0.282450	-1.0	0.7	1.20	488	7	98	2
A388_40_seq2	0.0149	12	0.00051	3	1.46719	1.88685	12	0.282477	25	0.282473	-0.4	0.9	1.16	477	7	95	2
A389_40_seq2	0.0148	12	0.00051	3	1.46720	1.88697	12	0.282488	21	0.282483	-0.2	0.8	1.14	469	7	94	2
A392_40_seq2	0.0092	7	0.00032	2	1.46720	1.88668	12	0.282473	21	0.282471	-0.9	0.7	1.17	457	7	92	2
A407_40_seq2	0.0093	8	0.00032	2	1.46722	1.88688	12	0.282500	23	0.282497	0.5	0.8	1.11	480	7	98	2
A416_40_seq2	0.0078	6	0.00027	2	1.46718	1.88678	13	0.282456	19	0.282454	-1.0	0.7	1.20	481	7	100	2
A419_40_seq2	0.0094	8	0.00035	2	1.46710	1.88668	13	0.282470	19	0.282466	0.0	0.7	1.16	506	8	100	2
A422_40_seq2	0.0118	9	0.00041	2	1.46719	1.88680	12	0.282464	21	0.282461	-1.7	0.8	1.20	438	6	101	2
A438_40_seq2	0.0002	0	0.00000	0	1.46717	1.88677	14	0.282627	22	0.282627	-5.6	0.8	1.05	0	0	0	2
A444_40_seq2	0.0006	1	0.00001	0	1.46713	1.88663	14	0.282631	22	0.282630	23.0	0.8	0.50	1267	221	28	2
A445_40_seq2	0.0004	0	0.00001	0	1.46717	1.88661	15	0.282618	20	0.282618	3.0	0.7	0.91	398	15	105	2
A446_40_seq2	0.0011	3	0.00002	1	1.46666	1.88319	7	0.282375	108	0.282375	-14.5	3.8	1.54	0	0	0	2
A448_40_seq2	0.0002	0	0.00001	0	1.46716	1.88643	19	0.282612	19	0.282612	-6.1	0.7	1.08	0	0	0	2
A450_40_seq2	0.0001	0	0.00000	0	1.46712	1.88643	14	0.282601	26	0.282601	-6.5	0.9	1.10	0	0	0	2
A451_40_seq2	0.0002	0	0.00001	0	1.46717	1.88665	14	0.282617	19	0.282617	2.8	0.7	0.91	393	9	99	2

Quoted uncertainties (absolute) relate to the last quoted figure. The effect of the inter-element fractionation on Lu/Hf was estimated to be about 6 % or less based on analyses of the GJ-1 and Plesoviče zircon. Accuracy and reproducibility was checked by repeated analyses of reference zircon GJ-1 and Plesoviče (data given as mean with 2 standard deviation uncertainties).

(a) $^{176}Yb/^{177}Hf = (^{176}Yb/^{173}Yb)_{true} \times (^{173}Yb/^{177}Hf)_{meas} \times (M_{173(Yb)}/M_{177(Hf)})^{\beta(Hf)}$, $\beta(Hf) = \ln((^{179}Hf/^{177}Hf_{true})/(^{179}Hf/^{177}Hf_{measured})) / \ln(M_{179(Hf)}/M_{177(Hf)})$, M = mass of respective isotopes. The $^{176}Lu/^{177}Hf$ was calculated in a similar way using $^{175}Lu/^{177}Hf$ and β(Yb).

(b) Mean Hf signal in volts.

(c) Uncertainties are quadratic additions of the within-run precision and the daily reproducibility of the 40ppb-JMC475 solution. Uncertainties for the JMC475 quoted at 2SD (2 standard deviation).

(d) Initial $^{176}Hf/^{177}Hf$ and εHf calculated using the apparent U-Pb age determined by LA-ICP-MS dating (see column f), and the CHUR parameters: $^{176}Lu/^{177}Hf$ = 0.0336, and $^{176}Hf/^{177}Hf$ = 0.282785 (Bouvier et al. 2008).

(e) Two stage model age in Ga using measured $^{176}Lu/^{177}Lu$ of each spot (first stage = age of zircon), a value of 0.0113 for the average continental crust (second stage, values compiled from Rudnick and Gao (2003), and depleted mantle $^{176}Lu/^{177}Lu$ = 0.0379, and $^{176}Hf/^{177}Hf$ = 0.283164.

(f) Apparent U-Pb age determined by LA-ICP-MS.

(g) U-Pb age concordance (%).

(h) Sequence in which Lu-Hf analyses were performed. Standard analyses for each sequence are showed on Table 12.

Table lg7-Hf

Lu, Yb and Hf LA-MC-ICPMS data of zircon crystals from sample GCH-23

Grain	$^{176}Yb/^{177}Hf$ [a]	±2σ	$^{176}Lu/^{177}Hf$ [a]	±2σ	$^{178}Hf/^{177}Hf$	$^{180}Hf/^{177}Hf$	Sig_{Hf} [b] (V)	$^{176}Hf/^{177}Hf$	±2σ[c]	$^{176}Hf/^{177}Hf_{(t)}$ [d]	$\varepsilon Hf_{(t)}$ [d]	±2σ [c] (εHf)	T_{DM} [e] (Ga)	age[f] (Ma)	±2σ (Ma)	U-Pb [g] conc	Lu-Hf [h] seq
A113_seq3_26	0.0145	30	0.00052	8	1.46707	1.88595	7	0.282616	47	0.282611	5.0	1.7	0.88	503	7	99	3
A115_seq3_40	0.0115	15	0.00043	4	1.46714	1.88619	12	0.282598	28	0.282594	4.3	1.0	0.92	495	7	98	3
A116_seq3_26	0.0123	25	0.00045	6	1.46655	1.88347	5	0.282324	78	0.282320	-5.3	2.8	1.45	502	8	99	3
A117_seq3_26	0.0403	59	0.00135	17	1.46700	1.88568	5	0.282589	57	0.282576	4.4	2.0	0.94	527	7	98	3
A121_seq3_26	0.0156	18	0.00055	5	1.46712	1.88627	6	0.282638	43	0.282633	5.6	1.5	0.84	491	7	95	3
A123_seq3_26	0.0158	34	0.00047	10	1.46693	1.88616	6	0.282567	43	0.282563	2.6	1.5	0.99	470	5	95	3
A124_seq3_26	0.0270	40	0.00087	11	1.46707	1.88569	6	0.282614	92	0.282606	4.4	3.3	0.90	480	7	96	3
A126_seq3_18	0.0202	42	0.00068	13	1.46705	1.88597	4	0.282733	40	0.282728	6.5	1.4	0.70	381	292	127	3
A129_seq3_26	0.0077	7	0.00026	2	1.46709	1.88633	7	0.281534	40	0.281526	-8.0	1.4	2.52	1624	61	52	3
A130_seq3_26	0.0529	92	0.00161	26	1.46684	1.88542	6	0.282540	71	0.282527	0.8	2.5	1.07	448	9	105	3
A131_seq3_26	0.0071	6	0.00028	2	1.46711	1.88592	6	0.282611	37	0.282608	5.1	1.3	0.88	507	7	99	3
A132_seq3_26	0.0151	20	0.00053	6	1.46713	1.88662	7	0.282669	29	0.282663	9.7	1.0	0.72	629	83	77	3
A133_seq3_26	0.0172	15	0.00059	4	1.46718	1.88642	7	0.282679	34	0.282673	7.6	1.2	0.75	519	52	88	3
A134_seq3_26	0.0200	50	0.00063	15	1.46709	1.88624	7	0.282679	29	0.282673	7.4	1.0	0.75	510	7	98	3
A135_seq3_26	0.0336	31	0.00126	10	1.46706	1.88596	6	0.282328	51	0.282313	-3.0	1.8	1.42	615	11	101	3
A136_seq3_26	0.0170	21	0.00054	6	1.46711	1.88685	6	0.282568	105	0.282559	12.3	3.7	0.81	908	91	56	3
A137_seq3_26	0.0216	26	0.00073	7	1.46706	1.88625	6	0.282614	32	0.282608	4.3	1.1	0.90	474	7	96	3
A139_seq3_26	0.0122	11	0.00038	2	1.46710	1.88638	6	0.282618	50	0.282614	6.4	1.8	0.85	559	118	86	3
A142_seq3_26	0.0340	62	0.00108	17	1.46705	1.88587	6	0.282664	40	0.282654	6.2	1.4	0.80	485	7	97	3
A144_seq3_40	0.0484	41	0.00161	10	1.46719	1.88657	13	0.282676	28	0.282662	6.4	1.0	0.79	481	6	102	3
A145_seq3_26	0.0072	6	0.00031	2	1.46713	1.88615	5	0.282661	36	0.282658	6.8	1.3	0.79	507	8	100	3
A151_seq3_26	0.0106	10	0.00041	3	1.46699	1.88586	5	0.282620	38	0.282617	4.5	1.3	0.88	468	8	102	3
A154_seq3_26	0.0220	38	0.00074	10	1.46704	1.88630	7	0.282622	55	0.282615	5.0	1.9	0.88	492	7	98	3
A159_seq3_26	0.0244	54	0.00076	16	1.46698	1.88582	7	0.282604	49	0.282597	4.3	1.7	0.91	491	7	98	3
A163_seq3_26	0.0345	35	0.00120	10	1.46701	1.88613	7	0.282622	27	0.282611	5.3	0.9	0.88	513	7	102	3

Quoted uncertainties (absolute) relate to the last quoted figure. The effect of the inter-element fractionation on Lu/Hf was estimated to be about 6 % or less based on analyses of the GJ-1 and Plesoviče zircon. Accuracy and reproducibility was checked by repeated analyses of reference zircon GJ-1 and Plesoviče (data given as mean with 2 standard deviation uncertainties).

(a) $^{176}Yb/^{177}Hf = (^{176}Yb/^{173}Yb)_{true} \times (^{173}Yb/^{177}Hf)_{meas} \times (M_{173(Yb)}/M_{177(Hf)})^{\beta(Hf)}$, $\beta(Hf) = \ln((^{179}Hf/^{177}Hf_{true})/(^{179}Hf/^{177}Hf_{measured})) / \ln(M_{179(Hf)}/M_{177(Hf)})$, M = mass of respective isotopes. The $^{176}Lu/^{177}Hf$ was calculated in a similar way using $^{175}Lu/^{177}Hf$ and β(Yb).

(b) Mean Hf signal in volts.

(c) Uncertainties are quadratic additions of the within-run precision and the daily reproducibility of the 40ppb-JMC475 solution. Uncertainties for the JMC475 quoted at 2SD (2 standard deviation).

(d) Initial $^{176}Hf/^{177}Hf$ and εHf calculated using the apparent U-Pb age determined by LA-ICP-MS dating (see column f), and the CHUR parameters: $^{176}Lu/^{177}Hf$ = 0.0336, and $^{176}Hf/^{177}Hf$ = 0.282785 (Bouvier et al. 2008).

(e) Two stage model age in Ga using measured $^{176}Lu/^{177}Lu$ of each spot (first stage = age of zircon), a value of 0.0113 for the average continental crust (second stage, values compiled from Rudnick and Gao (2003), and depleted mantle $^{176}Lu/^{177}Lu$ = 0.0379, and $^{176}Hf/^{177}Hf$ = 0.283164.

(f) Apparent U-Pb age determined by LA-ICP-MS.

(g) U-Pb age concordance (%).

(h) Sequence in which Lu-Hf analyses were performed. Standard analyses for each sequence are showed on Table 12.

Table Ig8-Hf

Lu, Yb and Hf LA-MC-ICPMS data of zircon crystals from sample GCH-01

Grain	$^{176}Yb/^{177}Hf$ [a]	±2σ	$^{176}Lu/^{177}Hf$ [a]	±2σ	$^{178}Hf/^{177}Hf$	$^{180}Hf/^{177}Hf$	Sig_{Hf} [b] (V)	$^{176}Hf/^{177}Hf$	±2σ[c]	$^{176}Hf/^{177}Hf_{(t)}$ [d]	$\varepsilon Hf_{(t)}$ [d]	±2σ [c] (εHf)	T_{DM} [e] (Ga)	age[f] (Ma)	±2σ (Ma)	U-Pb [g] conc	Lu-Hf [h] seq
A412_seq3_40	0.0819	68	0.00266	17	1.46720	1.88667	12	0.282764	20	0.282739	9.6	0.7	0.63	503	7	93	3
A414_seq3_40	0.0676	55	0.00223	14	1.46724	1.88671	13	0.282761	25	0.282731	14.1	0.9	0.55	717	114	69	3
A417_seq3_40	0.0400	32	0.00134	8	1.46721	1.88675	13	0.282750	22	0.282737	9.2	0.8	0.64	489	7	92	3
A418_seq3_40	0.0719	62	0.00236	16	1.46718	1.88683	14	0.282774	24	0.282752	10.0	0.8	0.60	500	7	90	3
A420_seq3_26	0.0838	73	0.00274	19	1.46706	1.88653	7	0.282711	32	0.282684	7.9	1.1	0.73	516	6	100	3
A424_seq3_26	0.0695	59	0.00234	15	1.46710	1.88635	5	0.282759	28	0.282737	9.4	1.0	0.63	500	6	101	3
A425_seq3_40	0.0496	42	0.00164	11	1.46721	1.88694	13	0.282752	25	0.282737	9.5	0.9	0.63	504	6	96	3
A426_seq3_40	0.0568	54	0.00185	15	1.46717	1.88670	13	0.282773	23	0.282756	9.7	0.8	0.60	478	6	90	3
A435_seq3_40	0.0401	41	0.00129	11	1.46718	1.88674	13	0.281920	25	0.281905	-17.6	0.9	2.21	605	7	90	3
A436_seq3_26	0.0665	84	0.00223	25	1.46720	1.88664	7	0.282819	38	0.282798	11.6	1.3	0.51	499	6	95	3
A445_seq3_26	0.0504	41	0.00176	11	1.46711	1.88641	7	0.282771	32	0.282755	9.9	1.1	0.60	491	7	90	3
A446_seq3_26	0.0013	1	0.00004	0	1.46719	1.88652	9	0.282754	28	0.282754	7.4	1.0	0.65	381	5	91	3
A448_seq3_26	0.0584	59	0.00200	17	1.46709	1.88634	6	0.282783	30	0.282765	10.3	1.1	0.58	496	6	91	3
A456_seq3_26	0.0006	1	0.00002	0	1.46726	1.88653	9	0.282322	33	0.282322	-7.5	1.2	1.49	401	5	101	3
A457_seq3_26	0.0284	24	0.00098	6	1.46704	1.88653	5	0.281948	29	0.281938	-17.6	1.0	2.16	558	8	90	3
A459_seq3_40	0.0307	26	0.00104	7	1.46717	1.88674	12	0.282735	18	0.282726	8.8	0.6	0.66	490	6	94	3
A465_seq3_26	0.0504	43	0.00170	11	1.46717	1.88668	7	0.282725	33	0.282709	8.4	1.2	0.69	497	7	91	3
A470_seq3_26	0.0575	47	0.00195	12	1.46712	1.88641	6	0.282775	25	0.282756	10.0	0.9	0.60	495	7	96	3
A477_seq3_26	0.0824	73	0.00268	18	1.46713	1.88635	6	0.282726	36	0.282688	13.3	1.3	0.62	750	42	66	3
A480_seq3_40	0.0258	23	0.00090	6	1.46707	1.88593	6	0.282714	43	0.282703	10.9	1.5	0.65	616	66	80	3
A482_seq3_26	0.0608	52	0.00207	14	1.46714	1.88625	6	0.282746	33	0.282727	8.9	1.2	0.66	491	7	97	3
A491_seq3_26	0.0017	2	0.00005	1	1.46717	1.88656	9	0.282770	21	0.282770	8.1	0.7	0.62	388	5	97	3
A514_seq3_26	0.0725	100	0.00241	30	1.46714	1.88635	8	0.282720	34	0.282697	8.0	1.2	0.71	498	7	97	3
A528_seq3_26	0.0228	19	0.00081	5	1.46713	1.88666	6	0.282022	26	0.282013	-14.7	0.9	2.02	566	7	92	3
A531_seq3_26	0.0365	34	0.00120	8	1.46719	1.88636	8	0.282608	28	0.282593	8.5	1.0	0.84	685	34	84	3
A539_seq3_26	0.0316	29	0.00104	8	1.46712	1.88636	8	0.282730	36	0.282722	7.4	1.3	0.69	433	6	101	3
A548_seq3_26	0.0018	2	0.00006	0	1.46713	1.88630	9	0.282745	32	0.282745	7.2	1.1	0.67	386	6	98	3
A555_seq3_26	0.0544	119	0.00205	46	1.46719	1.88687	7	0.282777	44	0.282761	8.3	1.6	0.63	410	6	101	3
A560_seq3_26	0.0529	57	0.00175	16	1.46729	1.88666	6	0.282790	30	0.282774	10.7	1.1	0.56	496	6	92	3
A564_seq3_40	0.0335	30	0.00109	8	1.46720	1.88673	11	0.282089	27	0.282077	-12.3	1.0	1.89	572	9	98	3
A565_seq3_40	0.0596	49	0.00198	13	1.46720	1.88673	13	0.282736	28	0.282717	8.8	1.0	0.67	501	6	96	3
A571_seq3_26	0.0044	4	0.00013	1	1.46711	1.88638	9	0.282747	45	0.282746	7.5	1.6	0.66	397	5	96	3
A574_seq3_26	0.0152	17	0.00054	5	1.46712	1.88633	5	0.282153	25	0.282148	-9.8	0.9	1.76	571	10	93	3
A578_seq3_26	0.0912	76	0.00304	20	1.46719	1.88648	6	0.282801	30	0.282773	10.5	1.1	0.57	487	7	96	3
A581_seq3_26	0.0582	81	0.00209	22	1.46721	1.88672	7	0.282797	34	0.282778	10.7	1.2	0.56	492	7	98	3
A584_seq3_26	0.0190	17	0.00116	8	1.46708	1.88555	9	0.282735	39	0.282726	6.8	1.4	0.70	399	8	95	3
A587_seq3_26	0.0408	69	0.00141	23	1.46713	1.88631	6	0.282788	28	0.282774	11.4	1.0	0.55	530	7	98	3

Quoted uncertainties (absolute) relate to the last quoted figure. The effect of the inter-element fractionation on Lu/Hf was estimated to be about 6 % or less based on analyses of the GJ-1 and Plesoviče zircon. Accuracy and reproducibility was checked by repeated analyses of reference zircon GJ-1 and Plesoviče (data given as mean with 2 standard deviation uncertainties).

(a) $^{176}Yb/^{177}Hf = (^{176}Yb/^{173}Yb)_{true} \times (^{173}Yb/^{177}Hf)_{meas} \times (M_{173(Yb)}/M_{177(Hf)})^{\beta(Hf)}$, $\beta(Hf) = \ln((^{179}Hf/^{177}Hf_{true})/(^{179}Hf/^{177}Hf_{measured})) / \ln(M_{179(Hf)}/M_{177(Hf)})$, M = mass of respective isotopes. The $^{176}Lu/^{177}Hf$ was calculated in a similar way using $^{175}Lu/^{177}Hf$ and β(Yb).

(b) Mean Hf signal in volts.

(c) Uncertainties are quadratic additions of the within-run precision and the daily reproducibility of the 40ppb-JMC475 solution. Uncertainties for the JMC475 quoted at 2SD (2 standard deviation).

(d) Initial $^{176}Hf/^{177}Hf$ and εHf calculated using the apparent U-Pb age determined by LA-ICP-MS dating (see column f), and the CHUR parameters: $^{176}Lu/^{177}Hf$ = 0.0336, and $^{176}Hf/^{177}Hf$ = 0.282785 (Bouvier et al. 2008).

(e) Two stage model age in Ga using measured $^{176}Lu/^{177}Lu$ of each spot (first stage = age of zircon), a value of 0.0113 for the average continental crust (second stage, values compiled from Rudnick and Gao (2003), and depleted mantle $^{176}Lu/^{177}Lu$ = 0.0379, and $^{176}Hf/^{177}Hf$ = 0.283164.

(f) Apparent U-Pb age determined by LA-ICP-MS.

(g) U-Pb age concordance (%).

(h) Sequence in which Lu-Hf analyses were performed. Standard analyses for each sequence are showed on Table 12.

Table lg9-Hf

Lu, Yb and Hf LA-MC-ICPMS data of zircon crystals from sample GCH-03

Grain	$^{176}Yb/^{177}Hf$ [a]	±2σ	$^{176}Lu/^{177}Hf$ [a]	±2σ	$^{178}Hf/^{177}Hf$	$^{180}Hf/^{177}Hf$	Sig_{Hf} [b] (V)	$^{176}Hf/^{177}Hf$	±2σ [c]	$^{176}Hf/^{177}Hf_{(t)}$ [d]	$\varepsilon Hf_{(t)}$ [d]	±2σ [c] (εHf)	T_{DM} [e] (Ga)	age [f] (Ma)	±2σ (Ma)	U-Pb [g] conc	Lu-Hf [h] seq
A46_40_seq2	0.0240	19	0.00079	5	1.46716	1.88675	13	0.282549	17	0.282541	2.2	0.6	1.02	487	7	99	2
A47_40_seq2	0.0465	67	0.00151	19	1.46716	1.88666	11	0.282710	27	0.282697	7.5	0.9	0.72	477	7	98	2
A49_26_seq2	0.0363	30	0.00124	8	1.46710	1.88635	4	0.282678	42	0.282667	6.6	1.5	0.78	485	6	99	2
A50_40_seq2	0.0424	88	0.00132	25	1.46720	1.88701	12	0.282689	22	0.282677	7.1	0.8	0.76	492	8	98	2
A53_40_seq2	0.0459	39	0.00148	10	1.46720	1.88683	13	0.282559	25	0.282545	2.2	0.9	1.02	480	7	97	2
A56_40_seq2	0.0344	58	0.00108	16	1.46711	1.88647	12	0.282675	27	0.282665	6.7	1.0	0.78	489	7	97	2
A58_40_seq2	0.0195	16	0.00063	4	1.46714	1.88653	11	0.282521	27	0.282515	1.3	1.0	1.07	489	10	100	2
A59_40_seq2	0.0394	38	0.00129	10	1.46719	1.88678	13	0.282577	23	0.282565	3.4	0.8	0.97	501	7	97	2
A60_40_seq2	0.0510	49	0.00168	14	1.46708	1.88637	9	0.282706	42	0.282691	7.1	1.5	0.74	466	9	96	2
A63_40_seq2	0.0284	23	0.00099	6	1.46723	1.88697	15	0.282620	25	0.282611	4.8	0.9	0.89	494	7	102	2
A64_40_seq2	0.0712	58	0.00216	13	1.46714	1.88633	12	0.282665	32	0.282645	6.2	1.1	0.82	498	9	101	2
A65_26_seq2	0.0162	13	0.00055	3	1.46711	1.88614	6	0.282550	36	0.282545	1.8	1.3	1.03	460	9	97	2
A72_40_seq2	0.0309	33	0.00097	8	1.46722	1.88690	11	0.282728	24	0.282719	8.2	0.8	0.68	472	7	97	2
A73_40_seq2	0.0243	40	0.00081	12	1.46727	1.88690	12	0.282688	28	0.282681	6.7	1.0	0.76	464	8	98	2
A74_40_seq2	0.0163	28	0.00055	8	1.46717	1.88702	13	0.282695	26	0.282691	6.9	0.9	0.74	457	6	97	2
A75_40_seq2	0.0135	16	0.00049	5	1.46719	1.88667	12	0.282656	22	0.282651	5.8	0.8	0.81	474	8	97	2
A77_40_seq2	0.0489	49	0.00156	13	1.46722	1.88669	11	0.282672	26	0.282657	6.6	0.9	0.79	500	8	96	2
A78_26_seq2	0.0134	19	0.00041	6	1.46712	1.88631	8	0.282613	39	0.282609	4.5	1.4	0.89	482	8	98	2
A81_26_seq2	0.0523	56	0.00167	16	1.46709	1.88621	7	0.282675	33	0.282660	6.2	1.2	0.80	474	7	96	2
A82_26_seq2	0.0453	38	0.00143	9	1.46711	1.88666	9	0.282712	25	0.282700	7.3	0.9	0.72	465	7	99	2
A84_40_seq2	0.0233	19	0.00080	5	1.46720	1.88660	13	0.282629	26	0.282621	4.8	0.9	0.87	473	8	98	2
A85_40_seq2	0.0634	61	0.00198	16	1.46715	1.88666	12	0.282720	23	0.282702	7.6	0.8	0.71	470	8	99	2
A86_40_seq2	0.0631	54	0.00199	13	1.46718	1.88691	13	0.282714	29	0.282695	7.8	1.0	0.72	493	7	92	2
A87_40_seq2	0.0590	51	0.00184	13	1.46723	1.88667	11	0.282700	26	0.282683	7.0	0.9	0.75	477	7	99	2
A89_40_seq2	0.0295	40	0.00093	12	1.46728	1.88678	10	0.282596	26	0.282588	3.9	0.9	0.93	486	8	96	2
A90_40_seq2	0.0558	53	0.00178	14	1.46716	1.88675	12	0.282606	26	0.282590	3.6	0.9	0.93	469	7	97	2
A91_40_seq2	0.0502	48	0.00161	12	1.46726	1.88675	13	0.282587	23	0.282573	3.1	0.8	0.97	476	8	96	2
A93_40_seq2	0.0654	66	0.00209	18	1.46715	1.88656	10	0.282712	31	0.282693	7.5	1.1	0.73	484	8	97	2
A94_40_seq2	0.0941	77	0.00282	18	1.46722	1.88662	9	0.282729	30	0.282704	7.8	1.1	0.71	478	7	100	2
A96_40_seq2	0.0687	70	0.00220	19	1.46723	1.88679	12	0.282699	26	0.282679	7.0	0.9	0.76	481	7	98	2
A98_40_seq2	0.0466	47	0.00153	13	1.46723	1.88673	11	0.282633	23	0.282619	5.2	0.8	0.87	495	9	98	2
A99_40_seq2	0.0825	72	0.00260	18	1.46726	1.88671	10	0.282717	26	0.282694	7.5	0.9	0.73	483	7	99	2
A100_40_seq2	0.0848	110	0.00260	31	1.46720	1.88665	11	0.282655	25	0.282633	4.9	0.9	0.86	463	7	95	2
A108_26_seq2	0.0245	44	0.00083	12	1.46722	1.88642	5	0.282610	34	0.282603	4.0	1.2	0.91	468	7	97	2
A112_40_seq2	0.0401	40	0.00125	11	1.46717	1.88679	12	0.282702	31	0.282691	7.5	1.1	0.73	484	8	99	2
A113_40_seq2	0.0824	84	0.00255	22	1.46716	1.88669	10	0.282747	38	0.282725	8.4	1.3	0.67	470	7	93	2
A117_40_seq2	0.0484	47	0.00150	12	1.46724	1.88680	16	0.282678	29	0.282664	6.8	1.0	0.78	499	7	100	2
A121_40_seq2	0.0399	38	0.00123	9	1.46721	1.88637	12	0.282546	23	0.282535	1.9	0.8	1.04	483	8	98	2
A124_40_seq2	0.0457	38	0.00144	9	1.46712	1.88648	12	0.282675	26	0.282662	6.6	0.9	0.79	490	7	99	2
A132_40_seq2	0.0478	42	0.00159	11	1.46721	1.88652	13	0.282611	21	0.282597	4.2	0.8	0.92	486	8	104	2
A138_40_seq2	0.1115	122	0.00328	30	1.46719	1.88683	12	0.282771	28	0.282742	9.2	1.0	0.63	479	7	99	2
A143_40_seq2	0.0317	30	0.00100	8	1.46719	1.88663	12	0.282678	24	0.282668	6.9	0.8	0.77	496	8	101	2
A164_26_seq2	0.0290	25	0.00098	7	1.46716	1.88620	5	0.282602	28	0.282592	4.6	1.0	0.91	512	7	99	2
A173_40_seq2	0.0457	44	0.00137	11	1.46714	1.88635	11	0.282692	23	0.282679	6.7	0.8	0.76	468	7	94	2
A178_40_seq2	0.0178	39	0.00055	12	1.46714	1.88637	14	0.282665	33	0.282660	6.2	1.2	0.80	478	7	97	2

Quoted uncertainties (absolute) relate to the last quoted figure. The effect of the inter-element fractionation on Lu/Hf was estimated to be about 6 % or less based on analyses of the GJ-1 and Plesoviče zircon. Accuracy and reproducibility was checked by repeated analyses of reference zircon GJ-1 and Plesoviče (data given as mean with 2 standard deviation uncertainties).

(a) $^{176}Yb/^{177}Hf = (^{176}Yb/^{173}Yb)_{true} \times (^{173}Yb/^{177}Hf)_{meas} \times (M_{173(Yb)}/M_{177(Hf)})^{\beta(Hf)}$, $\beta(Hf) = \ln((^{179}Hf/^{177}Hf_{true})/(^{179}Hf/^{177}Hf_{measured})) / \ln(M_{179(Hf)}/M_{177(Hf)})$, M = mass of respective isotopes. The $^{176}Lu/^{177}Hf$ was calculated in a similar way using $^{175}Lu/^{177}Hf$ and β(Yb).

(b) Mean Hf signal in volts.

(c) Uncertainties are quadratic additions of the within-run precision and the daily reproducibility of the 40ppb-JMC475 solution. Uncertainties for the JMC475 quoted at 2SD (2 standard deviation).

(d) Initial $^{176}Hf/^{177}Hf$ and εHf calculated using the apparent U-Pb age determined by LA-ICP-MS dating (see column f), and the CHUR parameters: $^{176}Lu/^{177}Hf$ = 0.0336, and $^{176}Hf/^{177}Hf$ = 0.282785 (Bouvier et al. 2008).

(e) Two stage model age in Ga using measured $^{176}Lu/^{177}Lu$ of each spot (first stage = age of zircon), a value of 0.0113 for the average continental crust (second stage, values compiled from Rudnick and Gao (2003), and depleted mantle $^{176}Lu/^{177}Lu$ = 0.0379, and $^{176}Hf/^{177}Hf$ = 0.283164.

(f) Apparent U-Pb age determined by LA-ICP-MS.

(g) U-Pb age concordance (%).

(h) Sequence in which Lu-Hf analyses were performed. Standard analyses for each sequence are showed on Table 12.

Table lg10-Hf

Lu, Yb and Hf LA-MC-ICPMS data of zircon crystals from sample GCH-13

Grain	$^{176}Yb/^{177}Hf$ [a]	±2σ	$^{176}Lu/^{177}Hf$ [a]	±2σ	$^{178}Hf/^{177}Hf$	$^{180}Hf/^{177}Hf$	Sig_{Hf} [b] (V)	$^{176}Hf/^{177}Hf$	±2σ[c]	$^{176}Hf/^{177}Hf_{(t)}$ [d]	$\varepsilon Hf_{(t)}$ [d]	±2σ [c] (εHf)	T_{DM} [e] (Ga)	age[f] (Ma)	±2σ (Ma)	U-Pb [g] conc	Lu-Hf [h] seq
A8_seq3_40	0.0349	29	0.00113	7	1.46718	1.88670	15	0.282187	21	0.282176	-10.5	0.7	1.73	497	7	99	3
A8_seq3_40	0.0349	29	0.00113	7	1.46718	1.88670	15	0.282187	21	0.282176	-10.5	0.7	1.73	497	7	99	3
A9_seq3_26	0.0285	26	0.00093	7	1.46714	1.88617	6	0.282628	33	0.282619	5.8	1.2	0.86	521	8	99	3
A10_seq3_26	0.0539	56	0.00169	15	1.46714	1.88651	7	0.282632	32	0.282616	5.5	1.1	0.87	516	8	97	3
A12_seq3_40	0.0219	18	0.00069	4	1.46718	1.88663	15	0.282492	24	0.282485	0.6	0.8	1.13	503	7	99	3
A17_seq3_40	0.0173	14	0.00059	4	1.46715	1.88655	12	0.281570	21	0.281547	3.2	0.8	2.27	2076	31	99	3
A18_seq3_40	0.0746	71	0.00223	18	1.46713	1.88648	13	0.282556	24	0.282534	2.6	0.9	1.03	515	8	99	3
A19_seq3_26	0.0810	97	0.00251	25	1.46712	1.88630	7	0.282634	31	0.282610	5.0	1.1	0.88	502	7	97	3
A20_seq3_26	0.0407	38	0.00127	10	1.46713	1.88665	7	0.282596	32	0.282584	4.0	1.1	0.94	498	7	100	3
A21_seq3_40	0.0946	90	0.00304	24	1.46719	1.88676	12	0.282404	24	0.282374	-3.0	0.8	1.34	515	7	99	3
A22_seq3_40	0.0278	23	0.00085	5	1.46712	1.88628	11	0.281575	22	0.281542	3.1	0.8	2.28	2079	23	100	3
A23_seq3_40	0.0297	31	0.00087	8	1.46712	1.88643	14	0.282488	31	0.282481	-0.1	1.1	1.15	479	7	93	3
A26_seq3_40	0.0191	15	0.00057	3	1.46714	1.88666	12	0.281206	21	0.281184	-10.0	0.8	2.99	2062	28	102	3
A27_seq3_40	0.0661	68	0.00206	18	1.46714	1.88663	13	0.282627	21	0.282608	4.6	0.7	0.89	486	7	102	3
A29_seq3_40	0.0372	30	0.00120	7	1.46713	1.88654	14	0.282607	17	0.282596	4.5	0.6	0.91	501	7	100	3
A30_seq3_40	0.0557	50	0.00166	12	1.46720	1.88682	14	0.282411	21	0.282395	-2.5	0.7	1.30	507	7	99	3
A38_seq3_40	0.0319	26	0.00096	6	1.46719	1.88670	13	0.282509	22	0.282500	1.1	0.8	1.10	503	6	98	3
A43_seq3_40	0.0356	32	0.00118	8	1.46708	1.88672	10	0.282621	23	0.282610	5.4	0.8	0.88	518	8	91	3
A45_seq3_40	0.0295	38	0.00098	10	1.46719	1.88658	13	0.282435	21	0.282426	-1.7	0.7	1.25	493	7	96	3
A46_seq3_40	0.0389	34	0.00119	9	1.46716	1.88685	12	0.282505	20	0.282495	0.3	0.7	1.12	474	7	91	3
A47_seq3_40	0.0581	88	0.00173	24	1.46706	1.88619	12	0.282506	26	0.282489	1.0	0.9	1.11	514	7	99	3
A49_seq3_40	0.0283	24	0.00087	5	1.46714	1.88660	14	0.282520	22	0.282512	1.7	0.8	1.07	510	6	100	3
A50_seq3_40	0.0286	23	0.00092	6	1.46713	1.88658	12	0.282683	21	0.282674	8.0	0.8	0.74	536	8	100	3
A65_seq3_40	0.0098	8	0.00034	2	1.46718	1.88660	11	0.281536	21	0.281523	2.6	0.7	2.32	2087	27	99	3
A72_seq3_40	0.0254	37	0.00079	11	1.46718	1.88649	14	0.282466	25	0.282459	-1.0	0.9	1.19	473	6	96	3
A85_seq3_40	0.0299	28	0.00093	7	1.46718	1.88656	11	0.282491	23	0.282479	4.9	0.8	1.06	703	154	73	3
A90_seq3_40	0.0151	13	0.00050	3	1.46706	1.88641	12	0.281551	28	0.281524	21.4	1.0	1.92	2889	69	99	3
A91_seq3_40	0.0534	47	0.00165	12	1.46713	1.88654	15	0.282143	29	0.282128	-12.4	1.0	1.83	487	8	98	3
A95_seq3_40	0.0259	37	0.00080	11	1.46715	1.88676	13	0.282495	21	0.282488	0.0	0.8	1.13	473	8	97	3

Quoted uncertainties (absolute) relate to the last quoted figure. The effect of the inter-element fractionation on Lu/Hf was estimated to be about 6 % or less based on analyses of the GJ-1 and Plesoviče zircon. Accuracy and reproducibility was checked by repeated analyses of reference zircon GJ-1 and Plesoviče (data given as mean with 2 standard deviation uncertainties).

(a) $^{176}Yb/^{177}Hf = (^{176}Yb/^{173}Yb)_{true} \times (^{173}Yb/^{177}Hf)_{meas} \times (M_{173(Yb)}/M_{177(Hf)})^{\beta(Hf)}$, $\beta(Hf) = \ln((^{179}Hf/^{177}Hf_{true})/(^{179}Hf/^{177}Hf_{measured})) / \ln(M_{179(Hf)}/M_{177(Hf)})$, M = mass of respective isotopes. The $^{176}Lu/^{177}Hf$ was calculated in a similar way using $^{175}Lu/^{177}Hf$ and β(Yb).

(b) Mean Hf signal in volts.

(c) Uncertainties are quadratic additions of the within-run precision and the daily reproducibility of the 40ppb-JMC475 solution. Uncertainties for the JMC475 quoted at 2SD (2 standard deviation).

(d) Initial $^{176}Hf/^{177}Hf$ and εHf calculated using the apparent U-Pb age determined by LA-ICP-MS dating (see column f), and the CHUR parameters: $^{176}Lu/^{177}Hf$ = 0.0336, and $^{176}Hf/^{177}Hf$ = 0.282785 (Bouvier et al. 2008).

(e) Two stage model age in Ga using measured $^{176}Lu/^{177}Lu$ of each spot (first stage = age of zircon), a value of 0.0113 for the average continental crust (second stage, values compiled from Rudnick and Gao (2003), and depleted mantle $^{176}Lu/^{177}Lu$ = 0.0379, and $^{176}Hf/^{177}Hf$ = 0.283164.

(f) Apparent U-Pb age determined by LA-ICP-MS.

(g) U-Pb age concordance (%).

(h) Sequence in which Lu-Hf analyses were performed. Standard analyses for each sequence are showed on Table 12.

Table Ig11-Hf

Lu, Yb and Hf LA-MC-ICPMS data of zircon crystals from sample GCH-14

Grain	$^{176}Yb/^{177}Hf$ [a]	±2σ	$^{176}Lu/^{177}Hf$ [a]	±2σ	$^{178}Hf/^{177}Hf$	$^{180}Hf/^{177}Hf$	Sig_{Hf} [b] (V)	$^{176}Hf/^{177}Hf$	±2σ [c]	$^{176}Hf/^{177}Hf_{(t)}$ [d]	$\varepsilon Hf_{(t)}$ [d]	±2σ [c] (εHf)	T_{DM} [e] (Ga)	age [f] (Ma)	±2σ (Ma)	U-Pb [g] conc	Lu-Hf [h] seq
A125_40_seq1	0.0687	62	0.00210	15	1.46710	1.88679	10	0.282571	26	0.282551	3.0	0.9	1.00	505	8	99	1
A126_40_seq1	0.0383	36	0.00125	9	1.46718	1.88685	12	0.282449	18	0.282437	-1.1	0.6	1.22	501	9	96	1
A129_40_seq1	0.0332	29	0.00108	7	1.46709	1.88668	10	0.282450	24	0.282441	-2.1	0.9	1.23	454	8	99	1
A131_40_seq1	0.0342	29	0.00111	7	1.46723	1.88680	12	0.282445	22	0.282435	-1.9	0.8	1.24	470	9	94	1
A139_40_seq1	0.0518	44	0.00169	11	1.46720	1.88695	9	0.282511	28	0.282499	-1.3	1.0	1.14	397	8	100	1
A143_40_seq1	0.0686	63	0.00214	16	1.46715	1.88683	14	0.282473	25	0.282453	-0.7	0.9	1.19	497	7	99	1
A144_26_seq1	0.0445	38	0.00139	9	1.46718	1.88688	11	0.282483	24	0.282470	0.0	0.8	1.16	498	7	100	1
A145_40_seq1	0.0085	9	0.00036	3	1.46725	1.88692	10	0.281587	22	0.281572	3.9	0.8	2.23	2068	16	97	1
A151_40_seq1	0.0809	67	0.00255	16	1.46720	1.88681	14	0.282448	24	0.282424	-1.4	0.8	1.24	508	8	99	1
A153_40_seq1	0.0381	31	0.00124	8	1.46718	1.88687	11	0.282385	23	0.282373	-3.5	0.8	1.35	499	7	99	1
A156_40_seq1	0.0229	18	0.00079	5	1.46716	1.88669	10	0.281598	24	0.281569	0.0	0.8	2.31	1904	30	100	1
A163_40_seq1	0.0484	42	0.00156	11	1.46716	1.88662	13	0.282354	26	0.282340	-4.7	0.9	1.41	497	7	100	1
A168_40_seq1	0.0255	26	0.00084	7	1.46711	1.88643	12	0.281771	29	0.281746	-1.3	1.0	2.11	1574	40	69	1
A169_26_seq1	0.0223	30	0.00070	9	1.46700	1.88628	8	0.281839	40	0.281818	0.2	1.4	1.99	1526	34	95	1
A174_40_seq1	0.0440	37	0.00140	9	1.46721	1.88695	13	0.282501	16	0.282488	0.8	0.6	1.12	506	103	86	1
A179_40_seq1	0.0435	48	0.00129	13	1.46716	1.88667	13	0.282580	23	0.282567	3.8	0.8	0.96	515	8	101	1
A180_40_seq1	0.0233	32	0.00074	9	1.46719	1.88681	15	0.282511	23	0.282504	1.0	0.8	1.09	491	8	100	1
A183_40_seq1	0.0729	60	0.00230	14	1.46720	1.88673	14	0.282409	21	0.282388	-3.3	0.7	1.33	482	7	100	1
A184_40_seq1	0.0447	44	0.00138	11	1.46716	1.88680	12	0.282462	27	0.282448	0.2	0.9	1.18	544	14	96	1
A185_40_seq1	0.0188	35	0.00058	10	1.46721	1.88679	14	0.282510	22	0.282506	-2.0	0.8	1.15	353	5	94	1
A186_40_seq1	0.0941	79	0.00291	19	1.46716	1.88657	11	0.282694	21	0.282667	6.9	0.8	0.77	496	7	97	1
A191_40_seq1	0.0419	36	0.00135	9	1.46711	1.88668	12	0.282402	26	0.282389	-2.8	0.9	1.31	504	9	100	1
A199_26_seq1	0.0399	34	0.00128	8	1.46711	1.88650	6	0.282382	39	0.282369	-2.9	1.4	1.34	528	8	100	1
A201_40_seq1	0.0262	51	0.00080	15	1.46729	1.88695	12	0.282574	32	0.282567	2.1	1.1	0.99	440	7	99	1
A204_26_seq1	0.0078	13	0.00026	4	1.46713	1.88642	6	0.282541	29	0.282541	-8.6	1.0	1.22	0	0	0	1
A206_40_seq1	0.0282	27	0.00093	7	1.46720	1.88680	10	0.282400	24	0.282391	-2.9	0.8	1.31	494	10	98	1
A212_40_seq1	0.0619	57	0.00189	15	1.46714	1.88646	9	0.282625	25	0.282608	4.7	0.9	0.89	493	7	99	1
A214_40_seq1	0.0402	40	0.00121	10	1.46717	1.88661	11	0.282643	24	0.282631	5.8	0.8	0.84	502	8	100	1
A217_40_seq1	0.0202	16	0.00064	4	1.46714	1.88670	11	0.281598	22	0.281573	3.4	0.8	2.24	2044	27	90	1
A221_40_seq1	0.0534	47	0.00170	12	1.46714	1.88676	12	0.282460	26	0.282444	-1.5	0.9	1.22	473	8	95	1
A227_40_seq1	0.0825	71	0.00255	18	1.46712	1.88664	12	0.282430	20	0.282407	-3.0	0.7	1.29	463	7	99	1
A233_40_seq1	0.0544	44	0.00167	10	1.46719	1.88688	14	0.282439	23	0.282423	-2.1	0.8	1.26	482	9	100	1
A243_40_seq1	0.0322	46	0.00102	13	1.46722	1.88705	12	0.282604	32	0.282595	4.1	1.1	0.92	487	8	99	1

Quoted uncertainties (absolute) relate to the last quoted figure. The effect of the inter-element fractionation on Lu/Hf was estimated to be about 6 % or less based on analyses of the GJ-1 and Plesoviče zircon. Accuracy and reproducibility was checked by repeated analyses of reference zircon GJ-1 and Plesoviče (data given as mean with 2 standard deviation uncertainties).

(a) $^{176}Yb/^{177}Hf = (^{176}Yb/^{173}Yb)_{true} \times (^{173}Yb/^{177}Hf)_{meas} \times (M_{173(Yb)}/M_{177(Hf)})^{\beta(Hf)}$, $\beta(Hf) = \ln((^{179}Hf/^{177}Hf_{true})/(^{179}Hf/^{177}Hf_{measured})) / \ln(M_{179(Hf)}/M_{177(Hf)})$, M = mass of respective isotopes. The $^{176}Lu/^{177}Hf$ was calculated in a similar way using $^{175}Lu/^{177}Hf$ and β(Yb).

(b) Mean Hf signal in volts.

(c) Uncertainties are quadratic additions of the within-run precision and the daily reproducibility of the 40ppb-JMC475 solution. Uncertainties for the JMC475 quoted at 2SD (2 standard deviation).

(d) Initial $^{176}Hf/^{177}Hf$ and εHf calculated using the apparent U-Pb age determined by LA-ICP-MS dating (see column f), and the CHUR parameters: $^{176}Lu/^{177}Hf$ = 0.0336, and $^{176}Hf/^{177}Hf$ = 0.282785 (Bouvier et al. 2008).

(e) Two stage model age in Ga using measured $^{176}Lu/^{177}Lu$ of each spot (first stage = age of zircon), a value of 0.0113 for the average continental crust (second stage, values compiled from Rudnick and Gao (2003), and depleted mantle $^{176}Lu/^{177}Lu$ = 0.0379, and $^{176}Hf/^{177}Hf$ = 0.283164.

(f) Apparent U-Pb age determined by LA-ICP-MS.

(g) U-Pb age concordance (%).

(h) Sequence in which Lu-Hf analyses were performed. Standard analyses for each sequence are showed on Table 12.

Table lg12-Hf

Lu, Yb and Hf LA-MC-ICPMS data of zircon crystals from sample GCH-18

Grain	$^{176}Yb/^{177}Hf$ [a]	±2σ	$^{176}Lu/^{177}Hf$ [a]	±2σ	$^{178}Hf/^{177}Hf$	$^{180}Hf/^{177}Hf$	Sig_{Hf} [b] (V)	$^{176}Hf/^{177}Hf$	±2σ [c]	$^{176}Hf/^{177}Hf_{(t)}$ [d]	$\varepsilon Hf_{(t)}$ [d]	±2σ [c] (εHf)	T_{DM} [e] (Ga)	age [f] (Ma)	±2σ (Ma)	U-Pb [g] conc	Lu-Hf [h] seq
A454_40_seq2	0.0368	34	0.00124	10	1.46712	1.88663	20	0.282332	18	0.282321	-5.3	0.6	1.45	499	7	99	1
A457_40_seq2	0.0404	33	0.00130	8	1.46716	1.88664	20	0.282333	17	0.282321	-5.0	0.6	1.44	513	7	100	1
A461_40_seq2	0.0414	34	0.00128	8	1.46718	1.88660	17	0.282317	22	0.282305	-5.7	0.8	1.48	503	7	101	1
A465_40_seq2	0.0358	30	0.00113	7	1.46713	1.88672	19	0.282328	21	0.282318	-5.4	0.7	1.45	500	7	99	1
A467_40_seq2	0.0364	30	0.00112	7	1.46714	1.88668	18	0.282318	16	0.282307	-5.6	0.6	1.47	508	7	98	1
A468_40_seq2	0.0381	31	0.00118	7	1.46718	1.88670	17	0.282345	16	0.282333	-4.5	0.6	1.42	513	7	98	1
A471_40_seq2	0.0473	48	0.00151	15	1.46715	1.88673	20	0.282322	20	0.282308	-5.7	0.7	1.47	501	8	99	1
A479_40_seq2	0.0509	64	0.00168	18	1.46712	1.88663	19	0.282332	21	0.282316	-5.5	0.7	1.46	495	7	100	1
A488_40_seq2	0.0340	31	0.00110	8	1.46718	1.88689	18	0.282357	17	0.282346	-4.5	0.6	1.40	495	6	98	1
A489_40_seq2	0.0458	39	0.00146	10	1.46716	1.88676	20	0.282338	20	0.282324	-5.0	0.7	1.44	508	7	101	1
A493_40_seq2	0.0524	90	0.00150	23	1.46718	1.88661	19	0.282326	21	0.282312	-5.8	0.7	1.47	492	7	100	1
A503_40_seq2	0.0676	80	0.00221	25	1.46710	1.88626	18	0.282299	22	0.282278	-6.5	0.8	1.53	515	7	100	1
A512_26_seq2	0.0356	31	0.00119	9	1.46706	1.88617	11	0.282279	29	0.282267	-6.9	1.0	1.55	511	7	98	1
A517_40_seq2	0.0144	12	0.00048	3	1.46720	1.88688	12	0.281003	22	0.280982	-10.2	0.8	3.25	2365	30	83	1
A518_40_seq2	0.0164	14	0.00046	3	1.46710	1.88650	12	0.281996	47	0.281986	-2.4	1.7	1.83	1151	62	101	1

Quoted uncertainties (absolute) relate to the last quoted figure. The effect of the inter-element fractionation on Lu/Hf was estimated to be about 6 % or less based on analyses of the GJ-1 and Plesoviče zircon. Accuracy and reproducibility was checked by repeated analyses of reference zircon GJ-1 and Plesoviče (data given as mean with 2 standard deviation uncertainties).

(a) $^{176}Yb/^{177}Hf = (^{176}Yb/^{173}Yb)_{true} \times (^{173}Yb/^{177}Hf)_{meas} \times (M_{173(Yb)}/M_{177(Hf)})^{\beta(Hf)}$, $\beta(Hf) = \ln((^{179}Hf/^{177}Hf_{true})/(^{179}Hf/^{177}Hf_{measured})) / \ln(M_{179(Hf)}/M_{177(Hf)})$, M = mass of respective isotopes. The $^{176}Lu/^{177}Hf$ was calculated in a similar way using $^{175}Lu/^{177}Hf$ and β(Yb).

(b) Mean Hf signal in volts.

(c) Uncertainties are quadratic additions of the within-run precision and the daily reproducibility of the 40ppb-JMC475 solution. Uncertainties for the JMC475 quoted at 2SD (2 standard deviation).

(d) Initial $^{176}Hf/^{177}Hf$ and εHf calculated using the apparent U-Pb age determined by LA-ICP-MS dating (see column f), and the CHUR parameters: $^{176}Lu/^{177}Hf$ = 0.0336, and $^{176}Hf/^{177}Hf$ = 0.282785 (Bouvier et al. 2008).

(e) Two stage model age in Ga using measured $^{176}Lu/^{177}Lu$ of each spot (first stage = age of zircon), a value of 0.0113 for the average continental crust (second stage, values compiled from Rudnick and Gao (2003), and depleted mantle $^{176}Lu/^{177}Lu$ = 0.0379, and $^{176}Hf/^{177}Hf$ = 0.283164.

(f) Apparent U-Pb age determined by LA-ICP-MS.

(g) U-Pb age concordance (%).

(h) Sequence in which Lu-Hf analyses were performed. Standard analyses for each sequence are showed on Table 12.

Table lg13-Hf

Lu, Yb and Hf LA-MC-ICPMS data of zircon crystals from sample GCH-31

Grain	$^{176}Yb/^{177}Hf$ [a]	±2σ	$^{176}Lu/^{177}Hf$ [a]	±2σ	$^{178}Hf/^{177}Hf$	$^{180}Hf/^{177}Hf$	Sig_{Hf} [b] (V)	$^{176}Hf/^{177}Hf$	±2σ [c]	$^{176}Hf/^{177}Hf_{(t)}$ [d]	$\varepsilon Hf_{(t)}$ [d]	±2σ [c] (εHf)	T_{DM} [e] (Ga)	age [f] (Ma)	±2σ (Ma)	U-Pb [g] conc	Lu-Hf [h] seq
GCH-31_220	0.0409	42	0.00139	12	1.46713	1.88641	5	0.282421	32	0.282408	-2.4	1.1	1.28	493	7	92	6
GCH-31_219	0.0382	32	0.00127	8	1.46717	1.88678	5	0.282466	40	0.282455	-1.0	1.4	1.20	480	7	91	6
GCH-31_218	0.0458	45	0.00159	13	1.46715	1.88650	4	0.282494	34	0.282480	-0.1	1.2	1.15	479	7	90	6
GCH-31_217	0.0362	31	0.00124	8	1.46712	1.88667	6	0.282458	27	0.282446	-1.4	1.0	1.21	474	6	100	6
GCH-31_216	0.0518	42	0.00173	11	1.46712	1.88674	5	0.282512	44	0.282497	0.4	1.6	1.12	475	7	71	6
GCH-31_215	0.0826	66	0.00279	17	1.46717	1.88662	7	0.282399	29	0.282373	-3.5	1.0	1.35	499	7	98	6
GCH-31_214	0.0480	40	0.00165	10	1.46702	1.88662	6	0.282388	31	0.282373	-3.4	1.1	1.35	502	8	68	6
GCH-31_213	0.0996	93	0.00335	26	1.46706	1.88655	5	0.282375	36	0.282345	-5.0	1.3	1.41	476	7	80	6
GCH-31_212	0.0306	26	0.00108	7	1.46705	1.88651	5	0.282387	29	0.282377	-3.6	1.0	1.34	486	7	92	6
GCH-31_211	0.0554	51	0.00189	14	1.46711	1.88677	6	0.282439	29	0.282421	-2.0	1.0	1.26	486	7	91	6
GCH-31_210	0.0090	7	0.00030	2	1.46709	1.88633	4	0.282433	47	0.282430	0.3	1.7	1.20	577	8	86	6
GCH-31_209	0.0148	12	0.00052	3	1.46712	1.88642	5	0.282440	32	0.282434	1.8	1.1	1.17	635	9	93	6
GCH-31_208	0.0490	42	0.00164	11	1.46714	1.88666	6	0.282391	30	0.282375	-3.4	1.0	1.34	496	7	91	6
GCH-31_207	0.0679	54	0.00230	14	1.46713	1.88664	6	0.282474	25	0.282451	0.1	0.9	1.18	534	8	83	6
GCH-31_206	0.0187	17	0.00069	5	1.46713	1.88636	5	0.281682	32	0.281676	-28.4	1.1	2.69	487	7	90	6
GCH-31_205	0.0695	56	0.00236	14	1.46712	1.88671	6	0.282423	33	0.282400	-2.2	1.2	1.29	510	7	95	6
GCH-31_204	0.0503	45	0.00172	12	1.46712	1.88660	6	0.282356	31	0.282340	-4.7	1.1	1.41	497	7	90	6
GCH-31_203	0.0638	55	0.00215	14	1.46712	1.88646	5	0.282416	39	0.282396	-2.8	1.4	1.30	493	9	79	6
GCH-31_202	0.0422	36	0.00143	10	1.46703	1.88648	5	0.282418	34	0.282405	-2.5	1.2	1.29	492	7	86	6
GCH-31_201	0.0539	44	0.00182	11	1.46717	1.88669	7	0.282439	24	0.282421	-1.3	0.8	1.25	519	8	95	6
GCH-31_200	0.0164	13	0.00068	4	1.46706	1.88642	4	0.281665	34	0.281638	7.9	1.2	2.06	2140	37	91	6
GCH-31_199	0.0830	67	0.00276	17	1.46715	1.88678	8	0.282391	27	0.282366	-3.9	1.0	1.37	488	8	96	6
GCH-31_198	0.0506	66	0.00171	20	1.46707	1.88676	5	0.282382	27	0.282366	-3.7	0.9	1.36	500	8	108	6
GCH-31_197	0.0316	30	0.00108	8	1.46714	1.88680	5	0.282408	29	0.282398	-2.3	1.0	1.30	510	7	93	6
GCH-31_196	0.0414	42	0.00141	12	1.46711	1.88659	5	0.282429	44	0.282416	-1.6	1.5	1.26	516	8	95	6

Quoted uncertainties (absolute) relate to the last quoted figure. The effect of the inter-element fractionation on Lu/Hf was estimated to be about 6 % or less based on analyses of the GJ-1 and Plesoviče zircon. Accuracy and reproducibility was checked by repeated analyses of reference zircon GJ-1 and Plesoviče (data given as mean with 2 standard deviation uncertainties).

(a) $^{176}Yb/^{177}Hf = (^{176}Yb/^{173}Yb)_{true} \times (^{173}Yb/^{177}Hf)_{meas} \times (M_{173(Yb)}/M_{177(Hf)})^{\beta(Hf)}$, $\beta(Hf) = \ln((^{179}Hf/^{177}Hf_{true})/(^{179}Hf/^{177}Hf_{measured})) / \ln(M_{179(Hf)}/M_{177(Hf)})$, M = mass of respective isotopes. The $^{176}Lu/^{177}Hf$ was calculated in a similar way using $^{175}Lu/^{177}Hf$ and β(Yb).

(b) Mean Hf signal in volts.

(c) Uncertainties are quadratic additions of the within-run precision and the daily reproducibility of the 40ppb-JMC475 solution. Uncertainties for the JMC475 quoted at 2SD (2 standard deviation).

(d) Initial $^{176}Hf/^{177}Hf$ and εHf calculated using the apparent U-Pb age determined by LA-ICP-MS dating (see column f), and the CHUR parameters: $^{176}Lu/^{177}Hf$ = 0.0336, and $^{176}Hf/^{177}Hf$ = 0.282785 (Bouvier et al. 2008).

(e) Two stage model age in Ga using measured $^{176}Lu/^{177}Lu$ of each spot (first stage = age of zircon), a value of 0.0113 for the average continental crust (second stage, values compiled from Rudnick and Gao (2003), and depleted mantle $^{176}Lu/^{177}Lu$ = 0.0379, and $^{176}Hf/^{177}Hf$ = 0.283164.

(f) Apparent U-Pb age determined by LA-ICP-MS.

(g) U-Pb age concordance (%).

(h) Sequence in which Lu-Hf analyses were performed. Standard analyses for each sequence are showed on Table 12.

Table lg-standards

Lu, Yb and Hf LA-MC-ICPMS data of standards

Grain	$^{176}Yb/^{177}Hf$ [a]	±2σ	$^{176}Lu/^{177}Hf$ [a]	±2σ	$^{178}Hf/^{177}Hf$	$^{180}Hf/^{177}Hf$	Sig_{Hf} [b] (V)	$^{176}Hf/^{177}Hf$	±2σ [c]	$^{176}Hf/^{177}Hf_{(t)}$ [d]	$\varepsilon Hf_{(t)}$ [d]	±2σ [c] (εHf)	T_{DM} [e] (Ga)	age [f] (Ma)
Sequence 1														
GJ1-40-1	0.0072	6	0.00025	1	1.46721	1.88688	10	0.282009	25	0.282006	-14.0	0.9	2.01	606
GJ1-40-2	0.0072	6	0.00025	1	1.46721	1.88693	11	0.282019	25	0.282016	-13.7	0.9	2.00	606
GJ1-40-3	0.0077	6	0.00024	1	1.46716	1.88669	11	0.281993	24	0.281990	-14.6	0.9	2.05	606
GJ1-40-4	0.0082	7	0.00025	1	1.46712	1.88657	12	0.281987	24	0.281984	-14.8	0.9	2.06	606
GJ1-40-5	0.0069	6	0.00023	1	1.46715	1.88661	9	0.282025	21	0.282022	-13.5	0.8	1.98	606
GJ1-40-6	0.0069	6	0.00024	1	1.46717	1.88678	10	0.282027	27	0.282025	-13.4	0.9	1.98	606
GJ1-40-7	0.0072	6	0.00025	1	1.46714	1.88673	8	0.282026	27	0.282024	-13.4	1.0	1.98	606
GJ1-40-8	0.0073	6	0.00025	1	1.46708	1.88645	9	0.282011	31	0.282008	-14.0	1.1	2.01	606
GJ1-40-9	0.0076	6	0.00025	1	1.46719	1.88679	9	0.282016	27	0.282013	-13.8	1.0	2.00	606
GJ1-40-10	0.0078	6	0.00025	1	1.46722	1.88672	9	0.282029	24	0.282026	-13.3	0.9	1.98	606
Sequence 2														
GJ1_40_90_1	0.0070	6	0.00024	1	1.46721	1.88677	8	0.281996	24	0.281993	-14.5	0.8	2.04	606
GJ1_40_90_2	0.0075	6	0.00025	2	1.46701	1.88634	5	0.281981	45	0.281978	-15.0	1.6	2.07	606
GJ1_40_90_3	0.0074	6	0.00025	1	1.46707	1.88663	8	0.282015	26	0.282013	-13.8	0.9	2.00	606
GJ1_40_90_4	0.0072	6	0.00025	2	1.46717	1.88679	8	0.282032	29	0.282029	-13.2	1.0	1.97	606
GJ1_40_90_5	0.0078	6	0.00025	1	1.46720	1.88687	9	0.282002	30	0.281999	-14.3	1.1	2.03	606
GJ1_40_90_6	0.0068	5	0.00023	1	1.46709	1.88668	8	0.282026	26	0.282024	-13.4	0.9	1.98	606
GJ1_40_90_7	0.0069	6	0.00023	1	1.46720	1.88676	9	0.282026	24	0.282023	-13.4	0.8	1.98	606
GJ1_40_90_8	0.0076	6	0.00025	1	1.46723	1.88678	9	0.282011	29	0.282008	-14.0	1.0	2.01	606
GJ1_40_90_9	0.0073	6	0.00023	1	1.46716	1.88667	9	0.282022	25	0.282019	-13.6	0.9	1.99	606
GJ1_40_90_10	0.0073	6	0.00024	1	1.46715	1.88667	9	0.282018	26	0.282016	-13.7	0.9	2.00	606
GJ1_40_90_11	0.0071	6	0.00023	1	1.46716	1.88667	9	0.282015	25	0.282012	-13.8	0.9	2.00	606
Sequence 3														
GJ1_6_100_100_line	0.0071	6	0.00025	2	1.46722	1.88687	14	0.282013	19	0.282010	-13.9	0.7	2.01	606
GJ1_6_100_100_line_2	0.0074	6	0.00025	1	1.46719	1.88687	16	0.281986	17	0.281983	-14.9	0.6	2.06	606
GJ1_40-5-90_1	0.0076	6	0.00026	2	1.46713	1.88657	10	0.281987	26	0.281984	-14.8	0.9	2.06	606
GJ1_40-5-90_2	0.0074	6	0.00026	2	1.46721	1.88668	10	0.282002	21	0.281999	-14.3	0.8	2.03	606
GJ1_40-5-90_3	0.0073	6	0.00025	2	1.46711	1.88662	7	0.282022	38	0.282020	-13.6	1.4	1.99	606
GJ1_40-5-90_4	0.0072	6	0.00025	2	1.46718	1.88674	8	0.282017	31	0.282014	-13.8	1.1	2.00	606
GJ1_40-5-90_5	0.0078	6	0.00025	2	1.46717	1.88661	10	0.282012	23	0.282009	-13.9	0.8	2.01	606
GJ1_40-5-90_6	0.0075	6	0.00025	2	1.46721	1.88663	9	0.282028	26	0.282025	-13.4	0.9	1.98	606
GJ1_40-5-90_7	0.0079	6	0.00025	2	1.46722	1.88673	10	0.282029	25	0.282026	-13.3	0.9	1.98	606
GJ1_40-5-90_8	0.0079	6	0.00025	1	1.46713	1.88669	10	0.281998	23	0.281995	-14.4	0.8	2.04	606
GJ1_40-5-90_9	0.0074	6	0.00025	2	1.46717	1.88678	8	0.282018	29	0.282016	-13.7	1.0	2.00	606
GJ1_40-5-90_10	0.0079	6	0.00025	1	1.46722	1.88674	9	0.282001	36	0.281998	-14.3	1.3	2.03	606
GJ1_40-5-90_11	0.0078	6	0.00025	1	1.46718	1.88662	9	0.282038	31	0.282035	-13.0	1.1	1.96	606
GJ1_40-5-90_12	0.0080	7	0.00024	1	1.46717	1.88656	11	0.282003	34	0.282001	-14.2	1.2	2.02	606
GJ1_40-5-90_13	0.0079	6	0.00024	1	1.46722	1.88686	10	0.282020	27	0.282017	-13.6	1.0	1.99	606
Sequence 6														
GJ1-50-100-6_line 1	0.0074	6	0.00026	2	1.46717	1.88691	14	0.281988	21	0.281985	-14.8	0.7	2.05	606
GJ1-50-100-6_12	0.0070	6	0.00025	2	1.46718	1.88680	9	0.281996	25	0.281994	-14.5	0.9	2.04	606
GJ1-50-100-6_11	0.0070	6	0.00025	2	1.46718	1.88669	9	0.282033	21	0.282030	-13.2	0.8	1.97	606
GJ1-50-100-6_10	0.0070	6	0.00025	2	1.46717	1.88673	9	0.281988	22	0.281985	-14.8	0.8	2.06	606
GJ1-50-100-6_9	0.0069	6	0.00025	2	1.46712	1.88682	9	0.282012	22	0.282010	-13.9	0.8	2.01	606
GJ1-50-100-6_8	0.0068	5	0.00025	2	1.46717	1.88670	9	0.282019	25	0.282016	-13.7	0.9	2.00	606
GJ1-50-100-6_7	0.0068	5	0.00025	2	1.46722	1.88677	9	0.282029	23	0.282026	-13.3	0.8	1.98	606
GJ1-50-100-6_6	0.0070	6	0.00025	2	1.46712	1.88677	9	0.282004	26	0.282001	-14.2	0.9	2.02	606
GJ1-50-100-6_5	0.0068	5	0.00026	2	1.46708	1.88639	4	0.282052	40	0.282049	-12.5	1.4	1.93	606
GJ1-50-100-6_4	0.0074	6	0.00026	2	1.46713	1.88681	11	0.282011	20	0.282008	-14.0	0.7	2.01	606
GJ1-50-100-6_3	0.0073	6	0.00026	2	1.46716	1.88666	11	0.282006	24	0.282003	-14.1	0.8	2.02	606
GJ1-50-100-6_2	0.0074	6	0.00026	2	1.46720	1.88688	11	0.282008	21	0.282005	-14.1	0.7	2.02	606

Grain	$^{176}Yb/^{177}Hf$ [a]	±2σ	$^{176}Lu/^{177}Hf$ [a]	±2σ	$^{178}Hf/^{177}Hf$	$^{180}Hf/^{177}Hf$	Sig_{Hf} [b] (V)	$^{176}Hf/^{177}Hf$	±2σ [c]	$^{176}Hf/^{177}Hf_{(t)}$ [d]	$\varepsilon Hf_{(t)}$	±2σ [c] (εHf)	T_{DM} [e] (Ga)	age [f] (Ma)
Sequence 1														
Plesovice 26_2	0.0050	4	0.00012	1	1.46710	1.88640	7	0.282457	24	0.282456	-4.1	0.9	1.25	338
Plesovice 32_1	0.0042	3	0.00010	1	1.46721	1.88669	13	0.282461	23	0.282460	-4.0	0.8	1.24	338
Plesovice 40_6	0.0061	5	0.00014	1	1.46720	1.88676	16	0.282469	26	0.282468	-3.7	0.9	1.23	338
Plesovice 40_7	0.0062	5	0.00014	1	1.46715	1.88667	16	0.282462	18	0.282461	-3.9	0.6	1.24	338
Plesovice 40_8	0.0062	5	0.00013	1	1.46716	1.88672	15	0.282444	20	0.282443	-4.6	0.7	1.28	338
Plesovice 40_9	0.0061	5	0.00013	1	1.46714	1.88675	14	0.282449	23	0.282448	-4.4	0.8	1.27	338
Plesovice 40_10	0.0077	6	0.00017	1	1.46712	1.88652	13	0.282454	22	0.282453	-4.2	0.8	1.26	338
Plesovice 48_4	0.0064	5	0.00015	1	1.46718	1.88682	26	0.282465	15	0.282464	-3.8	0.5	1.24	338
Plesovice 48_5	0.0065	5	0.00015	1	1.46717	1.88682	26	0.282455	17	0.282454	-4.2	0.6	1.26	338
Sequence 2														
Plesovice_40_90_1	0.0073	6	0.00017	1	1.46716	1.88668	13	0.282478	20	0.282477	-3.4	0.7	1.21	338
Plesovice_40_90_2	0.0076	6	0.00017	1	1.46720	1.88659	12	0.282456	22	0.282455	-4.2	0.8	1.25	338
Plesovice_40_90_3	0.0035	3	0.00008	0	1.46718	1.88672	12	0.282464	23	0.282463	-3.9	0.8	1.24	338
Plesovice_40_90_4	0.0059	5	0.00014	1	1.46718	1.88675	13	0.282460	17	0.282459	-4.0	0.6	1.25	338
Plesovice_40_90_5	0.0053	4	0.00013	1	1.46721	1.88667	12	0.282450	21	0.282449	-4.4	0.8	1.26	338
Sequence 3														
Plesovice_40-5-90_1	0.0037	3	0.00008	1	1.46718	1.88673	15	0.282470	23	0.282469	-3.6	0.8	1.23	338
Plesovice_40-5-90_2	0.0046	4	0.00011	1	1.46717	1.88670	11	0.282452	31	0.282452	-4.3	1.1	1.26	338
Plesovice_40-5-90_3	0.0060	5	0.00015	1	1.46725	1.88682	14	0.282463	28	0.282462	-3.9	1.0	1.24	338
Plesovice_40-5-90_4	0.0035	3	0.00008	0	1.46713	1.88687	14	0.282466	24	0.282465	-3.8	0.9	1.23	338
Plesovice_40-5-90_5	0.0025	2	0.00006	0	1.46723	1.88694	14	0.282480	25	0.282480	-3.3	0.9	1.20	338
Plesovice_40-5-90_6	0.0057	5	0.00013	1	1.46727	1.88698	13	0.282515	29	0.282514	-2.1	1.0	1.14	338
Plesovice_40-5-90_7	0.0038	3	0.00009	1	1.46717	1.88670	13	0.282442	22	0.282441	-4.6	0.8	1.28	338
Sequence 6														
Plesov-50-100-6_10	0.0058	5	0.00014	1	1.46719	1.88673	14	0.282455	22	0.282454	-4.2	0.8	1.25	338
Plesov-50-100-6_9	0.0063	5	0.00015	1	1.46718	1.88688	13	0.282436	16	0.282435	-4.9	0.6	1.29	338
Plesov-50-100-6_8	0.0059	5	0.00014	1	1.46710	1.88670	14	0.282468	17	0.282467	-3.7	0.6	1.23	338
Plesov-50-100-6_7	0.0063	5	0.00015	1	1.46711	1.88678	14	0.282442	18	0.282441	-4.7	0.6	1.28	338
Plesov-50-100-6_6	0.0064	5	0.00016	1	1.46716	1.88663	14	0.282463	19	0.282462	-3.9	0.7	1.24	338
Plesov-50-100-6_5	0.0061	5	0.00015	1	1.46716	1.88678	14	0.282463	18	0.282462	-3.9	0.6	1.24	338
Plesov-50-100-6_4	0.0062	5	0.00016	1	1.46711	1.88671	14	0.282445	16	0.282444	-4.6	0.6	1.28	338
Plesov-50-100-6_3	0.0062	5	0.00015	1	1.46716	1.88669	14	0.282467	17	0.282466	-3.8	0.6	1.23	338
Plesov-50-100-6_1	0.0064	5	0.00016	1	1.46715	1.88678	14	0.282452	21	0.282451	-4.3	0.8	1.26	338

Quoted uncertainties (absolute) relate to the last quoted figure. The effect of the inter-element fractionation on Lu/Hf was estimated to be about 6 % or less based on analyses of the GJ-1 and Plesoviče zircon. Accuracy and reproducibility was checked by repeated analyses of reference zircon GJ-1 and Plesoviče (data given as mean with 2 standard deviation uncertainties).

(a) $^{176}Yb/^{177}Hf = (^{176}Yb/^{173}Yb)_{true} \times (^{173}Yb/^{177}Hf)_{meas} \times (M_{173(Yb)}/M_{177(Hf)})^{\beta(Hf)}$, $\beta(Hf) = \ln((^{179}Hf/^{177}Hf_{true})/(^{179}Hf/^{177}Hf_{measured})) / \ln(M_{179(Hf)}/M_{177(Hf)})$, M = mass of respective isotopes. The $^{176}Lu/^{177}Hf$ was calculated in a similar way using $^{175}Lu/^{177}Hf$ and β(Yb).

(b) Mean Hf signal in volts.

(c) Uncertainties are quadratic additions of the within-run precision and the daily reproducibility of the 40ppb-JMC475 solution. Uncertainties for the JMC475 quoted at 2SD (2 standard deviation).

(d) Initial $^{176}Hf/^{177}Hf$ and εHf calculated using the apparent U-Pb age determined by LA-ICP-MS dating (see column f), and the CHUR parameters: $^{176}Lu/^{177}Hf = 0.0336$, and $^{176}Hf/^{177}Hf = 0.282785$ (Bouvier et al. 2008).

(e) Two stage model age in Ga using measured $^{176}Lu/^{177}Lu$ of each spot (first stage = age of zircon), a value of 0.0113 for the average continental crust (second stage, values compiled from Rudnick and Gao (2003), and depleted mantle $^{176}Lu/^{177}Lu = 0.0379$, and $^{176}Hf/^{177}Hf = 0.283164$.

(f) Apparent U-Pb age determined by LA-ICP-MS.